OHBM 2024
JUNE 23~27, SEOUL, KOREA

ABSTRACTS

Sunday, June 23 – Thursday, June 27
COEX CONVENTION & EXHIBITION CENTER | SEOUL

30TH ANNUAL MEETING OF THE
ORGANIZATION FOR HUMAN BRAIN MAPPING

Poster No 2334

Alzheimer's disease detection combining novel radiogenomics of ApoE, structural and function MRI

Nur Hafizah Mohad Azmi[1], Subapriya Suppiah[2], Nur Shahidatul Nabila Ibrahim[3], Buhari Ibrahim[4], Vengkatha Priya Seriramulu[4], Mazlyfarina Mohamad[5], Thilakavathy Karuppiah[6], Nur Farhayu Omar[6], Normala Ibrahim[6], Rizah Mazzuin Razali[7], Nor Harzana Harrun[8], Hakimah Mohamad Sallehuddin[4], Nisha Syed Nasser[9], Umar Ahmad[10]

[1]Universiti Putra Malaysia, Kajang, Selangor, [2]Universiti Putra Malaysia, Serdang, Selangor, [3]KPJ Healthcare University, Nilai, Negeri Sembilan, [4]Universiti Putra Malaysia, Serdang, Selangor, [5]Universiti Kebangsaan Malaysia, Kuala Lumpur, Wilayah persekutuan, [6]Universiti Putra Malaysia, Kuala Lumpur, Selangor, [7]Hospital Kuala Lumpur, Kuala Lumpur, Kuala Lumpur, [8]Klinik Kesihatan Pandamara, Klang, Selangor, [9]Nanyang Technological University, [50] Nanyang Avenue, [63]9798, Singapore, Singapore, Singapore, [10]Molecular Genetics Informatics, Department of Anatomy, Faculty of Basic Medical Science, Bauchi St, Gadau Bauchi, PMB 65

Introduction: The most common type of dementia in neurodegenerative diseases is Alzheimer's disease (AD), is a progressive neurological illness that causes memory loss. Neurophysiological tests including the Montreal cognitive assessment (MoCA), mini-mental state examination (MMSE), and clinical dementia rating (CDR) Scores are used to identify AD. Neuroimaging studies T1-weighted MRI scans assessed brain structural abnormalities. AD patients had grey matter volume (GMV) loss in brain structures when structural MRI data were analyzed using voxel-based morphometry (VBM). Neuroimaging studies resting state functional MRI (rs-fMRI) -blood oxygen level dependent (BOLD) sequence for brain imaging was process using the seed-based analysis (SBA) method to analyse functional connectivity (FC) in Default mode network (DMN), Sensorimotor network (SEN), Executive control network (ECN), Language network (LN), Visuospatial network (VN) and Salience network (SAN). Late onset AD can be studied utilising the apolipoprotein E gene (ApoE). ApoE has four alleles: ApoE 1, 2, 3, and 4, with LOAD patients having either a homozygous or heterozygous genotype of these alleles. The genotypes, particularly ApoE ε4, are associated with a more significant risk for AD pathogenesis. The combination of genotyping and MRI neuroimaging is a promising avenue for research that starts with protocol optimisation. Objective: to differentiate changes in structural brain volumetric and rs-fMRI functional connectivity strength with the diagnosis of AD and HC by combining APOE Ɛ4 genetic variations.

Methods: Thirty participants with AD, n = 15, and healthy control (HC), n = 15, for MRI study and six participants (n=6) with AD, n = 3, and HC, n = 3 for APOE genotyping. In this study we categorised the participants using neuropsychological tests i.e., MoCA, MMSE and CDR. Structural and functional MRI brain imaging was performed to identify network areas affected by AD. Structural voxel-based morphometry (VBM) models, and CONN Toolbox, which analysed functional MRI using seed-based analysis (SBA) were performed. Genotyping was done by extracting the DNA from the participants' blood samples. The isolated DNA underwent PCR-RFLP. Then, the restricted enzyme RE AFIII for rs429358 and the HAEII for rs7412 were performed.

Results: There was decreased grey matter volume (GMV) and reduced functional connectivity among AD participants involving the frontal lobe and anterior cingulate gyrus in DMN, SEN, ECN, LN, VN and SAN. We detected three participants with homozygous ApoE ε4 negative genotype (non-carriers), which was consistent with HC genotype. We also detected heterozygous genotype ApoE ε4 positive carriers, which indicated LOAD.

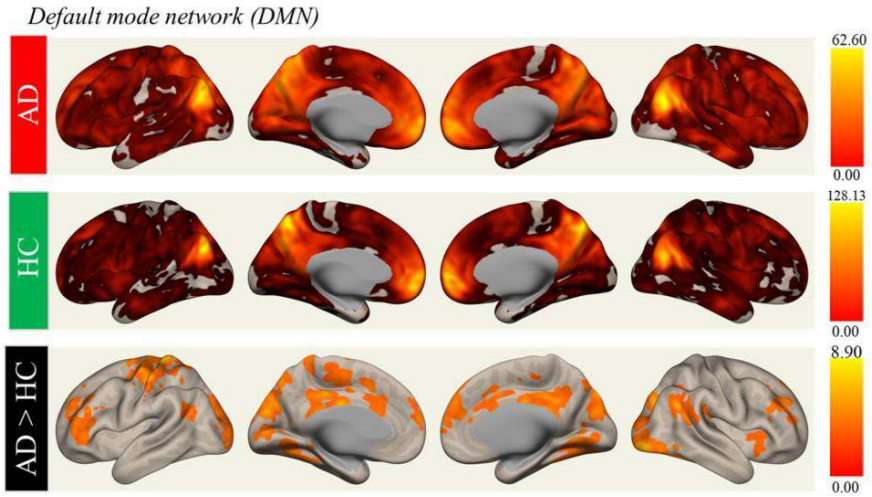

Table 1: Comparison of sociodemographic and neuropsychological profile of AD with HC.

Variable n=30		AD n=15 Freq. (%)	HC n=15 Freq. (%)	X^2 statistic[a] (df) P Value[a]
Demographic Data	**Gender**			0.001 (1) 1.0
	Male	5 (33.3%)	5 (33.3%)	
	Female	10 (66.7%)	10 (66.7%)	
	Education Level			1.15 (1) 0.28
	<6 years	3 (20.00%)	1 (6.67%)	
	>6 years	12 (80.00%)	14 (93.33%)	
	Marital Status			0.37 (1) 0.54
	Single	1 (6.67%)	2 (13.33%)	
	Married	14 (93.33%)	13 (26.67%)	
		Min-max (mean ± SD)	**Min-max (mean ± SD)**	t statistic[b] (df) P Value[b]
	n=30	**n=15**	**n=15**	
	Age Neuroimaging	59-83 (70.6 ±8.55)	60-82 (69.27 ±6.81)	-0.47 (28) 0.64
	n=6	**n=3**	**n=3**	
	Age Genotyping	61-83 (75.67 ±12.7)	60-79 (68±9.85)	-0.83 (3.77) 0.46
Neuropsychological test scores.	**MoCA**	0-22 (14.13± 6.82)	23-30 (28.13± 2.20)	7.56 (16.88) 0.001
	MMSE	0-29 (14.40±8.33)	24-30 (28.00±2.17)	-13.26 (14.00) 0.001
	CDR	1-3 (2.13±0.92)	0 (0.001±0.001)	6.12 (15.89) 0.001

Note: AD: Alzheimer's disease group, HC: healthy control group, MoCA: Montreal Cognitive Assessment, MMSE: Mini-Mental State Examination, CDR: Clinical Dementia Rating Score

[a] Chi-square test for independence n= Frequency df= Degree of Freedom with participant categories AD and HC.

[b] independent t test for independence n= Frequency df= Degree of Freedom with participant categories AD and HC.

Conclusions: There is altered GMV in VBM, decrease in brain activation and increase spatial activation size in rs-fMRI neuronal FC in some area of the brain with APOE ε4 carrier of AD Participants. Thus the imaging features of the AD participants are mapped well with their ApoE ε4 carrier status. Thus, we propose our radiogenomics techniques as a useful biomarker for the characterisation of AD patients.

References

1. Piersson AD, Ibrahim B, Suppiah S, Mohamad M, Hassan HA, Omar NF, et al. Multiparametric MRI for the improved diagnostic accuracy of Alzheimer's disease and mild cognitive impairment: Research protocol of a case-control study design. PLoS One. 2021;16(9):e0252883.
2. Ribeiro LG, Busatto GF. Voxel-based morphometry in Alzheimers disease and mild cognitive impairment: Systematic review of studies addressing the frontal lobe. Dement Neuropsychol. 2016;10(2):104-12.
3. Azmi M, Saripan M, Nordin A, Saad FA, Aziz SA, Adnan WW, et al. 18F-FDG PET brain images as features for Alzheimer classification. Radiation Physics and Chemistry. 2017;137:135-43.
4. Ibrahim B, Suppiah S, Ibrahim N, Mohamad M, Hassan HA, Nasser NS, et al. Diagnostic power of resting-state fMRI for detection of network connectivity in Alzheimer's disease and mild cognitive impairment: A systematic review. Hum Brain Mapp. 2021;42(9):2941-68.
5. Szabo-Reed AN, Vidoni E, Binder EF, Burns J, Cullum CM, Gahan WP, et al. Rationale and methods for a multicenter clinical trial assessing exercise and intensive vascular risk reduction in preventing dementia (rrAD Study). Contemp Clin Trials. 2019;79:44-54.
6. Su J, Huang Q, Ren S, Xie F, Zhai Y, Guan Y, et al. Altered Brain Glucose Metabolism Assessed by (18)F-FDG PET Imaging Is Associated with the Cognitive Impairment of CADASIL. Neuroscience. 2019;417:35-44.
7. Rankin KP, Toller G, Gavron L, La Joie R, Wu T, Shany-Ur T, et al. Social Behavior Observer Checklist: Patterns of Spontaneous Behaviors Differentiate Patients With Neurodegenerative Disease From Healthy Older Adults. Front Neurol. 2021;12:683162.
8. Zheng W, Su Z, Liu X, Zhang H, Han Y, Song H, et al. Modulation of functional activity and connectivity by acupuncture in patients with Alzheimer disease as measured by resting-state fMRI. PLoS One. 2018;13(5):e0196933.
9. Verfaillie SC, Tijms B, Versteeg A, Benedictus MR, Bouwman FH, Scheltens P, et al. Thinner temporal and parietal cortex is related to incident clinical progression to dementia in patients with subjective cognitive decline. Alzheimers Dement (Amst). 2016;5:43-52.
10. Tang Y, Xing Y, Zhu Z, He Y, Li F, Yang J, et al. The effects of 7-week cognitive training in patients with vascular cognitive impairment, no dementia (the Cog-VACCINE study): A randomized controlled trial. Alzheimers Dement. 2019;15(5):605-14.
11. Rubinov M, Sporns O. Complex network measures of brain connectivity: uses and interpretations. Neuroimage. 201

Poster No 2336

Dynamics of Brain Lateralization and Genetic Underpinnings during Chinese Natural Speech Processing

Ruohan Zhang[1], Shujie Geng[2], Xiaoqing Zheng[2], Wanwan Guo[2], Chun-Yi Lo[3], Jiaying Zhang[4], Xiao Chang[2], Xinran Wu[5], Jie Zhang[6], Miao Cao[2], Jianfeng Feng[7]

[1]University of Warwick, Coventry, West Midlands, [2]Fudan University, Shanghai, Shanghai, [3]Chung Yuan Christian University, Taoyuan, Chinese Taipei, [4]Beijing University of Posts and Telecommunications, Beijing, Beijing, [5]Institute of Science and Technology for Brain-inspired Intelligence, Fudan University, Shanghai, Shanghai, [6]Institute of Science and Technology for Brain-inspired Intelligence (ISTBI), Shanghai, Shanghai, [7]Institute of Science and Technology for Brain inspired Intelligence, Shanghai, Shanghai

Introduction: One notable aspect of language processing is brain lateralization, as the language system was traditionally assumed to be situated mainly in the left hemisphere, enhancing efficiency in multitask performance and reducing redundancy in neural organization. Nevertheless, lateralization has traditionally been treated as a static feature of the human brain. In a recent study, Wu et al. investigated dynamic lateralization in the brain in the resting state and its association with language functions and cognitive flexibility. This work suggests the potential of exploring dynamic lateralization across the whole brain during language processing. Furthermore, the impact of sex and contextual factors on dynamic lateralization patterns throughout the brain during language processing remains largely unknown.

Methods: We acquired fMRI data using an ultrahigh-field 7T Siemens Terra MR scanner with a cohort of 20 participants (with a mean age of 23.7 ± 1.8 years and 10 females for sex balance) while they performed a Chinese language natural listening task. During the task, all participants listened to two-hour narratives that replicated authentic language to simulate language processing in real-life situations. For the analyses, we employed a data-driven approach that combines a sliding window technique with the global signal-based laterality index to identify recurring whole-brain dynamic lateralization states. Then, we examined the spatial and temporal properties of the states as well as influences of sex and content. Next, we explored the genetic underpinnings of the observed dynamic lateralization states with publicly available postmortem brain-wide gene expression data. Finally, using resting-state fMRI data from the Human Connectome Project (HCP) cohort, we investigated whether the properties of the dynamic lateralization states observed during the Chinese natural listening task are related to inherent lateralization patterns.

Results: We investigated whole-brain functional dynamic lateralization patterns during Chinese language processing and potential sex disparities using functional MRI data of 20 subjects listening to narrative stories in a 7T MRI scanner. Our findings revealed two distinct dynamic lateralization states, with areas of the language system consistently exhibiting left-lateralized and converse lateralization patterns for both association areas and primary sensorimotor areas. These two states, characterized by areas of higher-order systems exhibiting left- or right-lateralization, corresponded to the processing of rational and emotional contents. We observed pronounced inclinations towards the former state in males and the latter state in females, especially during the processing of rational content. Finally, genetic analysis revealed that the sex differences in lateralization states were potentially influenced by sex hormones.

Conclusions: Our study provides valuable insights into the dynamic nature of brain lateralization during Chinese language processing. The identification of two distinct lateralization states improves our understanding of interhemispheric coordination during language processing, emphasizing the dynamic shift in higher-order cognitive functions between left and right lateralization patterns. Furthermore, the associations of these lateralization states with sex differences and the processed content (emotional or rational content) offer insights into sex-specific patterns in language processing. Moreover, our genetic-level analyses suggest that the observed sex differences in language lateralization may be influenced by sex hormones. Future research should focus on replicating and expanding our findings utilizing larger and more diverse sample populations, exploring different age groups, and investigating the functional significance of the observed dynamic lateralization states. This would advance our understanding of language processing mechanisms and their relevance in clinical and cognitive contexts.

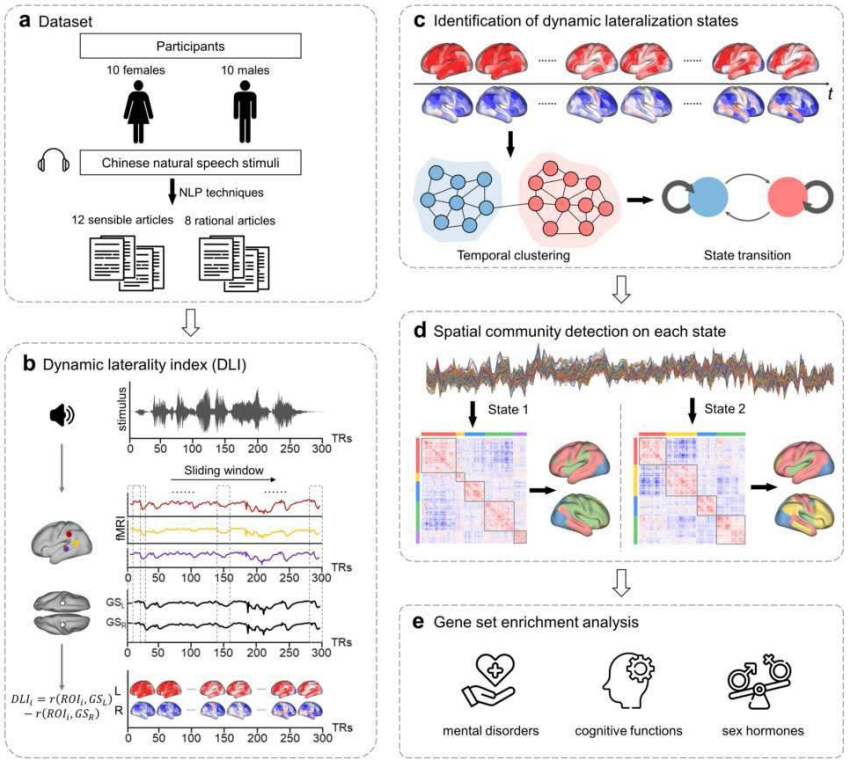

References

1. Wu, X. (2022), 'Dynamic changes in brain lateralization correlate with human cognitive performance', PLoS biology, 20(3), e3001560.
2. Xu, M. (2020), 'Sex differences in functional brain networks for language', Cerebral Cortex, 30(3), 1528-1537.
3. Huth, A. G. (2016), 'Natural speech reveals the semantic maps that tile human cerebral cortex', Nature, 532(7600), 453-458.
4. Peng, X. (2023), 'Robust dynamic brain coactivation states estimated in individuals', Science Advances, 9(3), eabq8566.

Poster No 2337

Cerebrovascular Reactivity Mapping Using Resting-State fMRI in Early Chronic Traumatic Brain Injury

Joon Yul Choi[1], Savannah Steer[2], Sung-min Kim[1], Daniel Brennan[2], Ines Guariguata[2], Taehyun Kim[1], Junghoon Kim[2]

[1]Yonsei University, Wonju, [2]The City University of New York, New York, NY

Introduction: Altered cerebrovascular reactivity (CVR) may reflect microvascular injury after traumatic brain injury (TBI) and serve as an indicator of cerebrovascular health[1-4]. However, current gas inhalation CVR assessment protocols and paradigms pose barriers to using CVR in clinical settings; most require complex designs and training[5,6]. Recently, an alternative to gas inhalation-based CVR protocol was proposed using resting-state BOLD MRI[5,7]. This study aims to examine test/retest reliability of resting-state based CVR (RS-CVR) and its alterations in moderate-to-severe TBI (msTBI) patients compared to matched healthy controls (HC).

Methods: Resting state fMRI (rsfMRI) images were acquired from 35 TBI patients at 3 months post-injury and 24 HC with the following parameters: TR/TE=3000/300 ms, matrix size=64x64, voxel size=3x3x3, and measurements=100. For 21 HC and 29 TBI subjects, two BOLD runs were available for reliability calculation. After preprocessing including motion correction and linear detrending, a bandpass filter with a range of 0 – 0.01164 Hz was applied to BOLD signals[7]. RS-CVR maps were obtained for each subject through a general linear model (GLM). To assess reliability, we computed intra-class correlations (ICCs) in two different ways: 1) ICC voxel-wise across runs within subjects and 2) ICC across subjects for each atlas based[8] region of interest (ROI). Aligned rank transformations (ART) ANOVA was conducted to compare differences in regional ICCs between groups and hemispheres. To compare RS-CVR values between TBI and HC, a GLM based on two sample t tests with covariates of age and gender was created. Whole-brain voxel-wise results from the GLM were evaluated using threshold free cluster enhancement (TFCE) inference and family-wise error (FWE) correction for multiple comparison correction.

Results: The average ICC across voxels (calculated within subjects) was 0.75 ± 0.12 and 0.69 ± 0.15 in HC and TBI, respectively. Figure 1A shows the regional ICCs for the left and right hemisphere ROIs (ROI N=118) in HC and TBI. The ICCs

for the left and right hemispheres in HC were 0.46 ± 0.16 and 0.48 ± 0.14, respectively while for TBI, these values were 0.37 ± 0.21 and 0.45 ± 0.17, respectively. The ART ANOVA revealed a significant difference in ICC between groups ($F1 = 7.6$, $p < 0.01$). However, in a subgroup analysis using only non-lesioned ROIs (N=50, Figure 1B), this group difference in ICC values disappeared, indicating that focal lesions lowered reliability of affected ROIs. When comparing RS-CVR between HC and TBI, HC exhibited significantly higher RS-CVR values in left cerebellum than TBI whereas TBI patients exhibited significantly higher RS-CVR values in cuneus than HC (Figure 2).

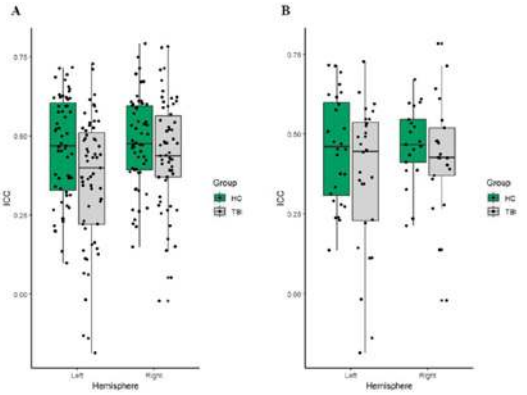

Figure 1. Intra-class correlation (ICC) across atlas based regions of interest (ROIs) in the left and right hemispheres of HC and TBI (panel A) and ICC for non-lesioned ROIs (panel B). HC: Healthy controls, TBI: Traumatic brain injury patients, LH: Left hemisphere, and RH: Right hemisphere.

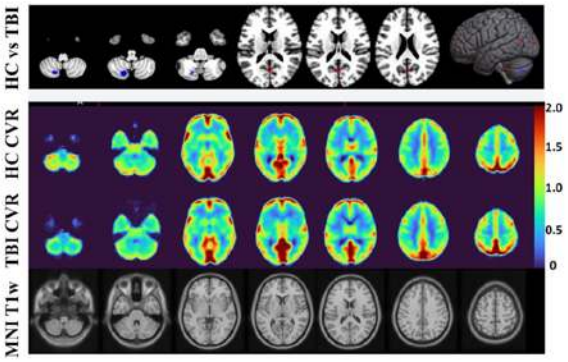

Figure 2. Statistical difference in RS-CVR between TBI and HC along with average RS-CVR maps. Blue: HC > TBI and Red: TBI > HC. HC: Healthy control, TBI: Traumatic brain injury, RS-CVR: Resting-state BOLD cerebrovascular reactivity. HC exhibited significantly higher RS-CVR values in cerebellum than TBI patients (Blue, $p < 0.05$, FWE corrected). TBI patients exhibited significantly higher RS-CVR values in cuneus than HC (Red, $p < 0.05$, FWE corrected).

Conclusions: Results from this study support previous studies' observations of good repeatability of within-subject RS-CVR maps quantified by voxelwise ICCs[5]. However, reliability measured by across-subject regional ICC values was substantially lower, especially for the ROIs affected by focal lesions. Group differences between msTBI and HC in the cerebellum in this study corroborate prior research implicating the cerebellum in TBI[4,9,10]. Lower RS-CVR values in the cuneus in HC compared to TBI might indicate that the cuneus is relatively preserved after msTBI.

References

1. Amyot F, Kenney K, Moore C, et al., Imaging of cerebrovascular function in chronic traumatic brain injury, J Neurotrauma, 35:1116-1123, 2018.
2. Amyot F, Kenney K, Spessert E, et al., Assessment of cerebrovascular dysfunction after traumatic brain injury with fMRI and fNIRS, Neuroimage Clin, 25:102086, 2020.
3. Chen JJ, Gauthier CJ, The role of cerebrovascular-reactivity mapping in functional MRI: Calibrated fMRI and resting-state fMRI, Front Physiol, 12:657362, 2021.
4. Kenny K, Amyot F, Haber M, et al., Cerebral vascular injury in traumatic brain injury, Exp Neurol, 3:353-366, 2016.
5. Liu P, Welch BG, Li Y, et al., Multiparametric imaging of brain hemodynamics and function using gas-inhalation MRI, Neuroimage, 146:715-723, 2017.
6. Pinto J, Bright MG, Bulte DP, et al., Cerebrovascular reactivity mapping without gas challenges: A methodological guide, Front Physiol, 11:608475, 2021.

7. Liu P, Liu G, Pinho MC, et al., Cerebrovascular reactivity mapping using resting-state BOLD functional MRI in healthy adults and patients with Moyamoya disease, Radiology, 299:419-425, 2021.
8. Landman B, Warfiled S, MICCAI 2012 workshop on multi-atlas labeling, in: MICCAI Grand Challenge and Workshop on Multi-Atlas Labeling, CreateSpace Independent Publishing Platform, Nice, France, 2012.
9. Gaggi NL, Ware JB, Dolui S, et al., Temporal dynamics of cerebral blood flow during the first year after moderate-severe traumatic brain injury: A longitudinal perfusion MRI study, Neuroimage Clin, 37:103344, 2023.
10. Hillary FG, Roman CA, Venkatesan U, et al., Hyperconnectivity is a fundamental response to neurological disruption, Neuropsychology, 29:59-75, 2015.

Poster No 2338

An rs-fMRI study of taVNS for Treatment-Resistant Depression and Non-Treatment-Resistant Depression

Qingyan Chen[1], Yi Luo[1], Yue Ma[1], Chunlei Guo[1], Shanshan Gao[1], Jiliang Fang[1]

[1]Guanganmen Hospital, China Academy of Chinese Medical Sciences, Beijing, China

Introduction: Major Depression Disorder (MDD) is a common emotional mental disorder. The main clinical characteristic are significant and persistent depression, loss of interest, sluggish thinking, persistent fatigue, and decreased volitional activity, etc., which has a high risk of disability and suicide[1]. The primary treatment for depression is pharmacological and psychological intervention. Nevertheless, significant proportion of patients, approximately 30%, remain resistant to treatment despite being administered two or more antidepressant medications with varying chemical structures in adequate doses and durations. This type of depression is classified as treatment-resistant depression (TRD)[2-3]. Therefore, searching for other non-drug therapies to effectively treat TRD has become the focus of research in the field of anti-depression. Transcutaneous auricular vagus nerve stimulation (taVNS) is a novel type of ear electroacupuncture therapy. Its theory mainly involves stimulating the auricular point - ear nail region with micro-current to regulate the function of the corresponding Zangfu. It has been widely used in the treatment of neurological diseases, mental and behavioral disorders. The team's previous research found that taVNS is effective in the treatment of mild to moderate depression and treatment-resistant depression[4-7], and its therapeutic effect is related to the regulation of default network[4], Salience network[8], visual processing network[9], cognitive control network[10] and other networks. However, there is still a lack of research on the brain effect mechanism of taVNS in TRD and nTRD.

Methods: In this study, 24 patients with TRD and 31 patients with nTRD were enrolled. Both groups received taVNS treatment for eight weeks respectively. Resting-state functional magnetic resonance imaging (rs-fMRI) was performed before and after treatment for two groups. The 17-item Hamilton Rating Scale for Depression (HAMD-17) was used as the primary clinical efficacy indicator, while the Ruminative Response Scale (RRS) served as the secondary indicator. The amplitude of low frequency fluctuation (ALFF) value before and after treatment between two groups was compared by mixed effect analysis.

Results: Both groups were found with significant reduction in HAMD-17 scores after treatment. The RRS scores of the nTRD group showed a notable reduction. The fMRI results showed that the nTRD group had significantly decreased ALFF in the left thalamus/hypothalamus/globus pallidum and primary visual cortex compared with the TRD group. After treatment, both groups demonstrated a significant increase in ALFF values in the left posterior central gyrus and a significant decrease in ALFF values in the right insular lobe. Furthermore, the nTRD group exhibited a significant increase in ALFF values in the right anterior central gyrus. Mixed-effect analysis results showed that the left orbitofrontal gyrus and right cerebellar Crus2 were the different brain regions between the TRD group and the nTRD group before and after treatment. nTRD group had significantly decreased ALFF in the left orbitofrontal gyrus and right cerebellar Crus2 after treatment, while the TRD group had significantly increased ALFF in the left orbitofrontal gyrus and the right cerebellum Crus2.

Conclusions: Transcutaneous auricular vagus nerve stimulation alleviated depressive symptoms in patients with treatment-resistant depression and non-treatment-resistant depression. There are brain function differences between TRDs and nTRDs in thalamus/hypothalamus/globus pallidum and primary visual cortex, so taVNS can regulate brain regions related to emotion, cognition and sensorimotor function in both groups of TRDs and nTRDs. While there are different regulatory patterns in the left orbitofrontal middle gyrus and cerebellum between two groups. This study could provide some basis for the targeted cortex of taVNS for TRD and nTRD.

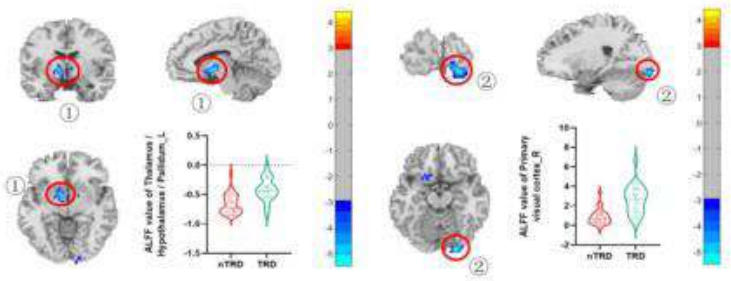

FIGURE 1 Brain regions with differences in ALFF values between the two groups before treatment: ① left thalamus/hypothalamus/pallidum (-12, 15, -12); ② right primary visual cortex (18, -19, -21). The color from blue to yellow indicates the degree of ALFF value from low to high (threshold voxel level $P<0.001$; cluster level $P<0.05$). The violin diagram above shows the difference in ALFF values between the two groups in the left thalamus/hypothalamus/pallidum and the right primary visual cortex.

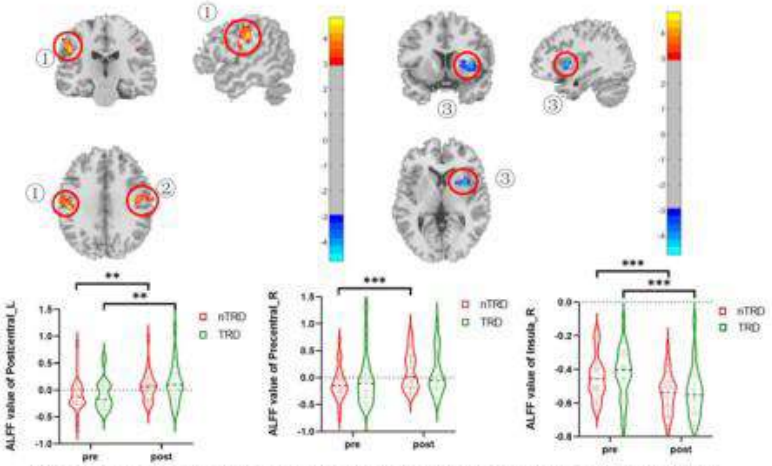

FIGURE 2 Brain regions with differences in ALFF values between the two groups after 8-week treatment: ① left postcentral gyrus (-51, -21, 33) ; ② right precentral gyrus (48, -9, 30); ③ right insula (45, -3, 12). The color from blue to yellow indicates the degree of ALFF value from low to high (threshold voxel level $P<0.005$; cluster level $P<0.05$). The violin diagram above shows the difference in ALFF values between the two groups in the left postcentral gyrus, right precentral gyrus, right insula. $^{**}P<0.005$, $^{***}P<0.001$.

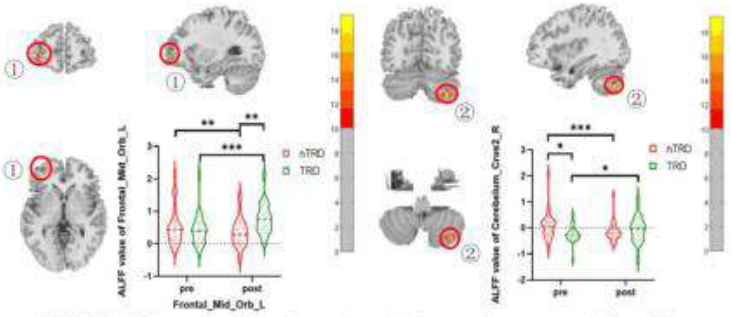

FIGURE 3 Differences in time and group interaction between the two groups: ① medial orbitofrontal gyrus (-30, 57, 0) ② right cerebelum_Crus2 (36, -72, -48). The color from blue to yellow indicates the degree of ALFF value from low to high (threshold voxel level $P<0.005$; cluster level $P<0.05$). The violin plots represent the difference in ALFF values of the left medial orbitofrontal gyrus and the right cerebellum_Crus2 before and after treatment in the two groups. $^{*}P<0.05$, $^{***}P<0.001$.

TABLE 1 Demographic and clinical characteristics of the study participants.($\bar{x} \pm s$)

Variable	TRD (n=24)	nTRD (n=31)	t/χ^2	*P*-value
Sex (M/F)	16/8	23/8	0.370	0.54[a]
Age (years)	43.38±11.00	43.42±10.68	0.015	0.99[b]
Educational level (years)	14.00±2.45	13.26±3.11	-0.853	0.40[b]

TRD, treatment-resistant depression; nTRD non treatment-resistant depression.
[a] The P-values of gender distribution between the two groups were obtained by chi-square test.
[b] The P-value obtained by two-sample t-test.

TABLE 2 Clinical data before and after 8-week treatment between TRD group and nTRD group.

Group	Time	HAMD-17			RRS		
		score	*t*-value	*P*-value	score	*t*-value	*P*-value
TRD (n=24)	pre	23.42±2.95	-10.67	<0.001[a*]	44.67±22.52	-2.00	0.058[a]
	post	7.92±6.75			35.21±17.80		
nTRD (n=31)	pre	23.19±3.29	-11.33	<0.001[a*]	40.90±13.86	-6.04	<0.001[a*]
	post	8.94±6.06			26.00±16.01		

HAMD-17, 17-item Hamilton Rating Scale for Depression; RRS, Ruminative Response Scale.
[a] The P-value obtained by two-sample t-test.
[*] Significant difference.

TABLE 3 Differences in ALFF between the TRD and nTRD groups.

Clusters	Brain Regions	R/L	BA	Voxel size	MNI Peak			*t*-value
					X	Y	Z	
Pre-treatment TRD group versus nTRD group								
1	Thalamus/Hypothalamus/Pallidum	L	-	143	-12	15	-12	-3.4887
2	Primary visual cortex	R	17	95	18	-19	-21	-3.4902
Post_ALFF versus Pre_ALFF								
1	Postcentral gyrus	L	1	161	-51	-21	33	-4.8189
2	Precentral gyrus	R	4	86	48	-9	30	-4.2275
3	Insula	R	13	96	45	-3	12	4.4164
Interaction effect between time and group of ALFF values								
1	Medial orbitofrontal gyrus	L	11	30	-30	57	0	19.0995
2	Cerebelum_Crus2	R	-	19	36	-72	-48	19.3092

ALFF, amplitude of low frequency fluctuation; BA, Brodmann area; MNI Peak, Coordinates of primary peak locations in the Montreal Neurological Institute space.

References

1. Geneva: World Health Organization.(2021),'Comprehensive mental health action plan 2013–2030', Licence:CC BY-NC-SA 3.0 IGO.
2. GAYNES B.N.(2020a),'Defining treatment-resistant depression', Depress Anxiety. vol.37,no.2,pp.134-145.
3. KVERNO K.S.(2021b),'Treatment-Resistant Depression: Approaches to Treatment', J Psychosoc Nurs Ment Health Serv. vol.59,no.9,pp.7-11.
4. FANG J.L.(2016a),'Transcutaneous vagus nerve stimulation modulates default mode network in major depressive disorder', Biol Psychiatry.vol.79,no.4,pp.266-273.
5. LI X.J.(2019a),'The effect of transcutaneous auricular vagus nerve stimulation on treatment-resistant depression monitored by resting-state fMRI and MRS: The first case report. Brain Stimul', vol.12,no.2,pp:377-379.
6. SUN J.F.(2022b),'Immediate modulation of transcutaneous auricular vagus nerve stimulation in patients with treatment-resistant depression: A resting-state functional magnetic resonance imaging study', Front Psychiatry. vol.13,pp:923783.
7. MA Y.(2022b),'Transcutaneous auricular vagus nerve immediate stimulation treatment for treatment-resistant depression: A functional magnetic resonance imaging study', Front Neurol. vol.13,pp:931838.
8. SUN J.F.(2022a),'A comparative study of regional homogeneity of resting-state fMRI between the early-onset and late-onset recurrent depression in adults', Front Psychol.vol.13,pp:849847.
9. SUN J.F.(2022a),'Comparison of functional connectivity of posterior cingulate cortex in resting-state between patients with treatment-resistant depression and non-treatment-resistant depression', Journal of Psychiatry. vol.35,no.1,pp:1-7.
10. SUN J.F.(2023a),'Immediate modulatory effects of transcutaneous auricular vagus nerve stimulation on the resting state of major depressive disorder', J Affect Disord.vol.325,pp:513-521.

Poster No 2339

Differential functional connectivity of the Sensorimotor Lateral r in football players

Wei Zou[1], Yidan Qiu[2], Fengguang Xia[3]

[1]School of Psychology, Key Laboratory of Brain, South China Normal University, Guangzhou, China, Guangzhou, China, China, [2]South China Normal University, Guangzhou, Guangdong, [3]Institute for Brain Research and Rehabilitation, South China Normal University, Guangzhou, China, China

Introduction: Long-term motor skill learning can induce plastic structural and functional reorganization of the brain[1,2]. Motor skill training refers to the process of repeated practice and interactions with the environment to achieve effortless movements[3]. Understanding the interactions between brain regions in football training can help to provide a more comprehensive of brain plasticity and the effects of training on brain function and brain connectivity. Further contributes to the design of more targeted measures in future physical education to improve soccer sport training[4,5]. In this study, rs-fMRI was used to investigate the differences in functional brain activity between football players and non-athletes. The resting-state functional connectivity indexes were calculated using CONN 20.b software, comparing the differences between the football group and the control group.

Methods: Subjects Twenty-three female football players (aged 20.60±4.1 years old) and 24 female non-athlete normal controls (aged 19.63±1.95 years old) were recruited.The study has been approved by the Human Research Ethnics Committee of South China Normal University. Written informed consent was obtained from each subject prior to this study. Data acquisition All Magnetic Resonance Imaging (MRI) datasets were obtained on a 3T Siemens Trio Tim MR scanner with the use of a 64 channel phased-array received-only head coil. The rest fMRI datasets were acquired using a gradient echo EPI sequence with the following parameters: TR/TE = 2000/30ms, thickness = 3.5mm, flip angle = 90°, field of view (FOV) = 224mm×224mm, matrix = 64×64. High-resolution structural brain images were obtained using a T1-weighted 3D MP-RAGE sequence (TR/TE = 2300/3.24ms, thickness = 1mm, flip angle = 9°, FOV = 256 mm×256 mm, bandwidth=210Hz/pixel. For each subject, the rest fMRI data and 3D high-resolution brain structural images were acquired in the same session. Data preprocessing The fMRI data were preprocessed using DPARSF and CONN based on Matlab (2018a). The preprocessing procedure contained the following steps: 1) Setup, 1. Manually enter the number of subjects=47, the repetition time TR=2 and the number of experimental sessions=1 and select the acquisition type and other basic experimental parameter settings. 2. Import Dpabi preprocessed functional and structural image data files, 3. Define the region of interest (ROI) based on the experimental hypothesis or the results of the pre-processing analysis. The ROI of this study is determined as Sensorimotor Lateral r, (2) Denoising, (3) First-level analyses functional connectivity analysis was performed by selecting the previously defined ROIs, (4) Second-level analyses.

Results: Figure 1 shows a significant difference in functional connectivity in the right Sensorimotor Lateral, the right Superior Temporal Gyrus, posterior division (pSTG r) between the football group and the control group.

Conclusions: The present study shows significant differences in functional connectivity between the football players and the control group in Superior Temporal Gyrus in the resting state. These plastic and adaptive changes in brain structure due to exercise training may improve the regulation of sensory, motor and cognitive functions.

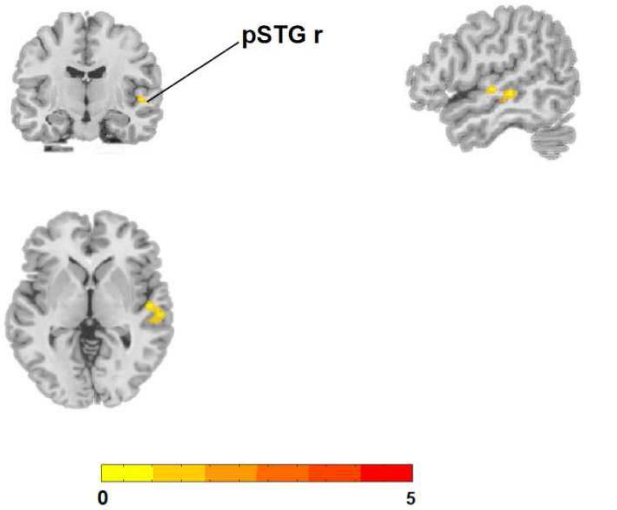

Fig.1 Brain areas with significant difference in Functional connectivity values in football players compared with the non-athlete normal controls.

References
1. Wang, J. J. et al. (2015). Exploring brain functional plasticity in world class gymnasts: a network analysis. Brain Structure and Function, 221(7), 3503–3519.
2. Deuker L, Bullmore ET, Smith M, Christensen S, Nathan PJ, Rockstroh B, Bassett DS (2009) Reproducibility of graph metrics of human brain functional networks. Neuroimage 47(4):1460–1468.
3. Willingham DB (1998) A neuropsychological theory of motor skill learning. Psychol Rev 105(3):558–584.
4. Coynel D, Marrelec G, Perlbarg V, Pelegrini-Issac M, Van de Moortele PF, Ugurbil K, Doyon J, Benali H, Lehericy S (2010) Dynamics of motor-related functional integration during motor sequence learning. Neuroimage 49(1):759–776.
5. Di X, Zhu S, Jin H, Wang P, Ye Z, Zhou K, Zhuo Y, Rao H (2012) Altered resting brain function and structure in professional badminton players. Brain Connect 2(4):225–233.

Poster No 2340

Simultaneous EEG-fMRI at 7T: Radiofrequency (RF) Heating and Shielding of a novel EEG cap

Rebecca Meagher[1], David Carmichael[2], Özlem Ipek[3], Tracy Warbrick[4]

[1]King's College London, London, United Kingdom, [2]King's College London, London, United Kingdom, [3]King's College London, London, London, [4]Brain Products GmbH, Gilching, Gilching

Introduction: The simultaneous acquisition of EEG and fMRI (EEG-fMRI) at 7T can provide very high temporal (sub-millisecond) resolution and spatial (sub-millimetre) resolution allowing non-invasive investigation of human brain function at the meso-scale. However, performing EEG-fMRI at ultra-high field comes with significant challenges because shorter RF wavelengths can facilitate increased coupling to the EEG cap (Phong Lê, Gruetter, Jorge, & Ipek, 2022), while also increasing the Specific Absorption Rate (SAR) produced by electric fields. In this study, we investigated a novel EEG cap incorporating segmented resistors, designed to avoid RF shielding at 7T, by measuring heating and transmit field (B1+) changes.

Methods: Data was acquired in 3 healthy volunteers. EEG measurements were recorded using the 32-channel 7T prototype cap with 4 carbon wire loops (BrainCap-MR7 FLEX, Brain Products GmbH). This novel cap design includes 5kOhm resistors placed on the flexprint PCB with another set of resistors on the EEG amplifier connection point to mitigate the formation of RF standing waves on long EEG cabling. (Phong Lê, Gruetter, Jorge, & Ipek, 2022) In addition, this design allows the modular connection between the EEG cap and the amplifiers through the 7T single-Tx birdcage coil (Nova Medical Inc., MA, USA) where the MR data was acquired at 7T (MAGNETOM Terra, Siemens Healthcare). Temperature probe measurements were acquired throughout the duration of the scan (Omniflex2, Neoptix, CA), with a sensitivity of +/- 0.1 °C, for each volunteer with 2 probes being placed underneath different EEG cap electrodes, and 1 placed on the ExG amplifier upper surface. The temperature data was sampled at a rate of 1Hz, and this data was subsequently smoothed with a 5s box kernel. For volunteers 1 and 2, the most lateral electrodes (FT9 and FT10) with the longest cabling, and therefore, the most susceptible to heating, were selected for temperature sampling. For volunteer 3, probes were placed at electrodes at the posterior region of the cap (TP9 and O1) as these are the electrodes closest to the coil Thermal images were captured (Seek Shot Thermal Camera, SeekThermal, CA, USA) before and after the scan. The specific pulse sequences used (localiser, B1+ maps, B0 maps 2D-TSE and MP2RAGE) and their SAR are described in Figure 1(b). At the end of the protocol the cap was removed and the subject repositioned within the coil then the localiser, B1+ maps, B0 maps were repeated.

Results: Figure 1(a) shows an overview of the temperature results. For all 3 volunteers, the temperature is seen to remain stable at both electrodes and at the ExG amplifier as both a function of time throughout the duration of the scan. There is minimal heating associated with scan onset apparent even for sequences with maximum normal mode SAR (TSE and MP2RAGE). Slow temperature drifts that are not related to scanning are visible, likely caused by natural variations in the thermal environment of the room, the cap, and the subjects head. These findings are reinforced by the thermal camera images, whereby there is no discernible difference between images captured before and after the scanning session, and no clear locations of increased heating. Figure 2 displays the B1+ maps for both the EEG cap on and cap off condition. Across all 3 volunteers, similar B1+ maps were obtained for both the cap on and cap off condition, with minimal visible RF reduction observed.

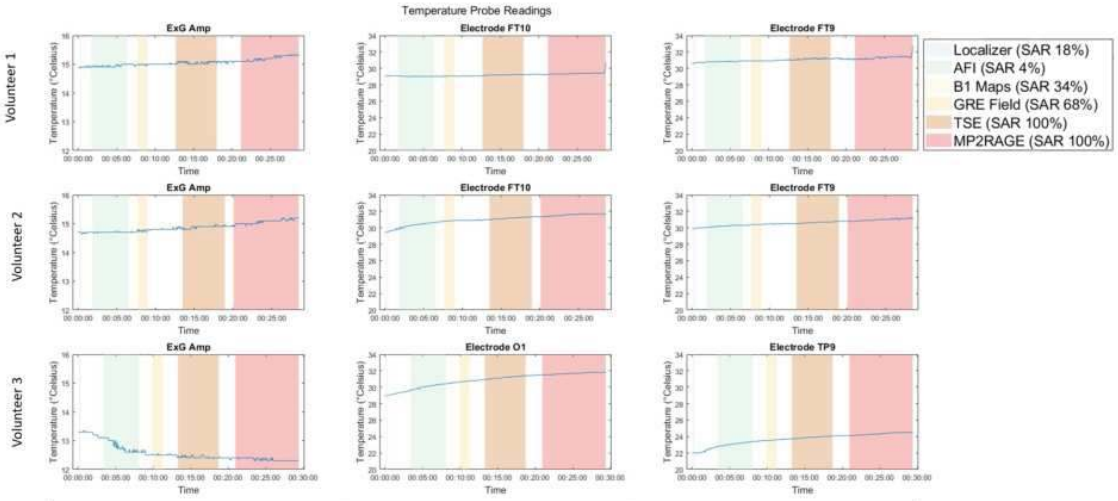

(b)

Sequence Name	Duration (mm:ss)	% SAR
Localizer	00:15	18
AFI B_1^+ map	04:38	4
2D B_1^+ map	00:09	34
GRE Field Mapping	01:22	68
TSE	05:54	100
MP2RAGE	07:21	100

Figure 1: (a) Temperature changes over time as detected by temperature probes. The different pulse sequences implemented, and their respective timings and SAR levels, are depicted by the shaded portions of the graphs, and in Figure 1(b)

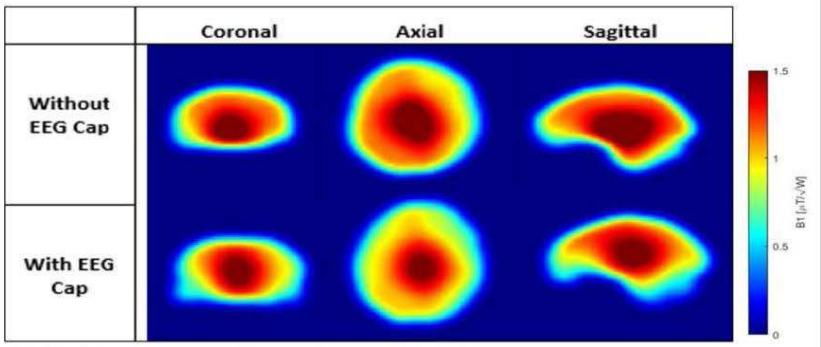

Figure 2: 3D B_1^+ map acquired with and without the EEG cap on healthy volunteer using AFI method, corrected with the measured B_0 maps

Conclusions: No measurable heating at the EEG electrodes or ExG amplifier was detected in any of the volunteers in this study, providing evidence that the risk of significant heating is low. Moreover, no visible RF reduction was observed between the EEG cap on and cap off conditions.

References

1. Phong Lê, T., Gruetter, R., Jorge, J., & Ipek, Ö. (2022). Segmenting electroencephalography wires reduces radiofrequency shielding artifacts in simultaneous electroencephalography and functional magnetic resonance imaging at 7 T. Magnetic Resonance Medicine, 1450–1464.

Acknowledgements
This project is co-funded by the UKRI MRC-DTP and BrainProducts GmbH

Poster No 2342

Functional Brain Networks and EEG Microstate Dynamics During Light Sleep: An EEG-fMRI Study

Yujie Long[1], Jing Xu[1], Shuqin Zhou[2], Guangyuan Zou[3,4], Jiayi Liu[3,4], Qihong Zou[3], Jia-hong Gao[3,4,5,1]

[1]Shanghai International Studies University, Shanghai, China, [2]McLean Imaging Center, McLean Hospital, Harvard Medical School, Belmont, MA 02478, USA, Boston, MA, [3]Center for MRI Research, Peking University, Beijing, China, [4]Beijing City Key Lab for Medical Physics and Engineering, Institution of Heavy Ion Physics, School of Physics, Peking University, Beijing, China, [5]McGovern Institute for Brain Research, Peking University, Beijing, China

Introduction: Light sleep, encompassing non-rapid eye movement stages N1 and N2, is vital for cognitive function and physical health, acting as a bridge to deeper sleep phases. Characterized by distinct EEG patterns, these stages are crucial

for understanding brain dynamics during sleep. Light sleep is composed of non-rapid eye movement stages including N1 and N2, characterized by distinct EEG patterns, with the latter stages serving as crucial transitions from wakefulness to deeper sleep phases. EEG microstates, brief quasi-stable periods of electric field topography, offer unique perspectives into these dynamic brain functions. In previous research, four consistent microstate maps (A-D), have been identified across wake and sleep stages. While recent EEG-fMRI advancements have identified their correlations with resting-state networks (RSNs), relationships during N1 and N2 remain unknown.

Methods: In this study, simultaneous EEG-fMRI data were acquired during the N1 and N2 stages to investigate the relationships between EEG microstates and fMRI networks. Stage-specific N1 and N2 template maps were applied to each subject's EEG data, enabling the computation of key microstate parameters including Mean Correlation, Global Explained Variance (GEV), Mean Duration, and Time Coverage. ANOVA with factors "stage" and "microstate" was performed on microstate parameters. Custom regressors based on microstate maps were used in a General Linear Model (GLM) to model BOLD responses, involving three critical steps: 1. Aligning group-level microstate template maps with individual EEG data; 2. Convolving spatial correlation time series with the hemodynamic response function for GLM analysis; 3. The beta maps resulting from the GLM analysis were analyzed using AFNI's 3dLMEr (Chen et al., 2013) for group-level linear mixed-effect analysis, considering sleep stages, sessions, and subjects. Multiple comparison corrections were applied using the autocorrelation function (ACF) modeling approach, involving 3dFWHMx for ACF estimation and 3dClustSim for determining the cluster-size threshold (Cox, 1996; Eklund et al., 2016). This methodology ensured a corrected significance level of $p < .05$ with a minimum cluster size of 150 voxels. The analysis was replicated for four different EEG microstate maps.

Results: ANOVA analysis showed that significant main effects were observed for sleep stages on mean correlation ($p < .05$), and for microstates on all four dependent microstate parameters ($p < .01$). Additionally, significant interaction effects between sleep stages and microstates were noted for each dependent variable ($p < .01$) (see Fig. 1). Notably, microstate B demonstrated larger values of GEV, mean duration, and time coverage in N1, a trend that reversed in N2 (see Fig. 1b-d). In contrast, microstate C showed smaller values in N1, which increased in N2 (see Fig. 1b-d). The main effects of sleep stage of beta values of microstate B and microstate D were found to be significant. Specifically, microstate B demonstrated a correlation with the right cerebellum, exhibiting activation during N1 and deactivation in N2, as detailed in post hoc analysis (see Fig. 2a). In the case of microstate D, correlations with the bilateral thalamus and the bilateral postcentral gyrus were observed. Interestingly, a transition from N1 to N2 in microstate D was characterized by a reversal in activation patterns: the thalamus shifted from deactivation to activation, while the motor network showed an opposite trend, moving from activation to deactivation (see Fig. 2b).

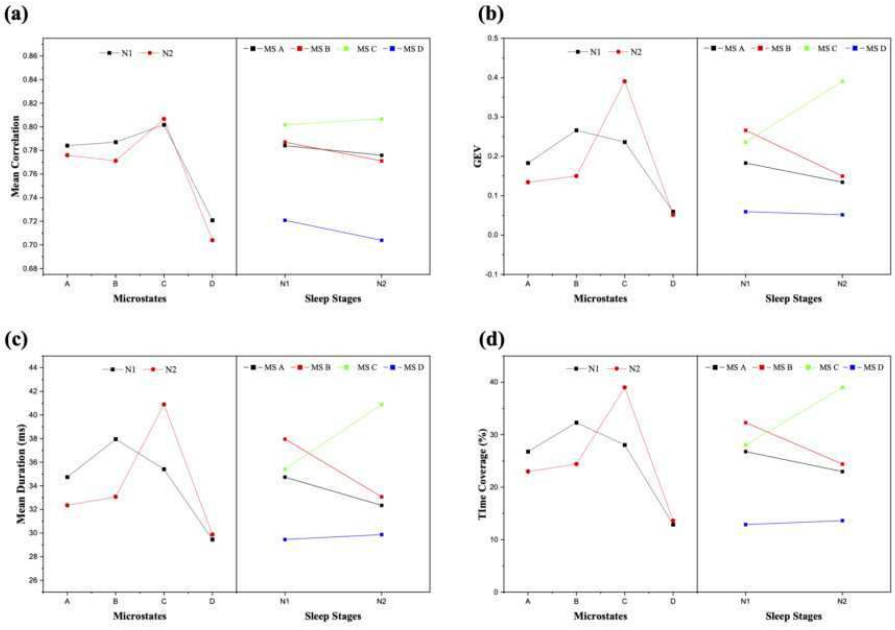

Fig. 1. 2 x 4 ANOVA of Sleep Stages and Microstates. This figure presents the interaction effects of sleep stages (N1 and N2) and microstates (A, B, C, D) on four different dependent variables: mean correlation, GEV (Global Explained Variance), mean duration, and time coverage. Each panel displays the means of the dependent variables for each microstate within each sleep stage.

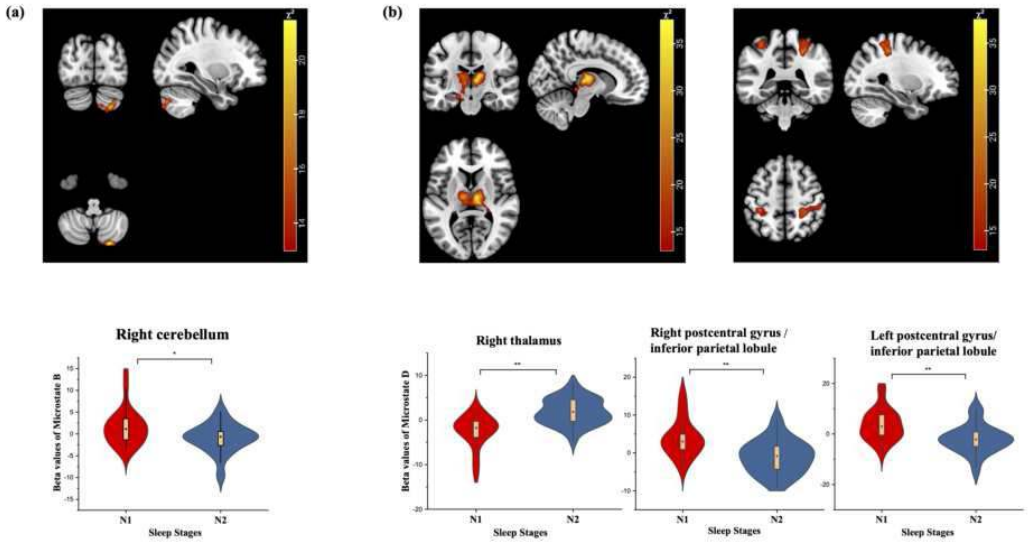

Fig. 2. The main effect of sleep stage of beta values of microstate B (Fig. 2a) and D (Fig. 2b). (N = 22 for N1, N = 38 for N2, $p < 0.001$ and clusterwise corrected $p < 0.05$). Average Fisher z-values (mean ± SEM) in the clusters with a sleep stage effect as shown in (a): The region includes the right cerebellum; In (b): The regions include bilateral thalamus and the bilateral postcentral gyrus (post hoc two-sample t-tests between the two groups, *p < .05, **p < .01).

Conclusions: In conclusion, our study sheds light on the relationships between EEG microstates and functional brain networks during the N1 and N2 stages of light sleep, establishing EEG microstates as crucial electrophysiological markers of these networks. Building upon prior research on thalamocortical network activity transitions from wakefulness to sleep, we postulate that microstates B and D represent EEG manifestations during early sleep stages.

References

1. Chen, G., Saad, Z. S., Britton, J. C., Pine, D. S., & Cox, R. W. (2013). Linear mixed-effects modeling approach to FMRI group analysis. NeuroImage, 73, 176–190. https://doi.org/10.1016/j.neuroimage.2013.01.047
2. Cox, R. W. (1996). AFNI: Software for Analysis and Visualization of Functional Magnetic Resonance Neuroimages. Computers and Biomedical Research, 29(3), 162–173. https://doi.org/10.1006/cbmr.1996.0014
3. Eklund, A., Nichols, T. E., & Knutsson, H. (2016). Cluster failure: Why fMRI inferences for spatial extent have inflated false-positive rates. Proceedings of the National Academy of Sciences, 113(28), 7900–7905. https://doi.org/10.1073/pnas.1602413113

Poster No 2343

Differences in layered activation of the insula during interoceptive vs. exteroceptive attention

Matthias Müller-Schrader[1], Frederike Petzschner[2], Jakob Heinzle[1], Lars Kasper[3], Katharina Wellstein[1], Johanna Bayer[4], Maria Engel[5], Lilian Weber[6], Klaas Prüssmann[5], Klaas Stephan[1]

[1]Translational Neuromodeling Unit (TNU), University of Zurich & ETH Zurich, Zurich, Zurich, [2]Brown University, Providence, RI, [3]University of Toronto, Toronto, Ontario, [4]Donders Institute for Brain, Cognition and Behaviour, Nijmegen, Gelderland, [5]Institute for Biomedical Engineering, ETH Zürich & University of Zurich, Zurich, Zurich, [6]Department of Psychiatry, University of Oxford, Oxford, Oxfordshire

Introduction: Attention modulates the processing of exteroceptive stimuli, such as visual inputs (Moore et al. 2017). Potential mechanisms include top-down cortical projections to lower sensory regions and neuromodulatory transmitter release via projections from brainstem nuclei, both of which occur in layer-specific manners. By contrast, the impact of attention on the perception of bodily states (interoception) remains less explored. Here, we present a preregistered analysis of layered 7T fMRI data, focusing on the insula, a central area for interoception. We investigated whether insular subregions show different BOLD activity between attention to one's own heartbeat and attention to auditory sounds, and whether this difference varied between upper vs. lower cortical layers.

Methods: 40 participants performed a heartbeat attention task (Petzschner et al. 2019). In each block (duration 20s, 16 per run), participants were instructed to either focus on their heartbeat (interoceptive condition) or on continuously present auditory white noise (exteroceptive condition). The study was approved by the cantonal ethics committee of Zurich (2016-

01297). FMRI images were acquired on a Philips Achieva 7T MR system with quadrature transmit and 32-channel head receive coils, using a high-resolution single-shot spiral-out trajectory with 0.9 mm in-plane resolution (R=4, TE=15ms, 50ms readout duration), 36 slices (0.9mm/0.1mm slice-gap/TR=3.128s) and fat suppression module (SPIR). Images were reconstructed by inversion of an advanced signal model, taking sensitivity encoding and static and dynamic field inhomogeneities into account (Kasper et al. 2022). Functional images were slice-timed, realigned and co-registered to an anatomical reference image. The first level GLM included two main regressors (attention to heart/sound), as well as regressors accounting for physiological noise, head motion, and motion censoring. Layered masks (upper/lower) were created for each individual by combining anatomical masks of insular regions (Fan et al. 2016) with 25%/75%-equivolume-cortical depth masks (Waehnert et al. 2014) obtained by segmentation of T1-weighted images [0.8mm isotropic resolution] with Freesurfer) and a functional mask for the contrast attention to heart vs. sound (from all other subjects, p_cluster<0.05 with CDT p<0.001), see Figure 1. Data processing and analyses followed a preregistered analysis plan (Müller-Schrader et al. 2023). A 2x2 repeated measures ANOVA was performed for each insular region (factors layer [upper/lower] and condition [attention to heart/sound]). We tested the layer-by-condition interaction and corrected for multiple comparisons across insular regions.

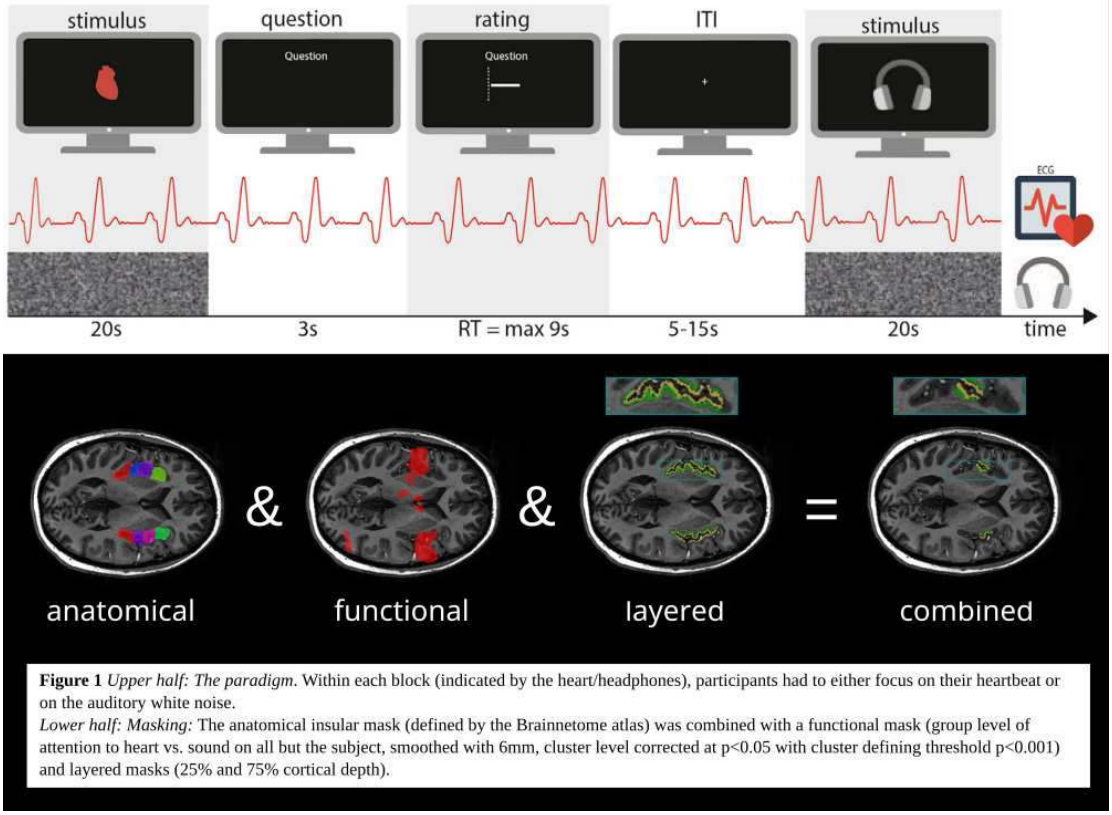

Figure 1 *Upper half: The paradigm.* Within each block (indicated by the heart/headphones), participants had to either focus on their heartbeat or on the auditory white noise.
Lower half: Masking: The anatomical insular mask (defined by the Brainnetome atlas) was combined with a functional mask (group level of attention to heart vs. sound on all but the subject, smoothed with 6mm, cluster level corrected at p<0.05 with cluster defining threshold p<0.001) and layered masks (25% and 75% cortical depth).

Results: Complete fMRI data were available for 25 out of 40 participants. 19 datasets could be reconstructed with sufficient quality for layered analyses. Within the functional mask, three insular regions had notable activations (>10 activated voxels). Attention to heartbeats activated the regions more strongly than attention to sound, and this difference was greater in upper vs. lower layers (Figure 2). This layer-by-condition interaction was significant in both left (p=0.00036, F = 19.55) and right (p=0.002, F=13.233) dorsal dysgranular insula, and exhibited a continuous trend across cortical depth (Figure 2).

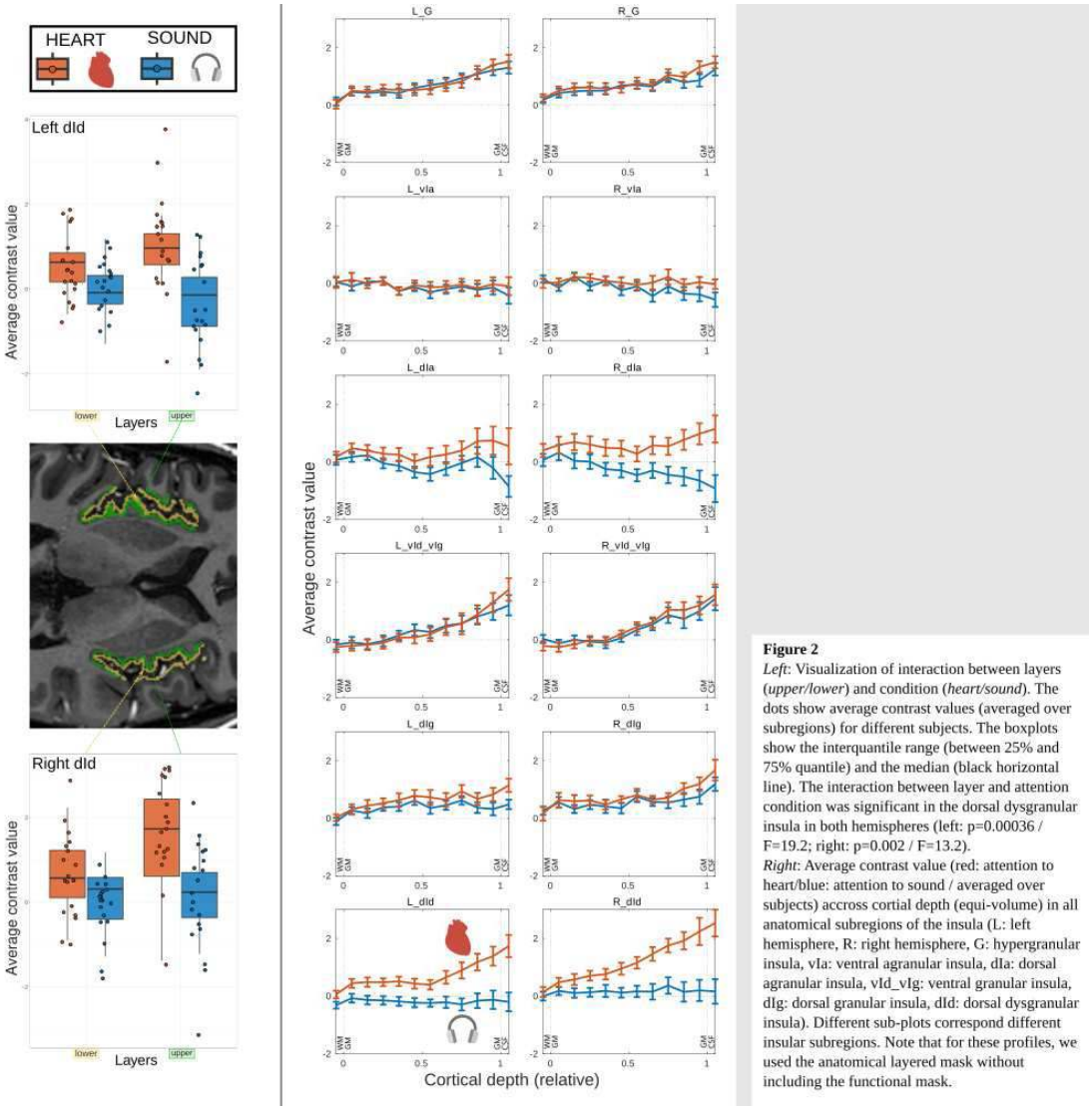

Figure 2
Left: Visualization of interaction between layers (*upper/lower*) and condition (*heart/sound*). The dots show average contrast values (averaged over subregions) for different subjects. The boxplots show the interquantile range (between 25% and 75% quantile) and the median (black horizontal line). The interaction between layer and attention condition was significant in the dorsal dysgranular insula in both hemispheres (left: p=0.00036 / F=19.2; right: p=0.002 / F=13.2).
Right: Average contrast value (red: attention to heart/blue: attention to sound / averaged over subjects) accross cortial depth (equi-volume) in all anatomical subregions of the insula (L: left hemisphere, R: right hemisphere, G: hypergranular insula, vIa: ventral agranular insula, dIa: dorsal agranular insula, vId_vIg: ventral granular insula, dIg: dorsal granular insula, dId: dorsal dysgranular insula). Different sub-plots correspond different insular subregions. Note that for these profiles, we used the anatomical layered mask without including the functional mask.

Conclusions: Previous layered fMRI have examined exteroceptive (visual) attention effects, with diverse results (Mourik et al, 2023, Liu et al, 2021, Muckli et al, 2015). This study is the first to report layer-specific attention effects for interoceptive stimuli. Our preregistered analysis found that activation of the insula by attending to heartbeats vs. sounds was modulated by cortical depth, revealing a layer-by-condition interaction, with larger differences in the upper layer. Notably, it is possible that these layer differences may have been influenced by venous blood inflow effects (from lower to upper layers); we will investigate this in further analyses.

References

1. Fan, L., et al. (2016), 'The Human Brainnetome Atlas: A New Brain Atlas Based on Connectional Architecture'. Cerebral Cortex (New York, N.Y.: 1991) 26 (8): 3508–26.
2. Kasper, L., et al. (2022), 'Advances in Spiral fMRI: A High-Resolution Study with Single-Shot Acquisition'. NeuroImage 246 (February): 118738.
3. Liu, C., et al (2021) „Layer-dependent multiplicative effects of spatial attention on contrast responses in human early visual cortex". Progress in Neurobiology, How high spatiotemporal resolution fMRI can advance neuroscience, 207 (1. Dezember 2021): 101897.
4. Moore, T., et al (2017) „Neural Mechanisms of Selective Visual Attention". Annual Review of Psychology 68, Nr. 1 (2017): 47–72.
5. Mourik, T., et al (2023) „Investigation of Layer-Specific BOLD Signal in the Human Visual Cortex during Visual Attention". Aperture Neuro 3 (29. August 2023): 1–18.
6. Muckli, L., et al (2015) „Contextual Feedback to Superficial Layers of V1". Current Biology 25, Nr. 20 (19. Oktober 2015): 2690–95.
7. Müller-Schrader, M., et al (2023), 'Analysis Plan: Layered Analysis of fMRI Data Acquired during Attention to Heartbeats'. Zenodo. https://doi.org/10.5281/zenodo.10015185.
8. Petzschner, F. H., et al (2019), 'Focus of Attention Modulates the Heartbeat Evoked Potential'. NeuroImage 186: 595–606.
9. Waehnert, M. D., et al (2014), 'Anatomically Motivated Modeling of Cortical Laminae'. NeuroImage, In-vivo Brodmann Mapping of the Human Brain, 93 (June): 210–20.

Poster No 2344

Activity in AI and aMCC of Clinicians Predicts Pain Assessment and Treatment via Stereotypes

Theoni Varoudaki[1], Nikta Khalilkhani[2], Morgan Gianola[3], Elizabeth Losin[2]

[1]Penn State Univeristy, State College, PA, [2]Penn State University, State College, PA, [3]University of Miami, Coral Gables, FL

Introduction: Non-Hispanic White populations are regularly over-prescribed opioids and other analgesics, which leads them to born a greater burden of the opioid epidemic, while minoritized groups and women are typically under-prescribed pain medication relative to clinical guidelines and experience poor pain management outcomes. One potential mechanism underlying this phenomenon is clinicians adjusting their prescription according to inaccurate stereotypes about the pain sensitivity and opioid abuse rates of different demographic groups or the idea that clinicians experience less shared pain when examining patients of a different demographics than their own, leading to lack of motivation to provide pain relief and an associated decrease in analgesic prescription. To understand the psychological and brain mechanisms underlying these health disparities, we conducted an fMRI study where clinicians watched vignettes of mock pain patients of different demographics.

Methods: 65 medical trainees (age: 22-32 years old, 34 female, 31 male) attended a single 3-hour visit. During the visit, they had an fMRI scan where they saw profiles and short videos of participants experiencing evoked pain, meant to represent the clinical exam of 36 musculoskeletal pain patients (12 non-Hispanic African American, 12 non-Hispanic White and 12 Hispanic White). For each patient, clinicians made pain assessment and treatment decisions. In order to understand how the pain expressions of patients and vicarious pain of clinicians contributed to the clinicians' decisions the following analyses took place: Pain facial expressions of the patients were analyzed using to draw conclusions about their effect on the clinicians' treatment decisions. A single-trial analysis focusing on two a priori regions (AI and aMCC) of interest from a meta-analysis on pain empathy was conducted. Z-scores of mean activation were extracted and added to a Structural Equation Model (SEM) to test the contributions of pain stereotypes, pain expression, neural indicators of vicarious pain (AI and aMCC activity), pain assessment, and treatment decisions in a single SEM model. The clinician-patient dyad was the unit of analysis with a total of 2,340 dyadic interactions.

Results: We found that clinicians assessed the pain of their patients based on the pain sensitivity stereotypes that they held about the patient's demographic. Activation in the AI and aMCC predicted both the clinician's treatment decisions via the clinicians' sensitivity stereotypes and pain assessment. However, the two areas had opposite effects on assessment and treatment when controlling for all other variables, with higher anterior insula activation predicting lower pain assessment and higher pain treatment, and higher anterior medial cingulate activation predicting higher pain assessment and lower pain treatment, indicating that they may play separate roles in the clinicians' decisions. The clinicians' gender was also an important predictor of pain assessment, sensitivity stereotypes and activation of the anterior insula, with women assessing all patients as more sensitive to pain and their pain as higher, but having a lower activation of their anterior insula when observing patients in pain than men. This finding could suggest that compared to male clinicians, female clinicians' pain treatment decisions may be driven more by affective (previously associated with the aMCC) than cognitive empathy (previously associated with the AI). Finally, clinicians with more years of medical education were less likely to prescribe any analgesics to patients but assessed patients' pain as higher and exhibited lower activation in the medial cingulate cortex when observing patients in pain during the mock clinical exam.

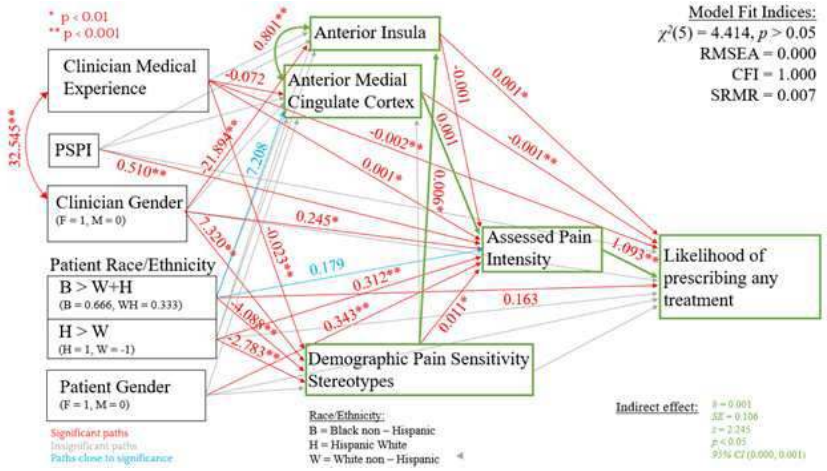

Fig. SEM Model Results

Conclusions: The finding that AI activity predicted treatment decisions whereas aMCC predicted pain assessment, could indicate that clinicians may share the pain of their patients but make their treatment decisions based on their objective impression of it.

References

1. Campbell, C. M., & Edwards, R. R. (2012). Ethnic differences in pain and pain management. Pain Manag, 2(3), 219-230. doi:10.2217/pmt.12.7
2. Hoffman, K. M., Trawalter, S., Axt, J. R., & Oliver, M. N. (2016). Racial bias in pain assessment and treatment recommendations, and false beliefs about biological differences between blacks and whites. Proc Natl Acad Sci U S A, 113(16), 4296-4301. doi:10.1073/pnas.1516047113
3. Kennel, J., Withers, E., Parsons, N., & Woo, H. (2019). Racial/Ethnic Disparities in Pain Treatment: Evidence From Oregon Emergency Medical Services Agencies. Med Care, 57(12), 924-929. doi:10.1097/mlr.0000000000001208
4. Lamm, C., Decety, J., & Singer, T. (2011). Meta-analytic evidence for common and distinct neural networks associated with directly experienced pain and empathy for pain. Neuroimage, 54(3), 2492-2502. doi:https://doi.org/10.1016/j.neuroimage.2010.10.014
5. Prkachin, K. M., & Solomon, P. E. (2008). The structure, reliability and validity of pain expression: evidence from patients with shoulder pain. Pain, 139(2), 267-274. doi:10.1016/j.pain.2008.04.010

Poster No 2345

A novel Virtual Reality based system for MR imaging of awake young children

Laura Bravo Balsa[1], Kun Qian[1], Lucilio Cordero-Grande[2,1], Molly Eddison[1], Jessica Cader[1], Jonathan O'Muircheartaigh[1,3,4], A. Edwards[1,5,3], Eva Loth[4], Joseph Hajnal[1], Tomoki Arichi[1,3,5]

[1]Centre for the Developing Brain, King's College London, London, UK, [2]Universidad Politécnica de Madrid & CIBER-BBN, Madrid, Spain, [3]Centre for Neurodevelopmental Disorders, King's College London, London, UK, [4]Department of Forensic and Neurodevelopmental Sciences, IoPPN, King's College London, London, UK, [5]Guy's and St Thomas' NHS Foundation Trust, London, UK

Introduction: The noisy and claustrophobic MRI environment is challenging for specific populations, particularly young children who may become distressed or struggle to keep still during image acquisition. Scans are therefore often performed during sleep[1] or with sedation or anesthesia in clinical practice[2]. This limits opportunities for neuroscience research to investigate the neural correlates of emerging facets of awake behaviour and cognition, and their a/typical neurodevelopmental trajectories[3]. To overcome this, we developed a novel Virtual Reality (VR) system which immerses the child in an interactive virtual world during scanning[4]. Eye tracking and an adaptive calibration free gaze estimation algorithm that is robust to subject movement enables continuous interaction with the VR environment[5] and can quantify visual attention for fMRI analysis. To resolve residual motion related image artifact, we implement the DISORDER method[6]. Here we describe the system itself and the results of pilot studies with awake toddlers, highlighting the potential to provide new insight into this understudied but critically important period of brain development.

Methods: The VR system consists of a light-tight 3D printed headset which mates precisely with the MR scanner head coil (figure 1a). Two MR compatible video cameras (12M-I, MRC systems) are mounted inside the headset, and a wall mounted video camera monitors the patient table position. Video content is projected onto a diffuser screen in the headset by an MR compatible projector (SV-8000 MR-Mini, Avotec Inc) placed on the examination table. Audio content is presented via noise cancelling headphones (OptoActive II, Optoacoustics Ltd). Content was developed following a series of workshops with children and families, which highlighted the need for tailored and flexible content using familiar characters. This is possible with content development using Unity (Unity Technologies) which enables easy customization for the preferences of each child. Interaction is enabled by holding gaze on items placed around the screen which trigger actions including games, videos, or character interaction. A progressive calibration algorithm which exploits additional information from each visual fixation ensures accurate motion-robust gaze estimation[5]. To maintain congruence with sensory experience, scanner table movement and gradient noise are linked to elements in the visual experience such as a moving visual perspective or work on a construction site. Retrospective motion correction of the images is done using the DISORDER framework which uses distributed and incoherent sampling orders, enabling resilience to head motion by encoding data redundancy[6]. The system has been tested with 3 healthy children under 3 years of age, using a Philips Achieva 3T scanner and a 32ch head coil.

Results: 2 out of 3 children successfully used the system inside the scanner bore in approximately 20-minute sessions. Children were able to immediately intuitively interact with the system, and sessions were only stopped when head movement had increased suggesting that the children had become bored. Data acquired during system use included high resolution MPRAGE images, TSE T2-weighted images, FLAIR images, and fMRI. Despite residual head movement, DISORDER reconstruction provided brain images suitable for both clinical reporting and volumetric analysis (figure 1b, c).

Conclusions: We describe and demonstrate the effectiveness of a novel framework which combines an immersive VR experience and motion tolerant imaging methods to open new possibilities for awake MR studies in young children for both clinical and research purposes. In addition to reducing the need for non-trivial interventions like anesthesia, this can enable a new generation of MR based studies of awake brain processing underlying key cognitive and behavioural functions during a critical time for their emergence and neurodevelopment.

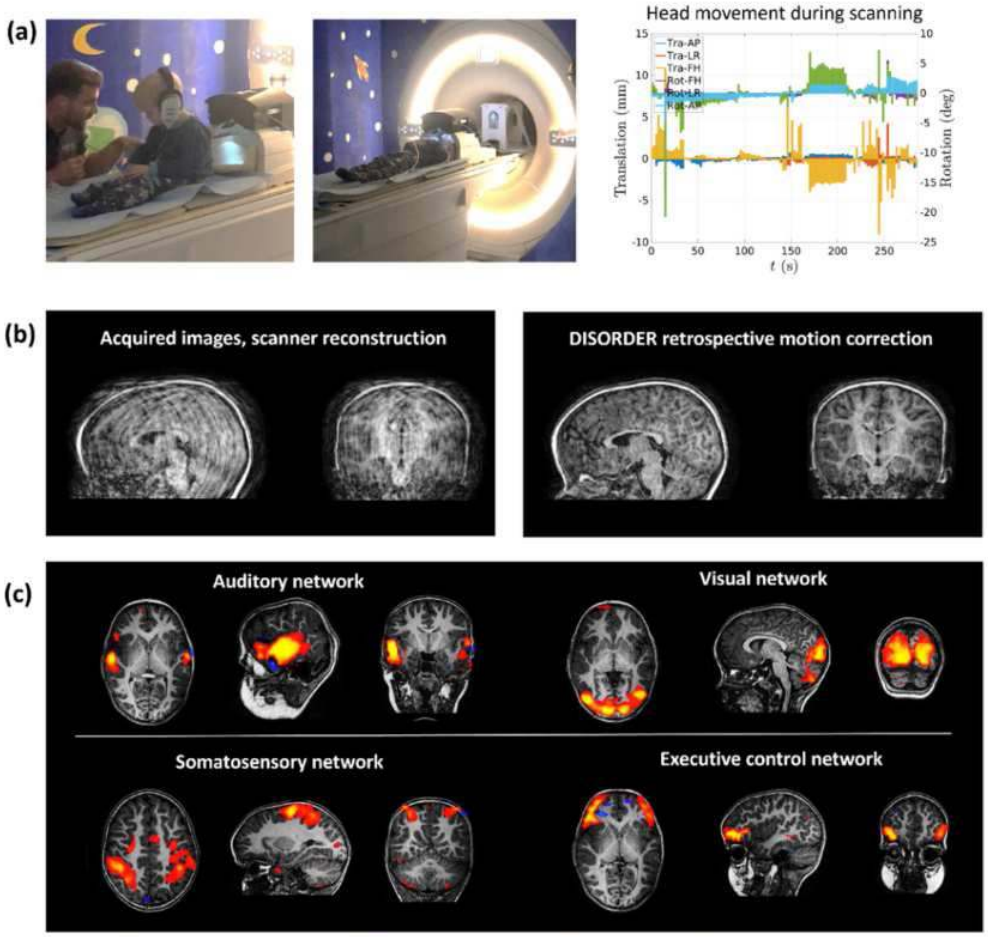

Figure 1. ***Example data from pilot MRI studies using the MR conditional VR system.*** *(a) 2.5-year-old child preparing for an MRI scan (left) and then entering the scanner bore whilst using the VR system once positioned inside the headset (middle). The system is designed to minimise head movement during image acquisition although some residual movement (up to 15mm translation and 10 degrees rotation) is still evident during use (right). (b) Residual image artefact due to head motion during scanning (left) can be resolved using the DISORDER retrospective motion correction framework developed in our department (right). (c) The VR system and image reconstruction framework enable the collection of high quality anatomical and functional data as evidenced by the well localised resting state networks characterised in an awake 2.5-year-old child.*

References

1. Copeland, A. et al. (2021), 'Infant and Child MRI: A Review of Scanning Procedures', Frontiers in neuroscience, 15, 666020.
2. Lawson, G.R. (2000), 'Controversy: sedation of children for magnetic resonance imaging', Archives of disease in childhood, 82(2), 150–153.
3. Ellis, C.T. et al. (2020), 'Re-imagining fMRI for awake behaving infants', Nature communications, 11(1), 4523.
4. Qian, K., et al. (2021), 'An eye tracking based virtual reality system for use inside Magnetic Resonance imaging Systems', Scientific Reports, 11(1), 16301.
5. Qian, K., et al. (2023), 'Instant Gaze (IG): an interaction driven adaptive gaze control interface', PREPRINT (Version 1) available at Research Square [https://doi.org/10.21203/rs.3.rs-3486222/v1]
6. Cordero-Grande, L. et al., (2020), 'Motion-corrected MRI with DISORDER: Distributed and incoherent sample orders for reconstruction deblurring using encoding redundancy', Magnetic Resonance in Medicine, 84(2), 713-726.

Poster No 2346

Sleep deprivation exhibits age-dependent effect on fMRI-based glymphatic measures

Yibing Yang[1], Yutong Mao[1], Tianxin Mao[2], Weiwei Zhao[2], Yao Deng[2], Xiaocui Zhang[2], Yifan Yang[1], Hengyi Rao[2,3], Xiao Liu[1,4]

[1]Department of Biomedical Engineering, The Pennsylvania State University, University Park, PA, 16802, USA, [2]Center for Functional Neuroimaging, Department of Neurology, University of Pennsylvania, Philadelphia, PA, USA, [3]Chronobiology and Sleep Institute, Department of Psychiatry, University of Pennsylvania, Philadelphia, PA, USA, [4]Institute for Computational and Data Sciences, The Pennsylvania State University, University Park, PA, 16802, USA

Introduction: Sleep plays a crucial role in various brain functions and essential homeostatic processes, particularly in the clearance of toxic proteins out of the brain. The brain glymphatic system, a recently proposed pathway for brain waste clearance, exhibits heightened activity during sleep[1]. Despite its significance, directly measuring glymphatic clearance in the human brain in vivo poses a considerable challenge. Recent research has unveiled a highly organized global brain activity at rest[2], manifested as prominent peaks in the global mean of resting-state fMRI (rsfMRI) BOLD signal (gBOLD), that is coupled to cerebrospinal fluid (CSF) movement and thus potentially linked to brain waste clearance[3]. Consequently, the coupling strength of gBOLD and CSF has been proposed as a surrogate measure of brain glymphatic function. This gBOLD-CSF coupling index has been found to correlate with neurodegenerative disease pathologies, including amyloid-beta (Aβ) and tau accumulation[4–6]. Given that sleep deprivation is known to impede waste clearance and increase Aβ and tau levels in the brain[7], it becomes intriguing to explore the impact of sleep deprivation on this fMRI-based glymphatic measure, particularly across different age groups with varying risk levels of Aβ and tau accumulation[8]. Our study investigates these questions with rsfMRI data acquired in a rigorously controlled in-laboratory sleep deprivation study[9].

Methods: Seventy subjects were enrolled in a 5-day, 4-night experiment and three of them were excluded due to significant head motion, technical issues and/or missing data. Among the remaining 67 participants (aged: 34.1 ± 8.9 years old, 29 females), 51 of them underwent total sleep deprivation on Night 2. RsfMRI sessions and PVT task were conducted in the mornings of Days 2 (Scan1), 3 (Scan2), and 5 (Scan3) (Fig. 1A). Eye-tracking was employed to ensure that subjects stayed awake during all scans. The CSF signal was extracted from the bottom slices of fMRI data near the cerebellum base, as the previous study[2]. The gBOLD was obtained by averaging fMRI signals within the entire gray matter regions (Fig. 1B). The gBOLD-CSF coupling was assessed at the negative peak (+4 seconds time lag) of their cross-correlation function (Fig. 1D), following the previous study[4].

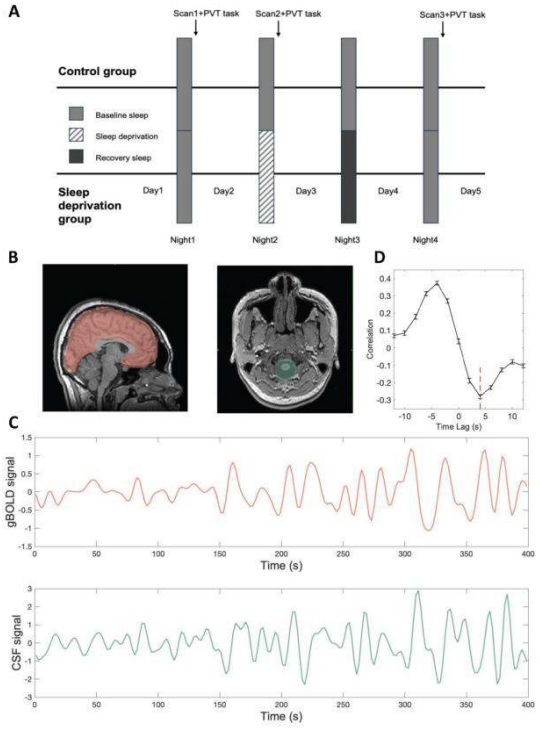

Figure 1. Experimental design and the gBOLD-CSF coupling. (A) Illustration of the experimental design and protocol. (B) Examples of the gray matter mask used to derive gBOLD (left) and the CSF mask for deriving CSF signal (right). (C) Examples of gBOLD and CSF signals from a representative subject. (D) The averaged cross-correlation function of gBOLD and CSF signals. The correlation at the negative peak (+4 seconds time lag), marked with a red dash line, was used to quantify the gBOLD-CSF coupling strength.

Results: Sleep deprivation had pronounced effects on the gBOLD-CSF coupling (Fig. 2A). Subjects after total sleep deprivation (N = 51) exhibited a large and significant increase (i.e., more negative) in the gBOLD-CSF coupling (p = 0.0071, paired t-test) in the Scan2 (Day3) right after the sleep deprivation, and then returned to baseline in Day5. In contrast, the gBOLD-CSF coupling remains stable and showed no significant changes (Scan2 vs. Scan1, p = 0.7823; Scan3 vs. Scan2, p = 0.8784, paired t-test) over the three scans in the control group. The above analysis was stratified by age groups among the sleep-deprived subjects (younger, age 20-30, N1 = 20; middle-aged, age 30-40, N2 = 14; older, age 40-50, N3 = 17) (Fig. 2B). Both the younger and middle-aged groups displayed a significant (younger, p = 0.0189; middle-aged, p = 0.0085, paired t-test) increase and then recovery (younger, p = 0.0132; middle-aged, p = 0.0037, paired t-test) of the gBOLD-CSF coupling, but this effect is much weaker and non-significant in the older group (Scan2 vs. Scan1, p = 0.8196; Scan3 vs. Scan2, p = 0.4410, paired t-test). Consistent with this observation, the age-scan interaction effect was found significant (p = 0.0367, two-way ANOVA), suggesting distinct effects of sleep deprivation on this fMRI measure across different age groups.

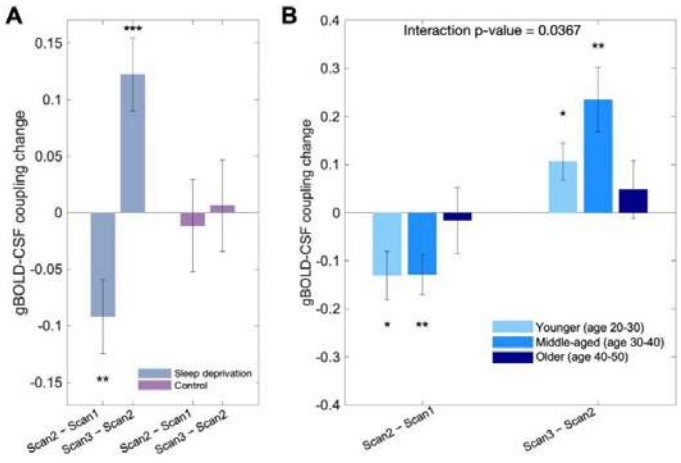

Figure 2. Changes in gBOLD–CSF coupling across scans. (A) Subjects with total sleep deprivation showed a significant increase in the gBOLD-CSF coupling ($p = 0.0071$, paired t-test) in Scan2 right after the sleep deprivation as compared to the baseline Scan1 in Day2, and the gBOLD-CSF coupling then changed back to the baseline level in Scan3 (Day 5). $*p < 0.05$, $**p < 0.01$, $***p < 0.001$. (B) The coupling changes across scans are significant for younger (N1 = 20) and middle-aged (N2 = 14) groups, but not the older group (N3 = 17). Two-way ANOVA has been applied to test the scan-age interaction for coupling change and a significant interaction was found. Error bars represent the standard error of the mean (SEM) across subjects.

Conclusions: Our results indicate a marked increase in gBOLD-CSF coupling following sleep deprivation, implying an enhanced clearance as a compensatory response to the lack of sleep. Yet, this compensatory mechanism seemed substantially diminished in participants of age 40-50, which might be a factor contributing to the age-related decline of brain waste clearance[8].

References

1. Xie, L. (2013). Sleep drives metabolite clearance from the adult brain. science, 342(6156), 373-377.
2. Fultz, N. E. (2019). Coupled electrophysiological, hemodynamic, and cerebrospinal fluid oscillations in human sleep. Science, 366(6465), 628-631.
3. Liu, X. (2023). Decoupling Between Brain Activity and Cerebrospinal Fluid Movement in Neurological Disorders. Journal of Magnetic Resonance Imaging.
4. Han, F. (2021). Reduced coupling between cerebrospinal fluid flow and global brain activity is linked to Alzheimer disease–related pathology. PLoS biology, 19(6), e3001233.
5. Han, F. (2021). Decoupling of global brain activity and cerebrospinal fluid flow in Parkinson's disease cognitive decline. Movement Disorders, 36(9), 2066-2076.
6. Han, F. (2023). Resting-state global brain activity affects early β-amyloid accumulation in default mode network. Nature Communications, 14(1), 7788.
7. Shokri-Kojori, E. (2018). β-Amyloid accumulation in the human brain after one night of sleep deprivation. Proceedings of the National Academy of Sciences, 115(17), 4483-4488.
8. Fyfe, I. (2020). Brain waste clearance reduced by ageing. Nature Reviews Neurology, 16(3), 128-128.
9. Yang, F. N. (2018). Sleep deprivation enhances inter-stimulus interval effect on vigilant attention performance. Sleep, 41(12), zsy189.

Poster No 2347

Simultaneous brain-spinal cord functional MRI with a force-matching task

Sandrine Bédard[1,2], Valeria Oliva[1], Christine Law[1], Dario Pfyffer[1], Merve Kaptan[1], Brett Chy[1], Susanna Aufrichtig[1], Nazrawit Berhe[1], John Ratliff[3], Serena Hu[4], Zachary Smith[5], Andrew Smith[6], Scott Delp[7], Akshay Chaudhari[8], Trevor Hastie[9], Gary Glover[8], Sean Mackey[1], Kenneth Weber[1]

[1]Systems Neuroscience and Pain Lab, Division of Pain Medicine, Stanford University School of Medicine, Palo Alto, CA, [2]NeuroPoly Lab, Institute of Biomedical Engineering, Polytechnique Montreal, Montréal, QC, Canada, [3]Department of Neurosurgery, Stanford University School of Medicine, Stanford, Palo Alto, CA, [4]Department of Orthopaedic Surgery, Stanford University School of Medicine, Stanford, Palo Alto, CA, [5]Department of Neurosurgery, University of Oklahoma Health Sciences Center, Oklahoma City, OK, [6]Department of Physical Medicine and Rehabilitation, University of Colorado School of Medicine, Aurora, CO, [7]Department of Bioengineering and Mechanical Engineering, Stanford University, Palo Alto, CA, [8]Department of Radiology, Stanford University School of Medicine, Palo Alto, CA, [9]Department of Statistics, Stanford University, Palo Alto, CA

Introduction: Spinal conditions affect nearly one billion individuals worldwide and rank among the primary causes of pain and physical disability[1]. Spinal cord and nerve root injury are characterized by hand weakness and impaired coordination[2]. Functional MRI (fMRI) can map motor-related brain activity and potentially characterize mechanisms underlying hand weakness and diminished coordination. Although some studies have investigated motor control mechanisms in the brain[3] research exploring these processes in the spinal cord has been limited[4,5], primarily due to technical challenges. In this study, we use simultaneous brain-spinal cord fMRI to capture descending motor signals, their interactions in the spinal cord, and the motor output during a force-matching task in healthy volunteers.

Methods: Eleven healthy volunteers (Age = 41 ± 14.8 years; 7 females, 4 males) were scanned using a 3T GE SIGNA Premier scanner with a 21-channel Head-Neck coil. We acquired simultaneous brain and spinal cord sequence[6] (EPI pulse sequence, dynamic per slice shimming; TR = 2.6 s, TE = 30 ms, GRAPPA = 2), with 30 brain slices (3.43 x 3.43 x 5.00 mm3) and 15 cervical spinal cord slices (1.25 x 1.25 x 5.00 mm3) centered at the C5-C6 intervertebral disc. The imaging protocol also included axial (FOV = 22 cm, matrix size = 128 x 128, ΔTE=1ms) and sagittal (FOV = 30 cm, matrix size = 256 x 64, ΔTE =1 ms) field maps for shimming, and anatomical scans of the brain (T1w 3DFSPGR; 1.0 x 1.0 x 1.0 mm3) and spinal cord (T2w reduced-FOV 3D turbo spin-echo; 0.8 x 0.8 x 0.8 mm3). The experimental design consisted of 30 sequences of 15 s blocks right-hand gripping using an MRI-compatible hand dynamometer with visual feedback with 15 s rest period between the task blocks. Participants matched three different force levels (10%, 20% and 30% of individual maximum voluntary contraction) during the experiment. Brain and spinal cord analysis included physiological noise correction, white matter and cerebrospinal fluid principal component regression, motion correction, temporal filtering, spatial normalization to the MNI[7] (brain) or PAM50[8] (spinal cord), and spatial smoothing using FSL[9] and the Spinal Cord Toolbox[10]. Subject-level activation maps were generated using a general linear model including three regressors corresponding to the three force task levels and then entered in group level analyses.

Results: In the brain, we identified activity in the contralateral motor and sensory cortices during the three different force levels. Additionally, BOLD signal change in the anterior cingulate cortex, the thalamus, cerebellum and occipital cortex linearly increased with force (Figure 1; mixed effects FLAME 1; $Z > 2.3$, cluster corrected $p < 0.05$). In the spinal cord, we identified activity in the right ventral horn for each force level at the C7 spinal segment. However, no significant linear increase in BOLD signal was identified across the three force levels (Figure 2; fixed effects, uncorrected $p < 0.05$).

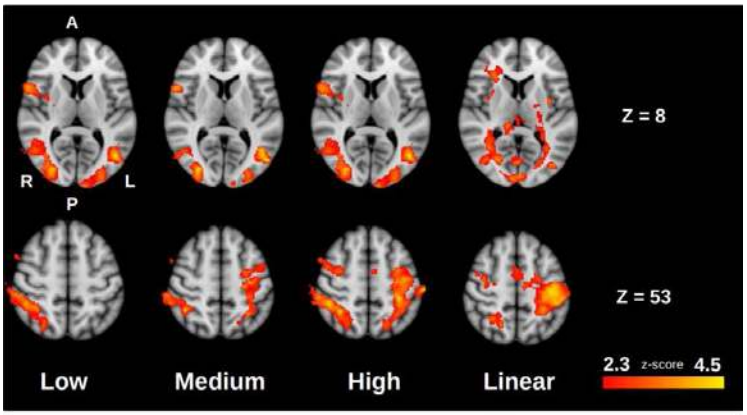

Figure 1. Brain activity in healthy volunteers during three levels of forces in a force matching task (N=10, Z > 3.1, cluster corrected for p < 0.05).

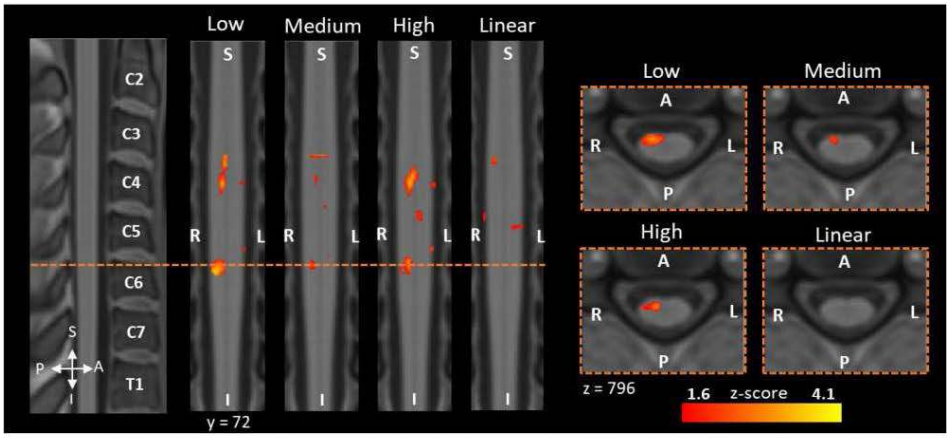

Figure 2. Spinal cord force matching group-level activation maps (n=11) for 3 levels of forces (low, medium, high) and linear increase in BOLD signal between the 3 levels. The average activation maps were thresholded at a z-score > 1.6 (uncorrected, $p < 0.05$). Orange line corresponds to the C7 spinal segment.

Conclusions: This study provides insights into the neural mechanisms of motor output in healthy volunteers with simultaneous brain and spinal cord fMRI and a force-matching task. The ipsilateral sensory and motor cortices show a linear increase in activity with higher force levels. In contrast, spinal cord activity, notably in the right ventral horn, did not demonstrate a similar linear relationship in this small sample. Studying motor control in the brain and spinal cord simultaneously has potential applications to spinal conditions such as spinal cord and nerve injury.

References

1. Abubakar, I. I., Tillmann, T. & Banerjee, A. Global, regional, and national age-sex specific all-cause and cause-specific mortality for 240 causes of death, 1990-2013: a systematic analysis for the Global Burden of Disease Study 2013. Lancet 385, 117–171 (2015).
2. Badhiwala, J. H. et al. Degenerative cervical myelopathy — update and future directions. Nat. Rev. Neurol. 16, 108–124 (2020).
3. Cramer, S. C. et al. Motor cortex activation is related to force of squeezing. Hum. Brain Mapp. 16, 197–205 (2002).
4. Hemmerling, K. J., Hoggarth, M. A., Sandhu, M. S., Parrish, T. B. & Bright, M. G. Spatial distribution of hand-grasp motor task activity in spinal cord functional magnetic resonance imaging. Hum. Brain Mapp. (2023) doi:10.1002/hbm.26458.
5. Weber, K. A., 2nd, Chen, Y., Wang, X., Kahnt, T. & Parrish, T. B. Lateralization of cervical spinal cord activity during an isometric upper extremity motor task with functional magnetic resonance imaging. Neuroimage 125, 233–243 (2016).
6. Islam, H., Law, C. S. W., Weber, K. A., Mackey, S. C. & Glover, G. H. Dynamic per slice shimming for simultaneous brain and spinal cord fMRI. Magn. Reson. Med. 81, 825–838 (2019).
7. Fonov, V. S., Evans, A. C., McKinstry, R. C., Almli, C. R. & Collins, D. L. Unbiased nonlinear average age-appropriate brain templates from birth to adulthood. Neuroimage 47, S102 (2009).
8. De Leener, B. et al. PAM50: Unbiased multimodal template of the brainstem and spinal cord aligned with the ICBM152 space. Neuroimage 165, 170–179 (2018).
9. Jenkinson, M., Beckmann, C. F., Behrens, T. E. J., Woolrich, M. W. & Smith, S. M. FSL. Neuroimage 62, 782–790 (2012).
10. De Leener, B. et al. SCT: Spinal Cord Toolbox, an open-source software for processing spinal cord MRI data. Neuroimage 145, 24–43 (2017).

Poster No 2348

Brain wide activation and connectivity analysis in awake mouse fMRI during forepaw force control

Vishwas Jindal[1,2], Daniel Wesson[3], David Vaillancourt[1,2], Shahab Vahdat[1,2]

[1]Department of Applied Physiology and Kinesiology, University of Florida, Gainesville, FL, [2]McKnight Brain Institute, University of Florida, Gainesville, FL, [3]Department of Pharmacology & Therapeutics, University of Florida, Gainesville, FL

Introduction: Controlling the level of upper limb force is crucial for performing daily activities. Despite knowing the areas involved in motor skill learning[1-3], the neural mechanisms involved in learning appropriate force control are not well understood. Functional magnetic resonance imaging (fMRI) in rodents allows unbiased tracking of whole-brain activation maps during learning to pinpoint key cortical, subcortical, and brainstem structures. However, there are no published fMRI studies performed during a motor task in mice. To fill this gap, we developed a novel-MR compatible head fixation apparatus for awake mouse fMRI during the forepaw force control task. This allowed us to shape mice during a motor behavior while minimizing noise and motion artifacts.

Methods: We built an accurate (resolution 0.005 N) MR-compatible miniature force transducer, as well as a 3D-printed head fixation system to shape and allow mice to engage in the forelimb force control task. We also designed and built a saddle linear MRI coil to fit our head fixation system. The training paradigm involves wild-type water-deprived mice undergoing a

reward-based forepaw press task. The mice were shaped to press the force transducer in a water-motivated press/no-press task for 7-14 days. After the training days, mice underwent an event-related awake SE-EPI fMRI scan in an 11T Bruker scanner while performing the right forepaw press task (resolution 0.35x0.35x0.5 mm3, TR = 2s). T2w anatomical scans (resolution 0.1x0.1x0.35 mm3) were also acquired for registration to the template. In aggregating activation maps (Fig. 1), an average was computed across 15 animals, each having a minimum of 2 functional scans. Subsequently, the average activation within each distinct brain region was computed to analyze the functional connectivity among them (Fig. 2).

Results: Our fMRI activation maps show (Fig. 1) significant ($p<0.05$, corrected) brain-wide activation related to forelimb force control across different cortical, subcortical, and cerebellar regions (Figure 1). The cortical structures mainly included M1, M2, ACC, RSG, and S1. The visible activation in subcortical structures included STR, hypothalamus, THL-VPL, THL-VL, SC & and IC, while, in the cerebellum, significant activation clusters were observed in Crus1 and the SIM lobules. We found that, although the activation was bilateral, it was more dominant on the contralateral side of the forepaw. The average motion during functional scans was minimal (less than 0.25 mm in all 3 directions), and additional motion correction parameters from the FSL software package were included as a confound in the regression model to ensure decoupling the effects of body motion from the activation maps. We used partial correlation analysis, by removing the effects of task paradigm, to assess functional connectivity. The functional connectivity analysis (Fig. 2) between the cortical, subcortical, and cerebellum areas showed 1) a significant correlation ($p < 0.05$, * Holm-Bonferroni correction) between various cortical and subcortical sensorimotor areas, including thalamus and striutum. 2) It is observed that, even though the results didn't reach statistical significance, a positive correlation exists between the cortical and cerebellar structures (SIM, AN, PRM with M1, M2, and ACC).

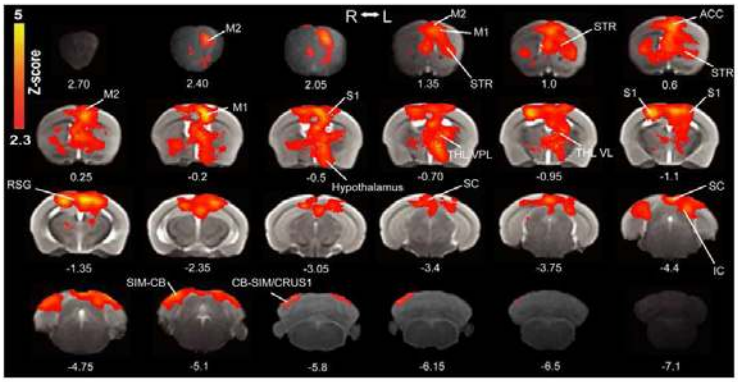

Figure 1. Brain-wide activation map during right forepaw force control task (n=15, $p < 0.05$, corrected). *Primary motor cortex (M1), secondary motor cortex (M2), anterior cingulate cortex (ACC), somatosensory cortex (S1), striatum (STR),* Ventral *posterolateral thalamus (THL VPL),* ventral *lateral thalamus (THL VL), retro splenial granular cortex (RSG), inferior and superior colliculus (SC & IC), cerebellum (CB) and simple lobule (SIM, lobule VI, VII-CB).*

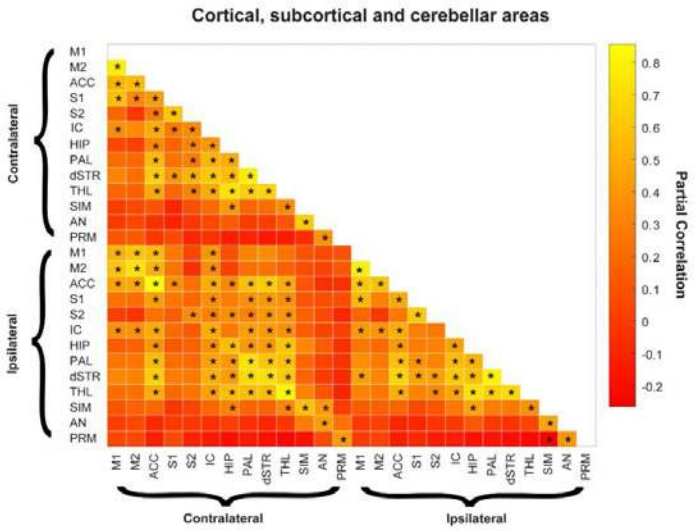

Figure 2. Region-based partial correlation analysis ($p < 0.05$,* Holm-Bonferroni correction). *Secondary somatosensory cortex (S2), insular cortex (IC), hippocampus (HIP), pallidum (PAL), dorsal striatum (dSTR), thalamus (THL), ansiform lobule (AN, lobule VII-CB) and paramedian lobule (PRM, lobule VIII-CB).*

Conclusions: Overall, our proposed method shows the feasibility of awake mouse fMRI in forelimb motor control and provides evidence for a widespread network of cortical and subcortical areas activated during force control. The functional connectivity analysis further helps us in determining functional interaction across various cortical, subcortical, and brainstrem regions. This method can further be used to study brain network reotganization following movement disorders and stroke in mice.

References

1. Kawai R, Markman T, Poddar R, Ko R, Fantana AL, Dhawale AK, Kampff AR, Ölveczky BP (2015) Motor cortex is required for learning but not for executing a motor skill. Neuron 86:800–812.
2. Yang W, Kanodia H, Arber S (2023) Structural and functional map for forelimb movement phases between cortex and medulla. Cell 186:162-177.e18
3. Yin HH, Mulcare SP, Hilário MRF, Clouse E, Holloway T, Davis MI, Hansson AC, Lovinger DM, Costa RM (2009) Dynamic reorganization of striatal circuits during the acquisition and consolidation of a skill. Nat Neurosci 12:333–34.

Poster No 2349

Where is Pain in the Brain? Unraveling Pain-Specific Functional Neurosignatures via 7 Tesla fMRI

Henning Reimann[1], Jurjen Heij[2], Thomas Gladytz[1], Thoralf Niendorf[1]

[1]Berlin Ultrahigh Field Facility, Max Delbrück Center for Molecular Medicine, Berlin, Germany, [2]Spinoza Centre for Neuroimaging, Amsterdam, Netherlands

Introduction: Functional MRI (fMRI) has failed to identify unambiguous and reliable signatures unique to pain[1,2]. Painful stimuli cause dynamic formation of large-scale functional networks related to stimulus prioritization (salience), attention, memory, interoception, autonomic control, and the initiation of motor patterns – all of which are highly characteristic but not specific to pain[1,2]. Here, we employ enhanced blood oxygen level-dependent (BOLD) contrast and spatial fidelity of 7T fMRI to disentangle pain-specific from domain-general representations via fine-grained cortical mapping. By comparing painful versus non-painful salient stimuli, we dissect the functional architecture of pain by specifying its domain-general core, probe its pain-specific features, and detail the large-scale orchestration of pain versus salience evoked networks.

Methods: fMRI of 8 volunteers (4/4, w/m), 4 runs, each 12 min. Stimuli (4 stimulus types, 8 per type and run) were applied briefly (duration ~100 ms) and pseudorandomized (interstimulus spacing 18-24s): contact heat (51°C), cutaneous electrical stimulation in 2 stimulus intensities: mildly painful (10 mA) and aversive but non-painful (6mA), and flashes of light (Fig. 1A). T2*-weighted fMRI (GE-EPI, TR/TE/FA = 2s/33.2ms/66°, FOV/matrix = 240x240mm/160x160, number of slices = 80, spatial resolution = 1.5mm isotropic, 220 volumes) acquired on MAGNETOM 7T scanner (Siemens Healthcare, Erlangen, Germany), single-channel-transmit/32-channel receive head coil (Nova Medical, Wilmington, MA, USA). fMRI data were motion/distortion corrected, smoothed, registered to MNI152, and statistically analyzed using FSL FLAME. Partial least squares (PLS) model trained and cross-validated on individual z maps (total 128 maps) to differentiate between stimulus modalities. 16 maps per volunteer (4 per stimulus) were normalized by their singular vector length in a singular value decomposition truncated after the 24th component. Leave-one-subject-out cross validation was performed to ensure transferability.

Results: Cortical representations across stimuli (Fig. 1B) intersected in a domain-general functional core GS(∩) (Fig. 1C,D). PLS regression revealed voxels that drive the classification of pain versus other salient stimuli (Fig. 2). The mean covariance coefficient (CC) map depicts voxels that drive classification across all stimulus modalities (Fig. 2A); reflecting the shared domain-general patterns of GS(∩). The mean CC map may be regarded as an offset from which the CC maps of each individual stimulus modality deviate (Fig. 2B). Comparing CC of painful heat with mildly painful electrical stimulation shows very similar patterns that highly classify for both conditions, but the orchestration of those patterns (i.e., how they vary from the offset) differs substantially. Particularly in insular (74-78) and opercular regions (42-48), the weighting was even inverted. Since some of these areas were positioned within GS(∩), we masked all individual z-maps with GS(∩) and calculated the area (AUC) under the receiver operator curve (ROC) for painful heat versus other salient stimuli. We found an AUC of 0.9 and higher for painful heat when only considering domain-general areas in GS(∩).

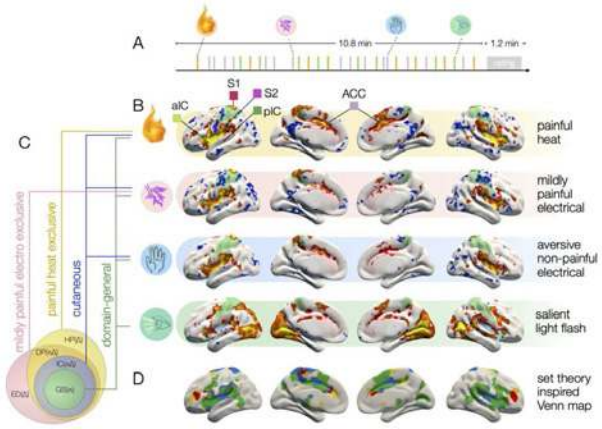

Fig. 1. **A**. Stimulation design. **B**. Functional networks formed in response to each stimulus modality. **C**,**D**. Set-theory-inspired intersection across modalities. Note domain-general functional core GS(∩) in green intersects across all stimuli.

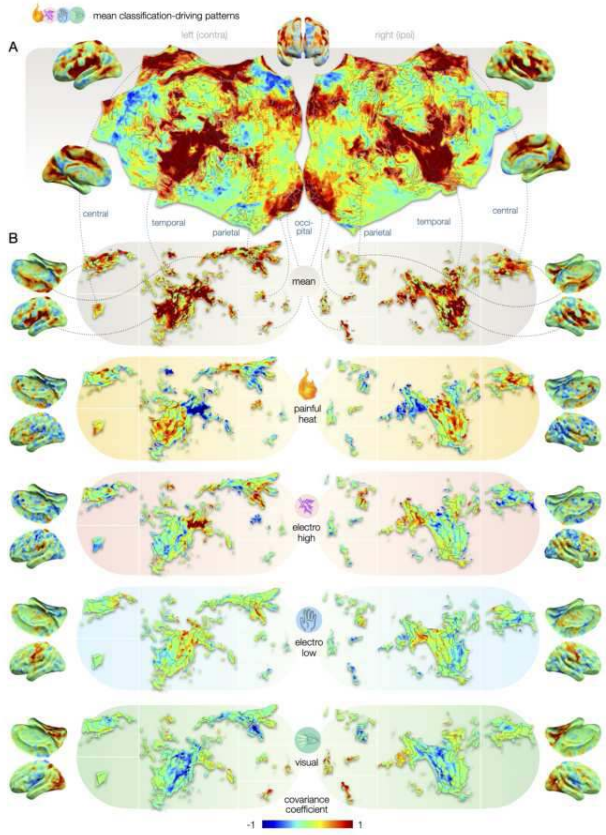

Fig. 2. Orchestration of functional networks across stimuli. CC maps display the classification strength for each voxel. **A**. Mean CC map reveals patterns that classify for all stimuli. **B**. Differences across stimuli reveal voxels classifying for specific modalities.

Conclusions: By combination of a set theory inspired intersection analysis of mass-univariate and multivariate analyses of painful versus non-painful salient fMRI data at 7T, we dissected the functional architecture of pain. Its domain-general functional core GS(∩) displays unique connectivity patterns for specific pain modalities and salient non-painful stimuli. GS(∩) exhibits great similarity to the recently introduced allostatic-interoceptive brain system3. This work deepens the understanding of pain-specific activity and its underlying mechanisms, operating upon an evolutionary well-conserved domain-general machinery for survival.

References

1. Lee et al. (2020), 'Distinguishing pain from nociception, salience, and arousal: How autonomic nervous system activity can improve neuroimaging tests of specificity', Arch Neurol, 204:1053-8119; [2] Jabakhanji et al. (2022), 'Limits of decoding mental states with fMRI', Cortex, 149: 101-122; [3] Katsumi et al. (2022), 'Allostasis as a core feature of hierarchical gradients in the human brain ', Network Neuroscience, 6 (4): 1010–1031.

Poster No 2350

Longitudinal BOLD variability change coincides with executive function change

Tzu-Chen Lung[1], Ekarin Pongpipat[1], Karen Rodrigue[1], Kristen Kennedy[1]

[1]*The University of Texas at Dallas, Dallas, TX*

Introduction: Variability in the fluctuations of the brain's functional activity has become a sensitive metric for explaining age-related cognitive performance[2,3]. Blood-oxygen-level-dependent (BOLD) variability decreases with increasing task demands and advanced age[7]. Most studies interpret BOLD variability as the dynamic range of the brain resources or coherence between regions[2,3]. However, our previous study showed the opposite result of greater BOLD variability associated with older age and worse performance[1]. One possible factor that could explain these divergent findings is the regions/networks utilized to retrieve BOLD variability signals[5]. Additionally, a recent longitudinal study on resting state BOLD variability indicated both cortical and subcortical contribution, with BOLD variability loss associated with loss of cognition. However, how BOLD variability and cognition may longitudinally change together during a task paradigm are still unknown. The current study explored BOLD variability change during an n-back paradigm over a period of 4-years, and examined how changes in BOLD variability were linked to age and cognition changes utilizing the behavioral partial least squares (PLS) method[6].

Methods: Participants included 87 healthy adults aged 20-86 yrs at baseline who returned for follow-up assessment. The mean square of successive differences (MSSD) was calculated as the proxy of BOLD variability. Participants' cognitive performance was assessed via 3 out-of-scanner tasks: fluid intelligence (Cattell culture fair intelligence test, CFIT), switching and inhibition (Delis-Kaplan executive function system, DKEFS) scores, and processing speed (digit symbol substitution task); and one in-scanner task: updating (mean accuracy on the n-back task). All change metrics from BOLD variability and cognition were calculated as Time 2 minus Time 1, and partialed out baseline age before the PLS analysis. Significance of the latent variable from the PLS analysis was assessed via 1000 permutations followed by 1000 bootstraps. The whole-brain bootstrap ratios (BSR; each voxel's weight/bootstrapped standard error) were thresholded at values of ±3. Each of the cognitive change scores were then correlated with the latent brain score, and the significance of the correlations were determined by 95% confidence intervals.

Results: PLS results indicated one significant latent component. The whole-brain, BSR-thresholded map of the first component resulted in widespread cortical and subcortical areas involving lingual gyrus, cingulate, cerebellum, superior frontal, pre/post central gyrus, and thalamus (Figure 1). The latent brain score was positively correlated with the latent behavioral score ($r(85) = 0.37$, $p < .001$). However, over time, changes in cognition per se indicated both positive and negative significant associations with the latent brain score of changes in BOLD MSSD. Specifically, increased BOLD variability was associated with better switching and inhibition performance, and worse updating and processing speed performance (Figure 2).

Conclusions: The current study explored longitudinal changes in task-based BOLD variability and cognition using PLS. By correlating the change in BOLD variability with change in age and cognition, widespread cortical and subcortical regions demonstrated significant change-change associations. Partially consistent with the previous longitudinal study[4], loss of switching and inhibition was associated with BOLD variability loss. Additionally, over time, loss of updating and processing speed with increasing BOLD variability was found, which supports our previous argument that increased BOLD variability might be a detrimental effect of aging[1]. These findings reveal the possibility that BOLD variability could be both beneficial and detrimental to aging, depending on the type of cognitive resources needed.

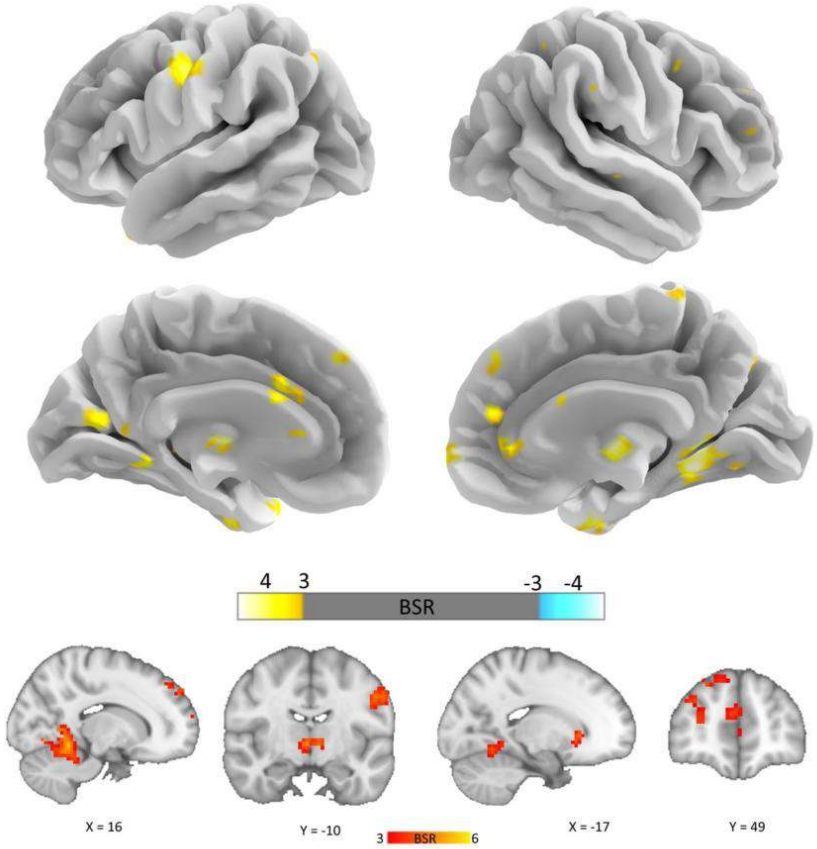

Figure 1. Brain regions showing significant positive association between 4-year change of $MSSD_{BOLD}$ & change in cognition. Increased BOLD MSSD in widespread cortical and subcortical regions was associated with increased switching and inhibition scores, and decrease of updating scores and processing speed. Figure shows brain regions with BSR > 3, and the brain slices show those with voxel size > 50 including bilateral lingual gyrus, cerebellum, cingulate, frontal pole, right superior frontal gyrus, left precentral gyrus, left postcentral gyrus, bilateral thalamus, and left caudate & putamen. None of the negative BSR voxel survived BSR < -3 threshold. BSR: bootstrap ratios.

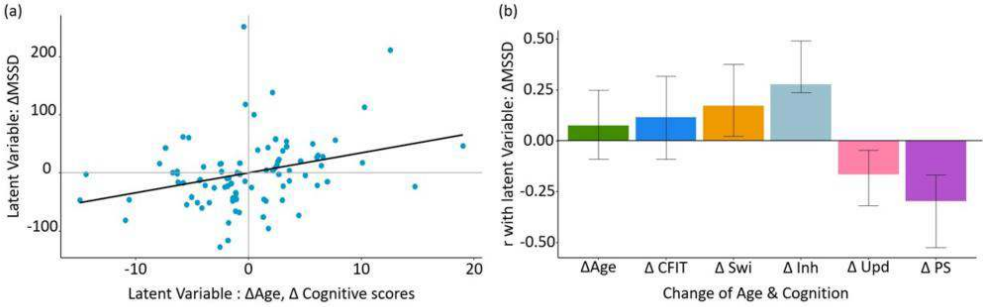

Figure 2. Behavioral PLS result showing association between 4-year change of $MSSD_{BOLD}$ & change of age and cognition. (a) In general, increased latent brain score (latent change of MSSD) was associated with increased behavior score (change of age and cognitive scores), $r(85) = 0.37$, $p < .001$. (b) Each bar represents the Pearson correlation between brain latent variable and each change score. Error bar shows bootstrap 95% CIs. Swi: switching, Inh: inhibition, Upd: updating, PS: processing speed.

References

1. Boylan, M.A. (2021), 'Greater BOLD Variability is Associated With Poorer Cognitive Function in an Adult Lifespan Sample', Cerebral Cortex, 31(1): p. 562-574.
2. Garrett, D.D. (2011), 'Moment-to-moment signal variability in the human brain can inform models of stochastic facilitation now', Nature Reviews Neuroscience,12(10).
3. Garrett, D.D. (2013), 'Moment-to-moment brain signal variability: A next frontier in human brain mapping?', Neuroscience and Biobehavioral Reviews, 37(4): p. 610-624.
4. Garrett, D.D. (2021), 'Lost Dynamics and the Dynamics of Loss: Longitudinal Compression of Brain Signal Variability is Coupled with Declines in Functional Integration and Cognitive Performance', Cerebral Cortex, 31(11): p. 5239-5252.
5. Goodman, Z.T. (2023), 'Brain Signal Variability and Executive Functions Across the Lifespan', Network Neuroscience, 2023: p. 1-36.
6. McIntosh, A.R. (2004), 'Partial least squares analysis of neuroimaging data: applications and advances', Neuroimage, 23: p. S250-S263.
7. Rieck, J.R. (2022), 'Reduced modulation of BOLD variability as a function of cognitive load in healthy aging', Neurobiology of Aging, 112: p. 215-230.

Poster No 2351

Functional Brain Networks Underlying Working Memory Deficit in Schizophrenia Detectable by Task fMRI

Tyrone Ly[1], Linda Chen[1], Todd Woodward[1]

[1]*University of British Columbia, Vancouver, British Columbia*

Introduction: In cognitive neuroscience, fMRI investigation of the working memory was most often acquired through analyzing the neural bases of behavior in performance of the Sternberg task. Originally developed by Robert J. Sternberg in 1966, this is a choice reaction time task that requires the usage of working memory. Though this has been a prominent research area for decades, the field has yet to arrive at a consensus for a set of functional brain networks. In the present study, we utilized a version of the task called Sternberg Item Recognition Paradigm to identify and characterize brain networks which demonstrated distinct patterns of activation during participants' performances of this task. We hypothesized that the Working Memory Big Five set of task-based functional brain networks will be detectable upon analysis of fMRI data for the performance of the Sternberg task: Response, Focus on Visual Features, Initiation, Internal Attention, and Default Mode Networks.

Methods: Thanks to open science, the fMRI data used in this project was obtained from the Function Biomedical Informatics Research Network phase II multi-site study, which is a publicly available database comprised of fMRI data collected at six different study sites across the US. Subjects included 54 healthy participants and 54 patients with schizophrenia or schizoaffective disorder who performed the Sternberg task while undergoing fMRI scanning sessions. For this task, subjects were instructed to memorize a set of one, three, or five digits (numbers between 0 and 9) in the beginning. After a short break, they would be presented with a series of digits and asked to indicate whether they have seen those before. Constrained Principal Component Analysis for fMRI (fMRI-CPCA) will be applied on the data to extract and characterize functional brain networks that emerged during task performance and their associated hemodynamic profiles.

Results: Upon fMRI-CPCA analysis, four functional brain networks were found to have been elicited during participants' performance of the Sternberg task. They included Auditory Attention for Response Network together with three of the Big Five which are Response, Initiation, and Traditional Default Mode Networks. Discovery of the Auditory Attention for Response network was an unexpected and surprising outcome. However, through further examination, we determined that this finding was reasonable because this network underwent deactivation when participants had to shift focus away from auditory stimuli and towards visual details of digits on the screen. All four networks demonstrated load dependency, meaning the more digits subjects had to memorized, the higher the response in their brain network activity. Initiation and Traditional Default Mode Networks both showed increased activity in schizophrenia patients compared to healthy participants, indicating their dysfunction may underlie cognitive impairments in schizophrenia. Finally, analyzing the features of the extracted Response network yielded that it was potentially merged with the Internal Attention network, which has been a common finding in our previous studies.

Conclusions: From these preliminary results, future research will investigate the effects of individual differences in demographics, personality, behavior, cognitive performance, and symptom of mental illnesses on the observed patterns of network activation. Additionally, since we were able to obtain a reasonably large sample of healthy subjects, further analyses of their data will serve as important implications for broadening our understanding about working memory deficits in several other neurological diseases. Hence, biological underpinnings in these diseases can be identified so that effective treatments can be developed to specifically target the impaired brain networks and move them to a healthier state.

References

1. Glover GH (2011). Overview of functional magnetic resonance imaging. Neurosurgery Clinics of North America 2011;22:133–9. doi:10.1016/j.nec.11.001.
2. Poldrack RA (2011). The future of fmri in Cognitive Neuroscience. NeuroImage 2012;62:1216–20. doi:10.1016/j.neuroimage.08.007.
3. Whitman JC, Metzak PD, Lavigne KM, Woodward TS (2013). Functional connectivity in a frontoparietal network involving the dorsal anterior cingulate cortex underlies decisions to accept a hypothesis. Neuropsychologia. 51:1132-1141. doi 10.1016/j.neuropsychologia.2013.02.016.
4. Klabes J, Babilon S, Zandi B, Khanh TQ (2021). The Sternberg Paradigm: Correcting encoding latencies in visual and auditory test designs. Vision; 5:21. doi:10.3390/vision5020021.
5. Sanford N, Whitman JC, Woodward TS (2020). Task-merging for finer separation of functional brain networks in working memory. Cortex;125:246–71. doi:10.1016/j.cortex.2019.12.014.
6. Sanford N, Woodward TS (2021). Functional delineation of prefrontal networks underlying working memory in schizophrenia: A cross-data-set examination. Journal of Cognitive Neuroscience;33:1880–908. doi:10.1162/jocn_a_01726.
7. Keator, D. B., Van Erp, T. G., Turner, J. A., Glover, G. H., Mueller, B. A., Liu, T. T., . . . Potkin, S. G. (2016). The function Biomedical Informatics Research Network Data Repository. NeuroImage, 124, 1074-1079. doi: 10.1016/j.neuroimage.2015.09.003

8. Hunter MA, Takane Y (2002). Constrained Principal Component Analysis: Various Applications. Journal of Educational and Behavioral Statistics;27:105–45. doi:10.3102/10769986027002105.
9. Takane Y, Shibayama T (1991). Principal component analysis with external information on both subjects and variables. Psychometrika;56:97–120. doi:10.1007/bf02294589.
10. Woodward TS, Feredoes E, Metzak PD, Takane Y, Manoach DS (2012). Epoch-specific functional networks involved in working memory. NeuroImage 2013;65:529–39. doi:10.1016/j.neuroimage.09.070.

Poster No 2352

Changes in cross-hierarchical propagating waves along the mode of connectivity-behavior covariation

Nattaporn Plub-In[1], Xiao Liu[1]

[1]The Pennsylvania State University, State College, PA

Introduction: The link between behavior and brain function and structure is an important topic in neuroscience. A data-driven analysis on large-scale neuroimaging data has identified a positive-negative mode of population covariation linking resting-state fMRI (rsfMRI) connectivity to behavioral and demographic measures[1]. This mode was subsequently found to be associated with changes in cortical thickness[2]. Along this mode direction, subjects' behavioral measures shift from negative to positive traits, whereas changes in imaging measures exhibit a cross-hierarchy contrast: both functional connectivity and cortical thickness increase in higher-order cognitive networks, mostly the default mode network (DMN), but decrease in lower-order sensory/motor (SM) areas[2]. Increasing evidence suggests rsfMRI connectivity arises from infra-slow spatiotemporal dynamics[3,4,5]. A specific form of such dynamics is infra-slow waves that propagate along the cortical hierarchy gradient between the lower-order SM areas and higher-order DMN. It thus raised an interesting question whether these cross-hierarchy propagating waves are systematically modulated along the connectivity-behavior mode and contribute to the hierarchy-dependent connectivity changes. Here we analyze a large-scale neuroimage dataset to address this question.

Methods: We used data of 818 subjects from the Human Connectome Project (HCP)[6]. We ran a canonical correlation analysis (CCA) between resting-state functional connectivity and 129 behavioral and demographic measures to derive the connectivity-behavior mode (1st canonical variate pair). Following a previous study[4], we detected and counted propagating waves along the cortical hierarchy gradient, described by the principal gradient (PG) direction[7]. We derived the patterns of both top-down (DMN-to-SM) and bottom-up (SM-to-DMN) propagations for each subject and then correlated them with the CCA score.

Results: Consist with the previous studies[3], our CCA analysis unveiled a significant mode ($r = 0.72$, $p = 1.7\times10\text{-}33$) that links the connectivity metrics to behavioral/demographic measures (Fig. 1A and 1B). The top behavioral measures positively correlated with this CCA mode are exclusively positive traits whereas those showing top negative correlations are all negative attributes (Fig. 1C). The number of the bottom-up (SM-to-DMN) propagations is significant correlated ($r = 0.16$, $p = 8.3\times10\text{-}6$) with the CCA scores, suggesting subjects with more positive traits tend to have more bottom-up propagations (Fig. 2A). This association was not observed for the top-down (DMN-to-SM) propagations ($r = -0.01$, $p = 0.86$). We divided the subjects into the high CCA (top 25%, N = 204), medium CCA (middle 50%, N = 410), and low CCA (bottom 25%, N = 204) groups. The high CCA group, which have more positive behavioral traits, has significantly more (high vs. medium, $p = 3.9\times10\text{-}3$; high vs. low, $p = 4.5\times10\text{-}4$) bottom-up propagations (Fig. 2B). The cross-hierarchy propagating wave patterns are modulated along the CCA mode direction. Correlations of the individuals' propagation pattern with their CCA scores showed significant values predominantly in the high-order brain regions with higher PG scores. This effect is more pronounced in the bottom-up propagations but also evident for the top-down propagations (Fig. 2D and 2G). A comparison of propagation patterns between the high CCA and low CCA groups found the same differences in the higher-order brain areas (Fig. 2E and 2H).

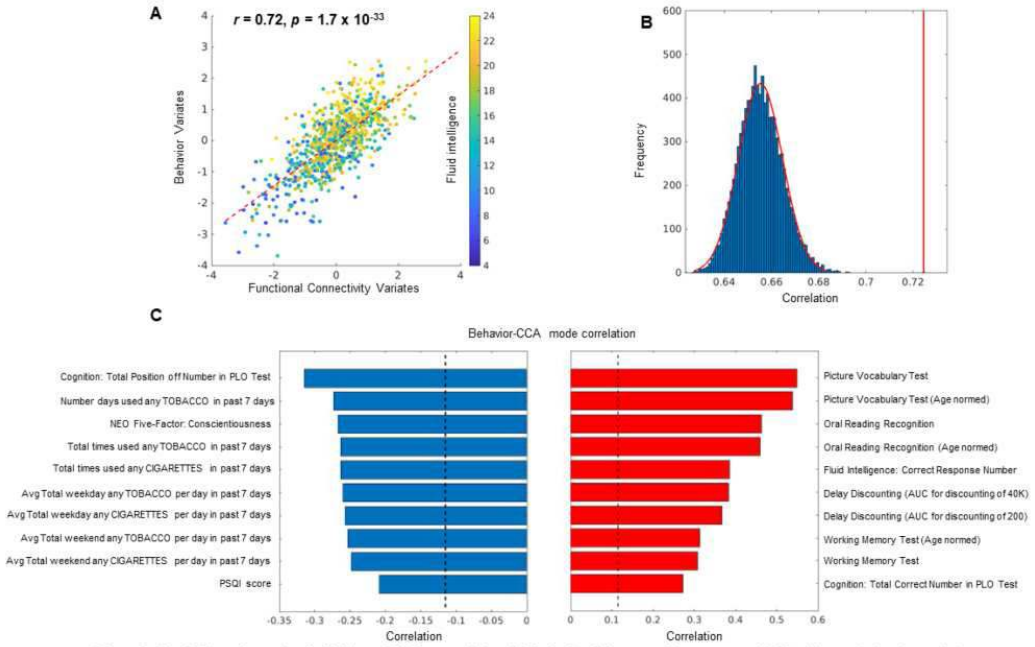

Figure 1. The CCA mode maximally linking rsfMRI connectivity with behavioral/demographic measures. (A) The 1st canonical variate pair (r = 0.72, p = 1.7 × 10^{-33}) as the CCA mode between rsfMRI connectivity and behavioral/demographic measures. Each dot represent a subject and its color encode his/her fluid intelligence score, one behavioral measure showing strong positive correlation with the CCA mode. (B) This mode correlation (the red vertical line) is compared to a null distribution of CCA correlations with permuting subject IDs. (C) Behavioral measures showing the strongest negative (left) and positive (right) correlation with the CCA mode.

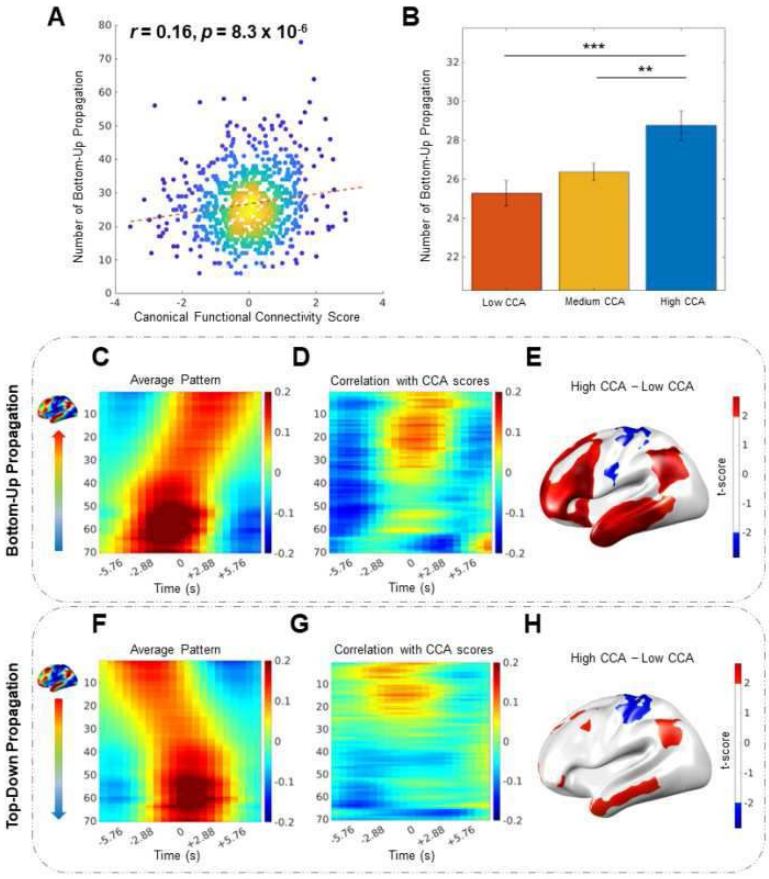

Figure 2. Modulation of propagating wave pattern along the connectivity-behavior CCA mode. (A) The number of bottom-up propagations is significantly correlated (r = 0.16, p = 8.3 × 10^{-6}) with functional connectivity CCA scores. (B) The number of bottom-up propagation exhibits significant differences (high vs. medium, p = 3.9 × 10^{-3}; high vs. low, p = 4.5 × 10^{-4}) in three groups of subjects with different CCA scores. Error bars represent the standard error of the mean (SEM). The average propagation pattern along the principal gradient (PG) shown in the time-position graph for both bottom-up (C) and top-down (F). Correlations between individuals' propagation patterns and their CCA scores (D and G) show significant values in the high-order regions. The propagations of the high-CCA group also showed stronger activations in the higher-order DMN regions than those of the low-CCA group, and their differences at the propagation center (t =0) are shown in (G) and (H).

Conclusions: The cross-hierarchy propagating waves are significantly modulated along the mode direction maximally linking functional connectivity and behavioral measures. Subjects exhibiting more positive traits tend to have more frequency bottom-up propagations, which involve higher-order bran networks more significantly. These findings provide insight into the link between resting-state infra-slow brain dynamics and human behaviors.

References

1. Smith, S. M. (2015), 'A positive-negative mode of population covariation links brain connectivity, demographics and behavior', Nature neuroscience, vol. 18, no. 11, pp. 1565-1567
2. Han, F. (2020), 'Neuroimaging contrast across the cortical hierarchy is the feature maximally linked to behavior and demographics', Neuroimage, vol. 215, pp. 116853
3. Abbas, A. (2019), 'Quasi-periodic patterns contribute to functional connectivity in the brain', Neuroimage, vol. 191, pp. 193-204
4. Gu, Y. (2021), 'Brain activity fluctuations propagate as waves traversing the cortical hierarchy', Cerebral cortex, vol. 31, no. 9, pp. 3986-4005 2
5. Mitra, A. (2015), 'Lag threads organize the brain's intrinsic activity', Proceedings of the National Academy of Sciences, vol. 112, no. 17, pp. E2235-E2244
6. Van Essen, D. C. (2013), 'The WU-Minn human connectome project: an overview', Neuroimage, vol. 80, pp. 62-79
7. Margulies, D. S. (2016), 'Situating the default-mode network along a principal gradient of macroscale cortical organization', Proceedings of the National Academy of Sciences, vol. 113, no. 44, pp. 12574-12579

Poster No 2353

Atypical joint density distribution of resting state dynamic spatial brain networks in Schizophrenia

Krishna Pusuluri[1], Armin Iraji[2], Vince Calhoun[3]

[1]Georgia State University, Dunwoody, GA, [2]Georgia State University, Atlanta, GA, [3]GSU/GATech/Emory, Decatur, GA

Introduction: Resting state functional magnetic resonance imaging (rsfMRI) studies in schizophrenia (SZ) usually focus on spatially static networks over the course of a scan. Recent studies addressed the spatial expansion or shrinkage (Iraji et al. 2020) and variations in coupling between spatially dynamic networks via a model of the spatial chronnectome (Iraji et al. 2019). In this work, we investigated spatially dynamic brain networks, their voxel-wise changes over time, and the joint density distributions of pairs of networks using 2D histograms, clustered across time windows. 2D histograms allow for the comparison of two networks, counting the occurrence of various combinations of voxel-level intensities/activities. We found that several clusters of 2D histograms across brain network pairs show significant group differences in occupancy time between healthy controls (CN) and SZ group.

Methods: rsfMRI data for 508 subjects with 315 controls (CN) and 193 SZ patients were obtained from three datasets – FBIRN (Damaraju et al. 2014), COBRE (Aine et al. 2017), and MPRC (Adhikari et al. 2019) – and preprocessed using SPM12 toolbox as described in (Iraji et al. 2022). We performed spatial independent component analysis (sICA) at the group level using the GIFT software package (Iraji et al. 2021) and identified 14 large-scale brain networks. The prior networks from group-level analysis were used as a reference for a spatially constrained ICA (integrated in GIFT as Multivariate Objective Optimization ICA with Reference) (Du et al. 2013) for each subject across sliding windows to ensure the correspondence of brain networks across subjects and time windows (window size is 30 times TR, the repetition time). For each brain network pair (see Fig.1), 2D histograms were computed for z-scored voxel-level activity at each window for each subject and clustered across all the subjects and windows using k-means algorithm (after subtracting the overall mean 2D histogram from the window-level data).

Results: Clustering results reveal changes in the joint density heat maps for several network pairs across subjects and time windows. We identified several clusters of 2D histograms that show significant group differences (with 2-sample t-tests) in subject-wise cluster occupancy time (defined as the ratio given by the number of windows per subject that fall within the cluster, divided by the total number of windows), revealing atypical joint density distributions of dynamic spatial brain network pairs in Schizophrenia. For 91 possible network pairs chosen across 14 brain networks, with 10 k-means clusters per network pair, we find that 290 of the clusters (out of a maximum of 91*10=910) show significant group differences after a 5% false discovery rate correction. A few of those clusters for the network pair cerebellar (CER) vs. secondary somatomotor (MTR-S) are shown in Fig.1.

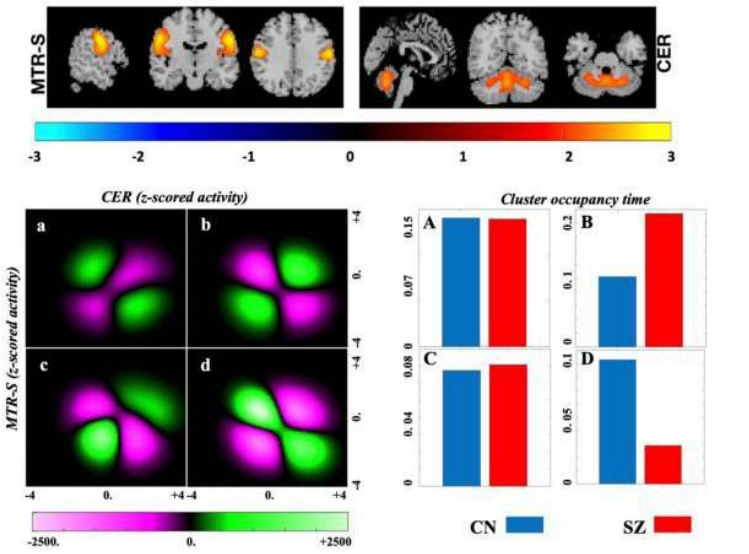

*Fig.1. (Top) Mean maps for secondary somatomotor (MTR-S) and cerebellar (CER) networks are shown along three orthogonal cross sections – sagittal, coronal and transverse – near the voxel with highest activity, with anatomical images in the background. Four example 2D histogram clusters for CER vs MTR-S are shown **(a-d)**, along with the corresponding cluster occupancy time (ratio) for CN and SZ **(A-D)**. Clusters shown in **(b/B)** and **(d/D)** show significant group differences in occupancy between CN and SZ, while those in **(a/A)** and **(c/C)** do not. 2-sample t-test p-values: (a) 0.932 (b) <10e-10 (c) 0.787 (d) <10e-6*

Conclusions: This work underscores the importance of studying spatiotemporally dynamic behaviors within/across brain networks and could lead to the development of novel biomarkers for brain function and dysfunction.

References

1. Adhikari, Bhim M., et al. "Functional network connectivity impairments and core cognitive deficits in schizophrenia." Human brain mapping 40.16 (2019): 4593-4605.
2. Aine, C. J., et al. "Multimodal neuroimaging in schizophrenia: description and dissemination." Neuroinformatics 15.4 (2017): 343-364.
3. Damaraju, Eswar, et al. "Dynamic functional connectivity analysis reveals transient states of dysconnectivity in schizophrenia." NeuroImage: Clinical 5 (2014): 298-308.
4. Du, Yuhui, and Yong Fan. "Group information guided ICA for fMRI data analysis." Neuroimage 69 (2013): 157-197.
5. Iraji, Armin, et al. "The spatial chronnectome reveals a dynamic interplay between functional segregation and integration." Human brain mapping 40.10 (2019): 3058-3077.
6. Iraji, Armin, et al. "Space: a missing piece of the dynamic puzzle." Trends in Cognitive Sciences 24.2 (2020):135-149.
7. Iraji, Armin, et al. "Tools of the trade: estimating time-varying connectivity patterns from fMRI data." Social Cognitive and Affective Neuroscience 16.8 (2021): 849-874
8. Iraji, Armin, et al. "Moving beyond the 'CAP'of the Iceberg: Intrinsic connectivity networks in fMRI are continuously engaging and overlapping." NeuroImage 251 (2022): 119013.

Poster No 2354

Connectome 2.0: Performance evaluation and initial in vivo human brain diffusion MRI results

Gabriel Ramos Llorden[1,2], Peter Dietz[3], Mathias Davids[1,2], Hong-Hsi Lee[1,2], Yixin Ma[1,2], Mirsad Mahmutovic[4], Alina Scholz[4], Hansol Lee[1,2], Chiara Maffei[1,2], Anastasia Yendiki[1,2], Berkin Bilgic[1,2], John E. Kirsch[1,2], Daniel J. Park[1], Bryan Clifford[5], Wei-Ching Lo[5], Stefan Stocker[3], Jasmine Fischer[3], Gudrun Ruyters[3], Manuela Roesler[3], Elmar Rummert[3], Andreas Krug[3], Andreas Potthast[3], Thomas Benner[3], Rebecca Ramb[3], Peter Basser[6], Thomas Witzel[7], Lawrence L. Wald[1,2], Bruce Rosen[1,2], Boris Keil[4,8], Susie Huang[1,2]

[1]Athinoula A. Martinos Center for Biomedical Imaging, Massachusetts General Hospital, Charlestown, MA, [2]Harvard Medical School, Boston, MA, [3]Siemens Healthineers, Erlangen, Germany, [4]Institute of Medical Physics and Radiation Protection, Mittelhessen University of Applied Science, Giessen, Germany, [5]Siemens Medical Solutions USA, Boston, MA, [6]Eunice Kennedy Shriver National Institute of Child Health and Human Development, NIH, Bethesda, Maryland, [7]Q Bio Inc, San Carlos, CA, [8]Department of Diagnostic and Interventional Radiology, University Hospital Marburg, Philipps University of Marburg, Marburg, Germany

Introduction: We present the Connectome 2.0 scanner[1], developed for next-generation human connectomics and microstructure imaging of human brain circuits across scales. Here, we report on the hardware's design, construction, and evaluation, and initial results for in vivo human brain diffusion MRI.

Methods: Scanner and gradient coil design The Connectome 2.0 system (Fig. 1a) (MAGNETOM Connectom.X, Siemens Healthineers, Erlangen, Germany) was designed on a 3T scanner platform and targeted in vivo human brain imaging using a maximum gradient strength (Gmax) of 500 mT/m and maximum slew rate (SRmax) of 600 T/m/s. The gradient coil is designed as an asymmetric head gradient following the stepped geometry of the Siemens 7T Impulse head gradient coil (Gmax=200 mT/m, SRmax=900 T/m/s),[2] but modified to include double-primary layers in all axes to achieve Gmax=500 mT/m. The gradient coil design was iterated upon using peripheral nerve stimulation (PNS) modeling to raise the PNS thresholds and maximize the usable gradient parameter space.[3,4] Radiofrequency (RF) coils design A 72-channel in vivo head receive coil[5] and a 64-channel ex vivo whole brain coil[6] were designed and constructed for high-sensitivity diffusion MRI acquisitions. Each receive array was outfitted with its own dedicated local transmit coil and 16-channel 19F clip-on field probe system for concurrent field monitoring.[7]

Results: Gradient system: (a) Geometry: The stepped design with shoulder cutouts and outer gradient coil diameter of 81 cm provides access for subjects of varying sizes. The inner gradient coil diameter is 44 cm, and the free bore diameter is 40 cm. (b) Gradient performance: The scanner achieves Gmax=500 mT/m and SRmax=600 T/m/s driven by 2 GPAs (1200A/2250V) per axis compared to the 4 GPAs (900A/2000V) of the original Connectome scanner.[8] The gradient coil has higher efficiency (0.42 mT/m/A) and lower inductance per axis than the original Connectome gradient coil (X=2250, Y=2450, Z=1800μH) with direct current resistance of 0.28 Ω. (c) Non-linearity: Maximum field linearity deviation in a 20cm sphere is X=6.7%, Y=8.2%, and Z=11.7%. (d) Cooling: The gradient coil incorporates direct liquid cooling technology to maximize thermal energy transfer and dissipation. (e) Active E-shims include 1st and 2nd-order harmonics. The gradient achieves 2.4-4.2x greater PNS thresholds than the Connectome 1.0 gradient coil. RF coils The 72-channel in vivo coil provides a 1.5x improvement in SNR in the peripheral regions of the brain compared to a standard 32-channel head coil. The 64-channel ex vivo coil outperforms the 72-channel in vivo coil by 1.73x in average SNR. Improvements in SNR for high b-value diffusion imaging: The stronger gradients of the Connectome 2.0 scanner enable significant reductions in diffusion time Δ and pulse width δ compared to Connectome 1.0, resulting in shorter TE by up to 50% (Fig. 1b). SNR gains are at least 4-fold compared to a state-of-the-art clinical scanner and up to double compared to Connectome 1.0 (Fig. 1c) at high b-values (Fig. 1d). In vivo human brain imaging High-resolution tractography was performed on a healthy volunteer (34F) on the Connectome 2.0 scanner using Connectome 2.0 and Connectome 1.0 protocols (see bottom of Fig. 2). Whole-brain tractograms were generated, seeding local probabilistic tractography in every voxel within a white matter mask.[9] SNR of Connectome 2.0 enables the delineation of fine fiber tracts like the mammillo-tegmental tract, which could not be seen with a matched protocol using Connectome 1.0 parameters.[10]

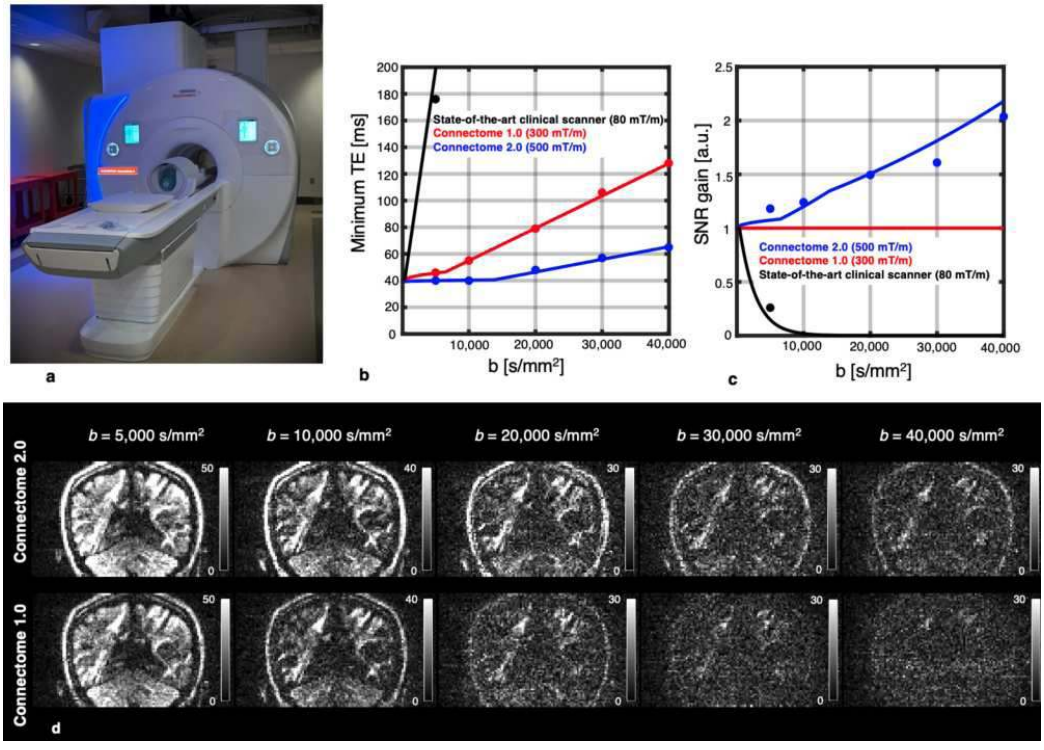

Fig. 1. a, Connectome 2.0 at MGH with the 72-channel in vivo coil. b, Minimum achievable TE at a given b-value. c, SNR gain with respect to Connectome 1.0 at a given b-value. d, In vivo DWIs at high-b value.

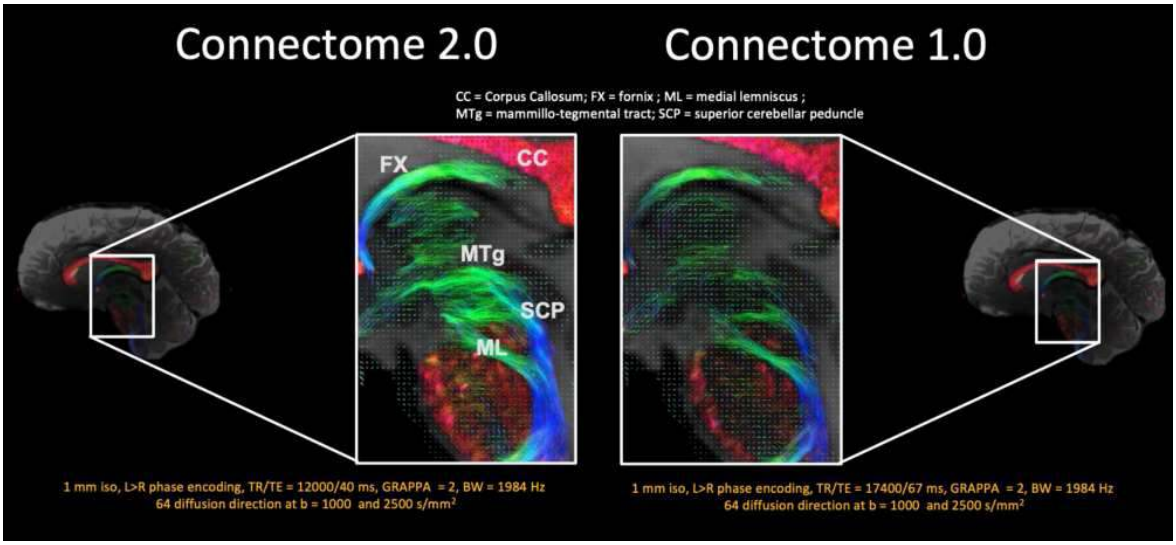

Fig. 2. High-spatial resolution diffusion MRI acquired at 1 mm isotropic resolution at b=1000 and 2500 s/mm2. Closeups of the midline sagittal view showing diencephalic and brainstem pathways.

Conclusions: The Connectome 2.0 scanner equipped with Gmax=500 mT/m and SRmax=600 T/m/s and the latest RF coil technology achieves unprecedented sensitivity and resolution for mesoscale diffusion MRI in the living human brain.

References

1. Davids M. (2023), 'Peripheral nerve stimulation informed design of a high-performance asymmetric head gradient coil', Magnetic Resonance in Medicine (2023) Aug, 90(2):784-801
2. Davids M. (2020), 'Optimization of MRI gradient coils with explicit peripheral nerve stimulation constraints', IEEE Transactions on Medical Imaging 40.1 (2020): 129-142.
3. Feinberg D.A. (2023), 'Next-generation MRI scanner designed for ultra-high-resolution human brain imaging at 7 Tesla', Nature Methods https://doi.org/10.1038/s41592-023-02068-7
4. Maffei C. (2024), 'Visualization of fine white matter bundles in the living human brain with diffusion MRI using 500 mT/m gradient strength', Submitted to the 2024 Annual Meeting of the International Society for Magnetic Resonance in Medicine.
5. Mahmutovic M. (2024), 'A 72-channel Head Coil with an Integrated 16-Channel Field Camera for the Connectome 2.0 Scanner', Submitted to the 2024 Annual Meeting of the International Society for Magnetic Resonance in Medicine.
6. Huang S.Y (2021), 'Connectome 2.0: Developing the next-generation ultra-high gradient strength human MRI scanner for bridging studies of the micro-, meso- and macro-connectome', Neuroimage. 2021 Nov;243:118530.
7. Scholz A. (2023), 'Design of a 64-channel ex vivo Brain Rx Array Coil with field monitoring and temperature control for DWI at 3T', Proceedings of the International Society of Magnetic Resonance in Medicine (2023) 0215
8. Setsompop K. (2013), 'Pushing the limits of in vivo diffusion MRI for the Human Connectome Project', Neuroimage 80 (2013): 220-233.
9. Tournier J.-D. (2010), 'Improved probabilistic streamlines tractography by 2nd order integration over fibre orientation distributions', Proceedings of the International Society of Magnetic Resonance in Medicine 18, (2010) 1670
10. Wilm B.J. (2015), 'Diffusion MRI with concurrent magnetic field monitoring', Magnetic Resonance in Medicine 2015;74(4):925-933. doi:10.1002/MRM.25827

Poster No 2355

Jointly Learning in *x-q* space for Fiber ODF Estimation

Chengdong Deng[1], Haotian Jiang[1], Jaeil Kim[2], Jiquan Ma[1], Geng Chen#[3]

[1]Department of Computer Science and Technology, Heilongjiang University, Harbin, China, [2]School of Computer Science and Engineering, Kyungpook National University, Daegu, South Korea, [3]School of Computer Science and Engineering, Northwestern Polytechnical University, Xi'an, China

Introduction: Fiber orientation distribution functions (fODFs) provide vital information for reconstructing the 3D geometric structure of brain white matter. Existing methods to predict fODFs are confronted by two inherent limitations. Firstly, the traditional methods necessitate densely sampled diffusion MRI (dMRI) data in q-space. Secondly, the deep learning methods neglect a comprehensive consideration of the x-q space information[1-3]. To address the aforementioned limitations, we propose a novel fiber orientation estimation method, called MXQ, which consists of an x-space learning model based on a 3D U-Net[4] and a q-space learning model based on spherical convolutional neural networks (SCNNs)[6-7]. Instead of considering a single domain, our joint learning framework exploits and fuses x-q space information to predict fODFs. The fusion is achieved

by a simple and effective integration module that can transform the features from two domains. Extensive experiments demonstrate that our MXQ model is effective in fODF estimation and outperforms cutting-edge models remarkably.

Methods: Our MXQ aims to improve the joint learning of x-space and q-space information through the use of a hybrid architecture consisting of a 3D U-Net and SCNNs, as illustrated in Figure 1 (a). The spatial relationship of each voxel in x-space is learned by the 3D U-Net, which is well-suited for capturing spatial correlation information, i.e.,

$$F_{\mathrm{x}} = \mathrm{MX}(A_{\mathrm{shc}}),$$

where MX represents our x-space module, which is used to learn the features of x-space Fx, and Ashc represents the input represented by spherical harmonic coefficients (SHCs). We use SCNNs to learn q-space information by mapping fODFs to spherical data, i.e.,

$$F_{\mathrm{q}} = \mathrm{MQ}(A_{\mathrm{amp}}),$$

where MQ represents our q-space module used to learn the features of q-space Fq, and Aamp denotes the spherical data transformed from Ashc. In SIF, as shown in Figure 1 (b), we fuse the x-space and q-space features by mining the commonality and individuality of two kinds of features with the channel attention components. Fianlly, the SIF module predicts the fODFs Yxq via

$$Y_{\mathrm{xq}} = \mathrm{SIF}(F_{\mathrm{x}}, F_{\mathrm{q}})$$

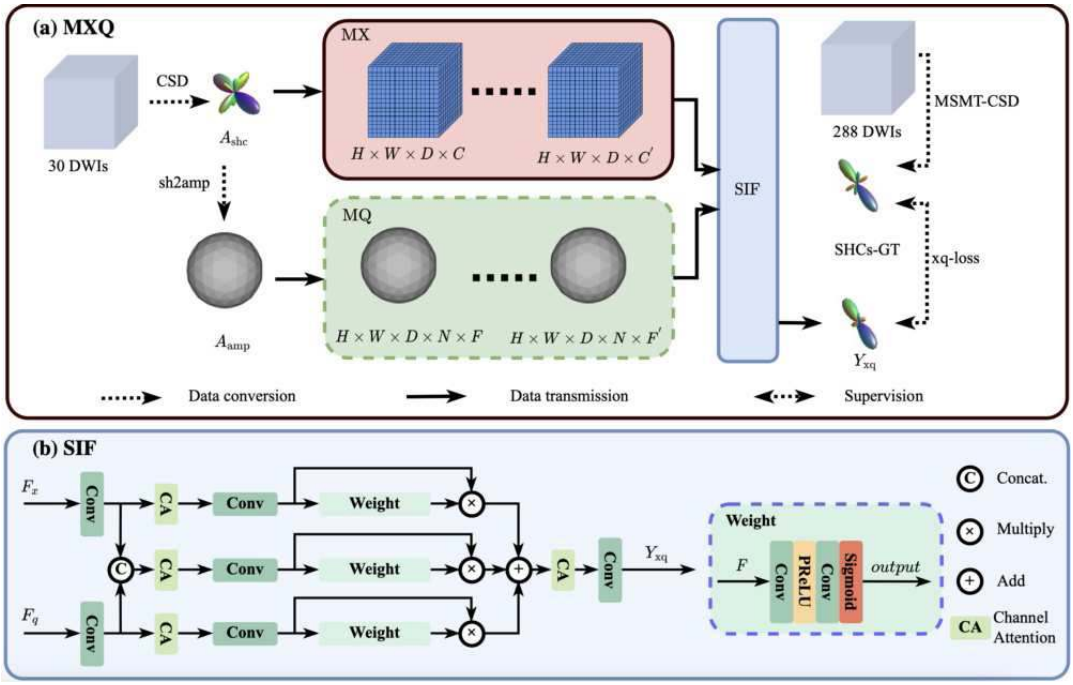

Figure 1: An Overview of our framework.

Results: Dataset: The dataset used in our experiments is from the human connectome project (HCP)[5]. We employed MSMT-CSD and the entire 270 gradient directions to compute the ground truth fODFs. To emulate data acquisition in a clinical setting, we downsampled the dMRI data by uniformly selecting 30 gradient directions at b = 1000 s/mm2. For the MX module, we set the size of input patches to 16 × 16 × 16. For the MQ module, we transformed the 45 SHCs into spherical data with 42 vertices. Experimental Results: As shown in Figure 2 (a) and (b), our MXQ provides the best ACC and MAE results. Figure 2 (c), indicate that our MXQ provides the best visualization results that are close to the ground truth. Exiting methods are capable of accurately predicting single-direction fODFs. However, when dealing with crossing fODFs, particularly those with three crossings, our MXQ demonstrates superior accuracy in comparison with existing methods.

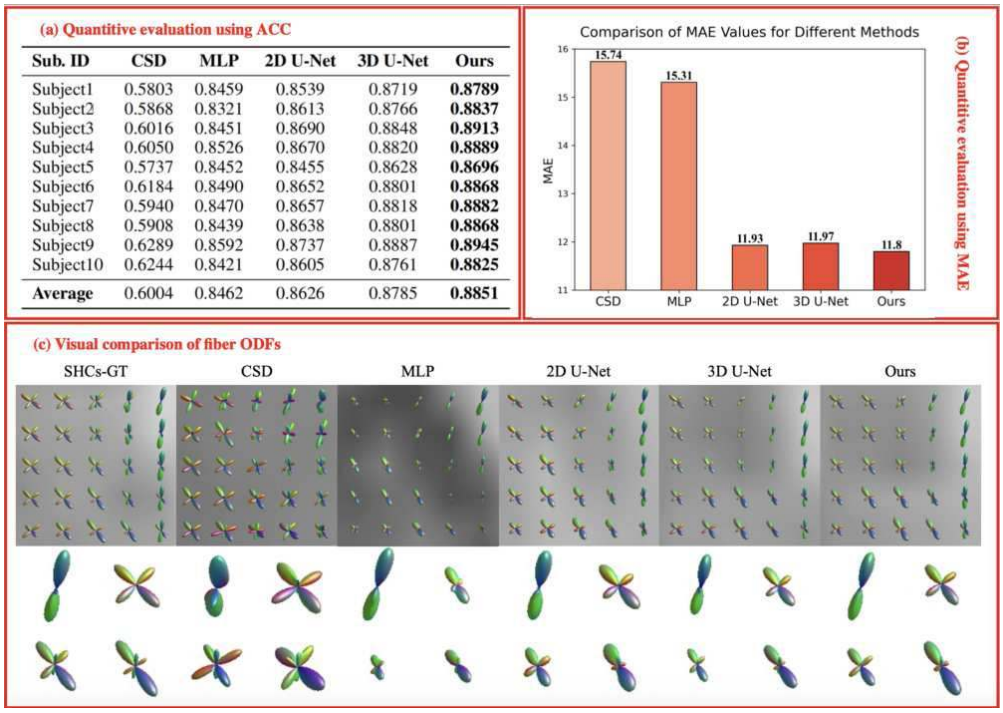

Figure 2: Quantitive and qualitative evaluation results.

Conclusions: We proposed MXQ, a deep learning-based fODF estimation model that exploits and fuses the x-q space features. Experimental results show that our MXQ outperforms existing models in terms of both quantitative and qualitative evaluations.

References

1. Jeurissen, B. (2019), 'Diffusion MRI fiber tractography of the brain', NMR in Biomedicine, 32(4): e3785.
2. Lin, Z. (2019), 'Fast learning of fiber orientation distribution function for MR tractography using convolutional neural network', Medical Physics, 46(7): 3101–3116.
3. Lucena, O. (2021), 'Enhancing the estimation of fiber orientation distributions using convolutional neural networks', Computers in Biology and Medicine, 135: 104643.
4. Ronneberger, O. (2015). 'U-Net: Convolutional networks for biomedical image segmentation'. In MICCAI 2015, Munich, Germany, October 5-9, 2015, Proceedings, Part III18, 234–241. Springer.
5. Van Essen, D. C. (2012), 'The Human Connectome Project: a data acquisition perspective'. NeuroImage, 62(4): 2222–2231.
6. Zhao, F. (2019). 'Spherical U-Net on cortical surfaces: methods and applications'. In IPMI 2019, Hong Kong, China, June 2–7, 2019, Proceedings 26, 855–866. Springer.
7. Zhao, F. (2021), 'Spherical deformable U-Net: Application to cortical surface parcellation and development prediction'. IEEE Transactions on Medical Imaging, 40(4): 1217–1228.

Poster No 2356

Associations between COVID-19 and neuroinflammation: A diffusion basis spectrum imaging study

Wei Zhang[1], Aaron Gorelik[1], Qing Wang[1], Sara Norton[1], Tmara Hershey[1], Arpana Agrawal[1], Ryan Bogdan[1], Janine Bijsterbosch[1]

[1]Washington University in St. Louis, Saint Louis, MO

Introduction: COVID-19 remains a significant international public health concern[1]. Yet, its underlying mechanisms have not been fully elucidated. Recent studies suggest that the SARS-CoV-2 infection may induce prolonged inflammation within the central nervous system, contributing to various "brain frog" symptoms[2]. However, the evidence so far primarily stems from limited small-scale case investigations[3]. To address this gap, the current study capitalized a longitudinal imaging dataset and a novel and non-invasive imaging technique to examine the associations between COVID-19 and neuroinflammation. We hypothesize that SARS-CoV-2 infection will be associated with non-invasively measured neuroinflammation markers of cellularity (indicative of increase in inflammatory cell fraction) and edema (extracellular accumulation of fluid).

Methods: This study used longitudinal data from the UK Biobank that included longitudinal neuroimaging data from a cohort of 416 individuals (Mage=58.6; n=244 female), including pre- and post-infection scans from n=224 COVID-19 cases (Mage=59.1; n=122 females). Putative neuroinflammation markers including restricted fraction (RF) indexing cellularity and hindered fraction

(HF) indexing vasogenic edema were generated using the Diffusion Basis Spectrum Imaging (DBSI) technique[4]. Regions of interest for gray matter structures were defined using FreeSurfer with automatic subcortical segmentation and Desikan-Killiany cortical atlases[5], and for white matter tracts using a probabilistic tractography atlas (JHU-ICBM-tracts[6]) with a threshold of 25%, resulting in 14 and 66 bilateral subcortical and cortical structures, as well as 20 white matter tracts. We conducted a series of linear regression analyses to model the putative neuroinflammation markers assessed after COVID-19 (i.e., at scan2) as a function of case-control membership, while accounting for the baseline neuroinflammation markers (i.e., at scan1), as well as confounding effects of sex, race, and changes in age, body mass index and smoking frequency. False discovery rate (FDR) was applied to account for multiple testing.

Results: After FDR corrections, COVID-19 was significantly associated with changes in DBSI-HF values in the pre- and post-central gyri, as well as the caudal middle frontal gyrus after FDR corrections (β's>0.3, FDR p's=0.03; Figure 1). Furthermore, a set of cortical regions and white matter tracts exhibited nominally significant associations, such as bilateral superior frontal gyrus, bilateral pars triangularis, and right cingulum bundle (β's>0.15, uncorrected p's<0.05). Conversely, COVID-19 was not associated with any changes in DBSI-RF values across all regional gray matter regions and white matter tracts apart from several trend-level associations (|β|'s>0.13, uncorrected p's<0.05; Figure 2).

Figure 1

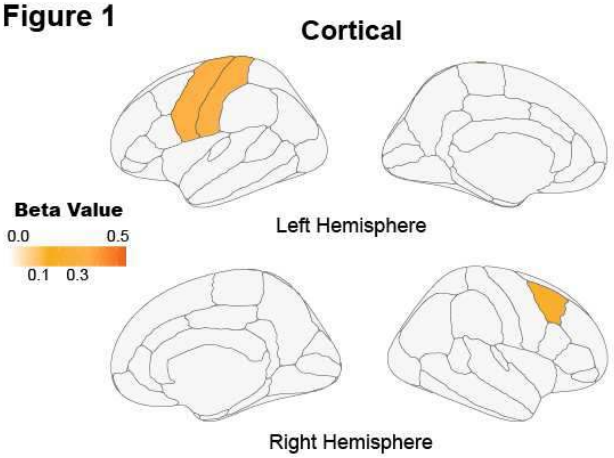

Figure 2

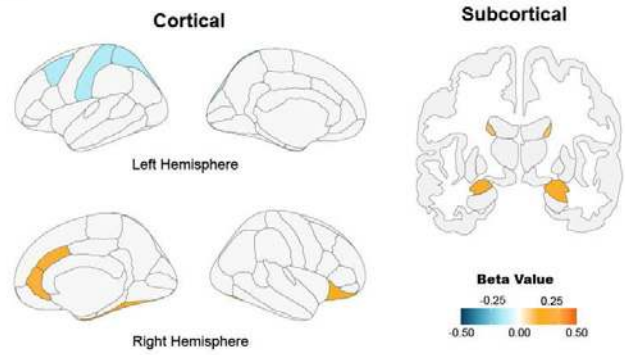

Conclusions: In line with our hypothesis, we found significant associations between increased vasogenic edema and SARS-CoV-2 infection. Interestingly, brain regions showing these associations also exhibited aberrant connectivity patterns[7], and increased brain activity at rest[8] in individuals with SARS-CoV-2 infection. Our results are also in line with evidence from a recent PET study showing increased [11C]PBR28 signal (i.e., indicative of microglia activation or neuroinflammation) in the same brain regions for individuals with long-COVID symptoms[9]. However, we did not find significant associations between COVID-19 and inflammation-related cellularity index, suggesting the vasogenic edema index as a more sensitive neuroinflammation marker to SARS-CoV-2 infection. This also broadly align with previous studies showing the associations of free water or extracellular water with other neuroinflammation-related disorders such as the Alzheimer Disease and obesity[10]. As this study lacks symptomology data, future research is warranted to explore the potential symptom-dependent neuroinflammatory relationship with SARS-CoV-2 infection.

References

1. Akinbami LJ. SARS-CoV-2 Serology and Self-Reported Infection Among Adults — National Health and Nutrition Examination Survey, United States, August 2021–May 2022. MMWR Morb Mortal Wkly Rep. 2022;71. doi:10.15585/mmwr.mm7148a4

2. Baj J, Karakuła-Juchnowicz H, Teresiński G, et al. COVID-19: Specific and Non-Specific Clinical Manifestations and Symptoms: The Current State of Knowledge. J Clin Med. 2020;9(6):1753. doi:10.3390/jcm9061753
3. Braga J, Lepra M, Kish SJ, et al. Neuroinflammation After COVID-19 With Persistent Depressive and Cognitive Symptoms. JAMA Psychiatry. Published online May 31, 2023. doi:10.1001/jamapsychiatry.2023.1321
4. Wang Y, Wang Q, Haldar JP, et al. Quantification of increased cellularity during inflammatory demyelination. Brain. 2011;134(12):3590-3601. doi:10.1093/brain/awr307
5. Fischl B. FreeSurfer. Neuroimage. 2012;62(2):774-781. doi:10.1016/j.neuroimage.2012.01.021
6. Hua K, Zhang J, Wakana S, et al. Tract Probability Maps in Stereotaxic Spaces: Analyses of White Matter Anatomy and Tract-Specific Quantification. Neuroimage. 2008;39(1):336-347. doi:10.1016/j.neuroimage.2007.07.053
7. Kafali HY, Dasgin H, Sahin D, et al. The effect of SARS-CoV-2 virus on resting-state functional connectivity during adolescence: Investigating brain correlates of psychotic-like experiences and SARS-CoV-2 related inflammation response. Psychiatry Research: Neuroimaging. Published online November 5, 2023:111746. doi:10.1016/j.pscychresns.2023.111746
8. Du YY, Zhao W, Zhou XL, et al. Survivors of COVID-19 exhibit altered amplitudes of low frequency fluctuation in the brain: a resting-state functional magnetic resonance imaging study at 1-year follow-up. Neural Regeneration Research. 2022;17(7):1576. doi:10.4103/1673-5374.327361
9. VanElzakker MB, Bues HF, Brusaferri L, et al. Neuroinflammation in post-acute sequelae of COVID-19 (PASC) as assessed by [11C]PBR28 PET correlates with vascular disease measures. bioRxiv. Published online October 20, 2023:2023.10.19.563117. doi:10.1101/2023.10.19.563117
10. Ly M, Raji CA, Yu GZ, et al. Obesity and White Matter Neuroinflammation Related Edema in Alzheimer's Disease Dementia Biomarker Negative Cognitively Normal Individuals. J Alzheimers Dis. 2021;79(4):1801-1811. doi:10.3233/JAD-201242

Poster No 2357

Distributed white matter abnormalities in primary trigeminal neuralgia: TBSS study

Elena Filimonova[1], Anton Pashkov[1], Galina Moysak[1], Azniv Martirosyan[1], Jamil Rzaev[1]

[1]Federal Neurosurgical Center, Novosibirsk, Russia

Introduction: Primary trigeminal neuralgia (PTN) is a prevalent chronic pain disorder whose pathogenesis is not limited to the trigeminal system. Despite the significant advances in uncovering underlying mechanisms, there is a paucity of comprehensive and consistent data regarding the role of white matter throughout the entire brain in PTN.

Methods: Sixty patients with PTN and 28 age- and sex-matched healthy controls were evaluated using diffusion tensor imaging (DTI). A tract-based spatial statistical approach was performed to investigate white matter impairment in patients with PTN with several metrics, including fractional anisotropy (FA), mean diffusivity (MD), radial diffusivity (RD) and axial diffusivity (AD). Additionally, ROI-based analysis was performed for each white matter tract to compare FA values between groups with correction for patient age and sex. Correlations between DTI data and nerve root compression severity, as well as pain severity, were also evaluated in patients with PTN.

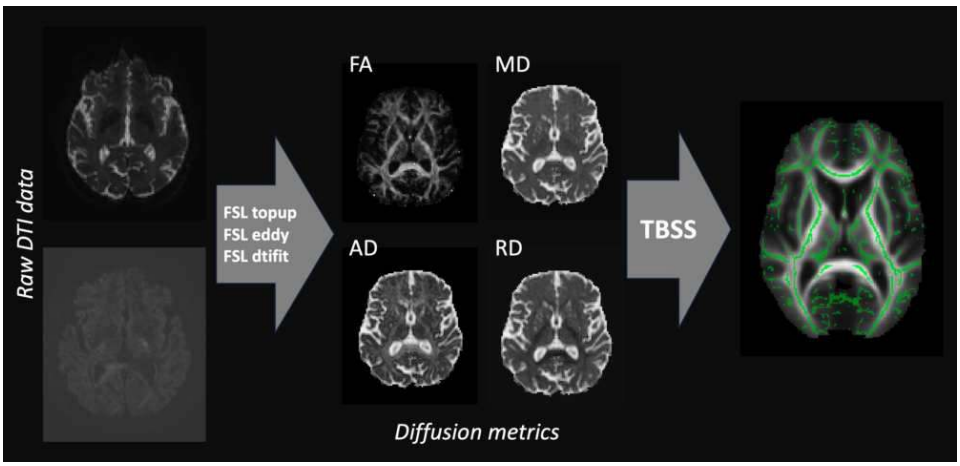

Fig. Schematic presentation of the DTI postprocessing algorithm

Results: Our analysis demonstrated a widespread and symmetrical reduction in FA values among TN patients when compared to the control group ($p < 0.05$). Specifically, this FA decrease was predominantly observed in regions such as the corona radiata, internal capsule, optic radiation, and thalami, as well as structures within the posterior fossa, notably the cerebellar peduncles. No statistically significant differences were found between patients and the control group during the MD, AD and RD map analyses. ROI-based analysis did not reveal statistically significant changes in FA values in white matter tracts ($p > 0.05$ in all comparisons, FDR-corrected); however, there were trends towards FA value decreases in the internal capsule ($p = 0.08$, FDR-corrected) and inferior fronto-occipital fasciculus ($p = 0.09$, FDR-corrected).

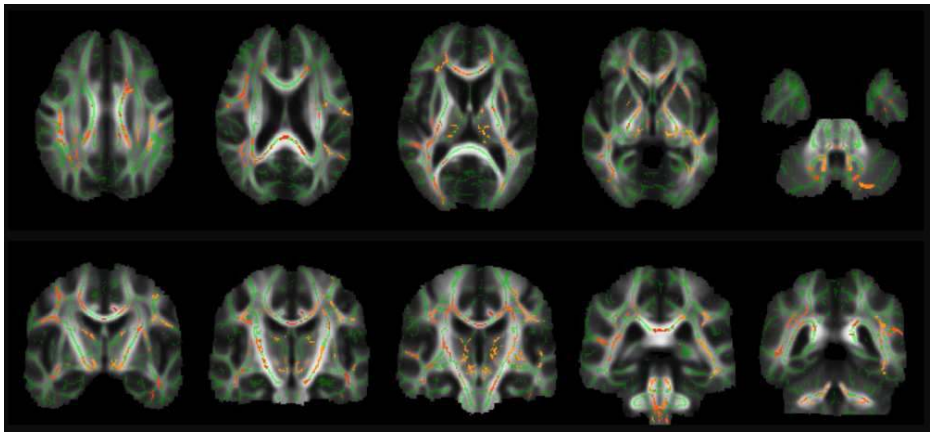

Fig. Differences in FA between groups (TBSS results). Green represents the anatomy of white matter tracts.

Conclusions: Our findings indicate the presence of microstructural abnormalities in white matter among individuals with primary trigeminal neuralgia, which may potentially play a role in the development and progression of the condition.

References

1. Gronemann, D. C., Koch, K., Bantel, C., & Sörös, P. (2020). Diffusion tensor imaging of white matter microstructure in chronic pain: a tract-based spatial statistics study and a systematic review. MedRxiv, 2020.04.16.20068197. https://doi.org/10.1101/2020.04.16.20068197
2. Kumaran, S., Gurram, S., Viswamitra, S., & Hegde, V. (2022). Utility of DTI (Diffusion Tensor Imaging) Metrics to Study Microstructural Changes of Trigeminal Nerve in Patients with Trigeminal Neuralgia (TN). Neurology India, 70(1), 270–274. https://doi.org/10.4103/0028-3886.338701
3. Liu, J., Zhu, J., Yuan, F., Zhang, X., & Zhang, Q. (2018). Abnormal brain white matter in patients with right trigeminal neuralgia: a diffusion tensor imaging study. The Journal of Headache and Pain, 19(1). https://doi.org/10.1186/S10194-018-0871-1

Poster No 2358

Tract profiles predict cognitive outomes associated with surgery in glioblastoma patients

Yizhou Wan[1,2], Ajay Halai[1,3], Rohitashwa Sinha[1,2], Haiyan Zheng[1,4], Richard Mair[1,2], Thomas Santarius[1,2], Robert Morris[1,2], Alexis Joannides[1,2], Matt Lambon-Ralph[1,3], Stephen Price[1,2]

[1]University of Cambridge, Cambridge, Cambridgeshire, [2]Division of Neurosurgery, Department of Clinical Neurosciences, Cambridge, United Kingdom, [3]MRC Cognition Brain Sciences Unit, Cambridge, United Kingdom, [4]MRC Biostatistics Unit, Cambridge, United Kingdom

Introduction: Glioblastoma is the most common and aggressive primary brain tumour. They are diffusely infiltrative and invade white-matter tracts. (Price et al. 2017) Cognitive deficits are common, affecting over 90% of patients. (Sinha, Stephenson, and Price 2019) The effect of the tumour and surgery on cognition is poorly understood. Tractometry has been used predict motor and language outcomes in glioma patients. (Shams et al. 2022; Prasse et al. 2022) We hypothesize that tractometry can be used to predict postoperative cognitive outcomes in glioblastoma patients by correlating microstructural measures from tract profiles with cognitive outcomes in a prospective cohort of glioblastoma patients undergoing surgery.

Methods: 40 patients were tested pre-surgery (t0) and post-surgery using the OCS-Bridge Cognitive Screening Tool (t2). Patients were scanned with anatomical and multi-shell diffusion sequences preoperatively and postoperatively. Cognitive scores at each timepoint were z-scored based the preoperative mean and standard-deviation. PCA was used to identify the latent dimensions. Anatomical processing involved tumour segmentation and lesion-filling. (Radwan et al. 2021) Whole-brain tractography was performed using Tractoflow. Diffusion tensor, Kurtosis, NODDI and RISH microstructural models were fitted. Tract segmentation was performed using TractSeg. (Wasserthal, Neher, and Maier-Hein 2018) Profiles were generated with 100 nodes per tract for 72 tracts in TractSeg. Longitudinal tract segmentations were used to calculate bundle reproducibility based on weighted-DICE. (Edde et al. 2023) Reproducible tracts (weighted DICE > 0.4) were selected for downstream analysis. Sparse group lasso regression (SGLR) was used to predict t0 and t2 cognitive scores using preoperative profiles. (Richie-Halford et al. 2021) Model performance was measured using cross-validated mean squared error between predicted and observed scores. (Halai, Woollams, and Lambon Ralph 2020)

Results: Attention and executive function accounted for 65% of the variance for OCS while perception and attention/visual memory accounted for 51% of the variance of the Cambridge perception screen. Overall weighted-DICE was low (range: 0 - 0.38, μ: 0.22). Reproducibility was higher for tracts contralateral to the tumour in resection compared to biopsy patients (n =

6) for both right-sided (0.302 vs. 0.235 FWE-corrected p = 0.02) (Fig 1) and left-sided tumours (0.468 vs 0.254, FWE-corrected p < 0.01) (Fig 2). 23 tracts were selected for statistical modelling. Microstructural features loaded onto two components representing measures of tissue “hindrance” and “complexity” accounting for 68% of the variance. Hindrance profiles predicted t0 and t2 scores. For t0 scores. K-fold cross-validated (k = 10) R2 were; attention (0.424, p = 5.45x10-6), executive function (0.294, p = 3.01-4), perception (0.177, 6.86x10-3), visual memory (0.229, p = 1.77x10--3). For t2 scores, the R2 values ranged between 0.154-0.565. Complexity explained higher variability in t2 scores (R2 range: 0.397 - 0.799) but not t0 scores.

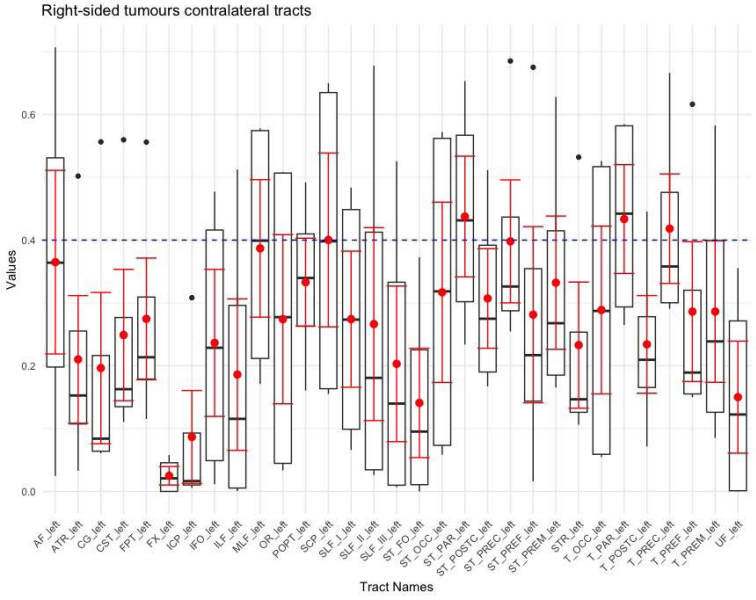

Fig. 1. Weighted DICE for contralateral tracts (Right-sided tumours))

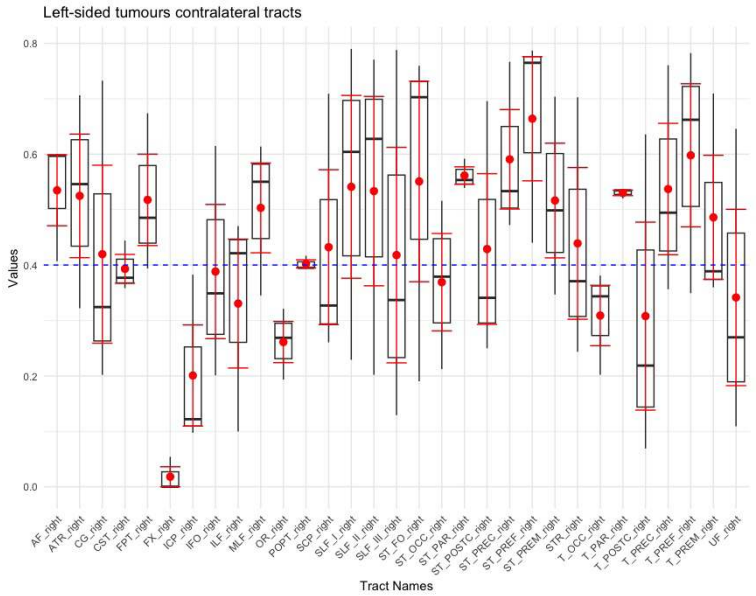

Fig. 2. Weighted DICE for contralateral tracts (Left-sided tumours))

Conclusions: Tractometry-derived profiles describing microstructural features of preoperative white-matter tracts may predict postoperative cognition, offering prognostic information for glioblastoma patients. A multivariable model accounting for features grouped into white-matter tracts show similar performance when predicting preoperative and postoperative outcomes. This suggests that postoperative cognition may be related to preoperative measures of white-matter damage related to brain-intrinsic or tumour effects. Features representing signal orientational-dispersion which may reflect local structural complexity shows higher correlations with postoperative scores. Future work should aim to investigate how anatomical changes related to surgery correlate with tract reproducibility and to validate these models using held-out datasets.

References
1. Edde, Manon, Guillaume Theaud, Matthieu Dumont, Antoine Théberge, Alex Valcourt
2. Caron, Guillaume Gilbert, Jean-Christophe Houde, et al. 2023. 'High-frequency Longitudinal White Matter Diffusion- and Myelin-based MRI Database: Reliability and Variability'. Human Brain Mapping 44 (9): 3758–80.
3. Halai, Ajay D., Anna M. Woollams, and Matthew A. Lambon Ralph. 2020. 'Investigating the Effect of Changing Parameters When Building Prediction Models for Post-Stroke Aphasia'. Nature Human Behaviour 4 (7): 725–35.
4. Prasse, Gordian, Hans-Jonas Meyer, Cordula Scherlach, Jens Maybaum, Anastasia Hoffmann, Johannes Kasper, Michael Karl Fehrenbach, et al. 2022. 'Preoperative Language Tract Integrity Is a Limiting Factor in Recovery from Aphasia after Glioma Surgery'. NeuroImage :
5. Clinical 37 (December): 103310.
6. Price, Stephen J., Kieren Allinson, Hongxiang Liu, Natalie R. Boonzaier, Jiun-Lin Yan, Victoria C. Lupson, and Timothy J. Larkin. 2017. 'Less Invasive Phenotype Found in Isocitrate Dehydrogenase–Mutated Glioblastomas than in Isocitrate Dehydrogenase Wild-Type
7. Glioblastomas: A Diffusion-Tensor Imaging Study'. Radiology 283 (1)
8. Radwan, Ahmed M., Louise Emsell, Jeroen Blommaert, Andrey Zhylka, Silvia Kovacs, Tom Theys, Nico Sollmann, Patrick Dupont, and Stefan Sunaert. 2021. 'Virtual Brain Grafting: Enabling Whole Brain Parcellation in the Presence of Large Lesions'. NeuroImage 229 (April): 117731.
9. Richie-Halford, Adam, Jason D. Yeatman, Noah Simon, and Ariel Rokem. 2021. 'Multidimensional Analysis and Detection of Informative Features in Human Brain White Matter'. PLOS Computational Biology 17 (6): e1009136.
10. Shams, Boshra, Ziqian Wang, Timo Roine, Dogu Baran Aydogan, Peter Vajkoczy, Christoph Lippert, Thomas Picht, and Lucius S. Fekonja. 2022. 'Machine Learning-Based Prediction of Motor Status in Glioma Patients Using Diffusion MRI Metrics along the Corticospinal Tract'. Brain Communications 4 (3): fcac141.
11. Sinha, Rohitashwa, Jade Marie Stephenson, and Stephen John Price. 2019. 'A Systematic Review of Cognitive Function in Patients with Glioblastoma Undergoing Surgery'. Neuro Oncology Practice.
12. Wasserthal, Jakob, Peter Neher, and Klaus H. Maier-Hein. 2018. 'TractSeg - Fast and Accurate White Matter Tract Segmentation'. NeuroImage 183 (December): 239–53.

Poster No 2359

Brain age prediction using fixel-based measures from advanced diffusion-weighted imaging

Remika Mito[1,2], Jocelyn Halim[1], Heath Pardoe[1], James Cole[3], Maria Di Biase[2], Andrew Zalesky[2,4]

[1]Florey Institute of Neuroscience and Mental Health, Melbourne, Victoria, Australia, [2]Department of Psychiatry, The University of Melbourne, Melbourne, Victoria, Australia, [3]Centre for Medical Image Computing, University College London, London, London, UK, [4]Department of Biomedical Engineering, The University of Melbourne, Melbourne, Victoria, Australia

Introduction: Machine learning applied to structural neuroimaging data can accurately predict chronological age in neurologically healthy individuals. Diffusion-weighted imaging (DWI) can be used to probe the in vivo white matter architecture of the brain, which is also known to exhibit substantial age-associated change. However, the ability of DWI to quantify changes in the brain's white matter fibre pathways depends on the way in which data are acquired, modelled and analysed. Previous work has demonstrated the ability to estimate brain age using both diffusion tensor imaging (DTI)-derived and advanced diffusion MRI measures(1,2). Here, we implement an advanced DWI modelling and analysis (fixel-based) approach to predict chronological age in a large cohort of older adults from the Human Connectome Project Lifespan study.

Methods: Participants from the Lifespan Human Connectome Project Aging (HCP-A; n=680 (382 females); age range: 36.0 – 89.8) were included. Multi-shell DWI data were collected(3) and preprocessed(4) as previously described. Following this, fibre orientation distribution (FOD) functions were extracted using multi-shell multi-tissue constrained spherical deconvolution (MSMT-CSD[5]). Spatial correspondence was achieved with a study-specific template through FOD-guided registration. The fixel-based analysis (FBA(6)) pipeline was used to extract a measure of fibre density and cross-section (FDC) at each white matter 'fixel' (fibre population within a voxel). Mean FDC values were extracted for each participant in 72 white matter fibre structures, defined by performing TractSeg(7) on the study-specific template FOD image. FreeSurfer-derived measures of cortical thickness and volume were extracted for the same participants from preprocessed structural imaging data (Lifespan 2.0 Release). 116 thickness and volume features were used for age prediction as per (8) (using Desikan-Killiany atlas and aseg Freesurfer atlas(9)). Brain-predicted age was calculated using Gaussian Process Regression, trained on the following imaging data: (i) Model 1: FDC values only (ii) Model 2: Cortical thickness and subcortical volumes (iii) Model 3: Combined FDC and cortical thickness and subcortical volumes For all models, predicted age was estimated using the same 80% training set and validated on a 20% test set. The predicted brain-age accuracy of each these models was assessed on the validation set using mean absolute error (MAE), root mean square error (RMSE) Pearson's r, and total variance explained (R2). Figure 1 provides an overview of the pipeline for this study.

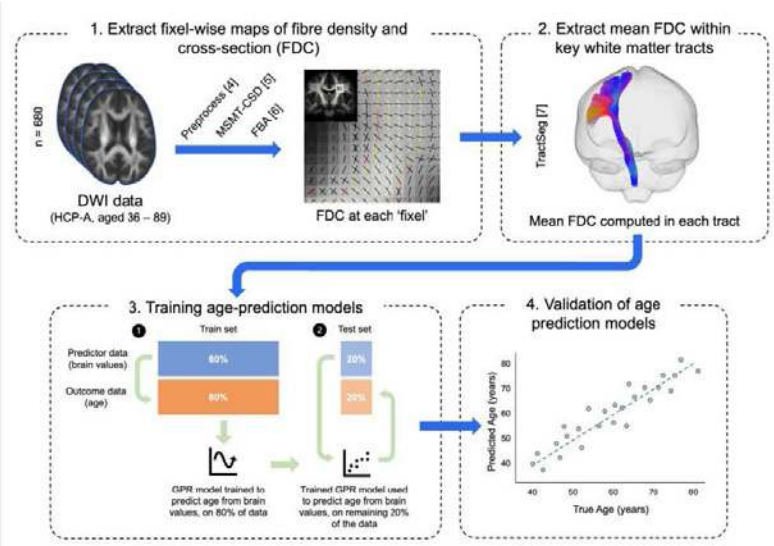

Figure 1: Pipeline for brain age prediction using the fibre density and cross-section (FDC) metric. Diffusion-weighted imaging (DWI) data from the HCP-A study were included. Measures of fibre density and cross-section (FDC) were obtained at each white matter 'fixel'. Following this, tract-summarised measures of mean FDC were obtained within 72 white matter fibre structures delineated using TractSeg. Brain age prediction was performed using Gaussian Process Regression using a train set of 80%, and prediction accuracy assessed on a 20% test (validation) set.

Results: Predictive model using only FDC inputs alone predicted chronological age with a mean average error (MAE) of 7.55 years, and a strong correlation with true age (r = 0.78; Figure 2). Using cortical thickness and subcortical volume values predicted chronological age with an MAE of 6.40 years, as well as a strong correlation with true age (r = 0.85). Combining the input values further improved model predictions (r = 0.87, MAE = 5.96 years).

Input data	MAE (years)	*r*	R^2	RMSE
FDC	7.55	0.78	0.61	9.50
Volume + thickness	6.40	0.85	0.72	7.92
FDC + volume + thickness	5.96	0.87	0.76	7.44

MAE = mean absolute error, *r* = Pearson's correlation between true and predicted age, RMSE = root mean squared error, FDC = fibre density and cross-section measure.

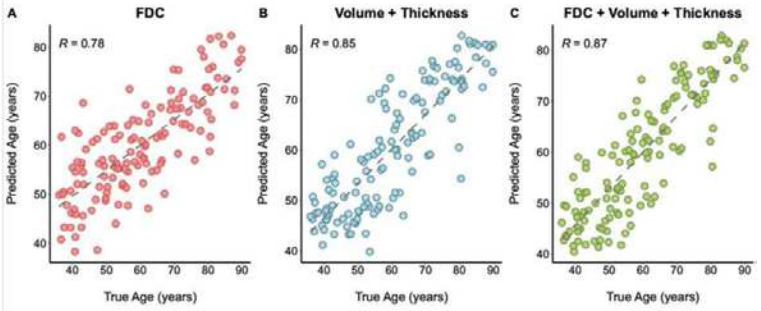

Figure 2: Accuracy of Gaussian Process Regression for age prediction from brain imaging data. Scatterplots displaying the correlation between true age (x-axis) and predicted age generated using a Gaussian Process Regression approach (y-axis). Subjects depicted here (N = 136) were from the test set of the HCP-A dataset. A) Predicted ages were generated from the model trained on mean FDC values only (Model 1). B) Predicted ages were generated from the model trained on cortical thickness and subcortical volumes (Model 2). C) Predicted ages were generated from the model trained on FDC values, cortical thickness, and subcortical volumes (Model 3).

Conclusions: Brain age prediction using an advanced DWI measure (FDC) demonstrated comparable prediction accuracy to previously published models using conventional diffusion tensor-based metrics(1,2), and improved the accuracy when combined with standard structural MRI measures. Combining DWI and structural brain measures yielded the most accurate predictions. Examining deviations in these brain age predictions could be valuable biomarkers in clinical cohorts where fibre-specific white matter abnormalities have been reported(10). Future studies may benefit from the use of fixel-level (rather than tract-summarised) measures of FDC in brain age prediction.

References
1. Tønnesen, S. et al. Brain Age Prediction Reveals Aberrant Brain White Matter in Schizophrenia and Bipolar Disorder: A Multisample Diffusion Tensor Imaging Study. Biol Psychiatry Cogn Neurosci Neuroimaging 5, 1095–1103 (2020).
2. Beck, D. et al. White matter microstructure across the adult lifespan: A mixed longitudinal and cross-sectional study using advanced diffusion models and brain-age prediction. Neuroimage 224, 117441 (2021).
3. Harms, M. P. et al. Extending the Human Connectome Project across ages: Imaging protocols for the Lifespan Development and Aging projects. Neuroimage 183, 972–984 (2018).
4. Glasser, M. F. et al. The minimal preprocessing pipelines for the Human Connectome Project. Neuroimage 80, 105–124 (2013).
5. Jeurissen, B., Tournier, J. D., Dhollander, T., Connelly, A. & Sijbers, J. Multi-tissue constrained spherical deconvolution for improved analysis of multi-shell diffusion MRI data. Neuroimage 103, 411–426 (2014).
6. Raffelt, D. A. et al. Investigating white matter fibre density and morphology using fixel-based analysis. Neuroimage 144, 58–73 (2017).
7. Wasserthal, J., Neher, P. & Maier-Hein, K. H. TractSeg-Fast and accurate white matter tract segmentation. Neuroimage 183, 239–253 (2018).
8. Dafflon, J. et al. An automated machine learning approach to predict brain age from cortical anatomical measures. Hum Brain Mapp 41, 3555–3566 (2020).
9. Desikan, R. S. et al. An automated labeling system for subdividing the human cerebral cortex on MRI scans into gyral based regions of interest. Neuroimage 31, 968–980 (2006).
10. Mito, R. et al. Fibre-specific white matter reductions in Alzheimer's disease and mild cognitive impairment. Brain 141, 888–902 (2018).

Poster No 2360

Precise Tracking of White Matter Integrity Following TBI in Densely Sampled Individuals

Aishwarya Rajesh[1], Ashley Meyer[1], Jason Hassenstab[1], Terrance Kummer[1], Evan Gordon[1], Nico Dosenbach[1]

[1]Washington University, St. Louis, MO

Introduction: Traumatic brain injury (TBI) has the highest incidence of all common neurological disorders, with enduring, debilitating impairments to quality of life (Maas et al., 2022). Accumulating evidence suggests that the global pathology underlying TBI-related impairment is axonal injury. Axonal injury can be noninvasively detected by a magnetic resonance imaging technique known as diffusion tensor imaging (DTI; Hulkower et al., 2013). Fractional anisotropy (FA)- a DTI-derived measure that describes the asymmetry of water diffusion within white matter bundles-is a commonly used surrogate marker for axonal injury that may serve as a biomarker for TBI severity and outcomes. However, interpreting FA in the context of TBI is difficult because the trajectory of FA changes after TBI is unclear: FA has been reported to both decrease and increase following TBI (Adnan et al., 2013, Chiou et al., 2019). To improve the utility of FA as a biomarker of TBI, a more comprehensive study of FA changes over time is critical. Here, we tracked weekly changes in FA over 27 weeks in 3 participants with TBI using an extended-acquisition, tract-based approach. For the first time, we show a precise and detailed characterization of the longitudinal recovery of white matter integrity after TBI.

Methods: Participant 1 identified as a 21yo female with pronounced right temporal subdural hematoma from a motor vehicle collision (MVC; GCS =15). She reported headaches, neck, and chest pain following injury. Participant 2 identified as a 31yo female with a right frontal subdural hematoma from an MVC. She reported headaches as well as pain/numbness in her left shoulder/arm following injury (GCS=14). Participant 3 identified as a 29 yo male who suffered a 10-foot fall. His CT scan revealed no obvious head trauma, but he reported persistent headaches and nausea symptoms following injury (GCS=13). DTI images were collected weekly over 27 weeks beginning ~two weeks after hospital admission and concluding 6 months later. DTI images were processed using FSL's DTIfit (Jenkinson, 2012). 18 white matter tracts were identified in each participant using TRACULA (Yendiki et al., 2011). For each session, FA values were extracted from each tract. Across sessions, FA changes were modeled against time using both linear and quadratic fits, and adjusted R-squared values were used to determine the best fit. In each participant, a two-way ANOVA was performed to analyze the effect of time and tract on FA, using the model: FA~time + tract + time*tract. The main effect of time (indicating the global effect of TBI recovery) was the primary effect of interest.

Results: The ANOVA revealed a significant main effect of time in each participant (ps < 10-7). Post-hoc testing indicated that in Participant 1, 13 of 18 tracts showed a significant change in FA over time. 12 of these tracts showed a positive parabolic relationship, such that FA values initially declined (~3 months), and then increased with time until the last tracked timepoint. Variance explained by this parabolic relationship reached 71% in some tracts. In Participant 2, 7 of 18 tracts showed a significant change in FA over time, with 3 tracts following a similar parabolic path. For Participant 3, 9 of 18 tracts showed a significant change, with FA showing a linear decline with time.

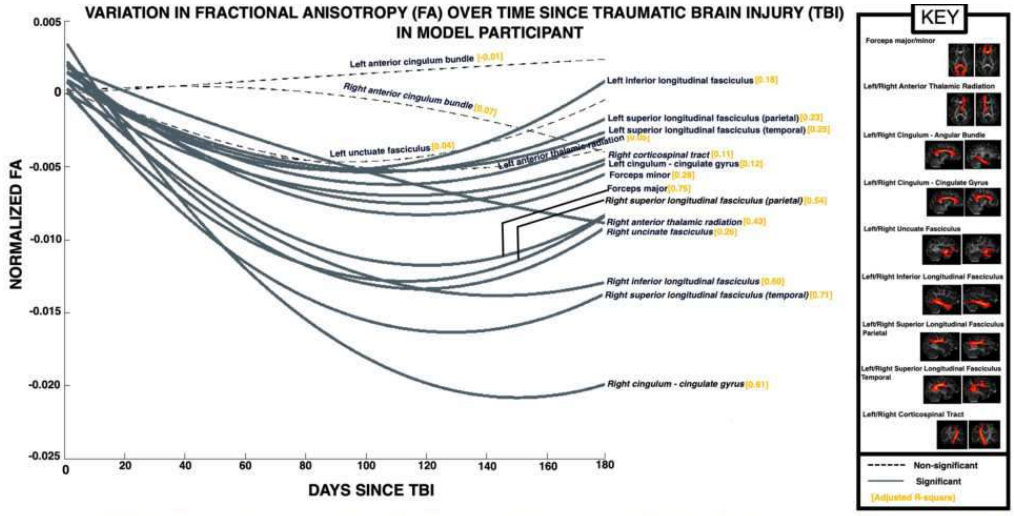

rajectory of White Matter Integrity indexed by Fractional Anisotropy (FA) for Participant 01 with Traumatic Brain njury (TBI). *Participant was a 21-year-old female with TBI from a motor vehicle collision and contusion to the right temporal pole. FA hanges were modeled against time. Adjusted R-squared values (shown in yellow brackets) were used to determine whether a linear or uadratic relationship better described the variation in FA across time. 12 of the 18 tracts for this participant showed a positive parabolic elationship between FA and time since injury.*

Conclusions: Across participants and tracts, changes in FA over time were generally described by positive parabolic relationships or linear decreases (which could be the initial stages of a positive parabolic effect). We speculate that the initial decline in FA may be associated with tract degeneration, and that the subsequent FA increase may reflect an adaptive neuroplasticity (Harris et al., 2016), enabling recovery to baseline. Together, this work significantly improves our understanding of recovery-related trajectories of a common neuroimaging marker of TBI, and thus may enable precise tracking of recovery processes in TBI patients.

References

1. Adnan, A., Crawley, A., Mikulis, D., Moscovitch, M., Colella, B., & Green, R. (2013). Moderate–severe traumatic brain injury causes delayed loss of white matter integrity: Evidence of fornix deterioration in the chronic stage of injury. Brain Injury, 27(12), 1415-1422.
2. Chiou, K. S., Jiang, T., Chiaravalloti, N., Hoptman, M. J., DeLuca, J., & Genova, H. (2019). Longitudinal examination of the relationship between changes in white matter organization and cognitive outcome in chronic TBI. Brain injury, 33(7), 846-853.
3. Cragun, B. N., Noorbakhsh, M. R., Philp, F. H., Suydam, E. R., Ditillo, M. F., Philp, A. S., & Murdock, A. D. (2020). Traumatic parafalcine subdural hematoma: a clinically benign finding. Journal of surgical research, 249, 99-103.
4. Harris, N. G., Verley, D. R., Gutman, B. A., & Sutton, R. L. (2016). Bi-directional changes in fractional anisotropy after experiment TBI: Disorganization and reorganization?. Neuroimage, 133, 129-143.
5. Hulkower, M. B., Poliak, D. B., Rosenbaum, S. B., Zimmerman, M. E., & Lipton, M. L. (2013). A decade of DTI in traumatic brain injury: 10 years and 100 articles later. American Journal of Neuroradiology, 34(11), 2064-2074.
6. Jenkinson, M., Beckmann, C. F., Behrens, T. E., Woolrich, M. W., & Smith, S. M. (2012). Fsl. Neuroimage, 62(2), 782-790.
7. Maas, A. I., Menon, D. K., Manley, G. T., Abrams, M., Åkerlund, C., Andelic, N., ... & Zemek, R. (2022). Traumatic brain injury: progress and challenges in prevention, clinical care, and research. The Lancet Neurology.
8. Yendiki, A., Panneck, P., Srinivasan, P., Stevens, A., Zöllei, L., Augustinack, J., ... & Fischl, B. (2011). Automated probabilistic reconstruction of white-matter pathways in health and disease using an atlas of the underlying anatomy. Frontiers in neuroinformatics, 5, 23.

Poster No 2361

Enhanced Structural Brain Connectivity Analyses Using High Diffusion-weighting Strengths

Leyao Yu[1], Adeen Flinker[2,1], Jelle Veraart[2]

[1]New York University Tandon School of Engineering, New York, NY, [2]New York University Grossman School of Medicine, New York, NY

Introduction: Tractography using diffusion-weighted Magnetic Resonance Imaging (dMRI) is an emerging tool in clinical and neuroscientific research, enabling presurgical planning (Nimsky et al., 2007) and the study of structural connectivity networks (Behrens & Sporns, 2012, Duffau, 2008; Glasser & Rilling, 2008; Turken & Dronkers, 2011). Recent studies showed that with increasing diffusion-weighting strength, probed by the b-value, dMRI becomes primarily sensitive to the intra-axonal signal (Veraart et al., 2016, 2020). Thus, increasing b-values may hold the untapped potential to increase the reliability of tractography. Here we test the hypothesis that exceeding current standard clinical b-values improve reliable reconstruction of longer-range connections using dMRI-based tractography, quantified based on nominal values and graph network metrics (Rubinov & Sporns, 2010).

Methods: Data: Multishell dMRI data was used from the publicly available MICRA dataset (Koller et al., 2021) where diffusion weighting was acquired with b=200, 500, 1200, 2400, and 6000 s/mm2 from 6 healthy participants with 5 repetitions. Analysis: Whole-brain, probabilistic tractography is performed using anatomical constraints (Tournier et al., 2019). The MRtrix3.0 package is used for fiber orientation estimation and tractography. Connectivity matrices (68 x 68 Desikan-Killiany (Desikan et al., 2006) nodes were constructed by computing the count and density of streamlines that connect corresponding cortical areas. Commonly used graph-theoretical metrics (average network degree and strength, betweenness, centrality, clustering coefficient, and normalized global efficiency) were calculated with the igraph toolbox in R.

Results: (i) More robust tracking of long-range connections (Fig 1): We first characterized the global and local change in the number and length of streamlines in long/short term range connections by fitting a polynomial mixed effect model. We found the total number of interhemispheric connections increased from 4.4% to 7.0% from b= 1200 to 6000s/mm2. Focusing on critical regions for the language network, we found that the average length of streamlines connecting the Inferior Frontal Gyrus (IFG) and Middle Frontal Gyrus (MFG) significantly increased by 24.08% and 34.70% in the same b-range. This is further reflected via increment in meaningful long-range nodal-to-nodal connections. For example, the number of streamlines seeded from left IFG to left STG increased by 160.6%. Further, spurious short-range connections and self-connections decreased with increasing b-value. (mean decrease in six major language ROIs -23.04%, std 7.76%; pars opercularis to caudal MFG -69.87%, MTG to STG -25.83%, all in left hemisphere). (ii) Impact on network analysis (Fig 2): We then characterized the changes of global and nodal graph network metrics by fitting a polynomial mixed effect model. Global changes in centrality of streamline count is limited to -13.79%, while certain regions are more vulnerable to b-value changes. In left STG and left MTG, the centrality decreases dramatically, (STG -48.27% and MTG -29.49%, from b= 1200 to 6000s/mm2), reflecting the heterogeneity of white matter tracts in the cortex. (iii) No loss in reproducibility: To quantify reproducibility, we calculated the coefficient of variation (CoV) and intraclass correlation coefficient for global and local networks. Using ANOVAN analysis, we do not observe loss in reproducibility of the findings for b-values above 1200s/mm2, despite the lower SNR at high b.

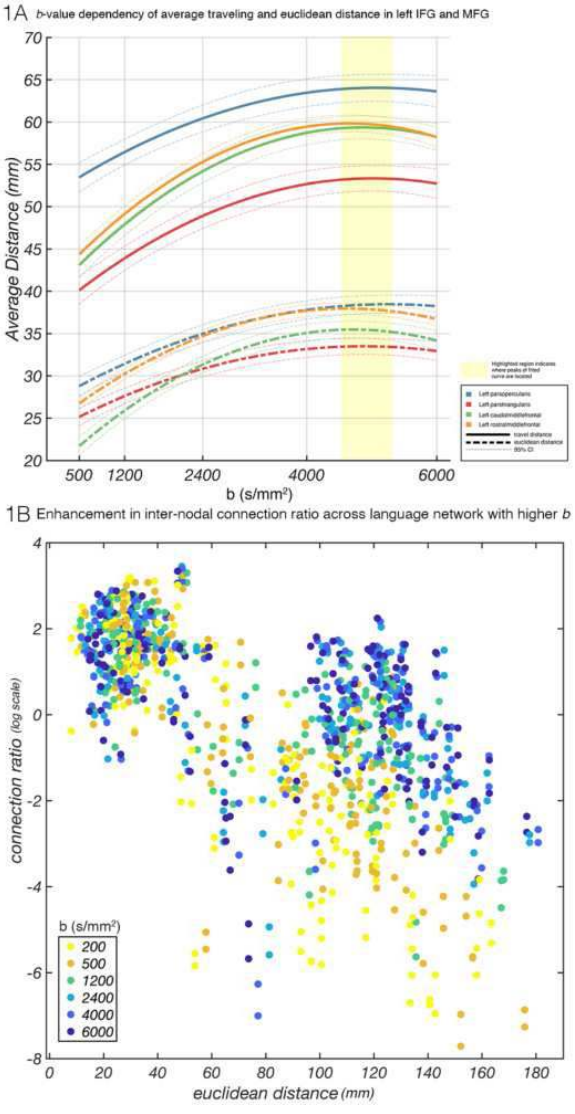

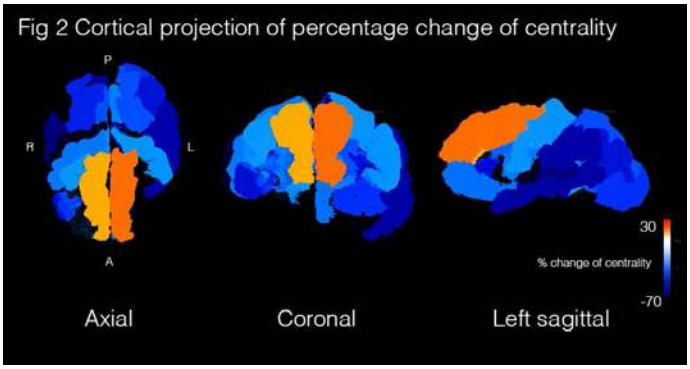

Conclusions: We observe that b-value is a critical experimental design factor that impacts tractography and structural connectivity analyses. Higher b-values are more robust in reconstructing long range connections, less impacted by spurious short-range connections, thereby advancing the study of structural brain connectivity.

References

1. Behrens, T. E. (2012). Human connectomics. Current Opinion in Neurobiology, 22(1), 144–153.
2. Desikan, R. S. (2006). An automated labeling system for subdividing the human cerebral cortex on MRI scans into gyral based regions of interest. NeuroImage, 31(3), 968–980.
3. Duffau, H. (2008). The anatomo-functional connectivity of language revisited. New insights provided by electrostimulation and tractography. Neuropsychologia, 46(4), 927–934.
4. Glasser, M. F. (2008). DTI tractography of the human brain's language pathways. Cerebral Cortex, 18(11), 2471–2482.
5. Koller, K. (2021). MICRA: Microstructural image compilation with repeated acquisitions. NeuroImage, 225, 117406.
6. Nimsky, C. (2007). Preoperative and intraoperative diffusion tensor imaging-based fiber tracking in glioma surgery. Neurosurgery, 61(1 Suppl), 178–185; discussion 186.
7. Rubinov, M. (2010). Complex network measures of brain connectivity: uses and interpretations. NeuroImage, 52(3), 1059–1069.
8. Tournier, J. D. (2019). MRtrix3: A fast, flexible and open software framework for medical image processing and visualisation. NeuroImage, 202, 116137.
9. Turken, A. U. (2011). The neural architecture of the language comprehension network: converging evidence from lesion and connectivity analyses. Frontiers in Systems Neuroscience, 5, 1.
10. Veraart, J. (2016). Universal power-law scaling of water diffusion in human brain defines what we see with MRI.
11. Veraart, J. (2020). Noninvasive quantification of axon radii using diffusion MRI. eLife, 9. https://doi.org/10.7554/eLife.49855

Poster No 2362

Structural Connectivity in Different Types of Reward Among Youth: A combined fMRI and DTI study

Siti Mariam Roslan[1], Asma Hayati Ahmad[2], Aini Ismafairus Abd Hamid[2]

[1]Universiti Sains Malaysia, Kubang Kerian, Kelantan, [2]Universiti Sains Malaysia, Kubang Kerian, Malaysia

Introduction: Neuroimaging studies have identified brain areas involved in reward processing. However, the connectivity of different types of reward remains unclear. This study aims to determine the structural connectivity in different types of reward cues among young adults.

Methods: Twenty right-handed students (11 males) with the mean age of 24±1 from School of Health Sciences, Universiti Sains Malaysia participated in this study. Participants underwent functional magnetic resonance imaging (fMRI) scan, while performing the 2-back tasks. Different cues (cash and filial) were displayed during the tasks. The participants remained inside the MRI scanner for diffusion MRI scan. Participants were divided into cash and filial groups based on their highest score during the 2-back tasks. Probabilistic tractography was performed to calculate the number of streamlines from the seed to targets. The seed was selected based on region-of-interests (ROI) extracted from random effects analysis (RFX) whereas the targets were selected based on previous literatures. The seed region was putamen, whereas ten targets were selected which included anterior cingulate cortex (ACC), posterior cingulate cortex (PCC), ventrolateral prefrontal cortex (VLPFC), amygdala, dorsolateral prefrontal cortex (DLPFC), anterior insula, and posterior insula.

Results: The highest connection probability in filial group was observed between the right putamen to the right amygdala. Whereas in cash group, the highest connectivity was between the right putamen to the right anterior insula.

Conclusions: Our findings suggest that differential structural connectivity exist in processing different rewards.

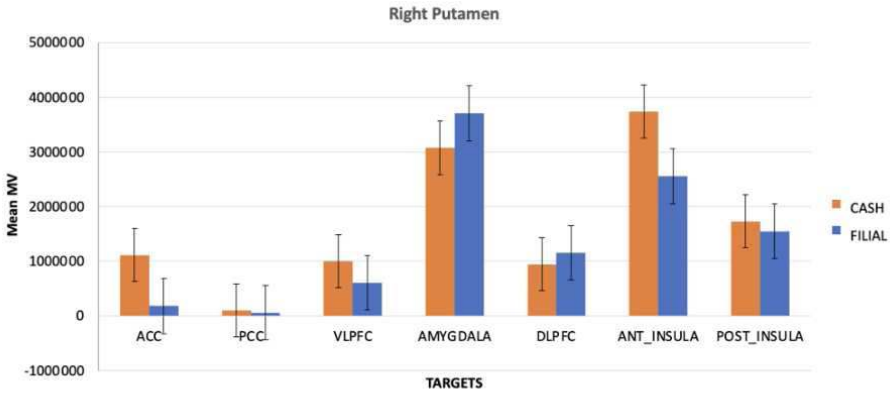

Fig. 1 Mean MV between right putamen to target regions in cash and filial group.

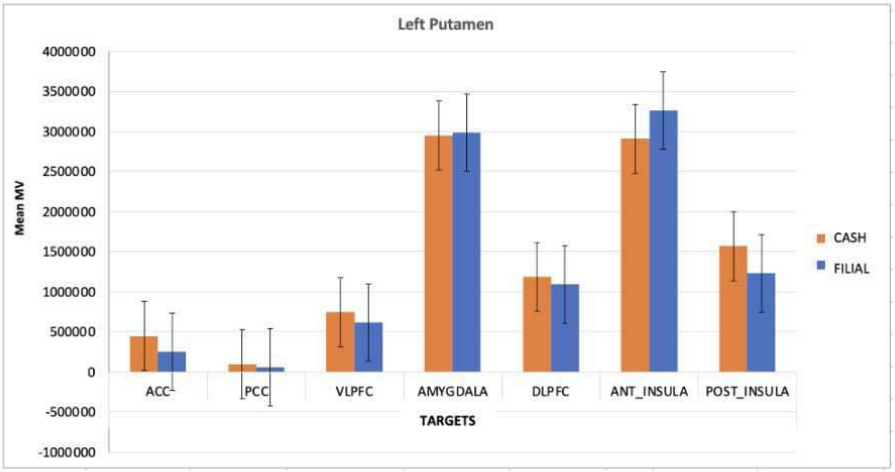

Fig. 2 Mean MV between left putamen to target regions in cash and filial group.

References

1. Banich, M.T. and Floresco, S. (2019) 'Reward systems, cognition, and emotion: Introduction to the special issue', Cognitive, Affective and Behavioral Neuroscience. Springer New York LLC, pp. 409–414. Available at: https://doi.org/10.3758/s13415-019-00725-z.
2. Bartra, O., McGuire, J.T. and Kable, J.W. (2013) 'The valuation system: A coordinate-based meta-analysis of BOLD fMRI experiments examining neural correlates of subjective value', NeuroImage, 76, pp. 412–427. Available at: https://doi.org/10.1016/j.neuroimage.2013.02.063.
3. Berry, A.S., Jagust, W.J. and Hsu, M. (2019) 'Age-related variability in decision-making: Insights from neurochemistry', Cognitive, Affective and Behavioral Neuroscience, 19(3), pp. 415–434. Available at: https://doi.org/10.3758/s13415-018-00678-9.
4. Bradley, K.A.L. et al. (2017) 'Neural correlates of RDoC reward constructs in adolescents with diverse psychiatric symptoms: A Reward Flanker Task pilot study', Journal of Affective Disorders, 216, pp. 36–45. Available at: https://doi.org/10.1016/j.jad.2016.11.042.
5. Camara, E. et al. (2009) 'Reward networks in the brain as captured by connectivity measures', 3(3), pp. 350–362.
6. Cao, Z. et al. (2019) 'Mapping adolescent reward anticipation, receipt, and prediction error during the monetary incentive delay task', Human Brain Mapping, 40(1), pp. 262–283. Available at: https://doi.org/10.1002/hbm.24370.
7. Chan, Y., Hsu, W. and Chou, T. (2018) 'Dissociation between the processing of humorous and monetary rewards in the " motivation " and " hedonic " brains', (May), pp. 1–11. Available at: https://doi.org/10.1038/s41598-018-33623-4.
8. Chan, Y.C., Wang, C.Y. and Chou, T.L. (2023) 'Money or funny: Effective connectivity during service recovery with a DCM-PEB approach', Biological Psychology, 176. Available at: https://doi.org/10.1016/j.biopsycho.2022.108464.
9. Chaplin, T.M., Mauro, K.L. and Niehaus, C.E. (2022) 'Effects of Parenting Environment on Child and Adolescent Social-Emotional Brain Function', Current topics in behavioral neurosciences, 54, pp. 341–372. Available at: https://doi.org/10.1007/7854_2021_276.
10. Chen, Z. et al. (2016) 'Maturation along white matter tracts in human brain using a diffusion tensor surface model tract-specific analysis', Frontiers in Neuroanatomy, 10(FEB), pp. 1–18.
11. Gibson, G. (2017) 'Cocaine and the Dopamine Hypothesis of Addiction FYS100C : Gotta Have It : Exploring the Science of Addiction', Chemistry: Student Scholarship & Creative Works, 7,

Poster No 2363

In vivo human brain submillimeter diffusion MRI on the Connectome 2.0 scanner

Gabriel Ramos Llorden[1,2], Mirsad Mahmutovic[3], Daniel J. Park[1], Chiara Maffei[1,2], Hong-Hsi Lee[1,2], Lawrence L. Wald[1,2], Thomas Witzel[4], Boris Keil[3,5], Susie Huang[1,2]

[1]Athinoula A. Martinos Center for Biomedical Imaging, Massachusetts General Hospital, Charlestown, MA, [2]Harvard Medical School, Boston, MA, [3]Institute of Medical Physics and Radiation Protection, Mittelhessen University of Applied Science, Giessen, Germany, [4]Q Bio Inc, San Carlos, CA, [5]Department of Diagnostic and Interventional Radiology, University Hospital Marburg, Philipps University of Marburg, Marburg, Germany

Introduction: Maximizing the benefits afforded by high-performance gradient technology[1,3,6] for diffusion MRI requires overcoming the technical challenges associated with strong diffusion gradients, including more pronounced high-order eddy currents and pervasive concomitant field effects. This work investigates the impact of eddy currents from ultra-strong diffusion gradients (500 mT/m) of the Connectome 2.0 scanner[6] on the long image readouts of high-spatial-resolution diffusion MRI acquisitions. We show the limitations of conventional ghosting-removal methods to provide high-quality images. We achieve eddy-current-induced geometric distortion- and ghosting-free submillimeter in vivo human diffusion MRI at unprecedentedly short echo time at Gmax = 500 mT/m with concurrent field monitoring integrated into a custom-built 72-ch in vivo coil.

Methods: Acquisition protocol: A healthy volunteer (23Y, female) underwent a diffusion MRI scan on the Connectome 2.0 scanner[6] (MAGNETOM Connectom.X, Siemens Healthineers, Erlangen, Germany) with a custom-built 72-ch head coil. The coil was equipped with a 16-channel 19F clip-on field probe system (Skope, Inc., Zurich, Switzerland) for concurrent field monitoring (Fig. 1a).[10] Whole brain was acquired with a 2D Pulsed-Field Gradient Spin Echo (PGSE) EPI sequence with axial slices, 0.9 mm in-plane resolution, slice thickness = 0.9 mm, TR/TE = 12,000/47 ms, phase encoding direction A>P, in-plane acceleration factor = 2, PF = 6/8, no SMS, BW = 1912 Hz, echo spacing = 0.57 ms. Readout time = 46 ms, Total acquisition time = 7.2 min. Thirty diffusion encoding directions at b = 1,200 s/mm2 (Gmax = 500 mT/m, Δ=8.7 ms, δ=2.9 ms) + 1b0-image. A gradient-recalled echo (GRE) scan was also performed to estimate the coil sensitivities. Image reconstruction: The 2D-PGSE EPI sequence was modified by incorporating triggers and synchronization pulses (beginning of the sequence) to ensure accurate synchronization between the monitored field and the k-space data during the image readout.[10] A third-order spherical harmonics (SH) model was fitted to the 16 NMR probes' signal phase with a linear least squares (LLS) algorithm.[10] B0-eddy-current compensation (B0-ECC) applied by the scanner was removed prior to reconstruction. Images were reconstructed within a SENSE reconstruction framework, with the image encoding matrix informed by the phase evolution[10,7] The ESPIRiT algorithm was used to estimate the coil sensitivities.[9] Validation: Concurrent field monitoring-based image reconstruction was compared with standard GRAPPA[4] reconstruction with 1D navigators[2] for Nyquist ghosting correction based on a linear phase model (1D LPC), and with Dual Polarity Grappa (DPG).[5] Reconstructed images with GRAPPA-1D LPC and DPG were corrected for eddy current-induced geometric distortion with the FSL post-processing tool 'eddy''.

Results: Eddy currents from the ultra-strong diffusion gradients perturb the image encoding, causing each DWI's k-space trajectory to deviate from the b0 k-space trajectory (Fig. 1b). High-order phase terms are also prominent with the asymmetric Connectome 2.0 head gradient coil (Fig. 1c) and diffusion-direction dependent due to remaining long-decay eddy currents. Phase differences between odd/even EPI lines are non-linear in space and vary among DWIs (Fig. 2a) Ghosting artifacts remain visible with GRAPPA-1D LPC but are largely mitigated with DPG and slightly more with concurrent field monitoring-based reconstruction (Fig. 2b). Axial, coronal, and sagittal views of a diffusion-weighted image reconstructed with concurrent field monitoring are shown in Fig. 2c as well as the averaged DWI map (Fig. 2d).

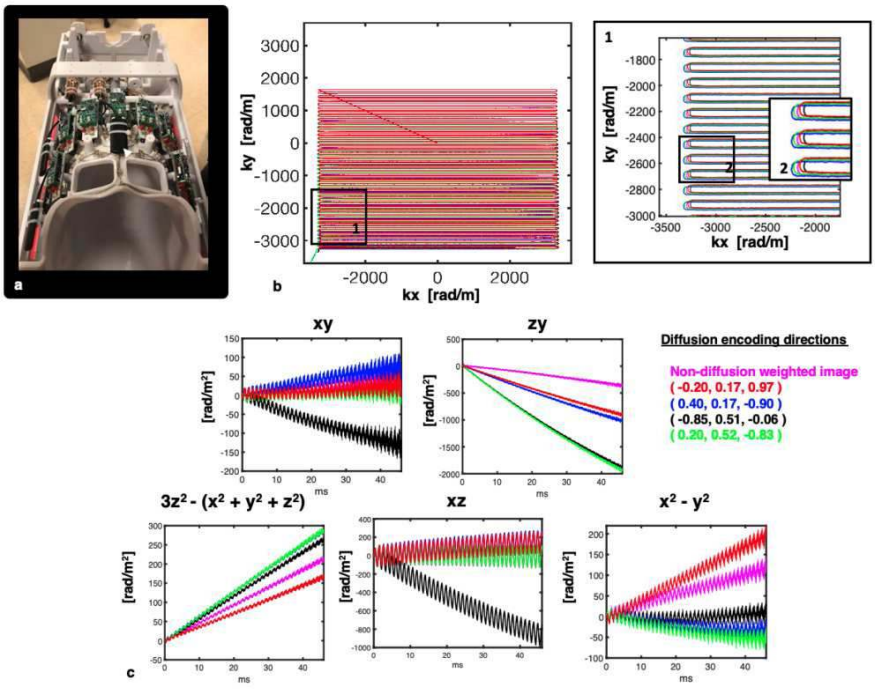

Fig. 1 a, 16-channel dynamic field monitoring system consisting of ^{19}F field probes (white arrowhead) integrated in the 72-channel *in vivo* coil. **b,** Measured imaging k-space trajectory of a non-diffusion weighted (b=0) image (magenta) and four representative DWIs acquired at b=1,200 s/mm^2 (G_{max}=500 mT/m, Δ=8.7 ms, δ=2.9 ms) with different diffusion directions at 0.9 mm isotropic resolution. Note that the *k*-space trajectories deviate from the nominal prescribed k-space trajectory (magenta) due to residual eddy currents from the diffusion gradients. **c,** Temporal evolution of 2nd order eddy current phase terms measured during image readout with the 16-channel dynamic field monitoring system.

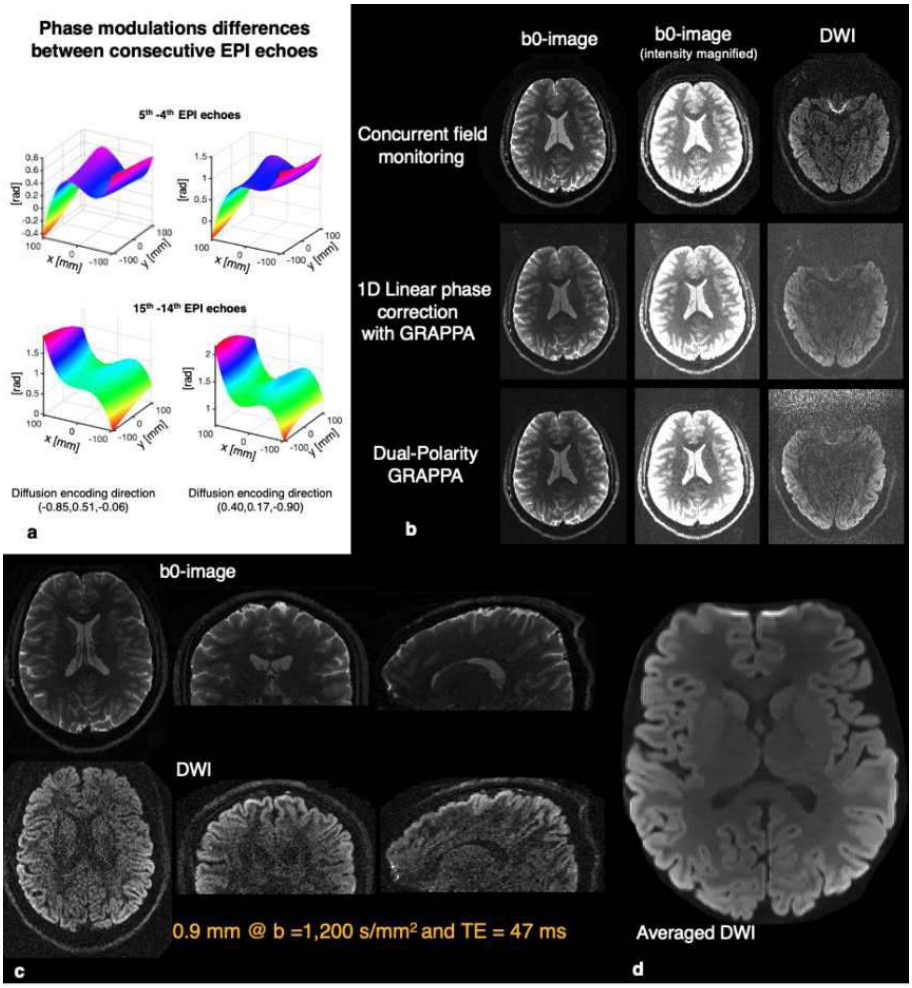

Fig. 2 | a, Spatial distribution of phase differences between consecutive EPI echoes at different time points of the image readout for different diffusion encoding directions. **b,** Nyquist ghosting removal results with concurrent field monitoring-based image reconstruction, one-dimensional linear phase correction with GRAPPA, and dual-polarity GRAPPA. **c,** Axial, coronal and sagittal views of a b0-image and DWI reconstructed with concurrent field monitoring. **d,** Averaged DWI map (averaged over diffusion encoding directions) obtained with concurrent-field monitoring reconstruction.

Conclusions: We show here that concurrent field monitoring effectively reduces non-linear Nyquist ghosting and geometric distortions generated by eddy currents from ultra-high-strength diffusion gradients on Connectome 2.0.

References

1. Feinberg, D.A., Beckett, A.J.S., Vu, A.T. et al. Next-generation MRI scanner designed for ultra-high-resolution human brain imaging at 7 Tesla. Nature Methods (2023).
2. Feiweier, T. Magnetic resonance method and apparatus to determine phase correction parameters. US Patent. 8,497,681. 2013
3. Foo TKF, Tan ET, Vermilyea ME, et al. Highly efficient head-only magnetic field insert gradient coil for achieving simultaneous high gradient amplitude and slew rate at 3.0T (MAGNUS) for brain microstructure imaging. Magn Reson Med. 2020 Jun;83(6):2356-2369. doi: 10.1002/mrm.28087. Epub 2019 Nov 25. PMID: 31763726.
4. Griswold MA, Jakob PM, Heidemann RM et al. Generalized autocalibrating partially parallel acquisitions (GRAPPA). Magn Reson Med. 2002 Jun;47(6):1202-10. doi: 10.1002/mrm.10171. PMID: 12111967.
5. Hoge WS, Polimeni JR. Dual-polarity GRAPPA for simultaneous reconstruction and ghost correction of echo planar imaging data. Magn Reson Med. 2016 Jul;76(1):32-44. doi: 10.1002/mrm.25839. Epub 2015 Jul 24. PMID: 26208304; PMCID: PMC4758917.
6. Huang SY, Witzel T, Keil B, et al. Connectome 2.0: Developing the next-generation ultra-high gradient strength human MRI scanner for bridging studies of the micro-, meso- and macro-connectome. Neuroimage. 2021 Nov;243:118530.
7. Ramos-Llordén G, Park DJ, Kirsch JE, et al. Eddy current-induced artifact correction in high b-value ex vivo human brain diffusion MRI with dynamic field monitoring. Magn Reson Med. 2023 Sep 27. doi: 10.1002/mrm.29873. Epub ahead of print. PMID: 37753621.
8. Setsompop K, Kimmlingen R, Eberlein E, et al. Pushing the limits of in vivo diffusion MRI for the Human Connectome Project. Neuroimage. 2013 Oct 15;80:220-33. doi: 10.1016/j.neuroimage.2013.05.078. Epub 2013 May 24. PMID: 23707579; PMCID: PMC3725309.
9. Uecker M, Lai P, Murphy MJ, et al. ESPIRiT--an eigenvalue approach to autocalibrating parallel MRI: where SENSE meets GRAPPA. Magn Reson Med. 2014 Mar;71(3):990-1001. doi: 10.1002/mrm.24751. PMID: 23649942; PMCID: PMC4142121.
10. Wilm BJ, Nagy Z, Barmet C, et al. Diffusion MRI with concurrent magnetic field monitoring. Magn Reson Med. 2015 Oct;74(4):925-33. doi: 10.1002/mrm.25827. Epub 2015 Jul 17. PMID: 26183218.

Poster No 2364

Diffusion MRI for Anatomical Nuclei Imaging (DiMANI): Visualizing Thalamic Subnuclei

Remi Patriat[1], Tara Palnitkar[1], Jayashree Chandrasekaran[1], Karianne Sretavan Wong[2], Henry Braun[1], Essa Yacoub[3], Robert McGovern III[1], Joshua Aman[1], Scott Cooper[1], Jerrold Vitek[1], Noam Harel[1]

[1]University of Minnesota, Minneapolis, MN, [2]University of Minnesota, Saint Louis Park, MN, [3]Center for Magnetic Resonance Research, Minneapolis, MN

Introduction: Conventional MRI has limited ability to visualize thalamic subnuclei, hindering precise targeting for interventions like deep brain stimulation (DBS) and MR-guided focused ultrasound (MRgFUS), resulting in variable patient outcomes (Agrawal et al., 2021; Flora et al., 2010) and repeat surgeries (Rolston et al., 2016). Several imaging methods have been developed for direct visualization, including susceptibility weighted imaging (Abosch et al., 2010; Najdenovska et al., 2019), quantitative magnetic susceptibility mapping (Deistung et al., 2013), and white-matter nulled T1 imaging, such as FGATIR (Sudhyadhom et al., 2009), 3D-EDGE (Middlebrooks et al., 2021), and WMn-MPRAGE (Su et al., 2019); however, these techniques have limitations for routine clinical use. Here, we present DiMANI, a novel method for directly visualizing thalamic subnuclei using diffusion MRI (dMRI).

Methods: One healthy control and six essential tremor (ET) patients underwent scanning on a 7T Siemens MRI scanner, supplemented by 3T and 7T data from a single Human Connectome Project (HCP) control subject. Standard preprocessing, including FSL's eddy and topup, was applied. DiMANI contrast was computed by averaging diffusion-weighted volumes (e.g., 50 b =1500s/mm^2 volumes). The resulting contrast was compared with THOMAS (Su et al., 2019) and Morel atlases (Morel et al., 1997). We evaluated the reproducibility of DiMANI by computing dice coefficients on manual segmentations performed on a unique dataset comprising eight scans of a single participant collected over a 3-year period. Inter-rater reliability was quantitatively evaluated for manual segmentations of thalamic subnuclei (3 raters and 5 patients). Then, DiMANI imaging data was qualitatively correlated with intra-operative electrophysiology obtained during ET-DBS surgery (for subnucleus identification), post-operative computed tomography (for DBS lead location), and clinical evaluations (final DBS stimulation settings).

Results: DiMANI provides enhanced contrast and enables direct visualization of thalamic subnuclei, including their borders (see Figure1 for manual segmentations). The DiMANI contrast corresponds to the overall anatomical organization as described by the THOMAS and Morel atlases. Dice coefficients (DCs) for manual segmentations of one volunteer's eight datasets, based on 12 nuclei from the THOMAS atlas nomenclature, averaged between 0.62 and 0.85, except for the habenula (DC = 0.50). Three raters independently segmented the subnuclei for 5 ET patients, yielding comparable DCs (0.46 to 0.81). DiMANI contrast enables the generation of 3D patient-specific models for thalamic subnuclei location depiction as shown in Figure 2 for 6 ET patients. All nine active DBS contacts were at or near the ventral lateral posterior (VLPv) – ventral lateral anterior

(VLa) border, which is consistent with expected lead locations. Micro-electrode recording tracks correlated with manual segmentations: 11 of 12 micro-electrode recording tracks, showed that regions of activity interpreted as neuronal firing of cells belonging to the ventral posterior lateral (VPL) overlapped fully with the manual segmentations of the VPL. The twelfth track was found just anterior to VPL within VLPv.

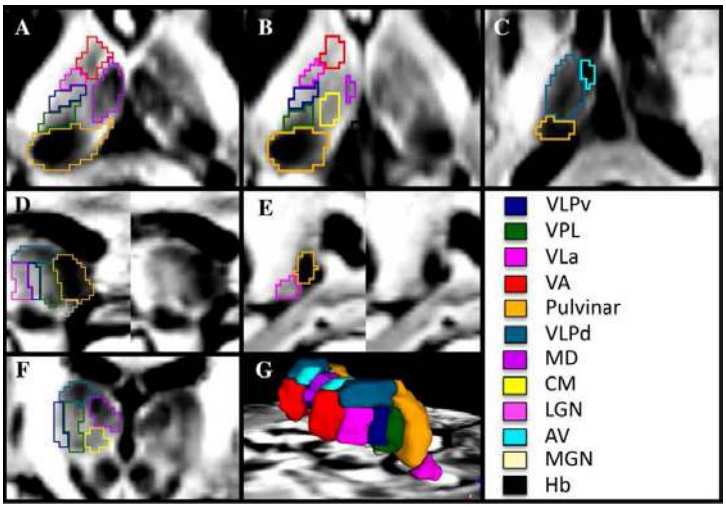

Figure 1: Manual segmentation of thalamic subnuclei using the DiMANI image following conventions from the THOMAS atlas in axial (A,B,C), sagittal (D and E), coronal (F), and in 3D (G).

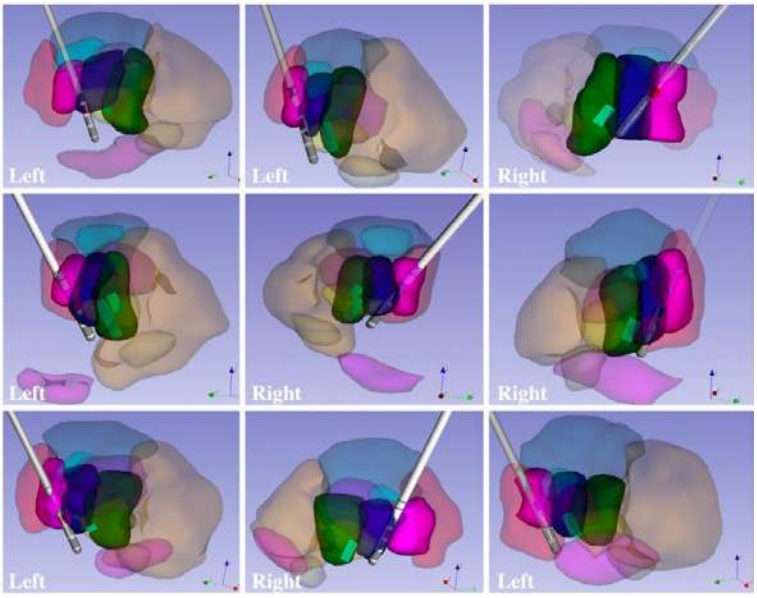

Figure 2: 3D models of patient-specific thalamic segmentations combined with DBS lead and VPL cell locations for six patients totaling nine leads.

Conclusions: DiMANI is a dMRI-based image contrast that facilitates direct visualization of numerous thalamic subnuclei. DiMANI holds significant potential for immediate clinical applications, aiding in segmentations, targeting, and optimizing thalamic therapies like DBS and MRgFUS. While the proof-of-concept displays common dMRI limitations, DiMANI shows promise for both research and clinical purposes. Ongoing work will leverage advanced acquisition and post-processing methods to enhance translational capabilities.

References

1. Abosch, A., Yacoub, E., Ugurbil, K., Harel, N., 2010. An assessment of current brain targets for deep brain stimulation surgery with susceptibility-weighted imaging at 7 tesla. Neurosurgery 67, 1745-1756; discussion 1756.
2. Agrawal, M., Garg, K., Samala, R., Rajan, R., Naik, V., Singh, M., 2021. Outcome and Complications of MR Guided Focused Ultrasound for Essential Tremor: A Systematic Review and Meta-Analysis. Front Neurol 12, 654711.
3. Deistung, A., Schäfer, A., Schweser, F., Biedermann, U., Turner, R., Reichenbach, J.R., 2013. Toward in vivo histology: a comparison of quantitative susceptibility mapping (QSM) with magnitude-, phase-, and R2*-imaging at ultra-high magnetic field strength. Neuroimage 65, 299-314.

4. Flora, E.D., Perera, C.L., Cameron, A.L., Maddern, G.J., 2010. Deep brain stimulation for essential tremor: a systematic review. Mov Disord 25, 1550-1559.
5. Middlebrooks, E.H., Okromelidze, L., Lin, C., Jain, A., Westerhold, E., Ritaccio, A., Quiñones-Hinojosa, A., Gupta, V., Grewal, S.S., 2021. Edge-enhancing gradient echo with multi-image co-registration and averaging (EDGE-MICRA) for targeting thalamic centromedian and parafascicular nuclei. Neuroradiol J 34, 667-675.
6. Morel, A., Magnin, M., Jeanmonod, D., 1997. Multiarchitectonic and stereotactic atlas of the human thalamus. J Comp Neurol 387, 588-630.
7. Najdenovska, E., Tuleasca, C., Jorge, J., Maeder, P., Marques, J.P., Roine, T., Gallichan, D., Thiran, J.P., Levivier, M., Bach Cuadra, M., 2019. Comparison of MRI-based automated segmentation methods and functional neurosurgery targeting with direct visualization of the Ventro-intermediate thalamic nucleus at 7T. Sci Rep 9, 1119.
8. Rolston, J.D., Englot, D.J., Starr, P.A., Larson, P.S., 2016. An unexpectedly high rate of revisions and removals in deep brain stimulation surgery: Analysis of multiple databases. Parkinsonism Relat Disord 33, 72-77.
9. Su, J.H., Thomas, F.T., Kasoff, W.S., Tourdias, T., Choi, E.Y., Rutt, B.K., Saranathan, M., 2019. Thalamus Optimized Multi Atlas Segmentation (THOMAS): fast, fully automated segmentation of thalamic nuclei from structural MRI. Neuroimage 194, 272-282.
10. Sudhyadhom, A., Haq, I.U., Foote, K.D., Okun, M.S., Bova, F.J., 2009. A high resolution and high contrast MRI for differentiation of subcortical structures for DBS targeting: the Fast Gray Matter Acquisition T1 Inversion Recovery (FGATIR). Neuroimage 47 Suppl 2, T44-52.

Poster No 2365

Analysis of cortical dysplasias using b-tensor encoding diffusion MRI in an animal model

Olimpia Ortega-Fimbres[1], Alonso Ramírez-Manzanares[2], Mónica López-Hidalgo[1], Ricardo Rios-Carrillo[1], Mirelta Regalado[1], Hiram Luna-Munguía[1], Luis Concha[1]

[1]Universidad Nacional Autónoma de México, Querétaro, Mexico, [2]Centro de Investigación en Matemáticas, Guanajuato, Mexico

Introduction: Focal cortical dysplasias (FCD) are cortical malformations that represent a major cause of drug-resistant focal epilepsy (Blümcke, 2011). Magnetic resonance images (MRI) are the main tool for their diagnosis and subsequent surgical intervention. However, despite clear histopathological changes, many FCDs lack macro-anatomical abnormalities, often going undetected (Guerrini & Barba, 2021). It is necessary to find better methods for their detection. Diffusion weighted MRI (dMRI) is ideally suited to probe the architecture of tissue. However, in complex structures such as the cortex, conventional dMRI methods (e.g. DTI) are insufficient (Benjamini, 2021). Novel dMRI methods have been used to reflect regional and layer-level abnormalities in the cerebral cortex of rodents (Villaseñor et al., 2023) and humans (Lampinen 2020, Lorio 2020). The b-tensor encoding method provides additional information contained in the dMRI signal and yields parameters more specific to the microstructure of tissue. Q-space trajectory imaging (QTI), an analysis technique for b-tensor encoding images, is used to derive micro fractional anisotropy (µFA) and orientation coherence (Cc), information that is not available with standard dMRI (Westin, 2016). We show the ability of b-tensor dMRI to evaluate the characteristics of the microarchitecture of the cerebral cortex in a rodent model of cortical dysplasia, aiming to improve the detection of FCDs in clinical populations.

Methods: Cortical abnormalities akin to those in FCD were created in Sprague-Dawley rats descended from females that were injected with either BCNU (20 mg/kg) or saline solution at the 15th day of pregnancy (Benardete & Kriegstein, 2002). The experimental animals (n=20/18 BCNU/control) were examined at 120 days after birth (P120). Scanning was performed on a pre-clinical 7T scanner. b-tensor encoding dMRI were acquired using the sequence available in the Preclinical Neuro MRI repository (https://osf.io/ngu4a/) and consisted of 3 b-tensor shapes: linear, spherical and planar (Szczepankiewicz, 2019). Gradient waveforms were optimized using the NOW toolbox (https://github.com/jsjol/NOW), tuned (Lundell, 2019), and scaled in magnitude to achieve 4 b-values (200, 700, 1400 and 2000 s/mm^2). Images were denoised with MP-PCA and corrected for geometric distortions. QTI was used to obtain fractional anisotropy (FA), axial diffusivity (AD), radial diffusivity (RD), mean diffusivity (MD), Cc and µFA. We used a curvilinear coordinate system to sample the dMRI parameters in the animal's cerebral cortex thus providing anatomical correspondence between animals. QTI metrics were obtained at each point, and t-tests were used to assess between-group differences. After scanning, the animals were euthanized, the brains removed, and Nissl staining and immunofluorescence of myelin (MBP), glial cells (GFAP) and neurons (NeuN) were performed.

Results: The largest and most widespread between-group differences corresponded to µFA, which showed reductions in BCNU-treated animals throughout the mid-cortical layers. Other diffusion metrics showed abnormalities interspersed throughout the cortex at different depths. Immunofluorescence analysis showed disorganized neuronal nuclei characteristic of cortical dysplasia. Moreover, myelin content was reduced in BCNU-treated animals, with overall less coherence in the spatial arrangement of myelinated fibers. Finally, experimental animals showed astrocytes that were increased in number and with enlarged processes.

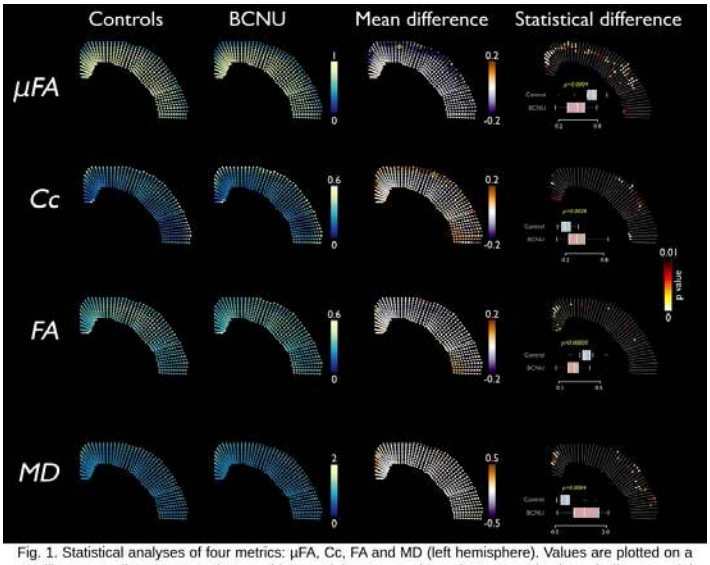

Fig. 1. Statistical analyses of four metrics: μFA, Cc, FA and MD (left hemisphere). Values are plotted on a curvilinear coordinate system that provides spatial correspondence between animals and allows spatial analyses along the depth of the cortex. Only the left hemisphere is shown. The first and the second column show the average values for each of the control and BCNU groups; the third column shows the mean group difference (BCNU-Control); and the fourth column shows the statistical differences (thresholded at $p < 0.01$). For each metric, a box plot from an exemplary point (shown as a yellow circle in the third column) illustrates the identified group differences. μFA shows more sensitivity to detect differences between control and experimental animals.

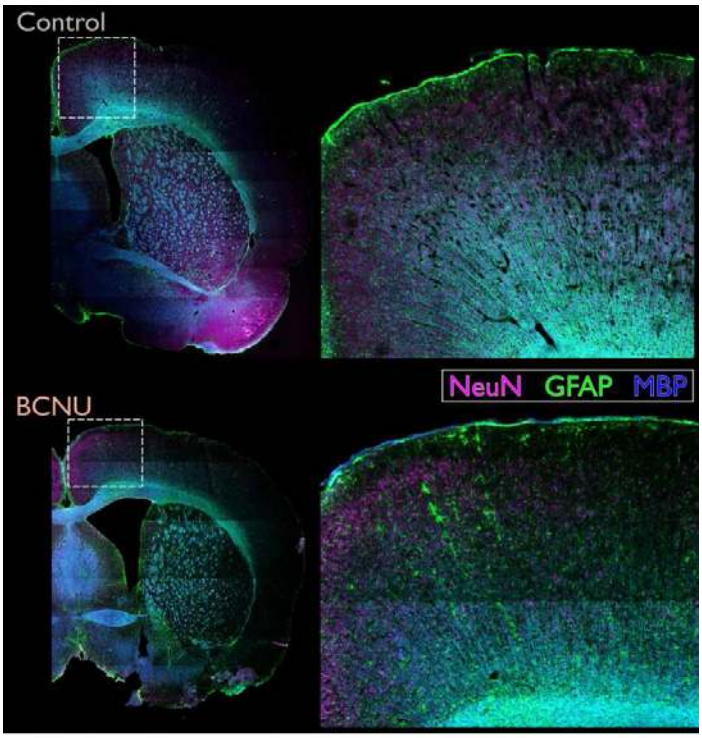

Fig. 2. Immunofluorescence marking Myelin basic protein (MBP), Glial fibrillary acidic protein (GFAP), and Neuronal nuclear protein (NeuN) in a Control and a BCNU-treated animal. Boxed regions in the left column are shown enlarged on the right. BCNU-treated rats have overall less intracortical myelin, neuronal dyslamination, and morphological differences of glial cells.

Conclusions: Advanced dMRI is able to detect abnormalities of the cortex in animals with histological features similar to those seen in FCD. μFA is highly sensitive to detect disorganized myeloarchitecture, which corresponds to alterations seen with immunofluorescence. Glial cells and neuronal dyslamination are also likely responsible for the identified diffusion alterations. b-tensor dMRI metrics are therefore promising for the detection of FCD in humans.

References

1. Benardete, E. A., & Kriegstein, A. R. (2002), 'Increased excitability and decreased sensitivity to GABA in an animal model of dysplastic cortex'. Epilepsia, vol. 43, no. 9, pp. 970-982.
2. Benjamini, D., et al. (2021), 'Diffuse axonal injury has a characteristic multidimensional MRI signature in the human brain', Brain: A Journal of Neurology, vol. 144, no. 3, 800-816.

3. Blümcke, I., Thom, M., Aronica, E., Armstrong, D. D., Vinters, H. V., Palmini, A., Jacques, T. S., Avanzini, G., Barkovich, A. J., Battaglia, G., Becker, A., Cepeda, C., Cendes, F., Colombo, N., Crino, P., Cross, J. H., Delalande, O., Dubeau, F., Duncan, J., Spreafico, R. (2011), 'The clinicopathologic spectrum of focal cortical dysplasias: A consensus classification proposed by an ad hoc Task Force of the ILAE Diagnostic Methods Commission', Epilepsia, vol. 52, no. 1, pp. 158-174.
4. Guerrini, R., & Barba, C. (2021), 'Focal cortical dysplasia: An update on diagnosis and treatment', Expert Review of Neurotherapeutics, vol. 21, no. 11, pp. 1213-1224.
5. Lampinen, B., Zampeli, A., Björkman-Burtscher, I. M., Szczepankiewicz, F., Källén, K.,
6. Compagno Strandberg, M., & Nilsson, M. (2020), 'Tensor-valued diffusion MRI differentiates cortex and white matter in malformations of cortical development associated with epilepsy', Epilepsia, vol. 61, no. 8, pp. 1701-1713.
7. Lorio, S., Adler, S., Gunny, R., D'Arco, F., Kaden, E., Wagstyl, K., Jacques, T. S., Clark, C. A., Cross, J. H., Baldeweg, T., & Carmichael, D. W. (2020), 'MRI profiling of focal cortical dysplasia using multi-compartment diffusion models', Epilepsia, vol. 61, no. 3, pp. 433-444.
8. Lundell, H., Nilsson, M., Dyrby, T. B., Parker, G. J. M., Cristinacce, P. L. H., Zhou, F.-L., Topgaard, D., & Lasič, S. (2019), 'Multidimensional diffusion MRI with spectrally modulated gradients reveals unprecedented microstructural detail', Scientific Reports, vol. 9, no. 1, 9026.
9. Szczepankiewicz, F., Hoge, S., & Westin, C.-F. (2019), 'Linear, planar and spherical tensor-valued diffusion MRI data by free waveform encoding in healthy brain, water, oil and liquid crystals', Data in Brief, vol. 25, 104208.
10. Villaseñor, P. J., Cortés-Servín, D., Pérez-Moriel, A., Aquiles, A., Luna-Munguía, H., Ramirez-Manzanares, A., Coronado-Leija, R., Larriva-Sahd, J., & Concha, L. (2023), 'Multi-tensor diffusion abnormalities of gray matter in an animal model of cortical dysplasia', Frontiers in Neurology, vol. 1

Poster No 2366

Assessing the Recovery of Spinal Cord on Traumatic Spinal Cord Injury using Diffusion Tensor Imaging

Bing Yao[1], Gail Forrest[1], Steven Kirshblum[1]

[1]Kessler Foundation, West Orange, NJ

Introduction: The challenges of spinal cord injury (SCI) extend far beyond physical damage; patients face severe disability, difficulty functioning, and expensive treatments. The questionnaires and exams used to measure recovery[1,2] have several shortcomings, including variability across examiners and not being able to evaluate the spinal cord function below the neurological level[3]. The conventional MRI, however, cannot fully reveal complexities of the change during recovery, providing very little information about the damage that occurs on a microstructural level. In this study, we investigated using the diffusion tensor imaging (DTI) to detect nerve fiber structural changes above and below the injury level in SC.

Methods: Participants: Thirteen acute SCI patients (age=41±17 y/o, F/M=3/10, AIS grade=B to D) and Twelve gender and age matched healthy controls (HCs) (age=43±17 y/o, F/M=3/9) have participated the study. All the participants went through five visits over the course of the first-year post injury (baseline, 2 weeks, 1, 3, and 6 months after the commencement of rehabilitative treatment). The outcome measurements including American Spinal Injury Association Impairment Scale (ASIA), Modified Ashworth Scale (MAS) and Spinal Cord Independence Measure III (SCIM III) were performed at each visit for the patient group. Image Acquisition: All MRIs were acquired at a 3T Siemens scanner. The axial DTI covering the entire cervical and thoracic sections of the cord was acquired with the following parameters: TE=97ms, TR=3600ms, Flip angle=90°; in-plane resolution=1.6x1.6mm, thickness = 3mm, 30 directions with b=1000s/mm. A high-resolution anatomical scan using T2*-weighted Multi-Echo Data Image Combination (MEDIC) sequence matching the DTI slice location was also acquired. Data Analysis: The raw DTI data were corrected for eddy current distortion and motion using FSL then further processed using Diffusion Toolkit. DTI indices including FA, MD, AD, and RD were computed for each voxel. Virtual nerve fibers were reconstructed using the fiber assignment through line propagation approach based on 2nd order Runge Kutta algorithm.

Results: Shorter and thinner fibers were seen on the SCI patients comparing to those on the HCs, suggesting the damaged white matter fibers. The outcome measures by SCIM showed a significant change over the 5 visits($f(4,28) = 13.7$, $p<.001$), suggesting a recovery over the six months post injury. The ASIA result showed the same recovery trend over time but not significantly (figure not shown). Fig. 1 shows the overall AD and FA in the SCI group were significantly lower than those in the HC group and the differences varies at spine locations. Higher values of AD, MD and RD were observed from T3 to T10 Level, indicating a possible structural variation in spine locations. Fig. 2 shows significant differences in AD (Above, below and LOI) and FA (Above and LOI) ($p<0.05$, Mixed Model Analysis) between the SCI and HC groups; All diffusivity measures demonstrated obvious significant changes over time at Below injury level ($p<0.05$, independent t-test). No significant changes over time were found at LOI.

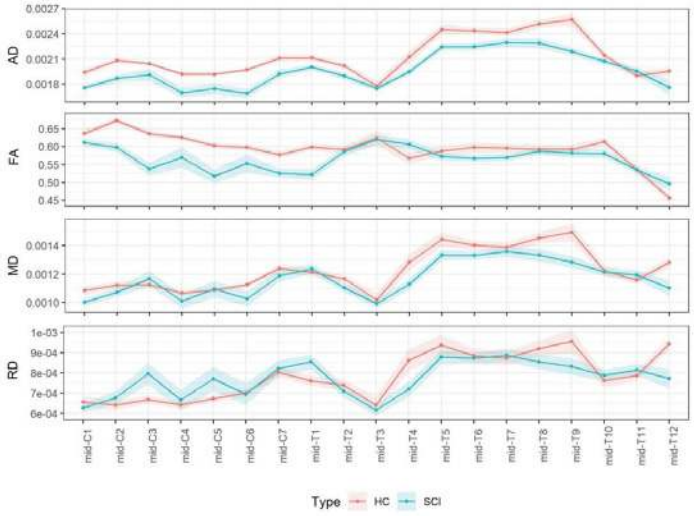

Fig. 1: Comparison of the mean values of the DTI indices (AD, FA, MD and RD) across all spine locations

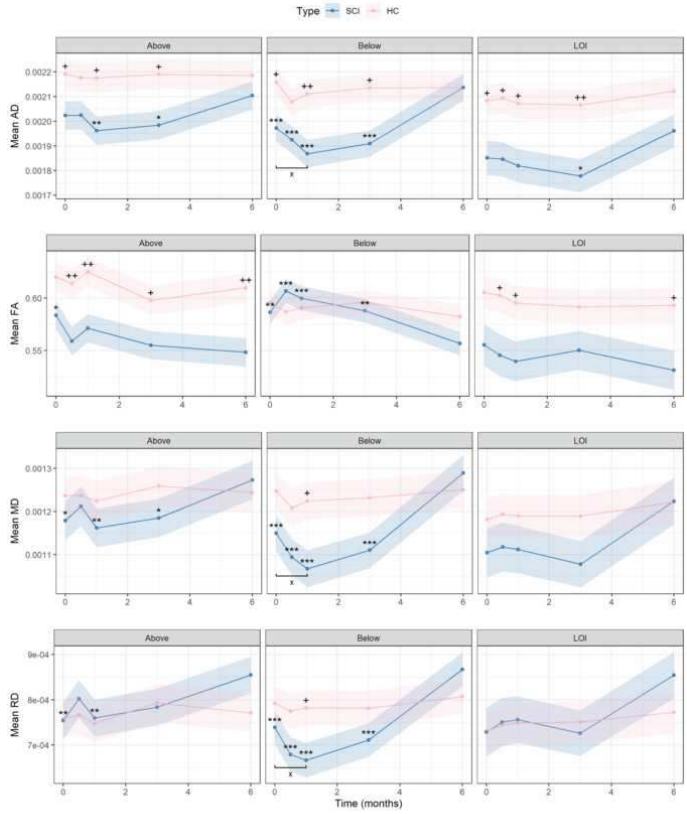

Fig. 2: Above, below and at the injury level comparison of the mean values of AD, FA, MD, and RD between SCI (blue) and Healthy Controls (red) over 6 months of recovery period. Values represent mean ± SEM. Significant differences were found between SCI and HC in AD (Above, below and LOI) and FA (Above and LOI), indicating by "+" ($p<0.05$); All diffusivity measures (AD, FA, MD and RD) demonstrated obvious significant changes over time at Below injury level, indicating by "*" ($p<0.05$, independent t-test). No significant changes over time was found at LOI.

Conclusions: Our data shows FA and AD had significantly lower values in the SCI group. A significant FA reductions above the injury in each visit after baseline, and at the injury level in visits 2, 3, and 5 was observed, which is consistent with the findings of reduced FA particularly at the injury level in previous reports on both acute and chronic patients[4]. It is also noteworthy that FA differed from controls above and at the injury but not below injury regions, suggesting that different impacts to the spine structure due to the injury. This is consistent with previous reports in acute and chronic patients, after injury[5]. Our study demonstrates that DTI may serve as a tool to assess the changes at different regions of the spine, of which information is usually hard to be obtained by traditional evaluation methods.

References
1. Kirshblum, S.C., et al. (2011), "International standards for neurological classification of spinal cord injury", J Spinal Cord Med, 34(6): p. 535- 46.
2. Marino, R.J. and D.E. Graves (2004), "Metric properties of the ASIA motor score: subscales improve correlation with functional activities", Arch Phys Med Rehabil, 85(11): p. 1804-10.
3. Mulachey, M. J., et al. (2013), "Neuromuscular scoliosis in children with spinal cord injury", Top Spinal Cord Inj Rehabil, 19(2): p. 96-103.
4. Chang, Y., et al., (2010), "Diffusion tensor imaging and fiber tractography of patients with cervical spinal cord injury", Journal of Neurotrauma, 27(11), 2033-40.
5. Koskinen, et al., (2013), "The current role of decompressive craniectomy in the management of neurological emergencies", Journal of Neurotrauma, 30(18), 1587-95.

Poster No 2367

A novel groupwise diffusion MRI registration framework using deep learning

Junyi Wang[1], Zhu Xi[1], Mubai Du[1], William Wells III[2], Lauren O'Donnell[2], Fan Zhang[1]

[1]University of Electronic Science and Technology of China, Chengdu, Sichuan, [2]Harvard Medical School, Boston, MA

Introduction: Diffusion MRI (dMRI)[1] enables the estimation of the underlying brain tissue microstructure and tracking of white matter (WM) fiber tracts in vivo[2]. Groupwise registration of dMRI data from multiple individuals is an important task for brain template construction[3] to identify normative brain structures and their variability across different populations for potential diagnosis and treatment of diseases[4,5]. However, groupwise dMRI registration is a challenging task due to the unique nature of dMRI data, which describes not only the strength but also the orientation of water diffusion in brain tissues. Widely used methods perform registration using dMRI-derived scalar images (e.g., fractional anisotropy; FA) across individuals and neglect the important orientation information that can reveal the underlying WM fiber orientation. We propose a novel deep-learning approach for simultaneous registration of dMRI data across multiple individuals into a common space. This work is built on our previous DDMReg[6] method for pairwise dMRI registration and further enables groupwise dMRI registration for brain template construction. Compared with a baseline and a state-of-the-art method, we show a significant improvement of fiber spatial alignment after registration, while maintaining a good volumetric overlap of segmented brain tissue structures.

Methods: From the dMRI data of each subject, we compute two types of input data: 1) FA, which is useful for aligning anatomical structures from the whole brain, and 2) 16 tract orientation maps (TOMs)[7], which are useful for aligning streamlines of specific anatomical WM tracts. The underlying network architecture is based on the popular conditional deformable template creation method[8]. To handle the large amount of input data, we use a two-step training process, including 1) pre-training a subnetwork on each TOM to compute tract-specific templates, and 2) overall network training on FA with the pre-trained tract-specific subnetworks as backbones. After learning, the network learns a deformable field for each subject to warp the FA and TOMs of all subjects into the common template space. In addition, we introduce bidirectional learning that allows reversed registration from the learned template to each subject. Our loss function is shown in Fig 1. For the experiment, we utilize dMRI data from 100 subjects from the Human Connectome Project (HCP)[9] (20 for training, 80 for testing). FA images are computed using SlicerDMRI[10] and TOMs are computed using TractSeg[7]. We compare our method with two template creation methods including the widely used SyN algorithm and the deep learning-based VoxelMorph method. The evaluation metric includes tract distance to assess fiber spatial alignment of the WM tracts, and tissue Dice for volume overlap of the tissue segmentations (i.e., gray matter, white matter, and cerebrospinal fluid).

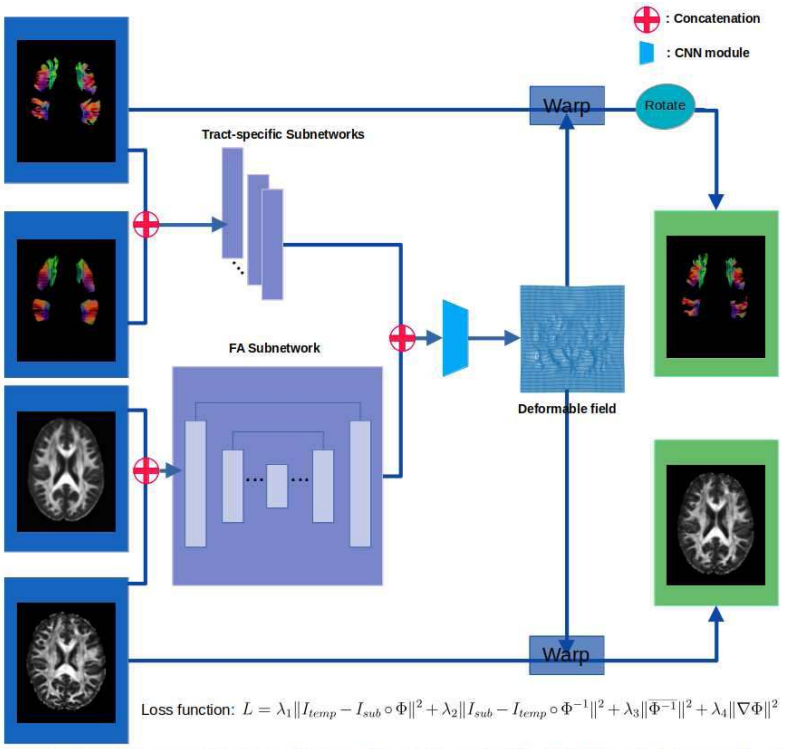

Fig 1. The network architecture of our proposed method. The inputs are the FA and TOM images from 20 subjects, which are concatenated together as a trainable template. Each of the subnetwork generates the deformation fields independently, which are merged with a two-layers CNN model to get the final deformation filed. The reorientation module is used to reorient the TOMs. Weights of the tract-specific subnetworks are pre-trained to reduce computational costs, while the templates generated by each subnetwork are still trainable during the overall training process.The loss function is shown at the bottom, where I_{temp} is the learned template, I_{sub} is an individual subject, ϕ is the deformable flow, $\nabla\phi$ is the gradient of the deformation field.

Results: Fig 2a gives visualization results of the three comparison methods. Our method obtains the warped TOMs that can better align the baseline image, showing a better groupwise registration across subjects. Fig 2b shows the fiber spatial alignment evaluation results. For each tract, there is a significant difference across the 3 methods (via an ANOVA test), where the proposed method obtains overall the best performance. Fig 2c shows the results of the tissue segmentation overlap, where the VoxelMorph and proposed methods generate significantly better performance than the baseline SyN method.

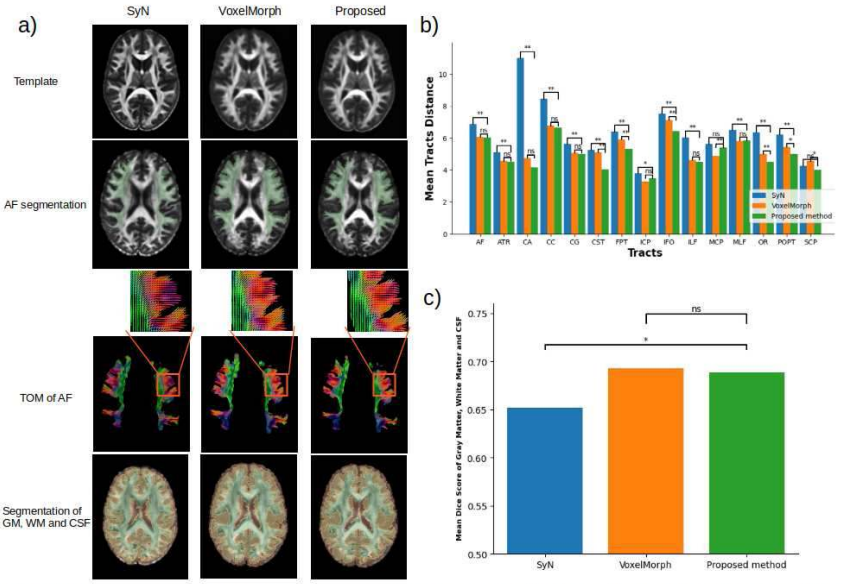

Fig 2. (a) Visualization of the registration results of the three comparison methods, including the generated template (first row), the warped tract segmentation (second row), the warped TOM (third row), and the warped whole brain tissue segmentation (fourth row). (b) Quantitative comparison of the tract distance between the warped fiber tracts across subjects . (c) Quantitative comparison of the volume overlap between the warped tissue segmentations across subjects. (ns - no significant difference; * p < 0.05, ** p < 0.01; AF - arcuate fasciculus).

Conclusions: We develop a deep learning framework that effectively combines tissue orientation and brain structure information for groupwise dMRI registration. We demonstrate advanced registration performance compared to existing groupwise dMRI registration methods. The proposed method can serve as an important tool for building brain atlases.

References
1. Basser, P. J. et al.(1996). Microstructural and physiological features of tissues elucidated by quantitative-diffusion-tensor MRI. Journal of Magnetic Resonance. Series B, 111(3), 209–219.
2. Zhang, F. et al. (2022). Quantitative mapping of the brain's structural connectivity using diffusion MRI tractography: A review. NeuroImage, 249, 118870.
3. Zhang, H. et al. (2007). Unbiased white matter atlas construction using diffusion tensor images. Medical Image Computing and Computer-Assisted Intervention: MICCAI ... International Conference on Medical Image Computing and Computer-Assisted Intervention, 10(Pt 2), 211–218.
4. Zhang, F. et al. (2018). An anatomically curated fiber clustering white matter atlas for consistent white matter tract parcellation across the lifespan. NeuroImage, 179, 429–447.
5. Yeh, F.-C. et al.(2018). Population-averaged atlas of the macroscale human structural connectome and its network topology. NeuroImage, 178, 57–68.
6. Zhang, F. et al. (2022). Deep Diffusion MRI Registration (DDMReg): A Deep Learning Method for Diffusion MRI Registration. IEEE Transactions on Medical Imaging, 41(6), 1454–1467.
7. Wasserthal, J.et al. (2019). Combined tract segmentation and orientation mapping for bundle-specific tractography. In arXiv [cs.CV]. arXiv. http://arxiv.org/abs/1901.10271
8. Dalca, A. et al. (2019). Learning conditional deformable templates with convolutional networks. Advances in Neural Information Processing Systems, 32. https://proceedings.neurips.cc/paper/2019/hash/bbcbff5c1f1ded46c25d28119a85c6c2-Abstract.html
9. Elam, J. S. et al. (2021). The Human Connectome Project: A retrospective. NeuroImage, 244, 118543.
10. Zhang, F. et al. (2020). SlicerDMRI: Diffusion MRI and Tractography Research Software for Brain Cancer Surgery Planning and Visualization. JCO Clinical Cancer Informatics, 4, 299–309.

Poster No 2368

Concurrent Mapping of Brain Connections in Neonates and Adults with dMRI Tractography

Wei Zhang[1], Yijie Li[1], Ruixi Zheng[1], Yuqian Chen[2], Leo Zekelman[2], Jarrett Rushmore[3], Yogesh Rathi[2], Nikos Makris[2], Lauren O'Donnell[2], Fan Zhang[1]

[1]University of Electronic Science and Technology of China, Chengdu, Sichuan, [2]Harvard Medical School, Boston, MA, [3]Boston University, Boston, MA

Introduction: Comparison of the white matter (WM) structural connections between adult and neonate brains via diffusion MRI (dMRI) can contribute to our understanding of normal brain development and assist identification of potential biomarkers for neurological disorders[1,2]. Brain WM atlases are an important tool to reveal WM differences between adults and neonates[3,4,5]. However, there have been no atlases that can concurrently map WM connections across adult and neonate populations. This study presents a novel dMRI tractography streamline clustering atlas consisting of WM connections from both adults and newborns. The atlas is created concurrently using the high-quality dMRI data from the Human Connectome Project (HCP)[6] and the Developing Human Connectome Project (dHCP)[7], where each cluster in the atlas includes streamlines from both populations. With the proposed atlas, we perform a comparative study of major WM fiber bundles (n=58) between the two populations and find widespread differences in WM structures across the brain.

Methods: Dataset: dMRI data from 100 healthy young adults (29±7 years; 50 F, 50 M) from the HCP database and 100 healthy new-born babies (33.43±8.86 post-conceptional weeks; 50 F, 50 M) were used. Atlas creation: Fig 1 gives the method overview. First, whole-brain tractography is performed to reconstruct whole brain WM streamlines. We use our two-tensor Unscented Kalman filter (UKF) algorithm[8], which accounts for crossing fibers and offers sensitive and reliable fiber tracking within a wide range of populations[5,9]. Second, streamline clustering is performed to subdivide the tractography into fine-scale clusters. We use our well-established whitematteranalysis pipeline[5] for simultaneous streamline clustering across all HCP and dHCP subjects. This generates a streamline clustering atlas including 800 clusters. Third, anatomical atlas curation is performed to annotate each cluster with an anatomical label according to our ORG atlas[5,10]. We calculate cluster distances between the new atlas and the ORG atlas, and then assign each new atlas cluster with the label of the closest ORG cluster. In total, our new atlas contains an anatomical tract parcellation including 58 major anatomical WM tracts. Finally, subject-specific tractography parcellation is performed by applying the curated atlas to the whole brain tractography of each individual in the HCP and dHCP datasets. Comparison between HCP and dHCP: Our atlas was created from both HCP and dHCP, with each cluster containing streamlines from both populations. This ensures that the atlas clustering is consistent across the two populations. We perform two types of comparisons. First, we measure the coefficient of variation (CoV) of the number of streamlines (NoF) of each tract in each population. This is to compare the variability of the corresponding WM tracts between the two populations. Second, we measure the lateralization index (LI) of NoF of each association tract in each population. This is to compare the differences of WM lateralization effect between the two populations.

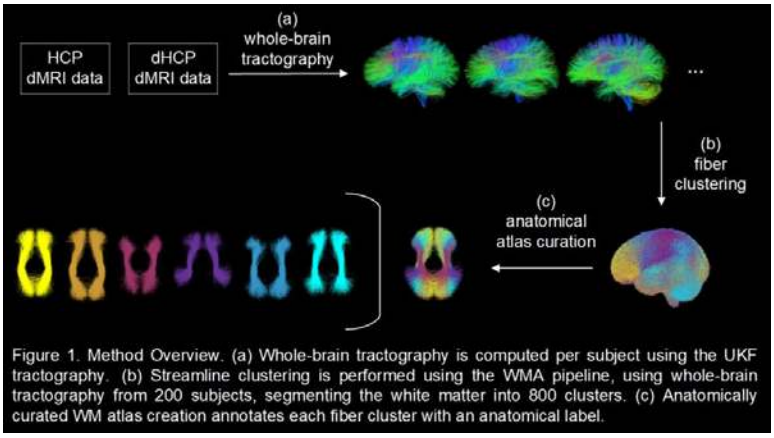

Figure 1. Method Overview. (a) Whole-brain tractography is computed per subject using the UKF tractography. (b) Streamline clustering is performed using the WMA pipeline, using whole-brain tractography from 200 subjects, segmenting the white matter into 800 clusters. (c) Anatomically curated WM atlas creation annotates each fiber cluster with an anatomical label.

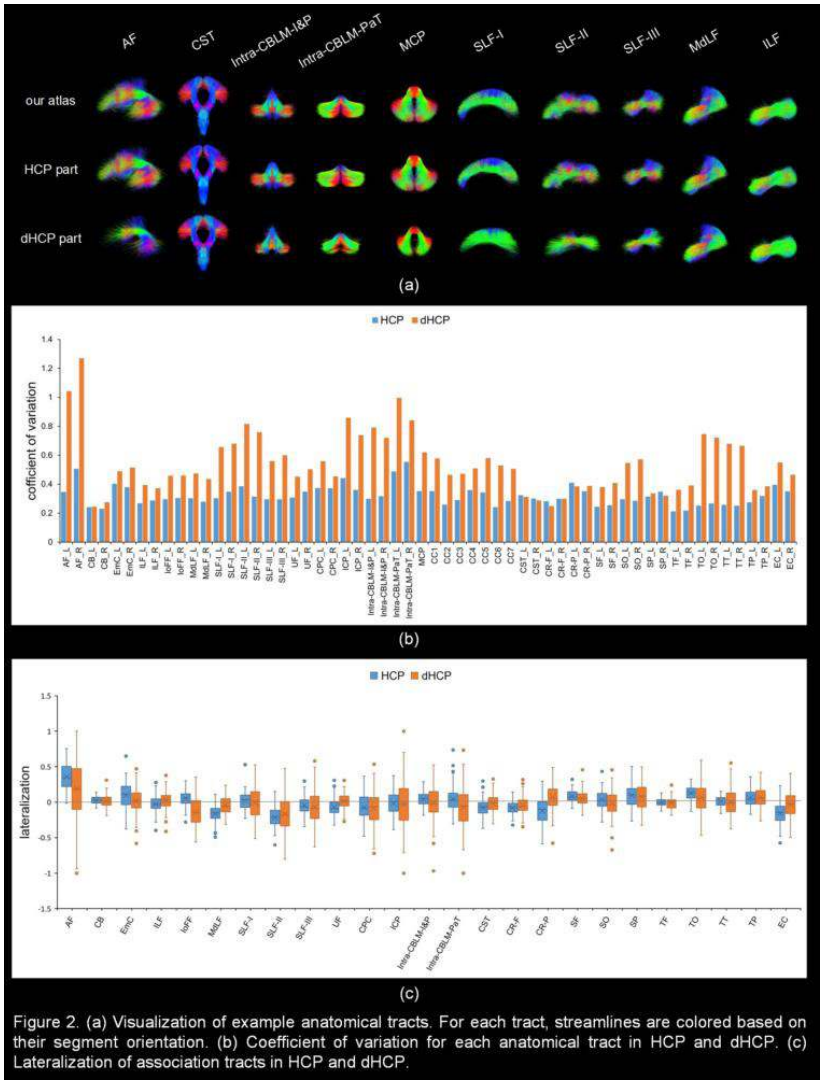

Figure 2. (a) Visualization of example anatomical tracts. For each tract, streamlines are colored based on their segment orientation. (b) Coefficient of variation for each anatomical tract in HCP and dHCP. (c) Lateralization of association tracts in HCP and dHCP.

Results: Fig 2a gives a visualization of example fiber tracts, showing while many tracts have visually different shapes between HCP and dHCP (e.g. AF and MCP), some are highly visually similar (e.g. CST and ILF). Fig 2b shows that dHCP has generally higher CoV of NoF across the fiber tracts, indicating a higher variability of the brain WM structures in the newborns than the adults. Fig 3c shows the lateralization effects in newborns are generally smaller than in adults. Interestingly, the AF tract has the highest LI scores across all association tracts in the atlas,where HCP has a stronger lateralization effect than dHCP.

Conclusions: This study presents a novel cross-population WM atlas for concurrent mapping of brain connections between adults and neonates. We perform a comparative assessment of the WM connections and identify widespread differences between the two populations in terms of streamline counts and tract visualization.

References
1. Zhai, G. (2003), 'Comparisons of regional white matter diffusion in healthy neonates and adults performed with a 3.0-T head-only MR imaging unit', Radiology, 229(3), 673–681.
2. Warrington, S. (2022), 'Concurrent mapping of brain ontogeny and phylogeny within a common space: Standardized tractography and applications', Science Advances, 8(42), eabq2022.
3. Wilkinson, M. (2017), 'Detection and Growth Pattern of Arcuate Fasciculus from Newborn to Adult', Frontiers in Neuroscience, 11, 389.
4. Liang, W. (2022), 'A comparative study of the superior longitudinal fasciculus subdivisions between neonates and young adults', Brain Structure & Function, 227(8), 2713–2730.
5. Zhang, F. (2018), 'An anatomically curated fiber clustering white matter atlas for consistent white matter tract parcellation across the lifespan', NeuroImage, 179, 429–447.
6. Elam, J. S. (2021), 'The Human Connectome Project: A retrospective', NeuroImage, 244, 118543.
7. Makropoulos, A. (2017), 'The Developing Human Connectome Project: a Minimal Processing Pipeline for Neonatal Cortical Surface Reconstruction', In bioRxiv (p. 125526). https://doi.org/10.1101/125526
8. Malcolm, J. G. (2010), 'Filtered multitensor tractography', IEEE Transactions on Medical Imaging, 29(9), 1664–1675.
9. Zhang, F. (2020), 'Deep white matter analysis (DeepWMA): Fast and consistent tractography segmentation', Medical Image Analysis, 65, 101761.
10. Zhang, F. (2019). 'Test-retest reproducibility of white matter parcellation using diffusion MRI tractography fiber clustering', Human Brain Mapping, 40(10), 3041–3057.

Poster No 2369

Changes of DTI scalars related to disease severity and cognitive impairment in PSP

Silja Kannenberg[1], Ann Carolin Hausmann[2], Alfons Schnitzler[3], Christian Hartmann[4], Luisa Wolf[5], Christian Rubbert[6], Julian Caspers[7]

[1]Institute of Clinical Neuroscience &Medical Psychology, Medical Faculty, Heinrich-Heine-University, Duesseldorf, Germany, [2]University Hospital Duesseldorf, Duesseldorf, Germany, [3]Institute of Clinical Neuroscience & Medical Psychology, Medical Faculty, Heinrich-Heine-University, Duesseldorf, Germany, [4]Department of Neurology, Medical Faculty, University Hospital Duesseldorf, Duesseldorf, Germany, [5]Department of Diagnostic and Interventional Radiology, Medical Faculty and University Hospital, Duesseldorf, NRW, [6]Medical Faculty and University Hospital Düsseldorf, Düsseldorf, NRW, [7]Heinrich Heine University, Düsseldorf, Nordrhein-Westfalen

Introduction: Progressive supranuclear palsy (PSP) is a rapidly progressive neurodegenerative disorder accompanied with specific clinical symptoms, such as postural instability with backward falls and vertical gaze palsy. Though magnetic resonance imaging (MRI) markers have been identified, there is no consensus on broader white matter (WM) atrophy patterns. Understanding how WM degeneration could account for the disease-specific symptom complex and the underlying pathologies is crucial. We aimed to identify changes in diffusion tensor imaging (DTI) parameter changes of WM tracts related to cognitive performance and disease severity in PSP.

Methods: 15 patients (5 male; age: 70.07±7.03 years; disease duration: 14.07±14.24 months) with PSP-Richardson's syndrome completed the Montreal Cognitive Assessment (MoCA) and PSP Rating Scale (PSPRS). Multi-shell diffusion MRI (dMRI) was acquired and preprocessed on a 3T Siemens Prisma with a protocol according to the Human Connectome Project in Aging (HCP-A; 64 head coil, voxel-size 1.5mm^3, 92 slices, FOV 210x210mm, TR=3200ms, TE=89ms, flip angle=90°, 185 gradient directions, b-values 0, 1500, 3000 s/mm^2). Fractional anisotropy (FA), mean diffusivity (MD), axial diffusivity (AD), and radial diffusivity (RD) images were created using dtifit in FSL v. 6.0 and further processed with TBSS. Voxel-wise analyses were applied on the skeletonized FA, MD, AD, and RD data for correlations with MoCA and PSPRS sum score using general linear models and permutation testing (5000 permutations) controlling for multiple comparisons and applying Threshold-Free Cluster Enhancement (TFCE; p≤0.05, FWE-corrected). Significant clusters were located and labelled anatomically to the Johns Hopkins University WM tractography atlas.

Results: We found clusters of reduced FA values correlated with increased PSPRS sum score (M=36.07±9.07) in the following WM tracts: corpus callosum (genu and body); bilateral superior, middle and inferior cerebellar peduncle; bilateral corticospinal tracts; bilateral medial lemniscus; bilateral anterior thalamic radiation (p=.028). The PSPRS gait sub score correlated highly with the mentioned WM tracts (p<.001). Complementing this, we found significant positive correlations between MD and RD and PSPRS scores in: bilateral anterior and posterior thalamic radiation; bilateral corticospinal tract; corpus callosum (genu;body;splenium); bilateral inferior and superior cerebellar peduncle; posterior corona radiata; bilateral superior longitudinal fasciculus (Fig. 1).FA and AD values exhibited significant positive correlations with MoCA scores (M=19.62±4.50) in the following WM tracts: bilateral middle cerebellar peduncle; external capsule; bilateral optic radiation; bilateral superior longitudinal fasciculus; bilateral anterior and posterior corona radiata; bilateral inferior fronto-occipital fasciculus; left internal capsule; forceps minor and major. Further, we found significant negative correlations of RD and MoCA in: bilateral anterior

thalamic radiation; bilateral corticospinal tract; corpus callosum (genu;body;splenium); bilateral inferior fronto-occipital fasciculus; bilateral superior longitudinal fasciculus (Fig. 2).

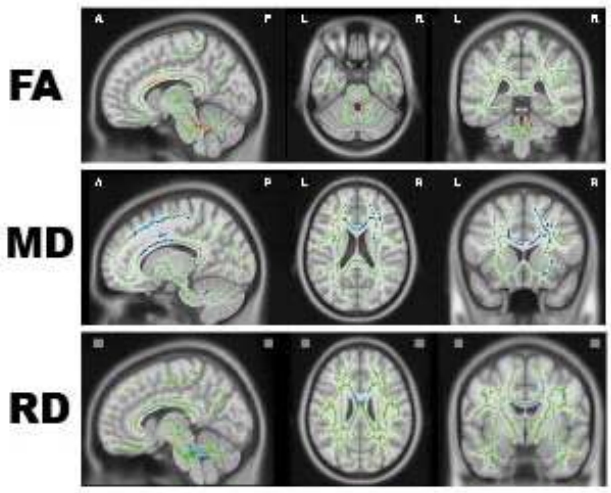

Fig. 1 TBSS results showing voxels where an increase in PSPRS score was significantly correlated with FA decrease (red-yellow) as well as MD increase (blue) and RD increase (blue).

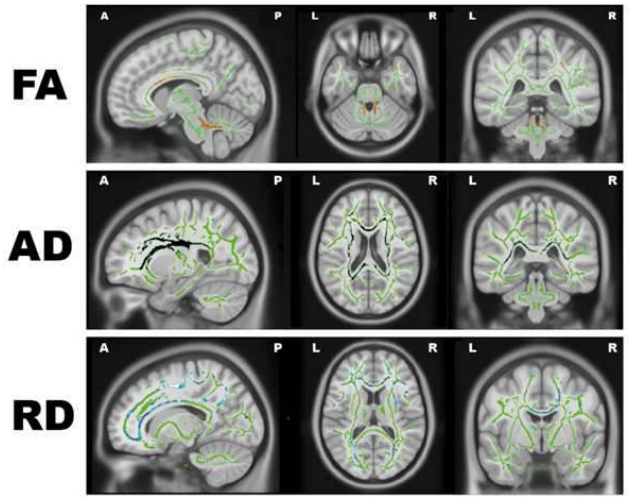

TBSS results showing voxels where a decrease in MoCA score was significantly correlated with FA decrease (red-yellow) as well as AD decrease (black) and RD increase (blue).

Conclusions: We revealed areas of significant WM tract degeneration related to markers of cognitive dysfunction and disease severity in PSP; reduced FA values complemented by increased MD and RD values observed in motor-related WM tracts incl. the corticospinal tract, corpus callosum and cerebellar peduncles are probably related to specific motor symptoms of the disease such as unbalanced gait and postural instability. FA decrease in the superior longitudinal fasciculus can be linked to cognitive decline through frontoparietal decoupling, especially regarding impairment of visuospatial abilities. As PSP might be a more network-based disorder, the present work confirms that considering disease-specific WM atrophy patterns might provide a better understanding of the complex symptom-characteristics of PSP.

References

1. Glasser, M. F., Sotiropoulos, S. N., Wilson, J. A., Coalson, T. S., Fischl, B., Andersson, J. L., ... & Wu-Minn HCP Consortium. (2013). The minimal preprocessing pipelines for the Human Connectome Project. Neuroimage, 80, 105-124.
2. Höglinger, G. U., Respondek, G., Stamelou, M., Kurz, C., Josephs, K. A., Lang, A. E., ... & Bordelon, Y. (2017). Clinical diagnosis of progressive supranuclear palsy: the movement disorder society criteria. Movement Disorders, 32(6), 853-864.
3. Koshiyama, D., Fukunaga, M., Okada, N., Morita, K., Nemoto, K., Yamashita, F., ... & Hashimoto, R. (2020). Association between the superior longitudinal fasciculus and perceptual organization and working memory: a diffusion tensor imaging study. Neuroscience Letters, 738, 135349.
4. Massey, L. A., Jäger, H. R., Paviour, D. C., O'Sullivan, S. S., Ling, H., Williams, D. R., ... & Micallef, C. (2013). The midbrain to pons ratio: a simple and specific MRI sign of progressive supranuclear palsy. Neurology, 80(20), 1856-1861.

5. Potrusil, T., Krismer, F., Beliveau, V., Seppi, K., Müller, C., Troger, F., ... & Scherfler, C. (2020). Diagnostic potential of automated tractography in progressive supranuclear palsy variants. Parkinsonism & Related Disorders, 72, 65-71.
6. Prasad, S., Rajan, A., Pasha, S. A., Mangalore, S., Saini, J., Ingalhalikar, M., & Pal, P. K. (2021). Abnormal structural connectivity in progressive supranuclear palsy—Richardson syndrome. Acta Neurologica Scandinavica, 143(4), 430-440.
7. Quattrone, A., Morelli, M., Nigro, S., Quattrone, A., Vescio, B., Arabia, G., ... & Caracciolo, M. (2018). A new MR imaging index for differentiation of progressive supranuclear palsy-parkinsonism from Parkinson's disease. Parkinsonism & related disorders, 54, 3-8.
8. Sintini, I., Kaufman, K., Botha, H., Martin, P. R., Loushin, S. R., Senjem, M. L., ... & Ali, F. (2021). Neuroimaging correlates of gait abnormalities in progressive supranuclear palsy. NeuroImage: Clinical, 32, 102850.
9. Whitwell, J. L., Master, A. V., Avula, R., Kantarci, K., Eggers, S. D., Edmonson, H. A., ... & Josephs, K. A. (2011). Clinical correlates of white matter tract degeneration in progressive supranuclear palsy. Archives of neurology, 68(6), 753-760.
10. Worker, A., Blain, C., Jarosz, J., Chaudhuri, K. R., Barker, G. J., Williams, S. C., ... & Simmons, A. (2014). Diffusion tensor imaging of Parkinson's disease, multiple system atrophy and progressives

Poster No 2370

Modulation of inhibitory control by stimulation of medial prefrontal cortex

Ahsan Khan[1], Raymond Kai-Yu Tong[1]

[1]*The Chinese University of Hong Kong, Ma Liu Shui, Shatin*

Introduction: Retrieval of target memories can result in forgetting of other related non-target memories, a phenomenon termed as retrieval induced forgetting (RIF). The psychological and neurobiological mechanisms underlying RIF, particularly the relationship between remembering and forgetting, are only partially understood. The objective of this study was to investigate the inhibitory control model, which posits that the act of remembering target memories inhibits non-target items, leading to subsequent forgetting. According to this model, these two processes, remembering and forgetting, occur independently of each other. We tested this model by stimulating the medial prefrontal cortex (MPC), a node implicated in inhibitory control and memory forgetting, to investigate RIF mechanisms. In addition, we investigated the electrophysiological correlates of stimulation induced modulation of inhibitory control.

Methods: The experiment was structured into 5 main parts, including, the study phase, stimulation, retrieval practice phase, distractor phase, and test phase. During the study phase, participants were instructed to study the items presented on the screen and were told that they would be tested later on those items. Following the study phase, stimulation was performed for 15 minutes, during which participants rested. Stimulation electrodes were placed in a ring configuration based on the 10-20 EEG electrode placement method. The target electrode was placed at the Fz location, whereas 4 return electrodes were placed at AF3, AF4, FC3, and FC4. Immediately after stimulation, retrieval practice was performed in which participants recalled some of the exemplars (RP+ items) when the category cue associated with the exemplar stem appeared on the screen. Participants performed three retrieval practices for each practiced item. Post-stimulation measurements then continued with a distractor phase lasting for 5 minutes followed by a final memory test phase during which memory for all the studied items was tested.

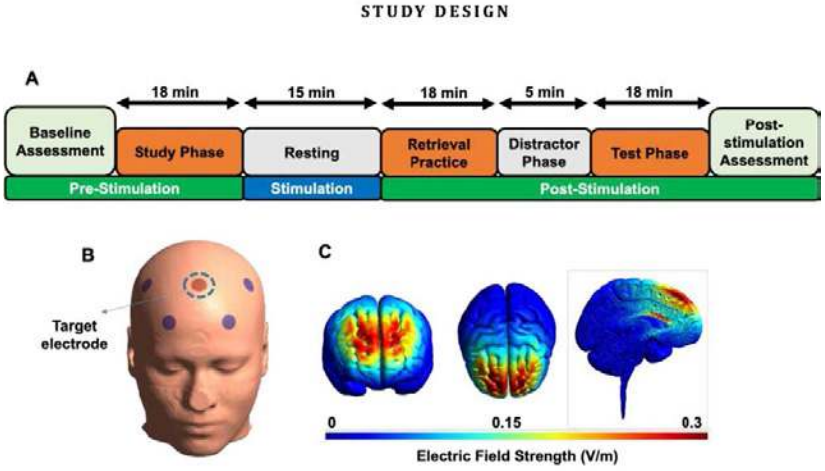

Results: MPC stimulation selectively reduced forgetting of non-target memories, aligning with the inhibitory control model, while leaving target memories unaffected. The observed decrease in RIF was associated with enhanced beta desynchronization in the left dorsolateral prefrontal cortex (left-DLPFC) in an early time window (<500 msec) during retrieval practice, followed by a stronger beta desynchronization in the parietal cortex.

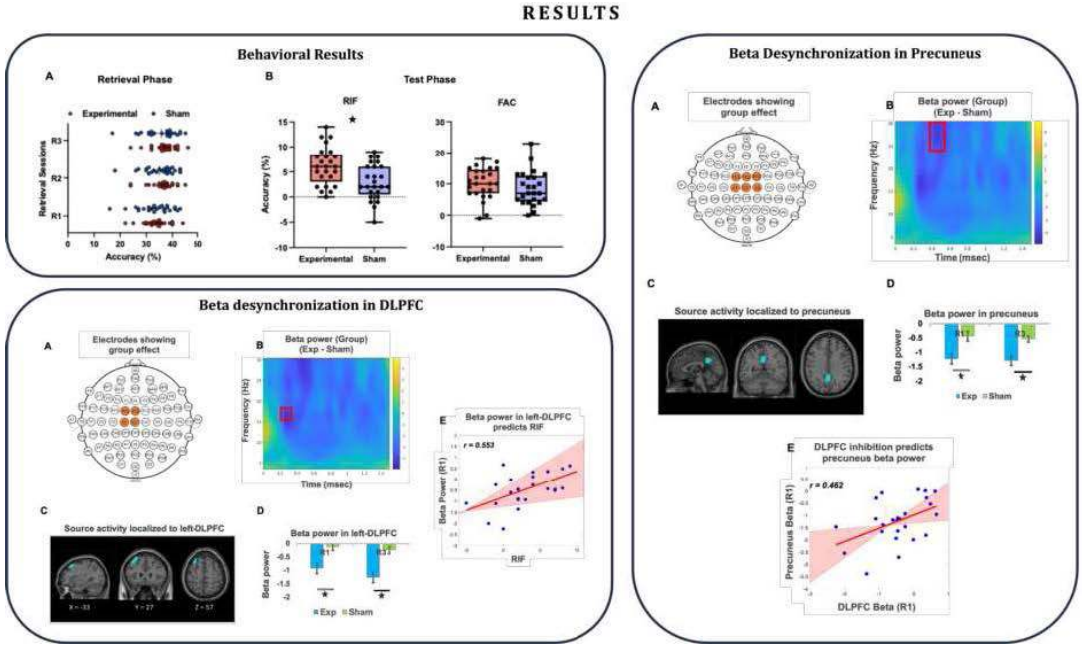

Conclusions: These findings suggest that MPC stimulation disrupts inhibitory control by desynchronizing beta band activity in the left-DLPFC, ultimately leading to increased retrieval of non-target memories and a more robust desynchronization in the parietal cortex, a recognized marker of successful memory retrieval.

References

1. Anderson MC (2003) Rethinking interference theory: Executive control and the mechanisms of forgetting. Journal of memory and language 49:415-445.
2. Anderson MC, Hulbert JC (2020) Active forgetting: Adaptation of memory by prefrontal control. Annual Review of Psychology 72.
3. Anderson MC, Bjork RA, Bjork EL (1994) Remembering can cause forgetting: retrieval dynamics in long-term memory. Journal of Experimental Psychology: Learning, Memory, and Cognition 20:1063.
4. Bäuml K-H, Kuhbandner C (2007) Remembering can cause forgetting—but not in negative moods. Psychological Science 18:111-115.
5. Castiglione A, Wagner J, Anderson M, Aron AR (2019) Preventing a Thought from Coming to Mind Elicits Increased Right Frontal Beta Just as Stopping Action Does. Cereb Cortex 29:2160-2172.
6. Ciaramelli E, Grady CL, Moscovitch M (2008) Top-down and bottom-up attention to memory: a hypothesis (AtoM) on the role of the posterior parietal cortex in memory retrieval. Neuropsychologia 46:1828-1851.
7. Cohen MX (2019) A better way to define and describe Morlet wavelets for time-frequency analysis. NeuroImage 199:81-86.
8. Crespo-García M, Wang Y, Jiang M, Anderson MC, Lei X (2022) Anterior cingulate cortex signals the need to control intrusive thoughts during motivated forgetting. Journal of Neuroscience 42:4342-4359.
9. Delorme A, Makeig S (2004) EEGLAB: an open source toolbox for analysis of single-trial EEG dynamics including independent component analysis. Journal of neuroscience methods 134:9-21.
10. Gross J, Kujala J, Hämäläinen M, Timmermann L, Schnitzler A, Salmelin R (2001) Dynamic imaging of coherent sources: studying neural interactions in the human brain. Proceedings of the National Academy of Sciences 98:694-699.
11. Hanslmayr S, Staudigl T, Fellner M-C (2012) Oscillatory power decreases and long-term memory: the information via desynchronization hypothesis. Frontiers in human neuroscience 6:74.
12. Hanslmayr S, Staudigl T, Aslan A, Bäuml K-H (2010) Theta oscillations predict the detrimental effects of memory retrieval. Cognitive, Affective, & Behavioral Neuroscience 10:329-338.
13. Hanslmayr S, Pastötter B, Bäuml K-H, Gruber S, Wimber M, Klimesch W (2008) The electrophysiological dynamics of interference during the Stroop task. Journal of cognitive neuroscience 20:215-225.
14. Hwang K, Ghuman AS, Manoach DS, Jones SR, Luna B (2014) Cortical neurodynamics of inhibitory control. Journal of Neuroscience 34:9551-9561.

Poster No 2371

Constructing EEG Networks to Detect Changes in Resting and Cognitive Brain Dynamics After Anesthesia

Elizabeth Teel[1], Kira Dolhan[2], George Mashour[3], Stefanie Blain-Moraes[2]

[1]Concordia University, Montréal, Quebec, [2]McGill University, Montreal, Quebec, [3]University of Michigan, Ann Arbor, MI

Introduction: Constructing graphs from neurophysiological data requires several input parameters[1-3] but the optimal parameters to study changes in cognitive function are unknown. Our objective was to compare EEG-derived brain network

outcomes from graphs constructed using different input parameters from data recorded at rest and during cognitive testing as healthy adults recovered from anesthetic-induced unconsciousness.

Methods: Healthy adults (age= 25.3 ± 2.2 years) were randomized into anesthesia (n=9) or control (n=6) groups. Anesthesia subjects were rendered deeply unconscious during a 3-hour intervention period, while controls were awake and minimally active (reading, watching TV, etc.). Subjects completed a cognitive testing battery 30mins before and 0-, 30-, 60-, 90-, and 120-mins post-intervention.[4] Subjects wore a 128-channel EEG headset (Electrical Geodesics, Inc.) throughout the study. EEG data were source localized using a forward model and mean source activity was calculated across each of the 82 regions of interest (ROI) defined by the Automated Anatomical Labelling brain atlas.[3] Functional connectivity (FC) matrices were derived from sensor- and source-space data. Pearson's correlations were calculated between the amplitude envelope (amplitude envelope coupling; AEC) or instantaneous phase (weighted phase lag index; wPLI) of each combination of pair-wise electrodes or ROIs.[3] Graphs were constructed on all FC matrices using weighted and binary methods. For binary graphs, the FC values were set to 0 or 1 based on an orthogonal minimally spanning tree threshold.[5] Path length, global efficiency, clustering coefficient (CC), small-world architecture (SWA), modularity, node strength, and betweenness centrality (BC) outcomes were calculated for each graph. Mixed linear effect models evaluated the effect of parameter, time, and their interaction, with random terms for participant and time. Significance was set at p=0.01.

Results: No significant interaction effects were observed for signal source and FC type. Main effects of time were observed, with more significant differences for AEC-derived network measures (CC: p=0.0007; SWA: p=0.0009; strength: p=0.0005). A significant interaction effect for modularity was observed (p=0.004) when comparing weighted and binary graphs, with the rate of change greater for binary graphs. There were also five significant main effects of time; the regression line was significantly steeper for binary graphs for four of the five variables (Figure 1). Binary graphs generated using sensor space data and AEC FC matrices best captured the effects of anesthetic-induced unconsciousness in resting data; cognitive graphs were constructed using this combination of input parameters. Five significant interaction effects (time by task-condition) were observed during the Digit Symbol Substitution Test (CC: p<0.0001, SWA: p<0.0001, modularity: p=0.0007, BC: p=0.002, & strength: p<0.0001). Significant interaction effects were also observed during administrations of the Visual Object Learning Test (modularity: p=0.005, strength: p=0.0009) and Fractal N-Back Test (strength: p=0.0009). Main effects of time were observed for node strength, with outcomes increasing across recovery from unconsciousness when comparing all cognitive tests to resting conditions (p≤0.004, Figure 2).

Conclusions: Under resting conditions, graphs were robust to input parameter selection with few interaction effects observed. Conversely, several main effects of time were found, suggesting that most input parameter selections can identify anesthetic-induced changes in functional brain networks. Network organization differed between cognitive and task-free conditions, with the strongest effects observed during memory tests. These findings add to the growing literature highlighting the potential for network measures to elucidate neural correlates of consciousness and cognitive function.[6,7]

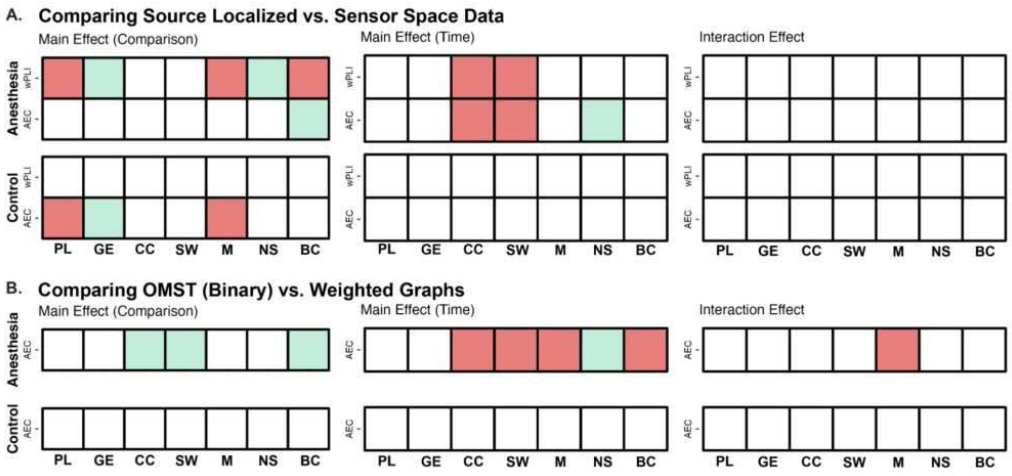

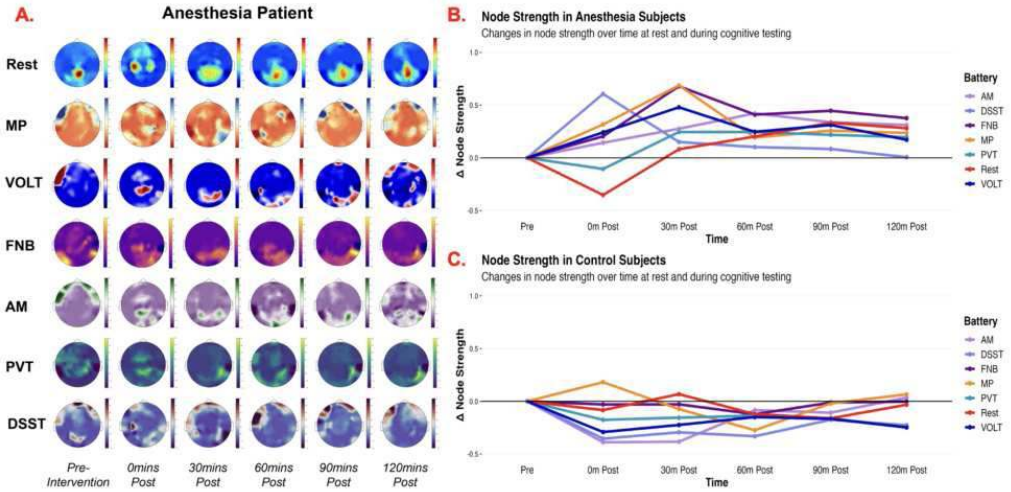

References

1. Engel, A. K., C. Gerloff, C. C. Hilgetag and G. Nolte (2013). "Intrinsic coupling modes: multiscale interactions in ongoing brain activity." Neuron 80(4): 867-886.
2. Bullmore, E. and O. Sporns (2009). "Complex brain networks: graph theoretical analysis of structural and functional systems." Nature reviews neuroscience 10(3): 186-198.
3. Duclos, C., C. Maschke, Y. Mahdid, K. Berkun, J. da Silva Castanheira, V. Tarnal, P. Picton, G. Vanini, G. Golmirzaie and E. Janke (2021). "Differential classification of states of consciousness using envelope-and phase-based functional connectivity." NeuroImage 237: 118171.
4. Maier, K. L., A. R. McKinstry-Wu, B. J. A. Palanca, V. Tarnal, S. Blain-Moraes, M. Basner, M. S. Avidan, G. A. Mashour and M. B. Kelz (2017). "Protocol for the Reconstructing Consciousness and Cognition (ReCCognition) Study." Front Hum Neurosci 11: 284.
5. Dimitriadis, S. I., M. Antonakakis, P. Simos, J. M. Fletcher and A. C. Papanicolaou (2017). "Data-driven topological filtering based on orthogonal minimal spanning trees: application to multigroup magnetoencephalography resting-state connectivity." Brain connectivity 7(10): 661-670.
6. Blain-Moraes, S., V. Tarnal, G. Vanini, T. Bel-Behar, E. Janke, P. Picton, G. Golmirzaie, B. J. Palanca, M. S. Avidan and M. B. Kelz (2017). "Network efficiency and posterior alpha patterns are markers of recovery from general anesthesia: a high-density electroencephalography study in healthy volunteers." Frontiers in human neuroscience 11: 328.
7. Wright, L. M., M. De Marco and A. Venneri (2021). "A graph theory approach to clarifying aging and disease related changes in cognitive networks." Frontiers in aging neuroscience 13: 676618.

Poster No 2372

Ballistocardiogram artifact removal in simultaneous EEG- fMRI using deep learning

Wing Yat Alpha Cheung[1], Wutao Lou[1]

[1]The Chinese University of Hong Kong, Hong Kong, Hong Kong

Introduction: Ballistocardiogram (BCG) artifacts caused by cardiac-induced movement in simultaneous EEG-fMRI data acquisition can seriously contaminate the EEG data. It is critical that BCG artifacts are eliminated from BCG-corrupted EEG signals. However, considering the unstable and time-varying changes in amplitude of BCG artifacts across different EEG channels, removing the BCG artifacts effectively is still a challenging task[1]. Optimal basis set (OBS) is a commonly used method for BCG artifact removal, but OBS depends on clean QRS complex detection from a high-quality ECG signal, which is not always available[2].

Methods: In the current study, we proposed a deep learning model based on the U-Net architecture to remove BCG artifacts automatically without the need for reference ECG signals (as shown in Figure 1). An open-access simultaneous EEG-fMRI dataset containing 22 sets of 61-channel ground truth clean EEG signals and BCG-corrupted EEG signals was used[3]. The MNE open-source Python library[4] was used to import the corrupted and clean data into Python (version 3.10.13). All channels were normalized with z-score normalization. Both corrupt and clean data were downsampled and segmented into 3-second epochs. Each epoch contained an EEG segment of 61 channels by 768 data points. Subsequently, time-synchronized corrupt and clean epochs of the same subject were concatenated, to generate mini-batches of data for model training and validation. The mini batches were then randomly assigned to training, validation and testing sets following a 70%, 15% and 15% split. A mean-squared error (MSE) loss function was used to evaluate the error generated between the outputs of network and ground truth, as shown in Figure 2.

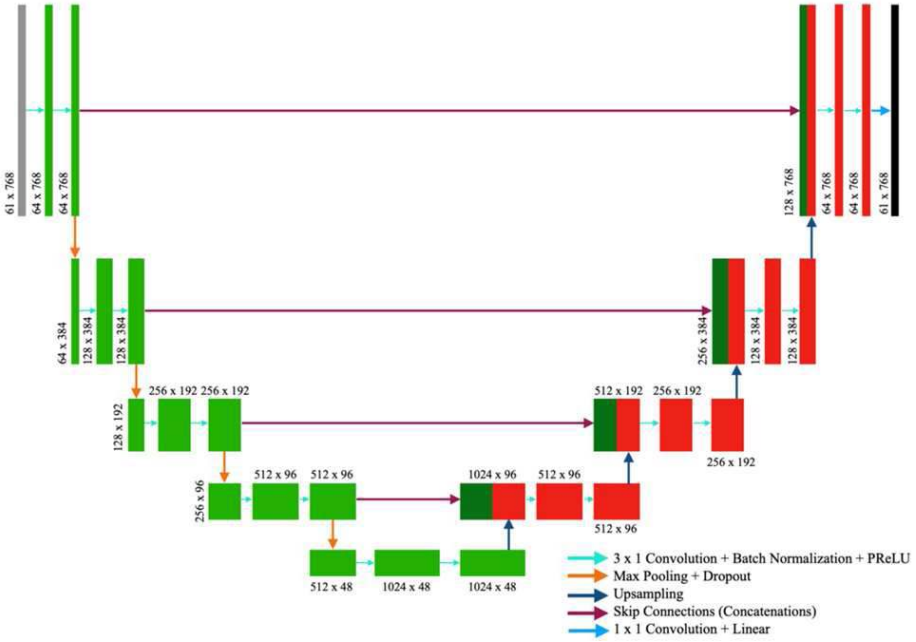

Figure 1. The proposed architecture of the network, based on U-Net, for BCG artifact removal.

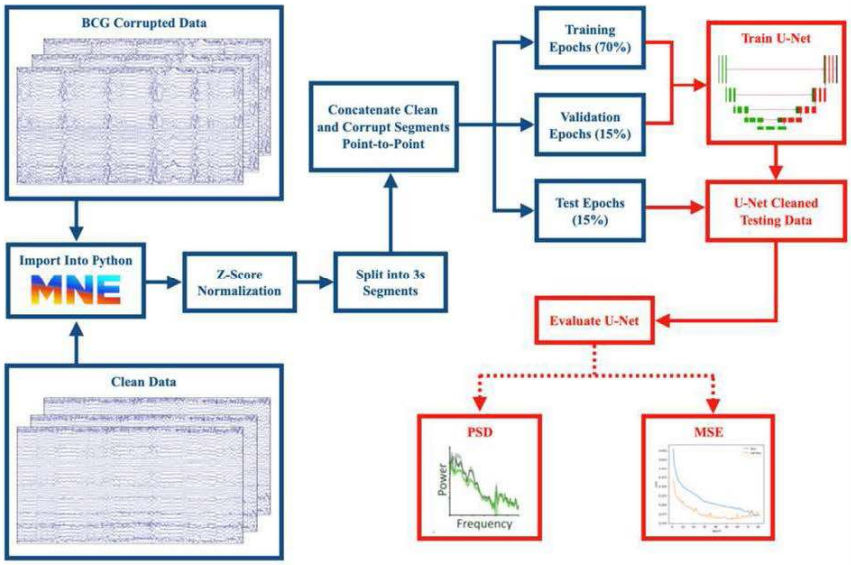

Figure 2. Processing pipeline, model training and evaluation.

Results: The model obtained an MSE of 0.26% on the training set and 0.39% on the validation set. The ratio of the power spectral density (PSD) between the model generated clean signals and ground truth clean signals were 1.163, 0.8336, 0.6508 and 0.6342 in the delta (0.5-4 Hz), theta (4-8 Hz), alpha (8-12 Hz) and beta (13-30 Hz) bands, respectively. The results indicate that the model was able to effectively remove BCG artifacts across all frequency bands, especially for the lower frequency bands.

Conclusions: This study has developed a novel deep learning-based method for direct removal of BCG artifacts in BCG-corrupted simultaneous EEG-fMRI recordings, without the need for a clean reference ECG signal. It provides a promising approach for recovering clean EEG signals in the event of low-quality ECG acquisition.

References

1. K. Vanderperren et al. (2010), "Removal of BCG artifacts from EEG recordings inside the Mr Scanner: A comparison of methodological and validation-related aspects," NeuroImage, vol. 50, no. 3, pp. 920–934
2. M. Marino et al.(2018), "Heart–brain interactions in the MR environment: Characterization of the Ballistocardiogram in EEG signals collected during simultaneous fmri," Brain Topography, vol. 31, no. 3, pp. 337–345.
3. Q. K. Telesford et al.(2023), "An open-access dataset of naturalistic viewing using simultaneous EEG-fMRI," Scientific Data, vol. 10, 554.
4. A. Gramfort et al.(2014), "MNE software for processing Meg and EEG Data," NeuroImage, vol. 86, pp. 446–460.

Poster No 2373

The Complexity of Brain Signals in Different Brain Regions Based on Resting State EEG (rs-EEG)

Li-Ting Lin[1], Albert Yang[2]

[1]National Yang Ming Chiao Tung University, Taipei, Taiwan, [2]National Yang Ming Chiao Tung University, Taipei City, Taiwan

Introduction: Violent issue in field of mental illness is worthy to pay attention, especially for becoming danger in society, e.g., harming others. Previous studies showed that some mental illness: schizophrenia, bipolar disorder have higher rates for aggression. However, it's hard to clarify how the mental symptoms affect on criminal behavior and there is lack of objective method for forensic psychiatry. Therefore, it's important to find the "biomarkers" for the interaction between mental illness and criminal behavior. Resting-state electroencephalogram (rs-EEG) is a non-invasive tool to measure brain signal and widely used in research and clinical use. And previous study showed that aggression behavior is associated with frontal, parietal, and temporal regions. In this study, we will focus on the highest rate for violent behavior in mental illness-schizophrenia spectrum disorder and aim to find the potential biomarkers or features for "criminal patients" and" aggression" based on re-EEG and focus on regions related to criminal behavior with non-linear analysis to contribute to clinical and practice.

Methods: Closed eye periods in rs-EEG data (21 channel, EB neuro) of criminal cases and health people were collected from the forensic psychiatry databases and healthy people databases in the Taoyuan Psychiatric Center, Taiwan, including 22 criminal cases with violent crime: harming others with weapons or unarmed attack (age: 39.86 ± 11.15, 95.45% in males), 13 criminal cases with non-violent crime (age: 42.69 ± 9.05, 53.85% in males) and 16 healthy people (age: 40.25± 11.54, 25% in male). Before entering the formal analysis for rs-EEG, all data were conducted pre-processing to remove noise with bandpass filter, notch filter, median filtering and removing outliers. And each signal will be segment into several epochs with 10s (overlap 5s). There are 156 epochs in violent group, 65 epochs in non-violent group and 250 epochs in healthy control group. With these data, we conducted non-linear analysis: sample entropy, multiscale entropy for time series data in different brain regions to measure the complexity of EEG signal to figure out the complexity of brain signal in different group.

Results: There is no significant difference in age among three group(p=.741). According to the analysis, we can find that there is difference in the complexity of time series in frontal, temporal, and parietal regions. To discuss the features for "criminal patients", there is lower complexity of brain signal in frontal and parietal regions and higher complexity of brain signal in temporal regions in first scale (sample entropy) in group of schizophrenics with criminal cases compared to healthy control. For the multiscale entropy, there is reverse performance for the complexity of brain signal in different scale in both frontal (after 4th scale) and parietal regions (after 2nd scale). Also, to discuss with the features for "aggression" in schizophrenia, non-violent crime groups showed highest complexity of brain signal (sample entropy) in all mentioned brain regions. For the multiscale entropy, there is higher complexity in temporal, parietal regions in 4th scale in violent group.

Conclusions: Our findings supported previous studies findings-there are changes for physiological signals under the interaction of behavior and mental illness and offered an idea that the complexity of brain signal in different scale may be potential features to distinguish schizophrenics who may have violent behavior or illicit non-violent behavior. However, the meaning of the changes for complexity for brain signal in different brain regions should be explored more with clinical investigation.

References

1. Cristofori, I. (2016). Brain regions influencing implicit violent attitudes: a lesion-mapping study. Journal of neuroscience, 36(9), 2757-2768.
2. Lindqvist, P. (1990). Schizophrenia and crime: a longitudinal follow-up of 644 schizophrenics in Stockholm. The British Journal of Psychiatry, 157(3), 345-350.
3. Potegal, M. (2012). Temporal and frontal lobe initiation and regulation of the top-down escalation of anger and aggression. Behavioural brain research, 231(2), 386-395.
4. Volavka, J. (2013). Violence in schizophrenia and bipolar disorder. Psychiatria danubina, 25(1), 0-33.
5. Werhahn, J. E. (2021). Aggression subtypes relate to distinct resting state functional connectivity in children and adolescents with disruptive behavior. European child & adolescent psychiatry, 30, 1237-1249.

Poster No 2374

Relationship between musical complexity, preference, and relative phase of brain network

Sunhyun Min[1,2], Younghwa Cha[1,2], Marcus Pearce[3], Joon-Young Moon[1,2]

[1]Center for Neuroscience Imaging Research, Institute for Basic Science (IBS), Suwon, Republic of Korea, [2]Sungkyunkwan University (SKKU), Suwon, Republic of Korea, [3]Queen Mary University of London, United Kingdom, London

Introduction: People have diverse preferences for music, yet there are also underlying commonalities. Previous studies have suggested that complexity could be a key to musical preference. Complexity can be quantified as Information Content (IC) and entropy, as measured by the Information Dynamics of Music (IDyOM) algorithm[1]. Interestingly, an inverted U-shaped relationship has been observed between complexity and liking ratings among general listeners. This observation raises several questions: Do experts have similar preferences as compared to general listeners? And if so, do preferences correlate with distinct brain responses? To investigate, we conducted simultaneous EEG-fMRI recordings while participants listened to various music samples and collected their rating data. Specifically, we measured the relative phase of the EEG response for each piece of music and compared the results with low, mid, and high IC across the expert and non-expert groups. Through this study, we aim to deepen the understanding of how musical preferences are formed and vary among different listener groups.

Methods: N>6 participants listened to classical music melodies inside the 3T fMRI scanner for 90 seconds each. Simultaneous EEG-fMRI measurement was carried out utilizing 64-channel EEG recording. These stimuli were generated using MIDI with the same tempo and the violin timbre of Joshua Bell (Kontakt 5). Following each piece, participants rated its complexity, likability, emotional content, familiarity, and attention using a 7-point Likert scale. Outside the scanner, participants responded to surveys including the Goldsmiths Musical Sophistication Index (Gold-MSI). For data analysis, the expertise of music for each participant was assessed based on their scores of Gold-MSI. IC of each stimulus was calculated using IDyOM. We explored correlations between IC, participants' ratings, and neural responses. For analyzing brain responses, we utilized a method focusing on relative phase. The relative phase was defined by subtracting the global mean phase from each electrode's phase across the whole brain area. Relative phase thus demonstrates the phase-lead/lag relationships of EEG signals at each time point, revealing temporal dynamics in the brain[2,3]. We also applied relative phase analysis to the eyes closed and eyes open resting state as the references to compare. We then applied the K-means clustering method to categorize the topographic patterns of the relative phase across the whole brain.

Results: From the ratings performed by each participant, we found a robust correlation between the perceived complexity and IC of each song regardless of their music expertise (Pearson correlation>0.7 with p-value<0.05). Also, we found an inverted U-shaped pattern when the likability and IC of each song were compared: songs with intermediate IC values were rated as most likable. In the relative phase analysis, we observe a robust switching pattern in the brain networks between top-down mode (where the parietal regions phase-lead the frontal regions) and bottom-up mode (where the frontal regions phase-lead parietal regions). There were also transient modes where either the left or right hemisphere was phase-leading against its counter-hemisphere. The dwell time in each mode was universally highest in the eyes closed state (~230ms), followed by the eyes open state (~180ms), which suggests that external stimuli trigger mode switching. Dwell time with the music stimuli was the shortest (~160ms), supporting our hypothesis that stimuli with more content will trigger more rapid mode switching.

Conclusions: Altogether, we found that participants, regardless of their music expertise, were able to identify the complexity of each music stimulus as identified by IDyOM. Also, there was a golden zone of IC for the music, which was most favored by the participants. Finally, our analysis showed that stimuli with more content triggered more rapid switching of the brain mode, as defined by the relative phases.

References

1. Gold, B. P. et al. (2019), 'Predictability and Uncertainty in the Pleasure of Music: A Reward for Learning?', Journal of Neuroscience. 39 (47) 9397-9409.
2. Moon, J.-Y. et al. (2015), 'General relationship of global topology, local dynamics, and directionality in large-scale brain networks', PLoS Computational Biology, 11(4) e1004225.
3. Moon, J.-Y. et al. (2017), 'Structure shapes dynamics and directionality in diverse brain networks: mathematical principles and empirical confirmation in three species', Scientific Reports, 7(1), 46606.

Poster No 2375

Anatomy-Aware Self-Attention Model for EEG-Based Emotion Recognition

Taeseong Kim[1], Won Hee Lee[1]

[1]Kyung Hee University, Yonginsi, Republic of Korea

Introduction: Emotion recognition using electroencephalogram (EEG) has gained significant attention in research due to its non-invasive, user-friendly and cost-effective nature. However, the challenge lies in the recognition of emotions from raw EEG signals, characterized by a low signal-to-noise ratio (SNR) and noise during data collection. Effective feature extraction is crucial for accurate EEG-based emotion recognition. While various studies have employed deep learning approaches such as DGCNN (Song, et al., 2018), STRNN (Zhang, et al., 2018), and BiLSTM (Joshi, et al., 2021) for emotion-related feature extraction,

they often neglect the consideration of the brain's anatomical characteristics. In this study, we propose a transformer-based deep learning model that captures inherent patterns based on the anatomical information of the brain for enhanced EEG-based emotion recognition.

Methods: We utilized the SJTU Emotion EEG Dataset (SEED), comprising EEG signals from 62 channels across 15 subjects (Zheng et al., 2015). EEG signals were recorded during 3 sessions for each subject, with 15 movie clips per session. For our analysis, we focused on 48 channels, excluding 14 channels challenging to categorize anatomically (Figure 1A). For feature extraction, we computed the differential entropy (DE) every second for five frequency bands: delta (1-3 Hz), theta (4-7 Hz), alpha (8-13 Hz), beta (14-30 Hz), and gamma (31-50 Hz). These features were stacked in 10-second intervals. Our proposed model comprises a spectral-channel attention module (SCAM) and two layers of the transformer encoder (Figure 1B). SCAM based on the squeeze-and-excitation (SE) block (Hu, et al., 2018) adaptively updates features in the spectral and EEG channel domains by assigning weights to prioritize crucial information in each domain, independently applied to each brain region (Figure 1C). The SCAM-generated embedding vectors for each brain region are then input into the transformer encoder. Within the transformer encoder, we incorporate anatomy-aware self-attention, deviating from conventional self-attention (Figure 1D). This anatomy-aware self-attention employs a masked mechanism, ensuring that attention is performed exclusively among embedding vectors corresponding to EEG channels associated with the same brain region. The transformer encoder outputs are flattened and processed through a fully-connected layer for emotion classification (neutral, positive, and negative). We conducted subject-dependent experiments on the SEED dataset. The model was trained on the first 9 trials as the training set and tested on the remaining 6 trials as the test set for each subject. Model performance was assessed by averaging accuracy and macro F1-scores across all subjects and sessions.

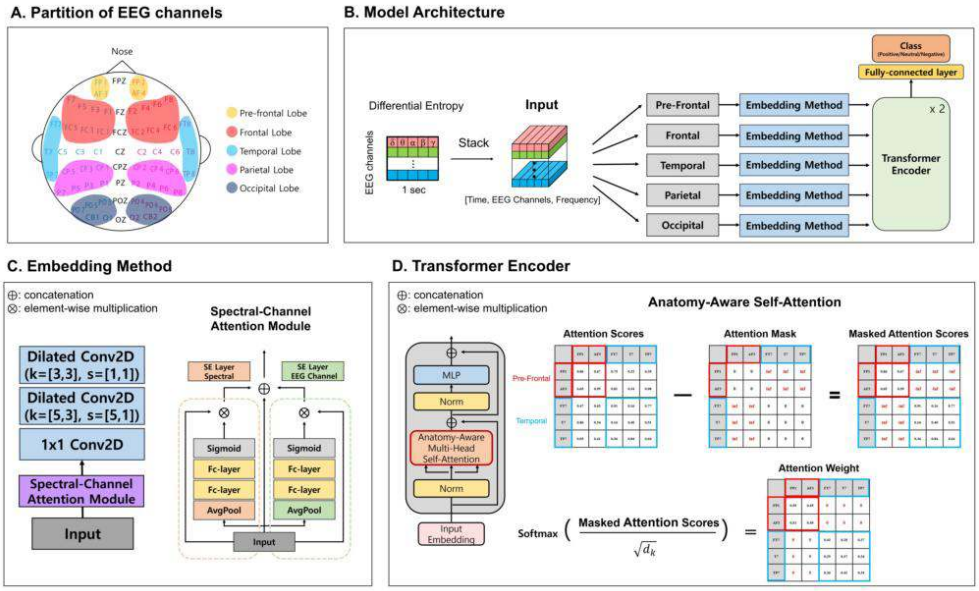

Figure 1. (A) Partition of EEG channels according to the anatomy of the brain. Electrodes are categorized into five lobes (pre-frontal, frontal, temporal, parietal, and occipital). (B) Model architecture. The model takes differential entropy (DE) as input, computed every second for five frequency bands, stacked in 10-second intervals. Independent embedding methods are applied to the EEG channels associated with each brain region, and embedding vectors pass through two layers of transformer encoders. (C) Embedding methods. Embedding method consists of spectral-channel attention module (SCAM), 1x1 2D convolutional neural networks (CNN), and dilated CNN. SCAM includes a spectral squeeze-and-excitation (SE) layer and an EEG channel SE layer. These layers use average pooling to squeeze the input tensor with respect to frequency and EEG channel. Subsequently, two fully-connected layers and a sigmoid function adaptively update features, weighting important information in each domain. The output of each SE layer is concatenated with the input tensor, and they are fused through a 1x1 2D CNN. We employ dilated CNN for capturing long-term dependency and reducing computational cost (Yu, et al., 2015). (D) Transformer encoder. Transformer encoder consists of normalization layers, anatomy-aware multi-head self-attention, and a multi-layer perceptron. Anatomy-aware self-attention involves masked self-attention, where infinity values are subtracted at positions corresponding to attention scores calculated among not-interested elements. This ensures that, after passing through softmax function, attention weights computed among EEG channels not belonging to the same brain region become 0. Consequently, the transformer encoder learns by considering only attention values computed within the same brain region.

Results: Figure 2 shows the subject-dependent emotion recognition performance with and without SCAM and anatomy-aware self-attention. The highest accuracy of 90.63% was achieved when both SCAM and anatomy-aware self-attention were incorporated. The model's performance decreased by 1.36% with the removal of SCAM and by 1.23% with the removal of anatomy-aware self-attention. When a portion of SCAM and anatomy-aware self-attention were removed, the classification accuracy decreased by 2.07%.

Model	Session	Macro F1 scores (std)	Accuracy (std)	Averaged Macro F1 scores (std)	Averaged Accuracy (std)
SCAM + Anatomy-Aware Self-Attention	Session1	92.99 (0.07)	93.19 (6.77)	**89.92 (0.10)**	**90.63 (8.41)**
	Session2	89.74 (0.11)	90.81 (8.71)		
	Session3	87.02 (0.10)	87.90 (8.76)		
SCAM + Self-Attention	Session1	91.52 (0.08)	91.95 (7.50)	88.49 (0.11)	89.40 (9.63)
	Session2	86.94 (0.13)	88.35 (10.19)		
	Session3	86.99 (0.12)	87.90 (10.39)		
w/o SCAM + Anatomy-Aware Self-Attention	Session1	91.71 (0.07)	91.95 (6.72)	88.67 (0.10)	89.27 (8.71)
	Session2	88.12 (0.11)	88.99 (10.10)		
	Session3	86.17 (0.09)	86.52 (8.22)		
w/o SCAM + Self-Attention	Session1	91.64 (0.07)	91.95 (6.72)	88.30 (0.10)	88.79 (9.04)
	Session2	87.14 (0.11)	87.80 (10.27)		
	Session3	86.11 (0.09)	86.62 (8.78)		

Figure 2. Subject-dependent emotion recognition performance, demonstrating the impact of SCAM and anatomy-aware self-attention on emotion recognition.

Conclusions: The results demonstrated that both SCAM and anatomy-aware self-attention improved the accuracy of emotion recognition compared to the model without these components. SCAM helped capture more relevant information in both spectral and EEG channel domains, while anatomy-aware self-attention leveraged the anatomical structure of the brain to extract meaningful patterns. The proposed transformer-based deep learning model shows promise for EEG-based emotion recognition with SCAM and anatomy-aware self-attention playing crucial roles in improving the accuracy of emotion recognition.

References

1. Song, T., Zheng, W., Song, P., & Cui, Z. (2018). EEG emotion recognition using dynamical graph convolutional neural networks. IEEE Transactions on Affective Computing, 11(3), 532-541.
2. Zhang, T., Zheng, W., Cui, Z., Zong, Y., & Li, Y. (2018). Spatial–temporal recurrent neural network for emotion recognition. IEEE transactions on cybernetics, 49(3), 839-847.
3. Joshi, V. M., & Ghongade, R. B. (2021). EEG based emotion detection using fourth order spectral moment and deep learning. Biomedical Signal Processing and Control, 68, 102755.
4. Zheng, W. L., & Lu, B. L. (2015). Investigating critical frequency bands and channels for EEG-based emotion recognition with deep neural networks. IEEE Transactions on autonomous mental development, 7(3), 162-175.
5. Hu, J., Shen, L., & Sun, G. (2018). Squeeze-and-excitation networks. In Proceedings of the IEEE conference on computer vision and pattern recognition (pp. 7132-7141).
6. Yu, F., & Koltun, V. (2015). Multi-scale context aggregation by dilated convolutions. arXiv preprint arXiv:1511.07122.

Poster No 2376

Inter-regional delays fluctuate in the human cerebral cortex

Joon-Young Moon[1,2], Charles Schroeder[3], Kathrin Müsch[4], Christopher Honey[4]

[1]Sungkyunkwan University, Suwon-si, Gyeonggi-do, Korea, Republic of, [2]Institute for Basic Science (IBS), Suwon-si, Gyeonggi-do, Korea, Republic of, [3]Nathan S. kline Institute for Psychiatric Research, Orangeburg, NY, [4]Johns Hopkins University, Baltimore, MD

Introduction: In electric signals such as field-potentials measured across regions of the human brain, parietal signals have a tendency to phase-lead signals in temporal and frontal cortex, while waves of activity propagates along parieto-temporal pathways. In order to better understand the functional properties of such large-scale pattern of signal flow, we asked: (i) are inter-regional delays stable or variable over time? (ii) do the patterns of signal propagation co-vary with endogenous cortical rhythms? (iii) do the patterns of signal flow vary with external stimulus properties?

Methods: We recorded electrocorticographic signals from the lateral cortical surface of 10 human participants as they listened to a 7-minute auditory narrative. In sliding 2-second windows, we identified inter-regional delays by computing the cross-correlation of voltage signals between nearby electrode pairs. For each time window, and for electrodes and electrode-pairs, we identified the time delay of maximal inter-electrode correlation from raw voltage signals, the power for different bands, and the mean broadband high-frequency power. We designed a computational model for the inter-regional flows using a Stuart-Landau coupled oscillator model, with structural topology based on human cortical anatomy.

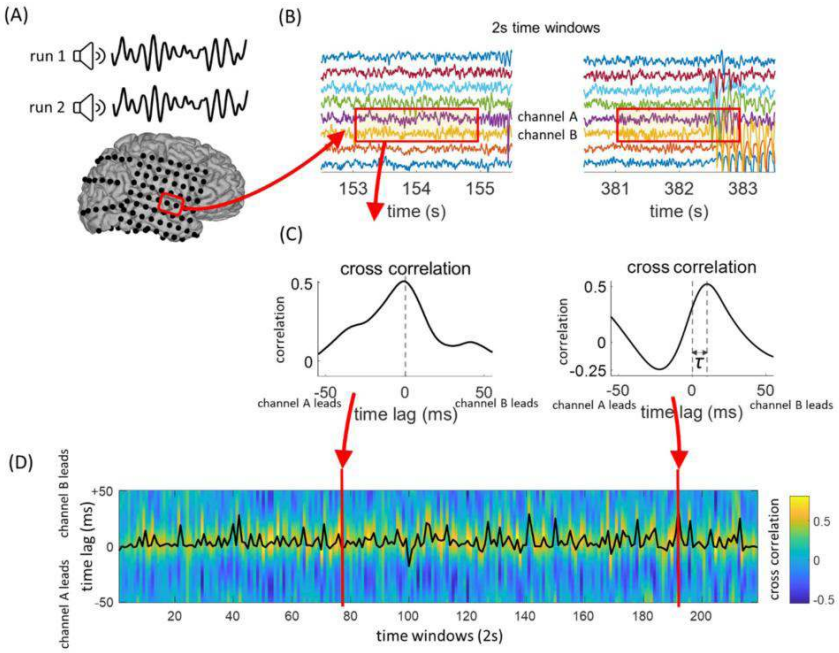

Figure 1. Scheme. (A) We presented a 7 minute auditory narrative twice to each participant. (B) Moving time windows were applied to each pair of ECoG channels. (C) For each time window, we measured the cross correlation between the chosen pair. The latency τ was defined as the time lag yielding the maximum cross-correlation. (D) Cross correlation and latency τ are illustrated for all time windows. The latency τ is represented as a black line. As observed from (D), the latency τ widely fluctuates.

Results: i) Inter-regional Latencies Vary Across Time: Consistent with prior reports[1,2], we found that the auditory pathway exhibited a gradient of delays, with posterior temporal regions leading anterior temporal regions on average. However, the latencies between stages of auditory processing were not stable, but fluctuated over time. Two distinct electrophysiological states were evident from data: one with longer inter-channel latencies ("propagating state"), and the other shorter latencies ("synchronized state"). ii) Latencies Correlates with Alpha Power Bursts: Latencies were longer during bursts of alpha power (propagating state) and were shorter during bursts of broadband power (synchronized state), consistent with models in which alpha oscillations regulate corticocortical interactions (van Kerkoerle et al., 2014). The inter-regional delays were mostly endogenous, as the correlation between responses under repeated stimulus was weak. Altogether, the changes in inter-regional latencies are not a random process, and reliably track features of the endogenous dynamics. iii) Global Latencies Changes between States: The transitions between synchronized and propagating states generalizes beyond the auditory pathway to the parietal, temporal and sensorimotor cortex. We observed that global latency patterns change between the synchronized state and the propagating state. When auditory drive was strong the latencies between many areas were reduced, and when auditory drive was absent the latencies increased. iv) Coupled Oscillator Model Reproduces Both States: We were able to reproduce the inter-regional correlation and delay pattern, by varying the coupling-strength between oscillators in the Stuart-Landau oscillator model, indicating that the large-scale dynamic shifts may be regulated by overall shifts in the efficacy of inter-regional influence.

Conclusions: Altogether, the data and models suggest that human cortical dynamics reliably transition between synchronized states (associated with increase of broadband power) and propagating states (associated with bursts of alpha-band power). These coupling dynamics may reflect a cortex-wide modulation of the relative influence of top-down and bottom-up signals in the human cerebral cortex[4].

References

1. Chapeton, J. I., Inati, S. K., & Zaghloul, K. A. (2017), Stable functional networks exhibit consistent timing in the human brain. Brain. 140, 628–640.
2. Zhang, H., Watrous, A. J., Patel, A., & Jacobs, J. (2018), Theta and Alpha Oscillations Are Traveling Waves in the Human Neocortex. Neuron. 98, 1269-1281.e4.
3. van Kerkoerle, T., Self, M. W., Dagnino, B., Gariel-Mathis, M.-A., Poort, J., van der Togt, C., & Roelfsema, P. R., (2014), Alpha and gamma oscillations characterize feedback and feedforward processing in monkey visual cortex, PNAS 111, 14332-14341.
4. Moon, J.-Y., Müsch, K., Schroeder, C. E., Honey, C. J. (2023)., Inter-regional delays fluctuate in the human cerebral cortex, bioRxiv, doi:10.1101/2022.06.01.494224, to be published in eLife.

Poster No 2377

Working memory load modulates frontal theta oscillation

Lucia Z Rivera[1], Andre Gómez-Lombardi[2], Begoña Góngora[2], Alejandra Figueroa-Vargas[3], Wael El-Deredy[4], Pablo Billeke[5]

[1]Universidad de Valparaiso, Valparaíso, Chile, [2]Universidad de Valparaíso, Valparaíso, Chile, [3]University of Desarrollo UDD · Centro de Investigación en Complejidad Social (CICS), Santiago, Santiago, [4]Universidad de Valparaíso, Valparaíso, Valparaíso, [5]University of Desarrollo UDD · Centro de Investigación en Complejidad Social (CICS), Santiago, Chile

Introduction: Neuroimaging studies of working memory [WM] show that it depends on a distributed functional network, primarily involving fronto-parietal association cortices (Ester et al., 2015; Christophel et al., 2017; Cabeza et al., 2008). The ability to sustain activity in these distributed networks depends on oscillatory activity in different frequency ranges (Roux et al., 2014). Specifically, it has been observed that EEG activity in the theta range (4-8 Hz) between fronto-parietal electrodes represents the maintenance of information in WM(Roux et al., 2014). Most EEG studies of WM test the modulation of the theta power by the WM load. Our study analyse WM performance under different load focusing on the individual theta frequency in a group of older adults. We show that individual theta frequency decreases with WM load, suggesting the recruitment of a more extensive cortical network, as proposed by (Lea-Carnall et al 2016).

Methods: EEG recordings from individuals aged over 60 (n=20) were utilized for this study. All participants were right-handed and exhibited a cognitive profile consistent with mild cognitive impairment, as per Petersen's criteria (2014), with a minimum of 6 years of formal schooling. To assess working memory, a modified version of the Sternberg task (Figueroa-Vargas, A. et al., 2020) was employed. This task focused on short-term memory retrieval and was presented at three difficulty levels: patterns of 2 (low load (LL)), 4 (medium load (ML)), and 6(high load (HL)) letters presented randomly. EEG data were recorded using a Biosemi Active-Two 64+8 channels according to the 10/20 system at a sampling rate of 1 kHz. Analyses were performed using EEGLab (Delorme and Makeig 2004) under MATLAB (Version 2021b, Mathworks Inc., Natick, USA). Time-frequency (TF) analyses were calculated using continuous wavelet transform. The individual theta frequency was computed in a window of 100–500 ms after stimulus presentation during memory encoding, in the average of central electrodes (Cz, C1, C2).

Results: A significant difference was found in participants' performance between low load (LL) and high load (HL) conditions ($p < 0.004$). Individual theta frequency was lower at the higher WM load, with a significant difference in theta frequency between LL and HL ($p < 0.039$). There was a significant correlation between individual theta frequency and accuracy, with lower frequency associated with lower accuracy and higher frequency linked to better performance.

Conclusions: The individual theta frequency varied during the execution of a variable-load working memory (WM) task. We demonstrate that, as the task becomes more challenging, a lower theta frequency is required, indicating a more extensive cortical network. This is due to the inversely proportional correlation between frequency and network size (Lea-Carnall et al 2016).

References

1. Ester, E. F., Sprague, T. C., & Serences, J. T. (2015). Parietal and frontal cortex encode stimulus-specific mnemonic representations during visual working memory. Neuron, 87(4), 893-905.
2. Christophel, T. B., Klink, P. C., Spitzer, B., Roelfsema, P. R., & Haynes, J.-D. (2017). The distributed nature of working memory. Trends in cognitive sciences, 21(2), 111-124.
3. Cabeza, R. (2002). Hemispheric asymmetry reduction in older adults: The HAROLD model. Psychology and Aging, 17(1), 85-100. https://doi.org/10.1037/0882-7974.17.1.85
4. Roux, F., & Uhlhaas, P. J. (2014). Working memory and neural oscillations: Alpha–gamma versus theta–gamma codes for distinct WM information? Trends in cognitive sciences, 18(1), 16-25.
5. Delorme, Arnaud, and Scott Makeig. 2004. "EEGLAB: An Open Source Toolbox for Analysis of Single-Trial EEG Dynamics Including Independent Component Analysis." Journal of Neuroscience Methods 134 (1): 9–21.
6. Lea-Carnall, C. A., Montemurro, M. A., Trujillo-Barreto, N. J., Parkes, L. M., & El-Deredy, W. (2016). Cortical resonance frequencies emerge from network size and connectivity. PLoS computational biology, 12(2), e1004740.

Poster No 2378

Modulatory Effects of mPFC-Derived Metabolites on P300 Responses in Schizophrenia

Berkhan Karsli[1], Genc Hasanaj[2], Marcel Kallweit[3], Verena Meisinger[1], Gizem Vural[4], Lukas Röll[3], Julian Melcher[5], Boris Papazov[6], Joanna Moussiopoulou[7], Vladislav Yakimov[3], Elias Wagner[3], Florian Raabe[8], Daniel Keeser[9]

[1]Ludwig Maximilian University, Munich, Germany, [2]Ludwig Maximillian University, Munich, Germany, [3]LMU University Hospital, Munich, Germany, [4]LMU Klinikum, Munich, Other, [5]LMU Klinikum, Munich, Bavaria, [6]LMU Munich, München, Bayern, [7]LMU Klinikum, München, Germany, [8]Department of Psychiatry and Psychotherapy, Ludwig-Maximilian University, Munich, Germany, [9]Department of Psychiatry and Psychotherapy, University Hospital LMU, Munich, Germany

Introduction: Frontal brain regions including the Anterior Cingulate Cortex play a crucial role in auditory deviance and cognitive control processing and metabolite levels in frontal regions vary and significantly modulate brain responses in schizophrenia spectrum disorder (SSD) (Duncan et al., 2014). Specifically, higher levels of glutamate and gamma-aminobutyric acid (GABA) are associated with an increased amplitude of the Mismatch Negativity (Rowland et al., 2016; Bartolomeo et al., 2012). Less known are the modulatory effects of these metabolites on the more complex P300 component, an event-related potential peaking around 300 ms post-stimulus in response to infrequently presented stimuli among frequently presented stimuli, a psychosis biomarker characterized by decreased amplitude and increased latency (Wang et al., 2022). In this study, we investigated the potential modulatory role of mPFC-derived Glutamate+Glutamine (Glx) and GABA on brain responses during the P300 task.

Methods: A total of 58 patients with SSD and 61 healthy controls (HC) participated in this study at the University Hospital LMU. They underwent multimodal MRI with a 3T MRI scanner, focusing on Single Voxel Spectroscopy at the mPFC (voxel size 20x20x20 mm^3) and task-based EEG measurement during the P300 task, in which they have to respond to the infrequent tone. The MRS data were processed using Osprey and LC-Model, and after excluding data based on Cramer-Rao lower bounds (>50% SD) and outliers (2.5 SD beyond the median), the analysis proceeded with data from 41 SSDs and 51 HCs. EEG data were preprocessed using an ICA preprocessing pipeline by Adams et al. (2022). Amplitude and latency of P300 were extracted for both frequent and infrequent tones within the 250-400 ms time window using MNE Python. Using multiple linear regression including patient group as a covariate, and Pearson correlation, metabolites were associated with P300 amplitude and latency at midline electrodes (Fz, Pz, Cz).

Results: Pz Amplitude was reduced for SSD for both infrequent ($t = -2.74$, $p = 0.008$) and frequent ($t = -2.32$, $p = 0.023$) tones. However, we did not find any other differences between two groups. The regression analysis revealed significant effects of the Group and Group x GABA on the amplitudes at midline electrodes. For the Fz amplitude, the Group x GABA was significant ($\beta = 2.74$, $t = 2.73$, $p = 0.008$). In the case of Pz amplitude, both the effect of Group ($\beta = -4.96$, $t = -2.82$, $p = 0.006$) and the Group x GABA ($\beta = 1.87$, $t = 1.99$, $p = 0.049$) were significant. Similarly, for the Cz amplitude, significant effects were observed for the effect of Group ($\beta = -4.91$, $t = -2.28$, $p = 0.025$) and the Group x GABA ($\beta = 2.77$, $t = 2.42$, $p = 0.018$). Reflecting these results, for SSD, GABA correlated with amplitudes of Fz ($r = 0.38$, $p = 0.014$), Cz ($r = 0.34$, $p = 0.031$), and Pz ($r = 0.37$, $p = 0.018$) for the frequent tone only, while for the HC group, there were no significant correlations.

Conclusions: The group comparison results showed reduced P300 amplitude over the Pz electrode in SSD patients for both infrequent and frequent tones, aligning with previous research that identified differences across temporoparietal regions (Wang et al., 2022). Significant interaction effects were observed between GABA levels and SSD on the amplitudes at midline electrodes (Fz, Cz, and Pz) for frequent tones. GABA concentration also showed a positive correlation with all three midline electrodes, suggesting a specific link between GABA concentration and reduced Pz amplitudes for SSD during auditory processing (Bartolomeo et al., 2012). These findings offer valuable insights into the neural mechanisms of auditory processing deficits in SSD and highlight the potential role of GABA in modulating P300 responses to frequent auditory stimuli in this group. Further research is needed to clarify how GABA influences neural responses to auditory stimuli in SSD and to investigate possible ways for developing targeted interventions for individuals with SSD.

References

1. Adams, R. A. (2022), 'Computational Modeling of Electroencephalography and Functional Magnetic Resonance Imaging Paradigms Indicates a Consistent Loss of Pyramidal Cell Synaptic Gain in Schizophrenia', Biological Psychiatry, vol. 91, no. 2, pp. 202–215
2. Bartolomeo, L. A. (2019), 'Relationship of auditory electrophysiological responses to magnetic resonance spectroscopy metabolites in Early Phase Psychosis', International Journal of Psychophysiology, vol. 145, pp. 15–22
3. Duncan, N. W. (2014), 'Associations of regional GABA and glutamate with intrinsic and extrinsic neural activity in humans—a review of multimodal imaging studies', Neuroscience and Biobehavioral Reviews, vol. 47, pp. 36–52
4. Rowland, L. M. (2016), 'Medial frontal GABA is lower in older schizophrenia: a MEGA-PRESS with macromolecule suppression study', Molecular Psychiatry, vol. 21, no. 2, pp. 198–204
5. Wang, B. (2022), 'Neurophysiology in psychosis: The quest for disease biomarkers', Translational Psychiatry, vol. 12, no. 1, pp. 100

Poster No 2379

MRF-gSlider: A High-resolution Multi-parameter Quantitative Magnetic Resonance Imaging Method

Dakun Hu[1], Huafeng Liu[1], Huihui Ye[1]

[1]*Zhejiang University, Hangzhou, Zhejiang*

Introduction: Magnetic resonance fingerprinting(MRF) (Ma et al., 2013) is an emerging technique that can obtain quantitative results of multiple magnetic parameters within a single MR scan. However, the slice thickness of common 2D MRF can only reach 3-5mm (Badve et al., 2017; Liao et al., 2018), which is quite limited for small lesion detection and fine structure characterization. Though 3D MRF (Liao et al., 2017; Ma et al., 2019) enables much higher slice resolution(~1mm), it suffers reconstruction burden from large data of 3D non-cartesian trajectory acquisition. We introduced the idea of gSlider(Generalized SLIce Dithered Enhanced Resolution) (Setsompop et al., 2018), which has a remarkable resolution improvement effect in diffusion MRI, into MRF, and proposed MRF-gSlider, to achieve high-resolution multi-parameter quantitative magnetic resonance imaging.

Methods: Based on the idea of gSlider, as shown in Fig.1, we designed 4 RF pulses and regarded the slice profile as composed of 4 sub-slices, where for each excitation, one sub-slice undergoes a π phase modulation. Gslider signals obtained after scanning with these four RF pulses are essentially different weighted combination of four sub-slice signals, which can be expressed in the form of a matrix as $Y4\times N\times t=A4\times 4S4\times N\times t$ (1) Among them, Y represents the 4 gSlider signals, S represents the independent signals of four sub-slices, A represents the weighted coefficient matrix, N represents the number of pixels in the image, and t represents the number of time points of the signal. Given A, we can easily solve for the independent signals of each sub-slice. Then perform dictionary matching separately, we can obtain quantitative results with 4 times higher resolution than common MRF. And A can be calculated through simulation experiments. We formulated 4 gSlider signals and 4 sub-slice signals from the dictionary based on the excitation profiles shown in Fig.1 and preset T1 and T2 maps. Then put the simulation signals into (1), we obtained the A matrix. To evaluate our method, we conducted multiple sets of scans. In phantom scans, We mainly validate the quantitative accuracy and uniformity across the slices of the T1 and T2 maps. Moreover, we also validate the robustness and repeatability. In vivo scans performed on a healthy adult's brain. Here we concerned about whether subtle structural changes in slice direction can be clearly distinguished. All scans were performed on a Siemens 3T Prisma scanner with a 20-channel coil based on a 2D FISP MRF sequence with gSlider pulses. Spiral trajectories and 36x downsampling were used to speed up the acquisition process with the in-plane resolution at $1x1mm^2$. A single acquisition takes about 20 seconds. The sub-slice thickness achieved is 1.5mm.

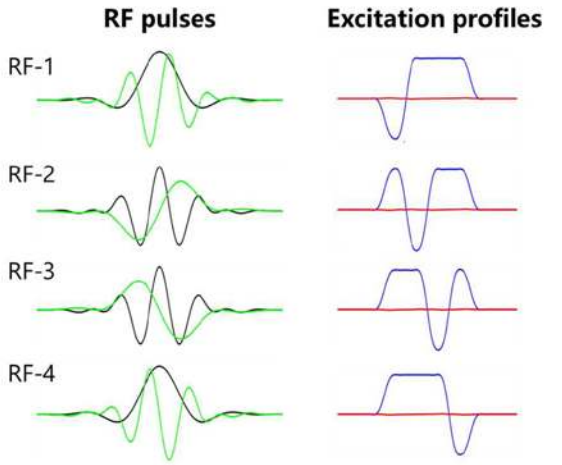

Fig.1 Our 4x-gSlider, 4 RF pulses are shown in the left column, with real and imaginary parts in black and green. The corresponding excitation profiles are shown in the right column, each case using a π phase modulation in a different sub-slice.

Results: Fig.2 shows the quantitative results for the phantom and brain. (a) is a T1 quantitative result of the phantom, including the golden standard and four sub-slice T1 map. Similarly, (b) is the corresponding T2 quantitative result of the phantom. It can be found that the quantitative results of T1 and T2 are highly consistent with the golden standard, and the results among the four sub-slices also show good consistency. In (c) and (d), The coordinates of each point represent the average quantitative value of a same ROI in two different scans of the phantom. It shows that the results of the two scans are stable and our method is repeatable. The T1 and T2 quantitative results of the brain are shown in (e) and (f). It can be seen that the subtle structural changes between adjacent sub-slices can be clearly distinguished.

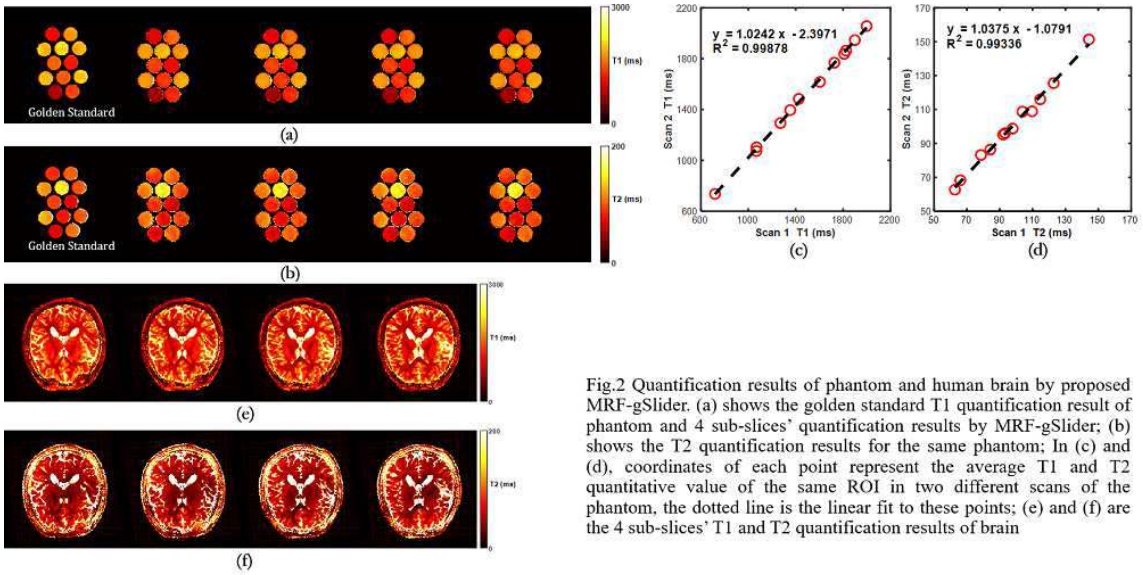

Fig.2 Quantification results of phantom and human brain by proposed MRF-gSlider. (a) shows the golden standard T1 quantification result of phantom and 4 sub-slices' quantification results by MRF-gSlider; (b) shows the T2 quantification results for the same phantom; In (c) and (d), coordinates of each point represent the average T1 and T2 quantitative value of the same ROI in two different scans of the phantom, the dotted line is the linear fit to these points; (e) and (f) are the 4 sub-slices' T1 and T2 quantification results of brain

Conclusions: Based on the idea of gSlider, we proposed a high-resolution multi-parameter quantitative MRI method that combines MRF and slice encoding, which can obtain a 4 times improvement on slice resolution compare with common MRF. Moreover, the proposed method has been validated on both phantom and in vivo scans, show that it can obtain accurate, uniform, and repeatable quantitative results.

References

1. Badve, C. et al. (2017) 'MR Fingerprinting of Adult Brain Tumors: Initial Experience', American Journal of Neuroradiology, 38(3), pp. 492–499.
2. Liao, C. et al. (2017) '3D MR fingerprinting with accelerated stack-of-spirals and hybrid sliding-window and GRAPPA reconstruction', NeuroImage, 162, pp. 13–22.
3. Liao, C. et al. (2018) 'Detection of Lesions in Mesial Temporal Lobe Epilepsy by Using MR Fingerprinting', Radiology, 288(3), pp. 804–812.
4. Ma, D. et al. (2013) 'Magnetic resonance fingerprinting', Nature, 495(7440), pp. 187–192.
5. Ma, D. et al. (2019) 'Development of high-resolution 3D MR fingerprinting for detection and characterization of epileptic lesions', Journal of Magnetic Resonance Imaging, 49(5), pp. 1333–1346.
6. Setsompop, K. et al. (2018) 'High-resolution in vivo diffusion imaging of the human brain with Generalized SLIce Dithered Enhanced Resolution Simultaneous MultiSlice (gSlider-SMS)', Magnetic resonance in medicine, 79(1), pp. 141–151.

Poster No 2380

Functional ultrasound reveals functional connectome adaptations in an NMDAR hypofunction model

Tudor Ionescu[1], Marion Ponserre[2], Alessa Franz[3], Serena Deiana[2], Niklas Schülert[2], Thorsten Lamla[2], Rhiannan Williams[2], Carsten Wotjak[2], Scott Hobson[2], Bastian Hengerer[2], Julien Dine[2], Azar Omrani[2]

[1]Boehringer Ingelheim, Biberach an der Riss, Baden Wuerttemberg, [2]Boehringer Ingelheim, Biberach an der Riss, Germany, [3]Boehringer Ingelheim, Biberach an Riss, Germany

Introduction: The development of animal models accurately capturing the complex features of schizophrenia has proven unfeasible due to the heterogeneity of the spectrum. However, certain clinical endphenotypes can be reproduced by animal models. In this context, NMDA receptor hypofunction achieved by acute or subchronic NMDA receptor antagonist administration to rodents has been extensively reported to recapitulate a wide range of relevant symptoms and biomarkers seen in patients. Functional ultrasound (fUS) is a newly-emerging technique which has shown significant promise in recent years as a viable alternative of retrieving neuronal information via neurovascular coupling to fMRI. Studies have shown that it can match fMRI in terms of spatiotemporal resolution and outperform it with regards to sensitivity, while being less expensive and generally easier to handle due to the lack of a strong magnetic field. Here, we revisited the NMDA hypofunction model using fUS, along with a number of additional state-of-the art technologies, such as optogenetic-assisted circuit mapping, accompanied by behavioral assessments of the model. We generated a unique set of biomarkers to characterize the model from molecules to cells and from local to macroscale circuitry, revealing aberrations centered around the PFC. The translational hallmarks described may offer a deeper understanding and enable a more precise use of the model in future studies.

Methods: For fUS experiments (60 minutes using the Iconeus One scanner, Iconeus) we used healthy C57BL/6JRj mice (10 mice per cohort, sedation induced using isoflurane and maintained using dexmedetomidine). The subchronic PCP model involved seven consecutive daily administrations of 10mg/kg PCP. We performed measurements at day 0, concomittently with the first dose, to capture the acute PCP effects, as well as at days 8 and 14, to identify subchronic alterations. We acquired a left-hemispheric oblique slice, covering the areas listed in Fig. 1. To temporally characterize the effects of PCP, we calculated FC dynamically using a sliding-window approach (10-minute windows, 30-second steps). We performed between-cohort edge-wise comparisons at all timepoints (two-sample t-tests, also yielding Z-score matrices for the differences between cohorts, FDR control was applied). In separate cohorts, we performed behavioral experiments to evaluate cognitive deficits (T-maze alternation and auditory steady-state responses), ex-vivo electrophysiology combined with optogenetics to evaluate the connectivity between ventral hippocampus and the prelimbic area, as well as immunonhistochemistry with high-throughput confocal microscopy to evaluate several prefrontal markers (among whic parvalbumin).

Results: At baseline, we observed highly similar connectomes between cohorts (Fig. 1A, D). Acute PCP increased FC globally (Fig. 1B, F and I. In contrast, we saw robust subchronic reductions in frontal (PL and ACg) and frontostriatal FC (between PL and CPu) at both days 8 (Fig. 1C, G) and 15 (Fig. 1D, H). The robustness of the dysconnectivity patterns is demonstrated by the strong correlation of the differences at days 8 and 15 (Fig. 1J-K). Overall, shifting from acute to subchronic NMDAR blockade led to a transition from a hyperconnected to a hypoconnected state with most pronounced aberrances across frontal and frontostriatal circuits. Using the same regime, we found, among others, impaired working memory (T-maze) and ASSR, impaired frontohippocampal connectivity (electrophysiology) and reduced prelimbic PV expression (Fig 2).

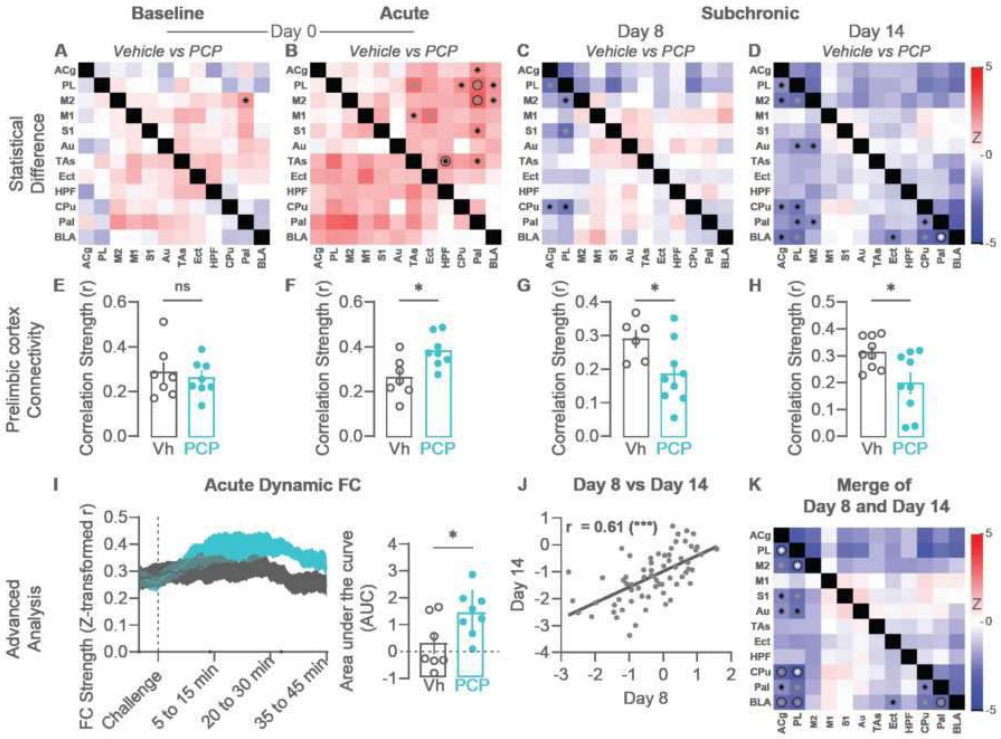

Figure 1: Functional connectivity analysis derived from fUS measurements upon acute and subchronic PCP treatment reveals abnormalities in brain networks. **A-D** Comparison of functional connectivity matrices of 12 regions covered by the acquired slice at **A** day 0 – baseline (minutes 5-15), **B** acute (minutes 25-35), **C** day 8 (minutes 5-60), and **D** day 15 (minutes 5-60). Matrices show the statistical differences (as Z-scores) between connectivity of the two cohorts. **E-H** Bar graphs at the bottom show connectivity strengths of the prelimbic cortex (averaged correlations of PL to all other regions) at day 0 (baseline **E** (For Vh, mean mPFC FC strength: 0.28 ± 0.12, n= 7 mice; For PCP, mean mPFC FC: 0.26 ± 0.07, n = 8 mice; 2-tailed unpaired t test: t(13) = 0.48, p = 0.64) and **F** acute (For Vh, mean mPFC FC strength: 0.26 ± 0.09, n= 7 mice; For PCP, mean mPFC FC: 0.38 ± 0.07, n = 8 mice; 2-tailed unpaired t test: t(13) = 2.94, p = 0.01)), **G** day 8 (For Vh, mean mPFC FC strength: 0.29 ± 0.06, n= 6 mice; For PCP, mean mPFC FC: 0.18 ± 0.09, n = 9 mice; 2-tailed unpaired t test: t(13) = 2.41, p = 0.03) , and **H** day 15 (For Vh, mean mPFC FC strength: 0.31 ± 0.05, n = 9 mice; For PCP, mean mPFC FC: 0.20 ± 0.11, n = 9 mice; 2-tailed unpaired t test: t(16) = 2.69, p = 0.02). **I** Dynamic prelimbic FC analysis for the day 0 timepoint. A sliding window approach depicts the prelimbic FC over 10-minute blocks slid forward in 20-second steps between the beginning and the end of the scan for both cohorts. Right panel: corresponding areas under the curve for prelimbic connectivity strengths (For Vh, mean mPFC FC AUC: 0.28 ± 0.98, n = 7 mice; For PCP, mean mPFC AUC FC: 1.42 ± 0.85, n = 8 mice; 2-tailed unpaired t test: t(13) = 2.39, p = 0.03). **J** Comparison of subchronic changes recorded at days 8 and 15 revealed strongly significant correlation between the respective Z-scores (r = 0.61, p < 0.0001). **K** Heatmap showing differences between both cohorts after merging the experiments performed at days 8 and 15. (*black: p < 0.05, *gray: p < 0.01, *white: p < 0.001, O: p < 0.05, FDR-corrected, two-sample t-tests). Bar graphs show mean ± SEM, each dot is the quantification a single animal. Graph in **D** show mean ±SD. Abbreviations: ACg = anterior cingulate, PL = prelimbic, M2 = secondary motor, M1 = primary motor, S1 = primary sensory, Au = auditory, TAs = temporal association, Ect = ectorhinal, HPF = hippocampal formation, CPu = caudate putamen, Pal = pallidum, BLA = basolateral amygdala.

Conclusions: Our data reveal which aspects of local and long-range circuitry are disturbed by the subchronic PCP model, which also recapitulate strongly translational hallmarks of the schizophrenia spectrum. Future studies may therefore more precisely target frontostriatal resting-state or frontohippocampal task-evoked dysconnectivity to assess whether pharmacological interventions can restore the observed deficits.

References

1. Brunner, C., Grillet, M., Urban, A., Roska, B., Montaldo, G., and Macé, E. (2021). Whole-brain functional ultrasound imaging in awake head-fixed mice. Nat Protoc 16, 3547–3571. 10.1038/s41596-021-00548-8.
2. Krystal, J.H., Karper, L.P., Seibyl, J.P., Freeman, G.K., Delaney, R., Bremner, J.D., Heninger, G.R., Bowers, M.B., and Charney, D.S. (1994). Subanesthetic Effects of the Noncompetitive NMDA Antagonist, Ketamine, in Humans: Psychotomimetic, Perceptual, Cognitive, and Neuroendocrine Responses. Arch. Gen. Psychiatry 51, 199–214. 10.1001/archpsyc.1994.03950030035004.
3. Osmanski, B.-F., Pezet, S., Ricobaraza, A., Lenkei, Z., and Tanter, M. (2014). Functional ultrasound imaging of intrinsic connectivity in the living rat brain with high spatiotemporal resolution. Nat Commun 5, 5023. 10.1038/ncomms6023.
4. Sigurdsson, T. (2016). Neural circuit dysfunction in schizophrenia: Insights from animal models. Neuroscience 321, 42–65. 10.1016/j.neuroscience.2015.06.059.

Poster No 2381

Glutamatergic Underpinnings of Within-Network Functional Connectivity in a Transdiagnostic Cohort

Margaret Pecsok[1], Ally Atkins[2], Alfredo Lucas[1], Monica Calkins[2], Adam Czernuszenko[3], Ruben Gur[4], Ravi Prakash Nanga Reddy[5], Ravinder Reddy[5], Heather Robinson[1], Kosha Ruparel[2], Nick Wellman[6], Daniel Wolf[1], Theodore Satterthwaite[4], David Roalf[7]

[1]University of Pennsylvania, Philadelphia, PA, [2]University of Pennsylvania, Department of Psychiatry, Philadelphia, PA, [3]University of Pennsylvania, Department of Psychiatry, Philadephia, PA, [4]UPenn, Philadelphia, PA, [5]University of Pennsylvania, Department of Radiology, Philadelphia, PA, [6]University of Pennsylvania, Department of Psychiatry, Philadelphia, PA, [7]Department of Psychiatry, Perelman School of Medicine, University of Pennsylvania, Philadelphia, PA

Introduction: Alterations in glutamate (Glu) concentration and resting state functional connectivity (FC) in cortical networks have independently been linked to psychosis spectrum (PS) symptoms (e.g., Sydnor & Roalf, 2020; O'Neill et al., 2019). However, the relationship between regional Glu and FC patterns in PS cohorts has been sparsely explored. The present study addresses this gap by leveraging 3T resting-state functional magnetic resonance imaging (rsfMRI) in conjunction with ultra-high field (7T) Glutamate Chemical Exchange Saturation Transfer (GluCEST), which allows for non-invasive, in vivo mapping of brain Glu with unprecedented sensitivity and spatial resolution. We seek to gain insights into the functional implications of cortical glutamatergic deficits across the sensorimotor-association (SA) axis in PS individuals and healthy controls (HC).

Methods: A transdiagnostic sample of 51 adults (23 HC, 28 PS) underwent 7T GluCEST and 3T rsfMRI within a 6-month period. The 2D GluCEST imaging parameters were: slice thickness=5 mm, FOV: 220×200, in-plane resolution=1.15×1.15 mm2, GRE read out TR=6.2 ms, TE=3 ms, number of averages=1, shot TR=10 500 ms, shots per slice=2, with a CEST saturation pulse at a B1rms of 3.06 μT with 800 ms duration. GluCEST data from cortical gray matter were processed using an in-house Python-based pipeline. In addition to GluCEST, participants also underwent 10 minutes of resting state fMRI (T2*-weighted gradient EPI, TR=3,000 ms, voxel size=2.0×2.0×2.0 mm3) obtained using a Siemens 3T scanner (Magnetom TrioTim). fMRI data were processed using fMRIPrep and XCP-D (Esteban et al., 2019; Mehta et al., 2023). All post-processing analyses were performed in Python. First, Glu levels were compared within and across 7 functional networks as defined by the Schaefer100 atlas (Schaefer et al., 2018). Finally, linear regression was used to compare within-network functional connectivity and network-wide GluCEST across all participants and within clinical groups.

Results: Across all participants, GluCEST was lower in the Limbic network (Limb) and higher in the visual network (Vis) compared to all other networks ($p<1*10-4$ and $p<1*10-8$, respectively, for all comparisons). Compared to HCs, PS participants had significantly lower GluCEST in the Salience/Ventral Attention network (SalVentAttn; $p=0.029$) and somatomotor network (SomMot; $p=0.038$). Linear regression revealed a positive association between SomMot GluCEST and FC ($R2=0.14$, $p=0.01$). A negative association between dorsal attention network (DorsAttn) GluCEST and FC ($R2=0.22$, $p=0.03$) was identified exclusively in the PS group.

Conclusions: The present analysis provides valuable preliminary insights into Glu-FC relationships. First, we replicated previous findings (Pecsok et al., 2022) of higher GluCEST in Vis and lower GluCEST in Limb; GluCEST may capture stable cortical features of these networks, potentially related to cortical architecture, synaptic plasticity, or baseline metabolic activity. Previous reports of lower Glu in PS groups (Pecsok et al., 2022, Roalf et al., 2017, Sydnor & Roalf, 2020) were also replicated, with lower GluCEST in PS within the SomMot and SalVentAttn networks. The positive association between SomMot GluCEST and FC suggests that the robustness of local excitatory glutamatergic signaling may underlie macroscale connectivity dynamics in this network. Interestingly, despite comparable GluCEST levels in DorsAttn, only the PS group showed a negative correlation between GluCEST and FC. This may stem from heightened vulnerability to Glu-mediated excitotoxicity in this region. Further investigation of Glu-FC coupling across cortical and subcortical networks is indicated.

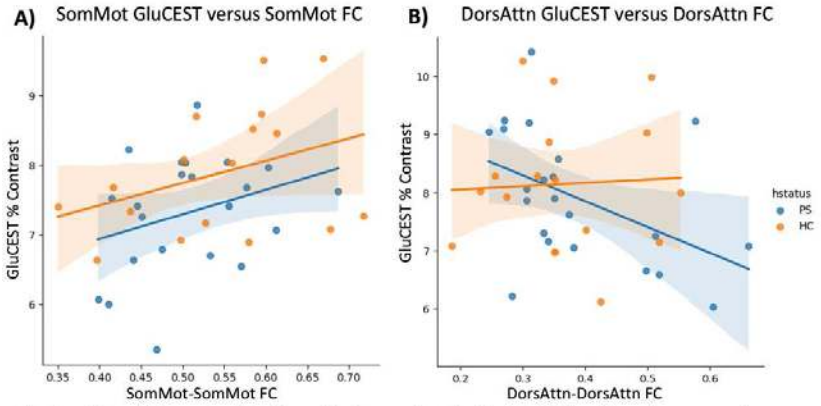

A) SomMot within-network FC is positively associated with GluCEST in this region across all participants (R^2=0.14, p=0.01). Trend-level associations are present in both the HC (R^2=0.13, p=0.15) and PS cohorts (R^2=0.10, p=0.16)

B) A trend-level association between DorsAttn GluCEST and FC across all participants (R^2=0.05, p=0.13). A negative association between DorsAttn GluCEST and FC (R^2=0.18, p=0.05) was present in the PS group.

References

1. Esteban, O., Markiewicz, C. J., Blair, R. W., Moodie, C. A., Isik, A. I., Erramuzpe, A., ... & Gorgolewski, K. J. (2019). fMRIPrep: a robust preprocessing pipeline for functional MRI. Nature methods, 16(1), 111-116.
2. Mehta, K. P., Salo, T., Madison, T., Adebimpe, A., Bassett, D. S., Bertolero, M., ... & Satterthwaite, T. D. (2023). XCP-D: A Robust Pipeline for the post-processing of fMRI data. bioRxiv, 2023-11.
3. O'Neill, A., Mechelli, A., & Bhattacharyya, S. (2019). Dysconnectivity of large-scale functional networks in early psychosis: a meta-analysis. Schizophrenia bulletin, 45(3), 579-590.
4. Pecsok, M., Jee, J., Mordy, A., Sydnor, V., Nanga, R. P., Shinohara, R., ... & Roalf, D. (2022). P321. Mapping Glutamate in Functional Cortical Networks. Biological Psychiatry, 91(9), S217.
5. Roalf, D. R., Nanga, R. P. R., Rupert, P. E., Hariharan, H., Quarmley, M., Calkins, M. E., ... & Turetsky, B. I. (2017). Glutamate imaging (GluCEST) reveals lower brain GluCEST contrast in patients on the psychosis spectrum. Molecular psychiatry, 22(9), 1298-1305.
6. Schaefer, A., Kong, R., Gordon, E. M., Laumann, T. O., Zuo, X. N., Holmes, A. J., ... & Yeo, B. T. (2018). Local-global parcellation of the human cerebral cortex from intrinsic functional connectivity MRI. Cerebral cortex, 28(9), 3095-3114.
7. Sydnor, V. J., & Roalf, D. R. (2020). A meta-analysis of ultra-high field glutamate, glutamine, GABA and glutathione 1HMRS in psychosis: Implications for studies of psychosis risk. Schizophrenia research, 226, 61-69.

Poster No 2382

Individual Markers Of Brain Inflammation in Acute Mild Traumatic Brain Injury: A Case Series

Mayan Bedggood[1], Christi Essex[1], Samantha Holdsworth[2,3], Amabelle Voice-Powell[1], Richard Faull[3], Alice Theadom[1], Mangor Pedersen[1]

[1]Auckland University of Technology, Auckland, New Zealand, [2]Mātai Medical Research Institute, Gisborne, New Zealand, [3]Centre for Brain Research, University of Auckland, Auckland, New Zealand

Introduction: Magnetic resonance imaging (MRI)-based T2 relaxometry is a quantitative technique measuring transverse components of the magnetisation dephase during an MRI scan. Importantly, T2 relaxation time increases as tissue water content increases (Liu et al., 2018). This indication of elevated fluid can indicate things such as gliosis (the proliferation of glial cells in injured brain areas), and increased inflammation (Cheng et al., 2012). This novel method can assess microstructural tissue alterations, such as inflammation, accompanying neurological conditions, such as mild traumatic brain injury (mTBI) (Pedersen et al., 2020). In the current study we aim to (1) investigate the utility of this objective method in discovering potential indicators of inflammation in individuals with acute mTBI (compared to healthy control estimates), and (2) link the findings to what their clinical radiologist report indicates about their brain health.

Methods: This is a case series with two groups of male participants: those with acute sports-related mTBI sustained within 14 days, (mean age = 21.4 years, n = 20) and controls with no mTBI in the last 12 months (mean age = 22.4 years, n = 44). MR images were acquired using a 3T Siemens MAGNETOM Vida fit scanner located at the Centre for Advanced Magnetic Resonance Imaging at The University of Auckland. T2 maps were acquired using a multi-echo relaxometry sequence and with 8 echoes (TE = 29.0, 58.0, 87.0, 120.0, 140.0, 170.0, 200.0, 230.0 ms, TR = 6s, voxel size = 2x 2x 2mm, FA = 180°. T1-weighted anatomical images were collected for quality control and normalisation using a magnetization-prepared rapid gradient echo (MPRAGE) sequence (TR = 1.94s, TE = 2.49ms, voxel size = 0.9x 0.9x 0.9 mm, FA = 9°). Processing and analyses were

conducted using Matlab version 9.13.0 (R2022b; MathWorks Inc., Natick, MA), including skullstripping, coregistering and normalising the images to MNI152 space. A monoexponential function with a baseline at each voxel was fitted to calculate the T2 relaxation time for each participant (Pedersen et al., 2020; Pell et al., 2004). Voxel-wise z-scores were obtained reflecting T2 relaxometry times between single mTBI participants and average T2 relaxometry times of all 44 controls, after applying a rank-based normalisation invariant algorithm. A False Discovery Rate at $p < .05$ was applied to derive statistically significant voxels for individual mTBI participants.

Results: 19/20 (95%) of mTBI participants had at least one voxel cluster with significantly higher T2 relaxometry times than controls (Figure 1). Although the majority of significant regions were unique to specific participants, we also observed areas common to several individuals, including the cingulate cortex, insula and superior parietal cortex (seen across ~1/3 of mTBI individuals, Figure 2). Furthermore, these potential pathologies were not aligned with the radiologist reports, that were all indicated to have either (a) no findings, or (b) incidental findings were not deemed to be clinically significant.

Figure 1
Individual Case Study Results Showing Voxel Clusters with Significantly Higher T2 Relaxometry Times Compared to Controls

Case	Region(s)	Raw T2 Relaxometry (ms)	Z-score compared to controls (SD)
1	L hippocampus; L lateral occipital	95.22; 71.83	5.00; 9.33
2	L superior parietal; L superior frontal (1); L superior frontal (2); L orbitofrontal cortex	146.50; 2.69e+06, 74.18; 79.78	8.40; 4.08; 4.38; 6.50
3	L superior parietal; R intraparietal sulcus; R temporoparietal junction (TPJ); R superior cerebellum	731456; 72.34; 65.49; 89.35	7.26; 14.39; 3.40; 8.72
4	L parahippocampal cortex; L orbitofrontal cortex; R anterior occipital; R orbitofrontal cortex	76.46; 6.50; 79.23; 74.74	10.37; 4.83; 10.22; 4.34
5	R superior cerebellum; R superior temporal sulcus	79.46; 69.54	13.15; 10.23
6	L anterior temporal	125.00	4.70
7	L supramarginal gyrus; L anterior occipital; L hippocampus; R premotor	70.15; 57.68; 274.06; 87.64	25.44; 13.83; 8.38; 19.60
8	L superior parietal; L anterior insula; R superior frontal	63.67; 63.72; 72.10	9.39; 18.65; 6.91
9	R inferior parietal; R posterior parietal; R superior cerebellum; R medial prefrontal cortex (mPFC)	70.64; 66.73; 104.69; 83.92	12.33; 19.85; 5.78; 8.13
10	R sensorimotor cortex	74.02	14.86
11	Cingulate cortex; L inferior supramarginal gyrus	73.47; 76.10	8.27; 16.31
12	R somatosensory cortex; R intraparietal sulcus	76.10; 51.54	8.66; 15.69
13	Cingulate cortex; L superior frontal; L posterior cerebellum	99.04; 259.39; 1.61e+08	11.08; 6.05; 5.37
14	L superior frontal	303.65	5.28
15	L anterior insula; L posterior cerebellum	68.26; 66.95	12.12; 7.04
16	None	N/A	N/A
17	L superior parietal; R posterior insula	65.66; 70.28	8.81; 5.31
18	R sensorimotor cortex	55.86	12.83
19	L cingulate cortex; L medial frontal; L sensorimotor cortex, L precuneous; L TPJ; R cingulate cortex; R superior parietal	66.32; 121.10; 79.65; 38.98; 100.25; 73.53; 22.05	17.51; 5.68; 4.57; 5.49; 5.60;15.48; 4.89
20	L superior parietal; R superior temporal; R superior parietal	54.89; 65.95; 70.83	15.92; 14.48; 8.46

Figure 2
Common Regions of Significant T2 Relaxometry (% of cases)

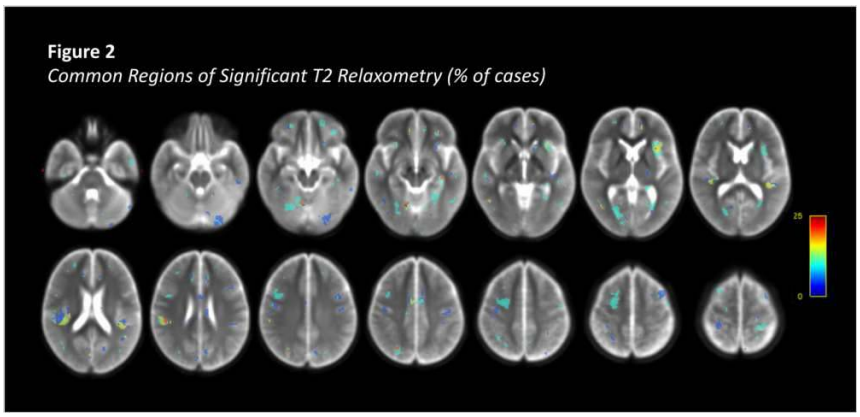

Conclusions: Increased T2 relaxometry in individuals with mTBI suggests the presence of acute inflammatory processes, despite no gross brain abnormalities on radiologist reports. As well as individual variation in T2 relaxometry times, there were significant voxel clusters that multiple participants had in common, including the cingulate cortex, insula, cerebellum and superior partietal cortex. This could indicate that certain regions are more susceptible to accumulated fluid content following mTBI. Understanding the role that inflammation plays acutely post-mTBI could have implications for individualised treatment and improved recovery outcome. T2 relaxometry provides individual, detailed maps of potential brain abnormalities and may offer new insights into a patient's injury. Future research would benefit from repeating all MRI scans to evaluate whether T2 relaxometry normalises at clinical recovery.

References

1. Cheng, H. L. M., Stikov, N., Ghugre, N. R., & Wright, G. A. (2012). Practical medical applications of quantitative MR relaxometry. Journal of Magnetic Resonance Imaging, 36(4), 805-824. https://doi.org/10.1002/jmri.23718
2. Liu, L. I., Yin, B. O., Shek, K., Geng, D., Lu, Y., Wen, J., Kuai, X., & Peng, W. (2018). Role of quantitative analysis of T2 relaxation time in differentiating benign from malignant breast lesions. Journal of International Medical Research, 46(5), 1928-1935. doi: 10.1177/0300060517721071
3. Pedersen, M., Makdissi, M., Parker, D. M., Barbour, T., Abbott, D. F., McCrory, P., & Jackson, G. D. (2020). Quantitative MRI as an imaging marker of concussion: evidence from studying repeated events. European Journal of Neurology, 27(10), e53-e54. https://doi.org/10.1111/ene.14377
4. Pell, G. S., Briellmann, R. S., Waites, A. B., Abbott, D. F. & Jackson, G. D. (2004). Voxel-based relaxometry: A new approach for analysis of T2 relaxometry changes in epilepsy. NeuroImage 21(2), 707–713. https://doi.org/10.1016/j.neuroimage.2003.09.059

Poster No 2383

Myelin water fraction in post-mortem brains: sequence comparison and behavior through fixation time

Liana Sanches[1], Roqaie Moqadam[1], Mallar Chakravarty[2], Mahsa Dadar[3], Yashar Zeighami[4]

[1]Cerebral Imaging Center, Douglas Mental Health University Institute, Montreal, Quebec, [2]Brain Imaging Centre, Douglas Research Centre, Montreal, Quebec, [3]Douglas Research Centre, McGill University, Montreal, QC, [4]Douglas Research Centre, McGill University, Montreal, Quebec

Introduction: The use of Magnetic resonance imaging (MRI) in neuroscience goes beyond the investigations of brain structure. Quantitative magnetic resonance imaging (qMRI) sequences provide an indirect proxy for tissue microstructure. Myelin water fraction (MWF) is a multi-compartmental modeling approach that uses the T2 relaxation time to calculate the amount of water trapped in the myelin sheets, which provides an indirect estimate of white matter integrity (Laule et al, 2004). For a method to be practical and feasible, all of this has to be accomplished in tolerated acquisition times and be applicable in clinical scanners. Studies in post-mortem MR of brain samples can help achieve these goals and validate the relationship between obtained MWF estimates and real microstructural structures. Finally, they can be compared with in vivo antemortem data and histology analysis. Therefore, post-mortem investigations can provide the ideal setting to develop and validate new biomarkers for neurodegenerative disorders (Shatil et al, 2018). Here we compare the standard 2D T2 (turbo) multi spin-echo (Neumann et al, 2014) and the 3D gradient and spin echo sequence (GRASE) (Piredda et al, 2020) acquisitions, in post-mortem brain samples fixed for different times. We calculate the correlation of MWF between the sequences and their behavior through the time since fixation.

Methods: Brain samples: Data included 12 post-mortem brain hemispheres from the Douglas Bell Canada Brain Bank (5 female, mean age = 80.7± 0.8). The donated brains were cut at the midsection, and one hemisphere (left or right, randomly assigned) was fixed in a 10% buffered formalin solution. The brains were scanned at different fixation times to allow us to assess the impact of fixation on the qMRI results (fixation time ranging between 0-20 years). All images were acquired at the Douglas CIC Research Centre, in a 3T scanner with 64 channel head-neck coil. The GRASE is a "work-in-progress" sequence obtained through a research agreement with the vendor. The following parameters were used: voxel size: 1.8 mm3, repetition time (TR): 1000 ms, 1 average, acceleration mode factor 3 in phase-encoding direction, and 2 in 3D. 32 echo times (TE) from 9 to 288 ms, echo-spacing 0.94 ms. The turbo spin-echo sequence has 27 slices and voxels of 0.3 x 0.3mm with 2.5 mm thickness, TR=4300 ms, 18 echo train per slice, turbo factor of 8, acceleration mode factor 3 in phase-encoding direction. This sequence was performed 7 times, changing the TE from 8 to 58 ms (echo spacing 8.25 ms). BISON (Dadar and Collins, 2021), a tissue segmentation tool was used to acquire white matter masks (WM) based on T1w images. The tissue masks were resampled to the spin-echo and GRASE images, providing regions of interest in which MWF and T2 values of the two sequences were compared. We assessed the correlation between average WM MWF estimations based on the two sequences, as well as the average WM MWF and fixation time, including post-mortem delay, sex, age, and hemisphere as covariates.

Results: Figure 1 shows an example of the derived MWF maps for one specimen, demonstrating the overall spatial agreements between the maps derived from the two sequences. Average white matter MWF estimations from the two sequences were highly correlated with each other (r = 0.90, p=0.0001), and positively correlated with fixation time (r = 0.78, p = 0.005 for standard T2 multi spin-echo and r = 0.63, p = 0.03 for GRASE). However, the average MWF estimates were consistently lower based on the multi-spin echo compared to the GRASE (t stat = -4.65, p<0.0001).

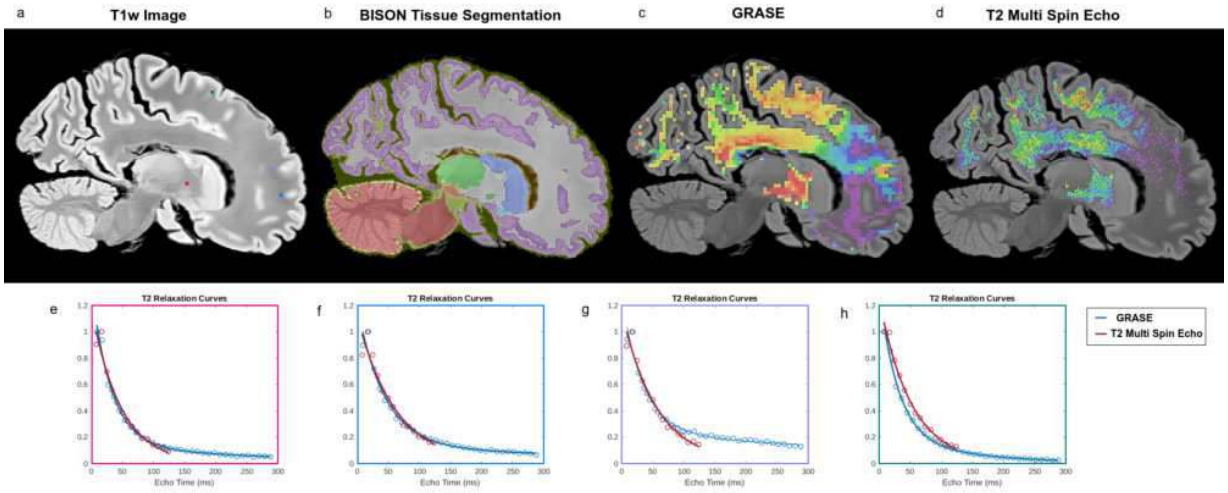

Figure 1. Comparison of T2 relaxation maps derived from GRASE and standard T2 multi spin echo sequences. a. post-mortem T1w image. b-d. Corresponding BISON tissue segmentation, GRASE MWF, and standard T2 multi spin-echo MWF maps overlaid on the T1w image, respectively. e-h. T2 relaxation curves for 4 voxels indicated with the same colors in panel a, showing similarly high (e), similarly low (f), and high versus low (g, h) MWF estimations across the two measures.

Conclusions: Our results showed that the GRASE sequence can provide a reliable proxy for the standard T2 multi spin-echo sequence, with the advantage of a better isotropic spatial resolution, brain coverage, and lower acquisition times (9:28 minutes compared to 15).

References

1. Dadar, M. (2021), 'BISON: Brain tissue segmentation pipeline using T1-weighted magnetic resonance images and a random forest classifier.' Magnetic Resonance in Medicine, 85(4), 1881-1894.
2. Laule C, (2004), 'Water content and myelin water fraction in multiple sclerosis. A T2 relaxation study.' Journal of neurology, Mar;251(3):284-93.
3. Neumann D, (2014), 'Simple recipe for accurate T(2) quantification with multi spin-echo acquisitions.' Magnetic Resonance Materials in Physics, Biology and Medicine. Dec;27(6):567-77.
4. Piredda, GF. (2020), 'Fast and high-resolution myelin water imaging: Accelerating multi-echo GRASE with CAIPIRINHA'. Magnetic Resonance in Medicine,; 85: 209–222.
5. Shatil AS. (2018), 'Quantitative Ex Vivo MRI Changes due to Progressive Formalin Fixation in Whole Human Brain Specimens: Longitudinal Characterization of Diffusion, Relaxometry, and Myelin Water Fraction Measurements at 3T. Frontiers in Medicine. 5:31.

Poster No 2384

Harmonization of an SMS-EPI fMRI protocol using Pulseq: Sequence implementation and ABCD QC metrics

Scott Peltier[1], Maximillian Egan[1], Rex Fung[1], Qingping Chen[2], Maxim Zaitsev[2], Jon-Fredrik Nielsen[1]

[1]University of Michigan, Ann Arbor, MI, [2]University Medical Center Freiburg, Freiburg, Germany

Introduction: Harmonizing fMRI acquisition protocols for multi-site studies can be a difficult and laborious task that may involve custom pulse sequence programming on each vendor platform and continued maintenance across scanner software updates. Moreover, protocols are typically only matched with respect to the high-level protocol parameters accessible to the end user such as field-of-view and resolution; subtle but potentially important differences in, e.g., sequence timing or RF and gradient pulse shapes, are typically not known to the researchers and are beyond their control. Furthermore, each vendor implements their own image reconstruction and post-processing (e.g., image filtering) algorithms. The impact of these vendor-specific protocol implementation details on the reproducibility of functional, structural, and quantitative MRI measures is generally unknown. Pulseq is an open, vendor-independent MR pulse programming platform that allows an MRI sequence to be created and analyzed in interactive programming environments such as MATLAB or Python, and executed on hardware using sequence-agnostic interpreters [Layton 2017]. Mature interpreters for the Pulseq sequence specification now exist for Siemens and GE scanners [Layton 2017, Nielsen 2018]. In addition, two independently-developed interpreters for Philips were

recently reported [Shaik 2023, Roos 2023]. The Pulseq platform enables, for the first time, exact harmonization of all low-level sequence details across sites and vendor platforms. Pulseq also greatly simplifies protocol maintenance, since only the interpreter needs to be recompiled every software upgrade. Here we report on a Pulseq implementation of a simultaneous multi-slice echo-planar imaging (SMS-EPI) protocol that is similar to the fMRI protocol used in the ABCD study, along with quality control (QC) metrics on two scanners from one vendor (GE) following the ABCD QC protocol.

Methods: Sequence design and scanner implementation: Using the Pulseq MATLAB toolbox we designed the SMS-EPI sequence shown in Figure 1, which consists of a fat saturation pulse, SMS excitation (multiband factor 6), and EPI readout. We compiled the GE Pulseq interpreter source code for three different software versions: For MR30.2 for the purpose of simulating the sequence with GE's 'Pulse Studio' sequence simulator; for MR29.1 for execution on a GE 3T MR750 scanner; and for RX28.0 for execution on a GE 3T UHP scanner. Data acquisition and QC metrics: We scanned the FBIRN phantom using the Pulseq SMS-EPI sequence on both scanners, using separate 32 channel Nova Medical head arrays. A total of 388 volumes were acquired, with the first 11 discarded (resulting in a time series duration of 5:01). We also acquired corresponding data using the ABCD QC protocol, and calculated several QC metrics, based on the fBIRN protocol, and as implemented in the ABCD study [https://github.com/ABCD-STUDY/FIONA-QC-PHANTOM]. Metrics were compared against average values obtained using the corresponding ABCD vendor-native sequences.

Results: Figure 1a shows the Pulseq SMS-EPI sequence in the Pulse Studio simulator, i.e., exactly as it appears on scanner hardware. Sequence waveforms and timing are identical to the Pulseq file description (not shown). Figure 1b shows representative images obtained with this sequence. Table 1 summarizes the calculated QC metrics. We observe that Pulseq performs favorably against the ABCD protocol. The higher SNR in the ABCD UHP acquisition is partly ascribed to the acquisition of full ky, as opposed to the fractional ky on the MR750 and in the Pulseq acquisition. As the Pulseq acquisition is the same across scanners, SNR values are more similar across the two scanners as compared to the ABCD protocol.

Conclusions: We implemented a Pulseq version of the ABCD SMS-EPI protocol and obtained similar or improved QC metrics compared to the vendor-native protocols. Future work will investigate its performance across vendors and different sequence types.

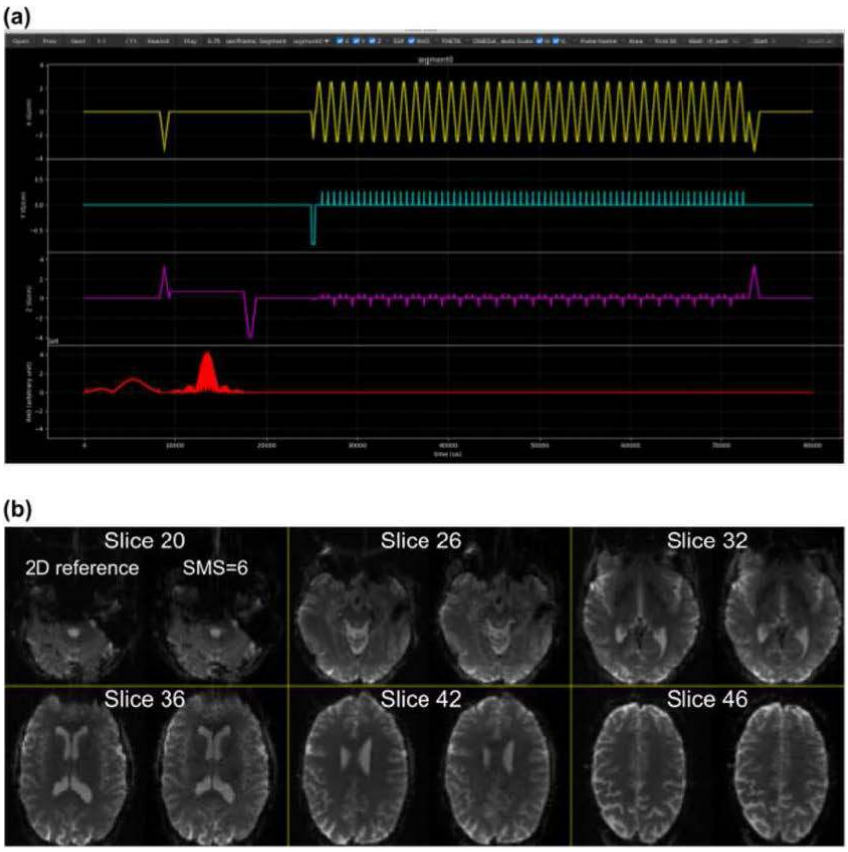

Figure 1. (a) A Pulseq SMS-EPI sequence simulated in GE's Pulse Studio (SMS factor 6; 2.4 mm iso; FOV = [21.6 21.6 14.4] cm). The TR is implemented as one segment consisting of 79 Pulseq blocks. (b) Human volunteer brain images obtained with the sequence in (a). Six slices are shown: each panel shows a non-SMS (2D) reference EPI image on the left, and the SMS=6 image on the right.

	ABCD	Pulseq	Scanner
SNR	69.0 (±6.1)	73.1	
SFNR	69.4 (±4.8)	73.0	
RMS	0.12 (±0.01)	0.11	
Drift	-0.82 (±0.88)	-0.28	
			MR750
RDC	12.7 (±1.1)	14.2	
FWHM x	2.77 (±0.04)	2.08	
FWHM y	2.14 (±0.05)	1.97	
	Partial ky	Partial ky	
SNR	93.2 (±6.8)	85.0	
SFNR	92.4 (±4.2)	82.2	
RMS	0.12 (±0.01)	0.12	
Drift	-0.52 (±0.29)	-0.67	
			UHP
RDC	9.5 (±0.62)	10.1	
FWHM x	2.79 (±0.01)	2.22	
FWHM y	2.51 (±0.01)	1.67	
	Full ky	Partial ky	

Table 1. FBIRN phantom metrics for MR750 (top) and UHP (bottom), using either ABCD (left) or Pulseq implementation of SMS-EPI. ABCD phantom data was taken as the average of multiple phantom scans (MR750: N=120, UHP:N=189). ABCD implementation of SMS used partial ky acquisition on MR750, full on UHP. SNR: image signal-to-noise ratio; SFNR: signal fluctuation to noise ratio; RMS: root mean square residual after polynomial fitting; RDC: radius of decorrelation; FWHM: spatial auto-correlation full width half maximum.

References

1. Layton KJ, Kroboth S, Jia F, Littin S, Yu H, Leupold J, Nielsen JF, Stöcker T, Zaitsev M. Pulseq: A rapid and hardware-independent pulse sequence prototyping framework. Magn Reson Med. 2017 Apr;77(4):1544-1552
2. Nielsen JF, Noll DC. TOPPE: A framework for rapid prototyping of MR pulse sequences. Magn Reson Med. 2018 Jun;79(6):3128-3134
3. Imam Shaik. A Pulseq Interpreter on Philips. ISMRM Virtual Meeting: Vendor-Agnostic Pulse Sequence Programming with Pulseq: From Basics to Advanced Topics. A Three-Day Virtual Meeting Series. 17 Nov 2023
4. Thomas Roos. Another Philips Pulseq Interpreter: from basics to pTX. ISMRM Virtual Meeting: Vendor-Agnostic Pulse Sequence Programming with Pulseq: From Basics to Advanced Topics. A Three-Day Virtual Meeting Series. 17 Nov 2023

Poster No 2385

A Monkey Mesoscopic Electrophysiology System to Bridge the Gap Between Cells, LFP, EEG and BOLD

Tobias Teichert[1]

[1]*University of Pittsburgh, Pittsburgh, PA*

Introduction: Key aspects of brain function can only be understood by recording from the entire brain in parallel, rather than parts of it in sequence. While fMRI has excellent full-brain coverage and spatial resolution, its temporal resolution is limited by the relatively slow hemodynamic response. And while electrophysiological approaches have excellent temporal resolution, they either 1) don't cover the entire brain (microscopic electrophysiology) or 2) have limited spatial resolution (macroscopic electrophysiology).

Methods: To address this methodological need, we developed the first electrophysiological mesoscope by distributing 992 electrode contacts across 62 multi-electrode shafts and then chronically implanting them in a regular grid that covers the entire right hemisphere of a monkey brain. Distances between electrode shafts were 5 mm in the antero-posterior dimension and 4 mm in the medio-lateral dimension. Each electrode shaft was custom designed and manufactured by hand for each grid location. The 16 electrode contacts on each shaft were distributed equidistantly across the entire length of brain penetrated by the shaft. Distance between electrode contacts on each shaft varied between 0.4 mm for the shortest shafts in orbitofrontal cortex and up to 2.7 mm for the much longer medial and posterior shafts.

Results: Our recordings show that mesoscopic electrophysiology is feasible, safe and provides extremely rich LFP recordings over a period of months, with no noticeable degradation over time. To showcase its wide field of view as well as its excellent temporal and spatial resolution, we recorded so-called frequency-following responses (FFRs), whose neural generators are still a matter of debate. Figure 1 shows FFRs with high signal-to-noise ratio across the entire monkey hemisphere. The large field of view and the high spatial resolution allowed us to follow the propagation and functional transformation of the FFRs along the ascending auditory pathway (Fig 1B). Next, we show that mesoscopic electrophysiology can capture brain-wide functional connectivity maps with a field of view that cannot be achieved using microscopic electrophysiology and a spectro-

temporal resolution that is not possible using fMRI. Figure 2A showcases seed-based functional connectivity maps for four example regions that emerge in different frequency bands. Furthermore, mesoscopic electrophysiology is ideally suited to identify brain-wide internal states. Using spatial correlations of activity patterns recorded at different times, mesoscopic electrophysiology shows the emergence and recurrence of stable brain-wide states that last on the order of tens of seconds that are abolished by sub-anesthetic doses of ketamine, but not midazolam (Fig 2B).

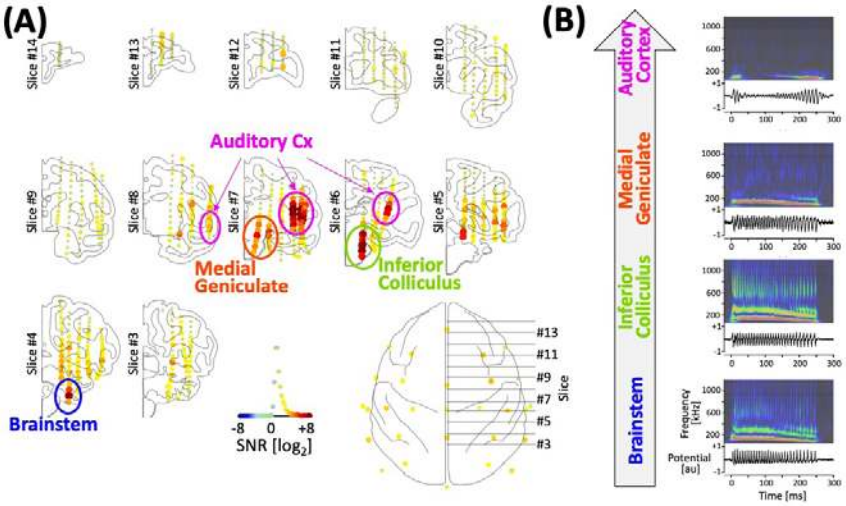

Figure 1 – Frequency Following Responses across the monkey brain. Mesoscopic electrophysiology was used to measure brain-wide frequency following responses to a clicktrain that mimicked the fundamental frequency of a 250 ms long falling Mandarin tone. (**A**) Each intracranial electrode contact is depicted as a colored dot superposed on the gray-matter outlines of 12 coronal slices. EEG electrode contacts are superposed on a top-down schematic of the monkey brain. Even with just 400 repetitions and 10 minutes of recording time, signal-to-noise exceeded a ratio of 100 at contacts close to key regions of the auditory system. (**B**) FFRs in the time and time-frequency domain for four example channels along the ascending auditory hierarchy. As the signal propagates through the auditory hierarchy, the latency gradually increases while the strength of the harmonics gradually decreases. Modeling identified contributions from Brainstem, Inferior Colliculus and Auditory Cortex to the scalp FFR (not shown). Brain-wide maps confirmed the model by tracing FFRs from the putative generators to the scalp (not shown).

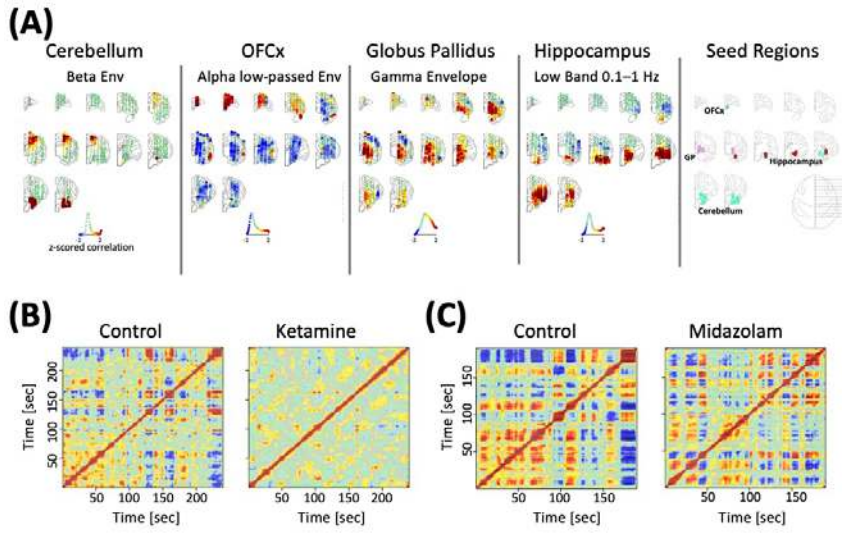

Figure 2 – Functional connectivity and large-scale brain states. A 3-minute long resting state recording was filtered into different frequency bands (low, delta, alpha, beta, gamma) and modes (band, envelope, low-passed envelope). (**A**) Seed-based functional connectivity maps for four example regions using different carrier frequencies and modes. (**B&C**) Images depict the spatial correlation of hemisphere-wide activity patterns at different time-points. Left and right panels depict sessions recorded before and after a sedative does of ketamine (B) or midazolam (C). Between periods of gradual change, the brain settles into stable states for periods of 10 – 20 seconds. The block-like structure of strong positive and negative correlations visible off the main diagonal suggests that these stable patterns tend to recur at different times. Interestingly, this entire structure is almost completely abolished following the injection of ketamine.

Conclusions: Mesoscopic electrophysiology combines the strengths of the two most important neuroscientific methods: the high temporal resolution of electrophysiology with the large field of view of fMRI. Methodologically, mesoscopic electrophysiology is closely related to other electrophysiolgical approaches. Conceptually, however, it differes from each of these approaches along at least one of three dimensions: (i) Its field of view is a three-dimensional volume rather than one- or

two-dimensional manifold; (ii) It spreads electrode contacts as widely as possible in order to maximise the field of view rather than spatial resolution; (iii) It prioritizes local field potentials over single-cell activity. These conceptual priorities of mesoscopic electrophysiology give rise to a functional profile of strengths and weaknesses that is unlike any other imaging method. Given this unique functional profile mesoscopic electrophysiology has the potential to facilitate the translation of findings across scales (micro – meso – macro), species (rodent – monkey – human), and recording modalities (electrophysiology – fMRI – optical).

Poster No 2386

Heart-rate variability during social stress task: effects of childhood trauma and neuro metabolites

Soroosh Golbabaei[1], Marina Krylova[1], Nathalie winter[2], Igor Izyurov[2], Hannes Meilicke[2], Larissa McClain[2], Jeannine Eichhorn[2], Daniel Güllmar[1], Laith Hamid[2], Anja Buder[2], Meng Li[1], Martin Walter[1], Lejla Colic[1]

[1]Jena University Hospital, Jena, Germany, [2]Department of Psychiatry and Psychotherapy, Jena University Hospital, Jena, Germany, Jena, Germany

Introduction: Altered stress response dynamics contribute to the development of psychiatric disorders (Berretz et al., 2020). The autonomic nervous system (ANS) alters its activity during stressful events. One commonly studied measure of ANS activation is heart rate variability (HRV), which refers to the fluctuations in consecutive interbeat intervals (IBIs; Immanuel et al., 2023). However, understanding the dynamics of stress response requires examining multiple factors. For instance, neurometabolic levels in brain regions related to stress regulation and psychiatric disorders, such as anterior insula (aINS) and pregenual anterior cingulate cortex (pgACC), may play a role (Rosso et al., 2014). Additionally, developmental factors such as childhood trauma may impact the ANS response during stress (Jiang et al., 2019). The present study aimed to investigate the influence of childhood trauma and glutamate and γ-Aminobutyric acid (GABA) levels in the aINS and pgACC on changes in HRV during stress task.

Methods: Fourteen participants (7 women, mean age=21.4, standard deviation=7.6) with no psychiatric or neurological diagnosis completed the Childhood Trauma Questionnaire (CTQ; Bernstein et al., 2003) and Magnetic Resonance Spectroscopy (MRS). After the MRS, participants completed the Scan Stress Task (Noack et al., 2019), during which their heart rate was recorded using Photoplethysmography (PPG; sampling frequency= 400 Hz). The Scan Stress included two sessions, pre- and post-verbal feedback. MRS was collected using the MEGA-PRESS protocol and pulse sequences from the CMRR Spectroscopy Package (Tremblay et al., 2014), in single-voxels left aINS and bilateral pgACC with parameters: 10×20×20 mm^3, echo-time=30 ms, repetition-time=3000 ms, flip angle=90°, averages=128 and water-averages=8. Spectra were analyzed using LCModel (V6.3; Provencher, 2001). Signal-to-noise ratio, Cramer-Rao lower bound, and full-width-at-half-maximum were used for quality checking, and we quantified glutamate, GABA, and total creatinine (tCr) as reference (Godlewska et al., 2017). From PPG, R-peaks and IBIs were extracted to construct Poincare plots (Brennan et al., 2001). The Poincare ratios (SD1/SD2) were calculated, and a normalized ratio between pre- and post-feedback was derived. Partial correlations were used to examine the relationships between glutamate/tCr and GABA/tCr from aINS and pgACC, CTQ-total score (CTQ-tot), and normalized Poincare ratio. Then, a backward regression was run with neuro metabolites, CTQ-tot, age, and sex to identify the best model for predicting the normalized Poincare ratio.

Results: When controlling for age and sex, the normalized Poincare ratio was positively correlated with CTQ-tot, r(10)=.6, p=.04, and glutamate/tCr in aINS, r(10)=.7, p=.01. Regression analysis showed that aINS Glu/tCR, β=.6, p=.03, age, β=.6, p=.032, and CTQ-tot, β=.4, p=.08 best predicted the Poincare ratio, R2=.6, F(10)=6.1, p=.01.

Conclusions: Our preliminary findings show that anterior insula glutamate and severity of childhood trauma contribute to stress dynamics measured via ANS in healthy participants. Both higher glutamate and childhood trauma were associated with higher ANS reactivity during a social stress task. Our findings emphasize the importance of both neural and physiological factors when examining the effects of stress on individuals.

References

1. Bernstein, D. P., Stein, J. A., Newcomb, M. D., Walker, E., Pogge, D., Ahluvalia, T., ... & Zule, W. (2003). Development and validation of a brief screening version of the Childhood Trauma Questionnaire. Child abuse & neglect, 27(2), 169-190.
2. Berretz, G., Wolf, O. T., Güntürkün, O., & Ocklenburg, S. (2020). Atypical lateralization in neurodevelopmental and psychiatric disorders: What is the role of stress?. cortex, 125, 215-232.
3. Brennan, M., Palaniswami, M., & Kamen, P. (2001). Do existing measures of Poincare plot geometry reflect nonlinear features of heart rate variability?. IEEE transactions on biomedical engineering, 48(11), 1342-1347.
4. Godlewska, B. R., Clare, S., Cowen, P. J., & Emir, U. E. (2017). Ultra-high-field magnetic resonance spectroscopy in psychiatry. Frontiers in psychiatry, 8, 123.

5. Immanuel, S., Teferra, M. N., Baumert, M., & Bidargaddi, N. (2023). Heart Rate Variability for Evaluating Psychological Stress Changes in Healthy Adults: A Scoping Review. Neuropsychobiology, 1-16.
6. Jiang, S., Postovit, L., Cattaneo, A., Binder, E. B., & Aitchison, K. J. (2019). Epigenetic modifications in stress response genes associated with childhood trauma. Frontiers in psychiatry, 10, 808.
7. Noack, H., Nolte, L., Nieratschker, V., Habel, U., & Derntl, B. (2019). Imaging stress: an overview of stress induction methods in the MR scanner. Journal of Neural Transmission, 126, 1187-1202.
8. Provencher, S. W. (2001). Automatic quantitation of localized in vivo 1H spectra with LCModel. NMR in Biomedicine: An International Journal Devoted to the Development and Application of Magnetic Resonance In Vivo, 14(4), 260-264.
9. Rosso, I. M., Weiner, M. R., Crowley, D. J., Silveri, M. M., Rauch, S. L., & Jensen, J. E. (2014). Insula and anterior cingulate GABA levels in posttraumatic stress disorder: preliminary findings using magnetic resonance spectroscopy. Depression and anxiety, 31(2), 115-123.
10. Tremblay, S., Beaulé, V., Proulx, S., Lafleur, L. P., Doyon, J., Marjańska, M., & Théoret, H. (2014). The use of magnetic resonance spectroscopy as a tool for the measurement of bi-hemispheric transcranial electric stimulation effects on primary motor cortex metabolism. JoVE (Journal of Visualized Experiments), (93), e51631.

Poster No 2387

Intervention-related changes in motor cortex GABA in children with perinatal stroke

Paulina Hart[1], Tiffany Bell[1], Ashley Harris[1], Helen Carlson[1], Adam Kirton[1]

[1]*University of Calgary, Calgary, Alberta*

Introduction: Perinatal stroke (PS) affects millions of children, damaging the motor system leading to lifelong motor disability in the form of hemiparetic cerebral palsy (Dunbar, 2020; Kirton, 2013). Most PS are either periventricular venous infarction (PVI) or arterial ischemic stroke (AIS). Magnetic resonance spectroscopy (MRS) has demonstrated differences in glutamate/glutamine and creatine levels between lesioned and non-lesioned hemisphere motor cortices in PS patients (Carlson, 2017). However, it is unknown if γ-aminobutyric acid (GABA), a primary inhibitory neurotransmitter critical for motor coordination, is altered. Current rehabilitation treatments for PS are limited but non-invasive neuromodulation is a promising adjuvant. Transcranial direct current stimulation (tDCS) uses weak electrical currents to modulate neuroplasticity and can enhance motor learning in children (Ciechanski, 2017) but effects on motor cortex chemistry are unknown. Studies have suggested that tDCS can induce changes to motor cortex GABA levels which are associated with improved cortical learning (Stagg, 2011). We aimed to quantify GABA levels in the lesioned and non-lesioned motor cortices in children with PS at baseline and following intensive motor learning paired with neurostimulation and explored associations with clinical function.

Methods: Participants (6-18 years) with unilateral, perinatal PVI or AIS were recruited to the Stimulation for Perinatal Stroke Optimizing Recovery Trajectory (SPORT) randomized, controlled, clinical trial. Participants attended a two-week day-camp including intensive, individualized, goal-directed therapy. Each received daily active or sham cathodal tDCS over the non-lesioned motor cortex. At baseline, post-camp, and 6-months later (follow-up), MRI was performed and motor function was assessed using the Assisting Hand Assessment (AHA), and Box and Blocks Test (affected hand, BBTA). MRI were performed on a 3.0 T GE MR750w MRI scanner. T1-weighted images were acquired. A ball-squeezing motor task-fMRI acquisition was used to localize the motor cortex bilaterally for MRS voxel placement. GABA-edited MEGA-PRESS was used to measure GABA levels (20x20x10mm3 voxels, TE=68ms, averages=128, 14ms editing pulses applied at 1.9ppm and 7.46 ppm). The MRS voxel was segmented by tissue type to maximize accuracy of tissue correction. GABA spectra (Figure 1) were processed using Gannet 9 (Edden, 2014). Statistical analyses were conducted using Jamovi.

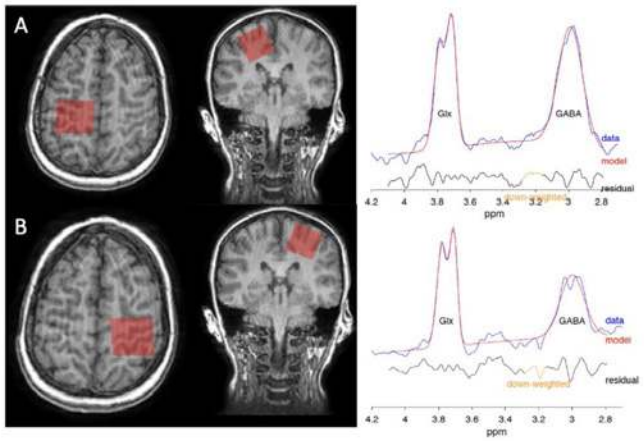

Figure 1. Baseline GABA spectra from Gannet output of MEGA-PRESS MRS for GABA quantification in the voxels placed in the motor cortices in the A) lesioned hemisphere and B) non-lesioned hemisphere.

Results: Forty-nine participants (AIS n=24, mean age 11.0(2.97) years; PVI n=25, age 10.3(1.74) years) were included. Three participants were excluded for missing baseline measurements or an MRS linewidth value (obtained from Gannet analysis) greater than 15Hz. Age, sex, and stroke laterality were comparable between groups. Twenty participants received active and 29 received sham tDCS. Linear mixed models (using age as a co-variate) showed a decrease in non-lesioned hemisphere GABA levels across the three time points (p=0.048) regardless of tDCS condition (Figure 2). There was no significant change in GABA levels observed in the lesioned hemisphere across the three time points (p=0.765) or between tDCS treatment groups. Motor function (AHA and BBTA) increased (p<0.001) across the three time points, however, increases in motor function were not associated with changes in GABA levels in either hemisphere (p>0.05).

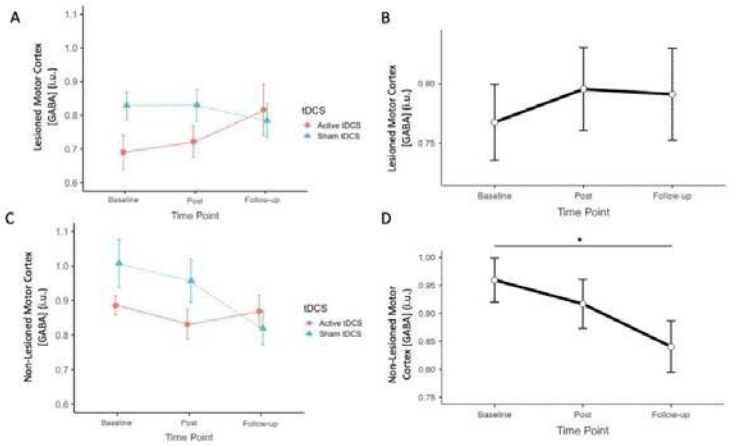

Figure 2. GABA levels with standard error across three time points in the A) lesioned and C) non-lesioned motor cortex of patients with PS receiving active or sham tDCS intervention. GABA levels across three time points, collapsed over tDCS condition in the B) lesioned and D) non-lesioned motor cortex (*p<0.05).

Conclusions: Bilateral motor cortex GABA is measurable in children with PS undergoing intensive therapy and neuromodulation. GABA levels may decrease in the non-lesioned motor cortex following intensive manual therapy with effects lasting 6 months or more. Simultaneous tDCS over the non-lesioned motor cortex does not appear to affect motor cortex GABA levels.

References

1. Carlson, H.L. (2017), 'Changes in spectroscopic biomarkers after transcranial direct current stimulation in children with perinatal stroke', Brain Stimulation, vol. 11, pp 94-103.
2. Ciechanski, P. (2017), 'Transcranial Direct-Current Stimulation Can Enhance Motor Learning in Children', Cerebral Cortex, vol. 27, no. 5, pp. 2758-2767.
3. Dunbar, M. (2020), 'Population Based Birth Prevalence of Disease-Specific Perinatal Stroke', Pediatrics, vol. 146, no. 5.
4. Edden, R.A.E. (2014), 'Gannet: A batch-processing tool for the quantitative analysis of gama-aminobutyric acid-edited MR spectroscopy spectra', Journal of Magnetic Resonance Imaging, vol. 40, pp. 1445-1452.
5. Kirton, A. (2013), 'Life after perinatal stroke', Stroke, vol. 44, no. 11, pp. 3265-3271.
6. Stagg, C. (2011), 'The Role of GABA in Human Motor Learning', Current Biology, vol. 21, no. 6, pp. 480-484.

Poster No 2388

Brain metabolite level differences between young and middle-aged adults assessed using 7T MRS

Flavie Detcheverry[1,2,3,4], Ikrame Housni[1,2,3,4], Sneha Senthil[5,6], Ali Filali-Mouhim[4], Rozie Arnaoutelis[5,6], Samson Antel[5,6], Douglas Arnold[5,6], Jamie Near[7], Sridar Narayanan[5,6], AmanPreet Badhwar[1,2,3,4]

[1]Multiomics Investigation of Neurodegenerative Diseases (MIND) lab, Montreal, Quebec, Canada, [2]Department of Pharmacology and Physiology, Faculty of Medicine, University of Montreal, Montreal, Quebec, Canada, [3]Institute of Biomedical Engineering, University of Montreal, Montreal, Quebec, Canada, [4]Centre de Recherche de l'Institut Universitaire de Gériatrie de Montréal (CRIUGM), Montreal, Quebec, Canada, [5]McConnell Brain Imaging Centre, Montreal Neurological Institute, Montreal, Quebec, Canada, [6]Department of Neurology and Neurosurgery, McGill University, Montreal, Quebec, Canada, [7]Sunnybrook Research Institute, Department of Medical Biophysics, University of Toronto, Toronto, Ontario, Canada

Introduction: Neurochemical changes take place in the brain as it ages, and readouts of brain metabolite levels from in vivo magnetic resonance spectroscopy (MRS) can provide key insight into the metabolic fingerprint of healthy aging. Our recent systematic review (Detcheverry et al., 2023) indicates that brain metabolite changes in healthy aging have not been fully characterized, especially in middle-aged adults (age range: 40-59 years (yrs)), an age where risk factors associated with age-

related dementia are known to appear. In addition, in the literature to date, only five papers investigated healthy adult group differences using 7T MRS, and mostly focused on N-acetylaspartate (NAA; a marker of neuroaxonal integrity, and the most prominent peak in the proton MRS spectrum) and glutamate (Glu; main excitatory neurotransmitter). Therefore, our study aims to characterize the concentration differences of 16 brain metabolites between young and middle-aged adults using 7T MRS, a magnet strength considered ideal for the detection of low-concentration, yet biologically relevant, metabolites.

Methods: Included in our age group comparison analysis were 23 adults (N=10 young, 20-29 yrs; N=13 middle-aged, 40-59 yrs; Figure 1A) from our ongoing healthy adult cohort study collecting 7T magnetic resonance imaging (MRI)/MRS and blood data. MRI/MRS data were acquired using a 7T Siemens Terra scanner (Siemens, Erlangen, Germany). The MRI protocol included a whole brain 3D T1-weighted MP2RAGE for localization. Metabolite levels were measured in posterior cingulate cortex (PCC) and centrum-semiovale white matter (CSWM) voxels using STimulated Echo Acquisition Mode (STEAM) MRS with the following parameters: TR/TE=5000/8ms, 64/96 averages for PCC/CSWM, 4096 points, and 5000 Hz spectral bandwidth (Figure 1B). Raw MRS data was preprocessed using the FID Appliance (FID-A) (Simpson et al., 2017), before spectral fitting, and Eddy current correction and spectral analysis were performed in LCModel (Provencher, 2001). We report metabolite concentrations in arbitrary units referenced to water. A series of linear models, controlled for brain region and sex, and adjusted for multiple comparisons (alpha=0.05), were applied to assess group differences between middle-aged and young adults. In addition, we performed linear regressions of metabolite concentrations with age for metabolites from all 32 participants (20-65 yrs) studied so far (Figure 1C).

A. Participants demographic information for age group comparison

	Young (20-29 yrs)	Middle-aged (40-59 yrs)
N	10	13
Age (yrs)	24.00±2.32	49.23±5.86
F/M	5/5	7/6

B. Age group comparison in the two ROIs

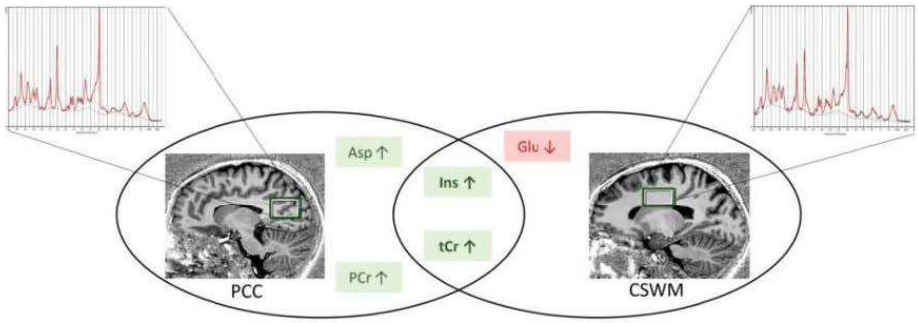

C. Linear regressions of metabolites with age

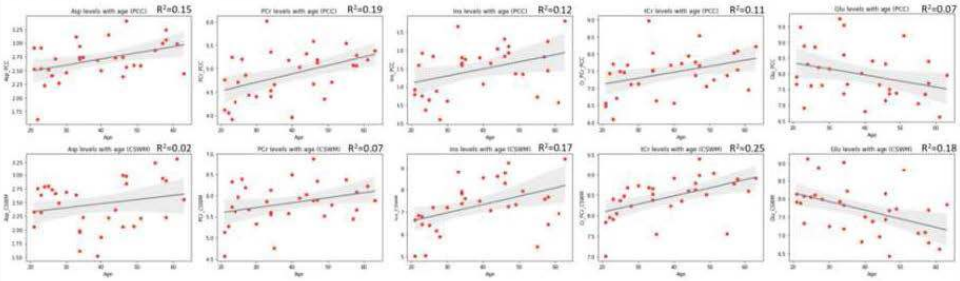

Figure 1. A. Demographic information about included participants in our age group comparison analysis; **B.** Metabolite level changes, per brain region, between young and middle-aged adults; and **C.** Linear regressions of metabolite with age, from young to old adults (20-65 yrs). The adjusted R^2 value is provided for every metabolite. *Abbreviations:* Asp, aspartate; CSWM, centrum semiovale white matter; F, female; Glu, glutamate; Ins, myo-inositol; M, male; PCC, posterior cingulate cortex; PCr, phosphocreatine; ROIs, regions of interest; tCr, total creatine = creatine + phosphocreatine; yrs, years; ↑, higher metabolite levels in middle-aged adults compared to young adults; ↓, lower metabolite levels in middle-aged compared to young adults.

Results: In middle-aged adults compared to young adults, we found (a) higher levels of myo-inositol (p=0.01 in PCC; p<0.01 in CSWM) and total creatine (tCr; p=0.02 in PCC; p=0.01 in CSWM) in both PCC and CSWM, (b) higher levels of aspartate (Asp; p=0.04) and phosphocreatine (PCr; p=0.04) in PCC, and (c) lower Glu (p=0.02) levels in CSWM (Figure 1B). In CSWM, while NAA and Glx (Glu + glutamine (Gln)) levels showed a trend for lower levels with increasing age, this finding did not survive multiple comparisons.

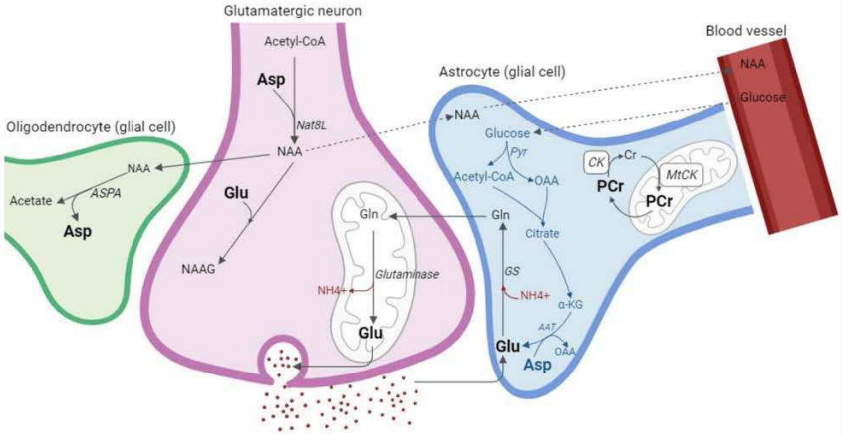

Figure 2. Neuroglial metabolite pathways. *Figure created with BioRender software (BioRender.com).* Compared to young adults, middle-aged adults showed level variations of Ins, tCr, Asp, PCr (increased levels) and Glu (decreased levels). Ins is a glial marker (not shown in the image) and its concentrations have been reported to be disturbed as a response to increased levels of ammonia (NH4+) in the astrocyte, due to abnormalities in the Glx signal as a consequence of a disturbed Glu-Gln cycle. Glu can be metabolized in two ways: the *de novo* synthesis (in blue) from glucose in the astrocyte, or from the Glu-Gln cycle in the neuron. Asp level variations can rise from a dysregulated NAA-Asp cycle in the neuron and the oligodendrocyte. Finally, higher levels of PCr and tCr (= PCr + Cr) can reflect perturbed PCr-Cr mitochondrial cycle in the astrocyte. *Abbreviations:* α-KG, α-Ketoglutaric acid; AAT, aspartate aminotransferase; Asp, aspartate; ASPA, aspartoacylase; Cr, creatine; CK, creatine kinase; Gln, glutamine; Glu, glutamate; GS, glutamine synthetase; Ins, myo-inositol; MtCK, mitochondrial CK; NAA, N-acetylaspartate; NAAG, N-acetylaspartylglutamic acid; Nat8L, N-acetyltransferae-8-like protein; OAA, oxaloacetate; PCr, phosphocreatine; Pyr, pyruvate. Note that enzymes are displayed in italic.

Conclusions: Overall, we demonstrate perturbations in brain metabolite levels in middle-aged adults, which may indicate alterations in the neuro-glial metabolite cycles, including the Glu-Gln, Cr-PCr, and NAA-Asp cycles (Figure 2) (Dingledine and McBain, 1999; Sherry, Lee and Choi, 2015). Proper functioning of these cycles, especially the Glu-Gln, ensures neuron-astrocyte integrity, preventing excitotoxicity caused by excess Glu levels in the extracellular space (Xu et al., 2016). Our future directions are to investigate these pathways in older adults using (a) 7T MRS and (b) plasma metabolomics data using mass spectrometry from our database.

References

1. Detcheverry, F. et al. (2023) 'Changes in levels of the antioxidant glutathione in brain and blood across the age span of healthy adults: A systematic review', NeuroImage: Clinical, p. 103503.
2. Dingledine, R. and McBain, C.J. (1999) Glutamate and Aspartate Are the Major Excitatory Transmitters in the Brain. Lippincott-Raven.
3. Provencher, S.W. (2001) 'Automatic quantitation of localized in vivo 1H spectra with LCModel', NMR in biomedicine, 14(4), pp. 260–264.
4. Sherry, E.B., Lee, P. and Choi, I.-Y. (2015) 'In Vivo NMR Studies of the Brain with Hereditary or Acquired Metabolic Disorders', Neurochemical research, 40(12), pp. 2647–2685.
5. Simpson, R. et al. (2017) 'Advanced processing and simulation of MRS data using the FID appliance (FID-A)-An open source, MATLAB-based toolkit', Magnetic resonance in medicine: official journal of the Society of Magnetic Resonance in Medicine / Society of Magnetic Resonance in Medicine, 77(1), pp. 23–33.
6. Xu, H. et al. (2016) 'Evaluation of neuron-glia integrity by in vivo proton magnetic resonance spectroscopy: Implications for psychiatric disorders', Neuroscience and biobehavioral reviews, 71, pp. 563–577.

Poster No 2389

Neurotransmitter Concentrations in Motor Neuron Disease using 1H MRS at 7 Tesla

Zeinab Eftekhari[1,2], Thomas Shaw[1,3,4], Robert Henderson[5,6], Wolfgang Bogner[7], Markus Barth[1,4,8]

[1]Centre for Advanced Imaging, The University of Queensland, Brisbane, Australia, [2]ARC Training Centre for Innovation in Biomedical Imaging Technology (CIBIT), The University of Queensland, Brisbane, Australia, [3]Neurology Department, Royal Brisbane and Women's Hospital, Brisbane, Australia, [4]School of Electrical Engineering and computer Science, The University of Queensland, Brisbane, Australia, [5]Neurology Department, Royal Brisbane and Women's Hospital, Brisbane, Australia, [6]Centre for Clinical Research, The University of Queensland, Brisbane, Australia, [7]High-field MR Centre, Department of Biomedical Imaging and Image-guided Therapy, Medical University, Vienna, Austria, [8]ARC Training Centre for Innovation in Biomedical Imaging Technology (CIBIT), The University of Queensland, Brisbane, Australia

Introduction: Motor neuron disease (MND) is a progressive condition marked by the degeneration of motor neurons, leading to physical deterioration and death. Magnetic Resonance Spectroscopy (MRS) provides a distinctive, non-invasive method for

quantifying neurochemical alterations at the molecular level in MND patients. Initial findings suggest that the concentrations of specific metabolites may be impacted in MND[1]. However, limited studies have explored 7T for measuring metabolite changes in MND with different onset locations/phenotypes or used sLASER MRS which is beneficial due to its enhanced signal-to-noise ratio, reduced chemical shift displacement, and more precise quantification of neurochemical changes[2]. This study aimed to investigate changes in metabolite ratios across the motor cortex using 7T MRS. Our investigation focused on N- Acetyl aspartate (NAA), Glutamate (Glu), and Glutamine (Gln) concentrations in cortical areas corresponding to MND symptoms, as well as regions unaffected by the disease. The goal was to improve diagnostic accuracy and enable effective early-stage disease monitoring.

Methods: Five non-neurodegenerative controls (NC) and five MND patients, (2 bulbar onset, 2 lower limb onset, and 1 upper limb onset), were scanned using a 7T whole-body research scanner (Siemens MAGNETOM) equipped with a 32-channel head coil (Nova Medical). The protocol included short-TE semi-LASER[3] (TE=28 ms, TR= 8s, 32 averages) and 3D T1-weighted MP2RAGE. MR spectra were collected from two distinct regions within the motor cortex for MND patients, one affected and one unaffected region (Figure 1). For the control group, the precentral gyrus (representing upper limb regions in the motor homunculus) and the paracentral lobule (representing lower limb regions) were selected. Data processing and analysis were conducted using the Osprey MRS analysis toolbox[4] in MATLAB (v.R2022a). Metabolite signals were quantified using LCModel (v6.3)[5] and the resulting mean absolute concentrations ± SD of NAA, Glu and Gln were reported for all comparative analyses.

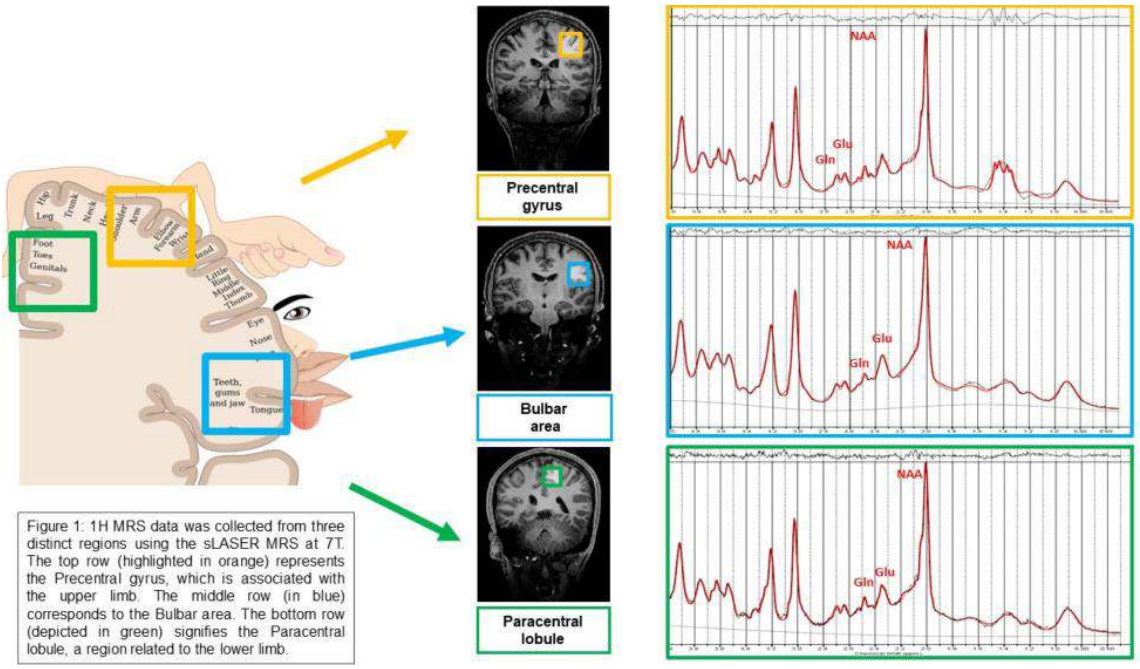

Figure 1: 1H MRS data was collected from three distinct regions using the sLASER MRS at 7T. The top row (highlighted in orange) represents the Precentral gyrus, which is associated with the upper limb. The middle row (in blue) corresponds to the Bulbar area. The bottom row (depicted in green) signifies the Paracentral lobule, a region related to the lower limb.

Results: We observed notable differences in neurochemical profiles between MND patients and NCs. NAA levels are 22.4% lower in affected regions (11.8 ± 1.5 mM) and 17% lower in non-affected regions (12.6 ± 1.3 mM) in MND patients, while NCs had mean absolute concentrations of 13.7 ± 0.7 mM in the lower limb and 15.2 ± 0.4 mM in the upper limb ROI. Gln levels were elevated by 23.3% in affected regions (3.8 ± 1 mM) and 5.9% in non-affected regions (2.8 ± 1 mM) in patients compared to NCs, who displayed mean absolute concentrations of 3.1 ± 0.6 mM in the lower limb and 2.6 ± 0.3 mM in the upper limb. Additionally, Glu levels were 14.6% lower in asymptomatic regions of MND patients (8.6 ± 0.6 mM) compared to NCs (9.4 ± 0.4 mM).

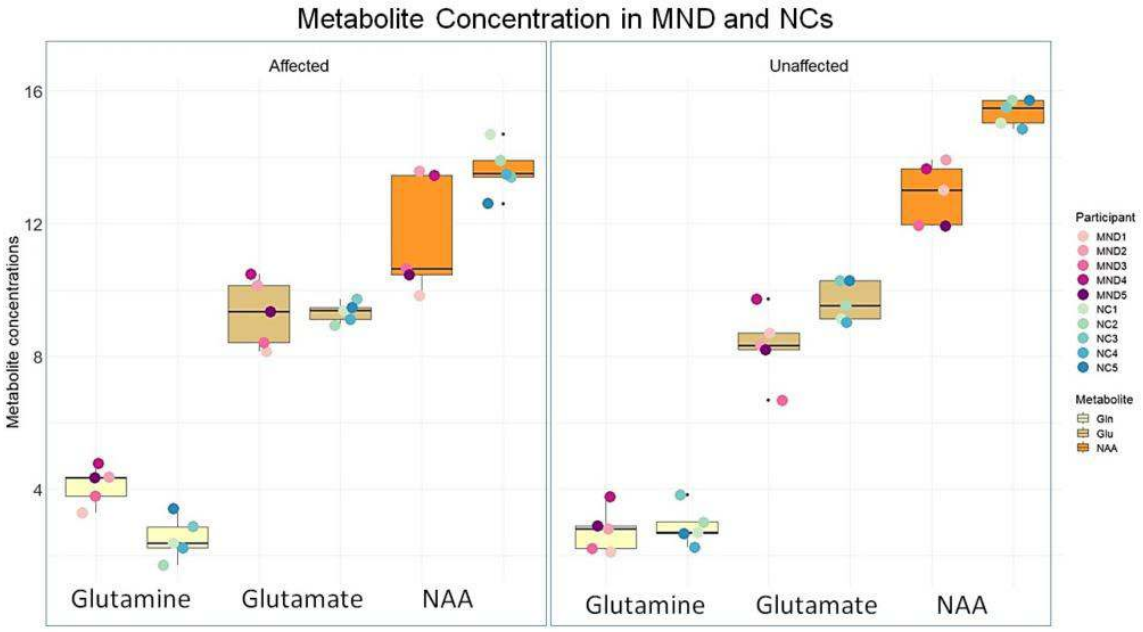

Figure 2: This visualization compares the absolute concentrations of three metabolites - Glutamine (Gln), Glutamate (Glu), and N-Acetyl Aspartate (NAA) - in the brains of five patients with Motor Neuron Disease (MND) and five Non neurodegenerative Controls (NCs). The data, acquired from a sLASER sequence at 7T, includes measurements from both affected and unaffected regions of the brain. In the case of the NCs, the Lower Limb regions are categorized as affected, while the Upper Limb regions are considered unaffected.

Conclusions: This study demonstrates the feasibility of robustly acquiring single voxel MRS data from different regions of the motor cortex at 7T within a reasonable acquisition time for the relevant patient groups and the capability of MRS to detect neurochemical alterations in regions without observable phenotypic symptoms. Our preliminary results suggest a potential trend of lower NAA, Glu and higher Gln levels in MND when compared to non-neurodegenerative controls (NCs). Metabolite ratios derived from MRS may serve as valuable in vivo diagnostic markers and enable the measurement and monitoring of hyperexcitability, which holds potential as a biomarker for subtype/phenotype categorization and disease monitoring. Our continued investigation aims to identify potential patterns in Glu and Gln levels throughout the disease progression, with the aim of measuring excitotoxicity in vivo.

References

1. G. Öz, Magnetic resonance spectroscopy of degenerative brain diseases. Springer, 2016.
2. S. Caldwell and D. L. Rothman, "1H magnetic resonance spectroscopy to understand the biological basis of als, diagnose patients earlier, and monitor disease progression," Frontiers in Neurology, vol. 12, p. 701170, 2021.
3. D. K. Deelchand et al., "Across-vendor standardization of semi-LASER for single-voxel MRS at 3T," NMR Biomed, vol. 34, no. 5, p. e4218, May 2021, doi: 10.1002/nbm.4218.
4. G. Oeltzschner et al., "Osprey: Open-source processing, reconstruction & estimation of magnetic resonance spectroscopy data," Journal of neuroscience methods, vol. 343, p. 108827, 2020.
5. S. W. Provencher, "Estimation of metabolite concentrations from localized in vivo proton NMR spectra," Magnetic resonance in medicine, vol. 30, no. 6, pp. 672-679, 1993.

Poster No 2390

Post-COVID depression in women – a higher symptom burden linked to lower glutamine in pgACC

Meng Li[1], Marina Krylova[1], Lejla Colic[1], Lena Danyeli[2], Benjamin Giszas[1], Gerd Wagner[3], Nils Opel[4], Daniel Güllmar[1], Kathrin Finke[1], Philipp Reuken[1], Andreas Stallmach[1], Martin Walter[1], Bianca Besteher[1]

[1]Jena University Hospital, Jena, Germany, [2]Department of Psychiatry and Psychotherapy, Jena University Hospital, Jena, Thuringia, [3]Jena University Hospital, Jena, Thuringia, [4]Jena University Hospital, Germany, Jena, Germany

Introduction: The COVID-19 pandemic not only increases mortality and morbidity rates during the acute phase of infection but also impairs mental health in the post-infection period. The depressive symptoms post COVID infection share several demographic and clinical characteristics with major depressive disorder (MDD), particularly in its higher prevalence in women. Investigating the underlying mechanism of vulnerability to depression onset after COVID-19 infection in women would be in favor of its treatment. MDD is suggested to be associated with the imbalance of neurotransmitter metabolism, especially the excitatory neurotransmitter system including glutamate (Glu) and glutamine (Gln) (Luykx et al. 2012; Mitchell and Baker 2010;

Yüksel and Öngür 2010; Moriguchi et al. 2019). Regionally specific alterations in glutamatergic neurotransmission have been reported in the anterior cingulate cortex (ACC) in MDD. A recent systematic review of neuroimaging studies revealed the ACC as one of the brain regions with sex differences in depression (Mohammadi et al. 2023). This study aims to investigate sex differences in distinct psychopathological features in COVID-19 survivors and their potential linkage with neurotransmitter metabolism in the pregenual anterior cingulate cortex (pgACC), which is crucial for the assessment of affective valence and reward-based learning (Phan et al. 2002; Rogers et al. 2004).

Methods: For the investigation of sex differences in depressive symptoms, 603 COVID-19 survivors after acute infection after acute infection were included (390 women, mean age= 48 years and 213 men, mean age= 50 years). Fifty-six individuals with post-COVID symptoms underwent thorough psychometric phenotyping and completed magnetic resonance spectroscopy at 3T, assessing Glu and Gln levels in the pgACC using the Siemens PRESS MRS sequences. All participants had verified COVID-19 via real-time reverse transcriptase-polymerase chain reaction during acute infection. To assess neuropsychiatric symptoms, participants completed the Montreal Cognitive Assessment (MoCA) for cognitive impairment, the Short-Form-36 questionnaire (SF-36) for quality-of-life measures, the Montgomery-Asberg Depression Rating Scale (MADRS), and the Fatigue Assessment Scale (FAS) for symptoms of depression and fatigue. We conducted group comparisons and Pearson correlation tests to assess group by sex differences and their associations to Glu and Gln levels in R.

Results: Our study revealed a significantly higher burden of mental health symptoms, especially depression, in women Post-COVID 19 survivors compared to men (Table 1). Psychometric phenotyping demonstrated a higher burden of depressive symptoms, fatigue, and subclinical stress, but not anhedonia, in women with long-COVID compared to men. Furthermore, depressive symptoms and reduced energy were linked to reduced Gln levels in the pgACC (MADRS: r= -0.49, p= 0.012; Energy, r= 0.45, p= 0.029). Notably, the Gln alteration in long-COVID participants were primarily driven by differences in women (p=0.01), not men (p = 0.52, Figure 1).

Table 1. Comparison of psychopathological phenotyping between female and male

Characteristic	female, N = 36[1]	male, N = 20[1]	p-value[2]
Age	45.0 (34.8, 52.3)	48.0 (40.5, 58.3)	0.3
PC	36 (100%)	20 (100%)	
WHO			0.9
1	1 (2.8%)	1 (5.0%)	
2	29 (81%)	16 (80%)	
3	2 (5.6%)	0 (0%)	
4	2 (5.6%)	1 (5.0%)	
5	2 (5.6%)	2 (10%)	
MoCA	26.0 (25.0, 28.0)	25.5 (23.8, 27.3)	0.2
MADRS	**12.5 (8.0, 20.3)**	**8.5 (4.0, 14.0)**	**0.026**
BDI_2	**15.5 (10.0, 21.0)**	**9.0 (7.0, 14.8)**	**0.027**
SSQ_25	**52.0 (38.8, 66.3)**	**30.0 (17.8, 44.0)**	**0.004**
FAS_gesamt	**38.5 (32.5, 42.0)**	**31.0 (21.3, 35.5)**	**0.023**
[1] Median (IQR); n (%)			
[2] Wilcoxon rank sum test; Fisher's exact test			

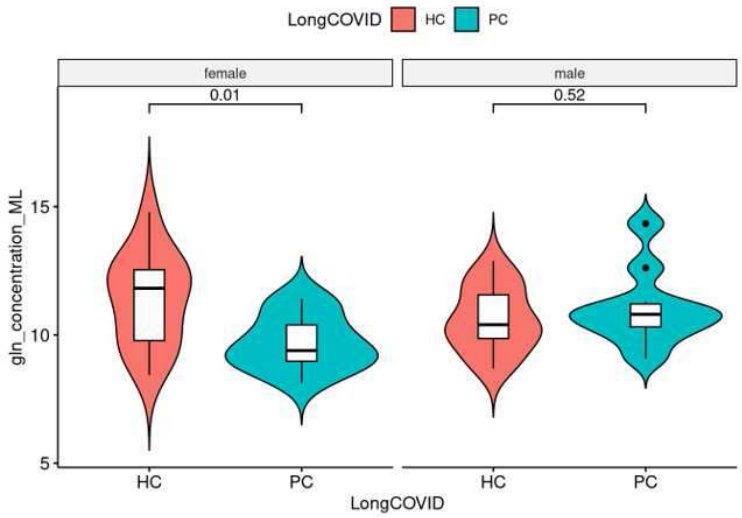

Fig. 1. Comparison of pgACC glutamine concentration between controls and patients in female an male.

Conclusions: In summary, we present evidence of distinct sex-specific features of long-COVID depression with an atypical symptom profile and lower Gln in the pgACC. Both features are likely connected to sex-specific persisting immunological alterations in long-COVID, leading to sickness behavior and limbic glutamatergic metabolism dysfunction.

References

1. Davey, C. G., B. J. Harrison, M. Yücel, and N. B. Allen. 2012. "Regionally Specific Alterations in Functional Connectivity of the Anterior Cingulate Cortex in Major Depressive Disorder." Psychological Medicine 42 (10): 2071–81. https://doi.org/10.1017/S0033291712000323.
2. Luykx, J.J., K.G. Laban, M.P. van den Heuvel, M.P.M. Boks, R.C.W. Mandl, R.S. Kahn, and S.C. Bakker. 2012. "Region and State Specific Glutamate Downregulation in Major Depressive Disorder: A Meta-Analysis of 1H-MRS Findings." Neuroscience & Biobehavioral Reviews 36 (1): 198–205. https://doi.org/10.1016/j.neubiorev.2011.05.014.
3. Mitchell, N. D., and G. B. Baker. 2010. "An Update on the Role of Glutamate in the Pathophysiology of Depression." Acta Psychiatrica Scandinavica 122 (3): 192–210. https://doi.org/10/b6fnbc.
4. Mohammadi, Soheil, Homa Seyedmirzaei, Mohammad Amin Salehi, Ali Jahanshahi, Seyed Sina Zakavi, Fatemeh Dehghani Firouzabadi, and David M. Yousem. 2023. "Brain-Based Sex Differences in Depression: A Systematic Review of Neuroimaging Studies." Brain Imaging and Behavior 17 (5): 541–69. https://doi.org/10.1007/s11682-023-00772-8.
5. Phan, K. Luan, Tor Wager, Stephan F. Taylor, and Israel Liberzon. 2002. "Functional Neuroanatomy of Emotion: A Meta-Analysis of Emotion Activation Studies in PET and fMRI." NeuroImage 16 (2): 331–48. https://doi.org/10.1006/nimg.2002.1087.
6. Rogers, Robert D., Narender Ramnani, Clare Mackay, James L. Wilson, Peter Jezzard, Cameron S. Carter, and Stephen M. Smith. 2004. "Distinct Portions of Anterior Cingulate Cortex and Medial Prefrontal Cortex Are Activated by Reward Processing in Separable Phases of Decision-Making Cognition." Biological Psychiatry 55 (6): 594–602. https://doi.org/10.1016/j.biopsych.2003.11.012.
7. Wu, Guo-Rong, and Chris Baeken. 2023. "Sex Determines Anterior Cingulate Cortex Cortical Thickness in the Course of Depression." Biological Psychiatry Global Open Science, August. https://doi.org/10.1016/j.bpsgos.2023.08.003.
8. Yüksel, Cagri, and Dost Öngür. 2010. "Magnetic Resonance Spectroscopy Studies of Glutamate-Related Abnormalities in Mood Disorders." Biological Psychiatry 68 (9): 785–94. https://doi.org/10.1016/j.biopsych.2010.06.016.

Poster No 2391

Comparison of STEAM and Semi-Laser for neurochemical separation at 7T

Tiffany Bell[1], Dana Goerzen[2], Jamie Near[3], Ashley Harris[1]

[1]University of Calgary, Calgary, Alberta, [2]Cornell University, Ithaca, NY, [3]University of Toronto, Toronto, Ontario

Introduction: Proton Magnetic Resonance Spectroscopy (MRS) is commonly used to quantify neurochemicals of interest. Typically quantified neurochemicals are: total N-acetyl aspartate (tNAA), total Creatine (tCr), total Choline (tCho), and Glx. However, these are composites of signals from multiple overlapping neurochemicals. For example, Glx signal consists of overlapping signals glutamate (Glu) and Glutamine (Gln). Higher field strengths (i.e. 7T) increase signal-to-noise ratio (SNR) and spectral resolution, allowing better signal separation. Several sequences have been proposed for 7T MRS. STEAM allows for very short echo times (TEs), minimizing signal modulation due to J-coupling and T2 relaxation, whereas Semi-LASER (sLASER) has reduced chemical shift displacement and better resilience to B1 inhomogeneity (Wilson et al., 2019). Previous work suggested sLASER (TE=28ms) produced a more robust measure of Glu than STEAM (TE=7.5ms) at 7T (Marsman et al., 2017). When comparing TEs 45-225ms with sLASER localization, the optimal echo time of Glu signal evolution was 105ms (Wong et al., 2018). However, these studies only focused on Glu. This 7T study directly compares the separation of neurochemicals using STEAM, short TE sLASER, and long TE sLASER acquisitions.

Methods: Simulations were conducted to assess the effects of measurement error on between- and within-subject variation to determine the best metric for comparisons. 14 healthy participants (18-40y) were scanned at 7T (Siemens Terra). Voxels were placed in the parietal cortex centred on the midline. Data were collected using 3 sequences: STEAM_8 (TE/TR/TM=8/6000/40ms), sLASER_34 (TE/TR=34/5000ms), and sLASER_105 (TE/TR=105/5000ms), all with 64 averages. Sequence order was counterbalanced across subjects. Data were preprocessed using FID-A (Simpson et al., 2017) and quantified with LCModel (Provencher, 2001). To assess repeatability, the scans were split into two (each with 32 averages), then processed as above. The analysis focused on the following combinations of metabolites: tNAA: NAA+N-acetylaspartylglutamate (NAAG), tCr: Cr+phosphocreatine (PCr), tCho: Cho+phosphocholine (PC)+glycerophosphocholine (GPC), Glx: Glutamate+Glutamine, and glutathione (GSH). The fit of the model was assessed using CRLB's, and repeatability was assessed using coefficient of variation (CV).

Results: Simulations showed that, for between subject variation, there was a large overlap between distributions of different measurement errors. In contrast, for within subject variation, there was little overlap between distributions from small measurement errors and large measurement errors. This indicates within subject variation is a better indicator of measurement error, and subsequently we chose this metric for comparing sequences (Figure 1). For most neurochemicals, sLASER_34 had the lowest CRLB and STEAM_8 had the lowest CV. However, for Cho and GPC, STEAM_8 had the lowest CRLB. For PC sLASER_105 had the lowest CRLBs, however these were still much higher than the typical cut-off points.

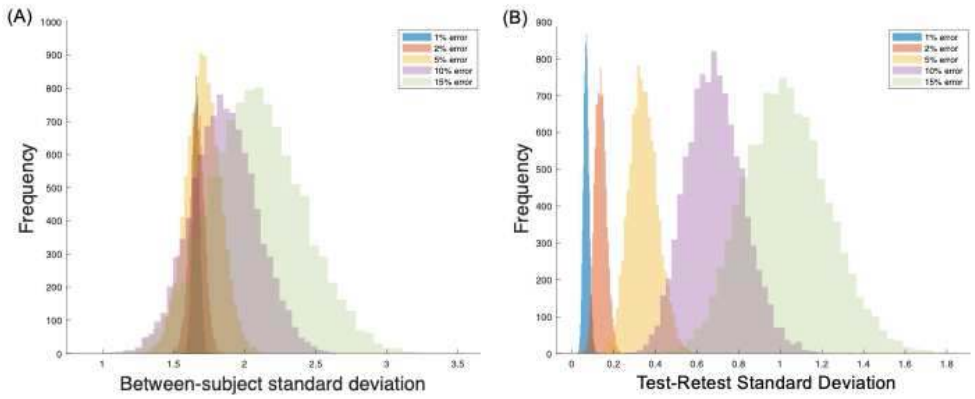

Figure 1: Distributions of (A) between-subject variability and (B) within subject variability using simulations with 5 different measurement errors (Blue: 1%, Orange: 2%, Yellow: 5%, Purple: 10%, Green: 15% error)

Conclusions: Overall, sLASER_34 best quantified both the individual and summed signals. However, Cho and GPC were best quantified with STEAM_8. PC wasn't quantified well with any sequence, likely due to the strong overlap between PC and GPC. STEAM_8 generally produced lower CV's, in contrast to previous work (Marsman et al., 2017), however this study compared measurements acquired two weeks apart. STEAM may produce more consistent results within session, but less consistent results across time. sLASER is likely less sensitive to repositioning effects due to reduced chemical shift displacement and better resilience to B1 inhomogeneity (Wilson et al., 2019). We conclude short TE sLASER is better for quantification of most standard neurochemicals than long TE sLASER or short TE STEAM at 7T. Depending however, if there is a specific neurochemical of interest (i.e., choline containing neurochemicals), short-echo STEAM or longer echo sLASER may be preferred.

References

1. Marsman et al., (2017). Detection of Glutamate Alterations in the Human Brain Using 1H-MRS: Comparison of STEAM and sLASER at 7 T. Frontiers in Psychiatry, 8, 60.
2. Provencher (2001). Automatic quantitation of localized in vivo 1H spectra with LCModel. NMR Biomed, 14, 260–264.
3. Simpson et al., (2017). Advanced processing and simulation of MRS data using the FID appliance (FID-A)—An open source, MATLAB-based toolkit. Magnetic Resonance in Medicine, 77(1), 23–33.
4. Wilson et al., (2019). Methodological consensus on clinical proton MRS of the brain: Review and recommendations. Magnetic Resonance in Medicine, 82(2), 527–550.
5. Wong et al (2018). Optimized in vivo brain glutamate measurement using long-echo-time semi-LASER at 7 T. NMR in Biomedicine, 31(11), 1–13.

Poster No 2392

Altered Neurochemical-Behavioral Interplay: dACC Glutamate and Awareness in Internet Gaming Disorder

Tiantian Hong[1], Hui Zhou[1,2], Wan Xi[1], Xiumei Li[1], Yusang Du[1], Jiaxin Liu[3], Yuzheng Hu[1,2,4]

[1]Department of Psychology and Behavioral Sciences, Zhejiang University, Hangzhou, Zhejiang, China, [2]The State Key Lab of Brain-Machine Intelligence, Zhejiang University, Hangzhou, Zhejiang, China, [3]College of Education, Zhejiang University, Hangzhou, Zhejiang, China, [4]MOE Frontiers Science Center for Brain Science & Brain-Machine Integration, Zhejiang University, Hangzhou, Zhejiang, China

Introduction: Repetitive and compulsive behavior is the core symptom of addiction including Internet Gaming Disorder (IGD). As a facet of mindfulness involving sustained awareness of one's actions during task engagement, the ability of acting with awareness (AWA) has a preventive role in both substance abuse and IGD. However, the neurochemical basis underlying the role of awareness in IGD remains unclear. The abnormalities of dorsal anterior cingulate cortex (dACC) have been linked to both IGD and awareness in a good number of studies. Our study endeavors to clarify the alterations in glutamate (Glu) levels within the dACC region and its correlation with AWA in individuals with IGD.

Methods: Participants and assessments. 53 participants were recruited through online advertisements. Poor fit of magnetic resonance spectroscopy (MRS,Cramer-Rao lower bounds≥10%, n=8) and participants failed attention-check (n=1) were excluded. IGD severity was assessed using the 9-criteria scale recommended by the DSM-5, with a diagnostic cutoff at a score of 5. In order to enhance the clarity of group classification, subjects with DSM scores equal to 4 (n=4) were also excluded,

resulting in 21 IGDs (scores>4, 20 males, age = 23.52±2.42) and 19 recreational game users (RGU, scores<4, 19 males, age = 23.42±2.59) in the final statistical analysis. There were no significant age difference (p = .898) and sex difference (p = .335) between two groups. AWA was measured using the "Acting with Awareness" sub-scale from the Five Facet Mindfulness Scale (FFMQ), in a 5-point Likert-type rating from rarely true to always true. Image acquisition and processing. MRS was collected using a 3T Siemens Prisma scanner equipped with a 20-channel coil. A 26×21×15 cm3 voxel of interest (VOI) were manually placed at dACC (Fig. 1A) for the MRS collection. We used a MEGA-PRESS sequence (TE/TR = 68/2000 ms) with 120 averages to measure the Glu concentration. Glu concentration was estimated using the 'LCModel' algorithm. Analysis. Independent samples t-tests were conducted to examine differences in Glu concentrations and AWA between IGD and RGU groups. Correlation analysis was employed to examine the relationship between dACC Glu and AWA in both groups. A comparison of the difference between two correlation coefficients was performed. The level of statistical significance was set at p < .05.

Results: Significant differences between the two groups have been observed in dACC Glu and AWA, with RGU exhibiting higher values than IGD (dACC Glu: t (38) = 2.17, p =.037; AWA: t (38) = 3.00, p = .005) (Fig. 1B, C). When considering the relationship between dACC Glu and AWA, different patterns have been found in the two groups. In the RGU group, participants with higher dACC Glu had a higher level of AWA (r = .46, p = .045). However, in the IGD group, we did not find a significant correlation between the two variables (r = -.11, p =.650) (Fig. 2). The difference of these two correlation coefficients reached a marginal significance (diff = -.57, Z = -1.77, p = .076).

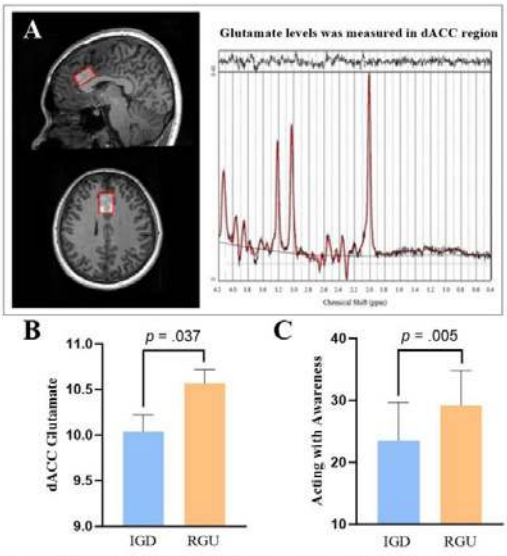

Figure 1. (A) Region of interest in the MRS experiment: A 26×21×15 cm^3 box was placed at the dACC for the MRS collection. (B) A significant group difference in glutamate concentration at the dACC was observed, with the dACC glutamate being significantly higher in the RGU group (orange compared to the IGD group (blue). (C) The RGU group had a significantly higher level of acting with awareness, as measured by FFMQ, than the IGD group.

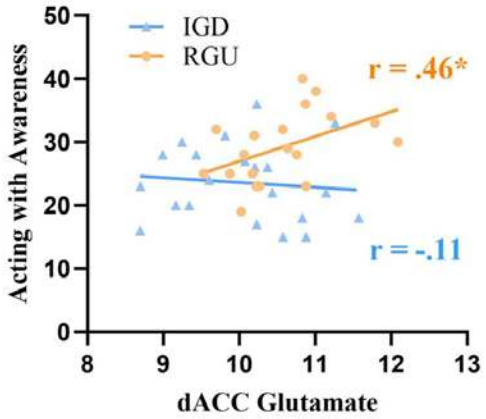

Figure 2. Different patterns in the relationship between glutamate concentration in the dACC and acting with awareness was observed in the IGD and RGU groups. In the RGU group, participants with higher dACC Glutamate exhibited a higher level of awareness (orange dot). However, in the IGD group, no significant correlation was found (blue triangle). * $p < .05$

Conclusions: The current study disclosed significant distinctions in dACC Glu and AWA between the IGD and RGU groups. Specifically, the RGU group exhibited higher values in dACC Glu and AWA compared to IGD group. Moreover, a significant positive correlation between dACC Glu and AWA was observed in the RGU group, not in the IGD group. Previous research has highlighted that acting without awareness mediated the link between negative affect and craving. Furthermore, 10h mindfulness training can elevate ACC Glu levels while concurrently increasing mindful attention awareness and reducing negative affect. Within the IGD group, we identified an altered neurochemical-behavioral interplay compared to RGU, suggesting that enhancing the excitability of the dACC through long-term mindfulness training may have the potential to improve AWA. Such improvement in AWA could contribute to better control over cravings for addictive substances triggered by negative affect.

References

1. American Psychiatric Association, D. (2013). 'Diagnostic and statistical manual of mental disorders: DSM-5 (Vol. 5, No. 5).' Washington, DC: American psychiatric association.
2. Baer, R. A. (2006). 'Using Self-Report Assessment Methods to Explore Facets of Mindfulness.' Assessment, 13(1), 27–45.
3. Enkema, M. C. (2020). 'Disrupting the path to craving: Acting without awareness mediates the link between negative affect and craving.' Psychology of Addictive Behaviors, 34(5), 620.
4. Fernandez, A. C. (2010). 'Measuring mindfulness and examining its relationship with alcohol use and negative consequences.' Psychology of Addictive Behaviors, 24(4), 608.
5. Goodman, A. (1990). 'Addiction: definition and implications.' British journal of addiction, 85(11), 1403-1408.
6. Kim, J. Y. (2019). 'The correlation between the frontostriatal network and impulsivity in internet gaming disorder.' Scientific reports, 9(1), 1191.
7. Orr, C. (2012). 'Error-related anterior cingulate cortex activity and the prediction of conscious error awareness.' Frontiers in human neuroscience, 6, 177.
8. Tang, Y. Y. (2020). 'Brief mindfulness training increased glutamate metabolism in the anterior cingulate cortex.' NeuroReport, 31(16), 1142-1145.
9. Yin, M. (2023). 'Depression and Internet Gaming Disorder among Chinese Adolescents: A Longitudinal Moderated Mediation Model.' International Journal of Environmental Research and Public Health, 20(4), 3633.

Poster No 2393

More for Less? Mapping Cortical Metabolites using Multi-Voxel Magnetic Resonance Spectroscopy

Thomas Shaw[1], Zeinab Eftekhari[1], Korbinian Eckstein[1], Bernhard Strasser[2], Fabian Niess[2], Wolfgang Bogner[2], Markus Barth[1]

[1]The University of Queensland, Brisbane, Australia, [2]Medical University of Vienna, Vienna, Austria

Introduction: Concentric ring trajectory-based free induction decay magnetic resonance spectroscopic imaging (MRSI) is a non-invasive technique for generating high-resolution maps of metabolites across the whole brain within reasonable timeframes at both 3T and 7T MRI[1]. Compared to single voxel spectroscopy, MRSI allows for the combination of metabolite maps with segmentations of grey and white matter (GM/WM), allowing for specific metabolite maps of glutamate, glutamine, N-Acetyl-Aspartate (NAA), and creatine across the cortex and some subcortical regions at 3T and 7T. Previous studies have explored the reproducibility of this technique[2,3], but comparison of MRSI across 3T and 7T in different brain regions have not been performed, which is vital for validation of the technique in GM and WM regions. Considering the improved SNR and spectral resolution at 7T[4], this technique is promising for mapping (sub)cortical metabolite profiles in research settings; while its application in 3T sites lends itself to easy clinical adoption in the future. Here, we show how the upper half of the cortex and white matter can be mapped reliably over time and discuss the implications for future MRS studies.

Methods: We conducted two scan sessions, 5-9 days apart, on five healthy participants (three female, age: 25-33) using both 7T (Siemens Magnetom 7T+) and 3T (Siemens Prisma) scanners. 3D-FID-MRSI parameters 3T: FOV=220x220x110mm, matrix size=32x32x21 at 6.3 mm^3 iso, TA=4:14 min; 7T: FOV=220x220x110mm, matrix size=64x64x31 at 3.4mm^3 iso, TA=11:30. A T1-w MP2RAGE was acquired for segmentation using FastSurfer[7] and metabolic maps were interpolated onto the Desikan-Killiany-Tourville (DKT) atlas' cortical surface for visualisation and as proof of concept for cortical metabolic mapping. MRSI spectroscopic quantification was performed in LCModel[6]. Maps were overlayed with T1w DKT segmentations (Fig 1). The FOV of MRSI allowed for quantification of 12 bilateral GM and one WM ROI (25 total). We report on three important metabolite ratios relevant for neurodegenerative diseases: NAA/tCr, Glx/tCr, and Glx/tNAA. Mean concentrations at each ROI and field-strength and the intra- and inter-subject Coefficient of Variation (CV) were calculated to assess reproducibility.

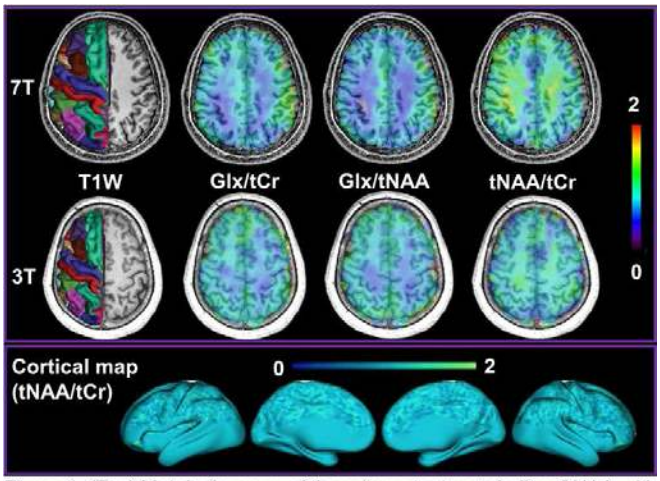

Figure 1: (Top) Metabolic maps of three important metabolites [tNAA = N-acetyl-aspartate (NAA)+ N-acetyl-aspartyl (NAAG); Glx= Glutamate (Glu) + Glutamine (Gln); tCr = Creatine (Cr) + phosphocreatine (PCr) together with anatomical T1-weighted (T1w) images acquired at 7T (top) and 3T (bottom). DKT parcellations are overlayed on the T1w image. (Bottom) The tNAA/tCr map sampled onto the cortical surface. Colour bars indicate relative concentrations.

Results: We examined reproducibility for three metabolite ratios across 25 DKT brain regions using test-retest at 3T and 7T. Across ROIs, the metabolite concentration ratio estimates were stable between subjects and within subject at both fields (Fig 2). Mean±SD concentrations were in line with literature[2,3]. The coefficient of variation (CV) for metabolite ratios across most ROIs did not exceed 12% (mean value, 6%; 3T, 7T), which indicated excellent reproducibility for both fields. Metabolic maps were successfully sampled onto FastSurfer cortical surfaces (Fig 1), revealing (for the first time) patterns of metabolic expression over the cortex. We observed higher variability in certain ROIs (e.g., rostral middle frontal) compared to others (e.g., paracentral lobule).

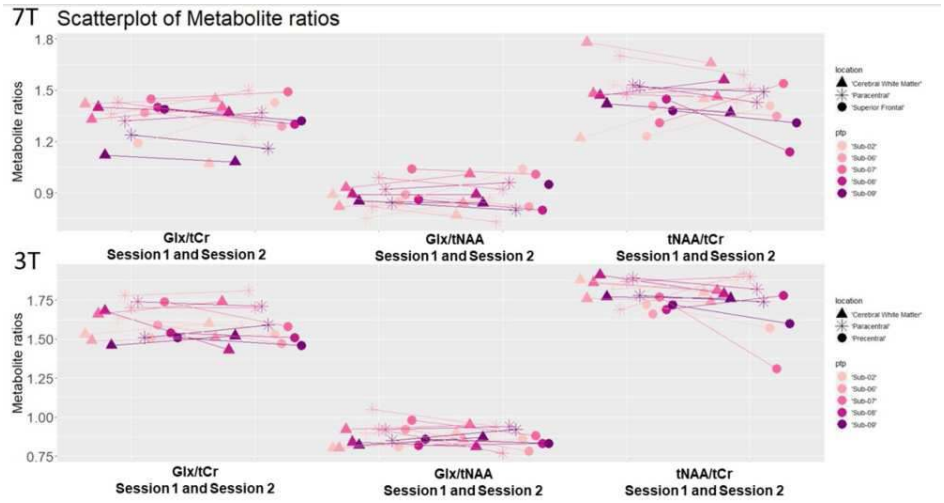

Figure 2: Relative changes of concentration ratios between two sessions with a week apart for three metabolite ratios across select brain regions at both 7T (top) and 3T (bottom). The outlier in the NAA ratios is likely due to a lipid artifact. Points are intentionally jittered.

Conclusions: The introduction of a cortical sampling technique for spectroscopy data unlocks the possibility of mapping the metabolic expression of the brain in a reliable, longitudinal manner. Results indicated a high degree of reproducibility for metabolites at both fields, with most ROIs demonstrating higher reproducibility at 3T compared to 7T, likely due to reduced participant movement over the shorter scan time. The variability of NAA/tCr across ROIs was substantial (2.1 CV% to 12 CV%), and besides actual biological variability, this may also be related to lipid contamination in some regions/subjects, warranting further investigation. Our results suggest that ratios of metabolite concentrations can be reproducibly measured with 3D-FID-MRSI at 3T and 7T, and these can be sampled onto the cortex of many brain regions. Scan time is an important factor for variability, and one could test to reduce scan time if lower spatial resolution is not an issue.

References

1. W. Bogner, R. Otazo, and A. Henning, (2021) "Accelerated MR spectroscopic imaging-a review of current and emerging techniques," NMR Biomed, vol. 34, no. 5, p. e4314, doi: 10.1002/nbm.4314.
2. P. Moser et al., (2020) "Intra-session and inter-subject variability of 3D-FID-MRSI using single-echo volumetric EPI navigators at 3T," Magnetic resonance in medicine, vol. 83, no. 6, pp. 1920-1929.
3. G. Hangel et al., (2021), "Inter-subject stability and regional concentration estimates of 3D-FID-MRSI in the human brain at 7 T," NMR in Biomedicine, vol. 34, no. 12, pp. e4596.
4. R. Mekle, V. Mlynárik, G. Gambarota, M. Hergt, G. Krueger, and R. Gruetter. (2009), "MR spectroscopy of the human brain with enhanced signal intensity at ultrashort echo times on a clinical platform at 3T and 7T," Magnetic Resonance in Medicine: An Official Journal of the International Society for Magnetic Resonance in Medicine, vol. 61, no. 6, pp. 1279-1285.
5. W. Bogner et al., (2014), "Real-time motion-and B0-correction for LASER-localized spiral-accelerated 3D-MRSI of the brain at 3 T," Neuroimage, vol. 88, pp. 22-31.
6. L. Hingerl et al., (2018), "Density-weighted concentric circle trajectories for high resolution brain magnetic resonance spectroscopic imaging at 7T," Magnetic resonance in medicine, vol. 79, no. 6, pp. 2874-2885.
7. L. Henschel, S. Conjeti, S. Estrada, K. Diers, B. Fischl, and M. Reuter, (2020), "Fastsurfer-a fast and accurate deep learning based neuroimaging pipeline," NeuroImage, vol. 219, pp. 117012.

Poster No 2394

Neurometabolic Changes in Visual Stimulation: Insights from a 3T Task fMRS Study

Iting Lee[1], Shang-Hua Lin[1], Rong-Rung Kuo[1], Ching-Po Lin[1,2], Li-Hung Chang[1]

[1]Institute of Neuroscience, National Yang Ming Chiao Tung University, Taipei, Taiwan, [2]Department of Education and Research, Taipei City Hospital, Taipei, Taiwan

Introduction: Proton magnetic resonance spectroscopy is a non-invasive technique used to measure the absolute concentrations of neurochemicals in the brain. Previous studies have shown that functional magnetic resonance spectroscopy (fMRS) is sensitive enough to detect task-related regional dynamics changes in neurotransmitters. Although fMRS studies have demonstrated task-related changes in glutamate during visual stimulation (Bednarik, Tkac et al. 2015, Ip, Berrington et al. 2017), most studies have been performed at ultra-high fields (>3T) and using specialized sequences. However, replication will be critical at lower, broader clinical domain intensities. In this study, we use time-resolved analysis to identified similar task-related changes during medium-field visual stimulation in a 3T system. Additionally, we aim to determine the physiological reaction time of neurotransmitters during a visual task and emphasize the significance of attention levels in the paradigm.

Methods: We recruited five healthy volunteers with visual acuity either normal or corrected-to-normal for the study. A total of 3 MRS sessions were delivered at noon on consecutive days under 3T Prisma-Fit scanner. In this study, visual stimulations were designed to modulate responses in the primary visual cortex, where the MRS voxel-of-interest (VOI) was positioned. The visual stimulation consisted of a baseline-stimulation block design, with a total time of 21.3 min. Throughout the experiment, a central fixation dot remained on the screen and a vigilance task was performed to encourage participants' central fixation and maintain consistent attention levels (Fig. 1). During data processing, to calculate the time course of metabolite concentrations, time-resolved and time-averaged analysis were used. In time-resolved analysis, 16 consecutive averages were summed into one spectrum and analyzed using an LCModel, resulting in a time course of 40 data points with a temporal resolution of 32 s. The first block was used to calculate the baseline signal variation and was therefore excluded from the statistical analysis. In contrast, in time-averaged analysis, 160 consecutive averages yielded a time course of 4 data points with a temporal resolution of 320 s. Spectra with a CRLB over 15% were excluded.

Fig. 1 **Experimental design: stimulus, VOI position**

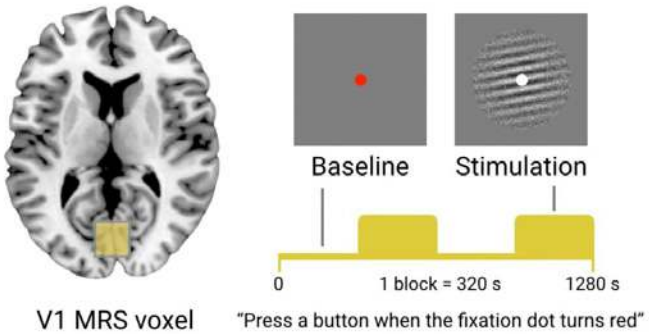

Results: The time-resolved analysis, in comparison with baseline periods, revealed a statistically significant increase in amplitude of change in Glutamate (Glu) and in the combined Glutamate+Glutamine (Glx) signals measured during visual stimulation periods (Glx [Stimulation: 1.18 ± 0.17/ baseline: –1.33 ± 0.94], $p < 0.001$; Glu [Stimulation: 1.83 ± 1.01/ baseline: – 0.29 ± 0.94], $p < 0.001$). On the other hand, GSH, NAA, and creatine did not differ significantly nor did the time-averaged analysis of all the aforementioned neurometabolites. Further, as measured repeatedly, the functional changes remained consistent. For the physiological reaction time of neurotransmitters, whether in visual stimulation or baseline conditions, the time exceeding the response threshold shows statistically significant breakthroughs in Glx and Glu concentrations compared with the baseline periods. The threshold is set by the baseline signal variation of the first block, reflecting a pure resting condition. The average response time requires approximately two data points (i.e., 64 s). A significant positive correlation was also observed between the time-resolved analysis of Glx concentration and the correction rate of the sustained attention ($r = 0.58$; $p = 0.039$).

Fig. 2 **Results of (A) time-resolved analysis, (B) time-averaged analysis**

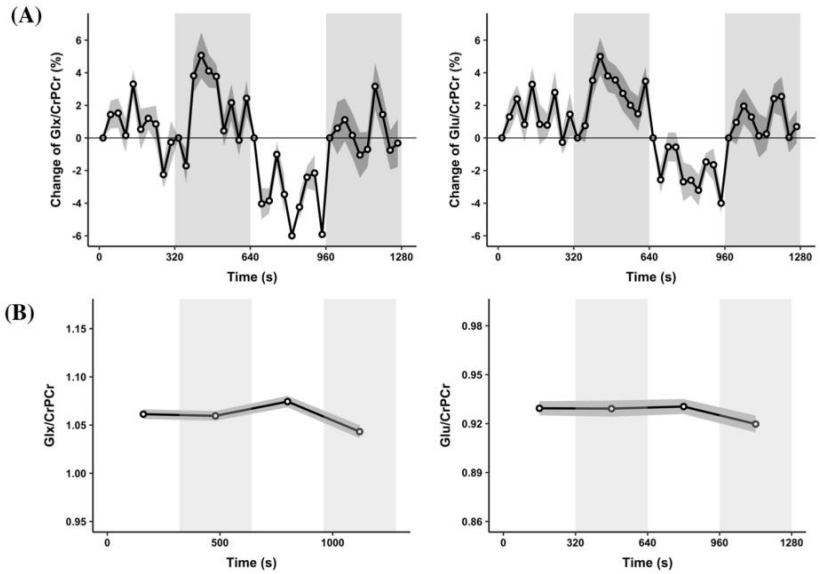

Conclusions: Our results suggest that varying time-course calculations might have influenced our observations of metabolite dynamics during a visual stimulation task on a 3T system. Additionally, we demonstrate the physiological reaction time of neurotransmitters and highlight the impact of attention levels on the concentration of neurotransmitters in the primary visual cortex. This study emphasizes the critical role of data analysis and the experimental paradigm in fMRS studies.

References

1. Bednarik, P., I. Tkac, F. Giove, M. DiNuzzo, D. K. Deelchand, U. E. Emir, L. E. Eberly and S. Mangia (2015). "Neurochemical and BOLD responses during neuronal activation measured in the human visual cortex at 7 Tesla." J Cereb Blood Flow Metab 35(4): 601-610.
2. Ip, I. B., A. Berrington, A. T. Hess, A. J. Parker, U. E. Emir and H. Bridge (2017). "Combined fMRI-MRS acquires simultaneous glutamate and BOLD-fMRI signals in the human brain." Neuroimage 155: 113-119.

Poster No 2395

Brain dynamics after acute stress task: moderating factors

Lejla Colic[1], Tara Chand[1], Soroosh Golbabaei[2], Larissa McClain[3], Hannes Meilicke[3], Luisa Herrmann[4], Louise Martens[4], Marina Krylova[5], Igor Izyurov[3], Meng Li[5], Martin Walter[6]

[1]Jena University Hospital, Jena, AK, [2]Jena University Hospital, Jena, Thuringia, [3]Department of Psychiatry and Psychotherapy, Jena University Hospital, Jena, Germany, Jena, Turingen, [4]University Tübingen, Tübingen, AS, [5]Jena University Hospital, Jena, Germany, [6]Department of Psychiatry and Psychotherapy, Jena University Hospital, Jena, Thuringia

Introduction: Whole brain resting state dynamics before and after acute stress task (Kühnel, 2022) may unravel alterations in brain stress response indicating maladaptive response (Hammen, 2015). Distal and proximal stress, measured as childhood adversity and recent chronic stress may modulate those dynamics (Kaiser, 2018; Söder, 2020). Moreover, other factors such as levels of excitatory neurometabolites in regions important for stress regulation, such as the pregenual anterior cingulate cortex (pgACC) (Arnsten, 2022) may further moderate these dynamics. Therefore, we investigated resting state brain dynamics and its associations with the aforementioned factors.

Methods: Thirty-seven healthy male participants (mean age= 26.6, stan.dev= 3 years) underwent 3 Tesla (Siemens, Germany) magnetic resonance scan comprising structural T1-weighted scan, two resting-state functional magnetic resonance imaging scans (rsfMRI) before and after psychosocial scan stress task and a single-voxel magnetic resonance imaging scan in bilateral pgACC (10×20×20 mm^3). RsfMRI data were preprocessed using fMRIPrep 20.1.1 (Esteban et al., 2019). Blood-oxygen-level-dependent time series of 100 regions were extracted using Schaefer-2018. Whole-brain dynamics were calculated using Kuramoto order parameter across time, i.e., "metastability" (Deco, 2017). Spectra were analyzed using LCModel (V6.3; Provencher, 2001). Signal-to-noise ratio, Cramer-Rao lower bound, and full-width-at-half-maximum were used for spectra quality checking and glutamate referenced to water signal were quantified. Participants were evaluated for childhood adversity via Childhood trauma questionnaire (CTQ-tot) and recent chronic stress via Perceived Stress Scale (PSS-tot). Outliers were detected with Rosner test. Linear-mixed models were set with stress (pre-post), CTQ-tot, PSS-tot and pgACC glutamate as fixed factors and a participant-specific random intercept (R-V4.1.3). Models tested main effect of stress on the brain dynamics and the interactions among the variables.

Results: Glutamate significantly moderated the stress dynamics (b= 0.007, st.error= 0.003, p= .04). There were main trend effects of childhood adversity (b= -0.006, st.error= 0.003, p= .09) but no interaction effects (b= 0.0003, st.error= 0.0005, p= .4). There were no main effects of acute stress task on metastability (b= 0.006, st.error= 0.004, p= .2), nor interaction with recent chronic stress (b= 0.0008, st.error= 0.0008, p= .3).

Conclusions: Results provide preliminary evidence for the relationship of whole-brain dynamics associations after stress and glutamate levels in a region important for stress and emotion regulation. Further, childhood adversity had a marginal man effect on the overall dynamics. Together, results point to possible mechanisms of maladaptive stress-psychopathology.

References

1. Kühnel, Anne, et al. "Spatiotemporal dynamics of stress-induced network reconfigurations reflect negative affectivity." Biological Psychiatry 92.2 (2022): 158-169.
2. Hammen, Constance L. "Stress and depression: old questions, new approaches." Current Opinion in Psychology 4 (2015): 80-85.
3. Kaiser, Roselinde H., et al. "Childhood stress, grown-up brain networks: corticolimbic correlates of threat-related early life stress and adult stress response." Psychological medicine 48.7 (2018): 1157-1166.
4. Söder, Eveline, Katarina Krkovic, and Tania M. Lincoln. "The relevance of chronic stress for the acute stress reaction in people at elevated risk for psychosis." Psychoneuroendocrinology 119 (2020): 104684.
5. Arnsten, Amy FT, Mary Kate P. Joyce, and Angela C. Roberts. "The Aversive Lens: Stress effects on the prefrontal-cingulate cortical pathways that regulate emotion." Neuroscience & Biobehavioral Reviews (2022): 105000.
6. Esteban, O., Markiewicz, C. J., Blair, R. W., Moodie, C. A., Isik, A. I., Erramuzpe, A., ... & Gorgolewski, K. J. (2019). fMRIPrep: a robust preprocessing pipeline for functional MRI. Nature methods, 16(1), 111-116.
7. Deco, G., Kringelbach, M. L., Jirsa, V. K., & Ritter, P. (2017). The dynamics of resting fluctuations in the brain: metastability and its dynamical cortical core. Scientific reports, 7(1), 3095.
8. Provencher, Stephen W. "Automatic quantitation of localized in vivo 1H spectra with LCModel." NMR in Biomedicine: An International Journal Devoted to the Development and Application of Magnetic Resonance In Vivo 14.4 (2001): 260-264.

Poster No 2396

An fNIRS study Exploring Cognitive Processes in Narrative Engagement

Leonhard Schreiner[1], Christy Li[2]

[1]g.tec Medical Engineering GmbH, Schiedlberg, Austria, [2]g.tec Neurotechnology Hong Kong Limited, Hong Kong, Hong Kong

Introduction: Narrative engagement encompasses attention, immersion, and memory, which are interconnected cognitive processes. This study delves into the relationship between narrativity and cognitive processes by categorizing narratives into four complexity and semantic content-based levels. Our goal is to differentiate between these varying degrees of narrativity by utilizing functional Near-Infrared Spectroscopy (fNIRS) as a metric to assess brain activity while exposing individuals to narratives of different content. The chosen stimuli were paintings from 4-narrative levels, a subset defined by Ryan (2007). In this exploratory study, we investigate the relationship between different levels of narrativity and attention, engagement, and memory aspects using Oxygenated (HBO) and deoxygenated (HBR) hemoglobin concentration features from the fNIRS data and behavioral analysis.

Methods: The wireless g.Nautilus fNIRS system (g.tec medical engineering GmbH) with 16 channels of EEG, combined with 8 channels of fNIRS, was used for data acquisition (Figure 1D). The 8 fNIRS channels were symmetrically placed bilaterally over the prefrontal cortex (PFC) (Figure 1B). To verify whether the general public would also categorize the paintings as per our pre-defined levels, we conducted an online validation test using the Clickworker platform (https://www.clickworker.com) with an independent panel of participants. Based on the participants' responses, we selected 10 pictures per category with the highest agreement percentage among the participants. Consequently, the stimuli used in this study comprised 40

paintings, with 10 paintings per narrativity level (Figure 1A). The procedure of the paradigm includes a short preparation phase, investigation of the pictures for 15 seconds followed by answering a questionnaire (Figure 1C). A support vector machine classifier with a 10x10 cross-fold (CV) approach was employed for the 4-class problem. A permutation test with shuffled labels was conducted 1000 times to identify statistically significant outcomes of the classifier.

Results: Figure 2 illustrates the grand average in cortical oxygenation and deoxygenation across all subjects the prefrontal cortex. The graph displays an elevation in the HBO changes particularly in class 1 (abstract-narrative) and class 4 (high-narrative) during the visual presentation, with the most pronounced oxygenation increase in the abstract narrative class occurring approximately 5 seconds after the stimulus was presented. The concentrations of HBR exhibit only a minor decline around the 5-second mark, with no significant variations between classes. The drop observed across all channels and categories shortly after the task concluded can be attributed to movement artifacts resulting from subjects adjusting their positions to complete the questionnaires.The abstract-Narrative stimulus shows an high increase in accuracy, reaching the maximum of 75% at around 8 second after picture presentation.

Conclusions: The findings from the behavioural analysis suggest that higher narrativity levels are associated with increased self-reported engagement while perceiving the stimulus. The relative HBO concentration changes show an increase in concentration across all levels, whereby the abstract-narrative and high-narrative classes have the highes concentration, which is in line with the outcome of the behavioural analysis. Therefore only the HBO feature channels were selected for classification. However, classification performance shows significant results only for the abstract-level class pictures. The brain might be processing abstract painting differently, such as analyzing colors, shapes, and textures, which could contribute to the classification outcome (Aviv, 2014).

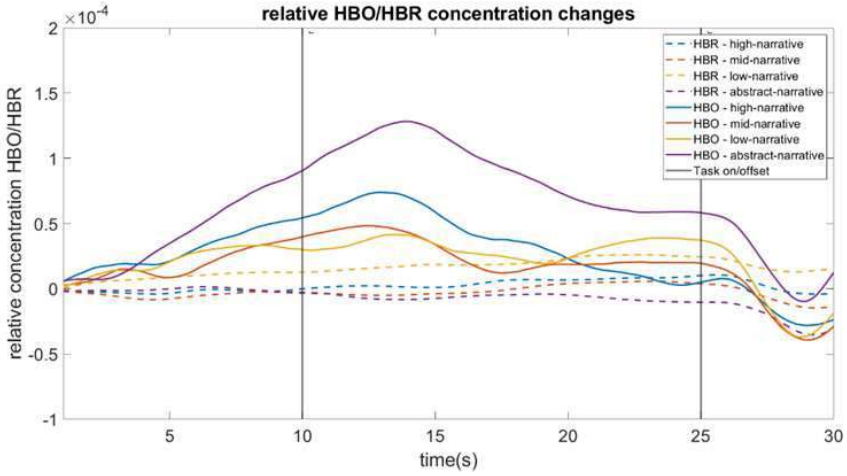

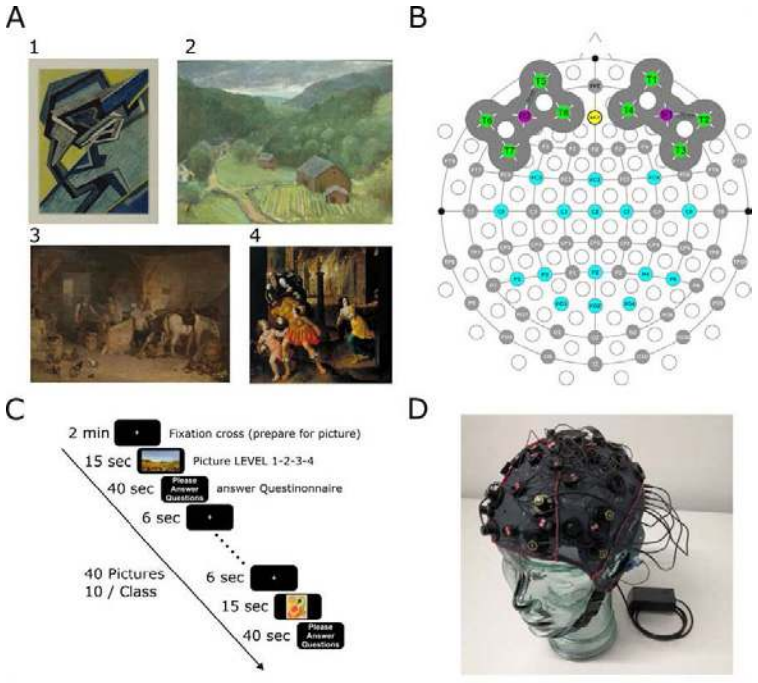

Poster No 2397

Simultaneous fPET/fMRI unveils nigrostriatal pathway mechanisms during optogenetic stimulation

Fernando Bravo[1], Sabrina Haas[2], Tudor Ionescu[2], Irene Gonzalez-Menendez[2], Leticia Quintanilla-Martinez[1], Gina Dunkel[2], Laura Kuebler[2], Bettina Weigelin[2], Gerald Reischl[2], Bernd Pichler[2], Kristina Herfert[1]

[1]University of Tübingen, Tübingen, Germany, [2]University of Tübingen, Tübingen, Germany

Introduction: The dopaminergic system is a unique modulatory component of the brain governing motor behavior, cognition and emotion. It plays a major role in various neurological and psychiatric conditions such as Parkinson's disease and schizophrenia. The nigrostriatal pathway delineates a critical circuit for dopamine projections from the substantia nigra pars compacta (SNc) to the striatum, representing a doorway for understanding many of the disease-related dysfunctions. Stand-alone fMRI is unable to characterize this circuit's interplay between brain activation and its molecular underpinnings. Here, the use of simultaneous [18F]FDG-fPET/BOLD-fMRI allowed us to demonstrate excitation-inhibition mechanisms of the nigrostriatal pathway during optogenetic stimulation, which are concealed in isolated fMRI readouts.

Methods: fMRI analysis: A block design was employed, modeling each of the six optogenetic stimulation and baseline blocks (Figure 1). Within-group subtractive/functional connectivity analyses were conducted in SPM12. fPET analysis: To enable functional PET (fPET) (Villien et al., 2014) we employed an [18F]FDG bolus+constant infusion protocol. Without requiring a priori assumptions on the shape of the expected [18F]FDG-fPET response, independent component analysis (ICA) has been successfully applied to [18F]FDG-fPET during task-related designs (Li et al., 2020). We advanced the ICA approach through an automatic kurtosis-sorting of ICA components to isolate task-related signals without priori timing information (Lu & Rajapakse, 2003). ICA and molecular connectivity analyses were implemented with the GIFT v4.0b and CONN v22a toolboxes.

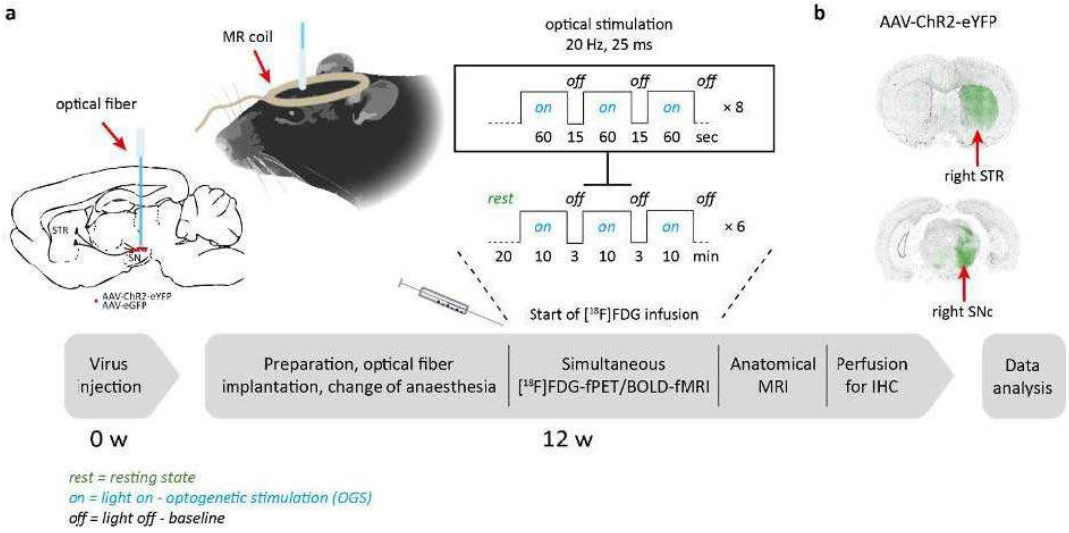

Fig. 1: Time course of simultaneous optogenetic [18F]FDG-fPET/fMRI experiments. (a) Optical stimulation of the right SNc. (b) Control virus expression in the STR and SNc by fluorescence microscopy.

Results: Comparison of hemodynamic and metabolic responses to stimulation: ICA revealed the optogenetic-stimulation response map as the first kurtosis-ranked component. Results showed significant [18F]FDG uptake in the expected right lateralised brain regions including the SNc, midbrain, thalamus, hypothalamus and striatum. Hemodynamic changes were observed in similar regions; however, important differences were found (Figure 2). BOLD-fMRI activation maps in the striatum showed a larger spatial extension than fPET glucose uptake maps, while the opposite was observed in the SNc. Ex vivo analysis of cFos expression in both corroborated our findings: increased cFos expression levels were evident in the dorsal striatum, but there were no discernible differences in the SNc. This occurred despite a high metabolic response in the SNc, suggesting an active suppression of neuronal firing during optogenetic stimulation. In agreement, metabolic connectivity analyses showed correlated glucose uptake in the right SNc, midbrain, thalamus and striatum; while functional connectivity evidenced BOLD signal interactions circumscribed to the right dorsal-ventral Striatum, supporting an active inhibition of nigrostriatal couplings during neuronal stimulation.

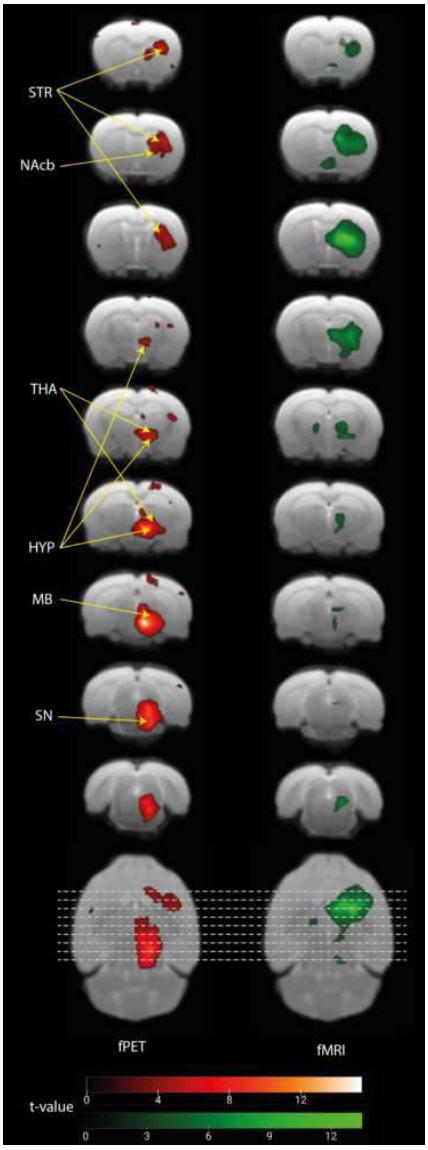

Fig. 2: Overlay of [18F]FDG-fPET and BOLD-fMRI activation maps. Results threshold: p < unc. 0.001 (voxellevel), p < 0.05 FWE (cluster-level).

Conclusions: Our study shed new light on the relationship between hemodynamic and metabolic responses during optogenetic stimulation of the dopaminergic pathway. fMRI results revealed a BOLD response which was strongly bound to the right striatum; fPET, on the other side, evidenced a significant [18F]FDG uptake along the entire dopaminergic circuit including the site of stimulation (SNc). The findings emphasize that a decrease or absence of the BOLD signal outside the striatal region does not necessarily correlate with neuronal inactivity. Dopamine release is modulated by numerous neuromodulators. One interpretation posits that optogenetic stimulation triggers the release of dopamine thereby activating dopamine D2 auto- and heteroreceptors and inhibiting further activation-induced dopamine release (Anzalone et al., 2012; Ford, 2014). This feedback control process may curtail the maximum attainable BOLD signal increase during stimulation (Benoit-Marand et al., 2001) and may be important to regulate neurotransmitter levels at the synapse for the effective operation of the dopaminergic system.

References

1. Anzalone, A., Lizardi-Ortiz, J. E., Ramos, M., Mei, C. D., Hopf, F. W., Iaccarino, C., Halbout, B., Jacobsen, J., Kinoshita, C., Welter, M., Caron, M. G., Bonci, A., Sulzer, D., & Borrelli, E. (2012). Dual Control of Dopamine Synthesis and Release by Presynaptic and Postsynaptic Dopamine D2 Receptors. Journal of Neuroscience, 32(26), 9023–9034. https://doi.org/10.1523/JNEUROSCI.0918-12.2012
2. Benoit-Marand, M., Borrelli, E., & Gonon, F. (2001). Inhibition of dopamine release via presynaptic D2 receptors: Time course and functional characteristics in vivo. The Journal of Neuroscience: The Official Journal of the Society for Neuroscience, 21(23), 9134–9141. https://doi.org/10.1523/JNEUROSCI.21-23-09134.2001
3. De Martino, F., Gentile, F., Esposito, F., Balsi, M., Di Salle, F., Goebel, R., & Formisano, E. (2007). Classification of fMRI independent components using IC-fingerprints and support vector machine classifiers. NeuroImage, 34(1), 177–194. https://doi.org/10.1016/j.neuroimage.2006.08.041

4. Ford, C. P. (2014). The Role of D2-Autoreceptors in Regulating Dopamine Neuron Activity and Transmission. Neuroscience, 282, 13–22. https://doi.org/10.1016/j.neuroscience.2014.01.025
5. Henson, R. (2007). Efficient Experimental Design for fMRI. In Statistical Parametric Mapping (pp. 193–210). Elsevier. https://doi.org/10.1016/B978-012372560-8/50015-2
6. Jamadar, S. D., Ward, P. GD., Li, S., Sforazzini, F., Baran, J., Chen, Z., & Egan, G. F. (2019). Simultaneous task-based BOLD-fMRI and [18-F] FDG functional PET for measurement of neuronal metabolism in the human visual cortex. NeuroImage, 189, 258–266. https://doi.org/10.1016/j.neuroimage.2019.01.003
7. Li, S., Jamadar, S. D., Ward, P. G. D., Premaratne, M., Egan, G. F., & Chen, Z. (2020). Analysis of continuous infusion functional PET (fPET) in the human brain. NeuroImage, 213, 116720. https://doi.org/10.1016/j.neuroimage.2020.116720
8. Lu, W., & Rajapakse, J. C. (2003). Eliminating indeterminacy in ICA. Neurocomputing, 50, 271–290. https://doi.org/10.1016/S0925-2312(01)00710-X
9. Villien, M., Wey, H.-Y., Mandeville, J. B., Catana, C., Polimeni, J. R., Sander, C. Y., Zürcher, N. R., Chonde, D. B., Fowler, J. S., Rosen, B. R., & Hooker, J. M. (2014). Dynamic functional imaging of brain glucose utilization using fPET-FDG. NeuroImage, 100, 192–199. https://doi.org/10.1016/j.neuroimage.2014.06.025

Poster No 2398

Data-driven latent alignment in simultaneous EEG-fMRI to fuse and generalize brain states

Reinmar Kobler[1,2], Toshikazu Kuroda[1], Takeshi Ogawa[1], Ce Ju[3], Motoaki Kawanabe[1,2]

[1]Advanced Telecommunications Research Institute International, Kyoto, Japan, [2]RIKEN AIP, Kyoto, Japan, [3]Nanyang Technological University, Singapore, Singapore

Introduction: Modalities like electroencephalography (EEG) and functional magnetic resonance imaging (fMRI) provide distinct views to human whole-brain dynamics owing to their contrasting spatiotemporal sensitivities and underlying neurophysiological coupling mechanisms. Advances in simultaneous EEG-fMRI instrumentation lays the groundwork for fusing these distinct views to recover whole-brain dynamics at high spatiotemporal resolution. However, fusing EEG and fMRI data poses a considerable challenge (Phil.+2021) due to low signal-to-noise ratios, non-stationarities, outliers, and a poorly understood non-linear coupling mechanism (Warb. 2022). To address these challenges, past methods relied on extensive domain-knowledge-based preprocessing and feature extraction before fusing both views (Warb. 2022, Sada.+2020). Our take on this problem is fundamentally different. Using minimally pre-processed data, we propose a data-driven approach to establish a latent representation space where EEG and fMRI dynamics vary consistently. To do so, we leverage cutting-edge EEG (Kobl.+2022) and fMRI (Thom.+2022) decoder architectures and train them to maximize geodesic correlation (Ju+in review) between their latent representations (Fig.1A).

Methods: In this study, we applied our proposed approach to two simultaneous EEG-fMRI datasets. The first (DS1), publicly available (v. d. Me.+2016), comprised resting subjects (n=8, 2 runs) in eyes closed vs. open conditions. We considered 6 subjects with clear alpha power changes between conditions. The second dataset (DS2), collected in-house, involved n-back task data (n=31, 2 days) in 0-back vs. 2-back conditions. For both datasets, fMRI data underwent preprocessing using fmriprep, followed by regressing out confounds and extracting ROI activity between 0.01 and 0.2 Hz. EEG data were preprocessed using a custom pipeline to mitigate artifacts and extract brain activity in channel-space between 1 and 36 Hz. Each run was segmented into short segments of paired EEG-fMRI data (10 s duration), which were robustly z-scored and concatenated. We generated train/test splits using cross-validation (CV), assessing generalization across subjects, days, and runs. Additionally, in DS2, we used unimodal EEG recordings to test generalization to data recorded outside the fMRI scanner.

Results: Fig.1B showcases the training convergence for DS 2, while Fig.1C displays t-SNE projections of learned representations for a representative CV split. Maximizing geodesic correlation between latent EEG and fMRI representations consistently preserved task structure. Employing explainable AI techniques (Fig.1D), we confirmed that the representations reflect task-relevant brain activity. The EEG decoder utilized power modulations in the alpha band within a large-scale network spanning frontal and parietal regions. For the fMRI decoder, we report self-attention maps that summarize the averaged self-attention layer output of the Transformer network per condition. They indicate engagement of executive (2-back) and saliency (0-back) networks. For DS1 (eyes open vs. closed), the latent representations reflect activity of occipital networks. Fig.2 lists CV test set scores. Moderate to high correlation scores indicate a robust coupling between the latent EEG and fMRI representations that generalizes to unseen data. Unimodal classification performance for distinguishing task conditions confirm that our end-to-end learning approach utilized task information, encoded in both EEG and fMRI, to fuse the latent representations.

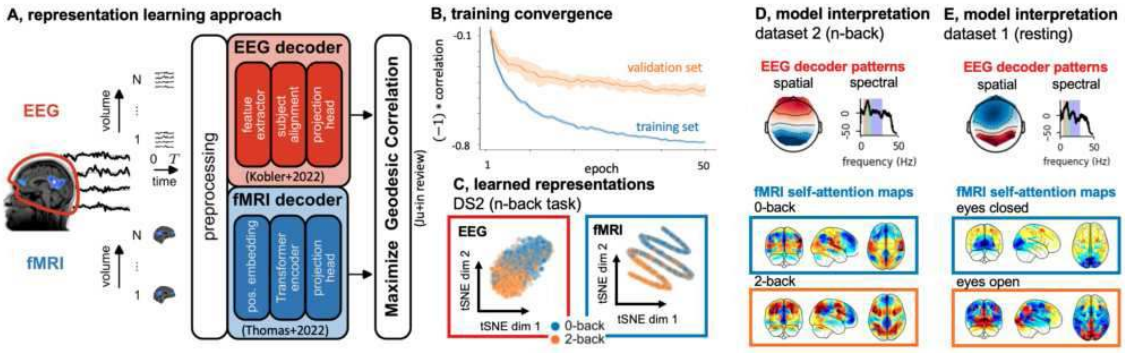

Fig.1: Data-driven EEG-fMRI representation learning. **A**, outline of the approach to maximize correlation of latent EEG and fMRI representations. **B**, convergence curve for DS2 (mean and bootstrapped confidence interval across CV folds; day scenario). **C**, t-SNE visualization of the learned EEG and fMRI representations (condition labels used to color the samples). **D**, Model interpretation results. EEG decoder patterns (spatial and spectral) for the most discriminative source (top) and fMRI self-attention maps per condition (bottom). **E**, as in **D** for DS1.

		pretraining correlation: mean (std)	condition classification balanced accuracy; mean (std)		
dataset	CV hold-out scenario	EEG ~ fMRI	fMRI	EEG inside → inside	EEG inside → outside
DS1 (resting)	run	0.72 (0.17)	88% (9%)	92% (18%)	N/A
	subject	0.69 (0.22)	87% (7%)	87% (18%)	N/A
DS2 (n-back)	day	0.44 (0.14)	74% (8%)	79% (8%)	85% (4%)
	subject	0.43 (0.12)	74% (4%)	79% (7%)	85% (7%)

Fig.2: Quantitative results for test-set folds (mean and std) across datasets and CV scenarios. Pretraining results (Pearson correlation between latent EEG and fMRI representations) exceeded estimated significance levels for DS1 (run: 0.20, subject: 0.16) and DS2 (day: 0.18, subject: 0.19). Condition classification results are reported for each modality. They summarize the performance of linear classifiers fitted to the latent representations (same train/test splits as in pretraining; unsupervised adaptation to outside EEG data). Estimated significance levels ranged from 57% (DS2, subject) to 60% (DS1, run).

Conclusions: We introduced a data-driven approach to fuse EEG-fMRI data and studied two datasets involving cognitive and resting conditions. The approach effectively preserved task-related information in the latent EEG and fMRI representations with the underlying neural patterns linked to specific cognitive processes. The approach exhibited promise in generalizing to simultaneous EEG-fMRI data, and even to EEG data of unseen subjects recorded outside the fMRI scanner.

References

1. Ju, C., Kober, R., Tang, L., Guan, C., & Kawanabe, M. (in review). Deep Geodesic Canonical Correlation Analysis for Covariance-Based Neuroimaging Data. International Conference on Learning Representations. https://openreview.net/pdf?id=PnR1MNen7u
2. Kobler, R., Hirayama, J., Zhao, Q., & Kawanabe, M. (2022). SPD domain-specific batch normalization to crack interpretable unsupervised domain adaptation in EEG. In Advances in Neural Information Processing Systems (Vol. 35, pp. 6219–6235).
3. Philiastides, M. G., Tu, T., & Sajda, P. (2021). Inferring Macroscale Brain Dynamics via Fusion of Simultaneous EEG-fMRI. Annual Review of Neuroscience, 44(1), 315–334. https://doi.org/10.1146/annurev-neuro-100220-093239
4. Sadaghiani, S., & Wirsich, J. (2020). Intrinsic connectome organization across temporal scales: New insights from cross-modal approaches. Network Neuroscience, 4(1), 1–29. https://doi.org/10.1162/netn_a_00114
5. Thomas, A., Ré, C., & Poldrack, R. (2022). Self-Supervised Learning of Brain Dynamics from Broad Neuroimaging Data. In Advances in Neural Information Processing Systems (Vol. 35, pp. 21255–21269).
6. van der Meer, J., Pampel, A., van Someren, E., Ramautar, J., van der Werf, Y., Gomez-Herrero,
7. G., Lepsien, J., Hellrung, L., Hinrichs, H., Möller, H., & Walter, M. (2016). “Eyes Open – Eyes Closed” EEG/fMRI data set including dedicated “Carbon Wire Loop” motion detection channels. Data in Brief, 7, 990–994. https://doi.org/10.1016/j.dib.2016.03.001
8. Warbrick, T. (2022). Simultaneous EEG-fMRI: What Have We Learned and What Does the Future Hold? Sensors, 22(6), 2262. https://doi.org/10.3390/s22062262

Poster No 2399

Exploring brain structure-function interactions associated with fluid cognition based on GCN

Jing Xia[1], Yi Hao Chan[1], Deepank Girish[1], Jagath Rajapakse[1]

[1]School of Computer Science and Engineering, Nanyang Technological University, Singapore

Introduction: Brain structural connectivity (SC) and functional connectivity (FC) not only have individual markers for fluid cognition[1,2], but their interaction may also contribute to cognition[3], given the inherent linkage between neural function and structure. Incorporating the interaction information between FC and SC could advance the prediction of fluid cognition and enhance our understanding of the fundamental neuroanatomical and neurophysiological bases of cognition. However, most graph neural network (GNN)-based studies on brain connectivity focus on a single imaging modality[4,5] and they do not capture the interaction between FC and SC. To this end, we propose an explainable structure-function interaction model based on

the graph convolution network (GCN) to predict fluid cognition and identify the significant edges and nodes for prediction, as shown in Fig. 1.

Methods: We use a dataset of 838 participants from HCP[6], including corresponding T1w, resting-state functional MRI (rs-fMRI), and DTI images, to evaluate the proposed method. Rs-fMRI and DTI images are preprocessed by the DPARSF 5.1 advanced toolkit and FSL software to construct the FC and SC with 116 regions of interest (ROIs), following the Anatomical Automatic Labeling protocol[7]. Fluid cognition scores are extracted from the phenotype list, ranging from 87 to 147. We develop an explainable structure-function interaction model to predict fluid cognition (Fig. 1A). Specifically, SC and FC graphs are modeled with brain ROIs as nodes and the connectivity between these ROIs as edges. A bottleneck MLP is employed on the concatenation matrix of structural and functional node features to learn the interactive weights between SC and FC (Fig. 1C). Then, a joint graph is constructed by inserting the learned interactive weights as edges between paired regions of FC and SC graphs. Finally, GCN is applied to the joint graph to predict fluid cognition scores. We adopt GNNExplainer[8] to elucidate salient aspects of the model, identifying a salient subgraph structure, and a salient subset of node features crucial to the prediction. Specifically, we identify the significant inter-edges between paired nodes of FC and SC, as well as key intra-regions within FC and SC contributing to fluid cognition (Fig. 1B).

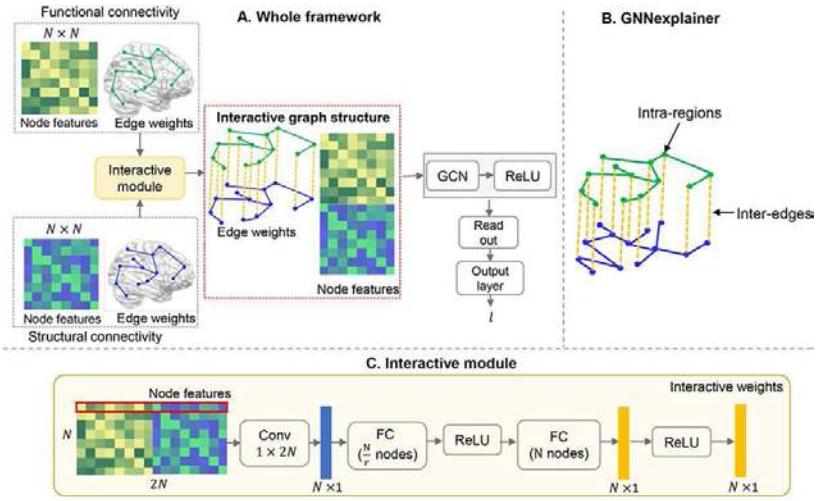

Figure 1. The architecture of the overall framework. SC and FC graphs are modeled with brain ROIs as nodes and the connectivity between these ROIs as edges. Each node's feature is the Pearson correlation with all other nodes. Then, an interactive module is designed to learn the interactions between corresponding regions of SC and FC graphs. A joint graph is constructed by inserting the learned interactive weights as edges between paired regions of FC and SC graphs. Finally, GCN is applied to the joint graph to predict fluid cognition scores.

Results: Pearson's correlation (r) between the actual and predicted fluid cognition scores was used to evaluate model performance. Our structure-function interaction model (r=0.3) outperformed other state-of-the-art multi-modal fusion approaches, including MV-GCN[9] (r=0.28) and Joint-GCN[10] (r=0.29). The most salient inter-edges found by GNNExplainer are located in the inferior frontal, precentral, postcentral, superior temporal, and cingulate cortices (Fig. 2). Fluid cognition involves the ability to executive function, such as planning, solving problems, and learning quickly. The structure-function coupling in the frontal, parietal, and temporal regions is mainly associated with executive functional networks engaged in high-level cognitive processes[3]. Therefore, the importance map from GNNExplainer identifies meaningful coupling regions related to fluid cognition. Moreover, Pearson correlation between the important weights and the learned interactive weights is 0.693 ($p<0.001$), indicating that our model can capture meaningful interactions for prediction. Furthermore, salient intra-regions related to fluid cognition within FC and SC are in the prefrontal, parietal, and occipital cortices, aligning with existing studies on brain structural and functional markers for fluid cognition[2].

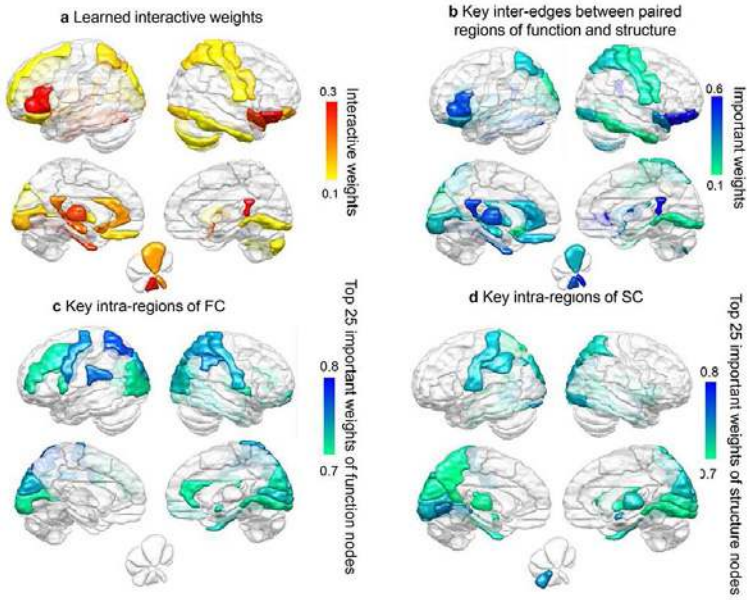

Figure 2. Visualized learned interactive weights, explainable key interactive edges, and key intra-regions of FC and SC for fluid cognition prediction.

Conclusions: We develop an explainable structure-function interaction framework to predict fluid cognition while identifying significant coupling regions between structure and function. This study provides a solution for fusing multi-model features and an explainable approach to explore biomarkers.

References

1. Ooi, L. Q. R., Chen, J., Zhang, S., et al. (2002), "Comparison of individualized behavioral predictions across anatomical, diffusion and functional connectivity mri", NeuroImage, vol. 263, pp. 119636.
2. Dhamala, E., Jamison, K.W., Jaywant, A., et al. (2021), "Distinct functional and structural connections predict crystallised and fluid cognition in healthy adults", Human brain mapping, vol. 42, no. 10, pp. 3102–3118.
3. Baum, G.L., Cui, Z., Roalf, D.R., et al. (2020), "Development of structure–function coupling in human
4. brain networks during youth", Proceedings of the National Academy of Sciences, vol. 117, no. 1, pp. 771–
5. He, T., Kong, R., Holmes, A.J., et al. (2020), "Deep neural networks and kernel regression achieve comparable accuracies for functional connectivity prediction of behavior and demographics", NeuroImage, vol. 206, pp. 116276.
6. Wen, X., Cao, Q., Zhang, D. (2022), "A multi-scale multi-hop graph convolution network for predicting fluid intelligence via functional connectivity", in 2022 IEEE International Conference on Bioinformatics and Biomedicine (BIBM). IEEE, pp. 1262–1267.
7. Van Essen, D.C., Smith, S.M., Barch, D.M., et al. (2013), "The wu-minn human connectome project: an overview", Neuroimage, vol. 80, pp. 62–79.
8. Tzourio-Mazoyer, N., Landeau, B., Papathanassiou, D., et al. (2002), "Automated anatomical labeling of activations in spm using a macroscopic anatomical parcellation of the mni mri single-subject brain", Neuroimage, vol. 15, no. 1, pp. 273–289.
9. Ying, Z., Bourgeois, D., You, J., et al. (2019), "Gnnexplainer: Generating explanations for graph neural networks", Advances in neural information processing systems 32.
10. Liu, J., Ma, G., Jiang, F., et al. (2019), "Community-preserving graph convolutions for structural and functional joint embedding of brain networks", in 2019 IEEE International Conference on Big Data (Big Data). IEEE, pp. 1163–1168.
11. Li, Y., Wei, Q., Adeli, E., et al. (2022), "Joint graph convolution for analyzing brain structural and functional connectomes,", in International Conference on Medical Image Computing and Computer-Assisted Intervention. Springer, pp. 231–240.

Poster No 2400

The Advanced BRain Imaging on ageing and Memory (ABRIM) data collection

Michelle Jansen[1], Marcel Zwiers[1], Jose Marques[1], Kwok-Shing Chan[1], Jitse Amelink[2], Mareike Altgassen[3], Joukje Oosterman[1], David Norris[1]

[1]Donders Institute for Brain, Cognition and Behaviour, Radboud University, Nijmegen, Gelderland, [2]Max Planck Institute for Psycholinguistics, Radboud University, Nijmegen, Gelderland, [3]Johannes Gutenberg-University Mainz, Mainz, Rheinland-Pfalz

Introduction: Ageing individuals display a marked variability in cognitive functioning. Recent scientific efforts have led to the growing availability of imaging cohort studies to further our understanding of the underlying mechanisms of normal cognitive aging, including the role of brain structure, brain function, and other factors relating to risk and resilience in ageing (e.g., education, sleep). To further understand healthy cognitive aging, a comprehensive characterization of brain health parameters is required in conjunction with other factors that contribute to individual risk and resilience. The Advanced BRain

Imaging on ageing and Memory (ABRIM) study aims to add to previously published datasets by offering researchers access to a cross-sectional, normative database of individuals aged between 18-80 years old, including numerous neuroimaging and behavioural parameters.

Methods: We included data of 295 participants from the general population in the Netherlands (median age 52, IQR 36-66, 53.2% females). The MRI protocol consisted of T1-weighted, T2-weighted, MP2RAGE and B1 mapping, multi-echo gradient echo (MEGRE), diffusion-weighted, and resting-state fMRI sequences. All images were defaced prior to further processing. All raw and preprocessed data, as well as applied code, was saved in accordance with the BIDS standard. We used BIDScoin for data management and generation of visual quality control reports (Zwiers et al., 2022). We processed our data using several standard BIDS-compliant pipelines, including MRIqc for quality assessment reports (Esteban et al., 2017). We used several MP2RAGE-related scripts to generate quantitative R1 maps (https://github.com/Donders-Institute/MP2RAGE-related-scripts), SEPIA to generate quantitative susceptibility maps from the MEGRE images (Chan et al., 2020), QSIprep to preprocess diffusion-weighted images and for reconstruction (Cieslak et al., 2021), fMRIprep to preprocess functional data (Esteban et al., 2019), with and without previous NORDIC denoising (Moeller et al., 2020). For a complete overview of the methodological steps that were applied to each imaging modality, see Figure 1. Participants underwent several neuropsychological tests tapping on global cognition, verbal intelligence, processing speed, executive functions, and memory. The Cognitive Reserve Index questionnaire was used to obtain measures for educational attainment, leisure activities, and occupational complexity. Several self-reported questionnaires were applied to obtain information on demographics, general health (e.g., medication use), depressive symptoms, pain, psychopathic traits, memory strategy use, subjective memory failure, and subjective cognitive functioning. In a sub-sample of 120 participants, actigraphy data was recorded for 7 consecutive days to infer sleep-wake rhythms.

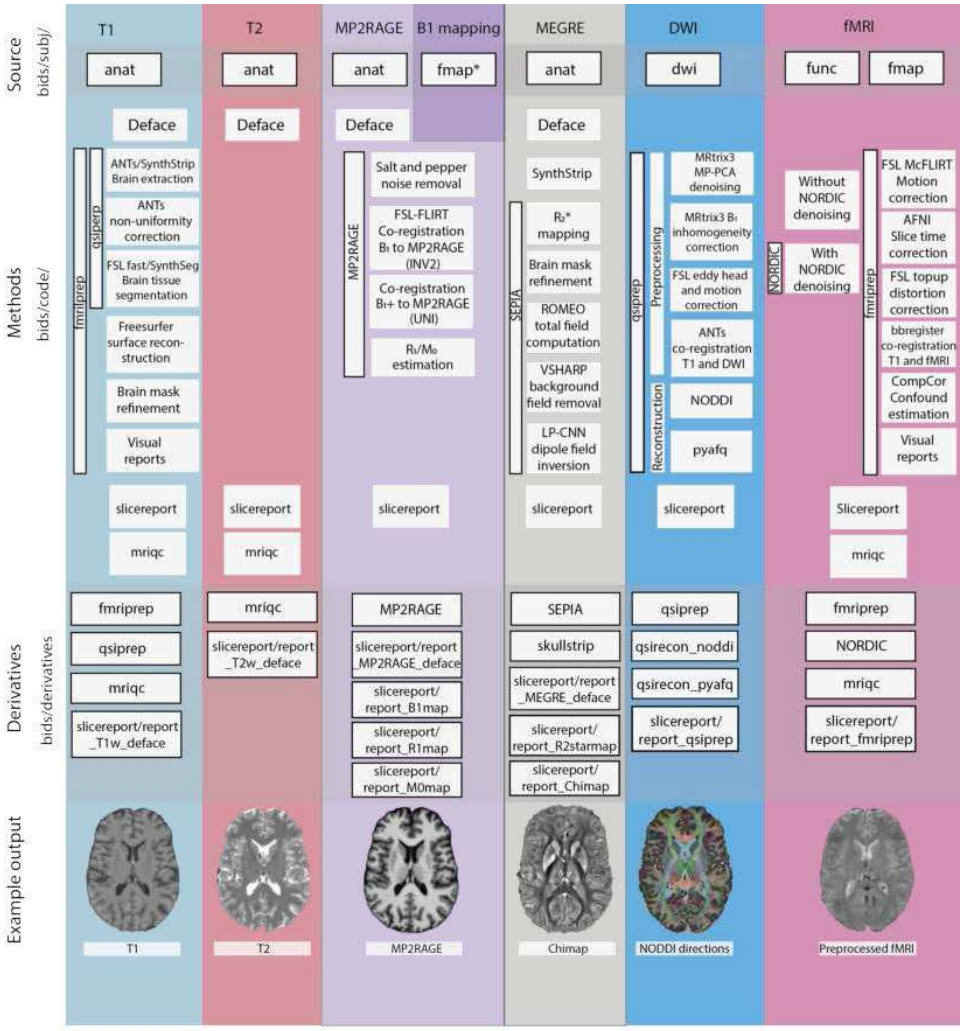

Figure 1. Schematic presentation of the diverse methodological steps applied to each imaging modality, and corresponding Brain Imaging Data Structure (BIDS) folders. Each coloured column indicates a different imaging modality. Each row represents a specific methodological step (e.g., fMRIprep) with corresponding sub-steps (e.g., brain extraction). BIDS folders are denoted with black frames. The process starts with the source data (e.g., bids/subj/anat/ folder) and progresses to the derivatives (e.g., bids/derivatives/fmriprep/ folder). Example outputs are displayed at the bottom. All code utilized can be found in the bids/code folder. Note that a certain imaging modality may be processed by multiple methods (e.g., T1 images with both fMRIprep and QSIprep).
*fmap is available under bids/subj/derivatives/SIEMENS/.

Results: ABRIM data is released through the Radboud Data Repository (https://data.ru.nl/). The ABRIM MRI collection consists of both the raw and pre-processed structural and functional MRI data in BIDS format, as well as corresponding scripts, to facilitate data usage among both expert and non-expert users. Basic demographics (e.g., age, sex) are also included. The ABRIM behavioural collection includes the detailed demographics (e.g., general health), outcomes of all neuropsychological tests, self-reported questionnaires and actigraphy data. While the ABRIM MRI collection is estimated to be released in November 2023 (https://doi.org/10.34973/7q0a-vj19), the behavioural collection will be released in November 2028. Data access is available for registered users (Data use agreement for identifiable human data – scientific use).

Conclusions: ABRIM provides a cross-sectional database on healthy participants throughout the adult lifespan, including an extensive characterization of both the brain as well as cognitive and behavioural characteristics. With ABRIM, we hope to further facilitate research into the underlying mechanisms of healthy cognitive ageing.

References

1. Chan K.S., Marques J.P. (2021), 'SEPIA-Susceptibility mapping pipeline tool for phase images.' NeuroImage, vol 227, pp. 117611.
2. Cieslak M., Cook P.A., He X., Yeh F.C., Dhollander T., Adebimpe A., et al. (2021), 'QSIPrep: an integrative platform for preprocessing and reconstructing diffusion MRI data.' Nature Methods, vol 18, no. 7, pp. 775-778.
3. Esteban O., Birman D., Schaer M., Koyejo O.O, Poldrack R.A., Gorgolewski K.J. (2017), 'MRIQC: Advancing the automatic prediction of image quality in MRI from unseen sites. PLoS One, vol 12, no. 9, pp. e0184661.
4. Esteban O., Markiewicz C.J., Blair R.W., Moodie C.A., Isik A.I., Erramuzpe A., et al. (2019), 'fMRIPrep: a robust preprocessing pipeline for functional MRI.' Nature Methods, vol 16, no. 1, pp. 111-116.
5. Moeller S., Pisharady P.K., Ramanna S., Lenglet C., Wu X., Dowdle L., et al. (2021), 'NOise reduction with DIstribution Corrected (NORDIC) PCA in dMRI with complex-valued parameter-free locally low-rank processing.' NeuroImage, vol 226, pp. 117539.
6. Zwiers M.P, Moia S., Oostenveld R. (2022), 'BIDScoin: A User-Friendly Application to Convert Source Data to Brain Imaging Data Structure'. Frontiers Neuroinformatics, vol 15, pp. 770608.

This page left intentionally blank

Poster No 2401

Multimodal thalamic features explain the different outcomes in tinnitus patients after sound therapy

Qian Chen[1], Yan Huang[1], Lining Dong[1], Zhenchang Wang[1]

[1]Beijing Friendship Hospital, Capital Medical University, Beijing, Beijing

Introduction: As the vital station to transform and integrate sensory afferent signals, the thalamus is crucial in tinnitus generation. The contributions of different thalamic subregions to tinnitus and its secondary dysfunction and the underlying mechanisms are undetermined. This study aimed to investigated thalamic structural and functional alterations using multimodal MRI and examined its clinical relevance in tinnitus patients with different outcomes after sound therapy.

Methods: In total, 60 patients with persistent tinnitus and 57 healthy controls (HCs) were recruited. Based on treatment efficacy, 28 patients were categorized into the effective group and 32 into the ineffective group. Five MRI measurements of the thalamus and its seven subregions, including gray matter volume, fractional anisotropy, fractional amplitude of low-frequency fluctuation, and functional connectivity (FC), were obtained for each participant and compared between the groups.

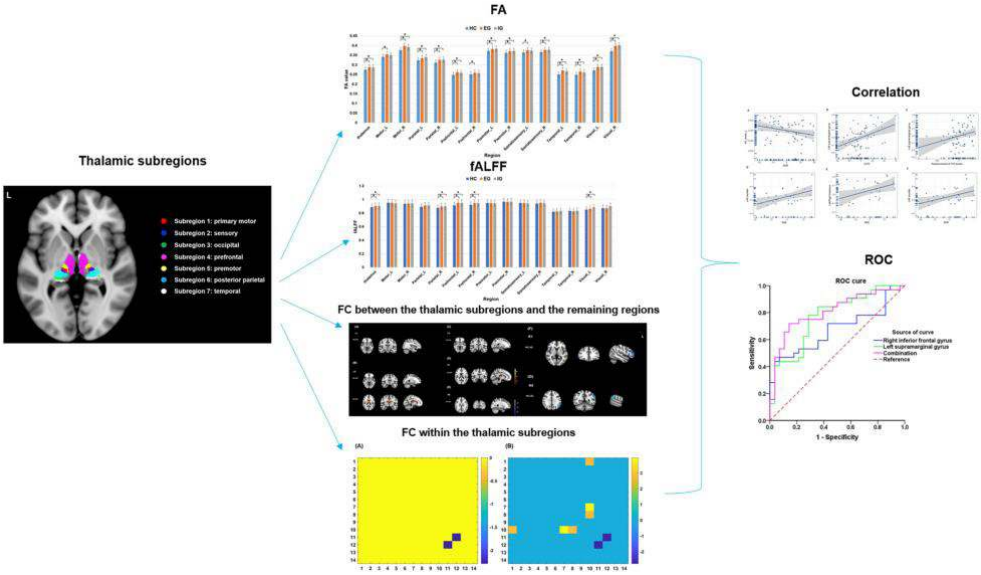

Fig. The whole analysis method of this study.

Results: Patients in both the groups exhibited widespread functional and diffusion abnormalities in the whole thalamus and several subregions, with more obvious changes observed in the effective group. All tinnitus patients had abnormal FC compared with the HCs; FC differences between the two patient groups were only observed in the striatal network, auditory-related cortex, and the core area of the limbic system. We combined the multimodal quantitative thalamic alterations and used it as an imaging indicator to evaluate prognosis before sound therapy and achieved a sensitivity of 71.9% and a specificity of 85.7%.

Conclusions: Similar patterns of thalamic alterations were identified in tinnitus patients with different outcomes, with more obvious changes observed in the effective group. Our findings support the tinnitus generation hypothesis of frontostriatal gating system dysfunction. A combination of multimodal quantitative thalamic properties may be used as indicators to predict tinnitus prognosis before sound therapy.

References

1. Lewis S, Chowdhury E, Stockdale D, Kennedy V. Assessment and management of tinnitus: summary of NICE guidance. BMJ. 2020 2020-03-31;368:m976.
2. Sereda M, Xia J, El Refaie A, Hall DA, Hoare DJ. Sound therapy (using amplification devices and/or sound generators) for tinnitus. The Cochrane database of systematic reviews. 2018 2018-01-01;12(12):D13094.
3. Chen Q, Lv H, Wang Z, Wei X, Liu J, Zhao P, et al. Pretreatment intranetwork connectivity can predict the outcomes in idiopathic tinnitus patients treated with sound therapy. HUM BRAIN MAPP. 2021 2021-07-07;42(14):4762-76.
4. Chen Q, Lv H, Wang Z, Wei X, Zhao P, Yang Z, et al. Outcomes at 6 months are related to brain structural and white matter microstructural reorganization in idiopathic tinnitus patients treated with sound therapy. HUM BRAIN MAPP. 2021 2021-02-15;42(3):753-65.
5. Ryu C, Park MS, Byun JY, Jahng G, Park S. White matter integrity associated with clinical symptoms in tinnitus patients: A tract-based spatial statistics study. EUR RADIOL. 2016;26(7):2223-32.

Poster No 2402

Whole-brain metabolic-effective coupling in healthy controls and its disruption in gliomas

Giulia Vallini[1], Giorgia Baron[1], Giulia Pagnin[1], John Lee[2], Andrei Vlassenko[2], Manu Goyal[2], Diego Cecchin[3], Maurizio Corbetta[4], Alessandra Bertoldo[3]

[1]University of Padua, Padua, Italy, [2]Neuroimaging Laboratories at the Mallinckrodt Institute of Radiology, St Louis, MO, [3]Padova Neuroscience Center, Padua, Italy, [4]Clinica Neurologica, Department of Neuroscience, University of Padova, Padova, Italy, Padova, Padova

Introduction: Glucose stands as the primary fuel source driving the energy-demanding process of neuronal activity. Glucose metabolism can be explored in vivo in human by [18F]FDG PET. DCM-based effective connectivity (EC) provides a linear mechanistic view of brain dynamics by conceiving it as a mixture of dissipative and solenoidal flow speaking to the concept of kinetic energy (Benozzo et al. 2023). This study aims to explore the association between kinetic energy and glucose metabolism by comparing EC-derived functional flow patterns with FDG PET measurements in healthy controls (HCs), finally investigating the disruption of this coupling in glioma patients.

Methods: The rsfMRI data of 42 HCs are fully described in (Volpi et al. 2022), while rsfMRI data of 43 patients are outlined in (Silvestri et al. 2022). EC matrices, estimated through sparse DCM (Prando et al. 2020), are decomposed into Σ-1 (partial correlation of the neuronal states) and S (differential cross-covariance, expressing the temporal directionality of neural activation) as in (Benozzo et al. 2023). From dynamic PET data (60-min acquisitions for both datasets), individual Metabolic Connectivity (MC) matrices, expressing the relationships between the metabolic states of different brain regions, are estimated according to (Volpi et al. 2022). Standardized Uptake Value Ratio (SUVR) is derived from static PET (sum of late frames 40-60 min) using whole-brain uptake for HCs (Byrnes et al. 2014) and ipsilateral cerebellum white matter for patients (Nozawa et al. 2015) as reference. We employ a clustered version of 100-area Yan Homotopic atlas (74 nodes, 7 RSNs) (Yan et al. 2023) plus 12 subcortical AAL3 ROIs (Rolls et al. 2020). Partial Least Square Correlation (PLSC) is applied to HC pairs: Σ-1-MC, S-MC (upper triangular matrices), SUVR-Σ-1 and SUVR-S (nodal strengths for Σ-1 and S, ROI values for SUVR). Generalizability of multivariate correlations were cross-validated using a 7-fold procedure. For each generalizable effective-metabolic pair, the regression line between the scores was identified, defining a normality band at the 90-percentile of the HC distances from the line. Finally, patients' metabolic and effective variables are projected onto the maximizing-covariance latent space identified in HCs. A tumor frequency map was obtained by combining tumor masks as weighted by the corresponding distance from the HC regression line (out-of-range patients only). Analysis workflow in Fig. 1.

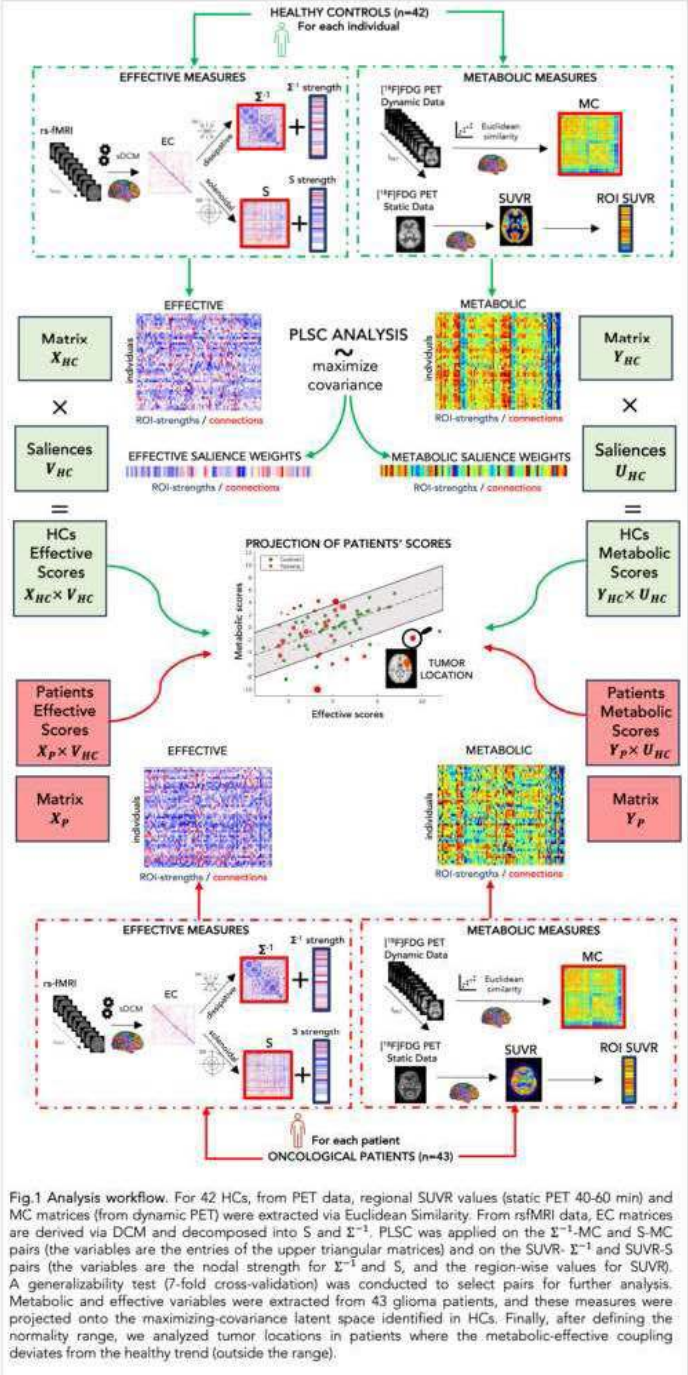

Fig.1 Analysis workflow. For 42 HCs, from PET data, regional SUVR values (static PET 40-60 min) and MC matrices (from dynamic PET) were extracted via Euclidean Similarity. From rsfMRI data, EC matrices are derived via DCM and decomposed into S and Σ^{-1}. PLSC was applied on the Σ^{-1}-MC and S-MC pairs (the variables are the entries of the upper triangular matrices) and on the SUVR- Σ^{-1} and SUVR-S pairs (the variables are the nodal strength for Σ^{-1} and S, and the region-wise values for SUVR). A generalizability test (7-fold cross-validation) was conducted to select pairs for further analysis. Metabolic and effective variables were extracted from 43 glioma patients, and these measures were projected onto the maximizing-covariance latent space identified in HCs. Finally, after defining the normality range, we analyzed tumor locations in patients where the metabolic-effective coupling deviates from the healthy trend (outside the range).

Results: Cross-validation reveals good generalizability for Σ-1-MC and SUVR-S associations (Pearson's r>0.76). The scatterplots between metabolic and effective scores for HCs and patient projections are in Fig. 2B. In both pairs, some patients notably diverge from the expected metabolic-effective coupling independently of tumor volume. As shown in Fig. 2C, SUVR-S pair is mostly altered for temporo-parietal tumors, while Σ-1-MC is mainly disrupted in patients with frontal lesions.

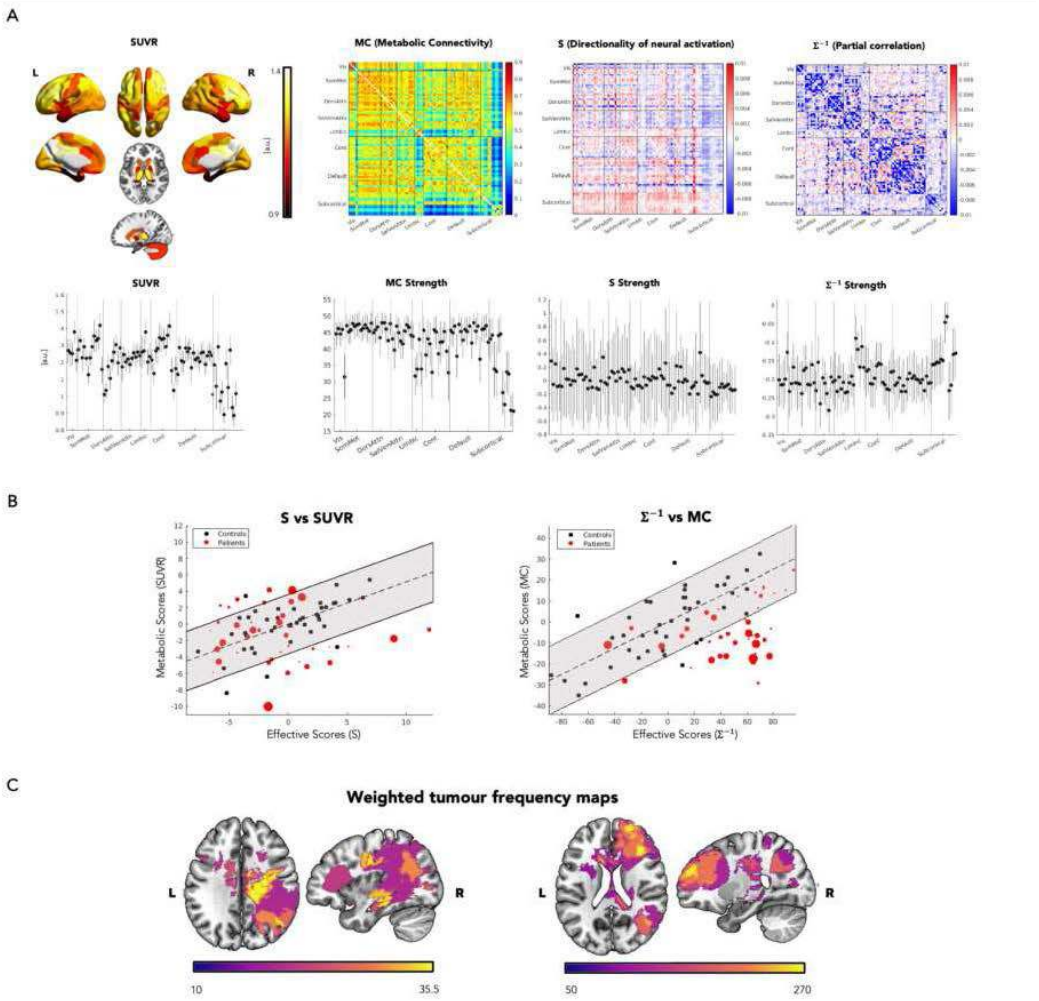

Fig. 2 (Fig. 2A) Region-wise SUVR values, Metabolic Connectivity, S and Σ^{-1} matrices averaged across individuals, with respective nodal strength values. (Fig. 2B) Scatterplots of the metabolic and effective scores of the HCs in black, and the projection of the patients' scores in red, with marker size proportional to tumour volume. In grey the normality band. (Fig. 2C) Tumour frequency maps (out-of-range patients only), where each tumour map was weighted according to the distance of the patient from the regression line. Σ^{-1}-MC pair on the right, S-SUVR pair on the left.

Conclusions: A dual metabolic-effective association emerges: one at local level (glucose uptake-node directionality) and one at network level (metabolic connectivity-partial correlation). Furthermore, our study unveils how these two distinct decoupling can differentiate patients based on the lesion location (and not its volume)-local disruption observed only for temporo-parietal lesions and network alterations for frontal lesions-providing novel insights into the physiopathology and the metabolic-kinetic link of glioma. While (Maleki Balajoo et al. 2022) already explored distinguishing pathologies (Alzheimer and Mild Cognitive Impairment) based on metabolism-function (FC metrics) coupling, our study is a pioneer in gliomas and the introduction of EC measures allows both to link metabolism to the concept of kinetic energy, but also to decouple neuronal activity from the adverse effects of hemodynamic convolution, proposing metabolic-effective coupling as a new biomarker.

References

1. Benozzo, Danilo, Giacomo Baggio, Giorgia Baron, Alessandro Chiuso, and Alessandra Bertoldo. 2023. "Analyzing Asymmetry in Brain Hierarchies with a Linear State-Space Model of Resting-State FMRI Data." https://doi.org/https://doi.org/10.1101/2023.11.04.565625.
2. Byrnes, Kimberly R., Colin M. Wilson, Fiona Brabazon, Ramona Von Leden, Jennifer S. Jurgens, Terrence R. Oakes, and Reed G. Selwyn. 2014. "FDG-PET Imaging in Mild Traumatic Brain Injury: A Critical Review." Frontiers in Neuroenergetics 6 (JAN).
3. Maleki Balajoo, Somayeh, Farzaneh Rahmani, Reza Khosrowabadi, Chun Meng, Simon B. Eickhoff, Timo Grimmer, Mojtaba Zarei, Alexander Drzezga, Christian Sorg, and Masoud Tahmasian. 2022. "Decoupling of Regional Neural Activity and Inter-Regional Functional Connectivity in Alzheimer's Disease: A Simultaneous PET/MR Study." European Journal of Nuclear Medicine and Molecular Imaging 49 (9): 3173–85.
4. Nozawa, Asae, Ali Hosseini Rivandi, Masayuki Kanematsu, Hiroaki Hoshi, David Piccioni, Santosh Kesari, and Carl K. Hoh. 2015. "Glucose-Corrected Standardized Uptake Value in the Differentiation of High-Grade Glioma versus Post-Treatment Changes." Nuclear Medicine Communications 36 (6): 573–81.
5. Prando, Giulia, Mattia Zorzi, Alessandra Bertoldo, Maurizio Corbetta, Marco Zorzi, and Alessandro Chiuso. 2020. "Sparse DCM for Whole-Brain Effective Connectivity from Resting-State FMRI Data." NeuroImage 208 (December 2019): 116367.

6. Rolls, Edmund T., Chu Chung Huang, Ching Po Lin, Jianfeng Feng, and Marc Joliot. 2020. “Automated Anatomical Labelling Atlas 3.” NeuroImage 206 (August 2019): 116189.
7. Silvestri, Erica, Manuela Moretto, Silvia Facchini, Marco Castellaro, Mariagiulia Anglani, Elena Monai, Domenico D’Avella, et al. 2022. “Widespread Cortical Functional Disconnection in Gliomas: An Individual Network Mapping Approach.” Brain Communications 4 (2): 1–14.
8. Volpi, Tommaso, Giulia Vallini, Erica Silvestri, Mattia De Francisci, Tony Durbin, Maurizio Corbetta, John J Lee, et al. 2022. “A New Framework for Metabolic Connectivity Mapping Using Bolus [18 F]FDG PET and Kinetic Modelling.” Journal of Cerebral Blood Flow and Metabolism, 1–21.
9. Yan, Xiaoxuan, Ru Kong, Aihuiping Xue, Qing Yang, Csaba Orban, Lijun An, Avram J. Holmes, et al. 2023. “Homotopic Local-Global Parcellation of the Human Cerebral Cortex from Resting-State Functional Connectivity.” NeuroImage 273 (October 2022): 120010.

Poster No 2403

Molecular basis underlying functional connectivity of premotor cortex subregions

Qian Wang[1], Zhang Yu[2], Jinfeng Hou[1], Shengfeng Liu[3], Tianzi Jiang[3], Lingzhong Fan[3], Luqi Cheng[1,2]

[1]School of Life and Environmental Sciences, Guilin University of Electronic Technology, Guilin, China, [2]Research Center for Augmented Intelligence, Zhejiang Lab, Hangzhou, China, [3]Brainnetome Center, Institute of Automation, Chinese Academy of Sciences, Beijing, China

Introduction: The premotor cortex (PM) is a cortical region within the frontal agranular cortex[1] that regulates motor and cognitive functions[2]. The functional diversity of the PM implies that it has functionally distinct subregions. Here, we identified the subdivisions of the PM based on structural connectivity and explored the corresponding behavioral domains and genetic association.

Methods: 40 right-handed healthy adults, including T1w images, diffusion-weighted images and resting-state functional MRI images were randomly selected from the Human Connectome Project (HCP)[3] database. The images had been preprocessed following the HCP’s minimal preprocessing pipeline[4]. The ROI of the PM was derived from HCP-MMP1.0[5] including regions of FEF, PEF, 55b, 6d, 6v, 6r, and 6a. Connectivity-based parcellation scheme[6] was used to identify the subregions of the PM. The appropriate cluster number was determined by evaluating the consistency of parcellation between subjects using the silhouette index. Functional decoding was conducted based on the Neurosynth database. Brain gene expression data were obtained from the AHBA dataset[7]. We obtained normalized expression data of 5013 genes for 1298 tissue samples. Cross-sample Pearson correlations between gene expression and rsFC were performed in a gene-wise manner, yielding 5013 correlation coefficients for each subject. Next, genes with significant correlations (using FDR-BH) in more than 90% of subjects were used for functional enrichment analyses with the Metascape portal[8] to characterize the biological functions and diseases of the rsFC-related gene sets.

Results: The PM could be subdivided into six subregions as the silhouette index showed the highest values in the six-cluster solution with the exception of the two-cluster solution (Fig1B). Three clusters were located in the dorsal part and three clusters in the ventral part(Fig1A). Meta-analysis showed that dorsal regions were mainly associated with movement and ventral regions were mainly associated with visual attention and linguistics. Particularly, the C1 of dorsal part was more associated with working memory, the C2 of dorsal part was more associated with visual and spatial motion while the C6 in left ventral part was more associated with language-related functions (Fig1C). For the functional enrichment, expression measures of 618, 2565, 2605, 2455, 1783 genes were associated with rsFC of the C2-C6, respectively, whereas no significant rsFC-related genes were found in the C1. In dorsal part, the rsFC-related genes of the C2 were especially enriched in adrenaline, and the C3 showed extra enrichment in Neuroinflammation and glutamatergic signaling pathway. RsFC-related genes of the ventral C4-C6 were primarily enriched for neurotransmitter pathways, with the C5 more related to hormone response and the C6 more related to muscle contraction (Fig2A). As for diseases, Absence Seizures was significantly enriched in the C2 of the dorsal part while Hypoxia, Subarachnoid Hemorrhage and Febrile Convulsions were enriched in the three ventral regions (Fig2B).

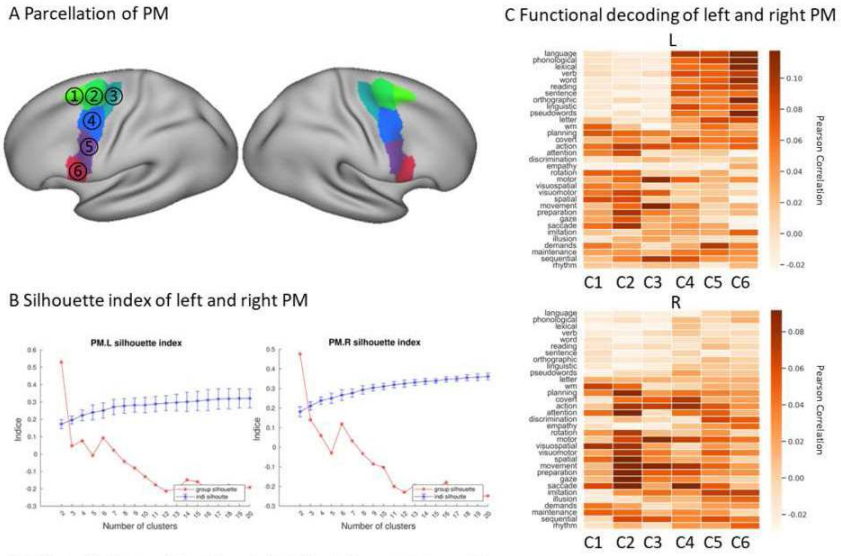

Fig1 Parcellation and functional decoding of premotor cortex

A Functional enrichment of the genes related to rsFC of PM subregions

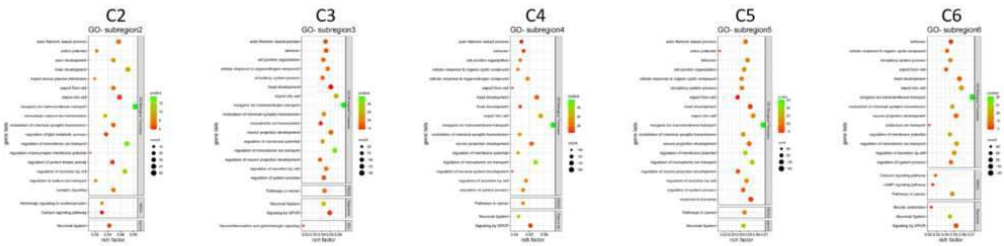

KEGG: KEGG Pathway; Reactome:Reactome Gene Sets; Wiki:WikiPathways

B Enriched disease expressions of the genes related to rsFC of PM subregions.

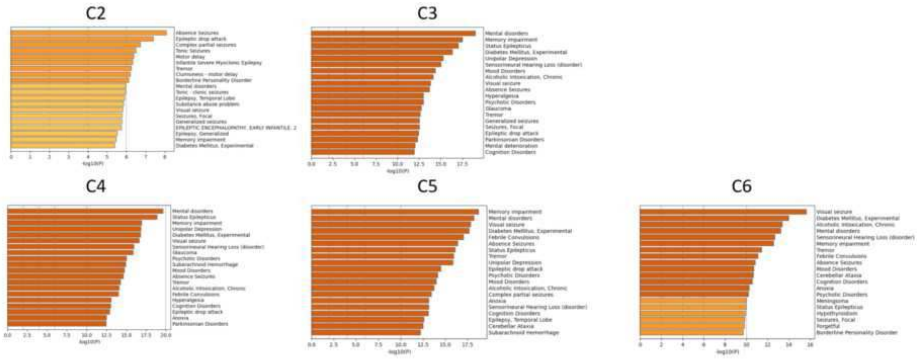

Fig2 Gene enrichment analysis of PM subregions

Conclusions: We demonstrated that the human PM can be subdivided into six distinct subregions based on their structural connectivity. Functional enrichment analyses suggested that rsFC of different PM subregions were modulated by their specific associated gene expression profiles. These findings may offer new insights into the molecular basis underlying the functional heterogeneity of the PM.

References

1. Wise SP.(1985), "The primate premotor cortex: past, present, and preparatory",Annu Rev Neurosci,vol.8,pp.1-19
2. Boussaoud D.(2001), "Attention versus intention in the primate premotor cortex", Neuroimage,vol.14,1 Pt 2,pp.40-45
3. Van Essen DC.(2013), "The WU-Minn Human Connectome Project: an overview",Neuroimage,vol.80,pp.62-79
4. Donahue CJ.(2018), "Quantitative assessment of prefrontal cortex in humans relative to nonhuman primates",Proc Natl Acad Sci U S A,vol.115,pp.E5183-E5192
5. Glasser MF.(2016), "A multi-modal parcellation of human cerebral cortex",Nature,vol.536,pp.171-178
6. Fan L.(2016), "The Human Brainnetome Atlas: A New Brain Atlas Based on Connectional Architecture",Cereb Cortex,vol.26,pp.3508-3526
7. Hawrylycz M.(2015), "Canonical genetic signatures of the adult human brain", Nat Neurosci,vol.18,pp.1832-1844
8. Zhou Y.(2019), "Metascape provides a biologist-oriented resource for the analysis of systems-level datasets",Nat Commun,vol.10,pp.1523

Poster No 2404

Impacts of Caffeine Consumption on Brain and CSF Dynamics: An EEG-fMRI Study

Lina Alqam[1], Kadir Yildirim[1], Kübra Eren[1], Belal Tavashi[1], Elif Can[1], Cem Karakuzu[1], Alp Dincer[2], Pinar S Ozbay[1]

[1]Bogazici University, Istanbul, Turkey, [2]Acibadem University, Istanbul, Turkey

Introduction: This study seeks to explore the relations between caffeine intake, brain activity, cerebrospinal fluid (CSF) flow during rest and alert conditions. We analyzed the correlations among specific brain regions, CSF flow patterns and EEG power in individuals post-caffeine consumption, emphasizing caffeine's impact on these neural and autonomic processes. Through these objectives, we aim to enhance our understanding of the complex relationship between caffeine, brain function, and physiological dynamics.

Methods: Resting state fMRI data were obtained at 3 T scanner with GRE-EPI (FA = 90, TR = 3 s, TE = 36 ms, in-place resolution = 2.5mm, number of TRs = 135). Cognitive task was elicited by an arithmetic task requiring solving an equation with one unknown. Problems were displayed against a gray background with a fixation dot. The experiment consisted of three blocks; each block began with a 45-second period of initial rest. This was followed by a 9-second mental arithmetic task, where a two-digit equation appeared. Afterward, there was a 36-second period of rest and focus on a fixation point, followed by a different mental task and another period of rest. EEG data was collected simultaneously with 32 channel head coil (Brain Products). 5 subjects were included in the analyses, 3 of which underwent simultaneous EEG-fMRI acquisition. Repeated scans were performed following immediate intake of caffeine pills, first scan 10 minutes second scan 30 minutes following intake. The subjects were not informed if the pill was caffeine or placebo. Preprocessing of fMRI data followed the suggested 'afni_proc' pipeline (AFNI (1)), including removal of signal drifts, slice-timing correction, realignment of consecutive volumes, registration to MNI template, smoothing (3 mm FWHM), and regression of motion parameters. Brain Products Analyzer's template approach was used to eliminate the MRI gradient and cardioballistic artifacts in the contaminated EEG data. This method required using average artifact subtraction (AAS)[3]. The EEG data was subjected to a band-pass filter with a frequency range of 0.5-35 Hz after applying ICA, and Fz was used as a reference channel. To investigate lag dependent correlations, we used various regions of interest and calculated cross-correlations 1) among themselves, 2) with CSF signal (4th ventricle), and 3) EEG alpha and beta power. We also performed connectivity analysis based on positive and negative peaks in cross-correlations.

Results: After caffeine intake, our study observed an increase in positive lag correlation between the 4th ventricle and the DMN regions, indicating a delay in CSF signal. We noted a general increase in positive peaks for correlations between resting state scans. Persistent negative correlation between CSF and ROIs, potentially linked to drowsiness. Arithmetic task shows an increased positive lag correlation at 0 lag between IPS and ACC, which are known for visual attention and awareness, suggesting a synchronization between these mechanisms. An increased correlation (Fig. 1) at 0 lag between CSF and EEG alpha and low beta powers, which may be related to increased CSF flow due to sympathetic activity after caffeine. EEG rest analysis indicated a reduced alpha power after caffeine intake while task analysis showed a rise in beta power following the caffeine specifically in the occipital and parietal electrodes. Subjects showed a decreased alpha band brainwave activity, signifying heightened alertness during the second resting session. Beta band, on the contrary, was enhanced by caffeine during the second arithmetic exercise suggesting higher level of cognitive processing (Fig. 2).

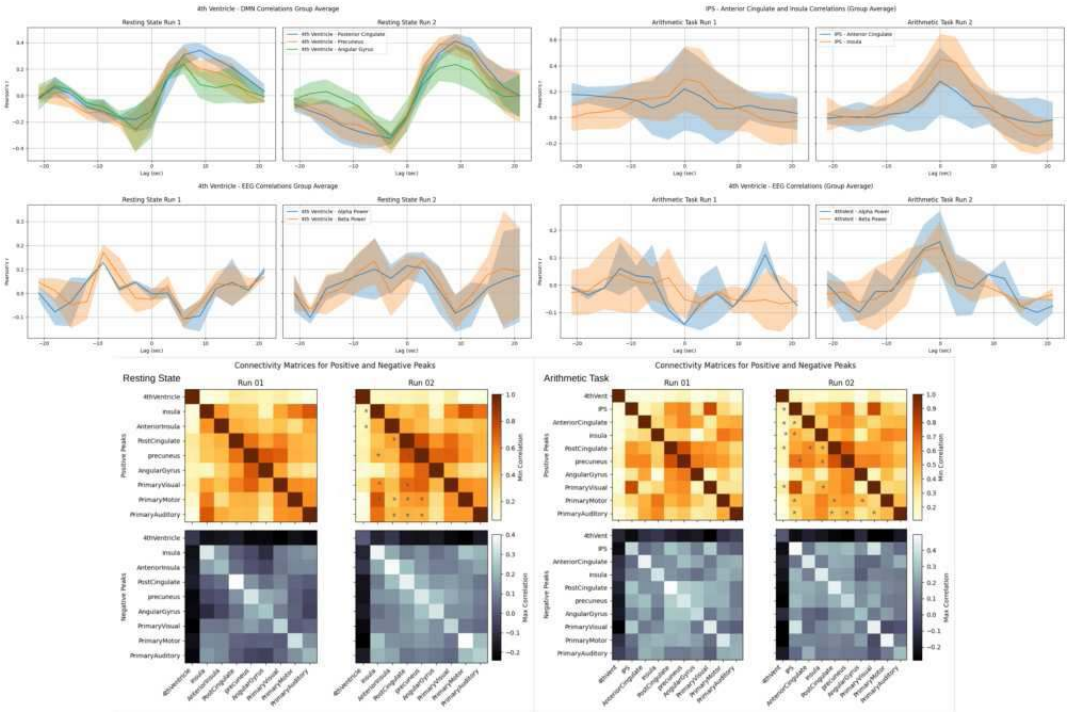

Fig. 1: Left: Resting state, Right: Arith task, (top row) Correlations between various ROIs (N=5), (middle row) Correlations between CSF and EEG powers (N=3), (bottom row) Connectivity matrices

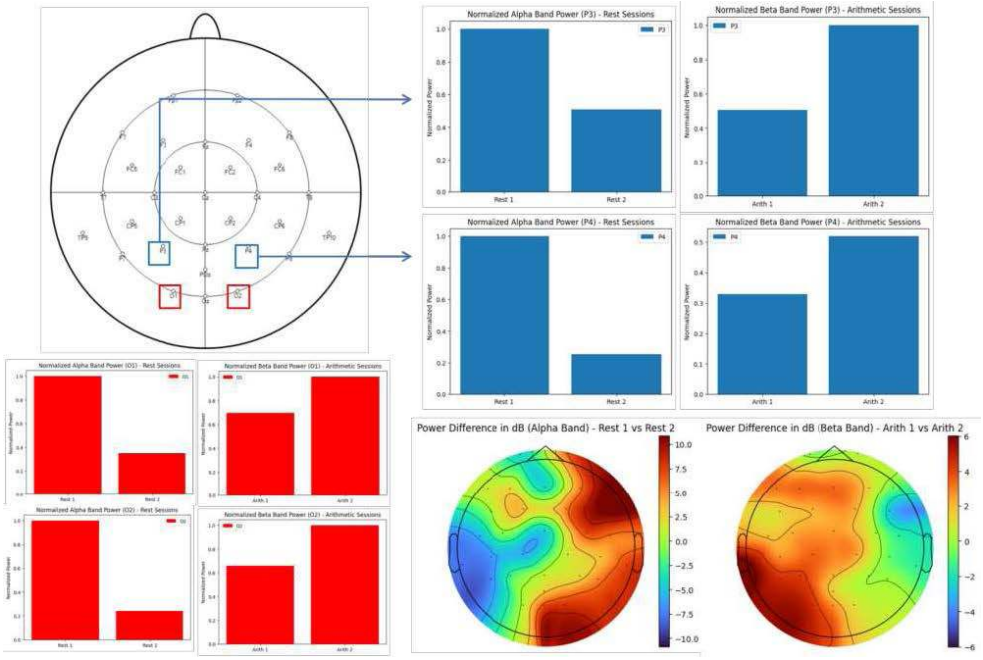

Fig. 2: (Left): EEG electrodes, (top right), (bottom left): Normalized alpha and beta powers across two different sessions, (bottom right): power difference in dB in both alpha and beta bands.

Conclusions: Our results suggest that caffeine influences the behavior of alpha and beta power difference in both mental arithmetic task and rest sessions. An increased connectivity for positive lag in regions of interest is also shown for both of these sessions, while the negative lag showed a decrease in only resting state scans.

References

1. Cox RW, Computers and biomedical research, 1996.
2. Birn RM et al. Neuroimage, 2006
3. Allen, P. J. et al., NeuroImage 2000
4. Ozbay P et al., Neuroimage, 2019
5. Picchioni D et al., Neuroimage, 2020

Poster No 2405

Hormones inside the early adolescent female brain: a multimodality brain MRI study

Muskan Khetan[1], Ye Tian[2], Nandita vijayakumar[3], Sarah Whittle[4]

[1]University of Melbourne, Melbourne, VIC, [2]University of Melbourne, Melbourne, Victoria, [3]Deakin university, Melbourne, Victoria, [4]University of Melbourne, Melbourne, Victoria

Introduction: During adolescence, about one-third of young people are diagnosed with internalizing disorders like depression and anxiety, with these disorders being more common in females than males. The sex difference in incidence rates may be related to pubertal factors, such as the influence of pubertal hormones on brain development. While some studies have examined the association between pubertal hormone levels and brain structure in adolescents, more research is needed to test associations between these hormone levels and both brain structure and function in adolescents, particularly during early adolescence when hormone levels begin to surge.

Methods: We used the Adolescent Brain Cognitive Development (ABCD) study baseline and second follow-up datasets (age 9-12 years) for female participants (N ~ 2204). Then, using elastic-net regression, we investigated the associations between pubertal hormone levels (oestradiol (E2), testosterone, Dehydroepiandrosterone (DHEA)) and brain structure (gray matter volumes, sulcal depth, cortical thickness and white matter microstructure) and function (resting-state connectivity, emotional n-back task-related function). Structure and function data were extracted from all regions across the whole brain (using the FreeSurfer Destrieux parcellation) and white matter tracts (using AtlasTrack). For analysis (Figure 1), data was randomly partitioned into training and test data. Then, using the MATLAB package GLMnet, a ten-fold, cross-validated elastic-net regression was applied to the training set for feature selection for each modality separately. From each modality, selected features that explained variance in hormones in the test data were included for further analysis. Next, within 10- iterations all significant features from each modality were modeled together in the same multi-modality model. The average r-square (R2) and correlation (r) for the fitted model were computed. To focus on the most important features, we interpreted only the top 20% fitted features.

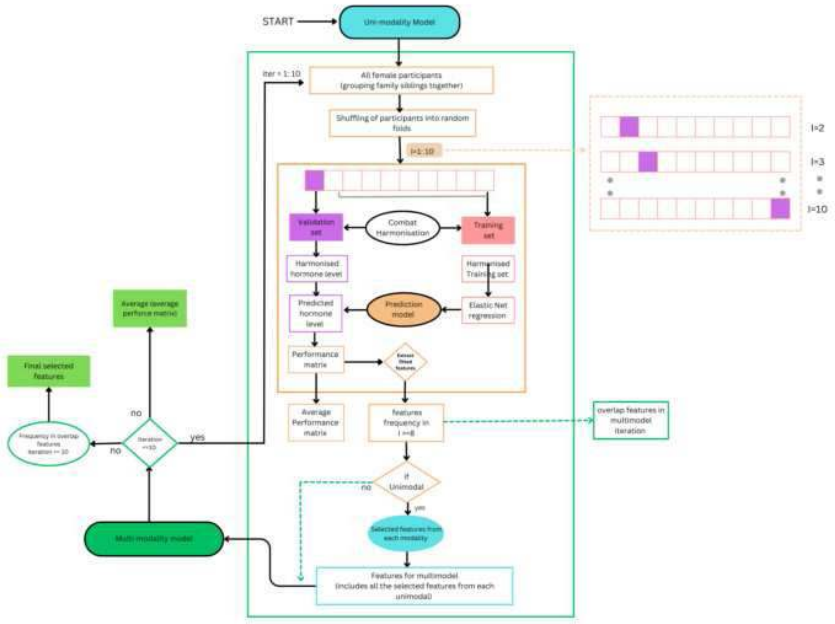

Results: In the multi-modality analysis, R2 and r values were 0.025 and 0.14 (E2), 0.18 and 0.46 (testosterone), and 0.036 and 0.32 (DHEA). From structural and functional features, we found that structural features, especially cortical thickness and sulcal depth, in addition to resting state functional connectivity, were among the most important features for all three hormones. The structure of frontal cortical regions (particularly middle frontal and subcallosal cortices) were negatively associated with E2, while parietal and temporal cortical structural properties were positively associated with testosterone and DHEA. Subcortical volumes were positively associated with testosterone (e.g., hippocampus) and DHEA (e.g., amygdala). In addition, resting-state connectivity between subcortical regions (such as thalamus or caudate) and cortical networks (such as default mode networks or fronto-parietal network) explained more variance in the hormones as compared to inter and intra cortical networks.

Conclusions: Associations between E2 and frontal structure, and testosterone and DHEA and temporal, parietal and subcortical regions, suggests a differential role of pubertal hormones in the development of brain regions underlying social, cognitive and emotional processes. The involvement of connectivity between subcortical regions and cortical networks further indicates the contribution of these hormones in organising cognitive and emotional brain networks. These findings are similar to studies that reported alterations in these brain regions in individuals with internalising symptoms. Thus, our findings indicate that more research is needed to understand the functional and behavioural implications of these hormone-brain associations.

References

1. L. Schmaal, D.J. (2016). Subcortical brain alterations in major depressive disorder: Findings from the ENIGMA Major Depressive Disorder working group. Mol. Psychiatry, 21, pp. 806-812
2. J.A. Silvers. (2017). vlPFC–vmPFC–amygdala interactions underlie age-related differences in cognitive regulation of emotion. Cereb. cortex, 27 (7), pp. 3502-3514
3. McLean, C. P. (2009). Brave men and timid women? A review of the gender differences in fear and anxiety. Clinical psychology review, 29(6), 496-505.
4. M.M. Herting.(2014). The role of testosterone and oestradiol in brain volume changes across adolescence: a longitudinal structural MRI study. Hum. Brain Mapp., 35 (11), pp. 5633-5645
5. Orlhac F (2022). A Guide to ComBat Harmonization of Imaging Biomarkers in Multicenter Studies. J Nucl Med, 63(2):172-179
6. Peper, J. S.(2009). Cerebral white matter in early puberty is associated with luteinizing hormone concentrations. Psychoneuroendocrinology, 34(5), 705-711.
7. Yee-Ming Chan. (2019) Effects of the Timing of Sex-Steroid Exposure in Adolescence on Adult Health Outcomes, The Journal of Clinical Endocrinology & Metabolism, Volume 104, Issue 10, Pages 4578–4586.
8. Vijayakumar, N. (2019). Puberty and the human brain: Insights into adolescent development. Neuroscience and Biobehavioral Reviews, 92, 417-436.

Poster No 2406

Voxel-wise normative models for abnormality-driven contrast of microstructural MRI

Olivier Parent[1], Yohan Yee[2], Gabriel Devenyi[2], Aurélie Bussy[3], Grace Pigeau[3], Manuela Costantino[3], Jérémie Fouquet[1], Daniela Quesada-Rodriguez[3], Mahsa Dadar[3], Mallar Chakravarty[4]

[1]Douglas Mental Health University Institute, Montreal, QC, [2]McGill University, Montreal, Quebec, [3]McGill University, Montreal, QC, [4]Brain Imaging Centre, Douglas Research Centre, Montreal, Quebec

Introduction: Microstructural magnetic resonance imaging (MRI) can be used to measure brain tissue properties in vivo and has been used extensively in scientific research to derive biomarkers sensitive to disease pathology and progression, like normal-appearing white matter alterations in multiple sclerosis (MS)[1] and small vessel disease (SVD)[2] and iron accumulation in the subcortical grey matter in Parkinson's disease (PD)[3]. However, these biomarkers have been seldom implemented in clinical practice. We posit that this limited clinical translation is due, in part, to the difficult interpretability of raw microstructural maps to detect subtle pathological tissue alterations distinct from normal variations. For example, white matter deterioration and subcortical grey matter iron accumulation are both normal age-related phenomena[4,5]. Here, we constructed voxel-wise normative models of microstructural MRI and produced subject-wise z-scored maps of microstructural abnormality relative to these age- and sex-specific averages. These maps bring important context regarding normal brain tissue integrity and permit intuitive visual assessment of brain tissue abnormalities at first glance.

Methods: We used data from 32,935 UK Biobank (UKB) subjects (32,014 healthy subjects and 921 subjects with a neurological diagnosis). T1-weighted (T1w) and Fluid-Attenuated Inversion Recovery (FLAIR) were used to segment the brain into 9 broad regions (labels) using the Brain tISsue segmentatiON (BISON) pipeline[6] (Fig. 1A). Diffusion-weighted images were used to derive diffusion tensor imaging (DTI) and neurite orientation dispersion and density imaging (NODDI) microstructural metrics, while susceptibility-weighted images were used to derive T2* and quantitative susceptibility mapping (QSM) metrics (resampled at 2 mm isotropic to match the diffusion resolution)[7]. Multispectral registration to a custom unbiased UKB template[8] was performed using T1w and fractional anisotropy (FA) maps as inputs in order to align tissue boundaries and white matter fibers, respectively. In this common space, we calculated voxel-wise and region-specific normative models using Bayesian linear regression with sex and age modelled with 4th-order B-splines with the PCN toolkit[9], using only healthy subject data. Importantly, in voxels where different regions are present across subjects due to imperfect registration, different normative models were fitted (Fig. 1B). Normative models were only calculated when the label prevalence was higher than 100 subjects (Fig. 1C). This process resulted in region-, age-, and sex-specific atlases of microstructure, which are then used to z-score subject microstructural maps (Fig. 1D). Microstructural maps were denoised prior to the z-scoring process[10].

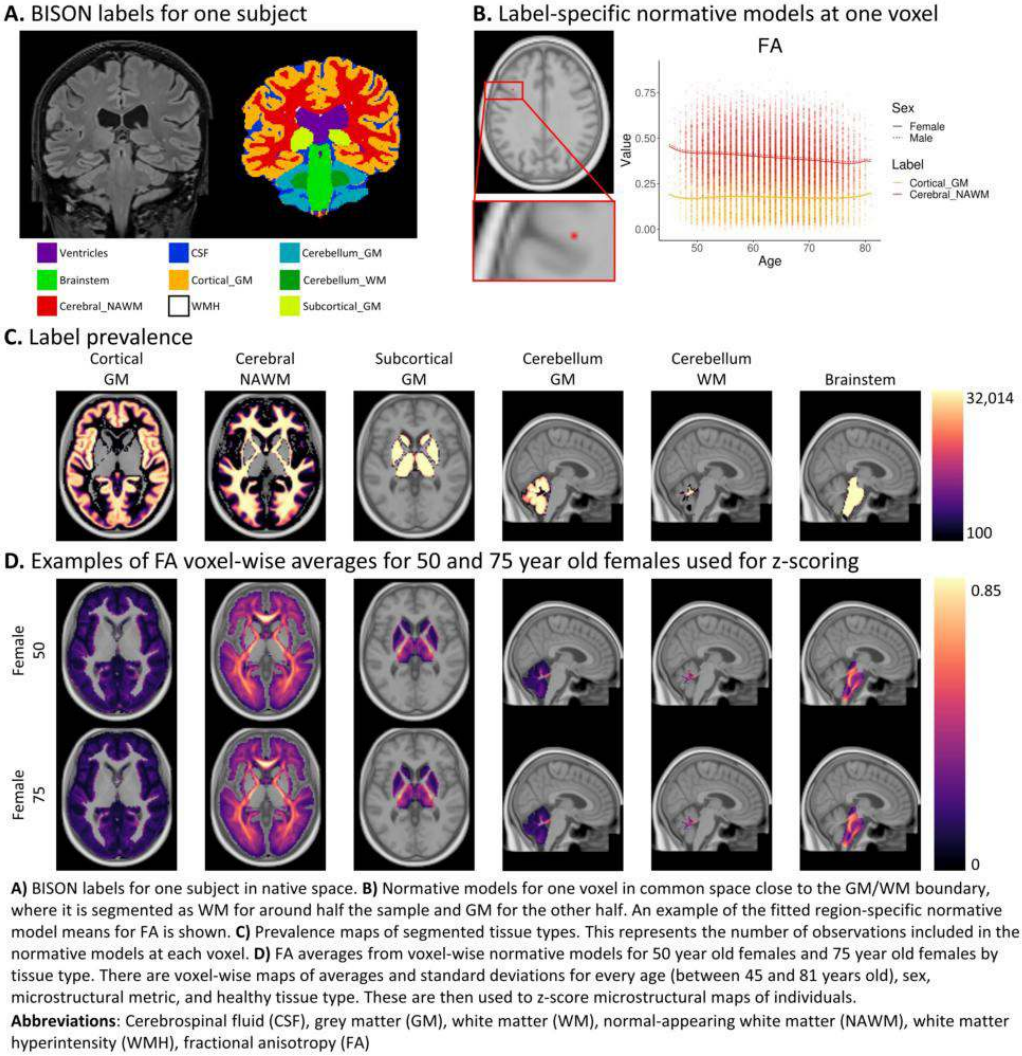

A) BISON labels for one subject in native space. **B)** Normative models for one voxel in common space close to the GM/WM boundary, where it is segmented as WM for around half the sample and GM for the other half. An example of the fitted region-specific normative model means for FA is shown. **C)** Prevalence maps of segmented tissue types. This represents the number of observations included in the normative models at each voxel. **D)** FA averages from voxel-wise normative models for 50 year old females and 75 year old females by tissue type. There are voxel-wise maps of averages and standard deviations for every age (between 45 and 81 years old), sex, microstructural metric, and healthy tissue type. These are then used to z-score microstructural maps of individuals.
Abbreviations: Cerebrospinal fluid (CSF), grey matter (GM), white matter (WM), normal-appearing white matter (NAWM), white matter hyperintensity (WMH), fractional anisotropy (FA)

Results: We present five case studies comparing raw and z-scored microstructural maps in common space (Fig. 2). Comparing two healthy subjects (Fig. 2A), the raw microstructural maps look highly similar (top rows) while z-scored maps reveal subvisible alterations in the white matter (bottom rows) for the second subject, potentially indicating SVD. Comparing two subjects with MS (Fig. 2B), z-scored maps reveal widespread microstructural alterations in white matter for the first subject, while being contained to lesions for the second subject. Lastly, z-scored maps for a subject with PD (Fig. 2C) reveal alterations in the subcortical grey matter, potentially indicating iron accumulation.

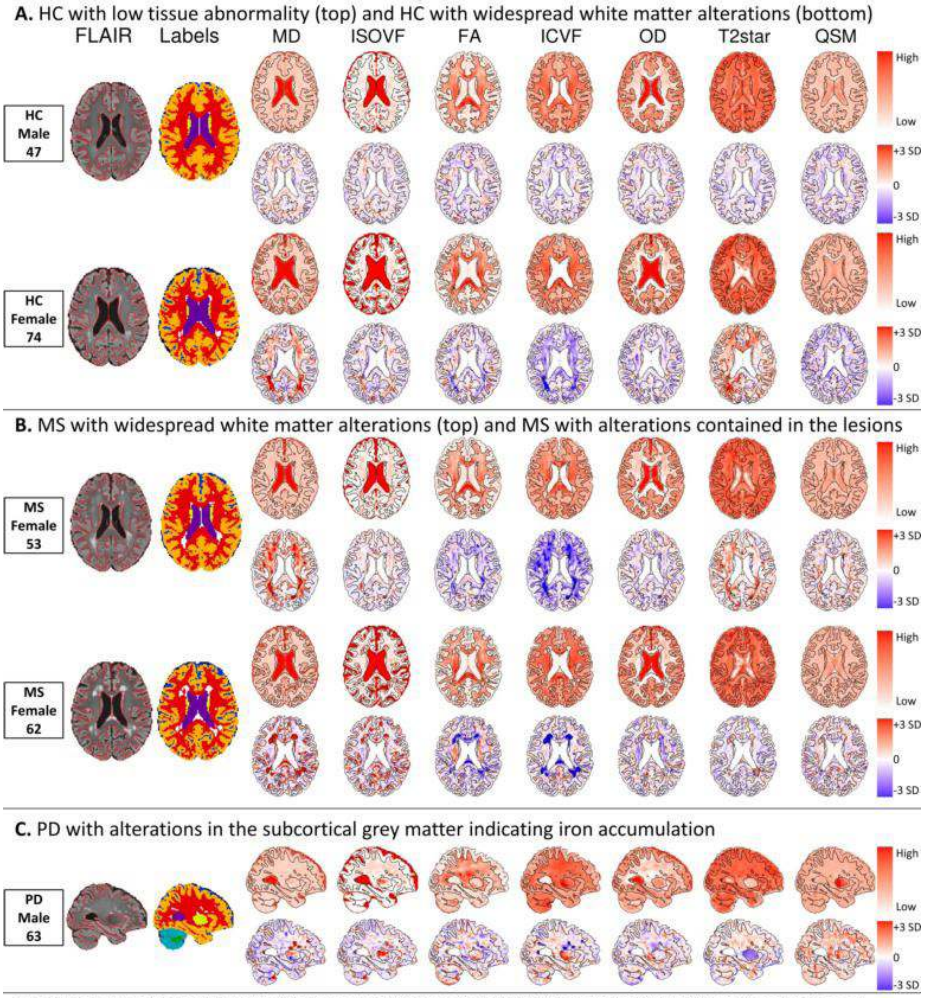

Single-subject raw and z-scored microstructural maps. The FLAIR image is shown with the contours of the UKB template regions to assess registration accuracy. BISON labels are shown to assess segmentation accuracy. Microstructural maps are shown with consistent color thresholds across subjects, with the black contours showing the subject region labels. **A)** Top: 47 year old male healthy control (HC) with low microstructural abnormality. Bottom: 74 year old female HC with posterior white matter hyperintensities and widespread sub-visible alterations in the white matter. **B)** Top: 53 year old female with multiple sclerosis (MS) with posterior lesions and widespread sub-visible alterations in the white matter. Bottom: 62 year old female with MS with alterations mostly restricted to the lesions. **C)** 63 year old male with Parkinson's disease (PD) with low T2* and high QSM in the sub-cortex indicating iron accumulation.

Abbreviations: FLAIR (fluid attenuated inversion recovery), MD (mean diffusivity), ISOVF (isotropic volume fraction), FA (fractional anisotropy), ICVF (intracellular volume fraction), OD (orientation dispersion), QSM (quantitative susceptibility mapping), HC (healthy control), MS (multiple sclerosis), PD (Parkinson's disease), SD (standard deviation)

Conclusions: Using normative models, we developed a visualization technique that simplifies tissue abnormality detection at the single-subject level. This technique permits a highly intuitive assessment of brain health and could help translate biomarker findings related to brain microstructure from research to clinical settings. Future work will focus on harmonization across sites and extending this principle to voxel-wise volumetric measurements.

References

1. West, J. (2014), 'Normal appearing and diffusely abnormal white matter in patients with multiple sclerosis assessed with quantitative MR', PLoS One, vol. 9, no. 4, pp. e95161
2. Muñoz-Maniega, S. (2015), 'White matter hyperintensities and normal-appearing white matter integrity in the aging brain', Neurobiology of Aging, vol. 36, no. 2, pp. 909–918
3. Biondetti, E. (2021), 'The spatiotemporal changes in dopamine, neuromelanin and iron characterizing Parkinson's disease', Brain, vol. 144, no. 10, pp. 3114–3125
4. Ward, R. J. (2014), 'The role of iron in brain ageing and neurodegenerative disorders', Lancet Neurology, vol. 13, no. 10, 1045-1060
5. Raghavan, S. (2021), 'Diffusion models reveal white matter microstructural changes with ageing, pathology and cognition', Brain Communications, vol. 3, no. 2
6. Dadar, M. (2021), 'BISON: Brain tissue segmentation pipeline using T1-weighted magnetic resonance images and a random forest classifier', Magnetic Resonance in Medicine, vol. 85, no. 4, pp. 1881-1894
7. Alfaro-Almagro, F. (2018), 'Image processing and Quality Control for the first 10,000 brain imaging datasets from UK Biobank', Neuroimage, vol. 166, pp. 400-424
8. Fonov, V. S. (2009), 'Unbiased nonlinear average age-appropriate brain templates from birth to adulthood', Neuroimage, vol. 47, pp. S102
9. Rutherford, S. (2022), 'The normative modeling framework for computational psychiatry', vol. 17, no. 7, pp. 1711-1734
10. Manjón, J. V. (2010), 'Adaptive non-local means denoising of MR images with spatially varying noise levels', Journal of Magnetic Resonance Imaging, vol. 31, no. 1, pp. 192-203

Poster No 2407

Invasive and noninvasive causal evidence of amygdala engagement by DLPFC stimulation

Xianqing Liu[1,2], Joel Bruss[3,4], Brandt Uitermarkt[3,4], Nicholas Trapp[1], Hiroyuki Oya[5], Aaron Boes[3,4], Jing Jiang[1,2]

[1]University of Iowa Hospitals and Clinics, Department of Psychiatry, Iowa City, IA, [2]University of Iowa Hospitals and Clinics, Stead Family Department of Pediatrics, Iowa City, IA, [3]University of Iowa Hospitals and Clinics, Neuroimaging & Noninvasive Brain Stimulation Laboratory, Iowa City, IA, [4]University of Iowa Hospitals and Clinics, Department of Neurology, Iowa City, IA, [5]University of Iowa Hospitals and Clinics, Department of Neurosurgery, Iowa City, IA

Introduction: While invasive modulation of amygdala activity has shown promise in treating certain refractory psychiatric cases, its widespread use among millions of treatment-resistant patients is impractical and entails inherent neurosurgery-related risks. Our recent studies indicate transcranial magnetic stimulation (TMS) of the dorsolateral prefrontal cortex (DLPFC) provides a potential noninvasive alternative (Eshel et al., 2020; Jiang, 2023). However, given the amygdala's deep location in the medial temporal lobe, there is a critical need for definitive causal evidence to determine whether and how DLPFC stimulation engages the amygdala. Therefore, the present study aims to get converging causal evidence of amygdala engagement to DLPFC stimulation from multimodal invasive and noninvasive imaging methods.

Methods: We performed 4 studies utilizing an unparalleled combination of invasive and noninvasive stimulation and recording methods in humans. We began with Study 1 in which we delivered single-pulse intracranial electrical stimulation (iES) to the left DLPFC while concurrently recording responses in the amygdala (n=11 electrodes) with intracranial EEG (iEEG) used in epilepsy patients being evaluated for surgery. The effect of iES to a control region, i.e., the left ventrolateral prefrontal cortex (VLPFC), in the amygdala was also assessed. To move towards clinical translatability, we performed another two noninvasive stimulation studies by delivering TMS to the left DLPFC while recording responses in the amygdala with iEEG in epilepsy patients (n=30 electrodes, Study 2) and with functional MRI (fMRI) in healthy individuals (N=85 subjects, Study 3). The effects of TMS to control regions, e.g., parietal cortex, in the amygdala were also assessed. Finally, we evaluated the potential role of DLPFC-amygdala connectivity assessed with resting state functional connectivity MRI in predicting amygdala responses induced by DLPFC stimulation in same participants from Study 2 and 3 (Study 4).

Results: In Study 1, we found single-pulse iES to the DLPFC evokes significant potential change in the amygdala in two separate time windows (119~165ms and 349~430ms) as compared to baseline ($t = 2.61$~3.36, corrected $p < 0.05$). In contrast, single-pulse iES to the VLPFC did not evoke similar amygdala response. In Study 2, we observed that single-pulse active TMS to the DLPFC also evokes significant potential difference in three time windows (52~91ms, 194~244ms, and 326~347ms) in amygdala as compared to sham TMS condition ($|t| = 2.68$~5.01, corrected $p < 0.05$). However, TMS to the parietal cortex did not evoke similar amygdala response. In Study 3, DLPFC TMS evokes strongest BOLD responses in the amygdala as assessed with concurrent functional MRI (fMRI) in healthy individuals among TMS to 11 TMS sites (Cohen's $d = 0.39$, Power = 0.92). Finally, in Study 4, we identified significant correlations between DLPFC-amygdala functional connectivity and amplitude in second time window where TMS vs Sham evoked potentials differ (194~244ms; $r = 0.54$, $p = 0.011$) and TMS-evoked BOLD responses ($r = 0.25$, $p = 0.035$) in the amygdala.

Conclusions: Together, our results provide converging and compelling causal evidence of amygdala engagement to DLPFC stimulation. The correlation between DLPFC-amygdala RSFC and DLPFC TMS-induced response in the amygdala suggests a possible functional connectivity-based strategy to target the amygdala, offering a circuit-based insight into the feasibility of noninvasive neuromodulatory therapies aiming at modulating the amygdala for psychiatric disorders.

References

1. Eshel, N., C. J. Keller, W. Wu, J. Jiang, C. Mills-Finnerty, J. Huemer, R. Wright, G. A. Fonzo, N. Ichikawa and D. Carreon (2020). 'Global connectivity and local excitability changes underlie antidepressant effects of repetitive transcranial magnetic stimulation.' Neuropsychopharmacology, vol. 45, no. 6 pp.1018-1025
2. Jiang, J. (2023). 'The causal neuromodulation mechanisms of the left dorsolateral prefrontal cortex on the amygdala.' Brain Stimulation: Basic, Translational, and Clinical Research in Neuromodulation, vol. 16, no. 1, pp. 391

Poster No 2408

Individualised mapping of the language system using ultra high-field fMRI

Nicole Eichert[1], Donna Gift Cabalo[2], Yezhou Wang[2], Shahin Tavakol[3], Jordan DeKraker[4], Alexander Weil[5], Raúl Rodriguez-Cruces[6], Boris Bernhardt[6]

[1]University of Oxford, Oxford, Oxfordshire, [2]McGill University, Montreal, Quebec, [3]McGill University, Montreal Neurological Institute and Hospital, Montreal, Quebec, [4]McGill University, Montreal, Canada, [5]Centre Hospitalier Universitaire Sainte-Justine, Montreal, Canada, [6]Montreal Neurological Institute and Hospital, Montreal, Quebec

Introduction: All humans share the fundamental neurobiological infrastructure that enables us to process language. Nevertheless, the brain's language system exhibits considerable inter-individual variability in both anatomy and function[1]. Mapping the language system, therefore, requires a nuanced approach that captures neuroanatomical features with high reliability to enable individualised analyses. Here, we performed high-precision individualised mapping of the language system using multimodal ultra high-field MRI. We leveraged a new MRI resource with unprecedented coverage: The openly-available 7T Precision NeuroImaging (PNI) dataset from the Montreal Neurological Institute features an extensive battery of repeated structural, quantitative and functional scans. Each participant underwent 4 sessions, one of which included an fMRI language task. This comprehensive dataset allows us to localise the brain's language system and to test associations with intrinsic neuroanatomical features.

Methods: The imaging protocol was implemented on a 7T Siemens Terra scanner. Pre-processed data from six participants (4F, median age: 25 years [22-32]) were accessed from the PNI dataset, specifically task BOLD fMRI data (1.9mm isotropic, TR=1690ms, multiband factor 3, echo spacing=0.53ms, multi-echo) and resting-state fMRI data (6 mins) from the same session. From other scanning sessions we accessed apparent diffusion coefficient (ADC), magnetization transfer saturation (MTSAT) and MP2RAGE-based quantitative T1 relaxometry (qT1). All metrics were sampled to individual surfaces reconstructed using FastSurfer and manually corrected. Pre-processing was performed using Micapipe[2]. The language task design and stimuli, matched for linguistic features, were adapted from a previous study[3]. Briefly, in blocks of 30s (10 trials of 3 seconds), participants were required to make a phonological, semantic, or visual judgement about a pair of words (Figure 1A). Task data were analysed using Python's nilearn to obtain a phonological-versus-semantic contrast. Group-level activation maps were based on t-test from individual z-maps and based on thresholded activation count maps. Group-level task peaks were identified on the surface and individual task peaks were located within a circular ROI of 2cm. To demonstrate specificity, random (i.e., displaced) peaks were selected within the same ROIs. Functional connectivity (FC) was determined using Pearson's correlation from rs-fMRI data. Associations of individual z-maps to microstructural markers were tested using a linear mixed effects model as implemented in Python's statsmodels.

Results: Behavioural responses indicated that all participants showed high performance throughout the task and comparable difficulty of phonological and semantic conditions (Figure 1B). Group-level activation and count maps demonstrate that expected language hubs in the brain were engaged during phonological and semantic processing with overall left-ward lateralization (Figure 1C). Group-level FC analyses demonstrated that phonological and semantic processing are relying on two distinct networks, which can be reliably extracted on the individual subject level (Figure 2A). A small displacement of the individual peaks results in a degraded connectivity matrix indicating high spatial specificity of the language task localizer. Spatial correlation to microstructural markers showed small but consistent associations across subjects, with semantic processing co-localising with cortex with lower ADC, lower MTSAT, and higher qT1 (Figure 2B).

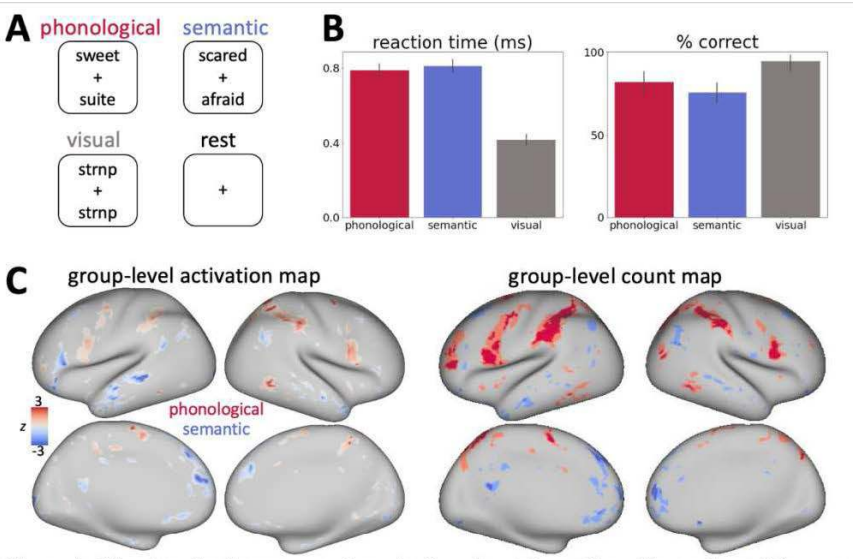

Figure 1. Mapping the language system. A: Experimental paradigm: For each condition, an example trial is shown, where the correct response is 'yes'. Task blocks were interleaved with rest blocks. **B**: Behavioural results (n=6). **C**: Left - Group-level activation map showing areas of significant activation from the phonological-versus-semantic contrast (one-sample t-test, p<0.05). Right – Group-level count map showing the overlap of significantly activated areas across the group (individual z-threshold: 1.96, count threshold: n>1).

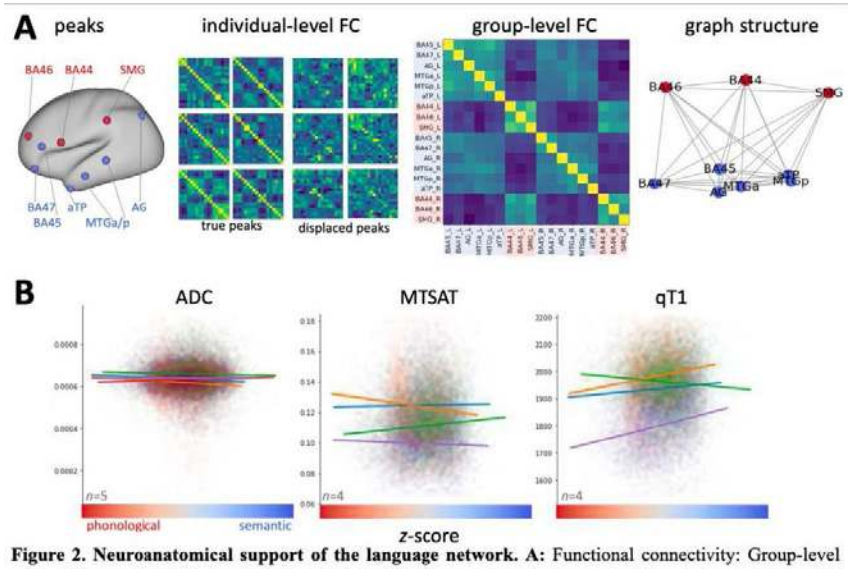

Figure 2. Neuroanatomical support of the language network. A: Functional connectivity: Group-level task peaks were identified on both hemispheres (SMG=supra marginal gyrus; aTP=anterior temporal pole; MTGa/p=anterior or posterior middle temporal gyrus; AG=angular gyrus). Each individual's FC matrix was determined for all pairs of individual task peaks and when selecting randomly displaced peaks within 2 cm. The average group-level FC matrix and the graph-based visualisation using Python's networkX highlight two distinct functional networks. **B:** Associations to microstructure: Normalised z-values correlate with ADC, MTSAT and qT1 (linear mixed effects model, p<0.001). Different colours indicate different subjects.

Conclusions: We successfully mapped the language system using a robust localizer task at 7T maintaining individual subject differences. The task scan is part of a densely sampled and multimodal MRI dataset, which will be openly available for the community. In our exemplary analysis on structure-function relations within the cortex, we showed that phonological and semantic processing are supported by distinct neuroanatomical make-up of the cortex.

References

1. Seghier, M. L. & Price, C. J. Interpreting and Utilising Intersubject Variability in Brain Function. Trends Cogn. Sci. 22, 517–530 (2018).
2. Cruces, R. R. et al. Micapipe: A pipeline for multimodal neuroimaging and connectome analysis. Neuroimage 263, 119612 (2022).
3. Devlin, J. T., Matthews, P. M. & Rushworth, M. F. S. Semantic processing in the left inferior prefrontal cortex: a combined functional magnetic resonance imaging and transcranial magnetic stimulation study. J. Cogn. Neurosci. 15, 71–84 (2003).

Poster No 2409

Temporally coupled FDG-fPET and BOLD-fMRI dynamics across task and naturalistic arousal

Sean Coursey[1,2], Shirley Feng[1], Jingyuan Chen[1,3]

[1]Athinoula A. Martinos Center for Biomedical Imaging, Massachusetts General Hospital, Charlestown, MA, [2]College of Science, Northeastern University, Boston, MA, [3]Department of Radiology, Harvard Medical School, Boston, MA

Introduction: The recent introduction of continuous-infusion FDG-PET (FDG-fPET) and modern PET-MRI scanners permits examining concurrent dynamics of glucose metabolism and blood-oxygenation-level-dependent (BOLD) signals in the human brain[1-3]. Despite fPET's higher temporal resolution than previous PET methods[4], most fPET-fMRI studies to date have centered on static spatial correlations[5-7]. Leveraging fPET's temporal resolution, our study introduces an analytical framework connecting the evolution of FDG-fPET signals with concurrent BOLD-fMRI data. Tested on visual-stimulus and naturalistic-arousal datasets, this methodology proved effective in linking glucose uptake and BOLD dynamics.

Methods: We first assessed the temporal coupling of BOLD-fMRI and FDG-fPET measures by analyzing a public visual-stimulation dataset[8]. The Monash vis-fPET-fMRI dataset comprises 70-minute simultaneous FDG-fPET and BOLD-fMRI scans of 10 healthy young adults (fMRI: voxel size = 3×3×3 mm3, TR = 2.45 s; fPET: reconstructed nominal voxel size = 1.39×1.39×2 mm3, temporal resolution = 1 min). Participants were shown a flickering checkerboard in an embedded block task design (Fig. 1a). We hypothesize that the power of the fMRI signal at the stimulus frequency is indicative of neural activity, so integrating this power over time will correspond to the concurrent FDG accumulation due to metabolic demand. To test this, we computed the average fMRI signal from the primary visual cortex (V1) across subjects, applied a Hilbert transform to determine the BOLD signal power over time, and integrated this power to use as a predictor variable for the FDG-fPET data (Fig. 1a). We removed long-term trends from both the predictor and the PET data using a third-order polynomial, focusing on the dynamic changes. To test our model for a naturalistic paradigm, we acquired and analyzed fPET-fMRI data from 23 healthy adults who were instructed to close their eyes and relax throughout a 75-120 min scan. Arousal states were inferred from simultaneous EEG recordings (18 subjects) or behavioral measures (5 subjects). All scans were performed on a 3T Siemens MR scanner with a BrainPET insert (fMRI: voxel size = 3×3×3 mm3, TR = 2/2.4 s; fPET: reconstructed nominal voxel size = 2.5×2.5×2.5 mm3, temporal resolution = 30 s). FDG was administered as a bolus plus continuous infusion. Following a similar framework as the visual dataset, we tested how much variance the integrated power of the global fMRI signal could explain in subjects' fPET time activity curves (TACs).

Results: Regression showed that our integrated V1 BOLD power predictor aligns with V1 FDG accumulation (Fig. 1a). Moreover, the significant correlation between the BOLD signal and FDG accumulation is specifically strong in the visual cortex (Fig. 1b). We also noticed metabolic activations in the frontal cortex, possibly owing to task-locked attention changes. Our tri-modal framework successfully tracked sleep-wake dynamics in both glucose uptake and hemodynamic changes (Fig. 2a). We identified strong coupling between the global BOLD and FDG time-courses (Fig. 2b). The metabolic regressor modeled by the global fMRI signal explained significant variance of fPET TACs in extensive cortical regions (Fig. 2c). These observations supported the applicability of the PET-MRI integration framework in naturalistic paradigms.

Conclusions: We created a framework that temporally links metabolic and hemodynamic signals. Functional MRI signals predicted concurrent FDG-fPET dynamics driven by visual stimulation and naturalistic arousal. Our results substantiate hemodynamic-metabolic temporal coupling, demonstrating the value of FDG-fPET in conjunction with BOLD-fMRI for characterizing time-resolved co-evolution of neurometabolic and neurovascular activity. Consequently, this study advances neuroimaging's exploration of hemodynamic-metabolic interdependence in the human brain.

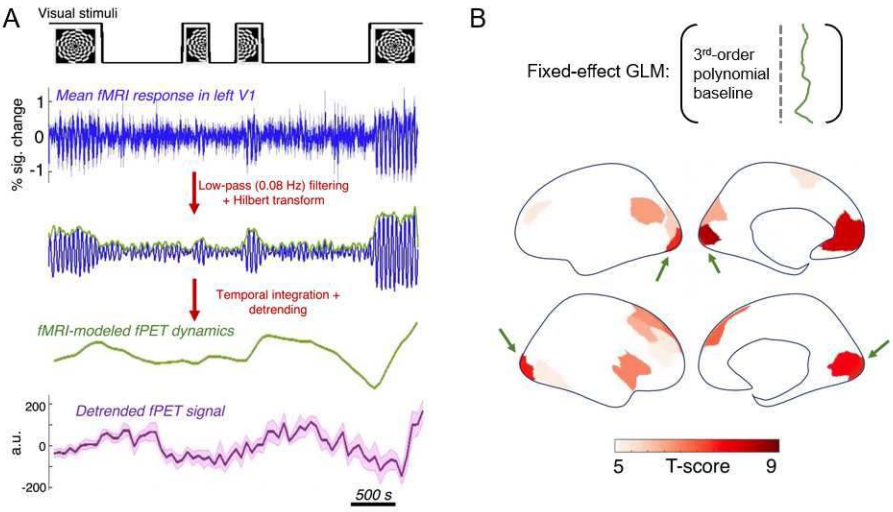

Figure 1.

(**A**) The overall scheme of modeling fPET time-activity curves from BOLD-fMRI time courses. Error bars of mean fMRI responses and detrended fPET signals indicate standard errors across subjects. (**B**) fPET metabolic activations identified using the fMRI-derived regressor (FDR, $p < 0.01$, fixed effects analysis given $N = 10$). Green arrows point towards the visual cortex.

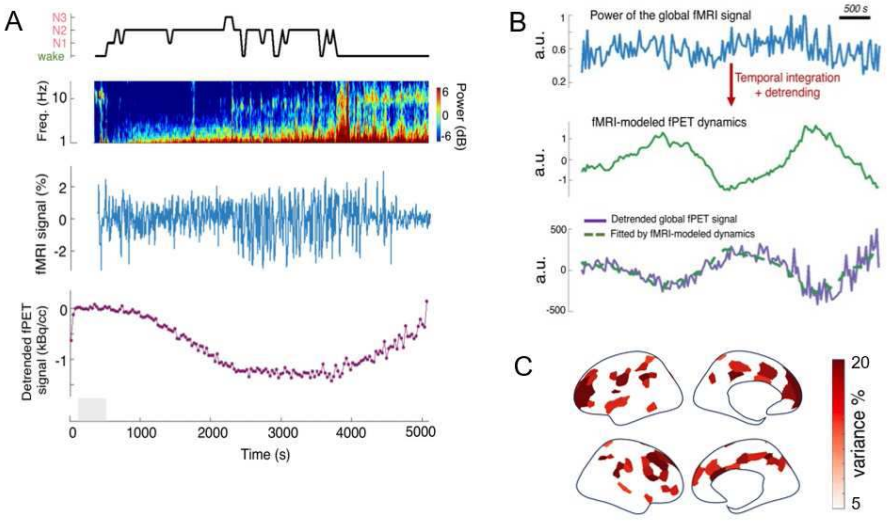

Figure 2.

(**A**) Tri-modal imaging of metabolic and BOLD dynamics accompanying arousal transitions. Changes in fMRI intensities and glucose metabolism (manifesting as altered slopes of PET signals, with an increase/decrease of slope indicated increased/decreased metabolism) were observed across arousal levels (including changes within the NREM phase, inferred from EEG, top). The fPET signal was detrended according to the initial wakeful period to help visualize its slope alterations at state transitions. (**B**) The analytical framework that links the fPET time-activity curves to the power of BOLD-fMRI signals. (**C**) Variance of fPET TACs explained by fMRI-modeled covariates in the sleep experiments. Only significant couplings are plotted (FDR, random-effects analysis, $p < 0.05$).

References

1. Villien, M. (2014), 'Dynamic functional imaging of brain glucose utilization using fPET-FDG', Neuroimage, 100, pp.192-199.
2. Hahn, A. (2016), 'Quantification of task-specific glucose metabolism with constant infusion of 18F-FDG', Journal of Nuclear Medicine, 57(12), pp.1933-1940.
3. Jamadar, S.D. (2019), 'Simultaneous task-based BOLD-fMRI and [18-F] FDG functional PET for measurement of neuronal metabolism in the human visual cortex', Neuroimage, 189, pp.258-266.
4. Rischka, L. (2018), 'Reduced task durations in functional PET imaging with [18F] FDG approaching that of functional MRI', Neuroimage, 181, pp.323-330.
5. Stiernman, L.J. (2021), 'Dissociations between glucose metabolism and blood oxygenation in the human default mode network revealed by simultaneous PET-fMRI', Proceedings of the National Academy of Sciences, 118(27), p.e2021913118.
6. Hahn, A. (2020), 'Reconfiguration of functional brain networks and metabolic cost converge during task performance', elife, 9, p.e52443.
7. Jamadar, S.D. (2021), 'Metabolic and hemodynamic resting-state connectivity of the human brain: a high-temporal resolution simultaneous BOLD-fMRI and FDG-fPET multimodality study', Cerebral Cortex, 31(6), pp.2855-2867.
8. Jamadar, S.D. (2021), 'Task-evoked simultaneous FDG-PET and fMRI data for measurement of neural metabolism in the human visual cortex', Scientific Data, 8(1), p.267.

Poster No 2410

Longitudinal iron in caudate related to control network connectivity and planning in older adults

Jing Zhou[1], Colleen Hughes[1], Alfie Wearn[1], Julia Huck[2], Giulia Baracchini[1], Elisabeth Sylvain[3], Jennifer Tremblay-Mercier[3], Judes Poirier[4], Sylvia Villeneuve[4], Christine Tardif[1], Claudine J. Gauthier[2], Gary Turner[5], R. Nathan Spreng[1]

[1]Montreal Neurological Institute, McGill University, Montreal, Québec, [2]Physics Department, Concordia University, Montreal, Québec, [3]Douglas Mental Health University Institute, Montreal, Québec, [4]Department of Psychiatry, McGill University, Montreal, Québec, [5]York University, Toronto, Ontario

Introduction: Cognitive functions attributed to the frontoparietal control network (FPCN) are central to goal-directed behaviors, and these abilities are vulnerable to decline with advancing age.[1] Age-related declines in executive function (EF) have been linked to dopaminergic striatal dysfunction[2]. Elevated striatal iron deposition has been associated with lower cognition[3], and differences in brain function, measured with fMRI[4]. Here, we examined the impact of longitudinal iron accumulation in the caudate, a core subcortical node of the FPCN, on resting state functional connectivity (RSFC) changes in the FPCN in a sample of older adults. We then examined caudate iron associations with brain function and impact on changes in EF.

Methods: Participants and cognitive assessment: 132 older adults (mean age, 67.64.6y, 34 men) at familial risk for AD from the PREVENT-AD cohort underwent MRI scanning at baseline and follow-up (mean interval, 2.7y). 81 completed the Cambridge Brain Sciences test battery (Planning, Token Search); 127 completed the Trail Making Task and Stroop at each timepoint. Data acquisition: MRI scanning was conducted on a Siemens Prisma 3T scanner with a 32-channel head coil array. QSM images were acquired from 3D GRE sequence with single-echo (TR=20ms; TE=7.29ms; Voxel size=0.8 x 0.8 x1.0mm3; scan time=5.31min). Resting-state multi-echo functional MRI were acquired from a multi-echo (ME) EPI sequence (TR=1000ms; TE1=12ms, TE2=30.11ms, TE3=48.22ms; Voxel size=3.0 x 3.0 x3.0mm3; scan time=10.24 min). T1w were acquired with 3D MP-RAGE sequence (TR=2300ms; TE=2.96ms; voxel size=1.0 x 1.0 x 1.2mm3; scan time=5.3min). Image processing: QSM: Phase images were combined to obtain offset-corrected images, using estimation from POEM[5]. QSM maps were reconstructed using TGV-based method[6]. FMRI: Functional images were submitted to ME-ICA[7]. Whole brain RSFC matrices were initialized to the 200-parcel Schaefer atlas[8] 7 networks. Parcels were then individualized to each participants' functional neuroanatomy using Group Prior Individualized Parcellation[9]. Product-moment correlation between parcels was computed for each timepoint, resulting in 2RSFC matrices for each participant (Fig.1), then restricted to the FPCN. MP-RAGE: Caudate ROI was obtained through Freesurfer subcortical segmentation and registered the QSM space. Analysis: We examined longitudinal change in iron and cognitive performance using a paired sample t-test predicting an increase in iron and decline in EF. The relationship between longitudinal change in iron and FPCN RSFC was conducted using a two condition (time 1, time 2) behavioral Partial Least Squares (bPLS) analysis. To test associations with EF, we used a linear mixed model. EF measures (planning, token search, Stroop inhibition time and TMT B-A RT) were assigned as dependent variables, with brain scores derived from bPLS and timepoint (baseline and follow-up) as fixed factors, and age, sex and education as covariates, allowing for random intercepts across subjects.

Results: Iron level significantly increased over time ($t(131)=2.4$, $p<.01$, single-tail). Increasing iron content in caudate was significantly associated with longitudinal FPCN RSFC ($p<.05$). Both positive and negative RSFC were observed within the FPCN to covary with iron over time. This multivariate association between iron accumulation in caudate and FPCN RSFC was then related to EF, noting a specific decline in planning ($t(80)=1.81$, $p<.05$, single-tail). Caudate iron - FPCN longitudinal effects were significantly associated with declines in planning ability ($r=.365$, $p<.005$) but not other measures of EF (Fig.2).

Conclusions: Iron deposition in the caudate in older adults is reliably associated with changes in brain connectivity within the FPCN. This relationship was associated with decline in planning ability. These findings suggest that iron accumulation may be a driving pathological factor in RSFC changes, and predicts EF decline with advancing age.

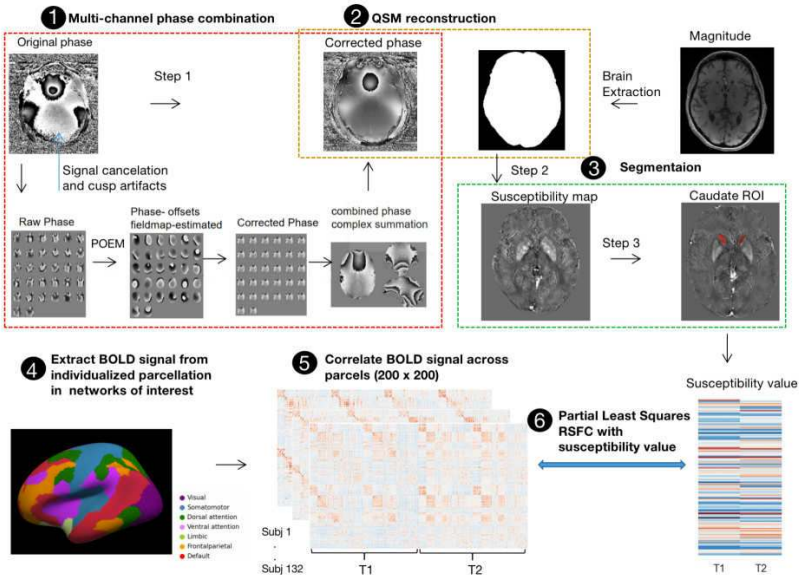

Fig.1 Preprocessing and analysis workflow. (1) Phase images from the 32-channel receiver were combined to obtain offset-corrected phase images using POEM.(2)The corrected phase image and magnitude image were then used for QSM reconstruction to obtain QSM maps.(3) Caudate ROI obtain through Freesurfer automatic subcortical segmentation was registered to QSM space to quantify susceptibility value. (4) BOLD resting-state data were extracted from subject-specific individual parcellation in seven networks of interest. (5) Functional connectivity between parcels were constructed, forming a 200 x 200 matrix. (6) PLS was used to identify patterns of RSFC that maximally covary with caudate iron across subjects over time.

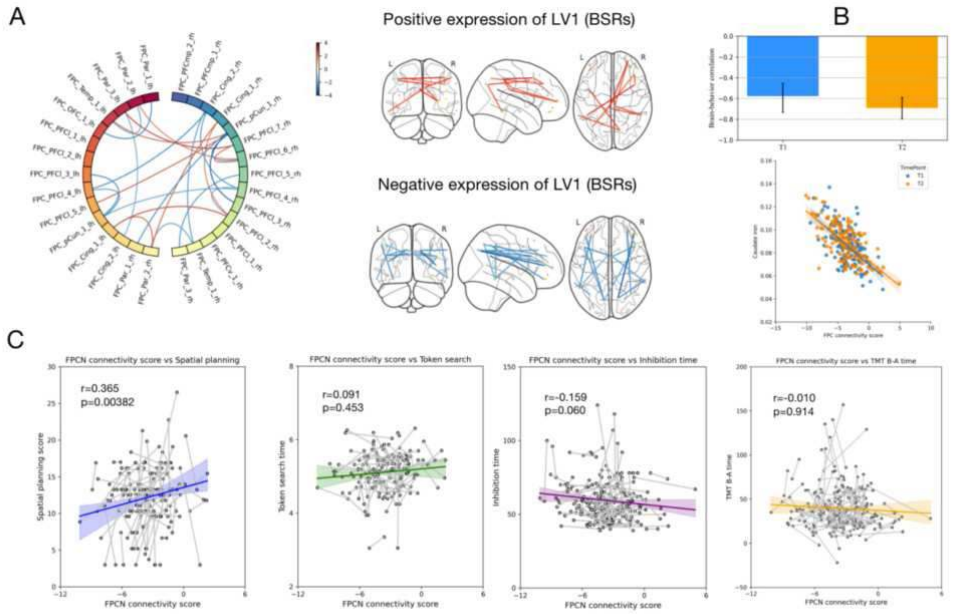

Fig.2. A) RSFC connectivity patterns within the PFCN related to iron. Warm colors indicate decreases in RSFC related to higher caudate iron. Cool colors indicate increases in RSFC related to higher caudate iron. B) Iron - FPCN RSFC associations. C) Association between iron - FPCN RSFC brain scores and four measures of EF: planning, token search, Stroop inhibition, TMT B-A time.

References

1. Campbell, K. L., Grady, C. L., Ng, C., & Hasher, L. (2012). Age differences in the frontoparietal cognitive control network: Implications for distractibility. Neuropsychologia, 50(9), 2212-2223. doi:https://doi.org/10.1016/j.neuropsychologia.2012.05.025
2. Bäckman, L., Lindenberger, U., Li, S.-C., & Nyberg, L. (2010). Linking cognitive aging to alterations in dopamine neurotransmitter functioning: Recent data and future avenues. Neuroscience & Biobehavioral Reviews, 34(5), 670-677. doi:https://doi.org/10.1016/j.neubiorev.2009.12.008
3. Spence, H., McNeil, C. J., & Waiter, G. D. (2020). The impact of brain iron accumulation on cognition: A systematic review. PLoS One, 15(10), e0240697. doi:10.1371/journal.pone.0240697
4. Salami, A., Avelar-Pereira, B., Garzon, B., Sitnikov, R., & Kalpouzos, G. (2018). Functional coherence of striatal resting-state networks is modulated by striatal iron content. Neuroimage, 183, 495-503. doi:10.1016/j.neuroimage.2018.08.036
5. Sun, H., Cleary, J. O., Glarin, R., Kolbe, S. C., Ordidge, R. J., Moffat, B. A., & Pike, G. B. (2020). Extracting more for less: multi-echo MP2RAGE for simultaneous T1-weighted imaging, T1 mapping, mapping, SWI, and QSM from a single acquisition. Magnetic Resonance in Medicine, 83(4), 1178-1191. doi:https://doi.org/10.1002/mrm.27975
6. Langkammer, C., Bredies, K., Poser, B. A., Barth, M., Reishofer, G., Fan, A. P., . . . Ropele, S. (2015). Fast quantitative susceptibility mapping using 3D EPI and total generalized variation. Neuroimage, 111, 622-630. doi:https://doi.org/10.1016/j.neuroimage.2015.02.041

7. Kundu, P., Brenowitz, N. D., Voon, V., Worbe, Y., Vértes, P. E., Inati, S. J., . . . Bullmore, E. T. (2013). Integrated strategy for improving functional connectivity mapping using multiecho fMRI. Proceedings of the National Academy of Sciences, 110(40), 16187-16192. doi:doi:10.1073/pnas.1301725110
8. Schaefer, A., Kong, R., Gordon, E. M., Laumann, T. O., Zuo, X.-N., Holmes, A. J., . . . Yeo, B. T. T. (2017). Local-Global Parcellation of the Human Cerebral Cortex from Intrinsic Functional Connectivity MRI. Cerebral Cortex, 28(9), 3095-3114. doi:10.1093/cercor/bhx179
9. Chong, M., Bhushan, C., Joshi, A.A., Choi, S.Y., Haldar, J.P., Shattuck, D.W., Spreng, R.N. & Leahy, R.M. (2017). Individual parcellation of resting fMRI with a group functional connectivity prior. NeuroImage, 156, 87–100.

Poster No 2411

The energetic costs of signaling as a proxy of cognition in health and disease

Gabriel Castrillon[1,2], Katarzyna Kurcyus[3], Samira Epp[1], Antonia Bose[3], Roman Belenya[3], Andreas Ranft[4], Igor Yakushev[5], Christine Preibisch[3], Valentin Riedl[1,3]

[1]Department of Neuroradiology, Uniklinikum Erlangen, Erlangen, Germany, [2]Research Group in Medical Imaging, SURA Ayudas Diagnósticas, Medellin, Colombia, [3]Department of Neuroradiology, Technical University of Munich, Munich, Germany, [4]Department of Anesthesiology, Technical University Munich, Munich, Germany, [5]Department of Nuclear Medicine, Technical University of Munich, Munich, Germany

Introduction: During evolution, the human brain has continuously expanded and increased its energy demands relative to the body[1]. The most expanded brain areas have been associated with higher cognitive functions in humans[2], increasing considerably the energy demands related to neural processing[3]. Patients with mental disorders often exhibit impaired cognitive functions[4]. We hypothesized that the distribution of energy metabolism along signaling pathways could reveal mechanisms of higher cognitive processing in the human brain and its deviation in disease.

Methods: Forty-seven quantitative FDG-PET and BOLD-fMRI data from thirty healthy participants from three independent cohorts of healthy participants were included. The cerebral metabolic rate of glucose (CMRglc) was derived using the Patlak plot model on the preprocessed PET images and the arterial input function. The degree of functional connectivity (dFC) was derived from the preprocessed BOLD images. We defined the energetic costs of signaling as the residual of the linear regression between the CMRglc and the dFC. Our findings were interpreted using the cortical expansion from non-human primates to humans[5], preprocessed microarray expression data from the Allen Human Brain Atlas (AHBA)[6], 28 previously published PET neuroreceptors maps[7], meta-analytic cognitive maps from the Neurosynth database[8,9], behavioral neural maps from psychotic disorders[10], and gene lists from genome-wide association studies (GWAS)[11-15]. The association between variables was assessed using the Pearson correlation's p-value corrected for autocorrelation (p_smash)[16].

Results: We identified a consistent cortical distribution with deviating energetic costs of signaling calculated as the residual CMRglc per dFC across all cohorts (Fig. 1A). From an evolutionary perspective, the energetic costs of signaling correlated significantly with the extent of cortex expansion from chimpanzees to humans (Fig. 1B), indicating that regions that expanded most during human evolution have a higher energy demand compared to the rest of the brain. Next, we analyzed the molecular profile associated with the distribution of energetic costs of signaling by running a gene ontology enrichment (GOE) analysis on the AHBA genes significantly correlated with the energetic costs map. We found that 95% of genes that are overexpressed in regions with high energetic costs are involved in signal transduction, mainly in metabotropic neuromodulation (Fig. 1C). This finding was replicated by entering 19 unique receptors, and transporters maps from 28 different PET studies into a partial least-squares (PLS) analysis, which explained 86% of the cortical variance in energetic costs (Fig. 1D), replicating that the cortical distribution of energetic costs of signaling is strongly related to the regional level of neuromodulator activity. Finally, we analyzed the relationship between the distribution of the energetic costs and cognition in health, observing that energetic costly regions were involved in high cognitive functions such as memory processing and reading but less involved in sensory-motor functions (Fig. 1E), whereas in disease, the distribution of the energetic costs was consistently correlated with psychotic disorders symptoms derived from behavioral (Fig. 1F, left) and genetic data in patients with schizophrenia (SCZ; Fig. 1F middle) and bipolar 1 disorder (BD; Fig. 1F right). In contrast, the energetic costs did not correlate with other non-psychotic disorders such as depression, autism spectrum disorder, or attention-deficit/hyperactivity disorder.

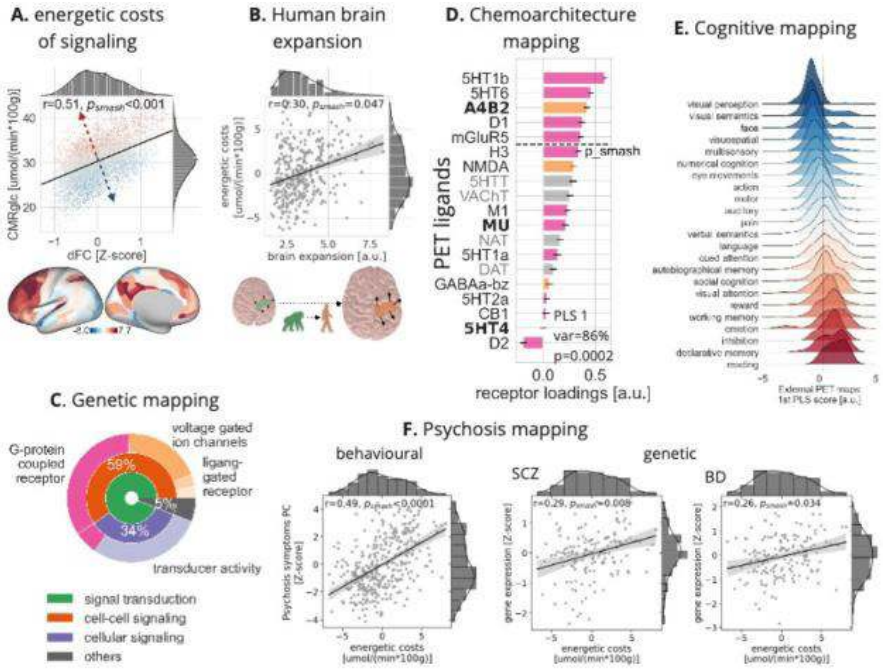

Figure 1. The energetic costs of signaling as a proxy of higher cognition in health and disease. A. The scatterplot of CMRglc (y-axis) and dFC (x-axis) is color-coded by the residual CMRglc, which corresponds to the distribution of energetic costs of signaling, indicating a higher (red) or lower (blue) energy demand per dFC (top). The brain surface shows the spatial pattern of energetic costs of signaling across all the subjects (bottom). **B**. Significant relationship between energetic costs (y-axis) and the degree of cortical expansion (x-axis) from non-human to human primates (r = 0.30, p_smash = 0.047). **C**. Summary of the gene ontology enrichment analysis showing the significant relationship of the energetic costs map with genes involved mainly in signal transduction (95%, green, inner pie), particularly of G protein–coupled, metabotropic, neuromodulation (40%, pink, external pie), and ionotropic signaling (26%, orange, external pie). **D**. Multi-dimensional PLS analysis reveals that 86% of the cortical distribution of energetic costs is explained by the linear combination of neurochemical signaling receptors derived from PET imaging of 19 neuromodulators and neurotransmitters (metabotropic: pink, ionotropic: orange, transporters: grey). Error bars represent 95% confidence intervals using bootstrap resampling (5000 permutations). **E**. Joyplot shows the voxel-wise distribution of the first latent PLS variable between energetic costs and chemoarchitecture profiles (z-score > 2.3) for each of 23 cognitive domains (y-axis) from the meta-analytic Neurosynth database. Color-coding illustrates the increasing rank (blue > red) of average energetic costs from sensory processing to higher cognitive functions. **F**. Significant relationship between the energetic costs and the principal component related to psychosis-spectrum (r > 0.25, p_smash < 0.05) derived from 36 behavioural measures (left) and the gene expression of genes related to schizophrenia (middle) and bipolar disorder (right) derived from genome-wide association studies (GWAS).

Conclusions: We derived a map of the energetic costs of signaling of the human brain, showing that energetic costly regions i) were most expanded during human evolution, ii) have upregulated neuromodulatory signaling, iii) are mainly involved in higher cognitive processing, and iv) are specifically related to pheno and genotypes from psychotic disorders but not to other mental disorders.

References

1. Herculano-Houzel, S. (2011). Scaling of brain metabolism with a fixed energy budget per neuron: implications for neuronal activity, plasticity and evolution. PloS one, 6(3)
2. Tomasello, M., & Call, J. (1997). Primate cognition. Oxford University Press
3. Aiello, L. C., & Wheeler, P . (1995). The expensive-tissue hypothesis: the brain and the digestive system in human and primate evolution. Current anthropology, 36(2)
4. Service, S.K., et al. (2020). Distinct and shared contributions of diagnosis and symptom domains to cognitive performance in severe mental illness in the Paisa population: a case-control study. The Lancet Psychiatry 7(5).
5. Wei, Y., et al. (2019). Genetic mapping and evolutionary analysis of human-expanded cognitive networks. Nature communications, 10(1).
6. Hawrylycz, M.J., et al. (2012). An anatomically comprehensive atlas of the adult human brain transcriptome. Nature, 489(7416).

7. Hansen, J. Y. (2022). Mapping neurotransmitter systems to the structural and functional organization of the human neocortex. Nature Neuroscience, 22.
8. Yarkoni, T., et al. (2011). Large-scale automated synthesis of human functional neuroimaging data. Nature methods, 8(8).
9. Margulies, et al.(2016). Situating the default-mode network along a principal gradient of macroscale cortical organization. Proceedings of the National Academy of Sciences, 113(44).
10. Ji, J.L., et al. (2021). Mapping brain-behavior space relationships along the psychosis spectrum. Elife, 10.
11. Stahl, E. A., et al. (2019). Genome-wide association study identifies 30 loci associated with bipolar disorder. Nature genetics, 51(5).
12. Pardiñas, A.F., et al. (2018). Common schizophrenia alleles are enriched in mutation-intolerant genes and in regions under strong background selection. Nature genetics, 50(3).
13. Howard, D.M., et al. (2019). Genome-wide meta-analysis of depression identifies 102 independent variants and highlights the importance of the prefrontal brain regions. Nature neuroscience, 22(3).
14. Grove, J., et al. (2019). Identification of common genetic risk variants for autism spectrum disorder. Nature genetics, 51(3).
15. Demontis, D., et al. (2019). Discovery of the first genome-wide significant risk loci for attention deficit/hyperactivity disorder. Nature genetics, 51(1).
16. Burt, J.B., et al. (2020). Generative modeling of brain maps with spatial autocorrelation. NeuroImage, 117038.

Poster No 2412

Adversarial Diffusion Models for Medical Image Translation

Hanyeol Yang[1], Seonggyu Kim[2], Yongseon Yoo[1], Jihwan Min[1], Jong-Min Lee[2]

[1]Department of Artificial Intelligence, Hanyang University, Seoul, Korea, Republic of, [2]Department of Electronic Engineering, Hanyang University, Seoul, Korea, Republic of

Introduction: Multi-modal imaging provides key insights for assessing the structure and function of the human body.[1]. Augmenting insights through multi-modal imaging enhances diagnostic accuracy and boosts performance in subsequent tasks[2]. However, the practical application of multimodal protocols includes realistic challenges due to labor and economic costs[3]. Medical image synthesis emerges as a solution to this issue, wherein the missing target modality is generated based on the acquired source modality[4,5,6]. In recent years, GAN models have shown remarkable success in image synthesis. Yet, inherent limitations in the quality and diversity of synthesized images persist[7]. To address these limitations, we have adopted diffusion model a recent focal point in generative model research[7,8]. Previous studies on image-to-image translation using existing diffusion models encounter drawbacks, slow sampling, a typical drawback of diffusion model[9,10]. In this context, we introduce an adversarial diffusion model for medical image synthesis. Our approach shows that adversarial loss to enhance sampling speed.

Methods: We used T1-weighted and FLAIR images obtained from 128 subjects from hospitals in south Korea. Each image underwent bias field correction, co-registration, and skull stripping. In each subject, 60 axial cross-sections with brain tissue were selected. The collected dataset was divided into 42 subjects for training and 86 subjects for testing purposes. Specifically, 2520 axial slices were used as training and 5160 axial slices were used as test. Traditional diffusion models undergo training across long time steps. Ongoing research aims to mitigate this inefficiency in both the learning and inference processes. To address this problem, an adversarial learning method is employed to minimize the time step[10]. Unlike the standard diffusion model, which predicts noise at each time step, our model is trained to consistently forecast the image at the 0th time step, regardless of the time sequence. The resultant predicted image is assessed through a discriminator to validate the successful removal of noise corresponding to each time step. For an accurate representation of the biological structure present in the T1w image throughout each time step, the T1w image is utilized as input to the G_θ. The L1 loss between the generated FLAIR and the input FLAIR is computed.

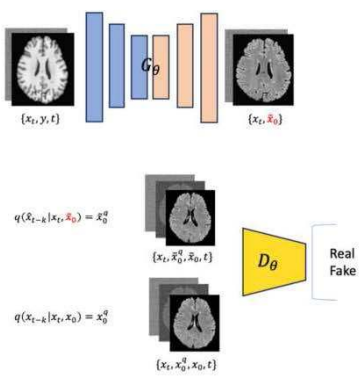

$$L_{G_\theta} = \mathbb{E}_{t,q(x_t|x_0,y),G_\theta(x_{t-k}|x_t,y)}[-log(D_\theta(\hat{x}_{t-k}))] + \mathbb{E}_{x\sim p(x)}[||x_0 - \tilde{x}_0||_1]$$

$$L_\theta = \mathbb{E}_{t,q(x_t|x_0,y)}[\mathbb{E}_{q(x_{t-k}|x_t,y)}[-log(D_\theta(x_{t-k}))] + \mathbb{E}_{G_\theta(x_{t-k}|x_t,y)}[-log(1 - D_\theta(\hat{x}_{t-k}))]]$$

Flg. Overview of Model and loss function

Results: Our model achieved 19.22 PSNR and 80.45 SSIM score on the test set. Notably, it employed approximately half the number of parameters compared to previous studies.

Conclusions: We propose a model that combines diffusion model and density constraints for medical image synthesis. The proposed model improves the sampling speed of diffusion model (1000->2).

References

1. Zhou, T., Liu, M., Thung, K.H., & Shen, D. (2019). Latent Representation Learning for Alzheimer's Disease Diagnosis With Incomplete Multi-Modality Neuroimaging and Genetic Data. IEEE Transactions on Medical Imaging, 38(10), 2411-2422.
2. Junghoon Lee, Aaron Carass, Amod Jog, Can Zhao, & Jerry L. Prince (2017). Multi-atlas-based CT synthesis from conventional MRI with patch-based refinement for MRI-based radiotherapy planning. In Medical Imaging 2017: Image Processing (pp. 101331I). SPIE.
3. Ye, D.H., Zikic, D., Glocker, B., Criminisi, A., Konukoglu, E. (2013). Modality Propagation: Coherent Synthesis of Subject-Specific Scans with Data-Driven Regularization. In: Mori, K., Sakuma, I., Sato, Y., Barillot, C., Navab, N. (eds) Medical Image Computing and Computer-Assisted Intervention – MICCAI 2013. MICCAI 2013. Lecture Notes in Computer Science, vol 8149. Springer, Berlin, Heidelberg. https://doi.org/10.1007/978-3-642-40811-3_76
4. Nie, D. et al. (2017). Medical Image Synthesis with Context-Aware Generative Adversarial Networks. In: Descoteaux, M., Maier-Hein, L., Franz, A., Jannin, P., Collins, D., Duchesne, S. (eds) Medical Image Computing and Computer Assisted Intervention − MICCAI 2017. MICCAI 2017. Lecture Notes in Computer Science(), vol 10435. Springer, Cham. https://doi.org/10.1007/978-3-319-66179-7_48
5. Huang, Y., Shao, L., & Frangi, A. (2018). Cross-Modality Image Synthesis via Weakly Coupled and Geometry Co-Regularized Joint Dictionary Learning. IEEE Transactions on Medical Imaging, 37(3), 815-827.
6. Yu, B., Zhou, L., Wang, L., Shi, Y., Fripp, J., & Bourgeat, P. (2019). Ea-GANs: Edge-Aware Generative Adversarial Networks for Cross-Modality MR Image Synthesis. IEEE Transactions on Medical Imaging, 38(7), 1750-1762.
7. Dhariwal, P., & Nichol, A. (2021). Diffusion Models Beat GANs on Image Synthesis. In Advances in Neural Information Processing Systems (pp. 8780–8794). Curran Associates, Inc..
8. Ho, J., Jain, A., & Abbeel, P. (2020). Denoising Diffusion Probabilistic Models. In Advances in Neural Information Processing Systems (pp. 6840–6851). Curran Associates, Inc..
9. Özbey, M., Dalmaz, O., Dar, S., Bedel, H., Özturk, Ş., Güngör, A., & Çukur, T. (2023). Unsupervised Medical Image Translation With Adversarial Diffusion Models. IEEE Transactions on Medical Imaging, 42(12), 3524-3539.
10. Zhisheng Xiao, Karsten Kreis, & Arash Vahdat (2022). Tackling the Generative Learning Trilemma with Denoising Diffusion GANs.ICLR

Acknowledgements
This work was supported by Institute of Information & communications Technology Planning & Evaluation (IITP) grant funded by the Korea government(MSIT) (No.2020-0-01373, Artificial Intelligence Graduate School Program(Hanyang University)).

Poster No 2413

Consistency of resting-state correlations between fMRI networks and EEG features

Marta Xavier[1], Inês Esteves[1], João Jorge[2], Rodolfo Abreu[3], Anne-Lise Giraud[4], Sepideh Sadaghiani[5], Jonathan Wirsich[6], Patricia Figueiredo[1]

[1]ISR-Lisboa and Department of Bioengineering, Instituto Superior Técnico, Universidade de Lisboa, Lisboa, Portugal, [2]CSEM, Swiss Center for Electronics and Microtechnology, Neuchâtel, Switzerland, [3]Coimbra Institute for Biomedical Imaging and Translational Research (CIBIT), University of Coimbra, Coimbra, Portugal, [4]Department of Neuroscience, University of Geneva, Genève, Switzerland, [5]Beckman Institute, Department of Psychology, University of Illinois at Urbana-Champaign, Urbana, IL, [6]University of Geneva, Genève, Switzerland

Introduction: Simultaneous EEG-fMRI acquisitions have been leveraged to investigate the electrophysiological correlates of fMRI resting-state networks (RSNs). Studies have reported temporal correlations between spontaneous activity of fMRI RSNs and concurrent fluctuations in EEG band-power[1,2]. However, inconsistencies in results exist, possibly due to varying acquisition conditions, pre-processing, and analysis methodologies. We investigated the consistency of correlations between EEG band-power and fMRI RSN activity across subjects and acquisition conditions, using 3 EEG-fMRI datasets at 1.5, 3, and 7T.

Methods: Data acquisition. 1.5T: 10 subjects, Siemens 1.5T MR-scanner, 10min eyes-open rest[3]; fMRI with GRE-EPI (TR/TE=2160/30ms, 3.3x3.3x4.0mm3); EEG with two 32-channel MR-compatible amplifiers (BrainAmpMR) and 63 electrodes (BrainCap). 3T: 23 subjects, Siemens 3T MR-Scanner, 30min eyes-closed rest[4]; fMRI with GRE-EPI (TR/TE=2000/50ms, 3mm isotropic); EEG with a 62-channels BrainAmpMRs. 7T: 9 subjects, Siemens 7T MR-scanner, 8min eyes-open rest[5]; fMRI with gradient-echo 2D-EPI sequence (TR/TE=1000/25ms, 2.2mm isotropic); EEG with two 32-channel BrainAmpMRs and 63 electrodes (EasyCap). Data analysis. fMRI underwent motion correction, nuisance regression of motion and physiological signals, high-pass temporal filtering (0.01Hz) and spatial smoothing. 7 canonical RSNs were identified by group-level ICA and template matching[6], and their fMRI time-series extracted in each subject by regression. EEG was corrected for scanner gradient and pulse artifacts, band-pass filtered (0.3-60Hz), re-referenced, and ICA-denoised. Source reconstructed data[7] was parcellated into the 68 ROIs of the Desikan-Killiany atlas[8]. EEG band-power was estimated with 4s Morlet wavelets for the delta(2-4Hz), theta(5-7Hz), alpha(8-12Hz), beta(15-29Hz), and gamma(3-60Hz) bands. EEG was down-sampled to

the fMRI TR and convolved with a hemodynamic response function (HRF), with overshoot delays of 2,4,5,6,8 and 10s. EEG TRs contaminated with motion were excluded[9]. Pearson's correlation was computed between EEG band-power and fMRI RSN time-series for each HRF delay and in each channel/ROI. Grand-mean scalp- and source-space correlation maps were estimated for each dataset. T-tests assessed the significance of the correlations across subjects. Multi-way ANOVA was performed to evaluate the impact on the channel/ROI-averaged EEG-fMRI correlations of factors dataset, EEG space (scalp/source), RSN, frequency-band, and HRF delay.

Results: Each RSN showed a distinct, frequency- and delay-dependent spatial distribution of EEG power correlations, without strong polarization, as illustrated in Fig.1 for the dorsal attention and default mode networks (DAN and DMN). Significant ($p<0.05$,FDR-corr.) correlations were found (Fig.2) for each dataset, mostly sharing the same direction (positive/negative) across datasets. Consistent observations across datasets included: visual network's positive delta and theta and negative alpha correlations; somatomotor network's positive delta and theta and negative beta and gamma correlations; DAN's negative alpha correlations; frontoparietal network's negative theta and positive gamma correlations; DMN's negative delta and theta and positive alpha and beta correlations. ANOVA showed significant main effects for dataset, RSN, frequency-band, and HRF delay, and various interactions, including a significant triple interaction among dataset, RSN, and frequency-band.

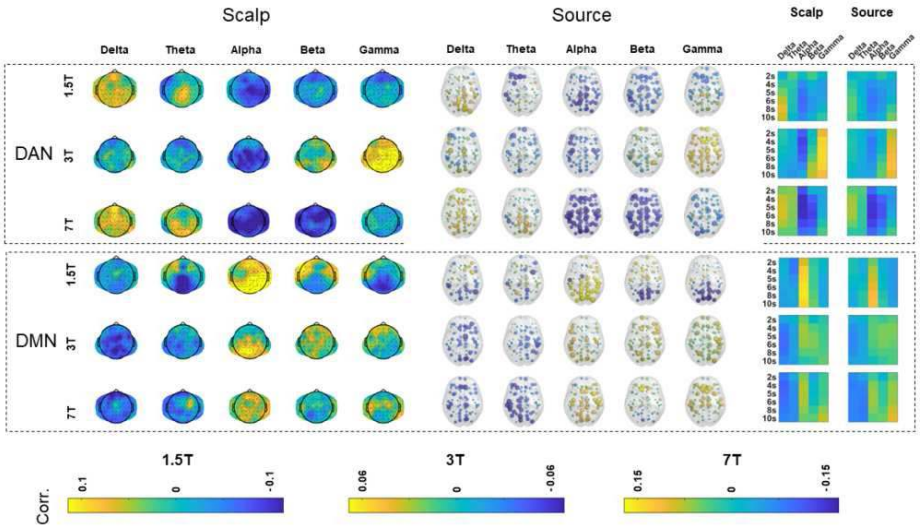

Fig1.Spatial maps of temporal correlations between EEG band-power (delta, theta, alpha, beta and gamma) and fMRI dorsal attention and default mode networks, for three independent datasets (1.5, 3, 7T)

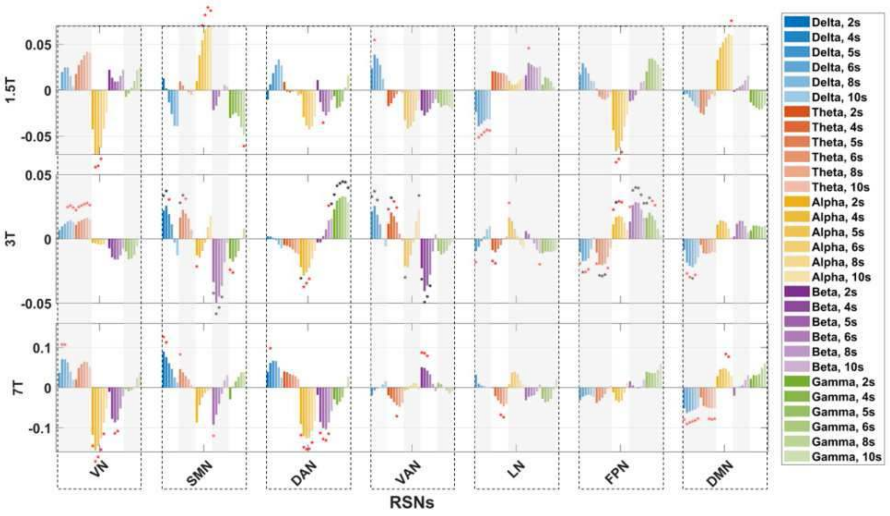

Fig2.Spatially averaged temporal correlations between EEG band-power (delta, theta, alpha, beta, and gamma) and seven canonical fMRI resting-state networks, for three independent datasets (1.5, 3, 7T)

Conclusions: We found consistent temporal correlations between fMRI RSN activity and EEG band-power across subjects in 3 datasets, with variations linked to RSN, EEG frequency-band, and HRF delay, but not EEG space (scalp/source). Despite

differences in field strength, subject number, and resting-state conditions, most correlations were qualitatively similar across datasets. Our findings support the consistency of specific EEG-fMRI correlations and highlight the importance of methodological considerations.

References
1. Mantini et al., National Academy of Sciences of the United States of America, 2007
2. Jann et al., PLoS ONE, 2010
3. Deligianni et al., Frontiers in Neuroscience, 2014
4. Sadaghiani et al., Journal of Neuroscience, 2010
5. Abreu et al., Brain Topography, 2021
6. Yeo et al., Journal of Neurophysiology, 2011
7. Tadel et al., Comput. Intell. Neurosci., 2011
8. Desikan et al., Neuroimage, 2006
9. Wirsich et al., Netw Neurosci., 2020.

Poster No 2414

Simulating how tissue microstructure affects MRI

Michiel Cottaar[1], Zhiyu Zheng[1], Benjamin Tendler[1], Karla Miller[1], Saad Jbabdi[1]

[1]Oxford University, Oxford, United Kingdom

Introduction: MRI has many different modalities that are sensitive to tissue microstructure, including diffusion-weighted MRI, susceptibility-weighted MRI, magnetisation transfer, and quantitative relaxometry. Because many of these modalities are sensitive to different aspects of the same microstructural components (e.g., myelin), combining these modalities may provide a more comprehensive view of those microstructural components. However, these different modalities are usually analysed in isolation with each modality coming with its own set of models and assumptions. Here we present a new Monte Carlo MR (MCMR) simulator[1] that aims to capture different ways that tissue microstructure affects the MRI signal evolution across a wide range of MR modalities, which are presented in Figure 1.

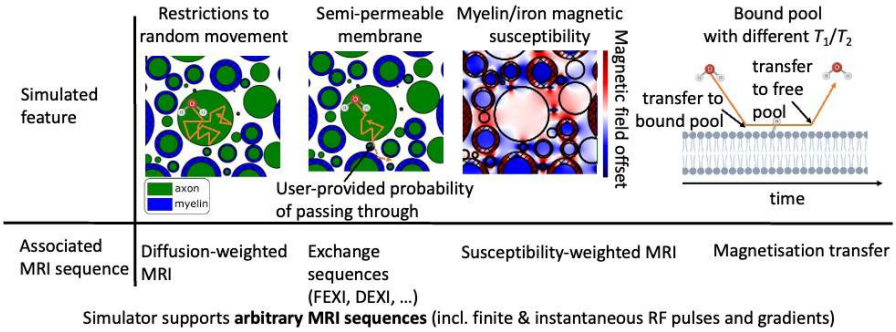

Methods: MCMR simulator has been implemented in the Julia programming language[2]. It has both a Julia and command line interface, with comprehensive documentation and tutorials available for both. An overview of the simulator methodology is shown in Figure 2. Briefly, the user synthesises a tissue geometry (consisting of any combination of infinite walls, infinite cylinders, spheres, and arbitrary meshes), and defines one or more MR sequences for which the MR signal will be computed in parallel. These sequences can include finite or instantaneous radiofrequency (RF) pulses and gradients and can be flexibly defined by the user or directly read from pulseq files[3]. For each sequence the simulator will predict the MRI signal for a single voxel. The simulator uses a Monte Carlo approach, which follows the random walk of individual spins, which is hindered by the user-provided tissue geometry. The spin magnetisation is updated using the Bloch equations, which includes the off-resonance field due to the tissue magnetic susceptibility of myelinated, infinite cylinders, or of arbitrary meshes. At each collision with the tissue, there is also user-defined probability of spins to pass through the surface, which enables the modelling of exchange. Otherwise, the spin will bounce back. Magnetisation transfer is implemented by allowing the spin magnetisation to transfer to a stationary “bound” pool during a collision with the tissue. The magnetisation transfer is controlled by a user-defined surface density and dwell time. The permeability, bound pool properties, and the magnetic susceptibility can be set on a global level or set to a different values for different simulated objects (down to individual triangles in any meshes), which would allow one to vary the permeability or myelination between cells or even along individual axons. Similarly, the relaxation rates of the free water are usually set globally, but can be updated within specific compartments. While the simulator does provide some support for generating geometries consisting of randomly distribution

cylinders or spheres, for more complicated geometries we recommend generating a mesh using an existing tool[4-7] (e.g., Config[5] which was used to generate the mesh in Figure 2).

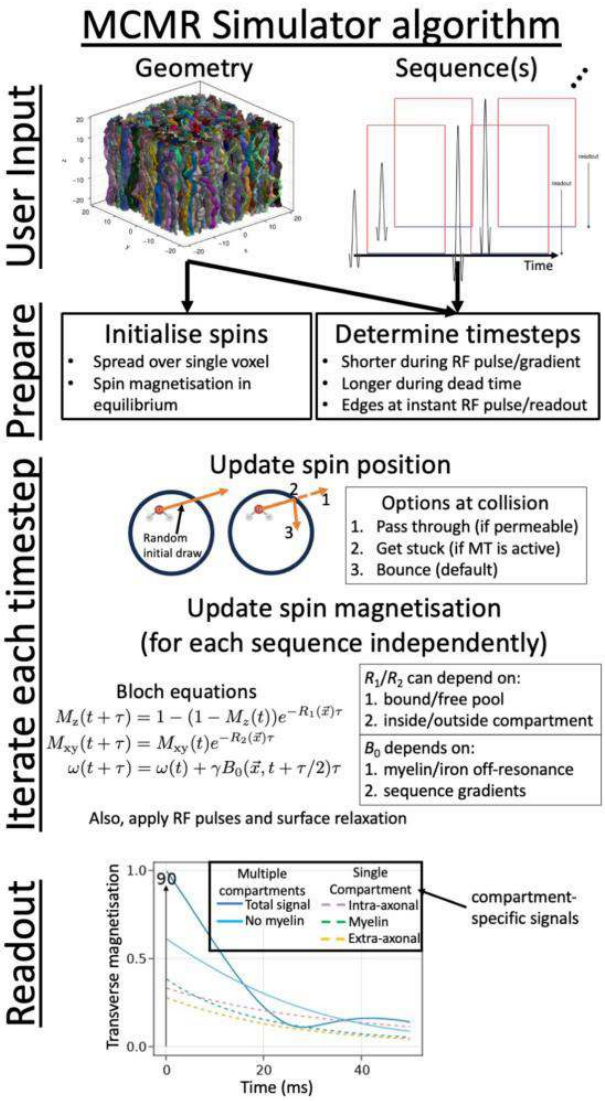

Results: By combining the effects of diffusion, permeability (exchange), magnetic susceptibility, and magnetisation transfer in the MCMR simulator, we allow for a more coherent analysis of these different ways microstructure affects the MRI signal. One could change one aspect of the tissue microstructure (e.g., reduce myelin thickness) and investigate its effect on a wide range of different MRI acquisitions. This could be used to help interpret changes seen in multi-modal MRI acquisitions or for the development of new acquisition protocols (or sequences) sensitive to specific aspects of the tissue microstructure.

Conclusions: Documentation including installation instructions and tutorials for both the Julia and command line interface is available at https://open.win.ox.ac.uk/pages/ndcn0236/mcmrsimulator.jl/stable/. The code is available at https://git.fmrib.ox.ac.uk/ndcn0236/mcmrsimulator.jl.

References

1. Cottaar, M. (2022) 'MCMRSimulator.jl'. Zenodo. doi:10.5281/zenodo.7318657.
2. Bezanson, J. et al. (2017) 'Julia: A fresh approach to numerical computing', SIAM review, 59(1), pp. 65–98.
3. Layton, K.J. et al. (2017) 'Pulseq: A rapid and hardware-independent pulse sequence prototyping framework', Magnetic Resonance in Medicine, 77(4), pp. 1544–1552. doi:10.1002/mrm.26235.
4. Palombo, M., Alexander, D.C. and Zhang, H. (2019) 'A generative model of realistic brain cells with application to numerical simulation of the diffusion-weighted MR signal', NeuroImage, 188, pp. 391–402. doi:10.1016/j.neuroimage.2018.12.025.
5. Callaghan, R. et al. (2020) 'Config: Contextual fibre growth to generate realistic axonal packing for diffusion mri simulation', NeuroImage, 220, p. 117107. doi:10.1016/j.neuroimage.2020.117107.
6. Ginsburger, K. et al. (2019) 'MEDUSA: A GPU-based tool to create realistic phantoms of the brain microstructure using tiny spheres.', Neuroimage, 193, pp. 10–24. doi:10.1016/j.neuroimage.2019.02.055.
7. Villarreal-Haro, J.L. et al. (2023) 'CACTUS: a computational framework for generating realistic white matter microstructure substrates', Frontiers in Neuroinformatics, 17. Available at: https://www.frontiersin.org/articles/10.3389/fninf.2023.1208073.

Poster No 2415

Beyond unimodal data: an fMRI-electrophysiological-hormonal account of brain signal variance

Giulia Baracchini[1], Jason da Silva Castanheira[1], Laura Pritschet[2], Tyler Santander[2], Hannah Grotzinger[2], Emily Jacobs[2], Mallar Chakravarty[3], R. Nathan Spreng[1]

[1]Montreal Neurological Institute and Hospital, McGill University, Montreal, Quebec, [2]University of California Santa Barbara, Santa Barbara, CA, [3]Brain Imaging Centre, Douglas Research Centre, Montreal, Quebec

Introduction: Within-subject variability of fMRI BOLD signals is often considered as mere noise[1], yet it is associated with behavior, age and clinical status[2-3]. The promising translational value of BOLD signal variability is constrained by a lack of understanding of its properties and drivers[4]. fMRI data alone cannot be used to gain insight into the sources of brain signal variance, given the limitations posed by the physics of fMRI BOLD. More broadly, the interplay between brain and body signals may be of particular importance. Here, we merge across neuroimaging and brain-body modalities to build a framework for BOLD signal variability that has the potential to accelerate discovery.

Methods: In the first experiment (Fig 1), we bridged across neuroimaging modalities to identify which signal properties drive brain signal variability. We leveraged empirical ranges of amplitude, frequency and background 'noise' of fMRI and electrophysiological data, to fit Fast Fourier Transforms and simulate multi-modal timeseries. We manipulated, one at a time, the afore-mentioned parameters (1000 iterations) and, for each iteration, we quantified signal variability via the root Mean Square of Successive Differences (rMSSD)[5]. In the second and third experiments (Fig 1), given the clinical applicability of fMRI, we aimed at identifying the within-subject reliability of BOLD signal variability, and quantified the interplay between brain-body signal variance. We leveraged an open-source, multi-modal, deeply phenotyped, micro-longitudinal (n=1, healthy female, age 23) dataset of fMRI BOLD and hormonal data, collected over 30 consecutive days[6]. fMRI data were preprocessed and denoised following previous studies[6-7]. For each day, we obtained rMSSD measures and hormonal concentrations of estrogen, progesterone, LH, FSH and testosterone from blood samples. To assess reliability of BOLD variability, we used product-to-moment correlations between whole-brain rMSSD measures across the 30 days. To quantify the interplay between daily rMSSD and hormonal scores, we used Multiple Factor Analysis (MFA)[8] – a multivariate method similar to Principal Component Analysis that aims at explaining the shared variance between repeated measures of separate sets of variables. Network-level rMSSD values were entered in MFA, as defined by the Schaefer 400 regions-7 network atlas[9].

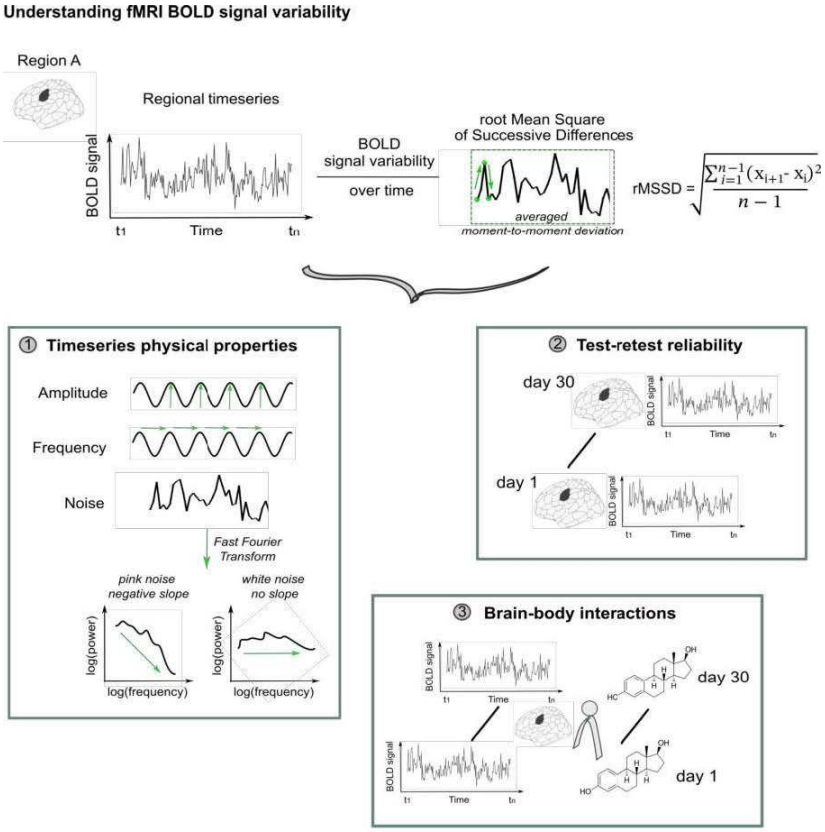

Figure 1. Here, we conducted three investigations aimed at building a comprehensive understanding of fMRI BOLD signal variability. In this figure, we summarize our three experimental paradigms.

Results: fMRI BOLD signal variability was driven by changes in signal amplitude and background 'noise', such that greater variability was obtained at higher amplitude and lower background 'noise' levels. Negligible effects were observed when manipulating BOLD signal frequency (Fig 2A). Electrophysiological simulations showed that signal variability can reflect changes in frequency, when a broader frequency range is provided than the one observed with fMRI. BOLD signal variability exhibited high test-retest reliability (median r=0.93; Fig 2B) and showed a positive association with daily fluctuations in estrogen levels (r=0.50, p=0.005). Daily fluctuations in brain signal variability strongly loaded together with daily hormonal fluctuations (PC1 38% variance; Fig 2C), highlighting how variations in the BOLD signal are rooted in complex interactions between brain and body. Estrogen variations preferentially mapped onto brain signal variations from modulatory networks (Salience and Default; PC2 31% variance; Fig 2C), and brain-body interactions additionally clustered based on the phases of the menstrual cycle (menses vs ovulatory window; Fig 2C).

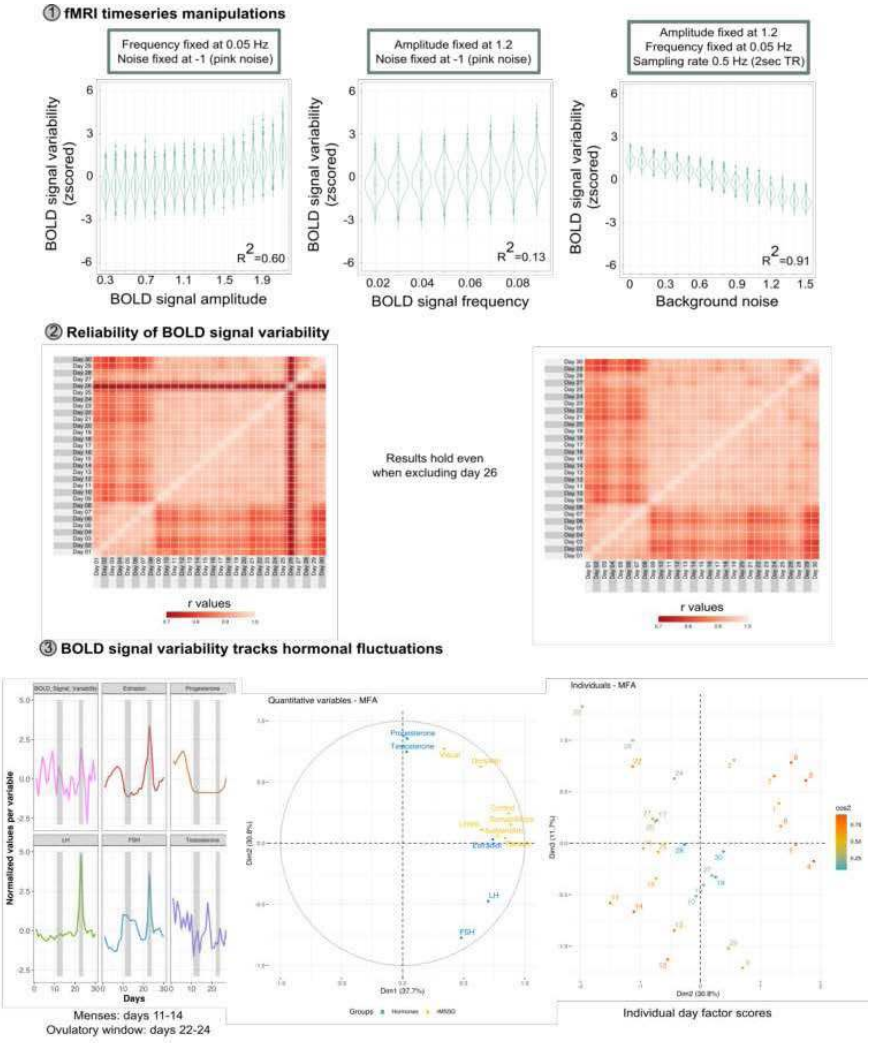

Figure 2. In our first experiment, we manipulated amplitude, frequency and background noise levels of simulated fMRI and electrophysiological timeseries. In Panel 1, we show the results for our fMRI simulations, where we identified amplitude and background noise changes to be the main drivers of BOLD signal variability. In our second experiment, we evaluated the test-retest reliability of BOLD signal variability. In Panel 2, we show the high reliability of BOLD variability across days. In our third experiment, we assessed the interaction between brain and body signal variance. In Panel 3, we show how BOLD signal variability tracked hormonal fluctuations across 30 days (left), how estrogen fluctuations preferentially mapped onto default and salience network fluctuations (middle), and how brain-body interactions clustered based on the phases of the menstrual cycle (days 11-14 vs days 22-24; right).

Conclusions: Altogether, our study demonstrates the significance of conducting cross-modal investigations on brain signal dynamics, as a way to more fully capture the complexity of a fundamental property of biological signals -variance-, and maximize the insights and translational applicability of brain signal variability.

References

1. Baracchini, G., et al. (2021). Inter-regional BOLD signal variability is an organizational feature of functional brain networks. NeuroImage, 237, 118149.
2. Rieck, J. R., et al. (2022). Reduced modulation of BOLD variability as a function of cognitive load in healthy aging. Neurobiology of Aging, 112, 215-230.
3. Månsson, K. N., et al. (2022). Moment-to-moment brain signal variability reliably predicts psychiatric treatment outcome. Biological Psychiatry, 91(7), 658-666.
4. Baracchini, G., et al. (2023). The biological role of local and global fMRI BOLD signal variability in human brain organization. bioRxiv, 2023-10.

5. Von Neumann, J., et al. (1941). The mean square successive difference. The Annals of Mathematical Statistics, 12(2), 153-162.
6. Pritschet, L., et al. (2020). Functional reorganization of brain networks across the human menstrual cycle. Neuroimage, 220, 117091.
7. Grotzinger, H., et al. (2023). Diurnal fluctuations in steroid hormones tied to variation in intrinsic functional connectivity in a densely sampled male. bioRxiv, 2023-10.
8. Abdi, H., et al. (2013). Multiple factor analysis: principal component analysis for multitable and multiblock data sets. Wiley Interdisciplinary reviews: computational statistics, 5(2), 149-179.
9. Schaefer, A., et al. (2018). Local-global parcellation of the human cerebral cortex from intrinsic functional connectivity MRI. Cerebral cortex, 28(9), 3095-3114.

Poster No 2416

Neuronal dynamics and functional topology of the rodent default mode network

Tzu-Hao Chao[1], Byeongwook Lee[2], LiMing Hsu[1], Domenic Cerri[1], Wei-Ting Zhang[1], Tzu-Wen Wang[1], Srikanth Ryali[2], Vinod Menon[2], Yen-Yu Shih[1]

[1]The University of North Carolina at Chapel Hill, Chapel Hill, NC, [2]Stanford University, Palo Alto, CA

Introduction: Brain imaging studies have shed light on the topology and function of large-scale brain networks. Given the inherent constraints of human studies, rodent models are uniquely positioned for probing the neural basis of DMN dynamics using invasive approaches; however, the translational utility of rodent models is currently limited by an incomplete understanding of rodent DMN. Here, we first examine the synchronization of neuronal activitiy in prelimbic (PrL), cingulate (Cg), retrosplenial (RSC), and anterior insular (AI) cortex in rat DMN during anesthetized resting-state. We then present salient stimuli to awake behaving rats, aiming to functionally characterize roles of putative DMN nodes. Together, these results revealed neuronal activity changes in PrL, Cg, and RSC preceding fMRI-derived DMN activations and cyclical transitions between brain network states. We also demonstrate that salient oddball stimuli suppress PrL, Cg, and RSC and enhance AI neuronal activity. These findings elucidate the neurophysiological foundations of rodent DMN, its spatiotemporal dynamical properties, paving the way for future translational studies[1]. Further, we simultaneously imaged two awake mice during spontaneous social behavior and observed robust synchronization in key DMN region. These techniques offer compelling advantages for future efforts mapping functional brain networks.

Methods: We concurrently measured neuronal calcium activity in the RSC, Cg, PrL, and AI of Thy1-GCaMP6f transgenic rats with an MR-compatible, 4-channel, fiber photometry platform (Fig. 1A). We used our platform and computational modeling to characterize DMN and AI neuronal dynamics under resting-state and awake, salient stimuli conditions. We further developed a silent fMRI method named Steady-state On-the-Ramp Detection of INduction-decay signal with Oversampling (SORDINO) for hyperscanning study between two awake face-to-face mice.

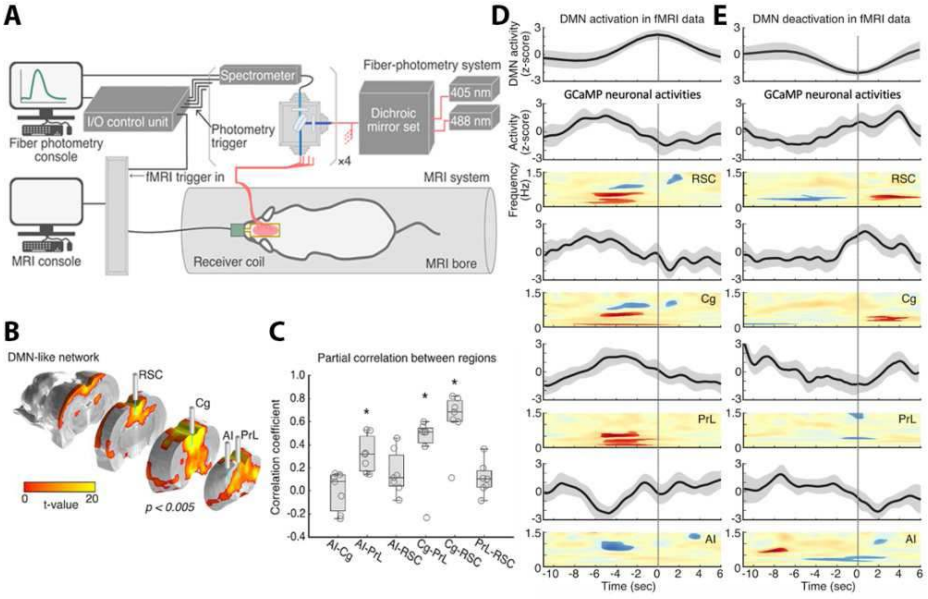

Figure 1.

Results: We found: 1) robust neuronal resting-state connectivity between RSC, Cg, and PrL (Fig. 1B, C); 2) specific patterns of neuronal activity in the AI and the RSC, Cg, and PrL in relation to fMRI-derived DMN activation and deactivation peaks (Fig. 1D, E); 3) significant neuronal inhibitory causal outflow from AI to RSC, Cg, and PrL during resting-state condition (Fig. 2A, B); 4)

cyclical state transitions characterized by neuronal activity in AI being intermittently in and out of phase with activity of RSC, Cg, and PrL during resting-state condition (Fig. 2C-E); 5) salient stimulus–induced activation of AI and deactivation of RSC, Cg, and PrL in free-moving rats (Fig. 2F, G); and 6) PrL synchronization across two face-to-face mouse brains during social interaction (Fig. 2H-K), whereas S1 showed no synchronization between the two mouse brains (Fig. 2L-N).

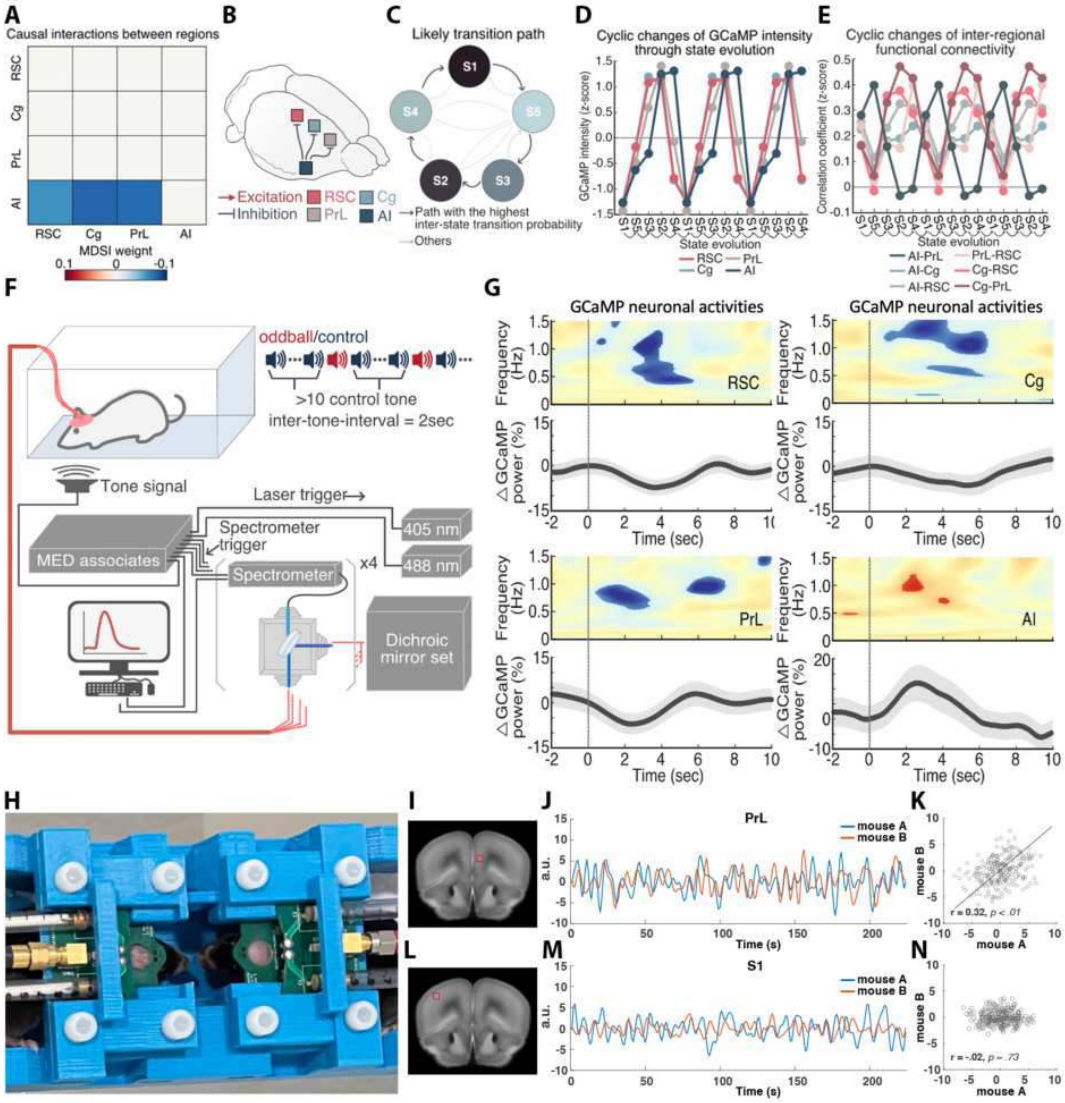

Figure 2.

Conclusions: Our results provide neuronal activity evidence that RSC, Cg, and PrL function as DMN nodes in rodent brain, with RSC and Cg showing the closest correspondence in their dynamics and PrL exhibiting a potentially dual-purpose role at the interface between DMN and SN. Our results also reveal a neuronal basis of causal inhibitory control from AI to RSC that facilitate access to attentional resources as observed in fMRI studies. These findings identify a translational and neural correspondence between AI and DMN responses in rats to salient task-relevant stimuli and show that rodent AI plays a causal role in DMN-SN dynamic switching. Our proof-of-concept hyperscanning study further corroborates the findings by showing PrL synchronization across two face-to-face mice, in agreement with human studies showing synchronized DMN during social interaction[2-4]. Together, our study paves the way for future translational studies using rodent models to investigate cellular basis of cognitive control circuits, which can help understand the dynamic properties of brain states, define their relationship to behaviors, and ultimately design network-based treatment regimens for neuropsychiatric and neurological disorders.

References

1. Chao, T.H. (2023) 'Neuronal dynamics of the default mode network and anterior insular cortex: Intrinsic properties and modulation by salient' stimuli', Science Advances, vol 9, pp. eade5732
2. Yeshurun, Y. (2021). The default mode network: where the idiosyncratic self meets the shared social world. Nature Reviews Neuroscience, vol. 22, no. 3, pp. 181-192.
3. Yoshioka, A. (2021). Neural substrates of shared visual experiences: a hyperscanning fMRI study. Social Cognitive and Affective Neuroscience, vol. 16, no. 12, pp. 1264-1275.
4. Liang, Z. (2022). Increased or decreased? Interpersonal neural synchronization in group creation. NeuroImage, vol. 260, pp. 119448.

Poster No 2417

Resecting BOLD Responses Related to Spikes and High Frequency Oscillations Improves Surgical Outcome

William Wilson[1], Daniel Pittman[1], Perry Dykens[1], Victoria Mosher[1], Laura Gill[1], Joseph Peedicail[1], Antis George[1], Craig Beers[1], Bradley Goodyear[1], Paolo Federico[1]

[1]*University of Calgary, Calgary, Alberta*

Introduction: Simultaneous intracranial EEG-fMRI (iEEG-fMRI) may be used to identify candidate regions for resection in patients with drug-resistant focal epilepsy. This is achieved by mapping the blood oxygen-level dependent (BOLD) activation associated with events of interest, typically epileptiform spikes, captured in the EEG. However, the activation maps associated with spikes have shown only moderate sensitivity and specificity for epileptogenic tissue essential for resection (Koupparis et al., 2021). High frequency oscillations (HFOs) have been proposed as a novel EEG marker that may better localize epileptogenic tissue than spikes in the pre-operative brain (Thomschewski et al., 2019). The hemodynamic response to HFOs measured using simultaneous iEEG-fMRI and its relation to epileptogenic tissue is not known. In this study, we evaluated the relationship between resection of areas of HFO-related BOLD activation and post-operative outcome. Further, we compared the post-operative predictive capabilities of both HFO-related BOLD activation and the BOLD activation associated with the more conventional marker, spikes.

Methods: Thirty-eight adult patients with focal epilepsy undergoing intracranial video-EEG monitoring were enrolled in this study. Each patient underwent a 60-minute iEEG-fMRI scan. Standard preprocessing steps were applied to the fMRI data (motion correction, slice-timing correction, non-brain removal, spatial smoothing, high-pass temporal filtering, and noise removal using independent component analysis). iEEG data were preprocessed by removing gradient switching artifact using an in-house algorithm and downsampling to 2500Hz. The timing of spikes and HFOs in the EEG recording were identified for each patient and used to generate statistical maps of related activity. The Maximum positive BOLD cluster was identified in each map. The resulting maps were then stratified into low, medium, and high confidence groups based on the magnitude of the z-score of the Maximum cluster relative to the second maximum cluster, a method shown to identify more localizing maps (Koupparis et al., 2021; Khoo et al., 2017). Patients then underwent epilepsy surgery guided by established clinical investigations, and not the iEEG-fMRI data. Spatial concordance of the Maximum cluster with the area of resection was determined using post-operative imaging. Concordance was related to post-operative outcome >12 months after surgery.

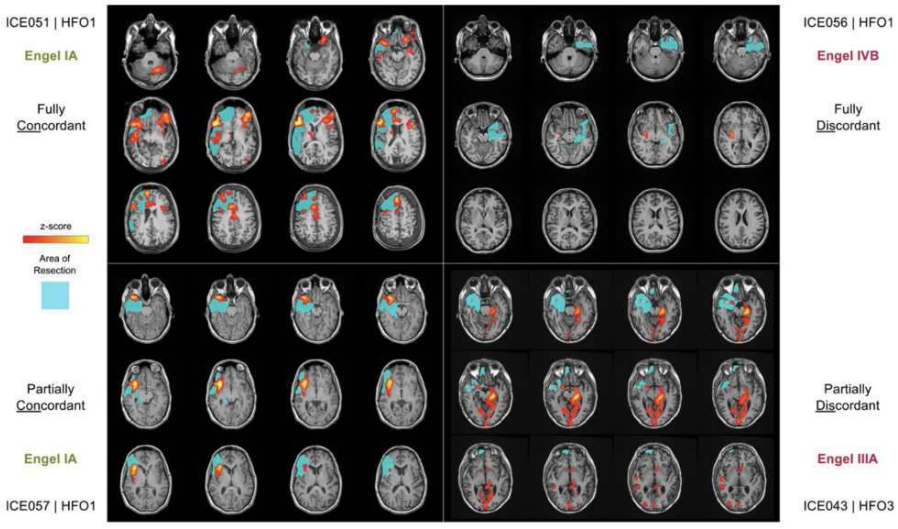

Figure 1: Classification of spatial concordance between the Max BOLD cluster and the area of resection. (Top left) Example of a subject where the Max BOLD cluster was fully concordant with the area of resection (i.e., peak voxel was resected) and the subject is seizure free (Engel IA). (Top right) Example of a subject where the Max BOLD cluster was fully discordant with the area of resection (i.e., no cluster was resected) and the subject continues to experience seizures (Engel IVB). (Bottom left) Example of a subject where the Max BOLD cluster was partially concordant with the area of resection (i.e., peak voxel not resected, but overlap with Max BOLD cluster) and the subject is seizure free (Engel IA). (Bottom right) Example of a subject where the Max BOLD cluster is partially discordant with the area of resection (i.e., no part of the Max BOLD cluster was resected, but another less significant cluster was resected) and the subject continues to experience seizures (Engel IIIA).

Results: At the time of last clinical follow up (mean interval = 4.5 years; range = 1.0 – 14.9 years), 21/38 (55%) subjects had a good post-operative outcome, and 17/38 (45%) subjects had a poor post-operative outcome. Resection of the peak voxel of high confidence Maximum clusters was associated with good post-operative outcomes for both spikes and HFOs (p = 0.040 and 0.035, Fisher exact test). HFOs were found to additionally predict outcome in cases where the peak voxel was not removed, but some other part of the Maximum cluster overlapped with the area of resection. More specifically, we found that resection of >30% of the Maximum HFO-related cluster was associated with good outcome (sensitivity = 80% and specificity = 80%). In all significant associations, a negative predictive value of 100% was observed accompanied by poor positive predictive values.

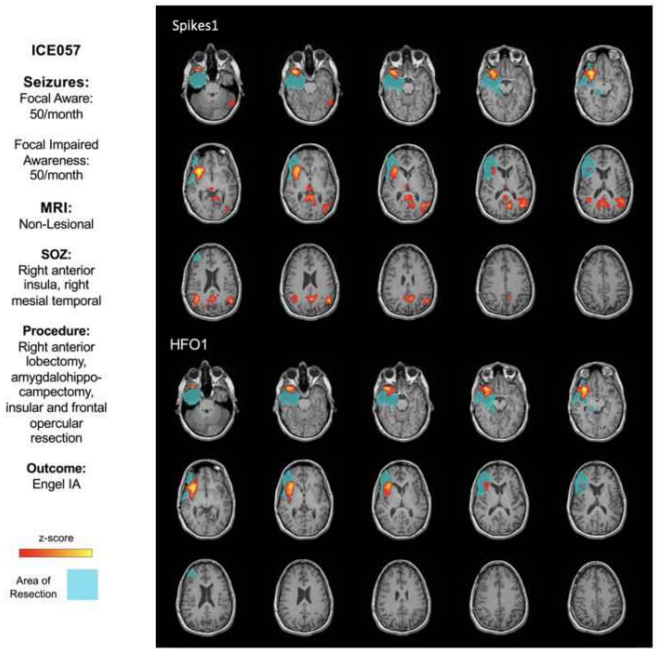

Figure 2: Spatial concordance between the Maximum BOLD cluster and the area of resection in subject ICE057. (Top) Activation map associated with spikes and its overlap with the area of resection (light blue). The Maximum BOLD cluster was fully concordant with the area of resection (i.e., peak voxel was resected) and the subject is seizure free (i.e., Engel IA). (Bottom) Activation map associated with HFOs.

Conclusions: Investigating the hemodynamic response to HFOs using iEEG-fMRI is feasible and generates maps of related activity that may further enhance localization of epileptogenic tissue critical to surgical planning. Furthermore, confidence level, which takes into account how distinct the Maximum cluster is relative to other areas of activation, should be considered when interpreting EEG-fMRI results of spikes and HFOs. Finally, removal of the peak voxel associated with both spikes and HFOs is necessary but not sufficient to achieve a good post-operative outcome. However, HFOs may provide useful spatial information in a broader range of patients undergoing intracranial monitoring.

References

1. Khoo, H. M. (2017), 'The hemodynamic response to interictal epileptic discharges localizes the seizure-onset zone', Epilepsia, vol. 58, no. 5, pp. 811–823
2. Koupparis, A. (2021), 'Association of EEG-fMRI Responses and Outcome After Epilepsy Surgery', Neurology, vol. 97, no. 15, pp. e1523–e1536
3. Thomschewski, A. (2019), 'Localization of the Epileptogenic Zone Using High Frequency Oscillations', Frontiers in Neurology, vol. 10, no. 94

Poster No 2418

Using structural-functional brain data fusion to explore adverse childhood experiences related PTSD

Richard Nkrumah[1], Claudius Claudius von Schröder[2], Traute Demirakca[3], Lemye Zehirlioglu[4], Sabine Vollstaedt-Klein[5], Christian Schmahl[6], Gabriele Ende[7]

[1]Dept. of Neuroimaging, Central Institute for Mental Health, Heidelberg University, Mannheim, Select a State or Province, [2]Department of Psychosomatic Medicine & Psychotherapy,Central Institute for Mental Health, Heidelberg, Mannheim, Baden württemberg, [3]Dept. of Neuroimaging, Central Institute for Mental Health, Heidelberg University, Mannheim, Germany, [4]Dept. of Psychosomatic & Psychotherapy, Central Institute for Mental Health, Heidelberg University, Mannheim, Baden württemberg, [5]Department of Addictive Behavior and Addiction Medicine, Central Institute for Mental Health, Heidel, Mannheim, Baden württemberg, [6]Department of Psychosomatic Medicine & Psychotherapy,Central Institute for Mental Health, Heidelberg, Mannheim, Germany, [7]Dept. of Neuroimaging, Central Institute for Mental Health, Heidelberg University, Mannheim, Baden württemberg

Introduction: Identifying neuroimaging biomarkers associated with ACE-related posttraumatic stress disorder (PTSD) is an active area of psychotraumatology research. Neuroimaging studies have demonstrated widespread abnormalities in brain structure and function in PTSD[1]. Fusing functional and structural imaging informed sources has also grown in interest based on the recent advances in neuroimaging data acquisition and analysis. Specifically, data-driven joint connectivity matrix independent component analysis of both structural (SC) and functional connectivity (FC) has recently been explored in a healthy subject sample and shows a promising method for connectivity-based multimodal neuroimaging data fusion[2]. Additionally, most of the previous PTSD studies focused on only one specific modality or not specific trauma-related PTSD, and thus the relationship between these isolated structural and functional alterations in ACE-related PTSD individuals remains poorly understood[3]. In this study, we performed joint connectivity matrix independent component analysis, in an ACE-related PTSD sample compared to ACE-exposed control. Based on the extant literature, we hypothesised that differences in fronto-parietal (FP) and salient (SN) networks differences between groups.

Methods: A total of 119 participants with any form of ACE were included in this study. Participants completed the Childhood Trauma Questionnaire (CTQ), the Structured Clinical Interview for DSM-5 (SCID-II), and the Life Event Checklist (LEC) for PTSD to ascertain the severity of ACE exposure, lifetime PTSD diagnosis, and the presence of other possible events associated with PTSD. PTSD=70, ACE severity (i.e. CTQtotal, PTSD=72.59, noPTSD=51.80), age (PTSD=31.67, noPTSD=29.22), sex (PTSD=64F, noPTSD=37F), and overall trauma load (PTSD=2.33, noPTSD=2.04) were computed. T1-weighted images were acquired, preprocessed, parcellated, and segmented into cortical and subcortical nodes. Diffusion and resting-state fMRI data were also collected and preprocessed, and SC and FC were retrieved using cmp3. The SC measure included individual measures of normalised fibre density and the number of fibres between nodes, while the FC measure included negative and positive correlation measures between nodes. All connectivity matrices were controlled for age, sex, ACE severity and trauma load and then normalised by rescaling the range of the data to a [0, 1] interval. Data-driven PCA/ICA was performed using a joint connectivity matrix that was obtained by fusing individual subjects by SC & FC measures data (Fig.1) using FIT. Finally, a shared mixing matrix between the four connectivity matrices was produced by taking an average of independent components (IC) computed over 10 runs, and a t-test was performed on shared weighted matrix data to identify components that were significantly different between groups. Conversely, the two previously reported brain networks in ACE/PTSD literature were then explored in the components that showed significant results.

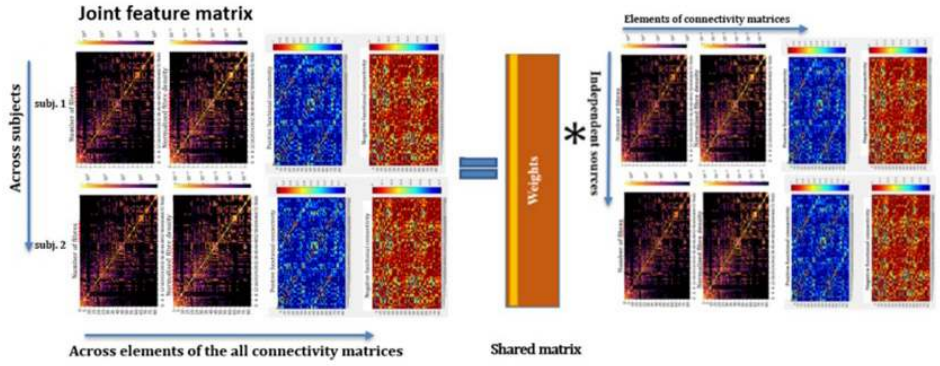

Figure 1. Number of fibres, normalized fibre density, positive functional connectivity and Negative functional connectivity features are stacked side by side to create a joint matrix. The number of IC is stacked vertically. The joint feature matrix is then modelled as a spatially independent sources and with shared weighted matrix. Figure was adapted from Khalilullah et. al, (2023).

Results: After correcting for multiple comparisons using Bonferroni, the joint mixing coefficient matrix for component 9 was significantly different between groups ($p < 0.001$, Figure 2A). Figure 2B shows the difference in the SC & FC measures between the noPTSD vs PTSD group from component 9. Overall, compared to the no-PTSD group, the PTSD group had reduced SC & FC measures in both SN & FP.

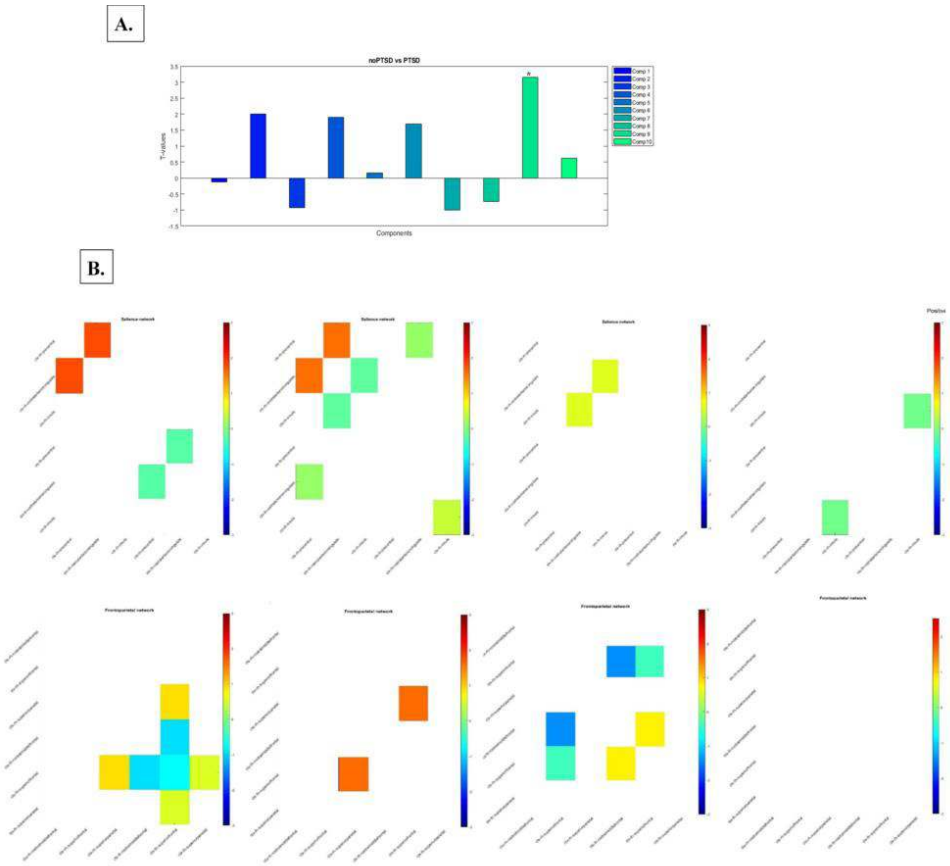

Figure 2. Two sample t-test was computed on the mixing coefficients between the noPTSD vs PTSD. **A.** Plot of the T-values of the t-test computed on all components. (*) shows component with significant pvalue after Bonferroni correction.

B. Networks in the number of fibres (column 1), normalised fibre density (column 2), negative functional connectivity (column 3), and positive functional connectivity (column 4) are measured in component 9. Networks include the bilateral regions in the salience network in row 1 (SN: precentral, rostralanteriorcingulate and insula) and the bilateral regions in the fronto-parietal network in row 2 (FP: rostralmiddlefrontal, superiorfrontal, and superiorparietal).

Conclusions: Using a joint connectivity matrix independent component analysis, we identified networks previously reported in literature to be statistically significant between ACE-exposed PTSD compared to ACE-exposed controls. Our findings in the salience network and frontal parietal network, which include regions such as the superior parietal lobe, extend the literature on the effect of PTSD on the brain, especially in regions involved in communication, social behaviour, self-awareness and attentional functioning[7,8].

References

1. McLaughlin, K. A., Koenen, K. C., Bromet, E. J., Karam, E. G., Liu, H., Petukhova, M., ... Kessler, R. C. (2017). Childhood adversities and post-traumatic stress disorder: Evidence for stress sensitisation in the World Mental Health Surveys
2. Wu, L., & Calhoun, V. (2023). Joint connectivity matrix independent component analysis: Auto-linking of structural and functional connectivities.
3. McLaughlin, K. A., Weissman, D., & Bitrán, D. (2019). Childhood Adversity and Neural Development: A Systematic Review.
4. Tourbier, S., Rue-Queralt, J., Glomb, K., Aleman-Gomez, Y., Mullier, E., Griffa, A., ... Hagmann, P. (2022). Connectome Mapper 3: A Flexible and Open-Source Pipeline Software for Multiscale Multimodal Human Connectome Mapping.
5. The FIT Documentation Team (2020). Fusion ICA (FIT). Retrieved from https://trends-public-website-fileshare.s3.amazonaws.com/public_website_files/software/fit/docs/v2.0e_FIT_Manual.pdf
6. Khalilullah, K. M. I., Agcaoglu, O., Sui, J., Adali, T., Duda, M., & Calhoun, V. D. (2023). Multimodal fusion of multiple rest fMRI networks and MRI gray matter via parallel multilink joint ICA reveals highly significant function/structure coupling in Alzheimer's disease.
7. Nkrumah, R. O., Schröder, C. von, Demirakca, T., Schmahl, C., & Ende, G. (2023). Cortical volume alteration in the superior parietal region mediates the relation between the childhood abuse and PTSD avoidance symptoms: a complementary multimodal neuroimaging study
8. Cardenas, V. A., Samuelson, K., Lenoci, M., Studholme, C., Neylan, T. C., Marmar, C. R., ... Weiner, M. W. (2011). Changes in brain anatomy during the course of posttraumatic stress disorder.

Poster No 2419

Developing Methods for Precision High-Density Diffuse Optical Tomography

Aahana Bajracharya[1], Dana Wilhelm[2], Zachary Markow[3], Morgan Fogarty[3], Wiete Fehner[3], Jonathan Peelle[4], Tmara Hershey[5], Joseph Culver[2]

[1]Washington University in St.Louis, St. Louis, MO, [2]Washington University School of Medicine, St. Louis, MO, [3]Washington University in St. Louis, St. Louis, MO, [4]Northeastern University, Boston, MA, [5]Washington University in St. Louis, Saint Louis, MO

Introduction: Neuroimaging research has traditionally approached data reliability through large-N consortium studies. However, in recent years, precision mapping studies, focusing on obtaining a high signal-to-noise ratio from a small group of individuals, have opened new avenues of exploring brain function[1]. Precision mapping takes a subject-specific approach to localize spatial and organizational variability in brain networks[2,3]. Although widely known in functional magnetic resonance imaging (fMRI) literature, this approach is yet to be established in optical imaging. In this study, we demonstrate the effectiveness of using High-Density Diffuse Optical Tomography (HD-DOT) to generate high-fidelity single-subject cortical maps[4]. HD-DOT is an optical imaging technique that uses dense, regularly spaced arrays of sources and detectors to obtain overlapping measurements of the underlying neuronal activity based on the absorption properties of hemoglobin in the blood[5-8]. We use an imaging system consisting of 128 sources and 125 detectors, with over 2500 measurements providing state-of-the-art HD-DOT image quality and extended cortical coverage (with a flatfield depth sensitivity >50% max, that extends to 20 mm beneath the scalp surface). Unlike fMRI, HD-DOT has a significant advantage of conducting scans while seated comfortably in a quiet and naturalistic environment.

Methods: We collected 4-6 hours of data from previously validated tasks (retinotopy, hearing words, finger tapping/tongue movement, and generating verbs) and resting-state paradigms over multiple visits on 4 subjects (2M, 2F) (Fig1A). While fMRI data can be easily co-registered to anatomical scans, HD-DOT depends on measured and simulated cap positions for image reconstruction. To address this issue, we developed an iterative process of comparing cortical activations using functional localizers and photometric validation of cap placement. This process involved placing the cap onto the participant's head by aligning the back row of fiber tips to the inion and symmetrically positioning the side panels over the ear with reference to the tragus (Fig1B). A silicone stencil with cap position marked from the first session was used to register subsequent sessions in addition to photometric references. Data pre-processing was done based on the principles of modeling light emission, diffusion, and detection through the head using the NeuroDOT toolbox[7]. We used global variance of temporal derivative (GVTD)[8] to identify motion artifacts in data frames and the strength of the cardiac pulse signal to assess data quality (Fig 1C). A voxel-wise general linear model framework was used to estimate the task responses and generate statistical maps of cortical activations.

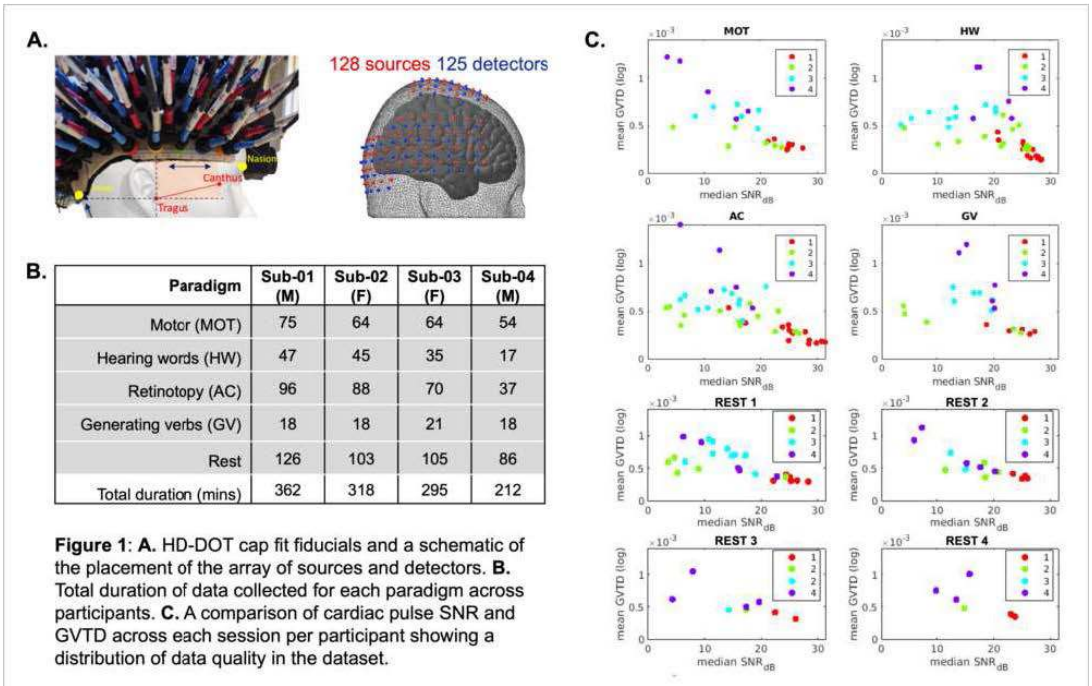

Paradigm	Sub-01 (M)	Sub-02 (F)	Sub-03 (F)	Sub-04 (M)
Motor (MOT)	75	64	64	54
Hearing words (HW)	47	45	35	17
Retinotopy (AC)	96	88	70	37
Generating verbs (GV)	18	18	21	18
Rest	126	103	105	86
Total duration (mins)	362	318	295	212

Figure 1: **A.** HD-DOT cap fit fiducials and a schematic of the placement of the array of sources and detectors. **B.** Total duration of data collected for each paradigm across participants. **C.** A comparison of cardiac pulse SNR and GVTD across each session per participant showing a distribution of data quality in the dataset.

Results: Fig 2A shows task activation maps averaged across all sessions of data in each participant. A spherical seed (radius = 5mm) around the peak activation voxel of the functional localizers was used to generate resting state functional connectivity

(RSFC) maps. Fig 2B shows five sessions of unthresholded beta maps while Sub-1 viewed a flashing checkerboard stimulus presented in the bottom right quadrant. Fig 2C shows RSFC map from five rest sessions with a seed placed in the left visual cortex. Fig 2D-E shows the correlation between the maps generated from concatenated sessions of data with smaller windows of this data. The overarching premise of precision mapping is that the maps become more stable as the number of trials or duration of data increases.

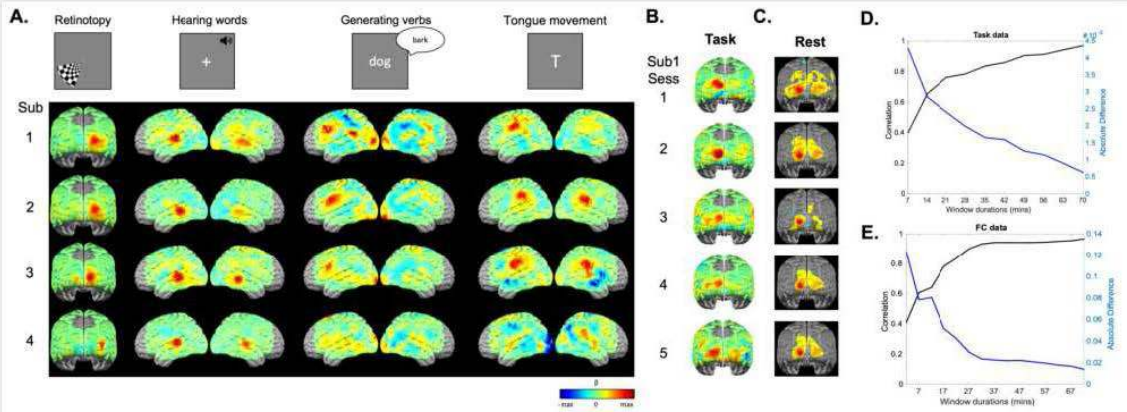

Figure 2: A. Single-subject functional localizers from retinotopy task (~8 mins with 6 trials of either left or right flashing checkboard each), passive listening to 6 blocks of 15 words (~4 mins), passively generating verbs for 6 blocks of 15 nouns (~4 mins), moving tongue side to side for 6 trials of each condition (~10 mins). **B.** Data from right visual stimulation and **C.** left visual seed RSFC for 5 sessions of data collection on Sub-1. Correlation and difference between the maps generated from concatenated sessions of data with smaller windows of this data for **D.** task and **E.** rest.

Conclusions: Accurate single-subject mapping can inform changes in functional brain activity over time. This valuable resource helps to understand individual brain organization while also improving group-level analyses. We demonstrate the feasibility of using HD-DOT to carry out precision mapping using task-based and resting state paradigms which can cater to a wide variety of participants, including children and individuals with implanted medical devices that are contraindicated by MRI.

References

1. Gratton C, Nelson SM, Gordon EM (2022): Brain-behavior correlations: Two paths toward reliability. Neuron.
2. Gordon EM, Laumann TO, Gilmore AW, Newbold DJ, Greene DJ, Berg JJ, Ortega M, Hoyt-Drazen C, Gratton C, Sun H, Hampton JM, Coalson RS, Nguyen AL, McDermott KB, Shimony JS, Snyder AZ, Schlaggar BL, Petersen SE, Nelson SM, Dosenbach NUF (2017): Precision Functional Mapping of Individual Human Brains. Neuron.
3. Laumann TO, Gordon EM, Adeyemo B, Snyder AZ, Joo SJ, Chen M-Y, Gilmore AW, McDermott KB, Nelson SM, Dosenbach NUF, Schlaggar BL, Mumford JA, Poldrack RA, Petersen SE (2015): Functional System and Areal Organization of a Highly Sampled Individual Human Brain. Neuron.
4. Bajracharya, A., Wilhelm, D., Markow, Z., Fogarty, M., Fehner, W., Peelle, J.E., Hershey, T., and Culver, J.P., "Precision Functional Mapping of Cortical Activity Using High-Density Diffuse Optical Tomography (HD-DOT)," in Optics and the Brain, JTu4B–15 (2023).
5. Wheelock MD, Culver JP, Eggebrecht AT (2019): High-density diffuse optical tomography for imaging human brain function. Review of Scientific Instruments.
6. Eggebrecht AT, Ferradal SL, Robichaux-Viehoever A, Hassanpour MS, Dehghani H, Snyder AZ, Hershey T, Culver JP (2014): Mapping distributed brain function and networks with diffuse optical tomography. Nat Photonics.
7. Eggebrecht AT, Culver JP (2019): NeuroDOT: an extensible Matlab toolbox for streamlined optical functional mapping. Diffuse Optical Spectroscopy and Imaging VII. International Society for Optics and Photonics.
8. Sherafati A, Snyder AZ, Eggebrecht AT, Bergonzi KM, Burns-Yocum TM, Lugar HM, Ferradal SL, Robichaux-Viehoever A, Smyser CD, Palanca BJ, Hershey T, Culver JP (2020): Global motion detection and censoring in high-density diffuse optical tomography. Hum Brain Mapp.

Poster No 2420

The Association of Mother-Infant Neural Synchrony and Bonding – Ad Interim Results

Debora Suppiger[1,2], Sabino Guglielmini[1,3], Tilman Reinelt[1,2], Martin Wolf[3,2], Giancarlo Natalucci[1,2,4]

[1]FLRF Center for Neurodevelopment, Growth and Nutrition of the Newborn, Zurich, Switzerland, [2]University of Zurich, Zurich, Switzerland, [3]Biomedical Optics Research Laboratory, Neonatology Research, University Hospital Zurich, Zurich, Switzerland, [4]University Hospital Zurich, Zurich, Switzerland

Introduction: Background Brain-to-brain coupling, or neural synchrony, refers to the time-dependent association of two or more brain signals[10,8]. In adults, increased neural, physiological or behavioral synchrony is associated with attachment and communication facilitation[7,8]. Various forms of physiological (e.g., heart rate) and behavioral (e.g., gaze) synchrony have been observed in infants and their parents in situations such as play or breastfeeding[2,5]. Furthermore, these forms of synchrony have been associated with attachment and bonding, as well as infant developmental outcomes[2,3]. First evidence of parent-

infant neural synchrony has been observed during parents singing nursery rhymes[6] or having proto-conversations with their infant[9], indicating the importance of neural synchrony in language development. Recently, neuro-behavioral coupling during mother-infant play was associated to caregiving profiles[1], portraying neural synchrony as a regulatory factor in infant social development. So far, no study has investigated whether neural synchrony is also associated with mother-infant relationship. The current project provides preliminary results on mother-infant neural and physiological synchrony. Research Questions • Do mother and infant brains synchronize during social play interactions? • Does neural synchrony increase with physical touch?

Methods: The sample consists of 15 mothers (Mage = 34.56 years) and their infants (52.94 % female; Mage = 220.17 days; Mgestational_age= 39.31 weeks). Three pairs were excluded from the analysis due to the lack of optical coupling between the optodes caused by the dense hair of the mother. In a free interaction situation, the mother and infant play with each other, whilst the infant sits in a highchair (5 min) or is held by their mother on the lap (2 min). During baseline, the pair watches a cartoon with no direct interaction (4 min). During all conditions, systemic-augmented fNIRS hyperscanning[4] is applied in bilateral prefrontal (PFC) and temporo-parietal regions (TP). Time and frequency dependent correlation between the concentration changes of oxyhemoglobin ([O2Hb]) was calculated using the wavelet transform coherence (WTC). Mean coherence was evaluated for two frequency bands: the low frequency band (LF, 0.015–0.15 Hz) and the heart rate band (HR, 1–2.5 Hz). Furthermore, the WTC for 1200 random pairs was calculated as a control analysis for each condition and frequency band.

Results: Preliminary results in the LF band showed a trend in all regions of interest: the mean coherence during the on-the-lap condition was higher compared to the other two conditions, especially compared to the baseline, this however remains non-significant. For the HR frequency band, statistically higher coherence was found in the left PFC during the on-the-lap condition compared to the baseline ($p = 0.036$). For the control analysis, we found statistically significant differences in the HR band during the on-the-lap condition in all the regions of interest ($p < 0.05$). The same was found for this frequency band during the face-to-face (left TP, right PFC) and the baseline condition (left and right PFC) ($p < 0.05$). The control analysis shows a statistically significant higher synchrony in real pairs than in random pairs.

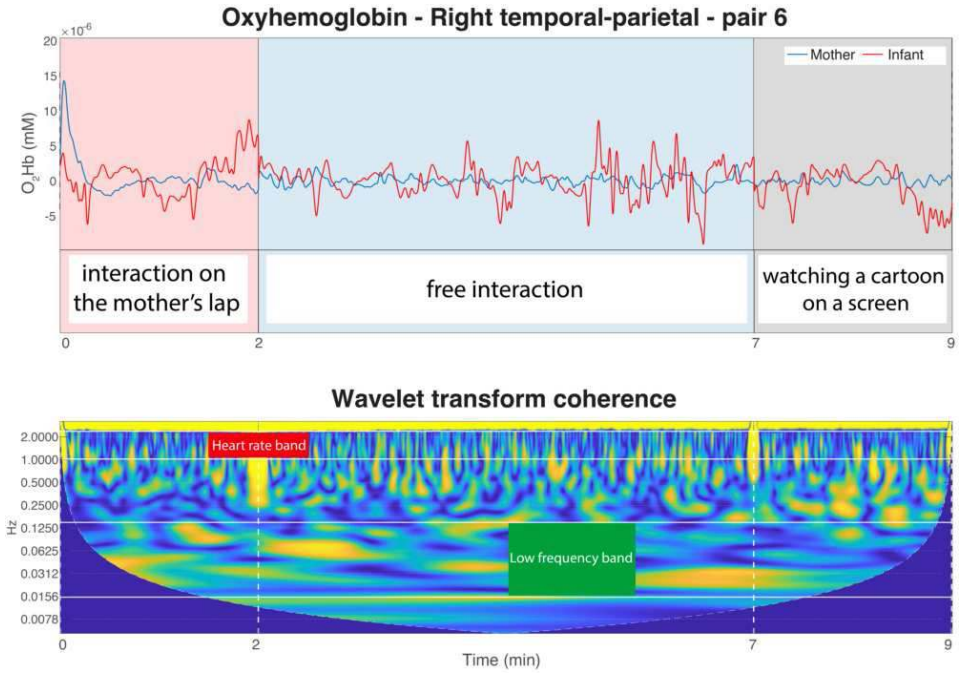

Figure 1 shows O2Hb in the right TP region of mother-infant pair 6. Below relative WTC between the signals, yellow indicating higher synchrony.

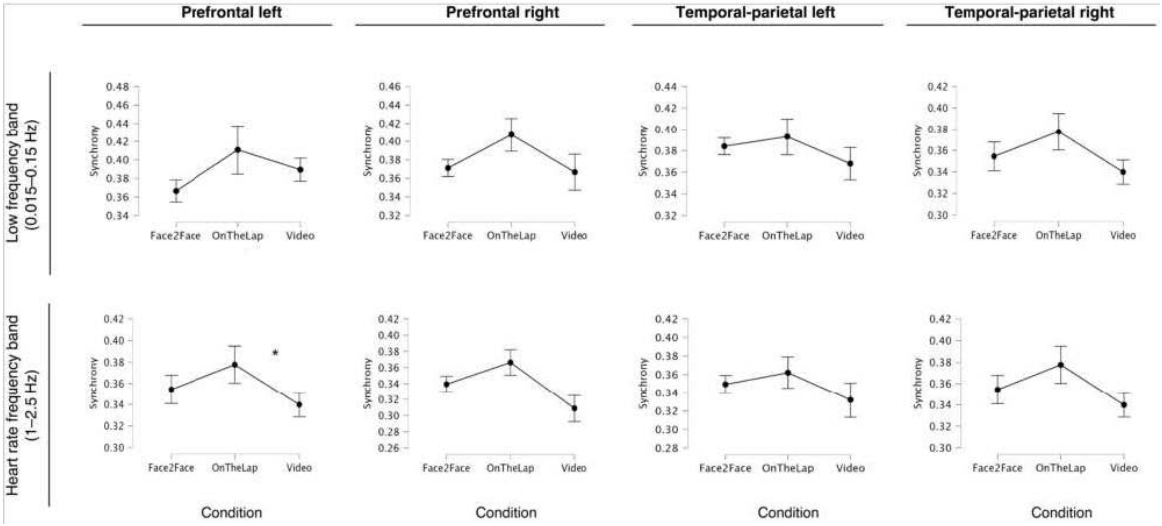

Figure 2 shows mean WTC in low (LF) and heart rate (HR) frequency band for all three conditions (1) playing face-to-face; (2) playing with infant on the lap; (3) baseline watching a cartoon.

Conclusions: Results present evidence of mother-infant brain coupling at 7.5 months during social play interaction, replicating recent findings[1]. Highest levels of synchrony were observed during physical contact and direct interaction in the heart-rate frequency band. Systemic-augmented fNIRS hyperscanning is proposed to be a valuable tool to investigate early parent-child interaction. Synchrony in the LF band was not statistically significant among the three conditions. This is most likely due to the small sample size.

References

1. Endevelt-Shapira, Y. (2023). "Mother-Infant Brain-to-Brain Synchrony Patterns Reflect Caregiving Profiles." Biology 12(2): 284.
2. Feldman, R. (2007). "Parent–Infant Synchrony:Biological Foundations and Developmental Outcomes." Current Directions in Psychological Science 16(6): 340-345.
3. Feldman R. (2012) . "Parent-infant synchrony: A biobehavioral model of mutual influences in the formation of affiliative bonds". Monographs of the Society for Research in Child Development, 77(2):42-51.
4. Guglielmini, S. (2022). "Systemic physiology augmented functional near-infrared spectroscopy hyperscanning: a first evaluation investigating entrainment of spontaneous activity of brain and body physiology between subjects". Neurophoton. 9(2) 026601. https://doi.org/10.1117/1.NPh.9.2.026601
5. Lan, Q.(2022). "Breastfeeding duration and vagal regulation of infants and mothers." Early Human Development 171: 105620.
6. Leong, V. (2017). "Speaker gaze increases information coupling between infant and adult brains." Proceedings of the National Academy of Sciences 114(50): 13290-13295.
7. Markova, G. (2019). "Neurobehavioral Interpersonal Synchrony in Early Development: The Role of Interactional Rhythms." Frontiers in Psychology 10.
8. Nguyen, T. (2020). Chapter 1 - Studying parent-child interaction with hyperscanning. Progress in Brain Research. S. Hunnius and M. Meyer, Elsevier. 254: 1-24.
9. Nguyen, T.2023). "Your turn, my turn. Neural synchrony in mother–infant proto-conversation." Philosophical Transactions of the Royal Society B: Biological Sciences 378(1875): 20210488.
10. Scholkmann, F.(2013). "A new methodical approach in neuroscience: assessing inter-personal brain coupling using functional near-infrared imaging (fNIRI) hyperscanning." Frontiers in Human Neuroscience 7.

Poster No 2421

Functional human brain mapping using whole head very-high-density diffuse optical tomography

Morgan Fogarty[1], Sean Rafferty[2], Anthony O'Sullivan[2], Calamity Svoboda[2], Zachary Markow[1], Edward Richter[1], Tessa George[1], Kelsey King[2], Dana Wilhelm[2], Kalyan Tripathy[2], Jason Trobaugh[1], Adam Eggebrecht[2], Joseph Culver[2]

[1]Washington University in St. Louis, St. Louis, MO, [2]Washington University School of Medicine, St. Louis, MO

Introduction: Functional neuroimaging has seen a rise in engaging and ecologically valid natural stimuli like podcasts and movies. While fMRI is the gold standard for functional neuroimaging, this technique involves a loud, unnatural scanning environment in the isolated magnet bore. Optical imaging with functional near infrared spectroscopy (fNIRS) allows for greater flexibility in imaging due to an open-air scanning environment, minimal (to no) acoustic noise, and portability (depending on the system). High-density diffuse optical tomography (HD-DOT) uses a dense array of optical elements to provide multiple multi-distance overlapping fNIRS light measurements. These measurements, together with tomographic reconstruction

techniques, improve image quality over traditional fNIRS and recover brain activations and resting state networks with fidelity comparable to fMRI (Eggebrecht et al., 2014). However, HD-DOT has a resolution of ~15 mm, which doesn't extend to the physical limits of this imaging method (Markow et al., 2023). Here we explore the image quality improvements achieved when doubling the optode count and decreasing the inter-optode spacing from 13 mm to 9.75 mm while maximizing whole-head coverage for usage in naturalistic and decoding imaging studies.

Methods: Our very-high-density DOT (VHD-DOT) system consists of 255 sources and 252 detectors in a regular rectangular grid of 9.75 mm nearest neighbor spacing (Fig 1A), resulting in approximately 5,000 measurements per wavelength. While only a 33% decrease in spacing from our HD-DOT system, this generates an approximately 200% increase in the number of measurements and directly translates to higher resolution and image quality as the point-spread function decreases in size with increasing grid density (Fig 1B-E). We also expanded the field of view to include bilateral aspects of occipital, temporal, parietal, and prefrontal areas (Fig 1F). The system was validated with 11 healthy adult participants completing a series of standard block-design localizer tasks (finger tapping, word hearing, verb generation, and retinotopy), and movie viewing in both VHD-DOT and MRI. The movie viewing task consisted of two viewings of the same 10-minute movie clip (Fishell et al., 2019). Beta value maps were generated using a GLM approach and responses were aggregated across subjects using random effect t-statistics. Functional localizer responses were also included in a six-way decoding task by generating a template from half of the blocks (3 blocks total) in each run and then computing the correlation between the template and the remaining 3 blocks individually. Similarly, correlations between the first and second movie viewing runs were used for template-based decoding across varying time durations.

Results: Through simulations, we prove our VHD-DOT system outperforms our HD-DOT system using standard image quality metrics (Fig 1B-E). Data quality was assessed in measurement space for each imaging session (Fig 1G-I). Functional localizer t-statistic maps appear consistent between fMRI and VHD-DOT across all tasks (Fig 1J-K). Localizer decoding offers insight into imaging performance across the cap for each subject (Fig 2A-C). Localizer decoding performance across all subjects resulted in an accuracy of 73.7% (Fig 2D) – well above the chance level of 17% when using oxy-, deoxy- and total hemoglobin (Fig 2E-G). For movie viewing, decoding accuracies remained above chance across the varying clip lengths and with an increasing number of clip choices (Fig 2H-K).

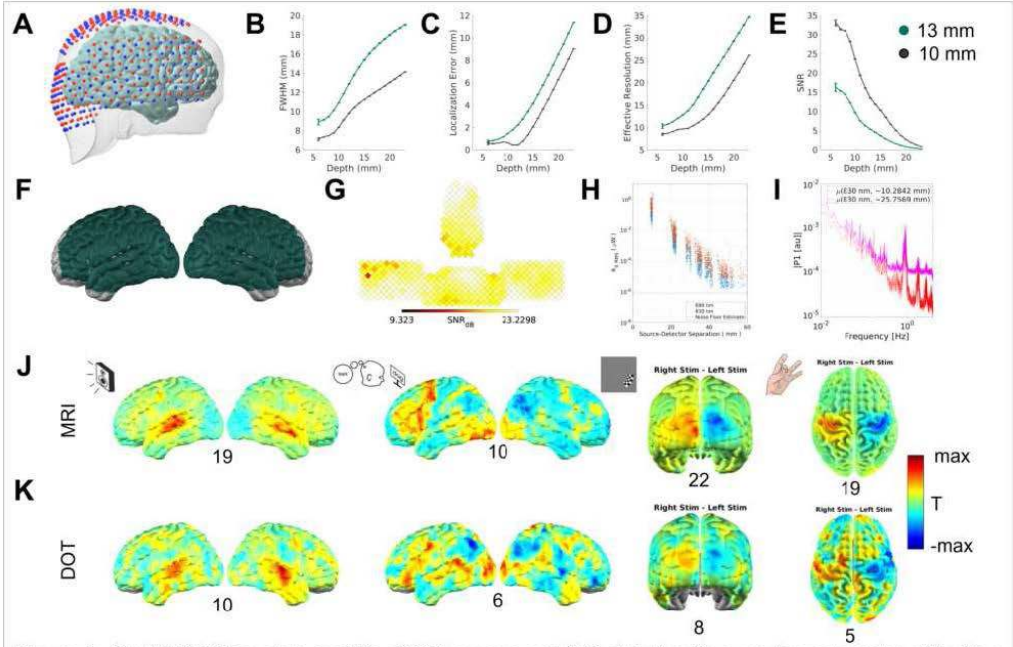

Figure 1: Our VHD-DOT system consists of 255 sources and 252 detectors in a regular rectangular grid with a source-detector separation of 9.75mm (A). Simulations comparing the VHD-DOT system and our previous HD-DOT system (13 mm) suggests improved image quality based on the FWHM of the point spread functions (B), localization error (C), effective resolution (D), and signal to noise ratio (E). The field of view of the system covers the majority of the cortex (F) and single subject data quality are presented using the mean band limited SNR (G), light fall off (H), and Fourier spectra (I). Group average t-statistic maps for the localizer tasks in fMRI (J) and DOT (K) display similar results suggesting our VHD-DOT system can achieve results comparable to fMRI.

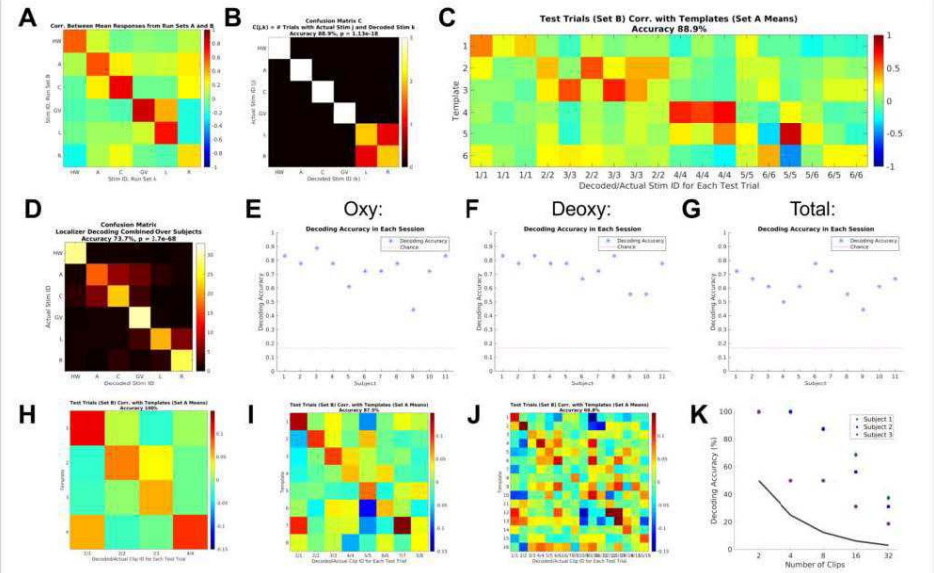

Figure 2: Six-way localizer decoding performance for a single subject (A-C) suggests that we can accurately discriminate between the six tasks (hearing words, left visual, right visual, verb generation, left motor, right motor). High correlations between matched task 3-block spatiotemporal templates and 3-block spatiotemporal test blocks demonstrates localizer mapping capabilities of the VHD-DOT system (A). Decoding performance is visualized in a single subject using a confusion matrix (B) and single trial correlations (C). Across subjects, we achieve a decoding accuracy of 73.7% and visualize results in a confusion matrix (D). Decoding accuracy for each subject using oxy- (E), deoxy- (F), and total (G) hemoglobin exhibits we can achieve high accuracy across chromophores. Audiovisual movie decoding in a single subject (H-J) shows high performance as the number of clip options increased and the length of the clips decreased. Decoding accuracy is shown for three subjects with the number of clips ranging from 2 to 32 clips (K).

Conclusions: Overall, these results show that we can map brain function across the majority of the cortex using our VHD-DOT system. This builds upon our previously reported HD-DOT systems to improve the image quality and resolution of whole-head optical imaging in adults. This system is promising for future work involving whole-head studies of resting state functional connectivity and expanding our decoding paradigms to more naturalistic opportunities (Tang et al., 2023).

References

1. Eggebrecht, A. T., Ferradal, S. L., Robichaux-Viehoever, A., Hassanpour, M. S., Dehghani, H., Snyder, A. Z., Hershey, T., & Culver, J. P. (2014). Mapping distributed brain function and networks with diffuse optical tomography. Nature Photonics, 8(6), 448-454. https://doi.org/10.1038/nphoton.2014.107
2. Fishell, A. K., Arbeláez, A. M., Valdés, C. P., Burns-Yocum, T. M., Sherafati, A., Richter, E. J., Torres, M., Eggebrecht, A. T., Smyser, C. D., & Culver, J. P. (2020). Portable, field-based neuroimaging using high-density diffuse optical tomography. NeuroImage, 215, 116541. https://doi.org/10.1016/j.neuroimage.2020.116541
3. Fishell, A. K., Burns-Yocum, T. M., Bergonzi, K. M., Eggebrecht, A. T., & Culver, J. P. (2019). Mapping brain function during naturalistic viewing using high-density diffuse optical tomography. Scientific Reports, 9(1). https://doi.org/10.1038/s41598-019-45555-8
4. Markow, Z. E., Trobaugh, J. W., Richter, E. J., Tripathy, K., Rafferty, S. M., Svoboda, A. M., Schroeder, M. L., Burns-Yocum, T. M., Bergonzi, K. M., Chevillet, M. A., Mugler, E. M., Eggebrecht, A. T., & Culver, J. P. (2023). Ultra-high density imaging arrays for diffuse optical tomography of human brain improve resolution, signal-to-noise, and information decoding. https://doi.org/10.1101/2023.07.21.549920
5. Tang, J., LeBel, A., Jain, S., & Huth, A. G. (2023). Semantic reconstruction of continuous language from non-invasive brain recordings. Nature Neuroscience. https://doi.org/10.1038/s41593-023-01304-9
6. Tripathy, K., Markow, Z. E., Fishell, A. K., Sherafati, A., Burns-Yocum, T. M., Schroeder, M. L., Svoboda, A. M., Eggebrecht, A. T., Anastasio, M. A., Schlaggar, B. L., & Culver, J. P. (2021). Decoding visual information from high-density diffuse optical tomography neuroimaging data. NeuroImage, 226. https://doi.org/10.1016/j.neuroimage.2020.117516

Poster No 2422

Measuring Neural Correlates of Motor Imitation in Autistic and Non-autistic Adults and Children

Tessa George[1], Dalin Yang[1], Chloe Sobolewski[1], Sophia McMorrow[2], Sung Min Park[3], René Vidal[4], Mary Nebel[5], Bahar Tunçgenç[6], Natasha Marrus[7], Stewart Mostofsky[5], Adam Eggebrecht[8]

[1]Washington University in St. Louis, St. Louis, MO, [2]Washington University School of Medicine in St. Louis, Saint Louis, MO, [3]Washington University in St. Louis, Saint Louis, MO, [4]University of Pennsylvania, Philadelphia, PA, [5]Kennedy Krieger Institute, Baltimore, MD, [6]University of Nottingham, Nottingham, United Kingdom, [7]Washington University School of Medciine, St. Louis, MO, [8]Washington University School of Medicine, St. Louis, MO

Introduction: Imitation is crucial to social-communicative development, and imitation deficits are linked to autism spectrum disorder[1,2]. Imitation measures at brain and behavioral levels could thereby provide biomarkers for advancing targeted

diagnosis and intervention[1,2]. Development of brain-based biomarkers of autism-associated differences in motor imitation has proved challenging. Gold standard neuroimaging with functional magnetic resonance imaging (fMRI) is limited by sensitivity to motion artifacts (of millimeters in extent), and the constrained, supine position is incompatible with overt naturalistic motion. High-density diffuse optical tomography (HD-DOT) provides fMRI-comparable image quality in an open scanning environment conducive to neuroimaging during naturalistic social behavior, including motor imitation[3]. We herein leverage advances in HD-DOT to investigate brain-behavior associations underlying motor imitation and observation in autistic (ASD) and non-autistic control (NAC) school-age and pre-school-age children, with an initial goal of establishing feasibility in a cohort of ASD and NAC adults and school-age children.

Methods: We imaged 97 adults (18-74 years) and 53 school-age children (7-16 years) (Table 1) with HD-DOT[3] (Figure 1A) during motor observation and motor imitation (Figure 1B). Participants observed or imitated videos of an actor completing sequences of arm movements while limiting head motion. Participants were concurrently recorded with Kinect 3D cameras for computer-vision-based assessment of motor imitation (CAMI), which has proven highly effective at distinguishing children with ASD from those without ASD2. Adult participants completed auditory, visual, and motor localizers, and passive movie-viewing. Children completed an auditory task and passive movie-viewing. Behavioral metrics included the Kaufmann Brief Intelligence Test (KBIT 2)[6] and the Social Responsiveness Scale (SRS-2)[5]. HD-DOT data were processed using NeuroDOT (https://www.nitrc.org/projects/neurodot) MATLAB pipelines, including head motion detection and censoring with global variance in the temporal derivative (GVTD), an established, data-driven motion censoring technique inspired by DVARS[4]. We used GLM to compute beta values of the stimulus response relative to rest (e.g., imitation>rest), which were then averaged across runs within participants. We then calculated group-level random effects t-tests for motor imitation, observation, and contrast (imitation>observation) for all groups.

Table 1. Participant demographics and group characteristics

Age		Adults (18-74 years)		Children (7-16 years)	
Group		NAC (n=77)	ASD (n=20)	NAC (n=34)	ASD (n=19)
Sex, Males: Females		29:48	12:8	17:17	13:6
Handedness, Right: Left		70:7	18:2	32:2	19:0
KBIT 2	Verbal	114.5 (18.2)	100.9 (19.2)	113.8 (17.6)	102.1 (18.5)
	Nonverbal	118.7 (14.2)	110.4 (14.5)	114.3 (14.4)	107.6 (14.4)
	IQ	118.8 (16.2)	106.2 (16.7)	116.6 (16.3)	105.9 (16.7)
SRS-2	Raw Score	41.8(29.8)	76.9 (31.2)	33.0 (40.3)	80.7 (41.4)
	T score	50.4 (10.5)	62.9 (11.0)	50.9 (16.1)	69.3 (16.4)

KBIT 2: Kaufmann Brief Intelligence Test, 2nd edition. SRS -2: Social Responsiveness Scale, 2nd edition

Results: For both adults and children, the observation, and imitation t-maps each exhibit expected visual and temporal cortex activations, with additional motor cortex activation during imitation (Figure 1D). The ASD adult contrast map indicates stronger imitation response in right pre-frontal and temporal cortex - patterns not observed in NAC adults. Further, during observation, while NAC and ASD children each show parietal activation, ASD children show increased motor and pre-motor activity.

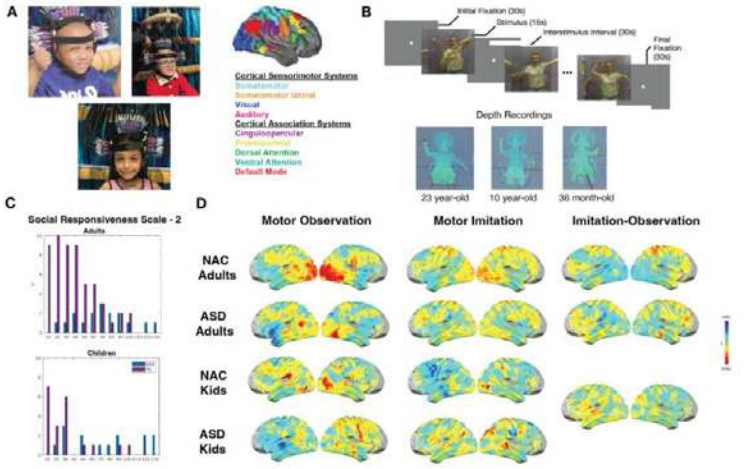

Figure 1 | HD-DOT system, Stimulus design, SRS distributions, motor observation and motor imitation t-maps| **A)** Three example child participants in our HD-DOT system. The field of view of the HD-DOT system on a side view of the cortex highlights multiple key functional cortical sensorimotor and cognitive systems that are modulated by naturalistic viewing of movies and that have been implicated in motor imitation in adults and atypical development associated with ASD. **B)** Stimulus design. The observation and imitation tasks included 30 seconds of initial fixation on a crosshair, followed by six 45-second blocks consisting of a 15-second video of an actor performing unfamiliar arm movements and a 30-second interstimulus interval, and then 30-seconds of final fixation on a crosshair. Stills from depth recordings acquired with a Kinect 3D camera and iPiSoft recording software from an adult and two child participants. **C)** Social Responsiveness Scale - 2 distributions. The SRS-2 is a measure of social reciprocity, with higher scores indicating a higher likelihood of ASD. **D)** Group t-maps of motor observation, imitation, and their contrast (imitation>observation) for adults and kids. Motor observation and imitation t-maps for NAC and ASD adults and children each exhibit expected visual and temporal cortex activations, with motor cortex activation during imitation. The ASD adult contrast map indicates stronger response in right pre-frontal and temporal cortex. In the observation t-maps, NAC, and ASD children each show parietal activations while ASD children show enhanced motor activations.

Conclusions: We herein established the feasibility of utilizing HD-DOT and CAMI to measure brain function underlying motor imitation and observation in ASD and NAC children and adults and highlight differential cortical activity in ASD participants in multiple brain regions such as prefrontal, temporal, and parietal cortex. Our future directions include examining diagnostic and differential transdiagnostic associations of neural signatures and imitation ability with quantitative measures of ASD traits, IQ, and motor ability. Ongoing studies include extending HD-DOT and CAMI to ASD and NAC pre-school-age children (3-6 years; currently n=45).

References

1. Nebel MB (2016). Intrinsic visual-motor synchrony correlates with social deficits in autism. Biological Psychiatry, 79(8),633-41
2. Tunçgenç B. (2021). Computerized assessment of motor imitation (CAMI) as a scalable method for distinguishing autism. Biological Psychiatry: CNNI.6,321-328
3. Eggebrecht AT.(2014). Mapping distributed brain function and networks with diffuse optical tomography. Nature Photonics. 8(6),448-54
4. Sherafati A. (2020) Global motion detection and censoring in high-density diffuse optical tomography. Human Brain Mapping 41(14),4093-4112.
5. Constantino JN. (2012). Social Responsiveness Scale, Second Edition (SRS-2). Torrance, CA: Western Psychological Services.
6. Kaufman, AS. (2004). Kaufman Brief Intelligence Test (2nd ed.). Circle Pines, MN: American Guidance Service.

Poster No 2423

Towards semantic visual decoding of naturalistic movies with high-density diffuse optical tomography

Wiete Fehner[1], Zachary Markow[1], Morgan Fogarty[1], Aahana Bajracharya[2], Dana Wilhelm[3], Alexander Huth[4], Joseph Culver[3]

[1]Washington University in St. Louis, St. Louis, MO, [2]Washington University in St.Louis, St. Louis, MO, [3]Washington University School of Medicine, St. Louis, MO, [4]The University of Texas at Austin, Austin, TX

Introduction: Functional magnetic resonance imaging (fMRI) studies have validated advanced decoding approaches for visual scenes, semantic categories, and natural language using naturalistic stimuli like movies and podcasts[5,6,9]. These advancements are pivotal for the evolution of brain-computer interfaces, which aim to restore communication capabilities impaired by conditions such as aphasia or locked-in syndrome[2]. While fMRI is the natural choice regarding signal-to-noise ratio, whole brain field of view (FOV), and spatial specificity, its use is limited in naturalistic settings due to its size, physical constraints, and cost. In contrast, high-density diffuse optical tomography (HD-DOT) is portable and cost-efficient, allowing the extension of cortical brain mapping to naturalistic environments. This study aims to develop an experimental paradigm to decode semantic categories from natural movie scenes using very high-density DOT (VHD-DOT). One of the primary challenges in using DOT is the lack of anatomical co-registration across sessions. Therefore, establishing repeatability and consistency in cap placements across different sessions is critical for successful decoding. Our group has shown that HD-DOT can decode visual stimuli such as checkerboards and naturalistic movie clips[4,7,10]. However, the field of view was limited to visual regions and the diversity of the training data was restricted. Here, we have expanded the FOV to include the entire head and incorporated a more diverse range of training movies. This marks a significant step towards decoding semantic categories from naturalistic movies. Having a detailed mapping of semantic categories is crucial for natural language decoding[5,9].

Methods: One participant underwent two 83-minute sessions of VHD-DOT imaging, employing a cap equipped with 255 sources and 252 detectors at 9.75 mm inter-optode spacing. To ensure repeatability, a precision protocol involving photometric alignment and facial markers was used for cap placement[1]. Each session included three 10-minute training and testing movie runs. Training movies were unique. In contrast, testing movie clips contained repetitions of three unique 1-minute clips. Clips were utilized from previously validated fMRI studies[5,6] that were manually categorized using semantic categories from WordNet[8] by[5]. Data processing followed an established DOT pipeline by[3], including pre-processing, reconstruction, and spectroscopy. Beta maps for individual runs were generated using a general linear model (GLM) for both auditory and visual localizer tasks. A correlation analysis was conducted to assess repeatability. The correlation coefficients between all possible combinations of task blocks across sessions were computed. The mean correlation value across these pairs was considered a measure of repeatability between sessions. Similarly, a correlation analysis was performed on the test movie clips to evaluate repeatability across runs. Template-based decoding was applied to the test movie data (Figure 1).

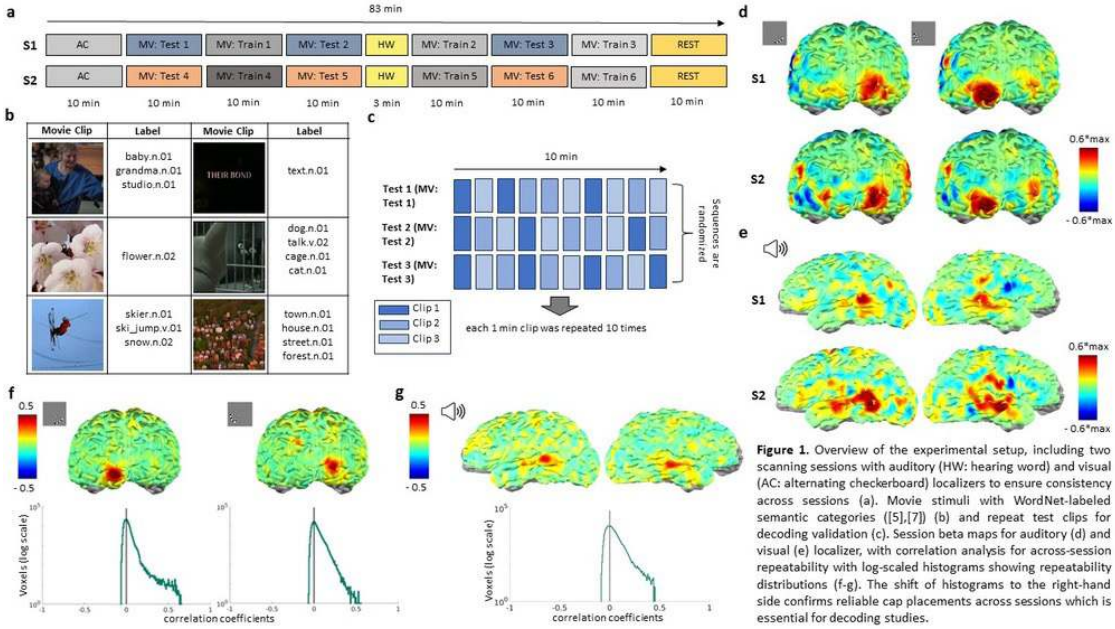

Figure 1. Overview of the experimental setup, including two scanning sessions with auditory (HW: hearing word) and visual (AC: alternating checkerboard) localizers to ensure consistency across sessions (a). Movie stimuli with WordNet-labeled semantic categories ([5],[7]) (b) and repeat test clips for decoding validation (c). Session beta maps for auditory (d) and visual (e) localizer, with correlation analysis for across-session repeatability with log-scaled histograms showing repeatability distributions (f-g). The shift of histograms to the right-hand side confirms reliable cap placements across sessions which is essential for decoding studies.

Results: An experimental design for using VHD-DOT for semantic visual decoding was developed. Correlation analysis indicates a high degree of repeatability across imaging sessions, as shown by localizer task repeatability (Figure 1). Within-session repeatability was established across different test movie runs for both imaging sessions. Repeatability was demonstrated by positively correlated voxels over time, shown by a right-shifted histogram, while the correlation distribution for non-matching clips was centered, confirming distinct clip-induced activation patterns. The template-based decoding results provided additional support for these findings, particularly for clips 1 and 2 from the first session (Figure 2).

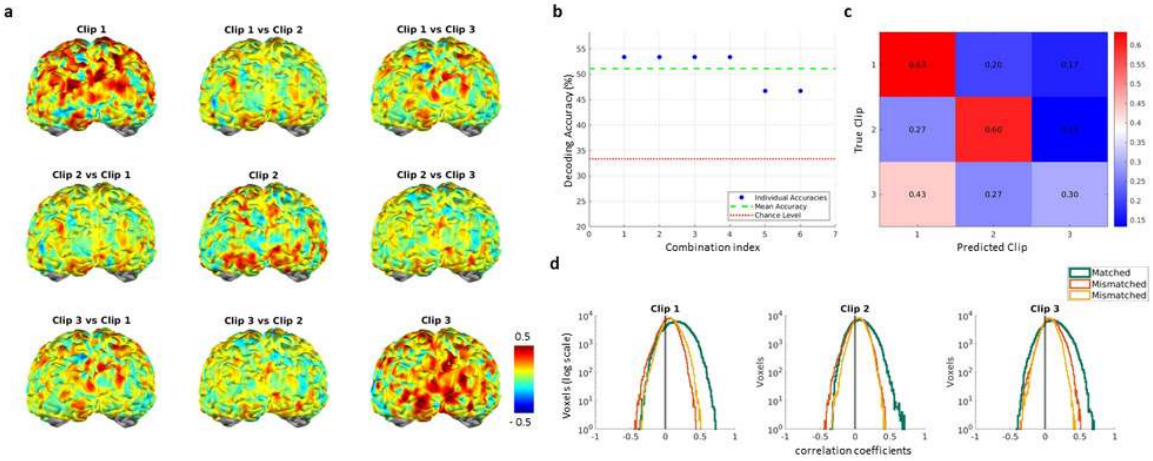

Figure 2. Assessment of within-session repeatability and decoding accuracy for test-movie clips for session 1 (S1). Time traces of clips were averaged within a run, then matched versus mismatched clips were correlated to evaluate repeatability across runs (a). Decoding accuracy was determined from six training/test splits, using 5/5 clip division for template formation and subsequent correlation-based decoding; accuracy reflects the ratio of correctly decoded over incorrectly decoded trials (b). A normalized confusion matrix illustrates decoding performance within session 1 (c), with log-scaled histograms showing repeatability distribution for matched and mismatched clips (d). The shift of histograms to the right-hand side for matched clips and centered histograms for mismatched clips confirms that we have a repeated pattern for matched clips and a non-repeatable pattern for mismatched clips.

Conclusions: The VHD-DOT task and movie data have shown high repeatability, which is crucial for intricate decoding tasks. This lays a foundation for semantic visual decoding of naturalistic movies using full-head VHD-DOT.

References

1. Bajracharya, A. et al (2023). Precision Functional Mapping of Cortical Activity Using High-Density Diffuse Optical Tomography (HD-DOT). https://doi.org/10.1364/boda.2023.jtu4b.15
2. Dobkin, B. H. (2007). Brain-computer interface technology as a tool to augment plasticity and outcomes for neurological rehabilitation. The Journal of Physiology, 579(3), 637–642. https://doi.org/10.1113/jphysiol.2006.123067
3. Eggebrecht, A. T. et al (2014). Mapping distributed brain function and networks with diffuse optical tomography. Nature Photonics, 8(6), 448–454. https://doi.org/10.1038/nphoton.2014.107
4. Fishell, A. K. et al (2019). Mapping brain function during naturalistic viewing using high-density diffuse optical tomography. Scientific Reports, 9(1). https://doi.org/10.1038/s41598-019-45555-8
5. Huth, A. G. et al (2012). A Continuous Semantic Space Describes the Representation of Thousands of Object and Action Categories across the Human Brain. Neuron, 76(6), 1210–1224. https://doi.org/10.1016/j.neuron.2012.10.014

6. Huth, A. G. et al (2016). Decoding the Semantic Content of Natural Movies from Human Brain Activity. Frontiers in Systems Neuroscience, 10. https://doi.org/10.3389/fnsys.2016.00081
7. Markow, Z. E. et al (2023). Template- and model-based decoding of movie identities with high-density diffuse optical tomography of neural hemodynamics. https://doi.org/10.1117/12.2649294
8. Miller, G.A. (1995) WordNet: A Lexical Database for English. Communications of the ACM, 38, 39-41. https://doi.org/10.1145/219717.219748
9. Tang, J. et al (2023). Semantic reconstruction of continuous language from non-invasive brain recordings. Nature Neuroscience, 26(5), 858–866. https://doi.org/10.1038/s41593-023-01304-9
10. Tripathy, K. et al (2021). Decoding visual information from high-density diffuse optical tomography neuroimaging data. NeuroImage, 226, 117516–117516. https://doi.org/10.1016/j.neuroimage.2020.117516

Poster No 2424

Neuroimaging During Motion with Portable, Wearable Diffuse Optical Tomography

Hannah DeVore[1], Alvin Agato[1], Calamity Svoboda[2], William Hamic[1], Anthony O'Sullivan[2], Michelle Hedlund[1], Sean Rafferty[2], Jason Trobaugh[1], Adam Eggebrecht[2], Edward Richter[1], Joseph Culver[2]

[1]Washington University in St. Louis, St. Louis, MO, [2]Washington University School of Medicine, St. Louis, MO

Introduction: While neuroimaging technologies have improved and expanded their capabilities, there has long been a gap in traditional neuroimaging technologies for a noninvasive, high-resolution, portable modality that tolerates participant movement. Established technologies like EEG may be used in real-world settings, but suffer from poor resolution, SNR, and motion susceptibility, while MRI has good spatial resolution, but creates a loud, cramped, unnatural scanning environment. MRI and PET are also stationary, and contraindicated in some populations. Wearable diffuse optical tomography (DOT) systems bridge this gap; our new wearable, high-density (WHD) DOT system offers portability and flexibility like EEG, spatial resolution similar to MRI, and improved robustness against motion artifacts versus fiber-based DOT systems. DOT is an optical technique that uses multiple, overlapping measurements from high-density imaging arrays to generate 3D tomographic reconstruction of cortical blood oxygenation dynamics (Fig 1a). As with MRI, neuronal activity is inferred from blood oxygenation via neurovascular coupling. While fiber-based DOT systems have been extensively validated against MRI over the last decade, full head fiber DOT systems require that the subject's head remains relatively still. New, wearable DOT systems have recently begun to provide similar imaging performance with the added advantage of permitting subject movement.

Methods: Our wearable DOT cap houses an array of modules with integrated optoelectronics and mechanics. The fully untethered system communicates with a control computer over Wi-Fi, and power is supplied via a battery in a backpack. Participants can move their head, stand, walk, and perform more complex movements (Fig 1bcd). 98 sources and 98 detectors are arranged in a high-density grid with a field of view covering most of the cortex. Spring-loaded optodes comb through hair to create and maintain scalp coupling. The system was validated both on the bench and in vivo, and compared to a conventional, fiber-based DOT system. In some cases, subjects were scanned while freely walking, which is impossible in MRI or fiber DOT.

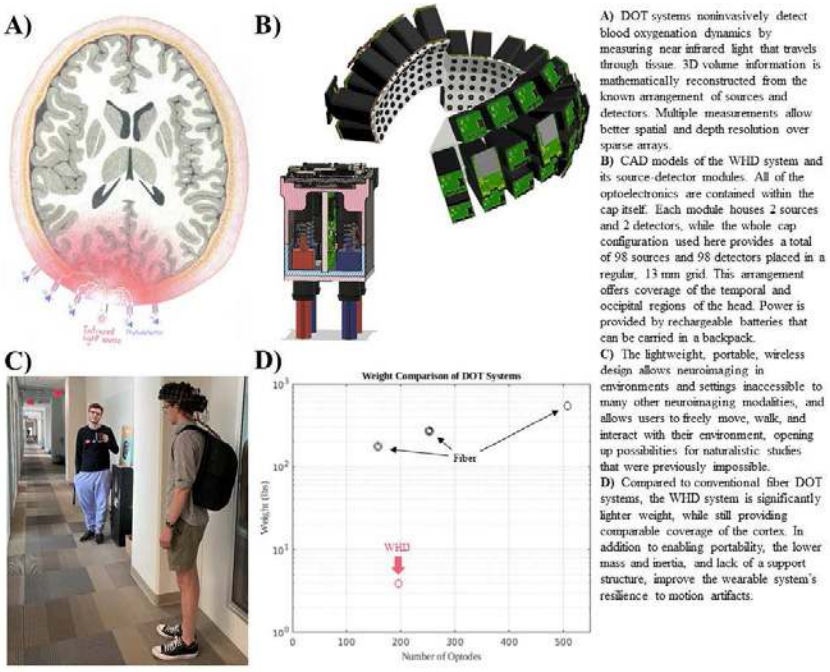

A) DOT systems noninvasively detect blood oxygenation dynamics by measuring near infrared light that travels through tissue. 3D volume information is mathematically reconstructed from the known arrangement of sources and detectors. Multiple measurements allow better spatial and depth resolution over sparse arrays.
B) CAD models of the WHD system and its source-detector modules. All of the optoelectronics are contained within the cap itself. Each module houses 2 sources and 2 detectors, while the whole cap configuration used here provides a total of 98 sources and 98 detectors placed in a regular, 13 mm grid. This arrangement offers coverage of the temporal and occipital regions of the head. Power is provided by rechargeable batteries that can be carried in a backpack.
C) The lightweight, portable, wireless design allows neuroimaging in environments and settings inaccessible to many other neuroimaging modalities, and allows users to freely move, walk, and interact with their environment, opening up possibilities for naturalistic studies that were previously impossible.
D) Compared to conventional fiber DOT systems, the WHD system is significantly lighter weight, while still providing comparable coverage of the cortex. In addition to enabling portability, the lower mass and inertia, and lack of a support structure, improve the wearable system's resilience to motion artifacts.

Results: In vivo data from varied behavioral tasks replicate the activation patterns expected from fMRI studies, including visual, auditory, motor, and language processing tasks. The SNR is sufficient for single session individual subject maps without group-averaging. In a 3-way visual decoding task, single-trial responses are robust enough for decoding with up to 100% accuracy. To verify robustness to subject movement, we used instructed motion from our WHD system and a comparable fiber DOT system. Multiple types of motion were compared, as well as the effects of motion artifacts on task maps and decoding performance. With instructed motion as great as 20 cm added to a visual task, the WHD system still output high quality maps with few motion artifacts, while on the fiber system, activations were completely obscured by motion artifacts (Fig 2a). Even during motion, the WHD system demonstrated high accuracy on a 3-way decoding task, while motion decimated the fiber system's decoding performance (Fig 2b). Quantifying motion artifacts with GVTD, akin to MRI's DVARS, shows rigid body motions on the WHD system gave GVTD values 1/3 of the mean and 1/5 of the amplitude of the GVTD on the fiber system.

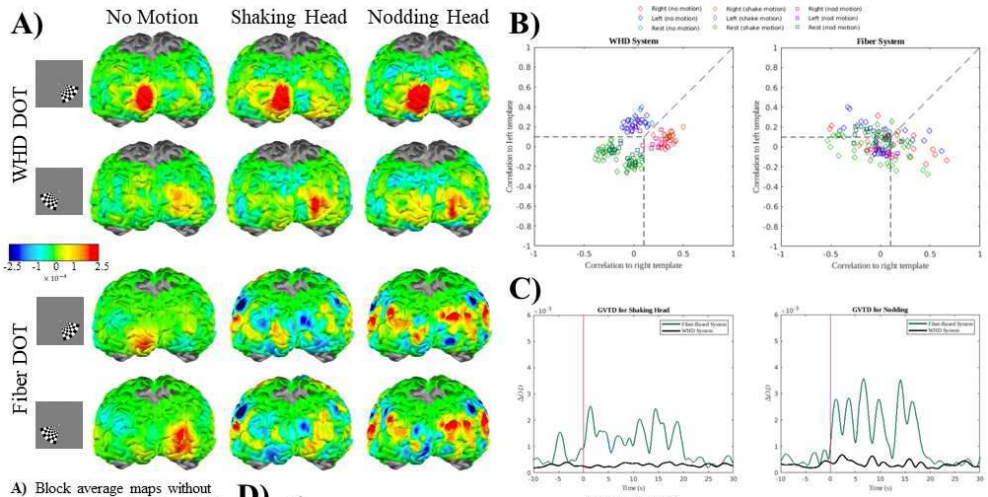

A) Block average maps without motion correction for left and right visual stimuli on a conventional fiber DOT system and the WHD system, under 3 motion conditions. Subjects performed no motion, side-to-side head shaking motions, or up-and-down nodding motions. Even during motion and without motion correction, the WHD system still detects the activations with minimal artifacts, while the fiber system is obscured by noise. **B)** 3-way decoding of left, right, and rest trials of visual stimuli under the same motion conditions, on a conventional fiber DOT system and the WHD system. No motion correction or compensation was applied. Decoding accuracy remained high on the WHD system even during motion, while the fiber system's performance drops markedly when motion is introduced. **C)** Exemplar GVTD timetraces for head shaking and head nodding motions on the WHD and fiber systems. GVTD values are much lower on the WHD system than fiber one. **D)** Exemplar GVTD traces from the WHD system during the visual/motion task. Despite the large amplitude motions, GVTD values remain low for the WHD system

Conclusions: We developed a WHD DOT system that bridges a gap in neuroimaging technologies, with wearable convenience, high resolution, and resistance to motion artifacts. Bench and in vivo testing demonstrate good performance, and it significantly outperformed fiber DOT systems during instructed motion. The portability and robustness to motion open new worlds of possibilities for scanning during tasks or in settings that were previously intractable; it is compatible with gross motor movement and locomotion, and with non-laboratory environments such as offices. Current work includes expanding the field of view and improving ergonomics.

References

1. Sherafati, A. (2020), 'Global motion detection and censoring in high-density diffuse optical tomography', Human Brain Mapping, pp. 4093–4112

Poster No 2425

Assisting Diagnostic Applications of Functional Near-Infrared Spectroscopy for Psychiatric disorders

JongKwan Choi[1], Yuna Kim[2], Yun Seong Park[2], Woojae Myung[2]

[1]OBELAB, Seoul, Korea, Republic of, [2]Seoul National University Bundang Hospital, Bundang, Korea, Republic of

Introduction: Major depressive disorder is known for its association with a high risk of persistent chronic symptoms that might cause modern social problems such as increase of suicide rates and reduction of economic outcomes. However, it is difficult to recognize early on patients' depressive symptoms and distinguish between major depressive disorder (MDD) patients and bipolar disorder (BP) patients, who require different treatment methods, through their behaviors and self-described reports.

According to an fMRI and PET study[1], functional activation followed by cognitive stimulation of MDD and BP patients were different between normal. However, due to constraints of space and cost, conventional neuromonitoring tools are not widely used. In this study, we employed fNIRS technology due to its affordability and user-friendly nature, aiming to validate its potential as an adjunctive tool in distinguishing various psychiatric disorders.

Methods: The MDD, BP and healthy control(HC) group participants were diagnosed using conventional methods, specifically the DSM-IV criteria, Hamilton Depression Rating Scale (HAMD), and Clinical Global Impression (CGI) score. Thirty healthy control group (HC) (ages: 32±11), thirty major depressive disorder group (MDD) (ages: 48±8) and thirty bipolar disorder group (BP) (ages: 28±7) were included. They performed verbal fluency task that was consisted of a 30 s pre-task period, 60 s task period, and a 70 s post-task period. During the pre- and post-task periods, participants were asked to say "ㅏ,ㅔ, ㅣ,ㅗ,ㅜ" (pronounce as "a,e,I,o,u") repeatedly. During the task period, they were instructed to generate as many words as possible, beginning with Korean letter as 'ㄱ', 'ㅅ' and 'o' (pronounce as "giek, siot, eong") for 20 s per letter[2]. The utilized fNIRS system is a NIRSIT (OBELAB Inc., Korea) described in figure 1 and it is composed by 24 lasers sources (780/850 nm) and 32 photo detectors with multiple source-detector spacing (1.5, 2.12, 3, 3.35 cm) and 48 channels implemented by 3cm separation were used. Detected signals were low pass filtered to decrease cardiovascular artifact and environmental noise. The hemodynamics responses extracted by modified beer-lambert law[3] and evaluated Integral and Centroid values to identify individuals with major diagnoses[4]. One-way ANOVA was performed between groups to evaluate significant different in each variables and analyses of variance (ANCOVA) to examine group differences of fNIRS features with age, education, and task performance.

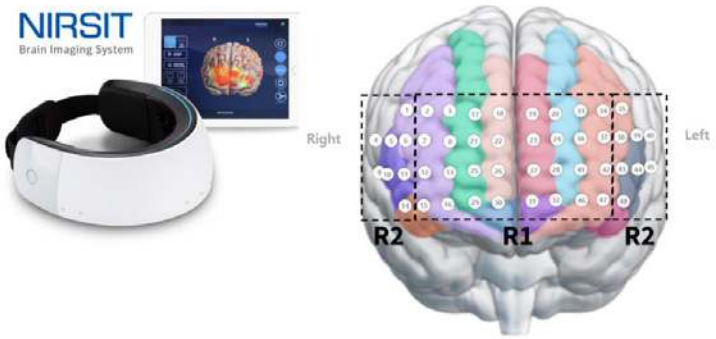

Fig. Region of interest frontal region (R1) and bilateral temporal region (R2)

Results: One-way ANOVA analysis demonstrated significant differences between groups concerning age and years of education, indicating that MDD tended to be older than their BP and HC groups ($F = 14.664$, $p < 0.005$). In terms of task performance, In terms of task performance, the total number of valid words used during the task in the MDD and HC groups was similar and higher than the BP group ($F = 5.622$, $p < 0.005$). One-way ANOVA showed a significant difference among groups in the Integral Value (IV) and post-hoc analyses showed a significant difference between HC and each psychiatric disorder group (HC vs BP, HC vs MD; $P < 0.05$), although no significant distinctions were found between any two patient groups for CV but showed differences in a representative patterns of each groups.

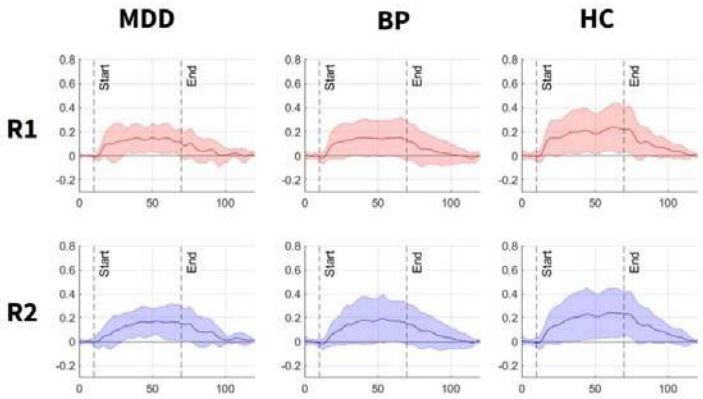

Fig. Average oxy-haemoglobin waveforms in the R1 and R2 regions in each groups

Conclusions: This fNIRS study aims to explore the potential of fNIRS as a practical tool for distinguishing between healthy individuals and those diagnosed with major psychiatric disorders. It is demonstrated that utilizing the integral and centroid

value extracted from hemoglobin changes have a potential in distinguishing individuals with mood disorders from healthy controls compared to distinguishing psychiatric disorders. These findings suggest that fNIRS has the potential to serve as a promising biomarker in the process of differentiating individuals with mood or psychosis disorders, marking a significant step towards tailoring treatments based on individual needs.

References

1. Kraus C, Kadriu B, Lanzenberger R, Zarate CA Jr, Kasper S. Prognosis and improved outcomes in major depression: a review. Transl Psychiatry. 2019 Apr 3;9(1):127.
2. Husain, S., Yu, R., Tang, TB. et al. Validating a functional near-infrared spectroscopy diagnostic paradigm for Major Depressive Disorder. Sci Rep 10, 9740 (2020).
3. Delpy, D. T., Cope, M., van der Zee, P., Arridge, S., Wray, S., & Wyatt, J. S. (1988). Estimation of optical pathlength through tissue from direct time of flight measurement. Physics in Medicine & Biology, 33(12), 1433.
4. Takizawa R, Fukuda M, Kawasaki S, Kasai K, Mimura M, Pu S, Noda T, Niwa S, Okazaki Y; Joint Project for Psychiatric Application of Near-Infrared Spectroscopy (JPSY-NIRS) Group. Neuroimaging-aided differential diagnosis of the depressive state. Neuroimage. 2014 Jan 15;85 Pt 1:498-507

Poster No 2426

Prefrontal functional near-infrared spectroscopy (fNIRS) as a tool for studying emotional regulation

Jihyun Cha[1], Taehoon Kim[1], Junggu Choi[2], JongKwan Choi[1], Sanghoon Han[2]

[1]OBELAB, Seoul, Korea, Republic of, [2]Yonsei University, Seoul, Korea, Republic of

Introduction: Daily stress affects individuals differently, with varying impacts on mental and physical health. Traditional stress biomarkers like salivary cortisol and ECG provide limited insights into the interaction between immediate stress responses and chronic stress levels. Individual traits and coping strategies further complicate the equation. Recent studies using fNIRS show prefrontal deactivation as a potential immediate biomarker for stress[1,2], but its universality remains unclear; it is uncertain whether the deactivation simply reflects a reduced cognitive response to the mental task given stress. This study explores prefrontal responses to stress without explicit tasks, employing fNIRS alongside traditional biomarkers and questionnaires to validate the feasibility of the fNIRS as an assessor of acute or prolonged stress.

Methods: A total of 78 participants (65 in the test and 13 in the control group) were recruited. The experiment consisted of three phases. First, the participants engaged in a resting-state fNIRS scanning (baseline phase). Second, during the Stress-induction phase, as the main "task," the test group watched a video clip of repulsive content (Fear Factor episode), whereas the control group watched neutral-to-positive content (cat video). Except for the content of the clips, all other aspects were identical across groups. Lastly, in the post-stress recovery phase, the participants underwent another resting-state scanning followed by their ratings on the video clips they watched, regarding the degree of stress change the clips caused on a scale of 1 to 7. In between these phases, salivary cortisol samples were collected. During the experiment, participants' prefrontal regions were measured using a NIRSIT LITE Adult (OBELAB, Inc., Rep. of Korea), a portable 15-channel continuous wave fNIRS system roughly covering BA 10. For analysis, the collected fNIRS signals were first converted to the delta optical density, on which a motion artifact correction algorithm (the Temporal Derivative Distribution Repair; TDDR) was applied[3]. The signals were then converted to relative oxygenated hemoglobin concentration (ΔHbO) changes via the modified Beer-Lambert law[4]. A General Linear Model (GLM) with an autoregressive, iteratively reweighted least-squares method (AR-IRLS)[5] was fitted to extract the beta amplitude during the baseline, stress-induction, and post-stress phase. To reduce the individual differences in the baseline activation, the baseline beta weights were subtracted from the following two phases. Thus, here, we mainly focus on the period when the stress was induced by the video content and the period when the participants engaged in the resting state following the stressful event.

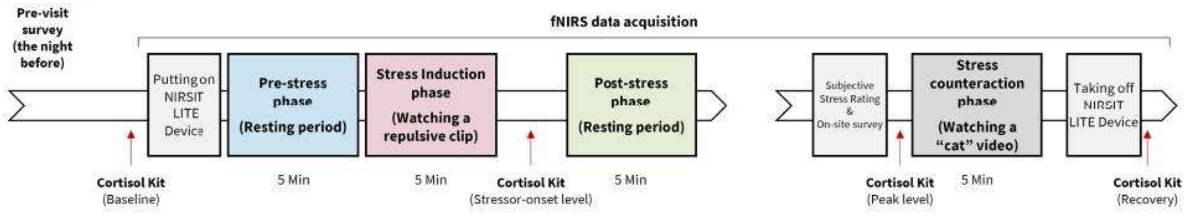

Fig. Stress-induction task procedure.

Results: Subjective stress ratings revealed an increase in the test group (+1.44) and a decrease in controls (-0.92), indicating successful stress induction ($p < .001$). ECG features showed marginal group x phase interactions, with elevated heart rate and

LF/HF ratio during post-stress in the test group. No significant cortisol level changes were observed after baseline correction. fNIRS data indicated a significant group x phase interaction in the left frontopolar cortex, showing lower activation during stress induction and elevated activation during post-stress. The post-stress activation correlated with subjective stress ratings of video content. Subsequent correlation analyses revealed that activation during the post-stress phase was related to Self-Compassion Scale and Coping Inventory for Stressful Situations.

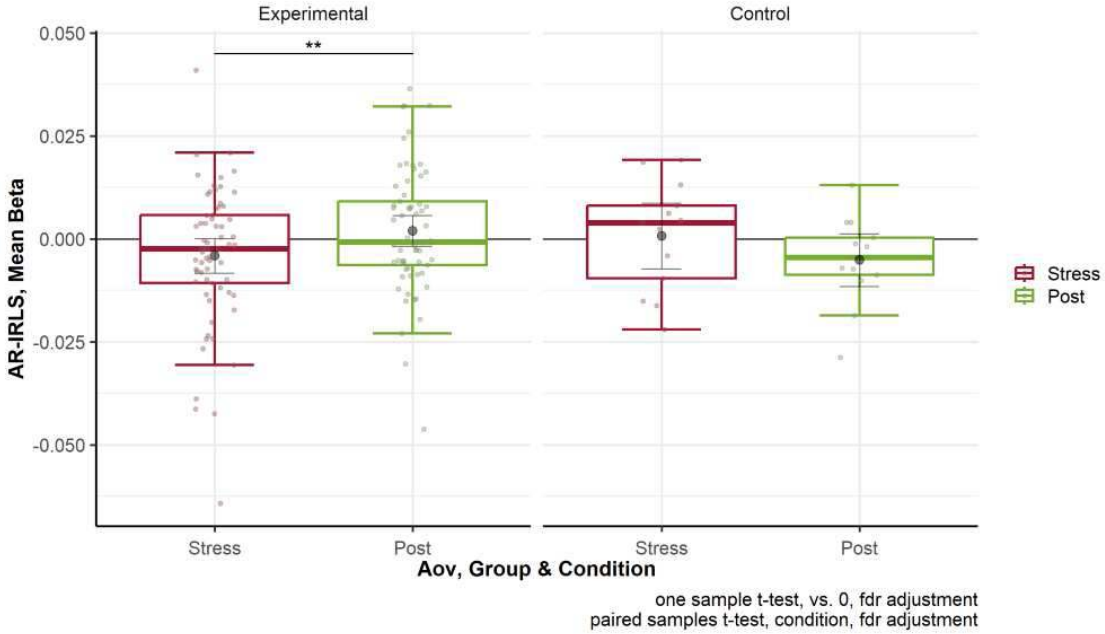

Flg. Baseline corrected prefrontal activation during stress-induction and post-stress phase.

Conclusions: Overall, prefrontal activation in response to stress reflects individuals' coping strategies rather than a direct physiological stress response. Unlike EGC signals, the frontal fNIRS signal may indicate rumination or emotional regulation post-stress. Traditional methods may struggle to detect stress in individuals effectively suppressing immediate responses, highlighting fNIRS's potential in uncovering hidden repercussions.

References

1. Al-Shargie, F.(2016). Mental stress assessment using simultaneous measurement of EEG and fNIRS. Biomedical Optics Express, 7(10), 3882.
2. Al-Shargie, F.(2017). Assessment of mental stress effects on prefrontal cortical activities using canonical correlation analysis: an fNIRS-EEG study. Biomedical Optics Express, 8(5), 2583.
3. Fishburn, F. A. (2019). Temporal Derivative Distribution Repair (TDDR): A motion correction method for fNIRS. NeuroImage, 184(June 2018), 171–179.
4. Delpy, D. T. (1988). Estimation of optical pathlength through tissue from direct time of flight measurement. Physics in Medicine and Biology, 33(12), 1433–1442.
5. Barker, J. W.(2013). Autoregressive model based algorithm for correcting motion and serially correlated errors in fNIRS. Biomedical Optics Express, 4(8), 1366.

Poster No 2427

NIRS data processing and statistical analysis: AnalyzIR toolbox

Hendrik Santosa[1], Xuetong Zhai[1], Theodore Huppert[1]

[1]*University of Pittsburgh, Pittsburgh, PA*

Introduction: Functional near-infrared spectroscopy (fNIRS) is a neuroimaging technique that uses low-levels of light (650-900 nm) to noninvasively measure changes in cerebral blood volume and oxygenation (Scholkmann, Kleiser et al. 2014). Over the last few years, this technique has been utilized in a growing number of resting-state and functional brain activity. However, the analysis of fNIRS data poses several challenges stemming from the unique physics of the technique, the unique statistical properties of data (Huppert 2016), and the growing diversity of non-traditional experimental design being utilized in studies due to the flexibility of this technology. For these reasons, specific analysis methods for this technology must be developed. In this poster, we introduce the NIRS Brain AnalyzIR toolbox as an open-source Matlab-based analysis package for

fNIRS data management, pre-processing, first- and second-level statistical analysis. Here, we describe the basic architectural format of this toolbox, which is based on the object-oriented programming paradigm. Algorithms detail for several of the major components of the toolbox including statistical analysis, probe registration, image reconstruction, and region-of-interest based statistics have been previously described (Santosa, Zhai et al. 2018).

Methods: Statistical Modules: The AnalyzIR toolbox contains number of processing modules for statistical analysis for both first- and higher-level models. These include time-series regression models (e.g., OLS (Huppert, Diamond et al. 2009) and AR-IRLS (Barker, Aarabi et al. 2013)), functional connectivity models (Santosa, Aarabi et al. 2017), image reconstruction methods (Zhai, Santosa et al. 2023), and higher order mixed effects and ANOVA models (Matlab: fitlme.m function). Image Reconstruction Modules: Based on the optical forward model, the toolbox reconstructs the subject image by solving the underdetermined linear system between changes in concentrations of HbO2 and Hb in the tissue and the changes in optical density using a hierarchal Bayesian inverse model (Zhai, Santosa et al. 2023). Connectivity and Hyper-Scanning Modules: The toolbox contains several modules for connectivity analysis and hyperscanning analysis (two or more subject are simultaneously recorded during an interactive task and the brain signals between subjects is analyzed). This analysis includes our proposed method for robust methods (Santosa, Aarabi et al. 2017). Toolbox Utilities: The toolbox offers additional utilities for probe registration and adjusting for head size, region-of-interest analysis, and other features.

Results: Architecture of Toolbox: The AnalyzIR toolbox is an open-source analysis package which utilizes both custom namespace and class definitions written in Matlab language to provide an object-oriented programming interface to performing fNIRS analysis. Pats of the toolbox interface to fNIRS forward models (models of the light propagation through tissue/brain) require separate download of the software such as NIRSFAST, Iso2mesh, MCextreme, MMC, tMCimg software packages. The toolbox currently also includes several functions for generating synthetic or semi-synthetic (experimental baseline data with synthetically added “evoked” response) data for testing purposes (ROC analysis) and offers several example scripts and tutorials including several full datasets that can be downloaded with code. Graphical Interfaces: Although the toolbox is primarily a command-line interface, there are available several GUIs, such as nirs.viz.jobmanager, nirs.viz.nirsviewer, nirs.viz.StimUtil, etc.

Conclusions: Future Direction: While the toolbox is written primarily for fNIRS data, it does provide limited support for EEG, MEG, and fMRI dense time-series data. We welcome more interaction with other researchers from various modalities on this toolbox with a particular focus on developing multimodal methods within this common framework.

References

1. Barker, J. W., A. Aarabi and T. J. Huppert (2013). “Autoregressive model based algorithm for correcting motion and serially correlated errors in fNIRS.” Biomedical Optics Express 4(8): 1366-1379.
2. Huppert, T. J. (2016). “Commentary on the statistical properties of noise and its implication on general linear models in functional near-infrared spectroscopy.” Neurophotonics 3(1).
3. Huppert, T. J., S. G. Diamond, M. A. Franceschini and D. A. Boas (2009). “HomER: a review of time-series analysis methods for near-infrared spectroscopy of the brain.” Applied Optics 48(10): D280-D298.
4. Santosa, H., A. Aarabi, S. B. Perlman and T. J. Huppert (2017). “Characterization and correction of the false-discovery rates in resting state connectivity using functional near-infrared spectroscopy.” J Biomed Opt 22(5): 55002.
5. Santosa, H., X. Zhai, F. Fishburn and T. Huppert (2018). “The NIRS brain AnalyzIR toolbox.” Algorithms 11(5): 73.
6. Scholkmann, F., S. Kleiser, A. J. Metz, R. Zimmermann, J. M. Pavia, U. Wolf and M. Wolf (2014). “A review on continuous wave functional near-infrared spectroscopy and imaging instrumentation and methodology.” NeuroImage 85: 6-27.
7. Zhai, X., H. Santosa, R. T. Krafty and T. J. Huppert (2023). “Brain space image reconstruction of functional near-infrared spectroscopy using a Bayesian adaptive fused sparse overlapping group lasso model.” Neurophotonics 10(2): 023516.

Poster No 2429

Exploring Prefrontal Function Alterations using fNIRS in Korean Baby Boomers with Suicidal Ideation

Hyeon Jin Kim[1,2], Hyunsan Cho[3,2], Sunhae Lee[1], Seong-Jin Son[4]

[1]Department of Neurology, Korea University Ansan Hospital, Ansan-si, Korea, Republic of, [2]Institute of Human Genomic Study, Korea University, College of Medicine, Seoul, Korea, Republic of, [3]BK 21 Four R&E Center for Learning Health Systems, Korea University, Seoul, Korea, Republic of, [4]Core Research & Development Center, Korea University Ansan Hospital, Ansan-si, Korea, Republic of

Introduction: Globally, suicide comprises 3% of mortality, with South Korea having the highest rate (24.6 per 100,000 persons) among OECD countries. The prefrontal cortex (PFC) is crucial for understanding the neurobiological basis of suicidal ideation, yet inconclusive findings persist due to limited samples. Korea’s baby boomers born between 1955 and 1963 represents a unique generation that encountered numerous either societal or personal traumatic experience throughout their lifetime, and

the prevalence of suicidal thoughts within this demographic represents a critical mental health concern. The present study aims to measure and analyze the hemodynamic responses in the PFC using functional Near-Infrared Spectroscopy (fNIRS) in Korean Baby Boomers, specifically focusing on individuals with a history of previous suicidal ideation.

Methods: About 360 participants completed the comprehensive questionnaire investigating various trauma experiences throughout their lifetime and psychological conditions. A total of 60 participants without any history of neurological problems participated in the fNIRS test, stratified by suicidality. This study was approved by the IRB of Korea University Ansan Hospital (2022AS0129). To compare hemodynamic signal differences over the FPC before and after the various emotional face recognition task, we designed five repeated fNIRS experiment sessions using Yonsei Face Database (YFaceDB). The fNIRS device utilized in this study was NIRSIT (OBELAB, www.obelab.com), and the acquired fNIRS data underwent meticulous preprocessing to enhance its quality and reliability. This involved filtering techniques to mitigate high-frequency noise, baseline correction to address signal drift, systematic removal of motion artifacts, and precise spatial registration to align channels across participants. The feature extraction process aimed to unveil meaningful patterns in prefrontal neural activity during emotional processing. Hemodynamic response modeling captured changes in oxygenated and deoxygenated hemoglobin concentrations, providing dynamic insights. All processing steps were performed using the Homer2 Toolbox within the MATLAB environment. Additional analyses were also conducted to explore potential relationships between prefrontal activity patterns, depression, and cognition scores.

Results: Among 359 participants who completed the comprehensive trauma history questionnaire, 175 (48.75%) participants were found to have experienced suicide ideation (n = 92, 25.56%), planning (n = 96, 26.74%), or attempts (n = 53, 14.85%) at least once throughout their lives. Significant differences in traumatic experiences, such as partner abuse and depression scores, were identified ($p < 0.001$), while no differences were found in sex or educational level. Compared to the control group, participants with suicidality history exhibited significantly decreased average signal value difference measured before and after the emotional face recognition task over the right and left dorsolateral PFC area channels by the fNIRS measurement. ($p < 0.001$).

Conclusions: In this study, we focus on functional alterations over the PFC in Korean Baby Boomers with suicidal ideation history, specifically linked to past traumatic experiences. Utilizing fNIRS, we examined cortical dynamics to identify the intricate interplay between prefrontal brain activity, suicidality, and trauma to understand underlying neural mechanisms contributing to psychological distress. This research significantly contributes to understanding prefrontal function in the context of suicide risk among Korean Baby Boomers, with implications for targeted therapeutic interventions and improved mental health support.

ACKNOWLEDGEMENT: This study was supported by grants from the Korea University Ansan Hospital [No. K2316061 to H.J.Kim], Basic Science Research Program through the National Research Foundation of Korea (NRF) funded by Ministry of Education [NRF-RS-NRF- 2021R1I1A1A01056054 to H. Cho and R2114233 to S. Son].

References

1. World Health Organization. (2019). Suicide in the world: global health estimates (No. WHO/MSD/MER/19.3). World Health Organization.
2. Chung, K. M., Kim, S., Jung, W. H., & Kim, Y. (2019). Development and validation of the Yonsei face database (YFace DB). Frontiers in psychology, 10, 2626.
3. Chen, C. F., Chen, W. N., & Zhang, B. (2022). Functional alterations of the suicidal brain: a coordinate-based meta-analysis of functional imaging studies. Brain Imaging and Behavior, 16(1), 291-304.
4. Gu, X., Yang, B., Gao, S., Yan, L. F., Xu, D., & Wang, W. (2021). Application of bi-modal signal in the classification and recognition of drug addiction degree based on machine learning. Math. Biosci. Eng, 18(5), 6926-6940.
5. Zhang, H., Dong, W., Dang, W., Quan, W., Tian, J., Chen, R., ... & Yu, X. (2015). Near-infrared spectroscopy for examination of prefrontal activation during cognitive tasks in patients with major depressive disorder: A meta-analysis of observational studies. Psychiatry and clinical neurosciences, 69(1), 22-33.

Poster No 2430

Predicting scholastic ability with resting-state functional near-Infrared spectroscopy

Taehoon Kim[1], Jihyun Cha[1], Junggu Choi[2], JongKwan Choi[1], Sanghoon Han[2]

[1]OBELAB, Seoul, Korea, Republic of, [2]Yonsei University, Seoul, Korea, Republic of

Introduction: Recent studies employing connectome-based predictive modeling (CPM), a robust data-driven approach for constructing predictive models of brain-behavior relationships from neural connectivity (Shen, et al., 2017), have shown promise in elucidating individual differences. This method has successfully predicted diverse aspects of human cognition and personality traits including fluid intelligence (Finn et al., 2015), creative ability (Beaty et al., 2018), and an individual's

level of anxiety (wang et al., 2021). The potential application of predicting real-life outcomes, such as professional aptitude or susceptibility to mental/physical disorders, is significant. Given the pivotal role the prefrontal cortex (PFC) plays in higher cognition, our study applies the CPM framework to resting-state functional near-infrared spectroscopy (fNIRS) signals acquired from the PFC. Specifically, we aim to examine the relationship between resting-state connectivity and academic ability, as represented by the scores on the Korean version of college scholastic assessment test (K-SAT).

Methods: We analyzed resting-state fNIRS data from 100 participants (mean age = 19.17, sd = 0.55, 60 females) who had recently taken the K-SAT. Their resting-state fNIRS data were collected using NIRSIT LITE (OBELAB, Inc., Rep. of Korea), a portable 15-channel fNIRS system covering BA 10. Participants underwent a 5-minute resting-state scan with their eyes open. The preprocessing involved converting raw light intensity to delta optical density, followed by motion artifact correction using spline interpolation (Scholkmann et al., 2010) and wavelet filtering (Molavi et al., 2012). The cleaned optical density data were then converted to the relative concentration changes in oxy- and deoxy-Hb based on the modified Beer-Lambert law (Delpy et al., 1988). A Butterworth filter (bandpass cutoff of 0.005 and 0.1 Hz, respectively) was applied to eliminate slow drift and physiological noise. In addition, short channel regression (Santosa et al, 2020) and an autogressive model (Lanka et al., 2020) were applied to remedy superficial physiological noise and serial correlation in the timeseries. Functional connectivity between 15 channels was calculated, forming connectivity matrices with 105 edges. This resulted in 100 matrices reflecting intrinsic PFC connectivity patterns of 100 individuals (Figure 1). Using a leave-one-out cross-validation (LOOCV) approach, we divided the data into training (99 participants) and testing sets (1 participant). In the training set, we tested a linear relationship between each edge's strength and K-SAT score. Edges with significant positive or negative correlations were extracted and combined to generate positive and negative weights for individual score prediction. The resulting model was then applied to the testing data to yield prediction on the K-SAT score. The process was iterated through cross-validation, providing predictions for the K-SAT scores of the entire 100 participants.

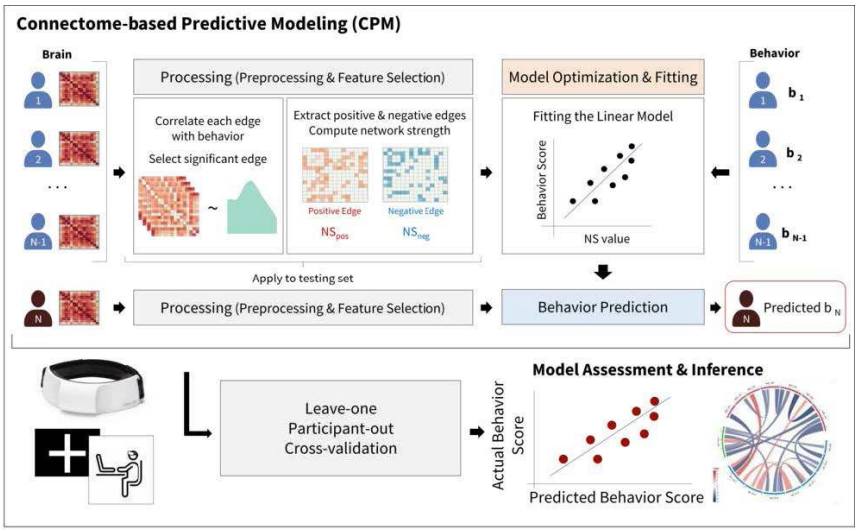

Results: Out of discrete sections of K-SAT probing diverse domains, we primarily focus on the prediction results for the language comprehension section. To evaluate the model performance, we calculated the spearman's rank correlation between the predicted and their actual scores (Figure 2). A moderate correlation ($r(98) = .37$, $p < .001$), comparable to reported CPM results based on whole-brain fMRI was observed. A separate analysis indicated no significant correlation between the predicted scores and the participant's Raven's progressive matrices scores. Overall, the results suggest that the predicted score uniquely reflects an individual's language comprehension ability, independent of their general IQ.

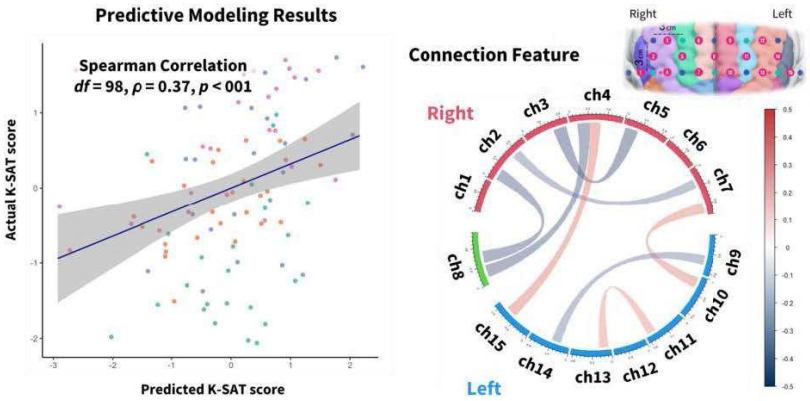

Conclusions: Our study highlights the potential of resting-state fNIRS in predicting academic ability, demonstrating the relevance of CPM even in its simpler form. Further exploration of these neural connections promises valuable insights into cognitive abilities and educational outcomes.

References

1. Beaty, R. E. (2018). Brain networks of the imaginative mind: Dynamic functional connectivity of default and cognitive control networks relates to openness to experience. Human Brain Mapping, 39(2), 811–821.
2. Delpy, D. T., Cope, M., Van Der Zee, P., Arridge, S., Wray, S., & Wyatt, J. (1988). Estimation of optical pathlength through tissue from direct time of flight measurement. Physics in Medicine and Biology, 33(12), 1433–1442.
3. Finn, E. S. (2015). Functional connectome fingerprinting: Identifying individuals using patterns of brain connectivity. Nature Neuroscience, 18(11), 1664–1671.
4. Lanka, P., Bortfeld, H., & Huppert, T. J. (2022). Correction of global physiology in resting-state functional near-infrared spectroscopy. Neurophotonics, 9(3), 035003-035003.
5. Molavi, B., & Dumont, G. A. (2012). Wavelet-based motion artifact removal for functional near-infrared spectroscopy. Physiological measurement, 33(2), 259.
6. Santosa, H., Zhai, X., Fishburn, F., Sparto, P. J., & Huppert, T. J. (2020). Quantitative comparison of correction techniques for removing systemic physiological signal in functional near-infrared spectroscopy studies. Neurophotonics, 7(3), 035009-035009.
7. Scholkmann, F., Spichtig, S., Muehlemann, T., & Wolf, M. (2010). How to detect and reduce movement artifacts in near-infrared imaging using moving standard deviation and spline interpolation. Physiological measurement, 31(5), 649.
8. Shen, X. (2017). Using connectome-based predictive modeling to predict individual behavior from brain connectivity. Nature Protocols, 12(3), 506–518.
9. Wang, Z., Goerlich, K. S., Ai, H., Aleman, A., Luo, Y. J., & Xu, P. (2021). Connectome-based predictive modeling of individual anxiety. Cerebral Cortex, 31(6), 3006-3020.

Poster No 2431

The origin of symbolic numerical knowledge in early development – an fNIRS Registered Report

Elizaveta Ivanova[1], Daniel Ansari[2], Mojtaba Soltanlou[1]

[1]University of Surrey, Guildford, Surrey, [2]Western University, London, Ontario

Introduction: Symbolic numerical knowledge is the basis of mathematical learning. Theoretical frameworks, supported by studies in adults and school children, propose left parietal involvement for processing number words and right parietal involvement for processing non-symbolic magnitudes (Bugden, et al., 2021; Pinhas et al., 2014; Vogel et al., 2017). Despite the insights from these studies, no study investigated the neuroimaging changes associated with the early acquisition of symbolic numerical knowledge. This study addresses this dilemma by focusing on a crucial concept of symbolic numerical knowledge acquired at around 3-4 years old – the cardinality principle (CP). wherein each number word in the count sequence denotes a set of items. We hypothesise that as the child becomes a CP-knower, parietal engagement during number word processing increases due to their advanced conceptual knowledge about the meaning of number words, as compared to when the child was a subset-knower. Increased parietal engagement is defined as increased left parietal activation and stronger bilateral parietal connectivity. We summarised the hypotheses in Figure 1.

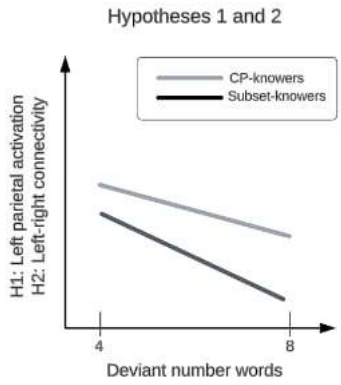

Figure 1: conceptual visualisation of the hypotheses for this study. Hypothesis 1 suggests CP-knowers will show increased left parietal activation compared to subset-knowers, while Hypothesis 2 suggests that CP-knowers will exhibit stronger bilateral parietal functional connectivity relative to subset-knowers.

Methods: Sample size calculation: Monte Carlo simulations using the BFDA package in R (Schönbrodt & Wagenmakers, 2018) were conducted for a paired t-test with covariates of Age and CP-status. Simulations showed that the probability of reaching BF10 = 10 before Nmax is 77.8%, at an average of 84 participants. However, to account for the challenges with noisy data in preschoolers, we recruited 110 typically developing preschoolers (43 girls, Mage = 3.55, SDage = 0.47). Procedure: Children completed a 'Give-a-Number' task (based on Krajcsi, 2021 and Marchand et al., 2022) and were classified as CP-knowers or subset-knowers based on their responses. In a block-designed fNIRS task based on a numerical adaptation paradigm (Vogel et al., 2017), children listened to a continuous stream of the number word 'two', interspersed by 'eight', 'four', and 'rin' (Figure 2). Data preprocessing is done with NIRS Brain AnalyzIR toolbox (Santosa et al., 2018), and systemic artefact correction is applied using a general linear model (GLM).

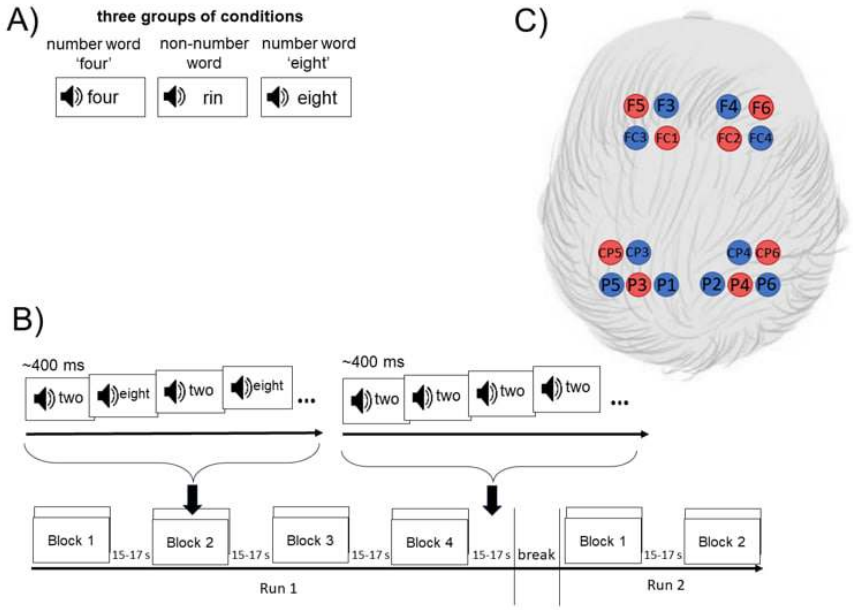

Figure 2: A) Trial types. The two deviant auditory number words differ by ½ and ¼ ratios from 'two'. B) The block design paradigm for stimuli with an example of trials in one of the blocks. There are 4 blocks in one run. Note that to improve the signal-to-noise ratio, there is one condition per run. Each stimulus takes approximately 400 ms, with an inter-stimulus interval of 1200 ms and a jittered inter-block interval between 15-17 seconds. Other conditions (deviant auditory number word 'four' and deviant auditory non-number word 'rin') follow the same procedure. C) Positions of the fNIRS optodes based on fNIRS Optodes' Location Decider (fOLD) toolbox (Zimeo Morais et al., 2018). The red circles depict the emitters, and the blue circles depict the detectors.

Results: The parietal response to the number word 'eight' condition vs. the number word 'four' condition is compared in paired t-tests (for left parietal activation and parietal connectivity separately) with factors of Age and CP status. Moderate BF10 of difference in activation in the left parietal region and connectivity within the bilateral parietal network in CP-knowers compared to subset-knowers is taken as strong evidence. The anecdotal BF10 of difference in activation and connectivity in

CP-knowers is taken as weak evidence. In the exploratory analysis, a multivariate pattern analysis is conducted to classify children as CP-knowers or subset-knowers depending on their parietal engagement when processing number words.

Conclusions: We discuss the findings in the context of two scenarios. On the one hand, higher activation in the left parietal region and connectivity within the bilateral parietal network in CP-knowers compared to subset-knowers can suggest that symbolic numerical knowledge relies on non-symbolic innate knowledge in the right the intraparietal sulcus (IPS). On the other hand, failure to find evidence for connectivity within the bilateral parietal network in CP-knowers compared to subset-knowers can suggest that symbolic numerical knowledge is related to the development of the left IPS independent of the right IPS. Regardless, the study is the first to measure the differences in processing number words in the parietal region between CP- and subset-knowers, as well as to build a classification of CP- and subset-knowers model based on the level of parietal engagement during number word processing.

References

1. Bugden, S. et al. (2021), 'The neural basis of number word processing in children and adults', Developmental Cognitive Neuroscience, 51, 101011
2. Krajcsi, A. (2021), 'Follow-up questions influence the measured number knowledge in the Give-a-number task', Cognitive Development, 57, 100968
3. Marchand, E. et al. (2022), 'Assessing the knower-level framework: How reliable is the Give-a-Number task?', Cognition, 222, 104998
4. Pinhas, M. et al. (2014), 'Electrophysiological evidence for the involvement of the approximate number system in preschoolers' processing of spoken number words', Journal of cognitive neuroscience, 26(9), 1891-1904
5. Santosa, H. et al. (2018), 'The NIRS brain AnalyzIR toolbox', Algorithms, 11(5), 73
6. Schönbrodt, F. D. et al. (2018), 'Bayes factor design analysis: Planning for compelling evidence', Psychonomic bulletin & review, 25(1), 128-142
7. Vogel, S. E. et al. (2017), 'The left intraparietal sulcus adapts to symbolic number in both the visual and auditory modalities: Evidence from fMRI', Neuroimage, 153, 16-27
8. Zimeo Morais, G. A. et al. (2018), 'fNIRS Optodes' Location Decider (fOLD): a toolbox for probe arrangement guided by brain regions-of-interest', Scientific reports, 8(1), 1-11

Poster No 2432

Examining dynamic functional connectivity during sleep in neonates using machine learning and HD-DOT

Katharine Lee[1], Topun Austin[2], Rob Cooper[3], Andrea Edwards[2], Jem Hebden[3], Kelly Pammenter[2], Julie Uchitel[4], Borja Blanco[5]

[1]University of Cambridge, Cambridge, United Kingdom, [2]Cambridge University Hospitals NHS Foundation Trust, Cambridge, Cambridgeshire, [3]Department of Medical Physics and Biomedical Engineering, University College London, London, Greater London, [4]Department of Paediatrics, University of Cambridge, Cambridge, Cambridgeshire, [5]Department of Psychology, University of Cambridge, Cambridge, Cambridgeshire

Introduction: Sleep is a critical factor in early brain development due to its impact on memory consolidation, synaptic plasticity, and neural network maintenance. High-Density Diffuse Optical Tomography (HD-DOT), a functional near-infrared spectroscopy (fNIRS) technology, has been used to investigate static resting state functional connectivity (FC) during active sleep (AS) and quiet sleep (QS) states in term-aged infants[1]. Dynamic FC analysis investigates time-varying patterns in brain activity to shed light on the non-stationary nature of resting state brain functionality. One functional magnetic resonance imaging (fMRI) method proposed for this objective identifies recurring co-activation patterns (CAPs) using machine learning clustering algorithms[2]. These CAPs represent instantaneous brain configurations at single time points and provide insight into the dynamics of spontaneous neural activity. Objective: This HD-DOT study examines dynamic functional connectivity during newborn infant sleep to shed light on early brain development in relation to sleep states. Specifically, this study adapts CAP analysis, an fMRI approach that employs unsupervised machine learning, for HD-DOT data.

Methods: In this observational study, HD-DOT data was acquired from a cohort of sleeping newborn infants at the Rosie Hospital, Cambridge UK (n=40, mean postmenstrual age=40+2). These datasets were classified as AS or QS based on behavioural analysis of synchronized video footage. The top 25% of frames for somato-motor and frontal networks were selected for each participant using a seed signal. Activation maps at these frames were clustered using the K-means algorithm into CAPs. CAP consistency was assessed by measuring intra-CAP spatial correlation. Other metrics such as CAP presence and CAP transition rate were compared in AS and QS datasets using rank sum t-tests to investigate how sleep states may modulate resting state networks.

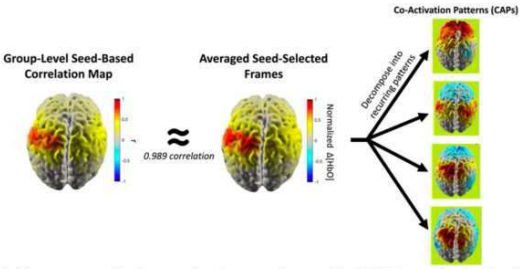

Figure 1. Standard static connectivity analysis vs. dynamic CAP analysis for left central network: CAPs are identified by clustering data frames at seed-selected time points. The average activation at these seed-selected time points is highly correlated with traditional static seed-driven analysis.

Results: Distinct CAPs were identified for AS and QS datasets, characterizing unique connectivity dynamics within somatomotor and frontal regions. These CAPs were found to have high consistency scores (left frontal region AS=0.51±0.03 and QS=0.50±0.04; left central region AS=0.53±0.04 and QS=0.51±0.04). Across iterations of CAP analysis, consistent trends emerged. Notably, CAPs with unilateral activation appear more frequently in the QS dataset.

Conclusions: This study is the first to apply CAP analysis to HD-DOT infant data, demonstrating the utility of unsupervised machine learning in dynamic FC analysis. Preliminary examination of CAP metrics reveals potential differences between AS and QS dynamic FC which may shed light on the function of sleep during early brain development. This study also focuses on dynamic FC as opposed to static FC, providing unique insight into the non-stationary nature of early resting state networks. The CAPs found in this study and the methodology used to identify them will support future infant studies that elucidate the relationship between sleep and neuronal connectivity in the developing brain.

References

1. Uchitel J. (2023). Cot-side imaging of functional connectivity in the developing brain using wearable high-density diffuse optical tomography. Neuroimage, 260:119784
2. Liu, X. (2018). Co-activation patterns in resting-state fMRI signals. NeuroImage, 180, 485-494.

Poster No 2433

Ultra-high-field fMRI mapping of layer-specific somatosensory processing in marmoset brain

Jiajia Yang[1], Hirohiko Imai[2], Masaki Fukunaga[3], Hiroki Yamamoto[4], Chenyu Wang[1], Yinghua Yu[1], Kazuhiko Seki[5], Takashi Hanakawa[6], Tatsuya Umeda[6]

[1]Faculty of Interdisciplinary Science and Engineering in Health Systems, Okayama University, Okayama, Japan, [2]Department of Informatics, Kyoto University Graduate School of Informatics, Kyoto, Japan, [3]Section of Brain Function Information, National Institute for Physiological Sciences, Aichi, Japan, [4]Graduate School of Human and Environmental Studies, Kyoto University, Kyoto, Japan, [5]Department of Neurophysiology, National Center of Neurology and Psychiatry, Tokyo, Japan, [6]Department of Integrated Neuroanatomy & Neuroimaging, Kyoto University Graduate School of Medicine, Kyoto, Japan

Introduction: The somatosensory systems share many similarities in anatomical and functional organization across the humans and nonhuman primates. It is well accepted in neuroscience that the primary somatosensory cortex (S1) can be divided into four sub-areas: 3a, 3b, 1, and 2. Area 3b is known to receive direct cutaneous tactile input of the contralateral body parts from the ventral posterolateral nucleus[1,2]. Then, the higher-order processing of tactile information occurs in areas 1 and 2, as well as the bilateral secondary somatosensory cortex (S2) and the somatosensory region of the posterior parietal cortex (PPC). To date, however, how tactile information is processed and updated through the layer-specific circuits across the whole brain remains poorly understood. Marmosets, compared to humans, have relatively thick cerebral cortex disproportionate to their overall brain size. This suggests the possibility of recording cortical layer-specific activities throughout the entire brain in marmosets. In the present study, we used a custom-designed MRI transmit and receiver coil set for marmoset at 7T MRI and acquired whole-brain layer-specific fMRI during tactile stimulation to identify the layer-specific hierarchical somatosensory processing in the marmoset brain.

Methods: One adult male common marmoset, weighting 356 g, was used in the experiment. All fMRI experiments were performed in a 7T/20-cm bore magnet (Bruker-Biospin). A saddle coil with an inner diameter of 80 mm was used as a transmit coil, and the MR signal was acquired from one loop coil placed around the marmoset head (Figure 1A) (Takashima Seisakusho Co., Ltd, Tokyo, Japan). On the day of the experiment, initial sedation was induced by a small dose of ketamine (20mg/kg) and

isoflurane (2.5%) inhaled via a facemask. After the marmoset received cannulation of a leg vein, anesthesia was switched to a constant intravenous infusion of dexmedetomidine (5ug/kg/hr) and 0.5% isoflurane. A dose of 20 mg/kg of 30-nm USPIO particles was injected. CBV weighted fMRI data were obtained with a GE-EPI sequence. FOV, 25.875 x 23 mm2; matrix, 72 x 64; slice thickness, 1 mm; nominal resolution, 0.36 x 0.36 x 1.0 mm3; TE, 9.9 ms; TR, 2000 ms. We used a 30s-on 30s-off block design, and the right hand of the marmoset was stimulated (200 ms air-puff of 0.2 kPa followed by an 800-ms null) during the on blocks. AFNI was used for the fMRI data preprocessing and GLM analysis. Laminar analyses were conducted with LayNii[3]. The study protocol was approved by the experimental animal committee at Kyoto University, Japan.

Results: Initially, we confirmed that the largest CBV signal changes in the gray matter rather than in large vessel regions. Then, we found that right hand tactile stimulation activated the left thalamus, S1 (area 3b, 1/2) and bilateral S2 in the marmoset brain (Figure 1B). We determined the ROIs of area 3b, 1/2, and S2 based on the previous findings[4,5] and generated laminar masks of each ROI. The layer-specific activities of each area are shown in Figure 1C, and we found clear hand corresponding activation in the middle layers of area 3b rather than in the upper and deep layers. In contrast, we did not find a clear middle layer activity peak signature in area 1/2 and S2.

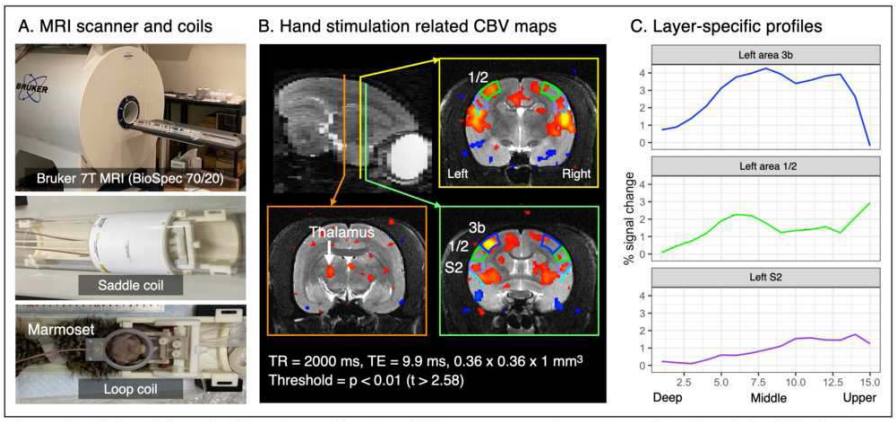

Figure 1. (A) A saddle coil with an inner diameter of 80 mm was used as a transmit coil, and the MR signal was acquired from one loop coil placed around the marmoset head at 7T. (B) Right hand tactile stimulation activated widespread areas in the whole marmoset brain. (C) Layer-specific profiles of left area 3b, 1/2 and S2.

Conclusions: Our custom-designed MRI transmit and receive coil set combined with a USPIO imaging contrast agent at 7T MRI was designed to provide enhanced signal sensitivity and high spatial specificity than BOLD for layer-specific fMRI. We succeeded in recording the layer-specific tactile stimulation-related responses in the marmoset whole brain. The middle layers' peak activity in area 3b was thought to reflect the somatosensory input via the thalamus, and the different layer-specific activity patterns in other areas may reflect the inter-area layer-specific interaction during the somatosensory processing. Our approach is expected to provide a new viewpoint on understanding the bidirectional hierarchical somatosensory processing.

References

1. Stringer EA, et al., (2014): Distinct fine-scale fMRI activation patterns of contra- and ipsilateral somatosensory areas 3b and 1 in humans. Hum Brain Mapp 35:4841–4857.
2. Yu Y, et al., (2019): Layer-specific activation of sensory input and predictive feedback in the human primary somatosensory cortex. Sci Adv 5:eaav9053.
3. Huber L (Renzo), et al., (2021): LayNii: A software suite for layer-fMRI. Neuroimage 237:118091.
4. Paxinos G, et al., (2012): The Marmoset Brain in Stereotaxic Coordinates. San Diego: Elsevier Academic Press.
5. Clery J, et al., (2020): Whole brain mapping of somatosensory responses in awake marmosets investigated with ultra-high-field fMRI. J Neurophysiol 124(6):1900-1913

Poster No 2434

Fast diffusion fMRI signals in the Superior Colliculus during the negative BOLD regime

Rita Gil[1], Noam Shemesh[1]

[1]Champalimaud Research, Champalimaud Foundation, Lisbon, Lisbon

Introduction: Positive BOLD Responses (PBRS) are known to correlate with increases in local field potentials (LFPs) and multi-unit activity (MUA) signals[1,2]. However, there is still debate on the biological underpinnings of Negative BOLD Responses (NBRs), with evidence pointing to neuronal suppression as the most probable biological scenario[3,4]. Recently, we employed a visual paradigm capable of modulating visual pathway BOLD responses from activation to suppression[5] (the latter achieved at high stimulation frequencies) and showed that they corresponded to PBR->NBR transitions. To better understand and

characterize the activation / suppression regimes, we harnessed diffusion functional MRI (dfMRI), whose fast responses were previously proposed to rely on neuromechanical coupling[6], thereby making them more specific to neural activity and less prone to blood vessel contamination[7]. Our findings reinforce the potential of dfMRI as a better tracker of neural activity.

Methods: Study in Long-Evans rats under medetomidine sedation in accordance with European Directive 2010/63. Stimulation: A blue LED (λ=470nm) was used for binocular stimulation at 1 and 25 Hz (Fig.1A). The paradigm is shown in Fig.1B. MRI: Data was acquired in a 9.4T BioSpec scanner at 95%O2 with an isotropically diffusion weighted SE-EPI sequence (TE/TR=37.3/750ms, FOV=18x18mm^2, resolution=250x250μm^2, slice thickness=1.5mm, b-value=0 and 1.5 ms/μm^2, two consecutive waveforms totalling 24.73 ms, tacq=6min and 45s) – schematic shown in Fig.1C. One tilted slice capturing the entire visual pathway was used (Fig.1D). MRI Pre-processing: Outlier, MP-PCA denoising with a 5x5 kernel, motion and slice-timing correction and isotropic smoothing. Runs were detrended with a polynomial fit to rest periods. Apparent diffusion coefficients (ADC) were calculated per timepoint: ADC=-(1/b)*ln(Sb/S0).

Results: As observed for the non-diffusion-weighted experiments, dfMRI responses in the superior colliculus (SC) and visual cortex (VC) show strong modulations with increasing stimulation frequency (Fig.2A). It is interesting to observe that dfMRI signals appear more localised to the superficial SC layers which correspond to the visual layers. Moreover, SC dfMRI time profiles show increased CNR for both BOLD regimes (Fig.2B) along with the sharp onset and offset peaks observed for the non-diffusion-weighted time profiles. Previous studies have reported ADC decreases in active brain regions; however the source of such ADC changes is not completely known with transient cell swelling/beading, increased turtuosity or a transition of water molecules from a faster to slower pool presenting as good candidates. While similar results are observed in this study for the PBR regime (Fig.2C), an ADC increase is observed for the NBR regime. In Fig.2D we propose a mechanism behind the observed ADC changes: A basal transient cell swelling (including dendritic and axonal beading as well as increased button size) exists during rest. These events dramatically increase upon neuronal activation leading to the already described ADC decrease due to increased extracellular tortuosity. Our previous work showing neuronal suppression during SC NBRs points to the hypothesis of reduced basal cell swelling upon neuronal suppression leading to increased ADC percentage resulting from decreased extracellular tortuosity.

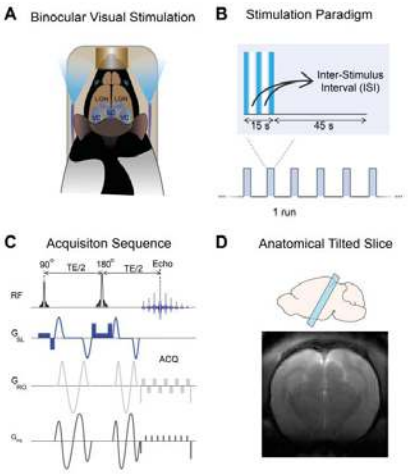

Figure 1: (A) Schematic of the animal's position in the fMRI bed along with the two LEDs for visual stimulation. The visual pathway is presented with structures used for the ROI analysis highlighted; **(B)** fMRI stimulation paradigm consisting of an initial resting period of 45s followed by 6 repetitions of the stimulation block: 15s of stimulation followed by 45s of rest; **(C)** Schematic of the isotropically DW SE-EPI sequence used for data acquisition; **(D)** Anatomical tilted slice in order to capture the entire visual pathway.

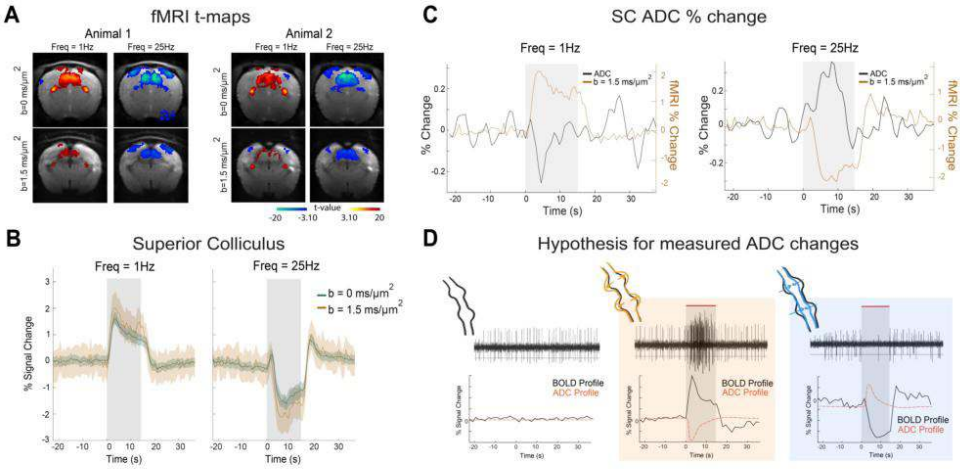

Figure 2: (A) fMRI t-maps: T-maps for 1Hz and 25Hz for the acquired tilted slice. Transitions from PBRs to NBRs are observed in cortical and subcortical areas when increasing visual stimulation frequency; **(B) fMRI Time profiles:** DfMRI signals show increased CNR in both stimulation regimes; **(C) ADC % changes:** Decreased ADC% is observed in the PBR regime while the opposite trend is observed in the NBR regime; **(D) Hypothesis for ADC changes:** A decrease of ADC can be thought of as a result from increased extracellular tortuosity due to cellular sewlling/beading which increase during neuronal activation. In the NBR regime (resulting from neuronal suppression as previous work shows) these events will be reduced compared to the resting state scenario, therefore leading to a decreased extracellular tortuosity and consequently an increased ADC.

Conclusions: Our results not only provide insight into the ongoing debate on the nature of negative BOLD signals but also open doors to investigate the biological mechanisms behind the measured ADC changes upon neuronal activation/suppression while highlighting the potential of dfMRI as a complementary and more cellular-oriented functional contrast mechanism.

References

1. Goense, J. B. M. & Logothetis, N. K. (2008), 'Neurophysiology of the BOLD fMRI Signal in Awake Monkeys.' Current Biology 18, 631–640.
2. Logothetis, N. K., et al. (2001), 'Neurophysiological investigation of the basis of the fMRI signal.' Nature 412, 150–157.
3. Shmuel, A., et al. (2006), 'Negative functional MRI response correlates with decreases in neuronal activity in monkey visual area V1.' Nature Neuroscience 9, 569–577.
4. Devor, A. et al. (2007), 'Suppressed Neuronal Activity and Concurrent Arteriolar Vasoconstriction May Explain Negative Blood Oxygenation Level-Dependent Signal.', Journal of Neuroscience 27, 4452–4459.
5. Gil, Rita, et al. (2022), 'Activation/suppression balances in rat Superior Colliculus encode the visual continuity illusion.' bioRxiv: 2022-11.
6. Nunes, D., et al. (2021) 'A rapid-onset diffusion functional MRI signal reflects neuromorphological coupling dynamics.', Neuroimage 231, 117862.
7. Kim, S.-G.,et al. (1999), 'Diffusion-weighted spin-echo fMRI at 9.4 T: Microvascular/tissue contribution to BOLD signal changes.', Magnetic Resonance in Medicine 42, 919–928.

Poster No 2435

Multi-scale brain function of tactile prediction processing: from cortical layers to whole brain

Yinghua Yu[1], Masaki Fukunaga[2], Laurentius (Renzo) Huber[3], Peter Bandettini[4,3], Norihiro Sadato[5], Jiajia Yang[1]

[1]Faculty of Interdisciplinary Science and Engineering in Health Systems, Okayama University, Okayama, Okayama, Japan, [2]Section of Brain Function Information, National Institute for Physiological Sciences, Okazaki, Aichi, Japan, [3]Functional MRI Core Facility, National Institute of Mental Health, Bethesda, MD, US, [4]Section on Functional Imaging Methods, National Institute of Mental Health, Bethesda, MD, US, [5]Research Organization of Science and Technology, Ritsumeikan University, Kyoto, Kyoto, Japan

Introduction: Human sensory processing is considered heirachally organized, having a series of discrete stages from a single cortical layer to the whole brain. In our previous studies[1,2], we demonstrated this bidirectional hierarchy processing at layer levels in the primary somatosensory cortex (S1) using laminar fMRI at 7T. We found that sensory input to S1 evoked activity in the middle layers, while prediction input yielded activity in the superficial and deep layers. Beyond the sensory cortex, our follow-up study[3] found the double-peak activity feature across midcingulate cortex (MCC) layers for tactile temporal prediction, indicating feedforward and feedback activity. Because of limited brain coverage of the VASO laminar fMRI approach, in order to explore connectivity between these regions subjects performed the prediction task both when using limited coverage laminar fMRI and whole brain lower resolution BOLD contrast.

Methods: Ten participants were asked to participate in the fMRI experiment, which consisted of one layer-specific medial surface of the cerebral hemisphere slab run and one whole brain run. We used three tactile temporal prediction (TP) tasks and one control task with random sensory input (RS) (Figure 1A). The participant was asked to predict when the left index finger will be poked in three TP tasks. The layer-specific fMRI data acquisition procedures at 7T were used as described in our previous study[1,2]. The interleaved BOLD and VASO contrasts – obtained as separate yet concomitant time series[4]. The effective TR is 4400 ms. The nominal resolution was 0.76 mm across cortical depths with 1.4-mm thick slices. For the whole brain data acquisition, multiband T2 ∗ -weighted echo planar imaging (EPI) sequence parameters were used: TR = 1785 ms, TE = 22 ms, axial slices = 90, iPAT = 2, multiband factor = 3 and spatial resolution = 1.6 × 1.6 × 1.6 mm3. The fMRI data preprocessing and general linear model analysis were conducted using AFNI and FSL. Laminar analyses were conducted with the open software suite LayNii[5]. The study protocol was approved by the local medical ethics committee at the Okayama University Hospital and National Institute for Physiological Sciences.

Results: We found that all four tasks activated widespread brain regions, including contralateral S1, bilateral S2, MCC, and other high-level regions. Task-state functional connectivity analysis and showed different connectivity patterns between prediction and prediction error tasks (Figure 1B). Furthermore, we confirmed that the layer-specific activity of MCC and SMA modulations across tasks could be detected (Figure 1C).

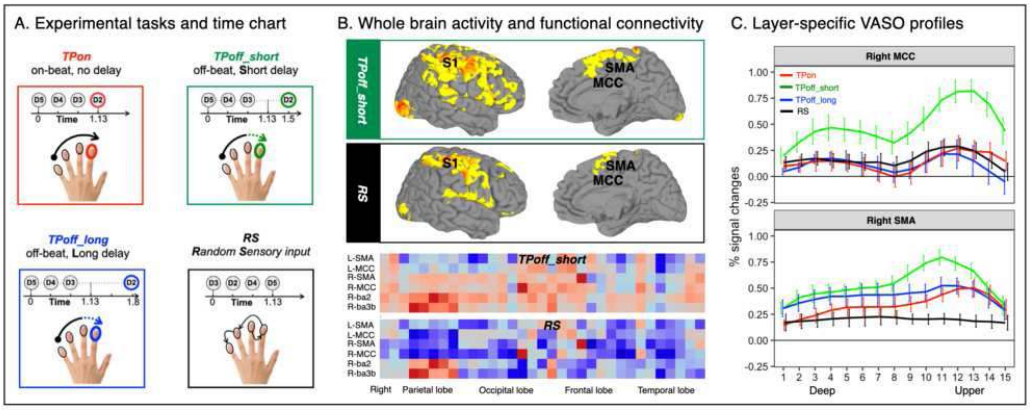

Figure 1. (A) Tactile stimulation sequences of the three temporal prediction (TP) tasks and the random sensory (RS) input control task. In the three TP tasks, the fingers were stimulated in set order (pinky to index), with the index finger receiving stimulation with the same interval as the other fingers (on-beat). In the TPoff_short and TPoff_long tasks, index finger stimulation was delayed by one beat (approximately 0.37 s) or by two beats (approximately 0.74 s), respectively. In the RS task, fingers were stimulated in a random order. (B) Whole brain mean activity maps and task-state functional connectivity (correlations) of TPoff_short and RS tasks. (C) Layer-specific VASO profiles of right MCC and SMA.

Conclusions: In the present study, we asked the participants to perform the same tactile temporal prediction tasks in a standard whole brain and a laminar BOLD/VASO fMRI session at 7T. We found that the prediction error modulated the functional connectivity between the somatosensory cortex and medial prefrontal cortex (i.e., MCC and SMA) from the whole brain session. We also found that the activity in MCC and SMA upper layers are selectively modulated by the error processing which occurred during the delayed period of the TPoff_short, but the increased upper layer activity was temporally turned by extending the off-beat interval in the TPoff_long task. One possible interpretation is that somewhat inhibitory processing may predominate during the longer delay period. These findings reflected the tactile temporal prediction processing at different spatial scales, which would be expected to provide insights into understanding our brain prediction system.

References

1. Yu Y, et al., (2019): Layer-specific activation of sensory input and predictive feedback in the human primary somatosensory cortex. Sci Adv 5:eaav9053.
2. Yu Y, et al., (2022): Layer-specific activation in human primary somatosensory cortex during tactile temporal prediction error processing. Neuroimage 248:118867.
3. Yang J, et al., (2021): Layer-specific activation of prediction in the human midcingulate cortex. Proc. Intel. Soc. Mag. Reson. Med. 29.
4. Huber L, et al., (2017): High-Resolution CBV-fMRI Allows Mapping of Laminar Activity and Connectivity of Cortical Input and Output in Human M1. Neuron 96(6):1253-1263.
5. Huber L, et al., (2021): LayNii: A software suite for layer-fMRI. Neuroimage 237:118091.

Poster No 2436

DiSpect reveals modulation and redistribution of venous blood flow caused by neural activation

Ekin Karasan[1], Chunlei Liu[1], Michael Lustig[1]

[1]Electrical Engineering and Computer Sciences, University of California, Berkeley, Berkeley, CA

Introduction: Functional MRI (fMRI) techniques probe the hemodynamic response resulting from neuronal activation. Among fMRI methods, blood-oxygenation-level-dependent (BOLD) contrast is most prominent[1,5,8]. One disadvantage is that BOLD is affected by the complex interplay of many processes[9-11], including blood oxygenation, cerebral blood volume (CBV) and cerebral blood flow (CBF). Vascular space occupancy[7] and Arterial Spin Labeling fMRI[2] are alternative methods that directly measure changes in a single process: CBV and arterial CBF, respectively. We recently introduced Displacement Spectrum Imaging (DiSpect), which is a method based on spin position tagging and imaging[3,4,12]. Previously[4], we showed that DiSpect can trace blood flow from the capillary bed into the superior cerebral veins and map venous territories (Figure 1a). Here, we show that DiSpect can consistently detect alterations in local venous blood flow due to motor cortex activation (Figure 1b).

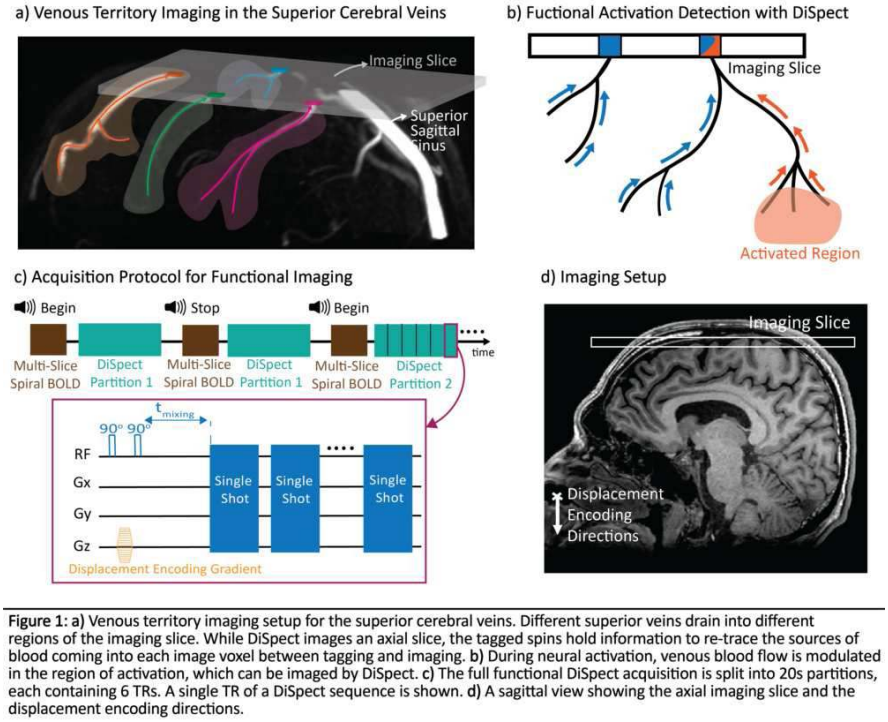

Figure 1: a) Venous territory imaging setup for the superior cerebral veins. Different superior veins drain into different regions of the imaging slice. While DiSpect images an axial slice, the tagged spins hold information to re-trace the sources of blood coming into each image voxel between tagging and imaging. b) During neural activation, venous blood flow is modulated in the region of activation, which can be imaged by DiSpect. c) The full functional DiSpect acquisition is split into 20s partitions, each containing 6 TRs. A single TR of a DiSpect sequence is shown. d) A sagittal view showing the axial imaging slice and the displacement encoding directions.

Methods: Pulse Sequence: The full DiSpect acquisition (20-30 minutes) was split into 20-second partitions to keep task durations short (Figure 1c). Partitions were repeated during task and at baseline before moving to the next. Multi-Slice Spiral-BOLD acquisitions were performed between partitions to ensure that activation is consistently occurring throughout the scan. Partitions were combined to form task and baseline blood source maps. Experiments: Two subjects were scanned using a 3T GE MR750W (GE Healthcare; Waukesha, WI). The superior cerebral veins were imaged with 2D DiSpect acquisitions during task and baseline with an axial imaging slice as placed in Figure 1d (resolution=4x4mm2/FOV=16x16cm2). Displacement encoding (displacement resolution=8x8mm2/FOV=11.2x8cm2) was performed along the LR and SI directions, producing coronal blood source maps (projected along AP). Data was collected for evolution times between 100ms to 3s after tagging (150ms increments). For the task, Subject 1 was instructed to squeeze both hands while Subject 2 was instructed to squeeze only their right hand. For each subject, a product 2D EPI-BOLD (res=3.3x3.3mm2/FOV=21x21cm2/TR=2s/TE=28ms) acquisition was performed. The subject was asked to perform the task for 20s on and 20s off for 5 minutes. Quantitative Susceptibility Mapping (QSM) was used to obtain venous structure, with protocol in[4]. STI Suite V3.0[13] was used to produce susceptibility maps using the iLSQR[6] method. A maximum intensity projection was used to visualize coronal vein structure. Data Analysis: BOLD datasets were analyzed with SPM12[14]. T-statistic images were produced with a cluster significance threshold of p=0.01. The percentage signal change in the blood source maps was determined as: %Signal Change = (Stask -Sbaseline)/ Sbaseline x 100%.

Results: Results from Subject 1 with bilateral motor cortex activation and Subject 2 with unilateral left motor cortex activation are shown (Figure 2). Two veins are selected for each subject. For Subject 1, two (orange) veins drain the activated motor cortices. For Subject 2, one (orange) vein drains the activated left motor cortex and one (blue) is selected as control. The blood source maps and their percentage change is shown (Figure 2c). In both subjects, the source maps of the activated veins show a large blood flow increase close to the BOLD activation. For Subject 1, a local decrease in blood flow is also observed in the right motor cortex, slightly further away from the neural activation, suggesting a possible redistribution of blood flow. The control vein for Subject 2 shows little percentage change.

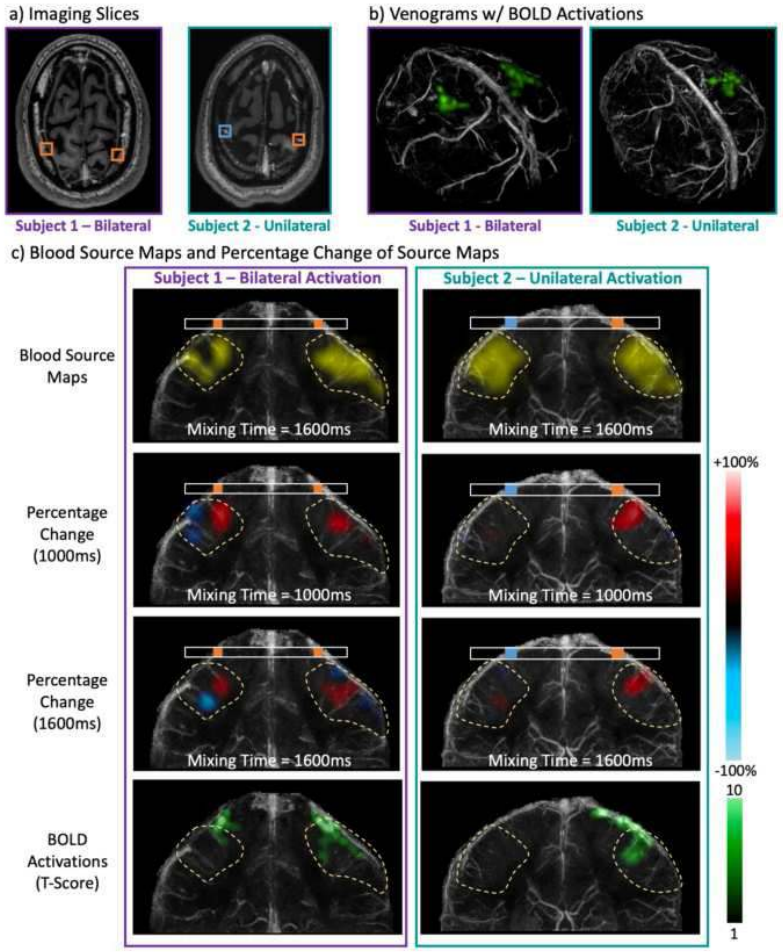

Figure 2: Bilateral motor cortex activation in Subject 1 and unilateral left motor cortex activation in Subject 2. **a)** Two veins are selected for each subject. For Subject 1, two (orange) veins drain the activated motor cortices. For Subject 2, one (orange) vein drains the activated left motor cortex and one (blue) does not and is selected as control. **b)** 3D QSM-venogram overlaid with BOLD activations (green) for both subjects. **c) Top:** Example blood source image for selected veins at a mixing time of 1600ms. **Middle:** The percentage change (at 1000ms and 1600ms mixing time) showing mostly positive and some negative blood flow change in veins draining the activated regions. Little or no percentage change is observed for the control (blue) vein. **Bottom:** BOLD activation map. Venous territories are marked with yellow dashed lines.

Conclusions: DiSpect can capture venous blood flow changes during a motor cortex task. BOLD contrast is affected by a complex interplay of several physiological processes. DiSpect probes changes in venous blood flow and can help to better understand the venous contributions in the BOLD signal.

References

1. Bandettini, P.A. (1992), 'Time course EPI of human brain function during task activation', Magnetic Resonance in Medicine, vol. 25, pp. 390.
2. Borogovac, A. (2012), 'Arterial Spin Labeling (ASL) fMRI: advantages, theoretical constrains, and experimental challenges in neurosciences.' International Journal of Biomedical Imaging, vol. 2012, pp. 818456.
3. Karasan, E. (2022), '"Reverse Perfusion" Imaging of the Cerebral Venous System with Displacement Spectrum Imaging (DiSpect).' Proceedings of International Society of Magnetic Resonance in Medicine.
4. Karasan, E. (2023), 'Advances in Post-Perfusion Venous Territories Imaging with Displacement Spectrum Imaging (DiSpect).' Proceedings of International Society of Magnetic Resonance in Medicine.
5. Kwong, K.K. (1992), 'Dynamic magnetic resonance imaging of human brain activity during primary sensory stimulation', Proceedings of National Academy of Sciences, vol. 89, pp. 5675.
6. Li, W. (2015), 'A method for estimating and removing streaking artifacts in quantitative susceptibility mapping.' Neuroimage, vol. 108, pp. 111-122.
7. Lu, H. (2003), 'Functional magnetic resonance imaging based on changes in vascular space occupancy', Magnetic Resonance in Medicine, vol. 50, no. 2, pp. 263-274.
8. Ogawa, S. (1992), 'Intrinsic signal changes accompanying sensory stimulation: functional brain mapping with magnetic resonance imaging', Proceedings of National Academy of Sciences, vol. 89, pp. 5951-5955.
9. Ogawa, S. (1993) 'Functional brain mapping by blood oxygenation level dependent contrast magnetic resonance imaging. A comparison of signal characteristics with a biophysical model', Biophysical Journal, vol. 64, pp. 803-812.
10. Turner, R. (1998), 'Echo-planar time course MRI of cat brain oxygenation changes.' Magnetic Resonance in Medicine, vol. 22, pp. 159-166.

11. van Zijl, P.C. (1998), 'Quantitative assessment of blood flow, blood volume and blood oxygenation effects in functional magnetic resonance imaging', Nature Medicine, vol. 4, pp. 159-167.
12. Zhang, Z. (2021), 'DiSpect: Displacement spectrum imaging of flow and tissue perfusion using spin-labeling and stimulated echoes.' Magnetic Resonance in Medicine, vol. 86, no. 5, pp. 2468-2481.
13. https://people.eecs.berkeley.edu/~chunlei.liu/software.html
14. http://fil.ion.ucl.ac.uk/spm/

Poster No 2437

Baseline hypoperfusion is associated with seizure severity in patients with epilepsy

Victoria Mosher[1], Tefani Perera[2], Laura Gill[2], Ismael Gaxiola-Valdez[1], Paolo Federico[1]

[1]University of Calgary, Calgary, Alberta, [2]Univeristy of Calgary, Calgary, Alberta

Introduction: Epilepsy is a serious neurological disease that affects millions of people worldwide and is characterized by recurrent, unprovoked seizures. Recently, it has been discovered that following a seizure, areas of the brain that are involved in the seizure onset become hypoxic due to a reduction in cerebral blood flow (CBF) for upwards of 60 minutes before returning to baseline (Farrell et al., 2016). Using perfusion imaging, we have generated CBF maps that detect hypoperfusion localizing to the region of seizure onset (Gaxiola-Valdez et al., 2017). While these postictal CBF maps can provide valuable localizing information for clinicians, it requires patients to be admitted to the hospital for 24-hour observation. For this reason, researchers have investigated the utility of baseline measures of hypoperfusion (i.e., hypoperfusion between seizures). Unfortunately, the utility of baseline hypoperfusion has not been established (Perera et al., 2020), possibly due to differences in seizure severity among the different seizure types. In this study, we measured baseline hypoperfusion in patients with epilepsy to determine whether the frequency of different focal seizure types influences the degree of hypoperfusion.

Methods: Twenty patients with a confirmed diagnosis of epilepsy participated in this study. Baseline arterial spin labelling scans (3T GE Discovery MR 750 system; 3D fast-spin-echo pseudo-continuous arterial spin labeling with background suppression; TR=4725ms, TE=10.152ms, post label delay=2025ms, NEX=4 and spiral acquisition with 512 points and 8 arms) were collected from patients after a seizure-free period of ≥ 24 hours to generate CBF maps. Each CBF map was compared to CBF maps of 100 healthy controls to identify regions of hypoperfusion. The mean CBF value (mL/100g/min) of the area of maximal hypoperfusion was extracted from each patient's CBF map and correlated with the frequency of three different focal seizure types: focal aware (FAS), focal impaired awareness (FIAS) and focal to bilateral tonic-clonic (FBTCS).

Results: Five patients did not display any baseline hypoperfusion and were excluded from further analysis. In the remaining 15 patients, mean disease duration was 17 years (range 6 months – 38 years), mean number of FAS was 14.5/month (range 0-135), mean number of FIAS was 8.1/month (range 0-40) and mean number of focal to bilateral tonic-clonic seizures was 0.5/month (range 0-5). There was a significant positive correlation between frequency of FBTCS and level of baseline hypoperfusion ($r=0.558$, $p=0.031$). No other significant correlations were found.

Conclusions: FBTCS are considered the most severe type of focal seizure, with longer seizure duration and a greater involvement of brain tissue relative to other seizure types (Steriade et al., 2022). It is possible that FBTCS have more long-lasting effects on the vascular dynamics in the brain. These findings provide evidence that baseline hypoperfusion measures may be more useful in cases where the patient experiences a higher frequency of FBTCS. This relationship between hypoperfusion and frequency of FBTCS may help shed light on why studies investigating baseline hypoperfusion in patients with epilepsy have generated conflicting results.

References

1. Farrell, J.S., Gaxiola-Valdez, I., Wolff, M.D., David, L.S., Dika, H.I., Geeraert, B.L., ... Teskey, G.C. (2016), 'Postictal behavioural impairments are due to a severe prolonged hypoperfusion/hypoxia event that is COS-2 depenedent, Elife, vol. 5, pp. e19352.
2. Gaxiola-Valdez, I., Singh, S., Perera T., Lie, E., Federico, P. (2017), 'Seizure onset zone localization using postictal hypoperfusion detected by arterial spin labelling MRI', Brain, vol. 140, no. 11, pp. 2895-2911.
3. Perera, T., Gaxiola-Valdez, I., Singh, S., Peedicail, J., Sandy, S., Lebel, R.M., Li, E., Milne-Ives, M., Szostakiwskyj, J., Federico, P. (2020), 'Localizing the seizure onset zone by comparing patient postictal hypoperfusion to healthy controls', Journal of Neuroscience Research, vol. 98, pp. 1517-1531.
4. Steriade, C., Sperling, M.R., DiVentura, B., Lozano, M., Shellhasss, R.A., Kessler, S.K., Dlugos, D., French, J. (2002), 'Proposal for an updated seizure classification framework in clinical trials', Epilepsia, vol. 63, pp. 565-572.

Poster No 2438

Comparing rapid direct neural evoked responses using non-selective MRI and simultaneous EEG

Peter Molfese[1], A. Morgan[1], J Derbyshire[1], Laurentius (Renzo) Huber[1], Peter Bandettini[1]

[1]National Institute of Mental Health, Bethesda, MD

Introduction: Several groups have reported attempts to directly measure neural responses using MRI sequences (DIANA) in mice[1,2] and humans[3,4,5]. Measuring brain responses with DIANA presents great potential for impact on the field of functional MRI, as it would circumvent the necessity for indirect inference of neural activity based on vascular signals[1,6]. The feasibility of measuring DIANA responses is still an open question, as these responses are reportedly very small1, requiring many trial to averages to measure useful signal[2]. Furthermore, the structure of 2D line-scanning sequences used to image DIANA responses necessitates trials be repeated for every acquired k-space line[5], inflating the required number of trials. We measured DIANA responses from the center of k-space using a fast (3 ms), non-selective MRI sequence without phase or frequency encoding, negating the need to repeat trials for multiple k-space lines. For comparison, we simultaneously acquired EEG during evoked auditory and visual stimulation experiments.

Methods: We tested a fast, non-selective, balanced steady-state free precession (bSSFP) sequence[7] without gradient encoding to record the center of k-space (Fig. 1). MRI scan parameters: TR=3 ms; TEs=0.75 to 2.25 ms; RF: hard pulse length=0.5 ms, FA=12°; ADC length=1.5 ms, BW=21370 Hz, vector size=64; RF and ADC phase progressed by 180° with every TR; an SSFP preparation preceded the first TR (FA=6°; TR=1.5 ms). Two participants underwent testing on a Siemens 3T Skyra with a Siemens 64-receiver coil. The first participant viewed a flashing strobe light (10 us; Grass Instruments PS33) via a fiber optic cable with an interstimulus interval (ISI) of 834 ms. The second participant heard two auditory tones (1000 and 2000 Hz; duration=300 ms), with random presentation order and pseudo-random ISIs (800-2000 ms). MRI time series were formed by Fourier transforming every ADC and taking the magnitude of the spectral peak response. Data were bandpass filtered between 0.5 and 50 Hz. MRI receiver coil locations were estimated by computing the center of mass of sensitivity maps within a skull ROI. We cut epochs between -100 and 800 ms from stimulus time and averaged within conditions. EEG data were recorded using a MR-conditional 256-channel EGI GES 400 (EGI; Eugene, OR). To reduce the impact of the BCG, QRS were estimated from the EEG channels, and subtracted using optimal basis sets[8], bandpass filtered 0.1-30Hz, segmented -100 to 700 ms from stimulus onset, baseline corrected, average referenced, and averaged.

Results: Evoked responses (MRI) and potentials (EEG) to visual flash stimulation are shown in Figure 2. We observe response dynamics in both MRI and EEG at 100 ms as well as correspondence between MRI and EEG topographical features. However, a prominent feature of the MRI time series for the visual stimulation paradigm is a substantial positive and negative peak at 200 ms. This feature is likely caused by a blink artifact, and is less visible in the EEG potentials due to semi-automated removal of epochs containing a blink. Responses and potentials to auditory stimulation are shown in Figure 3. These responses are more lateralized than the visual responses, and we see increased dynamics between conditions in the MRI signal, with an initial negative response for the 1000 Hz tone (100 ms) and a delayed positive response (500 ms). There is some correspondence between MRI and EEG topographies, though MRI responses are comparatively delayed. The initial negative response was not visible with the 2000 Hz tone and the response peak occurred earlier (250 ms).

Conclusions: We provide strong yet still preliminary evidence for evoked MRI response dynamics on the order of tens to hundreds of milliseconds, and compare the shape and topography of and responses to simultaneously acquired EEG measurements.

Figure 1

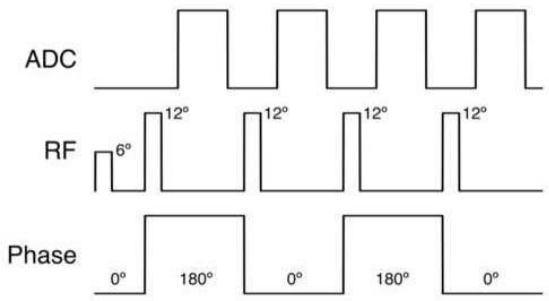

Figure 2

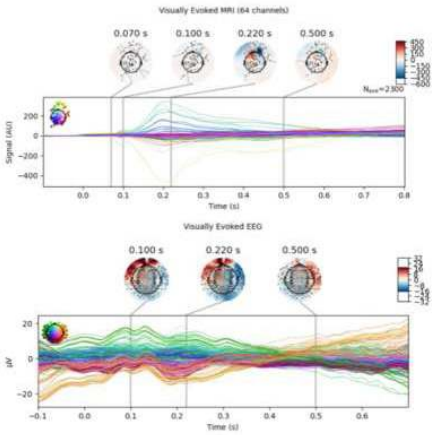

Figure 3

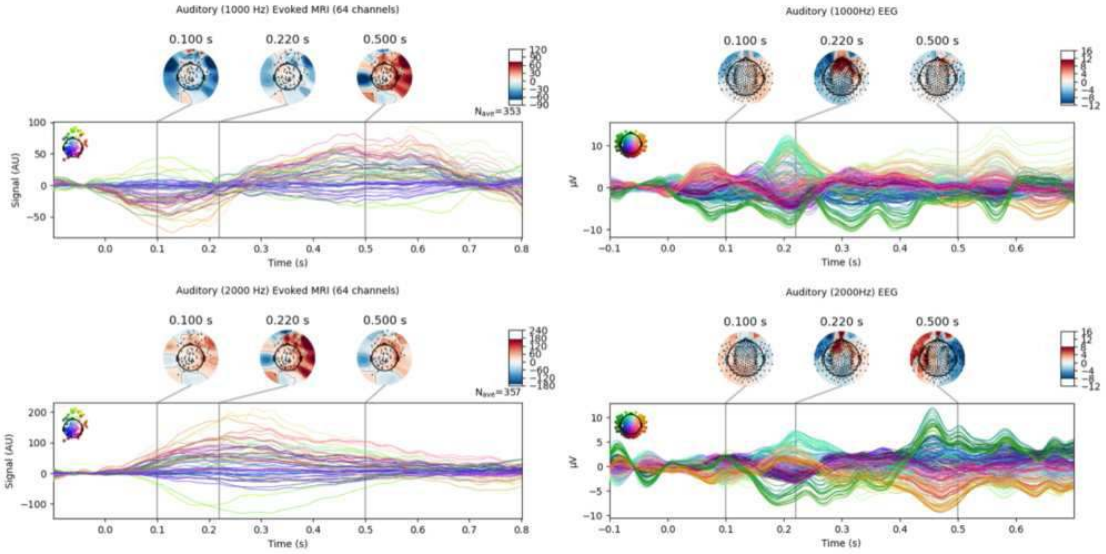

References

1. Toi, Phan Tan, Hyun Jae Jang, Kyeongseon Min, Sung-Phil Kim, Seung-Kyun Lee, Jongho Lee, Jeehyun Kwag, and Jang-Yeon Park. “In Vivo Direct Imaging of Neuronal Activity at High Temporospatial Resolution.” Science 378, no. 6616 (October 14, 2022): 160–68. https://doi.org/10.1126/science.abh4340.
2. Choi, Sang-Han, Geun Ho Im, Sangcheon Choi, Xin Yu, Peter A. Bandettini, Ravi S. Menon, and Seong-Gi Kim. “No Replication of Direct Neuronal Activity-Related (DIANA) fMRI in Anesthetized Mice.” bioRxiv, May 29, 2023. https://doi.org/10.1101/2023.05.26.542419.
3. Zhang, Yifei, Kaibao Sun, Jianxun Ren, Qingyu Hu, Yezhe Wang, Shiyi Li, Tienzheng Chen, et al. “High-Resolution Dynamic Human Brain Neural Activity Recording Using 3T MRI.” bioRxiv, June 4, 2023. https://doi.org/10.1101/2023.05.31.542967.
4. Hodono S, Rideaux R, van Kerkoerle T, Cloos MA. Initial experiences with Direct Imaging of Neuronal Activity (DIANA) in humans. 2023. https://arxiv.org/abs/2303.00161
5. Wilson, Joshua M., Hua Wu, Adam B. Kerr, Brian A. Wandell, and Justin L. Gardner. “Limitations of Line-Scan MRI for Directly Measuring Neural Activity.” bioRxiv, November 5, 2023. https://doi.org/10.1101/2023.11.03.565394.
6. O’Herron, Philip, Pratik Y. Chhatbar, Manuel Levy, Zhiming Shen, Adrien E. Schramm, Zhongyang Lu, and Prakash Kara. “Neural Correlates of Single-Vessel Haemodynamic Responses in Vivo.” Nature 534, no. 7607 (June 2016): 378–82. https://doi.org/10.1038/nature17965.
7. Scheffler, Klaus, and Stefan Lehnhardt. “Principles and Applications of Balanced SSFP Techniques.” European Radiology 13, no. 11 (November 1, 2003): 2409–18. https://doi.org/10.1007/s00330-003-1957-x.
8. Niazy, R. K., C. F. Beckmann, G. D. Iannetti, J. M. Brady, and S. M. Smith. “Removal of FMRI Environment Artifacts from EEG Data Using Optimal Basis Sets.” NeuroImage 28, no. 3 (November 15, 2005): 720–37. https://doi.org/10.1016/j.neuroimage.2005.06.067.

Poster No 2439

Imaging the brain during coughing: a unique PET study of cough

Yasuomi Ouchi[1,2], Takafumi Sugi[1], Etsuji Yoshikawa[3]

[1]Hamamatsu University School of Medicine, Hamamatsu, Japan, [2]Hamamatsu Medical Photonics Foundation, Hamamatsu, Japan, [3]Hamamatsu Photonics KK, Hamamatsu, Japan

Introduction: Coughing is known as a defensive reflex that protects the airways from harmful substances. Clinically, the cough reflex may be impaired by stroke While brain activity during cough was previously examined by functional magnetic resonance imaging (fMRI) with model analysis, this method does not capture the actual brain activity during coughing. To obtain accurate measurements of brain activity during coughing, we use an unrestrained positron emission tomography (PET) system with head motion correction to correct for head motion while a whole-brain scan was performed during a coughing task.

Methods: Twenty-four healthy right-handed men underwent multiple PET scans with [15O]H2O. We have recently developed a PET camera with a free-moving function that enables imaging during head movement by collecting positron signals every 1 second while correcting head movement every 4 milliseconds (Inubushi et al, Neuroimage 2021). Four tasks were performed during the scan: “resting”; “voluntary cough (VC)”, which is simply repeated spontaneous coughing; “induced cough (IC)”, where participants cough in response to the stimulating stimulus using the cough-inducing method with tartaric acid (CiTA); and “suppressed cough (SC),” in which cough was suppressed in response to CiTA. For CiTA, a 10% solution of L-tartaric acid was used in the IC and SC tasks, and saline was used as a placebo in the resting and VC tasks. We used 60 s of [15O]H2O data reconstructed after the increase in the PET count of the brain. The dose of [15O]H2O injected was 2.5 MBq/kg per scan. During the [15O]H2O experiment, the number of coughs and the intensity of coughing (cough peak flow) were measured. At the end of each scan, the urge to cough during the task was checked on a 10-point scale using the numerical rating scale. We performed whole brain analyses of [15O]H2O PET data with SPM12, applying a fixed-effect analysis with a multi-participant and multi-condition full factorial design, incorporating all scans from all participants into a single general linear model. This study was approved by the Hamamatsu University School of Medicine Ethics Committee.

Results: Whole brain analyses of motion-corrected data revealed that VC chiefly activated the supplementary motor cortex and the cerebellum extending to pons. In the IC condition, the infratentorial regions, including the pons, medulla oblongata and cerebellar regions, were activated. In the SC condition, significant activation was found in the superior frontal region covering the sensory cortex and the anterior and middle cingulate cortices. Furthermore, CiTA-related tasks (IC and SC) activated the higher sensory regions of the cerebral cortex and associated brain regions. When the urge to cough was taken into account in this analysis, we found that a wider range of cerebral regions including the cerebral cortex and diencephalon play a role in cough control under sensory stimulation.

Conclusions: Our PET system allows us to image brain activity without head restriction, and this study is the first to depict brain activity during coughing, suggesting that brain activity during simple cough is controlled chiefly by infratentorial areas. Cough control requires incorporating higher sensory areas of the brain to provide top-down control of information coming from the periphery. The current study partly clarified the underlying mechanism of CiTA, which allows clinicians to predict whether it will be effective before attempting it in stroke patients with brain lesions related to cough control.

References

1. Inubushi, T. et al. (2021), Neural correlates of head restraint: Unsolicited neuronal activation and dopamine release, Neuroimage, vol. 224,117434

Poster No 2440

Endogenous opioid receptor system mediates costly altruism in the human brain

Jinglu Chen[1], Vesa Putkinen[1], Kerttu Seppälä[1], Jussi Hirvonen[1], Kalliopi Ioumpa[2], Valeria Gazzola[2], Christian Keysers[2], Lauri Nummenmaa[1]

[1]Turku PET Centre, Turku, Finland, [2]The Netherlands Institute for Neuroscience, KNAW research institute, Amsterdam, The Netherlands

Introduction: Prosocial behavior is prevalent in humans and animals. It benefits the receiver, but also has a range of positive outcomes for the helper (De Waal & Preston, 2017). The neurocognitive link between empathy and prosociality has been investigated by quantifying responses in brain regions associated with empathy while witnessing the pain of others, and correlating these measures with individual differences in helping. However, the neuromolecular basis of individual differences

in vicarious pain and helping remain poorly understood. PET studies showed that mu-opioid receptor (MOR) availability is negatively associated with haemodynamic responses to seeing others in pain (Karjalainen et al., 2017), and positively correlated with prosocial motivation as indexed by social attachment styles (Nummenmaa et al., 2015; Turtonen et al., 2021). Against this background, here we investigated whether individual differences in the MOR availability translate into measurable differences in the willingness to forfeit money to reduce pain to others.

Methods: 30 women particate in the fMRI experiment and 14 of them in the PET scan. MOR density was measured with high-affinity agonist radioligand [11C]carfentanil during resting baseline with PET/CT. The fMRI study was run using the costly helping paradigm (Gallo et al., 2018). Participants met the confederate and were explained that the experiment would be performed in two separate rooms connected by a video camera. During the scan, participants, believing to witness the pain of the victim through a closed-circuit television, actually viewed pre-recorded videos of the confederate receiving the painful simulation. On each trial, subjects first saw a video of the confederate receiving a painful electric shock (1st video). The intensity of expressed pain ranged randomly from 2 (mild pain) to 6 (moderate pain) out of ten. After the video, subjects could decide how much money they were willing to donate on that trial to reduce the intensity of the second shock (2nd video) in that trial (Figure 1). FMRI data were analyzed in SPM12. First-level general linear models (GLM) were estimated by modeling the 1st video, donation phase, and the 2nd video by using boxcar regressors in the design matrix. Donation size (trial-wise donations for each subject) was entered as parametric modulator for the 1st video. Subject-wise contrast images were then generated for main effects of 1st video, donation phase, 2nd video. For PET baseline data, radiotracer binding was quantified using non-displaceable binding potential (BPND), calculated as the ratio of specific binding to non-displaceable binding in the tissue. To characterize the interactions between MOR availability and BOLD responses in pain perception and costly altruism, we first used PCA to reduce the dimensionality in the BPNDs across our ROIs, then used the first PC to predict the voxel-wise BOLD responses to the 1st video with donation size as a parametric modulator.

Results: People were in general willing to engage in costly helping, and donations increased as a function of the shock intensity shown in the first video, ß = 0.877, SE = 0.023, t = 37.591, $p < 0.001$. Haemodynamic activity in amydala, anterior insula, anterior cingulate cortex, striatum, primary motor cortex, primary somatosensory cortex, and thalamus increased when participants witnessed the pain of others. Insula, anterior cingulate cortex activated more strongly as the donation increased. These haemodynamic responses were negatively associated with MORs availability in the striatolimbic and cortical emotion circuits (Figure 2). In turn, haemodynamic responses during helping were positively associated with MOR availability in the anterior cingulate cortex and hippocampus.

Conclusions: Taken together, these results suggest that the opioid system is intimately involved in vicarious pain and neural processing of helping decisions.

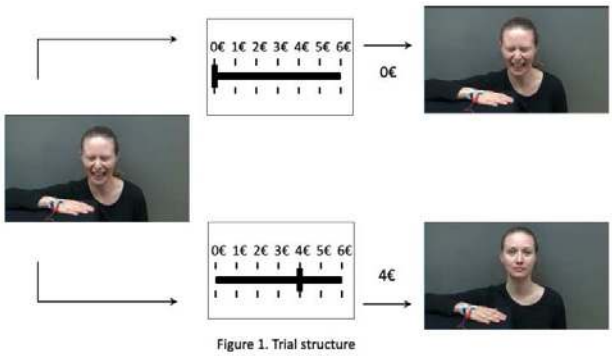

Figure 1. Trial structure

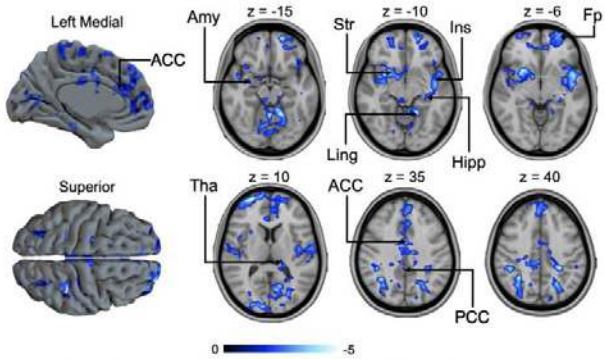

Figure 2. Negative correlation between the MOR availability and the parametric modulator of BOLD response to donation size during 1st video.

References
1. De Waal, F. B. M., & Preston, S. D. (2017). 'Mammalian empathy: Behavioural manifestations and neural basis', Nature Reviews Neuroscience, vol. 18, no. 8, pp. 498–509.
2. Karjalainen, T., Karlsson, H. K., Lahnakoski, J. M., Glerean, E., Nuutila, P., Jääskeläinen, I. P.,
3. Hari, R., Sams, M., & Nummenmaa, L. (2017). 'Dissociable roles of cerebral μ-opioid and type 2 dopamine receptors in vicarious pain: A combined PET-fMRI study'. Cerebral Cortex, vol. 27, no. 8, pp. 4257–4266
4. Nummenmaa, L., Manninen, S., Tuominen, L., Hirvonen, J., Kalliokoski, K. K., Nuutila, P., Jääskeläinen, I. P., Hari, R., Dunbar, R. I. M., & Sams, M. (2015). 'Adult attachment style is associated with cerebral μ-opioid receptor availability in humans'. Human Brain Mapping, vol. 36, no. 9, pp. 3621–3628.
5. Turtonen, O., Saarinen, A., Nummenmaa, L., Tuominen, L., Tikka, M., Armio, R. L., Hautamäki, A., Laurikainen, H., Raitakari, O., Keltikangas-Järvinen, L., & Hietala, J. (2021). 'Adult Attachment System Links With Brain Mu Opioid Receptor Availability In Vivo'. Biological Psychiatry: Cognitive Neuroscience and Neuroimaging, vol. 6, no. 3, pp. 360–369.
6. Gallo, S., Paracampo, R., Müller-Pinzler, L., Severo, M. C., Blömer, L., Fernandes-Henriques, C., Henschel, A., Lammes, B. K., Maskaljunas, T., Suttrup, J., Avenanti, A., Keysers, C., & Gazzola, V. (2018). 'The causal role of the somatosensory cortex in prosocial behaviour'. ELife, vol. 7, pp. 1–31.

Poster No 2441

Neuroinflammation in Human Immunodeficiency Virus-Related Neuropathic Pain

Minhae Kim[1], Angelica Sandstrom[1], Aarushi Tandon[1], Akila Weerasekera[1], Kelly Castro-Blanco[1], Shibani Mukerji[2], Vitaly Napadow[3], Robert Edwards[4], Eva-Maria Ratai[1], Marco Loggia[1]

[1]A.A. Martinos Center for Biomedical Imaging, Massachusetts General Hospital, Harvard Medical School, Boston, MA, [2]Massachusetts General Hospital, Harvard Medical School, Boston, MA, [3]Massachusetts General Hospital, Harvard Medical School, Charlestown, MA, [4]Brigham and Women's Hospital, Harvard Medical School, Boston, MA

Introduction: Approximately 38 million people worldwide live with human immunodeficiency virus (HIV). A common neurological complication of HIV and its treatment in people living with HIV (PWH) is HIV-associated sensory neuropathy, with neuropathic pain being its most highly prevalent and debilitating symptom. Our group has previously observed elevated levels of the 18kDa translocator protein (TSPO), a marker of glial activation and neuroinflammation, in human chronic pain and HIV using [11C]PBR28 positron emission tomography (PET)[1-2]. In this study, we used [11C]PBR28 PET to evaluate the hypothesis that HIV-related neuropathic pain is accompanied by elevated levels of TSPO expression in PWH.

Methods: Twenty-six PWH (11 with neuropathic pain, PWHpain; 15 without pain, PWHnopain) and 27 healthy controls (HC) completed [11C]PBR28 PET/MRI scans. All participants were genotyped for the Ala147Thr polymorphism in the TSPO gene, which predicts binding affinity to [11C]PBR28, and low affinity binders were considered ineligible. All PWH were on stable antiretroviral therapy and virally suppressed (plasma HIV RNA <200 copies/mL) at the time of screening. PWH completed the PainDETECT self-reported questionnaire, where higher scores (range: 0-38) indicate higher levels of neuropathic pain. Standardized uptake values (SUV) were computed from 60-90 min post-[11C]PBR28 injection data, spatially smoothed (FWHM=8mm), and normalized to the MNI template using FSL and FreeSurfer. A T1-weighted volume (MEMPRAGE; TR/TE1/TE2/TE3/TE4=2530/1.64/3.5/5.36/7.22ms, flip angle=7°, voxel size=1x1x1mm3) was used for attenuation correction of PET data and spatial normalization to the MNI space. Whole-brain voxel-wise analyses were run with Randomize, using a cluster-forming threshold of z=2.3 and including genotype as a covariate of no interest. PHW vs. HC comparison utilized occipital lobe normalization to increase sensitivity to widespread [11C]PBR28 signal, while within-PWH comparisons and correlation utilized whole brain normalization to detect regionally specific pain-related neuroinflammatory signals.

Results: PWH showed elevated TSPO expression compared to HC in the frontal white and grey matter including the ventrolateral, ventromedial, and dorsolateral prefrontal cortices, frontal pole, and secondary somatosensory cortex. PWHpain showed higher TSPO expression compared to PWHnopain in the anterior and posterior midcingulate (aMCC and pMCC, respectively) and posterior cingulate cortices, dorsolateral and dorsomedial prefrontal cortices (dLPFC and dMPFC, respectively), precentral gyrus, superior parietal lobule (SPL), supplementary motor area (SMA), and primary somatosensory and motor cortices (S1 and M1, respectively). In PWH, TSPO expression was positively correlated with PainDETECT scores in the cuneus, aMCC, pMCC, SMA, dMPFC, dLPFC, SPL, S1 and M1.

Conclusions: Overall, PWH showed elevated TSPO expression compared to HC, and PWHpain showed elevated [11C]PBR28 signal in the cingulate and prefrontal cortices and somatosensory and sensorimotor areas compared to PWHnopain. In PWH, [11C]PBR28 signal was positively correlated with PainDETECT scores in the prefrontal, cingulate, and primary somatosensory and motor cortices, suggesting an association between neuropathic pain and neuroinflammation. Future research with a larger sample size is required to assess the generalizability and validity of these observations.

References
1. Loggia et al. (2015). Evidence for brain glial activation in chronic pain patient. Brain, 138(3), 604-615.
2. Sari et al. (2022). Multimodal investigation of neuroinflammation in aviremic patients with HIV on antiretroviral therapy and HIV elite controllers. Neurology Neuroimmunology Neuroinflammation, 9(2), e1144.

Poster No 2442

Impact of Ageing on Memory and Dopaminergic Modulation: A Concurrent MR-PET Study with Fallypride

Yeo-Jin Yi[1], Jarkko Johansson[2], Berta Garcia-Garcia[1], Peter Schulze[1], Kathrin Baldauf[1], Matthew Betts[1], Marianne Patt[3], Oliver Speck[4], Osama Sabri[3], Michael Kreißl[5], Emrah Düzel[6], Dorothea Hämmerer[7]

[1]German Center for Neurodegenerative Diseases (DZNE), Magdeburg, Sachsen-Anhalt, [2]Department of Radiation Sciences, Umeå, [3]University Hospital Leipzig, Leipzig, Sachsen, [4]German Center for Neurodegenerative Diseases (DZNE), Magdeburg, Germany, [5]University Hospital Magdeburg, Magdeburg, Sachsen-Anhalt, [6]Institute of Cognitive Neurology and Dementia Research, Magdeburg, Germany, [7]Innsbruck University, Innsbruck, Tirol

Introduction: The dopaminergic system's profound impact on cognitive functions, particularly learning and memory, is well known (Lisman, Grace, & Düzel, 2011; Lisman & Grace, 2005). Dopamine (DA) is in particular essential for encoding and consolidating salient memories-key to our survival (Shohamy & Adcock, 2010). With an ageing population and rising neurodegenerative diseases, deciphering the DA system's memory link is crucial (Bäckman et al., 2010). Our study uses concurrent fMRI and dynamic [18F]fallypride PET imaging to examine age-related changes in D2/D3 receptor function's impact on memory.

Methods: Thirty-three healthy seniors (age: M=71.48, SD=5.52) underwent two concurrent MR-PET sessions with the high-affinity D2/D3 receptor antagonist [18F]fallypride. During the fMRI-PET sessions, subjects performed a reward task to investigate the link between reward, memory encoding, and DA receptor density. Approximately 15 minutes and 24 hours after the reward task, subjects performed recognition tests. PET data analyses included motion and physiological artefact correction, sMRI parcellation, and the radioactivity curve over time (time-activity curve [TAC]) extraction from regions of interests (Figure 1). Pharmacokinetic analysis of TACs using a simplified reference tissue model quantified the baseline BPND (BPBSL) (Lammertsma & Hume, 1996).

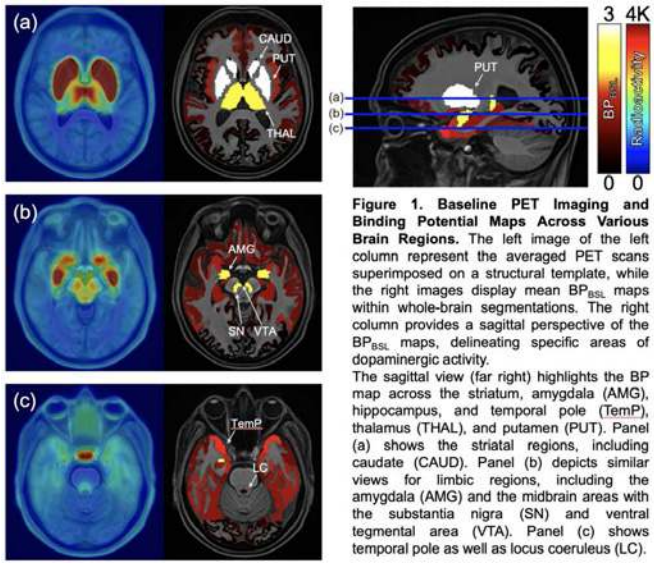

Figure 1. Baseline PET Imaging and Binding Potential Maps Across Various Brain Regions. The left image of the left column represent the averaged PET scans superimposed on a structural template, while the right images display mean BP_{BSL} maps within whole-brain segmentations. The right column provides a sagittal perspective of the BP_{BSL} maps, delineating specific areas of dopaminergic activity.
The sagittal view (far right) highlights the BP map across the striatum, amygdala (AMG), hippocampus, and temporal pole (TemP), thalamus (THAL), and putamen (PUT). Panel (a) shows the striatal regions, including caudate (CAUD). Panel (b) depicts similar views for limbic regions, including the amygdala (AMG) and the midbrain areas with the substantia nigra (SN) and ventral tegmental area (VTA). Panel (c) shows temporal pole as well as locus coeruleus (LC).

Results: Partial correlation analyses, controlling for age, revealed significant associations between BPBSL and recognition memory test performance quantified as loglinear D-prime (D'; Hautus 1995). A differential relationship between positive and negative relationships of receptor density and memory for neutral and rewarded stimuli was observed (Figure 2). Specifically, older adults with higher receptor densities in thalamus and nucleus accumbens (NAcc) showed better memory in particular for neutral scenes (thalamus: ρ=0.372, pFDRc=0.012; NAcc: ρ=0.294, pFDRc=0.058). Similarly, older adults with higher D2/D3 receptor density in the putamen showed better memory for reward-associated stimuli (ρ=0.305, p=0.041). On the other hand, higher D2/D3 receptor densities in substantia nigra (SN) and NAcc were related to worse memory for reward-associated stimuli (SN: ρ=-0.307, p=0.041; NAcc: ρ=-0.268, p=0.085).

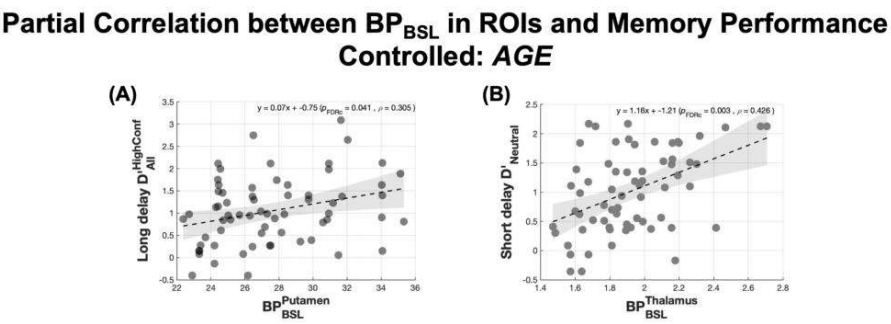

Figure 2. **Partial Correlations (Spearman's rho) Between Baseline Binding Potential and Memory Performance, Adjusted for Age.** Each point represents a single experimental session data. The dashed lines represent the best-fit linear regression for each dataset, with shaded areas indicating the 95% confidence interval for the regression line. **Panel (A)** displays a significant positive relationship between BP_{BSL} in the putamen and high-confidence memory performance for all stimuli in long delay recognition tests (p_{FDRc}=0.041, ρ=0.305). **Panel (B)** shows a significant positive correlation between BP_{BSL} in the thalamus and memory performance for neutral stimuli in short delay tests (p_{FDRc}=0.003, ρ=0.426).

Conclusions: Our study delineates the complex relationship between the DA system and memory encoding in ageing adults. We observed significant but varied correlations across different brain regions, which also distinguished memory performance for neutral and reward-associated stimuli. Particularly, enhanced memory for rewarded stimuli seemed particularly linked to higher D2/D3 receptor densities in the putamen, as opposed to findings in the SN and NAcc. In contrast, memory for neutral stimuli appeared to be associated with higher D2/D3 receptor densities in the thalamus and NAcc. These results may indicate a comparatively pronounced role in attention processing structures in the recognition of less the less salient neutral stimuli in ageing. We hope that our observations contribute to a better understanding of ageing memory capacities and underscore the potential of dopaminergic modulation as a target for interventions.

References

1. Bäckman, Lars, Ulman Lindenberger, Shu-Chen Li, and Lars Nyberg. (2010), 'Linking Cognitive Aging to Alterations in Dopamine Neurotransmitter Functioning: Recent Data and Future Avenues'. Neuroscience & Biobehavioral Reviews 34 (5): 670–77. https://doi.org/10.1016/j.neubiorev.2009.12.008.
2. Hautus, Michael J. (1995), 'Corrections for Extreme Proportions and Their Biasing Effects on Estimated Values Ofd''. Behavior Research Methods, Instruments, & Computers 27 (1): 46–51. https://doi.org/10.3758/BF03203619.
3. Lammertsma, Adriaan A., and Susan P. Hume. (1996), 'Simplified Reference Tissue Model for PET Receptor Studies'. NeuroImage 4 (3): 153–58. https://doi.org/10.1006/nimg.1996.0066.
4. Lisman, John E., and Anthony A. Grace. (2005), 'The Hippocampal-VTA Loop: Controlling the Entry of Information into Long-Term Memory'. Neuron 46 (5): 703–13. https://doi.org/10.1016/j.neuron.2005.05.002.
5. Lisman, John, Anthony A. Grace, and Emrah Duzel. (2011), 'A neoHebbian Framework for Episodic Memory; Role of Dopamine-Dependent Late LTP'. Trends in Neurosciences 34 (10): 536–47. https://doi.org/10.1016/j.tins.2011.07.006.
6. Shohamy, Daphna, and R. Alison Adcock. (2010), 'Dopamine and Adaptive Memory'. Trends in Cognitive Sciences 14 (10): 464–72. https://doi.org/10.1016/j.tics.2010.08.002.

Poster No 2443

Tau-PET pathology correlates with cognition and disease severity in Progressive Supranuclear Palsy

Roxane Dilcher[1], Charles Malpas[2], Terence O'Brien[1], Lucy Vivash[1]

[1]Dept. of Neuroscience, Monash University, Melbourne, VIC, [2]University of Melbourne, Melbourne, VIC

Introduction: For primary tau pathologies, such as Progressive Supranuclear Palsy (PSP), there are currently no specific biomarkers, limiting disease diagnosis and the development of treatments. The recently introduced positron emission tomography (PET) radiotracer 18F-PI-2620 has the potential to detect abnormal tau protein in PSP. This study investigates the correlation between tau-PET and clinical markers in PSP.

Methods: In this preliminary, cross-sectional analysis, 16 patients with clinically diagnosed probable PSP (Richardson's Syndrome) underwent T1-weighted MRI and 0-60 min dynamic 18F-PI-2620 PET scanning. Standardized uptake value ratios (SUVr) were generated for regions of interest (globus pallidus, frontal, and occipital lobe). Clinical assessments included the Digit Span Memory task, Hayling, Stroop, Trail Making Test, National Institutes of Health (NIH) toolbox subtasks, the Behaviour Rating Inventory of Executive Function (BRIEF-A, 'Never'-scores), and the PSP Rating Scale (PSP-RS). Voxel-wise and region-based multiple regression analyses tested the associations between SUVr and clinical markers. Data was pre-processed and analysed with FSL, SPM, and R.

Results: Tau uptake in the basal ganglia was negatively associated with the Digit Span Reverse task or the BRIEF-A (voxel-wise, p<0.01). Region-based analyses showed that tau uptake in the basal ganglia was significantly predicted by impairments in the Digit Span Forward and Reverse task (p<0.01), working memory subtask of the NIH toolbox (p<0.05), and the BRIEF-A (p<0.05). No positive associations were found in the frontal or occipital regions. There were significant clinical scales by region interactions, with the basal ganglia showing stronger negative associations in the Digit Span tasks, working memory subtask, oral reading recognition subtask, and BRIEF-A, compared to the frontal and the occipital lobe (p<0.05).

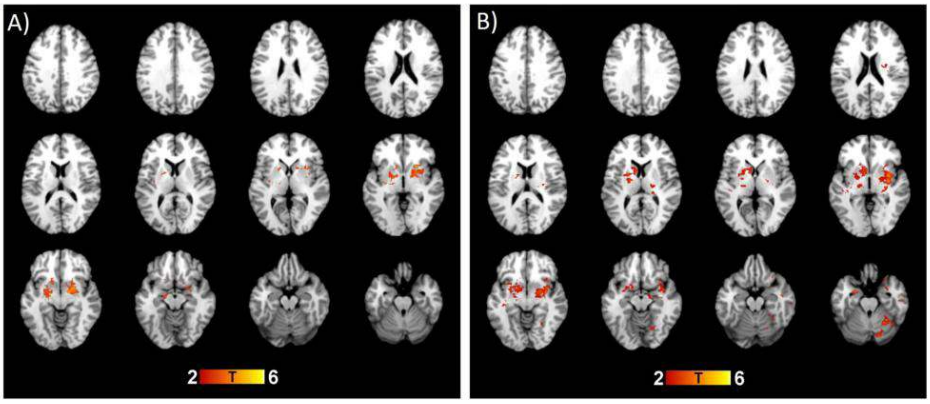

Figure 1. Significant associations between basal ganglia tau uptake (SUVr) and A) executive functions (Digit Span Memory Task Reverse) or B) disease severity (BRIEF-A, 'Never' scoring). Voxel-wise T-statistics are shown at *p*<0.01, *k*>500, overlaid on a standard template T1 MRI image.

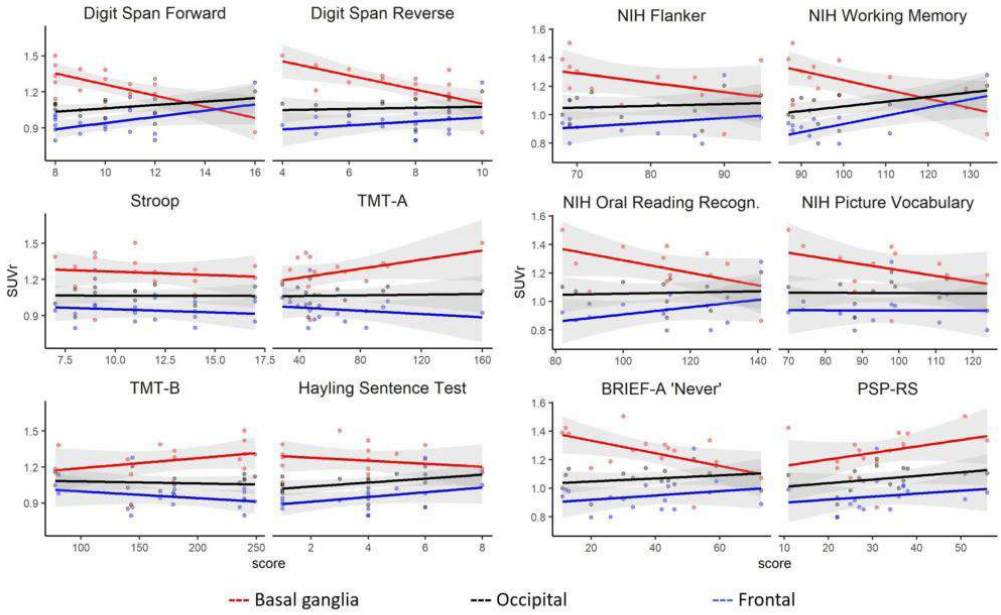

Figure 2. Region of interest associations for each clinical scale. Basal ganglia tau uptake (SUVr) is represented by the red line, occipital tau uptake by the black line, and frontal lobe tau uptake by the blue line.

Conclusions: Associations between executive dysfunctions, disease severity and tau uptake in the basal ganglia suggest suitability of the 18F-PI-2620 tracer as an in-vivo tau biomarker for the diagnosis and tracking of disease progression in PSP. New biomarkers are essential for the advancement of future clinical trials.

References

1. Brendel M. (2020), 'Assessment of 18F-PI-2620 as a Biomarker in Progressive Supranuclear Palsy'. JAMA Neurol. vol 77, no. 11, pp. 1408-1419
2. Kroth, H. (2019), 'Discovery and preclinical characterization of [18F]PI-2620, a next-generation tau PET tracer for the assessment of tau pathology in Alzheimer's disease and other tauopathies.' European journal of nuclear medicine and molecular imaging. vol. 46, no. 10, pp. 2178-2189

Poster No 2444

3D MRI to PET Translation using Constrained Denoising Diffusion Probabilistic Model

Minhui Yu[1], Mingxia Liu[1]

[1]*University of North Carolina at Chapel Hill, Chapel Hill, NC*

Introduction: Brain PET and MRI are non-invasive imaging techniques that play important roles in diagnosing and monitoring neurological conditions such as dementia and epilepsy. However, unlike MRI that is widely accessible in clinical practice, PET is usually unavailable due to its high cost and the complexities associated with radioactive tracers. To address this challenge, it is desirable to generate PET data from MRIs. Numerous prior studies employ generative adversarial networks (GANs) for MRI to PET translation but are generally limited by unstable model training, thus leading to less reliable results. To this end, we propose a novel constrained denoising diffusion probabilistic model (cDDPM) for PET synthesis based on corresponding MRI scans, which can enhance stability of model training while ensuing fidelity of generated PET images. In this framework, we propose to enhance the vanilla DDPM training process[1] by incorporating constraints on not only the noise component, but also the generated outcomes in final timestep derived from this noise. This improvement helps ensure the fidelity of synthesized PET images due to their one-to-one correspondence with input MRIs. This is among the first attempts to translate from 3D structural MRI to PET through a new constrained diffusion model at image level. Experimental results on 293 subjects suggest the superiority of our method in generating PET with high image quality, compared with state-of-the-arts.

Methods: The proposed cDDPM is a 3D generative framework based on a DDPM model that incorporates dual constraints during training process. As shown in Fig. 1, our cDDPM contains 3 downsampling blocks, 2 residual blocks, and 3 upsampling blocks, enhanced with cross-attention mechanisms and with the timestep embedded to intermediate convolutional layers. Each 3D MRI is incorporated as a condition, which is concatenated to the perturbed PET image (PET+Gaussion noise) as the input. The training process consists of (1) a forward process that incrementally adds Gaussian noise to the PET image across 1,000 timesteps, and (2) a reverse process that progressively denoises to reconstruct PET. In each timestep, a portion of noise is introduced with its proportion gradually increasing with time according to a predefined schedule, to avoid overly polluting the image at the onset. During training, a noisy image from a random intermediate timestep for each subject is used to predict the noise, to estimate the less noisy image at the preceding timestep. A noise-level constraint is used to encourage the estimated noise to be close to the real noise, and an image-level constraint is proposed to ensure the similarity between the synthetic PET (generated from the estimated noise) and its real image. The model undergoes 40 epochs of training with paired MRI and PET. In the test stage, our model is applied to input MR images along with Gaussian noise to synthesize their corresponding PET scans. Through 1,000 inference timesteps, the model removes the noise and ultimately yields the PET.

Results: The ADNI dataset[2] is used to validate the effectiveness of our method. The dataset contains 293 paired MRI and 18-fluoro-deoxyglucose PET scans of healthy control brains, among which we use approximately 90% of data (263 subjects) for training and 10% (30 subjects) for test. The peak signal noise ratio (PSNR) and structural similarity index measure (SSIM) of synthetic PET generated by our method on the test data is 22.884±0.584 dB and 0.680±0.008, respectively, with an improvement of 50.56% and 44.98% compared with its counterpart without the image-level constraint. We also compare our method with GAN[3] that yields the PSNR of 22.226±0.424 dB and SSIM of 0.676±0.0002. These results demonstrate the strong ability of our proposed model on modality translating from MRI to PET.

Conclusions: The proposed cDDPM translates 3D MRI to PET by introducing an image-level constraint on DDPM that greatly improves the accuracy of the one-to-one image synthesis.

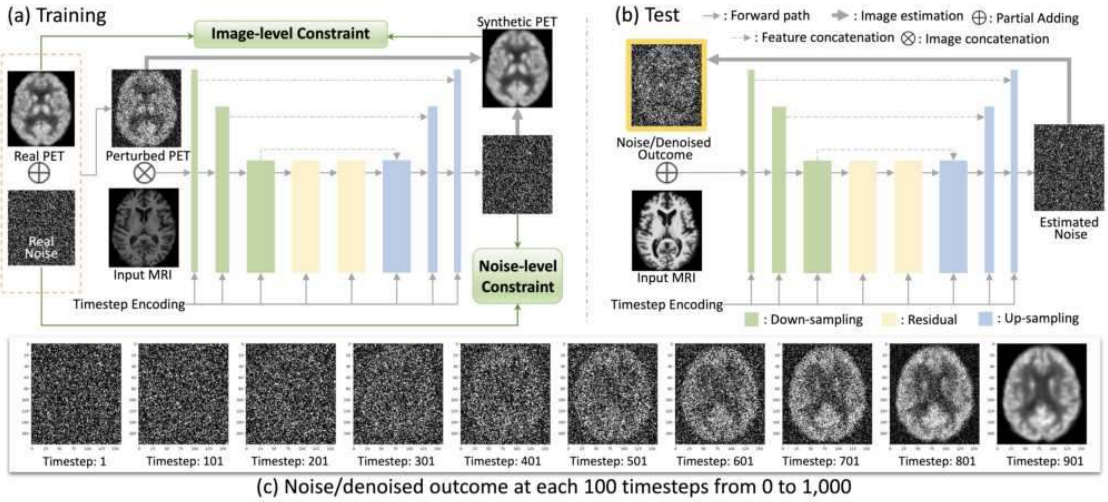

(c) Noise/denoised outcome at each 100 timesteps from 0 to 1,000

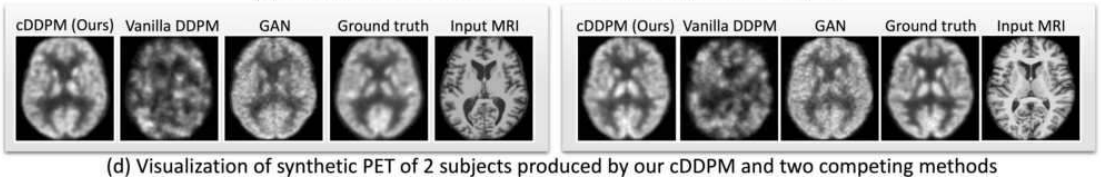

(d) Visualization of synthetic PET of 2 subjects produced by our cDDPM and two competing methods

References

1. Ho, J., Jain, A., & Abbeel, P. (2020). Denoising diffusion probabilistic models. Advances in neural information processing systems, 33, 6840-6851.
2. Jack Jr, C. R., Bernstein, M. A., Fox, N. C., Thompson, P., Alexander, G., Harvey, D., ... & Weiner, M. W. (2008). The Alzheimer's disease neuroimaging initiative (ADNI): MRI methods. Journal of Magnetic Resonance Imaging: An Official Journal of the International Society for Magnetic Resonance in Medicine, 27(4), 685-691.
3. Liu, Y., Yue, L., Xiao, S., Yang, W., Shen, D., & Liu, M. (2022). Assessing clinical progression from subjective cognitive decline to mild cognitive impairment with incomplete multi-modal neuroimages. Medical image analysis, 75, 102266.

Poster No 2445

The relationship between SV2A levels, neural activity, and cognitive function in healthy humans

Ekaterina Shatalina[1], Ellis Chika Onwordi[1], Thomas Whitehurst[2], Alexander Whittington[3], Ayla Mansur[3], Tiago Reis Marques[1], Roger Gunn[3], Sridhar Natesan[1], Matthew Nour[4], Eugenii Rabiner[3], Matthew Wall[3], Oliver Howes[1]

[1]Institute of Psychiatry, Psychology and Neuroscience, King's College London, London, United Kingdom, [2]Imperial College London, London, United Kingdom, [3]Invicro, London, United Kingdom, [4]Departement of Psychiatry, Oxford University, Oxford, United Kingdom

Introduction: Synapses are key sites of neuronal activity and are thought to be central to cognitive performance. [11C] UCB-J Positron Emission Tomography (PET) provides an index of synaptic terminal density, which has been linked with cognition in neurological and psychiatric populations. However, the link between synaptic terminal density and cognitive function has never been explored in healthy humans. We set out to investigate this and whether synaptic density is also positively associated with task-induced neural activity, measured by functional Magnetic Resonance Imaging (fMRI) of executive function.

Methods: Twenty-five healthy adults (22M,3F; mean age±SD 35.36±12.46) underwent a [11C]UCB-J PET and a fMRI scan where they performed an N-back working memory task and a task switching exercise (n=23). The N-back included two working memory conditions (1-back, 2-back) and an attentional control (0-back), a 1&2back>0back contrast was computed to model effects of working memory. Mean 1&2back accuracy was used as the main performance measure. The switching task had an event-related design, where participants responded to number-letter pairs appearing either in blue or green. Depending on the stimulus colour, they indicated if the number was odd/even or if the letter was a vowel/consonant. Trials where the colour changed were defined as switch trials and a switch>no-switch contrast was computed to model the effect of switching. Switch cost, defined as the difference in reaction time between switch and no-switch trials, was the main task performance measure. Voxel-wise kinetic modelling of [11C]UCB-J was carried out using a one-tissue compartment model to produce volume of distribution values. The centrum semiovale was then used as a reference region to produce a mean distribution volume ratio (DVRcs) for task-relevant predefined regions of interest (ROIs). A partial least squares (PLS) canonical analysis (CA) was used

to test relationships between [11C]UCB-J PET DVRcs and task-induced neural activity across 6 ROIs selected for each task. PLS-regression (PLS-R) was applied to test the relationship between [11C]UCB-J PET DVRcs and task performance. Exploratory Pearson's correlations were carried out to test relationships in individual regions.

Results: [11C]UCB-J PET DVRcs was significantly positively related to task-induced neural activity during task switching (PLS-CA second canonical component, r=0.63, p=0.043, figure 1), with the thalamus-putamen data positively contributing to this relationship (PLS-CA loading 0.679, exploratory Pearson's correlation r=0.42, p=0.044). [11C]UCB-J DVRcs was significantly predictive of behavioural switch cost (PLS-R, R2=0.45, RMSE=0.06, p=0.022, figure 2), with exploratory analyses showing significant negative correlations between switch cost and [11C]UCB-J DVRcs in the insula (r=−0.45, p=0.034), dorsolateral prefrontal cortex (r=−0.52, p=0.013), parietal-precuneus (r=−0.59, p=0.004), posterior frontal cortex (r=−0.56, p=0.007) and anterior cingulate cortex (r=−0.42, p=0.049). There were no relationships between [11C]UCB-J DVRcs and N-back working memory task-induced neural activity or task performance measures.

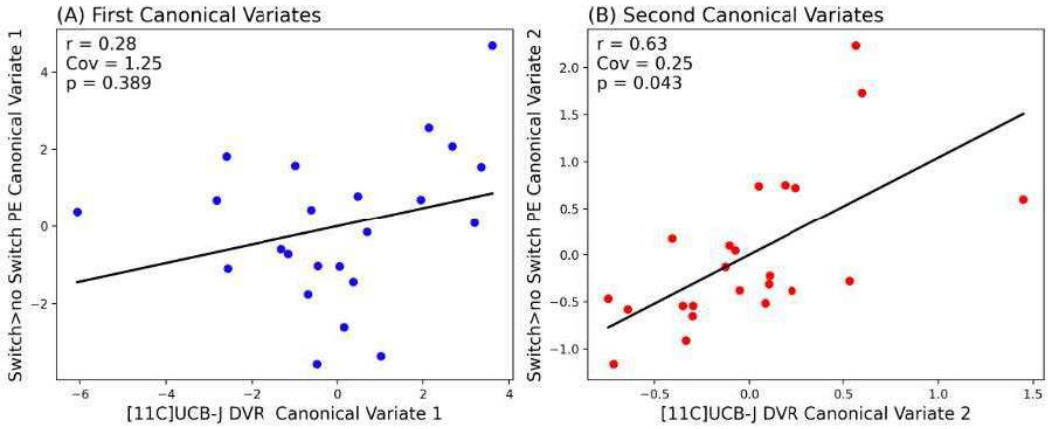

Fig. Partial Least Squares Canonical Analysis (PLS-CA) showing a strong positive correlation between [11C]UCB-J DVRcs and task switching related neural activity in the second canonical component (B)

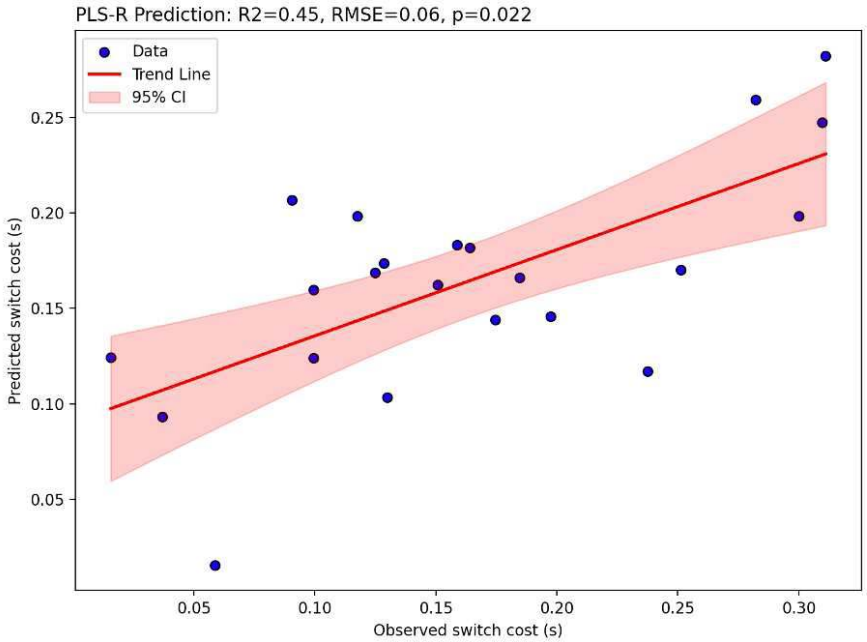

Fig. Partial-least-squares regression results showing switch cost (s) is significantly predicted by [11C]UCB-J DVRcs values across six task-switching relevant regions of interest

Conclusions: Interindividual differences in synaptic terminal density may be related to differences in switch cost and switching-related neural activity but not with working memory task performance or neural activity. Our results suggest some cognitive functions may be more closely related to synaptic terminal density which has implications for conditions associated with synaptic loss, as these functions may be more vulnerable to impairment.

Poster No 2447

Bridging Machine Learning and Clinical Diagnosis: An Explainable Biomarker for ß-Amyloid PET Imaging

János Barbero[1], Ana Franceschi[2], Luca Giliberto[1], Patrick Do[3], David Petrover[2], Jack Truong[4], Sean Clouston[5], Nha Nguyen[6], Marc Gordon[2], An Vo[1]

[1]The Feinstein Institutes for Medical Research, Manhasset, NY, [2]Donald and Barbara Zucker School of Medicine at Hofstra/Northwell, Hempstead, NY, [3]University of Massachusetts Amherst, Amherst, NY, [4]Adelphi University, Garden City, NY, [5]Renaissance School of Medicine at Stony Brook University, Stony Brook, NY, [6]Albert Einstein College of Medicine, New York, NY

Introduction: [18F]-florbetaben positron emission tomography (PET) imaging is an established marker of ß-Amyloid (Aß) that is being increasingly used to assess Aß deposition in Alzheimer's Disease (AD) [Sabri et al., 2015]. However, evaluation of these scans currently relies on expert interpretation. While prior machine learning classifiers for [18F]-florbetaben imaging exist [Lee et al., 2021], they lack the transparency needed for clinical decision-making. Our work bridges this gap, introducing an explainable machine learning biomarker for assessing Aß deposition in a more interpretable and clinically relevant manner.

Methods: We analyzed 163 [18F]-florbetaben PET scans acquired at our institution as part of a retrospective analysis [Franceschi et al., 2023]. Each scan was interpreted by two independent expert readers to assess Aß+ status, blinded to each other's assessments. We segmented and registered the scans into Montreal Neurological Institute (MNI) space using Statistical Parametric Mapping (SPM) 12, parcellated them using the Automated Anatomical Labeling (AAL) atlas [Tzourio-Mazoyer et al., 2002], then computed mean expression scores in each region normalized by mean cerebellar expression using a custom program in Matlab R2023a. We used the regional loadings to train a Cubic Support Vector Machine (SVM) classifier and tested the model using 5-fold cross-validation. To elucidate the model's decision-making process in aggregate, we employed local interpretable model-agnostic explanations (LIME) [Ribeiro et al., 2016], projecting the most influential features back onto the AAL atlas for visualization.

Results: Our cohort comprised 163 patients with [18F]-florbetaben imaging obtained from 2016 to 2018 (84M, 83F; 76.1 ± 6.8yo). There was high agreement (92.0%, k=0.84) between the readers, with 90 scans interpreted as positive and 60 as negative by both. The Cubic SVM classifier demonstrated robust performance, achieving 92.0% accuracy and 90.5% precision under 5-fold cross-validation. The model was highly sensitive (95.6%) and specific (87.7%) to Aß+ status, with an area under the curve (AUC) of 95.0% and an F1 score of 93.0% (Fig. 1). LIME analysis revealed that the model identified critical regions impacting Aß+ status, with notable contributions from the inferior frontal cortex, cuneus, olfactory cortex, postcentral gyrus, supramarginal gyrus, temporal pole, thalamus, and pallidum (Fig. 2). In our findings, amyloid deposition within the temporal pole emerged as the most significant factor in confirming Aß positivity. Conversely, the absence of amyloid deposition in the cuneus was identified as the key indicator for ruling out Aß+ status.

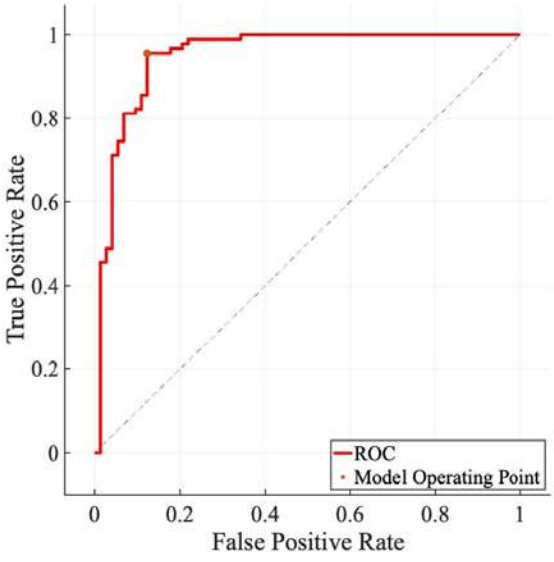

Figure 1: Receiver operating characteristic curve of a Cubic Support Vector Machine classifier to evaluate Aβ+ in [18F]-florbetaben PET scans. The model is highly sensitive (95.6%) and specific (87.7%), with a total AUC of 95.0%.

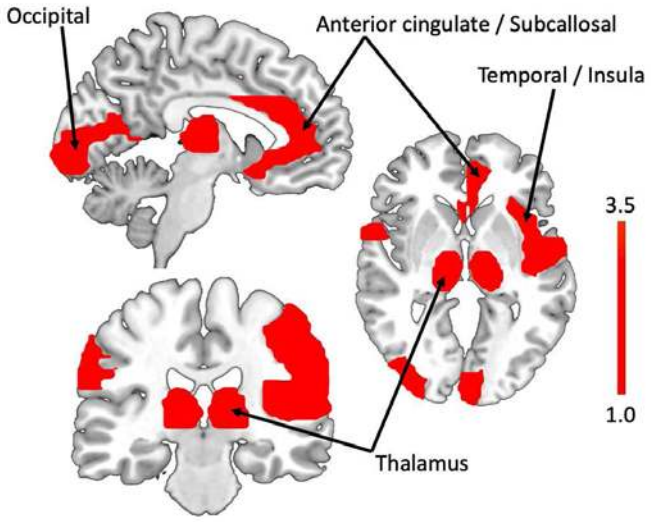

Figure 2: Local interpretable model-agnostic explanations (LIME) region weights for β-Amyloid (Aβ) positive predictions. Amyloid burden in regions that contributed significantly to predicting Aβ+ status include the temporal cortex, inferior frontal and orbitofrontal cortices, insula, postcentral gyrus, supramarginal gyrus, and thalamus.

Conclusions: This study presents a novel, explainable machine learning-based biomarker for assessing Aß+ positivity based on [18F]-florbetaben PET scans. The model showcases high accuracy, paralleling expert interpretation levels, and provides critical insights into the brain regions most affected by amyloid deposition. Unlike other black-box classifiers, our model transparently delineates the specific brain regions influencing its classifications. This clarity is crucial in a clinical setting, where the rationale behind diagnostic decisions must be both understandable and justifiable. In the context of emerging amyloid-focused disease-modifying therapies, the transparency and precision of our model make it a robust tool for patient selection, assessment of treatment efficacy, and monitoring of disease progression in a clinically interpretable manner. Finally, by elucidating the relationship between overall Aß+ status and specific brain regions, our approach holds promise for novel insights into the correlation between the spatial distribution of Aß and the clinical manifestations of Alzheimer's Disease.

4. References
5. Franceschi A.M. (2023), 'Semiquantitative Approach to Amyloid Positron Emission Tomography Interpretation in Clinical Practice', World J Nucl Med, 22:015–021.
6. Lee S.-Y. (2021), 'Performance evaluation in [18F]Florbetaben brain PET images classification using 3D Convolutional Neural Network', PLOS ONE, 16:e0258214.
7. Ribeiro M.T. (2016), '"Why Should I Trust You?": Explaining the Predictions of Any Classifier. In: . Proceedings of the 22nd ACM SIGKDD International Conference on Knowledge Discovery and Data Mining', Association for Computing Machinery KDD '16, pp 1135–1144.
8. Sabri O. (2015), 'Beta-amyloid imaging with florbetaben', Clin Transl Imaging, 3:13–26.
9. Tzourio-Mazoyer N. (2002), 'Automated Anatomical Labeling of Activations in SPM Using a Macroscopic Anatomical Parcellation of the MNI MRI Single-Subject Brain', NeuroImage, 15:273–289.

Poster No 2448

The modulation of cortical and cardiovascular arousal markers via volitional control of pupil size

Marieke Weijs[1], Silvia Missura[1], Bianca Badii[1], Manuel Carro Dominguez[1,2], Alan Kyle[1], Marc Bächinger[1], Nicole Wenderoth[1,2,3], Sarah Meissner[1]

[1]Neural Control of Movement Laboratory, Department of Health Sciences and Technology, ETH Zurich, Zurich, Switzerland, [2]Neuroscience Center Zurich, University and ETH Zurich, Zurich, Switzerland, [3]Future Health Technologies, Singapore-ETH Centre, Campus for Research Excellence and Technological Enterprise (CREATE), Singapore, Singapore

Introduction: The arousal levels of the human brain is key to cognitive functioning and mental well-being. Arousal is regulated by several neuromodulatory systems in the brainstem and basal forebrain, but one key regulator is the Locus Coeruleus (LC) (Joshi et al., 2016; Zerbi et al., 2019). The LC is the main source of noradrenaline (NA) for the central nervous system and modulates cardiovascular function via projections to the brainstem and spinal cord (Samuels & Szabadi, 2008). Interestingly, there is ample evidence for a link between LC activity and non-luminance dependent changes in pupil size (Samuels & Szabadi, 2008). Utilizing this link, we have recently shown that changes in pupil size can be volitionally induced via mental strategies and pupil-based biofeedback (pupil-BF) training and are associated with changes in LC activity (Meissner et al.,

2023). Here, we aim to investigate whether such volitional changes modulate (i) electrophysiological and (ii) cardiovascular arousal markers.

Methods: In experiment I, 23 healthy volunteers (21-41 years) received 3 days of pupil-BF training to learn to volitionally up- and downregulate pupil size. Eye tracking was performed to measure and feed back pupil size during training. On day 3, simultaneous electroencephalography (EEG) and electrocardiography (ECG) recordings were performed during pupil-BF training. In experiment II, we recorded EEG data while 20 already trained participants of an earlier cohort (Meissner et al., 2023) of pupil-BF training (21-47 years) were performing simultaneous pupil self-regulation (or a counting control task) and a two-tone auditory oddball task. EEG data were cleaned for artefacts using a slightly adapted automated EEG preprocessing pipeline Automagic. In experiment I, data were epoched in 3000 ms time windows during regulation of pupil size, the Welch's power spectrum was estimated, and the slope of the EEG power spectrum from 30-43 Hz was extracted using the fooof toolbox. ECG R-peaks were automatically detected using PhysioZoo, and RR-intervals were extracted to calculate heart rate and heart rate variability (HRV; root mean square of successive differences) during periods of up- and downregulation. In experiment II, we extracted epochs of 500 ms, from -1000 to 2500 ms around oddball tone for spectral slope calculations as in experiment I.

Results: Both at the end of training (i.e., day 3) and during the oddball task, participants of experiment I and II were able to successfully self-regulate their pupil size reflected by a difference between up- and downregulation. EEG and ECG analyses of experiment I revealed that pupil self-regulation was linked to systematic to changes in electrophysiological and cardiovascular arousal markers: we found shallower slopes of the EEG power spectrum from 30-43 Hz, higher heart rate, and lower HRV during blocks of volitional pupil size up- than downregulation. Similar effects on the EEG slope were observed during the auditory oddball task (n = 17). Overall, we found a steeper slope around oddball targets during blocks of down- than upregulation, or the counting control condition. Furthermore, the slope is shallower right after than before stimulus presentation but returns to pre-stimulus levels within the 2500 ms window for all three conditions.

Conclusions: Taken together, these results show that volitional self-regulation of arousal via pupil-BF using mental strategies not only changes pupil size but is also reflected in global electrophysiological and cardiovascular markers of arousal. Volitional control of pupil size modulated arousal in a pure self-regulation setting, as well as in a dual task setting during an oddball task. Thus, pupil-size can be used as a reliable marker of the brain's arousal system, and biofeedback can be used to make this system accessible for volitional control. Importantly, these findings bear tremendous translational potential for the development of arousal self-regulation applications in for example, stress-related disorders.

References

1. Behar, J. A. et al. (2018). PhysioZoo: A Novel Open Access Platform for Heart Rate Variability Analysis of Mammalian Electrocardiographic Data. Frontiers in Physiology, 9, 1390.
2. Donoghue, T. et al. (2020). Parameterizing neural power spectra into periodic and aperiodic components. Nature Neuroscience, 23, 1655–1665.
3. Joshi, S. et al. (2016). Relationships between Pupil Diameter and Neuronal Activity in the Locus Coeruleus, Colliculi, and Cingulate Cortex. Neuron 89, 221–234.
4. Meissner, S. N. et al. (2023). Self-regulating arousal via pupil-based biofeedback. Nature Human Behaviour, doi:10.1038/s41562-023-01729-z.
5. Pedroni, A. et al. (2019). Automagic: Standardized preprocessing of big EEG data. NeuroImage 200, 460–473.
6. Samuels, E. et al. (2008). Functional Neuroanatomy of the Noradrenergic Locus Coeruleus: Its Roles in the Regulation of Arousal and Autonomic Function Part II: Physiological and Pharmacological Manipulations and Pathological Alterations of Locus Coeruleus Activity in Humans. Current Neuropharmacology, 6, 254–285.
7. Zerbi, V. et al. (2019). Rapid Reconfiguration of the Functional Connectome after Chemogenetic Locus Coeruleus Activation. Neuron 103, 702-718.e5.

Poster No 2449

Dynamic alpha power modulations and slow negative potentials reflect spatio-temporal attention

Charline Peylo[1,2,3], Carola Romberg-Taylor[3], Larissa Behnke[1,2,3], Paul Sauseng[1,3]

[1]University of Zurich, Zurich, Switzerland, [2]Graduate School of Systemic Neurosciences, Planegg-Martinsried, Germany, [3]Ludwig Maximilian University, Munich, Germany

Introduction: Psychophysiological processes such as spatio-temporal top-down attention and its underlying neural signatures typically do not operate in isolation and can thus easily be confounded by secondary processes. Alpha power modulations and slow negative potentials, for example, have previously been associated with anticipatory processes in spatial and temporal top-down attention (e.g., Peylo et al., 2021; Praamstra et al., 2006; Rohenkohl & Nobre, 2011; Sauseng et al., 2005; Zanto et al., 2011), but neural responses triggered by transient stimulus onsets as well as decision- and/or- motor-related

processes (both of which are common to most traditional research designs) can interfere with attention-driven activity patterns and our interpretation of such (e.g., Di Russo et al., 2021; Kelly et al., 2006). Here, we investigated alpha power modulations and slow negative potentials as signatures of spatio-temporal attention in a dynamic paradigm that was designed to minimize these potential confounds.

Methods: Twenty-nine participants performed two parallel tasks while the electroencephalogram (EEG) was recorded. The first part of each trial consisted of a dynamic target detection task, in which participants attended the cued side of a bilateral stimulus rotation and mentally counted how often one of two remembered sample orientations (i.e., the target) was displayed while ignoring the uncued side and non-target orientation. In the second part of each trial, participants performed a delayed match-to-sample task, in which they indicated if the orientation of a probe stimulus matched the orientation of the corresponding sample stimulus (previously either target or non-target). We analyzed whether changes in alpha power and/or slow negative potentials during the dynamic target detection task mirrored the expected shifts of spatio-temporal attention towards task-relevant points in space and time (i.e., onset of the target orientation in the cued hemifield) and whether these dynamics were associated with performance in either of the two tasks.

Results: In line with our hypothesis, we observed dynamic alpha power decreases and slow negative waves around task-relevant locations and time points (i.e., onset of the target orientation on the cued side of the screen) over posterior electrodes contralateral to the locus of attention. In contrast to static alpha power lateralization, these dynamic signatures significantly correlated with performance in the subsequent delayed match-to-sample task (indicating decreased accuracy for probes of the counting-irrelevant non-target orientation with increasing alpha power reduction and slow wave negativity), suggesting a preferential allocation of attention to task-relevant points in space and time at the cost of reduced resources and impaired performance for information outside the current focus of attention.

Conclusions: Using a dynamic paradigm to minimize potentially interfering stimulus- and motor-related activity, we were able to reveal subtle yet behaviorally relevant dynamics of alpha power and slow negative potentials that mirrored attentional shifts towards relevant moments in time at relevant locations in space, thereby providing an important contribution to our knowledge about these two signatures of spatio-temporal top-down attention.

References

1. Di Russo et al. (2021), 'Sustained visuospatial attention enhances lateralized anticipatory ERP activity in sensory areas', Brain Structure and Function, vol. 226, pp. 457-470
2. Kelly et al. (2006), 'Increases in alpha oscillatory power reflect an active retinotopic mechanism for distracter suppression during sustained visuospatial attention', Journal of Neurophysiology, vol. 95, no. 6, pp. 3844-3851
3. Peylo et al. (2021), 'Cause or consequence? Alpha oscillations in visuospatial attention', Trends in Neurosciences, vol. 44, no. 9, pp. 705-713
4. Praamstra et al. (2006), 'Neurophysiology of implicit timing in serial choice reaction-time performance'. Journal of Neuroscience, vol. 26, no. 20, pp. 5448-5455
5. Rohenkohl et al. (2011), 'Alpha oscillations related to anticipatory attention follow temporal expectations', Journal of Neuroscience, vol. 31, no. 40, pp. 14076-14084
6. Sauseng et al. (2005), 'A shift of visual spatial attention is selectively associated with human EEG alpha activity', European Journal of Neuroscience, vol. 22, no. 11, pp. 2917-2926
7. Zanto et al. (2011), 'Age-related changes in orienting attention in time', Journal of Neuroscience, vol. 31, no. 35, pp. 12461-12470

Poster No 2450

The Neural Correlates of Visual Attention in Virtual Reality

Lukas Lorentz[1], André Schüppen[1], Boris Suchan[2], Ferdinand Binkofski[1]

[1]University Hospital Aachen, Aachen, Germany, [2]Ruhr-University Bochum, Bochum, Germany

Introduction: Virtual Reality technology is increasingly used in cognitive rehabilitation to train attentional functions[2,3]. However, the neural mechanisms by which Virtual Reality can presumably stimulate attention in a more ecologically valid way than conventional training methods are still mostly unstudied. The current study's objective is to examine the effects of different forms of binocular presentation (Virtual Reality-characteristic stereoscopic "3D" vs. monoscopic "2D") on neural processing during a visual attention task.

Methods: Thirty-two healthy participants performed a visual attention task in an immersive virtual environment that was displayed via MR-compatible video goggles in an MRI scanner. The paradigm required participants to change their first-person perspective in an underwater scenario (Figure 1) by using an MR-compatible trackball with the aim of hitting a particular target stimulus. The paradigm altered between trials requiring active engagement with the task and mere observation trials. Furthermore, the form of binocular presentation switched between monoscopic and stereoscopic presentation.

Results: Analyses yielded evidence for increased activation in stereoscopic compared to monoscopic trials in the tertiary visual cortex area V3A (Figure 2B) and elevated activation in the dorsal attention network when engaging in the attention task (Figure 2A). An additional ROI analysis of area V3A revealed significantly lower attentional engagement costs in stereoscopic conditions compared to monoscopic conditions (Figure 2C).

Conclusions: The results support previous findings indicating that V3A is involved in binocular depth perception[5]. Furthermore, heightened activation in V3A following stereoscopic presentation seemed to facilitate attentional engagement with the task (Figure 2C). Considering V3A's critical position as the origin of the dorso-dorsal, ventro-dorsal, and ventral visual processing pathways[1,4], the current findings suggest that it serves as a gating area distributing visual inputs to visuomotor systems partially contingent on binocular presentation.

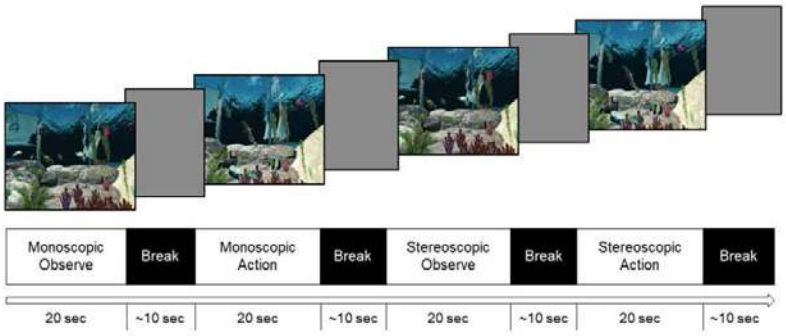

Flg. Schematic experimental timeline (in Methods)

5/17/24, 11:31 AM OHBM

https://

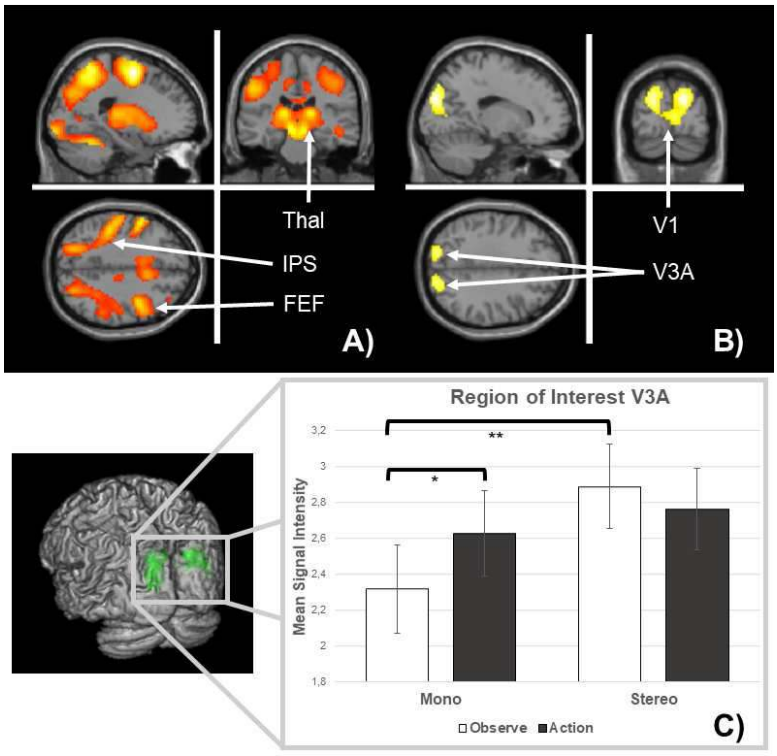

Flg. Main effects and interaction in ROI (in Restults)

References

1. Binkofski, F., & Buxbaum, L. J. (2013), "Two action systems in the human brain", Brain and Language, vol. 127, no. 2, pp. 222-229https://doi.org/10.1016/j.bandl.2012.07.007
2. Bioulac, S., Micoulaud-Franchi, J., Maire, J., Bouvard, M. P., Rizzo, A., Sagaspe, P., & Philip, P. (2020), "Virtual Remediation Versus Methylphenidate to Improve Distractibility in Children With ADHD. A Controlled Randomized Clinical Trial Study", Journal of Attention Disorders, vol. 24, no. 2, pp. 326–335 DOI: 10.1177/1087054718759751.

3. Gamito, P., Oliveira, J., Coelho, C., Morais, D., Lopes, P., Pacheco, J., Brito, R., Soares, F., Santos, N., & Barata, A. F. (2015), "Cognitive training on stroke patients via virtual reality-based serious games", Disability and Rehabilitation, vol. 39, no. 4, pp. 385-388 https://doi.org/10.3109/09638288.2014.934925
4. Tessari, A., Proietti, R., & Rumiati, R. I. (2021), "Bottom-up and top-down modulation of route selection in imitation", Cognitive Neuropsychology, vol. 38, no. 7-8, pp. 515–530 https://doi.org/10.1080/02643294.2022.2043264
5. Tsao, D. Y., Vanduffel, W., Sasaki, Y., Fize, D., Knutsen, T. A., Mandeville, J. B., Wald, L. L., Dale, A. M., Rosen, B. R., Van Essen, D. C., Livingstone, M. S., Orban, G. A., & Tootell, R. B. (2003), "Stereopsis activates V3A and caudal intraparietal areas in macaques and humans", Neuron, vol. 39, no. 3, pp. 555-568 https://doi.org/10.1016/s0896-6273(03)00459-8

Poster No 2451

Shared neural activation and co-fluctuations underlie auditory and visual sustained attention

Anna Corriveau[1], Jin Ke[1], Monica Rosenberg[1,2]

[1]Department of Psychology, The University of Chicago, Chicago, IL, [2]Neuroscience Institute, The University of Chicago, Chicago, IL

Introduction: Maintenance of attention over time to auditory and visual information relies, to some extent, on shared neural mechanisms[6,8]. Sustained attention ability is well-predicted by relationships between a distributed set of brain regions[5]. However, attention fluctuations occur over a matter of seconds, a time scale that is better-captured by dynamic brain measures, such as co-fluctuations in BOLD activity[2,4,10]. We compare the neural mechanisms–both activation and activity co-fluctuations–involved in maintaining attention to sounds and images. We identify a set of brain regions and connections that underlie sustained attention to information regardless of perceptual modality.

Methods: Participants performed a continuous performance task in which streams of trial-unique sounds and images were presented simultaneously during fMRI. Across two scan sessions, participants were tasked with pressing a button when relevant stimuli (either sounds or images) belonged to a frequent category (90%) and withholding response to infrequent stimuli (10%). Visual and auditory task analyses included 55 participants each. Of these, 51 participants are shared between analyses. Attention lapses were operationalized as incorrect responses to infrequent-category stimuli and attentional state was quantified using the reaction time variance time course [VTC; 1], which characterizes moments of in-the-zone (low variance) out-of-the-zone (high variance) pressing. BOLD activity was averaged within 268 functionally-defined regions of interest [ROIs; 7], yielding 268 ROI activation time series. Co-fluctuation times series between all pairs of regions (edges) were calculated as the element-wise product of z-scored time series (Figure 1). Activation and edge time series were convolved with a canonical HRF. To identify regions and pairs of regions involved in task performance, we contrasted trial-evoked activation and co-fluctuations to correct vs. incorrect responses to infrequent stimuli. To identify regions related to fluctuations in attentional state, activity and co-fluctuations were related to a parametric VTC regressor. Group-level analyses were tested within auditory and visual sessions separately. To correct for family-wise error rates, max-T and network-based statistic correction[9] were used for activation and co-fluctuation analyses, respectively.

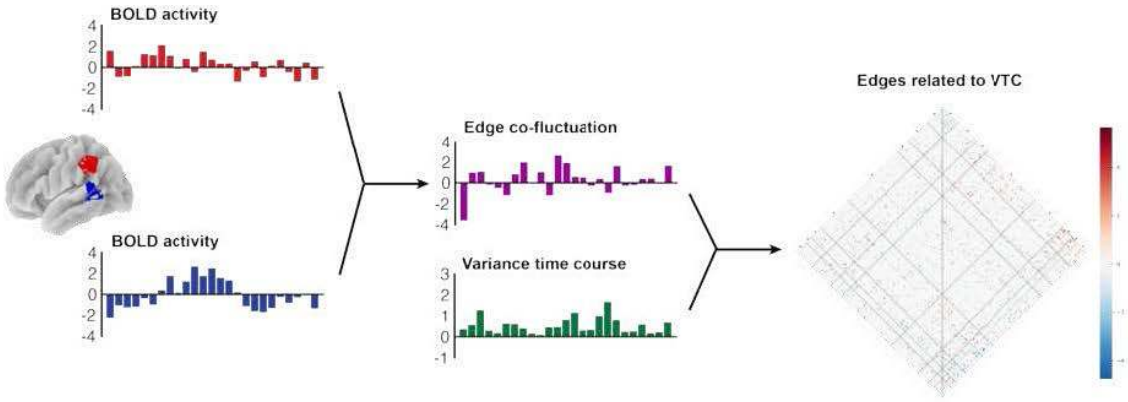

Figure 1. The within-subject co-fluctuation between all 268 ROIs was calculated as the element-wise product of z-scored BOLD time series. Variance time courses were convolved with a canonical HRF as well as its temporal derivative and fit with edge time series in a first-level model. Colors in the resulting matrix indicate T-statistics for edges in components larger than the 95th-percentile of a null distribution. The null distribution was created using an NBS approach by thresholding sign-flipped contrasts at $p<.01$ and recording the largest fully-connected component of each permutation.

Results: Contrasting activation on infrequent trials (correctly withheld responses - incorrect presses) revealed distributed regions more active on correct trials in both auditory and visual sessions (Figure 2). Co-fluctuation difference contrasts

revealed no significant edges in auditory sessions and therefore no overlapping edges between auditory and visual sessions. Activity in ROIs largely within the ventral attention network were positively related to the VTC in auditory and visual sessions (Figure 2), in line with previous work[3]. Auditory and visual sessions also shared more overlapping edges than chance ($p<.001$) whose co-fluctuation was significantly related (47 positive, 12 negative) to changes in VTC. Further, 22 of 47 edges positively related to response variance were not predicted by ROI time courses, suggesting edges carry additional information missed by activation alone.

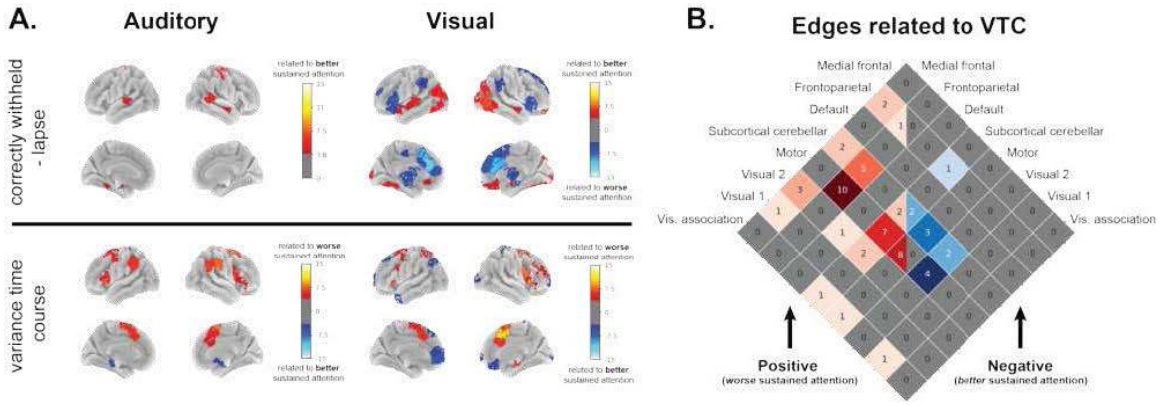

Figure 2. (A) Activation contrasts for ROI analyses. Colors indicate T-statistics greater than the 95th-percentile of a null distribution of sign-flipped contrasts using a max-T approach. (B) Number of edges significantly related to the variance time course, grouped by network, during both the auditory and visual sustained attention tasks.

Conclusions: Activation and co-fluctuation analyses identify regions and edges associated with sustained attention to auditory and visual information. A number of regions showed significant differences between correctly-withheld responses and attentional lapses in both auditory and visual sessions, suggesting a shared mechanism for performance on target trials during a continuous performance task. Additionally, shared activations and co-fluctuations tracked the VTC, a continuous measure of attentional state, during auditory and visual sessions, suggesting a common set of regions and edges related to attention fluctuations. These results identify perceptual modality-agnostic predictors of sustained attention performance.

References

1. Esterman, M. (2013). In the Zone or Zoning Out? Tracking Behavioral and Neural Fluctuations During Sustained Attention. Cerebral Cortex, 23(11), 2712–2723.
2. Faskowitz, J. (2020). Edge-centric functional network representations of human cerebral cortex reveal overlapping system-level architecture. Nature Neuroscience, 23(12), Article 12.
3. Fortenbaugh, F. C. (2018). Tracking behavioral and neural fluctuations during sustained attention: A robust replication and extension. NeuroImage, 171, 148–164.
4. Jones, H. M. (2023). Edge-based general linear models capture high-frequency fluctuations in attention (p. 2023.07.06.547966). bioRxiv.
5. Rosenberg, M. D. (2016). A neuromarker of sustained attention from whole-brain functional connectivity. Nature Neuroscience, 19(1), Article 1.
6. Seli, P. (2012). Consistency of sustained attention across modalities: Comparing visual and auditory versions of the SART. Canadian Journal of Experimental Psychology/Revue Canadienne de Psychologie Expérimentale, 66(1), 44–50.
7. Shen, X. (2013). Groupwise whole-brain parcellation from resting-state fMRI data for network node identification. NeuroImage, 82, 403–415.
8. Terashima, H. (2020). Common principles underlie the fluctuation of auditory and visual sustained attention. Quarterly Journal of Experimental Psychology, 1747021820972255.
9. Zalesky, A. (2010). Network-based statistic: Identifying differences in brain networks. NeuroImage, 53(4), 1197–1207.
10. Zamani Esfahlani, F. (2020). High-amplitude cofluctuations in cortical activity drive functional connectivity. Proceedings of the National Academy of Sciences, 117(45), 28393–28401.

Poster No 2452

Methylphenidate increases gamma-band oscillations power over parieto-occipital regions

Valentina Mancini[1], Caren Latreche[2], Vincent Rochas[2], Christoph Michel[2], Peter Uhlhaas[3], Stephan Eliez[2]

[1]Oxford University, Oxford, Oxfordshire, [2]University of Geneva, Geneva, Switzerland, [3]Charité, Berlin, Germany

Introduction: Methylphenidate (MPH), a widely prescribed psychostimulant drug, is commonly employed in the treatment of attention deficit hyperactivity disorder (ADHD). Despite its extensive clinical use, the precise mechanisms through which MPH exerts its therapeutic effects on attention is yet to be fully understood. MPH primarily acts as a norepinephrine and dopamine reuptake inhibitor, increasing the availability of these neurotransmitters in the synaptic cleft. However, it is not entirely

clear which neural circuits are preferentially modulated by MPH, and if there is a selective modulation of oscillatory activity. Gamma band oscillations (30-80 Hz) have been implicated in attention processes, especially within the visual system[1]. During sustained attentional processes, there is an increase in the synchronization of neural activity in the gamma frequency range, which effectively and precisely establishes communication within and between brain areas[2]. Despite the established link between gamma-band oscillations and attention, the impact of MPH on these oscillatory patterns has not yet been investigate so far. Investigating this aspect could provide valuable insights into the neural mechanisms underlying MPH's attention-enhancing effects.

Methods: This study was conducted as part of a randomized trial administering MPH to youths with 22q11.2 deletion syndrome[3], a neurodevelopmental condition that confers high risk of developing multiple psychiatric conditions, including ADHD[4]. Twenty-six deletion carriers (aged 8-24) completed the neuroimaging part of the study when they were on and off MPH. At each visit, we acquired high-density electroencephalography recordings with during two paradigms known to elicit a strong response in the gamma frequency range. We employed: a 40-Hz auditory steady state response (ASSR) task[5], and a visual inward moving grating task whereby participants are asked to report the change in speed of inward motion of the grating by button press[6]. The outcomes of the visual grating task (performance and reaction times) were examined. Stimulus-elicited oscillatory responses were analyzed with time-frequency analysis using Morlet wavelets decomposition at sensor and source level, and intertrial phase coherence (ITC), as in previous studies[7,8]. In all the analyses, the effects of treatment were compared on/off medication in a within-subject design.

Results: Deletion carriers on MPH had a better performance at the visual grating task ($t = 3.1$; $p<0.01$) and decreased reaction times ($t= 2.3$; $p< 0.05$) (figure 1). No differences in ASSR power or ITC were observed if deletion carriers were on or off MPH. Statistically significant differences were found at gamma-band frequencies over a cluster of parieto-occipital electrodes, with deletion carriers on MPH having higher gamma-band responses (60–70 Hz, 0.75–1.5 seconds, $t =3.2$, $p< 0.01$). At the source level, we found higher gamma-band responses at the level of the bilateral cuneus, precuneus, lingual gyrus and superior parietal cortex (figure 2).

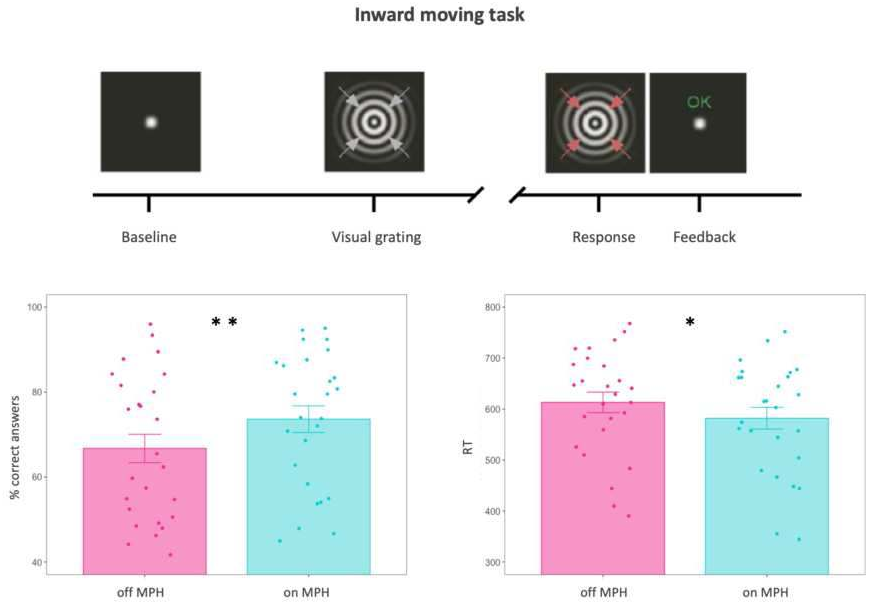

Fig.1 Behavioral results
Upper panel: diagram of the inward moving grating task. Participants are asked to report the change in speed of inward motion of the the grating by button press.
Lower panel: bar plots showing groups means and standard deviation for the percentage of correct answers and reaction times (ms). Asterisks indicate statically significant differences between deletion carriers on and off MPH.

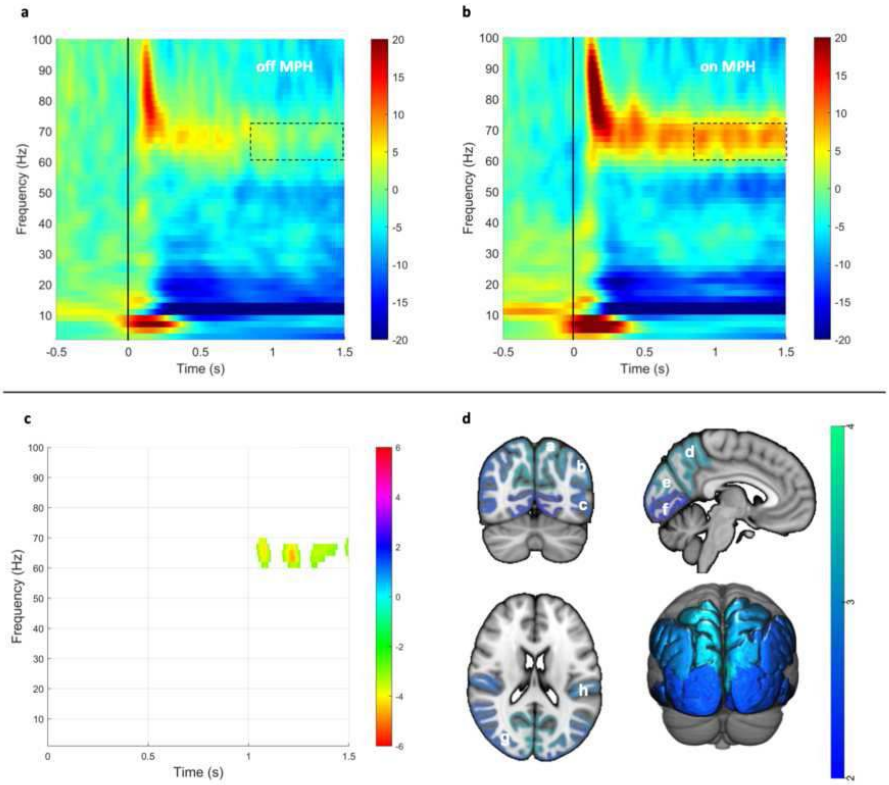

Figure 2. TF comparison between deletion carriers off and on MPH.
Time-frequency plots displaying the average pre- and post-stimulus event-related spectral perturbation (ERPS) in deletion carriers off (a) and on (b) MPH over a cluster of parieto-occipital electrodes. The outlined dotted boxes highlight the time-window of statistically significant group differences in gamma power (60-70 Hz). T-values of the difference between off and on MPH for the cluster of predetermined electrodes (c). Brain map with regions in the source space showing statistically significant increased gamma response (60-70 Hz, 0.75-1.5 sec) in deletion carriers on MPH (d). The colormap represents T-values for differences between deletion carriers off and on MPH plotted on the brain.

Conclusions: Our results indicate that MPH can successfully modulate attentional processes by increasing the number of correct responses to a visual attention task and decreasing the RT. Additionally, MPH can enhance gamma oscillations power during sustained attention in the visual grating task over regions involved in visual processing and attention. Conversely, in our data, MPH doesn't seem to influence the 40Hz-ASSR. A possible explanation is that the attentional demand of the 40Hz-ASSR task is much lower than in the visual grating task. Overall, MPH can improve the efficiency of attentional processing and increase gamma-band power over brain regions implicated in sustained visual attention. Since dopamine activation can enhance gamma-band oscillations[9], one hypothesis is that the observed action of MPH exerted on gamma power is mediated by the increased availability of dopamine at the level of synaptic cleft.

References

1. Fries P (2015): Rhythms for Cognition: Communication through Coherence. Neuron. 88: 220–235.
2. Fries P (2008): The Effects of Visual Stimulation and Selective Visual Attention on Rhythmic Neuronal Synchronization in Macaque Area V4. J Neurosci. 28: 4823–4835.
3. Maeder J (2022): Selective Effects of Methylphenidate on Attention and Inhibition in 22q11.2 Deletion Syndrome: Results From a Clinical Trial. Int J Neuropsychopharmacol. 25: 215–225.
4. Schneider M (2014): Psychiatric disorders from childhood to adulthood in 22q11.2 deletion syndrome: Results from the international consortium on brain and behavior in 22q11.2 deletion syndrome. Am J Psychiatry. 171: 627–639.
5. Grent-'t-Jong T (2021): 40-Hz Auditory Steady-State Responses Characterize Circuit Dysfunctions and Predict Clinical Outcomes in Clinical-High-Risk Participants: A MEG Study. Biol Psychiatry. . doi: 10.1016/j.biopsych.2021.03.018.
6. Hoogenboom N (2006): Localizing human visual gamma-band activity in frequency, time and space. Neuroimage. 29: 764–773.
7. Mancini V (2022): Oscillatory neural signatures of visual perception across developmental stages in individuals with 22q11.2 deletion syndrome. Biol Psychiatry. . doi: 10.1016/J.BIOPSYCH.2022.02.961.
8. Mancini V (2022): Aberrant Developmental Patterns of Gamma-Band Response and Long-Range Communication Disruption in Youths With 22q11.2 Deletion Syndrome. Am J Psychiatry. 179: 204–215.
9. Lohani S (2019): Dopamine Modulation of Prefrontal Cortex Activity Is Manifold and Operates at Multiple Temporal and Spatial Scales. Cell Rep. 27: 99-114.e6.

Poster No 2453

Adults born via C-section have visual attention deficits and aberrant brain network connectivity

W. Dale Stevens[1], Scott Adler[1], Laetitia Mwilambwe-Tshilobo[2], Diana Gorbet[1], Lily Solomon-Harris[1], Audrey Wong-Kee-You[1], Roni Setton[3], Gary Turner[1], R. Nathan Spreng[4]

[1]York University, Toronto, Ontario, [2]Princeton University, Princeton, NJ, [3]Harvard University, Cambridge, MA, [4]Montreal Neurological Institute, McGill University, Montreal, Quebec

Introduction: Caesarean section (C-section) is a relatively safe and potentially life-saving surgical procedure in the face of labor complications. However, there is evidence of abnormal brain and behavioral development associated with C-section birth in non-human mammals. Moreover, epidemiological/meta-analytic studies in humans have indicated increased rates of autism spectrum disorder (ASD) and attention deficit/hyperactivity disorder (ADHD) associated with C-section birth. But to our knowledge, no study to date has directly investigated the potential long-term neurocognitive effects of C-section in human adults. We previously reported visual attention deficits in 3-month-old human infants born via C-section vs. vaginal birth (V-birth), measured with eye-tracking in a cued visuospatial attention task. Here, we used multiple behavioral measures of visual attention, eye-tracking, and whole-brain connectomic analyses of resting-state functional MRI (rs-fMRI) data in multiple independent samples of human adults to investigate potential long-term effects of C-section birth on visual attention and brain network connectivity.

Methods: We used eye-tracking with the same cued visuospatial attention task previously used in infants in adults (n = 24: 12 C-section; 12 V-delivery). In an independent sample of adults (n = 94: 24 C-section; 70 V-delivery), visual attention and other cognitive domains were assessed using using a visual flanker task, as well as other tasks in the the NIH Toolbox, and the Symbol Digit Modalities Test (SDMT). Multi-echo rs-fMRI data (20 min) were acquired for 81 adults (20 C-section, 64 V-delivery). We used multi-echo independent components analysis (ME-ICA) and group prior individual parcellation (GPIP) to individually localize 400 cortical nodes across 7 large-scale canonical brain networks in each participant. The right and left superior colliculi (SC), subcortical regions responsible for eye movements, were also individually localized. We used the multivariate technique partial least squares (PLS) to compare patterns of intrinsic functional connectivity (RSFC) across all 402 brain regions.

Results: Replicating our findings in infants, C-section adults showed significantly longer saccade latencies in the cued visuospatial attention task, as measured with eye-tracking ($F(1,88) = 11.56$, $p = .001$, $\eta 2\rho = .12$). An independent sample of C-section adults showed a visual attention deficit relative to V-birth adults on the visual flanker task (Wilk's $F(1,84) = 4.21$; $p < .05$; partial $\eta 2\rho = .048$). We determined the specificity of this visual attention deficit by controlling for global processing speed, memory, and executive function, which did not differ between groups (t's < 1.2; p's >.20). In a hypothesis-driven ROI approach, we examined RSFC of early visual regions including primary visual cortex (V1) and SC with the rest of the brain; there was a significant difference between C-section and V-delivery adults (permuted $p = 0.04$, covariance explained = 100%; bootstrap resampling: $t(74) = 7.9$, $p < 0.001$, Cohen's $d = 2.06$). C-section adults showed hyperconnectivity of early visual regions within the visual network and, critically, with the default network, relative to V-birth adults. A control analysis ruled out more general/global group differences in RSFC, confirming the specificity of group differences in cortical connectivity to early visual regions.

Conclusions: To our knowledge, we report the first behavioral and neuroimaging evidence of potentially life-long neurocognitive abnormalities associated with C-section birth. These findings suggest a potential neural mechanism underlying increased rates of neurodevelopmental disorders (i.e., ASD and ADHD) associated with C-section. These findings warrant further investigation to determine the underlying causes and should be weighed among the critical risks and benefits considered by physicians and prospective parents in making informed decisions about optional, non-medically indicated C-section births.

Poster No 2454

Spatiotemporal dynamics of object-based attention: an MEG-fMRI-DNN fusion study

Chun-Hui Li[1], Bo-Cheng Kuo[1]

[1]National Taiwan University, Taipei, Taiwan

Introduction: Individuals typically receive continuous and unlimited sensory inputs from the external environment. The ability to selectively choose the most relevant information is contingent upon current behavioral goals. Recent advancements in multivariate methods have significantly contributed to unveiling the informational contents of object-based attention.

Employing these sophisticated methods allows the recording of spatial and temporal information in neural responses related to object-based attention through various neuroimaging modalities. Despite this progress, it remains uncertain whether and how information can be integrated across different imaging modalities and analysis methods. In this study, we adopted representational similarity analysis to investigate the spatiotemporal dynamics of neural representations that underlie object-based attention, utilizing magnetoencephalography (MEG), functional magnetic resonance imaging (fMRI), and deep neural networks (DNN).

Methods: Twenty-four participants viewed streams of face and building images in an MEG experiment and an fMRI experiment (Fig. 1A). MEG and fMRI data were acquired at National Taiwan University on a 306-channel Triux system (Elekta Neuromag) and a Siemens 3T Prisma MRI scanner, respectively. Participants were instructed to attend to faces or buildings and respond to pre-defined face or building targets while recording with MEG. They also performed a visual localizer task using the same face and building images and their scramble images in a block design with fMRI. We conducted an RSA-based fusion analysis to integrate MEG with either fMRI data or DNN data (Fig. 1B). Region-of-interests (ROIs) were defined based on the fMRI contrasts and the Automated Anatomical Labeling template, specifically focusing on fusiform face areas, FFA, and parahippocampal place areas, PPA. Pairwise dissimilarities were calculated across all combinations of conditions and stimuli, linking the multivariate measurements across different modalities. This process yielded representational dissimilarity matrices (RDMs). Each RDM generated from MEG, fMRI or DNN is symmetrical around the diagonal. The lower triangular part of each RDM was extracted and converted into a vector format. For each ROI, we calculated the Spearman correlation coefficients between the MEG RDMs and fMRI RDMs. This process was repeated separately for each face-selective and building-selective ROI, offering a temporal profile of representational similarities between fMRI and MEG for each ROI. Importantly, Spearman correlation coefficients were also computed between the MEG RDMs and DNN RDMs. RDM similarity estimations were carried out within each DNN RDM for two attention conditions separately. For all analyses, we built a linear model with face and building RDMs as two regressors to predict time-resolved RDMs from the MEG data thereby enabling a detailed exploration of the neural dynamics of object-based attention.

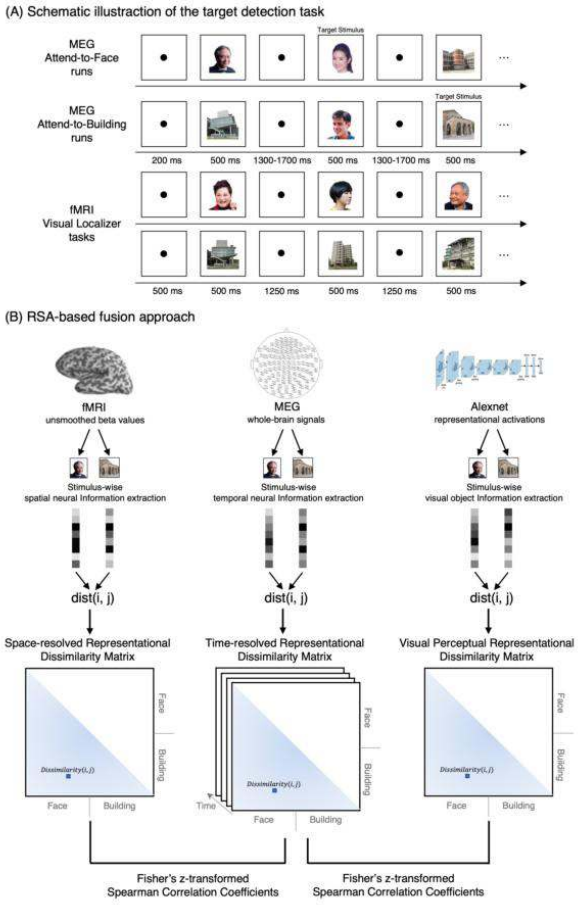

Figure 1. (A) Schematic illustration of the target detection tasks used in MEG and fMRI experiments. (B) The pipeline of RSA-based MEG-fMRI and MEG-DNN fusion approach.

Results: The fusion results showed attentional enhancement of representational similarity within category-selective brain areas. Moreover, we observed that the goal-directed modulation of representational similarity in the category-selective brain areas was influenced by the prefrontal cortex using the Granger causality analysis. Importantly, GLM-based RSA further confirmed the spatiotemporal representational dynamics in the category-selective brain areas for object-based attention (Fig. 2). Finally, the MEG-DNN fusion results revealed a similar attention effect on representational similarity (Fig. 2).

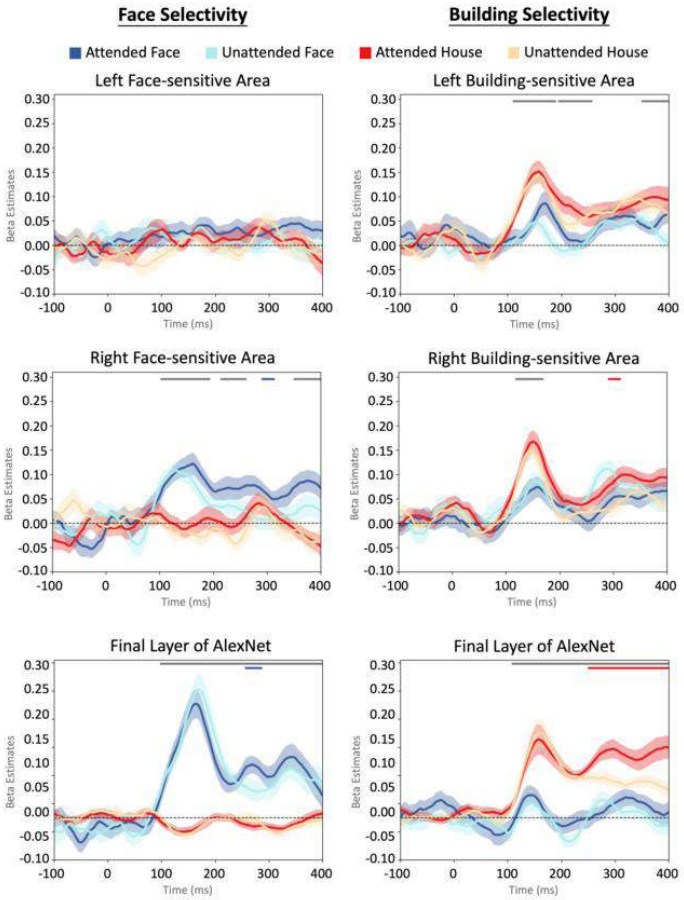

Figure 2. Beta estimate results of the GLM-based RSA. The grey lines on the top of the figures indicate significant preferential similarity for faces or for buildings in the category-sensitive areas as well as in the final layer of AlexNet. The blue and red lines on the top of the figures indicate significant attentional enhancement for faces and buildings, respectively.

Conclusions: Our fusion results demonstrated the modulation of spatiotemporal patterns of neural responses for object-based attention through the RSA-based MEG-fMRI and MEG-DNN fusion approaches. The study provides novel multivariate evidence of the cognitive operations and neural mechanisms underlying the attentional modulation of object selectivity.

References

1. Cohen, L. (2004). Specialization within the ventral stream: the case for the visual word form area. Neuroimage, 22(1), 466–476.
2. Dobs, K. (2019). How face perception unfolds over time. Nature Communications, 10(1), 1–10.
3. Epstein, R. (1999). The parahippocampal place area: recognition, navigation, or encoding? Neuron, 23(1), 115–125.
4. Grootswagers, T. (2017). Decoding dynamic brain patterns from evoked responses: a tutorial on multivariate pattern analysis applied to time series neuroimaging data. Journal of Cognitive Neuroscience, 29(4), 677–697.
5. Hubel, D.H. (1977). Ferrier lecture-Functional architecture of macaque monkey visual cortex. Proceedings of the Royal Society of London. Series B. Biological Sciences, 198(1130), 1–59.
6. Kanwisher, N. (1998). The effect of face inversion on the human fusiform face area. Cognition, 68(1), B1--B11.
7. Kriegeskorte, N. (2019). Interpreting encoding and decoding models. Current Opinion in Neurobiology, 55, 167–179.
8. Kuffler, S. W. (1953). Discharge patterns and functional organization of mammalian retina. Journal of Neurophysiology, 16(1), 37–68.
9. Kuo, B.-C. (2017). Top-down modulation of alpha power and pattern similarity for threatening representations in visual short-term memory. Neuropsychologia, 106, 21–30.
10. Li, C.-H. (2023). Tracking the temporal dynamics of the face-like inversion effect as revealed by Chinese characters using magnetoencephalography. Cerebral Cortex, bhad135.

Poster No 2455

Transient cortical activity predicts spontaneous attention shifts

Masakazu Inoue[1], Yasuo Kabe[1], Shuntaro Sasai[1]

[1]ARAYA Inc., Chiyoda, Tokyo

Introduction: We encounter a massive influx of environmental inputs in our daily lives, yet our attention is spontaneously allocated to only a subset thereof. With controlled experimental settings, parietal cortex was found to play an important role in attentional shift[1]. However, the neural mechanisms underlying spatial attention remains unclear in natural and voluntary settings. Using fMRI data obtained during movie-watching, we examine whether fMRI signals predict spontaneous changes of fixated locations. We localize brain regions contributing to the prediction and characterize the spatiotemporal neural dynamics underlying the spontaneous attentional allocation in natural settings.

Methods: dataset We used a publicly available, StudyForrest dataset[4] consisting of simultaneous fMRI (TR=2) and eye tracking (temporal resolution=1000 Hz) data during movie watching (Forrest Gump, 2h-long). We used data from twelve participants successfully completed their experiments. Twenty two ROIs were extracted according to Glasser et al.[5]. fMRI-based prediction of fixated locations We newly developed fMRI-based prediction of fixated locations as follows (Fig 1). Visual features of entire image and fixated location. We resampled the movie clips at a rate of 0.5Hz and generated masks blacking out non-fixated locations. We used five hidden layers' outputs of image encoder (ViT-g/14 from EVA-CLIP[6]) to construct visual features from entire images and masked images, respectively. For the masked image features, average pooling across spatial dimension was applied. After this procedure, we obtained patched features of entire image whose size was 5x16x16x1408 and features whose size was 5x1x1x1408 at each time point. Visual feature decoding from fMRI signal. We constructed linear models to predict the feature of fixated locations from BOLD signals of each ROI after voxel selection[7]. Prediction of fixation and evaluation. Pearson correlation between predicted feature vectors and those of each image patch was calculated. Patches with the top-k correlation were selected as predicted fixated locations. We used Intersection over Union (IoU) between these predicted patches and the true fixated patches as metrics for evaluation. The chance level was obtained by the same procedure using temporally shuffled fMRI signals.

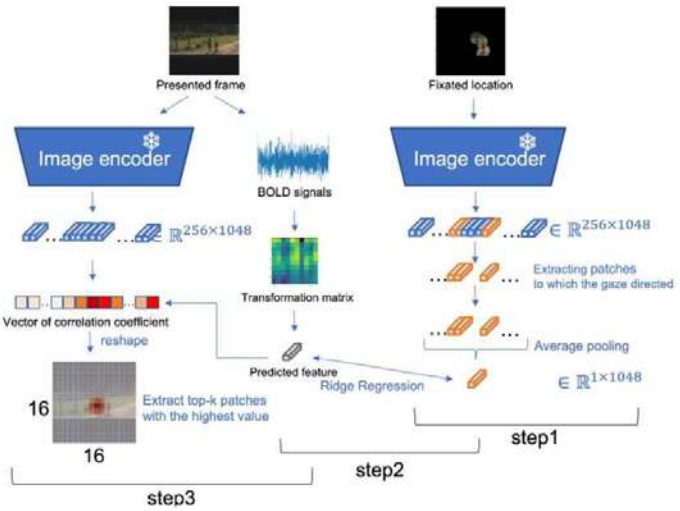

Fig 1.
fMRI-based prediction of fixated locations consists three steps. In step1, the visual feature vectors of fixated location are generated. In step2, linear regression model to predict the visual feature vectors of fixated location from BOLD signals is trained. In step3, Pearson correlation between predicted feature vectors and those of each image patch was calculated. Patches with the top-k correlation were selected as predicted fixated locations. We used ViT as image encoder, which transforms image into 16 x16 patches in the early stage and outputs the features of each patch.

Results: We examined whether fMRI signals in each ROI can predict changes in fixated locations through spontaneous attentional shifts. To do so, we focused time points where large eye movements occurred. We found that posterior, parietal ROIs can significantly predict the fixated locations before the occurrence of the eye movements (Fig. 2). In addition to these ROIs, activities in paracentral, middle cingulate, posterior cingulate, and dorsolateral prefrontal ROIs can successfully predict the fixated locations after the eye movements. Interestingly, paracentral and middle cingulate ROIs successfully decoded the relocated areas earlier than other cortices.

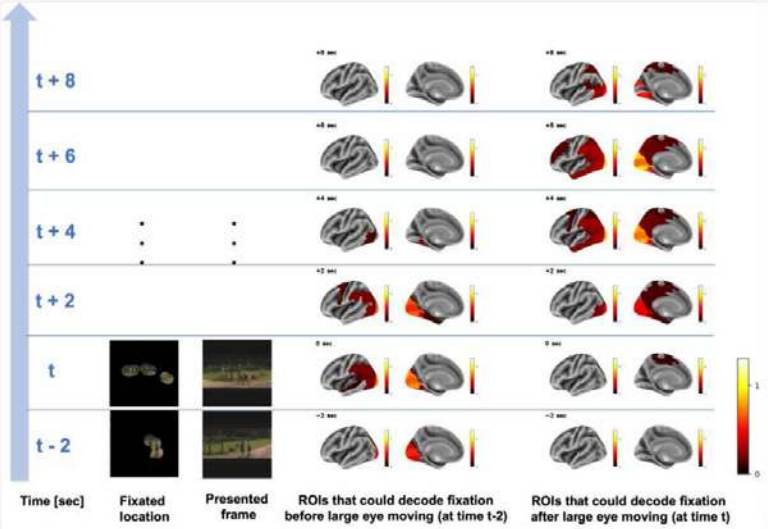

Fig 2.
Two left columns show examples of presented frame and fixated location before and after large eye movements occur respectively. Two right columns show the temporal transition of ROIs that could decode the fixated locations at time t-2 seconds and at time t. Only ROIs that could decode the fixated locations significantly above chance level at each time point (t-test, N=12, $p<0.05$, Bonferroni-corrected) are colored. The color represents the area calculated by subtracting IoU curve (obtained by arranging the IoU along k while moving k from 5, 10, 20, 40, 80, 100, 128.) of chance level from that of prediction.

Conclusions: We confirmed that the fixation with voluntary shift of attention could be significantly decoded from the BOLD signals of multiple time points. We also found that the neural activity in Paracentral lobular and mid cingulate can decode earlier than visual cortex, suggesting the ROI may be involved with generation or processing of voluntary attention.

References

1. Yantis, S. (2002), 'Transient neural activity in human parietal cortex during spatial attention shifts', Nat Neurosci 5, 995–1002
2. Jake Son (2020), 'Evaluating fMRI-Based Estimation of Eye Gaze During Naturalistic Viewing', Cerebral Cortex, Volume 30, Issue 3, Pages 1171–1184.
3. O'Connell (2018), 'Predicting eye movement patterns from fMRI responses to natural scenes', Nat Commun 9, 5159
4. Hanke, M. (2016), 'A studyforrest extension, simultaneous fMRI and eye gaze recordings during prolonged natural stimulation' Sci Data 3, 160092
5. Glasser, M. (2016), 'A multi-modal parcellation of human cerebral cortex' Nature 536, 171–178
6. Fang, Y. (2022), 'Eva: Exploring the limits of masked visual representation learning at scale' arXiv preprint arXiv:2211.07636
7. Horikawa, T. (2017), 'Generic decoding of seen and imagined objects using hierarchical visual features' Nat Commun 8, 15037

Poster No 2456

Genotype-Phenotype interaction in the attentive network in developmental dyslexia

Denis Peruzzo[1], Alice Giubergia[1,2], Filippo Arrigoni[3], Alessio Toraldo[4,5], Chiara Andreola[6], Martina Villa[7,8], Valentina Lampis[1,4], Giorda Roberto[1], Marco Villa[1], Sara Mascheretti[4,1]

[1]Scientific Institute IRCCS Eugenio Medea, Bosisio Parini (LC), Italy, [2]University of Padova, Padova (PD), Italy, [3]V. Buzzi Children's Hospital, Milano (MI), Italy, [4]University of Pavia, Pavia (PV), Italy, [5]Milan Centre for Neuroscience (NeuroMI), Milano (MI), Italy, [6]Université Paris Cité, Paris, France, [7]University of Connecticut, Storrs (CT), USA, [8]Yale Child Study Center Language Sciences Consortium, New Haven (CT), USA

Introduction: Developmental Dyslexia (DD) is a complex, heritable, language-based disorder resulting in impaired reading skills with no evident cognitive or sensory causes. Different candidate genes for DD have been identified, usually involved in neuronal migration, neurite outgrowth, cortical morphogenesis and ciliary structure and function[2]. In this study, we aim to exploit fMRI to investigate the relationship between the phenotype (i.e. the reading skills) and the genotype (i.e. the presence or absence of the deletion of the READ1 regulatory term in the DCDC2 gene). READ1 deletion (READ1-d) has already been associated with structural and functional alterations, both in children with DD and in TRs [1,3,5,6]. This study implements a genetic-imaging approach that uses the MRI derived measures as an intermediate phenotype to connect specific genetic variants (READS1-d) to cognitive phenotypes (Reading skills).

Methods: Participants: The recruited dataset comprised 79 subjects: 18 children with DD and READ1-d (DD+), 21 children with DD and without READ1-d (DD-), 19 typical readers with READ1-d (TR+), and 21 TR without READ1-d (TR-). TRs and children with DD showed significant differences in terms of age, gender distribution, QI, and DSM-IV-Inattention (DSM-IV-I) traits. fMRI Task and Acquisition: fMRI images (voxel size=2x2x2.7mm^3; TR=2s) were acquired during the administration of two visual tasks involving the Magno (M) dorsal, the Parvo (P) ventral pathways, and the attentive network were implemented, a full-field Sinusoidal Gratings (SG) and a sensitivity to Coherent Motion (CM)[4]. fMRI Data Processing: The fMRI data were processed following the FreeSurfer Functional Analysis Stream (FSFAST) to the computation of two contrast maps for the SG task (M-vs-B: M stimulus vs. Baseline; P-vs-B: P stimulus vs. Baseline) and three for the CM task depending on the coherence dot level in the stimulus (CML6-vs-B; CML15-vs-B; CML40-vs-B). Average contrast values were computed in each ROI following the HCP-MMP1 parcellation of the cortex. Statistical Analysis: contrast values were investigated using a univariate General Linear Model including as predictor the product between genetic variant and reading skills (i.e. READ1-d*Mean Reading) as a term to investigate the direct genotype-phenotype interaction we are interested in. The models included as covariates also other demographic (age, gender), cognitive (IQ, DSM-IV-I score, mean reading score) and genetic (READ1-d) predictors.

Results: At the Bonferroni-corrected level of significance ($p<0.00014$), we found a significant interaction effect between READ1-d and "Mean Reading'' in the left frontal opercular area 4 during the coherent motion sensitivity task at 15% dot coherence level. More specifically, among children with DD, READ1-d carriers had lower neural activation compared to their counterparts without READ1-d. Such a difference changes as a function of reading proficiency, with the gap closing and turning non-significant among TRs.

Conclusions: We showed here how MRI derived measures can be used as an intermediate phenotype to investigate the relationship between genetic variants and cognitive phenotypes. In particular, we identified a region lying in the Ventral Attention Network (VAN) showing an altered cortical activation during the processing of a visual motion task in the combination of genetic variant (READ1-d) and poor reading skills. This result supports the hypothesis of a sluggish attentional shifting during the processing of stimuli targeting the magno pathways in children with weak reading performance and READ1-d.

References

1. Cope, N. (2012) 'Variants in the DYX2 locus are associated with altered brain activation in reading-related brain regions in subjects with reading disability', NeuroImage, 63(1):148-156. doi:10.1016/j.neuroimage.2012.06.037
2. Lampis, V. (2021) 'Animal models of developmental dyslexia: Where we are and what we are missing', Neuroscience & Biobehavioral Reviews. 131:1180-1197. doi:10.1016/j.neubiorev.2021.10.022
3. Marino, C. (2014) 'The DCDC2/intron 2 deletion and white matter disorganization: focus on developmental dyslexia', Cortex, 57:227-243. doi:10.1016/j.cortex.2014.04.016
4. Mascheretti, S. (2021) 'Selecting the Most Relevant Brain Regions to Classify Children with Developmental Dyslexia and Typical Readers by Using Complex Magnocellular Stimuli and Multiple Kernel Learning', Brain Sciences, 11(6). doi:10.3390/brainsci11060722
5. Meda, S. A. (2008) 'Polymorphism of DCDC2 Reveals Differences in Cortical Morphology of Healthy Individuals—A Preliminary Voxel Based Morphometry Study', Brain Imaging and Behavior, 2(1):21-26. doi:10.1007/s11682-007-9012-1
6. Perani, D. (2021) 'White matter deficits correlate with visual motion perception impairments in dyslexic carriers of the DCDC2 genetic risk variant', Experimental Brain Research, 239(9):2725-2740. doi:10.1007/s00221-021-06137-1

Poster No 2457

Visuo-Spatial Attention Development is Modulated by Local Computations in the Dorsal Stream

Patricia Hoyos[1], Anna Williams[1], Edan Daniel-Hertz[1], Sabine Kastner[1], Jesse Gomez[1]

[1]Princeton University, Princeton, NJ

Introduction: Does development of visuo-spatial attention result from local computations in the visual cortex? The human visual system contains what is referred to as the "dorsal stream", a collection of retinotopic regions that process the visual image and play a key role in our ability to deploy visuo-spatial attention. However, the structural and functional properties of dorsal stream development across childhood have never been mapped, perhaps due to the difficulty of running attention-based experiments on young children. Overcoming this hurdle, we created two novel, child-friendly videogames designed to quantify how visuo-spatial computations develop in the dorsal stream. Because we will be measuring from visual cortex, we can quantify for each voxel the portion of visual space to which the population of neurons responds to a stimulus (the population receptive field, pRF). Modeling the pRF as a gaussian circle, we can quantify a pRF's position and size, as well as quantify how these parameters change when visuo-spatial attention is moved to test the hypothesis that pRF's become increasingly dynamic with development.

Methods: In the first game called "Cartoonotopy", participants fixate at the center of the screen as a colorful cartoon-filled sliding bar sweeps across the visual field. This allows us to map pRF's and delineate the borders of the visual field maps that comprise the dorsal stream (V1 to the IPS0-5 maps in the parietal lobe). In the second game, "gopheRField", participants fixate while gophers emerge randomly from a grid of holes spanning the visual field. In alternating blocks, participants attend to either the gophers or a central stimulus. This allows us to quantify how each voxel's pRF dynamically shifts in response to the allocation of visuo-spatial attention to the periphery.

Results: Outside the scanner, in a group of adults we demonstrate the gopheRField game can replicate known processing differences across the visual field (eccentricity and upper v. lower visual field effects), offering evidence that it is a tool sensitive to measuring visuo-spatial processing. We next performed functional MRI while participants played the gopherfield game to model pRF dynamics of the dorsal stream. In n=16 adults (mean age of 33.6), we find that the allocation of attention to the periphery significantly increases the size of pRF's particularly in higher-order regions of the dorsal stream such as IPS1-3 (pRF size center vs. peripheral condition; IPS1 $p<0.05$; IPS2 $p<0.005$; IPS3 $p< 0.0005$). Additionally, pRF's shift location and sample more eccentric portions of the visual field (IPS1-3 p's<0.005). However, pRF parameters were stable and not significantly different between conditions in areas of early visual cortex such as V1-V3. We additionally collected data from n=5 (mean age of 10.6) children to evaluate developmental effects on pRF dynamics. Contrary to adults, pRF's of IPS1-3 did not show any significant changes between central and peripheral conditions. Instead, we found a significant age group effect on receptive field eccentricity in V2d ($p<0.001$), with children's V2d receptive fields shifting 0.6 degrees more than adults on average. These results suggest that the dorsal stream is undergoing development and earlier areas in the dorsal stream may be compensating for the higher-order area's protracted development.

Conclusions: These data explicate the potential neural correlates of previous behavioral works showing that visuo-spatial attention undergoes protracted development. This developmental trajectory impacts the acquisition of skills that heavily rely on visuo-spatial attention, like reading (Hoyos et al., 2020). By studying the development of the attention network, we will provide useful benchmark data for future studies in children with ADHD and dyslexia, offering translational insight as to why there is a high comorbidity between the two disorders.

References

1. Hoyos, P. M. (2021), 'Development of spatial biases in school-aged children', Developmental Science, vol. 24, no.3, pp. e13053

Poster No 2459

Do Post-Concussion Cognitive Symptoms Include Deeper Inattention During Mind Wandering? An EEG Study

Ni An[1], Todd Handy[1]

[1]*University of British Columbia, Vancouver, British Columbia*

Introduction: Following concussions, many individuals report persisting (> 3 months) post-concussion symptoms (PCS), including lingering cognitive challenges. The goal of our study was to determine whether PCS may include alterations to normative patterns of mind wandering, or the natural propensity of our thinking to periodically drift away from the on-going task at hand. In particular, do those with PCS fall in to deeper states of inattention when mind wandering?

Methods: Two age-matched groups of participants were recruited through the Human Subject Pool (HSP) System of the University of British Columbia (UBC): those with PCS and health controls (HC). Eligibility criteria for the PCS group included adult individuals who have experienced one or more mild Traumatic Brain Injuries (mTBI) and self-report having persistent post-concussive cognitive symptoms. Exclusion criteria included individuals who have experienced moderate to severe traumatic brain injuries, have not fully recovered from their mTBI, or are currently in the acute stage of mTBI (injury happened in < 3 months). The exclusion criteria were included to eliminate the effects of acute symptoms of mTBI. The HC were screened for no history of neurological injury of any severity. A total of 17 individuals were included in the PCS group, and 19 individuals in the HC group. All participants were asked to complete a sustained-attention-to-response task (SART) while their EEG was recorded. The SART requires participants to (1) make a manual response to frequent numbers (1 to 9) presented in a serial fashion in the center of a computer screen, one every several seconds, while (2) withholding manual responses to infrequently-presented non-number stimuli (the letter X). Importantly, the SART is designed to be boring and repetitive, and so engenders frequent bouts of mind wandering. Each block of trials lasted from 30 to 90 seconds, and at the end of each block participants were instructed to report on their attentional state at the end of the block: were they paying attention to the

task when it ended, or had they just been mind wandering. Each participant performed a total of 40 trial blocks, producing 40 experience-sampling reports of being in an “on-task” or “mind wandering” attentional state.

Results: Data analysis centered on examining the amplitude of the P300 ERP component elicited by the target numbers presented in the 12 seconds immediately prior to the experience-sampling reports of being in an “on-task” or “mind wandering” attentional state. A repeated-measures ANOVA with one between-group factor (PCS vs. HC) and one within-group factor (on-task vs. mind wandering attentional state) revealed a main effect of attention, such that the mean amplitude of the P300 ERP component over midline parietal scalp locations was significantly higher during on-task vs. mind wandering attentional states ($F(1,33) = 5.02$; $p = .032$). However, there was no significant group x attention interaction ($F(1,33) = 1.63$; $p = .432$).

Conclusions: Consistent with prior studies of mind wandering, we found that the mean amplitude of the P300 ERP component elicited by target events in the SART was significantly lower when participants were mind wandering, relative when their attention was focused on the task. This provides normative validity for the data. Critically, however, this effect of attentional state on the P300 amplitude did not vary between groups. In other words, PCS was not associated with greater inattention during mind wandering, as indexed via cognitive electrophysiological measures. To the extent that mTBI can produce persisting cognitive challenges, these may not extend to pathologies in off-task attentional states.

Poster No 2460

Attentional Indicators and Quantitative EEG Alterations through Respiratory Pattern Manipulation

Dogeun Park[1], Young-Gi Ju[1], Dong-Ok Won[1,2]

[1]Dept. of Artificial Intelligence Convergence, Hallym University, Chuncheon, Kangwon, Korea, Republic of, [2]College of Medcine, Hallym University, Chuncheon, Kangwon, Korea, Republic of

Introduction: Attention enhancement is a valuable factor for attention-related disorders such as attention deficit/hyperactivity disorder (ADHD), and well-functioning in the work environment in modern society. Numerous studies have shown that theta/beta ratio (TBR) is elevated in ADHD, and these have provided evidence that TBR might be an electrophysiological marker for attentional control[1]. ERP-based BCI is a representative attention-based paradigm that could induce visual and cognitive fatigue[2]. One previous study showed improved performance through six minutes of meditative mindfulness induction. A study comparing four different respiratory patterns, including meditation, demonstrated that five minutes of physiological sighing were more effective than mindfulness meditation in terms of reducing physiological arousal, and another preliminary study showed that physiological sighing enhanced character recognition performance in ERP-based BCI. Therefore, we assumed that physiological sighing could improve attention through reducing stress and investigated the theta/beta ratio, which is one of the quantitative indicators of attentional control, to provide additional explanatory power for ERP-based BCI performance improvement.

Methods: As shown in Figure 1, physiological sighing consists of double inhalations and single extended exhalation. A second inhalation is performed to expand the alveoli. In this preliminary study, a total of five subjects participated. Each subject was requested to experience two sessions, and the experiment consists of two sessions: 1) Session A; 2) Session B, and two conditions: 1) Normal Condition; 2) Proposed Condition. An average of 15 minutes of break time was provided in the middle of the two sessions. We used MATLAB with the BBCI toolbox (http://bbci.de/toolbox) for pre-processing, and regularized linear discriminant analysis with shrinkage was applied with Python (version 3.7.11). To ascertain the feasibility of the hypothesis, Welch’s method and the composite Simpson’s rule were applied to estimate band power and the theta/beta ratio.

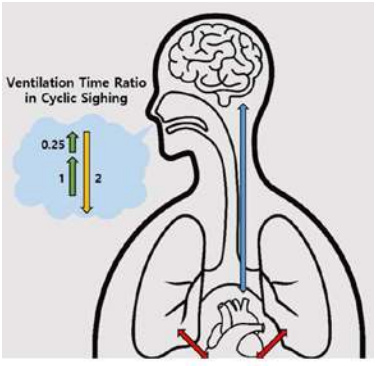

Figure 1

Results: This study demonstrated a lower mean TBR in the proposed conditions using physiological sighing (Figure 2). In addition, these results showed a lower mean TBR in the proposed respiratory patterns in both Session A and Session B. In individual analysis, we showed low TBR under all subjects' conditions except for the second session of subject 4. Interestingly, subject 4 had dry eye syndrome and showed low performance in BCI. This indicated that the BCI performance and the results of TBR are matched.

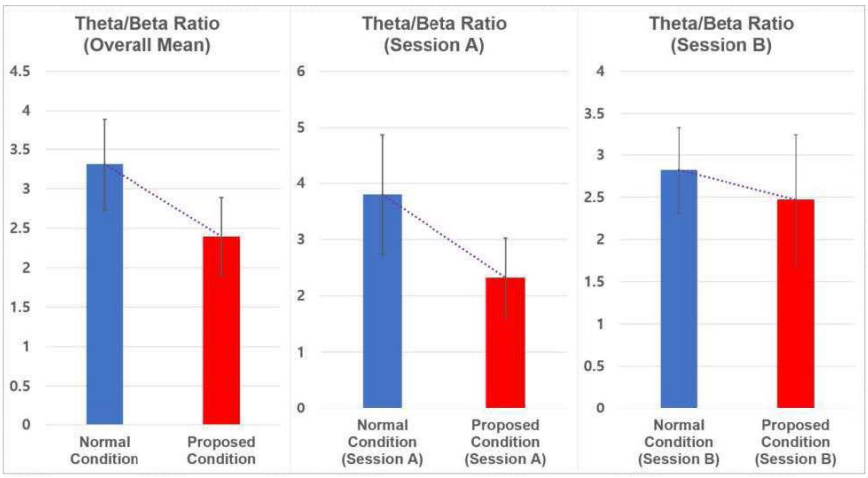

Figure 2

Conclusions: We examined the impact of proposed ventilation patterns with a 2-minute physiological sighing on users in ERP-based BCI tasks and investigated the impact of quantitative indicators. Generally, TBR and attention control have negative correlations [ref]. In Figure 2, overall, the proposed ventilation pattern showed a lower TBR than a normal ventilation pattern. This suggests that the proposed respiratory pattern using physiological sighing could enhance attentional control in various situations. In light of this, this provides additional explanatory power for the causal effect between physiological attention alterations and character recognition accuracy. Even though statistical analysis will be required for significance, this result leads our assumptions in an encouraging direction.

References

1. A. Angelidis, W. van der Does, L. Schakel, and P. Putman, 'Frontal EEG theta/beta ratio as an electrophysiological marker for attentional control and its test-retest reliability', Biological Psychology, vol. 121, pp. 49–52, 2016.
2. R. Fazel-Rezai, B. Allison, C. Guger, E. Sellers, S. Kleih, and A. Kübler, 'P300 brain computer interface: current challenges and emerging trends', Frontiers in Neuroengineering, vol. 5, 2012.
3. C. E. Lakey, D. R. Berry, and E. W. Sellers, 'Manipulating attention via mindfulness induction improves P300-based brain–computer interface performance', Journal of Neural Engineering, vol. 8, no. 2, p. 025019, Mar. 2011.
4. M. Y. Balban et al., 'Brief structured respiration practices enhance mood and reduce physiological arousal', Cell Reports Medicine, vol. 4, no. 1, p. 100895, 2023.
5. D. Park, Y.-G. Ju, and D.-O. Won, 'Stable Character Recognition Strategy Using Ventilation Manipulation in ERP-Based Brain-Computer Interface', in Pattern Recognition, 2023, pp. 15–25.

Poster No 2461

Structural connectivity of the olfaction network and its relation to aging and olfactory function

Xin Li[1], Jonas Olofsson[2], Jonas Persson[3]

[1]Karolinska Institutet, Stockholm, AB, [2]Stockholm University, Stockholm, AB, [3]Örebro universitet, Örebro, AB

Introduction: Olfactory function declines with age, significantly impacting the quality of everyday life. Emerging research has unveiled a compelling link between olfaction dysfunction and Alzheimer's disease. Olfactory performance has been related to specific brain regions, including the hippocampus (HC) and parahippocampal gyrus (PhG). However, how the primary olfaction cortex plays a role in olfaction is still unknown. The knowledge gap is partly due to the neural mechanism of the olfaction may lie in the connections among multiple brain regions. Taking a data-driven approach, a previous study parcellated the primary olfactory cortex into four distinct subregions and characterized their unique whole-brain functional connectivity profiles, unveiling the olfactory system's complexity. Currently, no study has explored the structural connectivity foundation of the olfaction system and its relationship with aging.

Methods: This study included 137 healthy adults without dementia (25-85 years), who underwent MRI scanning and olfaction tests, including smell identification and smell threshold (an index of smell sensitivity). Whole-brain Anatomically Constrained Tractography was performed on the preprocessed diffusion-weighted images in MRtrix 3.0. The primary olfaction cortex was parcellated into 4 subregions, anterior olfactory nucleus (AON), olfactory tubercle (TUB), and frontal and temporal piriform cortices (PriF and PriT), using the atlas from Zhou et al., 2019. Structural connectomes were constructed using tractograms and parcellation images. Connectivity strength was quantified using log-transformed fiber bundle capacity (FBC). After a two-step thresholding, 75 connections were included in subsequent analyses. We first investigated the age effects on the FBC of each connection within the connectome. To investigate the associations between the olfaction network with individual olfaction performance, we performed canonical regression using generalized additive models (GAMs). These models underwent hyperparameter tuning, model training, and testing through nested 2-fold cross-validation, which was repeated 100 times. The resulting feature weights were extracted to discern the significance of each connection to olfaction and cognitive performance.

Results: All 4 regions of the primary olfaction cortex are connected to several subcortical nuclei, including the HC, caudate (Cd), and putamen. Moreover, the subregions have unique connectivity patterns to the rest of the brain (Fig. 1). Importantly, only a small set of connections within the olfaction network demonstrated the age effects, including connections between AON to HC and PhG, between TUB to the HC, and Cd, and between PriT to insula ($P_{perm}<0.05$). We then examined if the connectivity strength (FBC) of the olfaction network (75 connections) can predict individual olfaction and other cognitive performance. Results show that the prediction models were significant for odor identification (mean Pearson's r = 0.25, mean MAE = 1.7 of range 0-12, $P_{perm} < 0.01$) and episodic memory (mean Pearson's r = 0.22, mean MAE = 7.1 of range 0-72, $P_{perm} < 0.05$), but not significant for other task domains. The weights of each connection in the prediction model of odor identification and episodic memory are shown in Fig. 2.

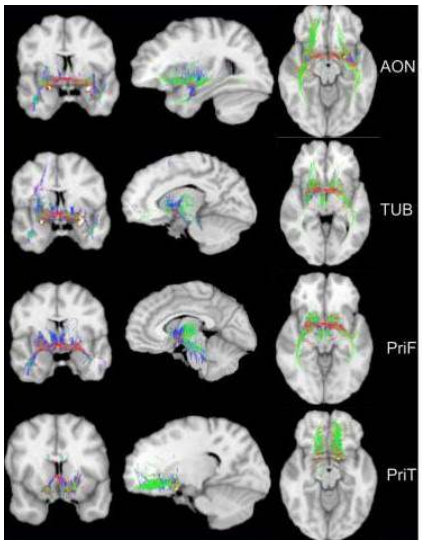

Fig. 1 White-matter conneciton from 4 subregions of the primary olfaction cortex, anterior olfactory nucleus (AON), olfactory tubercle (TUB), frontal piriform cortices (PriF), and temporal piriform cortices (PriT), to the rest of the brain. Color represents the fiber orientation. Tractogram. Tractogram is based on DWI from 1 participant of 25 years for illustrative purpose.

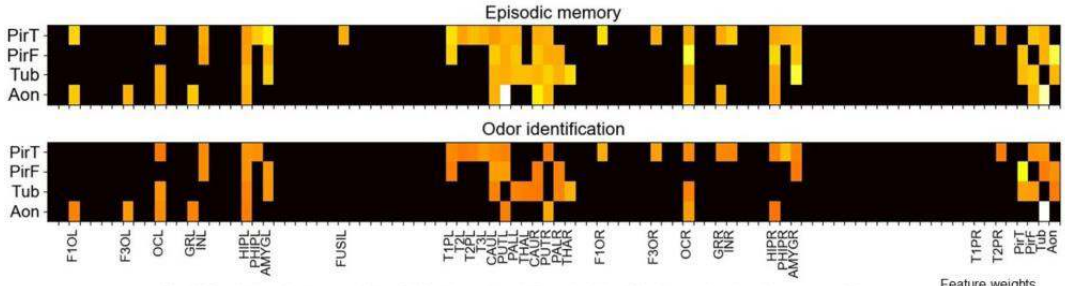

Fig. 2 Predictive-feature weights of olfaction network for odor identification and episodic memory. The values are standardized for illustrative purpose. Only significant features ($p<0.05$) are shown. R, right hemisphere; L, left hemisphere; HIP, hippocampus; PHIP, parahippocampus; AMYGL, amygdala; CAU, caudate; PUT, putamen; PAL, paladium; THA, thalamus.

Conclusions: The study is the first to reconstruct the brain connectome of the entire olfactory network. Using a wide age range, the study demonstrated age effects on connections between the olfaction cortex and key regions including the HC, Cd, and insula. Through quantifying the connectivity strength of the olfaction network, we were able to partially unveil the structural underpinnings of olfactory function. Notably, our findings demonstrated shared connectivity features that contribute to both odor identification and episodic memory. In summary, the study shed light on the neural mechanisms of olfactory function, providing novel insight into the intricate relationship among aging, olfaction, and episodic memory.

References
1. Kubota, S., Masaoka, Y., Sugiyama, H., Yoshida, M., Yoshikawa, A., Koiwa, N., Honma, M., Kinno, R., Watanabe, K., Iizuka, N., Ida, M., Ono, K., & Izumizaki, M. (2020). Hippocampus and Parahippocampus Volume Reduction Associated With Impaired Olfactory Abilities in Subjects Without Evidence of Cognitive Decline. Frontiers in Human Neuroscience, vol. 14
2. Smith, R.E., Tournier, J.D., Calamante, F., & Connelly, A. (2012). Anatomically-constrained tractography: improved diffusion MRI streamlines tractography through effective use of anatomical information. Neuroimage, vol. 62, pp. 1924-1938.
3. Tournier, J.D., Calamante, F., Gadian, D.G., & Connelly, A. (2004). Direct estimation of the fiber orientation density function from diffusion-weighted MRI data using spherical deconvolution. Neuroimage, vol. 23, pp. 1176-1185,
4. Zhou, G., Lane, G., Cooper, S. L., Kahnt, T., & Zelano, C. (2019). Characterizing functional pathways of the human olfactory system. Elife, vol. 8, article e47177.

Poster No 2462

Brain substates induced by DMT relate to sympathetic output and meaningfulness of the experience

Lorenzo Pasquini[1], Alexander Simon[2], Courtney Gallen[1], Hannes Kettner[1], Leor Roseman[3], Adam Gazzaley[1], Robin Carhart-Harris[1], Christian Timmermann[4]

[1]Department of Neurology, Neuroscape, University of California, San Francisco, San Francisco, CA, [2]Yale University, Interdepartmental Neuroscience Program, New Haven, CT, [3]Division of Psychiatry, Department of Brain Sciences, Centre for Psychedelic Research, Imperial Coll, London, UK, [4]Division of Psychiatry, Department of Brain Sciences, Centre for Psychedelic Research, Imperial Col, London, UK

Introduction: One's sense of self results from the integration of visceral and autonomic bodily functions into a distributed interoceptive brain network[1] and from the representation of autobiographical memories in midline parietal and medial temporal cortices[2]. N,N-Dimethyltryptamine (DMT) is a serotonergic psychedelic, known to rapidly induce short-lasting disruptions in the ordinary sense of self, characterized by auditory distortions, amplification of emotional states, and feelings of ego dissolution[3]. Multimodal neuroimaging work has started elucidating the impact of DMT on the human brain, by revealing brain network disintegration, heightened global connectivity, and increased EEG-based signal entropy after DMT administration[3]. Novel methods enable the identification of functional substates that emerge over the course of an entire scan[4–6], a valuable approach for identifying unique signatures of brain activity – and linked autonomic physiology – naturally evolving during the altered state of consciousness induced by DMT.

Methods: We leveraged neuroimaging data acquired in 14 healthy volunteers as part of a within-subject study assessing the effects of DMT on brain function[3]. Simultaneous fMRI and ECG data were acquired prior to, during, and after an intravenous bolus administration of 20 mg of DMT fumarate, and, separately, placebo. ECG data was used to derive continuous heart rate; fMRI data was preprocessed to derive nodal activity time series. Cosine similarity was applied on the nodal activity time series to derive individual dynamic activity matrices, reflecting the similarity of brain activity in time. Group-averaged dynamic activity matrices were subtracted, revealing periods of homogeneous brain activity under DMT and community detection methods were applied on this subtraction matrix to identify brain activity substates. Brain activity substate maps were compared across DMT and placebo and significant activity changes were linked to scores of auditory distortions, meaningfulness of the experience, and heart rate alterations.

Results: We identified three brain activity substates, one occurring before the injection of DMT and towards the end of the scanning session, a second directly following the injection of DMT, and a third state immediately following the previous post-injection substate. Only the second substate (i.e., the first occurring post-injection) showed significant brain activity changes when comparing the DMT to the placebo condition, revealing increased right superior temporal pole activity and decreased left hippocampal and medial parietal deactivations under DMT. Increased activation in the right superior temporal lobe correlated with the intensity of the auditory distortion, while deactivation of the hippocampus/medial parietal cortex correlated with scores of meaningfulness of the experience. During the first post-injection state, heart rate was increased during DMT, which correlated negatively with meaningfulness of the experience and positively with hippocampus/medial parietal deactivation.

Conclusions: Dynamic analyses and community detection algorithms applied to neuroimaging data acquired under DMT administration revealed a brain substate emerging during the peak effects, which was characterized by superior temporal lobe hyperactivity, and hippocampus and medial parietal cortex deactivation[7]. While hyperactivity correlated with altered sensory perception, deactivations related to the self-referential attribution of meaning to the psychedelic experience. Although the acute DMT experience is accompanied by increased heart rate[8], lower heart rate changes predicted meaningfulness of the experience and stronger hippocampal/medial parietal deactivation. These results indicate that sympathetic regulation[9] and

deactivation of hippocampal and medial parietal regions, which are associated with ego-dissolution under psychedelics, may contribute to fostering positive mental health outcomes in the context of psychedelic therapy.

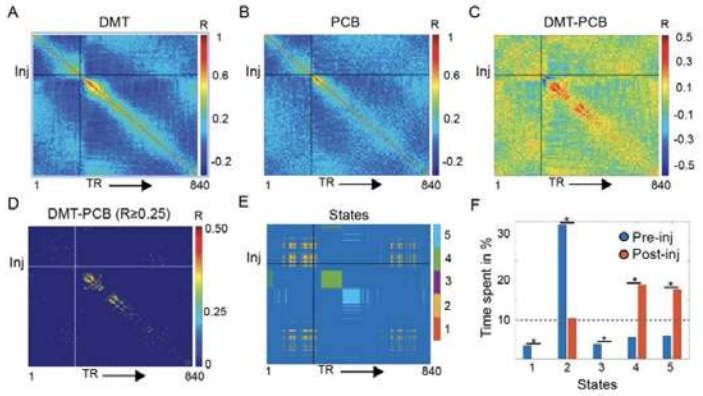

Figure 1. Analysis pipeline and metrics. Group-mean continuous brain activity similarity matrix, reflecting the homogeneity of brain activity in time during the DMT (**A**) and the placebo (PCB; **B**) conditions. (**C**) Mean subtraction matrix reflecting how continuous brain activity similarity varies across the DMT and placebo conditions. (**D**) The subtraction matrix was thresholded for similarity values maximizing the identification of brain activation substates occurring either during the pre-injection or post-injection phase (Pearson's correlation values $R \geq 0.25$) using an unsupervised community detection algorithm. This community detection algorithm identified five brain activation substates differentiating the DMT from the placebo condition (**E**). (**F**) These five substates were occupied at significant higher rate either during the pre- or post-injection periods, and only three were occupied for more that 10% of the duration of the entire scanning time. Following analyses focused on these three activation substates: State 2, 4, and 5. DMT = N,N-Dimethyltryptamine; Inj = injection; TR = MRI repetition time. $^*p < 0.05$

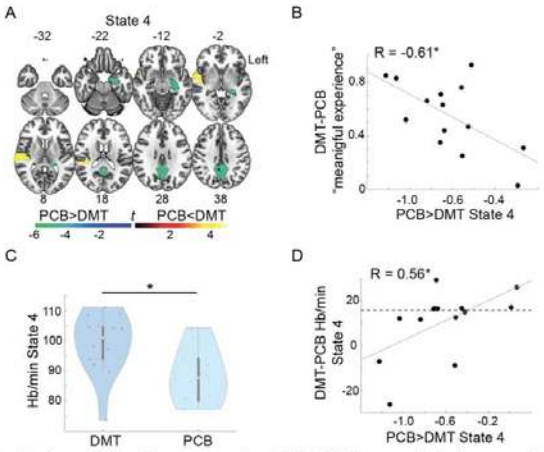

Figure 2. Brain activity changes under DMT. (A) Hyperactivity (warm colors) and hypoactivity (cold colors) in the first post-injection substate (State 4) under DMT when compared to placebo. Findings are FDR adjusted $p < 0.05$; color bar indicates associated *t*-values. (**B**) Hypoactivity of the hippocampus/medial parietal cortex in State 4 under DMT correlates with meaningfulness of the experience. (**C**) Increased heartrate during the first post-injection activation substate under DMT when compared to placebo. (**D**) The lower the heartrate change under the first post-injection DMT state, the stronger hippocampus and medial parietal deactivations under the same state. $^*p < 0.05$

References

1. Damasio, A. & Damasio, H. Homeostatic feelings and the biology of consciousness. Brain 145, 2231–2235 (2022).
2. Lyu, D. et al. Causal evidence for the processing of bodily self in the anterior precuneus. Neuron 111, 2502-2512.e4 (2023).
3. Timmermann, C. et al. Human brain effects of DMT assessed via EEG-fMRI. Proceedings of the National Academy of Sciences 120, 2023 (2023).
4. Rubinov, M. & Sporns, O. Complex network measures of brain connectivity: Uses and interpretations. Neuroimage 52, 1059–1069 (2010).
5. Deco, G. et al. Whole-Brain Multimodal Neuroimaging Model Using Serotonin Receptor Maps Explains Non-linear Functional Effects of LSD. Current Biology 28, 3065–3074.e6 (2018).
6. Lurie, D. J. et al. Questions and controversies in the study of time-varying functional connectivity in resting fMRI. Network Neuroscience 4, 30–69 (2020).
7. Carhart-Harris, R. L. et al. Neural correlates of the psychedelic state as determined by fMRI studies with psilocybin. Proc Natl Acad Sci U S A 109, 2138–2143 (2012).
8. Strassman, R. J. & Qualls, C. R. Dose-Response Study of N,N-Dimethyltryptamine in Humans: I. Neuroendocrine, Autonomic, and Cardiovascular Effects. Arch Gen Psychiatry 51, 85–97 (1994).
9. Critchley, H. D. & Harrison, N. A. Visceral Influences on Brain and Behavior. Neuron 77, 624–638 (2013).

Poster No 2463

The integrity of thalamo-dorsolateral prefrontal cortex tract: a key in consciousness disorders

Seonghoon Lim[1], Ji Yoon Jung[1], Sun Im[2], Tae-Woo Kim[3]

[1]Seoul St.Mary's Hospital College of Medicine, The Catholic University of Korea, Seoul, Korea, Republic of, [2]Bucheon St. Mary's Hospital, College of Medicine, The Catholic University of Korea, Seoul, Republic, Bucheon, Korea, Republic of, [3]National Traffic Injury Rehabilitation Hospital, Gyeongki-do, Republic of Korea, Gyeongki-do, Korea, Republic of

Introduction: The mesocircuit model describes a complex network that includes the prefrontal cortical-striatopallidal thalamocortical loop systems and is involved in the mechanism of consciousness in patients with disorders of consciousness (DoC). Inhibitory signals to the thalamus become hyperactive in DoC patients, leading to a loss of consciousness. Reactivating this mesocircuit system is key to recovering consciousness in these patients. We hypothesized that residual integrity of thalamo-dorsolateral prefrontal cortex tract (TDLPFCT) integrity may be key factor of consciousness in patients with DoC.

Methods: This retrospective case-control study included three groups: prolonged DoC (n=20), stroke without DoC (n=20), and normal controls (n=20). Diffusion tensor imaging (DTI) was performed at least 4 weeks after the onset. Thalamo-DLPFC tracts were reconstructed using diffusion tensor tractography, and fractional anisotropy (FA) and tract volume (TV) were measured for each hemisphere. Consciousness was assessed using revised coma recovery scale (CRS-R) within a week of brain imaging.

Results: All three groups exhibited significant differences in DLPFCT TV in both affected and less-affected lobes, with the DoC group showing greatest reduction($p = 0.002$). We found a significant correlation between the TV of the TDLPFCT in unaffected lobe, which can be referred to more preserved TDLPFCT, and the CRS-R score, as indicated by a Spearman's correlation coefficient of $r = 0.628$ ($p = 0.003$).

Conclusions: The integrity of the TDLPFCT, particularly in the less affected hemisphere, appears to play a crucial role in determining consciousness levels in prolonged DoC patients. Highlighting its potential importance in assessing prognosis and further developing therapeutic strategies for patients with DoC.

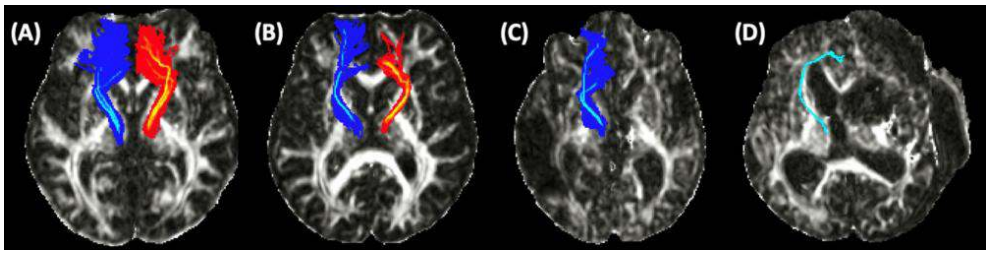

Fig. Representative diffusion tensor tractography images of the TDLPFCT. (A) Normal, (B) Stroke, (C) Disorders of consciousness with high CRS-R, (D) Disorders of consciousness with low CRS-R

References

1. Schiff ND. Recovery of consciousness after brain injury: a mesocircuit hypothesis. Trends Neurosci. 2010;33(1):1-9.
2. Schiff ND. Mesocircuit mechanisms in the diagnosis and treatment of disorders of consciousness. Presse Med. 2022;52(2):104161.

Poster No 2464

Measuring the Dynamic Balance of Integration and Segregation Underlying Conscious States

Hyunwoo Jang[1], George Mashour[1], Anthony Hudetz[1], Zirui Huang[1]

[1]University of Michigan, Ann Arbor, MI

Introduction: Integration and segregation are two key features of neural systems thought to mediate consciousness. Their balance in brain networks is critical for optimal function and has been a focus of research for over a decade. However, a consensus on how, precisely, to measure this balance has proven elusive. In this study we aimed to formulate a metric that captures two major surrogates of integration-segregation balance, i.e., functional connectivity strength and network topology. Through application to dynamic functional connectivity in humans, we investigate the potential of this metric to reflect shifts in conscious states during the loss and recovery of responsiveness (LOR and ROR, respectively). Furthermore, at a more granular level, we examine whether a sequential pattern of subnetwork changes in integration-segregation balance exists during the transitions to LOR and ROR. Finally, we use machine learning to identify if the topo-connectivity can reliably predict different states of consciousness.

Methods: Our approach involved analyzing two independent fMRI datasets encompassing scans taken before, during, and after the administration of the sedative-hypnotic drug propofol. Our analysis centered on dynamic functional connectivity of 450 regions of interest, employing a sliding-window technique. The goal was to incorporate both functional connectivity strength and network topology in a single metric, to advance beyond the status quo of assessing these properties independently. Functional connectivity strength was computed through the average of the functional connectivity matrix, while topology was measured using the small-worldness metric. The product of these two was termed the "Topo-Connectivity Index". This composite index was calculated for each time window both at a whole-brain level and within distinct subnetworks. We employed various machine learning techniques and tested the model performance both within datasets and in comparison between them.

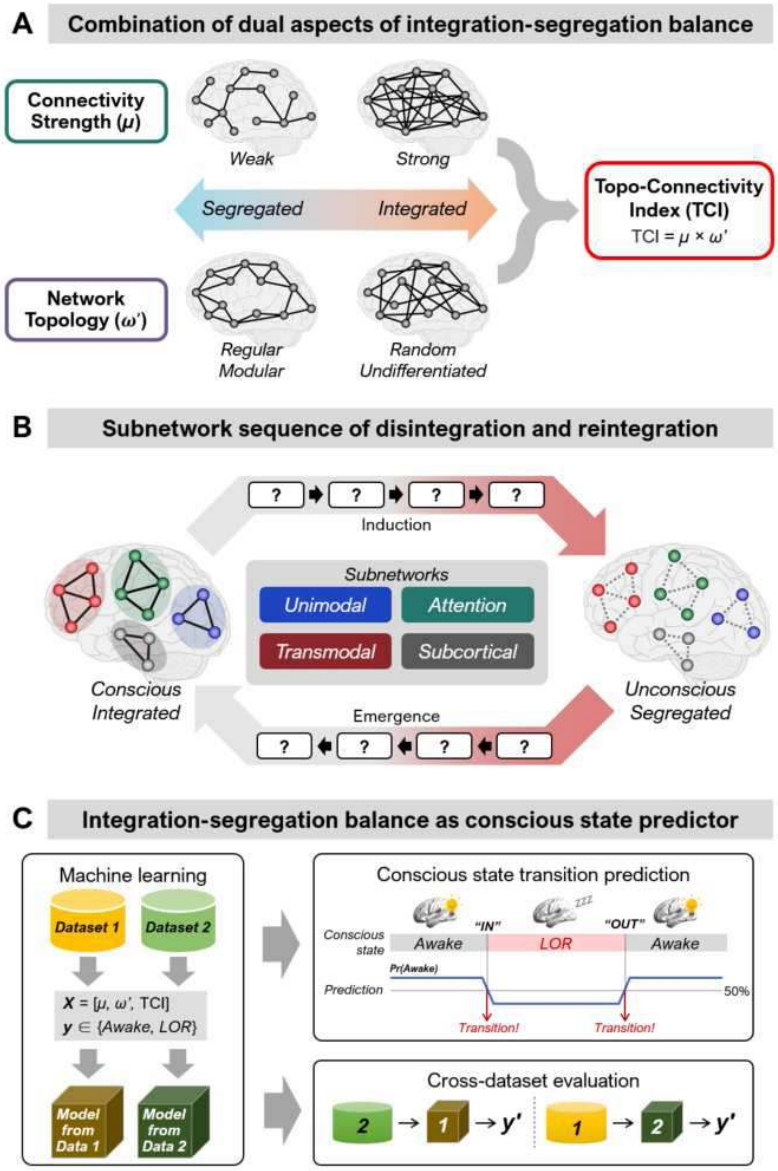

Results: Compared to conscious baseline, LOR was linked to a pronounced functional segregation in the brain. This was evidenced by a significant decrease in connectivity ($p=0.0022$) and a shift towards a lattice-like topology ($p=0.0022$). The descriminatory capability of TCI (AUC = 0.76) surpassed that of connectivity strength (AUC = 0.75) and topology (AUC = 0.69) in isolation, and other commonly used balance metrics. The whole-brain topo-connectivity exhibited a decline around the onset of LOR, continuing to decrease progressively over a span of 8 minutes. In contrast, as the transition to ROR approached, the topo-connectivity initiated a rebound 5 minutes prior to the ROR and continued to rise for 10 minutes. The analysis of brain subnetworks revealed a unique sequence of changes: the route to LOR was marked by an initial drop in topo-connectivity within unimodal networks (such as visual and somatomotor), followed by a decrease in transmodal (including fronto-parietal and default-mode) and subcortical networks. The course towards ROR was characterized by the restoration of transmodal networks, followed by the recovery of the unimodal and subcortical networks. Applying a support vector machine model, topo-connectivity emerged as a robust predictor of conscious states (accuracy ≈ 85%). Notably, our model predicted the

conscious state during critical transition periods with considerable accuracy (≃ 80%), even without presenting these periods in the training data.

Conclusions: Joint quantification of connectivity strength and network topology as a surrogate for integration-segregation balance is a novel and principled approach for assessing conscious states. Our findings also reveal a distinct temporal sequence of network changes that occur during the transition into and out of anesthetic-induced loss of consciousness. The application of the topo-connectivity and machine learning techniques demonstrates potential for objectively identifying conscious states or disorders of consciousness independently of behavior.

Poster No 2465

General anaesthesia reduces the uniqueness of brain connectivity across individuals and species

Andrea Luppi[1], Daniel Golkowski[2], Andreas Ranft[2], Rudiger Ilg[2], Denis Jordan[2], Danilo Bzdok[3], Adrian Owen[4], Lorina Naci[5], Emmanuel Stamatakis[6], Enrico Amico[7], Bratislav Misic[8]

[1]McGill University, Buguggiate, Italy, [2]Technical University Munich, Munich, Germany, [3]McConnell Brain Imaging Centre (BIC), Montreal Neurol, McGill Universityogical Institute (MNI), Montreal, Quebec, [4]Western University, London, Ontario, [5]Trinity College Dublin, Dublin, Ireland, [6]University of Cambridge, Cambridge, Cambridgeshire, [7]Ecole Polytechnique Federale de Lausanne, Lausanne, Switzerland, [8]McGill University, Montreal, Quebec

Introduction: The human brain is characterised by idiosyncratic patterns of spontaneous thought, rendering each brain uniquely identifiable from its neural activity (Amico and Goñi, 2018; Finn et al., 2015). However, deep general anaesthesia suppresses subjective experience. Does it also suppress what makes each brain unique? We attack this question from three conceptual angles. First, we compare brain connectivity within and across individuals. Second, we compare brain activity against the canonical brain maps of human cognition. Third, we ask whether anaesthesia makes the human brain less distinctive from another species: the macaque.

Methods: We consider resting-state functional MRI data from N=15 volunteers at baseline and at different levels of the anaesthetic sevoflurane: at burst-suppression, 3 vol%, 2 vol%, and post-anaesthetic recovery of responsiveness (Ranft et al., 2016). Here we use connectome fingerprinting of individuals based on fMRI scans to evaluate whether individuals become less distinguishable when under anaesthesia, based on the similarity (correlation) between functional connectivity patterns at different points in time (Amico and Goni, 2018; Finn et al., 2015). We compare the patterns of regional changes in identifiability against brain maps of evolutionary cortical expansion (Xu et al., 2020), human-accelerated gene expression (Wei et al., 2019), inter-individual variability (Mueller et al., 2013), and the archetypal sensory-association axis of cortical organisation (Sydnor et al., 2021), obtained from the neuromaps toolbox (Markello et al., 2022). To control for spatial autocorrelation, we employ autocorrelation-preserving null models (Markello et al., 2022). We also use 123 meta-analytic patterns from NeuroSynth (Yarkoni et al., 2011), and assess how well their spatial distribution matches the spatial patterns of spontaneous brain activity. Finally, we compare functional connectivity across levels of anaesthesia, against the functional connectivity of the macaque brain (Michael Milham et al., 2018). We replicate all results in an independent dataset of resting-state fMRI from N=16 volunteers scanned before, during, and after loss of responsiveness induced by propofol.

Results: When comparing two scans of the same individual while awake, it is easy to distinguish self from other. However, self-self correlations between awake and anaesthetised brains are significantly diminished compared to awake-recovery self-similarity (Fig.1a-d). We localise regional changes in identifiability, quantified as the mean change in intraclass correlation coefficient (ICC) across each region's edges (Amico and Goñi, 2018; Finn et al., 2015). We observe a significant spatial correlation with the brain's archetypal sensory-association axis ($\rho = 0.67$, $p < 0.001$) as well as inter-individual variability ($\rho = 0.63$, $p < 0.001$). Changes in regional identifiability correlate with molecular and morphometric markers of phylogenetic cortical differentiation between human and non-human primates: evolutionary expansion ($\rho = 0.35$, $p < 0.001$), and the regional mean expression of human-accelerated ("HAR") genes ($\rho = 0.42$, $p < 0.001$) (Fig.1e-h). As anaesthesia deepens, the quality of cognitive matching deteriorates: the best spatial correlation between brain activity and meta-analytic brain maps from NeuroSynth is lower at deeper levels of anaesthesia (Fig.2a,b). At increasing concentration of sevoflurane, we also observe increasing similarity between the regional functional connectivity patterns of humans and macaques (Fig.2c). The effects of sevoflurane anaesthesia are reversed upon recovery, and are replicated with a different anaesthetic, propofol.

Conclusions: Altogether, the present results indicate that regardless of the specific anaesthetic used, anaesthetised human brains are less unique, both across individuals and even across species, with regions that are most heterogeneous across individuals and across species being especially affected.

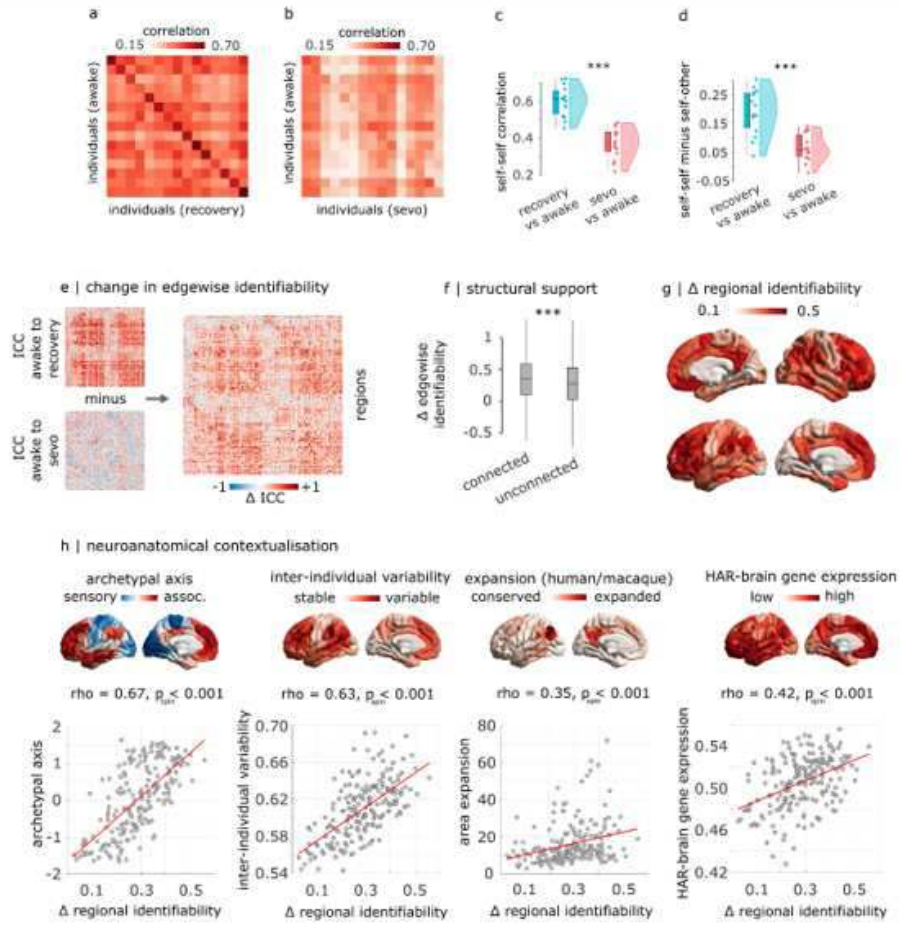

Fig.1. Identifiability of individual connectomes is reduced under sevoflurane anaesthesia | (**a**) Identifiability matrix between wakefulness and post-anaesthetic recovery. (**b**) Identifiability matrix between wakefulness and sevoflurane anaesthesia. Entries along the diagonal, represent self-self-similarity (correlation of FC patterns), whereas off-diagonal entries represent self-other similarity. (**c**) Self-self-similarity is significantly higher between two conscious states, than between wakefulness and anaesthesia. (**d**) Differential identifiability (the difference between self-self correlation and mean self-other correlation) is significantly higher between two conscious states, than between wakefulness and anaesthesia. (**e**) Edge-level difference in intra-class correlation coefficient between awake-recovery and awake-sevoflurane. (**f**) The anaesthetic-induced loss of ICC is significantly more pronounced for functional connections with an underlying structural direct connection, than without. (**g**) Regional distribution of anaesthetic-induced loss of ICC, projected onto the cortical surface. (**h**) The anaesthetic-induced regional loss of ICC is significantly spatially aligned with the archetypal sensory-association axis of cortical organisation; the regional distribution of inter-individual variability of functional connectivity; the regional distribution of cortical expansion between macaque and human brains; and the regional expression of human-accelerated genes pertaining to brain function and development ("HAR-brain genes"). ***, $p < 0.001$.

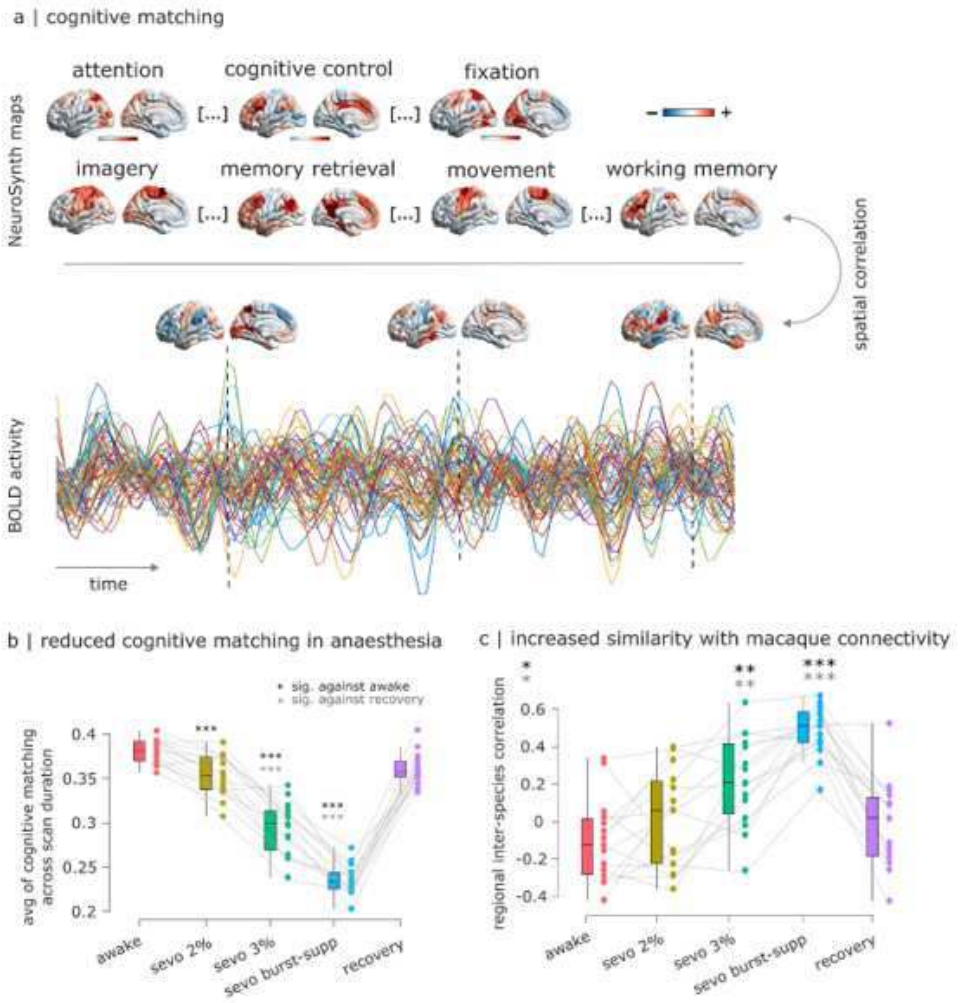

Fig.2. Anaesthesia reduces cognitive matching of brain activity with canonical meta-analytic patterns is diminished under anaesthesia, while increasing similarity with macaque functional connectivity | (a) At each point in time, the cognitive matching score is computed as the best spatial correlation between brain activity and 123 NeuroSynth meta-analytic maps. For each participant, an overall index of the quality of cognitive matching is then obtained by averaging the cognitive matching scores across the entire scan duration, within each condition. (b) Ordinate: mean across time of the cognitive matching score. *** (black), $p < 0.001$ against wakefulness (FDR-corrected). (c) Regional correlation of mean FC between human and macaque across wakefulness, anaesthesia, and recovery. **, $p < 0.01$, *** (black), $p < 0.001$ against wakefulness (FDR-corrected); ** (grey), $p < 0.01$ *** (grey), $p < 0.001$ against recovery (FDR-corrected).

References

1. Amico, E., (2018), 'The quest for identifiability in human functional connectomes'. Scientific Reports 8.
2. Finn, E.S., (2015, 'Functional connectome fingerprinting: identifying individuals using patterns of brain connectivity'. Nature Neuroscience 18, 1664–1671.
3. Markello, R.D. (2022), 'neuromaps: structural and functional interpretation of brain maps'. Nature Methods 19, 1472–1479.
4. Milham, M. (2018), 'An Open Resource for Non-human Primate Imaging'. Neuron 100, 61-74.e2.
5. Mueller, S., (2013), 'Individual variability in functional connectivity architecture of the human brain'. Neuron 77, 586–595.
6. Ranft, A., (2016), 'Neural Correlates of Sevoflurane-induced Unconsciousness Identified by Simultaneous Functional Magnetic Resonance Imaging and Electroencephalography'. Anesthesiology 125, 861–872.
7. Sydnor, V.J., (2021), 'Neurodevelopment of the association cortices: Patterns, mechanisms, and implications for psychopathology'. Neuron 109, 2820–2846.
8. Wei, Y., (2019), 'Genetic mapping and evolutionary analysis of human-expanded cognitive networks'. Nature Communications 10.
9. Xu, T., (2020), 'Cross-species functional alignment reveals evolutionary hierarchy within the connectome'. NeuroImage 223.
10. Yarkoni, T., (2011), 'Large-scale automated synthesis of human functional neuroimaging data'. Nature Methods 8, 665–670.

Poster No 2466

Is the prefrontal cortex necessary in conscious perception?

Kavindu Bandara[1], Elise Rowe[2], Stefan Bode[3], Marta Garrido[4]

[1]University of Melbourne, Carlton, Victoria, [2]The University of Melbourne, Melbourne, VIC, [3]University of Melbourne, Melbourne, Victoria, [4]The University of Melbourne, Melbourne, Australia

Introduction: The necessity of the prefrontal cortex (PFC) in generating consciousness remains a mystery. To date, empirical support has been largely mixed, with two theoretical camps suggesting two distinct brain regions involved in conscious perception. One family of theories (frontal theories) argues the PFC is necessary in the generation of consciousness, while the other (sensory theories) proposes that consciousness is accounted for by activity in posterior regions. Additionally, these sensory theories argue that PFC activity observed during conscious conditions may be contaminated by artefacts related to reporting one's percept – such as cognitive processes related to task-relevant processing (Tsuchiya et al., 2015). Consciousness has typically been experimentally manipulated using various visual phenomena, such as inattentional blindness (IB). IB is a phenomenon in which a stimulus presented in plain sight fails to reach conscious perception in some participants (Mack, 2003). IB is a particularly useful paradigm for consciousness researchers as the information entering the visual system is kept constant across participants, yet the IB stimulus reaches awareness for some but remains subliminal for others. Thus, any differences in neural activity across aware and unaware groups in an IB experiment may be accounting for consciousness. Here, we re-analysed EEG data from a no-report inattentional blindness paradigm conducted by Shafto and Pitts (2015) to assess the role of the PFC in the conscious perception of faces.

Methods: As shown in Figure 1, the task was designed to systematically manipulate awareness and task-relevance of face stimuli. Each phase was the same, with the only difference being experimental instructions, and all 30 participants completed the same experiment. In order to adjudicate between these theories we used DCM, a technique which enables estimating the directed influence that a brain region has on another (David et al., 2005). DCM begins with an anatomically-informed generative model to simulate neural time series (EEG) data given some parameters (effective connectivity). Using a data-driven approach, we specified a neuronal network consisting of the left and right occipital, fusiform, and inferior frontal gyri. These regions were used as nodes in the DCM model and the model was fully connected at every level. A second-level parametric empirical Bayes model was conducted over the modulatory connection parameters of the DCMs (Friston et al., 2016). This allowed us to estimate how connectivity was modulated at the group level across the main effects of awareness and task-relevancy.

Results: As shown in Figure 2, connectivity increased from right fusiform to the right PFC and decreased from the left PFC to the left occipital ROIs as a function of awareness (posterior probability > 0.95). This is surprising on multiple grounds. Firstly, various sensory theories predict feedback connectivity would increase under awareness within higher and lower-sensory regions – however this was not observed. Secondly, though frontal theories predict the PFC would increase feedback connectivity to sensory areas, instead a decrease was observed. Moreover, in line with neither theory, an increase in connectivity was observed from the right fusiform to the right PFC. For the effect of task-relevancy, connectivity from the right fusiform to the right PFC decreased, while intrinsic connections to the right occipital, left PFC, and right PFC all increased. This was unexpected as both theories predict PFC connectivity to sensory regions should increase with task-relevancy.

Conclusions: While this study did not provide conclusive evidence to side with either family of theories, this study advances consciousness research forward toward establishing where the seat of consciousness lies in the brain. The PFC remains a critical point of contention among theories and establishing its role in conscious processing remains vital in isolating the neural basis of consciousness.

Figure 1

Shafto and Pitts (2015) Inattentional Blindness Task

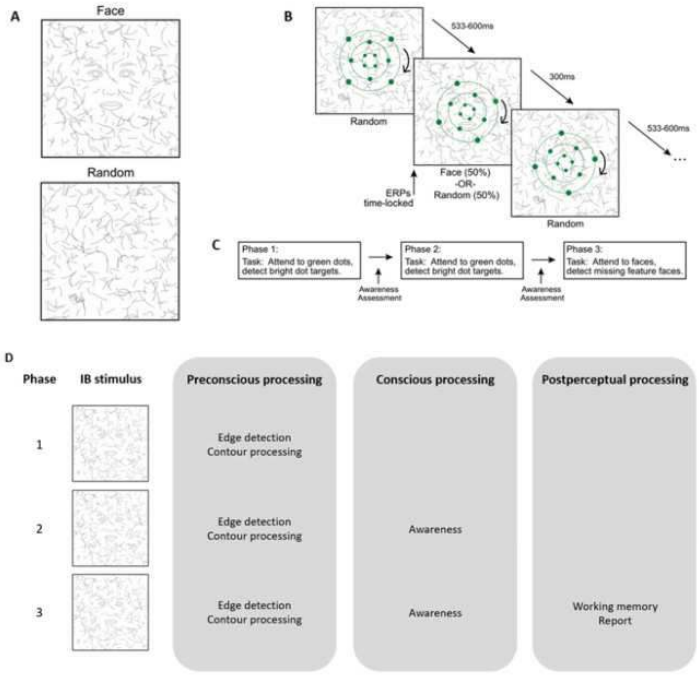

An overview of the experimental setup in Shafto and Pitts (2015) as well as the key manipulations. A): The two types of background stimuli presented to participants in this task. Here, the face is the critical inattentional blindness stimuli. B): In this task, participants are instructed to respond to either the green rings or the background lines. On occasion, the background lines will align to form a face – the critical IB stimulus. C): The three-phase design of the task, where task instructions are manipulated to isolate task-relevance from awareness. Crucially, all trials across phases are kept identical. In phase 1, participants are asked to attend to the green dots, where half the participants are inattentionally blind to the face and the other half are aware of the face. After surprise questioning, participants become aware of the face. Finally, in phase 3, participants are instructed to respond to the faces. D): Adapted from Pitts et al., 2014, this diagram shows the different levels of processing throughout the various phases of the task, assuming a participant is inattentionally blind.

Figure 2

Group Connectivity Modulation of DCMs for the Effects of Awareness and Task-relevance

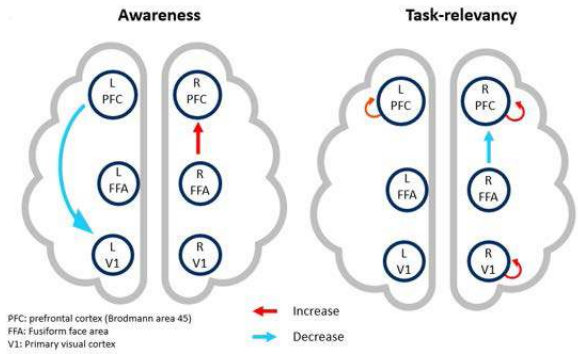

Results of the parametric empirical Bayes model on the first-order DCMs. The DCM models were fully connected, but here we show the connections which were modulated at the group level as a function of the main effects of awareness and task-relevance (with a posterior probability threshold of .95). Here, the left network shows the main effect of awareness across groups decreased connectivity between left PFC and left occipital ROIs, and increased connectivity from right fusiform to right PFC. The right network shows the main-effect of task-relevance, where connectivity from the right FFA to the right PFC decreased, while intrinsic connections to the right occipital, left PFC, and right PFC all increased. L and R refer to the left and right hemispheres; PFC: the prefrontal cortex node, here, Brodmann area 45 within the inferior frontal gyrus; FFA: fusiform face area; and V1: occipital area.

References
1. David, O. et al. (2005). Modelling event-related responses in the brain. NeuroImage, 25(3), 756–770. https://doi.org/10.1016/j.neuroimage.2004.12.030
2. Dehaene, S. et al. (2006). Conscious, preconscious, and subliminal processing: A testable taxonomy. Trends in Cognitive Sciences, 10(5), 204–211. https://doi.org/10.1016/j.tics.2006.03.007
3. Friston, K. J. et al. (2016). Bayesian model reduction and empirical Bayes for group (DCM) studies. NeuroImage, 128, 413-431.
4. Mack, A. (2003). Inattentional blindness: Looking without seeing. Current Directions in Psychological Science, 12(5), 180–184. https://doi.org/10.1111/1467-8721.01256
5. Pitts, M., Metzler, S., & Hillyard, S. (2014). Isolating neural correlates of conscious perception from neural correlates of reporting one's perception. Frontiers in Psychology, 5, 1078. https://doi.org/10.3389/fpsyg.2014.01078
6. Shafto, J. P. et al. (2015). Neural signatures of conscious face perception in an inattentional blindness paradigm. Journal of Neuroscience, 35(31), 10940–10948. https://doi.org/10.1523/JNEUROSCI.0145-15.2015
7. Tsuchiya, N. et al. (2015). No-report paradigms: Extracting the true neural correlates of consciousness. Trends in Cognitive Sciences, 19(12), 757–770. https://doi.org/10.1016/j.tics.2015.10.002

Poster No 2467

Consciousness and the Cerebellum

Yaron Caspi[1], Po-Jang Hsieh[1]

[1]Department of Psychology, National Taiwan University, Taipei, Taiwan

Introduction: Originally conceived as a purely motor-supporting structure of the brain, the scientific view regarding the cerebellum's function in non-motor-related processes underwent a revolution in the last two decades[1]. It is now recognized that the cerebellum contributes to multiple higher-order functions, ranging from language to social cognition[2]. Despite this development in understanding cerebellum functionality, discussions about the cerebellum concerning consciousness are rare. A prevalent view dominating the field of consciousness studies suggests that the cerebellum is dispensable for consciousness[3]. Yet, the discovery that the cerebellum participates in higher-order, non-motor-related functions, coupled with the accumulation of new data regarding its mode of operation, calls for a renewed analysis of the assumption that the cerebellum is dispensable for consciousness. In this abstract, we present such an analysis.

Methods: This work constitutes a literature review. We collected data from multiple published studies in brain research, forming a body of evidence regarding the relationships between the cerebellum and consciousness.

Results: The literature review identified several categories suggesting a role of the cerebellum in conscious experience. The well-known example is Cerebellar Cognitive Affective Syndrome, typically caused by insults to the posterior cerebellum[4]. Symptoms may include deficiencies in visuospatial cognition and emotion–affect. Some patients exhibit visuospatial disintegration (i.e., deficits in copying and conceptualizing drawn figures) and simultanagnosia (deficits in perceiving two objects simultaneously)[5], suggesting that the cerebellum can influence conscious experience. Another critical piece of evidence is the cerebellum's role in psychiatric conditions. For instance, the cerebellum was implicated in depression and remission from depression[6], as well as in autism[7], where structural cerebellar changes were found in individuals exhibiting such symptoms. Similarly, cerebellar gray matter volume was associated with symptoms of norm-violating behavior, psychosis, and anxiety among adolescents[8]. Additionally, numerous published pieces of evidence suggest cerebellum function in various conscious experiences, such as emotions, attention, hallucinations, pain, perception, sleep, and the sense of agency. These aspects will be discussed in this presentation.

Conclusions: Currently, no experiments aim to understand the cerebellum's role in conscious experience applied the gold standard paradigm for identifying the neural correlates of consciousness - namely, a comparison between conscious and unconscious experiences of similar stimuli. Therefore, one cannot definitively conclude such a role. However, this fact likely represents Cognitive Sciences cortical myopia[9] and an overemphasis on visual conscious perception[10]. In contrast, a plethora of circumstantial evidence suggests such a role. This work is a call for the scientific community to conduct experiments assessing this putative role, since such experiments can contribute intensively to our understanding of conscious experience. What can be concluded from such a review? We propose that, at least currently, the cerebellum can be conceived as a neural modulator of consciousness (NMC) - a part of a neuronal system that can modulate a conscious experience to produce a variation in some basic conscious experience. In other words, even if the conscious experience is the outcome of the brain activity of other parts of the brain, the conscious experience may be modulated by the coupling between the NMC and the parts of the brain representing the neural correlates of that conscious experience.

References
1. Zang Y, De Schutter E. (2023), 'Recent data on the cerebellum require new models and theories', Current Opinion in Neurobiology, vol. 82, pp. 102765

2. D'Angelo E. (2018) 'Physiology of the cerebellum', In: Manto M, Huisman TAGM, editors. Handbook of Clinical Neurology (The Cerebellum: From Embryology to Diagnostic Investigations; vol. 154), Elsevier, chapter 6, pp. 85–108,
3. Koch C. (2018) 'What Is Consciousness?', Nature, vol. 557, no. 7704, S8–12.
4. Argyropoulos GPD, van Dun K, Adamaszek M, Leggio M, Manto M, Masciullo M, et al. (2020), 'The Cerebellar Cognitive Affective/ Schmahmann Syndrome: a Task Force Paper', The Cerebellum, vol. 19, no. 1, 102–125
5. Schmahmann JD, Sherman JC (1998), 'The cerebellar cognitive affective syndrome', Brain, vol. 121, no. 4, pp. 561–579
6. Depping MS, Schmitgen MM, Kubera KM, Wolf RC (2018), 'Cerebellar Contributions to Major Depression', Frontiers in Psychiatry, vol. 9, pp. 00634
7. Mapelli L, Soda T, D'Angelo E, Prestori F (2022), 'The Cerebellar Involvement in Autism Spectrum Disorders: From the Social Brain to Mouse Models', International Journal of Molecular Sciences, vol. 23, no. 7, pp. 3894
8. Moberget T, Alnæs D, Kaufmann T, Doan NT, Córdova-Palomera A, Norbom LB, et al. (2019), 'Cerebellar Gray Matter Volume Is Associated With Cognitive Function and Psychopathology in Adolescence' Biological Psychiatry, vol. 86, no. 1, 65–75
9. Parvizi J (2019), 'Corticocentric myopia: old bias in new cognitive sciences', Trends in Cognitive Sciences, vol. 13, no. 8, 354–359
10. Faivre N, Arzi A, Lunghi C, Salomon R (2017), 'Consciousness is more than meets the eye: a call for a multisensory study of subjective experience', Neuroscience of Consciousness, vol. 2017, no. 1, pp. nix003

Poster No 2468

Phase of pupillary unrest corresponds with perceptual sensitivity, MEG, and whole brain fMRI signals

Victoria Gobo[1], Javier Gonzalez-Castillo[1], Joshua Teves[1], Micah Holness[1], Peter Bandettini[1], Sharif Kronemer[1]

[1]National Institute of Mental Health, Bethesda, MD

Introduction: Perceptual sensitivity – the likelihood of perceiving a sensory event – is closely linked to arousal state that is regulated by neuromodulatory activity from the thalamus and brainstem (Setzer, B. et al. 2022). A practical challenge is that these subcortical, arousal network foci are difficult to record from in humans. Therefore, an accessible, proxy measure of arousal would have numerous clinical and experimental benefits. One possible candidate is the spontaneous fluctuations in pupil size – pupillary unrest – independent of light stimulation. Previous research finds that changes in pupil size correspond to widespread subcortical and cortical activity across species (e.g., Bradshaw, J. 1967; Kronemer et al. 2022). To evaluate the relationship between the phase of pupillary unrest and perception sensitivity and brain activity, we aimed to: (1) examine how perceptual sensitivity changes are linked with the phase of pupillary unrest and (2) track and map the brain activity associated with the phase of pupillary unrest.

Methods: Healthy, adult participants (N = 4; Target N = 35) completed closed-loop auditory and visual perception tasks coupled with concurrent pupillometry (EyeLink 1000 Plus; SR Research, Inc.) and magnetoencephalography (MEG; 275-channel system; CTF Systems, Inc., Canada). The perception tasks involved a novel algorithm that detected four pupil phase events in real time: (1) local minima (troughs), (2) local maxima (peaks), (3) dilation, and (4) constriction periods. When a pupil phase event was detected, a near-perceptual threshold auditory tone was played in the left or right ear (auditory paradigm) or a near-perceptual threshold image was shown on the left or right side of the screen (visual paradigm). The participants were prompted to respond with a button press if they perceived the stimuli and indicate its location (either ear or screen side). In addition, a pupil phase independent stimulus condition presented stimuli at random, which served as a control. To map the brain networks linked with pupil phase, including subcortical regions inaccessible with MEG we analyzed a large (N > 100) healthy, adult human resting state fMRI dataset with concurrent pupillometry (7T; Human Connectome Project [HCP]). HCP pupillometry timecourses were analyzed retroactively to detect the pupil phase events. The whole brain fMRI signal preceding and following the pupil phase events were examined.

Results: Preliminary results demonstrate that the phase of pupillary unrest predicts perceptual sensitivity in audition and vision: decreased perception rate relative to baseline (i.e., random condition) perceptual sensitivity during constriction pupil phases (Figure 1). This result corresponds with MEG findings that show field potential divergences preceding pupil phase events. Particularly, field potential increases in parietal-occipital areas of the scalp are associated with pupil dilation and decreases with pupil constriction (Figure 2A). Finally, fMRI signals suggest that the areas most correlated with pupil phase are among sensory and arousal networks sites, including primary visual cortex and thalamus (Figure 2B).

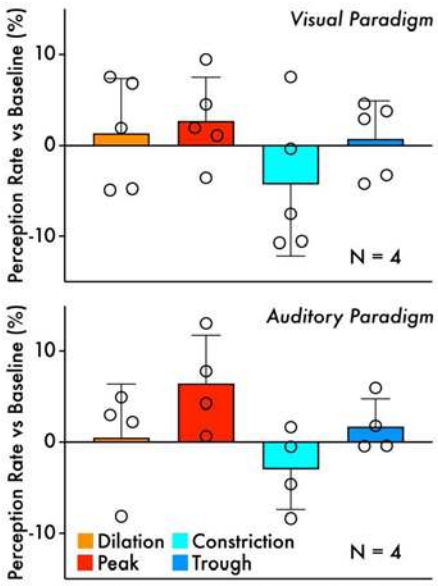

Figure 1. Pupil phase perception rate versus baseline perception rate (%) for visual (Visual Paradigm) and auditory (Auditory Paradigm) stimuli.

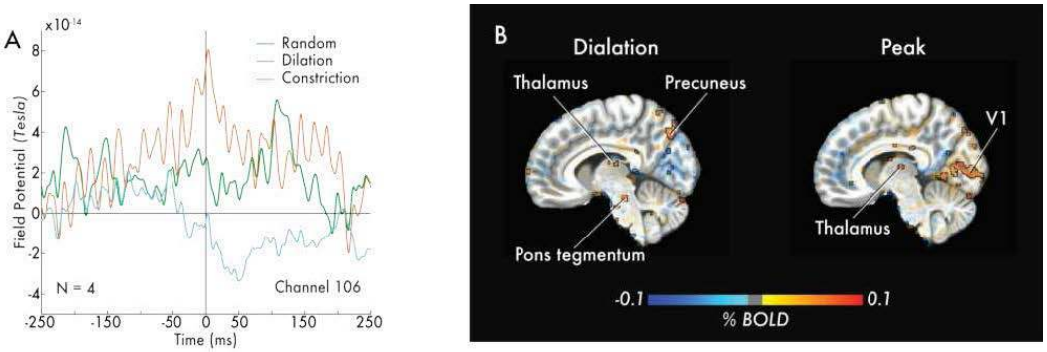

Figure 2. **A**) Single channel MEG field potential timecourses for the dilation and constriction pupil phase events versus the random (pupil phase independent) condition in the visual task. Field potentials were averaged across subjects per condition. Channel 106 was chosen for its location in the upper occipital parietal region. **B**) Uncorrected fMRI signals for dilation and peak (local maximum) pupil phases at 5 seconds prior to the event. Voxels above 0.05% BOLD threshold are shown with a black outline, all other activations are shown as transparent.

Conclusions: The phase of pupillary unrest may offer a real time readout of arousal state that previous research finds linked with behavior, cognition, and perception. Preliminary results demonstrate that pupil phase predicts perceptual sensitivity for auditory and visual stimuli. These perception state changes can be linked with field potentials in parietal-occipital scalp areas. In addition, fMRI signal divergences in sensory and arousal networks were observed according to the pupil phase. These results have the potential to elucidate the timecourse and neural origin of conscious state in healthy neurophysiology.

References

1. Bradshaw, J. (1967) 'Pupil Size as a Measure of Arousal during Information Processing', Nature, vol. 216, pp. 515-516
2. Kronemer, S.I., et al. (2022) 'Human Visual Consciousness involves large scale cortical and subcortical networks independent of task report and eye movement activity.' Nature Communication, vol. 13, 7342
3. Setzer, B., Fultz, N.E., Gomez, D.E.P. et al. (2022), 'A temporal sequence of thalamic activity unfolds at transitions in behavioral arousal state.', Nature Communications vol. 13, 5442 (2022).

Poster No 2469

A Spike in Entropy Precedes the Mismatch Negativity; Linking Entropy and Prediction Error

Michael Angyus[1], Fernando Rosas[2], Pedro Mediano[2], Robin Carhart-Harris[3]

[1]Imperial College London, Portland, OR, [2]Imperial College London, London, London, [3]Department of Neurology, Neuroscape, University of California, San Francisco, San Francisco, CA

Introduction: Karl Friston's free energy principle and predictive coding frame the brain as a hierarchically structured prediction machine that is iteratively testing neural models to achieve the most energy efficient arrangement of neural activity for

survival. One potential indicator of the inefficiency of neural activity is the information theoretical quantification of entropy. Entropy has become an umbrella term for several different approaches to analyzing neural activity, not all of which are as interchangeable as the terminology from statistical mechanics would suggest. Lempel-Ziv complexity (LZC) has been used to reliably distinguish between conscious states using brain imaging data from electroencephalography (EEG). At its information theoretical basis, LZC is an estimator of Shannon's entropy rate, which is a measure of predictability or surprise. Additionally, a corollary of the entropic brain hypothesis is that the unpredictability of neural activity is reflective of the brains inability to predict — and therefore suppress — bottom-up stimuli. This leads to the following conjecture: that an increase in 'richness' of conscious content is at least partly facilitated by a disruption in the prediction updating systems at the sensory level. While LZC has been used to examine global states of consciousness, it is still unknown whether increases in conscious activity of awake states are related to brain wide entropy increases of model prediction error.

Methods: This conjecture could be tested using the mismatch negativity (MMN) paradigm, which has been used to investigate model updating in the auditory system via an event related potential associated with a mismatch between expectation and stimuli. To our knowledge, research has not attempted to directly relate any measures of entropy to this neural adaptation process. A recently developed algorithm for estimating signal complexity via state space entropy rate (CSER) allows for entropy measurements at a high enough temporal resolution for the analysis of event related EEG data, enabling us to test the hypothesis that prediction error has an associated spike in complexity that is resolved by updating the predictive model.

Results: Our analyses reveal a significant spike in entropy occurring prior to the onset of the MMN, providing a first direct link between computational prediction error and neural activity associated with prediction error. Mixed effects regression revealed that the magnitude of this entropy spike was associated with strength of the MMN (Adjusted R2 = 0.385, ß = 0.012, $p < 0.001$). Mixed effects regression was also used to see if baseline entropy (prior to a given trial) was related to MMN magnitude, finding a significant positive relationship (Adjusted R2 = 0.239, ß = 0.023, $p < 0.001$).

Conclusions: The association between entropy and prediction error suggests brain entropy as a potential biomarker of the inability to suppress incoming stimuli. This examination of a low-level sensory model updating process provides first of its kind evidence for the interpretation of global entropy increases as a summation of various changing models across the brain. These results suggest that entropy is increased during the model updating process, providing support for predictive coding and the free energy principle.

References

1. Carhart-Harris, R. L., & Friston, K. J. (2019). REBUS and the Anarchic Brain: Toward a Unified Model of the Brain Action of Psychedelics. Pharmacological Reviews, 71(3), 316–344. https://doi.org/10.1124/pr.118.017160
2. Mediano, P. A. M., Rosas, F. E., Luppi, A. I., Noreika, V., Seth, A. K., Carhart-Harris, R. L., Barnett, L., & Bor, D. (2023). Spectrally and temporally resolved estimation of neural signal diversity (p. 2023.03.30.534922). bioRxiv. https://doi.org/10.1101/2023.03.30.534922
3. Spriggs, M. (2018). Electrophysiological Markers of Sensory Plasticity and Connectomics in Ageing and Mild Cognitive Impairment [Thesis, ResearchSpace@Auckland]. https://researchspace.auckland.ac.nz/handle/2292/47524

Poster No 2470

Frontoparietal contribution for conscious visual representations and related perceptual confidence

J. Amaro-Fuenzalida[1,2], Tomás Ossandón Valdés[3,4], Aurelio Cortese[5], Ranganatha Sitaram[6]

[1]Centro Interdisciplinario de Neurociencia, Pontificia Universidad Católica de Chile, Medicina, Santiago de Chile, Chile, [2]Neurodynamic of Cognition Laboratory, Departamento de Psiquiatría, Pontificia Universidad Católica de Chile, Santiago, Chile, [3]Neurodynamic of Cognition Laboratory, Departamento de Psiquiatría, Pontificia Universidad Católica d, Santiago de Chile, Chile, [4]Centro Interdisciplinario de Neurociencia, Pontificia Universidad Católica de Chile, Medicina, Santiago, Chile, [5]Department of Decoded Neurofeedback, ATR Computational Neuroscience Laboratories, Kyoto, Japan, [6]St. Jude Children's Research Hospital, Memphis, TN

Introduction: Consciousness as content refers to the experience of objects, commonly known as awareness (Searle, 2007). The Global Neuronal Workspace Model (GNWM) suggests that perceptual awareness relies on the activation of the fronto-parietal network (Mashour, 2020). Evidence indicates a frontal contribution to the awareness process when subjects report their experiences (Del Cul, 2007). However, GNWM does not explain how conscious contents are represented but focuses on the mechanisms required to access them. Theories like High Order Theory (HOT) address representation, proposing frontal meta-representation of posterior activity (Mashour, 2020). fMRI and neurofeedback experiments suggest perceptual content representations associate with posterior regions (Amano, 2017; Shibata, 2011). It remains unclear whether the representation of perceptual content is directly linked to frontal regions per se, even when reporting is necessary. Multi-Voxel Pattern Analysis techniques have identified that perceptual confidence can be decoded in frontal regions (Cortese, 2017) but objective

properties of stimuli seem linked to posterior regions. This research aims to determine the frontoparietal contribution to conscious visual representations and its connection with perceptual confidence.

Methods: fMRI data from 26 participants performing the Shadlen Random Dot Motion task (Cortese, 2017) were collected. We presented a set of random dots on a screen with a percentage of dots moving in a specific direction (coherence). We asked our participants to identify movement direction (objective rating) and perceptual confidence (subjective rating). Each participant underwent at least 160 trials. Each stimulus was calibrated under coherence threshold estimated for each participant by Quest Psychtoolbox function. Trials comprised Direction, Coherence, Score, and Confidence. Two fMRI analyses were conducted: I. ROI analysis, subtracting estimated beta values for dichotomic conditions (e.g. below or above threshold). II. Multi-Voxel Pattern Analysis, decoding brain activity with a Searchlight approach through The Decoding Toolbox, comparing voxel accuracy between lobes using the Desikan-Killany-Tourville atlas (Hatamimajoumerd, 2022). Data collection and sharing for this project was provided by the DecNef Department at the Advanced Telecommunication Research Institute International, Kyoto, Japan. FONDECYT regular 1230383

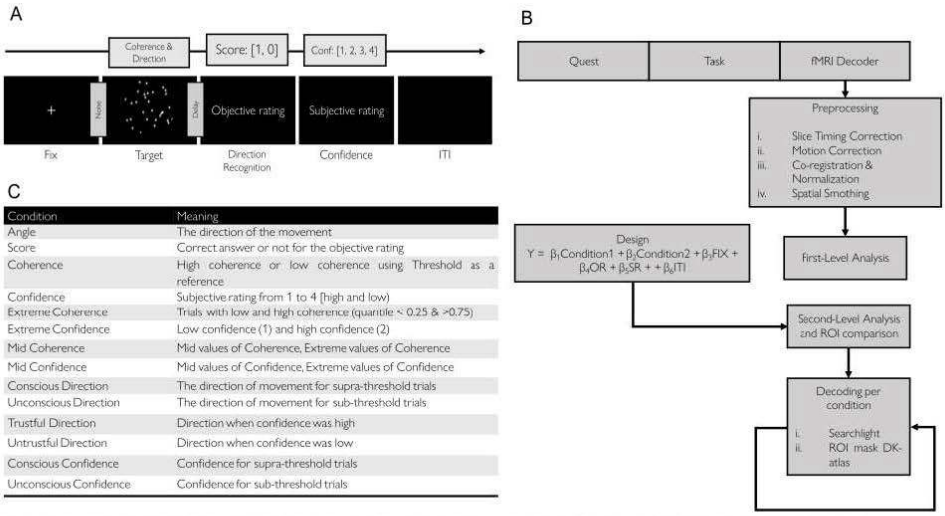

C

Condition	Meaning
Angle	The direction of the movement
Score	Correct answer or not for the objective rating
Coherence	High coherence or low coherence using Threshold as a reference
Confidence	Subjective rating from 1 to 4 (high and low)
Extreme Coherence	Trials with low and high coherence (quantile < 0.25 & >0.75)
Extreme Confidence	Low confidence (1) and high confidence (2)
Mid Coherence	Mid values of Coherence, Extreme values of Coherence
Mid Confidence	Mid values of Confidence, Extreme values of Confidence
Conscious Direction	The direction of movement for supra-threshold trials
Unconscious Direction	The direction of movement for sub-threshold trials
Trustful Direction	Direction when confidence was high
Untrustful Direction	Direction when confidence was low
Conscious Confidence	Confidence for supra-threshold trials
Unconscious Confidence	Confidence for sub-threshold trials

Figure 1. A: Shadlen Random Dot Motion task. After stimuli are presented in a certain direction and coherence, Objective and Subjective Ratings are evaluated. B. Data Analysis Steps: Following the task, an fMRI Decoder is developed. Preprocessing steps are listed, followed by ROI and MVPA (Searchlight followed by atlas masking). C. List of variables included in ROI analysis and MVPA during Second-Level Analysis.

Results: ROI analysis revealed significant differences in beta ROI activity between stimuli with 25% and 75% coherence as a function of topography ($p < 0.05$). The difference between frontal and posterior activity under low and high coherence was significantly higher. The left hemisphere also showed significant differences. Right hemisphere differences were observed between ROIs for conscious and nonconscious conditions ($p=0.0257$, $p=0.012$). The most accurate ROI for decoding movement direction below the awareness threshold included frontal regions. Significant differences in right hemisphere accuracy were observed in unconscious direction trials ($p=0.023$), while the left hemisphere showed differences between ROI accuracy for Score and Confidence.

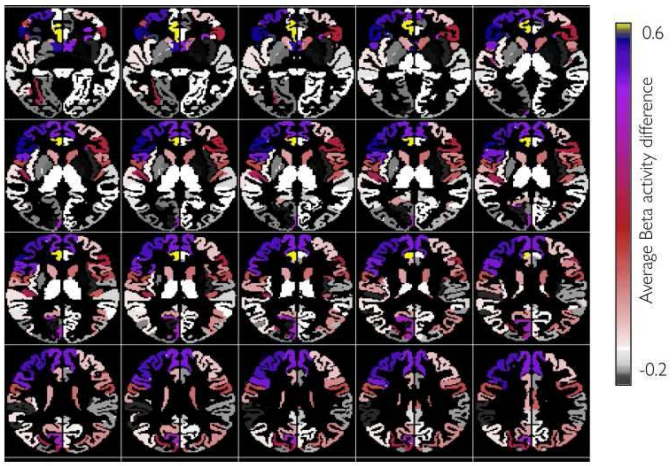

Figure 2. Average difference in beta activity for ROI when comparing activity in response to stimuli with 75% higher coherence and 25% lower coherence. The yellow area represents the region of interest where cortical activity is more activated in response to low coherence, while in gray, regions are highlighted that would be more activated in response to high coherence.

Conclusions: We expected to find high contribution when participants were aware of stimuli properties, while results suggest frontal region contribution, especially under low signal strength (low coherence). Decoding movement direction below the consciousness threshold highlighted the ventro-medial prefrontal cortex (vmPFC) significant contribution. This suggests frontal activity in perceptual tasks relates to working memory, acting as a memory buffer under conditions requiring more time for representation. This has been observed through no-report paradigm (Hatamimajoumerd, 2022). It is also possible that conscious experience about complex stimuli may be internally driven by priors (LeDoux & Lau, 2020) or imagination when stimuli is not strong enough to surpass subjective thresholds (Dijkstra & Fleming, 2023).

References

1. Amano, K., Shibata, K., Kawato, M., Sasaki, Y., & Watanabe, T. (2016). 'Learning to Associate Orientation with Color in Early Visual Areas by Associative Decoded fMRI Neurofeedback'. Curr Biol, 26(14), 1861-1866. doi:10.1016/j.cub.2016.05.014
2. Cortese, A., Amano, K., Koizumi, A., Lau, H., & Kawato, M. (2017). 'Decoded fMRI neurofeedback can induce bidirectional confidence changes within single participants'. Neuroimage, 149, 323-337. doi:10.1016/j.neuroimage.2017.01.069
3. Del Cul, A., Baillet, S., & Dehaene, S. (2007). 'Brain dynamics underlying the nonlinear threshold for access to consciousness'. PLoS biology, 5(10), e260.
4. Dijkstra, N., & Fleming, S. M. (2023). 'Subjective signal strength distinguishes reality from imagination'. Nature Communications, 14(1), 1627.
5. Hatamimajoumerd, E., Murty, N. A. R., Pitts, M., & Cohen, M. A. (2022). 'Decoding perceptual awareness across the brain with a no-report fMRI masking paradigm'. Current Biology, 32(19), 4139-4149.
6. LeDoux, J. E., & Lau, H. (2020). 'Seeing consciousness through the lens of memory'. Current Biology, 30(18), R1018-R1022.
7. Mashour, G. A., Roelfsema, P., Changeux, J. P., & Dehaene, S. (2020). 'Conscious processing and the global neuronal workspace hypothesis'. Neuron, 105(5), 776-798.
8. Searle, J. R. (2007). 'Dualism revisited'. Journal of Physiology-Paris, 101(4-6), 169-178.
9. Shibata, K., Watanabe, T., Sasaki, Y., & Kawato, M. (2011). 'Perceptual learning incepted by decoded fMRI neurofeedback without stimulus presentation'. Science, 334(6061), 1413-1415. doi:10.1126/science.1212003

Poster No 2471

Unveiling the Role of Thalamic Core-Matrix Functional Architecture in Loss of Consciousness

Zirui Huang[1], George Mashour[1], Anthony Hudetz[1]

[1]*University of Michigan, Ann Arbor, MI*

Introduction: Human neuroimaging data and biophysical modeling simulations suggest that loss of consciousness during general anesthesia is attributed to a targeted suppression of nonspecific, higher order thalamocortical connectivity (Liu et al., 2013; Munn et al., 2023). However, previous research predominantly examined the thalamus as a whole or concentrated on specific subregions, neglecting the identity of distinct neuronal subpopulations. The thalamus, characterized by a heterogeneous cytoarchitecture, comprises at least two discernible cell classes known as core and matrix cells, each sending distinct projections to the cortex. Given the widespread distribution of core and matrix cells throughout the thalamus from lower-order and higher-order nuclei, a comprehensive exploration of the spatial distribution of thalamocortical connectivity with a specific emphasis on the core-matrix architecture is justified. We hypothesized that loss of consciousness due to anesthesia would be associated with a disruption of core–matrix functional architecture of thalamocortical connectivity.

Methods: We performed functional magnetic resonance imaging (fMRI) investigation in twenty-seven healthy volunteers under conscious baseline, deep sedation, and the subsequent recovery phase. Deep sedation was achieved through a gradual increase of the effect site concentration of the anesthetic propofol until behavioral responsiveness was lost. We advanced the functional gradient mapping method (Margulies et al., 2016) to map the functional geometry of thalamocortical circuits by aligning it with the unimodal-transmodal functional axis of the cortex. First, we utilized cortical gradient mapping to transform the functional brain connectome into a non-linear diffusion space. Second, we examined the thalamic correlates of the unimodal-transmodal cortical gradient. We computed pair-wise correlations between the thalamocortical connectivity values of each thalamic voxel and the cortical gradient values, ultimately generating a topographical map of thalamocortical correlation coefficients. This map highlighted the correlations with the principal cortical gradient and was referred to as the gradient correlation coefficient (GCC). To determine the relative contributions of core and matrix cells in explaining the variations in GCC between conscious and unconscious states, we conducted a multiple regression analysis within a general linear model framework. In this analysis, we integrated the spatial densities of two calcium-binding proteins, Calbindin (abundant in matrix cells) and Parvalbumin (prevalent in core cells), provided by the Allen Human Brain Atlas (Hawrylycz et al., 2012; Müller et al., 2020), as covariates while considering the GCC difference between conscious and unconscious states as the dependent variable.

Results: We found that unconsciousness was associated with specific alterations in a functional hierarchy within thalamocortical circuits. Namely, there was a shift from a balanced unimodal-transmodal geometry during consciousness to a dominantly unimodal geometry during unconsciousness. This shift in functional geometry was depended on the spatial distribution of matrix cells within the thalamus. Specifically, thalamic regions with a high density of matrix cells exhibited a pronounced reduction in transmodal thalamocortical functional connectivity during unconsciousness.

Conclusions: Propofol-induced loss of consciousness is accompanied by a shift from balanced core–matrix functional geometry to unimodal core dominance. By synthesizing cellular-level data with systems-level findings, our research illuminates the pivotal role of thalamic matrix cells in understanding the neural mechanisms of states of consciousness.

References

1. Hawrylycz, M. J., et al. (2012), 'An anatomically comprehensive atlas of the adult human brain transcriptome', Nature, vol. 489, pp. 391-399.
2. Liu, X., et al. (2013), 'Differential effects of deep sedation with propofol on the specific and nonspecific thalamocortical systems', Anesthesiology, vol. 118, pp. 59-69.
3. Margulies, D. S., et al. (2016), 'Situating the default-mode network along a principal gradient of macroscale cortical organization', Proceedings of the National Academy of Sciences, vol. 113, pp. 12574-12579.
4. Munn, B. R., et al. (2023), 'A thalamocortical substrate for integrated information via critical synchronous bursting', Proceedings of the National Academy of Sciences, vol. 120, e2308670120.
5. Müller, E. J., et al. (2020), 'Core and matrix thalamic sub-populations relate to spatiotemporal cortical connectivity gradients', Neuroimage, vol. 222, 117224.

Poster No 2472

Changes in core structures of the network during propofol-induced unconsciousness using human iEEG

Mikyung Choe[1], Seung-Hyun Jin[1], Hyejin Kang[2], Dong Soo Lee[3,4], Seokhyun Lee[5], Chun Kee Chung[1,6]

[1]Neuroscience Research Institute, Seoul National University College of Medicine, Seoul, Korea, Republic of, [2]Biomedical Research Institute, Seoul National University Hospital, Seoul, Korea, Republic of, [3]Medical Research Center, Seoul National University, Seoul, Korea, Republic of, [4]School of Convergence Science and Technology, Pohang University of Science and Technology, Pohang, Korea, Republic of, [5]School of Psychology, Korea University, Seoul, Korea, Republic of, [6]Department of Neurosurgery, Seoul National University Hospital, Seoul, Korea, Republic of

Introduction: Consciousness is maintained through communication in the brain network. Hence, its characteristics should change as consciousness declines. k-core percolation could reveal the hierarchical structure of the brain network, with identifying the core structure by eliminating peripheral structures. The kmax-core of the network represents the pivotal hub of the networks with the densest connection. The kmax-core that is dominant in the parietooccipital area during the conscious state would change during the unconscious state accompanied by changes in the interaction strength. In the present study, we investigated changes in the core structure of the brain network during the propofol-induced anesthesia using k-core percolation with human intracranial electroencephalography (iEEG).

Methods: We recruited 6 patients diagnosed with medically intractable epilepsy (2 males and 4 females; age: mean = 30.5, SD = 6.8 years; 6 left hemispheres). In the conscious state, iEEG data was acquired in either the ward or operating room with subjects' eyes closed, and without any external stimuli. For the unconscious state, iEEG data was recorded after the subjects lost the ability to respond to verbal commands under general anesthesia, with target-controlled infusion of propofol and remifentanil (propofol concentration: mean = 4.08 μg/ml, SD = 0.34 μg/ml; remifentanil concentration: mean = 3.28 ng/ml, SD = 0.78 ng/ml). The average recording time for both conscious and unconscious states was 237.4 sec (standard deviation, 32.2 sec). Segmentation of iEEG data during conscious and unconscious states was performed into 12-sec epochs with a 50% overlap. We estimated functional connectivity using amplitude envelope correlation (AEC) and weighted phase lag index (wPLI). We calculated the functional connectivity matrix of each frequency band (delta: 1–3 Hz, theta: 4–7 Hz, alpha: 8–12 Hz, beta: 13–30 Hz, low gamma: 30–90 Hz, high gamma: 90–140 Hz). The adjacency matrix was constructed using a 40% threshold. We estimated k-max core structures and the number of nodes of k-max core structures. We investigated the number of nodes in cortical regions of k-maximum core structures between conscious and unconscious states ($p < 0.05/5$, with the Generalized Estimating Equation).

Results: In comparison to the conscious state, the number of k-max core nodes decreased in anterior regions, including frontal and sensorimotor regions, while it increased in the occipital regions during the propofol-induced unconscious state. No significant changes were observed in the number of k-max core nodes in the temporal and parietal regions.

Conclusions: k-core percolation revealed that the propofol-induced unconsciousness was accompanied with the reconstruction of core structure in the brain network, characterized by increased coreness in posterior regions and decreased coreness in anterior regions.

References

1. Jin, S. H. and C. K. Chung (2012). "Messages from the brain connectivity regarding neural correlates of consciousness." Exp Neurobiol 21(3): 113-122.
2. Lawn, T., D. Martins, O. O'Daly, S. Williams, M. Howard and O. Dipasquale (2023). "The effects of propofol anaesthesia on molecular-enriched networks during resting-state and naturalistic listening." NeuroImage 271: 120018.
3. Purdon, P. L., A. Sampson, K. J. Pavone and E. N. Brown (2015). "Clinical Electroencephalography for Anesthesiologists: Part I: Background and Basic Signatures." Anesthesiology 123(4): 937-960.
4. Stanford, W. C., P. J. Mucha and E. Dayan (2022). "A robust core architecture of functional brain networks supports topological resilience and cognitive performance in middle- and old-aged adults." Proceedings of the National Academy of Sciences 119(44): e2203682119.
5. Tononi, G. (2004). "An information integration theory of consciousness." BMC Neurosci 5: 42.
6. Whi, W., Y. Huh, S. Ha, H. Lee, H. Kang and D. S. Lee (2022). "Characteristic functional cores revealed by hyperbolic disc embedding and k-core percolation on resting-state fMRI." Scientific Reports 12(1): 4887.

Poster No 2473

Hedonia as a state of enhanced information integration: Illuminating ketamine's pro-hedonic effects

Maximilian Kathofer[1], Marie Spies[2], Pedro Mediano[3], Benjamin Eggerstorfer[2], Gregor Dörl[2], David Gomola[2], Christina Bieglmayer[1], Peter Stöhrmann[2], Julia Payer[1], Manfred Klöbl[2], Simon Mehler[1], Clemens Schmidt[2], Hanna Scharler[1], Gabriel Schlosser[2], Alexandra Mayerweg[2], Nina Granabetter[1], Lukas Artmeier[2], Benedikt Schmidt[1], Elisa Briem[2], Helmut Leder[1], Rupert Lanzenberger[2], Julia Crone[1,4]

[1]University Of Vienna, Vienna, Austria, [2]Medical University of Vienna, Vienna, Austria, [3]Imperial College London, London, United Kingdom, [4]University of California Los Angeles, Los Angeles, CA

Introduction: Originally devised as a potent anesthetic, subanesthetic doses of ketamine induce an altered state of consciousness and increase complex brain network dynamics[1]. This surge in network dynamics is thought to reflect ketamine's neuroplastic properties, ultimately enabling the brain to explore a broader range of possible states, and thus, increasing the integration of new information[2,3]. Leveraging recent advancements in information theory, we employ partial information decomposition (PID) to uncover higher-order dependencies that common bivariate approaches fail to uncover. By disentangling the observed neuronal information into redundant and synergistic parts, of which the latter serves as a measure of information integration, PID enables the detection of these higher-order dependencies across brain regions[4]. The still poorly understood rapid-acting, pro-hedonic properties of ketamine might be linked to its modulation of precisely these higher-order dependencies, reflecting a breakup of engrained connections inducing increased information integration. This seems convincing, as hedonic experiences – a product of various concurrent cognitive and affective processes - are themselves states of enhanced integration[5,6].

Methods: We use ketamine to alter hedonic experiences in response to music in 31 neurotypical subjects. The full within-subject design consists of 4 sessions; baseline, two treatment sessions (ketamine and placebo) counterbalanced across subjects, and a follow-up session. To assess the subacute state in which the beneficial effects start to emerge, participants complete a battery of standardized assessment scales (e.g., 5-Dimensional Altered States of Consciousness and Dimensional Anhedonia Rating Scale) as well as a resting-state scan and an aesthetic task using fMRI four hours after administration. The aesthetic task consists of self-selected highly moving and neutral music to examine ketamine's effect on the hedonic tone. Participants rate the induced experiences based on 3 dimensions: aesthetically moving, aesthetic chills, and valence. For the resting-state data, a linear mixed-effects model (LME) was implemented to evaluate whether ketamine increases synergistic information processing with the within-subjects factors of Treatment (ketamine & placebo) and Timepoint (treatment session 1 & 2). To probe whether altered synergistic information processing is associated with ketamine administration and peak hedonic experiences, we used the aesthetic task data and implemented a LME model with the factors of Hedonic Experience (high & low), Treatment (ketamine & placebo) and Timepoint (treatment session 1 & 2). Preliminary data of 9 participants is presented.

Results: The preliminary results of the resting state data show a main effect of Treatment, indicating that ketamine increases synergistic information processing compared to placebo (beta = 3.89, t(14) = 2.35, p = 0.047). Furthermore, the analysis of the aesthetic task data, revealed a main effect of Hedonic Experience, indicating that low hedonic experiences are associated with decreased synergistic processing compared to high hedonic experiences (beta = -32.26, t(24) = -2.35, p = 0.027). No main effect of Treatment was observed during the aesthetic task (beta = -4.41, t(24) = -0.32, p = 0.750).

Conclusions: In line with our hypothesis, we found an association between high hedonic experiences and increased information integration. In the resting state, ketamine – which is known to enhance neuroplasticity – also increased information integration. Interestingly, this effect was not evident during the presentation of moving and neutral music. However, in light of the limited power of this sample, we refrain from speculating about the meaning of this null result until the complete sample has been analyzed. Taken together, the present study poses an important contribution to the understanding of the intricate role of enhanced information integration for the emergence of hedonic experiences.

References

1. Schartner, M.M. (2017), 'Increased spontaneous MEG signal diversity for psychoactive doses of ketamine, LSD and psilocybin', Scientific Reports, 7(1), 46421
2. Aleksandrova, L. R., (2021), 'Neuroplasticity as a convergent mechanism of ketamine and classical psychedelics', Trends in pharmacological sciences, 42(11), pp. 929-942
3. Rubinov, M., (2010), 'Complex network measures of brain connectivity: uses and interpretations', Neuroimage, 52(3), pp.1059-1069
4. Luppi, A. I., (2022), 'A synergistic core for human brain evolution and cognition', Nature Neuroscience, 25(6), pp. 771-782
5. Kringelbach, M. L. (2005), 'The human orbitofrontal cortex: linking reward to hedonic experience', Nature Reviews Neuroscience, 6(9), pp. 691-702
6. Brattico, E., (2013), 'Toward a neural chronometry for the aesthetic experience of music', Frontiers in Psychology, 4, 206

Poster No 2474

Correlates of connected consciousness assessed by the isolated forearm technique during anaesthesia

Naji Alnagger[1], Javier Montupil[2], Paolo Cardone[2], Charlotte Martial[3], Jitka Annen[2], Olivia Gosseries[2], Aline Defresne[2], Arthur Bonnhomme[2], Atakan Şelte[4], Robert Sanders[5], Vincent Bonhomme[2], Coraline Mozin[2], Marie Miegebielle[2]

[1]University of Liège, Liège, Liège, [2]University of Liège, Liège, Liege, [3]University of Liège, Liège, Belgium, [4]University of Wisconsin-Madison, Madison, WI, [5]University of Sydney, Sydney, Sydney

Introduction: Connected consciousness (CC) is defined as the awareness of one's environment[1]. During general anaesthesia, around 5% of patients experience CC after a noxious stimulus[2]. The isolated forearm technique (IFT) consists of inflating a tourniquet on the arm before the injection of a neuromuscular blocker to allow voluntary hand movements. Those who responded to command via hand squeezing were deemed responders, thus demonstrating CC. Using fMRI, we aimed to identify the correlates of CC in responders during anaesthesia.

Methods: Using the IFT, 26 healthy volunteers were placed under general anaesthesia using remifentanil [constant 1 ng.mL-1 concentration] and propofol [stepwise increase until loss of responsiveness; 5.36(0.78)µg.mL-1] target-controlled infusions, and rocuronium [0.6 mg.Kg-1 single bolus after tourniquet inflation]. After laryngeal mask insertion, propofol was decreased following an up-and-down protocol in accordance with the previous volunteer 1.85(1.17)µg/ml. A noxious electrical stimulation prior to posing closed questions probed responsiveness, yielding 10 responders and 16 non responders. Resting state fMRI sequences were acquired in four conditions: awake (R1), unresponsiveness in all subjects (R2), after noxious stimulation (R3) and recovery (R4). We used meta-analytically derived maps from neurosynth.org to define a set of seven canonical resting-state networks (RSNs): default mode network (DMN), executive control network (ECN), thalamus (THAL), hippocampus (HPC), visual (VIS), and sensorimotor (SM), auditory (AUD) followed by a "dual regression" approach. Network integrity was assessed by mean parameter estimates (PE) for each network from the second stage of the dual regression. The time series from the first step of the dual regression were entered into a general linear model producing PE values representing strength of connectivity between pairs of RSNs. Both within and between network results were entered into a linear mixed-effects model which model incorporated session and group (responder vs. non-responder) as fixed effects, and subject as a random effect in addition to assessing interaction effects between session and group, and further pairwise comparisons between groups within session. Results were considered significant at $p<0.05$ (FDR corrected).

Results: In all subjects, several networks showed increased integrity during R2, including SM, AUD, THAL, and VIS. Whilst at R3, only SM showed increased integrity compared to R1. HPC, DMN and ECN showed no significant effect of session across all sessions. There was a significant interaction effect between group and R2 whereby responders show a stronger integrity compared with non-responders in THAL and VIS. There was also a significant interaction effect between group and R3 in AUD as non-responders had higher integrity than non-responders (Figure 1). Pairwise comparisons at R3 showed increases in connectivity between the thalamus and DMN in responders, whilst a decrease in connectivity between the thalamus and ECN, in addition to increased connectivity in responders between HPC and DMN compared to non-responders. There was also a significant interaction effect between group and R3 with SM and AUD (Figure 2).

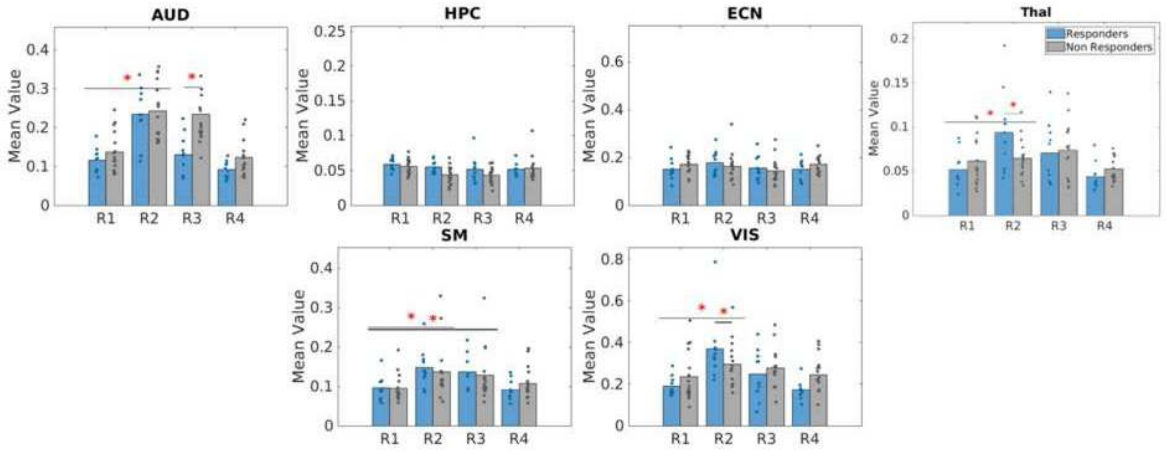

Fig. Mean parameter estimate values for each resting state network representing the network integrity.

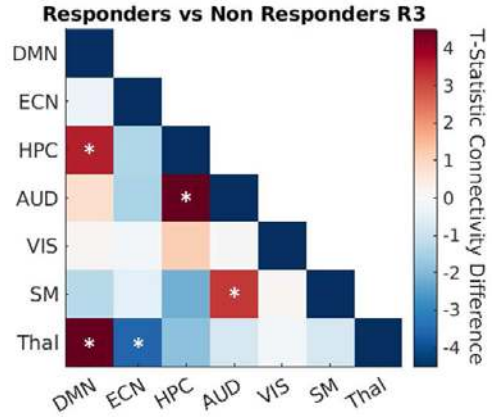

Fig. Pairwise comparisons of between-network connectivity between responders and non-responders during anaesthesia after stimualtion.

Conclusions: Unresponsiveness is not necessarily related to decreases in integrity of RSNs; in fact, we show increases in the integrity of several RSN. The thalamic hyperactivity pre-emptively displayed by responders during R2 could potentially signal the susceptibility for CC following stimulation. The increased connectivity between SM and AUD could indicate the preservation of auditory function both in hearing the questions and providing a motor response, whilst the increased connectivity between THAL and HPC might drive responders' conserved capacities for memory. Conserved cognition in responders is likely underwritten by the thalamic anchoring of the anticorrelation between the DMN and ECN.

References

1. Sanders RD. (2017), 'Incidence of Connected Consciousness after Tracheal Intubation: A Prospective, International, Multicenter Cohort Study of the Isolated Forearm Technique', Anesthesiology, 126(2):214-222.
2. Sanders RD. (2012) 'Unresponsiveness ≠ unconsciousness'. Anesthesiology, 116(4):946-59.

Poster No 2475

Profiling Neural Correlates of Consciousness based on Brain Biological Ontologies

Arianna Sala[1], Naji Alnagger[1], Simona Abagnale[2], Baris Kaan[1], Michiel Meys[1], Zhixin Wang[1], Marjorie Bardiau[1], Simon Eickhoff[3], Daniel Martins[4], Marco Tettamanti[5], Steven Laureys[1], Olivia Gosseries[1], Aurore Thibaut[1], Jitka Annen[1]

[1]University of Liege, Liege, Belgium, [2]University of Campania Luigi Vanvitelli, Naples, Italy, [3]Institute for Systems Neuroscience, Medical Faculty, Heinrich-Heine University Düsseldorf, Düsseldorf, Germany, [4]King's College London, London, United Kingdom, [5]University of Milano-Bicocca, Milano, Milano

Introduction: Studying the neural correlates of consciousness, i.e. the neural system whose state is causally linked with whether a subject is conscious or not (Chalmers, 1998), is non-trivial. Despite 25 years of neuroscientific research, the topography of the neural correlates of consciousness remains currently debated (Seth & Bayne, 2022) and even less is known

about the biological (e.g. molecular, microstructural) characteristics of the neural systems underlying consciousness. One way to study the neural correlates of consciousness is by comparing states of (un)consciousness, e.g. contrasting control subjects with patients with disorders of consciousness (DoC) after severe brain injury, reducing or nullifying awareness despite the presence of arousal. The present meta-analysis aims to shed light on the micro (molecular, microstructural) and macro (functional, evolutionary) biological ontologies of the neural correlates of consciousness, based on a quantitative synthesis of the existing evidence on brain structural, functional and molecular alterations in DoC.

Methods: In June 2023, we used MEDLINE via Ovid, and Scopus and Embase via Elsevier databases to search for resting-state MRI and PET studies, published from 2000 to 2023, and involving predominantly adults (≥16 years old) with prolonged DoC (≥28 days) and either a clinical diagnosis of DoC (unresponsive wakefulness syndrome or minimally conscious state) based on a validated behavioural scale (Schnakers et al., 2020). At least two referees (among AS, BK, NA, SA, JA) independently screened abstracts and full texts of selected studies and extracted coordinates of whole-brain, voxel-based comparisons performed between DoC patients and controls. Coordinate-based meta-analysis was performed via activation likelihood estimation. The resulting statistical maps of voxel-wise likelihoods were compared to the topography of 24 molecular, microstructural, functional and evolutionary biological ontologies, using standard settings in the neuromaps toolbox. All maps included were surface-type maps, i.e. including cortical areas only. Spatial correlations were deemed significant at $p<0.05$ Bonferroni-corrected for multiple comparison within map-type. The full protocol, including search strategy using controlled vocabulary and keyword terms, is available on PROSPERO (CRD42022327151).

Results: As of June 2023, of the resulting 2798 MRI and PET studies, 24 studies including 35 experiments (4 structural, 13 functional and 18 molecular) met criteria for inclusion, for a total of 665 patients (338 UWS; 327 MCS) and 351 controls (Fig. 1). Likelihood of consciousness-related alterations distributed following molecular, functional and evolutionary brain biological ontologies (Fig.2). No significant association was found with microstructural ontologies (T1w/T2w ratio and thickness). In details, likelihood of consciousness-related alterations spatially distributed following: - the degree of cerebral blood flow, with areas with higher cerebral blood flow most likely to be altered in disorders of consciousness - a unimodal-transmodal brain functional hierarchy, with higher-order associative areas (as opposed to sensory ones) most likely to be altered in disorders of consciousness - an evolutionary and allometric hierarchy, with areas that expanded the most in the evolution from macaque to human and that expand the most in the development from childhood to adulthood, most likely to be altered in disorders of consciousness.

Figure 1. Prisma flow diagram for MR and PET studies identified, screened and finally included in the meta-analysis

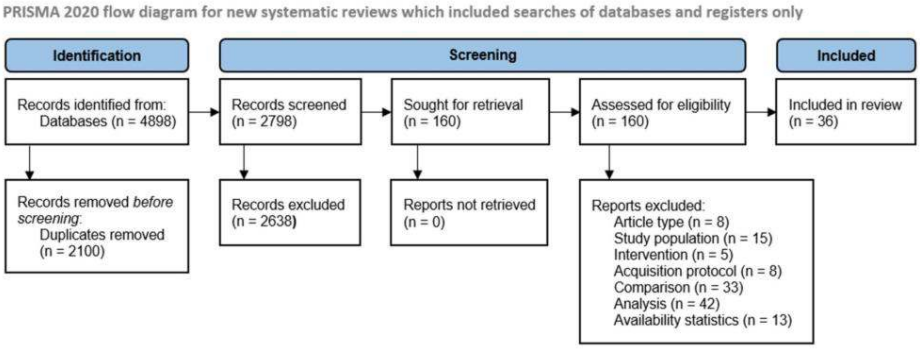

Figure 2. Significant spatial associations between likelihood map of consciousness-related alterations and biological ontologies

type	brain map	r	p	p-corrected	source
functional	functional gradient #1	0.25	<0.005	<0.05	Margulies et al. 2016
functional	sensory-association axis	0.24	<0.01	<0.05	Sydnor et al. 2021
molecular	cerebral blood flow	0.20	<0.005	<0.01	Vaishnavi et al. 2010
evolution/development	evolutionary expansion	0.25	<0.001	<0.01	Xu et al. 2020
evolution/development	allometric scaling (hcp)	0.21	<0.005	<0.05	Reardon et al. 2018

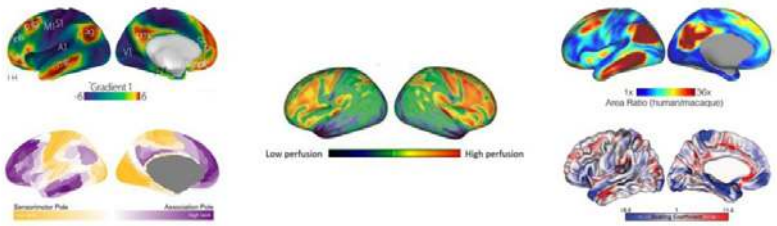

Conclusions: This meta-analysis provides the most extensive evidence to date on biological features of neural systems related to consciousness, where high-order cortical areas, that evolved the most in recent evolution and expand the most during development, and requiring higher cerebral perfusion, are most likely to be associated with the ability to express consciousness. Our findings should be independently confirmed based on evidence in other ordinary and non-ordinary states of consciousness (e.g. sleep, anesthesia).

References

1. Chalmers, D.J. (1998). 'The problems of consciousness'. Adv. Neurol. 77, 7–8.
2. Schnakers, C. (2020). 'Update on diagnosis in disorders of consciousness'. Expert Review of Neurotherapeutics, 20(10), 997-1004.
3. Seth, A. K., & Bayne, T. (2022). 'Theories of consciousness'. Nature Reviews Neuroscience, 23, 439–452

Poster No 2476

A thalamic perspective of consciousness in pharmacological and pathological states in humans

Dorottya Szocs[1], Dian Lyu[2], Rebecca Woodrow[1], Andrea I. Luppi[3], Peter Coppola[1], Judith Allanson[1], Ram Adapa[1], Guy B. Williams[1], JD Pickard[1], Adrian Owen[4], Lorina Naci[5], David Menon[1], Emmanuel Stamatakis[1]

[1]University of Cambridge, Cambridge, United Kingdom, [2]Stanford University, Palo Alto, CA, United States, [3]Montreal Neurological Institute, McGill University, Montreal, Québec, Canada, [4]Western University, London, Ontario, Canada, [5]Trinity College Dublin, Dublin, Ireland

Introduction: The thalamus is involved in modulation of arousal states (M. Shine et al., 2023, Fridman et al., 2022). Recent animal studies investigated the role of distinct thalamic nuclei in pharmacologically induced unconsciousness (Tasserie et al., 2022, Redinbaugh et al., 2020). Human studies highlighted thalamic interactions with the default mode network (DMN) in anaesthesia and disorders of consciousness (DOC) (Demertzi et al., 2019; Luppi et al., 2019). However, only few human studies differentiated the cytoarchitectonically and functionally distinct thalamic nuclei, to elucidate their relevance in altered states of consciousness (Setzer et al., 2022, Weiner et al., 2021, Liu et al., 2013). We investigated thalamic nuclei and their functional relationship to the cortex using functional MRI in both healthy anaesthetised volunteers and patients with disorders of consciousness, with implications for finding potential targets for deep brain stimulation (DBS).

Methods: We analysed the fMRI data of N=16 healthy controls under deep sedation (mean plasma propofol concentration 2.68µg/mL) and N=22 DOC patients (N=13 minimally conscious state, N=9 unresponsive wakefulness syndrome). All images were pre-processed in SPM12 and CONN. We used a thalamic parcellation atlas based on DW-MRI, where the thalamus is segmented into 7 regions of interest closely matching anatomical subparts (Najdenovska et al., 2018). Thalamic masks corresponded to nuclei (bilaterally): pulvinar (Pu), anterior (Ant), medio-dorsal (MD), ventral-latero-dorsal (VLD), central-lateral, lateral-posterior, medial-pulvinar (CL-LP-MPu), ventral-anterior (VA), and ventral-latero-ventral (VLV). Seed-to-voxel functional connectivity (FC) was computed between each nucleus and the whole brain, with a voxel level threshold of $p<0.005$ (uncorrected) and cluster level $p<0.05$ (FWE-corrected for multiple comparisons). Cortical SPM-t maps were derived from contrasts of FC (deep sedation vs. awake and DOC vs. control). To investigate which nucleus had the greatest magnitude of change in FC with loss of consciousness, we computed the average difference in FC (dFC) across the whole brain for the same contrasts as above.

Results: Cortical SPM-t maps revealed that Pu and VLV nuclei, but not others, increase their FC with DMN regions and decrease their FC with somatomotor (SM)-regions with loss of consciousness in both anaesthesia (Fig. 1a-i, g-i) and DOC (Fig. 2a-i, g-i). All other thalamic nuclei exhibited reversed effects with concomitant loss of consciousness (decreased FC with DMN-regions and increased connectivity with SM-regions). In DOC, most thalamic nuclei were found to disconnect from medial frontal regions (Fig. 2a-g). Box plots display z-scores for anaesthesia (Fig. 1) and DOC group comparisons (Fig. 2). Among all nuclei, Pu had the greatest magnitude of dFC in anaesthesia (Fig. 1h) and VLV had the greatest magnitude of dFC in DOC (Fig. 2h). Linear mixed models for within-subject analysis were used to compare magnitude of change in FC. In anaesthesia, the dFC for Pu was found to be significant in comparison to the rest of nuclei ($t = 2.081$, $p = 0.03861$). In DOC, the dFC for VLV was also found to be significant when tested against the rest of nuclei ($t = 12.336$, $p = 2.2e\text{-}16$).

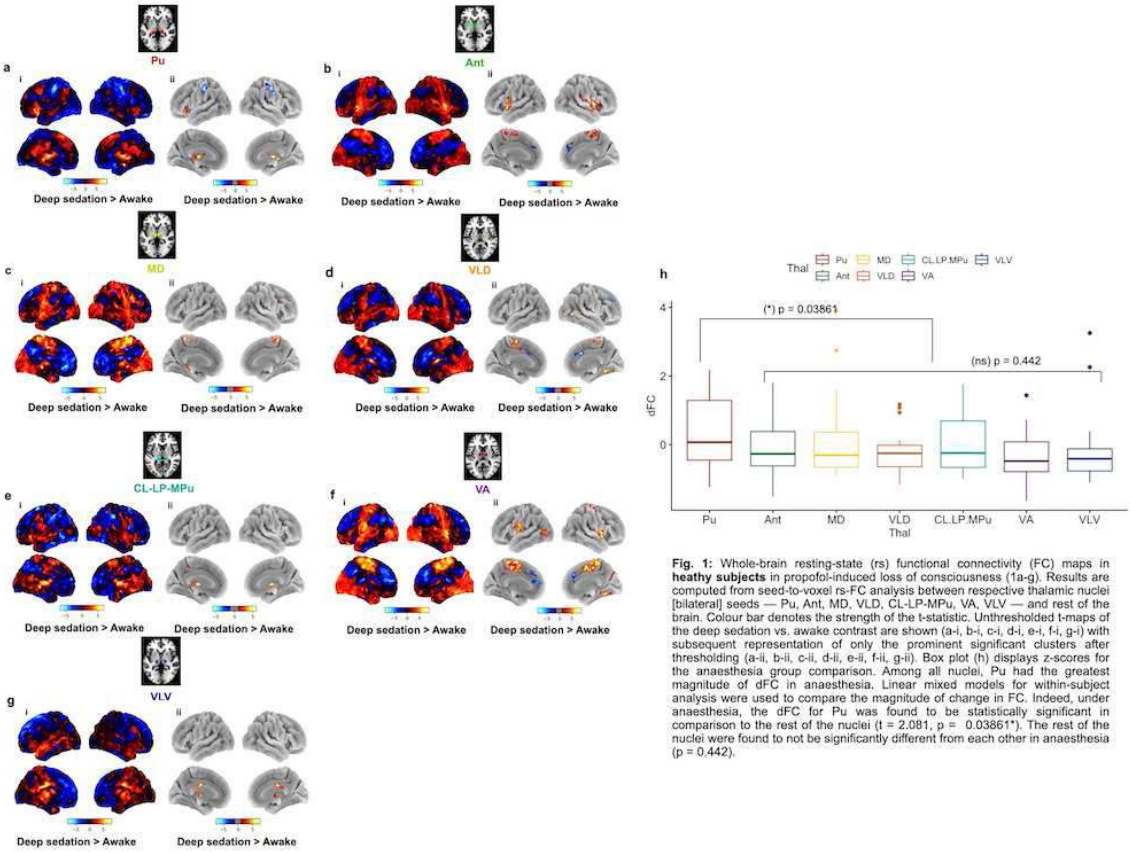

Fig. 1: Whole-brain resting-state (rs) functional connectivity (FC) maps in **heathy subjects** in propofol-induced loss of consciousness (1a-g). Results are computed from seed-to-voxel rs-FC analysis between respective thalamic nuclei [bilateral] seeds — Pu, Ant, MD, VLD, CL-LP-MPu, VA, VLV — and rest of the brain. Colour bar denotes the strength of the t-statistic. Unthresholded t-maps of the deep sedation vs. awake contrast are shown (a-i, b-i, c-i, d-i, e-i, f-i, g-i) with subsequent representation of only the prominent significant clusters after thresholding (a-ii, b-ii, c-ii, d-ii, e-ii, f-ii, g-ii). Box plot (h) displays z-scores for the anaesthesia group comparison. Among all nuclei, Pu had the greatest magnitude of dFC in anaesthesia. Linear mixed models for within-subject analysis were used to compare the magnitude of change in FC. Indeed, under anaesthesia, the dFC for Pu was found to be statistically significant in comparison to the rest of the nuclei (t = 2.081, p = 0.03861*). The rest of the nuclei were found to not be significantly different from each other in anaesthesia (p = 0.442).

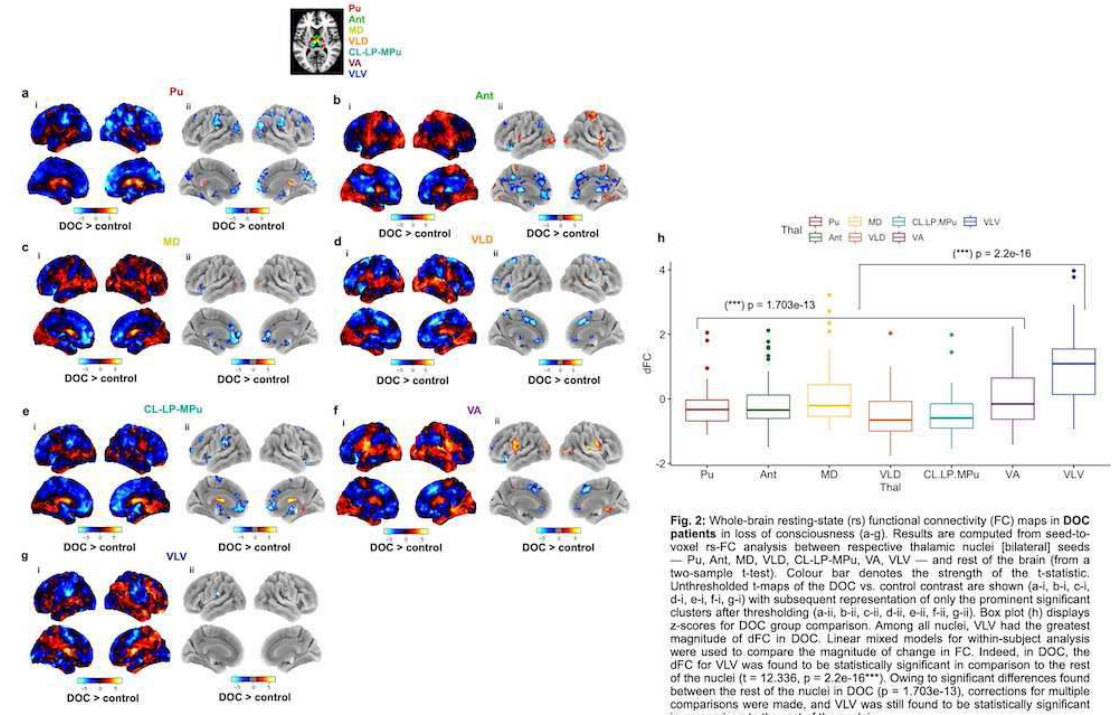

Fig. 2: Whole-brain resting-state (rs) functional connectivity (FC) maps in **DOC patients** in loss of consciousness (a-g). Results are computed from seed-to-voxel rs-FC analysis between respective thalamic nuclei [bilateral] seeds — Pu, Ant, MD, VLD, CL-LP-MPu, VA, VLV — and rest of the brain (from a two-sample t-test). Colour bar denotes the strength of the t-statistic. Unthresholded t-maps of the DOC vs. control contrast are shown (a-i, b-i, c-i, d-i, e-i, f-i, g-i) with subsequent representation of only the prominent significant clusters after thresholding (a-ii, b-ii, c-ii, d-ii, e-ii, f-ii, g-ii). Box plot (h) displays z-scores for DOC group comparison. Among all nuclei, VLV had the greatest magnitude of dFC in DOC. Linear mixed models for within-subject analysis were used to compare the magnitude of change in FC. Indeed, in DOC, the dFC for VLV was found to be statistically significant in comparison to the rest of the nuclei (t = 12.336, p = 2.2e-16***). Owing to significant differences found between the rest of the nuclei in DOC (p = 1.703e-13), corrections for multiple comparisons were made, and VLV was still found to be statistically significant in comparison to the rest of the nuclei.

Conclusions: We demonstrated, with fMRI, differentiated patterns of thalamic functional disconnections between pharmacological and pathological alterations in consciousness, in healthy volunteers and DOC patients, respectively. Whole-brain connectivity maps revealed that Pu and VLV nuclei in anaesthesia and DOC cohorts increased FC with DMN-regions and decreased FC with SM-regions with loss of consciousness. Additionally, among all nuclei, the Pu (in anaesthesia) and VLV (in

DOC) were found to have the strongest FC changes with pharmacological and pathological perturbations of consciousness, providing new evidence in the elucidation of individual thalamic nuclei's relevance in consciousness in both anaesthesia and disorders of consciousness.

References

1. Demertzi, A. (2019), 'Human consciousness is supported by dynamic complex patterns of brain signal coordination', Science Advances, 5(2), eaat7603. https://doi.org/10.1126/sciadv.aat7603
2. Fridman, E. A. (2022), 'Organizing a Rational Approach to Treatments of Disorders of Consciousness Using the Anterior Forebrain Mesocircuit Model', Journal of Clinical Neurophysiology: official publication of the American Electroencephalographic Society, 39(1), 40–48. https://doi.org/10.1097/WNP.0000000000000729
3. Liu, X. (2013), 'Differential effects of deep sedation with propofol on the specific and nonspecific thalamocortical systems: a functional magnetic resonance imaging study', Anesthesiology, 118(1), 59–69. https://doi.org/10.1097/ALN.0b013e318277a801
4. Luppi, A. I. (2019), 'Consciousness-specific dynamic interactions of brain integration and functional diversity', Nature Communications, 10(1), 4616. https://doi.org/10.1038/s41467-019-12658-9
5. Najdenovska, E. (2018), 'In-vivo probabilistic atlas of human thalamic nuclei based on diffusion- weighted magnetic resonance imaging', Scientific Data, 5, 180270. https://doi.org/10.1038/sdata.2018.270
6. Redinbaugh, M. J. (2020), 'Thalamus Modulates Consciousness via Layer-Specific Control of Cortex', Neuron, 106(1), 66–75.e12. https://doi.org/10.1016/j.neuron.2020.01.005
7. Setzer, B. (2022), 'A temporal sequence of thalamic activity unfolds at transitions in behavioral arousal state', Nature Communications, 13(1), 5442. https://doi.org/10.1038/s41467-022-33010-8
8. Shine, J. M. (2023), 'The impact of the human thalamus on brain-wide information processing', Nature Reviews Neuroscience, 24(7), 416–430. https://doi.org/10.1038/s41583-023-00701-0
9. Tasserie, J. (2022), 'Deep brain stimulation of the thalamus restores signatures of consciousness in a nonhuman primate model', Science Advances, 8(11), eabl5547. https://doi.org/10.1126/sciadv.abl5547
10. Weiner, V. S. (2023), 'Propofol disrupts alpha dynamics in functionally distinct thalamocortical networks during loss of consciousness', Proceedings of the National Academy of Sciences of the United States of America, 120(11), e2207831120. https://doi.org/10.1073/pnas.2207831120

Poster No 2477

Effects of Classical and Non-Classical Psychedelics on Regional Homogeneity in the Human Cortex

Rui Dai[1], Zirui Huang[1], George Mashour[1]

[1]*University of Michigan, Ann Arbor, MI*

Introduction: The neurobiology of the psychedelic experience is not fully understood. Identifying common neural changes induced by both classical (i.e., acting at the 5-HT2 receptor) and non-classical psychedelics would provide mechanistic insight into state-specific characteristics. Previous studies of psychedelic effects on the brain focused primarily on connectivity between different brain regions and networks. However, less is known about how psychedelics affect neural activity coordinated within local brain regions. To address this gap, we investigated the impact of nitrous oxide, ketamine and lysergic acid diethylamide (LSD) on regional homogeneity in human cortex.

Methods: This study was a reanalysis of three neuroimaging datasets from healthy human volunteers, who were assessed by fMRI during baseline (i.e., ordinary awake state) and during exposure to psychedelic concentrations of nitrous oxide (n=16), ketamine (n=12), and LSD (n=15). Regional homogeneity (ReHo) analysis was employed to assess the similarity or coherence of spontaneous neural activity within a specific region of the brain. The impact of different regional homogeneity cluster sizes (7 – 729 voxels) was also examined. Additionally, a support vector machine learning approach was utilized to classify baseline and psychedelic states based on the regional homogeneity features derived from distinct brain functional networks.

Results: Despite distinct molecular mechanisms and modes of delivery, all three psychedelics consistently reduced regional homogeneity in functional networks, including visual (nitrous oxide vs. baseline: p=0.033, ketamine vs. baseline: p=0.038, LSD vs. baseline: p=0.0002), dorsal attention (nitrous oxide vs. baseline: p=0.005, ketamine vs. baseline: p=0.010, LSD vs. baseline: p=0.0006), frontoparietal (nitrous oxide vs. baseline: p=0.0007, ketamine vs. baseline: p= 0.001, LSD vs. baseline: p<0.0001), and default mode (nitrous oxide vs. baseline: p=0.021, ketamine vs. baseline: p= 0.014, LSD vs. baseline: p=0.0005) networks. All p values were Bonferroni corrected. Furthermore, compared to baseline, psychedelic-induced changes in regional homogeneity was more consistent with small ReHo cluster size (e.g., 7-27 voxels). As the ReHo cluster size increased (e.g., 125-729 voxels), the difference between psychedelic states and baseline diminished. Lastly, the results from the support vector machine demonstrated the following prediction accuracies for distinguishing between baseline and psychedelic states: 75% for nitrous oxide, 67% for ketamine, and 83% for LSD.

Conclusions: We conclude that classical and non-classical psychedelics share a common effect of reducing local coherence of neural activity in areas of known relevance to consciousness, suggesting a common candidate mechanism for the psychedelic experience.

References
1. Carhart-Harris. (2016), 'Neural correlates of the LSD experience revealed by multimodal neuroimaging', Proceedings of the National Academy of Sciences, vol. 113, no. 17, pp. 4853-4858.
2. Dai, Rui. (2023), 'Classical and non-classical psychedelic drugs induce common network changes in human cortex', NeuroImage, vol. 273, no.120097.
3. Zang YF. (2004), 'Regional homogeneity approach to fMRI data analysis', NeuroImage, vol. 22, no. 1, pp. 394-400.

Poster No 2478

The Hierarchy of Psychedelic Effects: Three Systematic Reviews and Meta-Analyses

Kenneth Shinozuka[1]

[1]*University of Oxford, Oxford, Oxfordshire*

Introduction: Serotonergic psychedelics, including dimethyltryptamine (DMT), lysergic acid diethylamide (LSD), and psilocybin, induce altered states of consciousness. Yet their modes of action are currently not fully understood. Here, we provide three systematic reviews and meta-analyses of three hierarchical levels relevant to the effects of psychedelics, i.e., 1) their subjective experience (phenomenology), 2) whole-brain neuroimaging and 3) molecular pharmacology.

Methods: Phenomenology: We performed a meta-analysis on studies that measured the subjective experience of psychedelics through the Altered States of Consciousness (ASC) questionnaire. We conducted a three-level meta-analysis in order to account for statistical dependencies arising from the fact that ASC studies measured multiple subjective dimensions in the same group of participants. This three-level analysis models both the within-study heterogeneity and the between-study heterogeneity. Neuroimaging: To perform a meta-analysis on studies of FC, we essentially "re-parcellated" all of the data into the same parcellation: the seven resting-state Yeo networks. We conducted what amounted to a "vote-counting" meta-analysis. If a pair of ROIs became more connected under psychedelics, then a "vote" was cast in favour of the two Yeo networks that comprised this pair. To compute the significance of our results, we compared our results to a surrogate dataset formed from Human Connectome Project data. Pharmacology: We performed two meta-analyses of the pharmacology literature. The first was conducted on the selectivity of binding affinities, measured as the ratio between the affinity (Ki) for a given receptor and the affinity for a reference receptor, which we chose to be the 5-HT1A receptor. For the selectivity meta-analysis, we limited our literature search to four receptors – 5-HT1A, 5-HT2A, 5-HT2C, and D2 – expressed in human cells or cortical slices. The second meta-analysis was performed on relative functional activity, measured as Δlog(Emax/EC50), where Δ refers to the difference between this quantity for the psychedelic of interest and that of a reference ligand (e.g. serotonin). We examined three types of GPCR-mediated functional activity at the 5-HT2A receptor: calcium mobilisation and inositol phosphate formation, which capture Gq-protein signalling, and beta-arrestin-2 recruitment. For both the selectivity and relative activity meta-analyses, we constructed random-effects models, which model between-study heterogeneity.

Results: Phenomenology: At medium doses, 5D-ASC scores were significantly greater for LSD than psilocybin in the oceanic boundlessness dimension (OB; $p = 0.0283$), which corresponds to feelings of interconnectedness, and the visionary restructuralisation dimension (VR; $p = 0.0468$), which measures the quality and intensity of visual hallucinations. We also observed significant differences between LSD and psilocybin in the VR dimension ($p = 0.0417$) at high doses. Neuroimaging: All psychedelics significantly strengthened between-network connectivity. Within-network connectivity decreased in all networks except for the frontoparietal network. However, all reductions in within-network FC were deemed insignificant. Pharmacology: There were no significant differences between psychedelics in their selective affinity for the 5-HT2A, 5-HT2C, or D2 receptor, relative to the 5-HT1A receptor. There were also no significant differences in relative functional activity at the calcium mobilisation, inositol phosphate formation, or β-arrestin-2 recruitment pathways.

Conclusions: We found that the phenomenology, neuroimaging, and pharmacology of psychedelics exhibit a weak one-to-one correspondence with one another, which is not surprising given their highly non-linear relationships. We encourage future research to develop tools for modelling these relationships in order to improve our scientific understanding of psychedelics.

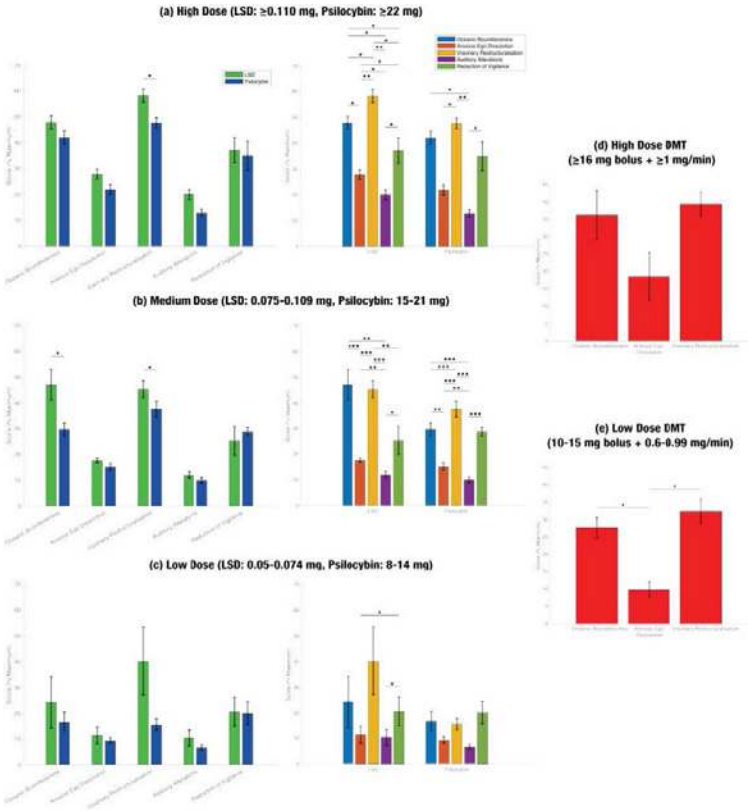

Fig. Results of the phenomenology meta-analysis.

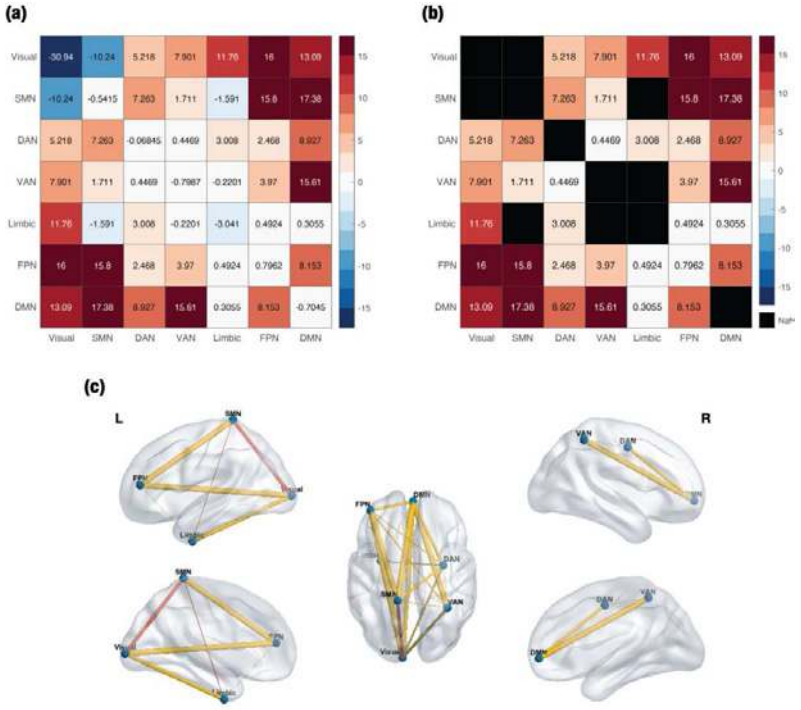

Fig. Results of the undirected functional connectivity meta-analysis.

References

1. Carhart-Harris, R. L., Erritzoe, D., Williams, T., Stone, J. M., Reed, L. J., Colasanti, A., Tyacke, R. J., Leech, R., Malizia, A. L., Murphy, K., Hobden, P., Evans, J., Feilding, A., Wise, R. G., & Nutt, D. J. (2012). Neural correlates of the psychedelic state as determined by fMRI studies with psilocybin. Proceedings of the National Academy of Sciences, 109(6), 2138–2143. https://doi.org/10.1073/pnas.111959810.
2. de Vos, C. M. H., Mason, N. L., & Kuypers, K. P. C. (2021). Psychedelics and Neuroplasticity: A Systematic Review Unraveling the Biological Underpinnings of Psychedelics. Frontiers in Psychiatry, 12. https://www.frontiersin.org/article/10.3389/fpsyt.2021.724606
3. Gonzalez-Maeso, J., & Sealfon, S. C. (2009). Agonist-Trafficking and Hallucinogens. Current Medicinal Chemistry, 16(8), 1017–1027.

4. Griffiths, R. R., Johnson, M. W., Richards, W. A., Richards, B. D., Jesse, R., MacLean, K. A., Barrett, F. S., Cosimano, M. P., & Klinedinst, M. A. (2018). Psilocybin-occasioned mystical-type experience in combination with meditation and other spiritual practices produces enduring positive changes in psychological functioning and in trait measures of prosocial attitudes and behaviors. Journal of Psychopharmacology (Oxford, England), 32(1), 49–69. https://doi.org/10.1177/0269881117731279
5. Harrer, M., Cuijpers, P., A, F. T., & Ebert, D. D. (2021). Doing Meta-Analysis With R: A Hands-On Guide (1st ed.). Chapman & Hall/CRC Press.
6. Hedges, L. V., Tipton, E., & Johnson, M. C. (2010). Robust variance estimation in meta-regression with dependent effect size estimates. Research Synthesis Methods, 1(1), 39–65. https://doi.org/10.1002/jrsm.5
7. Pustejovsky, J. E., & Tipton, E. (2022). Meta-analysis with Robust Variance Estimation: Expanding the Range of Working Models. Prevention Science, 23(3), 425–438. https://doi.org/10.1007/s11121-021-01246-3
8. Studerus, E., Gamma, A., & Vollenweider, F. X. (2010). Psychometric Evaluation of the Altered States of Consciousness Rating Scale (OAV). PLOS ONE, 5(8), e12412. https://doi.org/10.1371/journal.pone.0012412
9. Yaden, D. B., Johnson, M. W., Griffiths, R. R., Doss, M. K., Garcia-Romeu, A., Nayak, S., Gukasyan, N., Mathur, B. N., & Barrett, F. S. (2021). Psychedelics and consciousness: Distinctions, demarcations, and opportunities. International Journal of Neuropsychopharmacology, 24(8), 615–623. https://doi.org/10.1093/ijnp/pyab026

Poster No 2480

Neural correlates of emotional response to paintings of Caravaggio

Akitoshi Ogawa[1], Shigetoshi Osano[2], Tetsuya Matsuda[3], Masamichi Sakagami[3], Tatsuya Kameda[2]

[1]Juntendo University, Tokyo, Japan, [2]The University of Tokyo, Tokyo, Japan, [3]Tamagawa University, Tokyo, Japan

Introduction: An Italian Baroque painter, Caravaggio (1571-1610), innovated the Chiaroscuro technique, which uses light-dark intense contrasts. The limited information in the contrast elevates emotional responses to paintings[1]. Caravaggio's paintings depicting facial and body tension and movement in light-dark contrasts evoked subjective emotional elevation compared to his followers[2]. However, besides such art-historical observation, the neural basis of the distinctive emotional experiences associated with Caravaggio remains largely unknown. In this neuro-cognitive experiment that coupled eye-tracking and functional magnetic resonance imaging (fMRI), we explored the neural correlates of emotional elevation when viewing Caravaggio's paintings.

Methods: Eleven expert participants (students majoring in art history, 3 males and 8 females, ranging from 20 to 25 years) and twenty novice participants (other majors, 10 males and 10 females, ranging from 18 to 22 years) without neurological or psychiatric illness participated in this fMRI experiment. We prepared 10 Caravaggio's, 10 followers', and 10 Mondrian's paintings. In each trial, one single painting was presented for 25 s, followed by a fixation cross presented during the inter-trial interval (2, 3, or 4 s). Two senior experts in art history defined three areas of interest (AOIs) for each painting (Fig. 1A). During the fMRI experiment, the eye position was recorded using an MR-compatible eye tracker operating at 250 Hz (EyeLink 1000) (Fig. 1B). All MRI data were acquired using a 3-T MRI scanner (Prisma Fit) at Tamagawa University with a 32-ch head coil. Functional images were acquired using a multiband GRE EPI sequence (TR = 1.0 s, TE = 26 ms, FA = 59°, in-plane FOV = 192 mm × 192 mm, matrix size = 64 × 64, slice thickness = 3 mm, 45 contiguous slices, and multiband factor = 3[3]). We used SPM12 and FSL to process the acquired images. The functional images were motion-corrected, distortion-corrected, spatially normalized to the standard space of MNI coordinates, spatially smoothed (Gaussian FWHM = 8 mm), and high-pass filtered (cut off = 256 s). The design matrix of the general linear model included three regressors for the painting types (Caravaggio, Follower, and Mondrian) and six head-motion nuisance regressors. We used voxel-level and cluster-level thresholds to investigate significant activation ($P < 0.001$ for cluster identification and $P < 0.05$ for cluster-level significance with family-wise error correction).

Results: The eye-tracking results showed that the expert participants looked at the AOIs longer than the novice participants ($F(1,29) = 8.90$, $P = 0.0057$) (Fig. 1C). Imaging results showed that the anterior cingulate cortex, right fusiform gyrus, and right inferior frontal gyrus were significantly activated when viewing Caravaggio's paintings compared to those of his followers (Fig. 2A). Consistent with a previous study[4], Mondrian's paintings activated the early visual area, compared to Caravaggio's and his followers' paintings (Fig. 2B). The contrast between experts and novices when viewing Caravaggio's paintings showed significant activation in the right superior parietal lobule (Fig. 2C). As the amygdala is generally involved in emotional elevation, we compared the activity in the amygdala (Fig. 2D) while participants freely viewed the paintings of Caravaggio and his followers compared to the activity for the paintings of Mondrian. We collapsed experts and novices to examine the amygdala activity because of no significant difference in the amygdala activity; Caravaggio's paintings activated the amygdala more, compared to the followers' paintings ($t(30) = 2.08$, $P = 0.046$) (Fig. 2E).

Conclusions: These results suggest that experts and novices viewed the paintings cognitively differently, but the amygdala was activated similarly in both experts and novices while viewing Caravaggio's paintings, which evoked the characteristic emotional elevation.

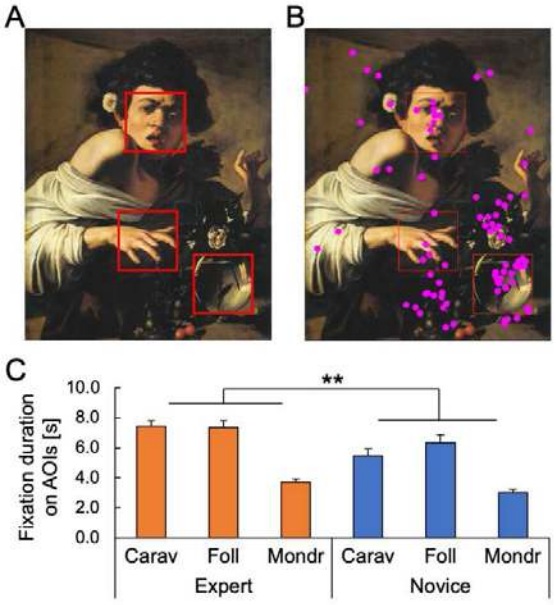

Figure 1. AOIs and fixations. **A.** Examples of AOIs indicated by squares shown in "Boy Bitten by a Lizard." Three AOIs had been defined for each of the thirty paintings before the experiment. **B.** An example of fixation records. Points show the fixation locations during viewing. Thin-line squares indicate the AOIs. **C.** Duration of fixation in the AOIs. Experts looked at the AOIs longer than Novices. The AOIs in representational paintings (i.e., Caravaggio and Follower) were also looked longer than abstract (Mondrian) paintings. Asterisks indicate statistical significance (**P < 0.01). Carav = Caravaggio, Foll = Follower, Modr = Mondrian.

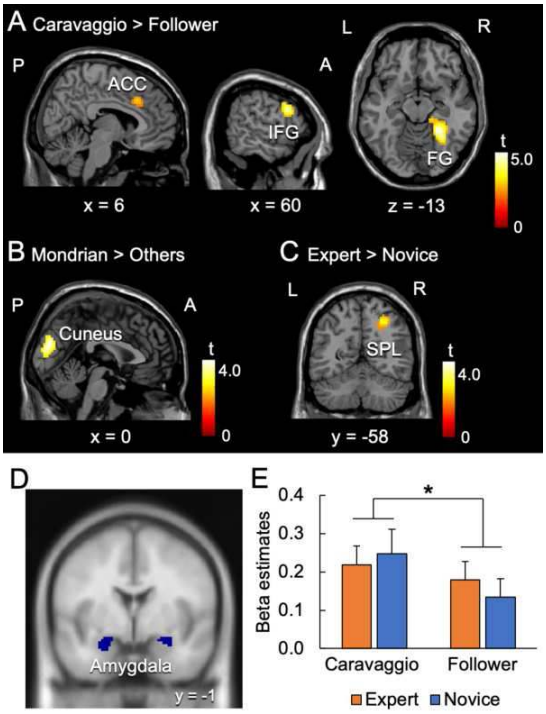

Figure 2. Imaging results. **A.** Activation while viewing Caravaggio's paintings. The ACC, FG, and IFG were activated for Caravaggio's paintings compared to the followers' paintings. **B.** Activation for Mondrian paintings compared to the other paintings. **C.** Activation observed in the contrast of Expert vs. Novice. The right superior parietal area, a putatively attention-related area, was more activated in the Expert group. **D.** Region of interest of the amygdala. **E.** Activation in the amygdala. The activity in Caravaggio was significantly higher than in Follower. The asterisk indicates the statistical significance (*P < 0.05).

References
1. Osano, S., 2020. Caravaggio. Hokkaido Shimbun Press, Hokkaido.
2. Szajnberg, N.M., 2013. Caravaggio Four Centuries Later. J Am Psychoanal Assoc 61, 311–332.
3. Xu, J., Moeller, S., Auerbach, E.J., Strupp, J., Smith, S.M., Feinberg, D.A., Yacoub, E., Uğurbil, K., 2013. Evaluation of slice accelerations using multiband echo planar imaging at 3T. Neuroimage 83, 991–1001.
4. McKeefry, D.J., Zeki, S., 1997. The position and topography of the human colour centre as revealed by functional magnetic resonance imaging. Brain 120, 2229–42.

Poster No 2481

Focal acetylcholinergic modulation of the human midcingulo-insular network during attention

Sudesna Chakraborty[1], Sun Kyun Lee[2], Sarah Arnold[3], Roy Haast[4], Ali Khan[1], Taylor Schmitz[1]

[1]University of Western Ontario, London, Ontario, [2]University of Toronto, Toronto, Ontario, [3]McMaster University, Hamilton, Ontario, [4]Aix-Marseille University, Marseille, Provence

Introduction: The cholinergic basal forebrain neurons send large projections to the cortex which are involved in rapid and spatially precise coordination of neuronal activity and behavior. The relatively recent discovery of 'wired' cholinergic neurotransmission modes comes mostly from non-human animal research but implies a central role of acetylcholine (ACh) in attention. However, the direct link between ACh signaling and attention has proven challenging to study experimentally in humans. Here, we used meta-analytic strategies targeting both pharmacological and non-pharmacological neuroimaging studies to examine the relationship between ACh and attention in humans (Chakraborty, Lee, et al. 2023).

Methods: We performed several meta-analyses including (1) focused meta-analysis on a well curated sample of placebo-controlled neuroimaging studies examining attention under pharmacological modulation with an ACh agonist and (2) discovery and validation meta-analyses on larger independent samples of non-pharmacological neuroimaging studies (Fig.1). First, we conducted a literature search on the PubMed database (https://pubmed.ncbi.nlm.nih.gov) to identify pharmacological functional imaging studies of potential relevance up to April 2023 (N=32 experiments in total). Relevant coordinates from the selected studies were extracted and converted into MNI coordinates, using the Lancaster transform included in GingerALE v.3.0.2 (Lancaster et al. 2007) (http://www.brainmap.org/ale/) to perform Activation Likelihood Estimation (ALE). We also extracted measures of response accuracy and response latency from these studies for a behavioral meta-analysis examining if and how ACh affects attentional task performance. For the discovery and validation meta-analyses of non-pharmacological imaging studies, we used Sleuth (https://brainmap.org/sleuth/) to perform meta-analytic connectivity mapping (MACM) on two seed regions of interest (ROIs). For the discovery MACM, we used the a priori anatomically defined nuclei of the BF as our ROI (Fig.1AB). For the validation MACM, we used the suprathreshold clusters identified in the previous ALE analysis of ACh pharmacological imaging studies (Fig.1C). The binarized MNI space masks for each ROI were entered into the BrainMap database, along with two other search criteria specifying (1) normal mapping and (2) activations. Using the search criteria, MACM queries the database for imaging studies which report coordinates for brain areas that are co-activated with the seed ROI during a particular task or under specific conditions. The coordinates are then entered into an ALE to identify brain regions that are consistently activated across studies. Finally, we used our previously defined "multimodal cholinergic map" (Chakraborty, Haast, et al. 2023) to perform spin test (Alexander-Bloch et al. 2018) to assess the spatial correspondences between the meta-analytic findings and the BF cortical cholinergic projectome (Fig.2).

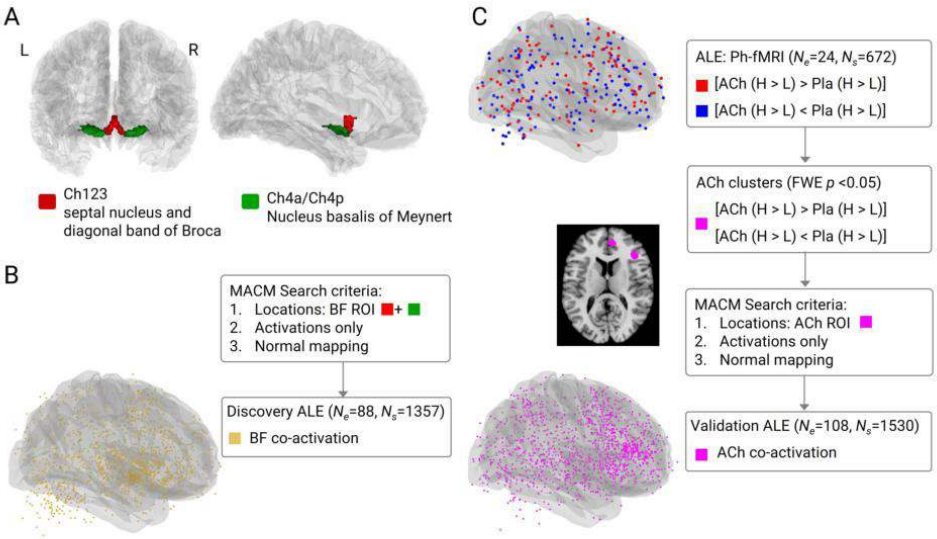

Figure 1: Overview of meta-analyses. (A) A probabilistic atlas of the Ch123,Ch4a/4p BF nuclei (Zaborszky et al., 2008) (B) The MACM localized coordinates for brain areas that co-activate with the BF under attentional engagement (goldenrod dots in semi-transparent render). (C) 24 placebo (Pla) controlled pharmacological neuroimaging studies that: (1) employed cholinergic agonists (ACh); (2) report explicit task comparisons of high versus low (H > L) attentional demand condition; (3) assessed cognitively normal younger adults (<50 years). ALE was performed separately on Drug x Task interactions where ACh either increased activation under ACh and attention (red dots: [ACh (H > L)] > [Pla (H > L)], or decreased activation under ACh and attention (blue dots: [ACh (H > L)] < [Pla (H > L)]. Suprathreshold ALE clusters for activation increases and decreases were merged into a seed region (magenta) for MACM. The MACM localized coordinates for brain areas that co-activate with the ACh modulated cortical regions under attentional engagement (magenta dots in semi-transparent render). These coordinates were submitted to validation ALE analysis.

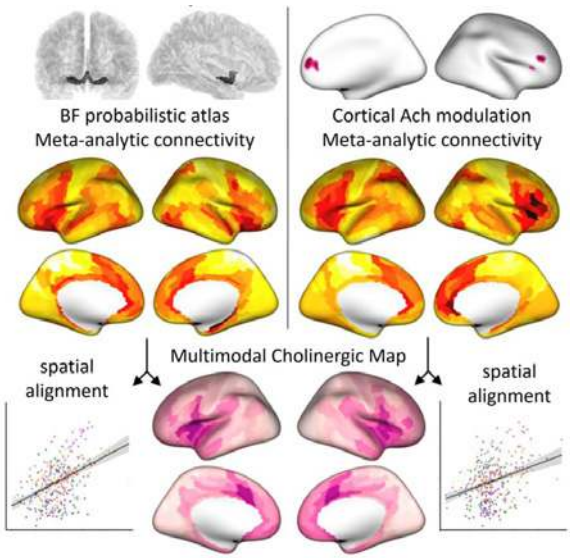

Figure 2: Overview of the study. (Top) Two seed regions of interest (ROIs) for the MACM. (Middle) Corresponding discovery and validation ALE analysis results. (Bottom) Multimodal cholinergic map (Chakraborty, Haast, et al. 2023) and spin test to assess the spatial alignment between the brain maps.

Results: We found that pharmaco-modulation of ACh evoked both increased activity in the anterior cingulate and decreased activity in the opercular and insular cortex. Behaviorally, ACh evoked a significant speeding of responses compared to placebo, with negligible tradeoff in accuracy, consistent with attentional enhancement. In large independent meta-analyses of non-pharmacological neuroimaging research, we demonstrate that during attentional engagement these same cortical areas exhibit (1) task-related co-activation with the basal forebrain, (2) task-related co-activation with one another, and (3) spatial overlap with dense cholinergic innervations originating from the BF, as estimated by multimodal cholinergic map.

Conclusions: In sum, the present meta-analytic findings provide further evidence that acetylcholinergic modulation of midcingulo-insular network via basal forebrain afferents may coordinate selection of task relevant information, thereby facilitating cognition and behavior.

References

1. Alexander-Bloch, Aaron F., Haochang Shou, Siyuan Liu, Theodore D. Satterthwaite, David C. Glahn, Russell T. Shinohara, Simon N. Vandekar, and Armin Raznahan. 2018. "On Testing for Spatial Correspondence between Maps of Human Brain Structure and Function." NeuroImage 178 (September): 540–51.
2. Chakraborty, Sudesna, Roy A. M. Haast, Prabesh Kanel, Ali R. Khan, and Taylor W. Schmitz. 2023. "Multimodal Gradients of Human Basal Forebrain Connectivity." BioRxiv. https://doi.org/10.1101/2023.05.26.541324.
3. Chakraborty, Sudesna, Sun Kyun Lee, Sarah M. Arnold, Roy A. M. Haast, Ali R. Khan, and Taylor W. Schmitz. 2023. "Focal Acetylcholinergic Modulation of the Human Midcingulo-Insular Network during Attention: Meta-Analytic Neuroimaging and Behavioral Evidence." Journal of Neurochemistry n/a (n/a). https://doi.org/10.1111/jnc.15990.
4. Lancaster, Jack L., Diana Tordesillas-Gutiérrez, Michael Martinez, Felipe Salinas, Alan Evans, Karl Zilles, John C. Mazziotta, and Peter T. Fox. 2007. "Bias between MNI and Talairach Coordinates Analyzed Using the ICBM-152 Brain Template." Human Brain Mapping 28 (11): 1194–1205.
5. Zaborszky, Laszlo, L. Hoemke, H. Mohlberg, A. Schleicher, K. Amunts, and K. Zilles. 2008. "Stereotaxic Probabilistic Maps of the Magnocellular Cell Groups in Human Basal Forebrain." NeuroImage 42 (3): 1127–41.

Poster No 2482

Attention Reshapes Receptive Fields for Thermal and Tactile Perception

Dongho Kim[1], Sohyun Han[2], Seongyun Kim[1], Seulgi Eun[1], Choong-Wan Woo[3], Min-Suk Kang[4], Seong-Gi Kim[5]

[1]Center for Neuroscience Imaging Research, IBS, Suwon-Si, Gyeonggi, [2]Res. Equipment Operations Div., Korea Basic Sci. Inst., Cheongju, Chungbuk, [3]Center for Neuroscience Imaging Research, IBS, Suwon-si, Gyeonggi-do, [4]Sungkyunkwan University, Seoul, Seoul, [5]Center for Neuroscience Imaging Research (CNIR), Institute for Basic Science (IBS), Suwon, Korea, Republic of

Introduction: Imagine a scenario where the wrist is subjected to high-temperature thermal stimulation, causing pain, while simultaneously, the finger receives a light vibrational stimulus. Intriguingly, shifting attention from the wrist to the finger has been found to temporarily reduce wrist pain(Kim, Woo et al. 2022). However, understanding the mechanisms of this pain reduction in the primary somatosensory cortex (S1) remains a challenge. The S1 cortex, comprising six neuronal layers with distinct neuron types and connections, plays a crucial role in sensory processing(Liang, Mouraux et al. 2013). Thalamic inputs predominantly synapse with neurons in the middle layer of S1. In contrast, feedback from higher-order brain areas typically targets both the deep and superficial layers(Yu, Huber et al. 2019). Additionally, feedforward lateral connections through the superficial layers of S1 are also important in the cortex's sensory processing functions(Douglas and Martin 2004). If attention diversion to the finger alleviates pain through cortico-cortical feedforward lateral inputs in the superficial layer near the wrist, we would expect an increase in BOLD (blood oxygen level-dependent) signals in the superficial layers of S1 associated with the wrist.

Methods: In the fMRI study, participants engaged in a tactile discrimination task focusing on finger stimuli, accompanied by an unattended tactile or heat stimulus (44 degrees Celsius) on the wrist. The fMRI protocol included 18-second stimulations on fingers and wrist, alternating with 36-second rest periods, over eight cycles per run, totaling eight runs. This setup was designed to monitor the BOLD signal within the S1 cortex, with a focus on signal sensitivity at 0.8 mm isotropic resolution and 35 slices, and a repetition time (TR) of 3 seconds for accurate BOLD contrast mapping(Han, Eun et al. 2021, Han, Eun et al. 2022). The behavioral experiments involved applying tactile stimuli to one of eight distinct forearm areas per trial, with participants identifying the stimuli locations. Additionally, in a dual-task condition, participants performed a frequency discrimination task on the fingers while locating stimuli on the forearm.

Results: The fMRI study revealed a significant reduction in BOLD signals across the middle, superficial, and deep layers of the S1 cortex in the wrist region when attention shifted to the finger. This reduction was notable not just in the layer receiving thalamic input but also in layers associated with feedback. These findings suggest that pain reduction mechanisms are more likely linked to diminished bottom-up input, modulated in the thalamus through attentional mechanisms, rather than to cortico-cortical feedforward inputs. Additionally, the S1 receptive field for the wrist's thermal stimulation showed a lateral shift. This shift led to a notable change in the BOLD signal, most pronounced in the middle layer. This pattern indicates that the receptive field shift is likely due to direct feedforward input from the thalamus, not cortico-cortical lateral feedforward input via the superficial layer, providing strong evidence of attention's role in shifting the receptive field within the human sensory cortex. In the behavioral experiments, participants showed higher accuracy in identifying stimuli at the forearm array's extremities compared to the middle, leading to the concept of 'endpoint bias'. This finding suggests increased sensitivity or responsiveness at the array's endpoints. During the dual-task condition, a perceptual shift was observed from the extremities to the middle of the forearm, indicating a reconfiguration of the receptive field for forearm stimulation when attention is focused on finger tasks.

Figure 1.

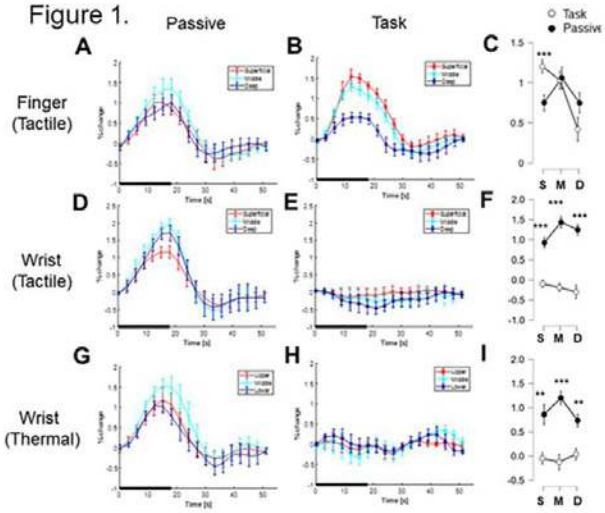

Layer-specific activation profiles in finger and wrist ROIs during task (attention to finger and passive (no attention) conditions
A. Passive condition with tactile stimulation in finger ROI.
B. Tactile discrimination task in finger ROI with attention focused on the finger.
C. Average BOLD signal (6-18 seconds) for superficial (S), middle (M), and deep (D) layers in task and passive conditions within finger ROI.
D-F correspond to A-C for the wrist ROI with unattended tactile stimuli, where E represents the passive condition and attention directed adjacent to the finger region.
G-I correspond to A-C for the wrist ROI with unattended thermal stimuli, where I represents the passive condition and attention directed adjacent to the finger region.
*Wrist ROI Defined in Passive Map; Finger ROI Found via Overlap of Passive & Task Maps at Finger Positions

Figure 2.

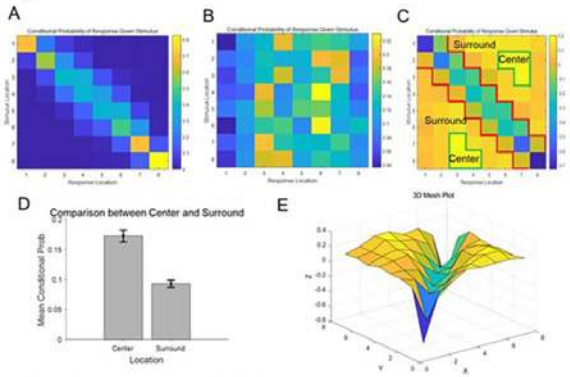

A. This panel displays the correlation between response probabilities and stimulus locations. Peaks along the diagonal represent correct identification of stimuli.

B. Illustrates the results from a subsequent dual-task experiment where participants simultaneously discerned stimuli on the forearm and matched tactile patterns on the fingers. Here, the diagonal peaks are lower, indicating increased difficulty in correct stimulus identification during the dual-task condition.

C and E. These panels compare outcomes from single and dual-task experiments. They show the emergence of non-diagonal peaks, which represent additional, unexpected response patterns.

D. Confirms that the central non-diagonal peaks are significantly higher than adjacent areas. This indicates the presence of distinct response patterns, which are different from the correct stimulus identification represented by the diagonal peaks.

Conclusions: The integration of fMRI and behavioral studies reveals how the receptive field for painful stimulation is dynamically reconfigured by diverting attention from the painful area. This reconfiguration is underpinned by mechanisms originating in the thalamus.

References

1. Douglas, R. J. (2004). “Neuronal circuits of the neocortex.” Annu Rev Neurosci 27: 419-451.
2. Han, S. (2021). “Improvement of sensitivity and specificity for laminar BOLD fMRI with double spin-echo EPI in humans at 7 T.” Neuroimage 241: 118435.
3. Han, S. (2022). “Improved laminar specificity and sensitivity by combining SE and GE BOLD signals.” Neuroimage 264: 119675.
4. Kim, D. (2022). “Neural mechanisms of pain relief through paying attention to painful stimuli.” Pain 163(6): 1130-1138.
5. Liang, M. (2013). “Primary sensory cortices contain distinguishable spatial patterns of activity for each sense.” Nat Commun 4: 1979.
6. Yu, Y. (2019). “Layer-specific activation of sensory input and predictive feedback in the human primary somatosensory cortex.” Sci Adv 5(5): eaav9053.

Poster No 2483

Two Default Modes, Internal and External, Revealed through Whole-brain Synchrony

Isaac Christian[1], Samuel Nastase[2], Michael Graziano[2]

[1]Princeton, Princeton, NJ, [2]Princeton University, Princeton, NJ

Introduction: The 'default mode' of cognition usually refers to an automatic propensity to simulate past, future, and hypothetical experiences, rather than attending to external events in the moment (Verschooren and Egner 2023). 'Mind wandering' usually refers to moments when people's attention drifts from external tasks to become engaged in internal, default-mode cognition. However, we suggest a more general formulation in which attention to external events can also become a default mode, when those events are information rich or salient. Likewise, mind wandering is not just movement of attention from an external task to internal cognition, but can also involve movement of attention from an internal task to external distractors. In this study, we used a focused attention task and whole brain synchrony to study involuntary shifts of attention bi-directionally, between external and internal states.

Methods: Forty participants completed an internal and external focused attention task in an MRI machine. In the external condition, participants were instructed to pay attention to a ~2 minute video clip and press a button if they noticed their mind had wandered from the video content. In the internal condition, participants viewed another video clip, this time tasked with ignoring the video and instead focusing on the rhythmic sensation of their breathing, while pressing a button if they noticed that their mind had wandered off their breathing. Each video was presented four times in succession. Thus, the video stimulus was more likely to attract attention on the first presentation, and less so by the fourth presentation. In addition, some videos were selected to be intrinsically interesting (high salience) and others to be uninteresting (low salience). Participants viewed a total of 6 videos, three high and three low salience. Self-reported mind wandering events (button presses) were used as an indirect measure of attention (more presses = less attention on task), and inter-subject correlation (ISC) was used to measure whole-brain attention synchrony to the video stimulus.

Results: When subjects tried to focus attention on the videos (the external focus condition), more mind wandering events occurred as the videos became less interesting (i.e. after more repetitions) and when less interesting videos were presented, suggesting a default mode of internal attention. When subjects focused on their breathing, more mind wandering events occurred when videos were most interesting (i.e. on the first repetition) and when more interesting videos were presented. In this case, subjects were biased toward an external default mode of attention, causing their minds to more frequently wander from the internal task. These behavioral results were reflected in brain activity. ISC analyses, which probe a neural signature of external attention, found that attention to the video was greater in the external focus condition than the internal focus condition; was greater to high salience videos than to low salience videos; and decreased as each video was repeated.

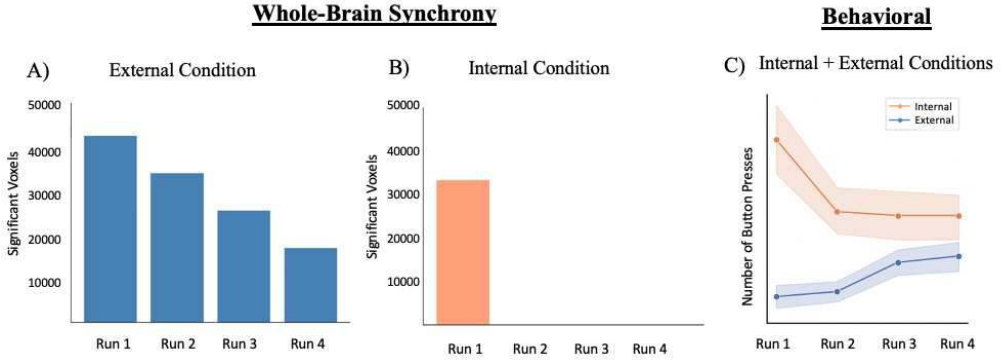

Figure 1. A) Whole-brain attention synchrony to the external stimulus when tasked with paying attention externally. B) Whole-brain attention synchrony to the external stimulus when focusing internally. C) Self-reported mind wandering event counts for internal and external conditions across repetitions. All results displayed from the Sherlock movie stimulus.

Conclusions: Our results illustrate that there are two default modes. When the external world is interesting, the default mode is to encode the external information. In contrast, when external information is not useful or exciting, the brain automatically decouples from the external environment and engages with internal simulation in a default manner. Automatic mind wandering from a desired task can therefore occur in either direction, depending on circumstances. This automatic orienting transcends an endogenous (voluntary and internally driven) and exogenous (involuntary and externally driven) distinction, showing that attention can be involuntarily drawn by an internal event just as it can by an external stimulus. Arbitrary top-down goals, such as focusing on the breath, or focusing on a video, can sometimes align with, and sometimes conflict with, the 'default' bias of orienting attention internally or externally.

References
1. Verschooren, S. and T. Egner (2023). "When the mind's eye prevails: The Internal Dominance over External Attention (IDEA) hypothesis." Psychon Bull Rev.

Poster No 2484

Subcortical White Matter Structural Alterations and Audio-Visual Attention Deficits in Schizophrenia

Hui-Yun Hsu[1], Albert Yang[1,2,3,4]

[1]Institute of Brain Science, National Yang Ming Chiao Tung University, Taipei, Taiwan, [2]Digital Medicine and Smart Healthcare Research Center, National Yang Ming Chiao Tung University, Taipei, Taiwan, [3]Department of Medical Research, Taipei Veterans General Hospital, Taipei, Taiwan, [4]Brain Research Center, National Yang Ming Chiao Tung University, Taipei, Taiwan

Introduction: Attention dysfunction represents one of the primary cognitive impairments in individuals with schizophrenia, leading to a significant impact on their long-term daily activities. Previous studies have highlighted that various functional and structural dysconnections in schizophrenia may contribute to cognitive symptoms. While numerous studies have explored cognitive function using functional magnetic resonance imaging and T1-weighted images, limited research has investigated the relationship between diffusion tensor imaging (DTI) features and attention function. By analyzing the features of white matter fiber tracts, several studies have suggested the aberrant subcortical microstructure could be the underlying mechanism of symptoms in schizophrenia. Therefore, our aim is to identify the correlation between white matter microstructure and abnormality of attention performance in individuals with schizophrenia.

Methods: Our study included 167 individuals with schizophrenia (age: 43.56 ± 12.24; 54.5% in females) and 167 healthy controls (age: 41.65 ± 10.95; 56.9% in females) from the Taiwan Aging and Mental Illness cohort. First, fractional anisotropy (FA) maps were constructed from DTI data for each participant. Second, the voxel-wise general linear model (GLM) was used to identify the FA maps difference between schizophrenia and healthy controls (cluster level > 100 voxels; PFWE < 0.001). The significant clusters were further defined into 48 white matter fiber tracts based on JHU-ICBM-labels-1mm atlas. The voxel numbers out of each tract's whole voxels over 50% was regarded as a meaningful difference. Third, we used the Mini-mental state examination (MMSE), digit span task and Wisconsin card sorting test (WCST) to evaluate multiple domains of attention function in the participants. Finally, to explore the group interaction between the FA maps and attention performance, the GLM with age, sex, and education as covariates was used in individuals with schizophrenia and healthy controls (cluster level > 100 voxels; PFWE < 0.001).

Results: We found 47 white matter tracts exhibited lower FA in individuals with schizophrenia compared to healthy controls, especially in the body of corpus callosum, fornix, right superior cerebellar peduncle, right sagittal stratum, right superior fronto-occipital fasciculus, and right uncinate fasciculus. In comparison to healthy controls, the overall cognitive assessments in schizophrenia performed worser. Furthermore, there was a significant positive correlation between the digit span task and two sub-indices of WCST (nonperseverative error, NPE; failure to maintain set, FMS), as well as FA maps. Individuals with schizophrenia presented decreased FA values with poorer attention performance. However, no significant relationship between MMSE and white matter microstructure was observed between the two groups. In our present findings, the regions that were significantly involved in auditory and visual attention dysfunction of schizophrenia included the right retrolenticular part of internal capsule, bilateral superior corona radiata, and right sagittal stratum.

Conclusions: We dedicated to exploring the structural mechanism of attention dysfunction of individuals with schizophrenia within the scope of white matter features. In conclusion, voxel-wise fractional anisotropy analysis could reflect distinct audio-visual attention patterns and aberrant white matter microstructure in individuals with schizophrenia. Additionally, these findings could reveal the abnormal attention function in schizophrenia, aligning with the neuropathological dysconnection hypothesis in white matter microstructure.

References
1. Friston, K. (2016), 'The dysconnection hypothesis (2016)', Schizophrenia research, vol. 176, no. 2-3, pp. 83-94
2. Hegde, R.R. (2020), 'Association of white matter microstructure and extracellular free-water with cognitive performance in the early course of schizophrenia', Psychiatry Research: Neuroimaging, vol. 305, 111159

Poster No 2485

Blue light exposure is associated with neural activity in the left anterior cingulate cortex

Madeline Daveney[1,2,3], Elise McGlashan[2,4], Sean Cain[1,2], Sharna Jamadar[1,2,3]

[1]Monash University, Melbourne, Australia, [2]Turner Institute for Brain and Mental Health, Melbourne, Australia, [3]Monash Biomedical Imaging, Melbourne, Australia, [4]The University of Melbourne, Melbourne, Australia

Introduction: The effect of light on humans ranges from its core role in vision to a wide array of non-visual effects on mood, physiology and brain activity (Chellappa et. al., 2011; McGlashan et. al., 2018; Vandewalle & Dijk, 2013). The non-visual effects of light in humans are thought to be mediated by the intrinsically photoreceptive retinal ganglion cells (ipRGCs) in the retina (Panda et. al., 2002; Schmidt et. al., 2011). ipRGCs contain the photopigment melanopsin, which becomes activated when exposed to light and are preferentially activated by short wavelength (blue) light compared to light of other wavelengths (Do & Yau, 2010). When activated by light, ipRGCs send signals to the brain through the retinohypothalamic tract. The aim of this study was to explore the effect of blue light on brain activity in a task-free, resting state paradigm.

Methods: Healthy individuals, free from sleep and circadian disorders (n=18, 50% female, age: M = 23.55, SD = 3.77) undertook functional MRI (fMRI) scans as part of the current study. As circadian rhythms show change with age, only participants aged 18 to 30 years were eligible for the study. Light was delivered using a custom-built fibre-optic LED light delivery system fitted to the MRI head coil. Participants were exposed to 30 second alternating blocks of blue-enriched (100 lux) and blue depleted (100 lux) light for a period of eight minutes. Half of the participants received blue-enriched light as their first exposure, and the other half received blue-depleted light as their first light exposure. Structural T1-weighted (TE = 2.07 ms; TR = 2.3 s, field of view: 256 mm; slice thickness: 1 mm) and functional T2*-weighted (TE = 30 ms; TR = 2 s, field of view: 192 mm; slice thickness: 2.2mm, interleaved acquisition) images were acquired. Participants did not engage in any task or activity during the imaging session. SPM12 was used to pre-process and analyse the results. A first-level general linear model and contrasts were computed for each participant to identify brain regions showing: (i) greater activity under blue-enriched compared to blue-depleted light and (ii) greater activity under blue-depleted compared to blue-enriched light. Voxels containing z-statistics with corresponding p-values of less than 0.001 were considered statistically significant. A second-level general linear model was then computed with the same statistical significance thresholds to view group results for both contrasts.

Results: A cluster of significantly activated voxels (k=48) was found in the left portion of the rostral cingulate zone (z=3.75, p<0.001, MNI coordinates [-8 48 4]). However, the results were not significant at the cluster level (p=0.114). No brain areas showed significantly greater brain activity when exposed to blue-depleted light compared to blue-enriched light.

Conclusions: The rostral cingulate zone is part of the anterior cingulate cortex. Activity in the anterior cingulate cortex, part of the limbic system, is associated with emotional regulation and various cognitive functions (Kober et. al., 2009; Rolls, 2019; Shackman et. al., 2011). It has also been implicated widely in mood disorder populations (Drevets et. al., 2008). Light exerts powerful positive effects on both mood and cognition and is associated with the activation of brain regions involved in these functions. As the non-visual effects of light - including those on mood and attention - are seen most prominently during blue light exposure, the results of the current study lend further support to this role of light in emotional and cognitive brain activity. Overall, these results provide evidence supporting the role of circadian photoreception in an area of the brain involved in mood, emotion and cognition, and cements the non-visual, non-image forming effects of light in humans at the neural level.

References

1. Chellappa, S. L., Steiner, R., Blattner, P., Oelhafen, P., Götz, T., & Cajochen, C. (2011). 'Non-visual effects of light on melatonin, alertness and cognitive performance: can blue-enriched light keep us alert?', PloS one, vol. 6, no. 1, pp. e16429.
2. Do, M. T. H., & Yau, K. W. (2010). 'Intrinsically photosensitive retinal ganglion cells', Physiological reviews, vol. 90, no. 4, pp. 1547-1581.
3. Drevets, W. C., Savitz, J., Trimble, M., (2008). 'The subgenual anterior circulate cortex in mood disorders', CNS spectrums, vol. 13, no. 8, pp. 663-681.
4. Kober, H., Barrett, L.F., Joseph, J., Bliss-Moreau, E., Lindquist, K. and Wager, T.D., 2008. 'Functional grouping and cortical–subcortical interactions in emotion: a meta-analysis of neuroimaging studies', Neuroimage, vol. 42, no. 2, pp. 998-1031.
5. McGlashan, E. M., Nandam, L. S., Vidafar, P., Mansfield, D. R., Rajaratnam, S. M. W., Cain, S. W. (2018). 'The SSRI citalopram increases the sensitivity of the human circadian system to light in an acute dose', Psychopharmacology, vol. 235, pp. 3201-3290.
6. Panda, S., Sato, T. K., Castrucci, A. M., Rollag, M. D., DeGrip, W. J., Hogenesch, J. B., Provencio, I., & Kay, S. A. (2002). 'Melanopsin (Opn4) requirement for normal light-induced circadian phase shifting', Science, vol. 298, no. 5601, pp. 2213-2216.
7. Rolls, E. T., (2019). 'The cingulate cortex and limbic systems for emotion, action, and memory', Brain Structure and Function, vol. 224, no. 9, pp. 3001-3018.
8. Schmidt, T. M., Chen, S.-K., & Hattar, S. (2011). 'Intrinsically photosensitive retinal ganglion cells: many subtypes, diverse functions.' Trends in neurosciences, vol. 34, no. 11, pp. 572-580.
9. Shackman, A.J., Salomons, T.V., Slagter, H.A., Fox, A.S., Winter, J.J. and Davidson, R.J., 2011. 'The integration of negative affect, pain and cognitive control in the cingulate cortex', Nature Reviews Neuroscience, vol. 12, no. 3, pp. 154-167.
10. Vandewalle, G., & Dijk, D.-J. (2013). 'Neuroimaging the effects of light on non-visual brain functions', Neuroimaging of sleep and sleep disorders, pp. 171-178.

Poster No 2486

Heart Rate Scales with Prediction Error

Maria Azanova[1,2], Lina Skora[3,4], Esra Al[5,1], Vadim Nikulin[1], Arno Villringer[1,6,7]

[1]Max Planck Institute for Human Cognitive and Brain Sciences, Leipzig, Germany, [2]Max Planck School of Cognition, Leipzig, Germany, [3]Heinrich-Heine-Universität Düsseldorf, Düsseldorf, Germany, [4]University of Sussex, Brighton, United Kingdom, [5]Columbia University, New York City, NY, [6]University Hospital Leipzig, Leipzig, Germany, [7]Humboldt University Berlin, Berlin, Germany

Introduction: Recent conceptualizations of cardiac deceleration in adaptive environments suggest that heart slowing could improve the precision of perception by reducing the frequency of noisy events associated with heartbeats (Skora et al., 2022). For instance, threat-related cardiac deceleration as part of freezing may not merely reflect a fear state but rather enable the integration of autonomic and central nervous reactions to coordinate an appropriate response (Roelofs & Dayan, 2023). Indeed, parts of the neural circuitry underlying freezing are also prominently involved in decision-making, learning, and interoception (e.g., ACC: Seamans & Floresco, 2022; insula: Zhao et al., 2023). This shared neural architecture suggests a more general role of heart rate in the integration of information. To further the knowledge of cardio-behavioral states involved in learning, we studied single-trial cardiac and neural reactions to feedback during a probabilistic learning task with non-threatening stimuli. We asked: (1) how exactly, if at all, does heart rate scale with prediction error? (2) how does it relate to the strength of the neural reaction to feedback?

Methods: To this end, we recorded combined EEG and ECG during the task in 37 participants. We used computational modeling (Q-learning) to extract prediction errors and Bayesian mixed linear models to obtain the results. We identified the Region of Practical Equivalence by assuming that effects of maximal change in prediction error can not be smaller than 1 ms change in IBI interval; in standardized coefficients, this resulted in 0.005 bounds. To study cardiac responses, we examined the change in the inter-beat interval (IBI) of the first heartbeat after feedback relative to the previous IBI. To study neural responses, we computed average amplitudes of feedback-related negativity (FRN) and P300, brain-evoked potentials that occur at around 270 and 380 ms post-feedback, respectively. We used the pseudo-trial approach (Wainio-Theberge et al., 2021) to confirm that observed ERP differences are not due to cardiac artifacts by adding random feedback triggers to the data and repeating the analysis.

Results: We found that heart rate slowed down more with larger prediction errors, even after controlling for the heart cycle phase at the moment of feedback presentation, its valence, as well as for the change and magnitude of the previous IBI: mode of standardized coefficient = .018, 95% highest density interval (HDI) = [.007,.032], Bayes Factor for coefficient >0 (BF>0) = 999, BF for null coefficient = 0.1. Furthermore, only when feedback appeared earlier in heart cycle phase (i.e., systole), change in heart rate was associated with the frontal P3a component of P300 (mode = -.058, HDI = [-.1,.-.16], BF<0 = 269.27, BF null =.12), and less so with FRN (mode = -.015, HDI = [-.06,.024], BF<0 = 4.41, BF null = 3.12) or posterior P3b component (mode = .04, HDI = [-.001,.08], BF>0 = 30.62, BF null = .84). Finally, we observed that heart rate change weakly predicted change of decision in the next trial with the same outcome-predictive stimulus (mode = .25, HDI = [.04,.488], BF>0 = 97.77, BF null = .34), indicating a direct relation to choices. All reported results were insensitive to a range of normal priors with 0 mean and uncertainty scaling from .05 to 1 sd.

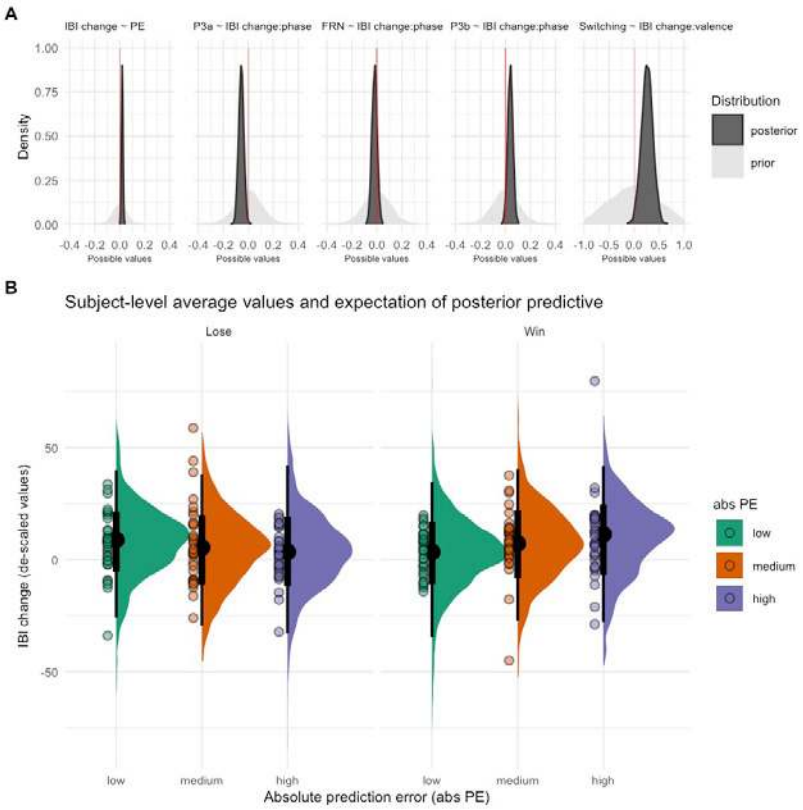

Fig. (A) Estimates of reported effects, including ROPE (red). (B) Fit results and actual data points demonstrate an interaction of absPE and valence of feedback - manifestation of PE.

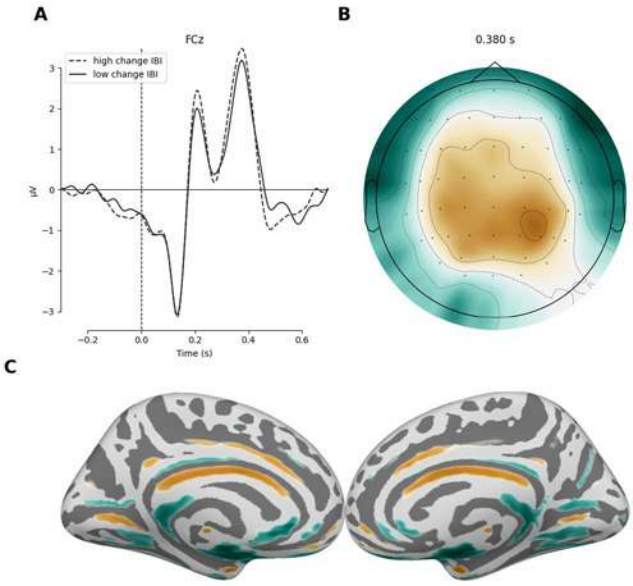

Fig. When feedback was given in systole, P3a is associated with IBI change. It is shown at FCz electrode (A), as a topography (B), and reconstructed activity (C). Warmer colors: positive association.

Conclusions: Therefore, we show it is possible to detect instant IBI scaling with prediction error in the order of tens of ms. Our findings provide insight into the mechanistic basis of the integration of cardio-behavioral states in learning and prediction. In particular, it seems that instantaneous heart rate change is mainly associated with frontal dopaminergic attentional involvement (Polich, 2007). This has further implications for understanding how cognitive processes are affected by various disturbances in heart-brain interactions, such as ones observed in anxiety (Tumati et al., 2021) and arrhythmia (Kumral et al., 2022).

References
1. Kumral, D. (2022). Attenuation of the heartbeat-evoked potential in patients with atrial fibrillation. Clinical Electrophysiology, 8(10), 1219-1230.
2. Polich, J. (2007). Updating P300: an integrative theory of P3a and P3b. Clinical neurophysiology, 118(10), 2128-2148.
3. Roelofs, K., & Dayan, P. (2022). Freezing revisited: coordinated autonomic and central optimization of threat coping. Nature Reviews Neuroscience, 23(9), 568-580.
4. Seamans, J. K. (2022). Event-based control of autonomic and emotional states by the anterior cingulate cortex. Neuroscience & Biobehavioral Reviews, 133, 104503.
5. Skora, L. I. (2022). The functional role of cardiac activity in perception and action. Neuroscience & Biobehavioral Reviews, 137, 104655.
6. Tumati, S. (2021). Out-of-step: brain-heart desynchronization in anxiety disorders. Molecular Psychiatry, 26(6), 1726-1737.
7. Wainio-Theberge, S. (2021). Dynamic relationships between spontaneous and evoked electrophysiological activity. Communications Biology, 4(1), 741.
8. Zhao, H. (2023). How distinct functional insular subdivisions mediate interacting neurocognitive systems. Cerebral Cortex, 33(5), 1739-1751.

Poster No 2487

The Neural Representation of Sound Locations by Functional Connectivity

Liwei Sun[1], Renjie Tong[1], Ying Liang[1], Jing Wei[1], Chunlin Li[1], Xu Zhang[1]

[1]School of Biomedical Engineering, Capital Medical University, Beijing, China

Introduction: The ability to localize sound sources rapidly allows human beings to understand the surrounding environment efficiently. Previous studies suggest that a dorsal "where" pathway on the cortex is functionally specialized for sound localization, which includes primary auditory cortex (PAC), planum temporale (PT), parietal regions, and prefrontal areas. However, it is still unclear how those regions within the "where" pathway interact with each other during sound localization. In the current study, we investigate how the multivariate functional connectivity (FC) patterns represent sound locations by collecting fMRI data from healthy participants during passive listening to sounds coming from different horizontal locations. Our result reveals a functional-connectivity-based system which encodes the lateralization angles of sound locations.

Methods: fMRI data from twenty-seven healthy participants (14 females; 20–34 years old) were collected during passive listening. Five 1.2-s sound clips of white noise from different horizontal directions (-90°, -45°, 0°, 45°, 90°) at 1.2 m were recorded in an isolation booth using a dummy head with a microphone in each ear. A sparse-sampling fMRI design was introduced to avoid the interference from scanner noise. For each trial, the scanner started with a 2-s BOLD signal collection period, followed by a 2-s pause for sound replay. Different sounds were presented by block. Each block included five trials of a sound clip from the same location. fMRI data was preprocessed using fMRIPrep and normalized into MNI152 space. Regions of interest (ROIs) were defined in our previous study (Sun et al., 2023) and projected to the BN246 atlas to gain a more granular parcellation of the "where" pathway (20 ROIs). FC patterns among the 20 ROIs were calculated for each participant. A leave-one-subject-out cross-validation procedure was carried out to estimate the mean classification accuracy of sound locations. Within each fold, we adopted F test for feature selection and multinomial logistic regression for classification. We varied the number of FC features selected to find the model with best performance. In addition, we compared the actual confusion matrix with confusion matrices predicted by three representational models, namely full model, left vs. right model, and lateralization angle model. Furthermore, we did exploratory analysis of FC patterns based on the whole-brain network.

Results: By feature selection, we found that as more FCs were included in the model, the decoding accuracy of sound locations initially increased, reached a peak at 29.63% (#FC = 15), and then gradually decreased. The best model with 15 FCs was used for following analysis. We calculated the Kendall's Tau correlation between the actual confusion matrix and three representational models. We found that the correlation between the observed confusion matrix and the lateralization angle model was significantly higher than the correlation between the confusion matrix and the left vs. right model ($t = 4.564$, $p < 0.001$) and marginally higher than the correlation between the confusion matrix and the full model ($t = 2.043$, $p = 0.051$). Furthermore, we found that sound locations could also be decoded from the whole-brain network with a peak accuracy of 32.6% (#FC = 35). The correlation between derived confusion matrix and the lateralization angle model was significantly higher than those between the confusion matrix and other two models (lateralization angle model > full model: $t = 2.228$, $p = 0.035$; lateralization angle model > left vs. right model: $t = 4.601$, $p < 0.001$).

Conclusions: In the current study, we were able to decode sound locations from the FC patterns within the dorsal "where" pathway. Our result indicates that FC patterns encode sound locations by lateralization angle, which is different from the opponent hemifield coding model suggested by previous activation studies.

References
1. Sun, L., Li, C., Wang, S., Si, Q., Lin, M., Wang, N., Sun, J., Li, H., Liang, Y., Wei, J., Zhang, X., & Zhang, J. (2023), 'Left frontal eye field encodes sound locations during passive listening', Cerebral Cortex, vol. 33, no. 6, pp. 3067–3079

Poster No 2488

Voxel-Based Morphometry and Subfield Volumetry Analysis Unveil the Involvement of the Limbic System

Sekwang Lee[1], Sung-Bom Pyun[1], Eui-Cheol Nam[2], Woo-Suk Tae[1]

[1]Korea University College of Medicine, Seoul, Korea, Republic of, [2]Kangwon National University, Chuncheon, Korea, Republic of

Introduction: Tinnitus, the perception of sound like ringing or buzzing without an external source, detrimentally impacts the quality of life, causing emotional difficulties and depressive symptoms. Despite its prevalence, the exact cause of tinnitus remains elusive. Recent studies propose the involvement of non-auditory brain structures, particularly the limbic system, responsible for emotional regulation and memory. Critical structures of interest include the amygdala, hippocampus, and thalamus. This study aimed to compare the volumes of these structures using voxel-based morphometry (VBM) and subfield volumetry in tinnitus patients and controls.

Methods: Fifty-three tinnitus patients (average age 52.7 years) and 52 normal controls, matched for age and gender, participated. Controls were devoid of hearing, otological, neurological, or psychological issues and were medication-free. High-resolution 3D T1-weighted brain images were acquired with a 3-T MRI scanner. MRI data were processed using the Computational Anatomy Toolbox (CAT12) for VBM and sulcal depth analysis. Automated subfield volumetry assessed specific brain structures (amygdala, hippocampus, thalamus).

Results: Tinnitus patients exhibited larger volumes in the entire amygdala, basal nucleus, right lateral nucleus, and left para-laminar nucleus than controls. Additionally, volumes of the subiculum-head, left fimbria, and left presubiculum-head in the hippocampus were greater in tinnitus patients than in normal controls. No differences emerged in thalamus volume and thalamus subnuclei between the tinnitus and normal control groups. Gray matter volumes of the thalamus, amygdala, and hippocampus were significantly higher in the tinnitus group than in the control group. Moreover, the bilateral precuneus and left parietal cortex cortical thickness was elevated in the tinnitus group.

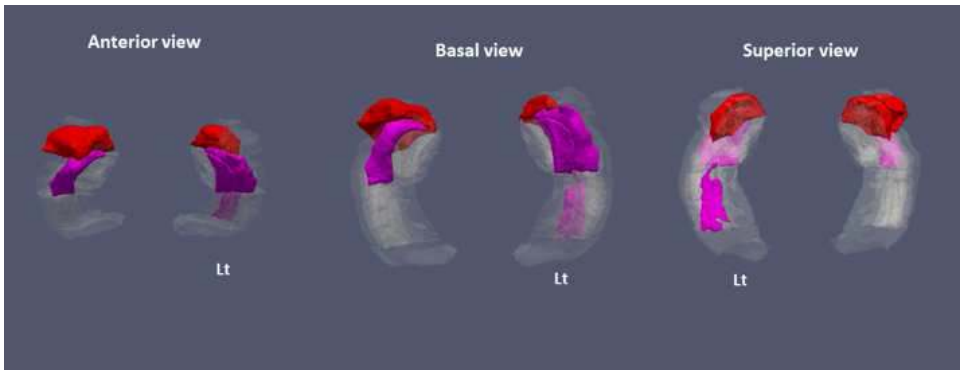

Fig. Elevated Volume in Hippocampal. Subregions Increased volume observed in hippocampal subregions (subiculum-head, left fimbria, and left presubiculum-head) during the analysis of tinnitus patie

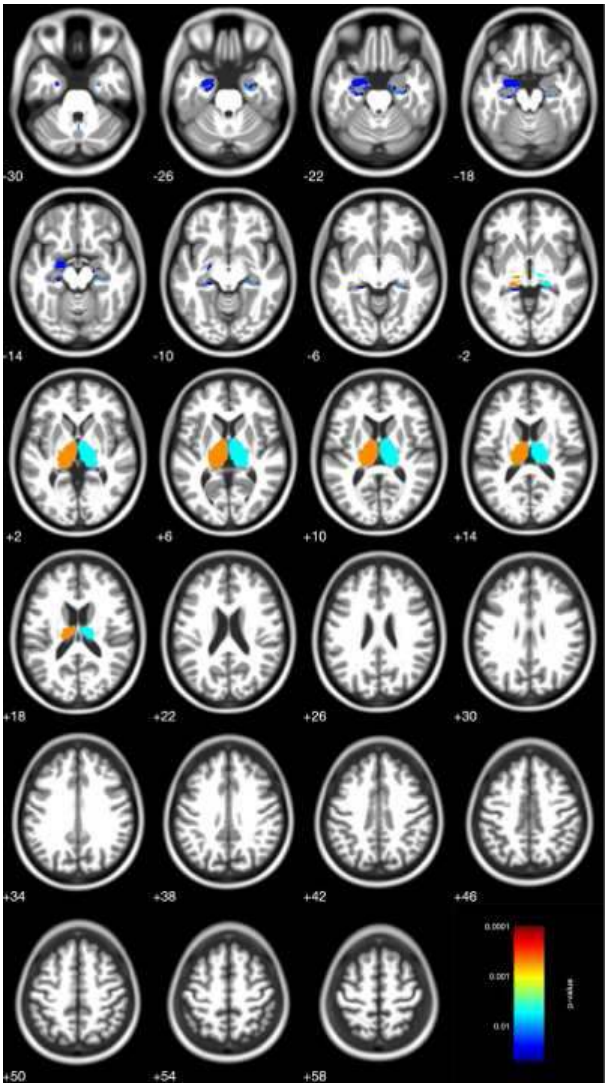

Fig. Gray Matter Volume Comparison. Significant increases in gray matter volume observed in the thalamus, amygdala, and hippocampus of the tinnitus group compared to the normal control group.

Conclusions: The findings suggest the involvement of the limbic system in tinnitus pathogenesis and provide a better understanding of the condition. The subfield volumetry technique used in this study may help identify more detailed structural changes associated with specific neurological and psychiatric conditions.

References

1. Adjamian, P. (2014). Neuroanatomical abnormalities in chronic tinnitus in the human brain. Neuroscience & Biobehavioral Reviews, 45, 119-133. https://doi.org/10.1016/j.neubiorev.2014.05.013
2. Bocchetta, M. (2019). Amygdala subnuclei are differentially affected in the different genetic and pathological forms of frontotemporal dementia. Alzheimer's & Dementia: Diagnosis, Assessment & Disease Monitoring, 11, 136-141. https://doi.org/10.1016/j.dadm.2018.12.006
3. Elgoyhen, A. B. (2015). Tinnitus: perspectives from human neuroimaging. Nature Reviews Neuroscience, 16(10), 632-642. https://doi.org/10.1038/nrn4003
4. Kapolowicz, M. R. (2020). Plasticity in Limbic Regions at Early Time Points in Experimental Models of Tinnitus [Review]. Frontiers in Systems Neuroscience, 13. https://doi.org/10.3389/fnsys.2019.00088
5. La Joie, R. (2013). Hippocampal subfield volumetry in mild cognitive impairment, Alzheimer's disease and semantic dementia. NeuroImage: Clinical, 3, 155-162. https://doi.org/https://doi.org/10.1016/j.nicl.2013.08.007
6. Leaver, A. M. (2011). Dysregulation of Limbic and Auditory Networks in Tinnitus. Neuron, 69(1), 33-43. https://doi.org/https://doi.org/10.1016/j.neuron.2010.12.002
7. O'Mara, S. M. (2009). Roles for the subiculum in spatial information processing, memory, motivation and the temporal control of behaviour. Progress in Neuropsychopharmacology & Biological Psychiatry, 33(5), 782-790. https://doi.org/10.1016/j.pnpbp.2009.03.040
8. Profant, O. (2020). The Influence of Aging, Hearing, and Tinnitus on the Morphology of Cortical Gray Matter, Amygdala, and Hippocampus [Original Research]. Frontiers in Aging Neuroscience, 12. https://doi.org/10.3389/fnagi.2020.553461
9. Saygin, Z. M. (2017). High-resolution magnetic resonance imaging reveals nuclei of the human amygdala: manual segmentation to automatic atlas. NeuroImage, 155, 370-382. https://doi.org/10.1016/j.neuroimage.2017.04.046
10. Tae, W.-S. (2018). Changes in the regional shape and volume of subcortical nuclei in patients with tinnitus comorbid with mild hearing loss. Neuroradiology, 60(11), 1203-1211. https://doi.org/10.1007/s00234-018-2093-2

Poster No 2489

Brain oscillations in hearing loss and mild cognitive impairment during speech-in-noise tests

Ji-Hye Han[1], Jihyun Lee[2], Hyo-Jeong Lee[3]

[1]Hallym University College of Medicine, Anyang-si, Gyeonggi-do, [2]Hallym University College of Medicine, Anyang, Gyeonggi, [3]Department of Otorhinolaryngology-Head and Neck Surgery, Hallym University College of Medici, Chuncheon, Kangwon-do

Introduction: Hearing loss stands as a primary risk factor for dementia, affecting central auditory function and cognitive abilities in elderly individuals. The speech-in-noise (SiN) test, encompassing sensory encoding and cognitive neural processing, serves as a clinical tool for evaluating central auditory function. Although Electroencephalogram (EEG) has a history of quantifying neural responses to speech stimuli, its application in investigating brain response changes concerning hearing and cognitive abilities in older adults has remained limited. This study aims to quantify brain oscillations during SiN listening and their correlation with cognitive abilities in older adults affected by hearing loss (HL) and/or mild cognitive impairment (MCI).

Methods: This study involved 20 participants, comprising 13 individuals with mild cognitive impairment (MCI), 10 with hearing loss (HL), and 7 experiencing both MCI and HL (MCI+HL). Additionally, 10 individuals with normal hearing (NH) were included as controls. Cognitive function assessment was conducted using the Montreal Cognitive Assessment (MOCA) test. EEG activity was recorded from 64 scalp electrodes while participants actively engaged in the Korean digit-in-noise test. DICS beamforming was employed to estimate the sources of neural activity for each frequency band.

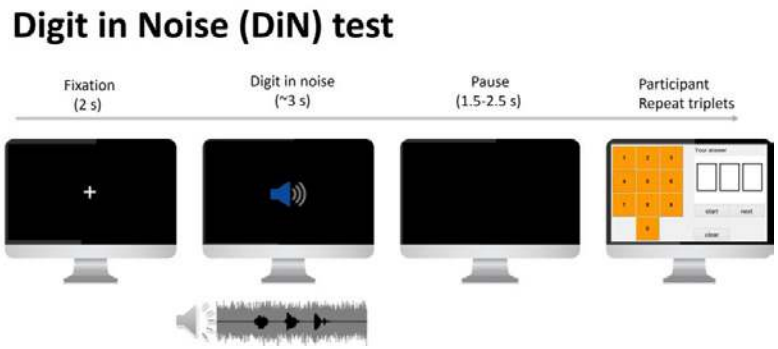

Results: In behavioral data, both HL groups (HL only and MCI+HL) exhibited lower DiN thresholds compared to the NH and MCI-only groups. Notably, the MCI+HL group demonstrated significanlty reduced DiN accuracy. The HL group displayed enhanced alpha event-related desynchrony (ERD) across broader brain areas compared to the other groups. Additionally, a positive correlation was found between alpha power in the right frontal lobe and DiN performance in the HL group. Conversely, the MCI+HL group revealed enhanced the theta activity in the frontal lobe. Furthermore, theta power in individuals with MCI exhibited a negative association with DiN performance and MOCA scores.

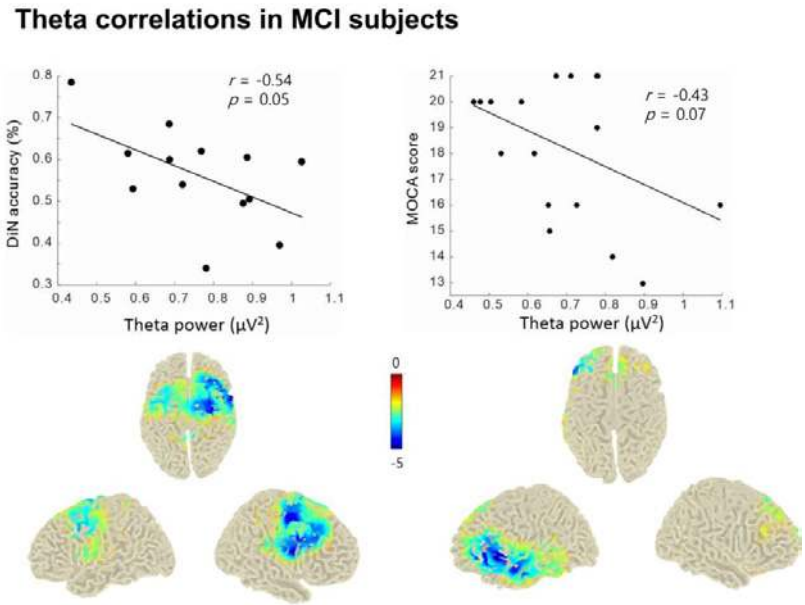

Conclusions: Our findings suggest that the alpha rhythm might function as a neural marker for auditory attention, whereas the theta rhythm seems to be more responsive to cognitive function. Moreover, neural activity during SiN listening demonstrates correlations not just with listening ability but also with cognitive function.

References

1. Caravaglios G, Muscoso EG, Di Maria G, Costanzo E (2013), 'Theta responses are abnormal in mild cognitive impairment: Evidence from analysis of theta event-related synchronization during a temporal expectancy task', Journal of Neural Transmission vol 120, pp. 1093–1107.
2. Dimitrijevic A, Smith ML, Kadis DS, Moore DR (2019), 'Neural indices of listening effort in noisy environments', Scientific reports vol. 9 no. 11278.
3. Gao M, Feng T, Zhao F, Shen J, Zheng Y, Liang J, Yang H (2023), 'Cognitive reserve disorder in age-related hearing loss: Cognitive cortical compensatory to auditory perceptual processing', Cerebral Cortex vol. 33 pp. 9616–9626.
4. Glick HA, Sharma A (2020), 'Cortical Neuroplasticity and Cognitive Function in Early-Stage, Mild-Moderate Hearing Loss: Evidence of Neurocognitive Benefit From Hearing Aid Use', Frontiers in Neuroscience vol. 14 pp. 1–22.
5. Griffiths TD (2023), 'Predicting speech-in-noise ability in normal and impaired hearing based on auditory cognitive measures', Frontiers in Neuroscience vol. 17 pp. 1–6.
6. Powell DS, Oh ES, Reed NS, Lin FR, Deal JA (2022), 'Hearing Loss and Cognition: What We Know and Where We Need to Go' Frontiers in Aging Neuroscience, vol. 13 pp. 1–18.

Poster No 2490

Microstructural changes in the auditory pathway in children with hearing loss

Peter Moon[1], Kristina Ward[1], Alan Cheng[1], Kristen Yeom[1], Iram Ahmad[1]

[1]Stanford University, Palo Alto, CA

Introduction: Early diagnosis of congenital sensorineural hearing loss (SNHL) is of paramount importance in preventing speech and language impairment. Prognostic factors following hearing rehabilitation are yet to be comprehensively standardized. Diffusion tensor imaging (DTI) MRI can identify brain microstructural changes that may potentially contribute towards prognosticating rehabilitation. As no previous study has assessed brainstem regions of the auditory pathway, the goal of our study was to investigate MRI-based microstructural changes along this pathway in pediatric patients with SNHL.

Methods: We retrospectively reviewed pediatric patients with SNHL who obtained DTI MRI between 2011 and 2019, identifying 16 pediatric patients (age <18 years) with at least moderate asymmetric/bilateral SNHL., and gender-matched controls without neurological, developmental, or MRI-based brain macrostructural abnormalities. The following brainstem regions and tracts of the auditory pathway were assessed: superior olivary nucleus (SON), inferior colliculus (IC), ipsilateral tracts between the inferior colliculus and superior olivary nucleus (IC-SON). Diffusion values for bilateral regions and tracts were generated, then averaged to calculate a mean value for fractional anisotropy (FA) and mean diffusivity (MD) for each subject. We performed tractography of the brainstem auditory pathway. We evaluated audiometric outcomes for out patients by evaluating speech reception thresholds on the patients.

Results: Significant differences were identified in FA values of the SON between the SNHL cohort and controls (0.3770.056 vs 0.4220.052; p=0.009). No other FA or MD values were significantly different. In children 5 years, MD was significantly decreased in the SNHL cohort compared to controls in the IC (0.9180.051 vs 1.1200.142; p<0.001). In children >5 years, there were no significant differences in MD (1.1240.198 vs 0.9970.103; p = 0.119). There were no significant differences in MD or FA in the white matter fibers of the IC-SON tract. When evaluating the audiometric findings, we noted a trending relation between speech awareness/recognition thresholds and mean FA SON.

Conclusions: This is the first study to assess microstructural changes in brainstem auditory pathway regions among children with SNHL. We also reconstructed and quantified diffusion along the fiber tracts between the IC and SON. Our results suggest abnormal neural tracts along the central auditory pathway among children with SNHL. Longitudinal studies should assess the prognostic value of these MRI-based findings for assessing long-term outcomes and determining intervention efficacy.

References

1. Moon P, Theruvath J, Chang J, Song Y, Shpanskaya K, Maleki M, Cheng AG, Ahmad IN, Yeom KW. MRI Correlates of Ototoxicity in the Auditory Pathway in Children Treated for Medulloblastoma. Otol Neurotol. 2022 Jan 1;43(1):e97-e104. doi: 10.1097/MAO.0000000000003336. PMID: 34739428.

Poster No 2491

Audiovision: activity in primary visual cortex is driven by musical information

Fernando Bravo[1], Emmanuel Stamatakis[2], Kristina Herfert[1]

[1]University of Tübingen, Tübingen, Germany, [2]University of Cambridge, Cambridge, UK

Introduction: The neuroscientific examination of music processing in audiovisual contexts offers a valuable framework to assess how auditory information influences the emotional encoding of visual information. Although one of the most common harmonic manipulations in film music (e.g., Spielberg's Jaws or Kubrick's The Shining), systematically controlled transformations of musical dissonance have not yet been neuroscientifically studied in regard to affective processing biases in the interpretation of visual contexts. We employed functional magnetic resonance imaging (fMRI) in a naturalistic film-viewing paradigm to investigate the effects of tonal dissonance on the affective processing of visual information.

Methods: During the present fMRI study, thirty-eight subjects watched the same short-film with systematically controlled consonant or dissonant music, in randomized order. Prior to the start of the audio-visual film clip subjects were instructed to "think about the intentions of the main character in the following film clip". Following the clip participants were asked to rate the valence of the movie character's intentions on a scale ranging from one (good intentions) to four (bad intentions). Two control conditions were included; i) visual alone category (i.e., film clip with no soundtrack but same instruction as above) and, ii) film clip with an instruction to describe the "physical" appearance of the character, to control for multimodal sensory processing, working memory and attentional demands of the task, without cueing subjects to attend specifically to mental states (Figure 1). Stimulus material: The stimuli employed in the present study were created for, and tested in two previous experiments (Bravo, 2013; Bravo et al., 2019). To construct the two music conditions, a choral piece was made to sound more or less consonant or dissonant by modifying its harmonic structure (i.e., interval content manipulation) producing two otherwise-identical versions of the same musical piece (Figure 2).

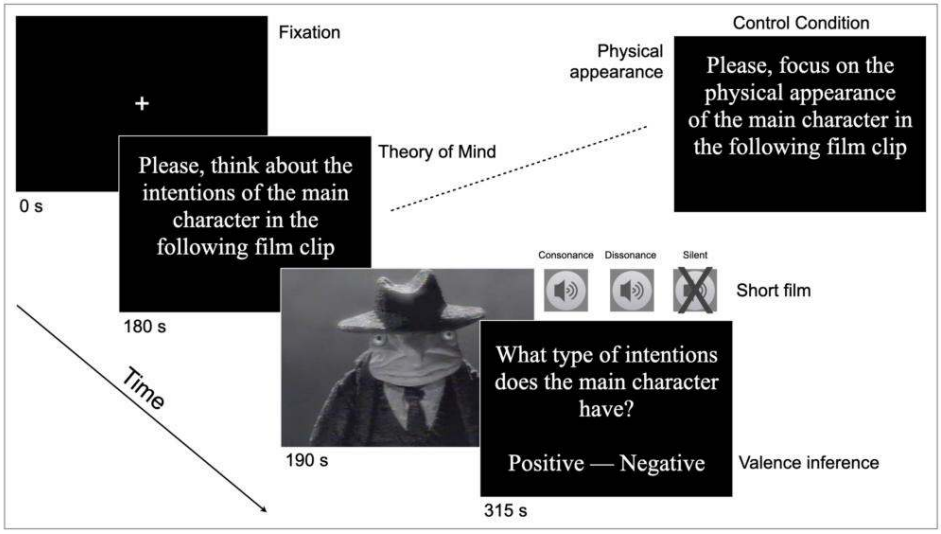

Figure 1. Experimental stimuli and design.

Results: The results showed that increasing levels of dissonance led to more negatively-valenced inferences, displaying the profound emotional impact of musical dissonance. Remarkably, at the neuroscientific level and despite music being the sole manipulation, dissonance evoked the response of the primary visual cortex response (V1). To our knowledge this is the first report of activations encompassing early visual cortices modulated by musical information. The function of the primary visual cortex in visual recognition is known to be strongly modulated by multisensory information (van Atteveldt et al., 2014). In particular, auditory feedback signals are the largest contributor (Murray et al., 2016). To further elucidate why dissonance recruited V1 and to examine potential top-down contextual influences influences on early visual processing, we measured functional and effective connectivity. The results showed a significant coupling between the auditory ventral stream (AVS) (Belin et al., 2000) and V1 in response to tonal dissonance, and demonstrated the modulation of early visual processing via top-down feedback inputs from the AVS to V1.

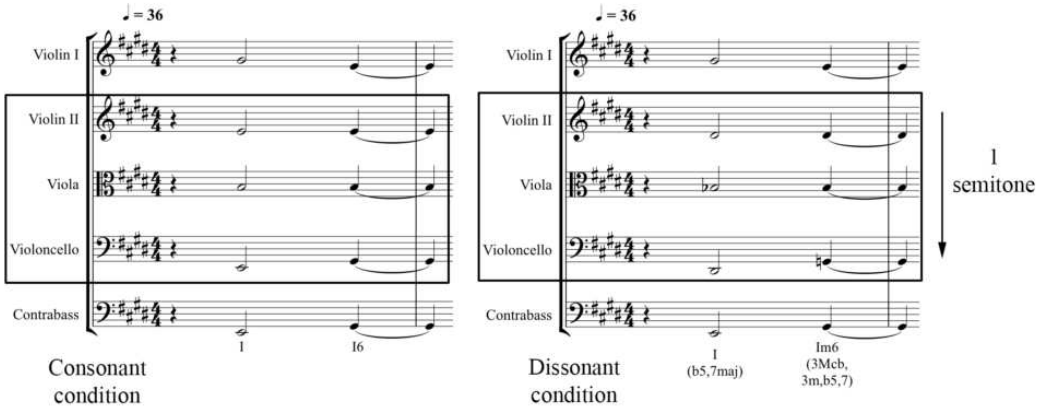

Figure 2. First measure of the consonant (left) and dissonant (right) music conditions.

Conclusions: The present study revealed responses in the primary visual cortex modulated by musical information: tonal dissonance recruited early visual processing via feedback interactions from the auditory ventral pathway to the primary visual cortex. We demonstrated that the auditory "what" ventral stream plays a role in assigning meaning to non-verbal sound cues, such as dissonant music conveying negative emotions, providing an interpretative framework that serves to process the audio-visual experience. Our results highlight the significance of employing systematically controlled music, which can isolate emotional valence from the arousal dimension, to elucidate the brain's sound-to-meaning interface and its distributive crossmodal effects on early visual encoding during naturalistic film viewing.

References

1. Belin, P., Zatorre, R. J., Romanski, L. M., Tian, B., Fritz, J. B., Mishkin, M., Goldman-Rakic, P. S., & Rauschecker, J. P. (2000). "What", "where" and "how" in auditory cortex [2]. Nature Neuroscience, 3(10), 965–966. Scopus. https://doi.org/10.1038/79890
2. Bravo, F. (2013). The Influence of Music on the Emotional Interpretation of Visual Contexts. Designing Interactive Multimedia Tools for Psychological Research. In M. Aramaki, M. Barthet, R. Kronland-Martinet, & S. Ystad (Eds.), From Sounds to Music and Emotions (Vol. 7900, pp. 366–377). Springer Berlin Heidelberg. https://doi.org/10.1007/978-3-642-41248-6_20
3. Bravo, F., Cross, I., Hopkins, C., Gonzalez, N., Docampo, J., Bruno, C., & Stamatakis, E. A. (2019). Anterior cingulate and medial prefrontal cortex response to systematically controlled tonal dissonance during passive music listening. Human Brain Mapping, 41(1). https://doi.org/10.1002/hbm.24786
4. Murray, M. M., Thelen, A., Thut, G., Romei, V., Martuzzi, R., & Matusz, P. J. (2016). The multisensory function of the human primary visual cortex. Neuropsychologia, 83, 161–169. https://doi.org/10.1016/j.neuropsychologia.2015.08.011
5. van Atteveldt, N., Murray, M. M., Thut, G., & Schroeder, C. E. (2014). Multisensory Integration: Flexible Use of General Operations. Neuron, 81(6), 1240–1253. https://doi.org/10.1016/j.neuron.2014.02.044

Poster No 2492

Neural correlates of prediction errors and learning rates during multisensory learning in children

Nina Raduner[1,2,3,4,5], Maya Schneebeli[1], Carmen Providoli[1,3,4,5], Sarah Di Pietro[1,4,5], Saurabh Bedi[6,5], Ella Casimiro[6,5], Nora Raschle[2,5,4], Michael Von Rhein[3,5], Christian Ruff[6,4,5,7], Silvia Brem[1,4,5,7]

[1]Department of Child and Adolescent Psychiatry and Psychotherapy, University Hospital of Psychiatry, Zurich, Switzerland, [2]Jacobs Center for Productive Youth Development, University of Zurich, Zurich, Switzerland, [3]University Children's Hospital Zurich and University of Zurich, Zurich, Switzerland, [4]Neuroscience Center Zurich ZNZ, Zurich, Switzerland, [5]URPP Adaptive Brain Circuits in Development and Learning, University of Zurich, Zurich, Switzerland, [6]Department of Neuroeconomics, University Zurich, Zurich, Switzerland, [7]equal contribution,

Introduction: Living in a multisensory world requires learning to integrate information from different sensory modalities. Multisensory integration is particularly important for language function, as it optimises behaviour by improving processing speed and memory performance[1–3]. From a brain perspective, learning and processing of multisensory information depend on an extended cortico-striato-thalamic network[4]. This study aimed to characterise the dynamics of multisensory learning across sensory modalities in children's brains.

Methods: We collected data from 18 healthy children (14 female, age=9.4±1.9 yrs) performing two audiovisual (AV) and two tactile-visual (TV) runs of a multisensory associative learning task during fMRI (3T). Each run involved learning associations between 4 visual (symbols) and 4 auditory (environmental sounds) or tactile (vibrations) stimuli. A sound or tactile stimulus was

presented with two visual symbols during stimulus presentation. Participants then chose the symbol matching the auditory/tactile stimulus and received feedback on their choice. We used 5 variations of the Rescorla-Wagner model[5] to describe the learning process. Successful parameter recovery on simulated data was only possible for 3 out of the 5 models, which were then used for further analyses. These described learning based on 1) the chosen visual stimuli, 2) the chosen AV/TV pair, and 3) on both presented AV/TV pairs. AIC and BIC of the three models were then compared within each participant. We also compared the best fitting model for AV runs to the best fitting model for TV runs. Further, model outputs (e.g., prediction error (PE) and learning rate) were correlated with the BOLD signal.

Results: Children achieved an overall accuracy of 73% in AV and 66% in TV runs. We observed faster reaction times (RT) and higher accuracies (ACC) towards the end of the runs (ps<.01). Generally, RTs were slower for TV runs compared to AV runs (ps<.001). When comparing the models, model 2 showed the best fit for both AV (BIC=53.3) and TV (BIC=58.0) runs, fitting the data best in 38 runs. Model 3 fitted slightly worse (AV: BIC = 54.7; TV: BIC = 60.2), being the best fit for 28 runs. As expected, activity in sensory areas was found in occipital and temporal regions during AV runs and in occipital and pre- and post-central regions during TV runs. PE modulated brain activity in the bilateral precuneus, parahippocampal gyri, nuclei accumbens, amygdalae and putamen. However, there was no difference in PE processing between AV and TV runs. In addition, the learning rate during stimulus presentation in AV runs covaried with brain activation in the right superior parietal lobule (SPL), right planum temporale (PT) and right central operculum.

Conclusions: Our results of decreasing RTs and increasing ACCs indicate that children in general were able to learn the associations of audio- visual and tactile-visual stimuli despite notable individual differences. During PE processing, expected areas in striatal and hippocampal regions showed increased activity. This suggests that children not only adjusted their knowledge based on the differences between expected and actual outcomes but also that these differences are encoded in their brain . Activation in the SPL and the PT are both linked to attention in relation to visual or auditory processing, respectively (Alahmadi, 2021; Jäncke et al., 2003). Activity in these regions, influenced by the AV learning rate, may reflect how attention is allocated to visual and auditory stimuli. Thus, higher learning rates might correspond to increased attention to auditory and visual cues, leading to more effective learning. To summarise, our findings suggest that our task provides a framework for exploring developmental changes and impairments in multisensory learning and integration.

References

1. Alahmadi, A. A. S. (2021). Investigating the sub-regions of the superior parietal cortex using functional magnetic resonance imaging connectivity. Insights into Imaging, 12(1). https://doi.org/10.1186/s13244-021-00993-9
2. Denervaud, S., Gentaz, E., Matusz, P. J., & Murray, M. M. (2020). Multisensory Gains in Simple Detection Predict Global Cognition in Schoolchildren. Scientific Reports, 10(1), 1394. https://doi.org/10.1038/s41598-020-58329-4
3. Jäncke, L., Specht, K., Shah, J. N., & Hugdahl, K. (2003). Focused attention in a simple dichotic listening task: An fMRI experiment. Cognitive Brain Research, 16(2). https://doi.org/10.1016/S0926-6410(02)00281-1
4. Rescorla, R. A., & Wagner, A. R. (1972). A Theory of Pavlovian Conditioning: Variations in the Effectiveness of Reinforcement and Nonreinforcement. Clasical Conditioning II: Current Research and Theory.
5. Van Den Brink, R. L., Cohen, M. X., Van Der Burg, E., Talsma, D., Vissers, M. E., & Slagter, H. A. (2014). Subcortical, modality-specific pathways contribute to multisensory processing in humans. Cerebral Cortex, 24(8). https://doi.org/10.1093/cercor/bht069

Poster No 2493

Geometrical Features of Neural Trajectory as Computational Motifs for Pain Cue-Stimulus Integration

Jungwoo Kim[1,2,3], Suhwan Gim[1,2], Seng Bum Yoo[1,2], Choong-Wan Woo[1,2,3]

[1]Center for Neuroscience Imaging Research, Institute for Basic Science, South Korea, [2]Department of Biomedical Engineering, Sungkyunkwan University, South Korea, [3]Department of Intelligent Precision Healthcare Convergence, Sungkyunkwan University, South Korea

Introduction: The brain integrates information from pain-predictive cues and noxious inputs to construct pain (Wiech, K, 2016). While previous studies have identified the neural correlates of individual pain components, the computational mechanisms of their integration remain elusive. Here, we used human fMRI to investigate neural trajectories within subspaces that preserve cue and stimulus information in network regions. We utilized the geometrical features of these trajectories to elucidate how the brain preserves and integrates information about pain components. We also explored the integration mechanism in large-scale networks aligned at the cortical hierarchy (Margulies et al, 2016), investigating whether progressive integration occurs from unimodal networks to transmodal networks. Our results show that while all networks preserve information about individual pain components in their respective subspaces, only the transmodal networks integrate it through the linear summation of information from subspaces.

Methods: In the fMRI scanner, we presented 56 participants with a 2-second visual pain-predictive cue (high, low, and no pain cue), followed by a heat stimulation at one of five intensity levels for 12.5 seconds (Fig. 1a). Participants then rated their pain experience. Using temporal fMRI data during participants' pain experiences, we applied targeted dimensionality reduction (Mante et al, 2013) to separate the subspace accounting for cue and stimulus information in each network region (Fig. 1f). We then projected the data onto each subspace and measured the distance between the neural trajectories of pain conditions. We used it to measure how well the subspace encodes the corresponding information (Fig. 1d, g) through a generalized linear model fit. We also calculated cue and stimulus effects by subtracting the encoding performances of the null subspace from the encoding performances of the subspace of interest to assess their significance. (Fig. 1d). We then linearly summed the distance information from each subspace and compared it with actual pain ratings (Fig. 1e) to investigate whether the network integrates the two types of information. Given the different scales for reconstructed and actual pain reports, we normalized the values after subtracting the middle condition value (i.e., the condition of no cue with stimulus intensity level 3) and dividing them by their variance. We measured the reconstruction fit by calculating the absolute difference between the two.

Results: Among the possible behavioral results (Fig. 1b), our behavioral results support the case of cue-stimulus integration, as evidenced by the significant effects of both the cue and stimulus intensity on the pain ratings (Fig. 1c). For the encoding performances of the subspaces, all seven large-scale networks exhibited significant cue and stimulus effects (Fig. 2a), implying that all network regions preserve both types of information in their respective subspaces. Example low-dimensional trajectories of the visual network and the limbic network are shown in Figs. 2b and c, respectively, from which the encoding performances were calculated. The linear summation of the distance measures from each subspace (Fig. 2d) indicated that the transmodal networks (the frontoparietal, limbic, and default networks) showed significant reconstruction fit (Figs. 2g-j), while the unimodal networks (the visual and somatomotor networks) did not (Figs. 2e-f, j), implying that only the transmodal networks integrate the information.

Conclusions: We have shown that all networks preserve information about pain expectations and noxious inputs. However, integration occurs only within the transmodal networks, through the linear summation of the information from each subspace. We demonstrated how distances between neural trajectories in networks' subspaces encode information about different pain components and could serve as a computational motif for eliciting actual pain behavior.

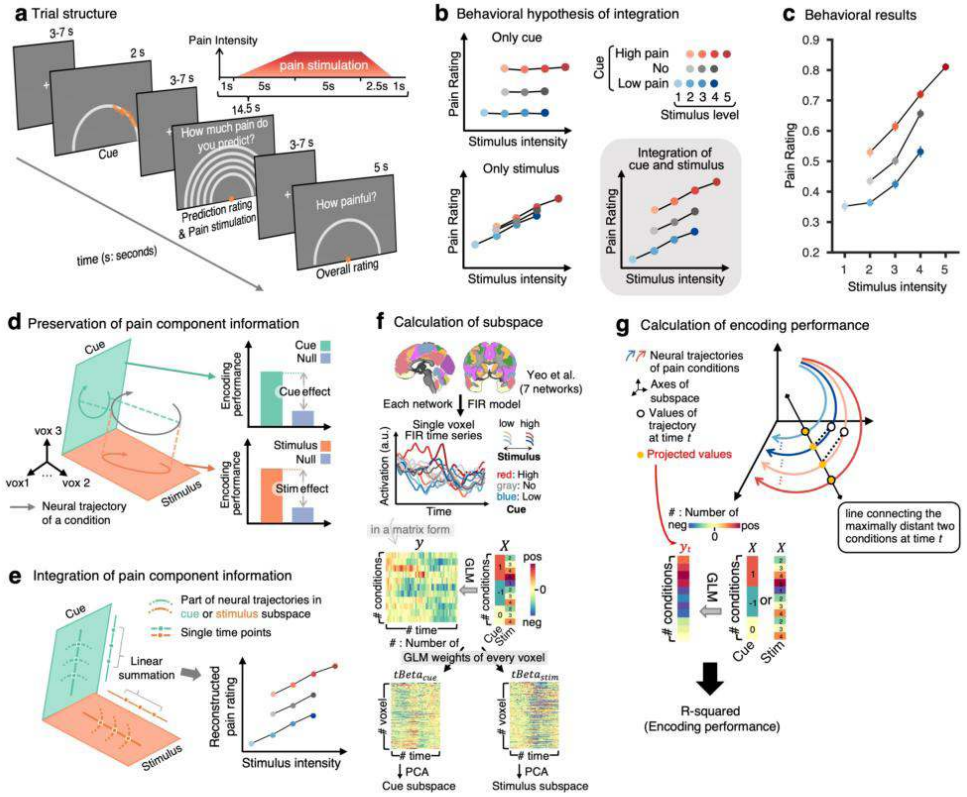

Figure 1. **(a)** The trial structure of the cue-induced pain modulation task. Participants were informed that the orange dots during the cue period represented pain ratings from 25 participants who previously participated in the experiment, serving as pain-predictive cues based on social information. After a few seconds of delay, a pain stimulus was administered for 12.5 seconds, followed by participants' reporting of how painful the overall stimulus was. **(b)** Hypothetical cases of behavioral results. **(c)** The average pain rating by subjects. **(d)** The schematic of information preservation through subspace formation. We assumed that cue and stimulus information is preserved in separate subspaces representing each and calculated encoding performance to quantify its extent. **(e)** The schematic of information integration. The straight lines and dots in the subspace represent distance between neural trajectories, calculated with the same procedure as **(g)**. We formalized the integration as a linear summation and validated it by comparing it with participants' pain reports. **(f)** Calculation of pain component subspaces. Temporal activations were regressed on cue and stimulus information, resulting in temporal GLM weights for each. Principal axes were then obtained to yield cue and stimulus subspaces. **(g)** Temporal activations projected onto cue and stimulus subspaces results in neural trajectories represented by colored lines. Using the two most distant conditions at a single time point, we obtained a one-dimensional vector depicted as yellow dots, encoding distance information between trajectories. We used it to calculate encoding performances and reconstruction fits of pain reports.

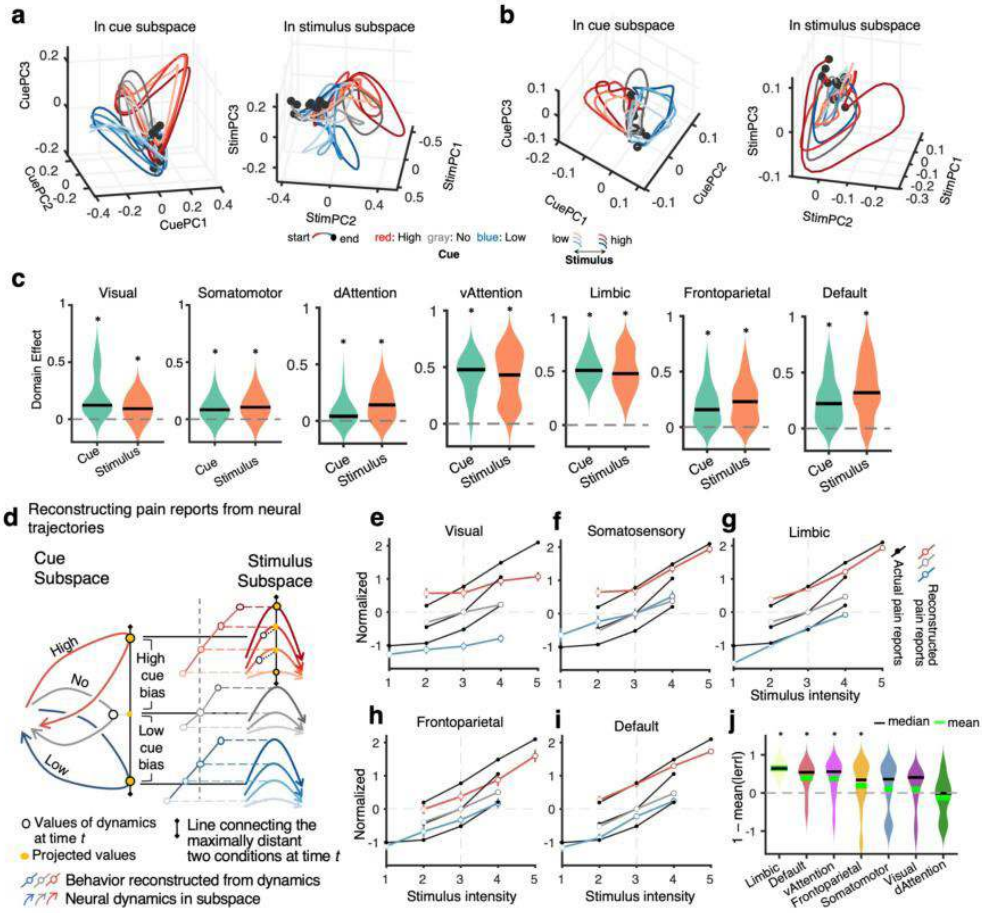

Figure 2. (a) Neural trajectories in the visual network. The left panel displays neural trajectories in the cue subspace, while the right panel shows neural trajectories in the stimulus subspace. **(b)** Neural trajectories in the limbic network. Panel order and displayed information are consistent with **(a)**. **(c)** Domain effects (i.e., cue and stimulus effects) in all seven large-scale networks. The asterisk indicates statistical significance (one-sample *t*-test, $df = 48$, $p < 1e\text{-}5$, two-tailed). **(d)** The schematic of information integration through linear summation. **(e-f)** Reconstructed pain reports and actual pain reports in unimodal networks. The colored (red, blue, and gray) lines indicate reconstructed reports from distances of neural trajectories, and black lines indicate averaged pain reports from participants. **(g-i)** Reconstructed pain reports and actual pain reports in the trasmodal networks. **(j)** Reconstruction fits of all networks. These were calculated by the absolute difference between actual pain reports and reconstructed reports for every time point. The asterisks indicate statistical significance. (one-sample *t*-test, $df = 48$, $p < 0.05$, two-tailed)

References

1. Wiech K., (2016), 'Deconstructing the sensation of pain: The influence of cognitive processes on pain perception', Science, 354(6312), 584–587.
2. Margulies et al., (2016), 'Situating the default-mode network along a principal gradient of macroscale cortical organization', Proceedings of the National Academy of Sciences, 113(44), 12574-12579.
3. Mante et al., (2013). 'Context-dependent computation by recurrent dynamics in prefrontal cortex', Nature, 503(7474),

Poster No 2494

Audiovisual integration during motion adaptation modulates brain activity in the early visual cortex

Minsun Park[1], Ghootae Kim[2], Chai-Youn Kim[1]

[1]Korea University, Seoul, Republic of Korea, [2]Cognitive Science Research Group, Korea Brain Research Institute, Seoul, Republic of Korea

Introduction: Recent neuroscientific findings challenge the traditional notion of the independence of unimodal sensory cortices (e.g., V1 for vision, A1 for audition) in multisensory integration. Studies, particularly on audio-visual (AV) interactions, demonstrated cross-modal processing, where auditory stimuli alone activated the visual cortex (Poirier et al., 2006), and various auditory information was decoded from the neural patterns in the visual cortex (Rezk et al., 2020; Vetter et al., 2020). Despite potential AV interaction through the visual cortex, a more direct assessment is still required, as sound and vision were not concurrently presented in these studies. In our study, we investigated whether integration of simultaneous AV signals modulate neural activity in the early visual areas. Our previous psychophysical works (Park et al., 2019; under review) utilizing

the motion aftereffect (MAE; Mather, 1980) showed an AV direction congruence effect, i.e., enhanced visual MAE when visual adapting motion was accompanied by directionally congruent auditory motion compared to incongruent auditory motion. Using fMRI, we probed the neural basis of such congruence effect by testing whether AV direction congruence in V1 and V2 areas is decoded through multi-voxel pattern analysis (MVPA).

Methods: Nineteen naïve individuals (24.09 ± 3.38 years) participated in an fMRI experiment (Siemens, 3T). Across 16 runs of the main experiment, adaptation and MAE phases were presented 8 times per run. During the adaptation phases (36 s initially and 12 s thereafter), the MAE was elicited by the 100%-coherence random-dot kinematograms (RDKs) moving leftward or rightward. Sound motions with the leftward or rightward direction were simulated by modulating white noise intensity presented between binaural channels of noise-canceling headphones. There were four sound conditions: congruent and incongruent conditions based on AV direction congruence, along with stationary and no-sound conditions. In the following 4-s MAE phase, participants reported the MAE duration and direction while viewing stationary RDKs. Using retinotopy and visual direction localizers, we identified a subset of motion-sensitive voxels in V1 and V2 (Figure 1a). Employing multi-class SVM, we performed MVPA to discriminate the four sound conditions for each adaptation and MAE phase. Whole-brain searchlight analysis was conducted to elucidate any regional specificity in patterns based on the sound conditions.

Results: Behavioral results replicated our previous finding, indicating a longer MAE duration in the congruent condition compared to the incongruent condition (Figure 1b). Univariate fMRI results mirrored this congruence effect, showing greater signal changes in V1 and V2 during adaptation in the congruent condition (Figure 1c), whereas no significant differences in signal changes during MAE. Notably, AV direction congruence could be reliably classified from neural patterns in V1 and V2, even in the absence of physical motion (i.e., MAE phase) as well as in the adaptation phase (Figure 1d). Whole-brain searchlight results identified a large part of bilateral superior temporal area including A1, transverse temporal gyrus, and insula during both phases (Figure 2).

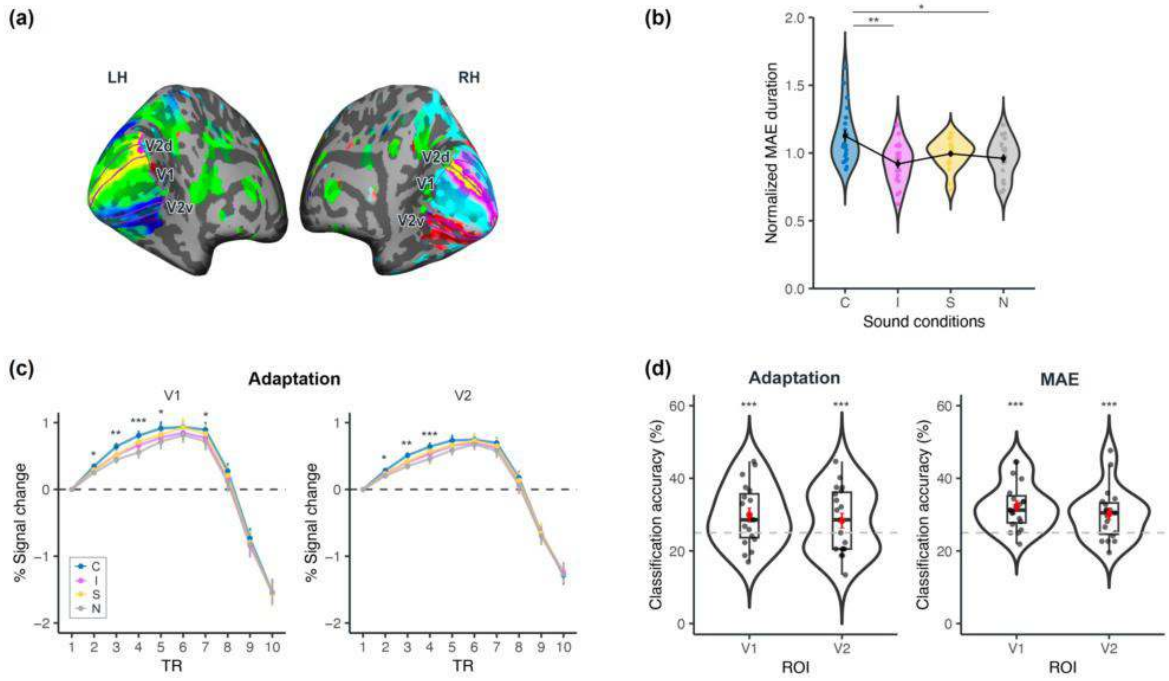

Figure 1. Behavioral and fMRI results. (a) Individually defined bilateral V1 and V2 of one representative participant. (b) Effect of AV direction congruency during adaptation on the duration of resulting visual MAE. Violin plots illustrate the estimated distributions of normalized MAE durations in each sound condition (congruent, C; incongruent, I; stationary, S; no-sound, N). Colored dots represent the individual normalized MAE duration, and the black dots represent the group means in each condition. Error bars show the standard error of the mean (SEM). Asterisks show the statistical significance of the post-hoc paired *t*-test (*FDR* corrected, * $p < .05$, ** $p < .01$). (c) Effect of AV direction congruency on the percentage of signal changes by TRs in each ROI during adaptation. Dots indicate the mean of individual %signal change. Error bars show the SEM. Asterisks show the statistical significance of the one-way ANOVA (*FDR* corrected, * $p < .05$, ** $p < .01$, *** $p < .001$). (d) Violin plots illustrate the estimated distributions of individual classification accuracy during adaptation (left panel) and MAE (right panel) phases in each ROI. Gray dots represent the individual classification accuracy. The middle and horizontal lines on the box plots indicate the median and the lower and upper ends of the box indicate the first and third quartiles. Red dots indicate the mean, and error bars show the SEM. Asterisks show the statistical significance of the non-parametric statistical testing with a 25% chance level (*** $p < .001$).

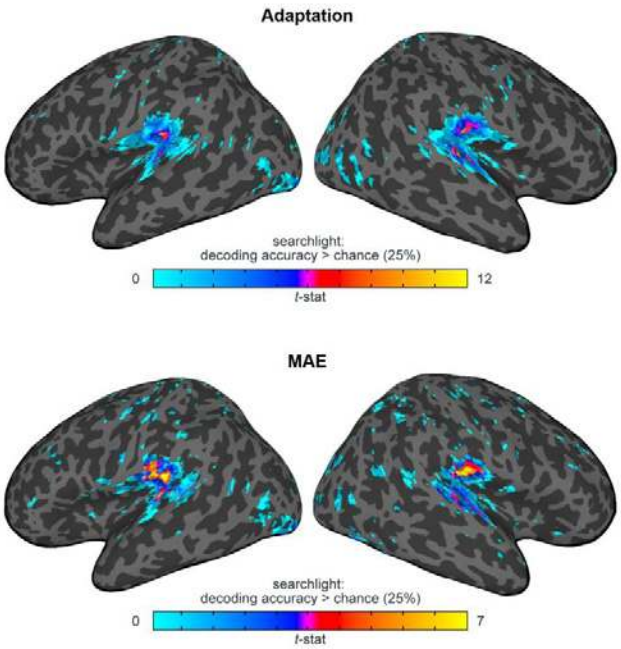

Figure 2. Results of the searchlight analysis. T-stat maps for decoding accuracy to discriminate the four sound conditions are shown for each adaptation (upper panel) and MAE (lower panel) phase. Significant clusters were identified in the statistical map at q-value < .05 (*FDR* corrected). Color indicates the level of t-value of a one-sample t-test if the decoding accuracy is above the chance level of 25%.

Conclusions: Our results suggest neural mechanisms underlying the AV congruence effect observed by MAE duration, demonstrating distinct neural patterns in the early visual cortex depending on AV integration. Searchlight findings suggest that neural signatures in V1 and V2, linked to AV congruence, may originate from feedback influences from higher-order multisensory areas such as STS and insula. The present work adds to the understanding of neural mechanisms governing cross-modal interactions within the retinotopic areas, offering direct examination of AV integration.

References

1. Mather, G. (1980). The movement aftereffect and a distribution-shift model for coding the direction of visual movement. Perception, 9, 379-392.
2. Park, M. Blake, R., & Kim, C. Y. (Under review). Audio-visual interactions outside of visual awareness during motion adaptation.
3. Park, M., Blake, R., Kim, Y., & Kim, C. Y. (2019). Congruent audio-visual stimulation during adaptation modulates the subsequently experienced visual motion aftereffect. Scientific Reports, 9(1), 1-11.
4. Poirier, C., Collignon, O., Scheiber, C., Renier, L., Vanlierde, A., Tranduy, D., Veraart, C., & de Volder, A. G. (2006). Auditory motion perception activates visual motion areas in early blind subjects. Neuroimage, 31, 279–285.
5. Rezk, M., Cattoir, S., Battal, C., Occelli, V., Mattioni, S., & Collignon, O. (2020). Shared representation of visual and auditory motion directions in the human middle-temporal cortex. Current Biology, 30(12), 2289-2299.
6. Vetter, P., Bola, Ł., Reich, L., Bennett, M., Muckli, L., & Amedi, A. (2020). Decoding natural sounds in early “visual” cortex of congenitally blind individuals. Current Biology, 30(15), 3039-3044.

Poster No 2495

Decoding sound-symbolic words in visual cortex

Stefano Ioannucci[1], Carole Jordan[2], Anne-Sophie Carnet[2], Carolyn McGettigan[3], Petra Vetter[2]

[1]University of Fribourg, Fribourg, Switzerland, [2]Visual and Cognitive Neuroscience Lab, University of Fribourg., Fribourg, Switzerland, [3]UCL Speech Hearing and Phonetic Sciences, University College London, London, United Kingdom

Introduction: Sound symbolism, also called the “bouba-kiki effect” is a fascinating phenomenon in psychology that demonstrates a non-arbitrary association between meaningless speech sounds and visual shapes. For example, participants routinely tend to associate rounded, curvy shapes with the word “bouba” and jagged, angular shapes with the word “kiki” (Lockwood & Dingemanse, 2015; Ramachandran & Hubbard, 2001). This suggests that there is a cross-modal association between certain speech sounds and specific visual characteristics. However, despite a long tradition of behavioral experiments manifesting the effect of sound symbolism, evidence for its neural correlates in the human brain is still sparse (Peiffer-Smadja & Cohen, 2019; Revill et al., 2014). Given that early visual cortex has been shown to respond to auditory

stimuli in a selective and content-specific way (Vetter et al., 2014, 2020), we sought to build upon these two separate lines of research to assess if visual cortices implicated in the processing of visual shape are sensible to the implicit shape conveyed by sound symbolic speech sounds. We hypothesized that sound-symbolic cross-modal shape associations should result in distinguishable neural activity patterns in the visual cortex, particularly in shape-selective brain regions.

Methods: We acquired 3T fMRI BOLD signals from 8 healthy adult participants while they were blindfolded and listened to a set of sound symbolic words (rounded, spiky and mixed). Participants' task was to categorize the associated visual shape of words (more spiky or more round on a 4-point scale). After standard fMRI pre-processing, we extracted beta weights from anatomically defined visual regions of interest (V1, V2, V3 and LOC). A within-subject multi-variate pattern classification analysis (MVPA) was then carried out with chance level and null distribution empirically generated via label permutation, to assess whether different sound-symbolic word categories were represented with differential neural activity patterns in our visual regions of interest.

Results: Behavioral results showed that we could replicate the "bouba-kiki" effect inside the MRI scanner, i.e. "rounded" words were judged as being associated more often with rounded shapes than "spiky" words, and vice versa. Preliminary fMRI data analyses indicate that it is possible to successfully decode sounds judged as "round" or "spiky" based on fMRI activity within visual cortical regions of interest in 5 out of 8 participants, indicating an expected Maximum A Posteriori effect size point estimate (Ince et al., 2021) of 68% as the most likely value for the general population parameter.

Conclusions: Our preliminary results show that sound symbolic words entailing a visual shape association can be decoded from fMRI activity patterns in early visual and shape selective cortical regions, even in the absence of visual stimulation. The present results provide evidence that the visual cortex can represent information from speech, even when it consists of meaningless non-words, as long as these words have a visual shape association. This supports the notion that sound symbolism may be a true effect of sensory and cross-modal association in the human brain rather than a linguistic epiphenomenon. Furthermore, our results add to the existing evidence that visual brain regions do not just process visual feed-forward information but are also sensitive to top-down, high-level auditory information. How fine-tuned the visual cortex is to different characteristics of auditory stimuli, revealing the depth of audiovisual interactions in the visual cortex, still remains to be explored.

References

1. Ince, R. A., Paton, A. T., Kay, J. W., & Schyns, P. G. (2021). Bayesian inference of population prevalence. eLife, 10, e62461. https://doi.org/10.7554/eLife.62461
2. Lockwood, G., & Dingemanse, M. (2015). Iconicity in the lab: A review of behavioral, developmental, and neuroimaging research into sound-symbolism. Frontiers in Psychology, 6, 1246. https://doi.org/10.3389/fpsyg.2015.01246
3. Peiffer-Smadja, N., & Cohen, L. (2019). The cerebral bases of the bouba-kiki effect. NeuroImage, 186, 679–689. https://doi.org/10.1016/j.neuroimage.2018.11.033
4. Ramachandran, V. S., & Hubbard, E. M. (2001). Synaesthesia—A window into perception, thought and language. Journal of Consciousness Studies, 8(12), 3–34.
5. Revill, K. P., Namy, L. L., DeFife, L. C., & Nygaard, L. C. (2014). Cross-linguistic sound symbolism and crossmodal correspondence: Evidence from fMRI and DTI. Brain and Language, 128(1), 18–24. https://doi.org/10.1016/j.bandl.2013.11.002
6. Vetter, P., Bola, Ł., Reich, L., Bennett, M., Muckli, L., & Amedi, A. (2020). Decoding Natural Sounds in Early "Visual" Cortex of Congenitally Blind Individuals. Current Biology, 30(15), 3039-3044.e2. https://doi.org/10.1016/j.cub.2020.05.071
7. Vetter, P., Smith, F. W., & Muckli, L. (2014). Decoding Sound and Imagery Content in Early Visual Cortex. Current Biology, 24(11), 1256–1262. https://doi.org/10.1016/j.cub.2014.04.020

Poster No 2496

Dissociable laminar profile of "what" and "when" predictions in the human auditory cortex

Caspar Schwiedrzik[1], Ryszard Auksztulewicz[2], Daniel Fabo[3], Johanna Szabo[3], Istvan Ulbert[3], Wittner Lucia[3], Thomas Thesen[4], Werner Doyle[5], Orrin Devinsky[5], Lucia Melloni[6]

[1]European Neuroscience Institute, Göttingen, Germany, [2]Freie Universität Berlin, Berlin, Berlin, [3]National Institute of Mental Health, Neurology and Neurosurgery, Budapest, Hungary, [4]New York University Comprehensive Epilepsy Center, New York, NY, USA, [5]New York University School of Medicine, New York, NY, USA, [6]Max Planck Institute for Empirical Aesthetics, Frankfurt am Main, Germany

Introduction: Predictions based on statistical regularities in the environment are fundamental for adaptive behaviour. However, while predictions of different stimulus features may facilitate sensory processing, they are likely mediated by dissociable neural mechanisms. In previous work [Auksztulewicz et al., 2018], based on direct electrophysiological recordings from the cortical surface in humans, we could elucidate the dissociable neural mechanisms of predicting the contents ("what") and timing ("when") of auditory stimuli. While some (e.g., frontal and premotor) cortical regions were preferentially modulated

by either “what” or “when” predictability, the superior temporal gyrus (STG), a higher-order auditory region, integrated predictability of both stimulus features. A Bayesian model fitted to the empirical data suggested that “what” and “when” predictability can be linked to complementary gain modulation mechanisms in the STG.

Methods: Here, we tested whether these functional dissociations can be mapped onto different laminar activity profiles in the STG. We analysed local field potentials (LFPs) and broadband activity recorded invasively from the STG using laminar probes. Recordings were conducted in five patients with pharmacologically intractable epilepsy undergoing surgical monitoring. Patients were asked to perform a speeded categorisation task on auditory syllables preceded by visual stimuli, allowing for a formation of “what” and/or “when” predictability (Fig. 1A). The laminar probes spanned the entire cortical sheet and signals were realigned across patients using the current source density profiles of auditory-evoked activity (Fig. 1B).

Results: “What” and “when” predictability was linked to dissociable laminar profiles of activity in the STG (Fig. 1C). Specifically, predictability of stimulus contents modulated activity in both supragranular and infragranular layers (receiving projections from higher-order regions), consistent with a recent study in macaque monkeys [Lakatos et al., 2020]. Predictability of stimulus timing had a more selective effect on infragranular layers, suggesting a partial laminar dissociation between the two types of predictions. Conversely, both types of predictions interactively modulated neural activity in infragranular layers but also in granular layers (receiving projections from lower-order regions), corroborating earlier theoretical proposals of how “what” and “when” predictions may be integrated in the cortex [Musacchia et al., 2014].

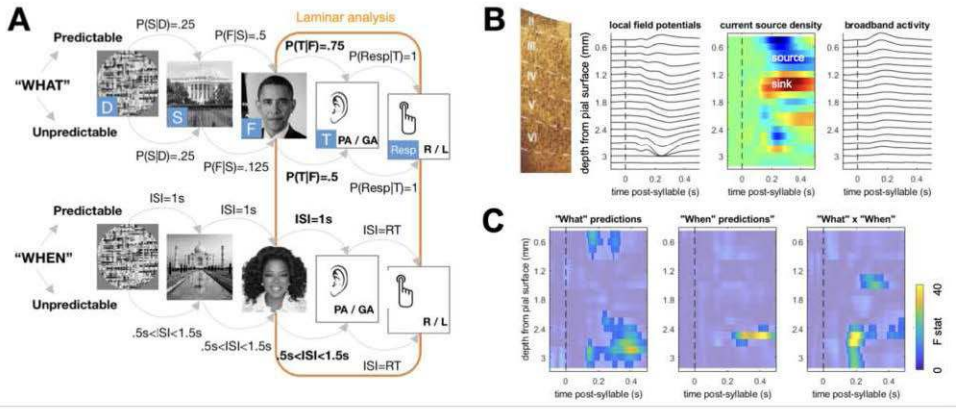

Figure 1. (A) Patients viewed a sequence of images, enabling them to form “what” and/or ”when” predictions of auditory syllables. **(B)** Laminar profiles of syllable-evoked STG responses mapped onto supragranular (II/III), granular (IV), and infragranular (V/VI) layers. **(C)** LFP profiles differentiated between the main effects of “what” predictability (left), “when” predictability (middle), and their interaction (right panel), suggesting their partial dissociation in terms of layer-specific activity.

Conclusions: Taken together, our results provide direct evidence for functional dissociations between different types of predictability in terms of their effects on cortical microcircuits.

References

1. Auksztulewicz, R., et al. (2018), ‘Not All Predictions Are Equal: “What” and “When” Predictions Modulate Activity in Auditory Cortex through Different Mechanisms’, Journal of Neuroscience, vol. 38, no. 40, pp. 8680-8693
2. Lakatos, P., et al. (2020), ‘The Thalamocortical Circuit of Auditory Mismatch Negativity’, Biological Psychiatry, vol. 87, no. 8, pp. 770-780
3. Musacchia, G., et al. (2014), ‘Thalamocortical mechanisms for integrating musical tone and rhythm’, Hearing Research, vol. 308, pp. 50-59

Poster No 2497

Spontaneous beta bursts shape HEP and somatosensory perception with opposing directions

Juanli Zhang[1], Paul Steinfath[1], Carina Forster[1], Christian Sander[2], Tilman Hensch[2], Ulrich Hegerl[3], Georg Schomerus[2], Veronica Witte[1], Arno Villringer[1], Vadim Nikulin[1]

[1]Max Planck Institute for Human Cognitive and Brain Sciences, Leipzig, Saxony, [2]University of Leipzig Medical Center, Leipzig, Saxony, [3]Goethe University, Frankfurt am Main, Hesse

Introduction: Large-scale ongoing brain activity, with oscillations being primarily generated in alpha and beta frequencies, has been consistently shown to shape the neural responses to external stimuli and thus affecting perceptual performance. While a

large body of studies focused on the amplitude of prestimulus activity, a few studies further showed that temporal dynamics, particularly reflected in transient beta events, could mask the perception of somatosensory stimuli (Shin et al., 2017; Karvat et al., 2021). However, the influence of transient beta events on interoception remains unexplored. In our study we investigated how spontaneous beta activity shapes interoception, particularly cardiac interoception. To this end, heartbeat evoked potential (HEP), an electrophysiological marker for processing cardiac information, was used to index cardiac interoception.

Methods: First, we attempted to replicate the previous findings relating prestimulus beta activity to the perception of somatosensory stimuli based on an independent dataset (N=40). Next, we analyzed a dataset based on a large-cohort study of the Leipzig Research Centre for Civilization Diseases (LIFE, N=~3000 participants). The participants underwent 20 minutes resting state EEG recording. By applying strict exclusion criteria for the elderly participants, the final sample includes 1466 healthy elderly subjects (age of 75.66±2.8 years, 680 females).

Results: We showed, in line with the previous studies, that 1) stronger beta activity, in the form of higher mean power (cluster-based permutation test in channel-time domain, p=9.995e-04) with the most pronounced effect at centro-parietal region, 2) longer burst duration (p=0.002) over the fronto-central area and 3) bursts occurring closer to the stimulus onset (p=0.032) over the right central region, were observed in undetected (Miss) compared to detected (Hit) trials. These results thus further confirmed a robust influence of spontaneous transient beta events on the exteroception in somatosensory domain. Additionally, we obtained HEP from LIFE dataset, and found that prestimulus (here “stimulus” is referred to the R peak in each cardiac cycle) beta activity positively shapes the brain’s response to heartbeat. More specifically, 1) stronger beta power (p=0.002) over bilateral centro-parietal region, 2) longer burst duration (p=0.002) over bilateral central area or 3) closer beta events (p=0.002) over frontal and parietal regions during the prestimulus time window corresponds to a larger amplitude of HEP. Crucially, we demonstrated that these effects are significantly locked to the R peaks, and are not attributed to the volume conducted cardiac field artifacts, leakage from the possibly sustained effect from the previous heartbeat, or due to the splitting procedure. Lastly, the prestimulus alpha power was also examined for both somatosensory perception task and cardiac interoception: stronger alpha power corresponds to weaker perception and lower HEP.

Conclusions: In sum, in addition to providing further support for the finding that beta bursting activity masks the perception of external stimuli, our study suggests its opposite influence on the cardiac interoception. A general suppressing role of spontaneous alpha activity on both exteroception and interocpetion might be consistent with the hypothesis that stronger alpha activity is related to a lower level of excitability. Moreover, divergent roles of spontaneous beta activity on sensory perception may well fit into a proposal that beta activity may be associated with the expectation of the external stimuli, together with the account that processing the internal and external stimuli information might be through distinct time windows (and probably related “brain states”) which could be optimal for one and in turn not for the other. Future research should focus on paradigms where external and internal stimuli are jointly presented and the reciprocal effect of transient beta activity could be investigated.

References

1. Karvat, G. (2021), ‘Spontaneous activity competes with externally evoked responses in sensory cortex’, Proc. Natl. Acad. Sci., USA 118
2. Shin, H. (2017), ‘The rate of transient beta frequency events predicts behavior across tasks and species’, eLife, 6:e29086

Poster No 2498

Heritability of movie-evoked brain activity and connectivity

David Gruskin[1], Gaurav Patel[1]

[1]*Columbia University, New York, NY*

Introduction: To what extent do our genes shape how we process movies? Studies involving retinotopic and task-free paradigms have established that various aspects of sensory-relevant brain function are under genetic control. However, the extent to which inherited genetic factors underlie individuals’ brain responses to complex audiovisual stimuli is still unclear. Additionally, recent work suggests that individual differences in fMRI activity and connectivity patterns are partially driven by lower-level features like functional topography (Haxby et al., 2020), but the extent to which the heritability of these high-dimensional patterns is driven by heritability of stimulus processing vs. functional topography is largely unknown. Here, we address these knowledge gaps by applying multidimensional heritability analyses to movie-watching and resting state 7T fMRI data from the Human Connectome Project (HCP).

Methods: Analyses were performed on fMRI data from the 176 subjects (including 50 monozygotic and 33 dizygotic twin pairs) who completed two hours of resting state and movie-watching runs across two days as part of the HCP Young Adult

7T release (Van Essen et al., 2013) following denoising with ICA-FIX and global signal regression. We used intersubject correlation (ISC) to measure vertex-level BOLD time course similarity between all pairs of participants and applied a multidimensional heritability analysis (Anderson et al., 2021) controlling for age, sex, and head motion to these ISC values to quantify BOLD time course heritability (h^2). To measure functional connectivity (FC) similarity across participants, we generated resting state and movie-watching FC matrices for each participant and each day of data collection by correlating time courses extracted from 400 Schaefer atlas parcels and then correlating FC profiles for each combination of 17 resting state networks (Schaefer et al., 2018). The resulting FC similarity values were then submitted to the multidimensional heritability analysis to estimate FC profile heritability. To quantify the extent to which this heritability is driven by genetic similarity in functional topography ("where" stimuli are processed) vs. stimulus processing ("how" stimuli are processed), we functionally aligned data from all subjects using both connectivity and response hyperalignment and repeated the ISC and FC heritability analyses on the aligned data. Importantly, we performed this alignment at multiple spatial resolutions to estimate point spread functions of heritable functional topographies.

Results: Vertex-level BOLD time courses were heritable across most of the cortex (max h^2 = .12, 65% of vertices heritable at FDR-corrected P<.05), especially in auditory and visual regions, and spatial heritability patterns were consistent across days of data collection (r = .94, Pspin<.001). Similarly, movie-watching FC profiles were heritable within and between all networks (avg. h^2 = .34, all network combinations heritable at FDR-corrected P<.05), and FC profile heritability was higher for sensory networks during movie-watching compared to rest. Movie-watching FC profile heritability patterns were also consistent across days of data collection (r = .96, P<.001). Following response and connectivity hyperalignment, activity and connectivity h^2 values were reduced across vertices and networks, especially for sensory regions. Activity h^2 decreased exponentially with hyperalignment resolution, and response hyperalignment at the coarsest spatial resolution decreased activity h^2 by 48% across the cortex.

Conclusions: Taken together, these results demonstrate the power of using ecologically rich stimuli to study the heritability of sensory processing in cortex. Specifically, these results establish that heritable brain responses to audiovisual stimuli reflect genetic control over multiple independent aspects of brain function, including both "where" vs. "how" information is processed.

Poster No 2499

Testing the Mediating Role of the Nucleus Accembens in Musically-Induced Hypoalgesia

Elise Desbarats[1], Mathieu Roy[1], Taryn Berman[1]

[1]McGill University, Montreal, Quebec

Introduction: Preferred music, particularly music that elicits the pleasurable musical chills response, has been shown to be the most effective type of music for pain relief (Garza-Villarreal et al., 2017; Valevicius et al., 2023). However, we lack an understanding of the specific mechanisms underlying this effect. Given that positive emotions elicited by music are influenced by the mesolimbic reward system (Mas-Herrero et al., 2021), activity in this system can serve as a potential mediator for the impact of music on pain. Specifically, activity in the nucleus accumbens (NAcc), predicts how enjoyable we find music to be, as well as the occurrence of musical chills (Salimpoor et al., 2011). Significantly, the NAcc is also an essential component of pain processing, appearing in a neurosignature that tracks subjective responses to pain (Woo et al., 2017). We present preliminary neuroimaging and behavioral results from a study aiming to investigate the role of musical pleasure and NAcc activity elicited by self-selected preferred music in determining musically-induced hypoalgesia.

Methods: 12 participants (%F = 92, M = 19) provided four pieces of music they find extremely pleasurable to listen to. First, participants listened to their self-selected music and control versions of those songs while giving continuous pleasure ratings. Auditory controls consisted of silence conditions and scrambled music, created by splitting the excerpts into two-second segments and randomizing their order. This method controls for the acoustic features of musical stimuli (eg. tonality, timbre) while disrupting musical structures that can contribute to enjoyment of the music. Participants then underwent a sensory calibration procedure to assess their pain tolerance. They then performed a music-listening task in an MRI scanner where they listened to 20 excerpts, each lasting 180s. Pleasurable music and control stimuli were presented once with four 8-second thermal pain stimulations and once without. Participants rated the pain of these stimulations and their enjoyment of each excerpt on scales of 0-100. High resolution T1-weighted structural images and whole-brain fMRI data (TR = 867ms, TE = 27.2 ms) were gathered on a 3T Siemens Prisma scanner. We assessed descriptive statistics of pain and enjoyment ratings and compared neural activation during pain stimulations in each condition.

Results: Preliminary behavioral data (n = 12) demonstrates that participants enjoyed listening to their favorite songs in the MRI scanner (M = 81.53, SD = 12.58), and that enjoyment ratings decreased significantly by an average of 43 points between scrambled and music conditions (t(190)= -17.60, p < .01, d = -2.54). Concurrent with previous studies, pain stimulations in the music condition (M = 50.73, SD = 13.65) were rated on average as 2.81 points less painful than pain stimulations paired with scrambled music (M = 53.54, SD = 16.59), and 4.23 points less painful than stimulations paired with silence (M = 54.96, SD = 17.06). Preliminary neuroimaging data (n = 8) showed that activation was higher in the left nucleus accumbens during pain stimulations in music conditions than during stimulations delivered in silence (t = 5.00, p <.001(unc.), x = -3.84, y = 13.68, z = -6.00). We also observed greater activity in the right nucleus accumbens (t = 6.47, p <.001(unc.), x = 11.03, y = 7.73, z = -18.00) and dorsomedial prefrontal cortex (t = 4.95, p <.001(unc.), x = 2.11, y = 25.57, z = 60.00) during pain stimulations in music conditions compared to stimulations in scrambled conditions.

Conclusions: These initial results follow existing literature describing hypoalgesia in response to preferred music. Results generated from this study may provide pre-clinical evidence to support the full integration of musical interventions in the treatment of pain conditions and in contexts involving acute pain such as dental procedures and vaccinations.

References

1. Garza-Villarreal, E. A. (2017). Music-Induced Analgesia in Chronic Pain Conditions: A Systematic Review and Meta-Analysis. Pain Physician, vol. 20, no. 7, pp. 597–610.
2. Mas-Herrero, E. (2021). Unraveling the Temporal Dynamics of Reward Signals in Music-Induced Pleasure with TMS. Journal of Neuroscience, vol. 41, no. 17, pp. 3889–3899.
3. Salimpoor, V. N. (2011). Anatomically distinct dopamine release during anticipation and experience of peak emotion to music. Nature Neuroscience, vol. 14, no. 2, pp. 257–262.
4. Valevicius, D. (2023). Emotional responses to favorite and relaxing music predict music-induced hypoalgesia. Frontiers in Pain Research, vol. 4.
5. Woo, C.-W. (2017). Quantifying cerebral contributions to pain beyond nociception. Nature Communications, vol. 8, no. 4211.

Poster No 2500

Improved performance of within- and between-individual pain prediction using multi-echo fMRI

Eui-Jin Jung[1,2], Suhwan Gim[1,2,3], Dong Hee Lee[1], Jae-Joong Lee[1], Choong-Wan Woo[1,2,3,4]

[1]Center for Neuroscience Imaging Research, Institute for Basic Science, Suwon, Korea, Republic of, [2]Department of Biomedical Engineering, Sungkyunkwan University, Suwon, Korea, Republic of, [3]Department of Intelligent Precision Healthcare Convergence, Sungkyunkwan University, Suwon, Korea, Republic of, [4]Life-inspired Neural Network for Prediction and Optimization Research Group, Suwon, Korea, Republic of

Introduction: Pain has multidimensional features, leading to individual differences in the experience of pain. To understand of these multidimensional features of pain, it is crucial to quantify pain as a subjective experience. Previous studies have developed neuroimaging biomarkers of pain using subjective pain reports (Wager et al., 2013; Woo et al., 2017; Lee et al., 2021). Recently, multi-echo fMRI (ME-fMRI) has emerged as an effective tool to alleviate the effect of non-neural signal such as head motion, physiological, and thermal noise. It notably improves the temporal signal-to-noise ratio (tSNR) by optimizing T2* decay rates at each voxel, thereby improving the reliability of functional connectivity in individuals (Lynch et al., 2020) and increasing effect size estimates and statistical power in task-fMRI (Lombardo et al., 2016). In addition, Multi-Echo Independent Component Analysis (ME-ICA), a denoising technique (Kundu et al., 2012), uses multiple echoes to distinguish between TE-dependent BOLD-like and TE-independent non-BOLD-like fluctuations based on T2* decay. Therefore, ME-fMRI combined with ME-ICA may better capture the brain representation of individual differences in pain than the previous fMRI sequence (i.e., single-echo fMRI). However, no previous studies have investigated the effects of the combination of ME-fMRI and ME-ICA on the brain representation of pain. Here we compared the performance of the pain prediction model between ME-fMRI and the single-echo fMRI.

Methods: Thirty-seven participants (19 female) underwent a thermal pain induction task during fMRI. Participants received thermal stimulation with fixed temperatures ranging from 45°C to 47.5°C, increasing in 0.5°C increments, and rated the level of intensity. Functional images were collected using a whole-brain T2* weighted echo-planar sequence (TR: 1sec; TE1: 13.00ms, TE2: 31.26ms, TE3: 49.52ms; FOV: 210mm; voxels: 3mm; 52 slices; in-plane acceleration factor: 2; multi-band factor: 4). In this study, there were three experimental conditions: single echo based on second echo (SE), multi-echo optimal combination (OC) and denoised by ME-ICA (ME). Initially, we compared tSNR to examine the effect of ME-fMRI. To understand the effect of ME-fMRI and ME-ICA on the brain representation of pain, we then performed two pain prediction models: 1) within-individual pain prediction model and 2) between-individual pain prediction.

Results: In this study, the ME condition showed significantly higher tSNR compared to SE and OC (Fig. 1a). We also examined the correlation between frame-wise displacement (FD) and tSNR difference between the OC minus SE and the ME minus OC conditions (Fig. 1b). In the OC minus SE condition, a negative correlation was observed between FD and tSNR difference (r=-0.66). Conversely, a positive correlation was observed in the ME minus OC condition (r=0.58). This implies that tSNR was increased with ME-fMRI and especially with ME-ICA, which can effectively reduce non-neuronal signals such as head movements. Within-individual pain prediction utilizing leave-one-subject-out cross-validation displayed significant predictive performance across all conditions (Fig. 2b). Notably, ME showed the highest predictive performance (r=0.53) compared to SE (r=0.49) and OC (r=0.51). Furthermore, in the between-individual pain prediction, ME condition (r=0.47) outperformed both SE (r=0.42) and OC (r=0.41;Fig. 2e). These results imply that the ME-fMRI combined with ME-ICA enhances tSNR throughout overall brain regions and reduces the influence of non-neuronal signals, thus capturing brain representation of pain than single-echo fMRI.

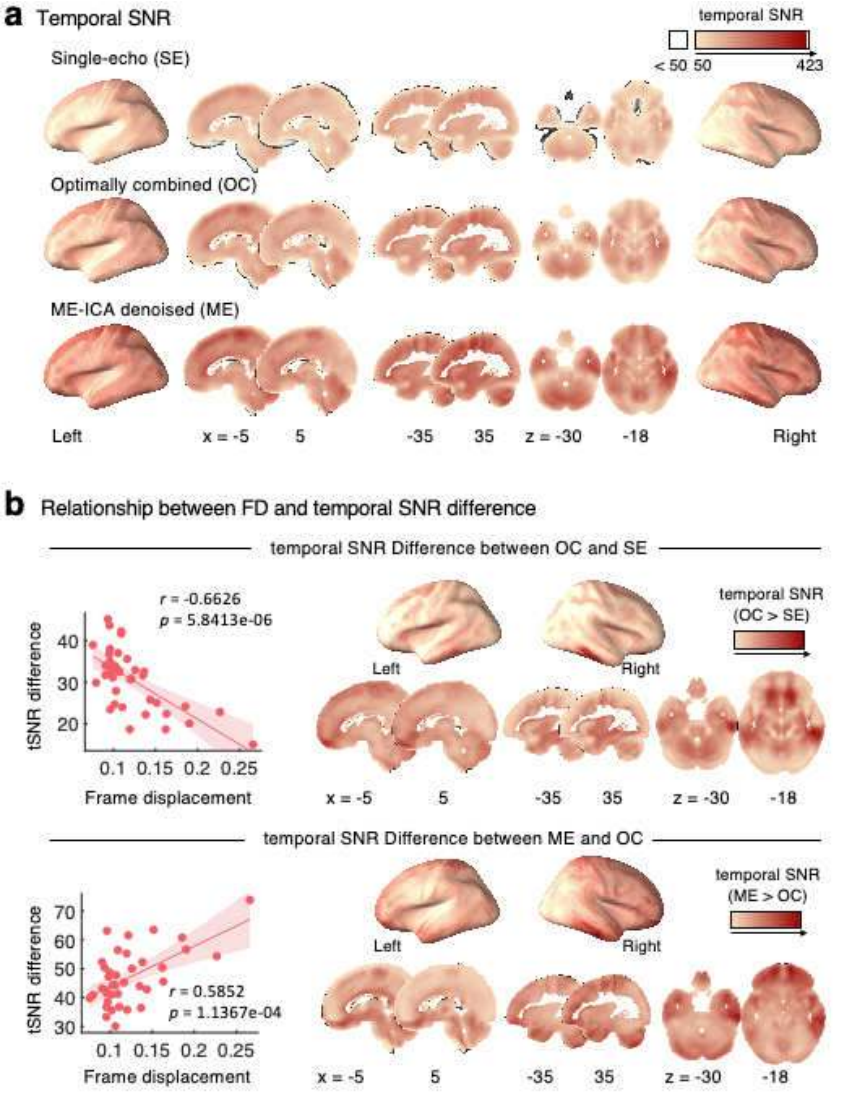

Figure 1. Temporal signal-to-noise ratio. **(a)** Multi-echo fMRI combined with multi-echo ICA showed improved tSNR compared to a single-echo fMRI sequence. tSNR was calculated by taking the mean activity divided by the standard deviation of the preprocessed heat-induction task images at each voxel. **(b)** The subject-level tSNR difference between OC and SE showed a negative relationship with FD (i.e., head movement), and the tSNR difference between ME and OC showed a positive relationship with FD. The tSNR difference was calculated by averaging the whole-brain tSNR difference and the FD was calculated by averaging the FD of the heat-induction task images.

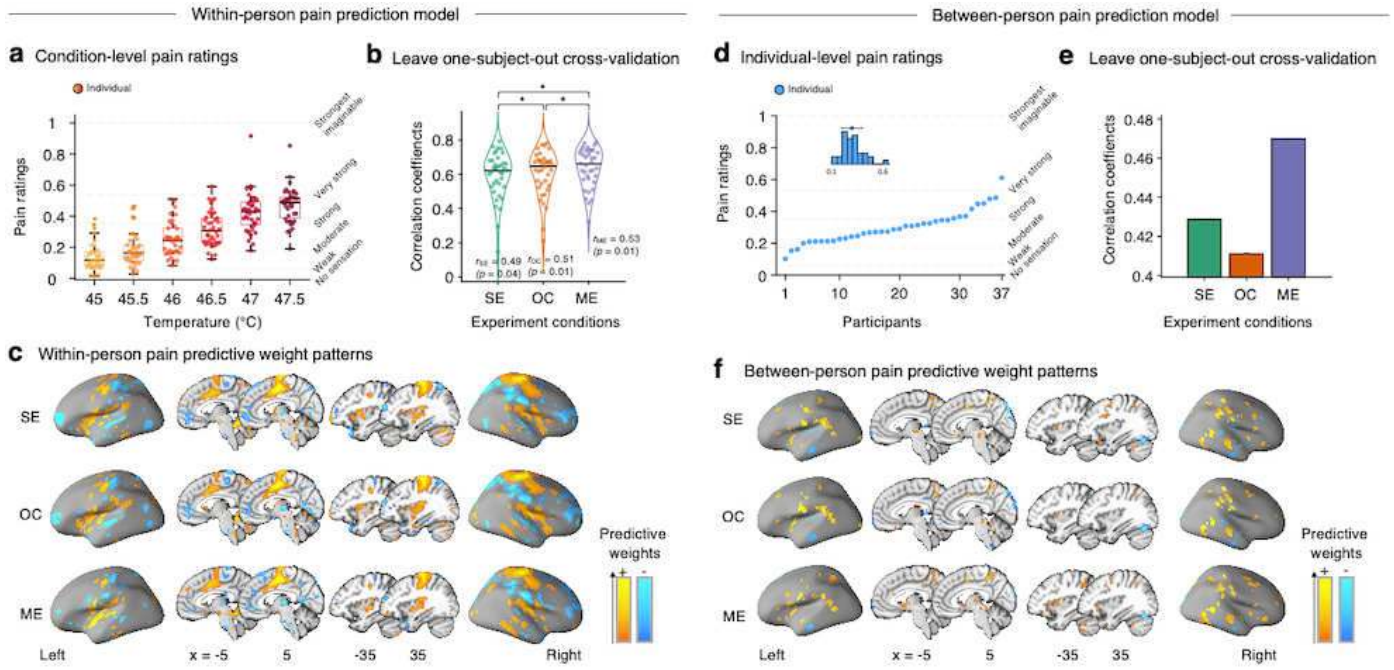

Figure 2. Within- and between-person pain prediction results. **(a-c)** Within-person pain prediction model. Pain predictive models were individually constructed for each participant using trial-by-trial pain ratings and heat-evoked brain activity, employing principal component regression (PCR). Model performance was evaluated through leave-one-subject-out cross-validation, averaging *N*-1 individual-level pain predictive patterns and calculating pattern expressions by taking dot-product of the trial-by-trial heat-evoked brain activities of the remaining participants. As a model performance, The correlation coefficient was then calculated between the trial-by-trial pattern expressions (i.e., predicted pain ratings) and actual pain ratings within remaining participant. **(a)** Condition-level pain ratings on generalized linear magnitude scale. Black line represents median of data. **(b)** Improved within-person pain prediction observed in the ME condition compared to SE and OC. **(c)** Predictive weight patterns displayed by condition, with significance tested using bootstrap test (5,000 resampling) and thresholded at $q < 0.05$ (after correcting multiple comparisons). **(d-e)** Between-person pain prediction model. For each condition, between-person pain predictive model was constructed using individual-level heat-evoked brain activities to predict individual-level pain ratings, employing LASSO-PCR. Model performance was evaluated through leave-one-subject-out cross-validation. Between-person pain predictive model was trained using *N*-1 participants' data and pattern expression was calculated by taking dot-product of the individual-level heat evoked brain activity of the remaining participants. As a model performance, the correlation coefficient was then calculated between pattern expressions and actual pain ratings. **(d)** Individual-level pain ratings on generalized linear magnitude scale which was sorted from the lowest to highest pain rating. **(e)** Improved between-person pain prediction observed in the ME ($r = 0.47$) condition compared to SE ($r = 0.42$) and OC ($r = 0.41$). **(f)** Predictive weight patterns displayed by condition, with significance tested using bootstrap test (5,000 resampling) and thresholded at uncorrected $p < 0.005$.

Conclusions: This research indicates a promising way to capture pain intra- and inter-individual variability in pain using ME-fMRI rather than single-echo fMRI. The utilization of ME-fMRI holds the potential to enhance personalized pain assessment and management strategies, consequently refining our understanding of the diverse range of pain experiences among individuals.

References

1. Wager, T. D., Atlas, L. Y., Lindquist, M. A., Roy, M., Woo, C. W., & Kross, E. (2013). An fMRI-based neurologic signature of physical pain. New England Journal of Medicine, 368(15), 1388-1397.
2. Woo, C. W., Schmidt, L., Krishnan, A., Jepma, M., Roy, M., Lindquist, M. A., ... & Wager, T. D. (2017). Quantifying cerebral contributions to pain beyond nociception. Nature communications, 8(1), 14211.
3. Lee, J. J., Kim, H. J., Čeko, M., Park, B. Y., Lee, S. A., Park, H., ... & Woo, C. W. (2021). A neuroimaging biomarker for sustained experimental and clinical pain. Nature medicine, 27(1), 174-182.
4. Lynch, C. J., Power, J. D., Scult, M. A., Dubin, M., Gunning, F. M., & Liston, C. (2020). Rapid precision functional mapping of individuals using multi-echo fMRI. Cell reports, 33(12).
5. Lombardo, M. V., Auyeung, B., Holt, R. J., Waldman, J., Ruigrok, A. N., Mooney, N., ... & Kundu, P. (2016). Improving effect size estimation and statistical power with multi-echo fMRI and its impact on understanding the neural systems supporting mentalizing. Neuroimage, 142, 55-66.
6. Kundu, P., Inati, S. J., Evans, J. W., Luh, W. M., & Bandettini, P. A. (2012). Differentiating BOLD and non-BOLD signals in fMRI time series using multi-echo EPI. Neuroimage, 60(3), 1759-1770.

Poster No 2501

Modulation effects of different treatments on PAG functional connectivity in KOA knee pain patients

Zhengjie Li[1], Jun Zhou[1]

[1]*Chengdu University of Traditional Chinese Medicine, Chengdu, Sichuan*

Introduction: The analgesic effect of acupuncture is widely recognized, but the mechanical characteristics of acupuncture for pain relief, compared to non-steroidal anti-inflammatory (NSAIDs) and placebo medication, remain unknown.

Methods: This study recruited 180 KOA patients with knee pain and 41 healthy controls (HCs). Individuals with KOA knee pain were divided randomly into groups of verum acupuncture (VA), sham acupuncture (SA), celecoxib (SC), placebo (PB),

and waiting list (WT), with 36 patients in each group. VA and SA groups included ten sessions of puncturing acupoints or puncturing non-acupoints acupuncture treatment for two successive weeks. Celecoxib capsules were continuously given orally to patients in the SC group at a dosage of 200 mg daily for two weeks. In the PB group, patients received a placebo capsule once a day for two weeks at the same dosage as celecoxib capsules. In the WL group, patients did not receive any treatment. Patients underwent a resting-state BOLD-fMRI scan pre- and post-receiving the therapy, whereas HCs only underwent a baseline scan. Seed (ventrolateral periaqueductal gray, vlPAG, a key node in DPMS) based resting-state functional connectivity (rs-FC) was applied in the data analysis.

Results: All groups demonstrated improved knee pain scores relative to the initial state. There was no statistical difference between the VA and SA groups in all clinical outcomes, and vlPAG rs-FC alterations. KOA knee pain individuals reported higher vlPAG rs-FC in the bilateral thalamus than HCs. KOA knee pain patients in the acupuncture group (verum + sham, AG) exhibited increased vlPAG rs-FC with the right dorsolateral prefrontal cortex (DLPFC) and the right angular, which is associated with knee pain improvement. In contrast with the SC and PB group, the AG exhibited significantly increased vlPAG rs-FC with the right DLPFC and angular. Contrary to the WT group, the AG showed greater vlPAG rs-FC with the right DLPFC and precuneus.

Conclusions: Acupuncture treatment, celecoxib, and placebo medication have different modulation effects on vlPAG DPMS in KOA knee pain patients. Acupuncture could modulate vlPAG rs-FC with brain regions associated with cognitive control, attention, and reappraisal for knee pain relief in KOA patients, compared with celecoxib and placebo medication.

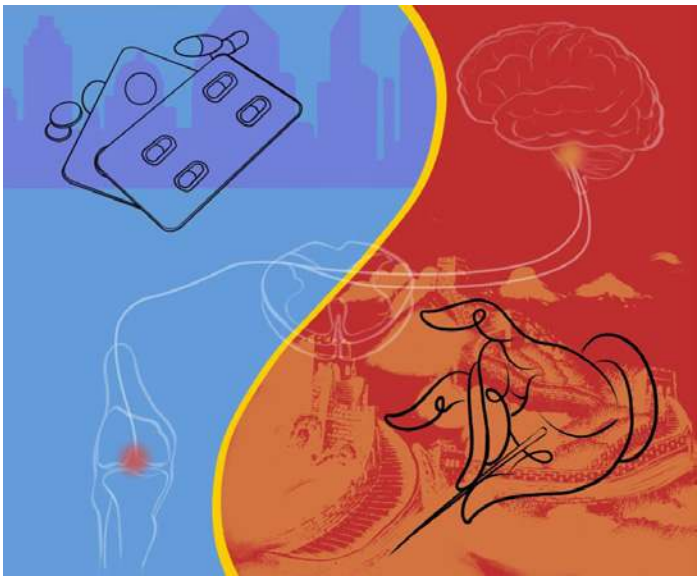

References

1. Li, ZJ. (2023), 'Modulation effects of different treatments on periaqueductal gray resting state functional connectivity in knee osteoarthritis knee pain patients', CNS Neuroscience & Therapeutics, vol. 29, no. 7, pp. 1965-1980.

Poster No 2502

Exploring pain perception: intracerebral EEG and ongoing oscillations in the human insula

Chiara Leu[1], Susana Ferrao Santos[1,2], Alexane Fierain[2], Vincent Joris[1,3], Patrice Finet[3], Giulia Liberati[1,4]

[1]Institute of Neuroscience, Université catholique de Louvain, Brussels, Belgium, [2]Department of Neurology, Saint-Luc University Hospital, Brussels, Belgium, [3]Department of Neurosurgery, Saint-Luc University Hospital, Brussels, Belgium, [4]Psychological Sciences Research Institute, Université catholique de Louvain, Louvain-La-Neuve, Belgium

Introduction: Intracerebral recordings from the posterior insula have shown that ongoing neural oscillations are preferentially modulated by sustained periodic nociceptive stimuli in the theta and alpha frequency band at the frequency of stimulation (Liberati et al. 2019). These findings suggest a relationship between nociception and ongoing oscillations in the posterior insula, but it remains unclear whether these modulations play a significant role in the perception of pain. If this is the case, cognitive processes known to affect pain perception (such as attention (Torta et al. 2017)) should also affect these ongoing oscillations. To investigate this link, we assessed the effect of an arithmetic distraction task on both perceived pain intensity and the modulation of ongoing oscillations in the insula measured using intracerebral electroencephalography (iEEG). We

hypothesized that the arithmetic task would lead to a decrease in the perceived intensity of thermonociceptive stimuli, concomitant to a decrease in amplitude of the modulation of ongoing oscillations exerted by thermonociceptive but not vibrotactile stimulation.

Methods: 5 patients (mean age: 34 ± 8 years, 1 f.) undergoing pre-surgical evaluation for refractory epilepsy were recruited at the Saint Luc University Hospital (Brussels, Belgium). As part of their evaluation, all patients had depth electrodes implanted in brain regions suspected to be the origin of their seizures. Only electrodes implanted in the anterior (n=25) and posterior (n=13) insula were considered for the present study. The protocol described in Leu et al. (2023) was used: Slow periodic sustained thermonociceptive and vibrotactile stimuli were used in separate trials, at a frequency of 0.2 Hz (range: 35 - 50°C) over a duration of 75s per trial. The arithmetic task consisted of continuously subtracting 7 from a 3-digit starting number throughout the stimulation. No task was presented during baseline trials. After each stimulus, the subjects provided a rating of the perceived stimulus intensity on a numerical ratings scale from 0 to 10 (0: no perception, 10: most intense imaginable). The modulation of ongoing oscillations was assessed in the theta (4-8 Hz) and alpha (8-12 Hz) frequency band using a "frequency-tagging of ongoing oscillations" approach (Leu et al. 2023; Liberati et al. 2019). Linear mixed models assessed the impact of condition, modality, and electrode contact location on perceived intensity and modulation of ongoing oscillations in different frequency bands, with post-hoc pairwise comparisons for significant interactions ($p<0.05$).

Results: During the arithmetic task, perceived stimulation intensity was significantly decreased only in the vibrotactile modality ($p<0.001$) (Fig.1). In the alpha frequency band, the modulation of ongoing oscillations was significantly larger in the posterior than in the anterior insula ($p<0.001$). Post-hoc pairwise comparisons illustrated that the modulation in the posterior insula was significantly larger in the baseline condition for thermonociceptive compared to vibrotactile stimuli ($p=0.02$). Additionally, the arithmetic task led to a significant reduction in the modulation for thermonociceptive stimuli ($p=0.007$) (Fig. 2). These differences can be observed on a single-subject level. In the theta frequency band, amplitudes were significantly larger in the posterior insula ($p<0.001$). No differences were observed between the modalities or conditions.

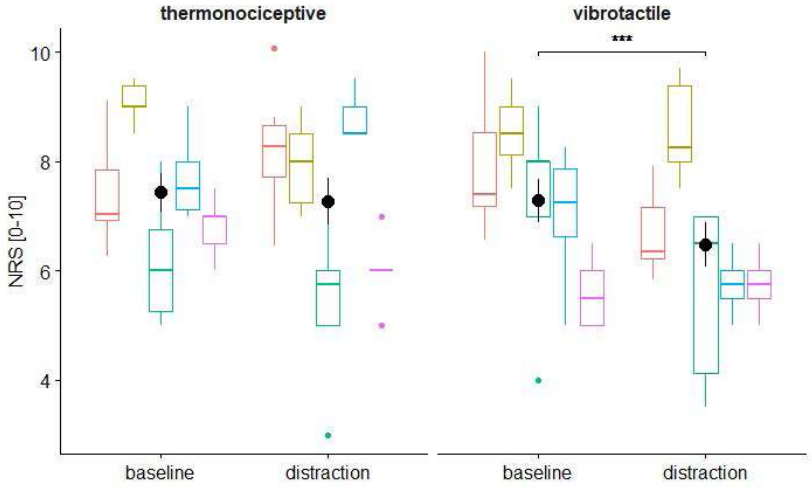

Fig. 1: Intensity ratings collected after each trial on a Numerical Rating Scale (NRS). Each colored boxplot is associated with one subject, black dots indicate the group mean.

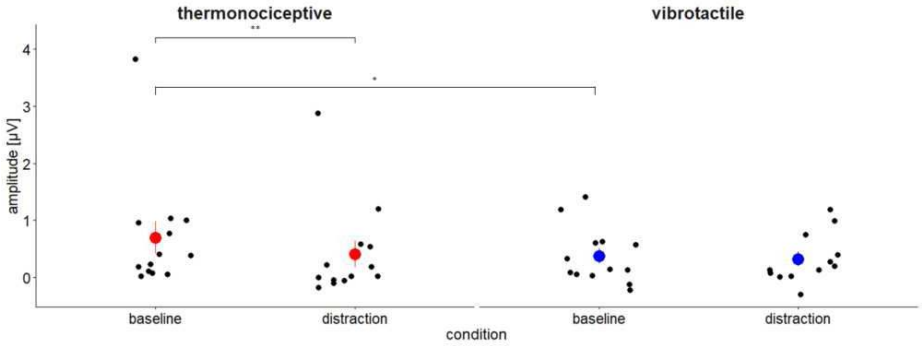

Fig. 2: Modulation of ongoing oscillations in the alpha frequency band in the posterior insula. Colored dots represent group means.

Conclusions: The obtained results demonstrate a dissociation between the ratings of perceived stimulus intensity and the modulation of ongoing oscillations in the alpha frequency band in the posterior insula following sustained periodic thermonociceptive stimuli. The difference in modulation between the modalities might reflect the preferential modulation of thermonociceptive stimuli within the posterior insula in the alpha frequency band and illustrates its potential involvement in the processing of thermonociceptive stimuli.

References
1. Leu, Chiara, et al. 2023. 'The role of ongoing oscillation in pain perception: Absence of modulation by a concomitant arithmetic task', Cortex, 168: 114-29.
2. Liberati, Giulia, et al. 2019. 'Tonic thermonociceptive stimulation selectively modulates ongoing neural oscillations in the human posterior insula: Evidence from intracerebral EEG', NeuroImage, 188: 70-83.
3. Torta, D. M., et al. 2017. 'Attention to pain! A neurocognitive perspective on attentional modulation of pain in neuroimaging studies', Cortex, 89: 120-34.

Poster No 2503

Understanding the Genetic Overlap and Causal Links Between Brain Morphometry and Chronic Pain

Miguel Renteria[1], Luis M. Garcia Marin[2], Natalia Ogonowski[2], Santiago Diaz-Torres[2], Freddy Chafota[2], Nicholas Martin[2]

[1]Mental Health & Neuroscience Program, QIMR Berghofer Medical Research Institute, Brisbane, QLD, [2]QIMR Berghofer Medical Research Institute, Brisbane, QLD

Introduction: Chronic pain is a complex condition with a substantial impact on quality of life, often associated with alterations in brain structure. However, the genetic underpinnings linking brain morphometry and chronic pain remain poorly understood. This study aims to elucidate the genetic correlations between brain morphometry and multisite chronic pain and to infer potential causal relationships.

Methods: We leveraged summary statistics from the largest genome-wide association studies (GWAS) of multisite chronic pain and neuroimaging phenotypes, focusing on cortical thickness and surface area, subcortical volumes, and intracranial volume. Pairwise genetic correlations between these neuroimaging phenotypes and chronic pain were estimated using LD-Score Regression (LDSC). For brain phenotypes showing significant correlations, we applied the GWAS-Pairwise method to estimate local genetic correlations. Further, we employed the novel LHC-Mendelian Randomisation (LHC-MR) method, designed to perform bi-directional causal estimation while addressing limitations of traditional Mendelian Randomization, such as sample overlap and sensitivity to heritable confounders.

Results: Our analyses revealed significant genetic correlations between several brain regions of interest and chronic pain. The GWAS-Pairwise method provided refined local genetic correlation estimates. Several genes, including RPP25, NFKB2, SCAMP5, PPCDC, ASXL3, and SLC44A2, were implicated as influencing chronic pain risk and at least one brain morphometric measure. The IHC-MR analysis indicated potential causal relationships between brain morphometry and chronic pain, with evidence of heritable factors influencing these associations.

Conclusions: This study provides novel insights into the genetic relationship between brain morphometry and chronic pain and highlights the potential for genetic factors to contribute to both brain structural changes and the susceptibility to chronic pain, offering avenues for future research into targeted interventions and personalised pain management strategies.

References
1. Dale, A.M., Fischl, B., Sereno, M.I., 1999. Cortical surface-based analysis. I. Segmentation and surface reconstruction. Neuroimage 9, 179-194.
2. Dale, A.M., Sereno, M.I., 1993. Improved localization of cortical activity by combining EEG and MEG with MRI cortical surface reconstruction: a linear approach. J Cogn Neurosci 5, 162-176.
3. Desikan, R.S., Segonne, F., Fischl, B., Quinn, B.T., Dickerson, B.C., Blacker, D., Buckner, R.L., Dale, A.M., Maguire, R.P., Hyman, B.T., Albert, M.S., Killiany, R.J., 2006. An automated labeling system for subdividing the human cerebral cortex on MRI scans into gyral based regions of interest. Neuroimage 31, 968-980.
4. Fischl, B., Dale, A.M., 2000. Measuring the thickness of the human cerebral cortex from magnetic resonance images. Proc Natl Acad Sci U S A 97, 11050-11055.
5. Fischl, B., Liu, A., Dale, A.M., 2001. Automated manifold surgery: constructing geometrically accurate and topologically correct models of the human cerebral cortex. IEEE Trans Med Imaging 20, 70-80.
6. Fischl, B., Salat, D.H., Busa, E., Albert, M., Dieterich, M., Haselgrove, C., van der Kouwe, A., Killiany, R., Kennedy, D., Klaveness, S., Montillo, A., Makris, N., Rosen, B., Dale, A.M., 2002. Whole brain segmentation: automated labeling of neuroanatomical structures in the human brain. Neuron 33, 341-355.
7. Fischl, B., Salat, D.H., van der Kouwe, A.J., Makris, N., Segonne, F., Quinn, B.T., Dale, A.M., 2004a. Sequence-independent segmentation of magnetic resonance images. Neuroimage 23 Suppl 1, S69-84.

8. Fischl, B., Sereno, M.I., Dale, A.M., 1999a. Cortical surface-based analysis. II: Inflation, flattening, and a surface-based coordinate system. Neuroimage 9, 195-207.
9. Fischl, B., Sereno, M.I., Tootell, R.B., Dale, A.M., 1999b. High-resolution intersubject averaging and a coordinate system for the cortical surface. Hum Brain Mapp 8, 272-284.
10. Fischl, B., van der Kouwe, A., Destrieux, C., Halgren, E., Segonne, F., Salat, D.H., Busa, E., Seidman, L.J., Goldstein, J., Kennedy, D., Caviness, V., Makris, N., Rosen, B., Dale, A.M., 2004b. Automatically parcellating the human cerebral cortex. Cereb Cortex 14, 11-22.
11. Han, X., Jovicich, J., Salat, D., van der Kouwe, A., Quinn, B., Czanner, S., Busa, E., Pacheco, J., Albert, M., Killiany, R., Maguire, P., Rosas, D., Makris, N., Dale, A., Dickerson, B., Fischl, B., 2006. Reliability of MRI-derived measurements of human cerebral cortical thickness: the effects of field strength, scanner upgrade and manufacturer. Neuroimage

Poster No 2504

White Matter Microstructural Abnormalities of the Trigeminal Nerve in Migraine - a 7T DTI study

Sarasa Tohyama[1,2], Michael Datko[1,2,3], Mackenzie Hyman[2], Alison Goldstein[1,2], Kassandra Round[1,2,3], Lillian Kinder[1,2,3], Ludovica Brusaferri[2], Ronald Garcia[2], Randy Gollub[2], Robert Edwards[4], Bruce Rosen[2], Nouchine Hadjikhani[2], Cheng Hsinlin[5], Zev Schuman-Olivier[3], Marco Loggia[2], Vitaly Napadow[1,2]

[1]Spaulding Rehabilitation Hospital, Harvard Medical School, Boston, MA, [2]A.A. Martinos Center for Biomedical Imaging, Massachusetts General Hospital, Harvard Medical School, Boston, MA, [3]Center for Mindfulness and Compassion, Cambridge Health Alliance, Harvard Medical School, Boston, MA, [4]Brigham and Women's Hospital, Harvard Medical School, Boston, MA, [5]Massachusetts General Hospital, Harvard Medical School, Boston, MA

Introduction: Migraine, a highly prevalent neurological condition, involves sensitization of the trigeminal nerve system (Charles, 2018; Noseda and Burstein, 2013). Magnetic resonance imaging (MRI) offers an in-vivo, non-invasive avenue to examine the trigeminal nerve in humans, and in particular, diffusion tensor imaging (DTI) can be used to assess white matter microstructural tissue characteristics (Alexander et al., 2007). Previous DTI studies have shown microstructural abnormalities of the trigeminal nerve root in neurological conditions such as trigeminal neuralgia (DeSouza et al., 2014) and temporomandibular disorder (Moayedi et al., 2012). Such abnormalities in migraine, however, have not been adequately studied. Here, we employed 7 Tesla DTI, allowing for improved spatial resolution, to investigate the microstructural properties of the trigeminal nerve root in patients with episodic migraine.

Methods: Our ongoing longitudinal study has enrolled 45 patients with episodic migraine (43F, mean age +/- SD: 35.98 +/- 11.57 years) and 18 age- and sex-matched healthy individuals (17F, mean age +/- SD: 35.82 +/- 13.83 years). All subjects completed a 4-week period of electronic daily headache diaries to confirm eligibility (i.e., 4-20 headache days for migraine patients and no headaches characteristic of migraine for healthy individuals). Each subject underwent a brainstem-focused diffusion-weighted imaging scan (7T MAGNETOM Terra equipped with an in-house built 64-channel coil, 64 directions, b = 1,000, repetition time = 5,900 ms, echo time = 68 ms, resolution = 1 mm isotropic) and two b0 scans with reversed phase-encode blips. The b0 images were used for susceptibility-induced distortion correction, followed by eddy current and motion correction. Scalar maps of fractional anisotropy (FA), radial diffusivity (RD), mean diffusivity (MD), and axial diffusivity (AD) were calculated. The four DTI metrics were manually extracted from the left and right trigeminal nerve roots in individual space and compared between migraine patients and healthy individuals. For multiple testing correction, false discovery rate correction was used.

Results: Ultra-high field 7 Tesla DTI successfully delineated the small-scale structure of the trigeminal nerve roots and enabled customization of the region-of-interest based on each subject's nerve root geometry. Migraine patients showed significantly reduced FA (U = 109, p = 2.8 x 10-5), and increased RD (U = 189, p = 0.0020) and MD (U = 231, p = 0.011), in the trigeminal nerve root compared with healthy individuals. No significant differences were found for AD (U = 320, p = 0.20). To assess laterality effects based on headache presentation, the left and right trigeminal nerve roots were compared for all four DTI metrics, which revealed no significant differences in both migraine patients and healthy individuals ($p > 0.20$ for all comparisons).

Conclusions: Our findings demonstrate that patients with episodic migraine have white matter microstructural abnormalities in the trigeminal nerve root, characterized by reduced FA, and increased RD and MD, and highlight the importance of DTI as a tool to investigate anatomopathological substrates of migraine disease that are not distinguishable on conventional MRI. Elevated RD and MD in migraine patients suggest myelin degeneration and inflammation-induced edema as previously described (Alexander et al., 2007) and shown in histological studies (Song et al., 2005, 2002). Trigeminal nerve root remodeling may be an important aspect of the dynamics underlying migraine pathophysiology.

References

1. Alexander, A.L., Lee, J.E., Lazar, M., Field, A.S., 2007. Diffusion tensor imaging of the brain. Neurotherapeutics 4, 316–329.
2. Charles, A., 2018. The pathophysiology of migraine: implications for clinical management. Lancet Neurol. 17, 174–182.

3. DeSouza, D.D., Hodaie, M., Davis, K.D., 2014. Abnormal trigeminal nerve microstructure and brain white matter in idiopathic trigeminal neuralgia. PAIN® 155, 37–44.
4. Moayedi, M., Weissman-Fogel, I., Salomons, T.V., Crawley, A.P., Goldberg, M.B., Freeman, B.V., Tenenbaum, H.C., Davis, K.D., 2012. White matter brain and trigeminal nerve abnormalities in temporomandibular disorder. PAIN® 153, 1467–1477.
5. Noseda, R., Burstein, R., 2013. Migraine pathophysiology: anatomy of the trigeminovascular pathway and associated neurological symptoms, cortical spreading depression, sensitization, and modulation of pain. PAIN® 154, S44–S53.
6. Song, S.-K., Sun, S.-W., Ramsbottom, M.J., Chang, C., Russell, J., Cross, A.H., 2002. Dysmyelination revealed through MRI as increased radial (but unchanged axial) diffusion of water. Neuroimage 17, 1429–1436.
7. Song, S.-K., Yoshino, J., Le, T.Q., Lin, S.-J., Sun, S.-W., Cross, A.H., Armstrong, R.C., 2005. Demyelination increases radial diffusivity in corpus callosum of mouse brain. Neuroimage 26, 132–140.

Poster No 2505

Beyond Internal Focus: Contrast between Extero/Interoceptive Attention on Heartbeat Evoked Responses

Su Hyun Bong[1], Dayoung Yoon[1], Jaewon Kim[1], Bumseok Jeong[1]

[1]Korea Advanced Institute of Science and Technology, Daejeon, Republic of Korea

Introduction: Interoception, the perception of the body's internal state, is linked to emotional awareness and various psychiatric disorders such as depression and anxiety. Heartbeat evoked responses (HER) have been regarded as neurophysiological markers of interoception[1]. Previous research indicates an elevation in HER amplitude with increased interoceptive attention, yet primarily contrasts it with resting states[2], resulting in ambiguous findings when comparing with exteroceptive attention . This study aims to elucidate differences in HER amplitudes between exteroceptive and interoceptive conditions and their association with psychiatric symptoms.

Methods: The study involved 42 participants, with final analyses conducted on 28 for the Heartbeat Counting Task (HCT)[4] and 30 for the Heart Rate Discrimination Task (HRD)[5]. During these tasks, EEG recordings were captured, focusing on the effects of exteroceptive/interoceptive attention on HER. Epoching was performed in the 200-650 ms range post-EKG R-peak, and statistical analyses included T-tests (HCT) and ANOVA (HRD), supplemented by regression analysis with covariates like interoceptive accuracy (HCT) and PHQ-9/STAI-X1(HRD). Statistics utilized EEGLAB's LIMO[6] toolbox, with cluster significance assessed via bootstrap at a 0.05 threshold.

Results: In the HCT, the interoception condition showed higher HER amplitude post R-peak (555-605ms) compared to resting. Higher interoceptive accuracy correlated with greater amplitude disparity (370-390ms). In HRD, while significant differences were noted among the three conditions (200-396ms, 400-632ms), no marked disparity was found between exteroception and interoception. Notably, increased PHQ-9/STAI-X1 scores (344-348ms, 344-364ms) were linked to greater HER amplitude contrasts in both exteroceptive and interoceptive conditions, suggesting a complex interaction with psychiatric symptoms.

Conclusions: Contrary to previous research, no significant HER amplitude differences were observed between exteroceptive and interoceptive conditions. However, the study highlights a significant link between psychiatric symptoms and HER amplitude variation within these attentional contexts. These findings suggest that exteroceptive attention can influence HER, reflecting a nuanced interplay between attentional types, HER changes, and psychiatric symptoms, indicating a need for a broader understanding of HER in dynamic neural mechanisms.

References

1. Schandry, R., Sparrer, B., & Weitkunat, R. (1986). From the heart to the brain: a study of heartbeat contingent scalp potentials. International Journal of Neuroscience, vol. 30, no.4, pp. 261-275.
2. Coll, M. P., Hobson, H., Bird, G., & Murphy, J. (2021). Systematic review and meta-analysis of the relationship between the heartbeat-evoked potential and interoception. Neuroscience & Biobehavioral Reviews, vol. 122, pp. 190-200.
3. Terhaar, J., Viola, F. C., Bär, K. J., & Debener, S. (2012). Heartbeat evoked potentials mirror altered body perception in depressed patients. Clinical neurophysiology, vol. 123, no.10, pp. 1950-1957.
4. Schandry, R. (1981). Heart beat perception and emotional experience. Psychophysiology, vol. 18, no.4, pp. 483-488.
5. Legrand, N., Nikolova, N., Correa, C., Brændholt, M., Stuckert, A., Kildahl, N., ... & Allen, M. (2022). The heart rate discrimination task: a psychophysical method to estimate the accuracy and precision of interoceptive beliefs. Biological Psychology, vol. 168, pp. 108239.
6. Pernet, C. R., Chauveau, N., Gaspar, C., & Rousselet, G. A. (2011). LIMO EEG: a toolbox for hierarchical LInear MOdeling of ElectroEncephaloGraphic data. Computational intelligence and neuroscience, vol. 2011, pp. 1-11.

Poster No 2506

Morphological and genetic decoding show heterogenous patterns of brain aging in chronic musculoskele

Lei Zhao[1], Yiheng Tu[1]

[1]*Institute of Psychology of the Chinese Academy of Sciences, Beijing, Beijing*

Introduction: Patients with chronic pain (CP) are at a higher risk of dementia, but the mechanism remains unclear. Dementia-risk-related biological impairments in the brain accumulate with age but vary in velocity across different conditions, suggesting the implication to decode the neurobiological mechanisms between CP and dementia via characterizing brain aging. Considering CP is a unifying symptom in a series of highly heterogeneous conditions, whether common CP types present a general or distinct brain aging patterns that are associated with patients' cognitive functions, dementia risks, and genetic predisposition, are still unknown.

Methods: To decode accelerated brain aging in CP, we developed an MRI-based brain age model in healthy adults (N = 6,725) and applied it to examine the brain aging acceleration (quantified by the predicted age difference [PAD]) in five common types of CP (Dataset 1; N = 2734) including knee pain, back pain, headache, neck pain, and hip pain. The findings of brain aging acceleration were further validated in an independent dataset (Dataset 2; N = 192) that had baseline and 5-year follow-up sessions. The associations between brain aging acceleration and pain symptoms, cognitive function, and dementia risks were assessed cross-sectionally and longitudinally. We also employed genetically pleiotropic, imaging-transcriptomic and enrichment analyses to identify the molecular genetic basis of brain aging acceleration in CP.

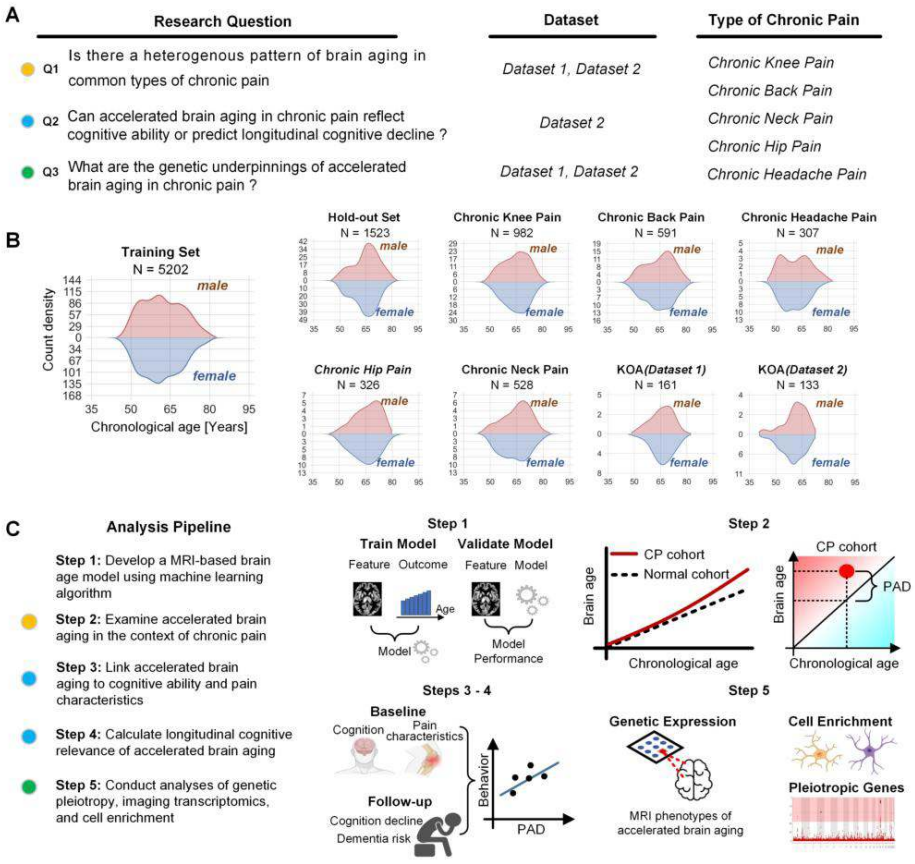

Results: Compared to healthy controls, a significantly increased PAD was only observed in chronic knee pain cohort (Cohen's d = 0.130). In the subgroups of chronic knee pain, a significant increase in PAD was found in the knee osteoarthritis (KOA) cohort (d = 0.437) but not in the subgroup without KOA. The increased PAD in KOA was replicated in Dataset 2 (d = 0.454) and was associated with memory decline (r = 0.348) and dementia risk (Spearman's rho = 0.278). The gene SLC39A8 showed pleiotropy between brain aging acceleration and KOA, as well as transcriptional associations with KOA neuroimaging phenotypes across both datasets. The genes exhibiting transcriptional associations with KOA neuroimaging phenotypes were highly expressed in microglial cells and astrocytes, and primarily enriched in synaptic structure and neurodevelopment.

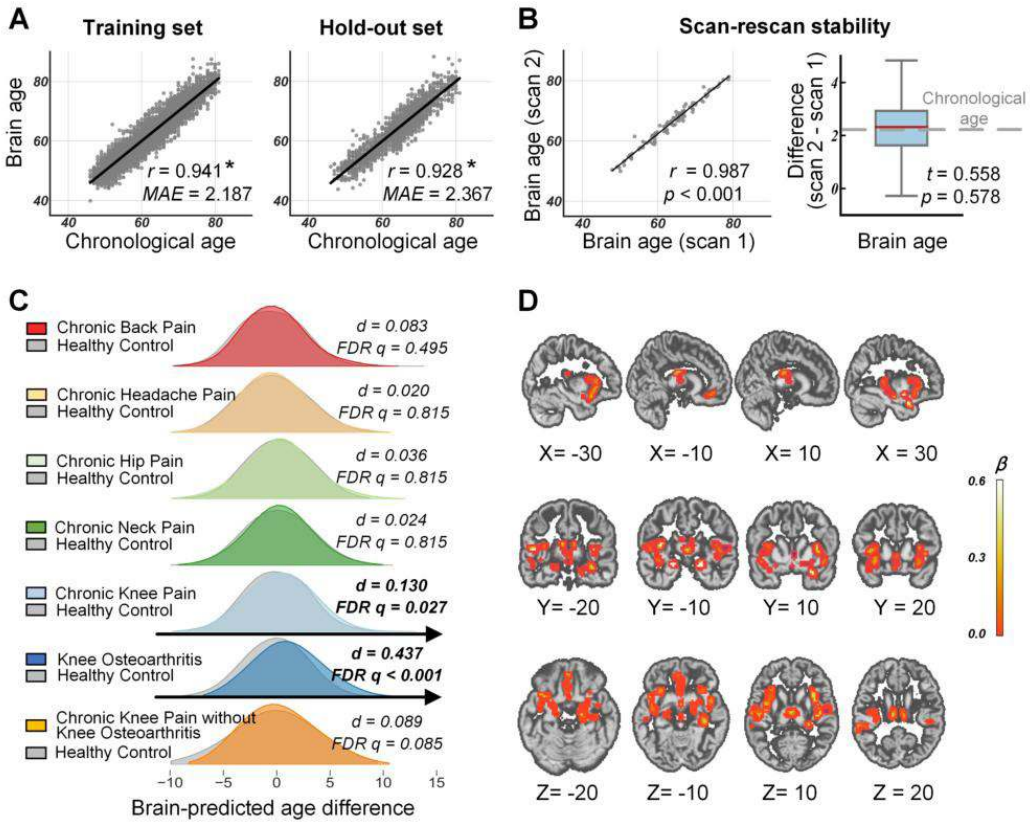

Conclusions: In summary, our study demonstrates the heterogeneity of brain aging in CP and unfolded a distinct heritable pattern that links KOA to dementia by providing an integrative biological profile that connects specific genes, molecular processes, and cell classes with morphological brain aging.

References

1. Anderson KM. (2020), Convergent molecular, cellular, and cortical neuroimaging signatures of major depressive disorder. Proceedings of the National Academy of Sciences of the United States of America, 117(40):25138-25149.
2. Andreassen OA. (2013) Improved detection of common variants associated with schizophrenia by leveraging pleiotropy with cardiovascular-disease risk factors. American journal of human genetics, 92(2):197-209.
3. Andreassen OA. (2014), Boosting the power of schizophrenia genetics by leveraging new statistical tools. Boosting the power of schizophrenia genetics by leveraging new statistical tools, 40(1):13-7.
4. Antal B. (2022), Type 2 diabetes mellitus accelerates brain aging and cognitive decline: Complementary findings from UK Biobank and meta-analyses. eLife, 11:e73138.
5. Bangen KJ. (2018), Baseline White Matter Hyperintensities and Hippocampal Volume are Associated With Conversion From Normal Cognition to Mild Cognitive Impairment in the Framingham Offspring Study. Alzheimer disease and associated disorders, 32(1):50-56.
6. Beck D. (2022), Cardiometabolic risk factors associated with brain age and accelerate brain ageing. Human brain mapping, 43(2):700-720.
7. Bethlehem RAI. (2022), Brain charts for the human lifespan. Nature. 604(7906):525-533.
8. Boyle R. (2021), Brain-predicted age difference score is related to specific cognitive functions: a multi-site replication analysis. Brain imaging and behavior, 15(1):327-345.
9. Broce. (2019), Dissecting the genetic relationship between cardiovascular risk factors and Alzheimer's disease. Acta neuropathologica, 137(2):209-226.
10. Brouwer. (2022), Genetic variants associated with longitudinal changes in brain structure across the lifespan. Nature neuroscience, 25(4):421-432.
11. Burt JB. (2018), Hierarchy of transcriptomic specialization across human cortex captured by structural neuroimaging topography. Nature neuroscience, 21(9):1251-1259.
12. Burt JB. (2020), Generative modeling of brain maps with spatial autocorrelation. Neuroimage. 220:117038.
13. Caillaud M. (2020), Evidence of a Relation Between Hippocampal Volume, White Matter Hyperintensities, and Cognition in Subjective Cognitive Decline and Mild Cognitive Impairment. The journals of gerontology. Series B, Psychological sciences and social sciences, 75(7):1382-1392.

Poster No 2507

Personalized Brain Decoding of Spontaneous Pain in Individuals with Chronic Pain

Jae-Joong Lee[1], Choong-Wan Woo[2]

[1]Institute for Basic Science (IBS), Suwon-si, Korea, Republic of, [2]Sungkyunkwan University, Suwon-si, Gyeonggi-do

Introduction: Current assessment of chronic pain lacks objective biomarkers. Neuroimaging has shown the potential as surrogates of subjective pain reports in healthy population, but whether this measurement has validity for single individuals with chronic pain remains unclear.

Methods: We studied a series of patients with fibromyalgia, characterized as chronic widespread pain. For extensive sampling of brain activity within individuals, participants underwent longitudinal sessions of functional magnetic resonance imaging (fMRI) scan on different days. Each session consisted of the three runs of 10 min fMRI scan, where we recorded the participants' whole-brain activity with their concurrent self-reports of spontaneous pain ratings. Machine learning algorithms were used to identify the personalized fMRI biomarkers that can decode continuous fluctuation of spontaneous pain.

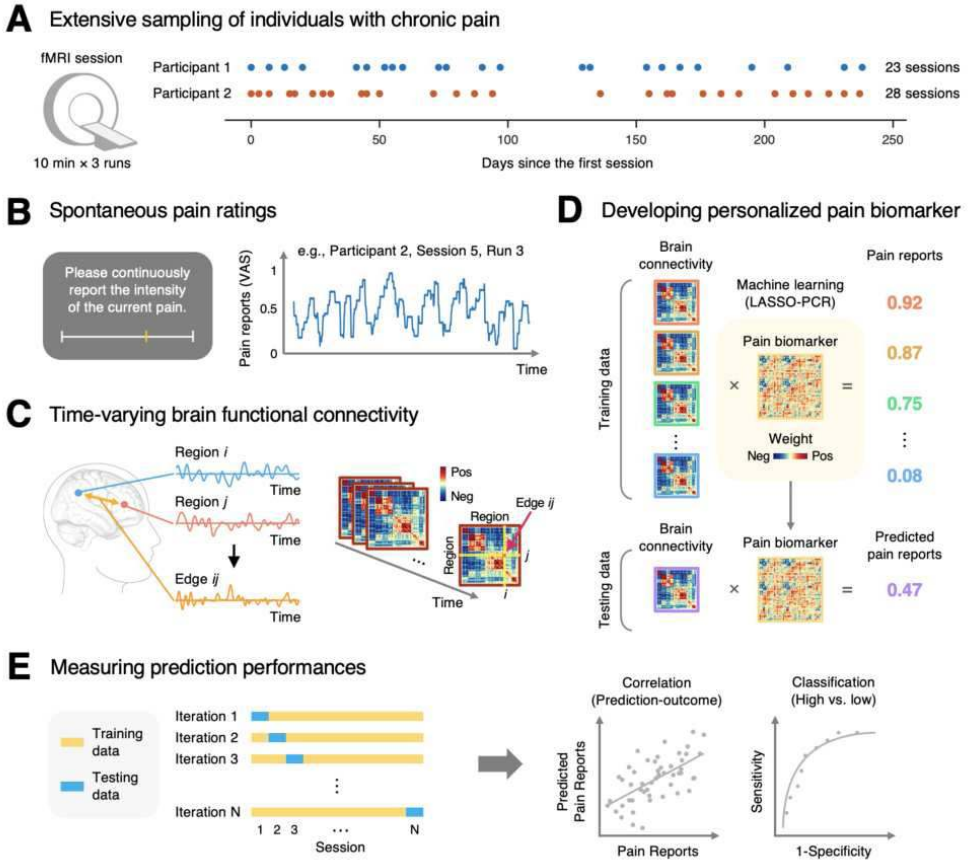

Results: Two out of three enrolled participants completed more than 15 required sessions of fMRI scan (Participant 1: 23 sessions; Participant 2: 28 sessions). The personalized biomarkers predicted changes in spontaneous pain ratings across sessions, runs, and minutes (Participant 1: Prediction-outcome correlation r = 0.40-0.61; Participant 2: r = 0.51-0.65), and discriminated the median-dichotomized high pain vs. low pain (Participant 1: Area under the curve [AUC] = 0.71-0.90; Participant 2: AUC = 0.76-0.94) with cross-validation. These biomarkers relied on individually unique patterns of whole-brain interaction for decoding, and were not predictive of the other participant's pain.

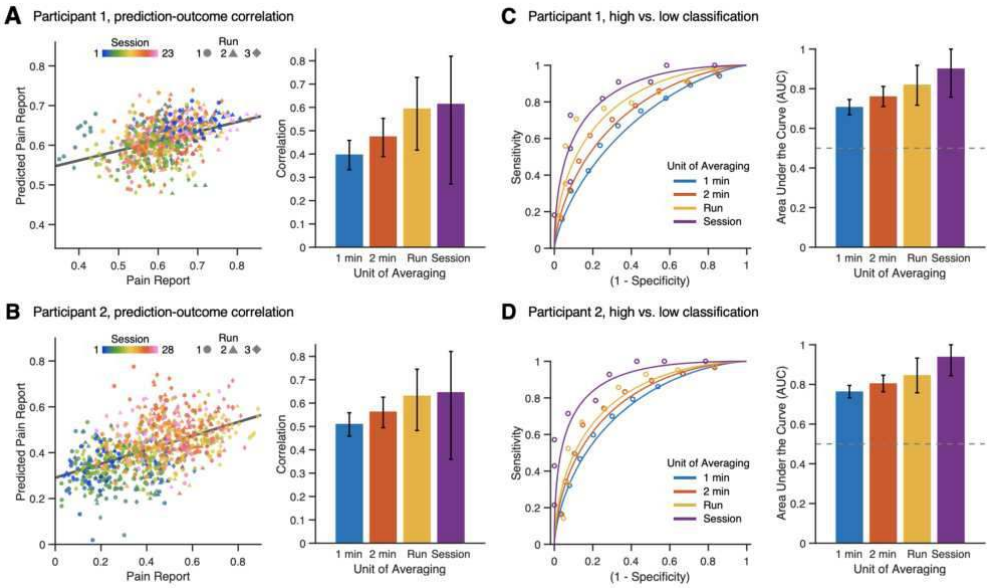

Conclusions: Neuroimaging can be used to decode spontaneous pain in single individuals with chronic pain.

References

1. Cheng, J. C., A. Rogachov, K. S. Hemington, A. Kucyi, R. L. Bosma, M. A. Lindquist, R. D. Inman and K. D. Davis (2018). "Multivariate machine learning distinguishes cross-network dynamic functional connectivity patterns in state and trait neuropathic pain." Pain 159(9): 1764-1776.
2. Gordon, E. M., T. O. Laumann, A. W. Gilmore, D. J. Newbold, D. J. Greene, J. J. Berg, M. Ortega, C. Hoyt-Drazen, C. Gratton, H. Sun, J. M. Hampton, R. S. Coalson, A. L. Nguyen, K. B. McDermott, J. S. Shimony, A. Z. Snyder, B. L. Schlaggar, S. E. Petersen, S. M. Nelson and N. U. F. Dosenbach (2017). "Precision Functional Mapping of Individual Human Brains." Neuron 95(4): 791-807 e797.
3. Lee, J., I. Mawla, J. Kim, M. L. Loggia, A. Ortiz, C. Jung, S. T. Chan, J. Gerber, V. J. Schmithorst, R. R. Edwards, A. D. Wasan, C. Berna, J. Kong, T. J. Kaptchuk, R. L. Gollub, B. R. Rosen and V. Napadow (2019). "Machine learning-based prediction of clinical pain using multimodal neuroimaging and autonomic metrics." Pain 160(3): 550-560.
4. Lee, J. J., H. J. Kim, M. Ceko, B. Y. Park, S. A. Lee, H. Park, M. Roy, S. G. Kim, T. D. Wager and C. W. Woo (2021). "A neuroimaging biomarker for sustained experimental and clinical pain." Nat Med 27(1): 174-182.
5. Mayr, A., P. Jahn, A. Stankewitz, B. Deak, A. Winkler, V. Witkovsky, O. Eren, A. Straube and E. Schulz (2022). "Patients with chronic pain exhibit individually unique cortical signatures of pain encoding." Hum Brain Mapp 43(5): 1676-1693.
6. Wager, T. D., L. Y. Atlas, M. A. Lindquist, M. Roy, C. W. Woo and E. Kross (2013). "An fMRI-based neurologic signature of physical pain." N Engl J Med 368(15): 1388-1397.

Poster No 2508

Reduced functional connectivity in patients with small fiber neuropathy: a resting state fMRI study

Sebastian Scheliga[1], Han-Gue Jo[2], Maike F. Dohrn[3], Thilo Kellermann[4], Angelika Lampert[5], Roman Rolke[6], Annette Lischka[7], Greta Peschke[3], Nortje Van den Braak[3], Ute Habel[8]

[1]RWTH Aachen University Hospital, Aachen, North Rhine-Westphalia, [2]Kunsan National University, Gunsan, Jeollabuk-do, [3]Department of Neurology, Medical Faculty RWTH Aachen University, Aachen, North Rhine-Westphalia, [4]Department of Psychiatry, Psychotherapy and Psychosomatics, Medical Faculty RWTH Aachen University, Aachen, North Rhine-Westphalia, [5]Institute of Neurophysiology, Medical Faculty RWTH Aachen University, Aachen, North Rhine-Westphalia, [6]Department of Palliative Medicine, Medical Faculty RWTH Aachen University, Aachen, North Rhine-Westphalia, [7]Institute for Human Genetics and Genomic Medicine, Medical Faculty RWTH Aachen University, Aachen, North Rhine-Westphalia, [8]Department of Psychiatry, Psychotherapy and Psychosomatics, RWTH Aachen University Hospital, Aachen, North Rhine-Westphalia

Introduction: Small fiber neuropathy (SFN) is clinically characterized by neuropathic pain and autonomic complaints[1]. Traditionally, SFN has been considered as a peripheral nervous system disorder. However, studies found aberrant brain functional connectivity during resting state (RS) in SFN patients[2]. Such functional changes were observed in neuropathic pain patients with different etiologies, e.g. diabetes mellitus[3]. To date, knowledge about RS alterations in idiopathic SFN is still lacking. Therefore, we used RS-fMRI to assess functional connectivity in a patient sample with idiopathic SFN. Gain-of-function mutations in voltage-gated sodium channels (Nav) have been discussed to play a role in the pathophysiology of SFN[4]. Therefore, we further analyzed RS connectivity in a homogenous subsample of SFN patients carrying missense Nav variants.

Methods: We recruited 31 healthy controls and 32 SFN patients. Patients with known neuropathy etiologies were excluded. In the patient sample, nine individuals carried rare heterozygous missense variants in SCN9A (n = 3), SCN10A (n = 3), or SCN11A (n = 4). One subject carried variants in SCN9A and SCN10A, respectively. We used seed-based voxel analysis; a whole-brain connectivity approach implemented in CONN toolbox, to compare RS connectivity between patients and controls. We defined right caudate nucleus as seed region for each analysis because we found reduced gray matter volume of that region in a previous voxel-based morphometry study from our lab[5]. We cluster-level threshold of $p < 0.05$ (FWE corrected). All regions showing significant group differences were considered for correlation analysis. Thereby, we extracted the respective connectivity coefficient and correlated it with total pain score from painDETECT questionnaire[6]. We used Pearson's correlation analysis implemented in SPSS 27. Finally, we calculated explorative seed-based analyses to compare the patient subsample carrying Nav variants with healthy controls and with patients without known genetic variants.

Results: Comparing SFN patients and controls, seed to voxel analysis revealed significantly reduced connectivity between right caudate nucleus seed and left supplementary motor area (SMA) in SFN patients. For the left caudate seed, there were no significant group differences. Moreover, comparing patients with missense variants and controls, explorative analysis yielded increased connectivity between right caudate seed and right Crus2 in Nav variant carriers compared with controls. Further, we compared patients without variants and healthy subjects. We identified increased connectivity between right caudate and left ACC for the patients. In controls, we found increased connectivity with bilateral SMA. There were no significant differences comparing patients with and without missense variants. We performed correlation analysis across all SFN patients. Here, we found a significant negative correlation between caudate-SMA connectivity and pain score ($r = -.364$, $p = 0.044$).

Conclusions: We found reduced RS connectivity between caudate nucleus and SMA in patients with SFN. These functional changes may point to deficits in the regulation of pain. Deficient RS connectivity may represent a disruption of endogenous pain modulatory systems elicited by long-term nociceptive input[7]. Further, the negative correlation between caudate-SMA connectivity and pain score suggests that lower RS connectivity may be linked with higher pain perception in SFN. Interestingly, we found higher connectivity between caudate nucleus and Crus2 in SFN patients with missense Nav variants compared with controls. Due to regulation deficits, increased connectivity may reflect compensatory functioning within endogenous pain-modulation networks[8] especially pronounced in patients with Nav variants. Future studies on SFN patients should further assess the involvement of sodium channel mutations in pain processing and the resulting brain functional changes.

References

1. Sopacua, M., Hoeijmakers, J. G., Merkies, I. S., Lauria, G., Waxman, S. G., & Faber, C. G. (2019). Small-fiber neuropathy: expanding the clinical pain universe. Journal of the Peripheral Nervous System, 24(1), 19-33.
2. Chao, C. C., Tseng, M. T., Lin, Y. H., Hsieh, P. C., Lin, C. H. J., Huang, S. L., ... & Chiang, M. C. (2021). Brain imaging signature of neuropathic pain phenotypes in small-fiber neuropathy: Altered thalamic connectome and its associations with skin nerve degeneration. Pain, 162(5), 1387-1399.
3. Zhang, Q., Zhang, P., Yan, R., Xu, X., Mao, C., Liu, X., ... & Wu, J. (2019). A single-blinded trial using resting-state functional magnetic resonance imaging of brain activity in patients with type 2 diabetes and painful neuropathy. Diabetes Therapy, 10, 135-147.
4. Lampert, A., Eberhardt, M., & Waxman, S. G. (2014). Altered sodium channel gating as molecular basis for pain: contribution of activation, inactivation, and resurgent currents. Voltage Gated Sodium Channels, 91-110.
5. Scheliga, S., Dohrn, M. F., Habel, U., Lampert, A., Rolke, R., Lischka, A., Van den Braak, N., Spehr, M., Jo, H. G., & Kellermann, T. Reduced gray matter volume and cortical thickness in patients with Small-Fiber Neuropathy (under review).
6. Freynhagen, R., Baron, R., Gockel, U., & Tölle, T. R. (2006). Pain DETECT: a new screening questionnaire to identify neuropathic components in patients with back pain. Current medical research and opinion, 22(10), 1911-1920.
7. Bushnell, M. C., Čeko, M., & Low, L. A. (2013). Cognitive and emotional control of pain and its disruption in chronic pain. Nature Reviews Neuroscience, 14(7), 502-511.
8. Mills, E. P., Di Pietro, F., Alshelh, Z., Peck, C. C., Murray, G. M., Vickers, E. R., & Henderson, L. A. (2018). Brainstem pain-control circuitry connectivity in chronic neuropathic pain. Journal of Neuroscience, 38(2), 465-473.

Poster No 2510

FMRI Deep Phenotyping of Experienced and Imagined Heat-Induced Somatotopy

Michael Sun[1], Ke Bo[1], Tor Wager[2]

[1]Dartmouth College, Hanover, NH, [2]Dartmouth College, Hanover, NH

Introduction: Pain perception is a complex neural process that involves encoding somatic nociception, aversive emotions, and contextual predictions about the persistence of stimuli causing pain. While previous research has established that the brain encodes pain differently across body sites and stimulation modalities, the specifics of this encoding – such as location, reliability, and individual differences – remain poorly understood. This study aims to understand (1) how different body sites vary in warmth sensitivity, heat tolerance, and pain perception; (2) the consistency of subjective pain experiences both within

and outside an fMRI environment; (3) differences in brain activity between actual and imagined heat stimulation, as compared to warm stimulation; (4) the brain regions involved in processing experienced versus imagined pain; and (5) the organization of activation within these regions.

Methods: The study was pre-registered on the Open Science Foundation platform (https://osf.io/zv4ec). We employed a longitudinal within-subject design of 9 participants (5 male, 4 female). Each participant was assigned individually calibrated High-Heat and Warm-Heat temperatures using an Ascending Method of Limits procedure. Participants then underwent fMRI scanning sessions where a Peltier thermode stimulated a skin-site on their body randomly with either high heat, warm heat, or an instruction to imagine themselves being burned by the thermode. Each participant underwent 40 runs of five repetitions of the thermode stimulating one of eight body sites. At the end of each run, participants were asked to rate the perceived heat intensity, valence (positive vs. negative), and overall bodily comfort.

Results: Experienced and imagined pain deactivated visual and and dorsal attention networks, but only experienced pain recruited the ventral attention network while deactivating the limbic network. Pattern similarity to neurotransmitter maps revealed that imagined pain deactivated regions with high GABA and 5HT receptor density, which is similar to experienced pain. Lexical analysis using Neurosynth topic maps of voxelwise principal components revealed that brain activity was distributed across 3 principal components of Pain Processing (73.94%), Motor Control (17.95%), and Spatial-Sensory Processing (8.12%). Predictably, brain activity across experienced and imagined pain (as well as warm stimulation) were similarly correlated with the first principal component, Pain processing, and similarly anticorrelated with the second principal component, Motor Control (warm stimulation was positively correlated). Experienced and imagined pain diverged on the third principal component, Spatial-Sensory Processing, where imagined pain was positively correlated, and experienced pain was negatively correlated. Warm stimulation was not correlated with this component. Imagined pain was significantly correlated with the Geuter Pain Signature (GPS) and Stimulus Intensity Independent Pain Signature (SIIPS), but not with Neurological Pain Signature (NPS) or Fibromyalgia Pain Signatures (FPS) suggesting that it largely recruits pain-related regions unrelated to nociception.

Conclusions: This study provides new insights into how brain activity is differentiated between experienced and imagined pain from different body sites. These findings have implications for our understanding of the neural basis of pain perception and its variability among individuals. Specifically, there may be a subset of individuals who can activate regions implicated in pain signatures such as the GPS, FPS, NPS, or SIIPS, which may be phenotypes relevant for potentiated pain or chronic pain experiences. The degree to which these signatures map onto reported pain exhibited significant bodysite and individual variability. There are potentially different bodysite-relevant pain patterns per individual, which suggests the need to fine-tune these signatures for individuals.

References

1. López-Solà, Marina, et al. “Towards a Neurophysiological Signature for Fibromyalgia.” Pain, vol. 158, no. 1, Jan. 2017, pp. 34–47.
2. Reddan, Marianne C., et al. “Effect Size Estimation in Neuroimaging.” JAMA Psychiatry, vol. 74, no. 3, 2017, p. 207, https://doi.org/10.1001/jamapsychiatry.2016.3356.
3. Wager, Tor D., et al. “An fMRI-Based Neurologic Signature of Physical Pain.” The New England Journal of Medicine, vol. 368, no. 15, 2013, pp. 1388–97.
4. Woo, Choong-Wan, et al. “Building Better Biomarkers: Brain Models in Translational Neuroimaging.” Nature Neuroscience, vol. 20, no. 3, Feb. 2017, pp. 365–77.
5. Zunhammer, Matthias, et al. “Placebo Effects on the Neurologic Pain Signature: A Meta-Analysis of Individual Participant Functional Magnetic Resonance Imaging Data.” JAMA Neurology, vol. 75, no. 11, Nov. 2018, pp. 1321–30.

Poster No 2511

Utilising Functional MRI and Psychophysics to Decode Descending Pain Modulation System

Joseph Taylor[1], Sonia Medina-Hernandez[2], Olivia Kowalcyck[1], Alessandra Venezia[1], Fawsitt-Jones Harriet[1], Elena Makovac[3], Timothy Lawn[1], Kirsty Bannister[1], Steven Williams[1], Matthew Howard[1]

[1]King’s College London, London, [2]Exeter Univeristy, Exeter, [3]Brunel University, London

Introduction: Conditioned pain modulation (CPM), a proposed measure of the efficiency of a person’s descending pain modulatory system (DPMS), refers to the phenomenon of increased pain thresholds and decreased intensity ratings in response to a given stimulus when applied in conjunction with a second noxious stimulus, compared to when applied in isolation. Dysfunction in this system has been reported in a variety of patient populations, but the results from these populations remain equivocal[1]. We used well-characterised noxious pressure stimulation, known to elicit robust and reliable responses in the brain[2] and a randomised, event-related fMRI design. It was hypothesised that pain ratings to unilateral

pressure stimuli would be reduced in the presence of a concurrent noxious stimulus, and that such reductions would be underpinned by cortical, midbrain and brainstem circuitry posited to be involved in endogenous pain control[3].

Methods: 50 participants completed a pain modulation paradigm involving delivery of a noxious "Test Stimulus" in the presence and absence of a concurrent noxious "Conditioning Stimulus", using custom designed thumb stimulators. Test and Conditioning stimuli were 2 and 8 seconds in duration respectively. The pressure eliciting approximately a 6/10 pain rating was titrated for each hand, then used as stimulation intensity. 36 stimuli were presented in a pseudorandomised trial structure, of "Test" trials, in which the test stimulus was presented on its own, and "Test+" trials, in which the test stimulus was presented with the conditioning stimulus. For every trial, participants rated the painfulness of the test stimulus, ignoring the conditioning stimulus, using a Visual Analogue Scale (VAS), anchored with 'no pain at all' and 'worst pain imaginable'. BOLD data were acquired at 3T and pre-processed using in FSL. First level explanatory variables (EVs) included the task regressors for Test, and Test+ trials and rating periods. Contrasts were performed for each trial type in isolation against baseline, with the main contrasts of interest being the two trial types compared against each other. Two first level analyses were performed: i) standard task analysis, ii) parametric modulation using first level trial-by-trial VAS ratings. For both, a second-level analysis was performed to derive mean brain activity across the group. Cluster significance was inferred at a family-wise error rate corrected threshold of 0.05.

Results: A two-way repeated measures ANOVA showed that the VAS ratings for the left hand were significantly lower than the right hand, but there were no significant differences in pain ratings between Test and Test+ trials, contrary to the hypothesised behavioural effect (Figure 1.). When considering the mean response to Test trials, there were significant clusters in bilateral S2 as well as contralateral Cerebellum. Group averaged contrasts between Test and Test+ stimulus classes also indicated significant clusters of stronger BOLD signal in bilateral S2 and contralateral cerebellum (see Figure 2.). Groupwise effects were not maintained in the parametric modulation analysis.

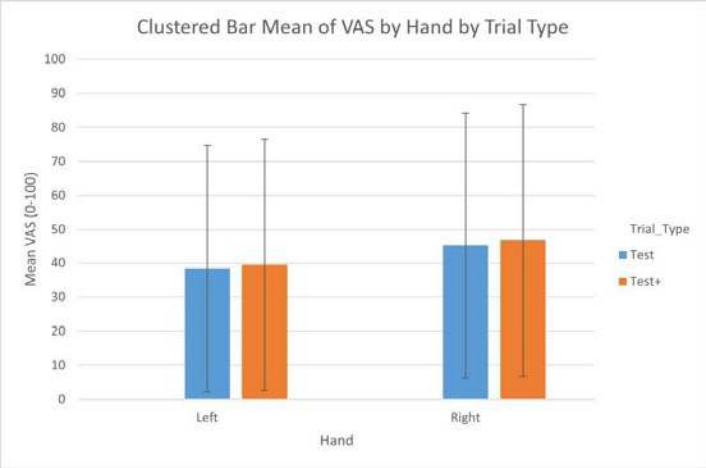

Figure 1. VAS ratings for each trial type and hand.

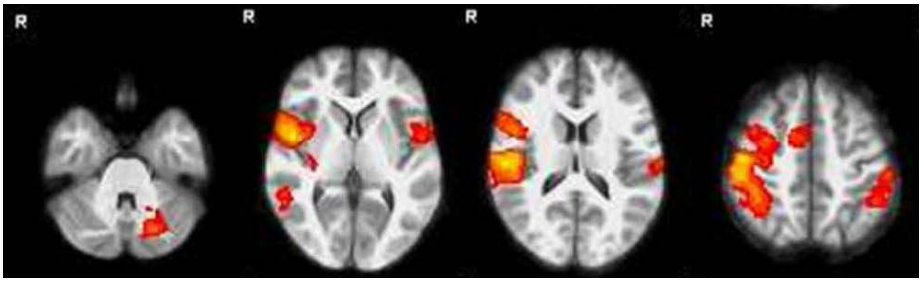

Figure 2. Significant clusters showing greater BOLD signal during Test+ trials compared to Test trials.

Conclusions: Despite the application of well-characterised pressure stimuli, we observed no behavioural effect implicating recruitment of the DPMS. While significant differences in BOLD signal between trial types were found, none were in cortical/sub-cortical regions suggested to be involved in descending pain control. Patterns of activity resembled previous reports of brain responses to pressure stimulation[2], which we interpret as more likely reflecting the effects of uni- vs bi-lateral stimulation. Our findings suggest that an experimental design optimised for maximising differences in BOLD activity may not be optimal for investigating the required behavioural effect. Since descending pain controls are an important therapeutic target, our study highlights the importance of paradigm design when it comes to understanding their mechanisms.

References
1. Fernandes, C., et al. (2019), 'Conditioned pain modulation as a biomarker of chronic pain: a systematic review of its concurrent validity.' Pain, 160(12), 2679-2690.
2. Jackson, J. B., et al. (2020), 'Noxious pressure stimulation demonstrates robust, reliable estimates of brain activity and self-reported pain.' Neuroimage, 221, 117178.
3. Nahman-Averbuch et al. (2022). 'Neural mechanisms underlying the conditioned pain modulation response: a narrative review of neuroimaging studies.' Pain, 10-1097.

Poster No 2512

Assessing the influence of uncertainty on pain perception

Mégane Lacombe-Thibault[1], Michel-Pierre Coll[1]

[1]Laval University, Québec, Quebec

Introduction: According to a learning account of pain, pain should be modulated to optimize learning and control (Seymour, 2019). Accordingly, previous evidence suggests that the subjective perception of pain is increased when pain leads to prediction errors that can be used to learn new information (Coll et al., 2023). Functional magnetic resonance imaging studies (fMRI) have measured brain activity during various cued pain paradigms and have found mediation effects of the anterior insular cortex on expectation of pain and on the integration of expectation and prediction errors of pain in healthy individuals (Strube et al., 2021; Fazeli and Büchel, 2018). Furthermore, pain perception is likely influenced by the uncertainty of the environment (De Berker et al., 2016) since, in uncertain settings, information gained from pain experiences could be more valuable. However, we still know little about the neural mechanisms underlying the modulation of pain perception by uncertainty. The current study aimed at validating a behavioural task in which pain stimuli could be used to learn cue-outcome contingencies under varying degrees of uncertainty. The ultimate goal is to employ this task in assessing the brain mechanisms responsible for how uncertainty modulates pain perception.

Methods: 50 healthy adults (mean age of 24.38 years old; 28F, 22M) participated in an experimental task (den Ouden et al., 2010) in which they had to learn to predict the associations between high or low tones and high or low painful electric stimuli. At each trial of this task (Figure 1A), a tone was presented and was followed by a painful stimulus. Participants had to indicate if the pain they received was high or low as quickly as possible. The probabilities related to the associations between the tones and painful stimuli changed throughout the task. The associations remained stable for several trials or changed rapidly in order to create periods of low or high uncertainty (Figure 1B). Different reinforcement learning models and a null model were compared to assess which model would best explain the data across participants. We then used trial-wise estimates of prediction errors and various types of uncertainty to attempt to predict changes in pain perception using linear mixed models.

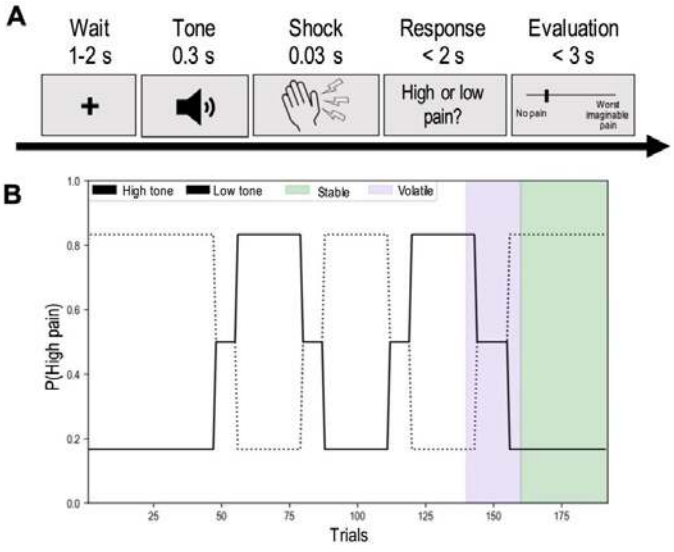

Results: Participants adequately learned to predict upcoming pain intensity, as confirmed by faster response times when the expected intensity was presented compared to unexpected outcomes (Figure 2A). Furthermore, model comparison confirmed that a hierarchical Bayesian learning model (Mathys et al., 2014) taking into account participants' uncertainty was the best model to explain participants' behaviour (Figure 2B), and this model adequately captured participants' changes in expectations and environmental uncertainty according to the changes in contingencies (Figure 2C and 2D). Computational

estimates of environmental uncertainty was a significant estimate of pain ratings (B = 2.15 - 95% CI [0.73, 3.6]), but this relationship interacted with stimulus intensity (B = -4.19 - 95% CI [-7.17, -2.46]) so that high pain stimuli were perceived as less intense under high uncertainty (B = -2.11 - 95% CI [-4.98, -0.18]) while low pain stimuli were perceived as more intense under higher uncertainty (B = 1.84 - 95% CI [0.28, 3.40]).

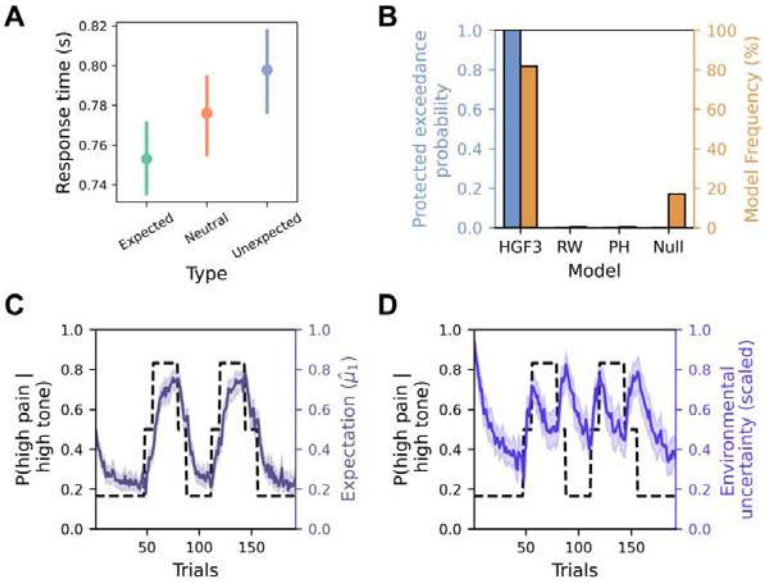

Figure 2. (A) Response time as a function of expectations of the intensity of the stimulus. **(B)** Results of the bayesian model comparison showing that the Hierarchical gaussian filter (HGF) best explained the behavioural data compared to Rescorla-Wagner (RW), Pearce-Hall (PH) models and a Null model assuming no learning. **(C)** The trajectory of average computational estimates of posterior expectations compared to actual contingencies. **(D)** The trajectory of average computational estimates of environmental uncertainty compared to actual contingencies. Error bars and shading show +/- 1 standard error of the mean.

Conclusions: The results obtained in this study suggest participants were able to accurately learn associations between tones and painful stimuli in the task developed and that pain perception was influenced by estimates of prediction errors and uncertainty. The developed task is therefore suitable to be used in future neuroimaging studies to evaluate how modulation of pain by these learning processes is implemented in the brain.

References

1. Coll, M.-P. et al. 2023. "Pain Reflects the Informational Value of Nociceptive Inputs". Preprint. Neuroscience. https://doi.org/10.1101/2023.07.14.549006.
2. de Berker, A. O. et al. 2016. "Computations of Uncertainty Mediate Acute Stress Responses in Humans." Nature Communications 7 (1): 10996. https://doi.org/10.1038/ncomms10996.
3. den Ouden, H. E. M. et al. 2010. "Striatal Prediction Error Modulates Cortical Coupling." Journal of Neuroscience 30 (9): 3210–19. https://doi.org/10.1523/JNEUROSCI.4458-09.2010.
4. Fazeli, S. and Büchel, C. 2018. "Pain-Related Expectation and Prediction Error Signals in the Anterior Insula Are Not Related to Aversiveness." The Journal of Neuroscience 38 (29): 6461–74. https://doi.org/10.1523/JNEUROSCI.0671-18.2018.
5. Mathys, C. D. et al. 2014. "Uncertainty in Perception and the Hierarchical Gaussian Filter." Frontiers in Human Neuroscience 8 (November). https://doi.org/10.3389/fnhum.2014.00825.
6. Seymour, B. 2019. "Pain: A Precision Signal for Reinforcement Learning and Control." Neuron 101 (6): 1029–41. https://doi.org/10.1016/j.neuron.2019.01.055.
7. Strube, A. et al. 2021. "The Temporal and Spectral Characteristics of Expectations and Prediction Errors in Pain and Thermoception." eLife 10 (February): e62809. https://doi.org/10.7554/eLife.62809.

Poster No 2513

K-means clustering to explore phenotypes of chronic ocular pain using resting fMRI and clinical data

Scott Holmes[1], Nicholas Reyes[2], Jaxon Huang[3], Anat Galor[2], Pradip Pattany[4], Elizabeth Felix[4], Eric Moulton[1]

[1]Boston Children's Hospital, Boston, MA, [2]Miami Veterans Administration Medical Center, Miami, FL, [3]Miami Veterans Affairs Administration Medical Center, Miami, FL, [4]University of Miami, Miami, FL

Introduction: The factors that mediate the expression of ocular pain and the mechanisms that promote chronic ocular pain symptoms are poorly understood. Central nervous system involvement is suspected based on observations of pain out of proportion to nociceptive stimuli in some patients. We focused on understanding functional connectivity between brain regions implicated in pain in persons reporting ocular pain symptoms.

Methods: Using a 3T Siemens MAGNETOM Vida scanner, we performed a resting state fMRI investigation using a region of interest (ROI) analysis that focused on subcortical brain structures including the trigeminal nucleus and performed a battery of ophthalmological examinations. 53 persons were divided into two cohorts: no ocular pain, and chronic ocular pain. A GE-EPI scan (TE/TR=30/2000ms, resolution: 1.94x1.94x1.50mm, duration: 10:06, volumes: 303) was collected with the participants instructed to keep their eyes open and to blink normally. Our field of view focused on brainstem and sub-cortical structures. ROIs included the thalamus, caudate, putamen, pallidum, amygdala, accumbens, brainstem, periaqueductal gray, and trigeminal nucleus. We also included bilateral precentral and postcentral gyrus based on prior work in persons with chronic pain[1]. fMRI data was processed using the CONN toolbox[2]. Standard pipeline settings were used, including realignment and unwarping, slice-timing correction, outlier detection, segmentation, normalization, spatial smoothing with an 8 mm filter. Resulting images were processed using a band-pass filter (0.008-0.09 Hz). Statistical significance for functional connectivity analysis was considered significant for $p<0.05$ (uncorrected for multiple comparisons). K-means clustering analysis was performed using Sklearn[3] on our chronic ocular pain cohort ($n = 37$) to separate these participants. We use silhouette coefficients to determine the number of clusters to use in our pain sub-cohorts. All clinical data were included as well as the output functional connectivity matrices from all ROIs. We performed a principal component analysis on the matrices from each participant and extracted the top 20 components that represented 80% of the variance. We chose two clusters based on the limited sample size of the starting population. We also determined the feature performance in differentiating the two pain cohorts using a K-means clustering analysis using the SelectKBest package and then back projected cluster data into original clinical metrics for clinical interpretation.

Results: The ocular pain cohort reported higher levels of pain symptoms relating to neuropathic pain and ocular surface disease, as well as more abnormal tear metrics (stability and tear production) than the non-pain cohort. Functional connectivity analysis between groups evinced multiple connections exemplifying both increases and decreases in connectivity including regions such as the trigeminal nucleus, amygdala, and sub-regions of the thalamus. K-based clustering analysis of the ocular pain cohort highlighted two new constituent pain sub-cohorts ($n=17$, $n=20$) presenting with unique phenotypes. Clinically, these groups represent individuals with lower (Group 1) and higher (Group 2) levels of ocular pain with neuropathic features. The top five distinguishing features were “Tear production in the left eye”, “Tear breakup time in the right eye”, “Resting State Network - Principal Component 13,” and “Ocular pain-before and after anesthesia,” and “Worst pain scores from the prior week.” This combination of features reflects fMRI and clinical metrics and suggests that even when considering pain and ocular surface metrics, functional brain connectivity remains an important differentiator between pain cohorts.

Conclusions: Our findings support centralized involvement in those patients reporting chronic ocular pain and allude to mechanisms through which pain treatment services may be directed in future research.

References

1. Holmes, S.A., Barakat, N., Bhasin, M., Lopez, N.I., Lebel A., Zurakowski D., et al. (2020), ‘Biological and behavioral markers of pain following nerve injury in humans’ Neurobiol Pain, vol. 7, p. 100038. doi: 10.1016/j.ynpai.2019.100038
2. Nieto-Castanon, A., Whitfield-Gabrieli, S. (2012), ‘Conn: a functional connectivity toolbox for correlated and anticorrelated brain networks’ Brain Connect. vol. 2, pp. 125–141. doi: 10.1089/brain.2012.0073
3. Pedregosa, F., Varoquaux, G., Gramfort, A., Michel, V., Thirion, B., Grisel, O., et al. (2011) ‘Scikit=−learn: machine learning in Python’ J Mach Learn Res. vol. 12, pp. 2825–2830.

Poster No 2514

Employing α-wave EEG-based neurofeedback in low-back pain management: a longitudinal study

Manal Ikram[1], Camille Grande[2], Djamel Dabli[3], Alexis Hom[3], Jean Paul Beregi[3], Arnaud Dupeyron[1], Fabricio Pereira[4]

[1]University of Montpellier, Montpellier, Occitanie, [2]Aix-Marseille University, Marseille, Provence-Alpes-Côte d’Azur, [3]University Hospital Center of Nimes, Nimes, Occitanie, [4]University of Nimes, Nimes, Occitanie

Introduction: Chronic low back pain (cLBP) is a pervasive issue impacting nearly a quarter of the population, highlighting its widespread prevalence and impact across various age groups.[1] This enduring condition, persisting for a minimum of 12 weeks, casts a significant shadow over the lives of those affected, subjecting them to prolonged discomfort and distress. Despite the manifold therapeutic approaches, including traditional pharmacological and manual treatments, many individuals grapple with ongoing pain, revealing the insufficiency of existing methods in providing lasting relief.[2] As this chronic ailment persists and substantially impairs the well-being of a significant portion of society, the quest for novel and more efficacious interventions becomes increasingly urgent. Studies suggest that higher power of alpha waves, neural oscillations ranging from 8 to 12 Hz, could lessen the intensity of pain. Thus, inducing alpha waves in cLBP individuals might offer a better pain management, though the exact mechanisms are still under exploration in neuroscience. In this longitudinal study, quantitative

EEG (qEEG) was utilized to capture real-time measurements of individuals' alpha-wave power and induce alpha-wave synchronization in patients experiencing chronic low back pain (cLBP). Daily sessions of neurofeedback were implemented and followed-up. EEG pattern was correlated with physical and mental pain. Finally, the efficacy of this intervention was assessed through comprehensive clinical evaluations. This comprehensive methodological framework aimed to provide a thorough understanding of the intervention's impact on both the subjective experiences of pain and the overall clinical status of individuals enduring chronic low back pain

Methods: The study was registered as Trial #NCT03929952, and all participants provided informed consent. Twelve patients diagnosed with cLBP aged from 28 to 58 years were enroled. Their pain intensity, rated above 5 on the Visual Analog Scale (EVA), significantly impacted their daily functionality, indicated by high scores on the Oswestry Disability Index (ODI). During the study, participants engaged in daily 30-minute sessions of an EEG-based closed-loop neurofeedback program for 20 consecutive days, focusing on a visual stimulus resembling a flame while real-time alpha-wave power was computed. They were rewarded based on achieving predominant EEG frequencies between 7 and 14 hertz. The collected EEG data underwent preprocessing, including file conversion, band-pass filtering, Independent Component Analysis (ICA), brain map generation, normalization, and statistical analyses, examining changes in alpha-synchrony and its correlation with clinical assessments

Results: Longitudinal analysis revealed a significant increase ($p<.05$) in alpha-wave power in the frontal regions, particularly around electrode Fz, while a decrease in activity was observed in parieto-temporal regions throughout the neurofeedback program [Figure 1: first (a) and last (b) sessions]. Additionally, statistical tendencies ($p<.06$) indicated negative correlations between F3, F4, and Fz with EVA (r=-.42/-.46/.51) and ODI (r=-.37/-.33/.43), whereas C3 and C4 electrodes exhibited positive correlations for EVA (r=.29/.32) and ODI (r=.25/.29).

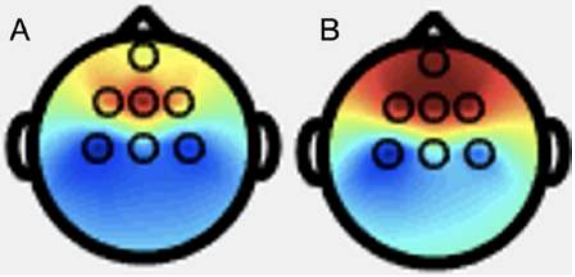

Fig. The alpha-synchrony levels were compared between the initial (a) and final (b) EEG sessions.

Conclusions: Neuromodulation based on alpha-synchronization is associated with electrical changes in frontal regions and may play a critical role in managing pain in cLBP

References

1. Balagué, F. (2012), 'Non-specific low back pain', The Lancet, 379(9814), 482–491
2. Bushnell, M. C. (2013), 'Cognitive and emotional control of pain and its disruption in chronic pain', Nature Reviews Neuroscience, 14(7), 502–511.

Poster No 2515

Greater integration across frontal networks and lower quality of life in youth with chronic pain

Saül Pascual-Diaz[1], Emma Biggs[2], Marie-Eve Hoeppli[3], Christopher King[4,5,6], Nima Aghaeepour[2], Martin Angst[7], Brice Gaudilliere[7], Jennifer Stinson[8,9], Massieh Moayedi[10,11], Robert Coghill[12], Laura Simons[2], Marina López-Solà[1]

[1]University of Barcelona, Barcelona, Spain, [2]Department of Anesthesiology, Perioperative and Pain Medicine, Stanford University, Stanford, CA, [3]CCHMC, Cincinnati, OH, [4]Department of Pediatrics, University of Cincinnati, Cincinnati, OH, [5]Division of Behavioral Medicine and Clinical Psychology, Cincinnati Children's Hospital Medical Center, Cincinnati, OH, [6]Pediatric Pain Research Center (PPRC), Cincinnati Children's Hospital Medical Center, Cincinnati, OH, [7]Centre for the Study of Pain, University of Toronto, Toronto, Ontario, [8]Department of Anesthesia and Pain Medicine, The Hospital for Sick Children, Toronto, Ontario, [9]The Research Institute, The Hospital for Sick Children, Toronto, Ontario, Canada, [10]Centre for Multimodal Sensorimotor and Pain Research, Faculty of Dentistry, University of Toronto, Toronto, Ontario, [11]Centre for the Study of Pain, University of Toronto, Toronto, Ontario, Canada, [12]Cincinnati Children's Hospital Medical Center, Cincinnati, OH

Introduction: Multisensory experiences significantly contribute to daily well-being, particularly in adolescents dealing with chronic musculoskeletal pain (CMP)[1]. Studies consistently demonstrate the correlation between hypersensitivity to multisensory stimulation and lower quality of life (QoL) in chronic pain patients, impacting school attendance and physical

activity[2,3]. Connectivity between the Default Mode Network (DMN), Frontoparietal Network (FPN), and Ventral Attention (or Salience Network; VAN) during resting-state has been linked to chronic pain[4,5]. Abnormal integration between the DMN and the VAN has been observed in individuals with chronic pain, suggesting its relevance to the experience of clinical pain[6]. This study aimed to determine whether (i) integration across medial frontal cortical brain networks including the DMN, the VAN, and the FPN[7]; and (ii) brain activation during a multisensory task could predict QoL in youth with chronic pain. We hypothesized that greater activation in regions important for multisensory integration and cognitive/evaluative response to multisensory stimulation such as the medial and lateral aspects of the prefrontal cortex and networks converging in medial prefrontal regions would predict QoL.

Methods: We included 129 participants (110 females, aged 12 to 18, mean age=15.58, SD=1.57) with CMP from Stanford University; Cincinnati Children's Hospital, and Sick Kids Hospital in Toronto. We used an fMRI multisensory task[8] and measured self-reported QoL (Pediatric QoL of Life Inventory (PedsQL)). The fMRI task involved four trials of concurrent presentation of visual, auditory, and tactile-motor stimulation and alternating rest periods. We preprocessed fMRI data to correct motion and noise using the CONN toolbox. GLMs identified voxels with significant activity changes during multisensory blocks compared to baseline, and we ran a voxel-wise regression to identify brain regions associated with the physical scale of PedsQL. We computed connectivity matrices (controlling for task-related oscillations) for each subject during the multisensory task to obtain between-network integration values. Nodes corresponded to Brainnetome atlas regions overlapping with each brain network[7,9], with edges representing brain connectivity amongst between-network ROI pairs.

Results: Augmented brain responses to non-painful multisensory stimulation in the rostral ACC predicted lower physical QoL (qFWEcluster-corrected=0.05, individual voxel p<.001). In females only, another cluster became significant in the dorsomedial prefrontal cortex (dmPFC) (qFWE=0.029). We ran bootstrap analyses (10000 permutations) revealing that the probability of obtaining the resulting clusters by chance was 0.09% (Fig 1). Greater between-network connectivity (FPN, VAN and DM networks) predicted augmented responses in the rostral ACC during the multisensory task, which in turn predicted lower QoL. Importantly, for these network connectivity analyses we excluded regions from the Brainnetome atlas showing overlap (≥1 voxel) with the ACC and dmPFC activation clusters. We did not find a direct effect of connectivity on QoL (Fig 2).

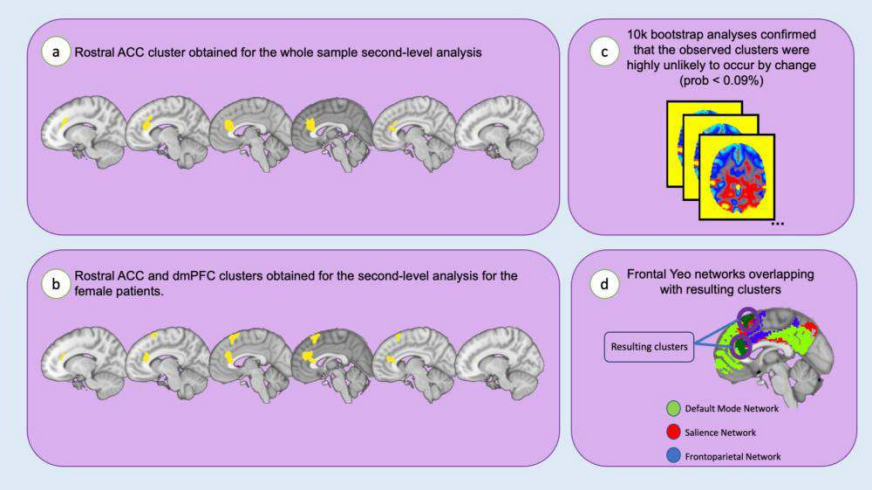

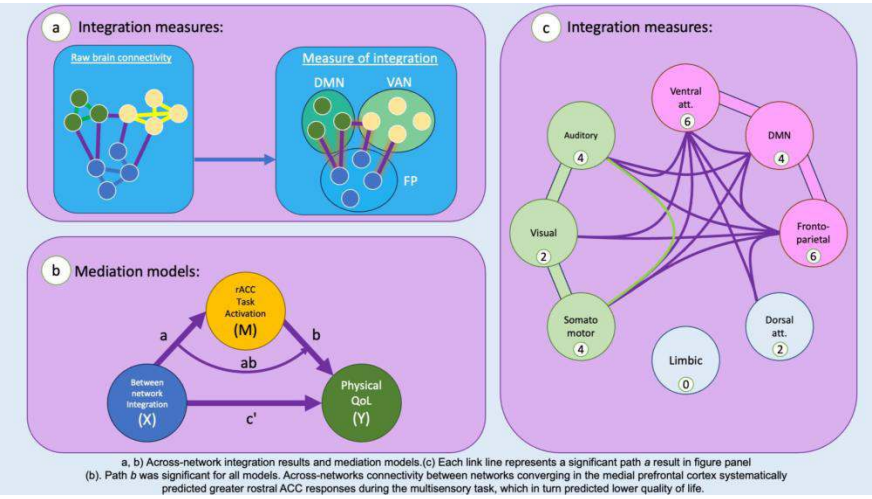

a, b) Across-network integration results and mediation models.(c) Each link line represents a significant path *a* result in figure panel (b). Path *b* was significant for all models. Across-networks connectivity between networks converging in the medial prefrontal cortex systematically predicted greater rostral ACC responses during the multisensory task, which in turn predicted lower quality of life.

Conclusions: We observed a robust association between heightened task-evoked activation in the rostral ACC and dmPFC and lower physical QoL in adolescents with CMP. Our findings suggest that adolescents with CMP exhibiting increased activation in affective/regulation circuits during a non-painful, unpleasant sensory task tend to experience lower QoL, affecting their ability to perform physical activities in daily life. The findings were coupled with greater signal integration between cortical networks with important medial prefrontal representation (DMN, VAN, and FPN). The results highlight the association between aberrant multisensory processing (both in terms of augmented activation and between-networks signal integration) and reduced quality of life in youth with CMP.

References

1. Kamper, S. J., & Williams, C. M. (2017). "Musculoskeletal Pain in Children and Adolescents: A Way Forward". The Journal of orthopaedic and sports physical therapy, 47(10), 702–704.
2. Seo, J. G., & Park, S. P. (2019). "Clinical significance of sensory hypersensitivities in migraine patients: does allodynia have a priority on it?". Neurological sciences : official journal of the Italian Neurological Society and of the Italian Society of Clinical Neurophysiology, 40(2), 393–398.
3. Wang, D., & Frey-Law, L. A. (2023). "Multisensory sensitivity differentiates between multiple chronic pain conditions and pain-free individuals". Pain, 164(2), e91–e102.
4. Baliki, M. N. (2014). "Functional reorganization of the default mode network across chronic pain conditions". PloS one, 9(9), e106133.
5. Hemington, K. S. "Abnormal cross-network functional connectivity in chronic pain and its association with clinical symptoms". Brain structure & function, 221(8), 4203–4219.
6. Ellingsen, D. M. (2021). "A picture is worth a thousand words: linking fibromyalgia pain widespreadness from digital pain drawings with pain catastrophizing and brain cross-network connectivity". Pain, 162(5), 1352–1363.
7. Yeo, B. T. (2011). "The organization of the human cerebral cortex estimated by intrinsic functional connectivity". Journal of neurophysiology, 106(3), 1125–1165.
8. López-Solà, M. (2014). "Altered functional magnetic resonance imaging responses to nonpainful sensory stimulation in fibromyalgia patients". Arthritis & rheumatology (Hoboken, N.J.), 66(11), 3200–3209.
9. Fan, L. (2016). "The Human Brainnetome Atlas: A New Brain Atlas Based on Connectional Architecture". Cerebral cortex (New York, N.Y. : 1991), 26(8), 3508–3526.

Poster No 2516

Deciphering the role of emotion in pain modulation by stimulus expectancy: an fMRI study

Hsin-Yun Tsai[1], Ming-Tsung Tseng[2]

[1]Taiwan International Graduate Program in Interdisciplinary Neuroscience, National Taiwan University, Taipei, Taiwan, [2]Graduate Institute of Brain and Mind Sciences, National Taiwan University College of Medicine, Taipei, Taiwan

Introduction: Human pain perception arises from the integration of prior expectations with sensory evidence. Although recent work has demonstrated that treatment expectancy effects (e.g., placebo hypoalgesia) can be explained by an integration framework incorporating the precision level of expectations and sensory inputs, the key factor modulating this integration in stimulus expectancy-induced pain modulation remains unclear.

Methods: In a stimulus expectancy paradigm combining emotion regulation in 31 healthy adults (both sexes), participants not only negatively or positively expected the upcoming electrocutaneous stimulus (i.e., expected an increased pain or a reduced pain, respectively) but were also instructed to attend to or downregulate their expectancy-associated emotions. By recording participants' skin conductance responses during the anticipation period, we confirmed the validity of emotion regulation on expectancy-induced emotions. Meanwhile, to investigate the underlying neural mechanisms, we collected participants' blood-oxygen-level-dependent (BOLD) signals by using the functional magnetic resonance imaging (fMRI) technology.

Results: At the behavioral level, we found that participants' voluntary reduction in anticipatory anxiety and pleasantness monotonically reduced the magnitude of pain modulation by negative and positive expectations, respectively, indicating a role of emotion in stimulus expectancy effects of pain perception. For both types of expectations, Bayesian model comparisons confirmed that an integration model using the respective emotion of expectations and sensory inputs explained stimulus expectancy effects on pain better than using their respective precision. For negative expectations, the role of anxiety is further supported by our fMRI findings that (i) functional coupling within anxiety-processing brain regions (amygdala and anterior cingulate cortex) reflected the integration of expectations with sensory inputs, and (ii) anxiety appeared to impair the updating of expectations via suppressed prediction error signals in the anterior cingulate cortex, thus perpetuating negative expectancy effects. Regarding positive expectations, their integration with sensory inputs relied on the functional coupling within brain structures processing positive emotion and inhibiting threat responding (medial orbitofrontal cortex and hippocampus).

Conclusions: In conclusion, the current study demonstrates that brain structures implicated in emotion processing integrate prior and novel pain experiences and may also influence the updating of pain predictions to underlie pain modulation by stimulus expectancy. Our findings add to the growing studies investigating the computational mechanisms behind expectancy modulation on pain.

References

1. Grahl, A. (2018), 'The periaqueductal gray and Bayesian integration in placebo analgesia', eLife, vol. 7.
2. Shih, Y.-W. (2019), 'Effects of Positive and Negative Expectations on Human Pain Perception Engage Separate But Interrelated and Dependently Regulated Cerebral Mechanisms', Journal of Neuroscience, vol. 39, pp. 1261-1274.

Poster No 2517

Dynamics of Cortical Thickness Alterations in Patients with Chronic Pain

Patcharaporn Srisaikaew[1], Timur Latypov[2], Alborz Noorani[2], Mojgan Hodaie[2,1]

[1]University Health Network, Toronto, Canada, [2]University of Toronto, Toronto, Canada

Introduction: Trigeminal neuralgia (TN) is a severe chronic neuropathic pain disorder characterized by intense shock-like pain in distributions of the trigeminal nerve branches. A distinctive feature of TN is the fear of recurring attacks, and the thought of recurrence of pain uniformly results in pain-related anxiety and stress. Previous structural brain imaging studies provide evidence of the association between chronic pain, pain-related stress and emotion, and the loss of gray matter (GM) volume. The prefrontal, anterior cingulate, and insular cortices are well-documented brain regions involved in pain mechanisms and are affected by stress and negative affect, and could be associated with the development of emotion disorders after experienced chronic pain (Obermann et al., 2013; Fritz et al., 2016; Hayes et al., 2017; Yuan et al., 2017). However, whether these altered cortical regions alter following surgical intervention for pain remain unclear. In this study, we aim to investigate the alterations of cortical thickness involved in pain mechanism and associated emotion-affective circuit in chronic pain patients. We used TN as a model to study pain and its potential resolution after surgery.

Methods: 3T anatomical T1-weighted images from 119 TN patients including pre-surgery (pre-sx) and 6 months after Gamma Knife radiosurgery (GKRS; post-sx) timepoints, and age-/sex-matched healthy controls (HC) were collected and analyzed. Freesurfer was used to perform the volumetric segmentation (cortical thickness, mm3) of the ventromedial prefrontal cortex (vmPFC), dorsolateral prefrontal cortex (dlPFC), anterior cingulate cortex (ACC), and insula cortex in both hemispheres. The estimated total intracranial volume in each hemisphere of each participant was calculated to account for the head size difference within the study cohorts. The significant statistical level was set at $p<.05$. All reported p-values were corrected for the multiple comparisons with the false discovery rate procedure ($q<.05$).

Results: The results showed the thickness (volume) of vmPFC, dlPFC, ACC, and insula cortices were significantly reduced in TN with persistent pain symptoms when compared to the controls ($q<0.01$). Comparing between pre- and post-surgical timepoints, these brain regions were significantly normalized (increased in volume) in TN only after successful pain relief ($q<0.001$). However, this effect was found only in patients who reported at least 75% pain relief after successful GKRS ($q<0.01$).

Conclusions: Our findings indicate the brain morphological changes observed in patients with TN are affected by chronic pain and may be linked to negative affect following pain experienced. Of importance, pain relief by surgical intervention normalizes these cortical alterations in the chronic pain cohort. The observed normalization pattern suggests dynamic cortical thickness alterations in chronic pain regarding neuronal plasticity. This also suggested that the investigation of the related mechanism (e.g., processing emotion and behaviour regulation) whereby these dynamic alterations take place should be considered in future studies. Recovery of pain-associated symptoms including negative affect is an important component in the management of chronic pain patients.

References

1. Fritz, H.C. et al. (2016) "Chronic Back Pain Is Associated With Decreased Prefrontal and Anterior Insular Gray Matter: Results From a Population-Based Cohort Study," The journal of pain: official journal of the American Pain Society, 17(1), pp. 111–118.
2. Hayes, D. J. et al. (2017) "Affective Circuitry Alterations in Patients with Trigeminal Neuralgia," Frontiers in neuroanatomy, 11, p. 73.
3. Obermann, M. et al. (2013) "Gray matter volume reduction reflects chronic pain in trigeminal neuralgia," NeuroImage, 74, pp. 352–358.
4. Yuan, C. et al. (2017) "Gray Matter Abnormalities Associated With Chronic Back Pain: A Meta-Analysis of Voxel-based Morphometric Studies," The Clinical journal of pain, 33(11), pp. 983–990.

Poster No 2518

Modeling dynamic brain responses of sustained pleasure and pain based on flexible basis functions

Soo Ahn Lee[1,2,3], Tor Wager[4], Choong-Wan Woo[1,2,3]

[1]Department of Biomedical Engineering, Sungkyunkwan University, Suwon-si, Korea, Republic of, [2]Center for Neuroscience Imaging Research, Institute for Basic Science, Suwon-si, Korea, Republic of, [3]Department of Intelligent Precision Healthcare Convergence, Sungkyunkwan University, Suwon-si, Korea, Republic of, [4]Department of Psychological and Brain Sciences, Dartmouth College, Hanover, NH

Introduction: Both sustained pleasure and pain induce dynamic affective brain states for longer time scales. Because these brain states slowly emerge and fluctuate over time, it is hard to specify the timings of the emergence and recovery of these state-related brain responses (Robinson et al. 2010). Here, we conducted a functional Magnetic Resonance Imaging (fMRI) experiment in which participants received the oral delivery of chocolate and capsaicin fluids. While experiencing multiple combinations of sustained pleasure and pain conditions, participants continuously rated their subjective pleasantness and unpleasantness. To model these brain responses more effectively, we used spline functions as flexible basis sets in the GLM analysis to identify encoding models of dynamic affective states.

Methods: We collected 14-minute fMRI data from 61 participants (28 females, mean of age = 22.74, SD of age = 2.66). We delivered capsaicin or chocolate fluids to participants' oral cavity through the MR-compatible fluid delivery system (Octaflow II, ALA Scientific Instruments Inc., Westbury, NY) and a custom-built MR-compatible mouthpiece. In the 'Capsaicin-Capsaicin (CC)', 'Capsaicin-Sweet (CS)', and 'Sweet-Sweet (SS)' conditions, we delivered capsaicin (Jinmifood, Inc.) or sweet chocolate (Hershey's, Inc.) fluids sequentially during each scan. The first and second deliveries occurred 90 seconds and 7 minutes after the start of the scan, respectively. In addition, there was 'Capsacin-water (C0)' condition, where we delivered capsaicin fluids only once 90 seconds after the start of the scan. During scans, we asked participants to continuously rate their moment-by-moment changes of subjective pleasantness or unpleasantness, based on the general Labeled Magnitude Scale (Bartoshuk et al. 2004). We conducted the spline-based univariate analysis that flexibly captures the fMRI signals related to pleasant and unpleasant states, obtaining the areas under the curve (AUCs) that indicate the overall activation magnitudes for each brain voxel.

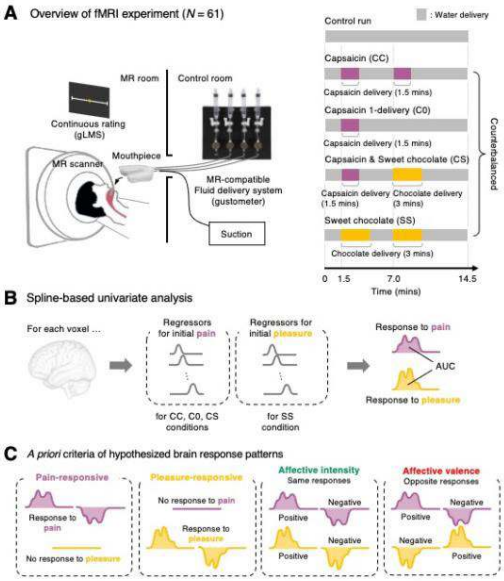

Figure 1. Overview of the fMRI experiment (*N* = 61) and spline-based GLM analysis. **(A)** fMRI experiment settings and multiple combinations of capsaicin and sweet chocolate conditions. **(B)** Overview of univariate GLM analysis using sets of spline functions as event regressors. **(C)** *A priori* criteria to characterize brain regions: (1) pain-responsive brain regions should show significant area under the curves (AUCs) to initial capsaicin, (2) pleasure-responsive brain regions should show significant AUCs to initial sweet chocolate, (3) brain regions of affective intensity should show the same patterns of AUCs to both initial capsaicin and sweet chocolate (i.e., both positive or negative AUCs for initial capsaicin and sweet chocolate), and (4) brain regions of affective valence should show the opposite patterns of AUCs to initial capsaicin and sweet chocolate (i.e., positive AUCs for initial capsaicin and negative AUCs for initial sweet chocolate, vice versa).

Results: We used the 265-region whole-brain parcellation combining Schaefer cortical atlas (Schaefer et al. 2018), subcortical and cerebellar regions from the Brainnetome atlas (Fan et al. 2016), and brainstem regions (Beissner et al. 2014; Roy et al. 2014). We examined brain response patterns based on the spline-based event regressors, toward initial sustained pain (i.e, the first capsaicin deliveries across CC, C0, and CS conditions) and initial sustained pleasure (i.e., the first sweet chocolate deliveries in SS conditions). There were significant AUCs in the dorsal posterior insula, cingulate cortex, somatosensory cortex, and ventromedial cortex for the initial capsaicin deliveries. There were significant AUCs in the amygdala, ventral anterior insula, and frontal parts of the medial prefrontal cortex for the initial chocolate deliveries. The results were consistent with the GLM results based on the canonical hemodynamic function. We categorized the brain regions based on the a priori criteria about their response patterns, similar to our previous study (Lee et al. 2023). (1) We found 58 pain-responsive brain regions that showed significant AUCs to initial capsaicin and (2) 49 pleasure-responsive brain regions that showed significant AUCs to initial sweet chocolate. 22 brain regions overlapped that satisfied both (1) and (2), and we found (3) 13 brain regions of affective intensity (weak vs. strong) that showed the same signs of AUCs and (4) 9 brain regions of affective valence (pleasant vs. unpleasant) that showed opposite signs of AUCs. The 22 brain regions showed large spatial overlaps with the predictive regions of the multivariate encoding models of the affective intensity and valence (Lee et al. 2023), tracking the overall trajectories of our hypothetical response patterns.

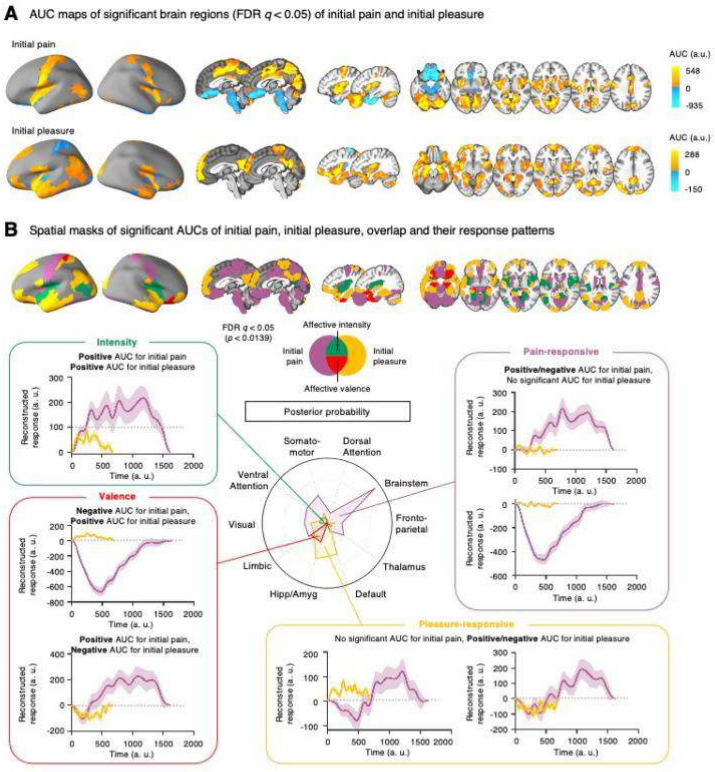

Figure 2. AUCs of significant brain regions among 265-region whole-brain parcellations and their response patterns.

(A) AUCs of significant brain regions for initial pain and pleasure across 265 brain regions ($p < 0.0139$, multiple comparisons based on the False Discovery Rate (FDR) $q < 0.05$). **(B)** Masks of the significant brain regions categorized as pain-responsive, pleasure-responsive, affective intensity, and affective valence. We provided their posterior probability given each large-scale functional brain network (Yeo et al. 2011) and response patterns to initial pain and pleasure.

Conclusions: This study characterized brain regions based on their response patterns toward sustained pleasure and pain, showing dynamic changes of brain responses over time.

References

1. Bartoshuk, L. M. (2004). 'Valid across-group comparisons with labeled scales: the gLMS versus magnitude matching', Physiology & behavior, vol. 82, no. 1, pp. 109-114.
2. Beissner, F. (2014). 'Advances in functional magnetic resonance imaging of the human brainstem', Neuroimage, vol. 86, pp. 91-98.
3. Fan, L. (2016). 'The human brainnetome atlas: a new brain atlas based on connectional architecture', Cerebral cortex, vol. 26, no. 8, pp. 3508-3526.
4. Lee, S. A. (2023). 'Brain Representations of Affective Valence and Intensity in Sustained Pleasure and Pain', bioRxiv. doi: 10.1101/2023.06.08.544230
5. Robinson, L. F. (2010). 'Change point estimation in multi-subject fMRI studies', Neuroimage, vol. 49, no. 2, pp. 1581-1592.

6. Roy, M. (2014). 'Representation of aversive prediction errors in the human periaqueductal gray', Nature neuroscience, vol. 17, no. 11, pp. 1607-1612.
7. Schaefer, A. (2018). 'Local-global parcellation of the human cerebral cortex from intrinsic functional connectivity MRI', Cerebral cortex, vol. 28, no. 9, pp. 3095-3114.
8. Yeo, B. T. (2011). 'The organization of the human cerebral cortex estimated by intrinsic functional connectivity', Journal of neurophysiology, vol. 106, no. 3, pp. 1125-1165.

Poster No 2519

Identifying brain systems in personalized and population-level predictive models of pain

Youngeun Park[1,2], Sungwoo Lee[2,1], Dong Hee Lee[2], Choong-Wan Woo[1,2]

[1]Sungkyunkwan University, Suwon, Korea, Republic of, [2]Center for Neuroscience Imaging Research, Institute for Basic Science, Suwon, Korea, Republic of

Introduction: Pain is a complex and subjective experience that extends beyond a simple nociceptive process. Various psychological and social factors influence pain experiences and contribute to individual variability in brain representations of pain (Fillingim, 2017; Kohoutova et al., 2022). In attempts to develop clinically useful pain biomarkers, current group-level fMRI pain biomarkers have demonstrated common representations of neural responses to pain and shown abilities to predict pain across different (Wager et al., 2013; Woo et al., 2017). However, their clinical potential remains elusive. On the other hand, the precision neuroimaging approach enables to describe individual-specific brain organization through extensive sampling of single individuals (Gordon et al., 2017). Using this approach, personalized models may have the potential to obtain stable and reliable within-individual measures (Kraus et al., 2023). In this study, we developed a personalized and population-level pain predictive models, examined its capacity to predict pain within and across individuals, and identified similarities and differences in the important brain regions involved in pain prediction.

Methods: A total of 125 healthy, right-handed participants participated in the study. One participant (author C.-W. W.) completed 33 sessions for a total of 66 hours of fMRI scanning for the individual dataset. The remaining 124 participants underwent a single session for the population dataset. During the fMRI scan, the participants experienced a series of thermal pain stimuli, ranging from 45 to 47.5℃ in 0.5℃ increments, and rated the intensity of pain induced by the stimulus across 96 trials per session. In the development of pain predictive models, we randomly divided single-trial fMRI datasets for the individual and population data into training, validation, and test sets based on sessions. We trained each model to predict pain ratings using principal component regression (PCR) with leave-one-session-out cross-validation (fig. 1a) and tested the models in the independent test sets (fig. 1b). To compare the weights of the two models, we measured searchlight-based pattern similarity, calculating the correlation coefficients between the predictive weights of the models within each searchlight. In the searchlight-based virtual lesion analysis, we excluded the predictive weights within searchlights, predicted pain ratings with the remaining predictive weights, and calculated the changes in the prediction performance.

Results: The personalized model exhibited the best predictive performance when predicting pain rating within the individual (mean r = 0.774) compared to the population model testing on the population data (mean r = 0.672) (Fig. 1b left). The two-sample t-test result showed significant differences between the prediction performances (Fig. 1b right). However, both models also could predict pain in the other dataset, indicating their utility as pain-predictive models. The weight patterns of the two models were highly similar in the regions including insula and supplementary motor cortex, while the regions including lateral thalamus and vmPFC showed low similarities (Fig. 1c & Fig. 1d). In the virtual lesion analysis, broader brain regions were important in predicting pain within the individual using the personalized model (one→one) compared to the population model (pop→one). The insula, sensorimotor areas, and high-order regions (dmPFC and dlPFC) were uniquely important in one→one (Fig. 1f).

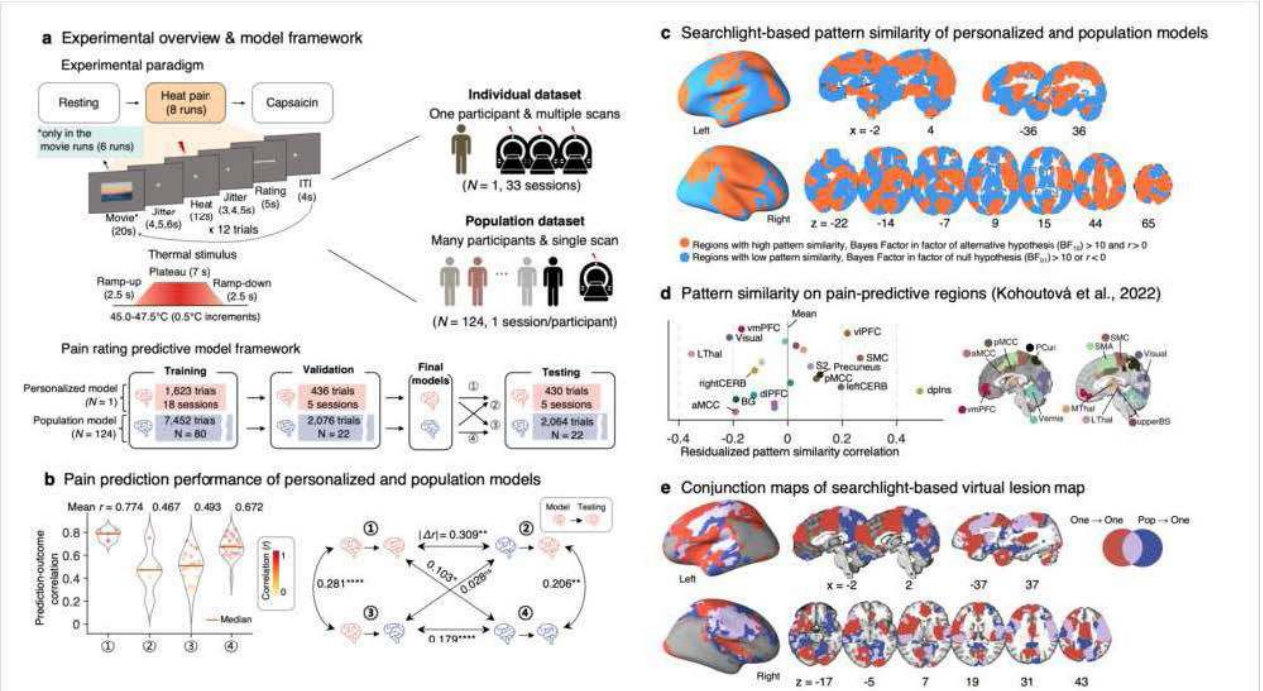

Figure 1. Experimental overview and results. (a) Experimental overview and predictive model framework: the predictive model were built to predict pain rating using principal component regression with leave-one-session-out cross-validation (b) Predictive model performances of the personalized and population pain predictive models were calculated in the test sets of the individual and population datasets. Two-sample t-test was performed to determine the difference between each performance result. (c) Searchlight-based pattern similarity . (d) Weight pattern similarity of the two models within important pain-predictive regions (Kohoutová et al., 2022): we regressed out the number of voxels from the calculated correlation to control the confounding effect of region size. (e) We excluded the predictive weights within searchlights, predicted pain ratings with the remaining predictive weights, and calculated the changes in the prediction performance (FDR corrected $q < 0.05$, $P < 0.016$, $\Delta r > 0$).

Conclusions: Overall, we showed that the personalized pain predictive model outperformed the group-level model for individual-specific pain prediction and exhibited importance in the high-order areas and the insula, which are responsible for pain processing and modulation, particularly cognitive and emotional aspects of pain experiences. These findings highlight the importance of developing personalized neuroimaging-based pain biomarkers, supporting personalized pain assessment and treatment.

References

1. Fillingim, R. B. (2017). Individual differences in pain: understanding the mosaic that makes pain personal. Pain, 158(Suppl 1), S11.
2. Kohoutová, L., Atlas, L. Y., Büchel, C., Buhle, J. T., Geuter, S., Jepma, M., ... & Woo, C. W. (2022). Individual variability in brain representations of pain. Nature neuroscience, 25(6), 749-759.
3. Wager, T. D., Atlas, L. Y., Lindquist, M. A., Roy, M., Woo, C. W., & Kross, E. (2013). An fMRI-based neurologic signature of physical pain. New England Journal of Medicine, 368(15), 1388-1397.
4. Woo, C. W., Schmidt, L., Krishnan, A., Jepma, M., Roy, M., Lindquist, M. A., ... & Wager, T. D. (2017). Quantifying cerebral contributions to pain beyond nociception. Nature communications, 8(1), 14211.
5. Gordon, E. M., Laumann, T. O., Gilmore, A. W., Newbold, D. J., Greene, D. J., Berg, J. J., ... & Dosenbach, N. U. (2017). Precision functional mapping of individual human brains. Neuron, 95(4), 791-807.
6. Kraus, B., Zinbarg, R., Braga, R. M., Nusslock, R., Mittal, V. A., & Gratton, C. (2023). Insights from Personalized Models of Brain and Behavior for Identifying Biomarkers in Psychiatry. Neuroscience & Biobehavioral Reviews, 105259.

Poster No 2520

Disability is primarily predicted by pain intensity and avoidance in patients with chronic back pain

Lejian Huang[1], Binbin Wu[2], Kenta Wakaizumi[1], Rami Jabakhanji[1], Apkar Apkarian[1], Marwan Baliki[1]

[1]Northwestern University, Chicago, IL, [2]The Second Affiliated Hospital and Yuying Children's Hospital of Wenzhou Medical University, Wenzhou, Zhejiang

Introduction: Chronic back pain (CBP) and pain disability represent a formidable challenge to scientists and health professionals. A better understanding of the behavioral and neural factors affecting disability can provide a conceptual framework for the evaluation and treatment of CBP. In this study, we demonstrated that disability (ODI) is primarily predicted by pain intensity (NRS) and avoidance (PASS_avoidance) and then identified the unique brain networks mediating their effects by analyzing resting-state fMRI (rs-fMRI) data.

Methods: Three hundred and eighty six patients (256 + 130) with CBP (CBPs) were recruited (179 M, 207 F; 44.6 ± 11.9 years old), 130 of which (82 M, 48 F; 43.9 ± 11.6 years old) were scanned for rs-fMRI data with the following parameters: voxel size = 3.4375 x 3.4375 x 3.5 mm3; TR/TE = 2500/30 ms; flip angle = 90°; in-plane resolution = 64 × 64; field of view = 220 x 220 mm2; number of volumes = 230; slices per volume = 42. All CBPs completed a battery of self-reported behavioral questionnaires related to pain including Oswestry Disability Index (ODI), Numerical Rating Scale (NRS), Beck Depression Inventory (BDI), Pain Anxiety Symptoms Scale (PASS), Positive and Negative Affect Schedule (PANAS), pain duration, Pain Sensitivity Questionnaire (PSQ), and Pain Catastrophizing Scale (PCS). The 256 CBPs without brain image were evenly allocated to either an exploratory group (Discovery) or a validation group (Validation) with matched demographics and behavioral characteristics. The correlations between pain disability and the brain network properties and local functional connectivity were investigated. 264 regions of interest (ROIs) were used to construct 13 functional networks (Power, Cohen et al. 2011). Linear regression was used to estimate ßij (i, j = 1, 2, ..., 264) for each brain functional connectivity between two ROIs in brain. The connections with their corresponding ROI coordinates and network assignment were recorded that exhibited significant association with ODI ($p < 0.001$) (80 significant connections were found at this stage). To determine whether this connectivity pattern mediated the effects of pain intensity and avoidance on disability, we first used a principal component analysis (PAC) to decompose the 80 “betas” into 20 orthogonal factors that accounted for 80.1% of the variance. Following this, the factors were submitted to perform mediation analysis.

Results: Only NRS and PASS-avoidance in behavioral factors showed significant regression across all folds ($r = 0.621$, $p < 0.001$ for Discovery group). This relationship was validated in the Validation group ($r = 0.577$, $p < 0.001$). The 80 pair-wise connections associated with ODI mainly localized in default-mode (DMN), somatosensory, and salience networks defined. PCA identified 20 components that accounted for 80.1% of variance of 80 connections that exhibited significant association with ODI across the 130 CBPs. Mediation analyses determined that the first component was the only one that significantly partially mediated both pain intensity and avoidance on pain disability.

Conclusions: Overall, our results show that disability in CBP patients is primarily predicted by pain intensity and avoidance. DMN exhibits most association between disability and functional connectivity. Besides, we found PASS-avoidance and NRS partially mediate ODI through a common DMN-dominated brain functional network. Taken together, these findings support a predicting role of pain intensity and pain-related avoidance for disability in CBPs, and further confirm the DMN including the mPFC may be the underlying biological mechanisms that mediate pain disability in CBP patients.

References

1. Power, J. D., A. L. Cohen, S. M. Nelson, G. S. Wig, K. A. Barnes, J. A. Church, A. C. Vogel, T. O. Laumann, F. M. Miezin, B. L. Schlaggar and S. E. Petersen (2011). “Functional network organization of the human brain.” Neuron 72(4): 665-678.

Poster No 2521

Comparison of resting state brain function in different subtypes of functional dyspepsia

Yi Luo[1], Yue Ma[1], Chunlei Guo[1], Shanshan Gao[1], Qingyan Chen[1], Jiliang Fang[1]

[1]Guanganmen Hospital, China Academy of Chinese Medical Sciences, Beijing, China, Beijing, China

Introduction: Functional dyspepsia is a group of clinical syndromes with postprandial fullness, early satiation, epigastric pain or burning as the main symptoms with no structural disease on routine investigations. According to different symptoms, it was divided into postprandial discomfort syndrome (PDS), upper abdominal pain syndrome (EPS) and overlap PDS/EPS[1], the pathogenesis is complex and needs to be further explored. The theory of “brain-gut axis” is a bidirectional information communication pathway between digestive tract and the center proposed in recent years[2]. The newly published Rome IV listed the dysfunction of brain-gut axis as one of the main pathogenesis. We aimed to collect resting state functional Magnetic Resonance Imaging(rest-fMRI) data and explore the brain mechanism of PDS and Overlap PDS/EPS by analyzing brain function abnormalities.

Methods: Eighty-three patients with FD were randomly enrolled and divided into 35 FD group with pain (Overlap PDS/EPS) and 48 FD group without pain (PDS) according to whether they were accompanied by epigastric pain, and 45 healthy controls (HCs) matched by age and sex were included. After the three groups were included, fMRI scans were performed, and 17 items of Hamilton Depression Scale (17-HAMD) and Hamilton Anxiety Scale (HAMA) were scored. Nepean Dyspepsia Index (NDI) and functional dyspepsia Quality of Life scale (FDDQL) were scored in PDS and Overlap PDS/EPS. Then we analyzed the differences in scale scores and partial correlations, further analyzed the differences in ALFF values of brain functions among the three groups, and compared the differences in FC values by using the brain areas with differences in ALFF values as Regions of Interest (ROI).

Results: The results of the clinical scales showed that the NDI scores in the Overlap PDS/EPS were significantly higher than those of the PDS (P < 0.05).The HAMD and HAMA scores of the Overlap PDS/EPS and PDS groups were significantly higher than those of the HC (P < 0.001).The sum of the scores of the first item of the NDI scale (epigastric pain) and the fifth item of the NDI scale (spasmodic pain in the epigastric region) in the Overlap PDS/EPS was significantly positively correlated with the HAMD score (P < 0.05). Analysis of brain imaging data showed that the ALFF values in the left precentral gyrus of the Overlap PDS/EPS were significantly higher than those of the PDS (P < 0.05), the ALFF values in the left insula of the Overlap PDS/EPS were significantly higher than those of the HC group (P < 0.05). Whole-brain FC analysis showed that the FC of the left precentral gyrus and bilateral postcentral gyrus was significantly higher than HC in the PDS (P < 0.05), the FC of the left insula and bilateral postcentral gyrus in the Overlap PDS/EPS was significantly lower than that in the PDS, which was significantly negatively correlated with the HAMD score(P < 0.05).

Table 1 Demographic and clinical characteristics of the study participants.

Variable	Overlap（*n*=35）	PDS（*n*=48）	HCs（*n*=45）	$F/t/\chi^2$	*P*-value
Age（years）	33.22±8.54	36.38±11.05	37.24±10.67	0.245	0.783[a]
Sex（M/F）	13/22	18/30	14/31	1.611	0.204[b]
NDI	68.11±29.04	55.50±22.25	NA	2.241	0.028[c]
FDDQI	65.97±22.10	62.69±19.37	NA	0.719	0.474[c]
17-HAMD	5.94±3.61	5.31±3.05	1.09±1.44	38.339	<0.001[d]
HAMA	8.14±3.90	7.86±4.24	1.29±1.70	55.035	<0.001[e]

Overlap, Overlap between postprandial distress syndrome and epigastric pain syndrome symptom; PDS, postprandial distress syndrome; NDI, Nepean Dyspepsia Index; FDDQI, quality of life questionnaire for functional digestive disorders; 17-HAMD, 17-item Hamilton Depression Scale; HAMA, Hamilton Anxiety scale; NA, not applicable

[a] P-value from one-way analysis of variance tests.

[b] P-values from chi-square test.

[c] P-value from two-sample t-test.

[d] The P-values of 17-HAMD and HAMA score among the three groups were obtained using the one-way analysis of variance tests. Post hoc t-test, 17-HAMD(Overlap VS PDS, P=0.311; Overlap VS HC,P≤0.001; PDS VS HC, P≤0.001), HAMA(Overlap VS PDS, P=0.790; Overlap VS HC, P≤0.001; PDS VS HC, PDS VS HC, P≤0.001)

Table2 ALFF differences in Overlap，PDS and HC

Clusters	Brian regions	MNI peak			Cluster size	F/T-value/peak
		X	Y	Z		
Overlap vs PDS						
1	PreCG.L	-39	9	51	54	4.693
Overlap vs HC						
1	INS.L	-36	-3	-12	43	4.770

MNI peak, coordinates of primary peak locations in the Montreal Neurological Institute space.

PreCG.L, left precental gyrus; INS.L, left insula.

Table3 FC differences in Overlap，PDS and HC

ROI	Clusters	Brian regions	MNI peak			Cluster size	F/T-value/peak
			X	Y	Z		
Precentral（L）							
PDS vs HC							
	1	PoCG.L	-21	-30	57	162	3.781
	2	PoCG.R	21	-45	54	165	4.292
Insula（L）							
Overlap vs PDS							
	1	PoCG.L	-21	-51	69	99	-4.727
	2	PoCG.R	27	-54	66	168	-4.229

MNI peak, coordinates of primary peak locations in the Montreal Neurological Institute space.

PoCG.L, left postcentral gyrus; PoCG.R, right postcentral gyrus.

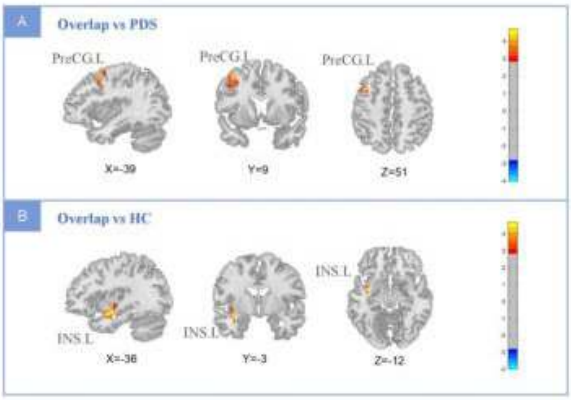

Fig1. ALFF differences in Overlap，PDS and HC.
The red color in the figure A indicates the areas with higher ALFF values in the Overlap group than in the PDS group. The red color in the figure B indicates the areas with higher ALFF values in the Overlap group than in the HCs group. The color bars indicate the P-value. (GRF, voxel *P*=0.005，cluster *P*=0.05). PreCG.L, left precental gyrus; INS.L, left insula.

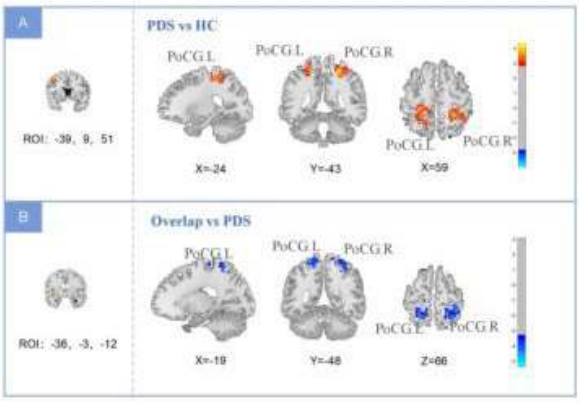

Fig2. FC differences in Overlap，PDS and HC.
Finger A represents the differential brain regions in whole-brain FC analysis based on left middle frontal gyrus/precentral gyrus, the red regions indicate the regions with higher FC values in the PDS group than in the HCs group (GRF, voxel *P*=0.005，cluster *P*=0.05). Finger B represents the differential brain regions in whole-brain FC analysis based on left insula, the red regions indicate the regions with higher FC values in the Overlap group than in the PDS group (GRF, voxel *P*=0.001，cluster *P*=0.05). The color bars indicate the P-value. PoCG.L, left postcentral gyrus; PoCG.R, right postcentral gyrus.

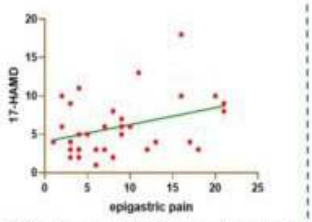

Fig 3. Positive correlation between The sum of the scores of the first item of the NDI scale (epigastric pain) and the fifth item of the NDI scale (spasmodic pain in the epigastric region) and 17-HAMD score in the Overlap group. (*r*=0.385, *P*=0.027).

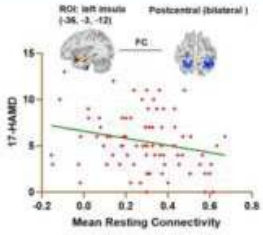

Fig 4. Negatively correlation between the FC of the left insula and bilateral postcentral gyrus in the Overlap and the HAMD score. (r=-0.214, P=0.034).

Conclusions: Patients with FD are often associated with anxiety and depression, and those with overlapping symptoms of PDS and EPS have more severe clinical symptoms and higher levels of depression than those with PDS alone, which is correlated with the degree of epigastric pain. The insula, which is related to emotion and visceral perception, and the sensorimotor network may be areas of differential brain functional activity in different subtypes of FD patients.

References

1. Stanghellini V, Talley N J, Chan F, et al. Rome IV -Gastroduodenal Disorders.[J]. Gastroenterology, 2016.
2. Wauters L, Talley NJ, Walker MM, Tack J, Vanuytsel T. Novel concepts in the pathophysiology and treatment of functional dyspepsia. Gut. 2020 Mar;69(3):591-600. doi: 10.1136/gutjnl-2019-318536. Epub 2019 Nov 29. PMID: 31784469.
3. No.5, Pavilion Street, North Line, Beijing, China

Poster No 2522

Reduced putamen activity precedes placebo analgesia: individual participant data meta-analysis

Balint Kincses[1], Tamás Spisák[2], Tor Wager[3], Ulrike Bingel[4], Placebo Imaging Consortium[5]

[1]University Hospital Essen, Essen, NRW, [2]University Medicine Essen, Essen, Germany, [3]Dartmouth College, Hanover, NH, [4]University Medicine Essen, Essen, NRW, [5]https://github.com/placebo-imaging-consortium/placebo-imaging-consortium.github.io

Introduction: Placebo analgesia (PA) is a widely investigated phenomenon, with a significant and considerable reduction of pain (Forsberg et al., 2017). A better understanding of its underlying neural mechanisms has promising implications for the exploitation of this effect in various clinical contexts. The neural correlates of PA during the pain delivery phase have previously been extensively investigated (Atlas & Wager, 2014; Zunhammer et al., 2018, 2021). However, brain activity preceding the pain stimulation, i.e. the anticipatory brain activity, has not thoroughly investigated. As anticipatory brain activity may reflect placebo-related expectations, its characterisation is an essential step towards the better understanding of mechanisms underlying PA. Here we investigated PA-related anticipatory brain activation changes with an unprecedented sample size in an individual participant data (IPD) meta-analysis.

Methods: IPD neuroimaging and behavioral data was collected on behalf of the Placebo Imaging Consortium, as previously described in (Zunhammer et al., 2018, 2021). The current analysis is based on an extended database, including 570 participants from 18 studies and focused on the differences in the anticipatory activity before pain stimulation with and without placebo-induction. Study plans were pre-registered at the Open Science Framework (https://osf.io/z4qu2). The preprocessing of IPD first-level anticipatory activation maps (ß or contrast images) consisted of re-slicing individual maps to MNI152 template, winsorizing voxel level data (outlier mitigation), and calculating meta-analytic summary scores with the voxel level generic inverse variance (GIV) approach, with studies as random effect. We investigated mean activation differences during the anticipation phase (placebo-control), as well as the correlation of these changes with behavioral placebo analgesia (pain rating differences). Permutation based (n permutation=5000) max statistics with probabilistic threshold free cluster enhancement (Spisák et al., 2019) was used to correct for the family-wise error rate with an alpha-value of 0.05 (two tailed). The analysis was done in MATLAB2021b and SPM12.

Results: With the extended dataset, we observed behavioural PA effects similar to the previously reported estimates (Zunhammer et al., 2018) (Hedge's g: -0.63). In terms of mean placebo-related differences in anticipatory brain activity, we observed a statistically significant decrease in three clusters in the occipital lobe: MNI peak coordinates: x=-5.7, y=-87.9, z=-9.8; x=-4.2, y=-74.6, z=26.3; x=-18.2, y=-64.3, z=13.8, FWER corrected, $p<0.05$) and in the cerebellum (x= -21.9, y=-79.8, z=-23.8, FWER corrected, $p<0.05$). No significant FWER corrected activity increase was observed. Placebo-related decreases in anticipatory brain activity were negatively correlated with behavioral PA in the left putamen (Figure 1, MNI peak coordinates: x=-24.1, y=0.6, z=2.0, FWER corrected, $p<0.05$, two-tailed). Specifically, decreased anticipatory activity in the placebo condition led to higher behavioral PA (Figure 2).

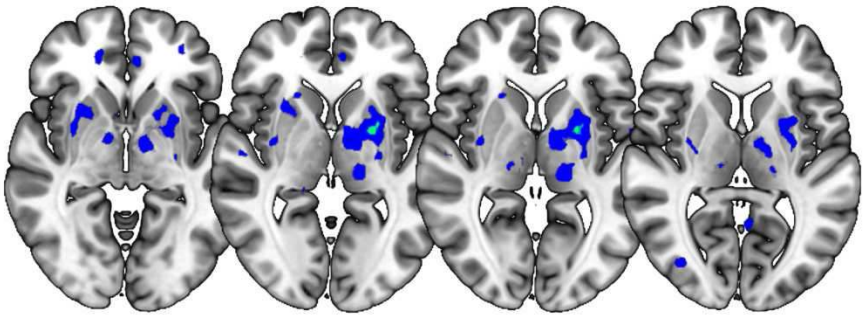

Figure 1 Correlation between placebo related deactivation and behavioral placebo analgesia. Lower activity during placebo related to higher behavioral analgesia. Blue uncorrected (two-sided), $p<0.01$.

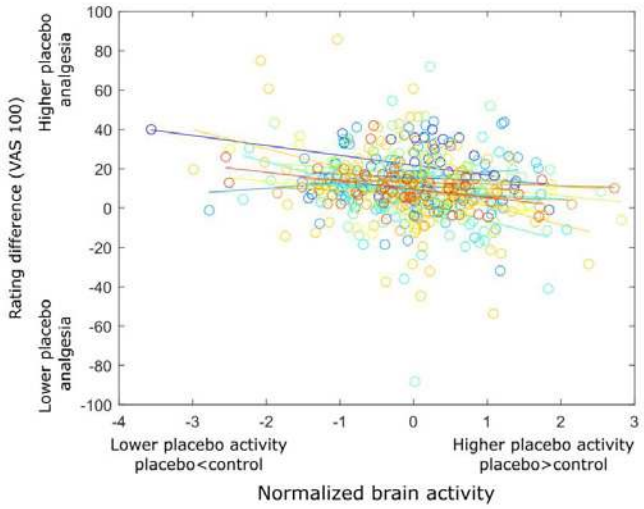

Figure 2 Correlation between behavior placebo analgesia (control-placebo) and brain activity difference in the anticipation phase in the putamen region.

Conclusions: Our previous meta-analytic results on the neural correlates of PA (Zunhammer et al., 2021) suggested that placebo is a multifaceted phenomenon, possibly driven by multiple complementary/parallel neural processes (e.g. in the presence and absence of conditioning). This heterogeneity may also apply to anticipatory activity and explain the lack of coherent increases across the investigated studies. The correlation analysis suggests that the involvement of the putamen is a common characteristic of different PA-related neural mechanisms during the anticipatory phase. It is therefore a promising target for further research aiming at the exploitation of PA in clinical contexts.

References

1. Atlas, L.Y. et al. (2014) 'A meta-analysis of brain mechanisms of placebo analgesia: Consistent findings and unanswered questions', Handbook of Experimental Pharmacology, 225. Available at: https://doi.org/10.1007/978-3-662-44519-8_3.
2. Forsberg, J.T. et al.(2017) 'The placebo analgesic effect in healthy individuals and patients: A meta-analysis', Psychosomatic Medicine. Available at: https://doi.org/10.1097/PSY.0000000000000432.
3. Spisák, T. et al. (2019) 'Probabilistic TFCE: A generalized combination of cluster size and voxel intensity to increase statistical power', NeuroImage, 185. Available at: https://doi.org/10.1016/j.neuroimage.2018.09.078.
4. Zunhammer, M. et al. (2021) 'Meta-analysis of neural systems underlying placebo analgesia from individual participant fMRI data', Nature Communications, 12(1). Available at: https://doi.org/10.1038/s41467-021-21179-3.
5. Zunhammer, M. et al. (2018) 'Placebo Effects on the Neurologic Pain Signature: A Meta-analysis of Individual Participant Functional Magnetic Resonance Imaging Data', JAMA Neurology, 75(11). Available at: https://doi.org/10.1001/jamaneurol.2018.2017.

Poster No 2523

External and construct validity of a standardised measure of neonatal noxious-evoked brain activity

Roshni Mansfield[1,2], Marianne Aspbury[1], Luke Baxter[1], Aomesh Bhatt[1], Maria Cobo[1,3], Caroline Hartley[1], Annalisa Hauck[1], Simon Marchant[1], Vaneesha Monk[1], Kirubin Pillay[1], Ravi Poorun[4,5], Marianne van der Vaart[1], Rebeccah Slater[1,6]

[1]Department of Paediatrics, University of Oxford, Oxford, United Kingdom, [2]Newborn Care Unit, John Radcliffe Hospital, Oxford University Hospitals NHS Foundation Trust, Oxford, United Kingdom, [3]Universidad San Francisco de Quito USFQ, Colegio de Ciencias Biologicas y Ambientales, Quito, Ecuador, [4]College of Medicine & Health, University of Exeter, Exeter, United Kingdom, [5]Children's Services, Royal Devon & Exeter NHS Foundation Trust, Exeter, United Kingdom, [6]Wellcome Centre for Integrative Neuroimaging, FMRIB, Nuffield Department of Clinical Neurosciences, University of Oxford, Oxford, United Kingdom

Introduction: Electroencephalography (EEG) can be used to measure neonatal noxious-evoked brain activity. Brain-derived measures of acute nociception are more objective than neonatal clinical pain scores, and clinical trials of neonatal analgesics would benefit from the improved reliability of these objective metrics. The external and construct validity of brain-derived measures must be demonstrated to support their use in clinical trials. The noxious neurodynamic response function (n-NRF) is an EEG-derived measure of neonatal noxious-evoked brain activity, developed in term neonates in Oxford, UK (Hartley et al. 2017). This study aimed to test the external and construct validity of the n-NRF in two independent datasets from University College London Hospital (UCL) and Royal Devon & Exeter Hospital.

Methods: The UCL dataset is publicly available (Jones et al. 2018). The Exeter dataset was collected from 2021 to 2023 (NHS ethics: 12/SC/0447, 21/LO/0523). Both datasets include term and preterm infants. Heel lances were clinically required. For control heel lances, the heel lance device was rotated 90 degrees so that the blade pierced the air. Stimuli were time-locked to the EEG as described previously (Worley et al. 2012). Data were acquired using Compumedics Grael V2 EEG System and recorded using CURRYscan8 neuroimaging suite, with eight electrodes on the scalp (Cz, CPz, C3, C4, FCz, T3, T4, Oz), a reference (Fz), ground (forehead) and ECG (left clavicle) electrode. EEG data from Cz electrode were pre-processed using an EEGLAB-based pipeline, including filtering (1Hz to 30Hz, 50Hz notch filter), epoching (0.5s pre- to 1s post-stimulus), and baseline correction to the pre-stimulus mean. Cz EEG data were regressed onto the n-NRF to calculate n-NRF magnitudes. We first aimed to reproduce the finding that the n-NRF magnitude is significantly larger following a clinical heel lance compared to a control heel lance (Hartley et al. 2017). We then tested whether the mean n-NRF magnitude (scaled to an average heel lance magnitude of 1.0 in the original Oxford dataset (Hartley et al. 2017)) is equivalent to 1.0±0.2 in independent cohorts. Lastly, we assessed whether the n-NRF magnitude following a heel lance increases with postmenstrual age (PMA) in preterm infants (Schmidt Mellado et al. 2022). The study protocol was peer-reviewed and pre-registered with the journal Cortex (https://doi.org/10.17605/OSF.IO/ZY9MS).

Results: The n-NRF magnitude was significantly greater following a heel lance than a control heel lance in both the UCL (n=60; mean difference (MD) 0.88; 95% confidence interval (CI) [0.64, 1.13]; one-tailed paired t-test p<0.0001) and Exeter datasets (n=31; MD=0.31; 95% CI=[0.02, 0.61]; p=0.02) (Figure 1). Using the TOST (two one-sided t-tests) procedure, we did not confirm equivalence of the n-NRF heel lance magnitude to 1.0 in either dataset (UCL: n=72, mean=1.33, 90% CI=[1.18, 1.52]; Exeter: n=35, mean=0.92, 90% CI=[0.74, 1.22]). An exploratory meta-analysis (Figure 2) including Oxford pilot data, UCL and Exeter data, showed significant heterogeneity between sites (random effects model mean n-NRF magnitude=1.10, 95% CI=[0.57, 1.62], X2=7.86, p-value=0.02). There was significant positive correlation between PMA up to 37 weeks and heel lance n-NRF magnitudes (n=65; one-sided Pearson's R, adjusted for site: 0.24; 95% CI=[0.06, 1.00]; p=0.03).

Conclusions: We reproduced two findings: the n-NRF magnitude was larger following a noxious than a non-noxious stimulus; the n-NRF magnitude increased with PMA up to 37 weeks. We did not reproduce equivalence of the heel lance n-NRF magnitude to 1.0 at other sites; we showed significant inter-site heterogeneity. This may relate to site differences in equipment, research staff, and study populations. Replicating these findings provides evidence supporting the external and construct validity of the n-NRF. However, if used for multisite trials, adjusting for site effects is required to account for inter-site differences in mean magnitude.

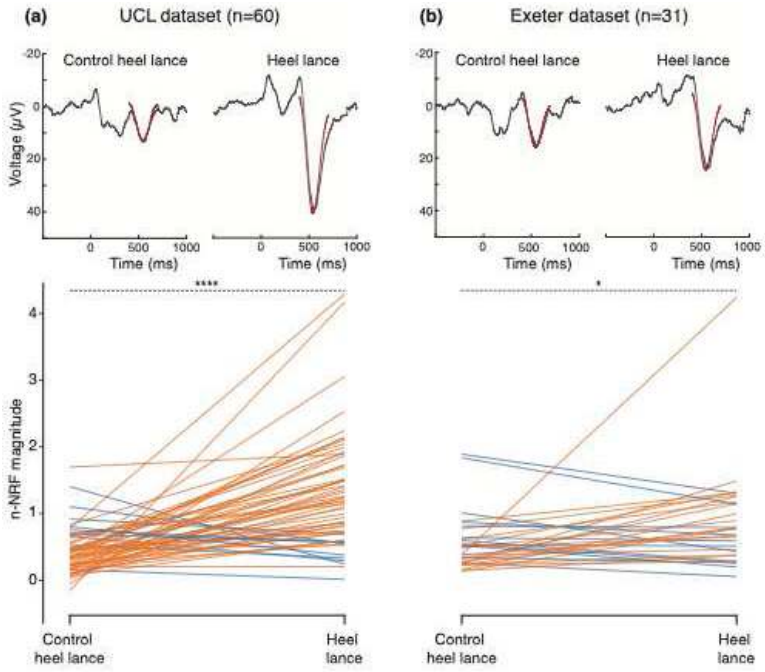

Figure 1: The top panel shows mean Woody filtered EEG traces for control heel lance data and heel lance data (grey) with the n-NRF fitted and overlaid on the data (red) for each dataset: (a) UCL (n=60) and (b) Exeter (n=31). The stimulus occurred at time point 0 ms. The bottom panel shows the heel lance and control heel lance n-NRF magnitudes at each site, paired by participant. Data is represented in orange for participants whose heel lance n-NRF magnitude was greater than their control heel lance n-NRF magnitude, and in blue for participants whose heel lance n-NRF magnitude was lower than their control heel lance n-NRF magnitude. *p<0.05; **** p<0.0001, differences assessed using a one-sided paired t-test.

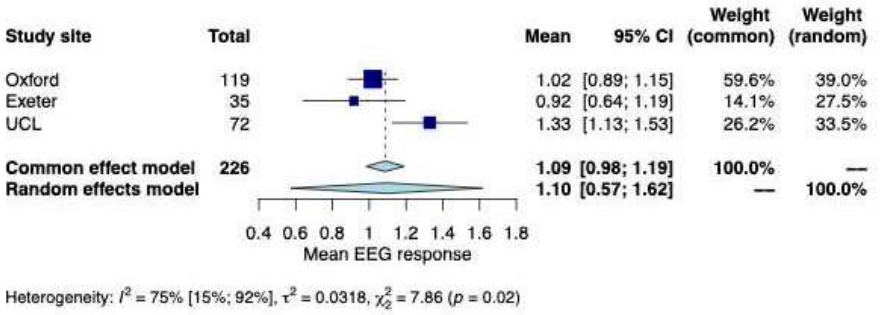

Figure 2: Forest plot showing the pooled mean and 95% confidence interval for the mean heel lance n-NRF magnitude at each site. The heterogeneity results are displayed below the forest plot. Both the common effects and random effects models are shown, though the latter is more appropriate in view of the high heterogeneity.

References

1. Hartley, Caroline, Eugene P. Duff, Gabrielle Green, Gabriela Schmidt Mellado, Alan Worley, Richard Rogers, and Rebeccah Slater. 2017. 'Nociceptive Brain Activity as a Measure of Analgesic Efficacy in Infants'. Science Translational Medicine 9 (388): eaah6122.
2. Jones, Laura, Maria Pureza Laudiano-Dray, Kimberley Whitehead, Madeleine Verriotis, Judith Meek, Maria Fitzgerald, and Lorenzo Fabrizi. 2018. 'EEG, Behavioural and Physiological Recordings Following a Painful Procedure in Human Neonates'. Scientific Data 5 (1): 180248.
3. Schmidt Mellado, Gabriela, Kirubin Pillay, Eleri Adams, Ana Alarcon, Foteini Andritsou, Maria M. Cobo, Ria Evans Fry, et al. 2022. 'The Impact of Premature Extrauterine Exposure on Infants' Stimulus-Evoked Brain Activity across Multiple Sensory Systems'. NeuroImage: Clinical 33 (1): 102914.
4. Worley, A, L Fabrizi, S Boyd, and R Slater. 2012. 'Multi-Modal Pain Measurements in Infants.' Journal of Neuroscience Methods 205 (2): 252–57.

Poster No 2524

Predictive Timing in Pain

Andreas Strube[1], Christian Büchel[2]

[1]University Medical Center Hamburg-Eppendorf, Hamburg, Hamburg, [2]University Medical Center Hamburg Eppendorf, Hamburg, Hamburg

Introduction: A key factor in the expectation of events is when an event will occur (e.g. Arnal & Giraud, 2012). This seems to be particularly the case with aversive factors that we want to avoid for our own protection. In an EEG study (N =35), we applied experimental phasic painful heat stimuli and non-painful cold stimuli and announced in advance for each stimulus whether the next stimulus would be applied immediately, early or late. In some cases, this cue was not reliable. This allows us to make statements about two important fields of research: First, can we find a signature in brain activity for predictive timing, i.e., temporal expectations and expectation errors? Second, does this allow us to draw conclusions about the role of expectations in the so-called dread effect — which shows that people choose to experience painful stimuli sooner rather than later (e.g. Story et al., 2013).

Methods: In this study, participants were confronted with painful heat stimuli and non-painful cold stimuli (4s stimulation / for heat stimuli: 46.5°C / for cold stimuli: 20.5°C). Before each stimulus, a cue announced whether the next stimulus would be applied immediately (0s), early (2s) or late (4s). These cues were not always reliable: In 50% of the cases, the cue correctly predicted the temporal contingency. In 25% of the cases, the temporal contingency was not correct. In the remaining 25% of cases, a catch trial was performed instead of the presentation of a stimulus. Participants had to rate the intensity of the stimulus after each stimulus. In addition, during the catch trials, participants had to report which cue they had just seen.

Results: An analysis of the intensity ratings showed that late expectations — regardless of the true temporal contingency of the stimuli — led to a significant increase in pain ratings. In contrast, the latency of the pain stimulus had no influence on pain ratings. A time-frequency analysis of the EEG data revealed that pain timing during pain application is encoded in a cluster in the theta band (4-8Hz) and in a cluster in the alpha-to-beta band (8-30Hz) — the greater the latency, the stronger the desynchronization in both clusters. Immediately after the cue, the timing expectation is represented in the alpha-to-beta band (8-30Hz). Expectation errors were encoded in a synchronization of theta (4-8Hz) and gamma band (>30Hz) activity.

Conclusions: In this study, we were able to show that late expectations regarding the latency of a pain stimulus are already sufficient to increase the intensity of the pain stimulus. This is in contradiction to ideas that the latency to the stimulus leads

to an increase in the pain stimulus. Furthermore, in this study we were able to show that predictive timing components were represented in the EEG and that typical pain signals are modulated by them.

References
1. Story, G. W., Vlaev, I., Seymour, B., Winston, J. S., Darzi, A., & Dolan, R. J. (2013). Dread and the disvalue of future pain. PLoS computational biology, 9(11), e1003335.
2. Arnal, L. H., & Giraud, A. L. (2012). Cortical oscillations and sensory predictions. Trends in cognitive sciences, 16(7), 390-398.

Poster No 2525

Insights in Structural and Functional Cortical Connectivity in Neuropathic and Non-Neuropathic Pain

Noah Lee[1], Martin Cole[2], Jennifer Gewandter[2], John Markman[2], Paul Geha[2]

[1]Yale University, New Haven, CT, [2]University of Rochester Medical Center, Rochester, NY

Introduction: Chronic back pain (CBP) represents a pervasive and debilitating health issue with substantial societal and economic implications.[1] It is estimated that up to 80% of individuals will experience back pain at some point in their lives, and a significant subset of these individuals will go on to develop chronic, persistent symptoms.[2] Continuing advancements in neuroimaging techniques have provided a unique opportunity to investigate the interplay between altered brain connectivity and the manifestation of chronic pain states. As neuroimaging studies have shown differences in connectivity measures between neuropathic and non-neuropathic pain, we hope to investigate structural and functional connectivity differences in neuropathic (i.e., back pain with sciatica) and non-neuropathic CBP.

Methods: We included 49 patients (age: 50 ± 16; female: 49%) with chronic back pain (> 1 year) along with 35 healthy controls (age: 49 ± 16; female: 74%) in this analysis. Out of the chronic back pain patients, 22 (age: 48 ± 17; female: 59%) of them were classified as neuropathic using the Standardized Evaluation of Pain (StEP) test, while 27 (age: 53 ± 16; female: 41%) of them were not. We collected diffusion-weighted, T1w, and rs-fMRI images from all subjects. All data were processed with the Surface-Based Connectivity Integration (SBCI) Pipeline and were confined to the cortex.[3] We examined group differences using ANCOVA corrected for age, sex, and BMI. Measures of connectivity tested included white matter-based structural connectivity (tractography, volume of tracts intersecting with cortical surface), seed-based connectivity using the accumbens and thalamus as seeds, coupling of structural-functional connectivity, and connectopy of primary somatosensory area S1.

Results: Contrary to our hypothesis of presumed differences between neuropathic and non-neuropathic CBP, ANCOVA did not yield any significant results (after correcting for multiple comparisons) using our connectivity measures. We therefore grouped the two CBP phenotypes and compared them to healthy controls. This approach uncovered significant (cluster corrected p-value: 0.03) group differences in the gradient of connectivity between S1 and primary sensory-motor areas and parts of the supplementary motor area (Fig.1).

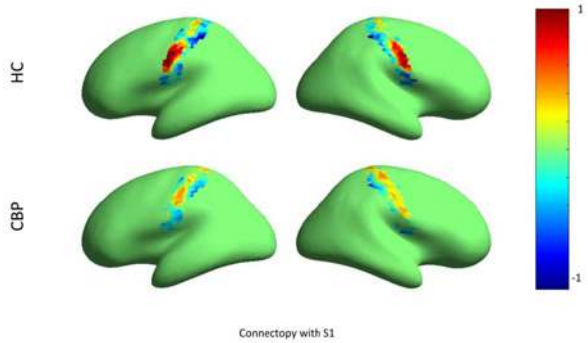

Conclusions: Clinical phenotypes do not appear to affect cortical connectivity in sub-groups of CBP. Nevertheless, we did identify differences in connectopy between CBP patients and healthy controls that are not yet reported in the literature. Further analysis will incorporate subcortical areas in our global measures of connectivity.

References
1. Duenas, M. et al. (2016). A review of chronic pain impact on patients, their social environment and the health care system. Journal of Pain Research, 9, 457–467. https://doi.org/10.2147/jpr.s105892
2. Hoy, D. et al. (2010). The Epidemiology of low back pain. Best practice & research. Clinical Rheumatology, 24(6), 769–781. https://doi.org/10.1016/j.berh.2010.10.002
3. Cole, M. et al. (2021). Surface-Based Connectivity Integration: An atlas-free approach to jointly study functional and structural connectivity. Human brain mapping, 42(11), 3481–3499. https://doi.org/10.1002/hbm.25447

Poster No 2526

Distinct fMRI connectivity patterns of posterior cingulate cortex subregions in fibromyalgia

Jeungchan Lee[1], Alessandra Anzolin[1], Asimina Lazaridou[2], Myrella Paschali[2], Dan-Mikael Ellingsen[3], Arvina Grahl[1], Marco Loggia[4], Ajay Wasan[5], Robert Edwards[6], Vitaly Napadow[7]

[1]Spaulding Rehabilitation Hospital, Charlestown, MA, [2]Brigham and Women's Hospital, Boston, MA, [3]Oslo University Hospital, Oslo, Norway, [4]A.A. Martinos Center for Biomedical Imaging, Massachusetts General Hospital, Harvard Medical School, Boston, MA, [5]University of Pittsburgh, Pittsburgh, PA, [6]Brigham and Women's Hospital, Harvard Medical School, Boston, MA, [7]Massachusetts General Hospital, Harvard Medical School, Charlestown, MA

Introduction: Previously we found that the posterior cingulate cortex (PCC) encodes pain catastrophizing in fibromyalgia (FM) patients (Lee et al., 2018), with distinct roles for different PCC subregions. For example, the level of self-reported engagement in catastrophizing thoughts was correlated with the activity in ventral PCC (vPCC, which supports self-referential cognition), while patients' pain severity was associated with activity in dorsal PCC (dPCC, which is associated with sensorimotor processing). It is not clear, however, if these different PCC subregions also show differential interactions with the rest of the brain during pain catastrophizing or sustained physical pain experience. In this study, we investigated functional connectivity for PCC subregions (vPCC and dPCC) in FM patients while they (separately) engaged in pain catastrophizing cognitions and experienced a sustained pain stimulus.

Methods: We enrolled 99 FM patients (all female, 41.4±12.0 years). Neuroimaging (fMRI: 3T, TR/TE=1250/33 ms, voxel dimension=2 mm isotropic, multiband acceleration factor=5) data were collected during (1) 6-minutes resting-state (REST), (2) sustained (6-minutes) experimental pain (PAIN) where patients' left lower leg was stimulated with cuff pressure (target pain=40/100), and (3) a cognitive pain catastrophizing task wherein patients viewed catastrophizing (CAT, taken from the validated Pain Catastrophizing Scale) or neutral (NEU) statements (presented in randomized order) and reflected on the statements' applicability to their daily experience of FM pain. From the CAT fMRI task, catastrophizing-specific brain regions were calculated using the contrast between CAT and NEU, and PCC subregions were used as ROI for subsequent connectivity analyses. Psychophysiological interaction (PPI) analysis was performed for the CAT task dataset to identify whole-brain functional connectivity patterns for each ROI during pain catastrophizing blocks. Seed-based connectivity analysis was also performed to assess whole-brain functional connectivity for ROIs during evoked pain, contrasting PAIN and REST scan runs. All analyses were cluster-corrected for multiple comparisons ($Z>3.1$, $P<0.05$).

Results: We found that CAT increased fMRI response in both PCC subregions (vPCC and dPCC) along with other default mode network (DMN) regions (vm/mPFC, PC, vlPFC, IPL, STS). However, during the pain catastrophizing period, vPCC was negatively correlated with other DMN subregions (PC, mPFC). In contrast, dPCC was negatively correlated with PC but positively correlated with the rest of the DMN (vlPFC, STS), dorsal attention network (DAN: SMA, PM), and frontoparietal network (FPN: dlPFC, ITG) subregions. In addition, compared to dPCC, vPCC showed greater anti-correlation with vmPFC during pain catastrophizing, while vmPFC was strongly and positively correlated with vPCC during both REST and PAIN states. In contrast, during REST and PAIN states, dPCC was more functionally connected with SLN (aMCC), FPN (FIC, dlPFC), and sensorimotor network (SMN: pINS) subregions, compared to vPCC. Interestingly, during PAIN, compared to REST, vPCC showed greater functional connectivity with SLN (aMCC, a/mINS), thalamus, SMN (S1/M1), SPL, and IPL. On the other hand, dPCC showed increased functional connectivity with SMA and thalamus during PAIN, compared to REST.

Conclusions: Pain catastrophizing induced both differential activation and connectivity patterns in PCC subregions, vPCC and dPCC. Our results suggest that the canonical correlation between vPCC and vmPFC, comprising the default mode network, was reversed during pain-catastrophizing rumination. The distinguishable connectivity patterns of PCC subregions might support their distinct roles in the processing of different modalities of pain-cognitive processing and somatic self-awareness by ventral and somatosensory processing by dorsal PCC.

References

1. Lee, J. (2018), 'Encoding of self-referential pain catastrophizing in posterior cingulate cortex in fibromyalgia', Arthritis & Rheumatology, vol. 70, no. 8, pp. 1308-1318.

Poster No 2527

Brain markers of chronic pain progression and resolution from a large-scale longitudinal study

Katerina Zorina-Lichtenwalter[1], Marta Čeko[1], Lydia Rader[1], Martin Lindquist[2], Naomi Friedman[1], Tor Wager[3]

[1]University of Colorado, Boulder, CO, [2]Johns Hopkins University, Baltimore, MD, [3]Dartmouth College, Hanover, NH

Introduction: Chronic pain patients have alterations in brain gray and white matter, as identified in MRI-based studies (Kregel et al. 2015; Vachon-Presseau et al. 2016). However, small samples have yielded largely inconsistent findings, and only recently have large-scale studies assessed brain structure and pain in samples sufficient to test these relationships with high power. In addition, whether these anomalies result from, lead to, or are merely comorbid with prolonged pain remains unclear. We investigated the relationship between T1 MRI-based measures of brain structure and chronic pain in 40,000 U. K. Biobank (UKB) participants (Littlejohns et al. 2020).

Methods: We analyzed longitudinal data on chronic pain (>3 months duration) in eight body sites (head, face, neck/shoulder, back, stomach, hip, knee, and all over) assessed at baseline (no MRI) and during an MRI visit four or more years later. We grouped participants into four categories: (1) pain-free controls (N = 14,150); (2) unresolved chronic pain at one or more body sites at both assessments (N = 10,532); (3) chronic pain at baseline that resolved by the MRI visit (N = 5,716); and (4) New-onset chronic pain at the MRI visit that was absent at the baseline visit (N = 4,656). We used multiple linear regression models to estimate associations between these categories and regional measures of gray matter volume, cortical thickness, and surface area, controlling for demographics (age, sex), intracranial volume, and scan site (four sites).

Results: Unresolved pain is associated with widespread gray matter volume and surface area reduction compared with pain-free controls in both cortical and subcortical regions, including bilateral sensorimotor and medial prefrontal cortices; new chronic pain is associated with limited gray matter volume reduction focused in cortical regions most affected in the unresolved pain group, and no changes in subcortical regions; resolved pain is associated with surface area reduction exclusively in the somatosensory cortex.

Conclusions: Collectively, these findings suggest a pervasive, partially reversible spreading of gray matter loss across the brain that correlates with chronic pain duration. We have thus identified brain markers of chronic pain progression and resolution, which may be targeted in novel treatment approaches, such as neuromodulation.

References

1. Kregel, J. (2015). 'Structural and Functional Brain Abnormalities in Chronic Low Back Pain: A Systematic Review.' Seminars in Arthritis and Rheumatism 45 (2), pp. 229–37.
2. Littlejohns, T. J. (2020), 'The UK Biobank imaging enhancement of 100,000 participants: rationale, data collection, management and future directions,' Nature communications, 11(1), pp. 2624.
3. Vachon-Presseau, E. (2016), 'Corticolimbic Anatomical Characteristics Predetermine Risk for Chronic Pain.' Brain: A Journal of Neurology 139 (Pt 7), pp. 1958–70.

Poster No 2528

Pain Response and Associations with Psychiatric Symptoms Using an Affordable Electric Shock Task

Benjamin Ely[1], Tram Nguyen[1], Zoe Baker[1], Jasmin Richard[1], Russell Tobe[2], Vilma Gabbay[3,2]

[1]Albert Einstein College of Medicine, Bronx, NY, [2]Nathan S. Kline Institute for Psychiatric Research, Orangeburg, NY, [3]University of Miami Miller School of Medicine, Miami, FL

Introduction: Pain is a key clinical feature of numerous physical and mental health conditions, including depression and substance use (Borsook 2016). However, stimulation methods commonly used to study pain (e.g. heat, pressure) require hardware that is expensive (>$50K US) and complex (e.g. pumped-water thermodes, pneumatic cuffs) to safely implement in an MR environment, leading fewer groups to study pain processing. Here, we describe a low-cost (<$10K US), solid-state electric pain task (ePain), modified from a previously published protocol (Ma 2016), and investigate pain response and associations with psychiatric symptoms in adolescents.

Methods: Task: Subjects first completed an out-of-scanner calibration. An electrode was placed on the dorsal surface of the right foot and connected to an electric stimulator (Biopac, Goleta CA). Shocks (100Hz, 0.5ms pulses) were delivered for 3s starting at 10V and raised in 2.5-5V increments (max 100V) to determine when shocks could be painlessly felt (detection threshold), became painful (pain threshold), and were as painful as could be tolerated (pain limit). Immediately prior to fMRI, calibration was repeated in-scanner to confirm/adjust thresholds using an MR-compatible variant of the electric stimulator. ePain trials consisted of: cue (2s), ISI (4-12s), shock (1s linear ramp-up, 2s peak), pain rating (6s, 0-10 VAS), and ITI (4-12s). Runs included 5 trials with painful cues/shocks (pain limit voltage -10%) and 5 with non-painful cues/shocks (detection limit voltage +10%) in pseudo-random. Data: Analyses were performed on a preliminary sample of 25 adolescents (age=15.4±2.5) with mood and anxiety symptoms enrolled in an actively recruiting study (see also our related abstract: Nguyen TNB et al. "Task fMRI Investigation of Pain Processing in Adolescent Cannabis Use"). Subjects filled out questionnaires to assess depression (BDI), anxiety (MASC), and anhedonia (TEPS) severity. Imaging was performed on a 3T Skyra scanner (Siemens, Germany)

using protocols similar to Human Connectome Project (HCP) Lifespan studies (Harms 2018), including T1w anatomical MPRAGE (0.9mm isotropic) and three runs of ePain task EPI (2.3mm isotropic, TR=1s, 280 volumes, 5x multiband). Data processing included template normalization, realignment, and mild spatial smoothing (4mm FWHM). We modeled activation during painful vs. non-painful cues, painful vs. non-painful shocks, and pain ratings, as well as associations with clinical scales. Results were analyzed using FSL FEAT v6.00 (Woolrich 2004) with FLAME1+2 and outlier deweighting and evaluated at the cluster-corrected Z>2.58, two-tailed p<0.05 level.

Results: As shown in Fig. 1, painful vs. non-painful shocks elicited activation throughout canonical pain circuitry (Wager 2013), including the primary (SI) and secondary (SII) somatosensory cortices and thalamus contralateral to the electrode as well as the insula, anterior cingulate (ACC), and mid-cingulate (MCC). Painful vs. non-painful cues evoked stronger activation in the periaqueductal gray (PAG), important for descending pain modulation (Behbehani 1995), as well as visual areas. Pain ratings engaged regions involved in salience and threat monitoring (Legrain 2011), including the ACC, anterior insula, habenula, and dopaminergic midbrain. Fig. 2 shows associations between task response and anticipatory anhedonia severity. Anhedonia correlated with activation in the bilateral insula, MCC, and posterior cingulate (PCC) during painful vs. non-painful cues; in the parahippocampus during painful vs. non-painful shocks; and in the pregenual and subgenual ACC during pain ratings.

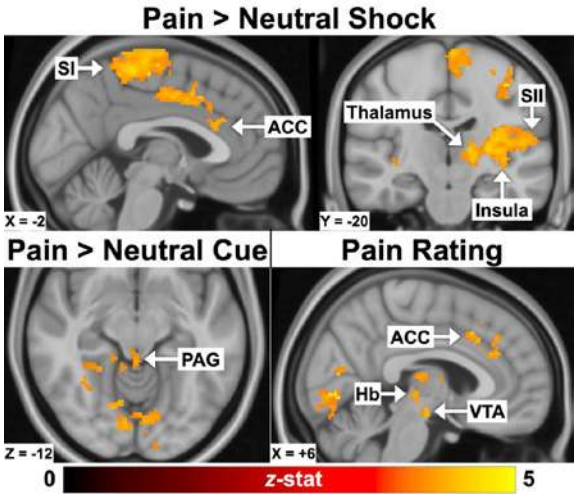

Figure 1. Response to painful vs. non-painful shocks, cues for painful vs. non-painful shocks, and pain ratings during the ePain task.

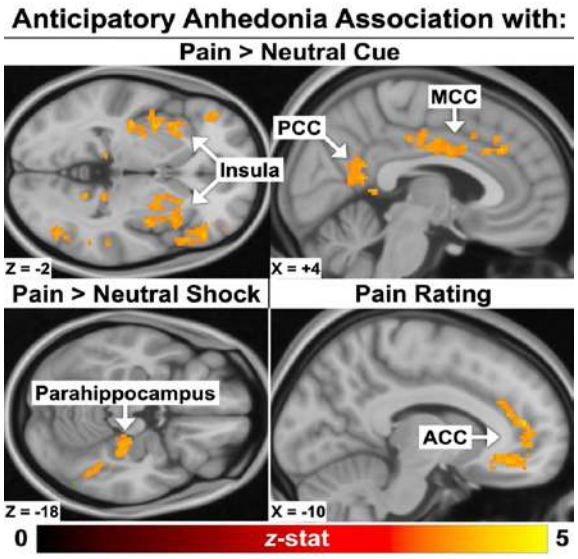

Figure 2. Correlations between anticipatory anhedonia severity and ePain task activation in adolescents with mood and anxiety symptoms.

Conclusions: The ePain task elicited a robust fMRI signal consistent with other noxious sensory stimuli, providing a straightforward way to probe pain circuitry without the need for highly specialized equipment. Moreover, we found extensive associations between neural pain responses and anhedonia severity, suggesting a link between reward dysfunction and aversion processing in youth.

References
1. Behbehani MM (1995), 'Functional characteristics of the midbrain periaqueductal gray', Prog Neurobiol, vol. 46, pp. 575-605.
2. Borsook D et al. (2016), 'Reward deficiency and anti-reward in pain chronification', Neurosci Biobehav Rev, vol. 68, pp. 282-297.
3. Harms MP et al. (2018), 'Extending the Human Connectome Project across ages: imaging protocols for the Lifespan Development and Aging projects', NeuroImage, vol. 183, pp. 972-984.
4. Legrain V et al. (2011), 'The pain matrix reloaded: a salience detection system for the body', Prog Neurobiol, vol. 93, pp. 111-124.
5. Ma Y et al. (2016), 'Serotonin transporter polymorphism alters citalopram effects on human pain responses to physical pain', NeuroImage, vol. 135, pp. 186-196.
6. Wager T et al. (2014), 'An fMRI-based neurologic signature of physical pain', N Engl J Med, vol. 368, pp. 1388-1397.
7. Woolrich MW et al., 'Multilevel linear modelling for FMRI group analysis using Bayesian inference', NeuroImage, vol. 21, pp. 1732-1747.

Poster No 2529

Brain structure and function in chronic widespread pain: a UK Biobank study

Valeria Oliva[1], Aditya Banerjee[1], Christine Law[1], Dokyoung You[1], Lola Falasinnu[1], Yiyu Wang[1], Gary Glover[1], Sean Mackey[1], Kenneth Weber[2]

[1]Stanford University, Palo Alto, CA, [2]Stanford University, Palo Alto, CA

Introduction: Chronic widespread pain is a debilitating condition affecting up to 10–15% of the global population[1]. Brain imaging studies, often with small sample sizes (n<50), have shown both functional and structural changes in the brain that are associated with chronic pain[2]. Here we aimed to identify structural and functional brain changes associated with chronic widespread pain in the large, heterogeneous brain imaging dataset available from the UK Biobank[3].

Methods: We identified 584 participants (377 females, 207 males, age = 60.9 ± 7.5 years) with chronic widespread pain (pain of >3 months duration within four or more body sites) at the initial imaging assessment as well as 584 (377 females, 207 males, age = 61.1 ± 7.3 years) pain-free controls that were matched based on sex, age, body mass index, imaging site, and date of imaging. T1-weighted structural (1 mm X 1 mm X 1 mm) and resting-state functional MRI (TR = 0.735, TE = 39ms, eyes-open, 6-minute duration) brain images were obtained. The UK Biobank's standard image processing pipeline was employed, which included the identification of the gray-white boundary surface and pial surface using FreeSurfer, automatic denoising of the resting-state functional images using FSL's FIX, and spatial normalization of the images[3]. Additional preprocessing steps included spatial smoothing (10 mm3 FWHM for the cortical thickness maps and 3 mm3 FWHM for the resting-state functional images) and bandpass temporal filtering of the resting-state functional images (0.01 Hz – 0.10 Hz). First, we performed mixed-effects between group comparisons in cortical thickness using FreeSurfer with cluster-based familywise error correction (cluster-forming threshold < 1.3, cluster-wise p-threshold < 0.05)[4]. Next, to uncover the functional corollaries of the structural differences, we placed 5 mm3 spheres at four brain regions corresponding to the peaks of group differences in cortical thickness, and we extracted the first principal component of the preprocessed fMRI time series from each region for each participant. For each seed, subject-level whole-brain connectivity maps were generated in FSL using the extracted time series. Then we performed mixed-effects between group comparisons in functional connectivity using FSL's flame with cluster-based familywise error correction (cluster-forming threshold < 3.1, cluster-wise p-threshold<0.05)[5]. Finally, we extracted the parameter estimates from regions showing significant differences in group-level functional connectivity and assessed whether the strength of functional connectivity was associated with the number of pain sites.

Results: We identified areas of decreased cortical thickness in the left dorsal anterior cingulate, left precuneus, left inferior parietal, right lateral precentral, bilateral superior parietal, and bilateral occipital cortices in chronic widespread pain (Figure 1). Chronic widespread chronic pain demonstrated decreased functional connectivity between the left dorsal anterior cingulate cortex and the right dlPFC as well as decreased functional connectivity between the precuneus and the right supramarginal gyrus (Figure 2). Neither the right lateral precentral or superior parietal seeds showed significant differences in functional connectivity between the two groups. The strength of functional connectivity was not significantly correlated with the number of pain sites.

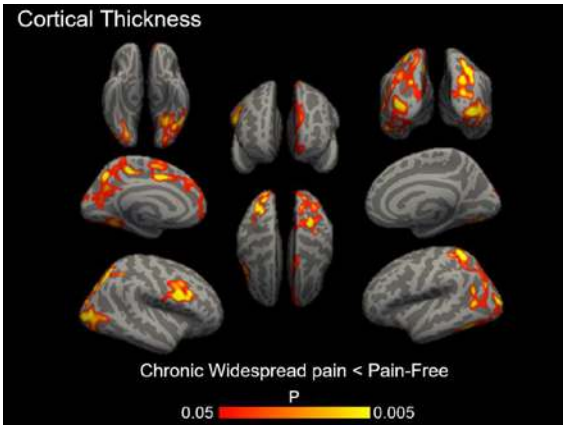

Figure 1. Cortical thickness differences between chronic widespread pain participants (N = 584) and pain-free controls (N = 584, $p < 0.05$).

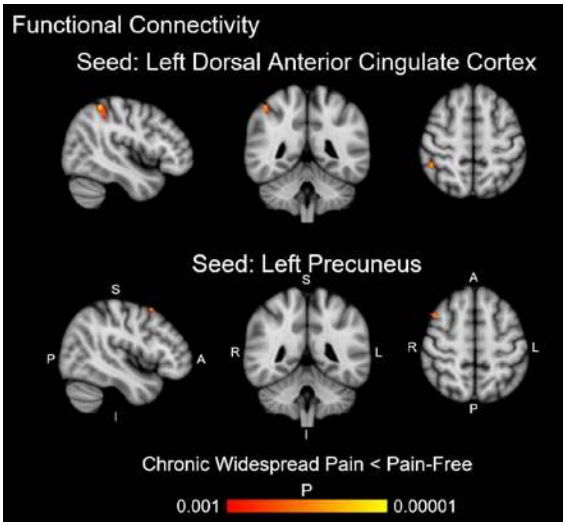

Figure 2. Functional connectivity differences between chronic widespread pain participants (N = 584) and painfree controls (N = 584, $p < 0.001$).

Conclusions: The findings, drawn from a large heterogeneous dataset, reveal altered brain structure and function in chronic widespread pain compared to matched pain-free volunteers. The link between the brain changes and clinical measures remains to be investigated and will require datasets with richer clinical information including pain severity, pain duration, and pain-related disability.

References

1. Andrew P et al. Eur J Pain. 2018 Jan;22(1):5-18.
2. Martucci KT and Mackey SC. Anesthesiology. 2018 Jun;128(6):1241-1254.
3. Alfaro-Almagro F et al. Neuroimage. 2018 Feb 1;166:400-424.
4. Fischl B. Neuroimage. 2012 Aug 15;62(2):774-81.
5. Jenkinson M et al. Neuroimage. 2012 Aug 15;62(2):782-90.

Poster No 2530

Distinct Characteristics between Somatosensory and Hippocampal Theta-Gamma Activities

Seokyun Ryun[1], Chun Kee Chung[1]

[1]Seoul National University, Seoul, Seoul

Introduction: High-gamma (HG) activity is a well-known and robust neurophysiological activity observed in various cortical regions, including the primary somatosensory cortex (S1) and hippocampus. However, its functional roles and mechanisms remain unclear. Specifically, although the relationship between theta-gamma activity is relatively well-established in the hippocampus, it is unclear whether this relationship can also be applied to other cortical regions, such as the S1 and the

primary visual cortex (V1). Here, we investigate this issue using phase-amplitude coupling and effective connectivity analysis. In this study, we first confirm the coupling between theta-HG activities and then evaluate the information flow between them.

Methods: Twelve patients with drug-resistant epilepsy were included in this study. Patients underwent electrocorticography (ECoG) grid or depth electrode insertion surgery. Eight patients with electrodes located on the S1 participated in the texture stimulation task, and four patients with electrodes located in the hippocampus performed a memory encoding task. We calculated theta-HG phase amplitude comodulation (PAC) using ECoG signals from the S1 and hippocampus during texture stimulation and encoding periods, respectively. To evaluate information flow between theta activity and HG envelope, we calculated partial directed coherence (PDC) between them. For significance testing, we created surrogate datasets using the multiple partitioning method for PAC and the fast Fourier transform (FFT)-surrogate method (phase randomization) for PDC. We then performed the simulation 1000 times and extracted the z-scores or p-values of each condition.

Results: We found that HG activities are phase-locked to the theta oscillations both in the S1 and hippocampus during tasks. However, the information flow between theta-HG activities showed distinct differences in S1 and hippocampus. That is, in the hippocampus, the theta oscillation drove the hippocampal HG activity. On the other hand, in the S1, the fluctuation of the HG envelope drove the theta oscillatory activity. These results were consistent across patients. Additionally, we found that HG activity in S1 modulates theta activity in surrounding cortical areas.

Conclusions: In this study, we showed that the relationship between theta and HG activities varies across cortical regions. Expressly, results from the S1 area indicated that S1 HG activity during stimulation is not induced by slow oscillatory activity such as theta oscillation but may be driven directly by external inputs. Therefore, we suggest that HG activities in the S1 and hippocampus have distinctly different generation mechanism.

References

1. Baccalá, L.A., Sameshima, K., (2001), 'Partial directed coherence: a new concept in neural structure determination', vol. 84, no. 6, pp. 463-474
2. Canolty, R.T. et al., (2006), 'High gamma power is phase-locked to theta oscillations in human neocortex', Science, vol. 313, no. 5793, pp. 1626-1628
3. Tort, A.B. et al., (2008), 'Dynamic cross-frequency couplings of local field potential oscillations in rat striatum and hippocampus during performance of a T-maze task', Proceedings of the National Academy of Sciences, vol. 105, no. 51, pp. 20517-20522

Poster No 2531

Facilitated hand proprioceptive processing in paraplegics with long-term wheelchair sports training

Eiichi Naito[1,2], Tomoyo Morita[1,2]

[1]CiNet, NICT, Suita, Japan, [2]Graduate School of Frontier Biosciences, Osaka University, Suita, Japan

Introduction: Previous studies have revealed drastic changes in motor processing in individuals with congenital or acquired limb deficiencies and dysfunction. However, little is known about whether their brains also exhibit characteristic proprioceptive processing. This study examined brain activity characteristics in four individuals with congenital or acquired paraplegia who had long-term wheelchair sports training (paraplegic group), when they passively experienced a right-hand movement (passive task) and when they actively performed a right-hand motor task (active task), compared to 37 able-bodied individuals (control group).

Methods: One participant with congenital paraplegia (P1) and three participants with acquired paraplegia (P2, P3, and P4) participated in this study. P1 was an active, top wheelchair racing Paralympian, aged 30 years. She began racing at the age of eight and underwent long-term wheelchair racing training. She won a total of 19 medals in six consecutive Summer Paralympic Games as of 2021. P2, P3, and P4 were not top athletes at the level of participant P1, but had more than 30 years of leg non-use period and long-term wheelchair sports training. P2 had paraplegia at the age of one and had 42 years of experience in wheelchair basketball and four years of experience in wheelchair table tennis. P3 had paraplegia at the age of 17 and had 27 years of experience in wheelchair table tennis. He was a Paralympian in Río de Janeiro. P4 had paraplegia at the age of 21 and had 31 years of experience in wheelchair basketball, 9 years of experience in wheelchair marathon, and 9 years of experience in wheelchair fencing. P1, P3, and P4 had no somatic sensations (light touch and pin prick) in their lower limbs and had complete immobility. P2 had complete immobility of his lower limbs; nonetheless, there were somatic sensations (light touch and pinprick). P1, P3, and P4 were right-handed, and P2 was ambidextrous. For the control participants, we recruited age-matched right-handed able-bodied adults (n = 37; 25 females) aged 37.4 ± 10.9 years (range 25–59 years). They had experience in various sports since their school days, but none of them were athletes participating in a particular sport. None of the able-bodied participants had a history of neurological, psychiatric, or movement disorders. Functional MRI images were

acquired using T2*-weighted gradient echo-planar imaging (EPI) sequences with a 3.0-Tesla MRI scanner (MAGNETOM Trio Tim; Siemens, Germany) and a 32-channel array coil when the paraplegic and able-bodied individuals performed the passive and active tasks. We performed both contrast analysis and region-of-interest analysis ($p < 0.05$ corrected). The study protocol was approved by the Ethics Committee of the National Institute of Information and Communications Technology (NICT) and the MRI Safety Committee of the Center for Information and Neural Networks (CiNet; no. 2003260010). The details of the experiment were explained to each participant before the experiment, after which they provided written informed consent. This study was conducted in accordance with the principles and guidelines of the Declaration of Helsinki (1975).

Results: The paraplegic group activated the foot section of the left primary motor cortex (M1) during the passive task, which was deactivated in the control group (Figure 1). Compared with the control group, the paraplegic group showed significantly greater activity in the inferior frontoparietal proprioceptive network (right inferior parietal lobule, area 44, and bilateral insula) during the passive task (Figure 2). None of the regions showed significantly greater activity in the paraplegic group during the active task. Similarly, no regions showed significantly greater activity in the control group for either task (Morita and Naito 2022).

Conclusions: This study demonstrated the facilitation of hand proprioceptive processing in the brains of paraplegic individuals with long-term wheelchair sports training.

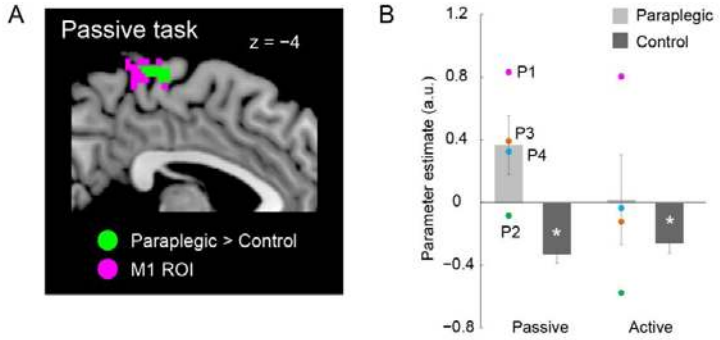

Figure 1 Results from ROI analysis for the foot section of M1

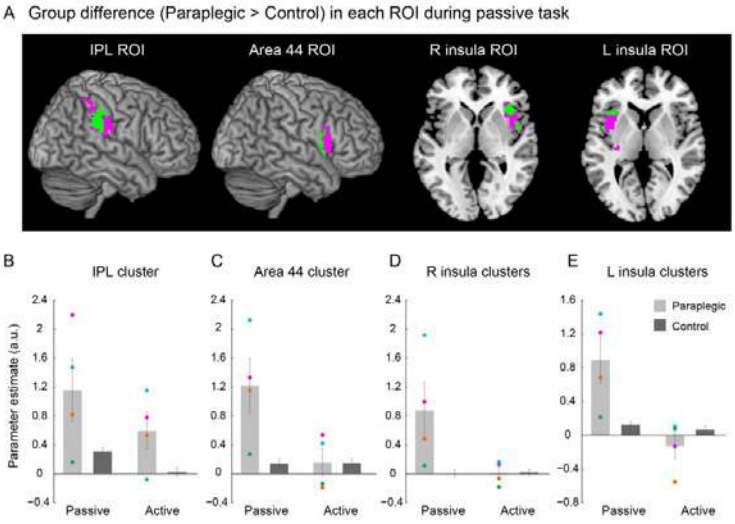

Figure 2 Results from ROI analysis for the inferior frontoparietal proprioceptive network

References

1. Morita, T. and Naito, E. (2022) 'Facilitation of hand proprioceptive processing in paraplegic individuals with long-term wheelchair sports training', Brain Sciences, 12(10), 1295; https://doi.org/10.3390/brainsci12101295.

Poster No 2532

EEG Hyperscanning: Maternal-Newborn Neural Activation in Response to Skin-to-Skin Affectionate Touch

Grace Kromm[1], Kelly Pammenter[2], Andrea Edwards[2], Stanimira Georgieva[3], Mohammed Adnan Azam[3], Victoria Leong[3], Topun Austin[2]

[1]University of Cambridge, Cambridge, United Kingdom, [2]Cambridge University Hospitals NHS Foundation Trust, Cambridge, United Kingdom, [3]Nanyang Technological University, Singapore, Singapore

Introduction: Affectionate touch is a fundamental aspect of the human experience from the very start of life. The sensory pathway for affectionate touch is anatomically segregated, primarily transmitted by unmyelinated, slow-conducting C-tactile (CT) afferents optimally activated by gentle stroking at 1-10 cm/s. In the neonatal period, skin-to-skin and stroking touch tune long-term somatosensory development, autonomic reactivity, social cognition, and bonding; however, neonatal neural processing of affectionate touch is not well understood. We aimed to examine neonatal brain activation in response to social/nonsocial and CT-targeted/non-CT-targeted touch stimuli and to interrogate the neural underpinnings of touch-mediated mother-infant interaction by recording simultaneous or "hyperscanning" maternal-newborn electroencephalography (EEG) at the neonatal cotside.

Methods: Before recruitment, we piloted with 14 mother-newborn dyads and incorporated their perspectives to develop a participant-driven paradigm. Our refined paradigm compares neural activation across touch context and touch mechanism in a 2x3 factorial design with order counterbalanced (Figure 1). For touch context, mothers and infants are skin-to-skin ("social") or separate ("nonsocial"). For touch mechanism, the infant receives still touch ("static"), slow stroking (~1-10 cm/s, "CT-optimal"), or fast stroking (~20 cm/s, "non-CT-optimal") across the back. Touch conditions are of 3-minute duration with alternating 3-minute periods of baseline (no touch) before and after. Simultaneous maternal-newborn EEG is recorded at 500 Hz on LiveAmp wireless amplifiers with actiCAP electrodes (Brain Products). With EEGLAB, recordings are highpass filtered at 0.5 Hz and lowpass filtered at 40 Hz, and artefacts are manually rejected. Hand position information is monitored with open-source QR pose estimation markers (ArUco) and a synchronised high frame rate video camera. Stroking speed is calculated from ArUco position information with a custom algorithm.

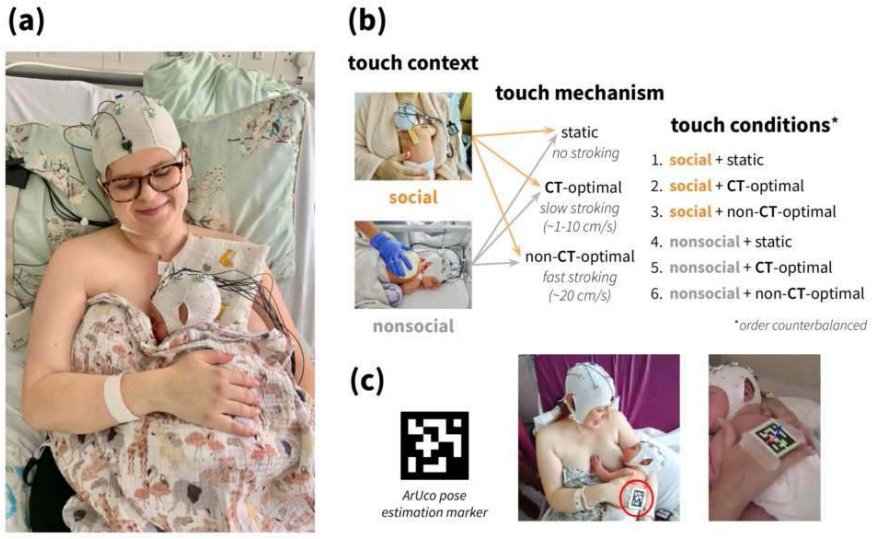

Figure 1. EEG hyperscanning paradigm at the neonatal cotside. (a) Wireless dual-EEG on a mother and her newborn infant during skin-to-skin contact on the postnatal wards of a maternity hospital. During a piloting period, we incorporated perspectives from mother-newborn dyads to develop a participant-driven, well-controlled paradigm that honours naturalistic processes. All images are shared with consent. **(b)** Neural activation is recorded across *touch context* (social vs. nonsocial) and *touch mechanism* (static vs. CT-optimal vs. non-CT-optimal) in a 2x3 factorial design with order counterbalanced. Touch conditions are of 3-minute duration with 3-minute baseline periods before and after. **(c)** Stroking speed is monitored with ArUco pose estimation markers and a high frame rate video camera.

Results: We applied EEG hyperscanning to study 43 mother-newborn dyads in the days after birth. Clean data from at least one touch condition was present in 30 healthy term-born newborns (11 female; mean 3409 grams, 39+4 weeks gestation, 1.7 days old) with their mothers (mean 32.0 years old). Stroking speed was calculated across stroking touch conditions. Average stroking speed was within 1-10 cm/s for all CT-optimal touch conditions and above this range for all non-CT-optimal touch conditions. We calculated neonatal broadband EEG power ($\mu V^2/Hz$) across 1-10 Hz in frontal, central, and parietal regions, subtracting baseline (N = 30). We found significant differences in EEG power between social and nonsocial contexts for static and CT-optimal, but not non-CT-optimal, touch (Figure 2). Specifically, we found decreased neonatal broadband EEG power,

representing increased neural activation, in the social context as compared to the nonsocial context for static touch and CT-optimal touch conditions.

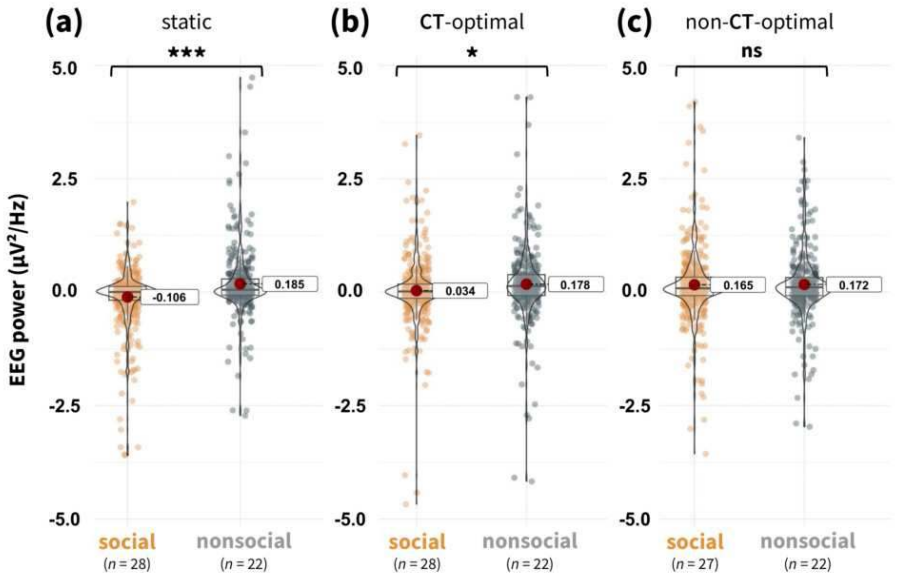

Figure 2. Neonatal EEG responses to touch conditions. Violin plots of broadband EEG power (μV²/Hz) during **(a)** static touch, **(b)** CT-optimal touch, and **(c)** non-CT-optimal touch in social and nonsocial contexts, subtracting baseline ($N = 30$). We found a significant two-way interaction between *touch context* (social vs. nonsocial) and *touch mechanism* (static vs. CT-optimal vs. non-CT-optimal) on EEG power, $F = 6.784$, $p = .001$. Individual dots represent power values in neonatal delta (1-2 Hz), theta (3-4 Hz), alpha (5-6 Hz), low beta (7-8 Hz), and high beta (9-10 Hz) bands in frontal electrodes, central electrodes, and parietal electrodes; red circles represent mean power; Bonferroni's post hoc tests between groups; *** = $p < 0.0001$, * = $p < 0.01$, ns = not significant.

Conclusions: We established and refined an EEG hyperscanning paradigm at the neonatal cotside across types of affectionate touch. Preliminary results indicate that static and CT-targeted touch stimuli elicit different neural activation responses in the newborn depending on the social context of the touch. Our findings are consistent with reports of decreased EEG power, or event-related desynchronization, during social as compared to nonsocial conditions in older infants. Additional recruitment and analyses of maternal-newborn neural synchronicity are currently underway. We hope our results will help elucidate the roles of social touch stimuli and the CT afferent pathway in early brain development as well as help characterise the beginnings of the mother-child inter-brain network.

References

1. Charpak, N. (2017), 'Twenty-year follow-up of kangaroo mother care versus traditional care', Pediatrics, vol. 139, no. 1, e20162063.
2. Löken, L. (2009), 'Coding of pleasant touch by unmyelinated afferents in humans', Nature Neuroscience, vol. 12, no. 5, pp. 547-548.
3. McGlone, F. (2014), 'Discriminative and affective touch: sensing and feeling', Neuron, vol. 82, no. 4, pp. 737-755.
4. St. John, A.M. (2016), 'Variation in infant EEG power across social and nonsocial contexts', Journal of Experimental Child Psychology, vol. 152, pp. 106-122.
5. Turk, E. (2022), 'Brains in sync: practical guideline for parent-infant EEG during natural interaction', Frontiers in Psychology, vol. 13, 833112.

Poster No 2533

Somatosensory abnormalities and rhythmic entrainment of gait in Parkinson's disease

Cheng-Wei Huang[1], Chin-Hsien Lin[2], Ming-Tsung Tseng[3]

[1]Graduate Institute of Brain and Mind Sciences, Taipei, Taiwan, [2]Department of Neurology, National Taiwan University Hospital, Taipei, Taiwan, [3]Graduate Institute of Brain and Mind Sciences, Taipei, Taiwan

Introduction: Accumulating evidence indicates that neurodegenerative diseases spread through the brain connectome. For Parkinson's disease (PD), non-motor manifestations may accompany motor dysfunction at an early disease stage when dopaminergic degeneration is limited to the basal ganglia. It remains unclear whether, based on the network-spread account, these abnormalities emanated from functional dysconnectivity with the basal ganglia, and whether interventions normalizing this connectivity could reverse these abnormalities.

Methods: To address this issue, we focused on somatosensory perception and employed functional MRI to record brain responses to tactile tasks in patients with mild-to-moderate PD and healthy controls before and after rhythmic auditory stimulation-assisted gait (RASg) training.

Results: Consistent with the presence of striatal degeneration, PD patients showed right posterior putamen (pPut) hypoactivation during both motor execution and detection of tactile stimuli. During tactile detection, they also exhibited reduced functional connectivity from the right pPut to IPL, whose activity reflected patients' impaired tactile detectability. Importantly, this hypoconnectivity predicted right IPL hypoactivation, indicating that pPut-IPL dysconnectivity underlay patients' somatosensory abnormalities. In addition, RASg training normalized patients' motor function and tactile detectability, which was accompanied by normalization of right IPL activation and pPut-IPL connectivity during tactile detection. Notably, training-induced changes in pPut-IPL connectivity predicted changes in IPL activation, indicating that normalizing pPut-IPL hypoconnectivity recovered patients' somatosensory abnormalities.

Conclusions: These findings suggest that somatosensory abnormalities in PD arise from the spread of striatal pathology to relevant cortical regions through striatal dysconnectivity. RASg training acts to reverse this dysconnectivity and thus improves somatosensory abnormalities in PD patients.

Poster No 2534

Cortical Representations of Vibrotactile Stimuli with Varying Frequency in Human S1

Ji-Hyun Kim[1], Junsuk Kim[2], Sung-Phil Kim[1]

[1]UNIST, Ulsan, Ulsan, [2]Kwangwoon University, Seoul, Seoul

Introduction: Animal studies showed that tactile sensations from slowly adapting receptors (SA) and rapidly adapting receptors (RA) elicit different spatial activation patterns within the primary somatosensory cortex (S1) (Mountcatle, 1957; Sur et al., 1981), suggesting similar neural representations in human S1. Using 3T fMRI with conventional BOLD signals, however, it is limited to uncover the receptor-specific neural responses in human S1. Therefore, in this study, we employed advanced high-resolution (0.7mm) fMRI at 7T with VASO-BOLD sequence to investigate the laminar and columnar characteristics of neural responses to vibrotactile stimulations with varying frequencies in human S1 (Brodmann Area 3b).

Methods: Thirteen healthy volunteers (8 male, 26.94 ± 3.2 years old) participated in this study. All neuroimaging measurements were conducted using a 7T scanner (MAGNETOM Terra, Siemens Healthineers, Erlangen, Germany) with a single channel transmitter and a 32-channel receiver head coil (NOVA Medical, Wilmington, MA). We used a multi-contrast VASO-BOLD sequence (Lu et al., 2003) with slices aligned to the central sulcus between the motor and sensory cortices of the participants. The imaging parameters were as follows: 0.7-mm isotropic resolution, in-plane reduction factor (Rin-plane) = 3, field of view (FOV) = 154 × 154 mm2, 12 slices, and TI1/TI2 = 67.14/2390.9 ms. Seven different frequency stimuli were applied to the left index fingertip of the participants (ranging from 2 to 38 Hz in 6 Hz increments), generated by piezoelectric devices equipped with 6-mm diameter electrodes (Dancerdesign, St. Helens, UK). Each participant completed eight runs to obtain VASO and BOLD images. During each run, the seven vibrotactile stimuli were randomly presented twice, resulting in fourteen task trials. We localized the brain regions that specify participants' index finger and set the region of interest (ROI) to fit BA 3b in S1. For laminar analysis, thirteen equivolume layers were calculated across the cortical depth of BA 3b. We calculated the mean VASO signal change within the voxels that corresponded to individual layer. For columnar analysis, ROIs were unfolded into 2D and similarity in cortical response patterns across columns was measured, expecting distinct spatial distributions between SA and RA columns. The columnar similarity was quantified using cosine similarity between vectors representing column activations at different frequencies. Laminar and columnar analyses were conducted using the software LAYNII (https://github.com/layerfMRI/LAYNII).

Results: We first confirmed that the vibrotactile stimuli activated BA 3b in contralateral S1. The laminar analysis showed that SA stimuli (2-Hz) elicited activation centered at the middle layer, while RA stimuli (38-Hz) elicited increasing activation towards the superficial layer. Other stimuli with intermediate frequencies between 8 Hz and 32 Hz resulted in activation patterns of both SA and RA, including activation in the middle-layer and increased activation towards the superficial layer. The columnar analysis revealed that responses of each column activated by 2-Hz and 38-Hz stimuli were the least similar to each other, indicating a distinct columnar distribution of cortical responses to SA and RA.

Conclusions: In this study, we reported that SA-, and RA-specific tactile stimuli elicited distinct spatial patterns of neural responses in human S1. Our finding in humans is in line with the previous report of peak activations in layer IV by SA stimulation in non-human primates (Mountcatle, 1957). Moreover, our results suggest spatial neural representations of vibrotactile frequency in S1 such that the superficial layer is more activated than the middle layer as the frequency increases. Our study may provide insights into the structural characteristics of S1 in processing the vibrotactile information.

References
1. Lu, H. (2003), 'Functional magnetic resonance imaging based on changes in vascular space occupancy', Magnetic Resonance in Medicine, vol. 50, no. 2, pp. 263-274.
2. Mountcastle, VB. (1957), 'Modality and topographic properties of single neurons of cat's somatic sensory cortex', Journal of Neurophysiology, vol 20, no. 6, pp. 408-434. doi:10.1152/jn.1957.20.4.408
3. Sur, M. (1981), 'Modular segregation of functional cell classes within the postcentral somatosensory cortex of monkeys', Science, vol. 212, no. 4498, pp.1059-1061

Poster No 2535

Identifying cortical columns for slow/rapid vibrotactile stimulation in human S1 using 7T fMRI

Ashley York[1], Harriet Dempsey-Jones[2], Thomas Shaw[3], Alexander Puckett[2], Markus Barth[4], Ross Cunnington[2]

[1]Centre for Advanced Imaging, University of Queensland, Brisbane, Queensland, [2]School of Psychology, University of Queensland, Brisbane, Queensland, [3]Centre for Advanced Imaging, The University of Queensland, Brisbane, Queensland, [4]Centre for Advanced Imaging, The University of Queensland, Brisbane, Australia

Introduction: Cortical columns are functionally distinct units of the cerebral cortex that are organized perpendicular to cortical layers and typically process similar types of information (e.g., orientation preference). The extensive identification of cortical columns across the cortex has led some to propose that columnar organization might be a fundamental principle of the entire neocortex. However, evidence for such columnar organization in the human primary somatosensory cortex (S1) remains limited (see[1,2]). Columnar organization presumed to relate to slowly adapting (SA) and rapidly adapting (RA) receptors, has been identified in primate SI[3,4]. Recent studies, however, suggest that S1 neurons are organized by feature selectivity (e.g., shape, movement, vibration) rather than strictly by receptor type[5]. Despite this, there may still be columnar organization in human S1 related to processing specific frequencies, such as 3Hz (SA, intermittent pressure) and 30Hz (RA, vibration), which merits further research[6]. Here, we seek to adapt approaches proven effective in identifying visual columns (e.g., ocular dominance) using UHF fMRI to probe for SI columnarity.

Methods: To specifically target separate bands of functionally dissociable cortex (based on feature or receptor preference) vibrotactile stimulation was administered at frequencies of 3 and 30Hz, to the distal fingertips of the right hand. Trials of 3/30Hz were interleaved with a short inter-trial interval for 6 runs (~62mins). In a separate session, somatotopic fingertip regions were localized through phase-encoded fingertip mapping. Data acquisition for 8 participants was conducted using 7T MRI (Fig.1). Anatomical images were captured with MP2RAGE (0.75mm iso), and functional data were obtained using a 3D-EPI sequence[7] (0.8mm iso, TR=1.92s) tilted to cover left S1. The surface-based analysis pipeline is detailed in Fig. 1. We analysed response delays from phasic fingertip stimulation, manually defining subject-specific regions of interest (ROIs) post-thresholding (FDR < 0.05; Fig2a). Within these ROIs, we used a general linear model (GLM) with motion and control regressors for deconvolution, conducting a general linear test (GLT) to compare responses to 3Hz and 30Hz stimulations.

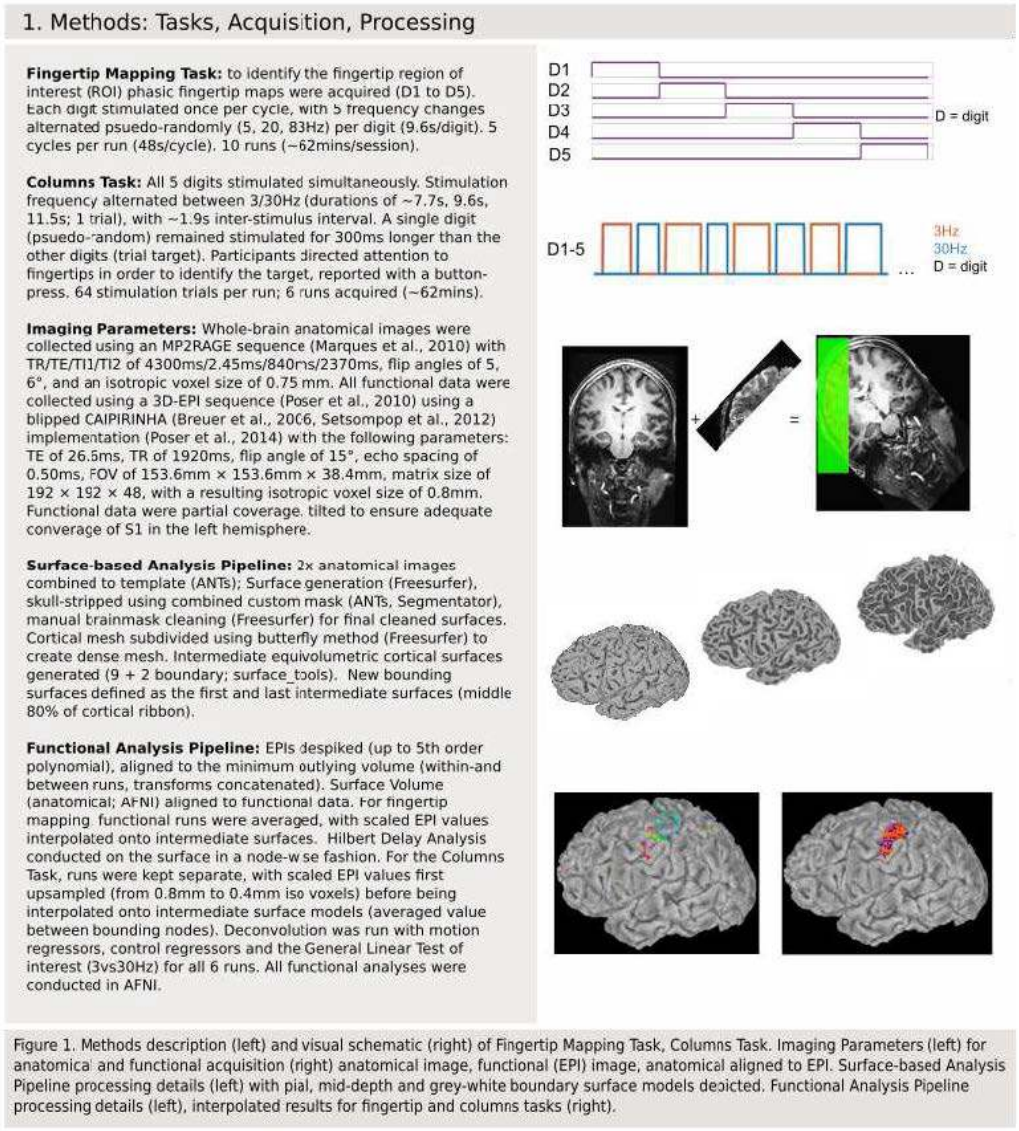

Figure 1. Methods description (left) and visual schematic (right) of Fingertip Mapping Task, Columns Task. Imaging Parameters (left) for anatomical and functional acquisition (right) anatomical image, functional (EPI) image, anatomical aligned to EPI. Surface-based Analysis Pipeline processing details (left) with pial, mid-depth and grey-white boundary surface models depicted. Functional Analysis Pipeline processing details (left), interpolated results for fingertip and columns tasks (right).

Results: We identified modular clusters in SI responding preferentially to 3Hz or 30Hz, suggestive of columnar organization (Fig.2b,c). We next binarized the GLT beta weights, and designated each vertex as 3/30Hz preferring. We assessed spatial consistency of these vibration preferences within sessions by comparing odd and even runs using a Jaccard index (0-1 scale; Fig.3a,b). We found the patterns were reliable, with ~64% vertices consistent across odd versus even runs. Furthermore, each of the observed Jaccard indices significantly exceeded the chance level established by a random-permutation null model, indicating a robust effect size (Fig.3b). For one participant, we collected an additional 12 runs of data in a separate session. Fig 3a shows the odd/even intersection map (vertices with the same signed beta-weight in odd/even runs), as well as the preference of each vertex for 3/30Hz within the mask. This analysis further supported the spatial consistency of 3/30Hz vertex preference. While column sizes appeared similar along the anterior bank and crown of the postcentral gyrus, the posterior bank showed a predominance of vertices preferring 3Hz. This pattern aligns with previous research suggesting an increase in receptive field size along the anterior to posterior axis of the postcentral gyrus.

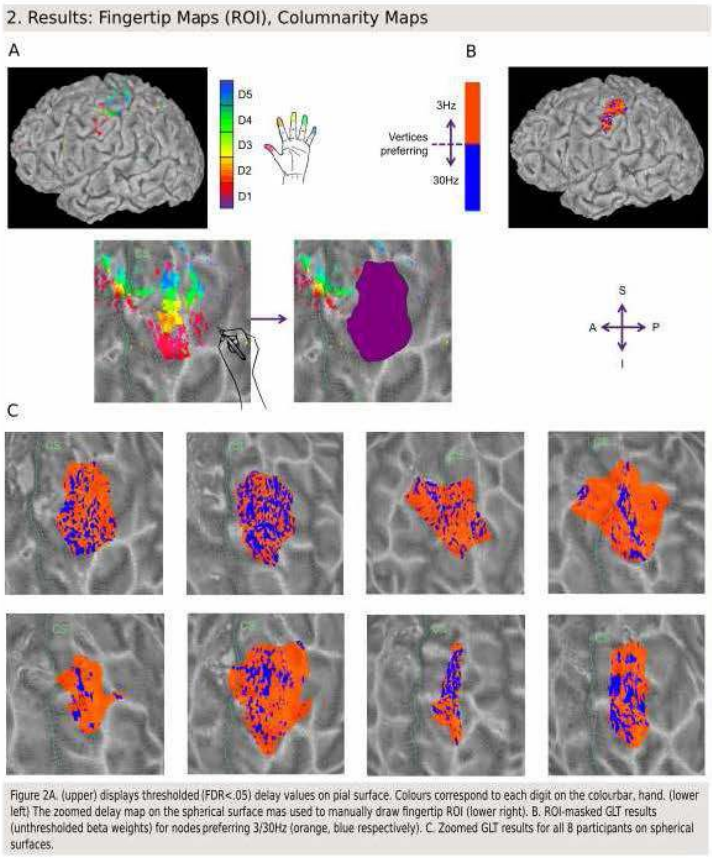

Figure 2A. (upper) displays thresholded (FDR<.05) delay values on pial surface. Colours correspond to each digit on the colourbar, hand. (lower left) The zoomed delay map on the spherical surface mas used to manually draw fingertip ROI (lower right). B. ROI-masked GLT results (unthresholded beta weights) for nodes preferring 3/30Hz (orange, blue respectively). C. Zoomed GLT results for all 8 participants on spherical surfaces.

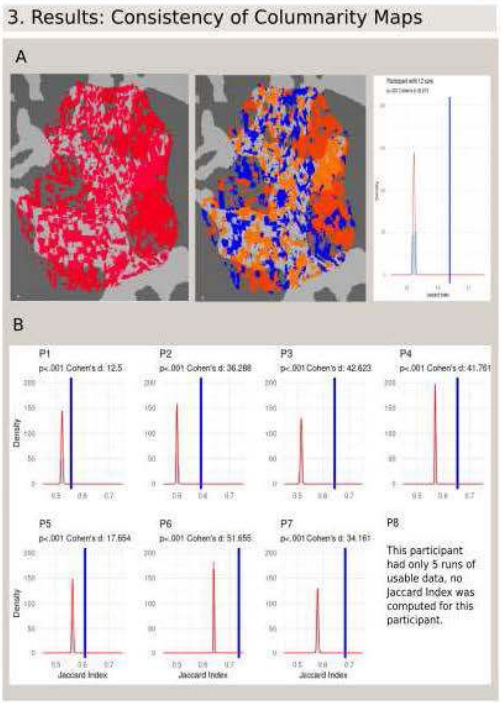

Figure 3A. (left) Map of the intersection of odds/evens runs for single participant with 12 runs of data (single session). (middle) intersection-masked columnarity map for all 12 runs of columns task data. (right) null distribution of Jaccard Indices based off permuted (shuffled) beta values (cyan) fitted with a normal curve (red) alongside the observed Jaccard Index calculated from the true odd/even runs (blue). P-value and effect size (Cohen's d) for the comparison of the observed Jaccard Index against the null. B. Jaccard Indices of the observed odds/evens for each participant (3 vs 3 runs), with their respective null distributions calculated as above. P-values and effect sizes also reported.

Conclusions: While columnar organisation was first identified in SI animal models[8], there has since been limited evidence reported in humans[1,2]. We found clear, reliable patterns of modular clusters responsive to different vibrotactile frequencies. Our results broaden our understanding of cortical organisation principles in sensory cortex, supporting the idea that this structure might be present in all sensory areas.

References

1. Yang et al., (2019). High-resolution fMRI maps of columnar organization in human primary somatosensory cortex. Paper presented at: 27 th Annual Meeting of ISMRM; May, 2019; Montreal, Canada. Abstract 617.
2. Kim et al., (2021). Laminar representations of vibrotactile stimuli with varying frequency in S1: a 7T fMRI study. Paper presented at: 27th Annual Meeting of the Organization for Human Brain Mapping, June, 2021., Glasgow, Scotland. Abstract 3847.
3. Sur et al., (1981). Modular segregation of functional cell classes within the postcentral somatosensory cortex of monkeys. Science,
4. Sur et al., (1984). Modular distribution of neurons with slowly adapting and rapidly adapting responses in area 3b of somatosensory cortex in monkeys. Journal of neurophysiology,
5. Saal & Bensmaia, (2014). Touch is a team effort: interplay of submodalities in cutaneous sensibility. Trends in neurosciences.
6. Keuhn & Pleger, (2020). Encoding schemes in somatosensation: from micro-to meta-topography. Neuroimage.
7. Poser, B. A. (2014), 'CAIPIRINHA-accelerated 3D EPI for temporal and/or spatial resolution EPI acquisitions'. Proc. of the ISMRM.
8. Mountcastle et al., (1955). Topographic organization and modality representation in first somatic area of cat's cerebral cortex by method of single unit analysis. Am. J. Physiol.

Poster No 2536

Perceptual Bistability in Occluded Digital Numbers: a Behavioral Study

Junxiang Luo[1], Isao Yokoi[1], Hiromasa Takemura[1,2,3]

[1]National Institute for Physiological Sciences, Okazaki, Japan, [2]The Graduate Institute of Advanced Studies, SOKENDAI, Hayama, Japan, [3]Center for Information and Neural Networks (CiNet), Advanced ICT Research Institute, NICT, Suita, Japan

Introduction: Number characters are essential visual stimuli widely used in modern society. Understanding the behavioral and neural mechanisms for processing number characters will improve the current understanding of how visual information can be hierarchically processed to establish semantic recognition of numbers. We found that the digital number, one of the popular number designs that frequently appear in our daily lives, can be a useful tool to study the recognition of number characters since a partial occlusion can cause perceptual ambiguities and induce bistable interpretations (Figure 1A). Here, we report a

behavioral study investigating how the perceptual bistability of occluded digital numbers can be manipulated by adapting to certain types of visual stimuli.

Methods: Fifteen adult human participants (8 females and 7 males) with normal or corrected-to-normal vision participated in the experiment after a written informed consent. Participants were instructed to see the visual stimuli appearing in a display, while maintaining a viewing distance of 65cm. Visual stimuli were designed by MATLAB Psychtoolbox extensions (Brainard, 1997; Pelli, 1997; Kleiner, 2007). During the experiment, participants were asked to maintain fixation to the point appearing at the center of the screen. Figure 1B describes the timeseries of the experiment. Participants were firstly asked to look at adaptation stimuli (digital numbers, Arabic numbers, digital elements, kanji characters, and white noise) for a certain amount of time, and were then asked to report whether a test stimulus (occluded number) presented afterwards can be seen as 6 or 8, or other numbers. Participants repeated 20 trials for each stimulus condition. In the data analysis, we calculated the bias index (BI): BI=(CR6 - CR8)/(CR6 + CR8), where CR6 and CR8 indicate the choice ratio of perceiving “6” and “8”, respectively. We performed the Krusukal-Wallis one-way analysis of variance for testing statistical significance by comparing the bias index in different adaptation conditions and calculated Cohen’s d for evaluating the effect size.

Results: The report from one participant clearly shows the perceptual biases caused by adaptation, after adapting to number 6 or the element corresponding to 6, the perceptual interpretation of occluded character tends to be 8; while adapting to number 8 tend to generate perception of number 6 from the occluded test stimuli (Figure 2A). Figure 2B depicts the population results of the BI from 15 participants. We found that adaptation to digital and Arabic numbers caused significant perceptual bias for test stimuli (occluded characters), in a consistent manner among participants. We also found statistically significant evidence of perceptual bias in the digital elements adaptation condition, although the effect size (d=1.96) was much smaller than those in digital and Arabic number conditions (d=8.22 and 4.11, respectively). We did not find a statistically significant perceptual bias in the condition of kanji characters adaptation.

Conclusions: Our results demonstrate that adaptation to number characters affects bistable perception of partially occluded digital number stimuli. We found that this effect can also be seen when adaptation stimuli were Arabic numbers and digital elements, suggesting that this perceptual bistability mainly originates in the middle level of visual processing, where shapes and number forms are encoded (Tanaka, 1996; Kravitz et al., 2013). A lack of evidence in kanji characters suggests that higher-order stage that represents numerosity or semantics did not take a significant role in generating this phenomenon (Nieder, 2016). The results of this behavioral study will provide an experimental design for future studies, testing how much activities in cortical regions processing shape and number forms (Shum et al., 2013; Cai et al., 2023) can be correlated with subjective experience in number perceptions.

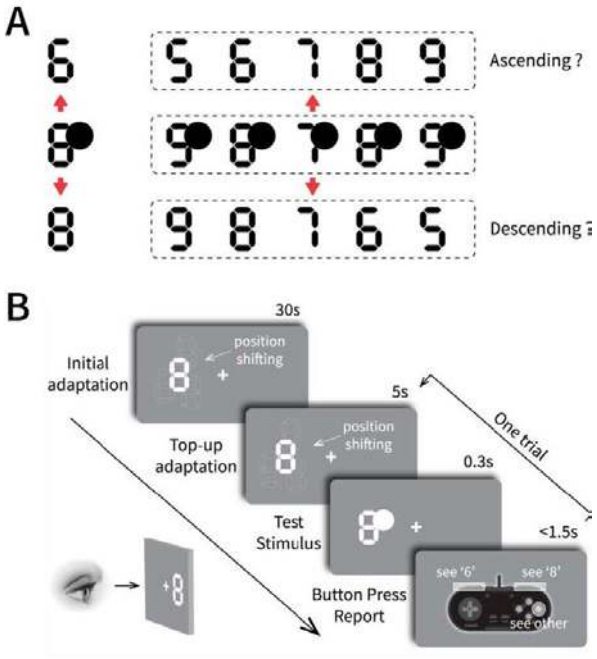

Figure 1. (A) Partial occlusion on the right-up corner of certain digital number characters induces two-way interpretation of their semanticmeaning. (B) Time series of the behavioral experiment.

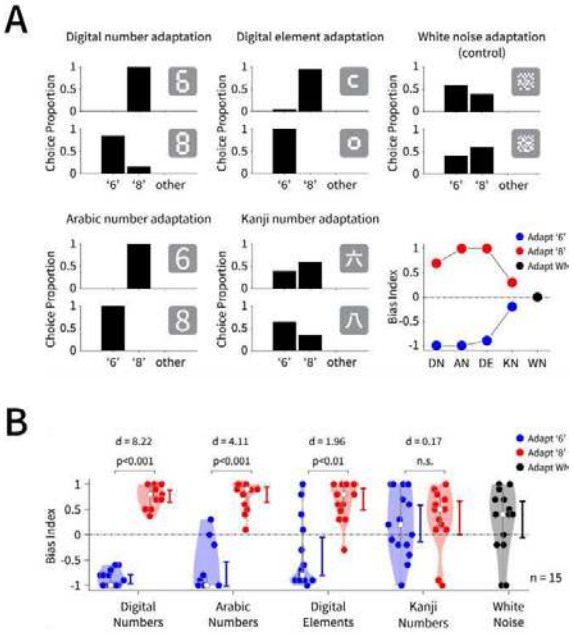

Figure 2. (A) Behavioral results of a single human participant. (B) Population results from 15 participants. The vertical axis indicates the bias index. Each colored dot depicts the data of individual participants (blue, adaptation to "6"; red, adaptation to "8"; black, adaptation to white noise). Values of Cohen's d are shown on the top of this coordinate. The error bar depicts ±95% confidence interval.

References

1. Brainard, D. H. (1997), 'The Psychophysics Toolbox', Spat. Vis., vol. 10, pp. 433–436.
2. Cai, Y. (2023), 'Nonsymbolic Numerosity Maps at the Occipitotemporal Cortex Respond to Symbolic Numbers', J Neurosci., vol. 43, no. 16, pp. 2950-2959.
3. Kleiner, M. (2007), 'What's new in psychtoolbox-3', Perception, vol. 36, pp. 1–16.
4. Kravitz, D. J. (2013). 'The ventral visual pathway: an expanded neural framework for the processing of object quality', Trends Cogn. Sci., vol. 17, pp. 26–49.
5. Nieder, A. (2016), 'The neuronal code for number', Nat. Rev. Neurosci. vol. 17, pp. 366–382.
6. Pelli, D. G. (1997), 'The VideoToolbox software for visual psychophysics: transforming numbers into movies', Spat. Vis., vol. 10, pp. 437–442.
7. Shum, J. (2013), 'A Brain Area for Visual Numerals', J Neurosci., vol. 33, no. 16, pp. 6709-6715.
8. Tanaka, K. (1996), 'Inferotemporal Cortex and Object Vision', Annu. Rev. Neurosci., vol. 19, pp. 109–139.

Poster No 2537

Sub-bundle based analysis reveals the role of human optic radiation in visual working memory

Yanming Wang[1], Huan wang[1], Sheng Hu[1], Benedictor Alexander Nguchu[1], Du Zhang[1], Shishuo Chen[1], Xiaoxiao Wang[1], Bensheng Qiu[1]

[1]*University of Science and Technology of China, Hefei, Anhui*

Introduction: White matter (WM) carries information between gray matter (GM) and is crucial for brain function. Studying the WM functional activities could help people understand the information processing mechanisms of the brain. BOLD fMRI has been widely used to evaluate the GM, but the WM BOLD signals have been rarely explored. Optic radiation (OR) is responsible for the transmission of visual information and is one of the most important WM tracts in the visual system. This study evaluated the population receptive field (pRF) characteristics of OR sub-bundles at the individual level to explore whether BOLD signals of individual OR sub-bundles can encode high-fidelity visual information. In addition, previous studies have reported that the human primary visual cortex (V1) is not only activated by incoming visual information but is also engaged by top-down cognitive processes, such as visual working memory (Lawrence et al., 2018), and that central vision has stronger top-down feedback (Zhaoping, 2021). OR is the most important WM tract connecting V1. This study thus also explored whether OR is involved in the transmission of feedback signals and evaluated the information transmission preferences in the foveal and peripheral sub-bundles.

Methods: The HCP 7T retinotopy dataset was used to reconstruct the OR. Then, OR was subdivided into sub-bundles based on the anatomical position of termination in V1. To suppress the influence of GM signals, WM masks set to different degrees of restraint were used. The OR sub-bundles were confined within the spaces of these masks, which were ranked as standard and strict sub-bundles. The pRF model was then applied to evaluate the retinotopic properties of these sub-bundles. Moreover, the consistency of the pRF properties of standard sub-bundles with those of V1 subfields at the endpoint of the sub-bundles was evaluated. Correlation analysis was performed to evaluate the relationships of the pRF parameters of the strict and standard sub-bundles. In addition, we applied the HCP working memory dataset to evaluate the activation of the foveal and peripheral OR sub-bundles (fOR, pOR) and LGN and V1 sub-fields (fLGN, pLGN, fV1, pV1) under 0bk and 2bk task and activation differences between 0bk and 2bk. Moreover, the 2bk-0bk contrast differences of foveal and peripheral sub-bundles or subfields were evaluated. Furthermore, we investigated the relationship between the 2bk-0bk contrast and the 2bk task d-prime.

Results: The OR was well reconstructed and the distribution of the sub-bundles was consistent with previous study (Kammen et al., 2016). For the standard sub-bundles, polar angles exhibited the characteristics of the contralateral visual field and were biased towards the horizontal meridian, Fig. 1A-C. Moreover, eccentricity was significantly positively correlated with pRF size, Fig. 1D. The findings showed that pRF parameters of standard sub-bundles were consistent with the standard retinotopic properties of OR (Wandell et al., 2007, Wang et al., 2023). Interestingly, there existed similar pRF properties in sub-bundles and corresponding V1 subfields. In addition, the pRF properties of strict sub-bundles also exhibited the standard retinotopic properties and significantly correlated with those of standard sub-bundles, indicating that OR sub-bundle evaluation was GM-free. Notably, the activation under the 2bk task was significantly stronger than that under the 0bk task in fOR, pOR, fLGN, pLGN, fV1 and pV1, Fig. 2A. The 2bk-0bk contrast of fV1 was significantly greater than that of pV1, Fig. 2B. More importantly, 2bk-0bk contrast only in fOR and pOR was significantly positively correlated with 2bk task d-prime, Fig. 2C.

Conclusions: The findings demonstrated that the BOLD signals of OR sub-bundles can encode high-fidelity visual information, indicating the feasibility of assessing WM functional activity at the tract sub-bundle level. Moreover, OR not only transmits visual information from bottom to up, but also engages visual working memory.

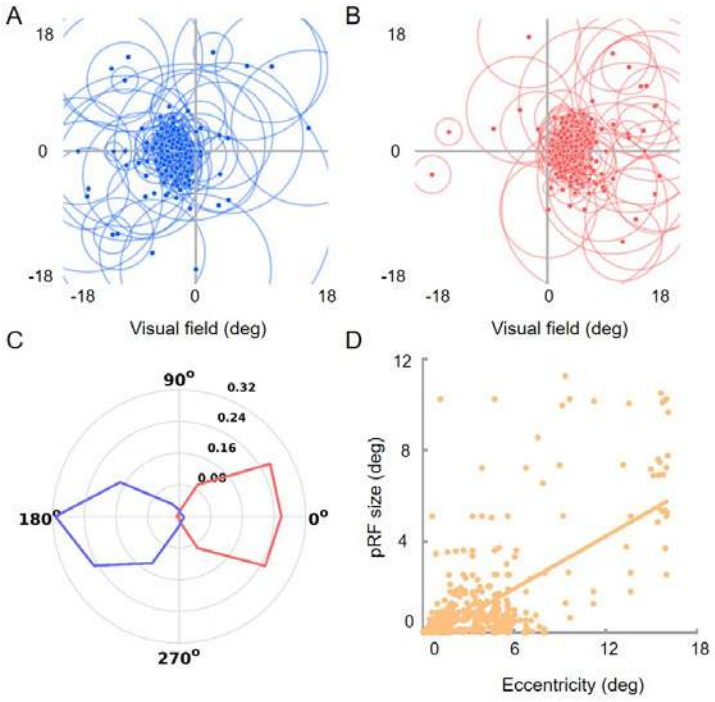

Figure1. Distribution of pRF properties of standard sub-bundles.

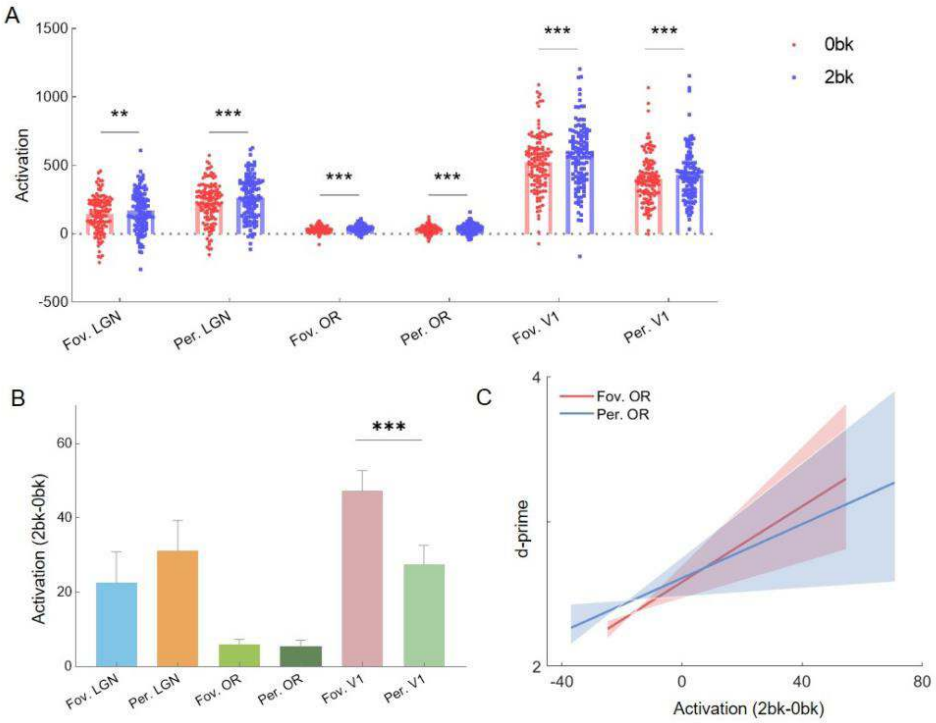

Figure 2. Activation analysis of OR sub-bundles and LGN and V1 sub-fields.

References

1. KAMMEN A, LAW M, TJAN B S, et al. 2016. Automated retinofugal visual pathway reconstruction with multi-shell HARDI and FOD-based analysis. Neuroimage [J], 125: 767-779.
2. LAWRENCE S J D, VAN MOURIK T, KOK P, et al. 2018. Laminar Organization of Working Memory Signals in Human Visual Cortex. Current Biology [J], 28: 3435-3440.
3. WANDELL B A, DUMOULIN S O, BREWER A A 2007. Visual field maps in human cortex. Neuron [J], 56: 366-383.
4. WANG H, WANG X, WANG Y, et al. 2023. White matter BOLD signals at 7 Tesla reveal visual field maps in optic radiation and vertical occipital fasciculus. Neuroimage [J], 269: 119916.
5. ZHAOPING L 2021. Contrast-reversed binocular dot-pairs in random-dot stereograms for depth perception in central visual field: Probing the dynamics of feedforward-feedback processes in visual inference. Vision Research [J], 186: 124-139.

Poster No 2538

Behavioral and neural correlates of impaired scene perception following saccadic eye movements

Yong Min Choi[1], Tzu-Yao Chiu[1], Julie Golomb[1]

[1]The Ohio State University, Columbus, OH

Introduction: Across frequent ballistic eye movements (i.e., saccades), the visual input projected to the retina shifts drastically. Although people are not aware of it, visual perception is impaired around the time of saccadic eye movements (Burr et al., 1994; Golomb et al., 2014). Most of these previous studies have used simple visual stimuli to assess perisaccadic visual perception, but how the processing of complex visual scene images is influenced by saccades remains less explored. Therefore, the current study explored behavioral evidence of impaired post-saccadic scene perception, and then further investigated underlying neural mechanisms by assessing 1) scene category information in high-level visual cortex, and 2) low-level visual information (i.e., spatial frequency) in early visual cortex.

Methods: In a series of behavioral and fMRI experiments assisted by eye-tracking, we presented scene images at different time points relative to saccade offset (Figure 1). Scene images contained either low- or high-spatial frequency information to investigate whether specific spatial frequency bands contribute differently to post-saccadic scene perception. In gaze-contingent behavioral experiments (Figure 1A), subjects followed a fixation dot and categorized briefly presented post-saccadic scene images (e.g., beach, mountain, forest, city, office, and highway). In Experiment 1, the scene image appeared either 5 ms or 500 ms after the saccade completion. Experiment 2 (pre-registered) included five post-saccadic delay conditions (5, 16, 50, 158, and 500 ms) to explore the time course of post-saccadic scene perception. In the fMRI experiment, instead of an explicit categorization task, subjects performed a 1-back task on scene images presented with jittered timing

after the saccade cue (Figure 1B). Trials were sorted according to post-saccadic delay based on post-hoc analysis of eye-tracking data.

Results: To answer how scene perception is behaviorally influenced by saccadic eye movement, we compared scene categorization accuracy between post-saccadic delay conditions. We found lower scene categorization accuracy in short than long delay trials, irrespective of spatial frequency of scene images (Experiment 1). Furthermore, Experiment 2 showed a lower scene categorization accuracy in the 5 ms and 16 ms post-saccadic delay condition compared to the baseline (500 ms), but not in the 50 ms and 158 ms delay conditions, suggesting rapid recovery within 50 ms after saccade completion. Additional analyses confirmed that the post-saccadic impairment was not attributable to eye movement velocity or saccade detection criterion. Next, we investigated neural correlates underlying the behavioral impairment. We assessed scene category and spatial frequency information in scene-selective region (parahippocampal place area; PPA) and early visual cortex (EVC), respectively, by running RSA-based decoding analysis (Haxby et al., 2001). First, the posterior PPA showed lower scene category information in the short compared to the long post-saccadic delay trials. Moreover, spatial frequency information in early visual cortex was also decreased in the short compared to long post-saccadic delay trials.

Conclusions: To summarize, we provided behavioral evidence for impaired perception of both high- and low- spatial frequency filtered scene images presented shortly after saccades. Neural evidence suggested that interrupted neural representations at different levels of visual hierarchies may underly impaired post-saccadic scene perception, affecting both high-level scene category information AND low-level visual information of a scene image. These results provide novel evidence for impaired perception of realistic scene images following saccadic eye movement, unlike seemingly intact visual perception across eye movements.

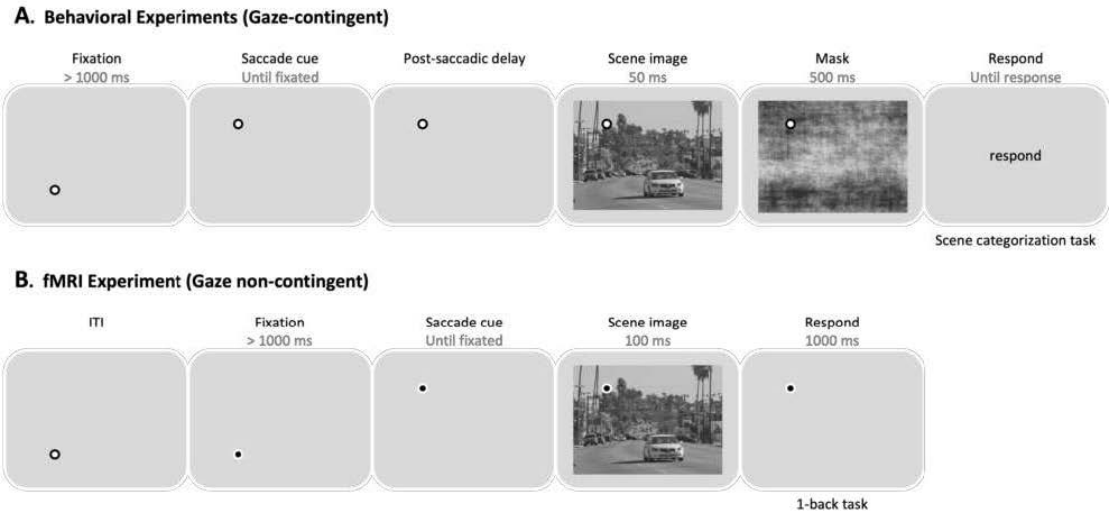

Figure 1. Illustration of trial sequence of (A) behavioral experiments and (B) fMRI experiment.
Subjects were asked to follow the fixation and make saccadic eye movements when the fixation shifted its location. Shortly after, the scene image flashed for a short duration and subjects reported the category of scene image (A) or reported when the scene image was identical to the previous trial (B).

References

1. Choi, Y. M., Chiu, T. Y., & Golomb, J. D. (2023). Behavioral and neural correlates of impaired scene perception following saccadic eye movements.

Poster No 2539

Individual differences in prefrontal coding of visual features

Qi Lin[1], Hakwan Lau[1]

[1]RIKEN, Wako, Saitama

Introduction: Sitting at the apex of the cortical hierarchy (Young, 1992), the lateral prefrontal cortex (LPFC) is most commonly associated with complex and high-level cognition. Does LPFC also play a role in visual perception? Evidence from nonhuman primates has characterized the representation of visual information in LPFC, even when there is no cognitive task involved (Riley et al., 2017; Tsao et al., 2008; Haile et al., 2019). In addition, feedback signals from LPFC seem necessary for recognizing

objects under challenging conditions (Kar & DiCarlo, 2021). Yet to date, with few exceptions (e.g., Huth et al., 2012), how LPFC may support perception in humans remains understudied. To fill in this gap, we built encoding models to relate visual features extracted from a deep neural network to predict brain activities in LPFC. We then contrasted the tuning profiles of LPFC for visual stimuli to those of the visual cortex. Strikingly, we found that the degrees of individual variability were higher in LPFC. That is, the stimuli that drove the maximal overall LPFC varied highly across individuals.

Methods: Results presented here are based on data from the Natural Scenes Dataset (Allen et al., 2022). Each of the 8 subjects viewed 9209~10,000 unique scene images while being scanned at 7T and performing a recognition memory task. To build encoding models of LPFC within each subject (see Figure 1A), for the presented images, we first extracted activations from the image encoder of a CLIP network (ViT-B/32 backbone; Radford et al., 2021). We divided the images into a training set and a test set. Separately for each vertex in a liberal LPFC mask (see the purple contours in Figure 1C), we built a ridge regression model to map the CLIP-img features to the single-trial beta estimates evoked by the training images. We only retained the top 10% vertices in terms of the explained variance from the regression models within the training set. For each of these selected vertices, we then tested the performance of the model in the held-out images. Performance was assessed as the Pearson's r between predicted vs. observed responses to the held-out images. Focusing on vertices within LPFC or the ventral visual stream (VVS) with cross-validated Pearson's r > 0.1, we built subject-specific encoding models to predict the average responses in these predictable vertices. We then screened all 73000 NSD images through these encoding models of LPFC/VVS activity. To quantify individual differences, we correlated the predicted responses for all images in LPFC/VVS across individuals.

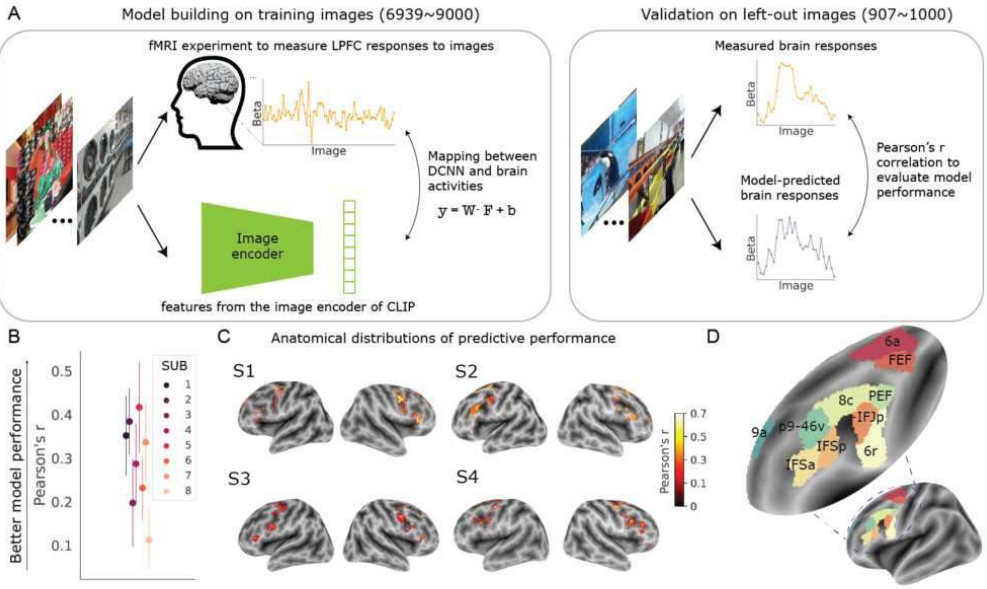

Figure 1. Encoding models robustly predict visual responses in patches of LPFC. (A) Schematic of the cross-validated prediction pipeline. (B) Average Pearson's r between predicted and observed responses in the top 10% LPFC vertices in the held-out data. Each dot represents a subject. Error bars represent +/- 1 SD. (C) Anatomical distributions of the predictive performance in four example subjects. The contour of the LPFC mask is marked in purple. (D) The 10 parcels with the largest average proportion of visually-sensitive vertices. Parcel labels are defined by Glasser et al. (2016).

Results: Across all 8 subjects, we observed robust prediction of LPFC in the held-out data (Figure 1B; all ps < .001 based on 10000 bootstrapping iterations). Figure 1C shows the anatomical distribution of prediction performance from 4 subjects. Figure 1D shows the 10 parcels (defined in Glasser et al., 2016) with the largest average proportion of visually-sensitive vertices (cross-validated r > 0.1). Shown in Figure 2A are the 5 images predicted to evoke the largest responses in the LPFC of 4 subjects. Inspection of these LPFC-activating images reveals a striking variance across individuals: each subject's LPFC seems to prefer a different kind of stimuli. Quantitively, the correlations of the predicted responses across individuals are lower in LPFC than in VVS (Figure 2B; Wilcoxon signed-rank test p < .001). To demonstrate that the observed pattern is not specific to NSD, we replicated the result with a larger independent image set (Figure 2C; Wilcoxon signed-rank test p < .001; Ecoset; Mehrer et al., 2021).

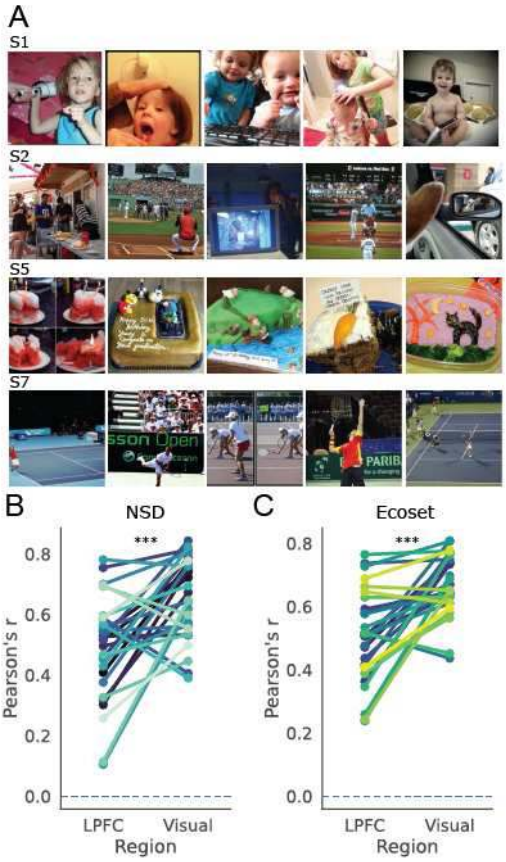

Figure 2. Individual differences in prefrontal coding of visual features. (A) The 5 images with the largest predicted LPFC responses in 4 representative subjects. Across-subject correlations of predicted responses in LPFC and visual regions in NSD (B) and Ecoset (C). Each line represents a pair of subjects.

Conclusions: Our study demonstrates the under-appreciated role of LPFC in visual processing and suggests that LPFC may underlie the idiosyncrasies in how different individuals experience the visual world. Methodologically, these findings may also explain why previous group studies have often failed to observe robust visual functions in LPFC, as subjects' responses may need to be calibrated individually.

References

1. Allen, E. J., St-Yves, G., Wu, Y., Breedlove, J. L., Prince, J. S., Dowdle, L. T., . . . Kay, K. (2022). A massive 7T fMRI dataset to bridge cognitive neuroscience and artificial intelligence. Nature Neuroscience, 25(1), 116–126.
2. Glasser, M. F., Coalson, T. S., Robinson, E. C., Hacker, C. D., Harwell, J., Yacoub, E., . . . Van Essen, D.C. (2016). A multi-modal parcellation of human cerebral cortex. Nature, 536(7615), 171–178.
3. Haile, T. M., Bohon, K. S., Romero, M. C., & Conway, B. R. (2019). Visual stimulus-driven functional organization of macaque prefrontal cortex. NeuroImage, 188, 427–444.
4. Huth, A. G., Nishimoto, S., Vu, A. T., & Gallant, J. L. (2012). A continuous semantic space describes the representation of thousands of object and action categories across the human brain. Neuron, 76(6), 1210–1224.
5. Kar, K., & DiCarlo, J. J. (2021). Fast recurrent processing via ventrolateral prefrontal cortex is needed by the primate ventral stream for robust core visual object recognition. Neuron, 109(1), 164–176.e5.
6. Mehrer, J., Spoerer, C. J., Jones, E. C., Kriegeskorte, N., & Kietzmann, T. C. (2021). An ecologically motivated image dataset for deep learning yields better models of human vision. Proceedings of the National Academy of Sciences, 118(8), e2011417118.
7. Radford, A., Kim, J. W., Hallacy, C., Ramesh, A., Goh, G., Agarwal, S., ... & Sutskever, I. (2021, July). Learning transferable visual models from natural language supervision. In International Conference on Machine Learning (pp. 8748-8763). PMLR.
8. Riley, M. R., Qi, X.-L., & Constantinidis, C. (2017). Functional specialization of areas along the anterior–posterior axis of the primate prefrontal cortex. Cerebral Cortex, 27(7), 3683–3697.
9. Tsao, D. Y., Schweers, N., Moeller, S., & Freiwald, W. A. (2008). Patches of face-selective cortex in the macaque frontal lobe. Nature Neuroscience, 11(8), 877–879.
10. Young, M. P. (1992). Objective analysis of the topological organization of the primate cortical visual system. Nature, 358(6382), 152–155.

Poster No 2540

Whole brain and primary visual cortex layer fMRI signatures of afterimage perception

Sharif Kronemer[1], Micah Holness[1], Burak Akin[1], Javier Gonzalez-Castillo[1], Laurentius (Renzo) Huber[2], Paul Taylor[1], A. Morgan[1], Joshua Teves[1], Victoria Gobo[1], Daniel Handwerker[1], Peter Bandettini[1]

[1]National Institute of Mental Health, Bethesda, MD, [2]Functional MRI Core Facility, National Institute of Mental Health, Bethesda, MD

Introduction: Afterimages are prolonged visual perceptions that typically follow adaptation to light stimulation. Afterimages have been a source of interest for centuries because they offer insight on the neural mechanisms of vision and conscious perception (Goethe, 1970). A lingering question is to what degree are retinal versus cortical processes involved in afterimages? Answering this query is significant for relating afterimages to other categories of conscious perception (e.g., imagery and hallucinations). While the retinal view of afterimages is dominant (e.g., the bleaching of photoreceptors; Brindley et al., 1962), there is evidence of post-retinal processes in the formation and modification of afterimages (e.g., Downey, 1901; Shimojo et al., 2001). Meanwhile, there is a limited number of neuroimaging studies on afterimages that would help to measure its central neural mechanisms. Accordingly, in the current experiment, we aimed to interrogate the whole brain and primary visual cortex layer fMRI signals underpinning afterimage perception.

Methods: Healthy, adult participants (N = 34) completed a visual perception task where participants were shown images and afterimages. Afterimages were induced by a human face silhouette image. In initial task phases, participants reported on the perceptual sharpness, contrast, and duration of their afterimages. Participant perception reporting accuracy was confirmed on images with known sharpness, contrast, and duration. The afterimage perception reports were used to reconstruct a mock afterimage: an image that perceptually-matched the sharpness and contrast overtime of each participants' afterimage. In the main task phase, participants reported the onset and offset of their mock and real afterimages, during simultaneous eye-tracking (EyeLink 1000 Plus; SR Research, Inc.) and whole brain 7T fMRI was recorded (BOLD; voxel size: 1.2mm3; TR: 1000ms; Siemens, Inc.). A subset of participants (N = 12) also completed the main task while recording primary visual cortex (V1) cortical-layer resolution 7T fMRI (BOLD/VASO; voxel size 0.8mm3; TR: 3000ms, Siemens, Inc.). Analysis were completed with MATLAB (MathWorks, Inc.) and Analysis of Functional Neuroimages (AFNI) software.

Results: The inducer stimulus reliably generated afterimages (>75% afterimage perception rate). Participants accurately reported on the image sharpness, contrast, and duration. The afterimage perceptual reports were sufficiently accurate such that a majority of participants (>90%) did not distinguish between their real and mock afterimages, even when they were presented side-by-side. Whole brain fMRI findings show that the mock and real afterimages recruit many of the same subcortical and cortical networks (Figure 1), including sensory regions (e.g., VI and fusiform gyrus [FG]), arousal and neuromodulatory regions (e.g., thalamus and brainstem), salience regions (e.g., insula and anterior cingulate cortex), and attention/detection regions (e.g., posterior parietal cortex [PPC] and dorsal lateral prefrontal cortex [DLPFC]). However, the mock afterimage showed greater fMRI responses relative to the real afterimage in several regions (e.g., FG, PPC, and DLPFC), and real afterimage revealed fMRI decreases absent in the mock afterimage, particularly in the prefrontal cortex (Figure 2). Preliminary analyses of the V1 cortical layer fMRI responses suggest similar dynamics between the mock and real afterimages.

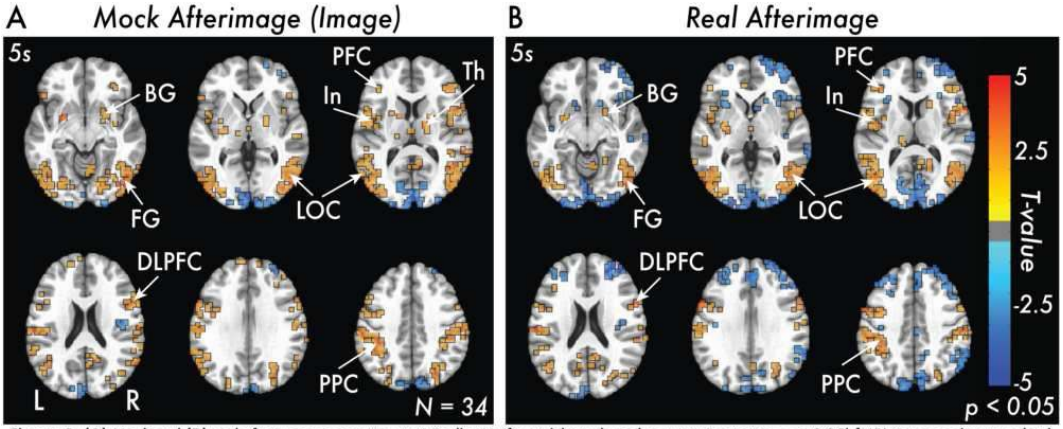

Figure 1. (A) Mock and **(B)** real afterimage perception statistically significant (cluster-based permutation testing, $p < 0.05$) fMRI increases (warm colors) and decreases (cool colors) at 5 seconds from afterimage onset. Basal ganglia (BG); fusiform gyrus (FG); dorsal lateral prefrontal cortex (DLPFC); lateral occipital cortex (LOC); posterior parietal cortex (PPC); insula (In); thalamus (Th); prefrontal cortex (PFC); left (L); right (R); seconds (s).

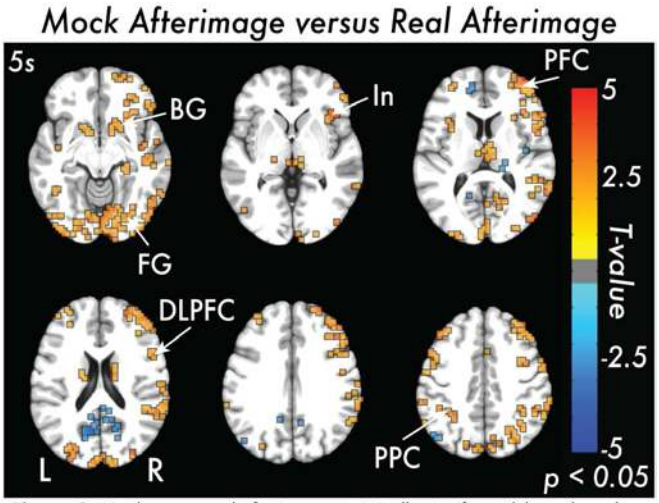

Figure 2. Mock versus real afterimage statistically significant (cluster-based permutation testing, $p < 0.05$) fMRI increases (warm colors) and decreases (cool colors) at 5 seconds from afterimage onset. Basal ganglia (BG); fusiform gyrus (FG); dorsal lateral prefrontal cortex (DLPFC), posterior parietal cortex (PPC); insula (In); prefrontal cortex (PFC); left (L); right (R); seconds (s).

Conclusions: As far as we know, the current investigation represents the first whole brain and layer fMRI study of human afterimage perception. These findings suggest that afterimages engage similar whole brain networks as normal sensory vision. However, in some brain areas, there are differences between mock and real afterimage conscious perception. Future analyses will interrogate subject-level dynamics (e.g., fMRI responses for participants with more or less vivid afterimage perception).

References

1. Brindley, G.S., (1962), 'Two new properties of foveal after-images and a photochemical hypothesis to explain them', The Journal of Physiology, vol. 164, no. 1, pp. 168-179.
2. Downey, J.E., (1901), 'An experiment on getting an after-image from a mental image', Psychological Review, vol. 8, no. 1, pp. 42-55.
3. Goethe, J.W.v., (1970), 'Theory of Colours', The MIT Press.
4. Shimojo, S., et al., (2001), 'Afterimage of perceptually filled-in surface', Science, vol. 293, no. 5535, pp. 1677-80.

Poster No 2541

Characterizing individual top-down depth-dependent human microcircuitry in ventro-temporal cortex

Luca Vizioli[1], Logan Dowdle[1], Geoff Ghose[1], Steen Moeller[1], Kamil Uğurbil[1], Essa Yacoub[1]

[1]Center for Magnetic Resonance Research, Minneapolis, MN

Introduction: Feedforward and feedback connections between different cortical areas define the sophisticated hierarchical processing of information in neocortex and have been characterized by distinct patterns of laminar connectivity using invasive methods in animals. Recent MR technological advances have enabled acquiring functional images with submillimeter resolution over small volumes, allowing noninvasive access to this mesoscopic scale. However, studying laminar connectivity non-invasively in humans remains challenging as extending these methods to large volumes encompassing multiple areas, critical for establishing the connectivity between regions, has remained elusive as the high level of acceleration required to achieve large coverage at high resolutions is restricted by thermal noise effects. Here we record functional images simultaneously from several regions of varying complexity across the cortical hierarchy to examine the impact of top-down task modulations during a high-level task.

Methods: We recorded 7T BOLD images in 4 individuals (Gradient echo (GE) EPI; TR: 2.03s; R=3; MB=2; 6/8th Partial Fourier; TE: 29.6ms; 56 slices). In two tasks, subjects viewed 8 blocks (12s on/off duration) of face stimuli. Faces were phase scrambled between 0 to 40% coherence1. Participants completed 6 runs of a face perception and 6 of a stimulus irrelevant fixation task. Before standard preprocessing (i.e., slice-timing; motion and detrending) images were denoised with NORDIC, which suppresses thermal noise without impacting functional spatial precision2. To identify face preferential regions such as the Fusiform face area (FFA) and Occipital face area (OFA), we used a separate face localizer. The retinotopic representation of the stimuli in V1 was instead localized using the first block of each task (discarded from subsequent analyses) in conjunction with probabilistic atlases. The regions of interest (ROIs) were converted into 3 cortical depths using LayNii3. Activation was estimated for each of the 48 single blocks, allowing enough statistical power to carry out within subject statistical analyses.

To evaluate top-down effects of task demands, we calculated the ratio of the activation during the face relative to the fixation task for each cortical depth. We then performed a depth dependent functional connectivity analysis, but in this case, it was done independently per task.

Results: Within each subject we show that, relative to the fixation, the face task elicited significantly larger BOLD responses in the inner compared to the outer layers of V1; and in the outer compared to the inner layers in the FFA (bootstrapped $p<0.05$, Bonferroni corrected). Moreover, we report a significant ($p<.05$, Bonferroni corrected) increase in functional connectivity between outer depths of FFA and inner depths of V1, during the face relative to the fixation task.

Conclusions: Cortical depth dependent fMRI allows non-invasive mesoscopic investigations of behaviors that are unique to humans. However, due to SNR and imaging challenges, prior studies have been mostly confined to primary sensory cortices using low-level stimuli, which do not tap into human specific behaviors. Here, we examine top-down cortical depth dependent modulations concomitantly across areas of different complexity in the visual hierarchy during a high level, socially meaningful task. Our layer dependent findings are consistent with animal reports of feedback being exchanged between deeper and superficial layers4. Furthermore, these results are consistent with a theorized mechanism of conscious perception involving apical dendritic amplification5. Importantly, the dissociation in laminar profiles between the FFA and V1 indicates that the results cannot be accounted for by spurious venous effects. Our work demonstrates the feasibility of carrying out depth dependent fMRI analyses at the single subject level, a crucial step towards characterizing mesoscopic differences in the diseased brain.

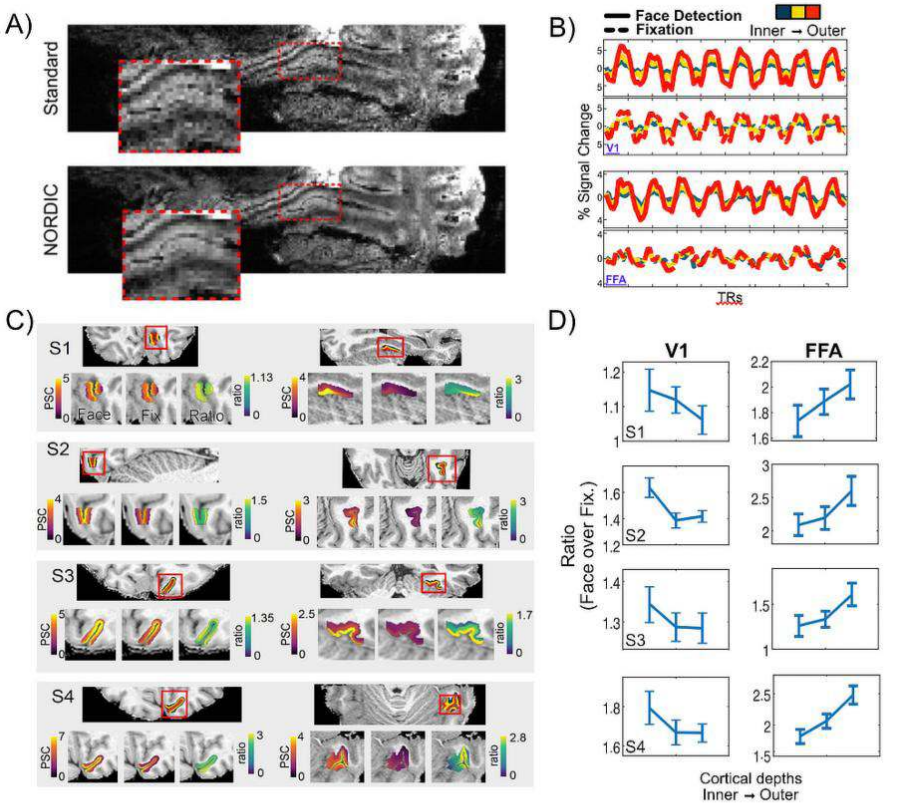

Figure1. A) Example of coverage (sagittal view) before and after NORDIC; B) example of single subject single run time courses for cortical depths in FFA and V1; C) Layer activation profiles; D) ratios across tasks; errorbars represent standard error across single blocks ratios. Asterisks indicate statistically significant ($p<.05$ corrected) differences.

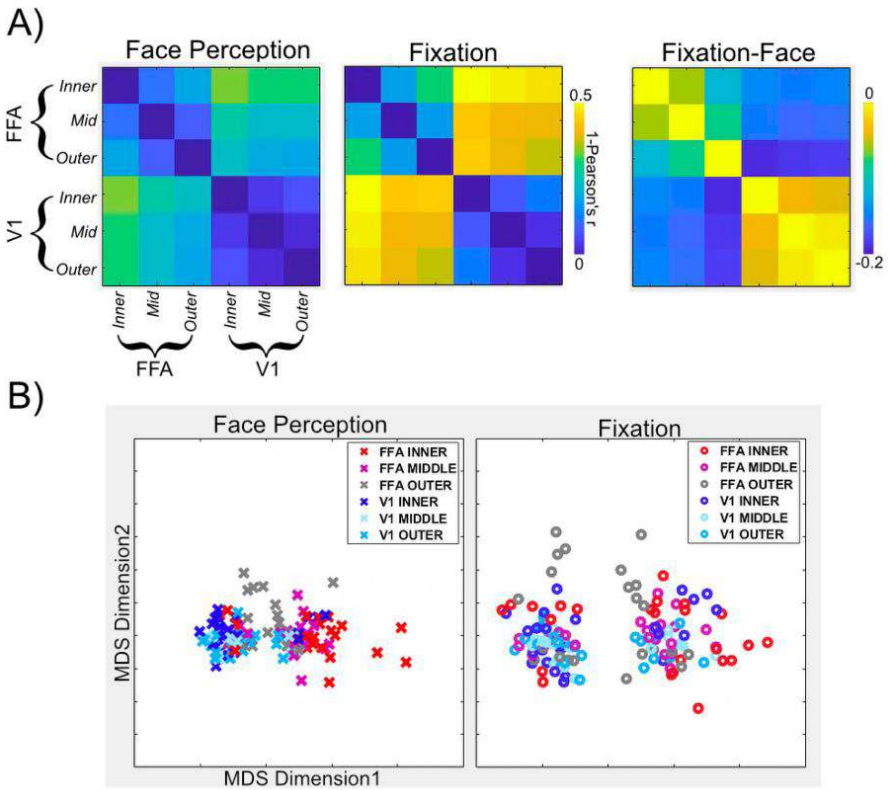

Figure2. A) Functional connectivity (FC) distance (1-Pearson's r) between FFA and V1; B) single subjects single runs multidimensional scaling of the FC matrices. Proximity between points indicates strength of connectivity. We observe an overall connectivity increase during the face task, being largest for outer layer of FFA and the inner layers of V1

References

1. Dowdle, L. T., Ghose, G., Ugurbil, K., Yacoub, E. & Vizioli, L.(2021) Clarifying the role of higher-level cortices in resolving perceptual ambiguity using ultra high field fMRI. NeuroImage 227, 117654 .
2. Vizioli, L. et al. (2021) Lowering the thermal noise barrier in functional brain mapping with magnetic resonance imaging. Nat Commun 12, 5181
3. Huber, L. (Renzo) et al. (2021) LayNii: A software suite for layer-fMRI. NeuroImage 118091 doi:10.1016/j.neuroimage.2021.118091.
4. Rockland, K. S. & Pandya, D. N. (1979) Laminar origins and terminations of cortical connections of the occipital lobe in the rhesus monkey. Brain Research 179, 3–20.
5. Marvan, T., Polák, M., Bachmann, T. & Phillips, W. A. (2021) Apical amplification—a cellular mechanism of conscious perception? Neuroscience of Consciousness.

Poster No 2542

Neural correlates of the perceptual spaces of low-level features and objects

Suniyya Waraich[1], Keith Jamison[2], Amy Kuceyeski[2], Jonathan Victor[3]

[1]Weill Cornell Graduate School, New York, NY, [2]Weill Cornell Medicine, New York City, NY, [3]Weill Cornell Medical College, New York, NY

Introduction: Low-level visual features and semantic information seem different: while low-level features, e.g., color, can vary continuously, objects often appear to be categorical. It has also been theorized that objects, unlike low-level features, are mentally represented in a tree-like structure (Kemp and Tenenbaum, 2008). To search for differences in the mental representations of low-level features and semantic information, we previously conducted psychophysical experiments to collect and analyze similarity judgments between different stimuli (Waraich and Victor, 2022) using a variant of multidimensional scaling (n=11-12 per domain, 8F). Five stimulus domains (Figure 1), which varied in their degree of semantic information were studied: a purely semantic domain of animal names, images of the animals, two intermediate domains of texturized images, and textures composed of colored checks. All five stimulus domains were derived from a common set of 37 animals. In separate experiments that probed the similarity structure of each stimulus domain individually, we found that indeed, even though all domains could be represented in a low-dimensional space, there was tree-like structure for the

stimulus domains containing more semantic information: the image-like, image, and word domains (Waraich and Victor, 2023). We next sought to find the neural correlates of this difference.

Methods: 9 of the participants (7F) who participated in the psychophysics experiments took part in an fMRI study. Over the course of four fMRI sessions, they were shown each of the stimuli (37 stimuli x 5 domains = 185) at least 7 times, while performing a one-back memory task to maintain central fixation and attention. Stimuli were presented in a slow event-related design (presentation time: 1s, ISI: 3.5s), but they appeared in blocks separated by 10s. Within a block, only stimuli from a single domain appeared. The data were acquired on a 3T Siemens scanner, with multiband acquisition and TR=0.8s. Data were preprocessed using fmriprep to perform motion correction, susceptibility distortion correction, and co-registration of functional scans with the anatomical scans. Two participants (2M) were excluded from further analysis due to excessive motion and poor performance on the one-back task. Response amplitudes to the five domains and individual images were separately obtained using two generalized linear models (Prince et al, 2022).

Results: Voxel-wise responses to the five stimulus domains showed different spatial patterns, with the texture-like, image-like, and image domains eliciting the greatest activity in the occipital areas, and overall decreased activation relative to baseline and a different pattern of activation in response to the words. We quantified these differences by computing the dissimilarities between the patterns of responses (beta estimates) for each domain (using two metrics: cosine distance and correlation distance) for voxels that were explained well by the GLM: $R^2 \geq 0.1$ (see Figure 2: fMRI) and $R^2 \geq 0.15$ separately. These voxels comprise most of visual cortex. We found that the greatest similarity in responses was observed for the texture-like, image-like, and image domains, with the responses to textures sometimes similar to these 3 domains, and with responses to words always the most dissimilar across participants. Psychophysical experiments also showed a difference between domains but the main difference was between the more semantic domains (image-like stimuli, images, and words) and the less-semantic domains (textures and texture-like stimuli).

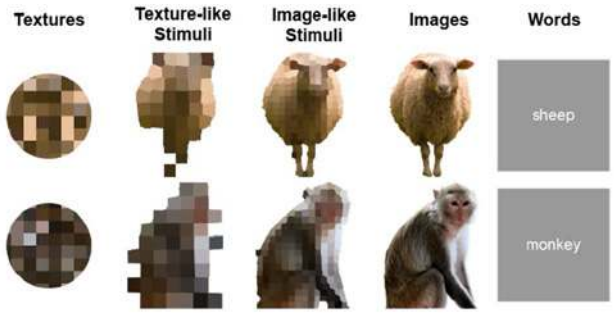

Fig. Example stimuli from each stimulus domain

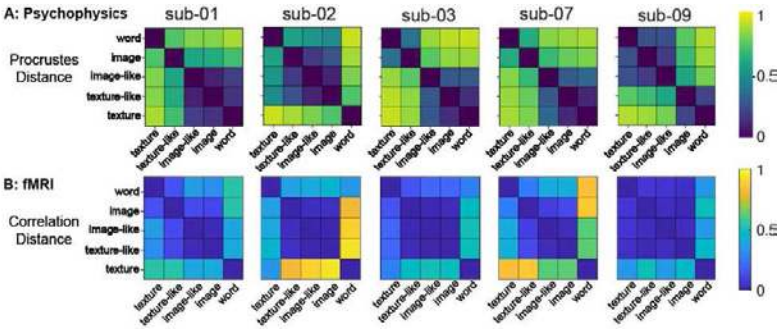

Fig. Differences between domains for 5 participants: Psychophysics: Procrustes distances between coordinates of points in each perceptual space. fMRI: correlation distance between betas for each domain

Conclusions: The psychophysical analysis compared within-domain similarities between stimuli and the fMRI analysis compared overall activation patterns between the domains. They both suggest a stepwise progression of representation in the brain, even though the correspondence between the representations based on similarity judgments and those based on neural activation patterns is not exact.

References

1. Kemp C. (2008), 'The discovery of structural form', Proceedings of the National Academy of Sciences, 105 (31) 10687-10692.
2. Prince J.S. (2022), 'Improving the accuracy of single-trial fMRI response estimates using GLMsingle', eLife 11:e77599.
3. Waraich S.A. (2022), 'A Psychophysics Paradigm for the Collection and Analysis of Similarity Judgments', The Journal of Visualized Experiments, (181), e63461.
4. Waraich S.A. (2023) 'The geometry of low- and high-level perceptual spaces', The Journal of Neuroscience, accepted.

Poster No 2543

Shared connectome and organization in the human cortex irrespective of sensory experience

Guo Jiahui[1], Francesca Setti[2], Ma Feilong[1], Davide Bottari[2], M. Ida Gobbini[3], Pietro Pietrini[2], Emiliano Ricciardi[2], James Haxby[1]

[1]Dartmouth College, Hanover, NH, [2]IMT School for Advanced Studies Lucca, Lucca, Italy, [3]University of Bologna, Bologna, Italy

Introduction: Human high-level visual cortex selectively responds to different visual categories (e.g., faces, places). Category-selective topographies exist in the ventral visual cortex, superior temporal sulcus, and extend to the frontal regions. The general layout of these topographies is similar across individuals, but idiosyncrasies exist in their precise conformation and location. Category-specific activations in response to tactile and auditory stimuli in both typically developed and sensory-deprived individuals[1–3] suggest a supramodal functional organization in these ventro-temporal and occipital areas. It has not been possible previously, however, to map individual-specific visual category-selective topographies in congenitally-blind participants.

Methods: Congenitally blind (BD, N = 11, mean age 46 years, 3 females) and deaf participants (DF, N = 9, mean age 24 years, 5 females) were presented with audio-only and video-only versions of the movie 101 Dalmatians[4], respectively. Three control groups either watched and/or listened to the audiovisual (AV, N = 10, mean age 35 years, 8 females), the audio-only (AD, N = 10, mean age 39 years, 7 females), and the video-only (VD, N = 10, mean age 37 years, 5 females) versions of the movie. It has been established that individualized category-selective topographies can be estimated with high fidelity across movies using connectivity hyperalignment (CHA)[5]. Another fMRI data[6] from an independent group of participants who watched the movie, The Grand Budapest Hotel, and performed a visual category functional localizer task (N = 20, mean age 27 years, 10 females), was included to predict the individualized topographies. The predictions were validated with another independent dataset (N = 24, mean age 26 years, 15 females), in which participants watched the movie Monkey Kingdom and also completed a similar functional localizer task.

Results: With CHA, category-selective topographies were successfully predicted in both congenitally blind and deaf participants by projecting the localizer data into their individual cortical space using transformation matrices derived from functional connectivity calculated from the movie data (Figure 1). The predicted topographies were distinctive for individuals in all groups (BD, DF, AV, AD, & VD). Notably, individual variability of category-selective topographies in the ventral visual pathway in congenitally blind participants was highly comparable to that of sighted participants (Figure 2). Functional connectomes were notably similar across the entire cortex, regardless of the modality of sensory input. When visual or auditory information was shared between groups, participants' connectomes showed higher similarity in the corresponding visual and auditory cortices. Connectomes in the bilateral superior temporal cortices, which are involved in multisensory information processing, were analogous across all groups. In the validation analysis with the Monkey Kingdom dataset, when we randomized the labels for the movie-localizer pairs across participants, prediction accuracy significantly dropped from near-noise-ceiling levels to baseline, demonstrating that our predictions using the correct labels are precise and specific to each individual.

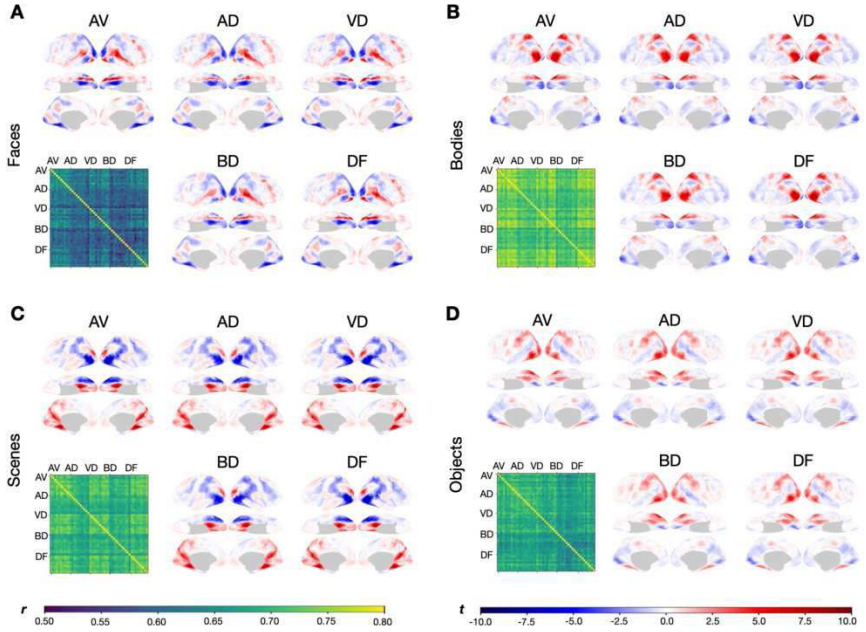

Figure 1. Similar Predicted Organizations across Groups. A. Predicted face-selective topographies (faces-vs-all) in control groups of participants either watched and/or listened to the audiovisual (AV), the audio-only (AD), and the video-only (VD) versions of the movie and patient groups of congenitally blind (BD) and deaf participants (DF). The similarity matrix at the lower left corner shows the Pearson correlation coefficients (*r*) between predicted topographies of each pair of individuals across the five groups. **B, C, & D.** Predicted and similarity matrices of body- (bodies-vs-all), scene- (scenes-vs-all), and object-selective (objects-vs-all) topographies accordingly.

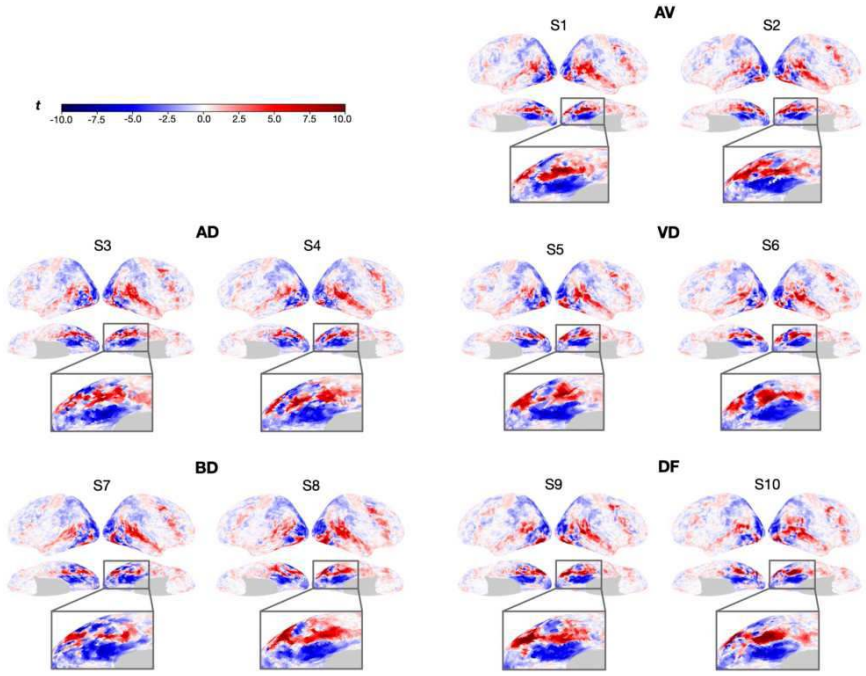

Figure 2. Sample contrast maps and enlarged views of the ventral temporal cortex in individual brains. Contrast maps for face-selective topographies (faces-vs-all) and their zoomed-in views of the ventral temporal cortex were plotted in two sample participants in each group of participants.

Conclusions: With real-world, naturalistic stimuli, this study demonstrates that the functional connectome maintains a similar organization across input from different sensory modalities and with different histories of congenital sensory deprivation. The structure of the part of the connectome that is associated with visual category-selective topographies is conserved even in adults with no history of visual experience. These results show that development of the functional organization of the human high-level visual cortex can occur independently of visual experience and introduce a method for identifying category-selective areas in adults who have never seen those categories.

References
1. P. Pietrini. (2004), 'Beyond sensory images: Object-based representation in the human ventral pathway', Proc. Natl. Acad. Sci. 101, 5658–5663
2. S. L. Fairhall. (2017), 'Plastic reorganization of neural systems for perception of others in the congenitally blind', NeuroImage 158, 126–135
3. S. Mattioni. (2020), 'Categorical representation from sound and sight in the ventral occipito-temporal cortex of sighted and blind'. eLife 9, e50732.
4. F. Setti. (2023), 'A modality-independent proto-organization of human multisensory areas', Nat. Hum. Behav., 1–14
5. G. Jiahui. (2023), 'Cross-movie prediction of individualized functional topography'. eLife 12, e86037
6. M. Visconti di Oleggio Castello. (2020), 'An fMRI dataset in response to "The Grand Budapest Hotel", a socially-rich, naturalistic movie', Sci. Data 7, 383

Poster No 2544

FMRI-based Encoding for Self-supervised Deep Predictive Coding in the Human Brain

Jungmin Lee[1,2,3], Sungwoo Lee[1,2,3], Sunghyoung Hong[1,2], Choong-Wan Woo[1,2,3], Seok Jun Hong[1,2,3,4]

[1]Center for Neuroscience Imaging Research, Institute for Basic Science, Suwon, Korea, Republic of, [2]Department of Biomedical Engineering, Sungkyunkwan University, Suwon, Korea, Republic of, [3]Life-inspired Neural networks for Prediction and Optimization (LNPO) Group, Suwon, Korea, Republic of, [4]Center for the Developing Brain, Child Mind Institute, New York, NY, United States

Introduction: The ability to anticipate future outcomes is of utmost importance in human cognition. Predictive coding theory[3] provides a parsimonious model for this phenomenon, conceptualizing the brain as a self-supervised hierarchical generative model minimizing prediction errors by reconciling top-down information with bottom-up sensory input. Despite its significance, the neuroscientific evidence supporting this theory remains scarce, especially at the whole-brain level. Here, we employed 'PredNet[2]', a predictive coding-inspired deep learning model, and correlated its temporal activation with movie-watching fMRI in order to explore the representation of prediction and prediction error across the human brain.

Methods: The model was trained on a 3-hour movie, 'Titanic', and subsequently tested on a 2-hour movie, 'ForrestGump'. The fMRI data of this test movie was obtained from StudyForrest[1], an open source repository providing audio-visual movie watching fMRI data from 15 subjects. For the next-frame video prediction task, we employed PredNet[2], a convLSTM model with four hierarchical layers, each containing four computational units: R (representation), Ahat (prediction), A (input), E (error) (Fig1A). Features from both prediction and prediction error units were extracted for voxel-wise encoding. Principal component analysis (PCA) was applied to this feature matrix to preserve 90% of its variance, followed by hemodynamic response convolution of 4 seconds and down-sampling to the actual fMRI rate. The feature matrix was used to train an encoding model via ridge regression, ensuring a robust evaluation through 9-fold cross-validation. During training, we estimated regression coefficients (β), which were then used to predict BOLD signals. Finally, we correlated this signal with experimental fMRI data to assess the encoding performance.

Results: We identified the distinct patterns of PredNet-Brain correspondence for both prediction and prediction error across the whole brain (Fig1B,D). Specifically, the prediction exhibited a more pronounced correlation in the early visual areas (i.e. V1-4), with average encoding performance values of 0.05, 0.13, and 0.19 in accordance with the hierarchy of PredNet (Fig1B). In comparison, the prediction error exhibited a stronger performance across widespread brain areas, persisting even at the lowest PredNet layer, and showed a layerwise increase, with averaged encoding accuracy values of 0.26, 0.33, and 0.40 (Fig1D). This implies that the computation of prediction error occurs on the whole-brain level, as sensory information is initiated for the processing and intensifies from the lower visual to higher dorsal attention networks. Subsequently, we focused on 8 regions of interest including V1-4, MT, and FFC, known for their relevance to visual processing, to assess how each prediction and prediction error could be mapped along the PredNet layer orders (Fig1C,E). For further analysis, we also mapped β as a means to identify the most explanatory features of prediction and prediction error within the layer, and examined their dominance ratio (Fig2A,C). Notably, at the layer 1, the prediction error initially showed a predominant pattern which, by the layer 2, gradually shifted towards the prediction taking over the dominance. At the highest layer, both the prediction and prediction error displayed a comparatively balanced dominance ratio (Fig2E).

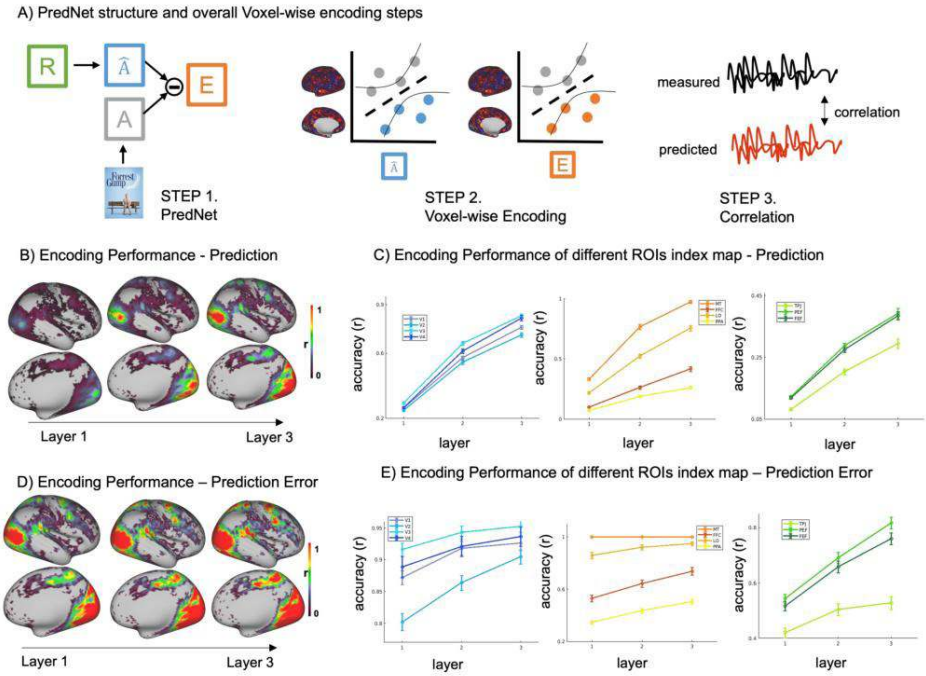

Figure 1. A) PredNet structure with overall encoding steps. B) Averaged encoding performance map across 15 subjects with on prediction from layer 1 to layer 3. Notably, the highest layer influences lower visual areas, demonstrating the impact of top-down prediction on the earliest layers of the visual pathway. C) The prediction encoding performance index map of ROIs associated with visual tasks. D) Averaged encoding performance map across 15 subjects with on error from layer 1 to layer 3. E) The error encoding performance index map of ROIs associated with visual tasks.

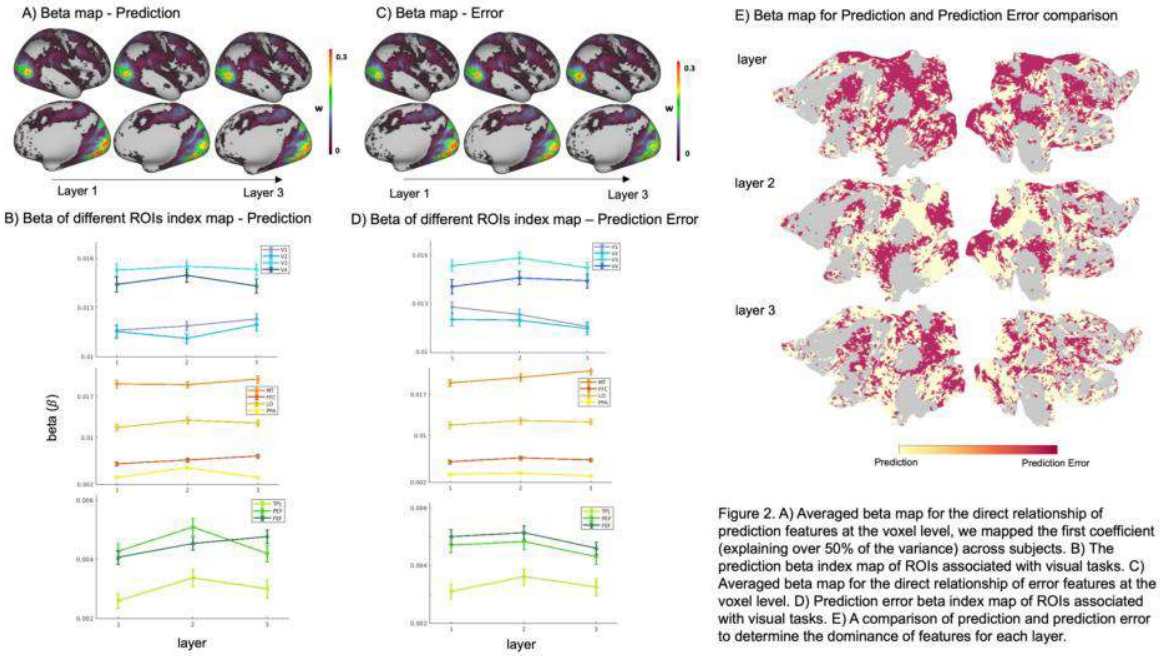

Figure 2. A) Averaged beta map for the direct relationship of prediction features at the voxel level, we mapped the first coefficient (explaining over 50% of the variance) across subjects. B) The prediction beta index map of ROIs associated with visual tasks. C) Averaged beta map for the direct relationship of error features at the voxel level. D) Prediction error beta index map of ROIs associated with visual tasks. E) A comparison of prediction and prediction error to determine the dominance of features for each layer.

Conclusions: The study showed unique signal pathways for each prediction and prediction error across the macroscale network, revealing a dynamic processing shift. By demonstrating a proof-of-concept for the biological plausibility of predictive coding, our study provides an important avenue to comprehending the intricate dynamics of macroscale information processing in the human brain.

References

1. Hanke, M., Adelhöfer, N., Kottke, D., Iacovella, V., Sengupta, A., Kaule, F. R., ... & Stadler, J. (2016). A studyforrest extension, simultaneous fMRI and eye gaze recordings during prolonged natural stimulation. Scientific data, 3(1), 1-15.
2. Lotter, W., Kreiman, G., & Cox, D. (2016). Deep predictive coding networks for video prediction and unsupervised learning. arXiv preprint arXiv:1605.08104
3. Rao, R. P., & Ballard, D. H. (1999). Predictive coding in the visual cortex: a functional interpretation of some extra- classical receptive-field effects. Nature neuroscience, 2(1), 79–87.

Poster No 2546

Category-selectivity, again: Hand-selective Visual Areas Support Action-related Behavioural Goals

Davide Cortinovis[1], Stefania Bracci[1]

[1]Center for Mind/Brain Sciences, University of Trento, Rovereto, Italy

Introduction: The occipitotemporal cortex (OTC) contains areas that preferentially respond to specific object categories like faces, body parts, and tools, with a mirrored organization across its lateral and ventral parts (Kanwisher, 2010; Taylor & Downing, 2011). However, the exact role of these areas in supporting action or object recognition and the dimensions they represent are still debated (Bracci & Op de Beeck, 2023; Peelen & Downing, 2017). Here, we investigate the role of the action dimension as one of the possible organizing principles of object space in visual cortex, by investigating the selectivity and the multivariate representations of category-selective clusters.

Methods: Across two experiments, we collected fMRI data from 47 participants who were presented with static images characterized by a different degree of action properties of either body parts (hands, whole-bodies, and faces) or objects (tools, manipulable objects, and non-manipulable objects). 19 participants participated in the first experiment, in which we collected task-based data with a blocked design to the investigate the selectivity of regions within OTC. To test category-selectivity, we adopted a vector-of-ROI analysis approach (Konkle & Caramazza, 2013). We created and extracted the activations from a series of partially overlapping spheres covering the ventral OTC (from parahippocampal gyrus to inferior temporal gyrus) and lateral OTC (from inferior temporal gyrus to transverse occipital sulcus). 28 participants participated in the second experiment, in which the same stimulus set was presented in an event-related design to characterize the multivariate representations behind the category-selective areas identified in the first experiment; specifically, we computed an action index that captures specific action-related components in OTC representational space. This index was computed by first correlating the patterns of activations between the six categories of objects, and then by subtracting to the correlation between each body-part with tools the correlation between each body-parts and the other inanimate object categories; this results in an index of how each body-part is selectively associated with tools (vs. the other inanimate objects). T-tests were then applied to the results to test for significance.

Results: In the first experiment, we found that left lateral OTC exhibits a dorsal-posterior to ventral-anterior topographically organized action gradient, with selective and partly overlapping activations for bodies, hands, tools, and manipulable objects, and a selective overlap between hands and tools. Left ventral OTC shows, from medial to lateral, the typical inanimate-animate division with further sub-characterizations: 1) an opposite action gradient in ventro-medial OTC with higher responses to non-manipulable, followed by manipulable and finally tools; 2) distinct responses for hands relative to faces and bodies in ventro-lateral OTC. In the second experiment, the action index analysis revealed that the action gradient was reflected at the level of multivariate representations only in hand-selective clusters in both left lateral and ventral OTC, i.e., these areas represented hands and tools as being more similar with each other compared to the other object categories.

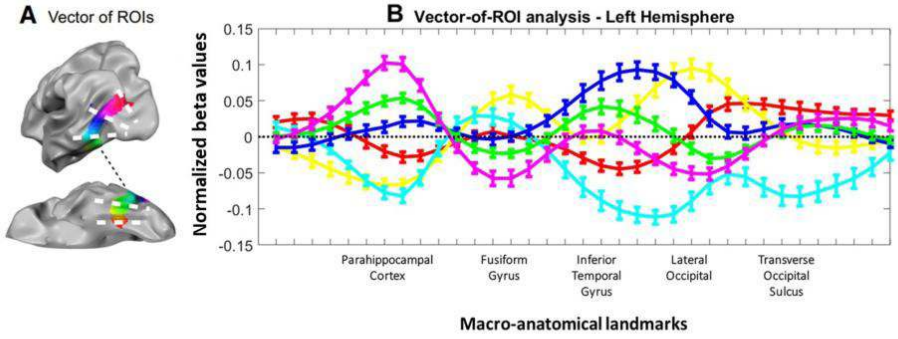

Figure 1. Vector-of-ROI analysis. A series of overlapping spheres was created, covering left ventral and lateral occipitotemporal cortex. Activations were extracted from each of the overlapping spheres, with y-axis showing normalized beta values and x axis the macro-anatomical landmarks of some spheres. Adapted from Konkle & Caramazza (2023).

Conclusions: Our results shed new light on the role of traditionally-defined category-selective areas: hand-selective clusters in visual cortex represent action-related properties of stimuli and their representational profile differentiate from the one of body- or face-selective areas. Altogether, our results show that the object space in hand-selective visual cortex reflects action-related behaviourally-relevant dimensions, and suggest future paths to generate a computational model of this object space (Ratan-Murty et al., 2021).

References
1. Bracci, S. (2023). Understanding human object vision: a picture is worth a thousand representations. Annual review of psychology, 74, 113-135.
2. Kanwisher, N. (2010). Functional specificity in the human brain: a window into the functional architecture of the mind. Proceedings of the national academy of sciences, 107(25), 11163-11170.
3. Konkle, T. (2013). Tripartite organization of the ventral stream by animacy and object size. Journal of Neuroscience, 33(25), 10235-10242.
4. Peelen, M. V. (2017). Category selectivity in human visual cortex: Beyond visual object recognition. Neuropsychologia, 105, 177-183.
5. Ratan Murty, N. A. Computational models of category-selective brain regions enable high-throughput tests of selectivity. Nature communications, 12(1), 5540.
6. Taylor, J. C. (2011). Division of labor between lateral and ventral extrastriate representations of faces, bodies, and objects. Journal of Cognitive Neuroscience, 23(12), 4122-4137.

Poster No 2547

Time-dependent contextual feedback signals increase V1 responses to unpredictable scene information

Zirui Zhang[1,2], Clement Abbatecola[1,2], Angus Paton[1,2], Lucy Petro[1,2], Lars Muckli[1,2]

[1]Centre for Cognitive Neuroimaging,School of Psycholog and Neuroscience, University of Glasgow, Glasgow, United Kingdom, [2]Imaging Centre for Excellence, Queen Elizabeth University Hospital, University of Glasgow, Glasgow, United Kingdom

Introduction: Introduction Information processing operations in the visual cortex are tuned to the statistical regularities of sensory inputs and are crucially dependent on context. Neurobiologically inspired computational frameworks of visual processing emphasise functional interactions between higher and lower cortical areas, whereby higher areas send feedback signals that influence feedforward processing in lower areas. Using a partial visual occlusion approach in which a mask covers the lower right quadrant of natural scene images, we can isolate feedback signals in the retinotopic visual cortex that processes the occluded image portion (Muckli et al., 2015, Morgan 2019, Muckli 2023). Based on our earlier findings using apparent motion stimulation where feedback signals suppress predictable sensory inputs (Alink et al., 2010), we hypothesised that a priming contextual scene would increase the response to subsequent unpredictable sensory information, while it would reduce or stabilise the response to consistent, expected sensory information.

Methods: Results are from 24 subjects, mean age = 26.34 years. We selected ten grey-scale images from five categories. We designed an event-related fMRI paradigm consisting of the 5 experimental conditions (consistent context before, inconsistent context before, consistent context after, inconsistent context after, and target only) and 1 baseline condition. The lower right quadrant of an image (Target) was always shown between 0.8s and 1.8s from trial start. In the target only condition, this was the whole trial. In the before conditions, contextual information was provided from 0s to 1s. In the after conditions, contextual information was provided from 1.6s to 2.6s. Contextual information was either consistent or inconsistent with target, yielding 5 conditions. We applied an ROI-wise deconvolution analysis to compare the effect of contextual consistency on the univariate BOLD response amplitude containing the peak of the signal in the Target region of V1.

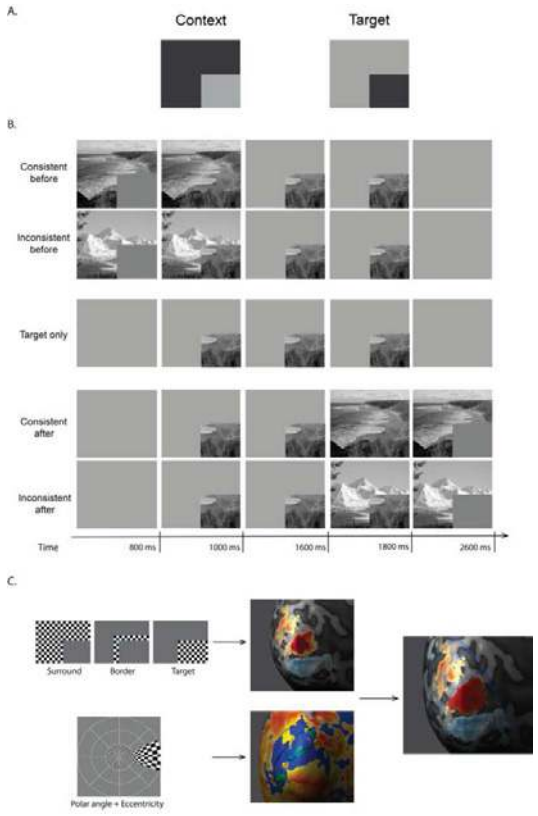

Fig 1. A) Two portions of image stimuli: the 'Context' (Left) and the 'Target' (Right). B) Experimental paradigm and example C) ROI defination: Processes of defining V1 Target area

Results: We found that the presence of contextual feedback signals increases the BOLD response in the Target region of V1 compared to when there was no contextual information available, t = 2.697. p = 0.007. Compared to the Target only condition, we found significantly higher activity when the Target was preceded by inconsistent contextual information, t = 2.737, p = 0.006. However, we found no significant difference between the Target only and consistent before conditions, t =0.635, p = 0.53, suggesting that bottom-up activation is not increased when there is preceding top-down information that predicts the content of the bottom-up activity. Furthermore, there was a significant difference when directly comparing consistent before vs inconsistent before, t = 2.101, p = 0.035. As a control, we also found that this unexpected later contextual information increased the response to the bottom-up Target compared to the Target only condition, which was true no matter whether this information was consistent with the Target (t = 2.139, p = 0.03) or not (t = 2.76, p =0.007). Further, there was no significant difference comparing the response to the Target when it was followed by either consistent or inconsistent contextual information, t = 0.572, p = 0.57.

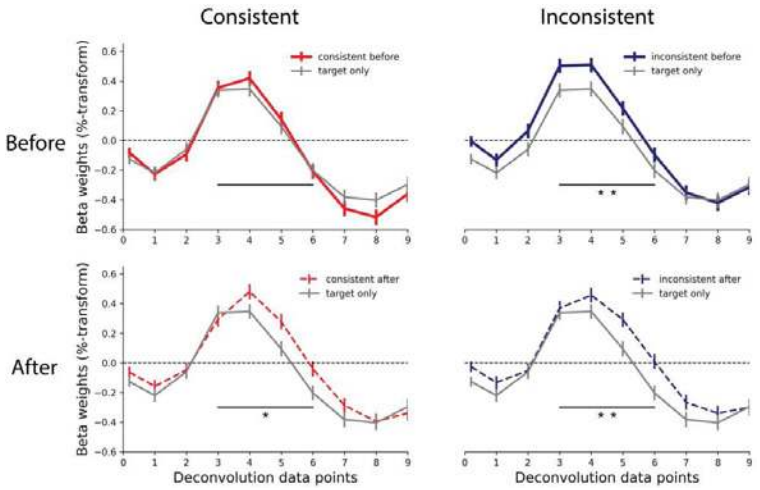

Fig 2. BOLD signal changes: consistent before vs target (upper left), inconsistent before vs target (upper right), consistent after vs target (lower left), inconsistent after vs target (lower right)

Conclusions: We found that top-down contextual modulation from other retinotopic regions contributes to the V1 BOLD signal in response to visual stimulation in a target region. This modulation causes attenuation when consistent and amplification when inconsistent, but only when context presented before the target region. Contextual top-down activity is 'explained-away' if presented with consistent stimulation. Contextual stimulation presented afterwards is unaffected by consistency. There is an interaction between bottom-up and top-down information related to natural scene processing in the early visual cortex, evidenced by BOLD response changes. This interaction depends on the consistency and timing of top-down and bottom-up information.

References

1. Alink, A., Schwiedrzik, C. M., Kohler, A., Singer, W., & Muckli, L. (2010). "Stimulus predictability reduces responses in primary visual cortex." The Journal of Neuroscience, 30(8), 2960-2966. https://doi.org/10.1523/JNEUROSCI.3730-10.2010
2. Muckli, L., De Martino, F., Vizioli, L., Petro, L., Smith, F., Ugurbil, K., Goebel, R., & Yacoub, E. (2015). "Contextual feedback to superficial layers of V1." Current Biology, 25(20), 2690-2695. https://doi.org/10.1016/j.cub.2015.08.057
3. Morgan, Andrew T., Lucy S. Petro, and Lars Muckli. 2019. "Scene Representations Conveyed by Cortical Feedback to Early Visual Cortex Can Be Described by Line Drawings." The Journal of Neuroscience: The Official Journal of the Society for Neuroscience 39 (47): 9410–23.
4. Muckli*, Lars, Lucy S. Petro*, Clement Abbatecola, Ahsan Adeel, Johanna Bergmann, Nicolas Deperrois, Alain Destexhe, et al. 2023. "The Cortical Microcircuitry of Predictions and Context – a Multi-Scale Perspective." Zenodo. https://doi.org/10.5281/ZENODO.8380093.

Poster No 2548

SSVEP Evidence: the Integration of Facing Dyads May be Explained by Domain General Attentional Cues

Xiao Fu[1], Etienne Roesch[1], Katie Gray[1]

[1]*University of Reading, Reading, Berkshire*

Introduction: Social perception research has tended to investigate the processing of individuals; however, people are often viewed interacting with each other. These social interactions are thought to be detected quickly, and may also recruit holistic processing (Vester et al., 2020), whereby multiple features are integrated into a non-decomposable whole. The current study used steady state visually evoked potentials (SSVEP) to investigate whether facing dyads (interactions viewed from a third-person perspective) are processed holistically, and whether this effect is specific to social interactions, or whether it is also generalised to objects.

Methods: Thirty-two participants were recruited to observe two images that were paired together to make a dyad. The two images were flickered at different rates, one at 5.45 Hz (F1) and the other at 7.5 Hz (F2) whilst participants' brain activity was recorded with EEG. The dyads were presented in different configurations (facing and non-facing), and there were three different image types (bodies, chairs, and lamps). At intermodulation frequencies (nF1 ± mF2), the two images in a dyad appeared on the screen simultaneously. Responses at these frequencies are considered to indicate the existence and degree of neural integration (Gordon et al., 2019). Signals were decomposed using the Fast Fourier Transform algorithm in python, with a frequency resolution of .0143 Hz. Responses were calculated as the power at the frequency of interest divided by the average power of its forty neighbouring frequency bins.

Results: We first tested whether activation at the frequencies of interest was significantly higher than baseline using one-sample t-tests. As expected, we found significant responses at the fundamental frequencies (F1, F2), and up to the third harmonic, showing that we were able to elicit SSVEPs in response to our stimuli. Importantly, we also found significant responses in the facing-body and facing-lamp conditions at an intermodulation frequency (F1+F2), indicating that facing bodies and lamps were integrated into a representation that was different from the sum of their parts. To explore the effect of dyad configuration and image type further, repeated measures ANOVAs were conducted on each frequency of interest separately. Responses at the fundamental frequencies (F1, F2), were significantly different between types of images, but not between their configurations. There was no significant effect of image type nor configuration on the responses at the second order intermodulation frequencies.

Conclusions: The findings indicate that facing body dyads show some evidence of recruiting holistic processing, whereas the same was not found for non-facing body dyads. However, this effect may not be specific to social interactions, as we also found the same effect in facing lamp stimuli. This leads to the possibility that domain general attentional cues might be responsible for the effects.

References
1. Vestner T, Gray KLH, Cook R. Why are social interactions found quickly in visual search tasks? Cognition. (2020). Jul;200:104270. doi: 10.1016/j.cognition.2020.104270. Epub 2020 Mar 26. PMID: 32220782; PMCID: PMC7315127.
2. Gordon, N., Hohwy, J., Davidson, M. J., van Boxtel, J. J. A., & Tsuchiya, N. (2019). From intermodulation components to visual perception and cognition-a review. Neuroimage, 199, 480e494. https://doi.org/10.1016/j.neuroimage.2019.06.008

Poster No 2549

Generating Stimuli for Simultaneously Mapping Retinotopic and Category-Selective Brain Regions

Insub Kim[1], Zhenzhen Weng[2], Kalanit Grill-Spector[1,3]

[1]Psychology, Stanford University, Stanford, CA, [2]Institute for Computational and Mathematical Engineering, Stanford University, Stanford, CA, [3]Wu Tsai Neurosciences Institute, Stanford University, Stanford, CA

Introduction: Mapping of retinotopic and category-selective regions in individual human brains using fMRI has become a routine task across multiple labs. As retinotopic and category-selective regions are selective to different properties of visual stimuli, two distinct experiments are conducted to map these brain regions. For example, traveling-wave stimuli with bars (Dumoulin and Wandell, 2008; Benson et al., 2018; Finzi et al., 2021; Kim et al., 2023) or with wedges and rings (Engel et al., 1997; Benson et al., 2018) are typically used to map population receptive fields (pRFs, Dumoulin and Wandell, 2008), identify visual field maps, and delineate borders of retinotopic visual regions (V1, V2, V3, hV4, VO, LO, TO, V3ab, and IPS). Whereas, functional localizer experiments (Kanwisher et al., 1997; Stigliani et al., 2015) using various categorical images of faces, bodies, scenes, and objects are used to define category-selective regions (mFus-faces, pFus-faces, mOTS-words, pOTS-words, OTS-bodies, CoS-places). Here, we developed a method that generates optimal stimuli for simultaneously mapping retinotopic and category-selective regions in a single fMRI experiment.

Methods: Using a large generative model (stable diffusion, Rombach et al., 2022) trained on large-scale datasets with classifier-free guidance (Nichol et al., 2021), we iteratively generated a sequence of naturalistic stimuli that have visual features from different categories (Fig. 1) while maximizing the ability to estimate pRF parameters. To ensure the successful mapping of category-selective regions, the sequence of generated images followed a block design in which 12 different images of the same category were presented for 12 seconds (1 second / image), and each block was repeated for 4 times in a randomized order. To also guarantee the mapping of retinotopic regions, images within each category block were generated to maximize the estimation of pRF parameters. This was achieved by assessing ability to generate distinct fMRI time courses of 100 simulated pRFs, which tiled a 12° visual field with varying pRF locations, sizes, and temporal parameters (Fig. 2A).

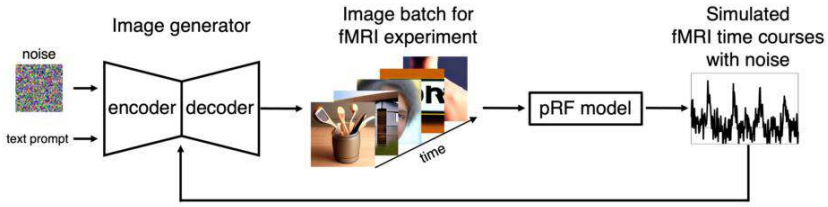

Figure 1. Architecture of fMRI experiment generation framework. A pre-trained latent diffusion model (i.e. Stable Diffusion) was used to synthesize natural images of five different functional categories. Each step of the iterative image denoising process was conditioned to maximally differentiate between simulated fMRI time courses, given different population receptive field parameters.

Results: We generated an optimal set of stimuli that were naturalistic and contained visual features associated with five categories (face, bodies, objects, places, and words). Despite the naturalistic and categorical nature of these generated images, there was variation in local contrast information among them. This variability across images allowed us to test the feasibility of estimating pRF parameters. Indeed, we found that in a simulated 240-second experiment with additive noise in a level similar to typical fMRI experiments, estimated pRF parameters were similar to the ground truth parameters with better estimation of central pRF parameters than pRFs close to the edges of the images (Fig. 2B). The median absolute percentage errors for pRF locations (x and y) and size (σ) were 26.4%, 29.73%, and 19.9%, respectively.

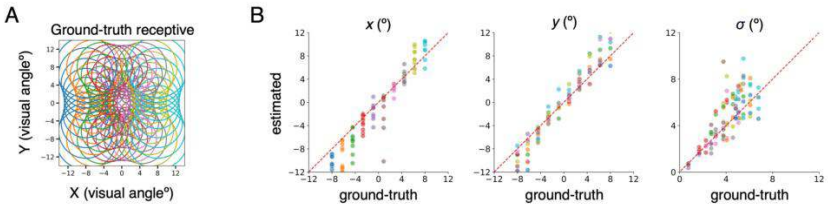

Figure 2. (A) Simulated 100 ground-truth receptive fields (pRFs) that tiled 12 degrees of the visual field. The size of receptive fields increased linearly with eccentricity to resemble properties of pRFs in human visual areas. Each pRF has 3 parameters (x, y, and σ) and is color-coded based on its x-coordinate. (B) Ground-truth parameter vs. model-estimated parameter for 100 simulated pRFs. Each dot indicates a parameter recovery profile for one pRF from a simulated fMRI time course on the synthesized images with additive noise. Same color conventions as (A).

Conclusions: We demonstrate the feasibility of an approach that can systematically generate optimized images for a fMRI experiment from natural images that can be used to define category selectivity and at the same time maximize the estimation of pRF parameters of each voxel. This approach can be used to optimize any fMRI experimental sequence based on any kind of image-computable models. This opens up new possibilities for designing optimal experiments that can: 1) reduce experimental time and resources, especially benefiting populations that are difficult to scan such as infants, children, and patients; 2) specifically target different subsets of brain regions; and 3) validate encoding models of the brain.

References

1. Benson, N. C., Jamison, K. W., Arcaro, M. J., Vu, A. T., Glasser, M. F., Coalson, T. S., ... & Kay, K. (2018). The Human Connectome Project 7 Tesla retinotopy dataset: Description and population receptive field analysis. Journal of vision, 18(13), 23-23.
2. Dumoulin, S. O., & Wandell, B. A. (2008). Population receptive field estimates in human visual cortex. Neuroimage, 39(2), 647-660.
3. Engel, S. A., Glover, G. H., & Wandell, B. A. (1997). Retinotopic organization in human visual cortex and the spatial precision of functional MRI. Cerebral cortex (New York, NY: 1991), 7(2), 181-192.
4. Finzi, D., Gomez, J., Nordt, M., Rezai, A. A., Poltoratski, S., & Grill-Spector, K. (2021). Differential spatial computations in ventral and lateral face-selective regions are scaffolded by structural connections. Nature communications, 12(1), 2278.
5. Kanwisher, N., McDermott, J., & Chun, M. M. (1997). The fusiform face area: a module in human extrastriate cortex specialized for face perception. Journal of neuroscience, 17(11), 4302-4311.
6. Kim, I., Kupers, E. R., Lerma-Usabiaga, G., & Grill-Spector, K. (2023). Characterizing spatiotemporal population receptive fields in human visual cortex with fMRI. bioRxiv, 2023-05.
7. Nichol, A., Dhariwal, P., Ramesh, A., Shyam, P., Mishkin, P., McGrew, B., ... & Chen, M. (2021). Glide: Towards photorealistic image generation and editing with text-guided diffusion models. arXiv preprint arXiv:2112.10741.
8. Rombach, R., Blattmann, A., Lorenz, D., Esser, P., & Ommer, B. (2022). High-resolution image synthesis with latent diffusion models. In Proceedings of the IEEE/CVF conference on computer vision and pattern recognition (pp. 10684-10695).
9. Stigliani, A., Weiner, K. S., & Grill-Spector, K. (2015). Temporal processing capacity in high-level visual cortex is domain specific. Journal of Neuroscience, 35(36), 12412-12424.

Poster No 2550

Top-down vs bottom-up origins of sensory uncertainty in early visual cortex

Joshua Corbett[1], Jacob Paul[1], Ruben van Bergen[2], Wouter Schellekens[2], Linzhi Tao[1], Floris de Lange[2], Marta Garrido[3]

[1]University of Melbourne, Melbourne, Australia, [2]Donders Institute for Brain, Cognition and Behaviour, Radboud University, Nijmegen, Netherlands, [3]The University of Melbourne, Melbourne, Australia

Introduction: Humans make better decisions by weighting sensory information according to its uncertainty. Despite behavioural evidence indicating the importance of sensory uncertainty in perception and action, little is known about how this information is encoded in the brain. We considered whether changes in sensory uncertainty are best explained by variability in bottom-up (feedforward) sensory processing (i.e., neural noise), or fluctuations in top-down (feedback) signals (i.e., attention), using a novel layer-specific fMRI approach.

Methods: We recorded BOLD activity from superficial, middle, and deep cortical layers of primary visual cortex while participants performed an orientation judgement task. Using this data in conjunction with a model-based decoding algorithm (TAFKAP; Van Bergen & Jehee, 2021), we gathered estimates of orientation and uncertainty for each layer separately, on each experimental trial. Given anatomical knowledge that bottom-up signals target middle layers and top-down signals target both superficial and deep layers (Felleman & Van Essen, 1991), we considered whether the encoding of uncertainty is implemented via feedforward or feedback processes.

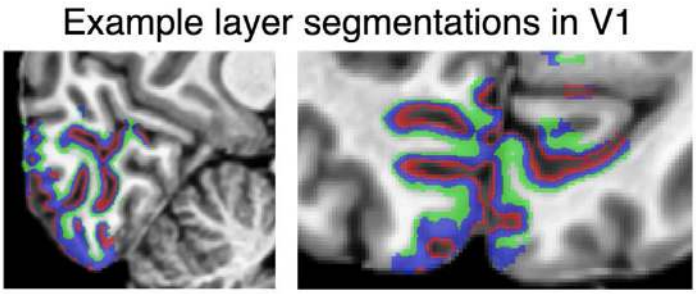

Results: In a sub-sample of 13 participants (out of a full sample of 30 participants that has already been collected), we found above chance orientation decoding from superficial (p=0.005), middle (p=0.002), and deep (p=0.002) layers. However, we did not find a relationship between uncertainty and behavioural variability for any layer in this sub-sample (ps > 0.05).

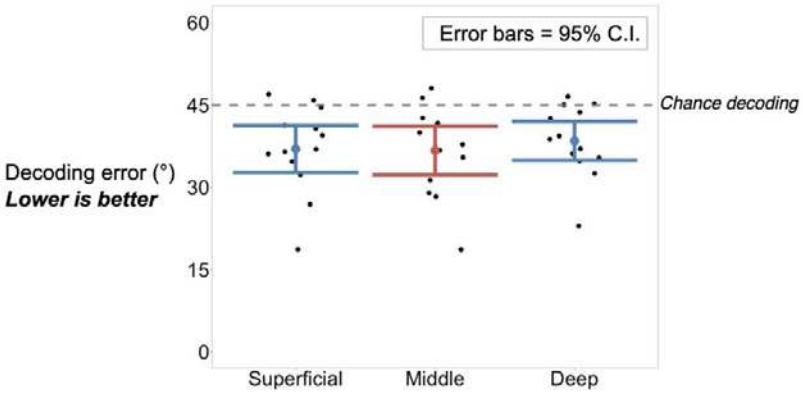

Fig. Layer specific decoding of orientation. Dots represent decoding error for individual participants.

Conclusions: Our findings excitingly demonstrate that orientation information is decodable at the laminar level. While we did not find a relationship between uncertainty and behavioural variability in this sub-sample, the next step will be to look at this relationship in the full (already collected) sample of N=30.

References

1. Felleman, D. J. (1991), 'Distributed hierarchical processing in the primate cerebral cortex', Cerebral cortex
2. Van Bergen, R. S. (2021), 'TAFKAP: An improved method for probabilistic decoding of cortical activity', bioRxiv

Poster No 2551

Functional connectivity of illusory surface representation in V1 with the default mode network

Ana Arsenovic[1,2], Natalia Zaretskaya[1,2]

[1]University of Graz, Graz, Austria, [2]BioTechMed-Graz, Graz, Austria

Introduction: Illusory surface is represented in a topographic manner in the brain, with distinct patterns of surface enhancement and suppression of the surrounding regions across multiple early and higher-level visual topographic areas (Arsenovic et al., 2022; Kok & de Lange, 2014). Here we tested if the topographic representations of the illusory surface in the primary visual cortex (V1) are functionally connected to other, possibly also topographic areas in the brain.

Methods: We present results from an fMRI study including 29 healthy participants. We measured BOLD responses while participants observed either illusory Kanizsa figures (diamond, left triangle or right triangle conditions) or inverted pac-man inducers (no illusion condition). Participants performed an unrelated detection task at the center of the visual field to ensure fixation. During the same session, we also acquired a functional localizer for each participant by presenting a flickering checkerboard at either surface, inducer, or background location of the illusory figure. We performed a seed-based functional connectivity (SBC) analysis, using the illusory surface and background representations in V1 as seeds. Changes in connectivity related to illusory surface presence were calculated as differences in functional connectivity between the illusory diamond condition and the no illusion condition, while accounting for the stimulus-evoked activity using a finite impulse response GLM analysis.

Results: We observed a significant functional connectivity reduction of both the left and the right V1 seeds representing illusory surface with the lateral parietal default mode network (DMN LP) region of the right hemisphere during illusory shape presence. For the right V1 seed (representing illusory surface in the left hemifield), 191 voxels (90%) of the negative cluster (212 voxels, pFDR = 0.001) with a peak at MNI [+42 -64 +28] overlapped with the DMN LP in the right hemisphere (Figure 1A). For the left V1 seed (representing illusory surface in the right hemifield), 118 voxels (91%) of the negative cluster (129 voxels, pFDR = 0.023) with a peak at MNI [+44 -64 +30], overlapped the same DMN LP in the right hemisphere (Figure 1B). More specifically, the correlation between these two areas changed from being positive or zero in the inverted condition to being below zero in the illusory diamond condition (Figure 1, bar graphs). During illusory surface perception, activity in the surface representation of V1 and the DMN cluster thus fluctuated in opposite directions. We did not find significant changes in functional connectivity of the background subregion seed in V1 in either hemisphere.

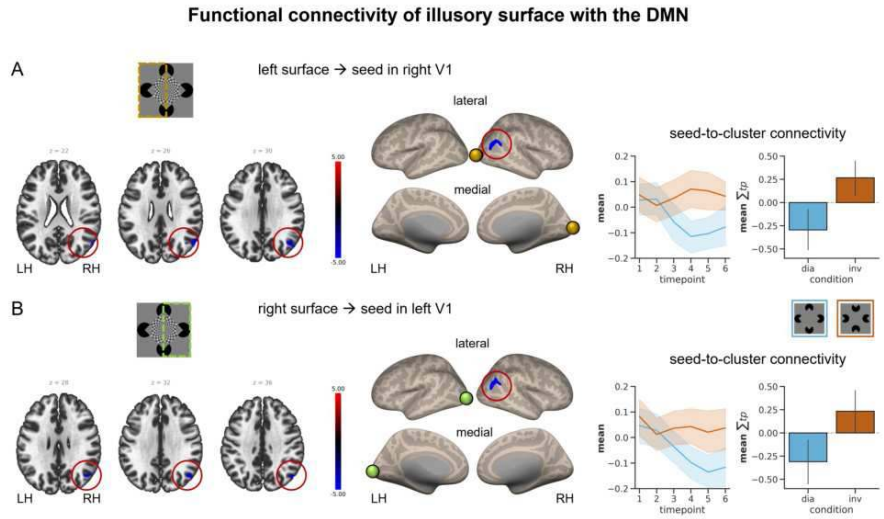

Figure 1. Results of the seed-based functional connectivity analysis for the V1 seed in the **A**: right and **B**: left hemisphere. The multiple comparison-corrected results are presented in MNI space (right) and on an inflated cortical surface (middle). Cluster-forming threshold was set at $p < 0.001$, FDR-corrected cluster-size threshold was set at $p < 0.05$. Bars plots (right) show summed connectivity values over the duration of each condition (6 timepoints, each with a duration of 2 s), averaged over participants. Error bars and shaded lines depict 95% CIs.

Conclusions: DMN can represent negative, but at the same time topographically specific visual responses (Szinte & Knapen, 2020). Our connectivity results point to the possible DMN involvement in illusory surface processing, with potentially overlapping topographic representation of the illusory surface with negative pRFs responding to visual stimulation. The latter hypothesis needs to be tested in future studies. Overall, our results add to the existing evidence for the DMN contribution to representing subjective aspects of perception (Gonzalez-Castillo & Bandettini, 2018; Lyu et al., 2022; Wilding et al., 2023).

References

1. Arsenovic, A. (2022). Dissociation between Attention-Dependent and Spatially Specific Illusory Shape Responses within the Topographic Areas of the Posterior Parietal Cortex. Journal of Neuroscience, 42(43), 8125–8135.
2. Gonzalez-Castillo, J. (2018). Task-based dynamic functional connectivity: Recent findings and open questions. NeuroImage, 180, 526–533.
3. Kok, P. (2014). Shape Perception Simultaneously Up- and Downregulates Neural Activity in the Primary Visual Cortex. Current Biology, 24(13), 1531–1535.
4. Lyu, D. (2022). Intrinsic brain dynamics in the Default Mode Network predict involuntary fluctuations of visual awareness. Nature Communications, 13(1), Article 1.
5. Szinte, M. (2020). Visual Organization of the Default Network. Cerebral Cortex, 30(6), 3518–3527.
6. Wilding, M. (2023). Resting-state neural correlates of visual Gestalt experience. Cerebral Cortex, bhad029.

Poster No 2552

Cortical depth-based variation of population receptive field size in human V1, V2 and V3

Maya Jastrzębowska[1], Nicolás Gravel[1], Polina Iamschchinina[1,2], Daniel Haenelt[3], Nikolaus Weiskopf[3,4], Radoslaw Cichy[1]

[1]Freie Universität Berlin, Berlin, Berlin, [2]Humboldt-Universität zu Berlin, Berlin, Germany, [3]Max Planck Institute for Human Cognitive and Brain Sciences, Leipzig, Germany, [4]Leipzig University, Leipzig, Germany

Introduction: The early visual cortex is governed by the well-established organizing principles of retinotopy and cortical magnification. Receptive field (RF) size varies systematically at the macroscopic scale, increasing with eccentricity from fovea

to periphery and along the visual hierarchy. However, the mesoscopic organization of RFs is not yet well understood. While neurophysiology studies in rodents and non-human primates have shown that RF size varies across cortical laminae, evidence in humans remains sparse (Fracasso et al., 2016). Here, we capitalize on recent advances in laminar fMRI to map RF properties in vivo at the submillimeter scale.

Methods: We used 7 Tesla fMRI (0.8 mm isotropic resolution) and population receptive field (pRF) mapping to measure gradient-echo blood oxygenation level-dependent (BOLD) responses to a drifting bar stimulus in four human participants. We projected the functional data to eight equivolumetric cortical surfaces based on white matter and pial surface reconstructions (Waehnert et al., 2014). For each vertex at each cortical depth, we fit a Difference of Gaussians (DoG) pRF model to the BOLD time series and estimated the location in visual space and pRF size that best explained visual field selectivity. We used the polar angle and eccentricity maps (Fig. 1A) to define regions of interest (ROIs): early visual areas V1, V2 and V3. Given the known variation of pRF size with eccentricity and across visual areas, we constrained our further analysis to an isoeccentricity band centered on 2 degrees. Analysis was limited to those vertices for which the goodness-of-fit of the pRF model exceeded the 75th percentile at the single participant level. For each participant and ROI, we computed the average center pRF and surround RF (sRF) of the DoG model. We characterized the p/sRF profiles across cortical depth by fitting a fourth order polynomial. Finally we computed a suppression index at each cortical depth, which represented the ratio of pRF surround suppression to center excitation (Sceniak et al., 2001).

Results: Addressing the need for validation in laminar fMRI, we first confirm that pRF size varies linearly with eccentricity across ROIs and is smallest in V1, followed by V2 and V3, as expected (Fig. 1B). We replicate previous findings of a U-shaped relation between pRF size and cortical depth in V1 (Fig. 1C; Fracasso et al., 2016), with larger pRF sizes in deep and superficial layers as compared to middle layers. We extend these findings by demonstrating depth-dependent patterns in V2 and V3. Similarly to V1, pRF sizes in V2 are largest in deep layers, followed by superficial and middle layers. Surround RF sizes also vary across cortical depth, though they tend to increase towards the pial surface. Nevertheless, the suppression index remains flat, consistent with previous reports, indicating that the ratio of surround suppression to center excitation does not change across cortical depth.

Conclusions: Our findings demonstrate the reliability of submillimeter fMRI in identifying RF properties at the scale of cortical laminar circuits. PRF size variation across cortical depth is robustly quantifiable in humans in vivo using the latest laminar fMRI processing tools, despite numerous differences in data processing compared to those previously reported (Fracasso et al., 2016). Our findings confirm and extend previous studies and lend support to future studies examining feedforward and feedback mechanisms of spatial vision.

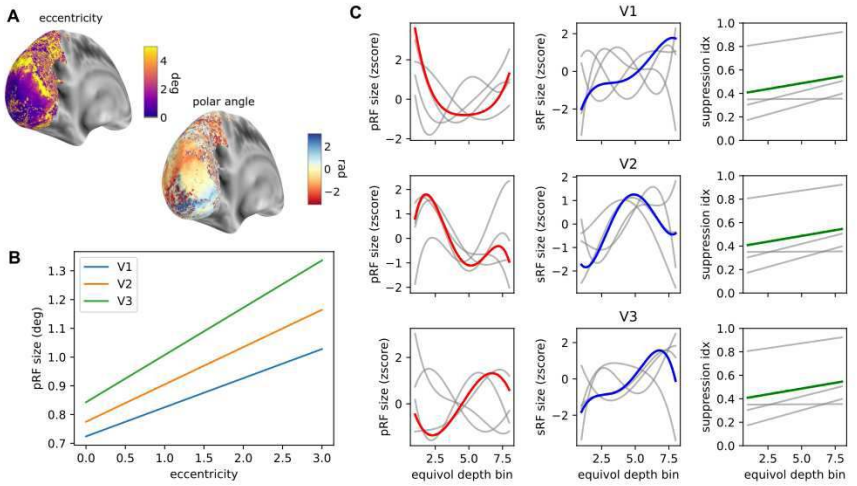

Figure 1. A Eccentricity and polar angle pRF maps for a single participant. The eccentricity map was used to define an isoeccentricity band centered on 2 degrees and extending from an eccentricity of 1 to 3 degrees, while the polar angle map was used to define regions of interest V1, V2 and V3. **B** Population receptive field size scales linearly with eccentricity and increases along the visual hierarchy. Line of best fit for each ROI shown for a single participant for illustration purposes. **C** Columns 1 and 2: center (pRF) and surround (sRF) size depth profiles for individual subjects (in gray) and average (red, blue, respectively). RF profiles across depth were fit with a fourth-order polynomial across 2000 bootstrapped samples. Column 3: suppression index across cortical depths for individual subjects (gray) and average (green). The slope of the suppression index was not significantly different from zero in any of the ROIs. Depth 1 corresponds to white matter surface, while depth 8 corresponds to the pial surface.

References

1. Fracasso, A. (2016), 'Systematic variation of population receptive field properties across cortical depth in human visual cortex', NeuroImage, vol. 139, pp. 427–438.
2. Sceniak, M.P. (2001), 'Visual spatial characterization of macaque V1 neurons', Journal of Neurophysiology, vol. 85, no. 5, pp. 1873–1887.
3. Waehnert, M.D. (2014), 'Anatomically motivated modeling of cortical laminae', NeuroImage, vol. 93, no. 2, pp. 210–220.

Poster No 2553

Activation and deactivation map during smooth and saccadic tracking in humans

Tetsuya Yamamoto[1,2], Kenichiro Miura[3], Keiji Matsuda[4], Junya Matsumoto[3], Ryota Hashimoto[3], Seiji Ono[5], Masaki Fukunaga[1,2], Norihiro Sadato[1,2,6]

[1]National Institute for Physiological Sciences, Okazaki, Japan, [2]The Graduate University for Advanced Studies (SOKENDAI), Hayama, Japan, [3]National Center of Neurology and Psychiatry, Kodaira, Japan, [4]National Institute of Advanced Industrial Science and Technology, Tsukuba, Japan, [5]University of Tsukuba, Tsukuba, Japan, [6]Ritsumeikan University, Kusatsu, Japan

Introduction: Two eye movement systems, smooth pursuit and saccade, are working together in visual tracking to maintain the fixation on an object moving in our surroundings and recognize its details. Abnormal visual tracking is often accompanied with neurological and psychiatric disorders. Elucidation of the neural mechanism underlying these oculomotor behaviors will give insight into the pathological mechanisms of diseases. The neural networks and their functions underlying smooth pursuit and saccade have been extensively discovered in non-human primates. Findings of brain activities during visual tracking are now being accumulated in humans using fMRI. More recently, the Human Connectome Project (HCP) is undertaking a systematic effort to map macroscopic human brain circuits and their relationship to behavior in a large population of healthy adults (Glasser et al., 2016). A set of the standardized image acquisition protocol (Van Essen et al., 2012) and data processing pipelines (Glasser et al., 2013) has enabled outstanding preprocessing of spatiotemporally high-resolution images. These applications in fMRI studies can thus provide more accurate activation maps during tasks, in turn resulting in novel findings. The present study attempted to elaborate brain activation during visually-guided smooth and saccadic tracking by acquiring whole-brain fMRI data with high spatiotemporal resolution in compliance with the HCP Protocol. Herein, we aimed to determine not only visual-tracking related activation but also deactivation and differences in activation between two different types of tracking, including subcortical regions.

Methods: All MRI data were acquired on a 3-T MRI scanner according to a modified HCP Protocol (fMRI scanning parameters: TR = 0.8 s; 2-mm isotropic resolution; 72 slices; multiband factor = 8). This enabled sophisticated preprocessing including image distortion corrections, noise removal of time series data based on independent component analysis (Griffanti et al., 2014), and cortical surface-based registration using Multimodal Surface Matching (Robinson et al., 2014), and non-parametric group analysis with the HCP Pipelines. 27 healthy normal volunteers participated in the study. They were instructed to look at a black and white random-dot patch presented on the screen. The patch was stationary (fixation block), moved smoothly (smooth tracking block) or moved in a stepwise manner (saccadic tracking block) along with a Lissajous trajectory in a given block (20 s). The 4 pursuit and 4 saccade blocks were randomly inserted after a fixation block during a single run. This run was repeated 4 times.

Results: In the contrast of the smooth tracking and steady fixation, we found significant activation in most of cortical areas reported in previous studies (Krauzlis, 2004; Lancer & Trillenberg, 2008) and also deactivation in several cortical areas (denoted with hot/cold colors in Figure 1, respectively). A similar (de)activation map was obtained for the contrast of the saccadic tracking and steady fixation. The comparison between the two types of tracking revealed smooth tracking predominance in early visual areas, the middle temporal complex, superior parietal lobule and posterior cingulate region, and saccadic tracking predominance in many parietal and frontal regions including the frontal, premotor, and supplementary and cingulate eye fields (FEF, PEF, and SCEF; denoted with hot/cold colors in Figure 2, respectively). In the cerebellum, a significant superiority of Lobule VII or lower was observed for the saccadic tracking. Additionally, a significant correspondence between these tracking-related cortical activation areas and heavily myelinated regions was confirmed.

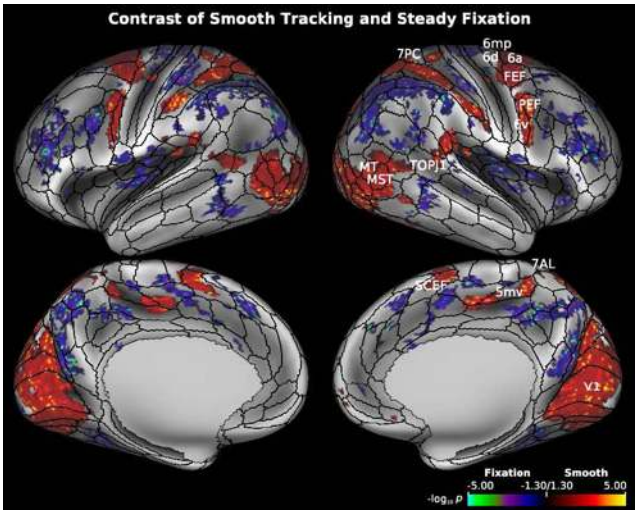

Figure 1: Contrast of smooth tracking and steady fixation.

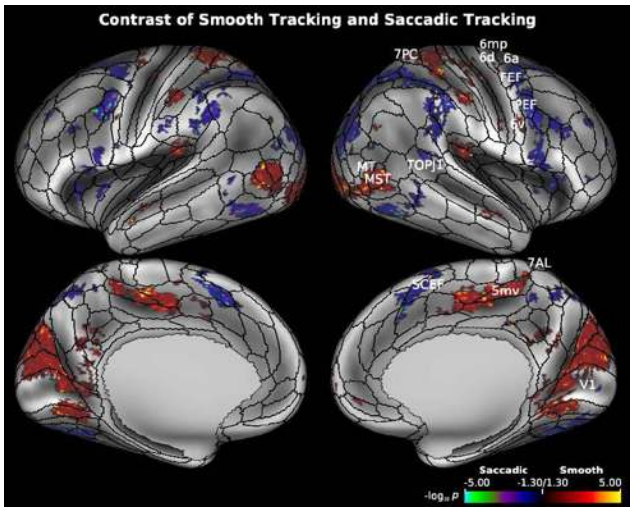

Figure 2: Contrast of smooth tracking and saccadic tracking.

Conclusions: These results strongly support regional contributions of eye movement functions known from previous literatures and extend our knowledges of the whole-brain functional circuitry of the visuo-oculomotor systems with novel regional activities and dependence on different eye movements.

References

1. Glasser, M.F. (2013), 'The minimal preprocessing pipelines for the Human Connectome Project', NeuroImage, vol. 80, pp. 105-124.
2. Glasser, M.F. (2016), 'A multi-modal parcellation of human cerebral cortex', Nature, vol. 536, no. 7615, pp. 171-178.
3. Griffanti, L. (2014), 'ICA-based artefact removal and accelerated fMRI acquisition for improved resting state network imaging', NeuroImage, vol. 95, pp. 232-247.
4. Krauzlis, R.J. (2004), 'Recasting the smooth pursuit eye movement system', Journal of Neurophysiology, vol. 91, no. 2, pp. 591-603.
5. Lencer, R. (2008), 'Neurophysiology and neuroanatomy of smooth pursuit in humans', Brain and Cognition, vol. 68, no. 3, pp. 219-228
6. Robinson E.C. (2014), 'MSM: a new flexible framework for Multimodal Surface Matching', NeuroImage, vol. 100, pp. 414-426.
7. Van Essen, D.C. (2012), 'The Human Connectome Project: a data acquisition perspective', NeuroImage, vol. 62, no. 4, pp. 2222-2231.

Poster No 2554

Feedback and feedforward laminar modulation of human motion perception: a 7T fMRI study

Alessandra Pizzuti[1], Omer Faruk Gulban[1,2], Laurentius (Renzo) Huber[3], Judith Peters[1], Rainer Goebel[1]

[1]Department of Cognitive Neuroscience, Faculty of Psychology and Neuroscience, Maastricht, Netherland, [2]Brain Innovation, Maastricht, Netherlands, [3]Functional MRI Core Facility, National Institute of Mental Health, Bethesda, MD

Introduction: Ultra-high field fMRI (≥7 Tesla) enables sub-millimeter investigation of human conscious perception. Prior studies dissociated perceptual interpretation of visual motion in the motion sensitive area (hMT+)[1]. Yet, how perceived

motion is constructed and modulated in the visual stream is unknown. Our 7T fMRI study explores how motion perception is orchestrated in visual areas (V1, V2, V3 and hMT+) and their laminar connectivity profiles. Using a bistable stimulus (physical and ambiguous motion quartet)[1], we dissociate feedforward from feedback signal integration and their neural correlates. Our results from V1 and hMT+ show differential laminar profiles for the two stimulus conditions.

Methods: The ambiguous quartet induced perception of horizontal or vertical movement through blinking squares at diagonally opposite corners (80s), alternating with a flicker condition (16s). Participants indicated percepts via a MR-compatible button box. In the physical quartet, squares moved along the same horizontal or vertical paths as targeted during the ambiguous motion. Five healthy participants underwent two 2-hour sessions using Siemens MAGNETOM Plus 7T at Scannexus (Maastricht, Netherlands). Per participant, we collected an MP2RAGE[4] (0.7 iso mm), a hMT+ functional localizer, 2 retinotopic mapping runs and 12 runs (12 min each) for the motion quartet stimulus (6 physical) using 2D gradient-echo (GE)-BOLD (0.8 iso mm, TR=2s)[5]. BOLD fMRI data (bilateral coverage) underwent preprocessing: slice time correction[6], motion correction[6], distortion correction[7], high-pass filter (5 cycles)[6] and co-registered to the anatomical images via boundary-based registration[6]. Two subjects were excluded due to motion. Anatomical images were bias field corrected[8], skull-stripped[7], upsampled to 0.35 iso mm. White (WM) and gray matter (GM) segmentation was performed[6] and manually corrected in ITK-SNAP[8]. GM cortical layers were defined by the equi-volume principle[9]. WM surfaces were reconstructed[6] and used to define the regions of interest (ROI). V1, V2, V3 ROIs were delineated using polar angle and eccentricity maps[10]. hMT+ ROI was defined using a separate visual motion localizer. A multi-run general linear model[6] characterized functional responses to physical and ambiguous conditions. Horizontal and vertical clusters (top 10% t-values, from the contrast: horizontal > vertical) in V1 and hMT+ were propagated to cover the whole cortical depth[9] and visualized on flattened GM[9]. Only voxels maintaining preference (horizontal or vertical) between two conditions (congruent voxels) were considered for laminar analysis (t-maps are upsampled to 0.35 iso mm).

Results: Although our ambiguous stimulus elicits a robust motion percept, fMRI responses are consistently lower compared to the physical condition, suggesting reduced brain response without sensory input. In the physical condition, V1 shows a stronger response than hMT+ (Fig.1 B, F), aligning with its expected retinotopic organization. Conversely, fMRI modulation is similar across ROIs in the ambiguous condition (Fig.1-C, G). hMT+ exhibits a higher percentage of congruent voxels between conditions (64%) than V1 (46%) on average. Cortical depth analysis reveals a consistent V1 middle layer peak in the physical condition, hinting at deep layer modulation in the ambiguous condition (Fig.1-C,D and Fig2-A). Laminar profiles in hMT+ lack a clear pattern across participants (Fig.2), we observe a demodulation of the middle layer in only one participant (Fig.1-L).

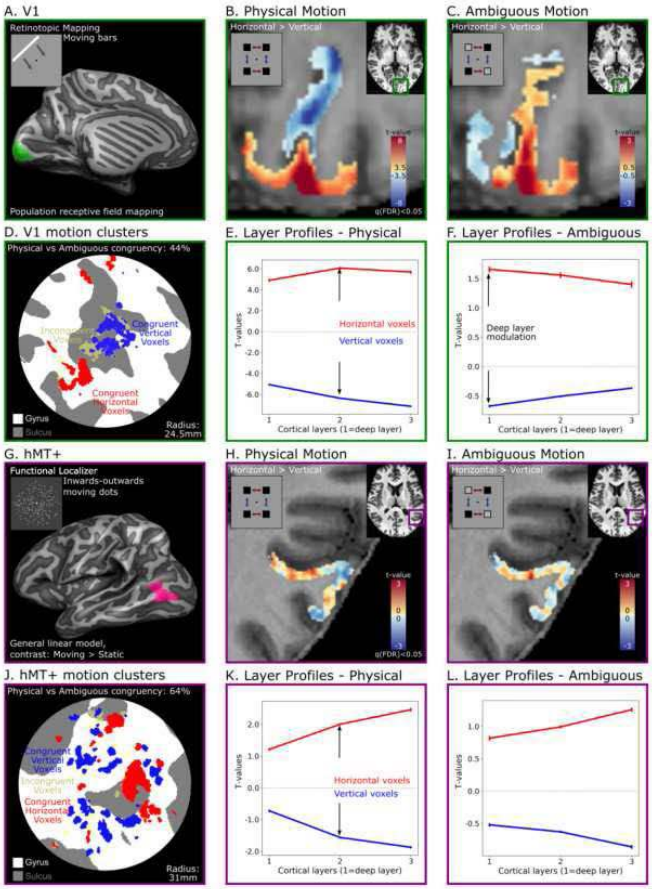

Figure 1: Overview of the main analysis steps to compute layer profiles in V1 and hMT+ (sub-01, left hemisphere). Delineation of V1 **(A)** and hMT+ **(G)** on the inflated white matter surface. V1 **(B,C)** and hMT+ **(K,L)** statistical t-maps for an exemplary slice are shown for both physical and ambiguous conditions. Top-left insert represents the used stimulus. V1 **(D)** and hMT+ **(J)** horizontal and vertical clusters with congruent voxels are shown on the flat cortex. V1 **(E, F)** and hMT+ **(K, L)** layer profiles are computed for each cluster and condition using t-map (contrast: horizontal > vertical). Positive profiles are expected for horizontal clusters, and negative profiles for vertical clusters. Mean and standard error of the mean is plotted for each layer. Arrows indicate where the main laminar modulation is more pronounced.

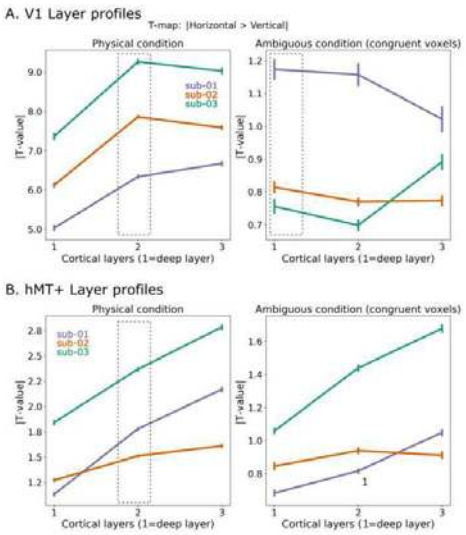

Figure 2: Participant-specific V1 **(A)** and hMT+ **(B)** layer profiles (left hemisphere). For both physical (left) and ambiguous (right) conditions, profiles are based on absolute differences between motion directions for congruent voxels (belonging to both horizontal and vertical clusters). Therefore, the absolute value of the contrast map (horizontal > vertical is considered) to compute means and the standard error of the mean for each cortical layer. Dotted areas highlight where the laminar modulation is more pronounced.

Conclusions: In conclusion, our high-resolution BOLD fMRI study disentangles feedforward and feedback modulation in V1. Preliminary results confirm feedforward influence on the middle layer and feedback on the deep layers during motion perception, aligning with previous V1 studies[3]. Further analysis is crucial to address the draining vein effect, conduct statistical inference on layer profiles, and explore laminar behavior in V2 and V3.

References

1. Schneider, M., Kemper, V. G., Emmerling, T. C., De Martino, F., & Goebel, R. (2019). Columnar clusters in the human motion complex reflect consciously perceived motion axis. Proceedings of the National Academy of Sciences of the United States of America, 116(11), 5096–5101. https://doi.org/10.1073/pnas.1814504116
2. Alessandra Pizzuti, Laurentius (Renzo) Huber, Omer Faruk Gulban, Amaia Benitez-Andonegui, Judith Peters, Rainer Goebel, Imaging the columnar functional organization of human area MT+ to axis-of-motion stimuli using VASO at 7 Tesla, Cerebral Cortex, Volume 33, Issue 13, 1 July 2023, Pages 8693–8711, https://doi.org/10.1093/cercor/bhad151
3. Peter Kok, Lauren J. Bains, Tim van Mourik, David G. Norris, Floris P. de Lange, Selective Activation of the Deep Layers of the Human Primary Visual Cortex by Top-Down Feedback, Current Biology, Volume 26, Issue 3, 2016, Pages 371-376, ISSN 0960-9822, https://doi.org/10.1016/j.cub.2015.12.038.
4. Marques, J. P. et al. (2010) 'MP2RAGE, a self bias-field corrected sequence for improved segmentation and T1-mapping at high field', NeuroImage, 49(2), pp. 1271–1281. doi: 10.1016/j.neuroimage.2009.10.002.
5. Moeller S, et al. (2010) Multiband multislice GE-EPI at 7 tesla, with 16-fold acceleration using partial parallel imaging with application to high spatial and temporal whole-brain FMRI. Magnetic Resonance in Medicine.
6. Goebel, R. (2012) 'BrainVoyager - Past, present, future', NeuroImage, 62(2), pp. 748–756. doi: 10.1016/j.neuroimage.2012.01.083.
7. Smith, S. M. et al. (2004) 'Advances in functional and structural MR image analysis and implementation as FSL', in NeuroImage. doi: 10.1016/j.neuroimage.2004.07.051.
8. Yushkevich, P. A. et al. (2006) 'User-guided 3D active contour segmentation of anatomical structures: Significantly improved efficiency and reliability', NeuroImage, 31(3), pp. 1116–1128. doi: 10.1016/j.neuroimage.2006.01.015.
9. Huber, L. (Renzo) R. et al. (2021) 'LayNii: A software suite for layer-fMRI', NeuroImage, 237(May), p. 118091. doi: 10.1016/j.neuroimage.2021.118091.
10. Senden M, Reithler J, Gijsen S, Goebel R (2014) Evaluating Population Receptive Field Estimation Frameworks in Terms of Robustness and Reproducibility. PLOS ONE 9(12): e114054. https://doi.org/10.1371/journal.pone.0114054

Poster No 2555

Spatially specific reward signals in visual areas during closed-loop naturalistic interaction

Royoung Kim[1,2], Jiwoong Park[1,2,3], Kendrick Kay[4], Won Mok Shim[1,2,3]

[1]Center for Neuroscience Imaging Research, Institute of Basic Science (IBS), Suwon, Korea, Republic of, [2]Dept. of Intelligent Precision Healthcare Convergence, Sungkyunkwan University (SKKU), Suwon, Korea, Republic of, [3]Dept. of Biomedical Engineering, Sungkyunkwan University (SKKU), Suwon, Korea, Republic of, [4]Center for Magnetic Resonance Research, Department of Radiology, University of Minnesota, Minneapolis, MN

Introduction: Our visual system actively gathers information from the environment to facilitate actions aligned with behavioral goals, and reward information plays a significant role in connecting sensory inputs with optimal actions. While previous animal studies have demonstrated that visually responsive brain regions, ranging from the primary visual cortex (V1)[1,2] to the frontal eye field (FEF)[3], show sensitivity to reward values within their receptive fields[4,5], the mechanism through which potential rewards modulate visual representations during goal-directed actions in dynamic naturalistic settings remains poorly understood, particularly in humans. To address this gap, we introduced an innovative Minecraft-based 3D interactive task, where participants strategically plan to achieve goals while navigating a virtual world. We hypothesized that rewards would elicit spatially specific responses, prioritizing the processing of important stimuli and supporting efficient visually guided actions towards them.

Methods: We collected data from shepherding task and population receptive field (pRF) experiments (N=7) as part of the 7T Naturalistic Perception, Action, and Cognition (NatPAC) dataset. In the shepherding task, participants continuously formulated plans and made actions within a Minecraft-based 3D interactive environment to herd as many sheep (i.e. potential rewards) as possible to a specified location while avoiding puddles and a fox (Fig 1A). This naturalistic task promotes deep engagement-a characteristic not typically associated with conventional laboratory tasks. We constructed a voxel-wise pRF model[6,7] from the pRF experiment data (Fig 1B) to estimate the pRFs for each voxel. Combining these pRFs with high-precision gaze estimates obtained through a novel head motion-corrected eye-tracking analysis method, we generated predicted BOLD signals based on gaze-centered visual inputs (Fig 1C, D). Subtracting these predicted signals from the actual BOLD signals allowed us to remove the effects of retinotopic visual stimulation (Fig 1D). We then modeled the residuals with regressors related to rewards. To examine the spatial specificity of rewards, we segmented the visual field into eight radial bins and explained their variance with the reward-related regressors (Fig 2A).

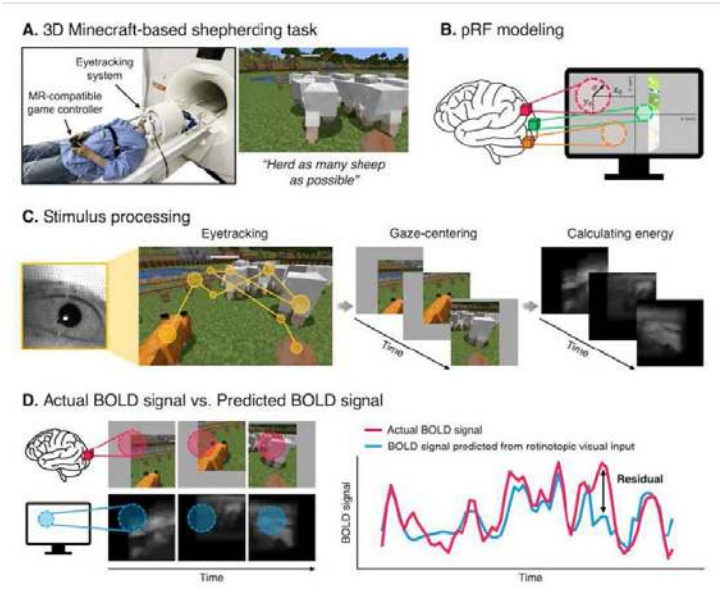

Figure 1. Task and analysis procedure. (A) The scanning setup featuring an eye-tracking system and an MR-compatible game controller, along with a screenshot of the shepherding task. (B) A schematic illustration of the pRF modeling. (C) Stimulus processing involved converting stimuli to gaze-centered input based on high-precision gaze estimates. Subsequently, we calculated stimulus energy by determining temporal and spatial standard deviation within predefined patches of the stimuli. (D) The predicted BOLD signal, generated from the retinotopic stimuli processed as in (C) using the model pRF at each voxel, was subtracted from the actual BOLD signals. This subtraction resulted in residuals indicating the portions of BOLD signals originating from sources other than retinotopic visual stimulation.

Results: Figs 2B and 2C show the spatial specificity of the coefficients for reward loss in V1, V2, V3, and the intraparietal sulcus (IPS) and FEF. Significant spatial specificity for reward loss was observed in V1 (p = .029), V3 (p = .037), IPS (p = .007), and FEF (p = .009). These results indicated that reward loss exhibits distinct spatial tuning in the visual field, with the actual BOLD signal being larger than the predicted BOLD signal based solely on retinotopic visual input. Notably, this effect was not evident for other attention-grabbing events, indicating the spatially specific effects were not due to attention in general but were specific to the anticipation of reward. In addition, our correlation analysis revealed that a higher level of reward-based spatial specificity was associated with more successful loss-avoidant behaviors in V1 (r = 0.70, p = .08), V2 (r = 0.71, p = .07), and V3 (r = 0.60, p = .15) (Fig 2D). This suggests that the integration of reward information into visual representations may facilitate optimal behaviors that effectively maximize rewards.

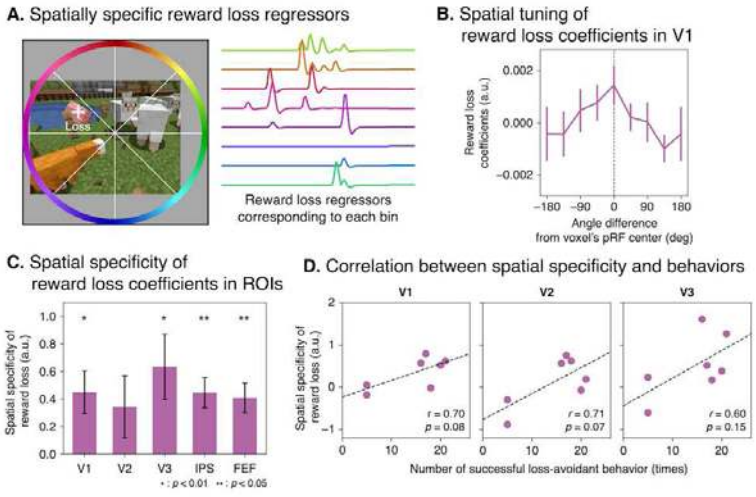

Figure 2. Spatial specificity of reward loss. (A) The visual field was divided into eight radial bins and regressors were created for each bin, each containing the timing information for reward gain (i.e. sheep entering the goal location) or loss (i.e. sheep falling into the puddles or being hunted by the fox). (B) Spatial tuning of reward loss coefficients in V1. Coefficients for reward loss were circularly shifted along the x-axis, aligning the coefficient from the bin where each voxel's pRF center belongs to the center of the x-axis. These aligned coefficients were then averaged to yield a single tuning of coefficients, indicating spatial specificity. Error bars denote ± standard error of mean across participants. (C) Spatial specificity of reward loss coefficients in ROIs. The spatial specificity was calculated by projecting coefficients at each degree onto a vector centered on zero and then calculating the mean of the projected vectors (V1: the primary visual cortex; V2 and V3: the extrastriate cortex; IPS: intraparietal sulcus; FEF: frontal eye field). (D) Correlation between spatial specificity and successful loss-avoidant behavior in V1, V2, and V3.

Conclusions: Using an immersive naturalistic task and high-precision eye-tracking data, we discovered reward-specific spatial responses within both visual and frontoparietal regions. This suggests that visual representations encoded in early visual areas and higher-order frontoparietal regions may effectively integrate cognitive information, such as the reward values associated with stimuli. This study illustrates the interplay of perception, action, and cognition as an integrative process unfolding in naturalistic settings, which is rarely studied in conventional laboratory paradigms.

References

1. Stănişor, L., Togt, C. van der, Pennartz, C. M. A., & Roelfsema, P. R. (2013). A unified selection signal for attention and reward in primary visual cortex. Proceedings of the National Academy of Sciences, 110(22), 9136–9141.
2. Henschke, J. U., Dylda, E., Katsanevaki, D., Dupuy, N., Currie, S. P., Amvrosiadis, T., Pakan, J. M. P., & Rochefort, N. L. (2020). Reward Association Enhances Stimulus-Specific Representations in Primary Visual Cortex. Current Biology, 30(10), 1866-1880.e5.
3. Glaser, J. I., Wood, D. K., Lawlor, P. N., Ramkumar, P., Kording, K. P., & Segraves, M. A. (2016). Role of expected reward in frontal eye field during natural scene search. Journal of Neurophysiology, 116(2), 645–657.
4. Hayhoe, M. M. (2016). Vision and Action. Annual Review of Vision Science, 3(1), 1–25.
5. Frankó, E., Seitz, A. R., & Vogels, R. (2010). Dissociable Neural Effects of Long-term Stimulus–Reward Pairing in Macaque Visual Cortex. Journal of Cognitive Neuroscience, 22(7), 1425–1439.
6. Dumoulin, S. O., & Wandell, B. A. (2008). Population receptive field estimates in human visual cortex. NeuroImage, 39(2), 647–660.
7. Kay, K. N., Winawer, J., Mezer, A., & Wandell, B. A. (2013). Compressive spatial summation in human visual cortex. Journal of Neurophysiology, 110(2), 481–494.

Poster No 2556

Parametrically regularised population receptive field (pRF) mapping

Michael Woletz[1], David Linhardt[2], Siddharth Mittal[1], Christian Windischberger[3]

[1]Medical University of Vienna, Vienna, Vienna, [2]Medical University of Vienna, Wien, Vienna, [3]Medical University of Vienna, Vienna, Austria

Introduction: Population receptive field (pRF) mapping (Dumoulin, 2008), is a method for mapping the visual cortex in terms of input from the visual field. By sampling the visual field using a stimulus, the BOLD response in the visual cortex can be used to assign each voxel a receptive field, typically modelled as a Gaussian with three parameters (μxx, μyand σ). In a standard analysis, this will be done for each voxel individually. The retinotopic organization of the visual cortex will in this case lead to neighbouring voxels having similar parameters, with gradual changes throughout the visual cortex. This topological organisation is not typically enforced, so large variations between neighbouring voxels may exist due the presence of measurement noise. While the topological organisation might be enforced during the fitting process (Tu, 2021), this enforcement is only possible on surface data and might strongly influence the results. In this work we propose a simpler solution, by adding a regularisation factor to the parameter estimation, penalising differences between the parameters between neighbouring voxels/vertices.

Methods: The proposed model optimises the sum of the explained variances of all voxels/vertices. We added a regularisation component that penalises the squared difference of the pRF parameters of neighbouring voxels/vertices. This regularisation is additionally weighted by the explained variance of each neighbour. In this way, the parameters of a voxel/vertex might be adjusted with respect to its neighbours, especially if the neighbours' pRF models fit the data well. The proposed model was implemented in the Python programming language and applied to the measured data of three subjects (3T, Siemens Prisma Fit) using a moving bar stimulus while acquiring EPI images (1s/38ms TR/TE, 1.5 mm isotropic, multiband 3). Algebraic properties of the model fitting process were used to enable the computation of the error function's gradient and the L-BFGS-B optimiser as implemented in SciPy was used to fit the model with and without regularisation to the data.

Results: Eccentricity and polar angle maps of the three subjects in V1 of the left hemisphere are shown in Figure 1. The regularisation led to smoother maps and fewer outliers compared to the results without regularisation.

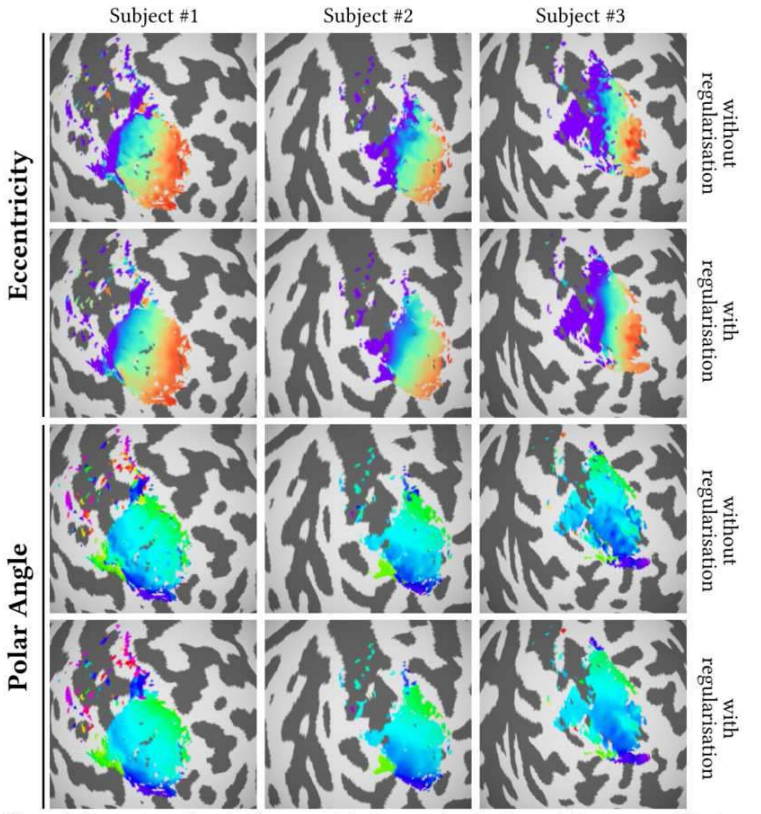

Figure 1. Comparison of results for eccentricity (top rows) and polar angle (bottom rows) for three subjects with and without regularisation between neighbouring vertices in a sweeping bar stimulus in V1. Results from the let hemisphere are shown on a spherically inflated brain. Regularisation adds smoothness to the results and eliminates some spurious outliers in the maps.

Conclusions: In this work, we presented a new method of adding a regularisation to pRF mapping. This method allows to better preserve the topological structure of the visual cortex and is able to reduce otherwise spurious outliers in the map. Further research is necessary to ensure that the regularised maps are consistent across runs and how the regularisation parameters should be best adjusted.

References

1. Dumoulin, S.O. (2008), 'Population receptive field estimates in human visual cortex', Neuroimage, vol. 39(2), pp. 647-660
2. Tu, Y. (2021), 'Topological Receptive Field Model for Human Retinotopic Mapping'. Med Image Comput Comput Assist Interv. pp. 639-649

Poster No 2557

A 7T fMRI correlate of visual perceptual filling-in in human visual cortex

Kenshu Koiso[1,2], Anna Razafindrahaba[1], Mark Roberts[1], Vincent van de Ven[1], Federico De Martino[1], Peter De Weerd[1]

[1]Maastricht University, Maastricht, the Netherlands, [2]The University of Electro-Communications, Tokyo, Japan

Introduction: We have used Troxler fading to probe fMRI correlates of visual surface perception in retinotopic visual cortex. In our version of this paradigm, subjects fixate a point away from a gray square surrounded by dynamic texture (1). After prolonged, steady fixation, the square is perceptually filled-in by the texture (perceptual filling-in) in the absence of physical changes to the stimulus. A neurophysiological study in monkeys (2) reported a signal increase in the representation of the square during perceptual filling-in. Here, we test whether a 7T fMRI correlate of perceptual filling-in is present in human visual cortex, and whether attention modulates its strength. We will also test the laminar distribution of the signal to evaluate the possibility that feedback contributes to the signal.

Methods: Stimulus: A dynamic texture was used consisting of small vertical bars refreshing at 30Hz. A 2.75 deg square texture-free, equiluminant gray square was placed over the texture, 5.5 deg away from the fixation spot. The luminance was set at 35 cd/m2 throughout the display. Six or seven functional runs, four localizer runs, and anatomical image acquisition were conducted in a 2h session per participant. In functional runs, a block design with 30.36 sec stimulus-on and 20.24 sec stimulus-off was used. In the standard condition, Filling-In was Enabled (FIE), whereas in a control condition Filling-In was

Prevented (FIP) by replacing the entire stimulus with an equiluminant full-screen gray for 0.2s every second (see 2). In both FIE and FIP conditions, attention was either directed to the square (by asking participants to press a button whenever they observed filling-in; ATT condition), or was directed away (using a difficult brightness detection task at fixation; NATT condition). Two blocks per condition were included in a run (~7 min). In the localizer run, we retinotopically mapped the location of the patch using a retionotopic phase-encoding design. A 16 Hz flickering checkerboard frame of 0.17 deg moved from the center of the patch to 1.5 deg outside with a total of 17 phase encoded steps at a rate of 1 TR/step. This mapping stimulus was repeated eight times per run (~6 min). Scanning: We used a Siemens 7T MAGNETOM scanner with a 1TX/32RX head coil at Scannexus (Maastricht, NLs). For functional and localizer runs, we collected GE-BOLD data with a resolution of 0.8 mm isotropic, 66 slices, and a TR of 2.53 sec. For anatomical imaging, a MP2RAGE protocol with a resolution of 0.7 mm isotropic was used. Participants: Two young healthy females with normal or corrected eye acuity were scanned. Analysis: BrainVoyager 22.4 (Brain Innovation, Maastricht, NLs) was used for fMRI data analysis (3). Standard preprocessing was applied. We identified the patch cortical location using standard retinotopic mapping. In preliminary analyses, the response to the different experimental conditions within the cortical location of the patch was determined by averaging the BOLD response across repetitions and runs.

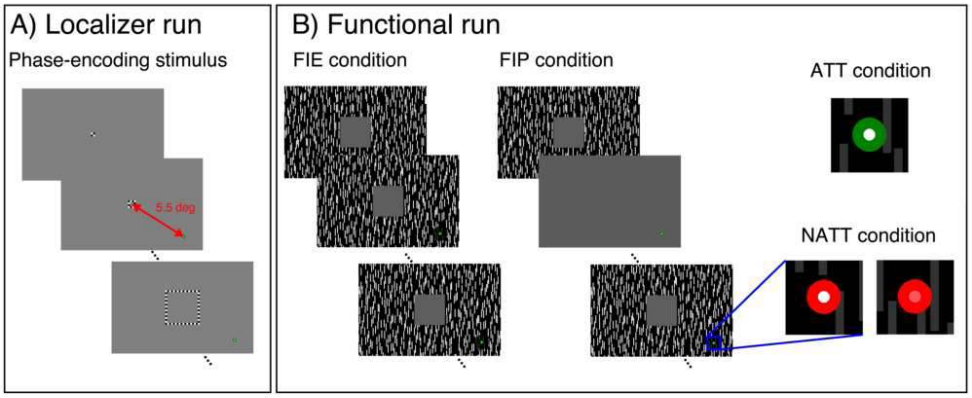

Figure 1

(A) Stimulus in localizer run. A phase-encoding flickering checkerboard at 16 Hz (expanding from small to large) was used. We divided the square patch into eight to determine one step size of the square ring (width = 2.75 deg / 8 / 2 = 0.172 deg) and extended nine steps (1.5 deg) beyond the edge of the patch to regress out influences from voxels surrounding the patch.
(B) Stimuli in functional run. We used a 2x2 experimental design. Using one factor, we aimed to enable filling-in (FIE) or prevent it (FIP). Using the second factor, we directed attention to the square (ATT) or away from it using a dimming task (NATT). The dimming task required participants to press a button when they perceived that the opacity of the white part of the fixation spot changed. The opacity change duration was 0.5 sec, the response window was 1 sec, and the interval among subsequent opacity changes was randomly 2, 2.5, or 3 sec. A 1up 2down staircase procedure was used to keep the difficulty of the attention task constant over time and between participants. The surround of the fixation spot cued participants which task to perform: green for ATT and red for NATT.

Results: We successfully mapped the cortical location of the patch in both V1 and V2 in the two participants (Fig. 2A). Within the cortical location of the patch, the FIE-ATT condition showed a unique signal change compared to all other conditions (Fig. 2B). The signal increase during the block was in agreement with previous behavioral (1) and neurophysiological (2) findings.

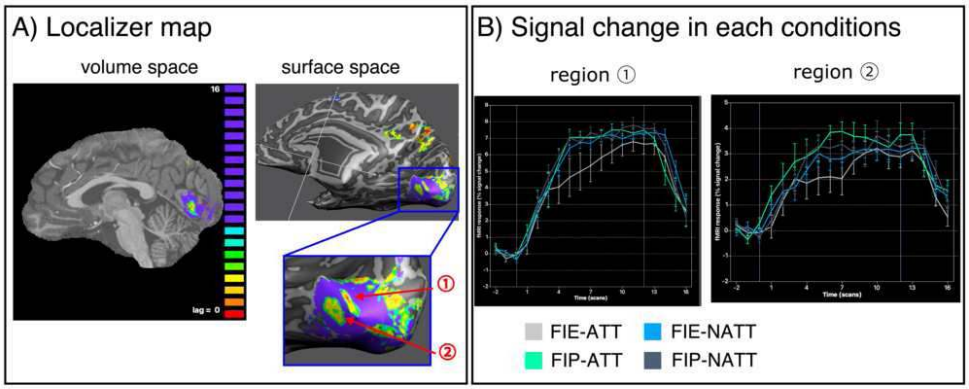

Figure 2

(C) Localizer map in volume space and surface space. Lag 0 represents the step at the square' s center, and 16 does the step farthest beyond the square' s boundary. Activity estimated to belong to the patch is rendered in non-purple colors, activity estimated coming from beyond the patch is color-coded in purple.
(D) GLM event-related signal change in each condition. Percent signal change (Y-axis) is plotted as a function of time (unit of TR = 2.53 sec). The two vertical lines represent the start and end timing of the filling-in block.

Conclusions: Our preliminary analysis demonstrates a correlate of perceptual filling-in using 7T fMRI at sub-millimiter resolution. These preliminary results seem to indicate that the expected response is only present when attention is directed to the patch. Future analyses will investigate the effect of filling-in and its interaction with attention at the laminar level.

References
1. De Weerd P, Desimone R, Ungerleider LG (1998), 'Perceptual filling-in: a parametric study', Vision Research 38 p2721-2734.
2. De Weerd P, Gattass R, Desimone R, Ungerleider LG (1995), 'Responses of cells in monkey visual cortex during perceptual filling-in of an artificial scotoma', Nature vol 377 p731-734.
3. Goebel R, Esposito F, Formisano E (2006), 'Analysis of FIAC data with BrainVoyager QX: From single subject to cortically aligned group GLM analysis and selforganizing group ICA', Human Brain Mapping.

Poster No 2558

Intrinsic Arousal Dynamics Alternately Support Sensory Encoding and Hippocampal Ripples

Yifan Yang[1], David Leopold[2], Jeff Duyn[3], Grayson Sipe[4], Xiao Liu[4]

[1]The Pennsylvania State University, State College, PA, [2]National Institute of Mental Health, Bethesda, MD, [3]National Institutes of Health, Bethesda, MD, [4]The Pennsylvania State University, State College, PA

Introduction: The variable nature of the brain's response to identical stimuli has long intrigued researchers. The state of arousal appears to be a critical factor given the enhancement of sensory responses during active behaviors, such as whisking or locomotion[1,2], and through manipulation of the noradrenergic and cholinergic systems[3,4]. However, in absence of overt active behaviors or external arousal modulators, response variability persists, even over time frames of a few seconds[5–7]. The nature and source of this seconds-scale fluctuation in the brain's response remains unclear. Recent studies revealed that ongoing spiking activity during rest is organized as a highly structured cascade dynamic that entrains ~70% of neurons across various regions into a temporal sequence of activations spanning multiple seconds[8]. Importantly, this cascade dynamic is phase coupled to rapid, seconds-scale arousal modulations, which may in turn contribute to the seconds-scale variance of neural responses. By analyzing large-scale neuronal recordings from mice, we investigated whether the cascade dynamic persists during periods of continuous external sensory stimulation and, if so, whether the dynamic affects how the brain processes sensory inputs.

Methods: We analyzed large-scale neuronal recordings in the Allen Visual Coding dataset[9], focusing on spiking activity of ~22,000 neurons recorded from 32 mice (Fig. 1A) across 4 experimental sessions, including three involving natural scene visual stimuli and one spontaneous session (Fig. 1B). We adopted the delay-profile decomposition method[8,10] to detect cascade events and formulate negative- and positive-delay neuron groups. To measure the efficacy of visual sensory processing, we trained and evaluated support vector machine (SVM) decoders to predict the image identity based on the evoked spiking activity (Fig. 2A).

Results: When sorted by their principal delay profile, the spiking activity of the population of recorded neurons showed clear cascade instances during immobile periods of visual stimulation that closely resembled cascades observed during rest (Fig. 1C and 1D). A state index, capturing the temporal population cascade dynamics using relative activation level of the negative- and positive-delay neurons, displayed a bimodal distribution, suggesting the existence of two distinct brain arousal states (Fig. 1E). The two states were associated with distinct pupil sizes (Fig. 1F) and correspond well to distinct phases of the cascades (Fig. 1C). The precision of visual information encoding, which was measured by the decoding accuracy of the trained SVM, showed a striking difference between the stationary high- and low-arousal states (Fig. 2B). In fact, state index and decoding accuracy displayed a strong and highly reproducible linear association (Fig. 2C). These associations appeared to be driven by the cascade dynamic. The decoding accuracy averaged over the cascades demonstrated systematic changes across the cycle and was tightly locked to the modulation of the state index (Fig. 2D). Further, the hippocampal sharp wave ripples (SPW-Rs), recorded simultaneously, were modulated in completely inverse way across the cascade cycle and peaked when sensory encoding was at its minimum (Fig. 2E).

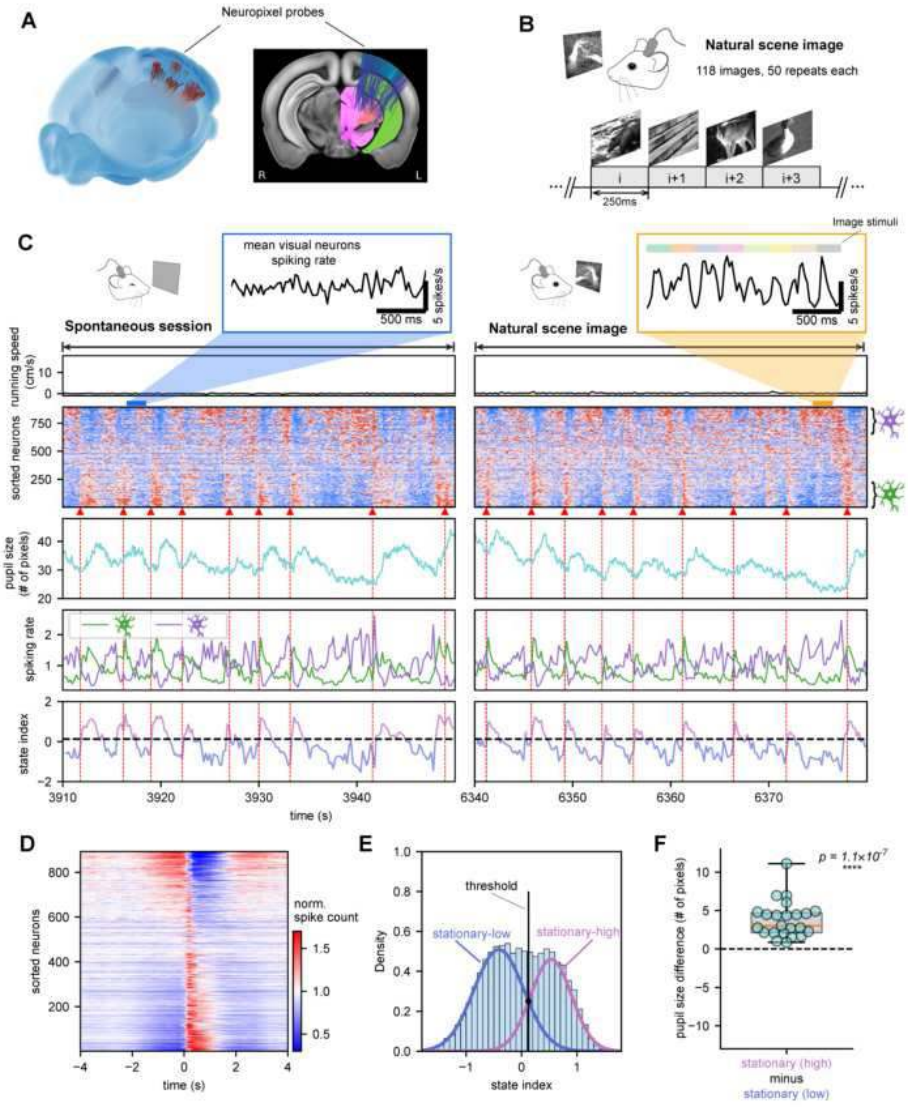

Figure 1. Spiking cascades of arousal relevance persist during continuous visual stimulation. (A) Neuropixel probes location. (B) Illustration of natural scene image session. (C) Example data from 40-s stationary period of spontaneous (Left) and image stimulation sessions (Right). From top to bottom: running speed, sorted spike rate, pupil, positive- (colored in green) and negative-delay neural activity (colored in purple), and state index. The pop-up panels at the top show the mean spiking rate of all visual neurons in example 2-sec time segments. (D) The average pattern of the spiking cascade during visual stimulation. (E) Bimodal distribution of state index. (F) Boxplot of pupil size difference between the two arousal states.

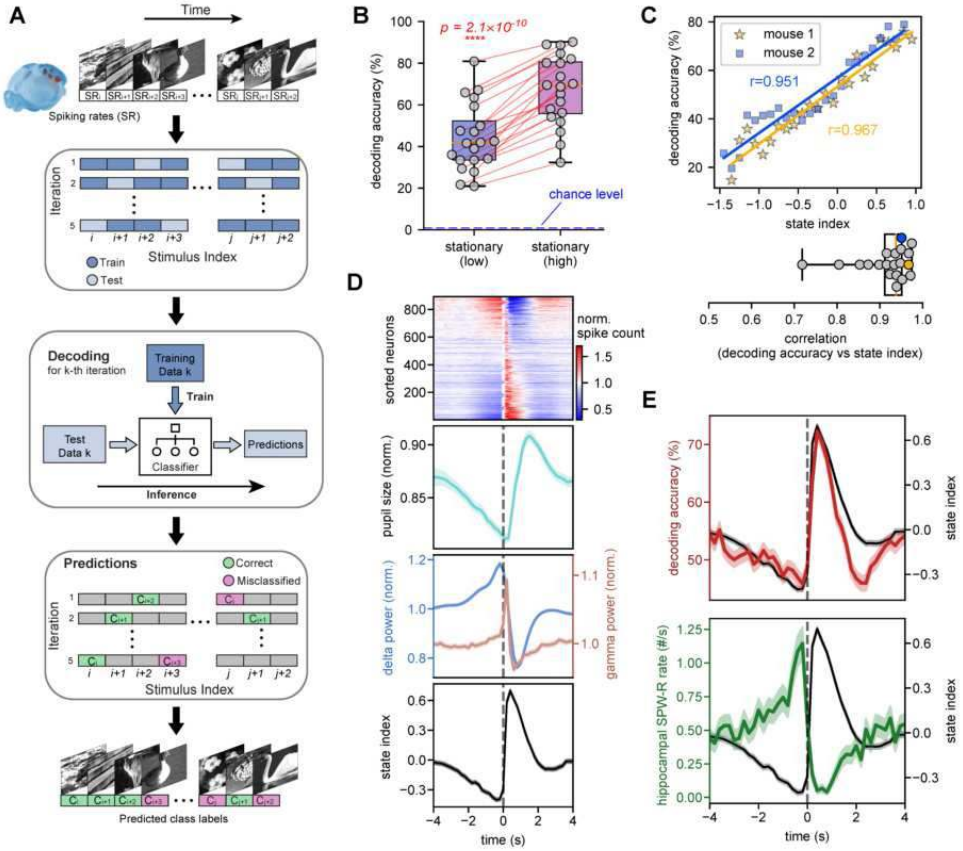

Figure 2. Population encoding of visual stimuli and SPW-Rs are inversely coupled with the cascade dynamics. (A) Pipeline for training a machine learning model to predict visual stimuli based on population spike data. (B) Box plot showing the decoding accuracy summarized for different conditions. (C) Relationship between state index and decoding accuracy is shown for two mice (Top) and summarized for all mice (Bottom). (D) Signals over 8-s cascade cycle, from top to bottom showing cascade pattern, pupil size, LFP band powers and state index. (E) Opposite modulation of decoding accuracy (top) and SPW-Rs rate (bottom) across cascade cycle. All of the time series data is shown as mean ± SEM from all cascade events (N=1401) across all 32 mice.

Conclusions: Here we show that the mouse brain, during stationary periods of passive visual stimulation, undergoes quasi-periodic state fluctuations indicated by stereotyped population dynamics spanning several seconds. Importantly, this cascade dynamic modulates sensory coding and hippocampal ripples in completely opposite ways. Thus, the brain alternates the brain between two functional modes that are optimized for external information processing and internal processes of memory relevance. These findings offer novel insights into the basis of neural variability over the timescale of seconds and the mechanisms by which the brain juggles competing demands on its computational resources.

References

1. Niell, C. M. (2010), 'Modulation of visual responses by behavioral state in mouse visual cortex', Neuron, 65(4), pp.472-479.
2. Saleem, A.B. (2013), 'Integration of visual motion and locomotion in mouse visual cortex', Nature neuroscience, 16(12), pp.1864-1869.
3. Pinto, L. (2013), 'Fast modulation of visual perception by basal forebrain cholinergic neurons', Nature neuroscience, 16(12), pp.1857-1863.
4. Fu, Y. (2014), 'A cortical circuit for gain control by behavioral state', Cell, 156(6), pp.1139-1152.
5. Fox, M.D. (2006), 'Coherent spontaneous activity accounts for trial-to-trial variability in human evoked brain responses', Nature neuroscience, 9(1), pp.23-25.
6. Reimer, J. (2014), 'Pupil fluctuations track fast switching of cortical states during quiet wakefulness', Neuron, 84(2), pp.355-362.
7. McGinley, M.J. (2015), 'Waking state: rapid variations modulate neural and behavioral responses', Neuron, 87(6), pp.1143-1161.
8. Liu, X. (2021), 'Single-neuron firing cascades underlie global spontaneous brain events', Proceedings of the National Academy of Sciences, 118(47), p.e2105395118.
9. Siegle, J.H. (2021), 'Survey of spiking in the mouse visual system reveals functional hierarchy', Nature, 592(7852), pp.86-92.
10. Yang, Y. (2022), 'Self-generated brain-wide spiking cascades govern replay dynamics in the hippocampus', bioRxiv, pp.2022-09.

Poster No 2559

The cortical microcircuitry of contextual processing in mice, monkeys, and humans

Lars Muckli[1], Christiaan Levelt[2], Tyler Morgan[3], Paolo Papale[4], Pieter Roelfsema[4], Koen Seignette[2], Matthew Self[2], Michele Svanera[5], Lucy Petro[6]

[1]University of Glasgow, Glasgow, Scotland, [2]Netherlands Institute for Neuroscience, Amsterdam, Netherlands, [3]National Institute of Mental Health, Bethesda, MD, [4]Netherlands Institute for Neuroscience (KNAW), Amsterdam, Netherlands, [5]University of Glasgow, Glasgow, United Kingdom, [6]School of Psycholog and Neuroscience, University of Glasgow, Glasgow, Scotland

Introduction: The architecture of the cerebral cortex supports the integration of sensory inputs with current demands, expectations and prior knowledge, in distinct processing streams flowing in bottom up and top down directions, embedded in laminar microcircuits (e.g. Larkum, 2013). However, the content of internal representations and the functional roles of top-down processing remain often theoretical or lack mechanistic detail. We present across-species studies using a visual occlusion paradigm designed to isolate the influence of top-down information. This approach masks a portion of an image (the "occluded" region). This region of the visual field in the primary visual cortex of humans, monkeys and mice does not receive bottom-up receptive field stimulation, and neuronal recordings therefore measure functional and structural principles of top-down processing.

Methods: (Humans) We recorded 3T (n=23) and laminar 7T (n = 8) fMRI data in human V1 while participants viewed partially occluded natural scene images. MRI acquisition was as follows: (3T: 18 slices; voxel size: 3 mm, isotropic; 0.3 mm inter-slice gap; TR = 1000 ms; TE = 30 ms; matrix size = 70×64; FOV = 210×192 mm, and 7T: 38 slices; isotropic 0.8 mm3; TE = 17 ms; TR= 2000 ms; FOV=128 x 128 mm2, matrix: 160 x 160). (Mice) We recorded chronic two-photon and wide-field calcium imaging in awake mice in L2/3 and L5. We mapped single cell receptive fields before presenting partially occluded natural scenes that were either novel or had been presented during a training phase. Animals trained to detect fullscreen natural scenes were subsequently presented with fullscreen or occluded natural scenes. (Monkeys) We recorded spiking activity in V1 neurons in two monkeys that were presented with an occluder over the receptive field. Partially occluded scenes were presented for 700ms. (Model) We built a generative encoder-decoder architecture to model human fMRI responses measuring cortical feedback processing (Svanera et al., 2021).

Results: In human, monkey and mouse V1, scene identity can be decoded using multivariate pattern analyses of data taken from a region processing only the occluded image patch. Laminar imaging localises this top-down contextual information to superficial layers of V1 (Muckli et al., 2015, Figure 1A). This contextual information in the non-stimulated retinotopic region of V1 correlates with orientation information found in internal model predictions of scenes, sampled in humans as behavioural line drawings of missing scene features (Morgan et al., 2019, Figure 1A). The dynamics of this contextual feedback information, studied using electrophysiology in monkeys, shows that V1 neurons in the occluded region (that don't receive feed-forward information) process scene-specific contextual information less than 20 ms later than neurons whose receptive fields are presented with the scene stimulus. These contextual representations were correlated between humans and monkeys, suggesting cross-species similarity in the content of perceptual internal models supplied by higher visual areas to V1 (Papale at al., 2023, Figure 1B). In mice, distinct populations of L2/3 neurons code for either sensory or feedback information, and contextual responses to occluded scenes are stronger in trained animals, suggesting that these responses can be explained in a predictive processing framework (Figure 1C, Seignette et al., 2023).

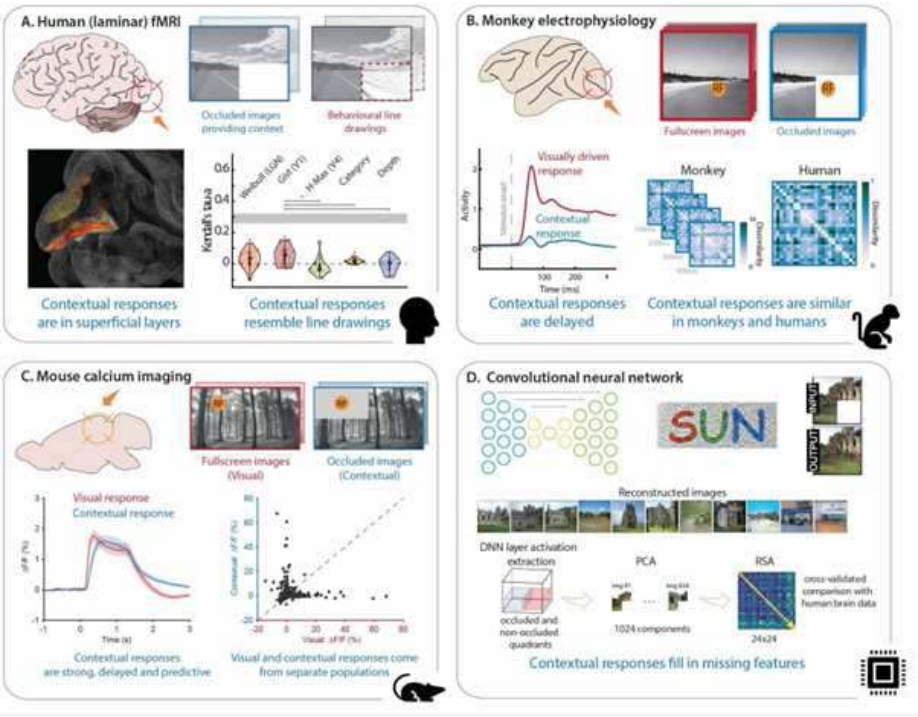

Fig. Multispecies contextual feedback in non-stimulated V1

Conclusions: Assessing cognitive functions and neuronal substrates of top-down microcircuits can be achieved with the occlusion paradigm. We showed evidence in humans that top-down signals include predictive world models that are updated by information from our senses. The occlusion paradigm can also be implemented in a multispecies approach, with surprisingly consistent results in human and nonhuman primates and mice, opening the door for studying the involvement of finer-grained (cellular) neural mechanisms in feedback processing (Muckli et al., 2023).

References

1. Larkum, M. (2013). A cellular mechanism for cortical associations: an organizing principle for the cerebral cortex. Trends in neurosciences, 36(3), 141-151.
2. Muckli, L., et al. (2015). Contextual feedback to superficial layers of V1. Current Biology, 25(20), 2690-2695.
3. Muckli,L et al. (2023). The cortical microcircuitry of predictions and context – a multi-scale perspective (v_0.1). Zenodo. https://doi.org/10.5281/zenodo.8380094
4. Papale, P., et al. (2023). The representation of occluded image regions in area V1 of monkeys and humans. Current Biology.
5. Seignette, K. et al. (2023). Layer-specific plasticity of feedforward and contextual neuronal population in mouse visual cortex. Society for Neuroscience 25.08.

Poster No 2560

The center-periphery bias in high level visual cortex follows a nonlinear topography

Edan Daniel-Hertz[1], Jewelia Yao[1], Sidney Gregorek[1], Patricia Hoyos[1], Anna Lyn Williams[1], Jesse Gomez[1]

[1]Princeton Neuroscience Institute, Princeton, NJ

Introduction: The current theory explaining the organization of category selective regions in the ventral visual stream posits that regions located laterally (i.e. fusiform face areas) or medially (i.e. place area) emerge there as a result of connections to foveal or peripheral retinotopic representations from earlier visual cortex (Hasson et al., 2002). This is also consistent with how faces and scenes are viewed, with foveal and peripheral vision respectively. If indeed the eccentricity selectivity follows a linear gradient from medial (peripheral) to lateral (foveal), a limb-selective region located laterally to the face region should have receptive fields (RFs) sampling foveal visual space. This, however, is inconsistent with how limbs are likely viewed statistically, with peripheral vision. Does this suggest that the single linear foveal-peripheral representation historically ascribed to the ventral stream is an inadequate description of its functional topography?

Methods: To answer this question, 27 participants (17 females, 18.6±0.75y) underwent functional MRI while completing a visual category localizer (Stigliani et al., 2015) and a population RF mapping experiment (Finzi et al., 2021). Data was preprocessed based on the HCP minimal preprocessing pipeline, and analyses were performed in each individual's native brain space.

Category-selective regions of interest (ROIs) were defined for each participant using data from the visual category localizer experiment. A separate group of 25 individuals (13 females, 23±8.6y) completed an eye-tracking experiment during naturalistic movie-watching, to characterize how bodies and limbs are sampled in retinal space.

Results: In the eye-tracking experiment we found that faces were more than three times more likely to be the focus of fixation compared to bodies (T[26]=19.6, P<.001), or to background/objects (T[26]=23.2, P<.001), indicating that limbs are most commonly processed using peripheral vision. Comparing pRF properties across visual categories, we found that pRFs in the previously uncharacterized occipitotemporal sulcus (OTS) limb-selective region were significantly more eccentric than in the neighboring Fusiform face-selective region (Limb: 5.8°, Face: 3.6°, T^{13}=3.36, P=.005). We found no significant difference in the size of the pRFs across those visual regions (Limb: 7.01°, Face: 6.49°, T^{13}=1.01, P=.33). These findings are surprisingly inconsistent with the linear gradient of eccentricity, and suggest that our visual experience drives the biases in spatial computations of high-level vision. Seeking to produce a parsimonious model of visual cortex organization, we quantified the graded changes in pRF eccentricity beyond the ventral surface by parcellating visual cortex into seven anatomically-defined ROIs according to cortical folds, from the medial collateral sulcus (CoS) to the lateral mid-temporal gyrus (MTG). We extracted average pRF properties from each bin in our dataset and the Human Connectome Project's 7T retinotopy dataset (Benson et al., 2018). In both datasets, we observe a non-linear gradient of pRF eccentricity, with pRFs being most foveal near the lateral fusiform gyrus and becoming increasingly peripheral as one travels laterally or medially.

Conclusions: We demonstrate that the spatial computations performed by the previously uncharacterized limb-selective region are inconsistent with predictions from a single linear gradient of eccentricity model. Limb-selective pRFs sample peripheral visual space, consistent with how they are experienced visually. We make the novel observation that there may in fact be two eccentricity gradients, forming a diverging non-linear topography across ventral visual cortex. This primary description supports a novel organization principle in which the ventral and lateral streams of visual processing may not be as separate as once described, but instead linked by a shared, parabolic-like gradient of RF properties.

References

1. Benson, N., Jamison, K., Vu, A., Winawer, J. & Kay, K. The HCP 7T Retinotopy Dataset: A new resource for investigating the organization of human visual cortex. J. Vis. 18, 215–215 (2018).
2. Finzi, D. et al. Differential spatial computations in ventral and lateral face-selective regions are scaffolded by structural connections. Nat. Commun. 12, 2278 (2021).
3. Hasson, U., Levy, I., Behrmann, M., Hendler, T. & Malach, R. Eccentricity bias as an organizing principle for human high-order object areas. Neuron 34, 479–490 (2002).
4. Stigliani, A., Weiner, K. S. & Grill-Spector, K. Temporal Processing Capacity in High-Level Visual Cortex Is Domain Specific. J. Neurosci. 35, 12412–12424 (2015).

Poster No 2561

Selectivity to object features and configuration in the ventral visual stream

Yuxuan Zeng[1], Ren Hentz[1], David Osher[1]

[1]*The Ohio State University, Columbus, OH*

Introduction: Visual processing of most stimuli involves feature-based visual processing (where stimuli are defined by the presence or absence of specific elements such as shape) whereas other stimulus classes like faces involve configural processing (information about relative locations of individual features e.g. interocular distance). Very little is known about the neural mechanisms that underlie feature and configural processing. We designed stimuli that vary based on either featural properties alone, or configural properties alone, and asked participants to learn to categorize them into groups through trial and error (Zeng et al., 2022). After participants learned to accurately categorize these stimuli in the lab, they performed the same task while fMRI data were collected. By contrasting blocks of featural stimuli against configural stimuli, we identified a mid-level visual region that is selectively recruited while participants extract stimulus features.

Methods: Participants were first trained to categorize stimuli into two groups, under two conditions: configural and feature-based, each comprising stimuli defined solely by configural or featural information. Participants had to achieve over 80% accuracy in both conditions in order to continue to the fMRI task. Six participants underwent scanning in a Siemens Prisma 3 Tesla MRI with a 64-channel headcoil, acquiring a high-resolution T1-weighted image (1mm isotropic, TR = 2300 ms, TE = 2.9 ms), and task-based fMRI (2mm isotropic, TR = 2000 ms, TE = 29 ms). We collected a 2-run localizer for high-level visual categories, including faces, bodies, object, scenes, and scrambled objects (Pitcher et al., 2011). We also collected 8 runs of fMRI while participants viewed stimuli and categorized them based on the previously learned categorization rules, in a block design that alternated between featural and configural stimuli. Data were processed with Freesurfer 7.2.0.

Results: We identified a bilateral region in the ventral visual stream that is specifically recruited while participants are extracting stimulus features. This region lies on the ventral surface just beyond areas V4/V8, and extends to the posterior fusiform gyrus. Interestingly, this region is not selective for any high-level visual category. It responds to faces, bodies, and scenes, and strongest to objects and even scrambled objects (object selectivity is typically defined by the contrast of objects > scrambled). In addition, we identified several visual fROIs, and compared configural and featural responses in each fROI. Only the bilateral posterior fusiform sulcus (an object selective region) showed a significant difference between these conditions, preferring featural over configurally processed stimuli.

Conclusions: Our findings reveal a region in the ventral visual stream associated with feature-based processing that does not overlap with other category-specific areas. We propose this could be an intermediary region that extracts featural information before stimulus identity is determined. Future work will focus on its connectivity with the rest of the ventral visual stream in order to investigate how this region interacts with visual processing at early and late stages of the perceptual process.

References

1. Pitcher, D. (2011), 'Differential selectivity for dynamic versus static information in face-selective cortical regions', Neuroimage, vol. 56, no. 4, pp. 2356-2363
2. Zeng, Y. (2023), 'A novel framework to study configural and holistic processing', Journal of Vision, vol. 23, no. 9, pp. 5471-5471

Poster No 2562

Mapping the Development of Spatial Computations from Childhood to Adolescence

Jewelia Yao[1], Justin Choo[1], Dawn Finzi[1], Kalanit Grill-Spector[1]

[1]*Stanford University, Stanford, CA*

Introduction: Reading and face recognition, skills essential for children's academic performance and socioemotional development, depend on spatial computations of receptive fields (RFs) – parts of visual space from which information is processed – throughout the ventral visual stream. These behaviors require the use of central vision, relying on RFs of groups of neurons, or population receptive fields (pRFs), which are centrally located (Levy et al., 2001; Hasson et al., 2002; Malach et al., 2002). Despite their significance, few studies have investigated pRFs – especially beyond early visual areas – in children, let alone adolescents. Given the ongoing development of reading and face recognition throughout adolescence, we employ a novel pRF mapping fMRI experiment (Toonoptopy, Finzi et al., 2021) that better drives high-level visual regions, to examine how spatial computations in the ventral visual stream develop from childhood through adolescence into adulthood.

Methods: 19 children (ages 8-17) and 28 adults (ages 22-32) participated in four runs of Toonotopy featuring sweeping bars (5.7° width, Field-of-View: 40° x 40°) filled with cartoon images presented at 8Hz. Each voxel's pRF was modeled using a 2D Gaussian with a compressive nonlinearity (Kay et al., 2013). Thresholded (>20% variance explained) eccentricity, phase, and size maps were generated, and retinotopic ROIs were hand-drawn based on previous definitions for every individual (Wang et al., 2015). pRF parameters (location, size) were estimated for each voxel. In each visual area, pRF parameters, upper visual field bias, the proportion of pRFs in the upper vs. lower visual field; and eccentricity bias, proportion of pRFs in the central 0-5° vs outer 5-20° were compared across development.

Results: Our approach revealed three main findings. First, 420/444 retinotopic ROIs (V1 – PHC) were identifiable across children and adults for the first time using Toonotopy (Fig 1). Second, linear mixed-effect models revealed little to no development in pRF properties in early visual areas V1 - V3 ($Fs < 4$, $p > .04$). Finally, while early visual areas exhibited minimal development, upstream regions continued developing past childhood. Notably, hV4 underwent the most significant change with pRFs becoming more foveal (Fig 2A) across in the right hemisphere ($F(1,34) = 13.3$, $p < 0.0001$) and upper visual field bias (Fig 2B) increasing in the right hemisphere ($F(1,34) = 4.96$, $p = 0.03$) but decreasing in the left ($F(1,35) = 4.37$, $p = 0.04$). Interestingly, in VO pRF size decreased with age in both hemispheres (Fig 2C; LH: $F(1, 35) = 6.42$, $p = 0.02$; RH: $F(1,33) = 4.76$, $p = 0.04$). Visual field coverage maps also complement these developments, as pRF coverage of the hV4 increases in density in the fovea but decreases in the periphery, and VO coverage spans more of the visual field, from childhood into adulthood.

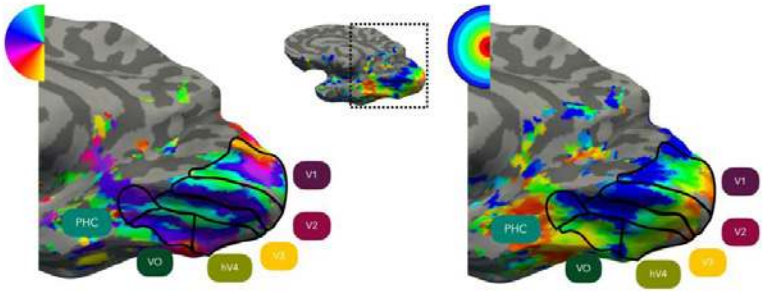

Figure 1. Retinotopic regions defined using toonotopy. An example cortical surface reconstruction in a representative 14 year old child. Example phase angle (left) and eccentricity (right) maps on the inflated right hemisphere. Maps are thresholded at 20% variance explained. Retinotopic regions denoted by solid black lines. Inset: zoomed medial view.

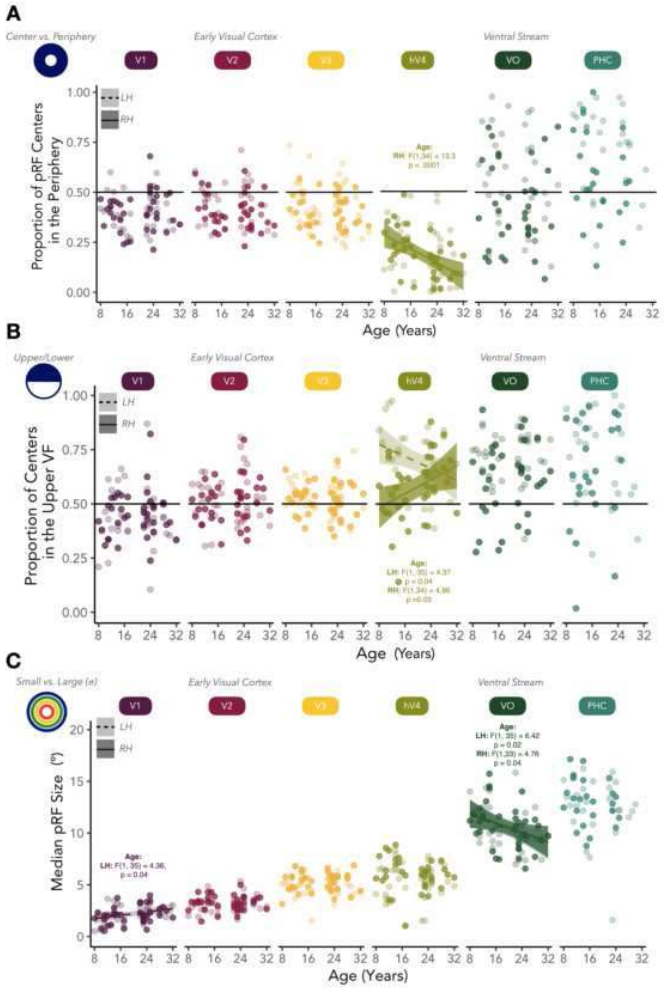

Figure 2. Development of pRF properties across the visual stream. *A:* Proportion of pRF centers in the center (0°-5°) versus periphery (> 5°) across early visual cortex ROIs V1 (purple), V2 (magenta), V3 (yellow) and upstream retinotopic ROIs hV4 (light green), VO (dark green), PHC (turquoise). Each dot is an individual. Lines indicate significant relationships between pRF center proportion and age measured in years. Left hemisphere show in light colors and dotted lines. Division in proportion of pRF centers shown by horizontal black line (0.5). *B:* Same as A but for proportion of pRF centers located in the upper visual field versus lower visual field. *C:* Same as A but for median pRF size (sigma, σ).

Conclusions: Taken together, these findings unveil surprisingly prolonged development through childhood and adolescence of basic spatial computations by population receptive fields in the human ventral visual stream. Importantly, using a novel experimental approach we show differential development across regions and hemispheres whereby intermediate (hV4 and VO) but not early (V1-V3) areas show prolonged development. The fact that basic spatial computations in the visual system continues to develop throughout childhood and adolescence has important ramifications for how the acquisition of centrally-biased visual behaviors crucial for academic and socioemotional growth may affect basic neural computations.

References
1. Finzi, D. (2021), 'Differential spatial computations in ventral and lateral face-selective regions are scaffolded by structural connections,' Nature Communications, 12(1), Article 1. https://doi.org/10.1038/s41467-021-22524-2
2. Hasson, U. (2002), 'Eccentricity bias as an organizing principle for human high-order object areas', Neuron, 34(3), 479-90. doi: 10.1016/s0896-6273(02)00662-1
3. Kay, K. N. (2013), 'Compressive spatial summation in human visual cortex. Journal of Neurophysiology', 110(2), 481–494. https://doi.org/10.1152/jn.00105.2013
4. Levy, I. (2001), 'Center–periphery organization of human object areas', Nature Neuroscience, 4(5), 533–539. https://doi.org/10.1038/87490
5. Malach, R. (2002), 'The topography of high-order human object areas', Trends in Cognitive Sciences, 6(4), 176–184. https://doi.org/10.1016/S1364-6613(02)01870-3
6. Wang, L. (2015). 'Probabilistic Maps of Visual Topography in Human Cortex', Cerebral Cortex, 25(10), 3911–3931. https://doi.org/10.1093/cercor/bhu277

Poster No 2563

Human cortical areas involved in perception of motion-in-depth

Sean Lee[1], Sylvia van Stijn[2], Bo-yong Park[3]

[1]Max Planck Institute for Empirical Aesthetics, Frankfurt, Germany, [2]Ernst Strüngmann Institute for Neuroscience in Cooperation with Max Planck Society, Frankfurt, Germany, [3]Inha University, Incheon, Incheon

Introduction: The middle temporal area (MT/V5) in the primate brain is thought to play a major role in processing of motion. For human motion-in-depth perception, the MT complex (hMT+) and its vicinities have been suggested to be involved (Likova and Tyler, 2007; Rokers et al., 2009). The human MT+ is a cluster of half a dozen subregions including MT. To answer which of these and possibly what other cortical areas are involved in the perception of motion-in-depth we measured the BOLD signal while the participant viewed the 3-D motion stimuli in a series of fMRI experiments.

Methods: To maintain overall appearance of the stimuli constant across conditions we employed a dynamic random-dot stereogram (RDS) to elicit perception of a frontoparallel plane moving in 3D. New sets of random-dots were plotted on eleven disparity-defined layers every 50ms. One of the layers contained white dots and the rest contained black dots. In each frame, the white dots were assigned to a different layer. When successive assignment occurred in a neighboring layer toward one direction, observers perceived the white plane smoothly traversing in depth (motion-in-depth, MID); when the switching occurred in arbitrary layers in succession, observers saw the white plane but perceived no coherent motion (shuffled-depth-plane, SDP. In the control condition the white dots were evenly distributed to all layers, in which the white dots formed no surface but appeared as amorphic cloud of white dots in depth (RDRD). Six adults were scanned in a 3T MRI scanner with an 8-channel RF head coil. The 1-mm isotropic whole-brain anatomical MRI was taken followed by the fMRIs (EPI: TR 2000 ms; TE 30 ms; FA 62, FOV 192 x 192 mm, 32 slices). The participant viewed the stimuli through the MR-compatible goggles and fixated a small red corss to perform a contrast discrimination task every 2 - 9 seconds. There were three contrast pairs in blocked design (12 seconds per block, repeated 8 times): MID-SDP, SDP-RDRD and MID-RDRD. Each contrast was ran 4 times (4mts each). EPI data processing: BrainVoyager QX software including field-distortion correction, slice-scan-time correction, motion correction, high-pass temporal filtering, and we used general linier model convolved with hemodynamic response function and tested in a univariate way. For multiple runs/subjects, GLM multi-study with a fixed effect analysis and z-transformation. The anatomical scan was processed with FreeSurfer and Werkbench to reconstruct the cortical surface and pacellated (Glasser et al., 2017). The brain areas labled according to Glasser et al.

Results: By alternating MID and RDRD conditions in a blocked design, we identified two concurrently activated areas: one in the dorso-occipital area (V3A/B) and the other in the tempero-occipital area (MST) anterior to MT. To determine which of the two areas is more directly involved in the perception of motion in depth, we compared the response pattern (BOLD percent signal change) of the two contrasts, MID-SDP and SDP-RDRD, in blocked designs. In the MID-SDP contrast, MST showed more prominent response compared to that of V3A/V3AB. In the SDP-RDRD contrast, V3A/V3B showed more prominent response than that of MST (Figure 1).

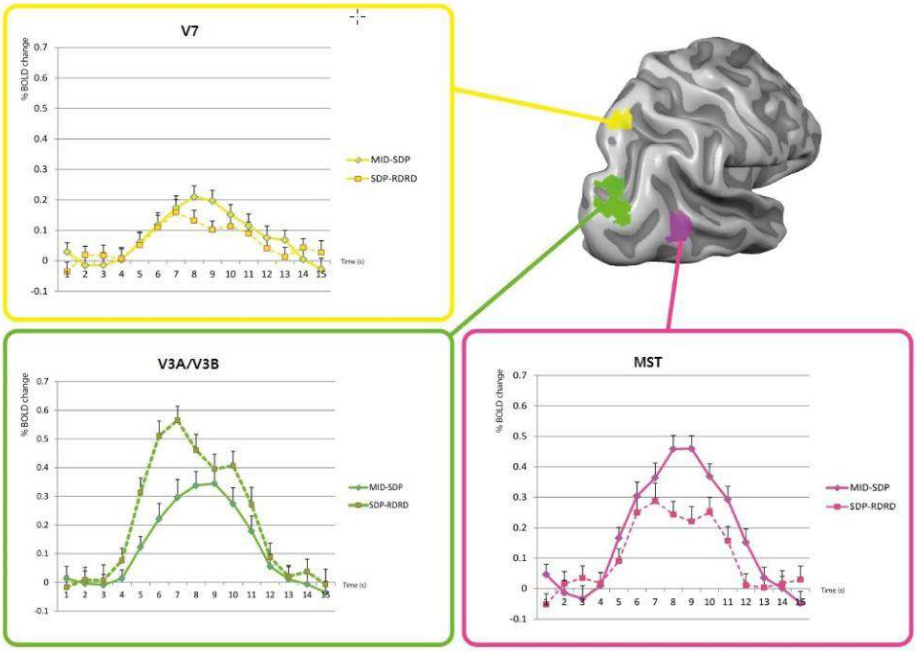

Conclusions: Our RDS stimuli were devised to control a single feature at a time. Between the MID and SDP conditions, disturbing only the time-series of the occurrence of the white-dot surface destroyed the perception of smooth motion in depth. Note that all other features, such as the number of random dots, overall contrast, and overall disparity distribution, remained identical for all stimulus conditions. Therefore, with a single-eye-only view, all three stimulus conditions appeared identical. Because seeing the surface in our RDS is a prerequisite for perceiving motion in depth, we conclude that V3A/B is a preceding area that is involved in segmenting/representing the surface in depth in the scene. On the other hand, MST showed a more direct signal change toward motion in depth.

References

1. Likova, L.T. (2007) 'Stereomotion processing in the human occipital cortex', Neuroimage vo. 38, pp. 293–305.
2. Rokers, B. (2009) 'Disparity- and velocity-based signals for three-dimensional motion perception in human MT+', Nature Neuroscience vol 12, pp.1050–1055.
3. Glasser, M.F. (2017) 'A multi-modal parcellation of human cerebral cortex", Nature, vol. 536, no. 7615, pp. 171-178

Poster No 2564

Brainwide fMRI patterns predict variations in EEG rhythms across sleep and wakefulness

Leandro Jacob[1], Sydney Bailes[1], Stephanie Williams[1], Carsen Stringer[2], Laura Lewis[1]

[1]Massachusetts Institute of Technology, Cambridge, MA, [2]Janelia, Ashburn, VA

Introduction: Arousal-related EEG oscillations are associated with major changes in cognition, but identifying brainwide dynamics underlying them is challenging, as EEG suffers from low spatial resolution. EEG can be simultaneously acquired with fMRI-which has higher spatial resolution and can image deeper brain regions-but analyzing these multimodal data is challenging. Prior work focused on univariate mass correlations to identify individual fMRI regions coupled to EEG oscillations, but this approach cannot detect network-scale patterns. Here, we aimed to identify brainwide fMRI dynamics that underlie variations in neural oscillations. We used machine learning to find fMRI patterns that predict variations in EEG alpha (8-12Hz) and delta (1-4Hz) power during fluctuations in vigilance.

Methods: We acquired simultaneous EEG and fast fMRI data in a 3T scanner (TR=378ms; voxel size=2.5mm isotropic) in subjects who spontaneously fell asleep (n=21 total, n=16 with alpha signals). We trained linear machine learning models to predict single timepoints of EEG power (5s window size) from 60 TRs of fMRI. fMRI data was parcellated in 84 regions—31 bilateral cortical, 7 bilateral subcortical, and 8 non-grey matter regions (white matter and ventricles). Models were iteratively trained on all subjects but one, and performance (correlation between predictions and ground truth) was assessed on held-out subjects. As control, we circularly shifted the fMRI by 2000 TRs in relation to the EEG (breaking the relationship between the modalities) prior to training and validation.

Results: We successfully predicted EEG alpha and delta power from fMRI dynamics, and distinct fMRI regions carried information for distinct EEG bands (Fig 1). Alpha power was only predicted by gray matter regions, while delta was also predicted by white matter and ventricles, likely owing to the known coupling between delta and cerebrospinal fluid flow[1]. Demonstrating that the model can identify fine-grained information, EEG was also differentially predicted by individual bilateral fMRI regions, with alpha significantly predicted by arousal-controlling subcortical regions and V1 (replicating previous literature[2–5]). Delta was only significantly predicted by the putamen in this single-region analysis, suggesting that delta power requires a higher number of regions for successful predictions. We thus investigated the spatial scales of alpha and delta by iteratively dropping low-weights regions (i.e. regions with redundant information) from the models (Fig 2A-B). Performance peaked at a much higher number for delta than for alpha, indicating that fMRI information predictive of delta is distributed widely (primarily through the cortex) while alpha is predicted by a much smaller set of subcortical and cortical regions. A clustering analysis showed that fMRI information predictive of delta is not only diffuse but not separable into distinct networks (Fig 2D). Alpha information, however, was clustered in two networks (Fig 2C): one primarily representing visual cortex and regions associated with higher-order cognition, and another highlighted by key arousal-controlling subcortical regions (Fig 2E-F). The regions in each network share the same predictive information, evidenced by worse within-cluster performance (mean r=-0.0163), while regions in different networks display distinct unique information, evidenced by improved between-cluster performance (mean r=0.0265; p<.001; Fig 2F-G).

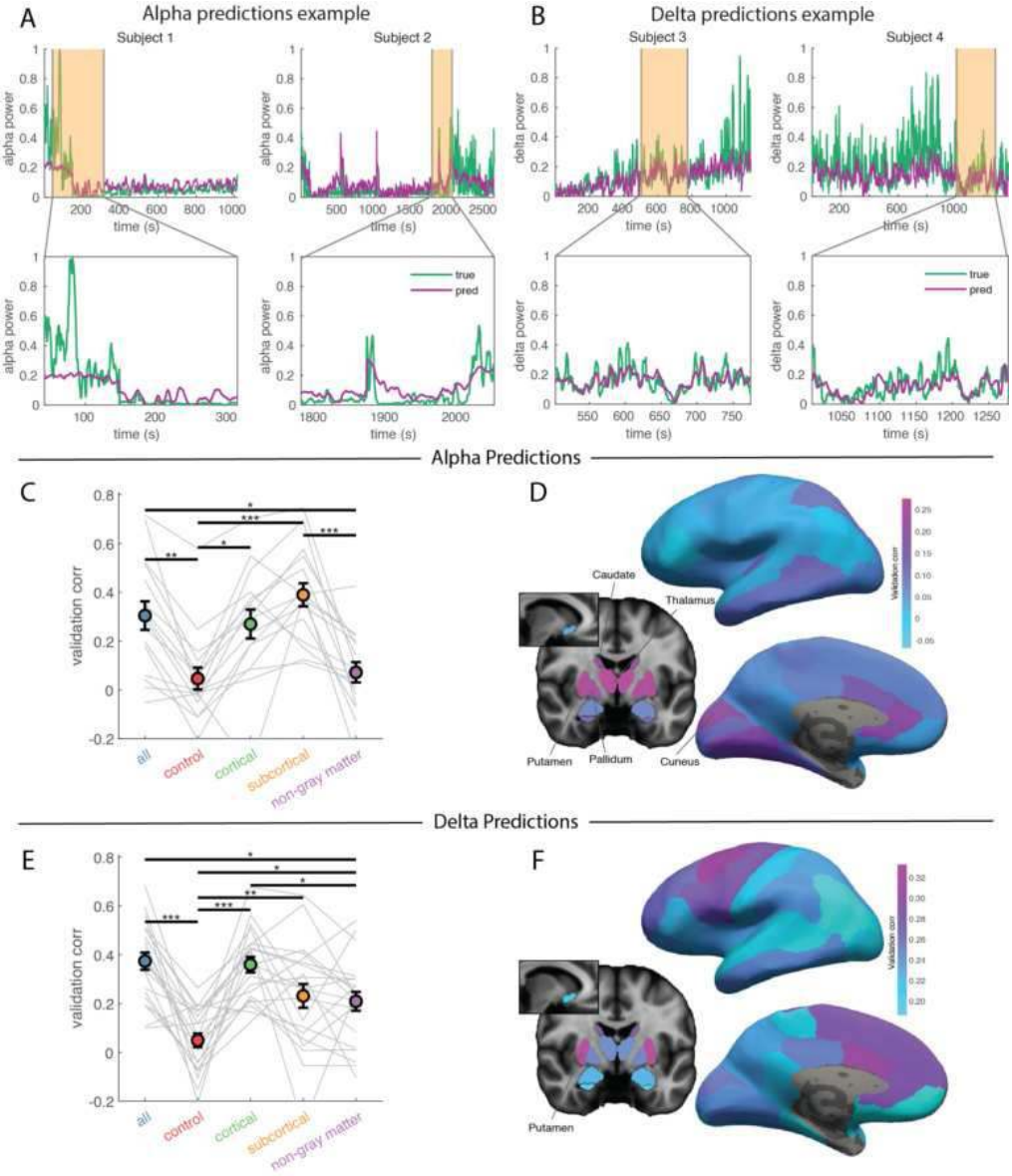

Fig 1: Alpha and delta power were predicted from fMRI with different prediction patterns based on input. **A-B:** representative predictions. **C, E:** validation performance (correlation between predictions on held-out subject and ground truth). See main text for conditions information. Gray lines represent subjects. Pairwise comparisons corrected using Tukey's HSD. * = p < .05, ** = p < .01, *** = p < 0.001. **D, F:** validation performance when model was trained on individual bilateral regions. For delta, given that non-gray matter regions were also predictive, these were included along with each bilateral region, as a way to correct for physiological components and to identify unique neural information. Marked regions were significantly different from control (D, alpha) or from non-gray matter regions by themselves (F, delta).

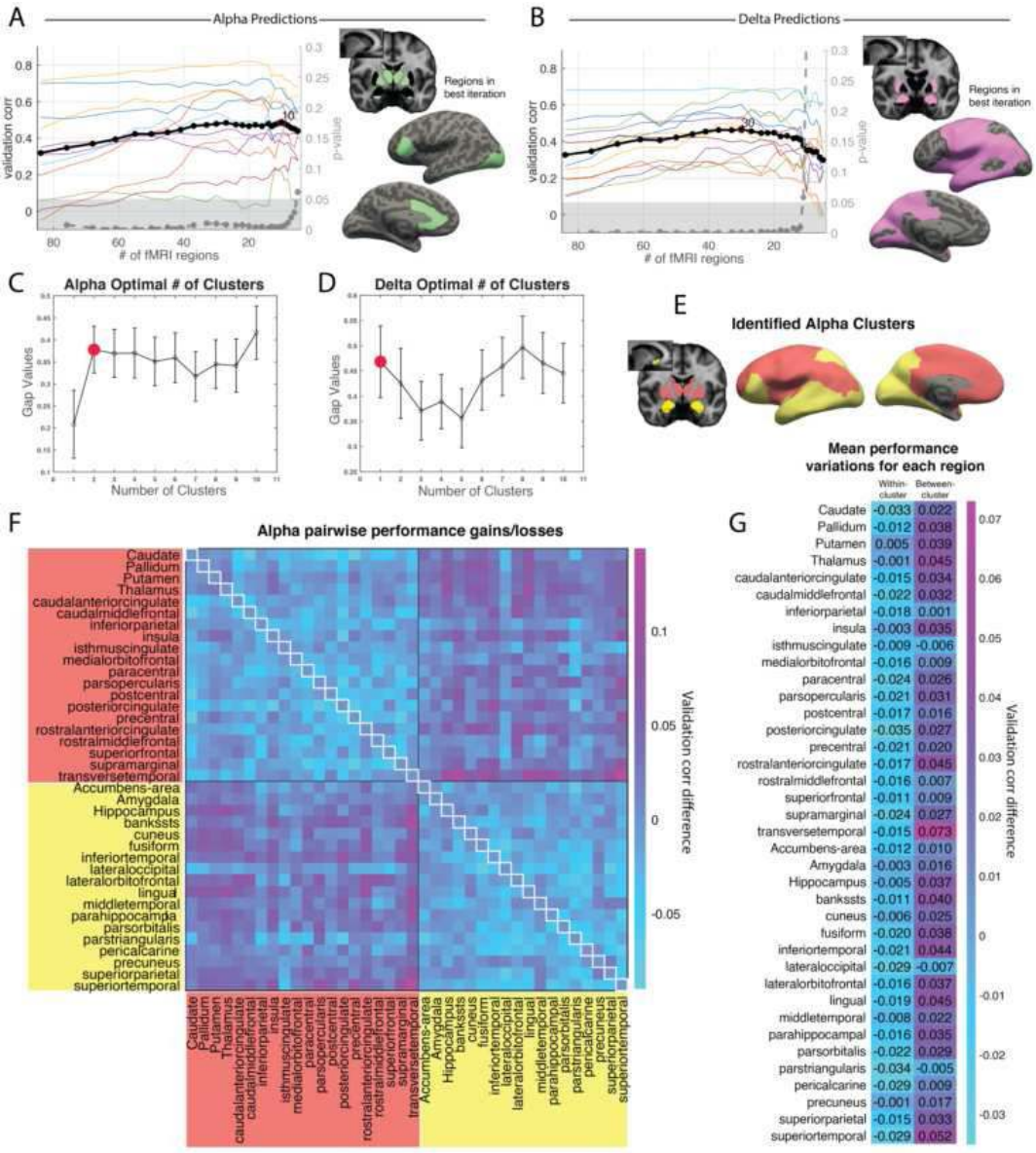

Fig 2: Machine learning identifies the brainwide structure of fMRI activity predictive of EEG power variations. **A-B:** Spatial scales of predictive information were revealed by iteratively dropping low-weights regions, which contain redundant or irrelevant information. Alpha performance peaked at a low number of regions which included subcortical regions (caudate, pallidum, hippocampus, thalamus), anterior cingulate, visual cortex, and frontal cortex. Delta performance peaked at a high number of primarily cortical regions along with the putamen and amygdala. **C-F:** To determine how information was distributed across the brain, we trained the model on each possible pair of regions and assessed how the pairs' performance differed from the best of its individual components (a performance loss implies the added region has redundant information, while a gain implies the added region has unique information). These performance variations were k-means clustered and evaluated with the gap statistic. **C-D:** The optimal clustering solution is the smallest k that satisfies Gap(k)≥GAPMAX−SE(GAPMAX), where Gap(k) is the gap value for the k-clusters solution, GAPMAX is the largest gap value, and SE is standard error. **E:** representation of the identified alpha clusters. **F:** (alpha) performance differences for the pairs, organized by clusters. **G:** (alpha) regions paired within their cluster consistently underperformed in relation to between-cluster pairs.

Conclusions: Our work identified the fMRI network correlates of EEG delta and alpha across sleep and wakefulness, going beyond mass univariate relationships by extending a predictive approach to continuous cross-modal data. We found that alpha variations can be predicted by a small number of fMRI regions and that the fMRI information is divided in two networks-one represented by the visual system, and the other by arousal-controlling subcortical regions-while delta variations are predicted by a large and unified array of primarily cortical regions.

References

1. Fultz, N. E. et al. (2019). Coupled electrophysiological, hemodynamic, and cerebrospinal fluid oscillations in human sleep. Science (80-.). 366, 628–631
2. de Munck, J. C. et al. (2007). The hemodynamic response of the alpha rhythm: An EEG/fMRI study. Neuroimage 35, 1142–1151
3. Feige, B. et al. (2005). Cortical and subcortical correlates of electroencephalographic alpha rhythm modulation. J. Neurophysiol. 93, 2864–2872
4. Goldman, R. et al. (2002). Simultaneous EEG and fMRI of the alpha rhythm. Neuroreport 2487–2492
5. Tyvaert, L. et al. (2008). Effects of fluctuating physiological rhythms during prolonged EEG-fMRI studies. Clin. Neurophysiol. 119, 2762–2774

Poster No 2565

Subcortical neuromodulation of arousal state transitions in the human brain

Nicholas Cicero[1], Beverly Setzer[2], Daniel Gomez[3], Ewa Beldzik[3], Makaila Banks[2], Juan Eugenio Iglesias[4], Giorgio Bonmassar[4], Brian Edlow[4], Laura Lewis[3]

[1]Boston University, Allston, MA, [2]Boston University, Boston, MA, [3]Massacusetts Institute of Technology, Cambridge, MA, [4]Athinoula A. Martinos Center for Biomedical Imaging, Charlestown, MA

Introduction: During sleep, our brains undergo a transformation in state, marked by profound changes in cognition and behavior[1]. During a typical night of sleep, the brain cycles through stereotyped stages of sleep[2-9], including many spontaneous, brief arousals from sleep. Emerging evidence indicates that several subcortical neuromodulatory nuclei, known as the ascending arousal network (AAN), generate and maintain this sleep architecture[2,3,6]. Individual nuclei within the AAN have been demonstrated in rodents to initiate arousal state transitions; however, it is unknown how the diverse components of this network operate together to generate and sustain sleep structure, and the small size of these brain regions has historically limited studies of the AAN in humans. To study the underlying neural mechanisms controlling sleep-wake state structure in humans, we performed simultaneous acquisition of electroencephalography (EEG) and ultra-high field functional magnetic resonance imaging (fMRI) to identify subcortical and cortical dynamics across sleep-wake state transitions.

Methods: Data were collected from nine healthy volunteers. Participants arrived at the lab around their typical bedtime and underwent simultaneous EEG-fMRI at 7 Tesla. After an MPRAGE scan (0.75mm isotropic), we performed a resting state fMRI scan using high spatial resolution sagittal partial-brain EPI acquisition covering the brainstem and midline cortex (voxel size=1.2mm isotropic; TR=0.98s; SMS=2, GRAPPA=4) (Fig 1A). Participants performed a self-paced button press task to indicate their behavioral state. Anatomical segmentation of the AAN was performed within each individual to localize nuclei with high spatial precision (Fig 1B). To delineate arousal dynamics within regions of the AAN, we extracted BOLD activity in each region of interest (ROI) at the moment of behavioral arousals, defined as the first button press after at least 20 seconds without a button press (Fig 2A). We next separated behavioral arousals into two types: sustained (at least 5 button presses following arousals) and transient (two or fewer button presses). We also separated behavioral arousals by the duration of the unresponsive period preceding the arousal. Significant differences between each ROI's fMRI signals in different arousal types were identified by computing a paired t-test across 1-s bins and the p-value was Bonferroni corrected for the number of time bins and ROIs tested.

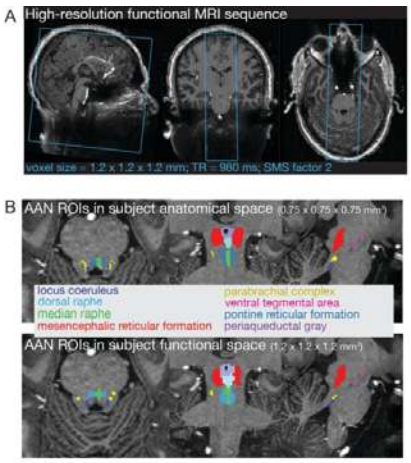

Figure 1. Demonstration of high spatial resolution sagittal partial-brain EPI acquisition and brainstem ROI extraction. A. Position of high spatial resolution EPI acquisition in an example subject in blue. B. (top) AAN ROIs segmented in subject anatomical space using a Bayesian algorithm based on individual anatomical landmarks and histological data. ROIs were manually reviewed and edited (bottom) AAN ROIs in subject functional space after nonlinear registration, interpolation, and thresholding.

Results: Analysis of fMRI dynamics at the moment of behavioral arousal revealed that all regions of the AAN activated prior to behavioral arousals (Fig 2B). We next tested whether specific regions were linked to subsequent maintenance of the arousal state following a sleep-to-wake transition. We found that select subcortical regions, namely the dorsal raphe, periaqueductal gray, mesencephalic reticular formation, ventral tegmental area, lateral hypothalamus, and thalamus, were more strongly activated following sustained compared to transient arousals (Bonferroni corrected paired t-test, $p<0.05$) (Fig 2C). The dynamics within specific subcortical regions also reflected the arousal state prior to behavioral arousal, with the locus coeruleus, pedunculopontine tegmentum, and lateral hypothalamus displaying significantly greater activation (Bonferroni corrected paired t-test, $p<0.05$) when subjects were emerging from a longer unresponsive period.

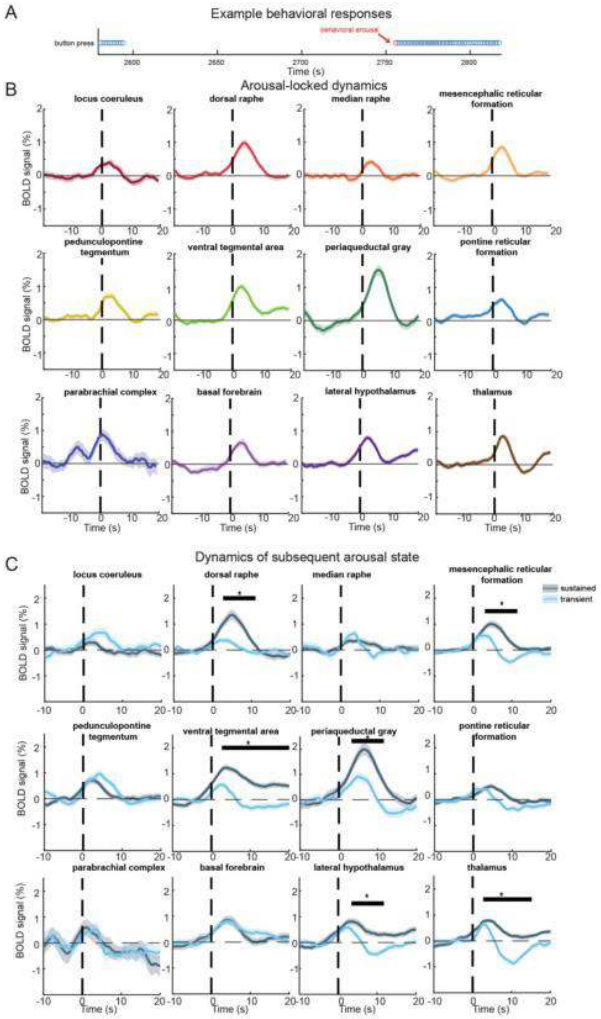

Figure 2. Arousal-locked dynamics of AAN ROIs. A. Example behavioral responses (circle = button press) with a behavioral arousal labeled in red. B. Subcortical regions of the AAN and the thalamus activate before the moment of behavioral arousal, (n=9 subjects, 82 behavioral arousals). C. Arousal-locked dynamics in the dorsal raphe, mesencephalic reticular formation, ventral tegmental area, periaqueductal gray, lateral hypothalamus, and thalamus are significantly greater (starred, black line, Bonferroni corrected paired t-test, at least $p<0.05$) in sustained compared to transient arousals. The dashed black line is behavioral arousal. The shaded region is SEM.

Conclusions: Using simultaneous EEG-fMRI at 7 Tesla, we identify distinct patterns of subcortical dynamics that reflect the moments before, during, and after arousal state transitions. We find that all regions of the AAN activate at the moment of a behavioral arousal state transition, but specific subsets of the AAN display activity are linked to the preceding depth and subsequent stability of an arousal state transition. This work identifies unified and unique properties of the AAN in humans and demonstrates that distinct dynamics within the AAN reflect different aspects of transitions between brain states.

References

1. McGinley, M. J. (2015), 'Waking state: Rapid variations modulate neural and behavioral responses', Neuron, vol. 87, pp. 1143-1161
2. Eban-Rothschild, A. (2018), 'Neuronal mechanisms for sleep/wake regulation and modulatory drive', Neuropsychopharmacology, vol. 43, pp. 937-952
3. Sulaman, B. A. (2022), 'Neuro-orchestration of sleep and wakefulness', Nature Neuroscience, vol. 26, pp. 196-212
4. Kroeger, D. (2023), 'To sleep or not to sleep – Effects on memory in normal aging and disease', Aging Brain, vol. 3, pp. 100068
5. Stickgold, R. (2005), 'Sleep-dependent memory consolidation', Nature, vol. 437, pp. 1272-1278
6. Kjaerby, C. (2022), 'Memory-enhancing properties of sleep depend on the oscillatory amplitude of norepinephrine', Nature Neuroscience, vol. 25, 1059-1070
7. Mason, I. C. (2022), 'Light exposure during sleep impairs cardiometabolic function', PNAS, vol. 119
8. Roth, T. (2013), 'Disrupted nighttime sleep in narcolepsy', J Clin Sleep Med., vol. 9, pp. 955-965
9. Johar, D. (2016), 'Impaired sleep predicts cognitive decline in old people: Findings from the prospective KORA age study', Sleep, vol. 39, pp. 217-226

Poster No 2566

Effects of mindfulness training on brain structure, depressive symptoms, and sleep in adolescence

Tara Samson[1], Benjamin Sipes[1], Angela Jakary[1], Tiffany Ngan[1], Yi Li[1], Eva Henje[2], Tony Yang[1], Olga Tymofiyeva[1]

[1]University of California, San Francisco, San Francisco, CA, [2]University of Umeå, Umeå, Sweden

Introduction: Quality sleep is a key component of healthy development in youth, yet many teens deal with chronic sleep disturbances (Seton et al., 2021). Research suggests mindfulness-based therapies can treat both depressive symptoms and associated sleep disturbances, and improving sleep quality may consequently alleviate depressive symptoms (Yang et al., 2022; Smith et al., 2021). Further, sleep disturbances, depressive symptoms, and mindfulness all have neural associations with the medial prefrontal cortex (mPFC) (Cheng et al., 2022; Scott et al., 2021). The Training for Awareness, Resilience, and Action (TARA) program addresses depressive symptoms including sleep disturbances in adolescents with mindfulness strategies such as breathing techniques, meditation, and yoga-based movements. The present study explores associations between (1) depressive symptoms and sleep disturbances and (2) the neural and behavioral effects TARA may have on these measures.

Methods: 121 healthy adolescents (15.9±1.3 yrs, range 14-18 yrs, 52 females) underwent a 3T MRI scan that included a T1-weighted sequence and a DTI sequence with 30 directions. Subjects were randomized to TARA (n=56) or a control waiting period (n=56) for 12 weeks, then scanned again. Our analyses focused on the ventromedial prefrontal cortex (vmPFC) which corresponds to the medial orbitofrontal cortex (mOFC) in the AAL atlas used in our study. Node strength was calculated as the sum of the connections from the vmPFC to all other brain regions weighted by the average fractional anisotropy (FA) along the tractography streamlines (Figure 1) (Rubinov et al., 2010). All participants completed self reports before and after the intervention which included the Insomnia Severity Index (ISI) and the Reynolds Adolescent Depression Scale-2nd edition (RADS-2).

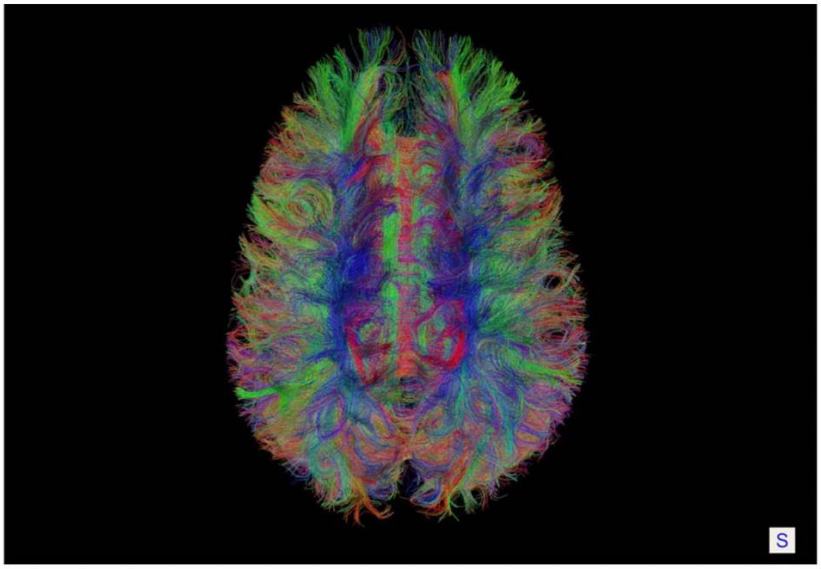

Figure 1. Tractography streamlines in an adolescent brain

Results: Firstly, we observed positive correlations between sleep disturbances (ISI) and depressive symptoms (RADS-2) at baseline ($r=0.531$; $p<0.001$) and follow-up ($r=0.574$; $p<0.001$) in all participants. Changes in sleep quality between baseline and follow-up were also positively associated with changes in depressive symptoms in the TARA group only ($r=0.296$; $p=0.027$). Sleep quality improved significantly more in adolescents who participated in TARA than in waitlist controls ($p=0.008$, Figure 2), while depressive symptoms did not improve in either group. Secondly, the structural node strength of the vmPFC was negatively correlated with sleep disturbances at both the baseline ($r=-0.214$; $p=0.020$) and follow-up ($r=-0.210$; $p=0.047$) scans. Changes in depressive symptoms were significantly associated with changes in vmPFC node strength ($r=-0.243$; $p=0.021$), but changes in sleep quality were not.

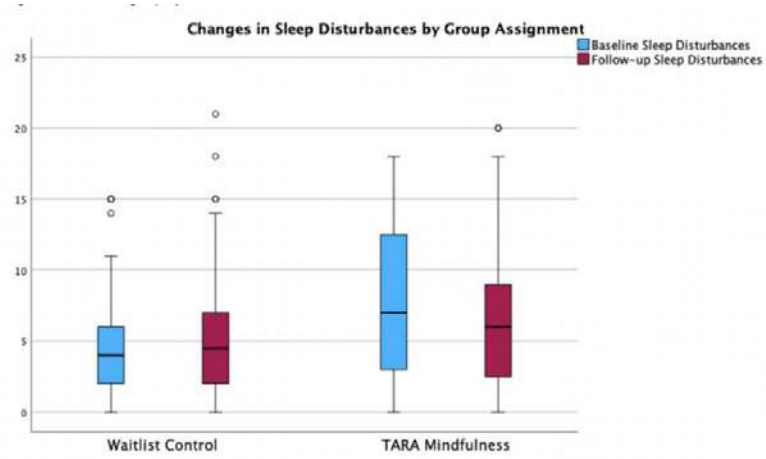

Figure 2. Boxplot comparing self reported sleep disturbances (ISI) in the waitlist control group vs. the TARA mindfulness group at baseline and after the 12-week intervention

Conclusions: In addition to supporting the well-established relationship between depressive symptoms and sleep disturbances, our study indicates that sleep disturbances may be more immediately impacted by mindfulness training than overall depressive symptoms. This finding aligns with prior work suggesting mindfulness training can improve sleep quality in the short-term without changing overall depressive symptoms (Smith et al., 2021). Our results also suggest that the vmPFC is a key brain region of interest for future work at the intersection of adolescent mindfulness, sleep, and depression. Such work may investigate the rates at which mindfulness training changes vmPFC structural or functional connectivity, improves sleep quality, and attenuates depressive symptoms in both healthy adolescents and those suffering from a depressive disorder.

References

1. Cheng, W. (2022), 'Sleep duration, brain structure, and psychiatric and cognitive problems in children', Molecular Psychiatry, vol. 26, no. 8, pp. 3992-4003
2. Rubinov, M. (2010), 'Complex network measures of brain connectivity: uses and interpretations', NeuroImage, vol. 52, no. 3, pp. 1059-1069
3. Scott, A. J. (2021), 'Improving sleep quality leads to better mental health: A meta-analysis of randomised controlled trials', Sleep Medicine Reviews, vol. 60, 101556
4. Seton, C. (2021), 'Chronic sleep deprivation in teenagers: Practical ways to help', Paediatric Respiratory Reviews, vol. 40, pp. 73-79
5. Smith, J. L. (2021), 'Impact of app-delivered mindfulness meditation on functional connectivity, mental health, and sleep disturbances among Physician Assistant students: Randomized, wait-list controlled pilot study', JMIR Formative Research, vol. 5, no. 10, e24208
6. Yang, F. N. (2022), 'Functional connectome mediates the association between sleep disturbance and mental health in preadolescence: A longitudinal mediation study', Human Brain Mapping, vol. 43, no. 6, pp. 2041-2050

Poster No 2567

CSF flow and neural activity associated with behavioral and physiological arousal state transitions

Danlei Chen[1], Beverly Setzer[2], Laura Lewis[3]

[1]MIT, Cambridge, MA, [2]Boston University, Boston, MA, [3]Massacusetts Institute of Technology, Cambridge, MA

Introduction: Cerebrospinal fluid (CSF) is an important component of the central nervous system that maintains essential biochemical and mechanical functions of the brain. Recent studies have found large waves of CSF flow in the fourth ventricle during non-rapid eye movement sleep (Fultz et al., 2019) and intense sensory stimulation (Williams et al., 2023), suggesting that CSF flow can be modulated by neural activity due to neurovascular coupling. In addition, autonomic arousal and global vascular dynamics can shape CSF flow (Picchioni et al., 2022). Here, we used accelerated, high-resolution fMRI to measure physiological and neural dynamics in the human brain during spontaneous transitions of both behavioral arousal and physiological arousal states. We hypothesized that arousal state transitions are associated with large-scale changes in CSF flow and whole-brain neural activity (Lewis et al., 2015; Raut et al., 2020; Setzer et al., 2022). We further used the high temporal resolution of these data to explore the temporal sequence across whole-brain networks that drive physiological changes during physiological arousal state transitions.

Methods: Ten participants who restricted their sleep to four hours the night prior to the experiment performed a behavioral task with fast fMRI at 7-Tesla (TR = 247 ms; 2.5mm isotropic voxels). Preprocessing included slice-time and motion correction. During the scan, participants were instructed to keep their eyes closed and press a button for every breath in and breath out.

Behavioral arousals were defined as the first response after at least 20 s of unresponsiveness (Fig. 1B). Physiological arousals were defined as the increase in respiratory volume. Any arousal events that included excessive motion (>0.3 mm) were excluded from the analysis. Using fast fMRI to measure flow-related enhancement, we extracted CSF flow signals in the fourth ventricle by selecting the brightest voxels in bottom edge slices (Fig. 1A).

Results: As hypothesized, we observed large-scale changes in CSF flow during the transitions of behavioral arousal states (Fig. 1C). Compared to the control region, CSF flow showed a significant increase in the 3.1 to 12.3 s window; i.e. the onset of arousal-locked increase in CSF flow appeared after the onset of arousal. The transition of behavioral arousal states also elicited an increase in respiratory volume (Fig. 1D). These results showed a system-wide changes in physiology and neural activity during behavioral arousal transitions. Next, we investigated transitions of arousal states defined by increases in respiratory volume. As hypothesized, we observed large changes in cortical, subcortical, and CSF signals during the transition of physiological arousal states (Fig. 2A). To characterize a temporal sequence of neural activity associated with changes in respiratory signals, we calculated cross-correlation to identify their maximal correlation coefficient and the corresponding temporal lag. We observed that most cortical regions were negatively correlated with and followed changes in respiratory volume, while subcortical regions were positively correlated with and preceded changes in respiratory volume (Fig. 2B). This result suggests a possible temporal sequence such that neural activity of the subcortical regions might elicit physiological changes which subsequently drive changes in neural activity and vascular constriction of cortical regions.

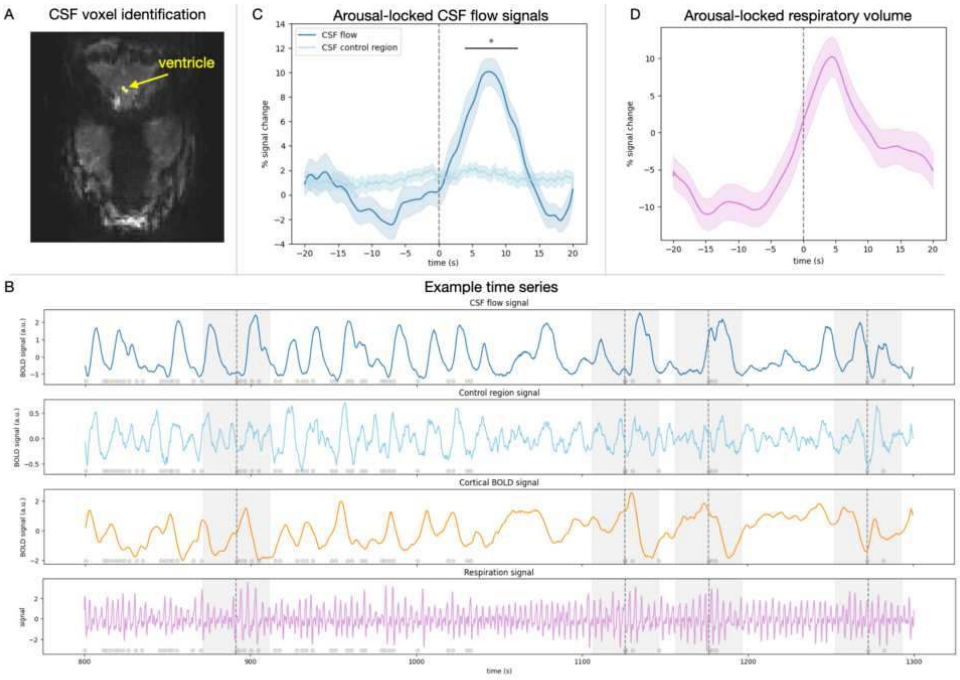

Figure 1. CSF flow is locked to transitions of behavioral arousal state. (A). CSF voxel identification. The brightest voxels in the fourth ventricle from the outermost slice were selected. (B). Example time series of CSF flow, a control region for CSF, the cortex, the thalamus, and respiration. Grey dots at the bottom indicate timing of button presses. Dashed lines indicate behavioral arousal defined as the first button press after at least 20 s of no responses. The shaded gray areas indicate 20 s before and after behavioral arousal events. (C). Arousal-locked CSF flow signals (dark blue) and BOLD signals in a size-matched control region (light blue), averaged across all arousal events (N = 73). CSF flow signals were low-pass filtered at 0.5 Hz. The CSF flow signals are significantly greater than the control region ($p<0.05$, paired t-test) in the 3.1 to 12.3 s window after transitions of behavioral arousal. (D). Arousal-locked respiratory volume and respiratory rate, averaged across all arousal events that passed quality check of respiratory signals (N = 69). The baseline was calculated as the mean signal of the entire run. Dashed grey line represents the onset of behavioral arousal, and shading represents standard error.

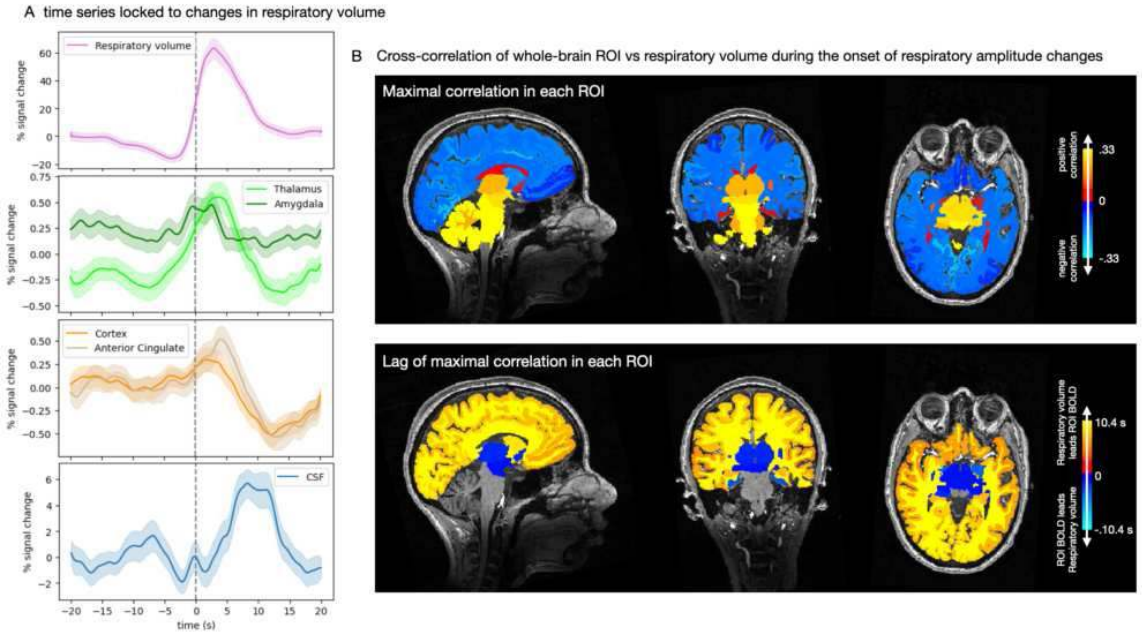

Figure 2. Subcortical BOLD signals rise before the increase in respiratory volume, while cortical signals follow. (A). Example time series locked to -20 to 20 s window around the increase in respiratory volume for 1) respiratory volume and 2) BOLD signals in entire cortex, anterior cingulate cortex, thalamus, amygdala, and CSF flow, averaged across all changes in respiratory volume (N = 78). BOLD signals were low-pass filtered at 0.5 Hz. The dashed lines indicate the onset of respiratory volume increase. The baseline was calculated as the mean signal of the entire run. Shading represents standard error. (B) Cross-correlation of whole-brain ROI vs respiratory volume during the onset of respiratory volume increase. The maximal correlation coefficient map indicates that most cortical regions are negatively correlated with respiratory volume, while most subcortical regions are positively correlated with respiratory volume. The lag of maximal correlation map (in s) indicates that most cortical regions followed respiratory volume, while, more importantly, some subcortical regions, including the thalamus, amygdala, and ventral diencephalon, preceded respiratory volume. This temporal sequence suggests a possible relationship where neural activity in subcortical regions induces changes in systemic physiology and, as a consequence, the cortical regions respond passively due to the changes in subcortical regions and systemic physiology.

Conclusions: Using accelerated fMRI, we identified CSF flow increases locked to behavioral and physiological arousal state transitions, which were also tightly coupled with both BOLD and respiratory signals. Further investigation also revealed a network-level temporal sequence which identified subcortical regions as a potential driver for physiological changes which in turn drives changes in cortical signals. Together, these results identify temporal sequences of neural and hemodynamic signals that couple CSF flow to behavioral and physiological arousal states.

References

1. Dreha-Kulaczewski, S., Joseph, A. A., Merboldt, K.-D., Ludwig, H.-C., Gärtner, J., & Frahm, J. (2015). Inspiration is the major regulator of human CSF flow. The Journal of Neuroscience: The Official Journal of the Society for Neuroscience, 35(6), 2485–2491. https://doi.org/10.1523/JNEUROSCI.3246-14.2015
2. Fultz, N. E., Bonmassar, G., Setsompop, K., Stickgold, R. A., Rosen, B. R., Polimeni, J. R., & Lewis, L. D. (2019). Coupled electrophysiological, hemodynamic, and cerebrospinal fluid oscillations in human sleep. Science (New York, N.Y.), 366(6465), 628–631. https://doi.org/10.1126/science.aax5440
3. Krohn, F., Novello, M., van der Giessen, R. S., De Zeeuw, C. I., Pel, J. J., & Bosman, L. W. (2023). The integrated brain network that controls respiration. eLife, 12, e83654. https://doi.org/10.7554/eLife.83654
4. Lewis, L. D., Voigts, J., Flores, F. J., Schmitt, L. I., Wilson, M. A., Halassa, M. M., & Brown, E. N. (2015). Thalamic reticular nucleus induces fast and local modulation of arousal state. eLife, 4, e08760. https://doi.org/10.7554/eLife.08760
5. Picchioni, D., Özbay, P. S., Mandelkow, H., de Zwart, J. A., Wang, Y., van Gelderen, P., & Duyn, J. H. (2022). Autonomic arousals contribute to brain fluid pulsations during sleep. NeuroImage, 249, 118888. https://doi.org/10.1016/j.neuroimage.2022.118888
6. Raut, R. V., Snyder, A. Z., & Raichle, M. E. (2020). Hierarchical dynamics as a macroscopic organizing principle of the human brain. Proceedings of the National Academy of Sciences, 117(34), 20890–20897. https://doi.org/10.1073/pnas.2003383117
7. Setzer, B., Fultz, N. E., Gomez, D. E. P., Williams, S. D., Bonmassar, G., Polimeni, J. R., & Lewis, L. D. (2022). A temporal sequence of thalamic activity unfolds at transitions in behavioral arousal state. Nature Communications, 13(1), 5442. https://doi.org/10.1038/s41467-022-33010-8
8. Williams, S. D., Setzer, B., Fultz, N. E., Valdiviezo, Z., Tacugue, N., Diamandis, Z., & Lewis, L. D. (2023). Neural activity induced by sensory stimulation can drive large-scale cerebrospinal fluid flow during wakefulness in humans. PLoS Biology, 21(3), e3002035. https://doi.org/10.1371/journal.pbio.3002035

Poster No 2568

Slow Oscillations Modulate Functional Brain Changes Supporting Working Memory Efficiency

Pin-Chun Chen[1], Jing Zhang[2], Arielle Tambini[3], Sara Mednick[4]

[1]University of Oxford, Oxford, United Kingdom, [2]Harvard Medical School and Massachusetts General Hospital, Boston, MA, USA, [3]The Nathan S. Kline Institute for Psychiatric Research, Orangeburg, NY, USA, [4]University of California Irvine, Irvine, CA, USA

Introduction: Working memory (WM), a cognitive process that temporarily stores and manipulates information to achieve a goal, is a skill that can improve with training (Jaeggi et al., 2008). Sleep, specifically slow oscillations (SOs; <1Hz), has been shown to benefit WM improvement (Diep et al., 2020; Pugin et al., 2015). Using simultaneous EEG-fMRI, the current study aims to explore neural mechanisms underlying sleep-dependent WM processing.

Methods: 34 participants (25.91 ± 5.29 yo, all right-handed) completed the entire study protocol consisting of two overnight visits. During each visit, participants performed an operation-span (OSPAN) WM task (see Faraco et al. 2011) in a 3T Siemens Prisma MRI scanner before and after sleep, with the first 2.5 hrs of sleep was monitored by simultaneous EEG-fMRI. EEG was acquired with an MR-compatible 12-channel EEG cap (BrainCap MR). SOs troughs were detected from each EEG channel on MATLAB (see Chen et al., 2021). Detected SOs were modeled as predictors in event-related analyses to assess fMRI BOLD activation and functional connectivity (similar to Ilhan-Bayrakcı et al. 2022). fMRI analyses were performed using SPM12 and Randomise (FSL). We examined how WM-related brain activity changed across a night of sleep, and whether overnight changes in WM were linked to neural processing during SOs. Our analysis took two approaches, a data-driven analysis that examined how WM-related brain activity changed across the night; and a priori network-driven analysis that focused on the Dorsal and Ventral Attention Networks, to examine SOs-related brain activity in these established networks that contribute to WM function (Majerus et al., 2018; Vossel et al., 2014).

Results: We reveal several insights into how the neural mechanisms supporting WM change over a night of sleep. First, we showed reliable changes in WM BOLD activity across sleep, with widespread decreases in WM-related activation patterns, specifically in the dorsal precuneus (FWE corrected at $p<0.05$). Using the dorsal precuneus as a seed ROI, we charted the whole-brain functional connectivity during OSPAN and SOs. During OSPAN, dorsal precuneus functionally interacted with multiple cortical sites, including the fusiform gyrus, superior parietal cortex, middle frontal gyrus, and premotor cortex (FWE corrected at $p<0.05$). During SOs, the dorsal precuneus showed a diffuse decrease in functional connectivity with frontal and parietal cortices during SOs relative to non-SO NREM sleep (FWE corrected at $p<0.05$). Moreover, we demonstrated that SOs modulated BOLD activation in WM-related regions, with portions of the dorsal mid-cingulate cortex and right thalamus activated during SOs and decreased activation in the anterior insular cortex. Critically, we uncovered multiple relationships between the extent of neural processing during SOs and changes in overnight WM activity. In particular, stronger activation in the vmPFC and premotor cortex during SOs was associated with greater overnight reductions in WM activity. Additionally, across voxels in the ventral attention network, there was a negative correlation between patterns of AM-PM OSPAN activation change and SO activation ($r=-0.27$, $p=0.01$, $N = 1000$ permutations). This indicates that voxels with greater overnight reductions in WM activation show stronger modulation during SO events. Together, these results provide evidence for a direct links between SO activity and overnight changes in WM function, which may underlie improvements WM across sleep.

Conclusions: To our knowledge, this is the first study to examine how functional changes time-locked to SOs contribute to neural processing during WM using simultaneous EEG-fMRI. Our findings elucidate the important role of sleep, specifically SOs, as a mechanism of functional changes in the brain associated with improvements in WM function across sleep. The more active WM-related regions are during SOs, the less they are recruited during subsequent WM task following a night of sleep.

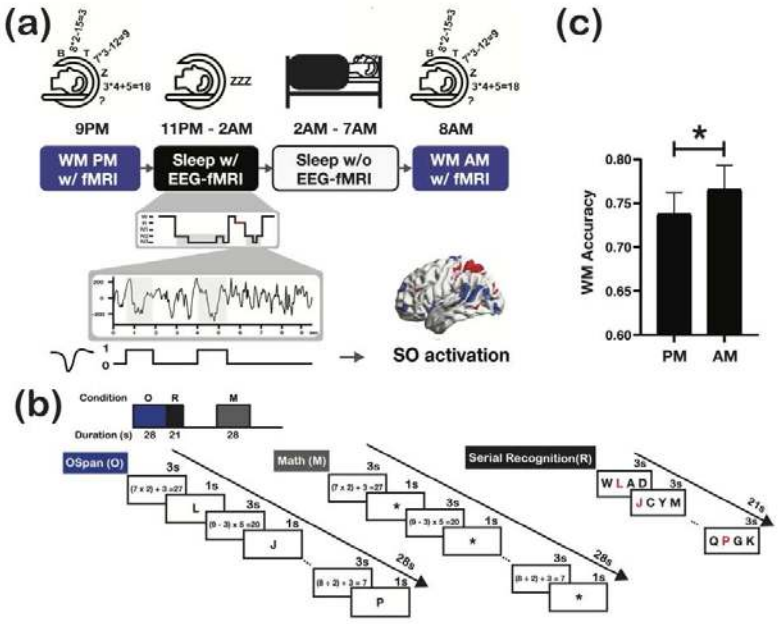

Fig. Study protocol (a), OSPAN task design (b), and behavioral results (c).

References

1. Chen, P.-C. (2021). Competitive dynamics underlie cognitive improvements during sleep. Proceedings of the National Academy of Sciences, 118(51), e2109339118.
2. Diep, C. (2020). Acoustic slow wave sleep enhancement via a novel, automated device improves executive function in middle-aged men. Sleep, 43(zsz197).
3. Faraco C.C., (2011) Complex span tasks and hippocampal recruitment during working memory. Neuroimage. 2011 Mar 15;55(2):773-87. doi: 10.1016/j.neuroimage.
4. Ilhan-Bayrakcı M, (2022) Individual slow wave events give rise to macroscopic fMRI signatures and drive the strength of the BOLD signal in human resting-state EEG-fMRI recordings. Cereb Cortex. 2022 Oct 20;32(21):4782-4796. doi: 10.1093/cercor/bhab516.
5. Jaeggi, S.M. (2008). Improving fluid intelligence with training on working memory. Proceedings of the National Academy of Sciences, 105(19), 6829–6833. https://doi.org/10.1073/pnas.0801268105
6. Majerus, S. (2018). The Dorsal Attention Network Reflects Both Encoding Load and Top–down Control during Working Memory. Journal of Cognitive Neuroscience, 30(2), 144–159.
7. Pugin, F. (2015) Local Increase of Sleep Slow Wave Activity after Three Weeks of Working Memory Training in Children and Adolescents, Sleep, Volume 38, Issue 4, 1 April 2015, Pages 607–614
8. Vossel, S. (2014). Dorsal and Ventral Attention Systems: Distinct Neural Circuits but Collaborative Roles. The Neuroscientist, 20(2), 150–159. https://doi.org/10.1177/1073858413494269

Poster No 2569

The relationship between sleep EEG-based brain age and cognitive function in OSA patients

Soonhyun Yook[1], Hae Ree Park[2], Eun Yeon Joo[3], Hosung Kim[4]

[1]University of Southern California, San Gabriel, CA, [2]Department of Neurology, Inje University College of Medicine, Ilsan Paik Hospital, Ilsan, Gyeonggi-do, [3]Department of Neurology, Neuroscience Center, Samsung Medical Center, Samsung Biomedical Research In, Seoul, Seoul, [4]University of Southern California, Los Angeles, CA

Introduction: Obstructive sleep apnea (OSA) is one of the most common sleep disorders, characterized by recurring breathing interruptions during sleep due to airway obstruction, resulting in intermittent hypoxemia and fragmented sleep.[1,2] These events contribute to oxidative stress, systemic inflammation, and adverse effects on brain structure and cognition in individuals with OSA.[3,4] Recent research from our group introduced a novel metric, the brain age index (BAI), derived from electroencephalogram (EEG) signals during sleep. BAI revealed an association with cortical thickness, suggesting a link between neuroelectrophysiological aging (BAI measured on EEG) and brain structural aging (cortical atrophy) in OSA. However, it remains unexplored whether faster aging observed on EEG is associated with declined cognitive function. This study thus attempts to answer this novel question by examining whether sleep EEG-BAI correlates with cognitive function, providing insights into reported cognitive impairments in OSA populations.

Methods: 1. Participants We studied individuals from Samsung Medical Center, including 78 OSA patients with an AHI > 15 and 77 normal subjects with an AHI < 5, all aged 18 and above. Normal subjects had an average age of 37.9 ± 11.0, while OSA patients had an average age of 47.8 ± 10.3. 2. Brain age prediction We utilized sleep EEG data, comprising six channels (F3, F4, C3, C4, O1, O2). The sleep EEG data were transformed into scalograms and fed into a 3D deep learning-based brain age prediction model.5 BAI was calculated by subtracting chronological age from predicted age. 3. Cognitive score Neuropsychological tests were conducted on 155 subjects, which we derived five composite score: 1) Attention and Executive Function, 2) Verbal Fluency, 3) Verbal Memory, 4) Visual Memory, and 5) Visuospatial Ability. 4. statistical analysis We conducted linear regression and Student's t-tests for group comparisons between the normal and OSA groups while correcting for possible confounding effects of age and body-mass index (BMI). Subsequently, we correlated cognitive composite scores with BAI within each normal and OSA group. All statistical results were adjusted using false discovery rate correction.

Results: 1. Comparison between normal and OSA groups The OSA group was on average 9.9 years older than the normal group. BAI in the OSA group was significantly higher at 2.5±7.8 years compared to -0.08±6.95 in the normal group. Furthermore, the normal group exhibited superior verbal fluency compared to the OSA group (t=3.14, p=0.01, Table 1). 2. Association between BAI and cognitive function In the normal group, none of the five cognitive scores exhibited a significant correlation with BAI. In contrast, within the OSA group, attention and executive function negatively correlated with BAI (ß=-3.52, p=0.01, Table 2).

	Normal (n=77)	OSA (n=78)	T-value	P-value
age	37.9 (11.0)	47.8 (10.3)	**5.82**	**<0.0001**
BAI	-0.08(6.95)	2.47 (7.83)	**3.14**	**0.001**
Attention & executive function	0.12 (0.61)	-0.02 (0.66)	1.38	0.17
Verbal fluency	0.16 (0.87)	-0.17 (0.78)	**2.50**	**0.01**
Verbal memory	0.17 (0.84)	-0.13 (0.78)	1.97	0.05
Visual memory	0.20 (0.78)	-0.03 (0.80)	1.80	0.07
Visuospatial function	0.14 (0.80)	-0.07 (0.87)	1.60	0.11

Table 1. Comparison between normal and OSA groups

	Normal (n=77)		OSA (n=78)	
	β	P-value	β	P-value
Attention & executive function	-1.80	0.28	-3.52	**0.01**
Verbal fluency	0.79	0.45	-0.10	0.93
Verbal memory	0.01	0.98	0.17	0.89
Visual memory	-1.99	0.09	-0.20	0.86
Visuospatial function	0.24	0.84	-0.13	0.91

Table 2. Association between cognitive function and BAI

Conclusions: In this study, we compared cognitive function between normal and OSA groups and explored the relationship between BAI and cognitive function. The OSA group had higher BAI and lower scores in verbal fluency. These differences may be linked to hypoxemia[6] and sleep fragmentation[7] that are main characteristics of OSA, which lead to neuroinflammation 8 and glymphatic dysfunction[9]. This may subsequently affect brain structural integrity and normal neural activity, thereby reducing cognitive function.[3] An interesting finding is that within the OSA group, attention and executive function correlated with BAI. Previous research has consistently noted impaired function in these domains among older adults with sleep apnea.[10] In the current study, a limitation is acknowledged in the notably younger healthy subjects compared to the OSA group. Further investigations focusing on old adults with OSA are required to elucidate whether brain aging mediates the cognitive decline associated with sleep apnea. In conclusion, our study proposes that BAI could be a valuable biomarker for assessing cognitive function, particularly in the context of OSA.

References

1. Park, J. G. (2011) Updates on definition, consequences, and management of obstructive sleep apnea. Mayo Clin Proc, 86, 549-54; quiz 554-5.
2. Jordan, A. S. (2014) Adult obstructive sleep apnoea. The Lancet, 383, 736-747.
3. Lim, D. C. (2014) Obstructive sleep apnea and cognitive impairment: Addressing the blood–brain barrier. Sleep Medicine Reviews, 18, 35-48.
4. Desseilles M. (2008) Neuroimaging Insights into the Pathophysiology of Sleep Disorders. Sleep, 31, 777-794.

5. Yook, S. (2022) Novel neuroelectrophysiological age index associated with imaging features of brain aging and sleep disorders. NeuroImage, 264, 119753.
6. Berr, C. (2000) Cognitive decline is associated with systemic oxidative stress: the EVA study. Journal of the American Geriatrics Society, 48, 1285-1291.
7. Benkirane, O. (2022) Impact of sleep fragmentation on cognition and fatigue. International journal of environmental research and public health, 19, 15485.
8. Daulatzai, M. A. (2015) Evidence of neurodegeneration in obstructive sleep apnea: Relationship between obstructive sleep apnea and cognitive dysfunction in the elderly. J Neurosci Res, 93, 1778-94.
9. Lee, H. (2022) Glymphatic system dysfunction in obstructive sleep apnea evidenced by DTI-ALPS. Sleep Medicine, 89, 176-181.
10. Alchanatis, M. (2008) Comparison of cognitive performance among different age groups in patients with obstructive sleep apnea. Sleep and breathing, 12, 17-24.

Poster No 2570

Robust Identification of Sleep States and Their Transitions Using Whole-Night fMRI Data

Nils Yang[1], Dante Picchioni[1], Jacco de Zwart[1], Yicun Wang[1], Peter van Gelderen[1], Jeff Duyn[1]

[1]National Institutes of Health, Bethesda, MD

Introduction: Sleep staging based on electroencephalography (EEG) and polysomnography (PSG) has been widely used to characterize sleep, but cannot track the detailed spatial and temporal features of brain activity across a night's sleep. For example, brain activity patterns involved with transitions or changes within and between sleep stages are not captured with common sleep staging approaches. Recent investigations have turned to functional magnetic resonance imaging (fMRI) to address this shortcoming[1,2]. Nevertheless, because of the sleep-adverse MRI environment, these studies have been limited to brief (~1 hour) sleep periods, limiting the ability to capture the full range of sleep stages and their cycling. Overcoming these challenges may provide valuable insights into conditions marked by disrupted sleep transitions, e.g. insomnia and various mental disorders.

Methods: Data acquisition was conducted as part of a previously described well-controlled sleep experiment[3] with two consecutive nights of concurrent fMRI-EEG recording from 23:00 to 7:00 for each night. Twelve participants (18-35 years old, 8 females) had at least one complete sleep cycle, encompassing all four sleep stages (N1-3 and REM), during both Night 1 and 2. Throughout each night, the fMRI experiments were intermittently disrupted by either acoustically stimulated or spontaneous awakenings. Detailed fMRI (with global signal regression), EEG, and photoplethysmography (PPG) preprocessing steps can be found elsewhere[3,4]. We employed an unsupervised learning approach - Hidden Markov Model (HMM)5,6 to analyze fMRI timecourses extracted from 300 ROIs7. See Figure 1. The HMM, trained on Night 2 data, encompassed 21 whole-brain states based on various model evaluation indexes. Each state was characterized as a multivariate Gaussian distribution including a mean fMRI activation distribution and a functional connectivity (FC) matrix. Furthermore, the HMM featured a transition probability matrix that detailed the likelihood of transitioning between states.

Results: Modular analysis of this transition probability matrix revealed five modules, each containing a set of states that had similar preferences to occur during a specific sleep stage or part thereof (See Figure 2). None of the states clearly preferred N1. Remarkably, the trained HMM predicted brain sleep states during Night 1 that had highly similar sleep stage preference ($r = 0.94$, $p < 0.001$). For mean activation, Wake-related HMM states 16 and 20 demonstrated the classic opposite activation pattern between the default-mode network (DMN) and frontal-parietal network (FPN). In contrast, during N3-related HMM states 8 and 10, DMN and FPN showed the same activation direction. For FC, similar patterns were found. In Wake-related HMM states 16 and 20, the FCs between DMN and Salience Network (SAL) / Control Network (CON) were negative, while during N3-related HMM states 8 and 10, these FCs were positive.

Conclusions: HMM analysis of overnight fMRI sleep data identified 21 brain states and their transition probability. A strong preference for specific sleep stages was observed that was highly reproducible across successive overnight scan sessions. Furthermore, analysis of the transition preference between states naturally grouped the states into the classical sleep stages. These observations suggest that HMM may provide valuable information about sleep-state-specific brain activity patterns that extend well beyond the information provided by classical sleep staging. For example, cursory inspection of the HMM results suggests a subdivision of N2 in two groups of multiple states with different transition probabilities to Wake; analysis of brain activation and FC patterns of HMM states indicated that the connections between DMN and SAL/CON may play a critical role in the transition from wake to light sleep and, to deep sleep. A more detailed analysis of the HMM states and their FC patterns is currently underway.

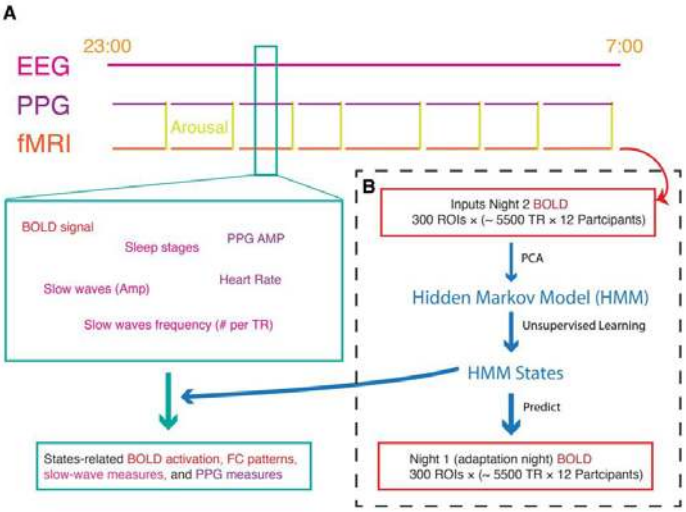

Figure 1. Whole-brain dynamics identified from fMRI sleep recording using a Hidden Markov Model. **A**. Participants slept inside a scanner from 23:00 to 7:00 for two consecutive nights, with concurrent EEG, fMRI, and PPG recording. During each night, the fMRI experiments were intermittently disrupted by either acoustical arousals or spontaneous awakenings. Variables derived from those three recordings were depicted in the green box. **B**. HMM was trained using BOLD signals of Night 2. Then the identified HMM states were generalized to Night 1 BOLD signals. Finally, we studied the states-related variations in BOLD activation, FC patterns, etc.

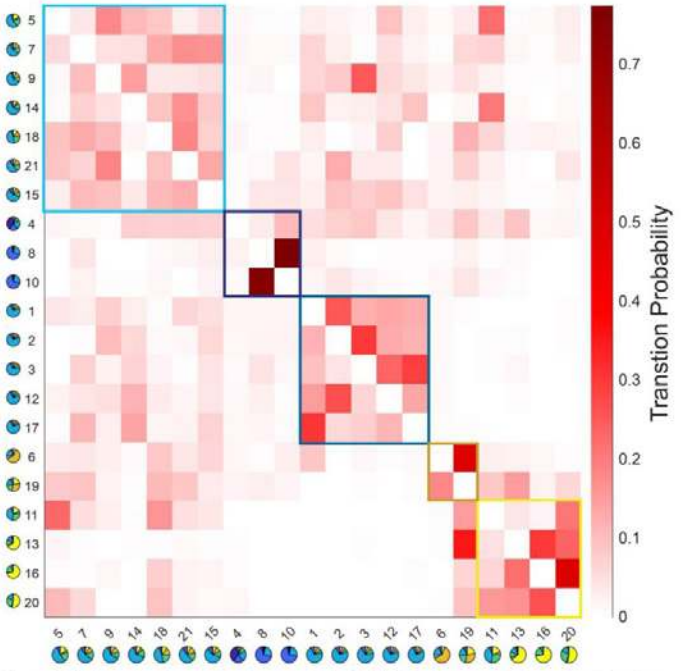

Figure 2. Modular analysis based on transition probability of HMM states independent of sleep stages. Twenty-one HMM states were categorized into five modules: from left to right, light-N2 module (light blue: states 5, 7, 9, 14, 18, 21), N3 module (dark blue: states 4, 8, 10), deep-N2 module (blue: states 1, 2, 3, 12, 17), REM module (orange: states 6 and 19), and Wake module (yellow: states 11, 13, 16, 20). The pie chart under each state represents the sleep stage distribution for the state (Dark Blue - undefined, Blue - N3, Light Blue - N2, Green - N1, Orange - REM, Yellow - Wake).

References

1. Stevner, A. B. A. et al. Discovery of key whole-brain transitions and dynamics during human wakefulness and non-REM sleep. Nat. Commun. 10, 1035 (2019).
2. Zhou, S. et al. Dynamic functional connectivity states characterize NREM sleep and wakefulness. Hum. Brain Mapp. 40, 5256–5268 (2019).
3. Moehlman, T. M. et al. All-night functional magnetic resonance imaging sleep studies. J. Neurosci. Methods 316, 83–98 (2019).
4. Picchioni, D. et al. Autonomic arousals contribute to brain fluid pulsations during sleep. NeuroImage 249, 118888 (2022).
5. Vidaurre, D., Smith, S. M. & Woolrich, M. W. Brain network dynamics are hierarchically organized in time. Proc. Natl. Acad. Sci. 114, 12827–12832 (2017).
6. Vidaurre, D. et al. Discovering dynamic brain networks from big data in rest and task. NeuroImage 180, 646–656 (2018).
7. Seitzman, B. et al. A set of functionally-defined brain regions with improved representation of the subcortex and cerebellum. NeuroImage 206, 116290 (2019).

Poster No 2571

Cerebrospinal fluid flow closely tracks behavioral performance during an attention task

Zinong Yang[1], Stephanie Williams[2], Stephanie Anakwe[3], Emilia Schimmelpfennig[1], Laura Lewis[4]

[1]Boston University, bosotn, MA, [2]Boston University, Boston, MA, [3]Boston University, Bosotn, MA, [4]Massachusetts Institute of Technology, Cambridge, MA

Introduction: Sufficient sleep plays an essential role in maintaining optimal cognitive function and brain health in humans. A single night of lost sleep causes substantial negative cognitive consequences, such as attentional lapses[1]. Recent studies suggest that sleep is the critical stage for cleaning brain neurotoxic waste products that accumulate during wake periods via the glymphatic system, in which metabolites transit through the cerebrospinal fluid (CSF)[2]. A key mechanism driving CSF and clearance is the pulsation of blood vessels in the brain, and sleep enhances this vascular pulsatility and in turn increases CSF flow. However, despite the critical role of sleep and CSF flow in brain health, it remains unclear whether CSF dynamics change after sleep deprivation (SD), and how CSF activity correlates with SD-induced cognitive impairment. Here we characterized how large-scale brain dynamics are altered after acute SD. We first tested the effects of SD on global brain dynamics and CSF activity during wakefulness. We then assessed the correlation between CSF activity and attentional states fluctuation assessed by changes in reaction times, using combined EEG and fast fMRI to simultaneously measure CSF flow.

Methods: To study the effects of SD on CSF dynamics and cognitive deficits, we imaged 26 healthy adults. Each subject was scanned in morning MRI sessions, one after typical sleep and one after SD, in counterbalanced order. During the SD session, subjects underwent a 24-hour period of SD under continuous monitoring of study staff, with EEG performed every 3 hours, followed by EEG-fMRI-Eyetracking during wakefulness in the morning. Functional images were acquired using fast BOLD-fMRI (TR=378ms, 2.5 mm isotropic). Accelerated fMRI paradigms contain flow-related enhancement signals in which high-velocity fluids produce bright signals in the outermost image slices[3]. Our acquisition paradigm exploited these signals and has been successfully used previously to measure BOLD dynamics and CSF flow[4,5]. Subjects underwent 4 runs of the psychomotor vigilance task (PVT) and 1 resting-state. No global signal regression nor ventricle regression was used. The fourth ventricle was identified anatomically as a region of interest (ROI) and was extracted to measure CSF flow signals generated by flow-related enhancement.

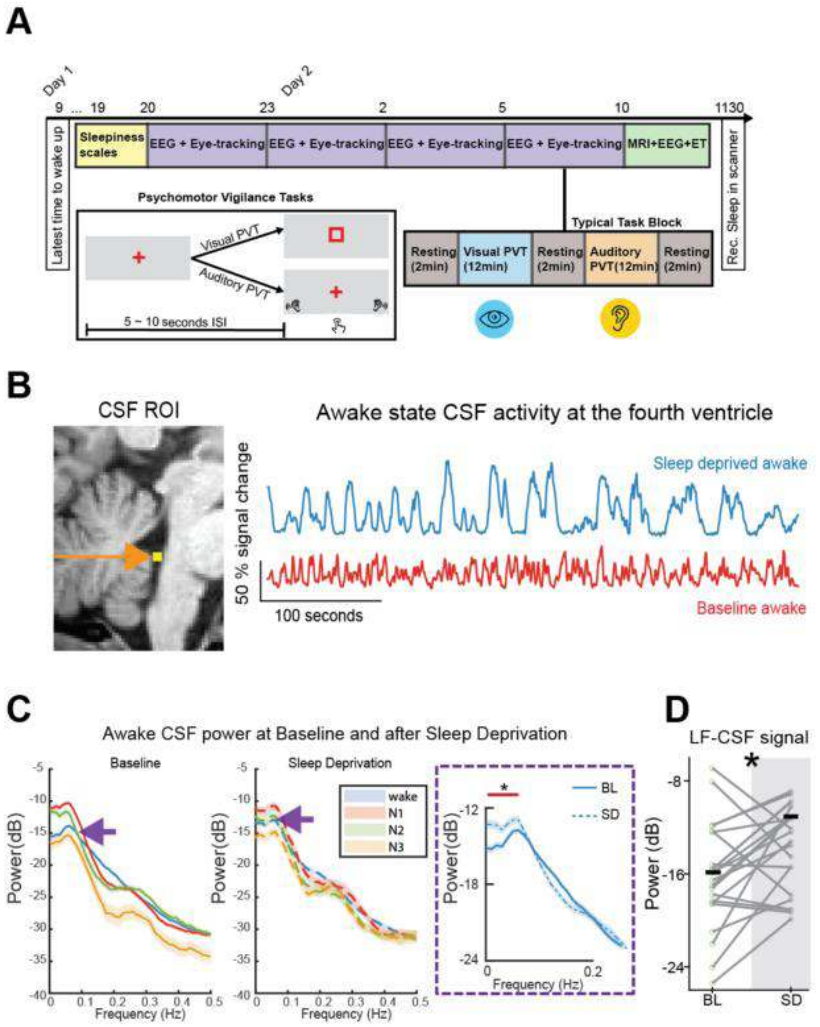

Figure 1. Brain dynamics show sleep-like activity during wakefulness after 24 hours of sleep deprivation. A. Experimental paradigm: Subjects arrived at the laboratory at 7PM of the sleep deprived night. Resting state eyes-open and eyes-closed EEG and eye-tracking were acquired every 3 hours throughout the night. The EEG-fMRI scan time for both baseline and sleep deprived sessions were matched. Each subject performed a visual and auditory psychomotor vigilance task (PVT) every 3 hours throughout the 24 hours of sleep deprivation. B. Left: Example placement of CSF ROI (yellow) in the fourth ventricle in one subject. Right: CSF timeseries from the one representative subject during rested wakefulness at baseline and after sleep deprivation. C. Spectral analysis shows increased ultra-low frequency (0-0.1 Hz) power during rested wakefulness (permutation test with Bonferroni correction: p<0.05 from 0-0.04Hz). D. Ultra-low frequency CSF power increased during wakefulness after SD (n = 23 participants for pairwise comparison).

Results: Consistent with prior studies, spectral power analysis demonstrated that the EEG slow-delta frequency (SWA, 0.5-4 Hz) power increased after SD. We calculated the power spectrum density of the CSF signal at each sleep stage (wake, or stages N1/2/3 of NREM sleep) to test whether SD induces increased CSF flow at ultra-low frequencies (<0.1 Hz) at awake state. We observed a large oscillation in the CSF signal centered around 0.05 Hz during wakefulness after SD, similar to what has been reported during typical rested NREM sleep[4]. We further found a positive correlation between CSF peaks and reaction times during PVT both at baseline and after SD ($p<0.05$, permutation test). We analyzed the SWA, global cortex BOLD and pupil size relative to the peak of the CSF waves and found that neural, BOLD, pupil size and CSF activity were coupled (1736 peaks identified). Cross-correlation analysis (n=26) indicated that peaks in EEG SWA preceded CSF inflow by 6-8s, suggesting that even during wakefulness a transient local increase in slow wave activity is predictive of CSF inflow.

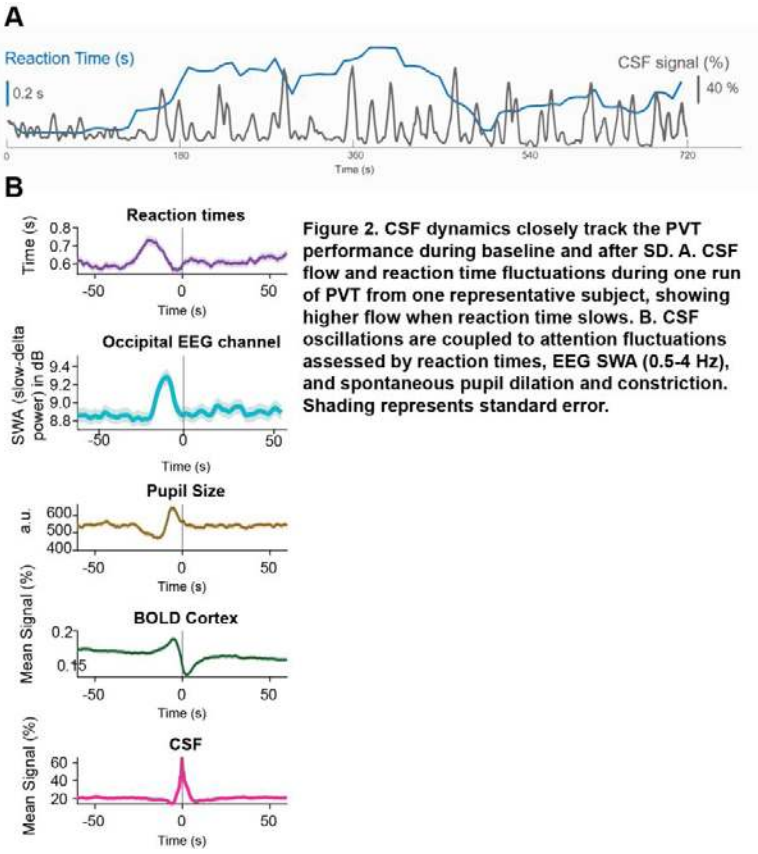

Figure 2. CSF dynamics closely track the PVT performance during baseline and after SD. A. CSF flow and reaction time fluctuations during one run of PVT from one representative subject, showing higher flow when reaction time slows. B. CSF oscillations are coupled to attention fluctuations assessed by reaction times, EEG SWA (0.5-4 Hz), and spontaneous pupil dilation and constriction. Shading represents standard error.

Conclusions: We found that the increased slow wave activity after total sleep deprivation is linked to large-scale CSF inflow through the fourth ventricle during wakefulness. The coupling between CSF inflow and neuronal activity can be detected in drowsy human subjects during behavioral tasks. Sleep deprivation is detrimental to cognitive ability, and cognitive lapses come at a high cost for organismal function. Our results suggest that SD-induced cognitive impairments reflect moments of increased cerebrospinal fluid flow, due to the need for sleep-like restorative physiology after SD.

References

1. Durmer JS, Dinges DF. Neurocognitive consequences of sleep deprivation. Semin Neurol. 2005;25(1):117-129. doi:10.1055/s-2005-867080
2. Yang HC (Shawn), Inglis B, Talavage TM, et al. Coupling between Cerebrovascular Oscillations and CSF Flow Fluctuation during Wakefulness: An fMRI Study. Neuroscience; 2021. doi:10.1101/2021.03.29.437406
3. Gao JH, Miller I, Lai S, Xiong J, Fox PT. Quantitative assessment of blood inflow effects in functional MRI signals - Gao - 1996 - Magnetic Resonance in Medicine - Wiley Online Library. Accessed November 28, 2023.
4. Fultz NE, Bonmassar G, Setsompop K, et al. Coupled electrophysiological, hemodynamic, and cerebrospinal fluid oscillations in human sleep. Science. 2019;366(6465):628-631. doi:10.1126/science.aax5440
5. Williams SD, Setzer B, Fultz NE, et al. Neural activity induced by sensory stimulation can drive large-scale cerebrospinal fluid flow during wakefulness in humans. PLOS Biol. 2023;21(3):e3002035. doi:10.1371/journal.pbio.3002035

Poster No 2572

Deep NREM sleep lowers the amplitude of global cerebral hemodynamic oscillations

Vidhya Vijayakrishnan Nair[1], Brianna R. Kish[1], Hideyuki Oshima[2], A.J Schwichtenberg[1], Yunjie Tong[1]

[1]Purdue University, West Lafayette, IN, [2]Shibaura Institute of Technology, Tokyo, Japan

Introduction: A recently postulated function of slow-wave Non-Rapid Eye Movement (NREM) sleep is brain-metabolic waste clearance via the glymphatic system. The cerebrospinal fluid (CSF) flow through the brain's perivascular pathways and further exchange with interstitial fluid, as described in the glymphatic model, increases dramatically during slow-wave NREM sleep in live mice(Nedergaard, 2013; Xie et al., 2013). In agreement with this observation, recent functional magnetic resonance imaging (fMRI) studies in humans report large amplitude CSF fluctuations moving craniad into the brain during light NREM (NREM-1 and NREM-2) sleep(Fultz et al., 2019; Picchioni et al., 2022). Similar increases in the amplitude of cerebral hemodynamic oscillations are reported during light NREM sleep(Vijayakrishnan Nair et al., 2023). These large CSF movements

have also been shown to be mechanistically driven by low-frequency changes in cerebral hemodynamic oscillations(Fultz et al., 2019; Vijayakrishnan Nair et al., 2023; Yang et al., 2022). However, it is unknown if the amplitude of cerebral hemodynamic oscillations also exhibits a similar increase during deep (slow-wave) NREM sleep (NREM-3). Here, we investigate the amplitude variations in both cerebral hemodynamic oscillations and craniad CSF movement, as well as the strength of coupling between them during NREM-3.

Methods: All participants' structural and functional MRI data were acquired using a 3T SIEMENS MRI scanner (Magnetom Prisma, Siemens Medical Solutions, Erlangen, Germany) with a 64-channel head coil. The scans included structural T1-weighted MPRAGE and fMRI. 32-channel Electroencephalography (EEG) was also concurrently acquired using an MRI-compatible EEG system (BrainAmp MR, Brain Products GmbH, Gilching, Germany) during fMRI scans for sleep scoring. The fMRI scans employed here were carefully designed to concurrently capture the craniad CSF movement at the fourth ventricle utilizing the inflow effect(Fultz et al., 2019; Vijayakrishnan Nair et al., 2022, 2023; Yang et al., 2022) and the global cerebral hemodynamic oscillations across the entire brain (see Figure 1 for an overview of the experimental design). To quantify the variations in amplitude, the standard deviations of detrended (MATLAB detrend) global signal (GS) and CSF signals were calculated across continuous segments (at least 3 minutes in duration) of wakefulness, NREM-1, NREM-2, and NREM-3 for each participant. Similarly, the cross-correlations between changes in GS and CSF movement signals (in the low-frequency range of 0.01 – 0.1 Hz) were also quantified across continuous segments of wakefulness, NREM-1, NREM-2 and NREM-3.

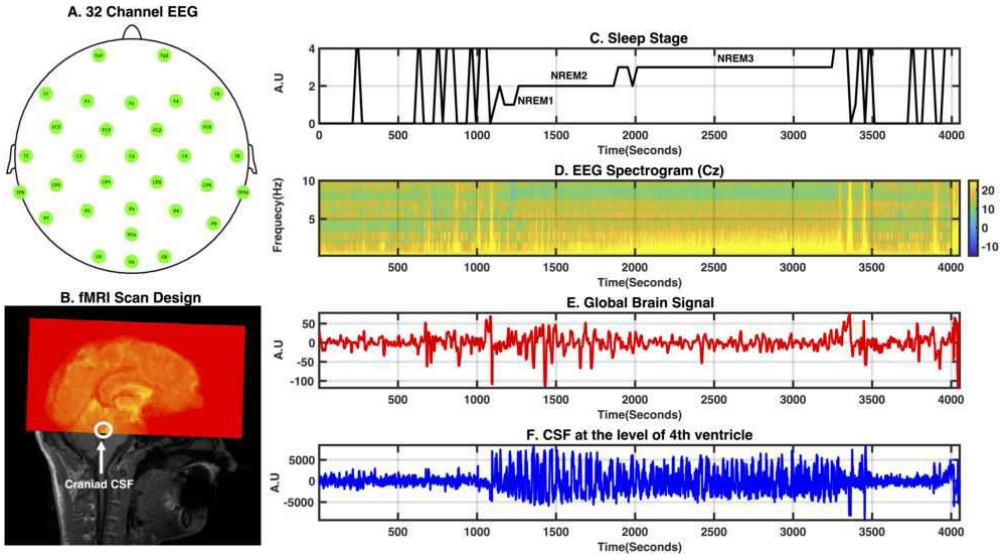

Figure 1: Overview of the experimental design indicating (A) locations of 32-channel EEG electrodes on the head and (B) typical fMRI scan design illustrating the concurrent capture of craniad CSF movement into the brain scan volume utilizing inflow effect and global brain signal as well as the corresponding (C) Sleep stage scoring, (D) EEG spectrogram from central (Cz) electrode, (E) global brain signal and (F) CSF movement signal. A.U – Arbitrary units; CSF - Cerebrospinal Fluid; EEG – Electroencephalogram; fMRI – functional magnetic resonance imaging; NREM – Non-Rapid Eye Movement sleep.

Results: The time series plots of detrended GS and CSF signals clearly illustrate that the amplitude of both GS and CSF increase during light NREM sleep states compared to wakefulness. However, the amplitude of only the GS lowers and resembles wakefulness patterns, whereas CSF movement remains elevated during NREM sleep (figure 2A & 2B). Group results also reveal the same pattern with no statistically significant changes across wake and sleep states (figure 2C). In terms of mechanistic coupling between low-frequency changes in the GS and craniad CSF movement, a strong coupling is apparent (Correlations < -0.3) regardless of the wake/sleep states with change in GS temporally leading/driving CSF movement into the brain with delays of ~2 seconds during wakefulness and ~3-4 seconds during NREM sleep (figure 2D, 2E and 2F).

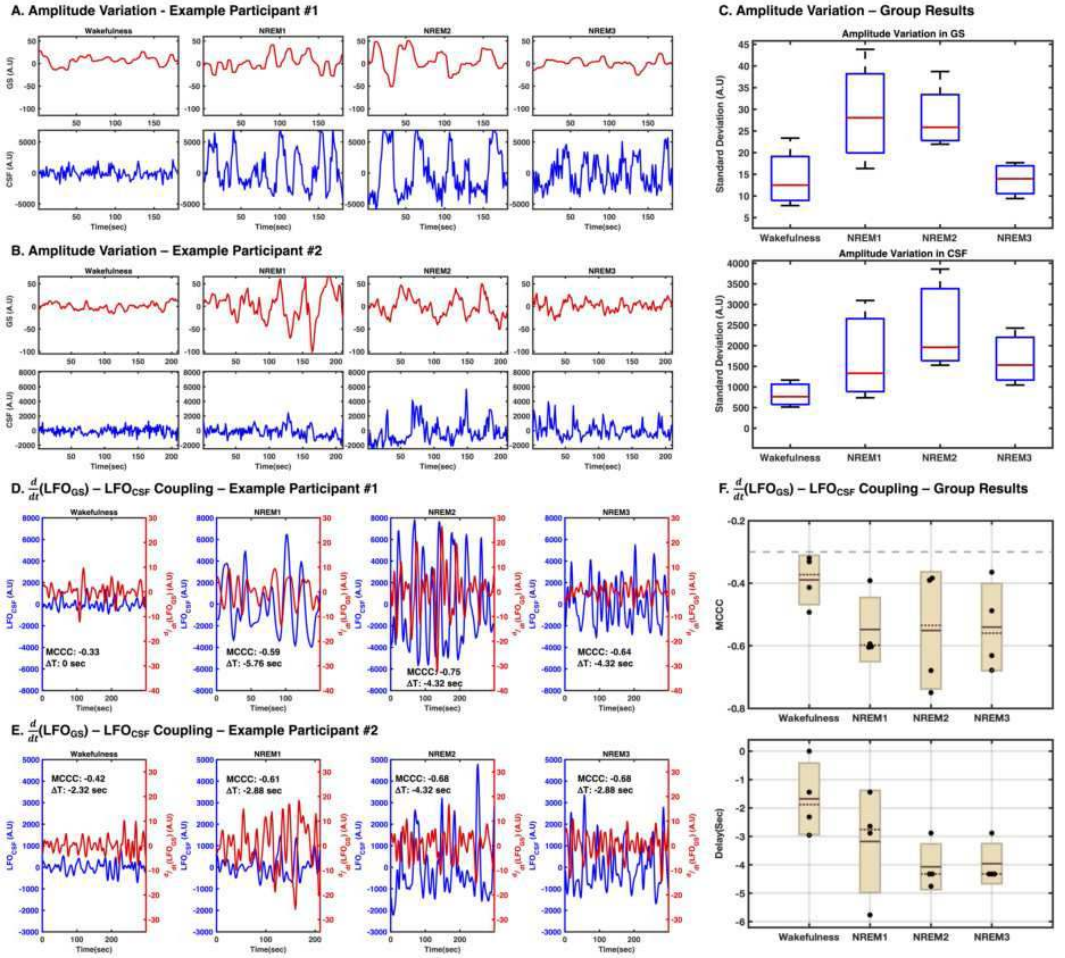

Figure 2: Results - Amplitude variation in GS and CSF signals and low-frequency coupling between them across wake and sleep states in two example participants (panels A, B, D, and E) and the corresponding group results (panels C and F). A.U – Arbitrary Units; CSF - Cerebrospinal Fluid; GS – Global Signal; LFO – Low-frequency Oscillation (0.01 Hz – 0.1 Hz); MCCC – Maximum Cross-Correlation Coefficient; NREM – Non-Rapid Eye Movement sleep. In group results (F), the brown solid line represents the mean, the brown dotted line represents the median, the brown whiskers represent one standard deviation of the raw data points jittered over a 95 percent confidence interval in cream, and the gray dashed line represent the threshold of statistical significance for MCCCs in the LFO range.

Conclusions: Data illustrate that deep NREM sleep lowers the amplitude of cerebral hemodynamic oscillations, whereas the CSF movement oscillation amplitudes stay elevated during all NREM sleep stages. This difference in amplitudes between cerebral hemodynamics and CSF movement during NREM-3 sleep does not affect their mechanistic coupling in the low-frequency range. This implies that mechanisms or forces capable of driving CSF movement without initiating changes in cerebral hemodynamics may be at play during deep NREM sleep.

References

1. Fultz, N. E., Bonmassar, G., Setsompop, K., Stickgold, R. A., Rosen, B. R., Polimeni, J. R., & Lewis, L. D. (2019). Coupled electrophysiological, hemodynamic, and cerebrospinal fluid oscillations in human sleep. Science, 366(6465), 628–631. https://doi.org/10.1126/science.aax5440
2. Nedergaard, M. (2013). Garbage Truck of the Brain. Science, 340(6140), 1529–1530. https://doi.org/10.1126/science.1240514
3. Picchioni, D., Özbay, P. S., Mandelkow, H., de Zwart, J. A., Wang, Y., van Gelderen, P., & Duyn, J. H. (2022). Autonomic arousals contribute to brain fluid pulsations during sleep. NeuroImage, 249(January), 118888. https://doi.org/10.1016/j.neuroimage.2022.118888
4. Vijayakrishnan Nair, V., Kish, B. R., Chong, P. L., Yang, H.-C. (Shawn), Wu, Y.-C., Tong, Y., & Schwichtenberg, A. J. (2023). Neurofluid coupling during sleep and wake states. Sleep Medicine. https://doi.org/https://doi.org/10.1016/j.sleep.2023.07.021
5. Vijayakrishnan Nair, V., Kish, B. R., Inglis, B., Yang, H.-C. (Shawn), Wright, A. M., Wu, Y.-C., Zhou, X., Schwichtenberg, A. J., & Tong, Y. (2022). Human CSF movement influenced by vascular low frequency oscillations and respiration. Frontiers in Physiology, 13. https://doi.org/10.3389/fphys.2022.940140
6. Xie, L., Kang, H., Xu, Q., Chen, M. J., Liao, Y., Thiyagarajan, M., O'Donnell, J., Christensen, D. J., Nicholson, C., Iliff, J. J., Takano, T., Deane, R., & Nedergaard, M. (2013). Sleep drives metabolite clearance from the adult brain. Science (New York, N.Y.), 342(6156), 373–377. https://doi.org/10.1126/science.1241224
7. Yang, H. C., Inglis, B., Talavage, T. M., Nair, V. V., Yao, J., Fitzgerald, B., Schwichtenberg, A. J., & Tong, Y. (2022). Coupling between cerebrovascular oscillations and CSF flow fluctuations during wakefulness: An fMRI study. Journal of Cerebral Blood Flow and Metabolism. https://doi.org/10.1177/0271678X221074639

Poster No 2573

Reciprocal causation relationship between rumination and sleep quality: a resting-state fMRI study

Shiyan Yang[1,2], Xu Lei[1,2]

[1]Sleep and NeuroImaging Center, Faculty of Psychology, Southwest University, Chongqing, China, [2]Key Laboratory of Cognition and Personality (Southwest University), Ministry of Education, chongqing, China

Introduction: Rumination thinking is a type of negative repetitive thinking, a tendency to constantly focus on the causes, consequences and other aspects of negative events, which has implications for a variety of psychiatric disorders. Previous studies have confirmed a strong association between rumination thinking and poor sleep or insomnia, but the direction of causality between the two is not entirely clear. In this study, we investigated the direction of causality between rumination thinking and sleep quality by constructing a cross-lagged model using a longitudinal study with a two-year interval and explored the possible brain-neurological basis of the association using resting-state functional magnetic resonance imaging(fMRI) data.

Methods: Participants were 373 current university students (males: n = 84,8.67±0.76 years old) who completed the Ruminative Responses Scale (RRS) and the Pittsburgh Sleep Quality Index (PSQI) at two time points and had resting-state MRI data collected. First, descriptive statistics and Pearson correlation analysis were performed on the questionnaires at each time point, followed by the construction of a cross-lagged model to explore the causal relationship; Then, the precuneus (x=0, y=-53, z=61 mm) was selected as the seed point based on previous literature, and the average correlation coefficient between the precuneus and whole-brain voxels were normalized to z-scores using Fisher's r-to-z transformation(zFC, z-transformed functional connectivity), to further explore the neural basis of the mutual influence of rumination thinking and sleep quality, the bivariate correlation was calculated between three variables (zFC of the precuneus and whole brain, sleep quality, and rumination thinking), and then the mediation analysis was conducted using PROCESS, with gender and FD (frame-wise displacement, a head motion parameter) as covariables. In the mediation modeling process, X was FC, the mediating variable was PSQI or RRS score at time 1, and Y was PSQI or RRS score at time 2.

Results: The results of the cross-lagged model analysis indicate that sleep quality predicts rumination both concurrently (β=0.34, p<0.001; β=0.17, p<0.01) and across time (β=0.16, p<0.01); similarly, rumination predicts sleep quality both concurrently and across time (β=0.15, p<0.01). We processed partial correlation analysis of the zFC of the precuneus and whole-brain voxels with the scale scores at T1, and the results showed that FC of the precuneus and the lingual gyrus (x=10, y=-88, z=-10) was significantly negatively correlated with RRS_T1 scores (r=-0.251, p<0.001), and not significantly negatively correlated with PSQI_T1 scores (r=-0.089, p=0.112). Considering the cross path of TI rumination thinking affecting T2 sleep quality in the cross-lag model, partial correlation analysis was also conducted between the FC and T2 sleep quality, and the results showed that the FC was significantly negatively correlated with PSQI_T2 scores (r=-0.12, p<0.05). The mediation results showed that T1 rumination plays a fully mediating role between FC of Precuneus-Lingual_R and T2 sleep quality, after regressed out the gender, age and FD, the total effect (c=-2.476, SE=1.147, 95%CI=[-4.7319, -.2202]) and the indirect effect(a×b=-1.753, SE=0.501, 95%CI=[-2.8318, -.8526]) are significant, and a nonsignificant direct effect (c=0.723, SE=1.121, 95%CI=[-2.9282, 1.4822]).

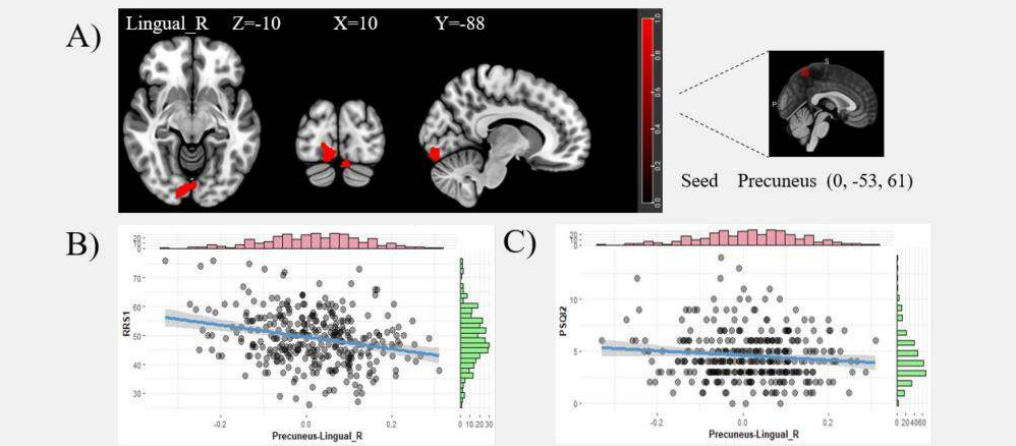

Figure 3. (A)With the Precuneus as the seed point, the right lingual gyrus is the brain region with significant FC related to rumination, GRF corrected(voxel *p* value<0.005, cluster *p* value<0.05); (B) Relationship between the FC of Precuneus-Lingual_R and RRS scores in Time 1;(C) Relationship between the FC of precuneus-Lingual_R and PSQI scores in Time 2. The gray dots represent the data of each participant and the blue line refers to the fitting line (the shadow refers to the 95 % confidence interval). The pink bars in (B) and (C) illustrate the distribution of Precuneus-Lingual_R. The green bars in (B) illustrate the distribution of rumination thinking score of RRS and the green bars in (C) illustrate the distribution of subjective sleep quality score of PSQI. (Note: FC: functional connectivity)

Conclusions: rumination thinking and sleep quality are causally related in a bidirectional manner; and the FC of the precuneus and lingual gyrus may be the neural basis for rumination thinking to predict sleep quality.

References

1. Baker, L. D., Baldwin, D. S., & Garner, M. (2015). Daytime intrusive thoughts and subjective insomnia symptoms. Psychiatry Research, 229(3), 1038-1042.
2. Buysse, D. J., Reynolds, C. F., Monk, T. H., Berman, S. R., & Kupfer, D. J. (1989). The Pittsburgh Sleep Quality Index: a new instrument for psychiatric practice and research. Psychiatry Research, 28(2), 193-213.
3. Harvey, A. G. (2002). A cognitive model of insomnia. Behaviour Research and Therapy, 40(8), 869-893.
4. Ma, L., & Zhang, C. (2021). The Function and Structure of Precuneus Is Associated With Subjective Sleep Quality in Major Depression. Frontiers In Psychiatry, 12, 831524.
5. Nolen-Hoeksema, S., Wisco, B. E., & Lyubomirsky, S. (2008). Rethinking Rumination. Perspectives On Psychological Science : a Journal of the Association For Psychological Science, 3(5), 400-424.
6. Wang, L., Wang, K., Liu, J.-H., & Wang, Y.-P. (2018). Altered Default Mode and Sensorimotor Network Connectivity With Striatal Subregions in Primary Insomnia: A Resting-State Multi-Band fMRI Study. Frontiers In Neuroscience, 12, 917.
7. Tang, N. K. Y., & Harvey, A. G. (2004). Effects of cognitive arousal and physiological arousal on sleep perception. Sleep, 27(1), 69-78.

Poster No 2574

Associations between sleep, brain, and cognitive performance using the ENIGMA-Sleep data

Hanwen Bi[1,2], Robin Bülow[3], Michele Deantoni[4], David Elmenhorst[5,6,7], Eva-Maria Elmenhorst[8,9], Ralf Ewert[10], Fabio Ferrarelli[11], Stefan Frenzel[12], Hans Grabe[12,13], Felix Hoffstaedter[1,2], Neda Jahanshad[14], Ahmadreza Keihani[11], Vincent Küppers[6,1], Ahmad Mayeli[11], Nasrin Mortazavi[4], Gustav Nilsonne[15,16], Julia Rupp[11], Amin Saberi[17,1,2], Christina Schmidt[4,18], Kai Spiegelhalder[19], Sandra Tamm[15,16], Sophia Thomopoulos[14], Paul Thompson[14], Sofie Valk[17,1,2], Gilles Vandewalle[4], Antoine Weihs[12,13], Joseph Wexler[20,15], Katharina Wittfeld[12], Simon Eickhoff[1,2], Kaustubh Patil[1,2], Federico Raimondo[1,2], Masoud Tahmasian[1,2,6]

[1]Institute of Neuroscience and Medicine, Brain and Behaviour (INM-7), Research Center Jülich, Jülich, Germany, [2]Institute of Systems Neuroscience, Medical Faculty and University Hospital Düsseldorf; Heinrich Heine University, Düsseldorf, Germany, [3]Institute of Diagnostic Radiology and Neuroradiology, University Medicine Greifswald, Greifswald, Germany, [4]GIGA-Institute, Cyclotron Research Center/In Vivo Imaging, Sleep and Chronobiology Lab, University of Liège, Liège, Belgium, [5]Research Center Jülich, Research Center Jülich, Jülich, Germany, [6]Department of Nuclear Medicine, Faculty of Medicine, University Hospital Cologne, University of Cologne, Cologne, Germany, [7]Division of Medical Psychology, Rheinische Friedrich-Wilhelms-University Bonn, Bonn, Germany, [8]Department of Sleep and Human Factors Research, German Aerospace Center, Cologne, Germany, [9]Institute for Occupational, Social and Environmental Medicine, Medical Faculty, RWTH Aachen University, Aachen, Germany, [10]Internal Medicine B, Pneumology, University Medicine Greifswald, Greifswald, Germany, [11]Department of Psychiatry, University of Pittsburgh, Pittsburgh, PA, USA, [12]Department of Psychiatry and Psychotherapy, University Medicine Greifswald, Greifswald, Germany, [13]German Center for Neurodegenerative Diseases (DZNE), Greifswald, Germany, [14]Imaging Genetics Center, Keck School of Medicine of University of Southern California, Los Angeles, CA, USA, [15]Department of Clinical Neuroscience, Karolinska Institutet, Stockholm, Sweden, [16]Department of Psychology, Stress Research Institute, Stockholm University, Stockholm, Sweden, [17]Otto Hahn Research Group for Cognitive Neurogenetics, Max Planck Institute for Human Cognitive and Brain Sciences, Leipzig, Germany, [18]Psychology and Neuroscience of Cognition Research Unit, Faculty of Psychology and Educational Sciences, University of Liège, Liège, Belgium, [19]Department of Psychiatry and Psychotherapy, Medical Center - University of Freiburg, Faculty of Medicine, University of Freiburg, Freiburg im Breisgau, Germany, [20]Department of Psychology, Stanford University, Stanford, CA, USA

Introduction: Sleep disturbances potentially exacerbate cognitive decline and dementia[1,2], necessitating large-scale studies to explore the neurobiological interplay between sleep and cognitive performance. While previous studies highlighted a non-linear relationship between sleep duration and cognitive performance, their effect size was small[3,4], they used group comparison statistical approaches, focused on subjective sleep assessment, and were limited to a particular sample, limiting the generalizability of their findings in other samples. Machine learning (ML) methods enable individual-level predictions and can validate models on unseen data, providing a more robust analytical framework. Here, we performed ML analysis based on objective and subjective sleep measurements and brain structure data from the ENIGMA-Sleep working group[5] to predict cognitive performance.

Methods: A total of 1,023 participants from SHIP-Trend[6] Greifswald (N=831) and Liege[7] (N=192) have been included. Sleep measurements were sleep duration and sleep efficiency extracted from Polysomnography data and Pittsburgh Sleep Quality Index. Cognitive performance was measured using Stroop scores (SHIP-Trend and Liege) and N-back working memory (Liege). Subcortical volumes derived from the Aseg atlas via FreeSurfer for brain structure data[8]. In addition, age, sex, BMI, and depressive symptoms (Beck Depression Inventory-II) scores were added as model input as demographic/behavioral factors.

Three machine learning models were utilized in this study: the support vector machine (SVM) with RBF kernel, random forest (RF), and AutoGluon[9]. These models were trained on the SHIP-Trend and Liege datasets separately using nested cross-validation, with the performance metrics being derived from the average results across this process (Figure 1A). Out-of-sample predictions were conducted by applying the models, which were trained on the SHIP-Trend dataset, to the Liege dataset (Figure 1B). The performance of ML models was evaluated by mean absolute error, mean squared error, R2, and Pearson correlation. Different feature combinations of sleep measurement, subcortical volume, and demographic/behavioral factors were used as model inputs. SHAP toolbox[10] was utilized for model explanation, elucidating the importance and influence of various features on the predictions.

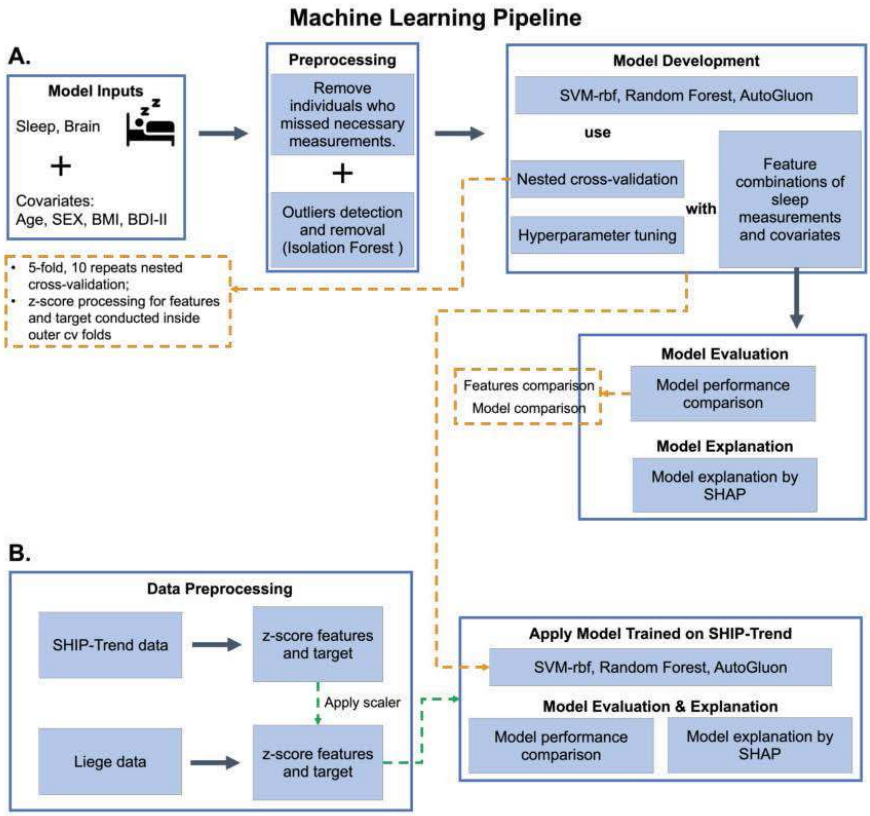

Figure 1: Machine learning pipeline for cognitive performance prediction in SHIP-Trend and Liege datasets. A: Before model development, datasets were preprocessed by removing individuals who missed necessary measurements and outliers. Support vector machine (SVM) with RBF kernel, random forest (RF), and AutoGluon were used as the machine learning models for prediction. Hyperparameters were tuned in the inner cross-validation (cv) of nested cv. Different feature combinations of sleep measurement, subcortical volume, and covariates were used as model inputs. Features and targets were standardized using z-score in a CV-consistent manner. B: Pipeline for out-of-sample prediction by applying models trained on SHIP-Trend dataset to Liege dataset. First get z-score scaler from SHIP-Trend dataset then apply on Liege dataset. Then apply the models trained on SHIP-Trend dataset to predict Stroop interference score.

Results: Sleep measurements and covariates predicted Stroop reaction times in SHIP-Trend (AutoGluon: R2=0.1308, Pearson correlation=0.3812) and interference scores in Liege (AutoGluon: R2=0.2716, Pearson correlation=0.5593) using SVM, RF, and AutoGluon (Figure 2A). The best performance was achieved when using sleep measurement, subcortical volumes, and covariates together in the SHIP-Trend dataset (AutoGluon: R2=0.1409, Pearson correlation=0.3959) (Figure 2B). In the out-of-sample validation using the AutoGluon model, although there was a strong correlation between the predicted values and the actual Stroop interference scores in the Liege dataset (Pearson correlation=0.4186) (Figure 2C), the R2 was adversely affected due to the differing scales of Stroop interference scores between the SHIP-Trend and Liege datasets. Across all models and both datasets, age emerged as a key predictive feature (Figure 2D). However, in the Liege dataset, the models were unable to predict working memory accuracy.

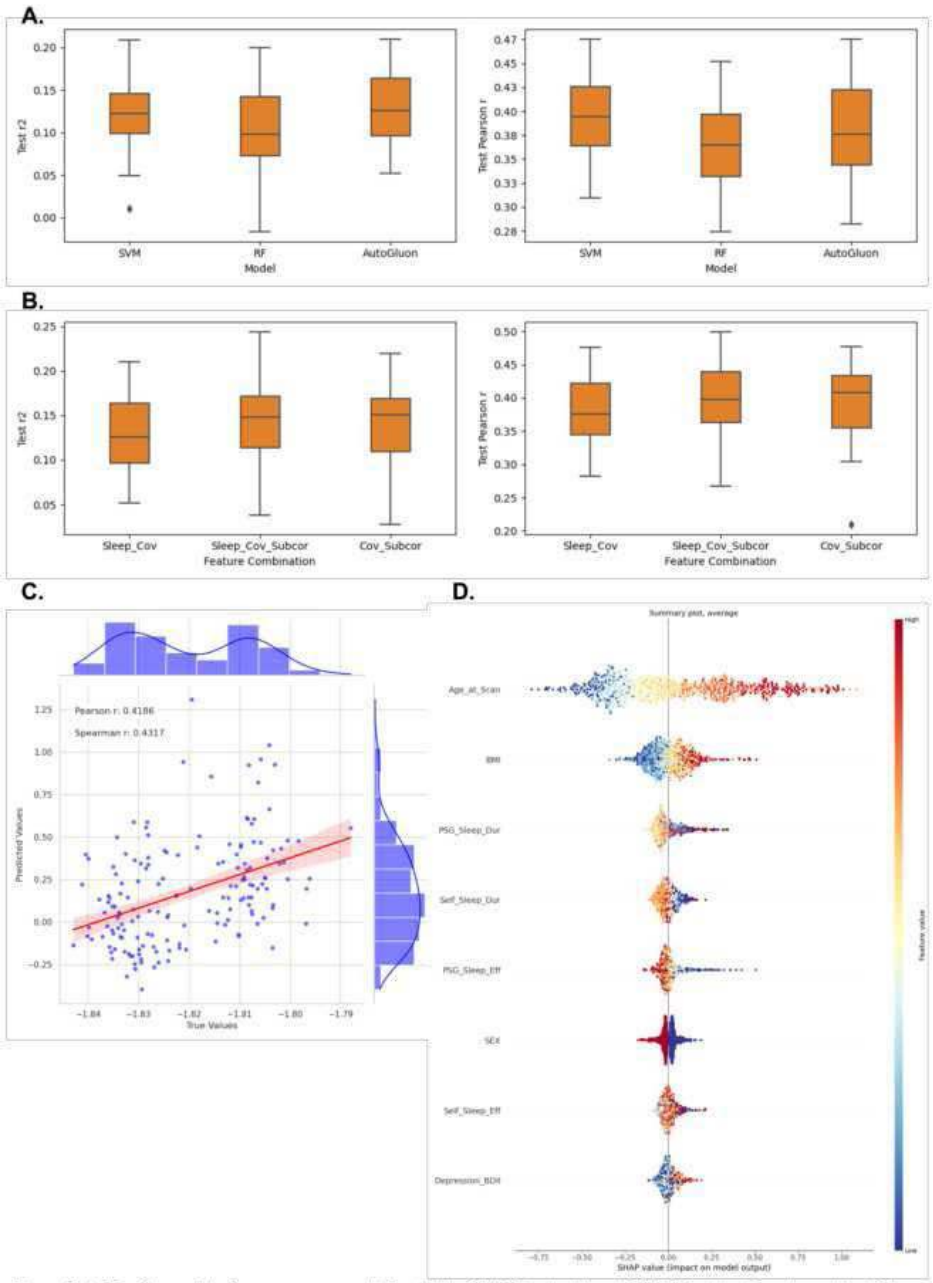

Figure 2: A: For Stroop interference score prediction in the SHIP-Trend dataset, SVM, Random Forest, and AutoGluon showed the successful prediction referring to the R2 and correlation score; B: Stroop interference score can be predicted by AutoGluon in the SHIP-Trend dataset with sleep measurements, subcortical volume, demographic and depression data; C: Since the scale of Stroop interference score in SHIP-Trend and Liege dataset is different, the out-of-sample prediction by trained AutoGluon showed good correlation between the predicted value and true target but bad R2. D: Age is the most important feature.

Conclusions: Although the predictive strength is modest, non-linear ML models have a consistent and stable capacity to predict Stroop interference and reaction time scores using our input features across both samples. The SHAP findings showed that age was the most important contributing factor to our predictive model. Particularly, older individuals exhibiting shorter sleep durations and younger individuals with longer sleep durations contribute to prediction, indicating the complex relationships between sleep, brain, and aging to predict cognitive function at the individual subject level.

References

1. Emamian, F. et al. The Association Between Obstructive Sleep Apnea and Alzheimer's Disease: A Meta-Analysis Perspective. Frontiers in Aging Neuroscience 8, (2016).
2. Koren, T., Fisher, E., Webster, L., Livingston, G. & Rapaport, P. Prevalence of sleep disturbances in people with dementia living in the community: A systematic review and meta-analysis. Ageing Research Reviews 83, 101782 (2023).
3. Kyle, S. D. et al. Sleep and cognitive performance: cross-sectional associations in the UK Biobank. Sleep Medicine 38, 85–91 (2017).
4. Li, Y. et al. The brain structure and genetic mechanisms underlying the nonlinear association between sleep duration, cognition and mental health. Nat Aging 2, 425–437 (2022).
5. Tahmasian, M. et al. ENIGMA-Sleep: Challenges, opportunities, and the road map. J. Sleep Res. 30, (2021).

6. Völzke, H. et al. Cohort Profile Update: The Study of Health in Pomerania (SHIP). International Journal of Epidemiology 51, e372–e383 (2022).
7. Deantoni, M. et al. Association between sleep slow-wave activity and in-vivo estimates of myelin in healthy young men. NeuroImage 272, 120045 (2023).
8. Fischl, B. et al. Whole Brain Segmentation: Automated Labeling of Neuroanatomical Structures in the Human Brain. Neuron 33, 341–355 (2002).
9. Erickson, N. et al. AutoGluon-Tabular: Robust and Accurate AutoML for Structured Data. Preprint at http://arxiv.org/abs/2003.06505 (2020).
10. Lundberg, S. M. & Lee, S.-I. A unified approach to interpreting model predictions. in Proceedings of the 31st International Conference on Neural Information Processing Systems 4768–4777 (Curran Associates Inc., 2017).

Poster No 2575

Exploring sleep problem, cognitive function, and frontal surface using human connectome project

Chung-I Su[1], Ya-Chuan Huang[2], Ting-Ting Chang[1,2], Shang-Yueh Tsai[1,3], Chien-Ming Yang[1,2]

[1]Research Center for Mind, Brain, and Learning, National Chengchi University, Taipei, Taiwan, [2]Department of Psychology, National Chengchi University, Taipei, Taiwan, [3]Graduate Institute of Applied Physics, National Chengchi University, Taipei, Taiwan

Introduction: It has been documented that shorter sleep duration and increased sleep problems reduce individuals' general cognitive function and volumetric subcortical structures (Fjell et al., 2023). However, different cognitive domains may exhibit different associations with sleep. Utilizing the HCP dataset, the present study aims to elucidate whether specific cognitive domains are particularly vulnerable to variations in sleep duration and problems, and whether these cognitive changes correspond to noticeable brain structure alterations.

Methods: The sleep indexes, cognitive performances, and brain structural measurements were acquired from the HCP Young Adult 1200 Subject Data Release at https://db.humanconnectome.org/data/projects/HCP_1200. Figure 1 lists the participant selection criteria for the present study. In sleep group analyses, 666 participants fulfilled the classification criteria, and no missing data on cognitive and brain measurements were included. Participants were screened into four groups based on responses from the Pittsburgh Sleep Quality Index (PSQI) in sleep duration (short ≤ 6 hours vs. recommended 7~8 hours) and sleep problems (none vs. multiple), following the same criteria used by Fjell et al. (2023). Different cognitive functions were accessed based on age-adjusted scores on different tasks of the NIH toolbox. The Crystallized cognitive score represented the averaging of the two language tasks (Picture Vocabulary and Reading Recognition), Fluid cognitive score represented the averaging of five other tasks (Flanker, Dimensional Change Card Sort, Picture Sequence Memory, List Sorting and Pattern Comparison, and Pattern Completion), and individual score for each task were included in analyses. Among global/regional cortical/subcortical morphometric measurements, only several cortical frontal surface areas were included as the regions of interest due to their roles in higher cognitive functions, including superior frontal, rostral, and caudal middle frontal, lateral, and medial orbitofrontal, pars opercularis, triangularis, and orbitalis areas. In sleep group analyses, including four sleep groups: Short sleep & No sleep problem (SN), Short sleep & Multiple sleep problems (SM), Recommended sleep & No sleep problem (RN), and Recommended sleep & Multiple sleep problems (RM), and multiple comparisons were conducted to examine group differences in cognitive performances and frontal surface areas. In mediation analyses, 1096 participants with no missing data were included to examine whether significant frontal surface areas mediate the associations between sleep duration or problems with the crystallized cognitive score.

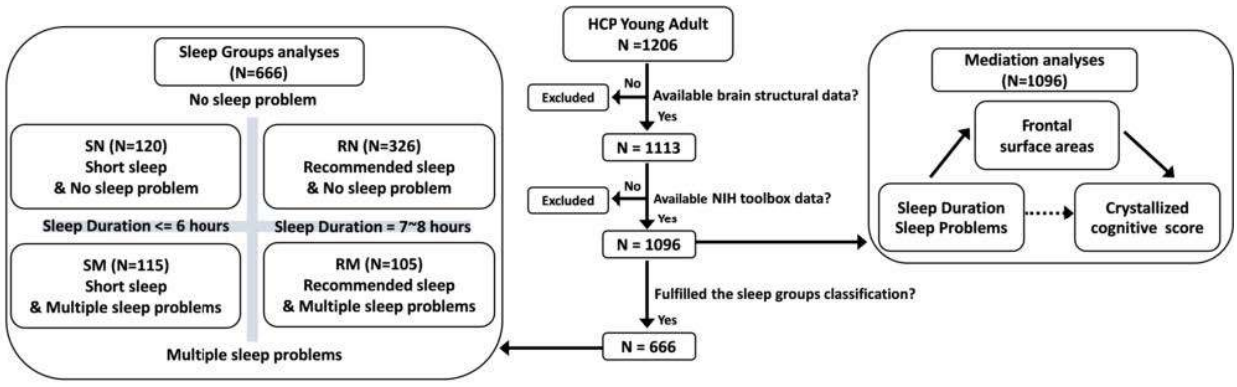

Figure 1. Participant selection criteria.

Results: Among short sleepers (SM vs. SN), SM demonstrated significantly lower cognitive performance in picture vocabulary (t=-4.43, p=.036), reading recognition (t=-4.86, p=.019), and crystallized cognitive score (t=-5.74, p=.016). A similar pattern of results was observed in comparisons between recommended sleepers (RM vs. RN), with t=-3.89 & p=.016, t=-5.14 & p<.001, and t=-5.75 & p<.001, respectively. Among frontal surface areas, significant differences between groups were observed only among short sleepers, with SM showing significant reductions in left and right superior frontal (t=-283.73, p=.009; t=-233.34, p=.035), left caudal middle frontal (t=-115.95, p=.034), right lateral orbitofrontal (t= -99.29, p=.017), and right pars opercularis areas (t=-63.15, p=.04). Mediation analyses revealed that specific frontal surface areas significantly mediate the associations between sleep duration or problems and crystallized cognitive scores (see Figure 2).

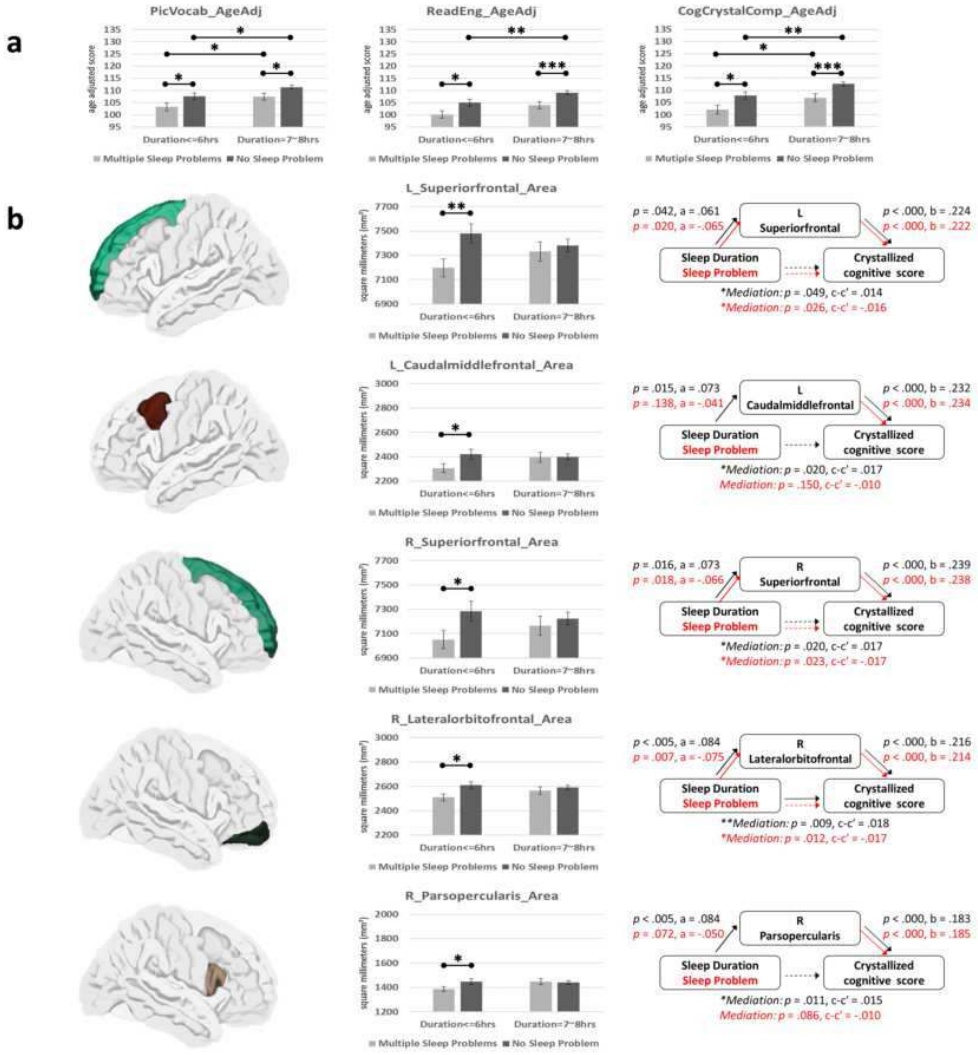

Figure 2. Summary of the results. a, cognitive tasks showed significant differences across groups. b, brain frontal surface areas showed significant differences across groups, and the results of mediation analyses with sleep duration (in black) or problems (in red) as the independent variable, each significant frontal surface area as the mediator, and the crystallized cognitive score as the dependent variable. The template of cortical parcellation generated by Freesurfer. *p ≤ .05; **p ≤ .01; ***p ≤ .001.

Conclusions: Sleep problems adversely impact crystallized cognitive functions regardless of variations in sleep duration, while a sleep duration below 6 hours is linked to reduced frontal surface areas. To further understand these differences, future studies should explore underling mechanisms and investigate additional sleep indexes as potential brain health markers.

References

1. Fjell, A. (2023), 'Is short sleep bad for the brain? Brain structure and cognitive function in short sleepers', Journal of Neuroscience, vol. 43, no. 28, pp 5241-5250.

Poster No 2576

Cerebrospinal fluid dynamics are coupled to sleep brain oscillations during NREM and REM sleep

Makoto Uji[1], Xuemei Li[1], An Saotome[1,2], Ryosuke Katsumata[1,3], Chisato Suzuki[1], Kenichi Ueno[1], Sayaka Aritake[1,2], Masako Tamaki[1,4]

[1]RIKEN Center for Brain Science, Wako, Japan, [2]Saitama Prefectural University, Saitama, Japan, [3]Chiba University, Chiba, Japan, [4]RIKEN Cluster for Pioneering Research, Wako, Japan

Introduction: While cerebrospinal fluid (CSF) dynamics during sleep have recently been implicated in cleansing metabolic waste products in animals[1], how CSF is modulated with neural activities and events during deep NREM and REM sleep in humans[2] remains unclear. Previous studies in human subjects have shown that CSF fluctuations during light NREM sleep are coupled with K-complexes, a type of slow oscillations typically associated with arousals[3,4]. CSF during REM sleep has never been investigated in animals or humans. Does an arousal mechanism solely contribute to CSF dynamics or are any sleep-specific neural processes also linked to fluid changes during NREM and REM sleep? Our recent data revealed that deep NREM and REM sleep involved faster frequency components (0.06-0.12Hz and >0.12Hz) in CSF signals (Fig.1)[5], suggesting that abundant brain oscillations and events during deep stable sleep may play a crucial role in CSF dynamics and a waste clearance mechanism. In the present study we investigate whether sleep-specific brain oscillations and events during stable NREM and REM sleep are in fact associated with CSF dynamics in human subjects.

Methods: 25 healthy subjects (15 females, mean 23.6±4.8 years old) participated in two 90-min early afternoon naps with polysomnography (PSG) in a 3T Siemens Prisma MRI scanner. MRI data were acquired using a sparse GE-EPI sequence (TR/TE=3000/30ms, FA=85°, Multiband=3, 42 transverse slices, voxel size = 3x3x3mm3, 1800 volumes, B1+RMS=0.5μT, MR acquisition time=0.9s, quiet period=2.1s)[6]. An anatomical image, respiration and heartbeat signals were also acquired. PSG data were corrected for gradient and pulse artefacts[7]. Sleep stages were scored into wakefulness (stage W), NREM sleep stages 1-3 (N1-N3), and REM sleep. Events during sleep, including sleep spindles, slow-oscillations, rapid eye movements (REMs), and sawtooth waves were detected. Epochs containing arousals or motion artifacts were removed from further analyses. MRI data were denoised using cardiac and respiration, motion corrected, normalized, and averaged across all voxels in the lateral ventricles as CSF signals. CSF signals (0 to 30s) were baseline corrected (-9 to 0s) to investigate CSF changes for each sleep event.

Results: The average sleep duration was 69.6±20.7 min and the proportion of each stage was 22.5%, 28.6%, 34.3%, 12.3%, and 2.4% for stages W, N1, N2, N3, and REM sleep, respectively. The interval of each sleep event showed that slow oscillations occurred every 43s during N2 and 6s during N3. Sleep spindles occurred every 5-6s during N2 and N3. REMs and sawtooth waves occurred every 8s during REM sleep (Fig.2). These intervals corresponded to frequency profiles in the CSF signals that we previously reported (faster frequency components,[5]). We next found that a large CSF fluctuation was induced at 8s after the onset of slow oscillations detected from N2. Slow oscillations during N3, which occurred more abundantly than N2, accompanied a smaller CSF peak at 5.5s after the onset (Fig.2A1). Additionally, sleep spindles also induced CSF fluctuation at 3-4s after the onset, lasting for about 20s (Fig.2A2). We further found that REM events and sawtooth waves during REM sleep coupled to CSF fluctuations, inducing fluctuations at 20s after the onset of the events (Fig.2A3).

Conclusions: Our results demonstrate that sleep brain oscillations and events, such as slow oscillations and spindles during NREM sleep, and REMs and sawtooth waves during REM sleep, are indeed coupled to CSF signal fluctuations. This study reveals CSF signals are dynamically varied across different sleep depths and that CSF signal changes are coordinated with sleep-specific neural activities. These brain oscillations and events during deep NREM and REM sleep, associated with neural plasticity processes, may also play an essential role in a waste clearance mechanism for healthy brain functions in humans.

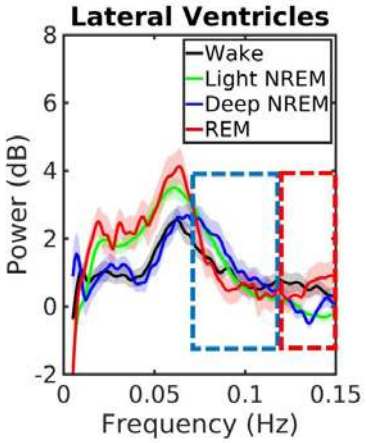

Figure 1. Group (n=25) mean (+SE) CSF signal periodic power spectral density (PSD) across all sleep stages (Wake, Light NREM (N1 & N2), Deep NREM (N3), REM) in the lateral ventricles. Slow component frequency (<0.06Hz) power of CSF signals measured from the lateral ventricles during light NREM was significantly larger than Wake or deep NREM ($p<0.05$). Fast component frequency (0.06-0.12Hz) power in the lateral ventricles during deep NREM was significantly larger than Wake, light NREM, and REM (blue box, $p<0.05$). During REM, very fast component frequency (>0.12Hz) power in CSF was significantly larger than light NREM (red box, $p<0.05$), as well as the slow component frequency (<0.06Hz) power was significantly larger than wake and deep NREM ($p < 0.05$).

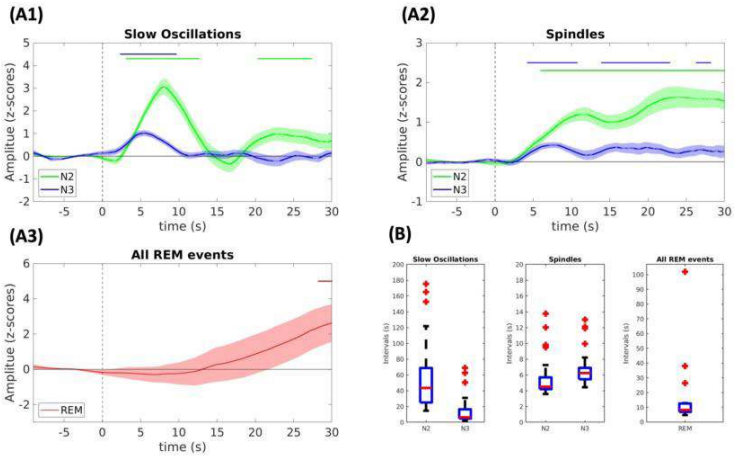

Figure 2. (A) Group (n=25) mean (+SE) fMRI signal time-courses locked to sleep event onsets in the lateral ventricles. (**A1**) time-courses related to slow oscillation onsets. (**A2**) time-courses related to spindle onsets. (**A3**) time-courses related to all REM event onsets including rapid eye movement events and sawtooth waves. The horizontal bars represent significances (FDR corrected $p<0.05$).
(B) Box plots demonstrating time intervals for slow oscillations (Left), spindles (Middle), and all REM events including rapid eye movement (REM) events and sawtooth events (Right).

References

1. Xie, L., Kang, H., Xu, Q., Chen, M.J., Liao, Y., Meenakshisundaram, T., O'Donnell, J., Christensen, D.J., Nicholson, C., Iliff, J.J., Takano, T., Deane, R., Nedergaard, M. (2013) Sleep drives interstitial metabolite clearance from the adult brain. Science 342:373–377. https://doi.org/10.1126/science.1241224
2. Uji, M., Tamaki, M. (2023). Sleep, learning, and memory in human research using noninvasive neuroimaging techniques. Neuroscience Research. https://doi.org/10.1016/j.neures.2022.12.013
3. Fultz, N.E., Bonmassar, G., Setsompop, K., Stickgold, R.A., Rosen, B.R., Polimeni, J.R., & Lewis, L.D. (2019). Coupled electrophysiological, hemodynamic, and cerebrospinal fluid oscillations in human sleep. Science, 366(6465), 628-631. https://doi.org/10.1126/science.aax5440
4. Picchioni, D., Özbay, P. S., Mandelkow, H., de Zwart, J. A., Wang, Y., van Gelderen, P., & Duyn, J. H. (2022). Autonomic arousals contribute to brain fluid pulsations during sleep. NeuroImage, 249, 118888. https://doi.org/10.1016/j.neuroimage.2022.118888
5. Uji, M., Li, X., Saotome, A., Katsumata, R., Aritake, S., Suzuki, C., Ueno, K., M. Tamaki, M. (2023). Cerebrospinal fluid dynamics during NREM and REM sleep by a simultaneous sparse-fMRI and EEG method. OHBM 2023 in Montreal, Canada.
6. Uji, M., Wilson, R., Francis, S.T., Mullinger, K.J., & Mayhew, S.D. (2018). Exploring the advantages of multiband fMRI with simultaneous EEG to investigate coupling between gamma frequency neural activity and the BOLD response in humans. Human Brain Mapping, 39(4), 1673-1687. https://doi.org/10.1002/hbm.23943
7. Warbrick, T. (2022). Simultaneous EEG-fMRI: What Have We Learned and What Does the Future Hold? Sensors, 22(6), 2262. https://doi.org/10.3390/s22062262

Poster No 2577

Locus Coeruleus Activity during Wake Is Associated with Rapid Eye Movement Sleep Intensity

Nasrin Mortazavi[1], Ekaterina Koshmanova[1], Roya Sharifpour[1], Alexandre Berger[2,3], Elise Beckers[1,4], Islay Campbell[1], Ilenia Paparella[1], Fermin Aizpurua[1], Laurent Lamalle[1], Puneet Talwar[1], Siya Sherif[1], Gilles Vandewalle[1]

[1]Sleep and Chronobiology Lab, GIGA-Institute, CRC-In Vivo Imaging Unit, University of Liège, Liège, Belgium, [2]Institute of Neuroscience (IoNS), Université Catholique de Louvain (UCLouvain), Brussels, Belgium, [3]Synergia Medical SA, Mont-Saint-Guibert, Belgium, [4]Faculty of Health, Medicine and Life Sciences, School for Mental Health and Neuroscience, Alzheimer Centre Limburg, Maastricht University, Maastricht, Netherlands

Introduction: The locus coeruleus (LC) is the main source of norepinephrine in the brain (Szabadi, 2013). The LC contributes to the transition between sleep and wakefulness, and between slow wave sleep (SWS) and rapid eye movement sleep (REMS) (Cirelli et al., 2005). It is tightly linked to the oscillatory modes found during sleep, such as sleep spindles and slow waves in animals (Eschenko et al., 2012). While the LC appears to be an important structure for sleep, only a few imaging studies evaluated whether the LC is related to sleep variability due to the difficulty of imaging such a small size nucleus in vivo (Keren et al., 2009). We aimed to investigate the link between LC activity during wakefulness assessed by 7-Tesla MRI and electroencephalogram (EEG) features of sleep. To trigger a response of the LC, we used a visual perceptual rivalry task and an auditory attentional task. Subjects saw an ambiguous stimulus which could trigger spontaneous switches between two perceptions of the same image (Blake et al., 2002). Switches are considered to recruit the LC (Einhauser et al., 2008; Murphy et al., 2014). Participants also did an auditory oddball task, which can activate LC (Murphy et al., 2014).

Methods: 52 healthy volunteers, including 33 young (22.3 ± 3.2 y; 28 women) and 19 late middle-aged (61.05 ± 5.3 y; 14 women) individuals completed the protocol. They first underwent a structural 7T MRI session, which allowed collecting high-resolution whole-brain T1-weighted images as well as magnetization transfer-weighted turbo-flash (MT-TFL) sequence over a 6 cm slab placed around the LC. The latter was used to create an individual LC-mask in the brain space of each participant. All individual LC-masks were gathered into a probabilistic LC-mask in a standardized group brain space. Following 1 week of regular sleep times, participants completed an fMRI session in the morning, 2h to 3h after wake-up time, during which they were administered the perceptual rivalry task and oddball task (TR= 2.34s; voxel size 1.4x1.4x1.4 mm^3). Participant's habitual and baseline sleep was recorded in-lab under EEG to extract 4 sleep features of interest depicting some of the most canonical characteristics of sleep (i.e., cumulated power of the theta frequency band during REMS, slow wave energy (SWE), sleep onset latency, and REMS percentage). We computed a general linear model by the Statistical Parametric Mapping 12 package (SPM12) over the entire brain in individual space. Subject level maps were normalized to MNI space for group statistic visualization. We then extracted the activity estimates over individual LC masks and then conducted generalized linear mixed models (GLMMs) to test for associations between the activity of the LC during both tasks and EEG features of sleep, including age, sex, BMI, and total sleep time as covariates.

Results: Inspection of whole brain group data identified increased activation within the left LC group template associated with perceptual switches (uncorrected $p<0.001$; $t > 3.27$) and the detection of the target sound of the oddball task (uncorrected $p<0.001$; $t >3.26$) (Figure 1). This supported the extraction of individual LC activity in the individual space to associate with sleep EEG metrics. GLMMs on the LC activity and sleep EEG metrics revealed a positive association between the left LC activity during perceptual rivalry task and EEG cumulated power of the theta frequency band (4-8Hz) during REMS ($p = 0.004$, $t=3.02$), which reflects the intensity of REMS. A negative association was found between the left LC activity during oddball task and this sleep metric in the older ($p = 0.024$, $t = -2.33$) but not in the younger group.

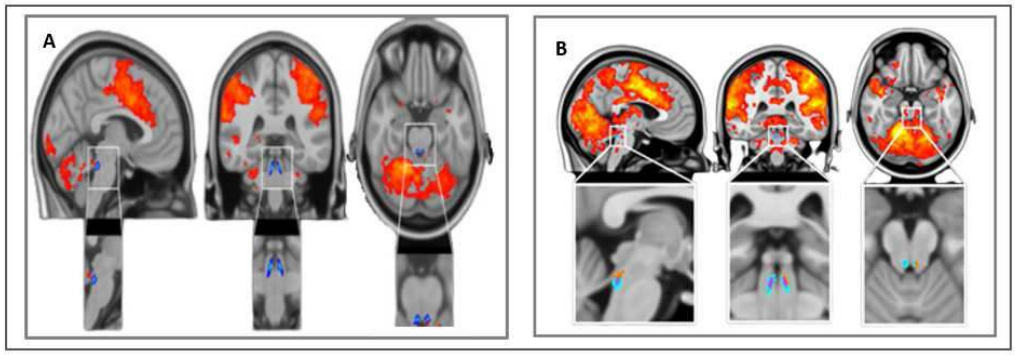

Figure 1. Locus coeruleus activity at perception switch during perceptual rivalry task (A) and oddball task (B)

(A) Top: whole-brain response to perceptual switches ($p < 0.001$ uncorrected, $t > 3.27$). Images at the bottom show the LC probabilistic template and the significant activation detected within this mask.
(B) Top: whole-brain response to the detection of the target sound ($p < 0.001$ uncorrected, $t > 3.26$). Images at the bottom show the LC probabilistic template and the significant activation detected within this mask.

The images are shown with the radiological convention for the orientation.

Conclusions: The results suggest that maybe there is an inverted U-shape relationship between LC activity during wakefulness and REMS intensity. These results contribute to the understanding of sleep physiology.

References

1. Blake, R. (2002) 'Visual competition', Nature Reviews Neuroscience, vol. 3, no.1, pp. 13–21.
2. Einhauser, W. (2008) 'Pupil dilation reflects perceptual selection and predicts subsequent stability in perceptual rivalry', Proceedings of the National Academy of Sciences, vol. 105, no. 5, pp. 1704–1709.
3. Eschenko, O. (2012) 'Noradrenergic neurons of the locus coeruleus are phase locked to cortical up-down states during sleep', Cerebral Cortex, vol. 22, no. 2, pp. 426–435.
4. Keren, N.I. (2009) 'In vivo mapping of the human locus coeruleus', NeuroImage, vol. 47, no. 4, pp. 1261–1267.
5. Murphy, P.R. (2014) 'Pupil diameter covaries with BOLD activity in human locus coeruleus', Human Brain Mapping, vol. 35, no. 8, pp. 4140–4154.
6. Szabadi, E. (2013) 'Functional neuroanatomy of the central noradrenergic system', Journal of Psychopharmacology, vol. 27, no. 8, pp. 659–693.

Acknowledgements

Funding: FNRS Belgium, ULiège, FEDER, Alzheimer Foundation (SAO-FRA), Wallonia-Brussels federation

Poster No 2578

Sleep disorders cause myelin reduction in gray matter mediated by glymphatic system dysfunction

Christina Andica[1,2], Koji Kamagata[2], Kaito Takabayashi[2], Zaimire Mahemuti[2], Akifumi Hagiwara[2], Shigeki Aoki[1,2]

[1]Faculty of Health Data Science, Juntendo University, Chiba, Japan, [2]Department of Radiology, Juntendo University, Tokyo, Japan

Introduction: Emerging evidence suggests that sleep deprivation alters gray matter (GM) microstructure (Voldsbekk, Bjornerud et al. 2022) and impairs the glymphatic system, a brain-wide perivascular network crucial for clearing central nervous system waste (Hablitz, Pla et al. 2020, Mestre, Mori et al. 2020), as indicated by the diffusion tensor Imaging analysis along the perivascular space (DTI-ALPS) index (Siow, Toh et al. 2022). Nevertheless, the relationship between GM microstructural changes and with glymphatic efficiency in sleep disorders, remain elusive. Our proposed study aims to utilize magnetization transfer (MT) imaging and neurite orientation dispersion and density imaging (NODDI) to elucidate the GM microstructural changes, and the DTI-ALPS index to assess glymphatic function in older adults with sleep disorders.

Methods: In the present study, we evaluated 50 individuals with sleep disorders (24 males; aged 71.08 ± 4.69 years; Pittsburgh sleep quality index [PSQI] >5] and 50 individuals without sleep disorders [24 males; 73.04 ± aged 5.80 years; PSQI ≤5) who has participated in the Bunkyo Health Study (Someya, Tamura et al. 2019). MT imaging (to obtain myelin volume fraction

[MVF]) and diffusion-weighted imaging (to obtain NODDI metrics [b-values of 1000 and 2000 s/mm^2] and ALPS index [b-value of 1000 s/mm^2]) for all study participants were performed using a 3 T MAGNETOM Prisma system (Siemens Healthcare, Erlangen, Germany) equipped with a 64-channel head coil. GM was parcellated using the Desikan-Killiany atlas and overlaid onto the GM-based spatial statistics skeleton (Ball, Srinivasan et al. 2013), to exclude any white matter and cerebrospinal fluid voxels. Median values for MVF, NDI, ODI, and ISO were measured from 34 cerebral cortices, cerebellar cortex, and seven subcortical regions on the left and right hemispheres (42 regions of interest [ROIs]). The ALPS index was calculated with a validated semiautomated pipeline (Taoka, Ito et al. 2022). The ALPS index, MVF, and NODDI measures (neurite density index [NDI], orientation dispersion index [ODI], and isotropic volume fraction [ISO]) were compared between groups using a general linear model (GLM), adjusting for age, sex, years of education, and intracranial volume as covariates. An false discovery rate (FDR)-corrected (42 ROIs) P-value <0.05 was considered significant. Multivariate linear regression (MLR), considering these covariates, assessed the relationship between the ALPS index and MVF in GM areas with significant differences between the sleep-disordered and non-sleep-disordered groups. Finally, the PROCESS Procedure for SPSS Version 4.2 was employed for mediation analysis to investigate the relationship between the PSQI, ALPS index, and GM MVF in those areas.

Results: Individuals with sleep disorders exhibited a significantly lower ALPS index (1.37 ± 0.17, P = 0.026) compared to those without sleep disorders (1.44 ± 0.16). Additionally, a significantly lower MVF, with FDR-corrected P-values ranging from 0.010 to 0.049, was also observed in the sleep-disordered group across GM regions (Table 1). MLR analyses demonstrated positive associations between the ALPS index and GM MVF values, with standardized β ranging from 0.313 to 0.639 (P = 0.00059 to 0.033). Mediation analysis revealed an indirect effect of the PSQI total on GM MVF mediated by the ALPS index in GM areas that were significant in the MLR analyses (Figure 1). However, GLM analysis showed no significant findings for NDI, ODI, and ISO. Moreover, MLR and mediation analyses yielded no significant results for individuals without sleep disorders.

Table 1. Comparison of myelin volume fraction in the gray matter regions where differences were observed between individuals without and with sleep disorders

Myelin volume fraction	Without sleep disorders		With sleep disorders		FDR-corrected *P*
	Mean	SD	Mean	SD	
Frontal lobe					
Caudal middle frontal	0.35	0.03	0.32	0.03	**0.010**
Lateral orbitofrontal	0.26	0.02	0.25	0.02	**0.023**
Medial orbitofrontal	0.27	0.02	0.26	0.02	**0.010**
Parstriangularis	0.25	0.02	0.24	0.02	**0.030**
Precentral	0.32	0.02	0.31	0.02	**0.028**
Superior frontal	0.32	0.03	0.30	0.03	**0.010**
Temporal lobe					
Banks of the superior temporal sulcus	0.23	0.02	0.21	0.02	**0.010**
Fusiform	0.21	0.01	0.20	0.01	**0.010**
Inferior Temporal	0.23	0.02	0.22	0.01	**0.017**
Middle temporal	0.23	0.02	0.22	0.01	**0.017**
Superior temporal	0.25	0.02	0.23	0.02	**0.017**
Parietal lobe					
Inferior parietal	0.24	0.02	0.22	0.02	**0.014**
Postcentral	0.28	0.02	0.27	0.02	**0.036**
Precuneus	0.21	0.02	0.20	0.02	**0.017**
Supramarginal	0.25	0.02	0.24	0.02	**0.038**
Occipital lobe					
Lateral occipital	0.23	0.02	0.21	0.02	**0.010**
Limbic regions					
Caudal anterior cingulate	0.27	0.02	0.25	0.02	**0.010**
Isthmus cingulate	0.21	0.02	0.20	0.02	**0.010**
Posterior cingulate	0.25	0.02	0.24	0.02	**0.010**
Rostral anterior cingulate	0.26	0.02	0.25	0.02	**0.011**
Insula	0.24	0.01	0.23	0.01	**0.014**
Deep gray matter					
Thalamus	0.21	0.01	0.20	0.01	**0.016**
Caudate	0.23	0.02	0.22	0.02	**0.028**
Putamen	0.23	0.01	0.22	0.01	**0.012**
Hippocampus	0.20	0.01	0.19	0.01	**0.036**
Cerebellum-Cortex	0.18	0.01	0.18	0.01	**0.049**

Abbreviations: FDR, family discovery rate; SD, standard deviation.

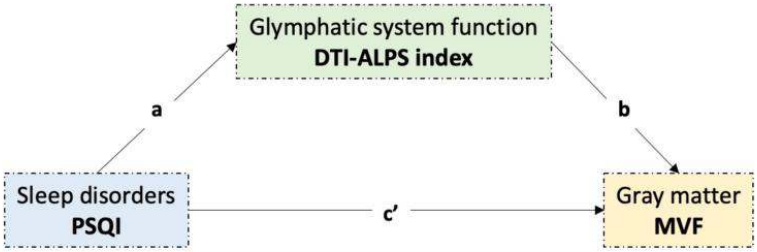

	a		b		Dirrect effect (c')		Indirect effect	
	Coefficient	P	Coefficient	P	Effect	P	Effect	CI
Caudal anterior cingulate	0.021	**0.041**	0.041	**0.024**	0.0009	0.506	0.0009	-0.0001–0.002
Inferior parietal	0.021	**0.041**	0.044	**0.008**	-0.002	0.193	0.0009	0.000–0.003
Isthmus cingulate	0.021	**0.041**	0.045	**0.0009**	0.0005	0.569	0.001	0.0001–0.002
Lateral occipital	0.021	**0.041**	0.060	**0.0005**	-0.0006	0.625	0.001	0.0001–0.003
Postcentral	0.021	**0.041**	0.042	**0.016**	0.0006	0.611	0.0009	-0.0001–0.002
Posterior cingulate	0.021	**0.041**	0.036	**0.015**	0.0005	0.671	0.0008	0.000–0.002
Precentral	0.021	**0.041**	0.038	**0.038**	0.001	0.421	0.0008	-0.0003–0.003
Precuneus	0.021	**0.041**	0.044	**0.003**	0.0001	0.959	0.0009	0.000–0.003
Superior frontal	0.021	**0.041**	0.051	**0.020**	0.0000	0.986	0.001	-0.0003–0.003
Superior temporal	0.021	**0.041**	0.036	**0.024**	0.0004	0.715	0.0008	0.000–0.002
Supra marginalis	0.021	**0.041**	0.038	**0.020**	0.0000	0.977	0.0008	-0.0001–0.002

Figure 2. Mediation analysis between sleep disorders, glymphatic function, and gray matter MVF in individuals with sleep disorders. *Abbreviations*: PSQI, Pittsburgh sleep quality index; DTI-ALPS, diffusion tensor Imaging analysis along the perivascular space; MVF, myelin volume fraction.

Conclusions: Our findings using multimodal MRI-based measures indicated that individuals with sleep disorders exhibited reduced diffusivity along perivascular spaces, as measured by the ALPS index, and showed demyelination in the GM, in contrast to those without such disorders. Mediation analysis also suggested glymphatic dysfunction as a possible mediator between sleep disorders and GM demyelination.

References

1. Ball, G. (2013), 'Development of cortical microstructure in the preterm human brain', Proc Natl Acad Sci USA, vol. 110, no. 23, pp. 9541-9546.
2. Hablitz, L. (2020), 'Circadian control of brain glymphatic and lymphatic fluid flow', Nat Commun, vol. 11, no. 1, pp. 4411.
3. Mestre, H. (2020), 'The Brain's Glymphatic System: Current Controversies', Trends Neurosci, vol. 43, no. 7, pp. 458-466.
4. Siow, T. Y. (2022), 'Association of Sleep, Neuropsychological Performance, and Gray Matter Volume With Glymphatic Function in Community-Dwelling Older Adults', Neurology, vol. 98, no. 8, pp. e829-e838.
5. Someya, Y. (2019), 'Skeletal muscle function and need for long-term care of urban elderly people in Japan (the Bunkyo Health Study): a prospective cohort study', BMJ Open, vol. 9, no. 9, pp. e031584.
6. Taoka, T. (2022), 'Reproducibility of diffusion tensor image analysis along the perivascular space (DTI-ALPS) for evaluating interstitial fluid diffusivity and glymphatic function: CHanges in Alps index on Multiple conditiON acqulsition eXperiment (CHAMONIX) study', Jpn J Radiol, vol. 40, no. 2, pp. 147-158.
7. Voldsbekk, I. (2022), 'Evidence for widespread alterations in cortical microstructure after 32 h of sleep deprivation', Transl Psychiatry, vol. 12, no. 1, pp. 161.

Poster No 2579

The dynamics of hemispheric global signal with the fluctuation of wakefulness during resting state

Xiangyu Kong[1], Gaolang Gong[1]

[1]State Key Laboratory of Cognitive Neuroscience and Learning & IDG/McGovern Institute for Brain Resea, Beijing, Beijing

Introduction: Wakefulness reflects responsiveness to external stimuli and internal consciousness, which is vital for understanding brain function[1,2]. Changes in wakefulness states accompany with alteration of brain activity, including the global signal (GS)[3,4]. Interestingly, such alteration showed distinct patterns between the left and right hemispheres during the wakefulness-to-sleep transition[5,6]. To date, it remains largely unknown whether and how the change of wakefulness states during non-sleeping conditions is associated with hemisphere-specific brain activity changes. This study was designed to systematically assess the dynamics of the GS within each hemisphere, along with the fluctuation of non-sleeping wakefulness during resting state.

Methods: The study used 7T dataset from the Human Connectome Project (HCP) S1200 release[7]. It includes 184 subjects with 723 resting-state fMRI scans and concurrent eye-tracking data. The eye-tracking data was processed following Gonzalez-Castillo et al, and resting-state fMRI data was preprocessed using the HCP minimal pipeline. As did previously[8], 30-second nonoverlap sliding windows were applied to calculate the percentage of eye closure (PERCLOS) as a quantitative measure of wakefulness. For each sliding time window, the hemispheric GS timeseries were derived by averaging preprocessed BOLD signals across all cortical vertices within each hemisphere. The global signal fluctuation (GSF) and global signal topography (GST) were then calculated[3,9]. A linear mixed model was applied to evaluate the main effects of PERCLOS and hemisphere, as well as their interaction effect, while controlling for age, sex, and handedness as covariates. Multiple comparison was corrected by permutation-based family-wise error method.

Results: As shown in Fig 1, there was significant main effects of both PERCLOS and hemisphere on the GSF (the PERCLOS effect: left hemisphere, $r = 0.24$, $p < 0.001$; right hemisphere, $r = 0.23$, $p < 0.001$; the hemisphere effect: right-greater-than-left, $t = 6.664$, $p < 0.001$). No significant hemisphere *PERCLOS interaction effect was observed. Regarding the main PERCLOS effect on the GST, positive correlation with PERCLOS (warm-colored) was mainly located around the primary somatosensory cortex and temporo-occipital cortex. In contrast, the intraparietal sulcus, parieto-occipital sulcus, and primary visual cortex showed negative correlation with PERCLOS (cold-colored) (Fig. 2A). Significant main hemisphere effects on the GST were also observed. Specifically, compared with the right hemisphere, the left hemisphere showed higher GST values (warm-colored) in the inferior parietal cortex, primary auditory cortex, and ventral posterior cingulate cortex, but lower GST values around the inferior parietal lobule, parieto-occipital sulcus, and superior parietal lobule (cold-colored) (Fig. 2B). Finally, there were significant PERCLOS* hemisphere interaction effect (Fig 2C). For example, the supramarginal gyrus and inferior frontal junction area showed a positive correlation with PERCLOS in the left hemisphere but a negative correlation in the right hemisphere.

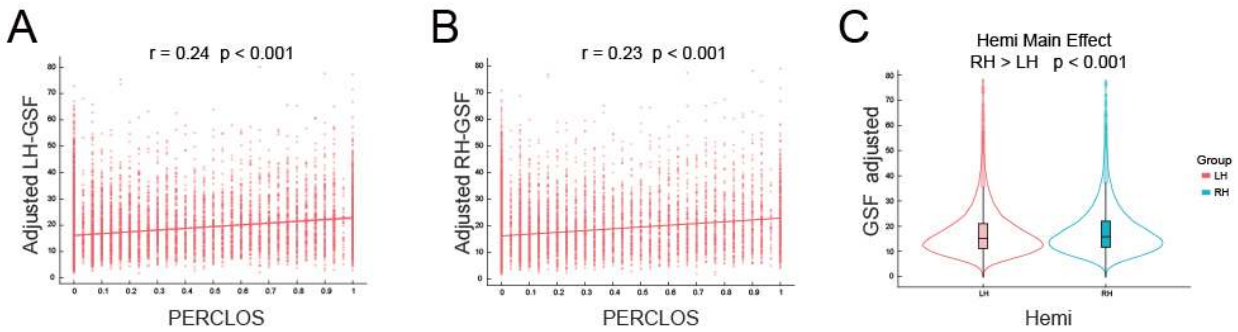

Fig1. Relationship between hemispheric GSF and wakefulness and asymmetry of GSF. Hemispheric GSF was obtained by computing the standard deviation of the left and right hemispheric GS timeseries separately. **(A)** Adjusted GSF in the left hemisphere was positively correlated with PERCLOS. **(B)** Adjusted GSF in the right hemisphere was positively correlated with PERCLOS. **(C)** Comparative results of GSF in the right and left hemispheres, with the right hemisphere having a higher GSF than the left hemisphere (regardless of the level of wakefulness)

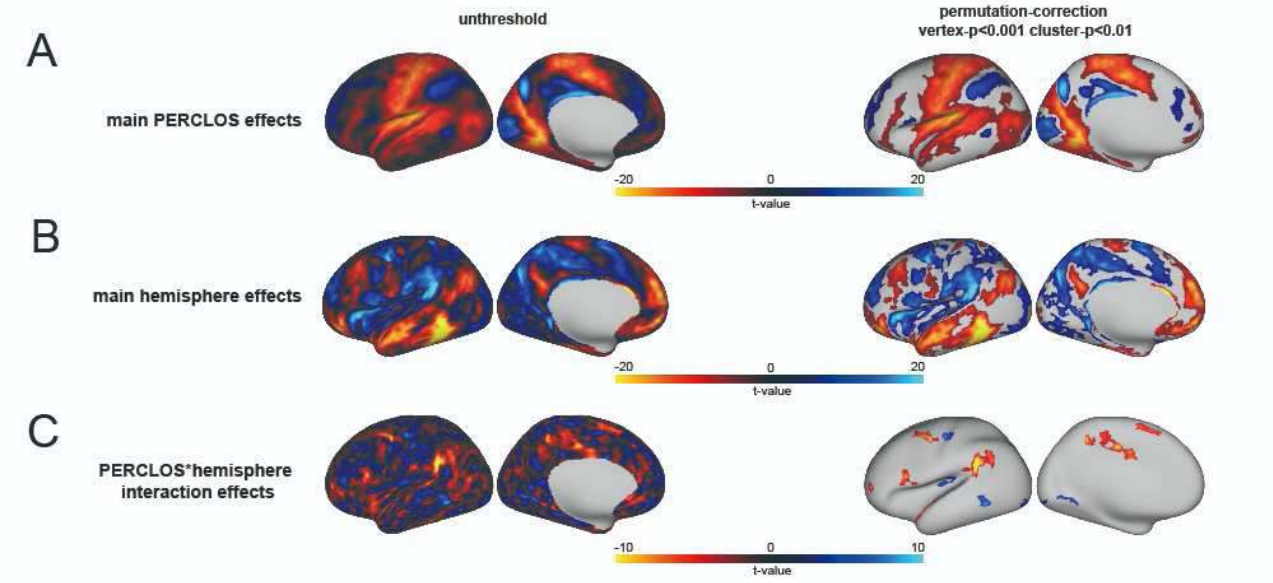

Fig2. The asymmetry of hemispheric GST and modulation of GST in association with wakefulness, and interaction. Hemispheric GST was derived by calculating pairwise Pearson correlation between hemispheric GS time series and each vertex's time series in the same hemisphere, followed by Fisher's r-to-z transformation. The left column is the unthreshold t-map, and the right column is after multiple comparisons correction (vertex-p<0.001 cluster-p<0.01). **(A)** Main PERCLOS effect on the GST, positive correlation between GST and PERCLOS is indicated by warm-colored. **(B)** Main hemisphere effects on the GST, higher GST values in the left hemisphere compared to the right hemisphere is indicated by warm-colored.**(C)** PERCLOS* hemisphere interaction effect .

Conclusions: The present study demonstrated an association of dynamic change of hemispheric global signal (e.g., GSF and GST) with fluctuation of wakefulness during resting state. Particularly, the two hemispheres exhibited significant difference in the global signal, which could be modulated by the wakefulness state.

References

1. Brown, R.E. (2012), 'Control of Sleep and Wakefulness', Physiological Reviews, vol. 92, no. 3, pp. 1087–1187
2. Scammell, T.E. (2017), 'Neural Circuitry of Wakefulness and Sleep', Neuron, vol. 93, no. 4, pp. 747–765
3. Wong, C.W. (2013), 'The amplitude of the resting-state fMRI global signal is related to EEG vigilance measures', NeuroImage, vol. 83, pp. 983–990
4. Turchi, J. (2018), 'The Basal Forebrain Regulates Global Resting-State fMRI Fluctuations', Neuron, vol. 97, no. 4, pp. 940-952.e4
5. Bolduc, C. (2003), 'Hemispheric lateralization of the EEG during wakefulness and REM sleep in young healthy adults', Brain and Cognition, vol. 53, no. 2, pp. 193–196
6. Tamaki, M. (2016), 'Night Watch in One Brain Hemisphere during Sleep Associated with the First-Night Effect in Humans', Current Biology, vol. 26, no. 9, pp. 1190–1194
7. Glasser, M.F. (2013), 'The minimal preprocessing pipelines for the Human Connectome Project', NeuroImage, vol. 80, pp. 105–124
8. Wilson, R.S. (2015), 'Influence of epoch length on measurement of dynamic functional connectivity in wakefulness and behavioural validation in sleep', NeuroImage, vol. 112, pp. 169–179
9. Yang, G.J. (2016), 'Altered Global Signal Topography in Schizophrenia', Cerebral Cortex, vol. 27, pp. 5156–5169

Poster No 2580

Phase-specific reactivation modulates motor memory via hippocampal and striatal-mediated plasticity

Judith Nicolas[1], Bradley King[2], David Levesque[3], Latifa Lazzouni[4], David Wang[5], Nir Grossman[6], Stephan Swinnen[7], Julien Doyon[4], Julie Carrier[8], Genevieve Albouy[9]

[1]Centre de Recherche en Neurosciences de Lyon, BRON, [2]Department of Health and Kinesiology, College of Health, University of Utah, Salt Lake City, UT, [3]Center for Advanced Research in Sleep Medicine, Centre Intégré Universitaire de Santé et de Servi, Montreal, Quebec, [4]McConnell Brain Imaging Centre, Department of Neurology and Neurosurgery, Montreal Neurological Inst, Montreal, Quebec, [5]Elemind Technologies Inc Massachusetts Institute of Technology, Cambridge, MA, [6]Faculty of Medicine, Department of Brain Sciences, Imperial College London, London, [7]KU Leuven, Leuven, Vlaams Brabant, [8]Department of Psychology, Université de Montréal, Montreal, Quebec, [9]KU Leuven, Leuven, Belgium

Introduction: Motor memory consolidation can be enhanced by targeted memory reactivation (TMR) during post-learning sleep (reviewed in Hu et al., 2020). Inspired by studies showing that auditory clicks delivered in a closed-loop (CL) fashion at the up state of the slow wave (SW) can optimize declarative memory consolidation, we tested whether applying TMR at specific phases of the SW (e.g., up vs. down stimulation) could influence motor memory consolidation. We used both EEG and fMRI to characterize the underlying neurophysiological processes. Inspired by studies showing that auditory clicks delivered in a closed-loop fashion at the up state of the SW can optimize declarative memory consolidation, we tested whether applying TMR at specific phases of the SW (e.g., up vs. down stimulation) could influence motor memory consolidation.

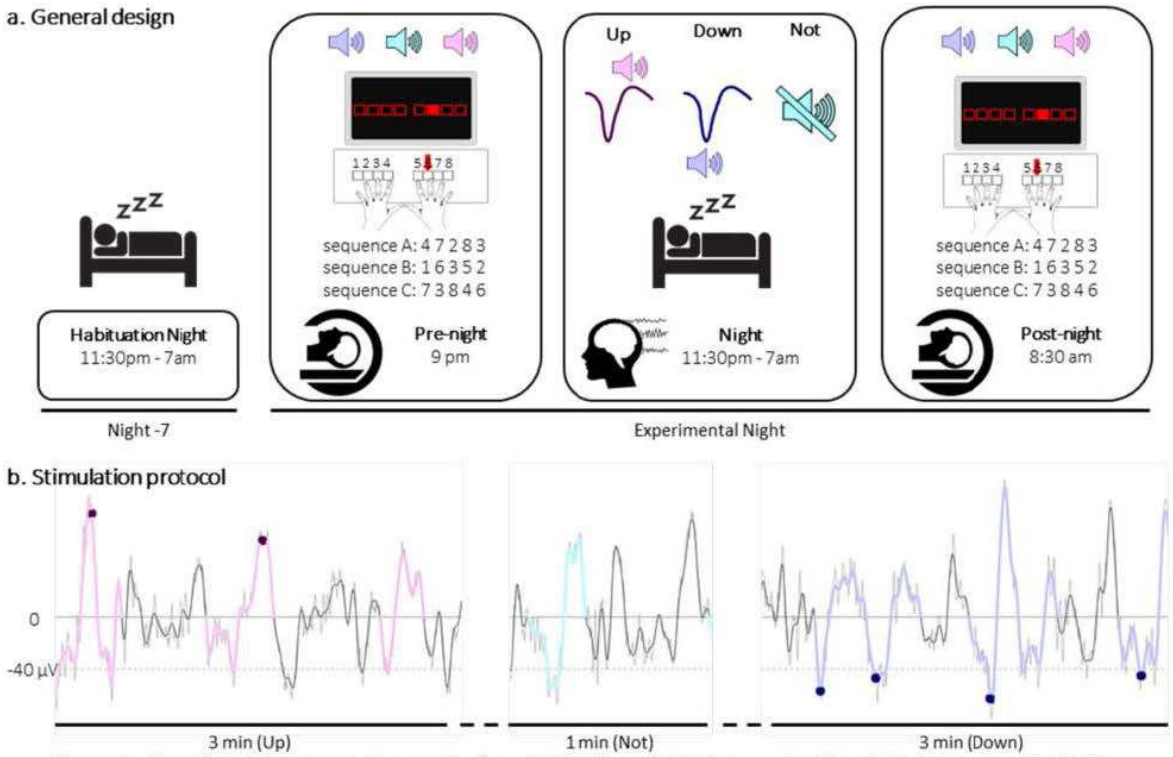

Figure 1: Experimental protocol. One week after a habituation night, 28 young healthy adults (age range 18-30, 15 females) completed a pre-night experimental session in the MR scanner during which they performed a MSL task including three different movement sequences. During task practice, each of the motor sequences was associated to a specific sound. After the MRI session, participants were invited for an experimental night in the sleep lab during which their sleep was monitored with EEG. Participants were retested on the MSL task the next morning during the post-night practice session that also took place in the MRI scanner. **b. Stimulation protocol**. During NREM 2-3 sleep stages of the first 2 sleep cycles of the post-learning night, two of the three sounds were presented (reactivated conditions) while the third sound was not presented and served a no reactivation condition (not-reactivated). For the 2 reactivated conditions, online EEG analyses were performed to apply closed-loop auditory stimulation on different phases of the detected slow oscillations so that one sound was presented at the peak of the slow oscillation (up-reactivated) while the other sound was presented at the trough of the slow oscillation (down-reactivated).

Methods: Twenty-eight young healthy adults (age range 18-30, 15 females) participated in this study. Each participant performed, in the fMRI scanner, a motor sequence learning (MSL) task including three different movement sequences before and after a night of sleep monitored with EEG (see details in Fig. 1). Sounds associated to the 3 different motor sequences were not replayed (control) or replayed either on the up or the down phase of the SW detected online during post-learning sleep. EEG data collected during reactivation were preprocessed using Fieldtrip with standard procedures (e.g., Nicolas et al., 2022). MRI data collected during task practice (TR = 2s, voxel size = 2.5x2.5x2.5mm; Philips Achieva 3T MR scanner) were preprocessed and analyzed using SPM12 with standard procedures (e.g., Dolfen et al., 2021). Based on previous evidence that the hippocampus and the striatum are critically involved in MSL (e.g., Albouy et al., 2015), task-related brain activity and connectivity were examined in these ROIs as well as motor areas.

Results: Behavioral data analyses indicate that the offline overnight changes in performance speed were greater for the up-, as compared to the down-, reactivated sequences (up vs. down: $t = 2.32$, $p = 0.014$ (p-FDR = 0.035), Cohen's $d = 0.44$, Fig. 2a). Analyses of the sleep EEG data revealed a phase-specific modulation of sleep oscillations such that up-stimulated SW exhibited higher amplitude and greater sigma power nested in the SW peak than down-stimulated SW (p-value = 0.0040; Cohen's $d = 0.67$ and $p = 0.0080$; Cohen's $d = 0.66$ respectively, corrected with cluster-based permutations, Fig. 2b). Moreover, up-stimulation resulted in a greater overnight increase in task-related brain activity in striato-motor networks (up vs. down: $x = 20$, $y = 18$, $z = 12$, p-Small Volume Corrected (p-svc) = 0.009; up vs not: $x = 18$, $y = 28$, $z = 4$, p-svc = 0.02; down vs not: $x = 16$, $y = -2$, $z = 26$, p-svc = 0.016) while it prevented hippocampal activity to decrease as compared to the not-reactivated condition (up vs. not: $x = 36$, $y = -36$, $z = -4$, p-svc = 0.028, Fig. 2c). Connectivity analyses showed that down stimulation resulted in an overnight increase in striatal connectivity (up vs not: $x = -32$, $y = -20$, $z = 50$, p-svc = 0.02, Fig 2d). Interestingly, this down-reactivated increase in striato-motor connectivity was associated to poorer overnight performance improvement ($x = 26$, $y = -8$, $z = 44$, p-svc = 0.025) whereas the increase in striato-hippocampal connectivity was associated to greater performance improvement ($x = -16$, $y = -40$, $z = 6$, p-svc = 0.014, Fig 2e).

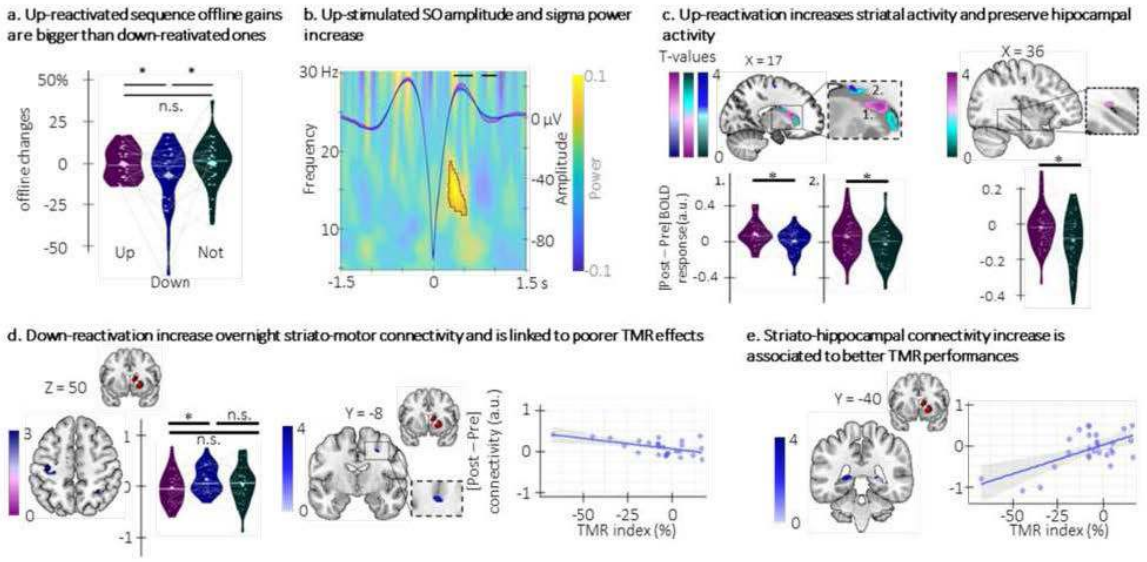

Figure 2: Phase-specific modulation of motor memory consolidation. **a**. Offline changes in performance were greater for the up- and not-reactivated as compared to the down-reactivated sequence. **b**. Up-stimulation during the night resulted in enhanced SO amplitude as well as a stronger sigma power during the phase of high excitability of the SO. **c**. The overnight increase in striatal activity was greater for the up-reactivated sequence while hippocampal activity was preserved. **d**. Striato-motor connectivity increased only in the down-reactivated condition and this increase is associated to poorer TMR performances. **e**. Down-reactivated hippocampo-straital increase in connectivity is linked to greater TMR performances.

Conclusions: Altogether, these results suggest that slow-oscillation closed-loop TMR induced phase-specific modulations of (i) motor performance, (ii) activity and connectivity in task-relevant networks including the striatum, the hippocampus and the motor cortex and (iii) characteristics of sleep EEG features involved in plasticity processes. Interestingly, the different brain connectivity patterns observed at retest during practice of the down-reactivated sequence were effective or not to compensate for the deleterious effect of down stimulation on performance.

References

1. Albouy, G., Fogel, S., King, B. R., Laventure, S., Benali, H., Karni, A., Carrier, J., Robertson, E. M., & Doyon, J. (2015). Maintaining vs. enhancing motor sequence memories : Respective roles of striatal and hippocampal systems. NeuroImage, 108, 423-434. https://doi.org/10.1016/j.neuroimage.2014.12.049
2. Dolfen, N., King, B. R., Schwabe, L., Gann, M. A., Veldman, M. P., von Leupoldt, A., Swinnen, S. P., & Albouy, G. (2021). Stress Modulates the Balance between Hippocampal and Motor Networks during Motor Memory Processing. Cerebral Cortex, 31(2), 1365-1382. https://doi.org/10.1093/cercor/bhaa302
3. Hu, X., Cheng, L. Y., Chiu, M. H., & Paller, K. A. (2020). Promoting memory consolidation during sleep : A meta-analysis of targeted memory reactivation. Psychological Bulletin, 146(3), 218-244. https://doi.org/10.1037/bul0000223
4. Nicolas, J., King, B. R., Levesque, D., Lazzouni, L., Coffey, E., Swinnen, S., Doyon, J., Carrier, J., & Albouy, G. (2022). Sigma oscillations protect or reinstate motor memory depending on their temporal coordination with slow waves. eLife, 11, e73930. https://doi.org/10.7554/eLife.73930

Poster No 2581

The Neurobiology of Chronotype: Insights from a Comprehensive Multimodal Population Study

Le Zhou[1,2], Karin Saltoun[1,2], Danilo Bzdok[1,2,3,4]

[1]McConnell Brain Imaging Centre, Montreal Neurological Institute (MNI), McGill University, Montreal, Canada, [2]Mila - Quebec Artificial Intelligence Institute, Montreal, Canada, [3]Department of Biomedical Engineering, Faculty of Medicine, McGill University, Montreal, Canada, [4]School of Computer Science, McGill University, Montreal, Canada

Introduction: The advent of the industrial age has precipitated noteworthy alterations in daily routines and lifestyles. The widespread use of electronic devices has been particularly transformative, significantly impacting people's sleep patterns and social interactions[1]. These shifts have sparked interest in understanding the impact of chronotype on brain and behavior, a clear manifestation of circadian rhythms that can be effectively assessed through self-reporting[2]. However, the brain basis of chronotype differences in humans are rarely examined, let alone on a population scale. In our population neuroscience study, we combine the data field of chronotype and various phenotypes and three brain image modalities (region volume, white-matter fiber tracts and functional connectivity) in 27030 UK-biobank participants to investigate the association between chronotype and a rich portfolio of ~1,000 health and lifestyle markers.

Methods: Using self-report chronotype data from the UK-biobank, we categorized subjects as 0 for morningness and 1 for eveningness. Moreover, we excluded subjects with inconsistent assessments between the initial assessment and imaging visit, as well as those with shift work experiences. Finally, we selected 27030 subjects who had complete data for structure MRI, diffusion MRI, and resting-state fMRI. We first conducted Phenome-Wide Association Study(PheWAS) between chronotype and 976 other phenotypes[3] in our population dataset. Then, in our main analysis, we applied the linear discriminant model to investigate the multivariate brain patterns linked to chronotype across three neuroimaging modalities separately. For each neuroimaging feature, we regressed out the effects of head motion, head size, head position, body mass index (BMI), position of scanner table, data acquisition site, sleep duration, insomnia, snoring, dozing, and nap. To identify the most important brain features, we implemented 100 bootstraps to extract the relevant coefficients.

Results: In our PheWAS analysis, 161 phenotypes exceeded the threshold at $p<0.05$ after Bonferroni's family-wise error correction (Figure 1). Lifestyle factors, including leisure activity, exercise, smoking and alcohol consumption, were highly associated with chronotype. Additionally, BMI, vitamin D, and 56 self-reported mental health phenotypes were also highlighted. We further examined the association between chronotype and three neuroimaging modalities. The significant coefficients of regional gray matter volume and white matter tracts are shown in Figure 2a, while resting-state functional connectivity is presented in Figure 2b.

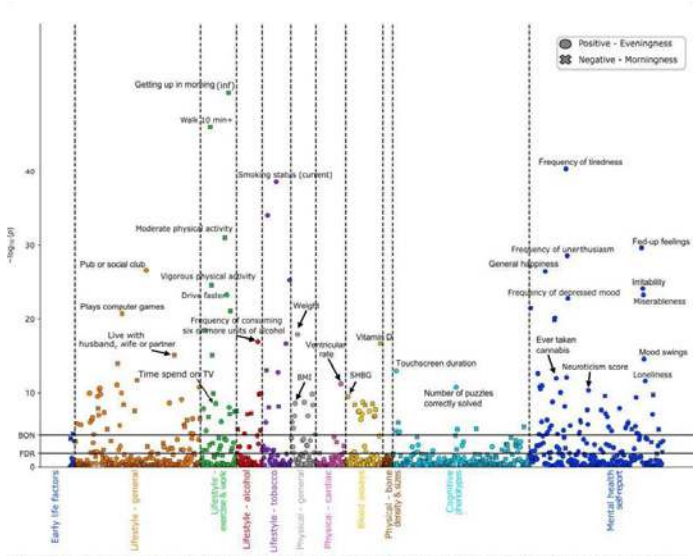

Figure 1. ***Manhattan plot of Phenome-Wide Association Study (PheWAS) based on chronotypes.*** For each phenotype, association coefficients are plotted in units on logarithmic scale of the associated p value. Horizontal lines indicate the significance thresholds at Bonferroni correction for phenotypes (0.05/976), and at FDR correction labelled BON and FDR. Based on the direction between the chronotype (morningness decoded as 0, eveninningness decoded as 1) and other phenotypes, circle indicate the positive direction, and cross indicates negative direction.

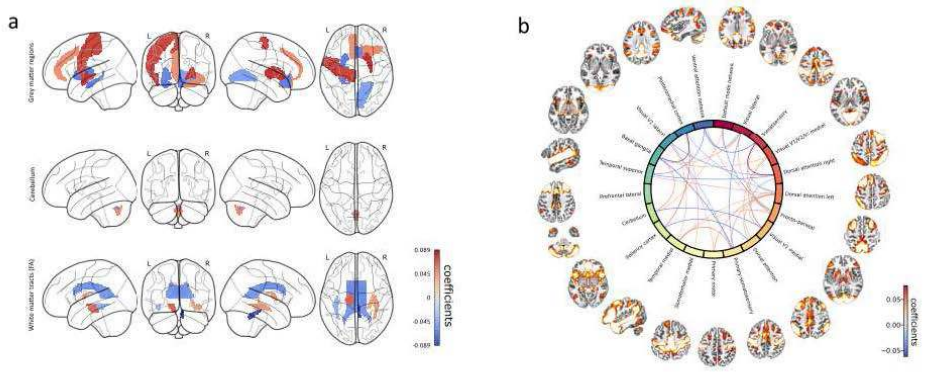

Figure 2: Revealing the multivariate brain patterns linked to chronotypes. We implemented the linear discriminant model to investigate the association between chronotype and brain features. Regional gray matter volume of 139 distinct brain regions were extracted based on the Harvard-Oxford atlas, and 48 examined major white matter tracts were derived from the John-Hopkins atlas, and the resting-state functional connectivity between the 21 brain components were extracted from group ICA analysis of spatiotemporally coherent brain networks. Three neuroimaging modalities were used as separate input variables to predict morningness (negative class) and eveningness (positive class). To assess the significance of each brain feature, we evaluated the distributions of the coefficients across 100 bootstrap resampling iterations, presenting the results with a 10-90% confidence intervals threshold. **a**, significant brain regions of cerebrum and cerebellum, and significant white matter tracts. **b**, the significant resting-state functional connectivity between 21 network components.

Conclusions: Our study confirmed the evident disparities in lifestyles between morningness and eveningness. Aligning with prior research, the eveningness tends to be more vulnerability to mood disorder and unfavorable habits[4,5]. Complementary to behavioral observations, our neurobiological findings emphasize the involvement of key brain regions, including the basal ganglia, orbital frontal cortex, hippocampus, precentral cortex and cerebellum, crucial in the establishment of new habits[6]. These regions also exert influence over the hypothalamic-pituitary-adrenal (HPA) axis[7] and play a pivotal role in the reward system[8]. Furthermore, the subcallosal cortex, paracingulate gyrus, and parahippocampal areas were also significantly associated with chronotype. These regions, integral to the limbic system, are strongly linked to emotional regulations[9,10]. The observed white matter tracts of the fornix and the confirmed functional connectivity patterns involving the basal ganglia, cerebellum, primary somatosensory cortex, temporal medial cortex, and frontal-parietal cortex provide additional support for our neurobiological insights. In summary, our population study delved into the neurobiological associations of chronotypes, shedding light on their associations with brain regions pivotal in habit formation, HPA axis, and emotional regulation.

References

1. Fossum, I.N., et al., (2014) The Association Between Use of Electronic Media in Bed Before Going to Sleep and Insomnia Symptoms, Daytime Sleepiness, Morningness, and Chronotype. Behavioral Sleep Medicine, Taylor & Francis, 12, 343–357. https://doi.org/10.1080/15402002.2013.819468.
2. Levandovski, R., et al., (2013) Chronotype: A Review of the Advances, Limits and Applicability of the Main Instruments Used in the Literature to Assess Human Phenotype. Trends in Psychiatry and Psychotherapy, 35, 3–11. https://doi.org/10.1590/s2237-60892013000100002.
3. Saltoun, K., et al., (2023) Dissociable Brain Structural Asymmetry Patterns Reveal Unique Phenome-Wide Profiles. Nature Human Behaviour, Nature Publishing Group, 7, 251–268. https://doi.org/10.1038/s41562-022-01461-0.
4. Kianersi, S., et al., (2023) Chronotype, Unhealthy Lifestyle, and Diabetes Risk in Middle-Aged U.S. Women. Annals of Internal Medicine, American College of Physicians. https://doi.org/10.7326/M23-0728.
5. Monk, T.H., et al., (2004) Morningness-Eveningness and Lifestyle Regularity. Chronobiology International, Taylor & Francis, 21, 435–443. https://doi.org/10.1081/CBI-120038614.
6. Yin, H.H., et al., (2006) The Role of the Basal Ganglia in Habit Formation. Nature Reviews Neuroscience, Nature Publishing Group, 7, 464–476. https://doi.org/10.1038/nrn1919.
7. Dedovic, K., et al., (2009) The Brain and the Stress Axis: The Neural Correlates of Cortisol Regulation in Response to Stress. NeuroImage, 47, 864–871. https://doi.org/10.1016/j.neuroimage.2009.05.074.
8. Stalnaker, T.A., et al., (2015) What the Orbitofrontal Cortex Does Not Do. Nature Neuroscience, Nature Publishing Group, 18, 620–627. https://doi.org/10.1038/nn.3982.
9. Rudebeck, P.H., et al., (2014) A Role for Primate Subgenual Cingulate Cortex in Sustaining Autonomic Arousal. Proceedings of the National Academy of Sciences, Proceedings of the National Academy of Sciences, 111, 5391–5396. https://doi.org/10.1073/pnas.1317695111.
10. Rolls, E.T. (2015) Limbic Systems for Emotion and for Memory, but No Single Limbic System. Cortex, 62, 119–157. https://doi.org/10.1016/j.cortex.2013.12.005.

Poster No 2582

Neurophysiological mechanisms of sleep overheating: insights on the insular cortex connectivity

Erfan Naghavi[1], Amirhussein Abdolalizadeh[2]

[1]School of Medicine, Tehran university of medical sciences, Tehran, Iran, [2]School of Medicine and Health Sciences, Carl Von Ossietzky Universität Oldenburg, Oldenburg, Germany

Introduction: Sleep is a crucial factor in maintaining overall health, and its poor quality has been linked to various medical conditions, such as cardiovascular disease, cancer, and depression (Irwin 2015). Feeling overheated during sleep without any heat source, commonly referred to as hot flashes, contributes to lower sleep efficiency and perceived sleep quality (Joffe et al. 2013). The right insular cortex (rIC) is involved in linking subjective and objective sensory perceptions: the dorsal posterior part provides the foundation for the primary interoceptive representation, while the right anterior region plays an important role in subjective emotional awareness and perception of warmth (Olausson et al. 2005; Davis et al. 2023; Craig 2009). We propose that impaired connectivity between the posterior and anterior rIC may be associated with the hot flashes, irrespective of the room temperature.

Methods: The minimally-preprocessed resting-state functional magnetic resonance imaging (rfMRI) data of the 1200 subjects human connectome project young adults (HCP-YA) was used in this study (Essen et al. 2013), including data on age, gender, depression, the Pittsburgh sleepiness questionnaire index (PSQI), while excluding participants with incomplete data (less than 4 rfMRI runs) or a positive drug test. We then included the subjects with poor sleep quality (PSQI > 5). Then, they were categorized into two groups based on the frequency of sleep disruption due to hot flashes in the last month: at least two times a week (hot sensitive group: HSG), and less than that (not-hot sensitive group: NHSG). We divided the rIC into three functional areas based on prior literature (Menon et al. 2020): dorsal anterior insula (dAI), ventral anterior insula (vAI), and posterior insula

(PI). These three areas respectively correspond to AVI+MI+FOP3, AAIC, and PoI1+PoI2+Ig+FOP2 based on the Glasser's atlas (Glasser et al. 2016) (Figure 1). Pairwise functional connectivity was calculated across four functional runs, r-to-z-transformed, and averaged. We then statistically compared the pairwise functional connectivity (PI-dAI, PI-vAI, dAI-vAI) between HSG and NHSG. Age, gender, and depression were included as covariates in the analysis.

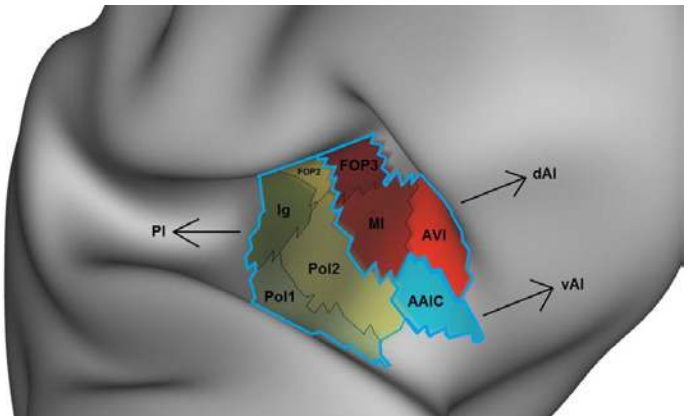

Figure 1. The rIC components and their corresponding subdivisions.

Results: In total, there were 245 participants, comprising 106 men and 139 women, with a mean age of 28.67 ± 3.50 years. There was no significant difference in age, gender, depression, and PSQI score between the NHSG and the HSG. The demographic data are available in detail in Table 1. Our results indicated that the functional connectivity between the PI and the dAI was significantly lower in the HSG compared to NHSG ($F(1, df) = 4.387$, p value = 0.037). However, the analysis did not support a significant difference in the PI and the vAI ($F(1, df) = 0.539$, $p = 0.463$), as well as the dAI and the vAI ($F(1, df) = 0.349$, $p = 0.554$) functional connectivity between the two groups (Figure 2).

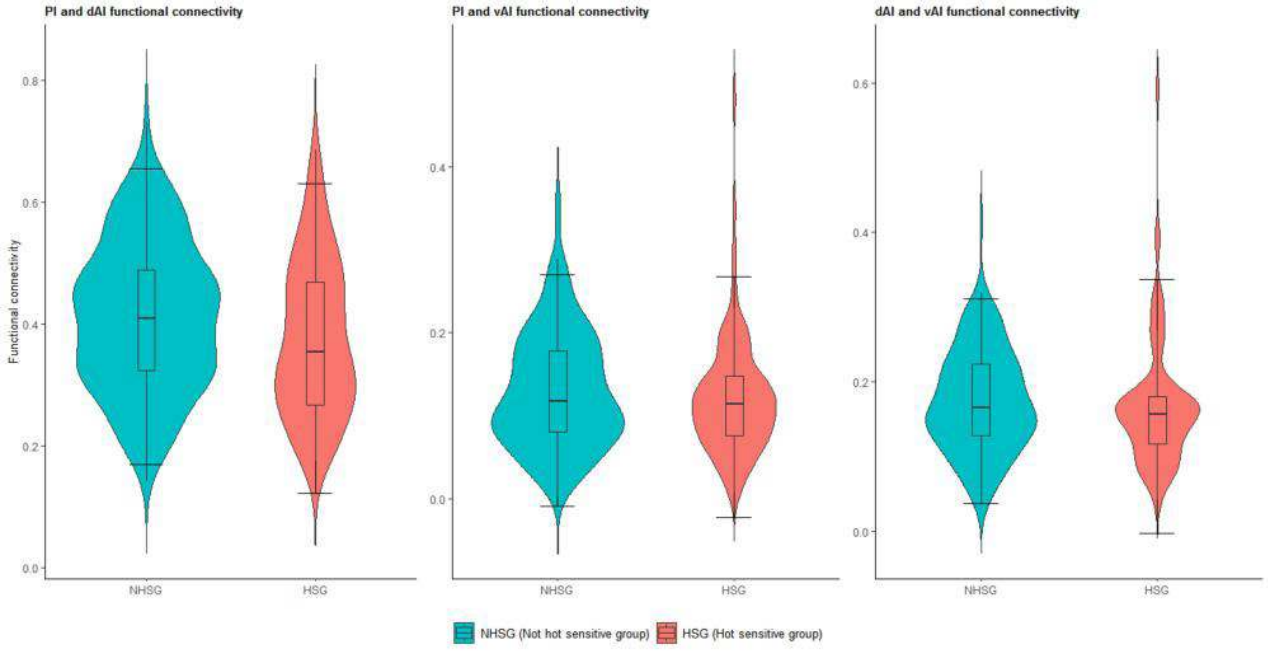

Figure 2. Comparing PI, dAI, and vAI pairwise functional connectivity between the NHSG and HSG.

Conclusions: In conclusion, the PI and the dAI functional connectivity was significantly lower in the HSG compared to the NHSG. These findings support our hypothesis that the impaired functional connectivity between the right dorsal posterior and the anterior insular cortex may contribute to hot flashes in healthy subjects. Our findings may offer additional insights into the neurophysiological role of the insular cortex in the occurrence of hot flashes during sleep.

References

1. Craig, A D Bud. 2009. "How Do You Feel — Now? The Anterior Insula and Human Awareness" 10 (JANuARy).
2. Davis, K D, G E Pope, A P Crawley, and D J Mikulis. 2023. "Perceptual Illusion of ' Paradoxical Heat ' Engages the Insular Cortex," 1248–51.

3. Essen, David C Van, Stephen M Smith, Deanna M Barch, Timothy E J Behrens, Essa Yacoub, Kamil Ugurbil, and Wu-minn H C P Consortium. 2013. "NeuroImage The WU-Minn Human Connectome Project : An Overview." NeuroImage 80: 62–79. https://doi.org/10.1016/j.neuroimage.2013.05.041.
4. Glasser, Matthew F, Timothy S Coalson, Emma C Robinson, Carl D Hacker, John Harwell, and Essa Yacoub. 2016. "A Multi-Modal Parcellation of Human Cerebral Cortex." Nature Publishing Group 536 (7615): 171–78. https://doi.org/10.1038/nature18933.
5. Irwin, Michael R. 2015. "Why Sleep Is Important for Health: A Psychoneuroimmunology Perspective." Annual Review of Psychology 66 (January): 143–72. https://doi.org/10.1146/annurev-psych-010213-115205.
6. Joffe, Hadine, David P White, Sybil L Crawford, Kristin E McCurnin, Nicole Economou, Stephanie Connors, and Janet E Hall. 2013. "Adverse Effects of Induced Hot Flashes on Objectively Recorded and Subjectively Reported Sleep: Results of a Gonadotropin-Releasing Hormone Agonist Experimental Protocol." Menopause (New York, N.Y.) 20 (9): 905–14. https://doi.org/10.1097/GME.0b013e31828292d1.
7. Menon, Vinod, Guillermo Gallardo, Mark A Pinsk, Van-dang Nguyen, United States, and Inria Sophia Antipolis. 2020. "Microstructural Organization of Human Insula Is Linked to Its Macrofunctional Circuitry and Predicts Cognitive Control," 1–27.
8. Olausson, H, J Charron, S Marchand, C Villemure, I A Strigo, and M C Bushnell. 2005. "Feelings of Warmth Correlate with Neural Activity in Right Anterior Insular Cortex" 389: 1–5. https://doi.org/10.1016/j.neulet.2005.06.065.

Poster No 2583

Synchronous 4D magnitude and phase fMRI reveals sleep induced changes in respiratory brain

Saara Syväoja[1], Lauri Raitamaa[2], Vesa Kiviniemi[3]

[1]University of Oulu, Oulu, Finland, [2]University of Oulu, Oulu, Pohjois-Pohjanmaa, [3]Oulu University Hospital, Oulu, Finland

Introduction: Sleep is crucial for the proper functioning of the brain, including memory consolidation, emotional regulation, restoration and repair, and overall brain health. Physiological brain pulsations are thought to have a role in sleep, which however is not fully understood. To study pulsations in awake and sleep stages we used fMRI magnetic resonance encephalography (MREG) imaging sequence to simultaneously capture both phase and magnitude 4D brain data at ultrafast 10 Hz sampling rate, ergo 10 whole brain images per second. This approach allowed us to visualize physiological pulsations across the entire brain and obtain information that would otherwise be overlooked using traditional methods. In this study, our focus is on analyzing phase signal due to the phase fMRI signal increased sensitivity to physiological phenomena as compared to the magnitude signal. Our findings revealed a significant increase in respiratory amplitudes, as observed in both phase and magnitude maps during sleep compared to wakefulness.

Methods: The study involved twelve healthy volunteers (age 26.2 ± 4.3 years, 5 females). During the awake scan session, the participants were asked to rest with their eyes open and focus on a cross displayed on the screen for 10 minutes. Three days later, the sleep scans were conducted. Subjects were scanned using a Siemens 3T SKYRA scanner with a 32-channel head coil and a 3D whole brain MREG sequence (TR 100ms, TE 3.6ms, flip angle 25, matrix=643, FOV=192mm). Data preprocessing involved motion spike removal with AFNI's 3dDespike, standard FSL pipeline with high-pass filtering at 0.008 Hz, motion correction using FSL MCFLIRT, and brain extraction with FSL BET. Anatomical MPRAGE images aided in registering MREG data to MNI152 standard space. We used a modified ALFF method to study amplitude of fluctuation (AF) of very low frequency (AFVLF), respiratory (AFresp), and cardiac (AFcard) pulsations. The frequency band for AFVLF was 0.01-0.1 Hz, corresponding to the classical ALFF, while the bands for AFresp and AFcard were 0.1 Hz wide, centered around the previously defined individual peaks (i.e., peak ± 0.05 Hz). For every subject, the time courses of each voxel from whole brain temporal MREG data were transformed using AFNI 3dPeriodogram to the frequency domain via a fast Fourier transformation, which yielded the voxel-wise power spectrum. The square root of the power spectral density was calculated, and amplitudes calculated over the frequency bands of interest were summed to obtain a corresponding AF map[5]. Voxel-wise comparisons of the AF maps between awake and sleep states were performed by a two-sample t-test using a paired non-parametric threshold-free permutation test (5000 permutations) implemented in randomise from FSL. The tests were corrected for the family-wise error rate (FWER) at a significance level of $p<0.05$.

Results: Our findings revealed a significant increase in respiratory amplitudes, as observed in both phase and magnitude maps during sleep compared to wakefulness. Notably, the brainstem, cerebellum, and temporal lobe exhibited the highest amplitudes in the phase maps, while the frontal lobe, parietal lobe, and temporal lobe exhibited the strongest amplitudes in the magnitude maps. Comparison of the phase and magnitude maps revealed both differences and similarities, highlighting the potential for expanding the amount of information obtained in a single imaging session of the brain.

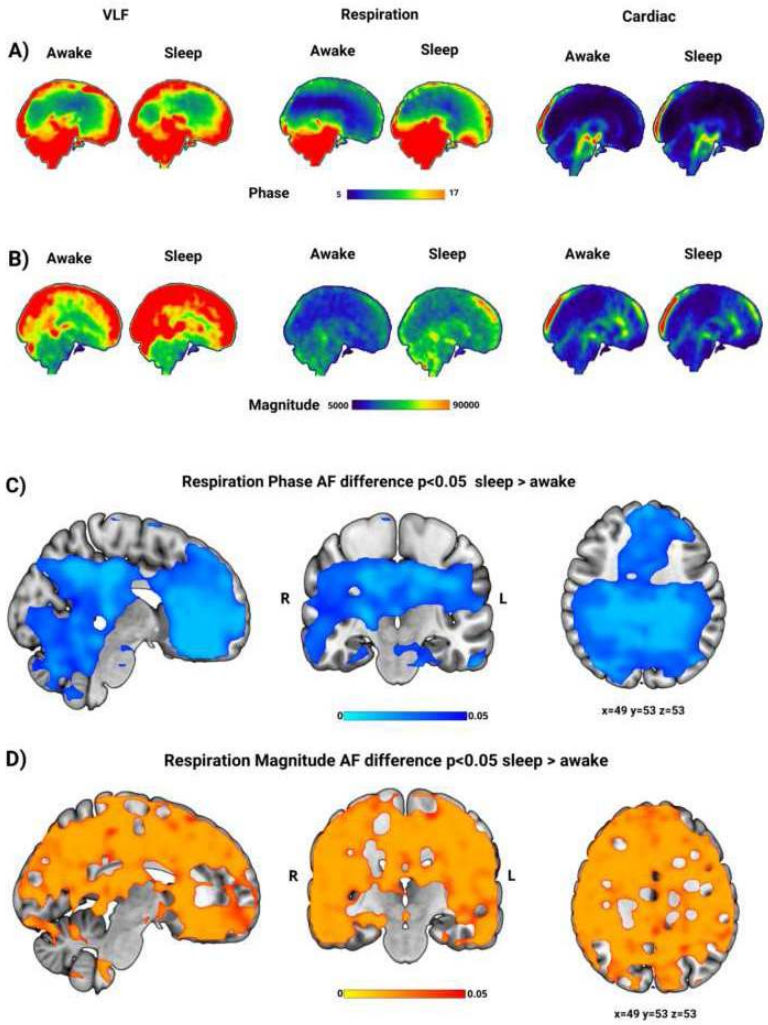

Fig. Mean values of amplitude of fluctuation (AF) from phase and magnitude maps in VLF, respiratory and cardiovascular bands.

Conclusions: The present findings imply that the concurrent utilization of phase and magnitude information using MREG scanning offers a more comprehensive insight into the dynamics of the brain physiological pulsations during sleep compared to solely analyzing the magnitude maps.

Poster No 2584

Effect of age on the relationship between sleep quality and cortical thickness: a HCP-A Study

Hyun Kim[1], Elizabeth Rueppel[2], Yisha Zhang[2], Aren Tucker[2], Maria Purcell[2], Terry Goldberg[1], Seonjoo Lee[1]

[1]Columbia University Irving Medical Center, New York, NY, [2]New York State Psychiatric Institute, New York, NY

Introduction: While the association between sleep quality and brain health is well established, the role of aging in this relationship is largely unknown. Understanding the interaction between sleep and age is especially important in brain aging and outcomes research, given that disease outcomes can be modified with age-related changes in brain structures and networks (Yagi et al., 2020). Therefore, this study employed a sample of adults across a wide age range and examined the interaction between sleep and age on cortical thickness. Age was examined in both linear and non-linear (quadratic) terms, in order to determine the presence of critical age ranges that may exhibit more significant sleep-related brain structural changes.

Methods: Sample included 700 adults (mean age 59.63 [age range 36-90], 55.9% female) from the Human Connectome Project-Aging (HCP-A) database (Bookheimer et al., 2019). Sleep quality was measured using the Pittsburgh Sleep Quality Index (PSQI). Magnetic resonance imaging (MRI) data was obtained from T1-weighted structural images using a 3T scanner, and cortical thickness indices were derived using the FreeSurfer pipeline. The interaction between sleep and age on

cortical thickness was tested using the moderation analysis using linear regression models, with sex, race, and use of sleep medication as covariates.

Results: There was a significant interaction term between the PSQI and non-linear age term (age2) on the insular thickness (β=0.67, CI=0.03-1.30, p=.04), indicating that sleep quality may be associated with the structure of insula distinctly in different age groups. A visual examination of this relationship indicated that the insular thickness for individuals between the ages 53 and 78 was most sensitive to poor sleep quality.

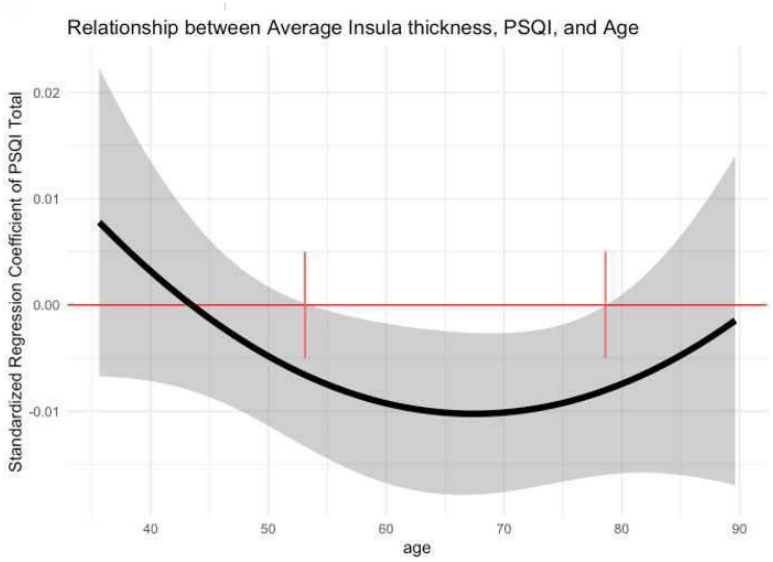

Fig. Association between Pittsburg Sleep Quality Index (PSQI) and insular thickness by age. The relationship between PSQI and insular thickness is presented as the standardized regression coefficient.

Conclusions: Age may have a significant role in the relationship between sleep and cortical thickness, particularly the insular thickness. As part of the salience network, the insula has been involved in crucial emotional and cognitive functioning and has been shown to be impacted by both sleep disorders and Alzheimer's disease (Wang et al., 2021; Wang et al., 2022; Menon et al., 2010). Therefore, the insula may be more significantly associated with sleep disturbance, particularly in the aging population. Our results also suggest that middle-aged and older adults may be most vulnerable to sleep-related changes in the brain structures.

References

1. Bookheimer, S. Y., et al. (2019). 'The Lifespan Human Connectome Project in Aging: An overview', Neuroimage, vol. 185, pp. 335-348.
2. Menon, V. et al. (2010), 'Saliency, switching, attention and control: a network model of insula function', Brain Structure and Function, vol. 214, pp. 655–67.
3. Wang, C. et al. (2021), 'Cortical Thinning and Abnormal Structural Covariance Network After Three Hours Sleep Restriction', Frontiers in Psychiatry, 12:664811.
4. Wang, Y. et al. (2022), 'Is the insula linked to sleep? A systematic review and narrative synthesis', Heliyon, vol. 8, no11, e11406.
5. Yagi, A. et al. (2020), 'The Role of Cognitive Control in Age-Related Changes in Well-Being', Frontiers in Aging Neuroscience, vol. 12, 198.

Poster No 2585

Can REM Sleep Behavior Disorder Be Differentiated by Using Neural Dynamics during Sleep?

Younghan Lee[1,2], Youngseo Kim[3], Hyeon Jin Kim[4,5,6], Ho Bae[7], Yunheung Paek[1,2], Hyang Woon Lee[3,8,5,6]

[1]Department of Electrical and Computer Engineering (ECE),Seoul National University, Seoul, Korea, Republic of, [2]Inter-University Semiconductor Research Center (ISRC), Seoul National University, Seoul, Korea, Republic of, [3]Graduate Program of Artificial Intelligence Convergence, Ewha Womans University, Seoul, Korea, Republic of, [4]Department of Neurology, Korea University Ansan Hospital, Ansan-si, Gyeonggi-do, [5]Departments of Neurology Ewha Womans University School of Medicine and Ewha Medical Research, Seoul, Korea, Republic of, [6]Departments of Medical Science, Ewha Womans University School of Medicine and Ewha Medical Research, Seoul, Korea, Republic of, [7]Department of Cyber Security, Ewha Womans University, Seoul, Korea, Republic of, [8]Computational Medicine, System Health Science & Engineering, Graduate School of Ewha Womans University, Seoul, Korea, Republic of

Introduction: The diagnosis of REM sleep behavior disorder (RBD) relies upon the meticulous analysis of polysomnography (PSG), wherein recurrent instances of sleep-related vocalization and physically aggressive behaviors during dream enactment are observed. Confirmation of this diagnosis is achieved through the identification of REM sleep without atonia in the PSG recordings. Such complex cognitive processes occurring during sleep are intricately tied to the interactions of neural activities. Consequently, many studies have delved into the examination of specific frequency components within electroencephalography (EEG), exploring their correlation with diverse neuropsychological outcomes. In response to the current limitations in research methodology, predominantly characterized by a low-resolution framework, our endeavor is to represent personal brain activity during sleep independently of the temporal evolution of sleep architecture. In this research initiative, we aim to discern distinctive individualized neural dynamics between cohorts of patients with and without RBD.

Methods: A total of 220 anonymous polysomnography (PSG) datasets from subjects were analyzed in the course of unrelated research, following approval from the Institutional Review Board (IRB) of Ewha Womans University Mokdong Hospital. Within this cohort, exactly 50% (110 subjects) were diagnosed with RBD, comprising 49 females and 61 males, with an average age of 62.22 years. To uphold methodological integrity, the sex and age parameters of the control dataset were matched, maintaining an average age of 62.24 years, with an equal distribution of 49 females and 61 males. The EEG data, sampled at 200 Hz, underwent analysis focusing on the C3-A1 electrode derivation. Employing the multitaper approach for spectral estimation, sleep EEG spectrograms were computed for each subject. The relative slow-oscillation (SO, 0.5-2.0 Hz) power, serving as a quantitative surrogate indicator of sleep depth, was extracted. Subsequently, the average spectral power (0.5-30 Hz) corresponding to the SO-power was computed to generate histograms. To facilitate inter-subject or intra-subject comparison, standardized segments were established by fixing the size of SO-power ranges into 41 sections (segment 0~40, respectively).

Results: The mean value of each segment within the two groups (those with and without RBD) exhibited a noticeable distinction. To quantify this difference, we employed the mean squared error (MSE), a metric that gauges the average of the squared differences between two vectors. The extent of difference varied across SO-power segments. Notably, segments with both lower (segment 1-6) and higher (segment 33-40) SO-power ranges exhibited more pronounced differences between the two groups. This suggests that, for discerning subjects with RBD based on neural dynamics, attention should be focused on specific regions. For instance, segment 16, representing the middle section of the histogram, demonstrated visually no difference between the two groups.

Conclusions: In conclusion, our study explored the feasibility of differentiating RBD by analyzing neural dynamics during sleep. Our approach utilized EEG to examine SO-power, aiming to overcome methodological limitations. Analyzing 220 subjects, half diagnosed with RBD, we observed significant differences in SO-power segments particularly with both lower and higher ranges. MSE metric was employed to quantify these distinctions, emphasizing the importance of specific SO-power ranges in the differentiation process.

References

1. American Academy of Sleep Medicine. International Classification of Sleep Disorders, 3rd ed.; American Academy of Sleep Medicine: Darien, IL, USA, 2014.
2. Choi, Gyeong Seon, et al. “Can corticomuscular coherence differentiate between rem sleep behavior disorder with or without parkinsonism?.” Journal of Clinical Medicine 10.23 (2021): 5585.
3. Prerau, Michael J., et al. “Sleep neurophysiological dynamics through the lens of multitaper spectral analysis.” Physiology 32.1 (2017): 60-92.
4. H. J. Kim, S. Chen, U. T. Eden and M. J. Prerau, “A quantitative representation of continuous brain state during sleep,” 2021 10th International IEEE/EMBS Conference on Neural Engineering (NER), Italy, 2021, pp. 103-106, doi: 10.1109/NER49283.2021.9441276.

Acknowledgments

Supported by the National Research Foundation of Korea (NRF) (No. 2019M3C1B8090803, 2020R1A2C2013216, and RS-2023-00265524), Institute of Information & Communication Technology Planning & Evaluation (IITP) grant (No. RS-2022-00155966) by the Korea government (MSIT), and BK21-plus FOUR and Artificial Intelligence Convergence Innovation Human Resources Development programs of Ewha Womans University to H.W.Lee. This study was supported by grants from the Korea University Ansan Hospital [No. K2316061 to H.J.Kim], the Korea Health Technology R & D Project through the Korea Health Industry Development Institute (KHIDI), funded by the Ministry of Health & Welfare, Republic of Korea [HI19C1065 to H.J.Kim]. This work was supported by the BK21 FOUR program of the Education and Research Program for Future ICT Pioneers, Seoul National University in 2023. Also, it was supported by the National Research Foundation of Korea(NRF) grant funded by the Korea government(MSIT) (RS-2023-00277326).

Poster No 2586

Age-related differences in the electrophysiological and hemodynamic signatures of arousal

Sydney Bailes[1,2], Stephanie Williams[1,2], Baarbod Ashenagar[1,2], Dabriel Zimmerman[3], Laura Lewis[4]

[1]Boston University, Boston, MA, [2]Massachusetts Institute of Technology, Cambridge, MA, [3]University of Philadelphia, Philadelphia, PA, [4]Massacusetts Institute of Technology, Cambridge, MA

Introduction: Sleep plays a crucial role in maintaining brain health and cognition, yet as we age our ability to initiate and maintain sleep is impaired[1]. Changes in sleep architecture are typical even in healthy aging, but greater sleep impairment has been linked to occurrences of neurodegenerative diseases[2]. Transitions in behavioral arousal state have previously been shown to follow a distinct sequence of thalamic activation followed by cortical deactivation[3]. Additionally, older adults have been shown to have increases in thalamocortical connectivity not observed in younger individuals paired with a reduced capacity to functionally disconnect regions related to attentional, sensory, and higher cognitive functions during NREM sleep[4]. The thalamus is a hub for sensory integration and modulation of arousal state with profuse connections to the cortex, thus, investigating differences in thalamocortical interactions could provide insight towards understanding age-related sleep impairments. We used simultaneous EEG-fMRI to investigate age-related differences in electrophysiological and hemodynamic changes around transitions in behavioral arousal state.

Methods: We simultaneously measured BOLD fMRI and EEG in 30 human subjects (16 female) during sleep. Participants were sorted into two age groups: young (N=11, 18-39 years) and older (N=19, 60-80 years). BOLD fMRI data was acquired at 3 Tesla (TR=378 ms, 2.5mm isotropic voxels). EEG data was acquired using a 32-channel MR compatible EEG cap. Subjects closed their eyes and performed a self-paced breathing task – pressing a button on every breath in. We identified behavioral arousals, defined as the first button press after 30 seconds of inactivity, and rejected arousals with excessive motion (>0.3mm). We calculated the EEG spectrogram around each arousal and calculated occipital alpha power (8-13 Hz) and frontal delta power (0.5-4 Hz). The fMRI time series 10 s before and 20 s after each arousal were also extracted to calculate the mean fMRI response for each group.

Results: Occipital alpha power increased following arousal, visible on both an individual event level and on a group level, as expected (Fig. 1). In the young group the alpha power peaked before the moment of arousal, while it continued to rise post-arousal in the older group (Fig 1B). Delta power dynamics were also distinct between the groups: in the young group, delta power began to decrease before arousal, whereas in the older group, it decreased after arousal (Fig. 1C). These results showed that older adults exhibited a mixed state after arousal, reflecting EEG signatures of both sleep and wakefulness. We next investigated the fMRI activity linked to arousal and observed cortical deactivation following and thalamic activation before arousal, consistent with prior work[3]. Notably, the thalamus reached its peak earlier in the older group (Fig. 2B). To spatially characterize age-related changes, we extracted 32 cortical regions of interest (ROIs) and estimated their time to peak. Most regions reached their peak deactivation earlier in the older group while a minority of cortical regions reach their peak deactivation earlier in the young group (Fig. 2C).

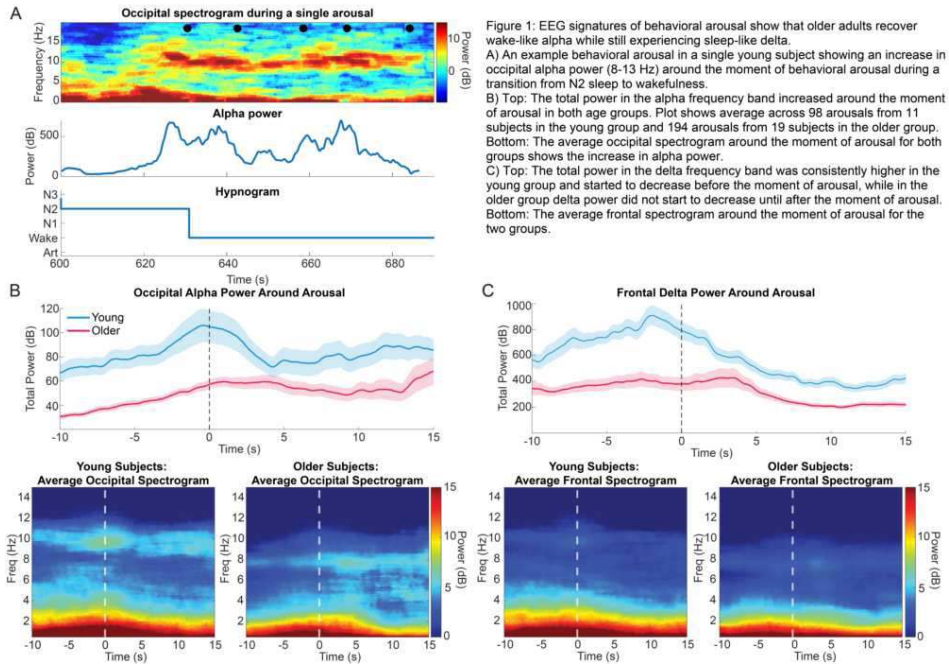

Figure 1: EEG signatures of behavioral arousal show that older adults recover wake-like alpha while still experiencing sleep-like delta.
A) An example behavioral arousal in a single young subject showing an increase in occipital alpha power (8-13 Hz) around the moment of behavioral arousal during a transition from N2 sleep to wakefulness.
B) Top: The total power in the alpha frequency band increased around the moment of arousal in both age groups. Plot shows average across 98 arousals from 11 subjects in the young group and 194 arousals from 19 subjects in the older group. Bottom: The average occipital spectrogram around the moment of arousal for both groups shows the increase in alpha power.
C) Top: The total power in the delta frequency band was consistently higher in the young group and started to decrease before the moment of arousal, while in the older group delta power did not start to decrease until after the moment of arousal. Bottom: The average frontal spectrogram around the moment of arousal for the two groups.

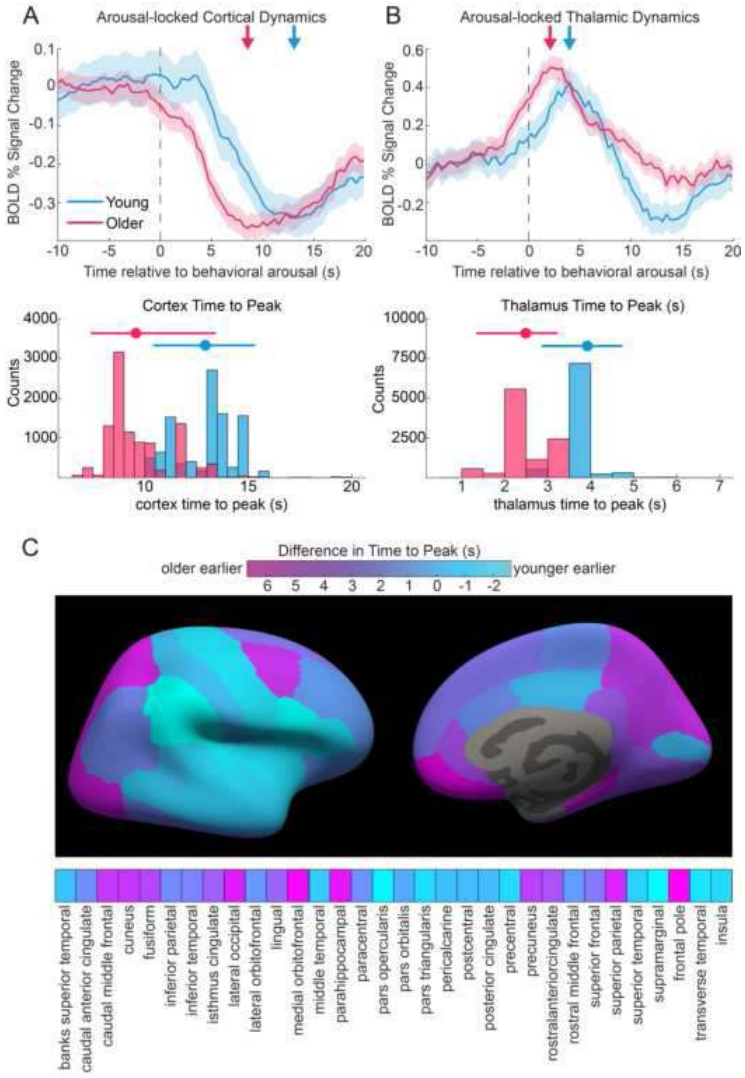

Figure 2: BOLD fMRI signatures of behavioral arousal show faster transition to wake-like activity in the older group.
A) Top: In both age groups, the cortex deactivated following behavioral arousal as expected. Arrows denote the time to the absolute maximum (i.e., maximum deactivation). Bottom: In the older group the cortex trended toward an earlier activation ($p=0.074$) as shown by the histogram of time to peak values across 10,000 bootstraps (older average = 9.00 s, 95% CIs = [7.77, 13.44] s; young average = 12.59 s, 95% CIs = [10.79, 15.33] s).
B) Top: In both groups, the thalamus began to activate before the behavioral arousal and reached its peak activation in the seconds following the arousal. Arrows denote the time to the absolute maximum. Bottom: In the older group, the thalamus reaches its peak activation earlier ($p=0.004$) than in the young group as shown by the histogram of time to peak values across 10,000 bootstraps (older average = 2.45 sec, 95% CIs = [1.72, 3.23] s; young average = 3.94 s, 95% CIs = [3.23, 4.36] s).
C) A majority of cortical regions reach their peak deactivation earlier in the older group compared to the young group. Reported values are the average of 10,000 bootstraps. P-values were obtained through permutation testing of group differences.

Conclusions: We found that despite sharing a general pattern of dynamics that unfold around arousal, the timing of the EEG and fMRI changes differs between the age groups. Older adults exhibited a mixed electrophysiological state following arousal containing EEG signatures of both wakefulness and sleep that was not observed in the young group. Conversely, the older adults had faster changes in the fMRI signatures of arousal compared to the young group. These results demonstrate that the mechanisms controlling arousal state transitions are occurring on different time scales for the two groups. Furthermore, we found slower electrophysiological arousals and faster hemodynamics in aging, suggesting an alteration of arousal circuitry in the older brain.

References

1. Mander, B.A. (2017), 'Sleep and Human Aging,' Neuron, vol. 94, no. 1, pp. 19-36
2. Sabia, S. (2021), 'Association of sleep duration in middle and old age with incidence of demential,' Nature Communications, vol. 12, no. 1, pp. 2289
3. Setzer, B (2022), 'A temporal sequence of thalamic activity unfolds at transitions in behavioral arousal state,' Nature Communications, vol. 13, no. 1, pp. 5442
4. Daneault, V (2021), 'Cerebral functional networks during sleep in younger and older individuals,' vol. 11, no. 1, pp. 4905

Poster No 2587

Individualized Neural Dynamics Patterns During Sleep by High-Resolution Phenotype Mapping

Hyeon Jin Kim[1,2], Younghan Lee[3], Sophie Saremsky[4], Habiba Noamany[4], Youngseo Kim[5], Ho Bae[5], Yunheung Paek[3], Michael J. Prerau[4], Hyang Woon Lee[5,2]

[1]Department of Neurology, Korea University Ansan Hospital, Ansan, Republic of Korea, [2]Departments of Neurology and Medical Science, Ewha Womans University School of Medicine and Ewha Medical Research Institute, Seoul, Korea, Republic of, [3]Department of Electrical and Computer Engineering (ECE) and Inter-University Semiconductor Research Center (ISRC), Seoul National University, Seoul, Korea, Republic of, [4]Division of Sleep and Circadian Disorders, Brigham and Women's Hospital, Boston, MA, [5]Artificial Intelligence Convergence and Computational Medicine, System Health Science & Engineering, Graduate School of Ewha Womans University, Seoul, Korea, Republic of

Introduction: Cognitive processing during sleep has been revealed to rely on the precisely synchronized interactions of rhythmic oscillation of neural activities. Current practice, however, significantly limits our ability to explore the continuously evolving neurophysiological dynamics by the low-resolution framework, which discretizes the neural states during sleep only into 5 categories with a temporal constraint of a non-overlapping 30-sec epoch. Recent studies have shown that the slow oscillation (SO) power can be used as a continuous correlate of depth of sleep. In this study, we aim to represent the personal intrinsic neural dynamic patterns during sleep by high-resolution phenotype mapping, which is independent of the temporal evolution of sleep architecture or night-to-night variability.

Methods: We analyzed 80 polysomnography (PSG) data previously recorded from 20 middle-aged female subjects (mean age of 56.45 ± 3.97 years) for unrelated research, approved by the IRB of Ewha Womans University Mokdong Hospital and was registered with the Clinical Research Information Service (CRIS; study number KCT0001867). For all subjects, four PSGs at one-month intervals were recorded at the hospital sleep laboratory. We analyzed each night's EEG signal from the C3-A1 electrode derivation, and the data segment was from the time of lights out to the time of lights on. SO-power was computed as the total power in the artifact-free EEG multitaper spectrogram between .5 – 2.0 Hz within a 60s window with 5s step (TW=30, L=29). Then, mean spectral power from .5-30 Hz was computed as a function of SO-power to obtain the state-based histogram. For dimensionality reduction, a low-resolution (60 x 41) representation of the SO-power histogram was created for each PSG recording. To evaluate the intra-subject stability of the suggested framework, the similarity of the four SO-power histogram matrices from each participant was determined through mean square error (MSE) and Euclidian distance, which measures the average squared differences.

Results: The average length (time-in-bed) of our PSG recordings was 309.34 ± 46.41 minutes, and the sleep efficiency was 78.73 ± 10.85%. According to the standard guidelines of the AASM, 84.19 ± 6.94% was NREM sleep, of which the slow wave sleep was 4.85 ± 4.92%. Despite night-to-night variability in sleep architecture evolution over time within each subject, the repeatedly calculated SO-power histograms from one's own four PSG recordings exhibited marked similar patterns, showing consistency in the neural dynamics of each individual. Moreover, we also confirmed the heterogeneity of the SO-power histogram between subjects. The MSE between the first night PSG recording and the other three PSG recordings obtained from the same subject was lower than the MSE between different subjects.

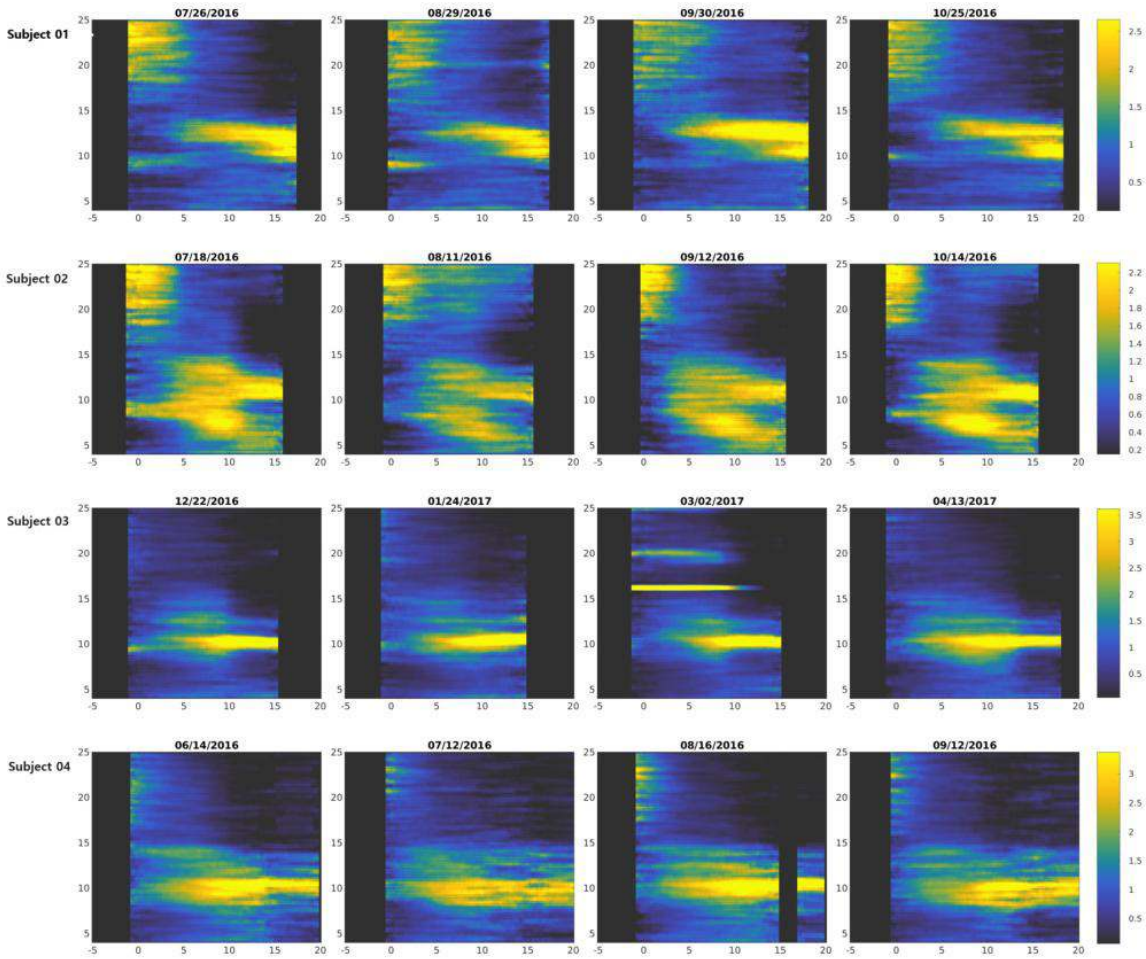

Fig. Intra-individual stability and Inter-individual variability of the suggested framework

Conclusions: In this study, we build on previous work (Kim et. al, Stokes et. al) and compute a SO-power histogram, which visualizes the median spectral power as a function of frequency and SO-power. In this work, we extend previous findings of night-to-night stability to show clear month-to-month stability. This allows us to observe how non-stationary oscillatory dynamics of the brain during sleep can comprehensively and quantitatively be represented using continuous-valued correlates of sleep depth without being affected by different temporal sleep evolution patterns. By choosing a high-dimensional, low-variability representation of sleep EEG data, we can create a high-resolution phenotype mapping framework that is more sensitive to changes in nneural dynamic states, and thus a powerful tool for assessing potential changes in neurological health.

References

1. Kim, H. J., Chen, S., Eden, U. T., & Prerau, M. J. (2021, May). A quantitative representation of continuous brain state during sleep. In 2021 10th International IEEE/EMBS Conference on Neural Engineering (NER) (pp. 103-106). IEEE.
2. Prerau, M. J., Brown, R. E., Bianchi, M. T., Ellenbogen, J. M., & Purdon, P. L. (2017). Sleep neurophysiological dynamics through the lens of multitaper spectral analysis. Physiology, 32(1), 60-92.
3. Stokes, P. A., Rath, P., Possidente, T., He, M., Purcell, S., Manoach, D. S., ... & Prerau, M. J. (2023). Transient oscillation dynamics during sleep provide a robust basis for electroencephalographic phenotyping and biomarker identification. Sleep, 46(1), zsac223.
4. Kim, H. J., Kim, J., Lee, S., Kim, B., Kwon, E., Lee, J. E., ... & Lee, H. W. (2019). A double-blind, randomized, placebo-controlled crossover clinical study of the effects of alpha-s1 casein hydrolysate on sleep disturbance. Nutrients, 11(7), 1466.

Acknowledgments

This study was supported by grants from the Korea University Ansan Hospital [K2316061 to H.J.Kim], the Korea Health Technology R & D Project through the KHIDI, funded by the Ministry of Health & Welfare [HI19C1065 to H.J.Kim], the National Research Foundation of Korea [NRF-2019M3C1B8090803 and 2020R1A2C2013216 to H.W.Lee], the IITP grant through the MSIT/Ministry of Education & Future Planning [RS-2022-00155966 to H.W.Lee and RS-2023-00277326 to Y.Lee], and by the BK21 FOUR program of the Education and Research Program for Future ICT Pioneers programs of Ewha Womans University and Seoul National University in 2023.

Poster No 2588

REM sleep is characterized by infra-slow waves propagating across the neocortical hierarchy

Xufu Liu[1], Dante Picchioni[2], Yifan Yang[1], Hendrik Mandelkow[2], Jacco de Zwart[2], Jeff Duyn[2], Xiao Liu[1]

[1]The Pennsylvania State University, State College, PA, [2]National Institutes of Health, Bethesda, MD

Introduction: Infra-slow (<0.1 Hz) spatiotemporal dynamics play a crucial role in shaping resting-state functional connectivity, which has been linked to various aspects of brain function and dysfunction[1,2]. Newly reported propagating waves represent a specific form of these infra-slow dynamics, which travel along the cortical hierarchical gradient between sensory/motor (SM) cortices and the higher-order default mode network (DMN)[3]. This propagating direction is consistent with flows of information required for optimizing artificial neural networks[4], suggesting a possible link of these propagating waves to learning and memory. Cross-hierarchy information flow has also been hypothesized to be critical for sleep, particularly rapid eye movement (REM) sleep[5], to fulfill its known role in offline learning and memory. Nevertheless, it remains unclear how the cross-hierarchy propagating waves are modulated across sleep stages, particularly during REM sleep. Here, we examined the cross-hierarchy fMRI propagating waves across various sleep stages through whole-night fMRI/electroencephalography (EEG) recordings.

Methods: We analyzed 12 subjects, each with two nights of simultaneous fMRI/EEG[6]. Among them, 18 nights showed REM sleep. We identified cross-hierarchy propagating waves[3] in bottom-up (SM to DMN) and top-down (DMN to SM) directions and compared their occurrence fraction under various sleep stages. We focused on stable sleep periods during which a specific sleep stage lasted longer than one minute. We aligned and averaged fMRI propagations according to the global mean BOLD (gBOLD) peak within each identified propagation and converted the result into t-score maps. Relative phase delay of a specific region in bottom-up propagation is the time delay between its peak activation and the propagation center defined as the gBOLD peak. We quantified eye movements based on two independent measurements: the electrooculogram (EOG) signal variation and motion signals derived from concurrent video recordings[7]. We identified isolated eye movements (at least 8 seconds of stable eye position on either side, duration less than 3 seconds), and examined fMRI changes around them.

Results: Bottom-up propagations gradually increased from wakefulness to deeper NREM sleep stages (N1 to N3), peaking during REM sleep (Fig.1A). Top-down propagations followed a similar trend during wakefulness and NREM stages but exhibited an opposite change and reached its minimum during REM sleep (Fig.1B). Hence, REM sleep featured the largest rate difference between the two types of propagations (Fig.1C). Importantly, the bottom-up propagating waves during REM sleep showed distinct dynamics in the thalamus, pons and visual cortex, key regions with established involvement in ponto-geniculo-occipital (PGO) waves of REM signature (Fig.1D and 1E). Their phase in the bottom-up propagations (i.e., relative time delay to the propagation center) was significantly advanced to earlier time as compared to other conditions (Fig.1E), and this effect is absent in the control somatosensory areas. The bottom-up propagations during REM sleep were also associated with systematic eye movements, as estimated by EOG variation (Fig.2A). Consistent with this, fMRI changes at eye movements detected via EOG showed progressively increasing time delays along the cortical hierarchical gradient, as described by a principal gradient (PG) direction (Fig.2B). This pattern manifested as a bottom-up propagation on the cortical surface (Fig.2C) and is associated with early thalamic and pontine activity (Fig.2C). In addition, fMRI changes at isolated eye movements detected through concurrent video recordings displayed similar dynamics of bottom-up propagating waves (Fig.2D-2F).

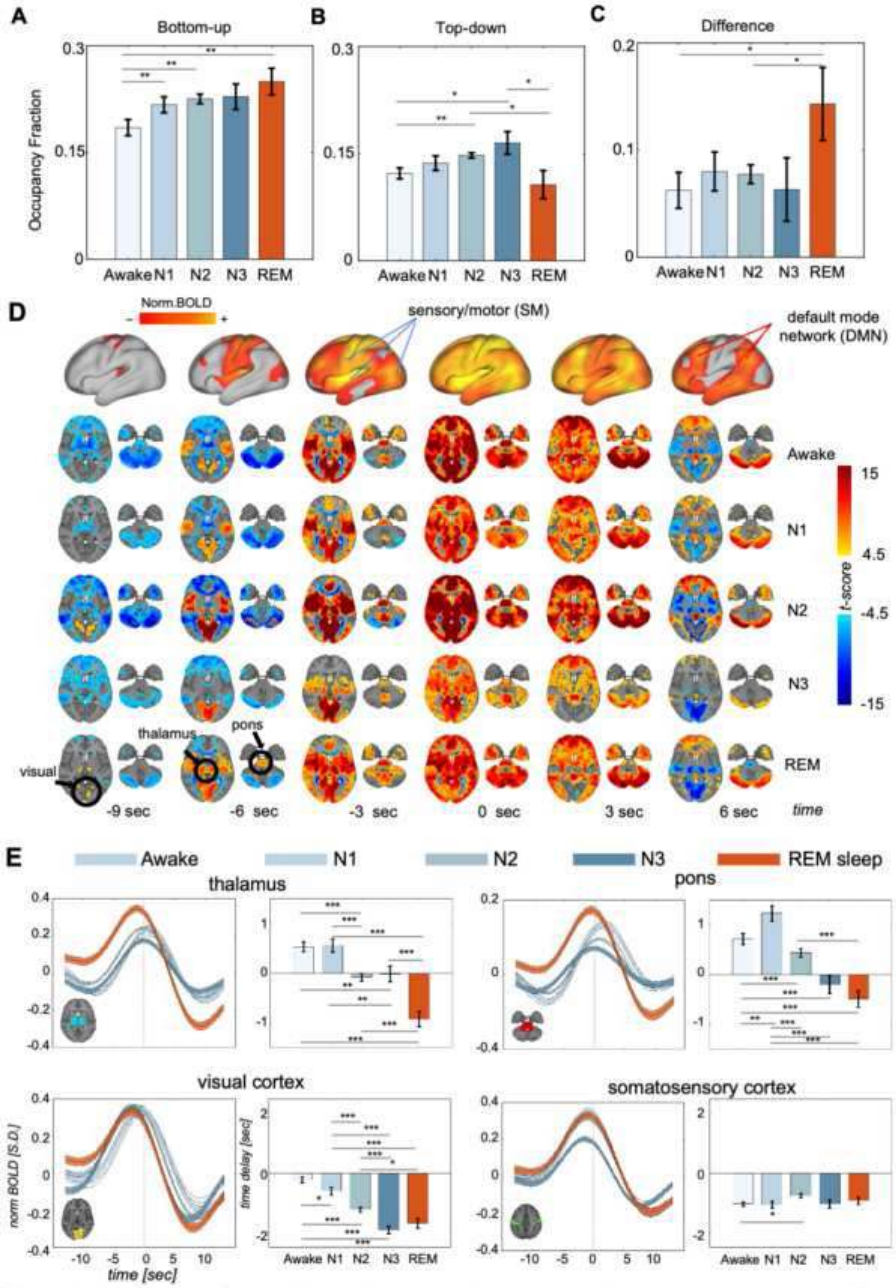

Figure 1. Modulation of cross-hierarchy propagating waves varies across sleep stages. The occupancy fraction of bottom-up (A) and top-down (B) propagating waves, as well as their differences (C). Significant changes are marked by asterisks. (D) The averaged pattern of bottom-up propagations under awake, N1, N2, N3, and REM sleep. The top row shows averaged bottom-up propagations across all conditions on a brain surface. (E) For each of the four regions, the left panel shows the averaged fMRI time courses of bottom-up propagations under the various arousal states, whereas the right panel summarized the relative time delays between their peak activation and the propagation center. (*: $p<0.05$; **: $p<0.01$; ***: $p<0.001$). Error bars and shaded regions represent the range within one standard error of the mean (SEM).

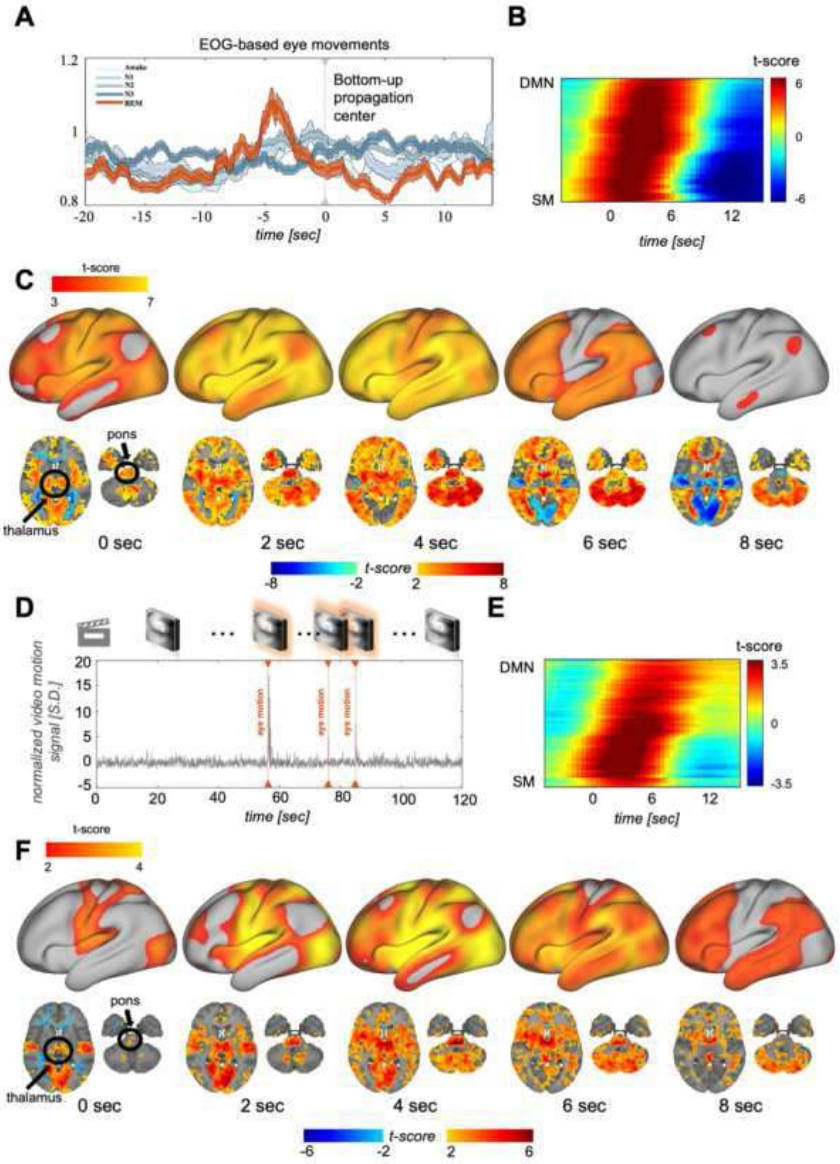

Figure 2. Bottom-up propagations during REM sleep are associated with eye movements.
(A) EOG-based estimates of eye movements show a big peak at the early phase (~ –4.5 seconds) of bottom-up propagations during REM sleep. (B) Averaged fMRI changes, sorted according to the PG, around isolated eye movements detected by EOG during REM sleep. (C) fMRI changes at EOG-detected eye movements displayed on a cortical surface and in two axial slices. (D) Examples of isolated eye motion based on concurrent video recordings. (E, F) Same as (B, C) but for video-detected eye movements.

Conclusions: Cross-hierarchy propagating waves of fMRI activity are significantly modulated across sleep stages. REM sleep is characterized by notably dominant bottom-up propagations, which appear linked to PGO waves and eye movements.

References

1. Mitra, A. (2017), 'The Lag Structure of Intrinsic Activity is Focally Altered in High Functioning Adults with Autism', Cerebral Cortex, vol. 27, no. 2, pp. 1083-1093
2. Mitra, A. (2015), 'Propagated infra-slow intrinsic brain activity reorganizes across wake and slow wave sleep', Elife, vol. 4, e10781.
3. Gu, Y. (2021), 'Brain Activity Fluctuations Propagate as Waves Traversing the Cortical Hierarchy', Cerebral Cortex, vol. 31, no. 9, pp. 3986–4005
4. Goh, A. T. C. (1995), 'Back-propagation neural networks for modeling complex systems', Artificial Intelligence in Engineering, vol. 9, no. 3, pp. 143–151
5. Hobson, J. A. (2014), 'Virtual reality and consciousness inference in dreaming', Frontiers in psychology, vol. 5.
6. Moehlman, T. M. (2019), 'All-night functional magnetic resonance imaging sleep studies', Journal of Neuroscience Methods, vol. 316, pp. 83–98.
7. Stringer, C. (2019), 'Spontaneous behaviors drive multidimensional, brainwide activity', Science, vol. 364, no. 6437, pp. eaav7893.

Poster No 2589

Transient Sleep EEG Oscillation Dynamics Reveal Novel Changes in Brain State Across the Lifespan

Michael Prerau[1], Thomas Possidente[2], Habiba Noamany[2], Mingjian He[2,3,4], Sophie Saremsky[2]

[1]Brigham and Women's Hospital/Harvard Medical School, Boston, MA, [2]Division of Sleep and Circadian Disorders, Brigham and Women's Hospital, Boston, MA, [3]MIT-HST Program, Cambridge, MA, [4]Department of Anesthesia, Critical Care, and Pain Management, Massachusetts General Hospital, Boston, MA

Introduction: Transient oscillatory events in the sleep electroencephalogram (EEG), such as sleep spindles, have been linked to memory consolidation, and changes in spindle activity have been associated with numerous psychiatric, neurodevelopmental, and neurodegenerative disorders. However, our recent studies have shown that traditional sleep spindles represent only a subset of a larger class of transient oscillatory events and that classes of spindle-like events at other frequencies, such as those occurring at low-alpha and theta ranges, can act as a biomarker of disorders such as schizophrenia. Moreover, we have shown that transient oscillation dynamics are fingerprint-like: highly heterogeneous between individuals, yet strongly consistent night-to-night. While sleep spindles change throughout the lifespan, there is little characterization of general classes of transient oscillations and their dynamics. In this study, we describe oscillation activity as a function of slow oscillation (SO) power (a continuous depth-of-sleep metric), and SO-coupled phase (a correlate of cortical up/down states) to expand our view of potential biomarkers in neurodevelopment and aging.

Methods: Transient oscillations were detected as time-frequency peaks (TF-peaks) in the sleep EEG spectrogram from the Cleveland Family Study (N=735, ages 7-89) using the DYNAM-O toolbox (sleepEEG.org), an extended implementation of methods described in detail in Stokes et. al 2022. In short: we first identify time-frequency peaks in the topography of the multitaper spectrogram of the sleep EEG using a variant of the watershed method. We then summarize the dynamics of the tens of thousands of detected TF-peaks per subject in visualizations called SO-power and SO-phase histograms, which plot TF-peak rate as a function of continuous depth of sleep (SO-power) and SO-phase. SO-power and phase histograms were computed for all CFS subjects and stratified by age. Statistical comparisons across population-averaged age groups were computed using FDR-corrected two-sample t-tests.

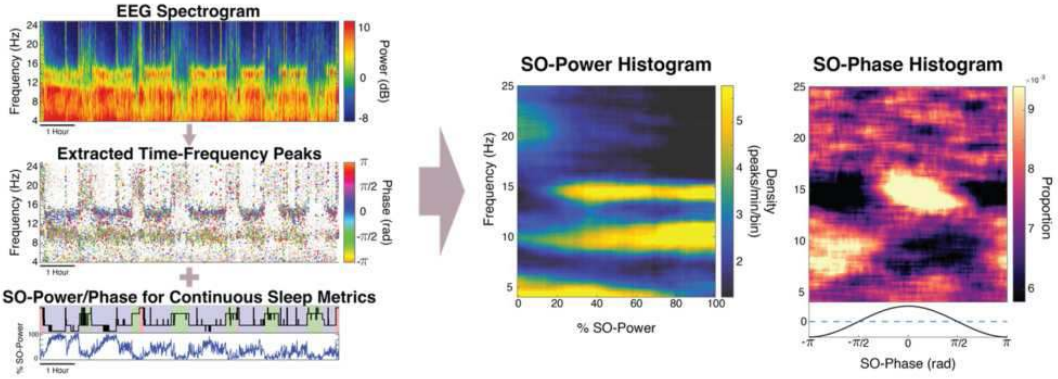

Figure 1: The dynamics of thousands of time-frequency peaks (TF-peaks) are summarized in slow oscillation (SO) power and phase spectrograms. Using a variant of the watershed algorithm, we extract salient topographical peaks from the sleep EEG spectrogram. For each peak, we extract the corresponding SO power (a continuous correlate of sleep depth) and SO phase (a marker of thalamocortical up/down state). TF-peak rate is visualized as a function of frequency and these correlates, forming the SO-power and SO-phase histograms.

Results: Significant differences in transient oscillation activity mode strength, frequency, SO-power, and SO-phase were observed across the lifespan. We identified stereotyped dynamics in sleep depth/frequency/amplitude in traditional "fast" spindle activity, rising from ~11 to 15 Hz, as well in a class of rising 6 to 10 Hz transient oscillation events during neurodevelopment, and the appearance of slow spindle activity at approximately 25 years of age. Moreover, we observe an initial mismatch between the frequencies of maximal SO-phase coupling and maximal transient oscillation density, which converge during development, suggesting the gradual emergence of coordination between networks essential for memory consolidation.

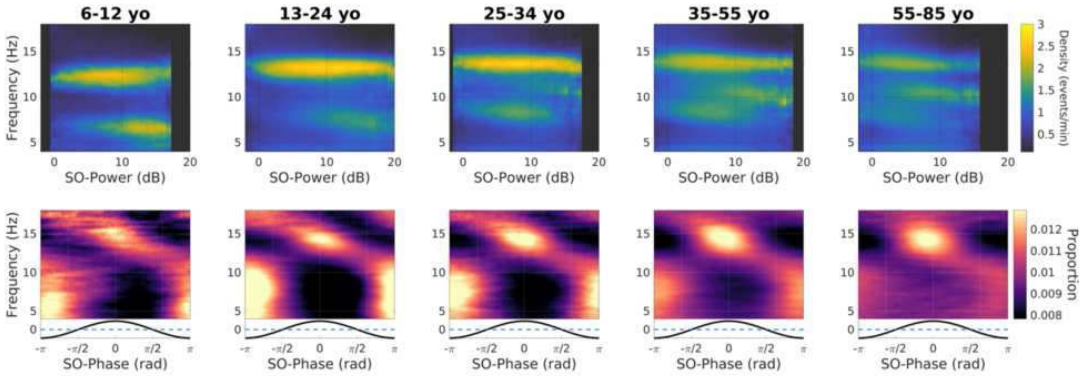

Figure 2: Changes in transient oscillation dynamics across the lifespan. Using data from the Cleveland Family Study (N=735, age 7-89) we computed SO-power and phase histograms for all subjects, which were averaged in age groups. In the SO-power histograms, we observe clear changes in multiple modes across maturation and aging. In particular, we observe a rise in frequency from ~11-14 Hz in the "fast" spindle mode, an increase from ~6-8 Hz in the lower frequency mode, and the appearance of a "slow" spindle mode in the 25 to 34 year-old group. In the SO-phase histograms, we observe the characteristic negative phase shift in the 12-15Hz mode with age, along with global changes in phase coupling structure across the lifespan.

Conclusions: By characterizing general classes of transient oscillation activity across frequency, we identify unreported features of the sleep EEG and their associated dynamics throughout the lifespan. The framework constitutes a dramatic shift in approach for population analysis of sleep EEG activity-characterizing the distributional properties of general event classes rather than attempting to detect specific waveforms. These modal dynamics raise important mechanistic questions and act as new windows into the intersection of sleep physiology and the pathophysiology of related disorders. Finally, these dynamics provide a powerful new basis for the development of EEG biomarkers for tracking and detection of neurological disorders.

References

1. Dimitrov, T. (2021), "Sleep Spindles Comprise a Subset of a Broader Class of Electroencephalogram Events." Sleep, April. https://doi.org/10.1093/sleep/zsab099.
2. Fernandez, L.M. (2020), "Sleep Spindles: Mechanisms and Functions." Physiological Reviews 100 (2): 805–68. https://doi.org/10.1152/physrev.00042.2018.
3. Prerau, M. J. (2017), "Sleep Neurophysiological Dynamics through the Lens of Multitaper Spectral Analysis." Physiology 32 (1): 60–92. https://doi.org/10.1152/physiol.00062.2015.
4. Purcell, S.M. (2017), "Characterizing Sleep Spindles in 11,630 Individuals from the National Sleep Research Resource." Nature Communications 8 (June): 15930. https://doi.org/10.1038/ncomms15930.
5. Redline, S. (1995), "The Familial Aggregation of Obstructive Sleep Apnea." American Journal of Respiratory and Critical Care Medicine 151 (3 Pt 1): 682–87. https://doi.org/10.1164/ajrccm/151.3_Pt_1.682.
6. Stokes, P.A. (2023), "Transient Oscillation Dynamics during Sleep Provide a Robust Basis for Electroencephalographic Phenotyping and Biomarker Identification." Sleep 46 (1): zsac223. https://doi.org/10.1093/sleep/zsac223.
7. Zhang, G. (2018), "The National Sleep Research Resource: Towards a Sleep Data Commons." Journal of the American Medical Informatics Association 25 (10): 1351–58. https://doi.org/10.1093/jamia/ocy064.

Poster No 2590

Features of slow rhythmic fMRI activity in the thalamus are linked to changes in arousal state

Beverly Setzer[1,2], Sydney Bailes[1,2], Carsen Stringer[3], Laura Lewis[4,5]

[1]Boston University, Boston, MA, [2]Massachusets Institute of Technology, Cambridge, MA, [3]Janelia Research Campus, Ashburn, VA, [4]Massachusetts Institute of Technology, Cambridge, MA, [5]Athinoula A. Martinos Center for Biomedical Imaging, Charlestown, MA

Introduction: In light sleep and drowsiness, the brain exhibits low-frequency oscillations. These can be observed in both electrical neural signals by electroencephalography (EEG) and in blood-oxygen level dependent (BOLD) signals by fast functional magnetic resonance imaging (fMRI) (Horovitz et al., 2008; Watson, 2018). EEG infraslow oscillations have been linked to changes in arousal levels (Monto et al., 2008; Sihn & Kim, 2022), and a peak in BOLD signal locks to changes in physiological arousal state (Raut et al., 2021). However, precisely how rhythmic slow BOLD dynamics are related to behavioral arousal state, the ability to sustain behavior, is unknown. A key question is whether the distinct spatio-temporal features, like amplitude, frequency, and propagation dynamics of BOLD signal peaks have behavioral significance. Interestingly, peaks in the BOLD signal locked to changes in physiological arousal state propagate across the brain, from unimodal (early sensory processing) to transmodal (higher-order cognition) regions (Gu et al., 2021; Raut et al., 2021). On a fine-grained level, a precise

spatio-temporal pattern of BOLD activity propagates across the thalamus with fluctuating arousal (Gu et al., 2021; Raut et al., 2021; Setzer et al., 2021), which is a core deep-brain structure comprised of sub-nuclei with diverse functional roles in cognition. Therefore, slow, rhythmic brain dynamics have some functional and spatial structure. We thus aimed to use fast fMRI to discover how slow BOLD dynamics in the thalamus are linked to arousal state, and investigate if specific spatio-temporal features of these dynamics affect behavior.

Methods: We used fMRI to capture activity throughout the brain while subject's arousal state varied across sleep and wakefulness. In Experiment 1, we used ultra-high field (7 Tesla) functional magnetic resonance imaging (fMRI) to capture high resolution (n=15 subjects, TR=247 mS, 2.5 mm isotropic voxels) dynamics. Subjects performed a simple button pressing task to track behavioral state (Prerau et al., 2014), and were allowed to fall asleep inside the scanner. In Experiment 2, we used simultaneous EEG-fMRI at 3 Tesla (n=5 subjects, TR=367 mS, 2.5 mm isotropic voxels) to capture how canonical arousal-related EEG rhythms were coupled to peaks in the BOLD oscillation. First, we evaluated how both behavioral and EEG arousal state was linked to BOLD oscillation peaks by averaging behavior and EEG signals during all BOLD peaks. Then, to group peaks together with similar spatio-temporal features and evaluate arousal differences between groups in a data driven way, we clustered BOLD activity across thalamic voxels using unsupervised machine learning (Stringer et al., 2023). This analysis captured both how temporal dynamics vary across the thalamus spatially and between individual peaks in the rhythmic activity. To assess the relationship directly between peak features with behavior, we averaged behavior across different amplitude and frequencies independently.

Results: We identified two distinct clusters that had different features of thalamic activity dynamics: one with low-amplitude fast oscillations, and one with slower, larger oscillations (Figure 1a). The slow, large amplitude peaks had a stronger coupling to behavior (Figure 1b) and EEG rhythms than the fast, low amplitude peaks, which were associated with a higher baseline EEG arousal state. We found that peak amplitude was directly coupled to transitions in behavior, and that frequency was coupled to overall behavioral arousal state. Therefore, thalamic activity was linked to behavior and EEG rhythms in a state-dependent manner, with changes in behavior and EEG rhythms occurring more strongly in clusters of thalamic peaks with specific features.

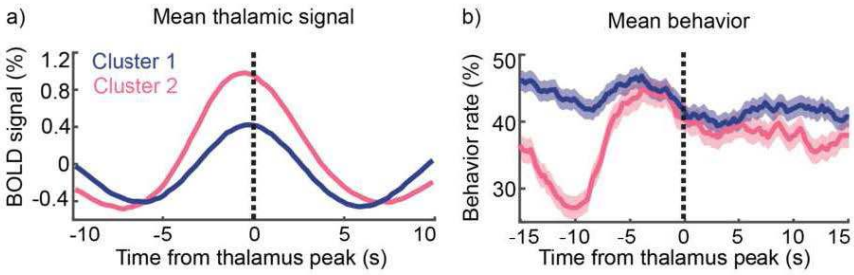

Figure 1. Thalamic BOLD signal peaks with higher amplitude and lower frequency correspond to a transition in behavioral state. (a) Unsupervised machine learning identified two clusters of thalamic BOLD signal peaks: one with low-amplitude fast oscillations (blue, n=1036 peaks), and one with slower, larger oscillations (pink, n=656 peaks). b) A greater change in behavior (click rate) occurs in the cluster with larger amplitude, lower frequency peaks. The smaller thalamic peaks occur during higher, more stable arousal states. Shading is standard error.

Conclusions: This study reveals functional differences in rhythmic BOLD signal activity linked to drowsiness and light sleep. Additionally, we identified distinct states of thalamic activity that coupled to different behavior and EEG arousal levels.

References

1. Gu, Y. (2021). 'Brain Activity Fluctuations Propagate as Waves Traversing the Cortical Hierarchy', Cerebral Cortex (New York, N.Y.: 1991), 31(9), 3986–4005.
2. Horovitz, S. (2008). 'Low frequency BOLD fluctuations during resting wakefulness and light sleep: A simultaneous EEG-fMRI study', Human Brain Mapping, 29(6), 671–682.
3. Monto, S. (2008). Very Slow EEG Fluctuations Predict the Dynamics of Stimulus Detection and Oscillation Amplitudes in Humans. Journal of Neuroscience, 28(33), 8268–8272.
4. Prerau, M. J. (2014). Tracking the Sleep Onset Process: An Empirical Model of Behavioral and Physiological Dynamics. PLoS Computational Biology, 10(10), e1003866.
5. Raut, R. (2021). Global waves synchronize the brain's functional systems with fluctuating arousal. Science Advances, 7(30), eabf2709.
6. Setzer, B. (2021). A temporal sequence of thalamic activity unfolds at transitions in behavioral arousal state (p. 2021.12.01.470627).
7. Sihn, D. (2022). Brain Infraslow Activity Correlates With Arousal Levels. Frontiers in Neuroscience, 16.
8. Stringer, C. (2023). Rastermap: A discovery method for neural population recordings [Preprint]. Neuroscience.
9. Watson, B. O. (2018). Cognitive and Physiologic Impacts of the Infraslow Oscillation. Frontiers in Systems Neuroscience, 12.

Poster No 2591

Characteristics of Sleep Neural Dynamics between Men and Women with Obstructive Sleep Apnea

Younghan Lee[1,2], Youngseo Kim[3], Hyeon Jin Kim[4,5,6], Ho Bae[7], Yunheung Paek[1,2], Hyang Woon Lee[3,5,6,8]

[1]Department of Electrical and Computer Engineering (ECE),Seoul National University, Seoul, Korea, Republic of, [2]Inter-University Semiconductor Research Center (ISRC), Seoul National University, Seoul, Korea, Republic of, [3]Graduate Program of Artificial Intelligence Convergence, Ewha Womans University, Seoul, Korea, Republic of, [4]Department of Neurology, Korea University Ansan Hospital, Ansan-si, Gyeonggi-do, [5]Departments of Neurology Ewha Womans University School of Medicine and Ewha Medical Research, Seoul, Korea, Republic of, [6]Departments of Medical Science, Ewha Womans University School of Medicine and Ewha Medical Research, Seoul, Korea, Republic of, [7]Department of Cyber Security, Ewha Womans University, Seoul, Korea, Republic of, [8]Computational Medicine, System Health Science & Engineering, Graduate School of Ewha Womans University, Seoul, Korea, Republic of

Introduction: Among the myriad sleep disorders, Severe Obstructive Sleep Apnea (OSA) stands out as a prevalent and potentially debilitating condition, characterized by recurrent upper airway obstruction leading to disrupted breathing patterns during sleep. While the physiological impact of OSA on sleep architecture is well-established, the intricate neural dynamics underlying these disruptions remain an area of active investigation. In this study, we focus on unraveling the distinctions in neural activity during sleep between men and women with severe OSA in comparison to those with mild to moderate OSA and healthy controls without OSA. Through advanced methodologies using high-resolution neurodynamic analyses, we aimed to elucidate the differences of quantitative sleep characteristics in severe OSA patients in comparison to those in mild to moderate OSA and in control subjects without OSA. Additionally, we thrive to compare these sleep characteristics between male and female patients.

Methods: A total of 852 anonymous polysomnography (PSG) datasets which were collected for an unrelated research initiative, having received approval from the Institutional Review Board (IRB) at Ewha Womans University Mokdong Hospital. Within this dataset, 284 individuals were identified with severe OSA, comprising 44 females and 240 males, with an average age of 52.54 years and 284 individuals with mild to moderate OSA with the same ratio of sex and the average age of 52.23 years. To ensure methodological robustness, we matched the sex and age parameters of the healthy control dataset without OSA preserving an average age of 51.78 years, with an equal distribution of 44 females and 240 males. The EEG data which is sampled at a rate of 200 Hz is used for spectral estimation through multitaper approach. We only focused on the C3 electrode and EEg spectrograms were drawn for each subject. Firstly, we extracted slow-oscillation (SO) power in a range of 0.5-2.0Hz. Subsequently carried out a calculation to generate histograms that indicates the average SO-power within the rage of 0.5-30 Hz. To facilitate mathematical analysis and identify characteristics of sleep neural dynamics in OSA, it is essential to standardize the vector of SO-power divided equally into 41 segments (0-39, respectively) across subjects. We employed the mean squared error (MSE) metric which aids in the precise evaluation of distinctions, contributing to a comprehensive understanding of the unique features of sleep neural dynamics in individuals with OSA.

Results: We computed the average of SO-powers in each segment within three groups: those with severe OSA, those with mild to moderate OSA, and those without OSA. We utilized the mean squared error (MSE) for each SO-power segment to identify the differences between these three groups. Smaller MSE values indicate greater similarity in the characteristics of sleep neural dynamics. Our results revealed notable variations across segments between groups. In particular, the differences were significant in SO-powers with lower (segments 1-6) and higher (segments 43-40) ranges between the severe OSA and healthy control groups.

Conclusions: Through the generation of sleep EEG spectrograms and computation of histograms for SO-power, we unveiled notable differences between OSA patients and controls, especially between severe OSA and control groups, particularly evident in lower and higher ranges. The potential clinical implications of our proposed method, combined with high-resolution neural dynamic analyses, include investigation of sleep quality in OSA patients with different disease severity as well as regular monitoring for the sleep improvement before and after therapeutic intervention.

References

1. Malhotra, Atul, et al. “Metrics of sleep apnea severity: beyond the apnea-hypopnea index.” Sleep 44.7 (2021): zsab030.
2. Prerau, Michael J., et al. “Sleep neurophysiological dynamics through the lens of multitaper spectral analysis.” Physiology 32.1 (2017): 60-92.
3. H. J. Kim, S. Chen, U. T. Eden and M. J. Prerau, “A quantitative representation of continuous brain state during sleep,” 2021 10th International IEEE/EMBS Conference on Neural Engineering (NER), Italy, 2021, pp. 103-106, doi: 10.1109/NER49283.2021.9441276.
4. Han, H., Oh, J. Application of various machine learning techniques to predict obstructive sleep apnea syndrome severity. Sci Rep 13, 6379 (2023). https://doi.org/10.1038/s41598-023-33170-7

Acknowledgments
Supported by the National Research Foundation of Korea (NRF) (No. 2019M3C1B8090803, 2020R1A2C2013216, and RS-2023-00265524), Institute of Information & Communication Technology Planning & Evaluation (IITP) grant (No. RS-2022-00155966) by the Korea government (MSIT), and BK21-plus FOUR and Artificial Intelligence Convergence Innovation Human Resources Development programs of Ewha Womans University. to H.W.Lee. This study was supported by grants from the Korea University Ansan Hospital [No. K2316061 to H.J.Kim], the Korea Health Technology R & D Project through the Korea Health Industry Development Institute (KHIDI), funded by the Ministry of Health & Welfare, Republic of Korea [HI19C1065 to H.J.Kim]. This work was supported by the BK21 FOUR program of the Education and Research Program for Future ICT Pioneers, Seoul National University in 2023. Also, it was supported by the National Research Foundation of Korea(NRF) grant funded by the Korea government(MSIT) (RS-2023-00277326).

Poster No 2592

Short-Term CBF and FC Response to Moderate Exercise Differs in Congenital Heart Disease Patients

Vanessa Schmithorst[1], Aurelia Sahel[2], Vince Lee[1], Julia Wallace[2], Ashok Panigrahy[2]

[1]UPMC Children's Hospital, Pittsburgh, PA, [2]UPMC Children's Hospital of Pittsburgh, Pittsburgh, PA

Introduction: Aerobic exercise causes short-term changes in cerebral blood flow (CBF) (Querido & Sheel, 2007; Olivo et al., 2021) and functional connectivity (Ko et al., 2023); and long-term neurocognitive benefits (Colcombe & Kramer, 2003) mediated by vascular changes (Hillman et al., 2008). Congenital heart disease (CHD) patients show neurocognitive deficits in a variety of domains (Donofrio & Massaro, 2010) and aerobic exercise may be a promising intervention. We investigated the short-term effects of moderate intensity exercise on CBF and functional connectivity strength (FCS), in CHD patients and normal controls.

Methods: Participants were10 normal controls (age = 23.3 +/- 4.0 years, 7 M, 3 F) and 7 CHD patients (age = 27.7 +/= 6.4 years, 2 M, 5 F). Participants exercised for 15 minutes on a cycle ergometer preceded and followed by 3-minute warm up and cool down periods. Peak exercise intensity was performed at 60-70% of the maximum predicted heart rate (estimated as 220 – age(yrs)). Images were obtained on a 3 T Siemens Skyra scanner. PCASL: 2D-EPI, resolution = 4 X 4 X 4 mm, label duration = 1500 ms, post-label delay = 1500 ms, 45 label/tag image pairs acquired. BOLD: 2D-EPI, resolution = 4 X 4 X 4 mm, TE = 30 ms, TR = 2000 ms (MB factor = 1) / 800 ms (MB factor = 4). For the CHD participants, the MB factor was chosen as either 1 or 4 dependent on the presence of a metal shunt (MB factor > 1 being prohibited in these cases). For the controls, MB factor was randomized to either 1 or 4. Functional connectivity strength (FCS) maps and CBF maps were computed and spatially coregistered. A mixed-effects general linear model (GLM) was performed on a voxelwise basis investigating main effect of session (pre- or post-exercise) and CHD status X session interaction. Age and sex were included as covariates for all analyses. For CBF, GM probability was also included as a covariate. For FCS, MB factor and total number of frames acquired (square root) were included as covariates of no interest. Standard methods were used to correct for multiple comparisons (FWE).

Results: Decreases in CBF were seen (Figure 1, left) in prefrontal/medial frontal cortex, insula, putamen, as well as sensory regions. Increases were seen in the right cerebellum and fusiform/lingual gyri. Significant interactions were seen mainly in posterior regions (Figure 1, right) but also in the cerebellum and fusiform/lingual gyri. FCS increases were seen (Figure 2, left) in the inferior and superior parietal lobules, the inferior temporal lobe, and the superior temporal gyrus. FCS decreases were seen in the posterior DMN, supplementary motor cortex, and visual association areas (lingual gyrus/middle occipital gyrus). Positive interactions were seen (Figure 2, right) mainly in the basal ganglia (putamen/caudate) and thalamus, inferior temporal gyrus and supramarginal gyrus. Negative interactions were seen in the cuneus/precuneus, prefrontal cortex and inferior occipital lobe.

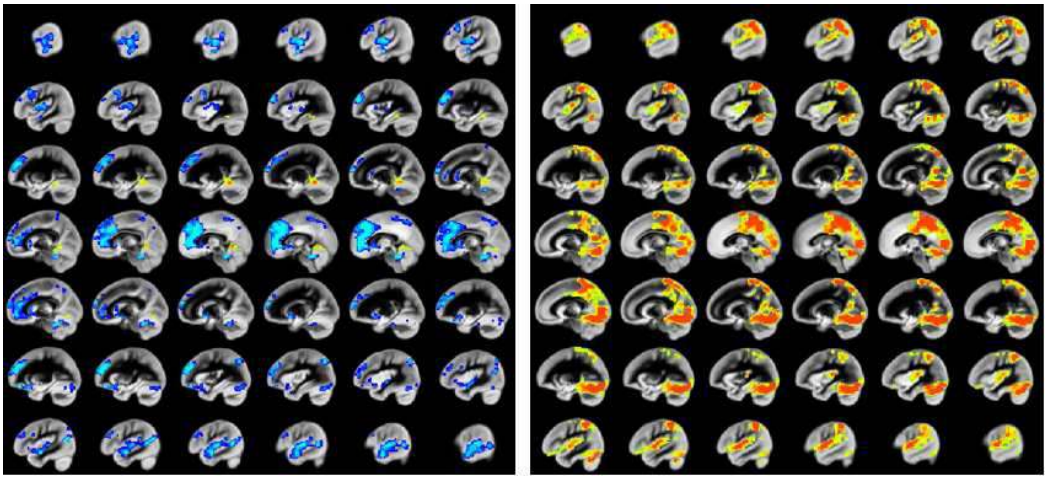

Figure 1. (Left) Regions with increased (hot colors) or decreased (cold colors) CBF after exercise. (Right) Regions with CHD status - X - session interactions.

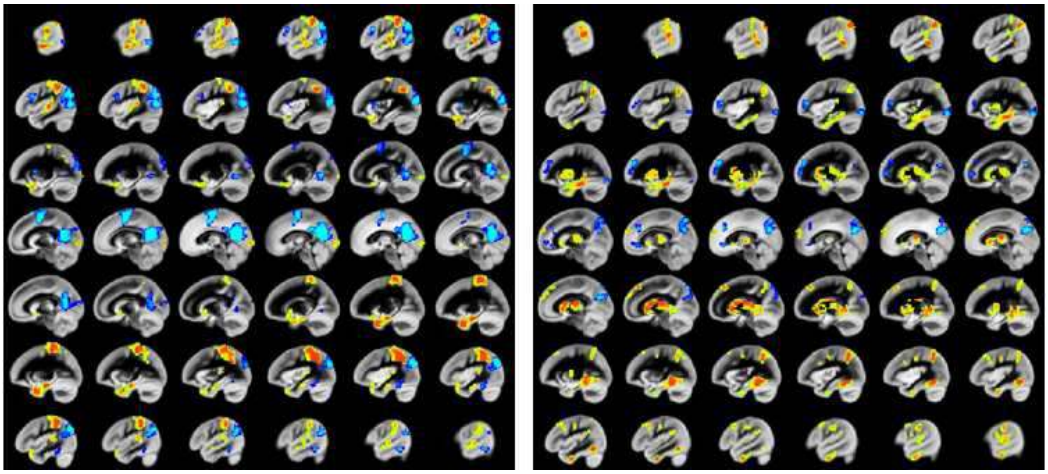

Figure 2. (Left) Regions with increased (hot colors) or decreased (cold colors) FCS after exercise. (Right) Regions with CHD status - X - session interactions.

Conclusions: Our results agree with previous reports (Querido & Sheel, 2007) showing overall CBF reductions after exercise likely due to vasoconstriction subsequent to hypercapnia. CHD patients show less CBF reductions in regions supplied via the cortical branches of the posterior carotid artery (PCA), which may indicate increased stiffness and less cerebrovascular reactivity in CHD patients (Hou et al., 2015; Sandhu et al., 2021). Our results also show increased FCS after exercise mainly in primary motor and sensory processing regions but decreased FCS primarily in the posterior DMN. CHD patients display increased FCS in the basal ganglia and thalamus after exercise, while showing less effects in the DMN and visual processing regions. Increased cerebellar-thalamic and thalamic-prefrontal connectivity has been previously shown in CHD patients (Sahel et al., 2023). The impact of these differences on long-term effects of exercise in CHD patients will be investigated in future research.

References

1. Donofrio, M. T. and A. N. Massaro (2010). “Impact of congenital heart disease on brain development and neurodevelopmental outcome.” Int J Pediatr 2010.
2. Hou, Y., L. J. Yuan, C. Y. Xing, F. J. Shang and Y. Y. Duan (2015). “Carotid Arterial Stiffness in Patients with Congenital Heart Disease-Related Pulmonary Hypertension Assessed with Radio Frequency Data Technique.” Echocardiography 32(11): 1676-1680.
3. Ko, Y. W., S. M. Kim, K. D. Kang and D. H. Han (2023). “Changes in Functional Connectivity Between Default Mode Network and Attention Network in Response to Changes in Aerobic Exercise Intensity.” Psychiatry Investig 20(1): 27-34.
4. Olivo, G., J. Nilsson, B. Garzon, A. Lebedev, A. Wahlin, O. Tarassova, M. Ekblom and M. Lovden (2021). “Immediate effects of a single session of physical exercise on cognition and cerebral blood flow: A randomized controlled study of older adults.” Neuroimage 225: 117500.
5. Querido, J. S. and A. W. Sheel (2007). “Regulation of cerebral blood flow during exercise.” Sports Med 37(9): 765-782.
6. Sahel, A., R. Ceschin, D. Badaly, M. Lewis, V. K. Lee, J. Wallace, J. Weinberg, V. Schmithorst, C. Lo and A. Panigrahy (2023). “Increased Cerebello-Prefrontal Connectivity Predicts Poor Executive Function in Congenital Heart Disease.” J Clin Med 12(16).
7. Sandhu, K., S. Pepe, J. J. Smolich, M. M. H. Cheung and J. P. Mynard (2021). “Arterial Stiffness in Congenital Heart Disease.” Heart Lung Circ 30(11): 1602-1612.

Poster No 2593

ASL-derived cerebrovascular brain-age improves associations with cognitive decline

Mathijs Dijsselhof[1,2], Floor Duits[3,4,5], Wibeke Nordhøy[6], Dani Beck[7,8,9], Lars Westlye[7,8,10], James Cole[11,12], Wiesje Van der Flier[3,4,13], Frederik Barkhof[1,2,14], Jan Petr[1,15], Henk Mutsaerts[1,2]

[1]Radiology and Nuclear Medicine, Amsterdam University Medical Centers, Vrije Universiteit, Amsterdam, Netherlands, [2]Amsterdam Neuroscience, Brain Imaging, Amsterdam, Netherlands, [3]Alzheimer Center Amsterdam, Neurology, Vrije Universiteit Amsterdam, Amsterdam UMC location VUmc, Amsterdam, Netherlands, [4]Amsterdam Neuroscience, Neurodegeneration, Amsterdam, Netherlands, [5]Neurochemistry lab, Department of Clinical Chemistry, Amsterdam Neuroscience, Amsterdam UMC, Amsterdam, Netherlands, [6]Physics and Computational Radiology, Radiology and Nuclear Medicine, Oslo University Hospital, Oslo, Norway, [7]Norwegian Centre for Mental Disorders Research (NORMENT), Oslo University Hospital, Oslo, Norway, [8]Department of Psychology, University of Oslo, Oslo, Norway, [9]Department of Psychiatric Research, Diakonhjemmet Hospital, Oslo, Norway, [10]KG Jebsen Centre for Neurodevelopmental Disorders, University of Oslo, Oslo, Norway, [11]Dementia Research Centre, Queen Square Institute of Neurology, UCL, London, United Kingdom, [12]Centre for Medical Imaging Computing, Computer Science, UCL, London, United Kingdom, [13]Epidemiology and Data Science, Vrije Universiteit Amsterdam, Amsterdam UMC location VUmc, Amsterdam, Netherlands, [14]Queen Square Institute of Neurology and Centre for Medical Image Computing, UCL, London, United Kingdom, [15]Helmholtz-Zentrum Dresden-Rossendorf, Institute of Radiopharmaceutical Cancer Research, Dresden, Germany

Introduction: Accelerated brain ageing is associated with cognitive decline and dementia[1], and can be estimated using structural brain MRI and machine learning methods, which subtracted with the chronological age results in the brain-predicted age difference (brain-PAD). However, structural MRI is mostly sensitive to irreversible structural changes, and there is increasing evidence that accelerated cerebrovascular compromise is an important factor for cognitive dysfunction[2]. The addition of arterial spin labelling (ASL) perfusion scans has been shown to improve brain-PAD accuracy in healthy ageing and brain-PAD-based classification of Alzheimer's Disease (AD)[3,4]. However, the added value of cerebrovascular ageing, its underlying mechanisms, and their relation to (domain-specific) cognitive decline are not yet fully understood. In this study, we assessed the relationship between brain-PAD and 1) stages of cognitive decline, and 2) global cognitive scores and domain-specific cognitive tests. We compared brain-PAD results between structural-only (T1w+FLAIR), ASL-only, and structural+ASL models.

Methods: Study design/data: Healthy controls (HC, n=1107, 52% male, 49±16.9 years, 17.7–94.7 years) were drawn from the StrokeMRI and TOP datasets[5]. From the Amsterdam Dementia Cohort[6] (ADC; n=213, 54.9% male, 63.9±7.5 years, 43-97 years), patients with Subjective Cognitive Decline (SCD, n=77), Mild Cognitive Impairment (MCI, n=63), and probable Alzheimer's Disease (AD, n=73) were selected. All ASL datasets were acquired with the same 3D spiral-FSE PCASL protocol (3T GE MR750, post-labelling delay=2025ms, labelling duration=1450ms) and processed with ExploreASL. Cognitive tests (ADC only) were z-scored and averaged per domain[7]. Features[3] were created from: GM and WM volumetrics (T1w), WMH volumetrics (FLAIR), and vascular territory-based CBF and spatial coefficient of variation (sCoV; ASL). Brain-age predictions: The three brain-age estimation models (T1w+FLAIR+ASL, T1w+FLAIR, or ASL-only) were trained on the HC dataset, and ADC Brain-PADs were determined. Model performance was compared using the mean absolute error (MAE), and (absolute) Brain-PAD group differences were assessed per model, using one-way ANOVA with Tukey's HSD post-hoc test. Relationships between cognitive performance, per domain, and brain-PADs, per model, were assessed using linear regression.

Results: The T1w+FLAIR+ASL model performed best (MAE=7.8 years), and model performance did not differ between diagnostic groups ($p>0.05$, all models, Figure 1). Brain-PADs differed ($p<0.05$, Figure 1) between SCD and AD (all models) and between SCD and MCI (ASL model). The T1w+FLAIR+ASL brain-PADs were associated with MMSE (ß=-0.031,$p<0.001$), language (ß=-0.013,$p=0.04$), attention & executive (ß=-0.012,$p=0.02$) and visuospatial (ß=-0.02,$p<0.001$) domains (Figure 2). The T1w+FLAIR Brain-PADs were associated with MMSE (ß=-0.021,$p<0.001$), attention & executive (ß=-0.010,$p=0.03$) and visuospatial (ß=-0.020,$p=0.006$) domains (Figure 2). The ASL-only brain-PADs were associated with the memory domain (ß=0.20,$p=0.01$; Figure 2).

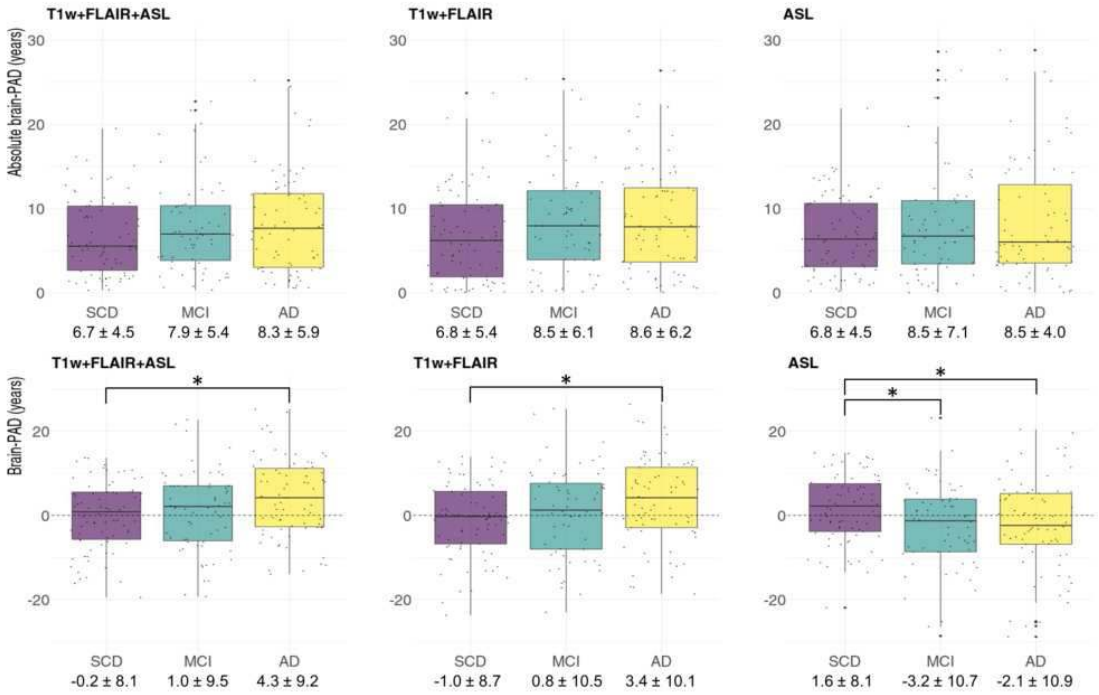

Figure 1: Boxplots showing model performance (absolute brain-PAD) in years (row 1), and brain-PAD in years (row 2) per diagnosis group for each model. Values shown are mean ± standard deviation in years. The asterisks denote statistical significance (p<0.05). *AD = Alzheimer's disease; ASL = arterial spin labeling; brain-PAD = brain-predicted age difference; MCI = mild cognitive impairment; SCD = subjective cognitive decline.*

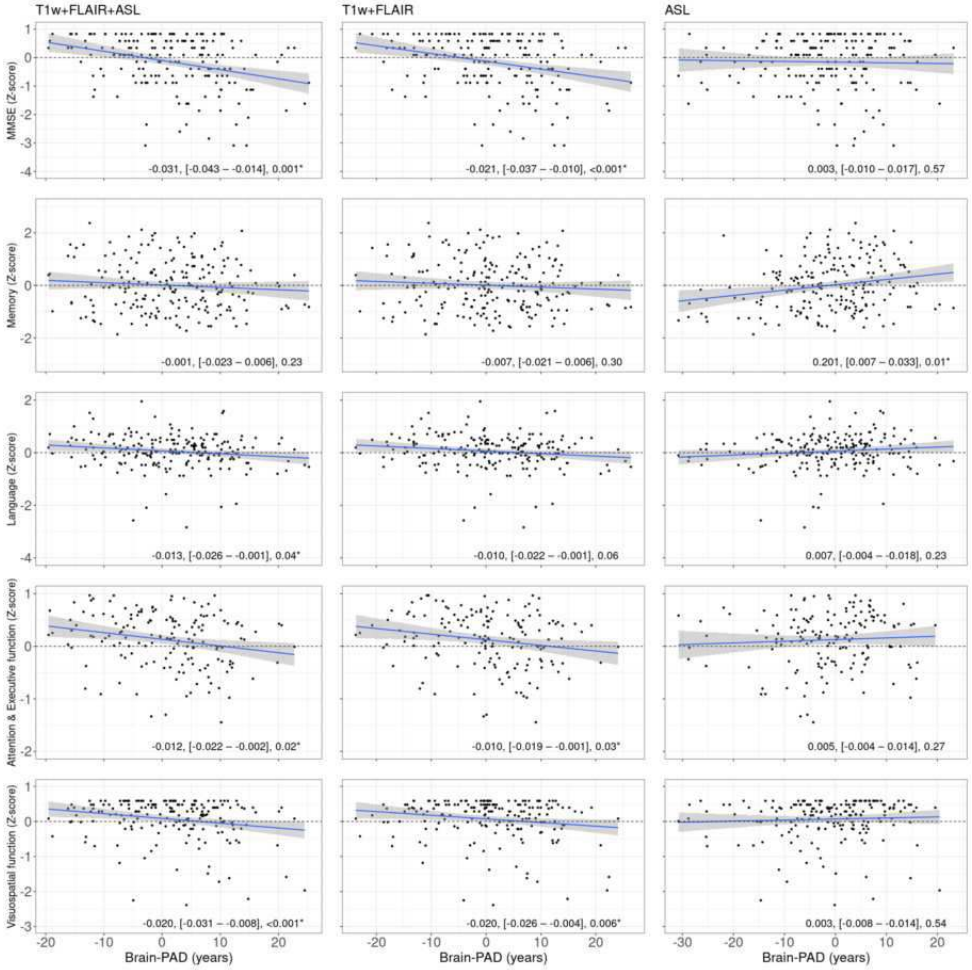

Figure 2: Associations between global and domain-specific cognitive composites and brain-PADs per model. Regression results are presented in ß, [95% confidence interval], p-value. The asterisks denote statistical significance (p<0.05). *ASL = arterial spin labeling; brain-PAD = brain-predicted age difference.*

Conclusions: SCD brain-PADS were similar to HC, and increased with cognitive decline staging, confirming previous studies[1]. The addition of ASL improved Brain-age sensitivity to global and domain-specific cognitive decline. Only the ASL-only model was associated with cognitive staging and memory, which is unexpected as structural derivatives such as hippocampal and parietal volume usually show stronger effects[8]. Also unexpectedly, a lower ASL-only brain-PAD (i.e., a biologically younger brain) was related with poorer cognition. Perhaps, the observed relationships might be explained by early-stage compensatory perfusion effects described in initial stages of AD-related cognitive decline[9], or because ADC contains many young-onset AD patients. These findings encourage larger multi-stage AD studies to assess if and how ASL mediates the association between structural and cognitive changes.

References

1. Dijsselhof, M. B. J., et al. (2023). The value of arterial spin labelling perfusion MRI in brain age prediction. Human Brain Mapping, 44(7), 2754–2766.
2. Franke, K., et al. (2019). Ten Years of BrainAGE as a Neuroimaging Biomarker of Brain Aging: What Insights Have We Gained? Frontiers in Neurology, 10, 789.
3. Hänggi, J., et al. (2011). Volumes of lateral temporal and parietal structures distinguish between healthy aging, mild cognitive impairment, and Alzheimer's disease. Journal of Alzheimer's Disease: JAD, 26(4), 719–734.
4. Iadecola, C., et al. (2019). Neurovascular and Cognitive Dysfunction in Hypertension. Circulation Research, 124(7), 1025–1044.
5. Richard, G., et al. (2018). Assessing distinct patterns of cognitive aging using tissue-specific brain age prediction based on diffusion tensor imaging and brain morphometry. PeerJ, 6, e5908.
6. Rokicki, J., et al. (2021). Multimodal imaging improves brain age prediction and reveals distinct abnormalities in patients with psychiatric and neurological disorders. Human Brain Mapping, 42(6), 1714–1726.
7. Scheltens, N. M. E., et al. (2017). Cognitive subtypes of probable Alzheimer's disease robustly identified in four cohorts. Alzheimer's & Dementia: The Journal of the Alzheimer's Association, 13(11), 1226–1236.
8. Thomas, K. R., et al. (2021). Regional hyperperfusion in older adults with objectively-defined subtle cognitive decline. Journal of Cerebral Blood Flow and Metabolism: Official Journal of the International Society of Cerebral Blood Flow and Metabolism, 41(5), 1001–1012.
9. van der Flier, W. M., et al. (2018). Amsterdam Dementia Cohort: Performing Research to Optimize Care. Journal of Alzheimer's Disease: JAD, 62(3), 1091–1111.

Poster No 2594

High resolution pCASL mapping of perfusion in a mouse model of stroke

Sara Monteiro[1,2], Lydiane Hirschler[3], Emmanuel Barbier[4], Patricia Figueiredo[2], Noam Shemesh[1]

[1]Champalimaud Research, Champalimaud Foundation, Lisbon, Portugal, [2]Instituto Superior Técnico, Universidade de Lisboa, Lisbon, Portugal, [3]C.J. Gorter Center for High Field MRI, Department of Radiology, Leiden University Medical Center, Leiden, Netherlands, [4]Université Grenoble Alpes, Inserm, Grenoble Institut des Neurosciences, Grenoble, France

Introduction: pCASL enables efficient perfusion mapping in-vivo without injection of contrast agents.[1] Despite its great potential, state-of-the-art pCASL in preclinical settings is still characterized by low spatial resolution and high variability in CBF maps.[1-3] Compared to rats, pCASL measurements are particularly challenging in mice due to mouse-specific anatomical constraints that limit labeling efficiency due to the way carotids are placed.[4] Here, we address this gap and develop a novel experimental setup that optimizes carotid placement and further harnesses dramatic SNR increases from cryogenic coils[5] to achieve high-resolution and reliable pCASL imaging in mice at 9.4 T and test our approach in an animal model of stroke.

Methods: All animal experiments received proper ethical approval. Experimental Setup: A custom-built ramp was designed for better animal positioning (Fig.1A). Animal Preparation: Female C57BL/g mice (N=16, ~12 weeks old, weights 20–25g) were sedated using ~2% isoflurane. In N=3 animals, a photothrombotic stroke[6] was induced. The animals were scanned using the ramp at t=0h, 24h and 5days after stroke. MRI experiments: Experiments were conducted on a 9.4 T Bruker Biospec Scanner using an unbalanced pCASL sequence[7] (labelling plane (LP) positioned at the mouse neck (~8mm below the isocenter), labeling duration of 3s, post-labelling delay of 300ms, TR/TE=4000/17ms, 30 repetitions). N=7 animals were scanned with a LP tilt of 0° (no ramp 0°) and 45° (no ramp 45°) and N=6 animals were scanned with the LP angle of 0° and on top of a ramp (Fig.1A), both at low and high-resolution. Low-resolution pCASL acquisitions: FOV=14x14mm2, slice thickness=1mm, slice gap=0.2mm, matrix=96x96 resulting in a spatial resolution of 146x146µm2. For high-resolution pCASL: FOV=12x12mm2, slice thickness=0.5mm, slice gap=0.35mm, matrix=120x120 resulting in a spatial resolution of 100x100µm2. For cerebral blood flow (CBF) quantification, the T1 map was obtained from an inversion recovery sequence[7]. A pCASL encoded FLASH was employed to estimate the inversion efficiency (IE) 3mm above the LP (PLD=0ms, LD=200ms).[7] Data Analysis: CBF (ml/100g/min) was calculated from the relative ASL signal difference between control and label images (rASL).[8] In the rASL and CBF high-resolution maps, two ROIs were defined (cortical and thalamic) and used for averaging rASL and CBF. The IE was calculated by manually drawing a ROI in each carotid.

Results: The IE was calculated for each setup: no ramp 0°=0.57±0.20, no ramp 45°=0.80±0.63 and ramp=0.78±0.04. Note the dramatically smaller variance in the ramp setup. Additionally, only the ramp setup reveals the expected linear relationship between rASL and IE (Fig.1C). Figure 2A shows CBF maps from the mice scanned at the low and high-resolution for the 3 conditions. In controls, only the acquisitions using the ramp present the expected CBF patterns in the healthy mouse brain, with little variability across animals both at low- and high-resolution. In the high-resolution images, differences in perfusion within different hippocampal layers, descending cortical vessels can be discerned (Fig.2A). In the stroke model, we detected CBF impairments across the brain that were changing over time (Fig.2C).

Conclusions: By using a novel experimental setup, we managed to increase state-of-the-art resolution[2] of pCASL perfusion images of the mouse brain by a factor of 15 and obtain highly reliable CBF maps. Our findings include enhanced stability of the images acquired with the ramp (lower standard deviation in the IE measure) and a better delineation of brain areas including in an animal model of stroke, unveiling pCASL's potential to detect alterations in CBF in mouse models of disease or healthy longitudinal processes. Our findings bode well for future applications of CBF mapping in mice.

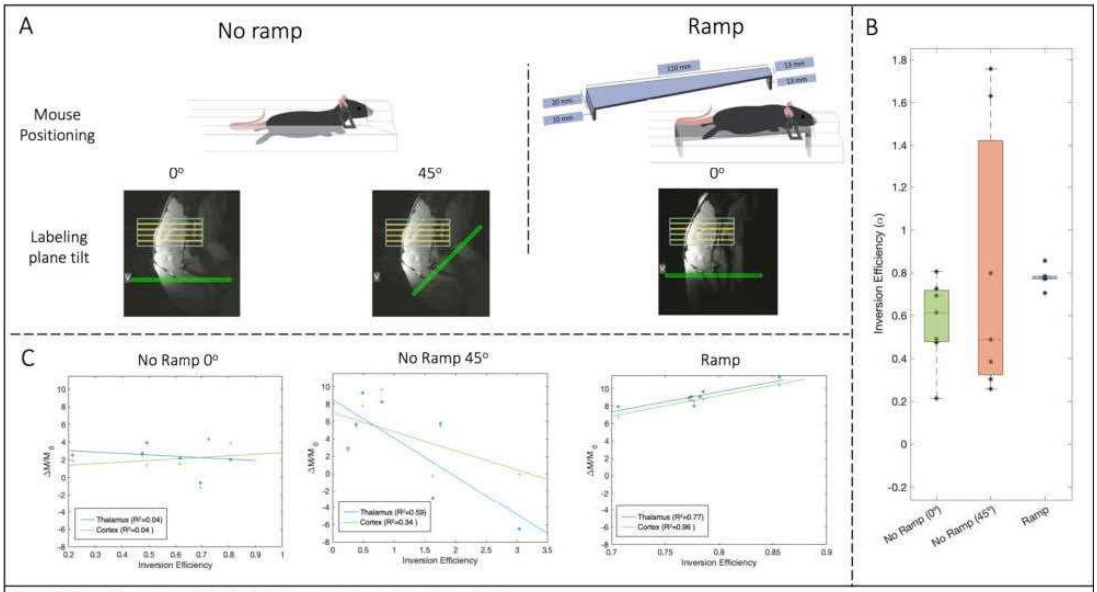

Figure 1. Setups for mouse positioning in the scanner when using a cryogenic coil
A) No ramp setup: labeling plane tilt of 0° (*no ramp 0°*) and 45° (*no ramp 45°*) in relation to the imaging region and ramp setup: labeling plane angle set to 0° and mice positioned on top of a *ramp*. B) Inversion Efficiency (IE) estimation for the 3 setups at the level of the carotids. Note that there is a dramatically smaller variance in the ramp compared to the other conditions. C) Relationship between ΔM and IE across setups in two specific ROIs (thalamic and cortical). Only in the ramp setup there is the expected linear relationship.

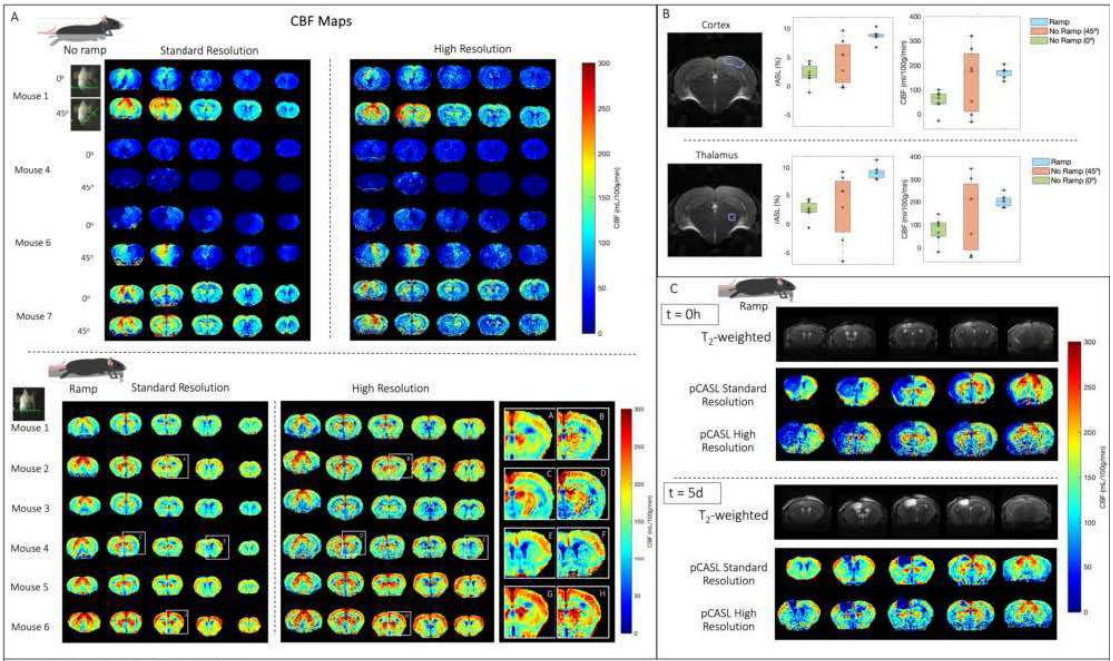

Figure 2. CBF mapping in the mouse brain
A) Quantitative CBF maps for low and high-resolution acquisitions for the 3 setups analysed: TOP) no ramp (0° and 45°).There is high disparity between setups, along with extremely low CBF values brain- wide. BOTTOM) ramp. Insets on the right display differences between low and high-resolution acquisitions.
B) Comparison of rASL and CBF in two ROIs between setups. Ramp setup shows lower standard-deviation and higher rASL.
C) CBF maps of a representative mouse induced with phototrombotic stroke, scanned at 2 different timepoints. Visible differences can be observed from a more acute stage to a more chronic stage.

References

1. Buck J, Larkin JR, Simard MA, et al. Sensitivity of multiphase pseudocontinuous arterial spin labelling (MP pCASL) magnetic resonance imaging for measuring brain and tumour blood flow in mice. Contrast Media Mol Imaging. 2018;2018.
2. Duhamel G, Callot V, Tachrount M, et al. Pseudo-continuous arterial spin labeling at very high magnetic field (11.75 T) for high-resolution mouse brain perfusion imaging. Magn Reson Med. 2012;67(5):1225-1236.
3. Hirschler L, Munting LP, Khmelinskii A, et al. Transit time mapping in the mouse brain using time-encoded pCASL. NMR Biomed. 2018;31(2):1- 11.
4. Larkin JR, Simard MA, Khrapitchev AA, et al. Quantitative blood flow measurement in rat brain with multiphase arterial spin labelling magnetic resonance imaging. Journal of Cerebral Blood Flow and Metabolism. 2019;39(8):1557-1569.
5. Rating D, Baltes C, Nordmeyer-Massner J, et al. Performance of a 200-MHz cryogenic RF probe designed for MRI and MRS of the murine brain. Magn Reson Med. 2008;59(6):1440-1447.
6. Watson BD, Dalton Dietrich W, Busto R, et al. Induction of Reproducible Brain Infarction by Photochemically Initiated Thrombosis, Ann. Neurol., vol. 17, no. 5, pp. 497–504, 1985.
7. Hirschler L, Debacker CS, Voiron J, et al. Interpulse phase corrections for unbalanced pseudo-continuous arterial spin labeling at high magnetic field. Magn Reson Med. 2018;79(3):1314-1324.
8. Alsop DC, Detre JA, Golay X, et al. Recommended Implementation of ASL Perfusion MRI for Clinical Applications. Magn Reson Med. 2015;73(1):102-116

Poster No 2595

Contribution of energy metabolism to structure and function of the human brain

Moohebat Pourmajidian[1], Bratislav Misic[1], Alain Dagher[2]

[1]McGill University, Montreal, Quebec, [2]Montreal Neurological Institute and Hospital, McGill University, Montreal, QC

Introduction: The brain relies on energy from glucose metabolism to maintain its structure and carry out its functional repertoire. Perturbations of energy distribution in the brain can therefore lead to physiological and cognitive dysfunction. Abnormal neurovascular and neurometabolic coupling, oxidative metabolism, and mitochondrial function have been observed in the aging brain and several neurodevelopmental and neurodegenerative disorders, including Parkinson's disease (PD), Alzheimer's disease (AD). Metabolic dysfunctions appear early in disease progression (Watts et al., 2018) and mitochondrial dysfunction has been associated with protein aggregation in both AD and PD (Cho et al., 2010). Here, by leveraging gene expression data, we investigate how different energy metabolism pathways are distributed in the human cortex.

Methods: We curated gene sets of known pathways of glucose and lactate metabolism using Gene Ontology and Reactome databases. Microarray data from the Allen Human Brain Atlas (AHBA) was preprocessed using the abagen package (Markello et al., 2021) and parcellated into 400 cortical regions in the Schaefer parcellation (Schaefer et al., 2018). Average gene expression maps of glucose-specific metabolic pathways were produced and used as an indicator of metabolic activity across the human cortex. Distribution of metabolic expression maps across functional and cytoarchitectural classes of the human cortex were explored (Thomas Yeo et al., 2011; Triarhou, 2007) Metabolic PET maps including glucose uptake, oxygen consumption, cerebral blood flow and glycolytic index, as well as MEG maps from the Human Connectome Project (HCP) S900 release were acquired and parcellated using the Neuromaps package (Markello et al., 2022). Structural and functional connectivity matrices were obtained from the HCP S900 release (Vos De Wael et al., 2018). Cell type gene expression maps were produced using curated data from five single-cell RNA sequencing studies (Seidlitz et al., 2020). The relationship between metabolic pathway maps and PET maps, cell type maps, structural and functional connectivity measures were explored using Pearson correlation and partial least squares (PLS) analysis. Spatial null models and bootstrap resampling were employed to test the reliability and statistical significance of the results.

Results: Curated gene sets were used to generate mean expression maps of glycolysis, pentose phosphate pathway (PPP), tricarboxylic acid cycle (TCA), oxidative phosphorylation (OXPHOS) and lactate metabolism. These metabolic maps generally show higher average expression in the somatosensory and motor cortices and lower expression in the limbic and visual regions (Fig.1a, b). The PPP map is different from the five other metabolic pathway maps, which show a very similar distribution to each other. Correlation analysis showed significant positive correlations between the PPP and lactate maps and metabolic PET maps. The glycolysis and OXPHOS maps only show significant positive correlation with the glycolytic index PET map (Fig.1c). PLS analysis of metabolic PET maps with the multi-modal brain maps, shows a general dichotomy: lactate and PPP pathways, neuronal and endothelial cells, lower MEG frequencies and functional connectivity measures spatially covary in the same direction as the PET metabolic maps of glucose, oxygen and cerebral blood flow. On the other end, the negative loadings seem to be dominated by glial cells, higher MEG frequencies and measures of structural connectivity (Fig.2).

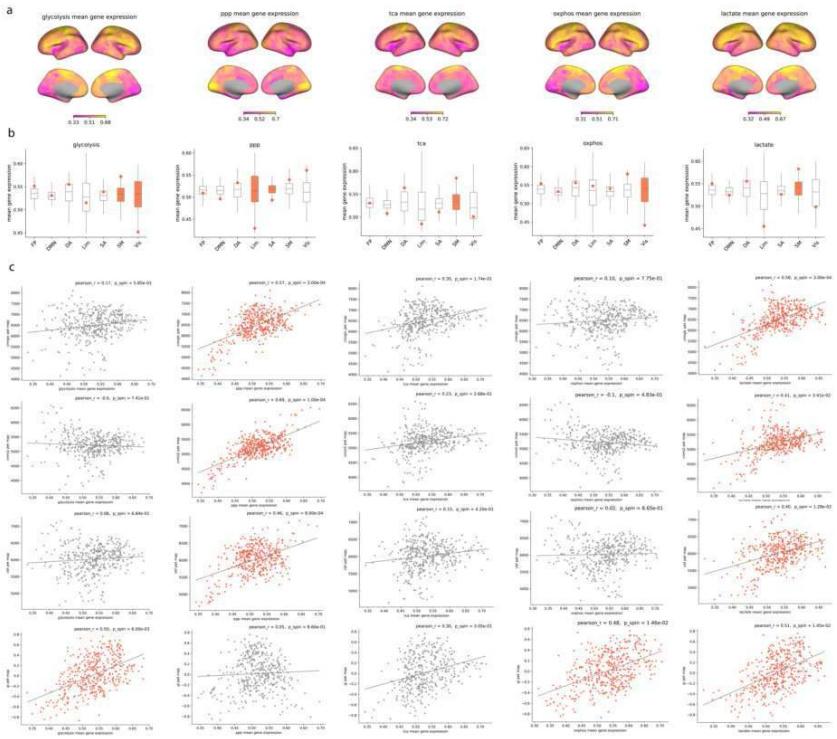

Figure 1. Distribution of glucose metabolic pathways across the human cortex. (a) Average gene expression maps where used as a proxy to glucose metabolic pathways. (b) Box plot showing the null distribution of means generated using spin test for glucose metabolic patwhays across seven intrinstic functional networks of Yeo et al., 2011. Filled circles indicate mean gene expression of glucose metabolic maps. Highlighted boxes indicate p_spin< 0.05. (c) Correlation between the glucose metabolism maps and metabolic PET maps. Highlighted scatter plots show significant correlations after spin test (p_spin < 0.05). PPP and lactate maps show significant positive correlations with PET maps of glucose uptake, oxygen and cerebral blood flow.

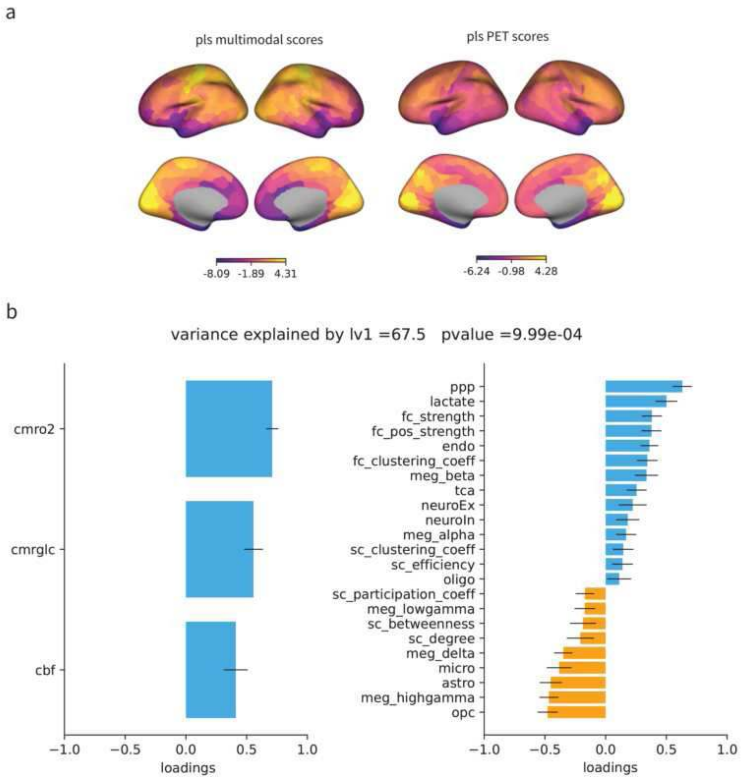

Figure. 2. relationship between PET metabolic maps and multimodal maps of brain structure and function. Partial Least Squares analysis was used to explore covarying patterns of metabolic PET maps and maps of glucose metabolism, cell types, neurophysiological oscillations and structural and functional connectivity measures of the cortex. (a) Original data was projected back onto the first latent variable of the PLS analysis to visualize covarying spatial patterns of PET and multimodal maps. (b) PET and multimodal loadings of the first latent variable., showing the extent to which each map contributes to the covariance pattern in the data.

Conclusions: Here, using gene expression as a proxy, we produced maps of glucose metabolism pathways and investigated their distribution across the human cortex. We show a dichotomy between PPP and maps related to glycolysis. As well, we explored the spatial alignment between glucose metabolic pathway maps and metabolic PET maps, cell type distribution, neurophysiological oscillations, and structural/functional network topology.

References

1. Cho, D. H. (2010). Mitochondrial dynamics in cell death and neurodegeneration. In Cellular and Molecular Life Sciences (Vol. 67, Issue 20, pp. 3435–3447). https://doi.org/10.1007/s00018-010-0435-2
2. Markello, R. D. (2021). Standardizing workflows in imaging transcriptomics with the abagen toolbox. eLife, 10, e72129. https://doi.org/10.7554/eLife.72129
3. Markello, R. D. (2022). neuromaps: Structural and functional interpretation of brain maps. Nature Methods, 19(11), 1472–1479. https://doi.org/10.1038/s41592-022-01625-w
4. Schaefer, A. (2018). Local-Global Parcellation of the Human Cerebral Cortex from Intrinsic Functional Connectivity MRI. Cerebral Cortex, 28(9), 3095–3114. https://doi.org/10.1093/cercor/bhx179
5. Seidlitz, J. (2020). Transcriptomic and cellular decoding of regional brain vulnerability to neurogenetic disorders. Nature Communications, 11(1). https://doi.org/10.1038/s41467-020-17051-5
6. Thomas Yeo. (2011). The organization of the human cerebral cortex estimated by intrinsic functional connectivity. Journal of Neurophysiology, 106(3), 1125–1165. https://doi.org/10.1152/jn.00338.2011
7. Triarhou, L. C. (2007). The Economo-Koskinas atlas revisited: Cytoarchitectonics and functional context. In Stereotactic and Functional Neurosurgery (Vol. 85, Issue 5, pp. 195–203). https://doi.org/10.1159/000103258
8. Vos De Wael, R. (2018). Anatomical and microstructural determinants of hippocampal subfield functional connectome embedding. Proceedings of the National Academy of Sciences, 115(40), 10154–10159. https://doi.org/10.1073/pnas.1803667115
9. Watts, M. E. (2018). Brain energy and oxygen metabolism: Emerging role in normal function and disease. In Frontiers in Molecular Neuroscience (Vol. 11). Frontiers Media S.A. https://doi.org/10.3389/fnmol.2018.00216

Poster No 2596

BOLD-fMRI Lag-Time Mapping: A Novel Biomarker for Early-stage Cerebral Small Vessel Disease

Wan-Ting Hsieh[1], Pei-Lin Lee[2], Yi-Hua Huang[1], Nai-Fan Chi[3], Liang-Kung Chen[2,4], Ching-Po Lin[1,5,6], Chih-Ping Chung[2,3,7], Kun-Hsien Chou[1,8]

[1]Institute of Neuroscience, National Yang Ming Chiao Tung University, Taipei, Taiwan, [2]Center for Healthy Longevity and Aging Sciences, National Yang Ming Chiao Tung University, Taipei, Taiwan, [3]Department of Neurology, Neurological Institute, Taipei Veterans General Hospital, Taipei, Taiwan, [4]Taipei Municipal Gan-Dau Hospital (managed by Taipei Veterans General Hospital), Taipei, Taiwan, [5]Brain Research Center and National Yang Ming Chiao Tung University, Taipei, Taiwan, [6]Deptartment of Education and Research, Taipei City Hospital, Taipei, Taiwan, [7]School of Medicine, National Yang Ming Chiao Tung University, Taipei, Taiwan, [8]Brain Research Center, National Yang Ming Chiao Tung University, Taipei, Taiwan

Introduction: Cerebral Small Vessel Disease (CSVD) represents a spectrum of pathological changes in the brain's microvasculature, playing a pivotal role in dementia, disable and stroke in older people. Due to challenges in assessing the pathology within the brain's microvasculature, the diagnosis of CSVD is currently reliant on the identification of diverse ischemic and hemorrhagic lesions. These include white matter hyperintensities, lacunes, cerebral microbleeds, and dilated perivascular spaces. This diagnostic approach primarily identifies CSVD during later stages characterized by the emergence of brain parenchymal lesions. It lacks the ability to directly capture the underlying neurovascular abnormalities or dysfunctions. To address this research gap, the present study employs rs-fMRI, with a specific focus on BOLD lag-time mapping. This non-invasive technique facilitates a comprehensive examination of neurovascular blood flow dynamics, specifically the transit time, offering potential insights into microvasculature function. The study's objective is to investigate whether this approach can effectively differentiate between participants with and without CSVD, serving as a measurement of brain microvasculature at an early stage of CSVD.

Methods: This study evaluated 101 asymptomatic CSVD patients and 539 healthy controls (HC). We processed rs-fMRI data using a standard pre-processing pipeline[1]. Various quantitative indices pertaining to vascular transit-time were calculated following the previously delineated methodology[1]. This involving extracting the global mean signal as an initial reference and further iteratively shifted by ±0.5 seconds to map temporal lag properties up to a ±7.0 sec shift. Afterwards, the arterial transit time was calculated by averaging lag-time greater than the peak location of the histogram, indicating upstream locations from this peak. Conversely, venous transit time was calculated using downstream voxels. The sum of these times provided the global transit time. We employed two separate ANCOVA models to address distinct research inquiries. The first model evaluated significant differences in transit times between CSVD and HC groups. The second model investigated the association between transit times and CSVD severity based on Fazekas scores[2]. Through the use of bidirectional linear contrasts, we delineated trends in the alterations of these indices across different stages of CSVD.

Results: 1. Transit Time Differences Between CSVD and HC Groups (Fig. 1): A comparison between CSVD and HC revealed a notable increase in arterial transit time for CSVD group, reaching statistical significance (p=0.045). No significant differences were detected in arterial or venous transit times 2. Association Between Transit Times and CSVD Severity (Fig. 2): Analysis spanning the spectrum of CSVD severity revealed notable trends in transit times. A discernible elevation in arterial (p-trend=0.003), venous (p-trend=0.031), and global transit times (p-trend=0.005) correlated with increasing CSVD severity.

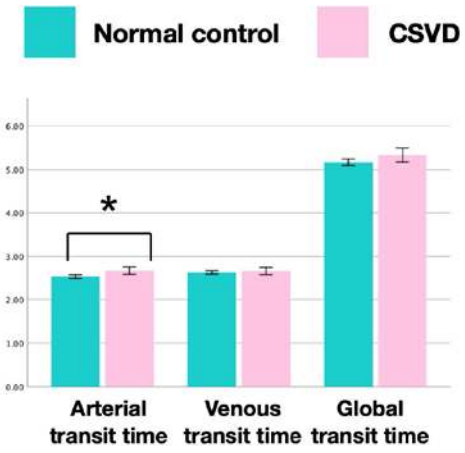

Fig. 1: The difference in arterial and venous transit time between CSVD and non-CSVD groups.

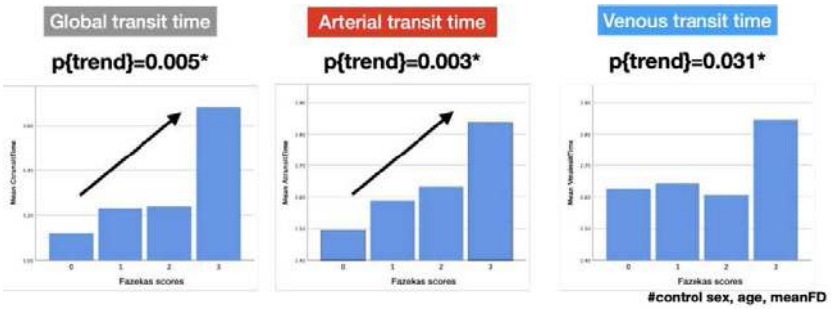

Fig. 2: The histograms of the severity of CSVD with respect to different transit times.

Conclusions: Our findings illuminate the intricate relationship between brain CSVD lesions and microvascular transit times. A significant increase in arterial transit time was observed in CSVD, establishing it as a potential non-invasive biomarker for CSVD detection. Furthermore, the ascending trends in transit times in relation to CSVD severity underscore their potential as indicators of disease progression. These results suggest that BOLD-fMRI-derived transit times could serve as valuable tools in the early detection and monitoring of CSVD, contributing to better clinical outcomes through timely interventions. Future studies could prioritize longitudinal data to better understand the changes in transit times throughout the disease progression. This could involve the inclusion of symptomatic CSVD patients, validating the tool for clinical applications and potentially unveiling new insights into the pathophysiological processes associated with CSVD.

References

1. Aso, Toshihiko, et al. “A venous mechanism of ventriculomegaly shared between traumatic brain injury and normal ageing.” Brain 143.6 (2020): 1843-1856.
2. Fazekas, Franz, et al. “MR signal abnormalities at 1.5 T in Alzheimer’s dementia and normal aging.” American Journal of Neuroradiology 8.3 (1987): 421-426.

Poster No 2597

Cerebrovascular reactivity mapping using resting-state functional MRI in infants aged 0 to 6 months

Baorong Gu[1], Rui Qian[1], Zilong Ye[1], Bowen Qiu[1], Zixuan Lin[1], Dan Wu[1]

[1]Department of Biomedical Engineering, Zhejiang University, Hangzhou, China

Introduction: Cerebrovascular reactivity (CVR), the ability of cerebral vessels to dilate or constrict, was proven to be altered in various cerebrovascular diseases such as arterial stenosis (Gupta et al., 2012), stroke (Geranmayeh et al., 2015), and small vessel disease. The common methods of measuring CVR require acetazolamide injection or hypercapnia challenge (Liu, De

Vis and Lu, 2019), which is not suitable for infants. Therefore, we utilized a recently developed resting-state based method to map CVR in infants aged 0 to 6 months and explored the relationship between CVR and age, gender as well as cognition.

Methods: Participants: Resting-state fMRI data of 67 subjects aged 0-6 months from the UNC/UMN Baby Connectome Project (BCP) (Howell et al., 2019) was included in this study. The information of the participants is elaborated in Figure 1A. All subjects were imaged without sedation and during natural sleep. Mullen Scales of Early Learning (MSEL) (Mullen, 1995) test results were available in a subset of 53 subjects. Data processing: As shown in Figure 1B, BOLD images were first pre-processed and then temporally filtered using the optimal frequency range of 0 to 0.1164Hz (Liu et al., 2021). The resulted filtered signal time-courses were averaged across whole brain to obtain the reference time course. Then the relative CVR index was calculated by regressing the voxel-wise BOLD signal against the reference signal. CVR maps for all subjects were registered to their respective month templates (Figure 1C) (Chen et al., 2022) and then to the March template with the purpose of voxel-wise analyses. Voxel-wise analyses: Multiple regression analysis was first used to examine the effect of age or gender on CVR. Then, age-standardized T-scores for visual reception (VR), fine motor (FM), expressive language (EL), receptive language (RL), gross motor (GM) and early learning composite (ELC) scores (Mullen, 1995) were obtained from MSEL tests and their relationships with CVR were analyzed using regression model as well, with age and gender as covariates. All analyses were conducted using SPM12 with a primary threshold of $p<0.0005$, cluster extent threshold of 1500 continuous voxels and Family-Wise Error (FWE) correction at $p<0.05$.

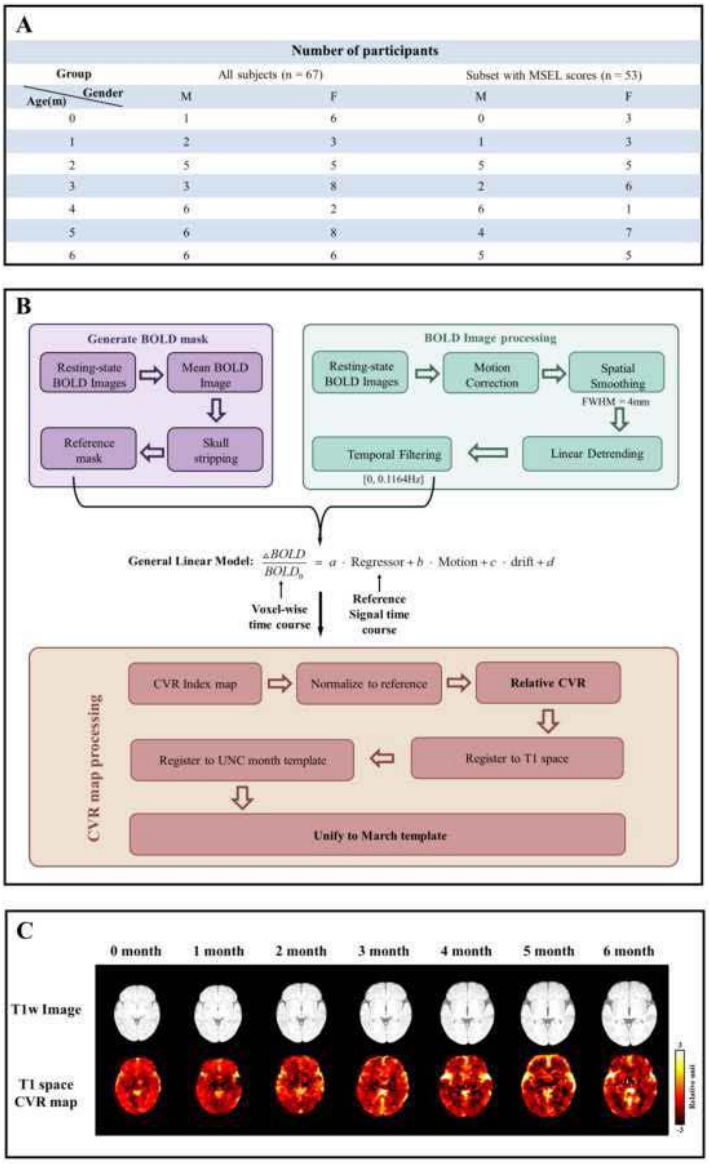

Figure 1. CVR quantification methods and representative results. (A) Demographic information of subjects included in current study. (B) CVR data processing pipeline. (C) Representative T1w structural images and CVR maps registered to standard month templates.

Results: Our results (Figure 2A) demonstrated that there was a significant positive relationship between CVR and age at prefrontal lobe (bilateral frontal pole), temporal lobe (bilateral inferior temporal gyrus, bilateral fusiform gyrus), the right lingual gyrus, the right parietal lobe (superior parietal gyrus, precuneus), as well as the central sulcus (right paracentral lobules, right precentral gyrus), which are reported to be associated with visual processing (Roland and Gulyás, 1995), visual memory (Gilboa, 2004) and movement (Yousry, 1997); Besides, CVR in deep white matter significantly declined with age, reflecting an inclination of blood supply towards the gray matter after birth. However, we did not find significant developmental differences in CVR between males and females. As for the subset with MSEL scores, CVR in the left precentral gyrus, thalamus, and brainstem had a significant positive association with gross motor T-score, reflecting the need of cerebrovascular supply for motor tasks (Yousry, 1997) during early development. The p-values and number of voxels for all significant clusters were given in Figure 2B. Additionally, Figure 2C presents the scatterplot of the average CVR of each significant cluster and its corresponding regressions.

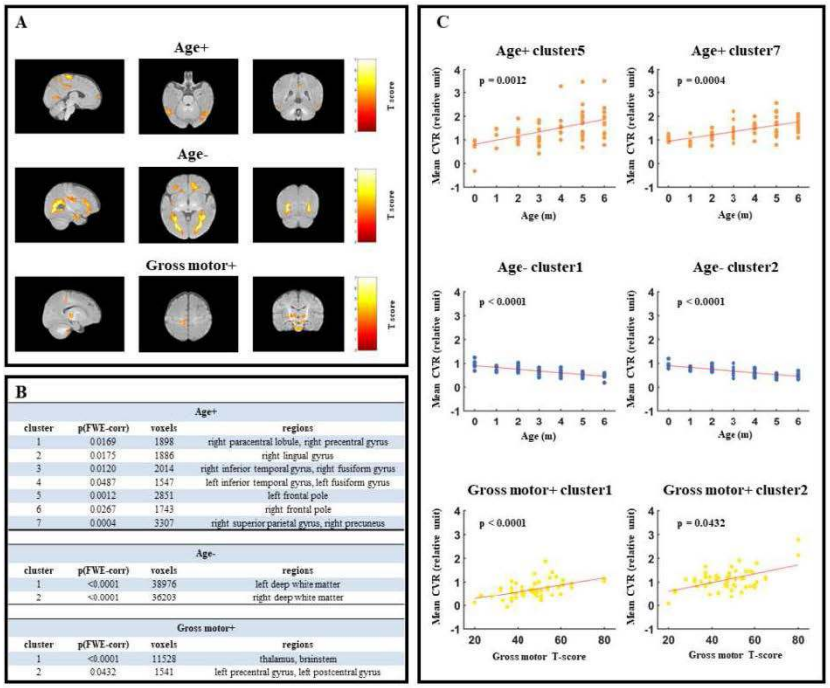

Figure 2. Significant results obtained from multiple regression analysis. Age+ and Age- respectively represent positive and negative association with age while Gross motor+ indicates a positive correlation between CVR and gross motor T-score. (A) Brain regions where CVR was significantly associated with age and gross motor function in infants from 0 to 6 months. (B) Detailed information of significant clusters where CVR was associated with age or gross motor function. (C) Scatterplots of the mean cluster CVR and age or gross motor function.

Conclusions: In this study, for the first, we mapped the CVR during early 6 months in life using a resting-state based method and identified key regions during brain development, as well as areas associated with early learning ability, supporting the potential role of CVR as a biomarker in the cerebrovascular diseases during early infancy.

References

1. Chen, L. (2022), 'A 4D infant brain volumetric atlas based on the UNC/UMN baby connectome project (BCP) cohort', NeuroImage, 253, p. 119097.
2. Geranmayeh, F. (2015), 'Measuring vascular reactivity with breath-holds after stroke: A method to aid interpretation of group-level BOLD signal changes in longitudinal fMRI studies', Human Brain Mapping, 36(5), pp. 1755–1771.
3. Gilboa, A. (2004), 'Remembering Our Past: Functional Neuroanatomy of Recollection of Recent and Very Remote Personal Events', Cerebral Cortex, 14(11), pp. 1214–1225.
4. Gupta, A. (2012), 'Cerebrovascular Reserve and Stroke Risk in Patients With Carotid Stenosis or Occlusion', Stroke, 43(11), pp. 2884–2891.
5. Howell, B.R. (2019), 'The UNC/UMN Baby Connectome Project (BCP): An overview of the study design and protocol development', Neuroimage, 185, pp. 891–905.
6. Liu, P. (2021), 'Cerebrovascular Reactivity Mapping Using Resting-State BOLD Functional MRI in Healthy Adults and Patients with Moyamoya Disease', Radiology, 299(2), pp. 419–425.
7. Liu, P. (2019), 'Cerebrovascular reactivity (CVR) MRI with CO2 challenge: A technical review', Neuroimage, 187, pp. 104–115.
8. Mullen, E. (1995), Mullen Scales of early learning. Bloomington, Mn.: NCS Pearson.
9. Roland, P.E. (1995), 'Visual Memory, Visual Imagery, and Visual Recognition of Large Field Patterns by the Human Brain: Functional Anatomy by Positron Emission Tomography', Cerebral Cortex, 5(1), pp. 79–93.
10. Yousry, T. (1997), 'Localization of the motor hand area to a knob on the precentral gyrus. A new landmark', Brain, 120(1), pp. 141–157.

Poster No 2598

Connectivity-Energy Coupling in the human brain: Mapping Glucose Demands of Structural Connectivity

Yifan Mayr[1,2], Aldana Lizarraga[1], Arianna Sala[3,1], Igor Yakushev[1,2]

[1]Technical University of Munich, Department of Nuclear Medicine, Munich, Germany, [2]Graduate School of Systemic Neurosciences GSN-LMU, Munich, Germany, [3]Université De Liège, Liege, Belgium

Introduction: Operation of any communication system requires energy input. Recently, energy demands of the brain were shown to be closely linked to its structural connectivity (SC). The goal of the present study was to map region-wise glucose demands of SC.

Methods: We analyzed diffusion tensor imaging (DWI), and fluorodeoxyglucose (FDG) positron emission tomography (PET) data of 55 healthy, middle-aged individuals. Each subject underwent 2 identical scanning sessions, separated by 8 weeks . Images were spatially parcellated into 106 brain regions. SC was measured by probabilistic tractography. From each scanning session, we obtained 55x106=5830 observations of relative FDG uptake. For each FDG uptake observation, 106 connection weights were available. To understand how each connection individually contributes to a region's energy consumption, we fitted a multilinear regression model between structural connection weights and relative FDG uptake. The complete dataset was split into a training (80%) and a test (20%) set, stratified by brain region. Significance level was set at 0.05 with Bonferroni correction; confidence interval was estimated from 10,000 bootstraps.

Results: The model consistently explained nearly half of the variance in regional FDG uptake (Session 1: training R2 = 0.49, test R2 = 0.48; Session 2: training R2 = 0.51, test R2 = 0.49). Among the 106 model coefficients, 40 were statistically significant in session 1, and 36 in session 2 (Figure 1). Of those, 32 were present in both sessions and were highly consistent (Figure 2, Pearson r=0.99, p<0.001). The top three most and least glucose-demanding connections were preserved in both sessions. The most glucose-demanding connections were to the right posterior cingulate, left posterior cingulate, and the right insula; the least glucose-demanding connections were to the left superior temporal pole, left hippocampus, and the left mid-temporal pole (Figure 1).

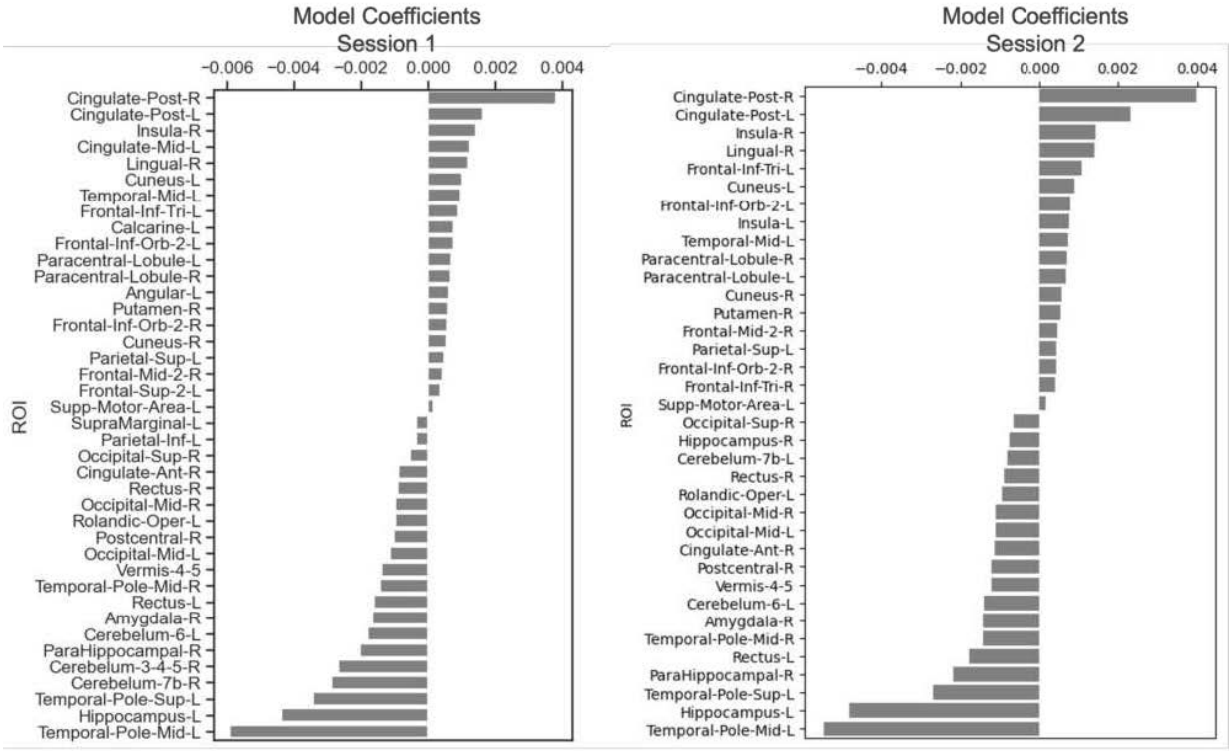

Figure 1. Multilinear regression model coefficients from session 1 (left) and session 2 (right).

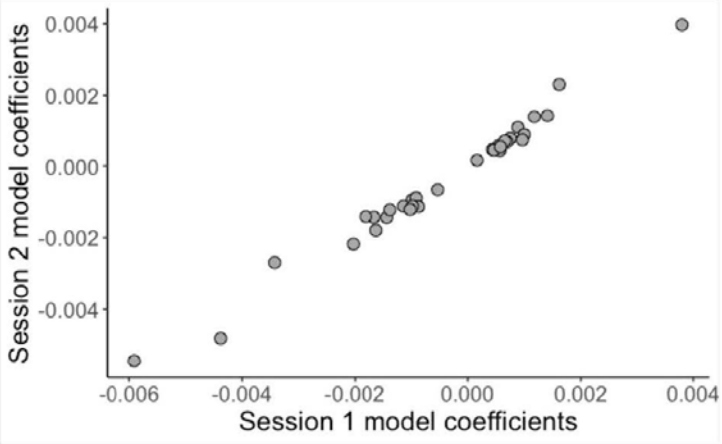

Figure 2. Scatter plot of the 32 model coefficients common in session 1 and session 2.

Conclusions: In the healthy human brain, there is a specific relationship between communication infrastructure and energy demands. Neural fibers contribute differently to a brain region's glucose metabolism, and this coupling pattern is reproducible. This normal map builds a reference for studying connectivity-energy coupling, or likely decoupling, in the diseased brain.

Poster No 2599

Predicting regional glucose metabolism from structural vs. functional connectivity

Yifan Mayr[1,2], Aldana Lizarraga[1], Arianna Sala[3,1], Igor Yakushev[1,2]

[1]Technical University of Munich, Department of Nuclear Medicine, Munich, Germany, [2]Graduate School of Systemic Neurosciences GSN-LMU, Munich, Germany, [3]Université De Liège, Liege, Belgium

Introduction: Operation of any communication system requires energy input. Both structural and functional connectivity of the brain were recently shown to be positively linked to its energy consumption, but the strength of this link remains unclear. Here, we directly compared structural connectivity (SC) and functional connectivity (FC) in their ability to predict glucose metabolism of the brain.

Methods: We analyzed diffusion tensor imaging (DWI), and fluorodeoxyglucose (FDG) positron emission tomography (PET) data of 55 healthy, middle-aged individuals. Images were spatially parcellated into 106 brain regions. FDG uptake was intensity normalized by the mean uptake in the whole brain gray matter. SC was measured by probabilistic tractography. FC was estimated from fMRI data. FC weights were computed as Pearson correlation between blood-oxygen-level-dependent signals of each pair of regions. In total, we obtained 55x106=5830 observations of FDG uptake. For each FDG uptake observation, 106 connection weights were available. Linear regression explores the linear association between connection weights and FDG uptake, nonlinear regression models allow more complex relationships. We tested 5 types of regression models: linear regression, k-nearest neighbors, support vector, extremely randomized trees, and gradient boosting. We fitted 3 sets of regression models: one set with SC as predictors, another with FC as predictors, and a third set with both SC and FC as predictors. Each set included the 5 regression models listed above. The complete dataset was split into a training (80%) and a test set (20%), stratified by brain region. All regression models were trained using the same training set, with 5-fold cross validation repeated 5 times. Mean training R2 scores and root mean squared error (RMSE), and standard deviation were reported for each model. Test R2 score and RMSE were evaluated on the test set using the best regression model.

Results: Up to 75% of the variance in the brain's relative FDG uptake was explained by SC, but only 30% by FC. Across all regressors, the SC models performed substantially better than FC models: the mean R2 of each SC model is more than double that of its counterpart FC model (Figure 1), and the mean RMSE of each SC model is lower than its counterpart FC model (Figure 2). The test R2 score and RMSE were similar to the training scores. Additionally, including FC predictors did not enhance model performance achievable by SC alone.

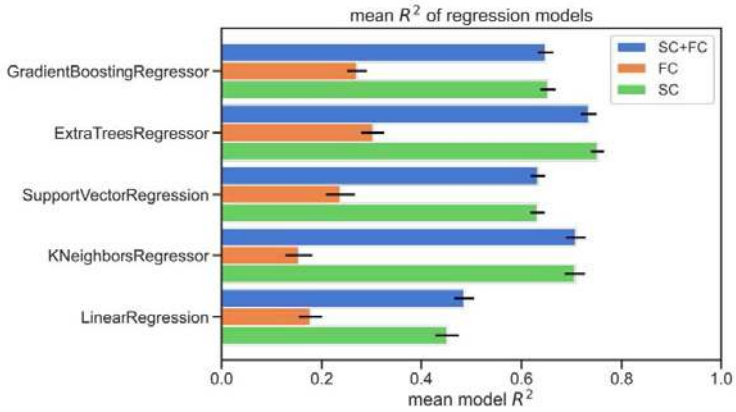

Figure 1. Mean R^2 of all models during training from 5 repeats of cross validation. Standard deviation as error bars.

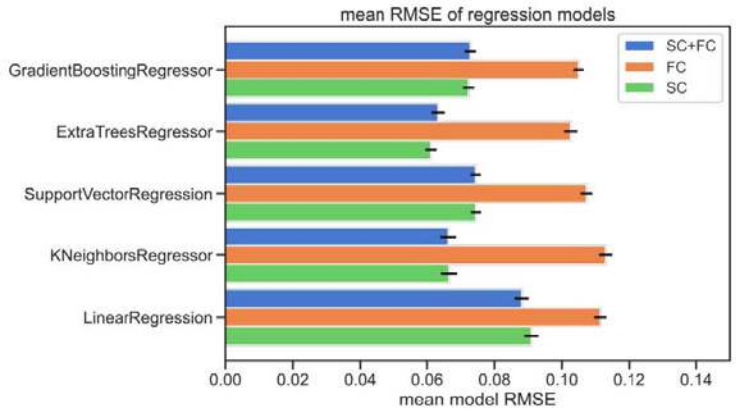

Figure 2. Mean RMSE of all models during training from 5 repeats of cross validation. Standard deviation as error bars.

Conclusions: SC predicts glucose metabolism more accurately and strongly than FC, in both linear and nonlinear models, regardless of the model complexity. FC does not add to the predictive power when combined with SC. Our results indicate that brain energy demands are closer linked to its white matter infrastructure than to its functional communication.

Poster No 2601

Improved cerebrovascular brain-age accuracy by multi-sequence, multi-center harmonisation

Mathijs Dijsselhof[1,2], Candace Moore[3], Wibeke Nordhøy[4], Dani Beck[5,6,7], Lars Westlye[5,6,8], Nishi Chaturvedi[9,10], Alun Hughes[9], David Cash[11,12], Jonathan Schott[11], Frederik Barkhof[1,2,13], James Cole[14,15], Henk Mutsaerts[1,2], Jan Petr[1,16]

[1]Radiology and Nuclear Medicine, Amsterdam University Medical Centers, Vrije Universiteit, Amsterdam, Netherlands, [2]Amsterdam Neuroscience, Brain Imaging, Amsterdam, Netherlands, [3]Netherlands eScience Center, Amsterdam, Netherlands, [4]Physics and Computational Radiology, Radiology and Nuclear Medicine, Oslo University Hospital, Oslo, Norway, [5]Norwegian Centre for Mental Disorders Research (NORMENT), Oslo University Hospital, Oslo, Norway, [6]Department of Psychology, University of Oslo, Oslo, Norway, [7]Division of Mental Health and Substance Abuse, Diakonhjemmet Hospital, Oslo, Norway, [8]KG Jebsen Centre for Neurodevelopmental Disorders, University of Oslo, Oslo, Norway, [9]MRC Unit for Lifelong Health & Ageing, Department of Population Science, University College London, London, United Kingdom, [10]Population Sciences and Experimental Medicine, Institute of Cardiovascular Science, University College London, London, United Kingdom, [11]Dementia Research Centre, UCL Queen Square Institute of Neurology, London, United Kingdom, [12]UK Dementia Research Institute at UCL, University College London, London, United Kingdom, [13]Queen Square Institute of Neurology and Centre for Medical Image Computing, University College London, Amsterdam, Netherlands, [14]Dementia Research Centre, Queen Square Institute of Neurology, UCL, London, United Kingdom, [15]Centre for Medical Imaging Computing, Computer Science, UCL, London, United Kingdom, [16]Helmholtz-Zentrum Dresden-Rossendorf, Institute of Radiopharmaceutical Cancer Research, Dresden, Germany

Introduction: Accelerated brain ageing is associated with increased risks of dementia and mortality, and can be assessed with machine learning and structural brain MRI data to determine the predicted age difference (brain-PAD) between biological and chronological age[1]. Advanced brain-PAD approaches aim to increase accuracy and sensitivity to specific pathologies by adding sequences able to assess cerebrovascular health, a contributor to cognitive decline[2]. Improved brain-PAD accuracy, and classification of Alzheimer's Disease (AD) patients, were shown with Cerebrovascular Brain-age by adding Arterial Spin Labeling (ASL) perfusion MRI to T1w and FLAIR data in a single-site study[3,4]. Such a pre-trained model has, however, a limited value for data from different MRI vendors or acquired with different parameters. While combining (ASL) studies is often a prerequisite to reach sufficient sample sizes for machine learning, acquisition differences can lead to a systematic bias of brain-PAD. The impact of commonly used harmonisation techniques on this bias is not sufficiently studied. Here, we assessed the influence of feature harmonisation with NeuroCombat[5] on Cerebrovascular brain-PAD, trained in a large dataset with T1w, FLAIR, and ASL sequences and applied in clinical datasets differing in sequence parameters and age range.

Methods: Imaging data MRI data was obtained from three population-based studies: NORMENT[4] (GE, n=1107, 54.9% female, 49.7±16.9 years, 18-95 years) with PCASL 3D spiral-FSE (PLD=2025ms, LD=1450ms), SABRE[6] (Philips, n=727, 53% male, 71.2±6.6 years, 37-90 years) with PCASL 2D EPI (PLD=2000ms, LD=1800ms), and Insight46[7] (Siemens, n=282, 50.7% female, 70.6±0.66 years, 69–72 years) with PCASL 3D GraSE (PLD=1800ms, LD=1800ms). Additionally, structural (T1w and FLAIR) images were included. Data was pre-processed with ExploreASL (v1.10). Machine learning Brain-age model features were created from GM and WM volumetrics (T1w), (log-transform) WMH volumetrics (FLAIR), and vascular territory-based CBF and spatial coefficient of variation (sCoV; ASL)3. Training was performed using the ExtraTrees regressor (scikit-learn 1.3.2) on NORMENT, validated using 5-fold cross-validation, and tested on Insight46 and SABRE. Dataset features were harmonised using NeuroCombat[5], and performance between unharmonised (UH) and harmonised (H) features was assessed by comparing brain-PAD and the mean (MAE) and standard deviation of the absolute brain-PAD.

Results: Harmonisation decreased mean differences between all groups in all individual features (Figure 1). The harmonisation had no effect on the results (UH/H MAE = 4.8±3.9/4.7±3.8 years; p=0.87) within the validation dataset. Without harmonisation, brain-PADs were -14.0 ± 5.1 (Insight46) and -10.6 ± 6.6 (SABRE) years. Harmonisation reduced brain-PAD (p<0.001) in both datasets to -2.6±4.7 and -4.1±5.9 years, respectively, and also reduced MAE significantly to 3.9±3.6 (Insight46) and 5.7±4.4 (SABRE) years.

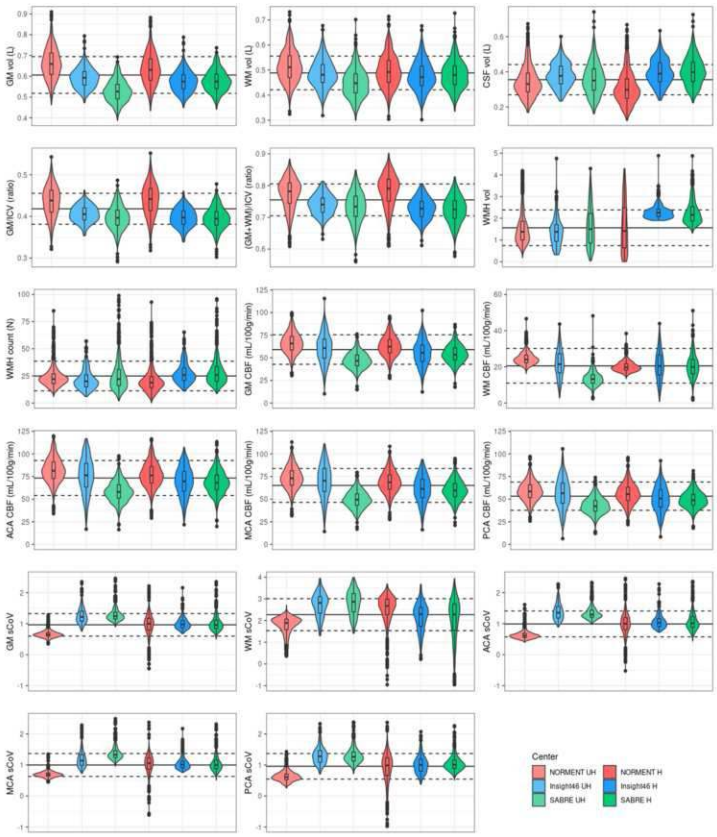

Figure 1: Imaging features of T1w, FLAIR and ASL sequences, per dataset, before and after harmonisation. Mean (black) and two standard deviations (dotted) lines are based on the three datasets before harmonisation. Abbreviations: GM = grey matter; WM = white matter; CSF = cerebrospinal fluid; ICV = intracranial volume; WMH = white matter hyperintensity; CBF = cerebral blood flow; sCoV = spatial coefficient of variation; ACA = anterior cerebral artery; MCA = middle cerebral artery; PCA = posterior cerebral artery; UH = unharmonised; H = harmonised.

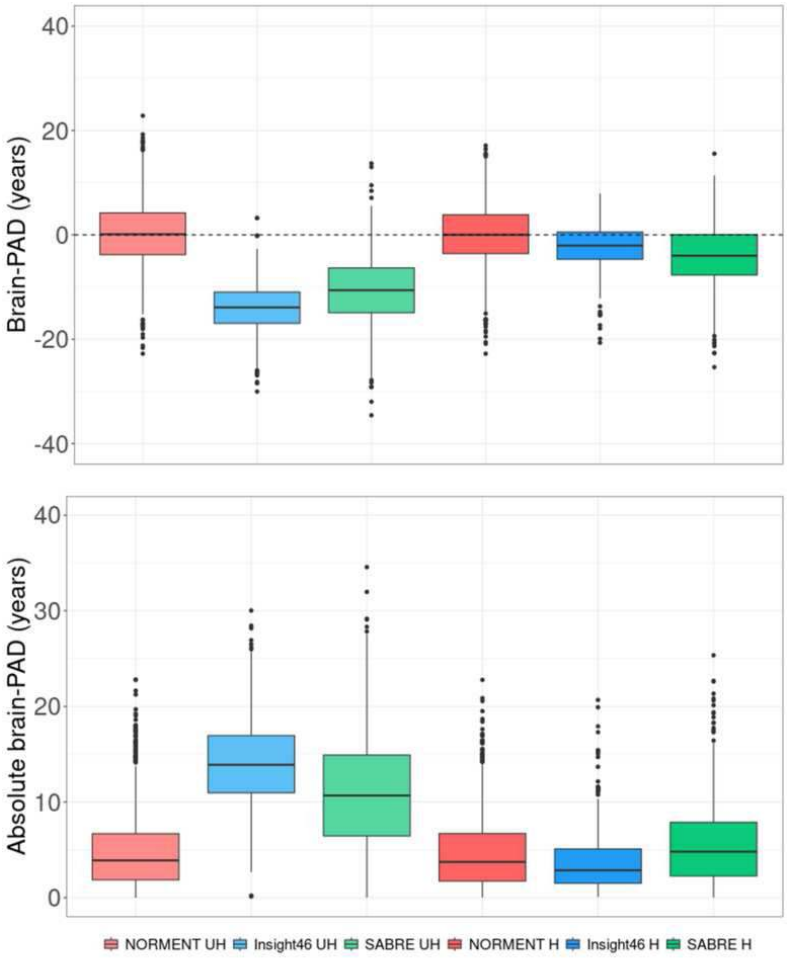

Figure 2: Boxplots showing brain-PAD in years (row 1), and absolute brain-PAD in years (row 2) for every (un)harmonised dataset. *Brain-PAD = brain-predicted age difference; H = harmonised; UH = unharmonised.*

Conclusions: Harmonisation effects between Insight46 and SABRE affected the ASL features the most, perhaps due to more variation in the different ASL sequence parameters having a direct impact on CBF, compared to the structural scans[8]. The remaining differences, especially in GM volume and CBF, could be attributed to dataset age differences. Harmonisation improved Brain-PAD and MAE values for Insight46 and SABRE, with more similar results to NORMENT, with brain-PADS of Insight46 agreeing with previous literature (-2.8±8.0 years)[9]. Both testing datasets showed negative average brain-PADs, perhaps due to known brain-age prediction biases at an older age[10]. To conclude, harmonisation reduces sequence- and site-specific biases in brain-age predictions using structural and, especially, ASL features. Further efforts should investigate applications in broader age ranges with a range of cognitive function to ensure that variance due to pathology and heterogeneous ageing remains present after harmonisation.

References

1. Cole, J. H. (2020) Multimodality neuroimaging brain-age in UK biobank: relationship to biomedical, lifestyle, and cognitive factors. Neurobiol. Aging 92, 34–42.
2. Iadecola, C. et al., (2019) Neurovascular and Cognitive Dysfunction in Hypertension. Circ. Res. 124, 1025–1044.
3. Dijsselhof, M. B. J. et al. (2023) The value of arterial spin labelling perfusion MRI in brain age prediction. Hum. Brain Mapp. 44, 2754–2766.
4. Rokicki, J. et al. (2021) Multimodal imaging improves brain age prediction and reveals distinct abnormalities in patients with psychiatric and neurological disorders. Hum. Brain Mapp. 42, 1714–1726.
5. Fortin, J.-P. et al. (2017) Harmonization of multi-site diffusion tensor imaging data. Neuroimage 161, 149–170.
6. Jones, S. et al. (2020) Cohort Profile Update: Southall and Brent Revisited (SABRE) study: a UK population-based comparison of cardiovascular disease and diabetes in people of European, South Asian and African Caribbean heritage. Int. J. Epidemiol. 49, 1441–1442e.
7. James, S.-N. et al. (2018) Using a birth cohort to study brain health and preclinical dementia: recruitment and participation rates in Insight 46. BMC Res. Notes 11, 885.
8. Baas, K. P. A. et al. (2021) Effects of Acquisition Parameter Modifications and Field Strength on the Reproducibility of Brain Perfusion Measurements Using Arterial Spin-Labeling. AJNR Am. J. Neuroradiol. 42, 109–115.
9. Wagen, A. Z. et al. (2022) Life course, genetic, and neuropathological associations with brain age in the 1946 British Birth Cohort: a population-based study. Lancet Healthy Longev 3, e607–e616.
10. de Lange, A.-M. G. et al., (2020) Commentary: Correction procedures in brain-age prediction. NeuroImage. Clinical vol. 26 102229.

Poster No 2603

Effect of hypertension and diabetes on CVR follows networks in grey and white matter

Nuwan Nanayakkara[1], Liesel-Ann Meusel[1], Nicole Anderson[1,2], J. Jean Chen[1,2]

[1]Baycrest Health Sciences, Toronto, Ontario, Canada, [2]University of Toronto, Toronto, Ontario, Canada

Introduction: Cerebrovascular reactivity (CVR) changes in gray matter (GM) have been reported in hypertension and diabetes (Ivankovic et al., 2013; Tchistiakova et al., 2014; Li et al., 2021), but have only been reported sparsely in the white matter (WM) (Nanayakkara et al., 2023b). Studies of CVR changes in functionally and structurally connected brain circuits are not reported even with recent trends for integrated analysis of regions within functional networks. This study assessed differences in the amplitude and time delay of CVR among patients with hypertension (HT), hypertension and type 2 diabetes (HT+DM), and age-matched controls (CTL) in joint WM and GM atlas contributing to resting-state (RS) networks (Nozais et al., 2023).

Methods: The study consisted of 18 CTL, 20 HT, and 11 HT+DM subjects with mean ages of 71.42, 72.22 and 70.22 years, respectively. Each subject followed a 30 s resting and 2 s exhale followed by a 15 s breath-hold (period = 47 s), repeated 6 times during an fMRI image acquisition with T2*-weighted EPI (voxel size = 3.4x3.4x6.0 mm, TE1/TE2/TR = 9.1/25/4000 ms). Respiratory bellows were recorded using the scanner's built-in belt. A T1-anatomical scan was acquired to generate brain parcellations by registering to standard atlases. The time series data were preprocessed using FSL and AFNI tools. AFNI's 3dretroicor was used to generate BOLD data corrected for physiological noise (i.e., heartbeat, respiration). Neighbouring control and tag frames were averaged in a sliding-window manner to produce 78 frames of BOLD data. These were then high-pass filtered at a 0.01 Hz cut-off frequency, from which CVR metrics were derived using the Fourier transform using our recently published method (Nanayakkara et al., 2023a, 2023c). CVR amplitude and time delay were computed in corresponding WM and GM atlases (Nozais et al., 2023) contributing to RS networks, with GM separated from WM using dilated FreeSurfer GM parcellations. The CVR time delay was expressed in reference to the respiratory belt signal. The 2-way ANOVA was used in each RS network to compare CVR metrics between groups corrected for multiple comparisons by controlling the false discovery rate.

Results: Figure 1 shows RS network-wise mean CVR amplitudes and time delays compared between subject groups in the GM, the WM and the combined GM and WM regions. All regions show similar differences between groups. The CVR amplitude is significantly higher in CTL than in both HT and HT+DM and the time delay is significantly shorter in HT than in both CTL and HT+DM. HT+DM subjects have the lowest CVR amplitudes and longest time delays. Figure 2 shows the network-wise comparison of the GM-WM combined CVR amplitudes and time delays between groups. CVR time delays show more significant differences between groups than amplitudes in RS networks.

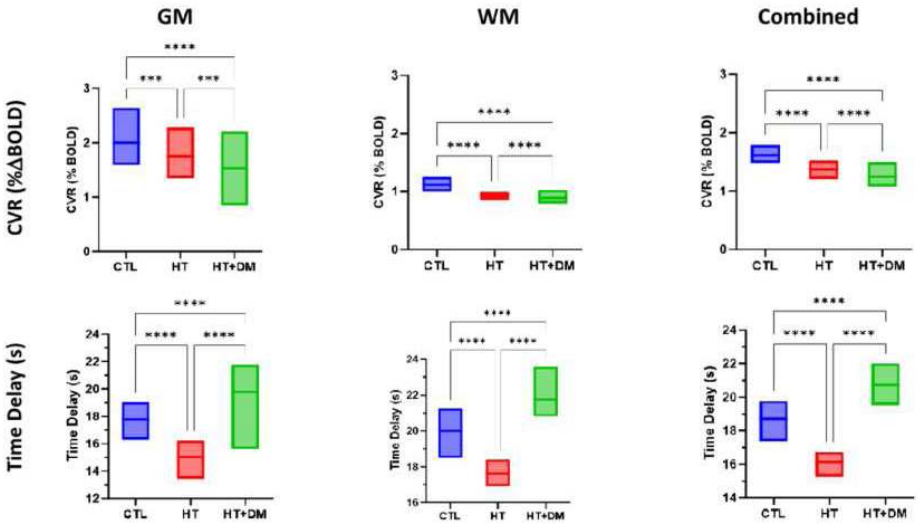

Figure 1. Mean CVR amplitude and time delay across all RS networks compared between subject groups for GM, WM, and combined GM and WM regions in each RS network. The statistically significant differences detected by ANOVA corrected for multiple comparisons by controlling the false discovery rate using the Benjamini-Hochberg procedure indicated by *** ($q < 0.001$) and **** ($q < 0.0001$).

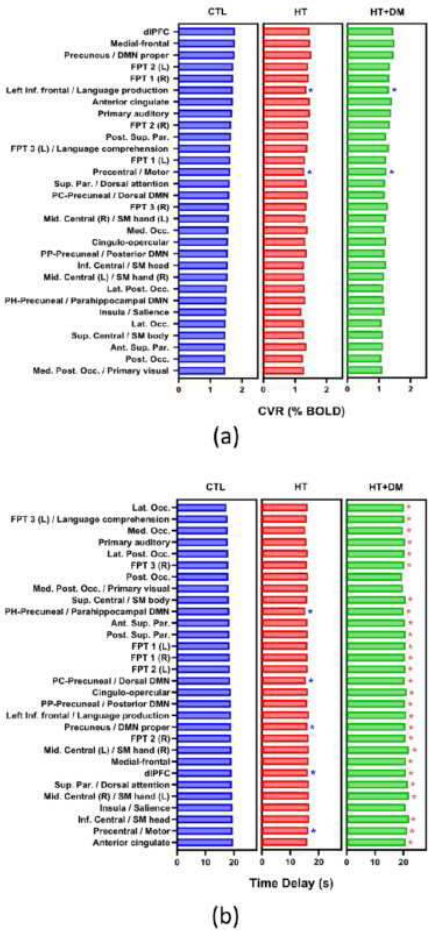

Figure 2. (a) Mean RS network-wise CVR amplitude arranged in descending order of CTL values in RS networks. Statistically significant lower CVR amplitudes compared to CTL are marked by blue (*) asterisks. (b) Mean RS network-wise CVR time delay arranged in the ascending order of CTL in RS networks. Statistically significant shorter CVR time delay compared to CTL is marked with blue (*) and longer CVR time delays compared to HT are marked by red (*) asterisks.

Conclusions: In this work, we demonstrate that CVR varies across CTL, HT and HT+DM groups in a network-specific manner, in line with vascular-density differences across tracts (Bernier, Viessmann and Ohringer, 2020). This complements our previous work in which CVR amplitude and delay were shown to differ across these groups in a parcellation-specific manner (Nanayakkara et al., 2023c). The CVR amplitude was lowest in HT+DM for both GM and WM, consistent with previous studies in the GM (Tchistiakova et al., 2014), whereas the HT group exhibited a lower CVR than CTL, also consistent with previous GM studies(Lee et al., 2021; Li et al., 2021). Interestingly, the CVR time delay in RS networks was far more sensitive than CVR amplitude to differences across the groups; this was the case in both GM and WM. While HT+DM seems to confer longer CVR delays, HT seems to confer shorter delays than CTL, suggesting the unique effect of hypertension on vascular dynamics. These findings suggest that the cerebrovasculature may be affected by disease in a network-wise manner, spanning both GM and WM that are connected within the same networks.

References

1. Bernier, M., Viessmann, O. and Ohringer, N. (2020) 'Human cerebral white-matter vasculature imaged using the blood-Pool contrast agent ferumoxytol: bundle-specific vessels and vascular density', Proc Intl Soc Mag [Preprint]. Available at: https://archive.ismrm.org/2020/0016.html.
2. Bright, M.G. and Murphy, K. (2013) 'Reliable quantification of BOLD fMRI cerebrovascular reactivity despite poor breath-hold performance', NeuroImage, 83, pp. 559–568.
3. Ivankovic, M. et al. (2013) 'Influence of hypertension and type 2 diabetes mellitus on cerebrovascular reactivity in diabetics with retinopathy', Annals of Saudi medicine, 33(2), pp. 130–133.
4. Lee, B.-C. et al. (2021) 'Arterial Spin Labeling Imaging Assessment of Cerebrovascular Reactivity in Hypertensive Small Vessel Disease', Frontiers in neurology, 12, p. 640069.
5. Li, Y. et al. (2021) 'MRI study of cerebral blood flow, vascular reactivity, and vascular coupling in systemic hypertension', Brain research, 1753, p. 147224.
6. Nanayakkara, N.D. et al. (2023a) 'A robust method for estimating CVR dynamics from breath-hold BOLD data without end-tidal carbon dioxide recordings', in Proceedings of International Society for Magnetic Resonance in Medicine (ISMRM), p. 2025.

7. Nanayakkara, N.D. et al. (2023b) 'Effects of hypertension and type 2 diabetes on cerebrovascular reactivity in white matter', in Organization for Human Brain Mapping (OHBM) Annual Meeting, p. 1319.
8. Nanayakkara, N.D. et al. (2023c) 'Robust estimation of dynamic cerebrovascular reactivity using breath-holding fMRI: application in diabetes and hypertension', medRxiv. Available at: https://doi.org/10.1101/2023.05.20.23290209.
9. Nozais, V. et al. (2023) 'Atlasing white matter and grey matter joint contributions to resting-state networks in the human brain', Communications biology, 6(1), p. 726.
10. Tchistiakova, E. et al. (2014) 'Combined effects of type 2 diabetes and hypertension associated with cortical thinning and impaired cerebrovascular reactivity relative to hypertension alone in older adults', NeuroImage. Clinical, 5, pp. 36–41.

Poster No 2604

Functional networks link grey and white matter cerebrovascular reactivity in healthy elderly adults

Nuwan Nanayakkara[1], Liesel-Ann Meusel[1], Nicole Anderson[1,2], J. Jean Chen[1,2]

[1]Baycrest Health Sciences, Toronto, Ontario, [2]University of Toronto, Toronto, Ontario, Canada

Introduction: The cerebrovasculature was previously shown to be regulated in a network-like manner that coincides with the anatomy of cortical functional networks (Bright et al., 2020), consistent with early works that support the development of vasculature according to function (Shellshear, 1924). Thus, cerebrovascular reactivity (CVR), a hemodynamic metric often used to assess vascular regulation (e.g., diameter, resistance), may vary between these "vascular networks". Functional networks are fundamentally sustained by subcortical white-matter (WM) networks, and indeed, WM vascular density was found to vary by tract (Bernier, Viessmann and Ohringer, 2020), but the relationship between associated grey matter (GM) and WM hemodynamics remains unclear. Based on the literature on fetal development (Smirnov, Destrieux and Maldonado, 2021), we expect the vasculature feeding neighboring GM and WM regions within the same network to be congruent. Moreover, it is expected that the WM would be associated with longer hemodynamic delays than GM (Van den Bergh, 1969). This was previously reported for WM cerebrovascular reactivity (CVR) (Thomas et al., 2014). In this work, we investigate the relationships between CVR in paired GM and WM networks.

Methods: This study consisted of 18 healthy volunteers aged 71.42 years (mean). Each subject followed a 30 s resting and 2 s exhale followed by a 15 s breath-hold (period = 47 s), repeated 6 times during an dual-echo pCASL fMRI acquisition (voxel size = 3.4x3.4x6.0 mm, TE1/TE2/TR = 9.1/25/4000 ms). Respiratory bellows were recorded using the scanner's built-in belt and used as CVR delay reference. The time series data were preprocessed using FSL and AFNI tools. AFNI's 3dretroicor was used to generate BOLD data corrected for noise associated with physiological motion (i.e., heartbeat, respiration). Neighbouring control and tag frames were averaged in a sliding-window manner to produce 78 frames of BOLD data. These were then high-pass filtered at a 0.01 Hz cut-off frequency. CVR amplitude and delay were etimated using our Fourier-based method (Nanayakkara et al., 2023b), then divided into corresponding white matter and grey matter networks based on the functionnectome (Nozais et al., 2023). To minimize partial-volume effects, dilated FreeSurfer GM parcellations were used to separate GM from WM. The correlation between GM and WM of the CVR amplitude and time delay within each network was analyzed using Pearson correlation.

Results: Fig. 1 shows the differences in mean CVR amplitude and time delay between GM and WM across the 30 resting-state networks. The CVR amplitude in WM was statistically significantly ($p < 0.0001$) lower and the time delay in WM was statistically significantly longer ($p < 0.0001$) than in GM as detected by paired t-test. These results are consistent with previous research (Thomas et al., 2014). Means and standard deviations in network-wise GM and WM regions exhibited a statistically significant correlation (Fig. 2). The mean time delay showed the strongest correlation between GM and WM.

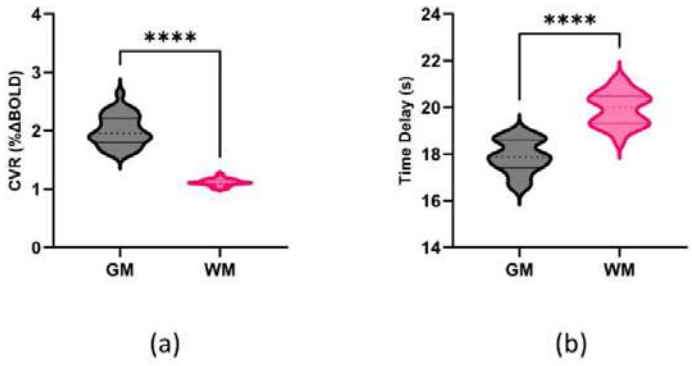

Figure 1. (a) The differences in mean CVR (a) amplitude and (b) time delay between GM and WM in RS networks. The statistically significant differences ($p < 0.0001$) were detected by paired *t*-test.

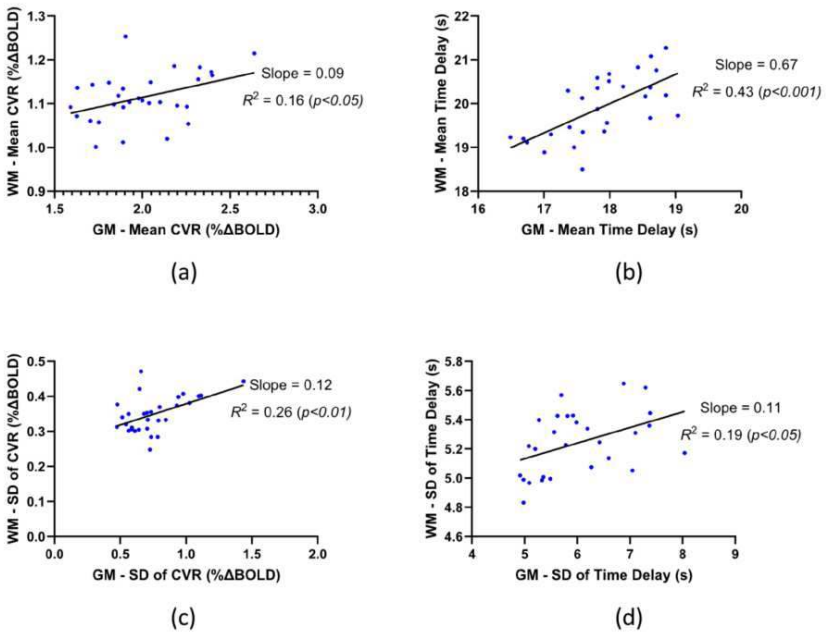

Figure 2. The means of CVR (a) amplitude and (b) time delay of the study population showed a statistically significant correlation between network-wise GM and WM regions. The standard deviations of CVR (c) amplitude and (d) time delay also showed a statistically significant correlation for the same regions. This data shows a similar distribution of subject CVR in each RS network.

Conclusions: This study was motivated by previous work by Bright et al. that demonstrated network behaviour in the BOLD response to carbon dioxide (Bright et al., 2020). Our results suggest CVR amplitudes are correlated across WM and GM regions within the same networks, but CVR delays even more so. The group-wise variability in these quantities are also coherent between WM and GM in the same network. BOLD-based CVR is determined by both vascular resistances (Duffin et al., 2018) and blood oxygenation, and CVR delay reflect both blood transit and the hemodynamic response time. For blood vessels in a given WM-GM network to exhibit similar CVR amplitude and delays, they should presumably exhibit similarities in some or all of the above factors that govern CVR.

References

1. Bernier, M., Viessmann, O. and Ohringer, N. (2020) 'Human cerebral white-matter vasculature imaged using the blood-Pool contrast agent ferumoxytol: bundle-specific vessels and vascular density', Proc Intl Soc Mag [Preprint]. Available at: https://archive.ismrm.org/2020/0016.html.
2. Bright, M.G. et al. (2020) 'Vascular physiology drives functional brain networks', NeuroImage, p. 116907.
3. Duffin, J. et al. (2018) 'Cerebrovascular Resistance: The Basis of Cerebrovascular Reactivity', Frontiers in neuroscience, 12. Available at: https://doi.org/10.3389/fnins.2018.00409.
4. Nanayakkara, N.D. et al. (2023a) 'Effects of hypertension and type 2 diabetes on cerebrovascular reactivity in white matter', in Organization for Human Brain Mapping (OHBM) Annual Meeting, p. 1319.
5. Nanayakkara, N.D. et al. (2023b) 'Robust estimation of dynamic cerebrovascular reactivity using breath-holding fMRI: application in diabetes and hypertension', medRxiv. Available at: https://doi.org/10.1101/2023.05.20.23290209.
6. Nozais, V. et al. (2023) 'Atlasing white matter and grey matter joint contributions to resting-state networks in the human brain', Communications biology, 6(1), p. 726.
7. Shellshear, J.L. (1924) 'The Basal Arteries of the Forebrain and Their Functional Significance', The Journal of nervous and mental disease, 60(3), p. 296.
8. Smirnov, M., Destrieux, C. and Maldonado, I.L. (2021) 'Cerebral white matter vasculature: still uncharted?', Brain: a journal of neurology, 144(12), pp. 3561–3575.
9. Thomas, B.P. et al. (2014) 'Cerebrovascular Reactivity in the Brain White Matter: Magnitude, Temporal Characteristics, and Age Effects', Journal of cerebral blood flow and metabolism: official journal of the International Society of Cerebral Blood Flow and Metabolism, 34(2), pp. 242–247.
10. Van den Bergh, R. (1969) 'Centrifugal elements in the vascular pattern of the deep intracerebral blood supply', Angiology, 20(2), pp. 88–94.

Poster No 2605

Developmental trajectory of the coupling between CSF and cerebral hemodynamics across human lifespan

Lin Hua[1], Canpeng Huang[1], Zhen Yuan[1], Zhiying Zhao[1]

[1]*University of Macau, Taipa, Macau*

Introduction: The lymphatic system of brain, known as glymphatic system, plays an important role in waste clearance and maintaining the water homeostasis of the central nervous system. Recent studies have reported that the movement of the cerebrospinal fluid (CSF) in the ventricles during slow-wave sleep, which are coupled with high-amplitude spontaneous brain activations, contributes to increased metabolite transportation and clearance[1,2]. This phenomenon, hereinafter referred to as the CSF-BOLD coupling, is also present in the wakeful brain and has been associated with aging and neurodegenerative diseases[3]. However, no reference standards currently exist to quantify the glymphatic function over time using this measurement as a proxy, which hinders the understanding of the glymphatic changes across the human lifespan. Therefore, the current study aims to elucidate the developmental trajectory of CSF-BOLD coupling across the lifespan.

Methods: A total of 2159 subjects with the age span from 5 to 100 years were retrieved from three Human Connectome Project (HCP) datasets, including HCP Development (HCP-D; n = 628; age range: 5-21), HCP Young Adult (HCP-YA; n = 811; age range: 22-35) and HCP Aging (HCP-A; n = 720; age range: 36-100). After image preprocessing, the global BOLD signal and the CSF inflow signal were extracted from the gray matter mask and the bottom slice of CSF mask, respectively. Cross-correlation analysis was performed to measure the coupling strength between the global BOLD signal and the CSF inflow signal (Figure 1). Then, the Generalized Additive Models for Location, Scale, and Shape (GAMLSS) modelling with fractional polynomials was used to model the changes in CSF-BOLD coupling strength and brain structural measures across the lifespan separately. Finally, correlation analysis was conducted to examine the relationship between the coupling strengths and brain morphological and behavioral measures.

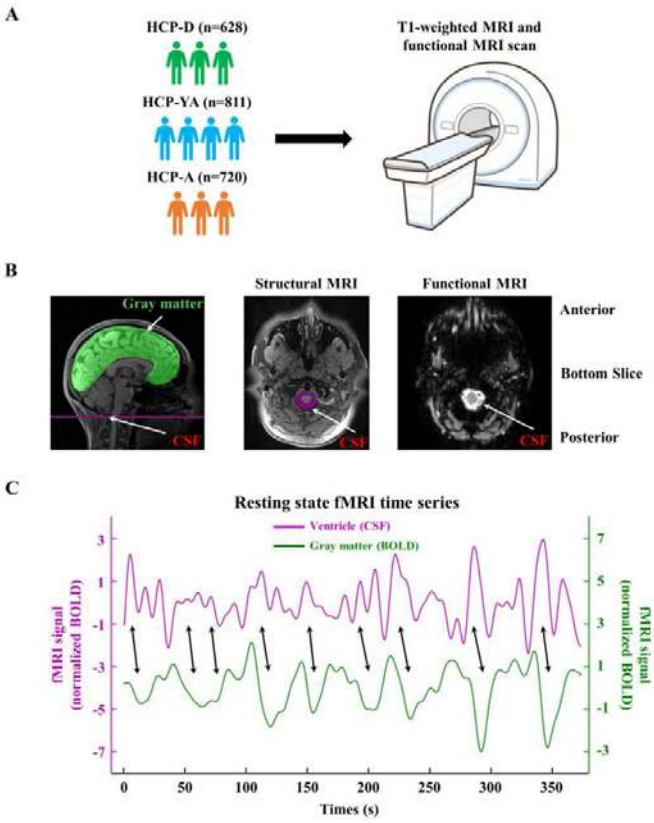

Figure 1. Procedures of the coupling relationship between the global BOLD signal and CSF inflow signal across human lifespan

Results: The CSF-BOLD coupling showed a significantly negative peak at the 3.2-second lag ($r = -0.45$; $p < 0.001$, permutation test) across whole subjects. Fitting with fractional polynomials, CSF-BOLD coupling strength presented an initial trend of a steep drop from early childhood (5 years) to early adulthood (peaking around 35 years), followed by an increase till the late life stage (age 90-100) in both sexes (Figure2). This developmental trajectory is similar between males and females with the negative peak arriving earlier in females. In the late adulthood (50-100 years), females showed a significantly stronger CSF-

BOLD coupling relationship than males (t = -2.10, p = 0.036). Moreover, the developmental trajectory of intracranial tissue volume and CSF-BOLD coupling suggested that age-related change in CSF-BOLD coupling was in synchrony with the white matter development. Regarding behavioral measures, after adjusting for age and sex, CSF-BOLD coupling strength positively correlated with item scores of hours of actual sleep (r = 0.131, p < 0.001) and frequency of sleep medicine (r = 0.077, p = 0.002) in Pittsburg Sleep Quality Index (PSQI). Finally, CSF-BOLD coupling coefficient was correlated with cognitive function scores assessed by the NIH Toolbox for the Assessment of Neurological Behavior and Function Cognition Battery (NIHTB-CB) adjusted for age. Significant negative correlations are with the working memory domain (r = -0.070, p = 0.003) and total cognition score of NIHTB-CB (r = -0.092, p < 0.001). Both fluid (r = -0.107, p < 0.001) and crystal intelligence (r = -0.067, p = 0.004) score also negatively correlated with CSF-BOLD coupling strength.

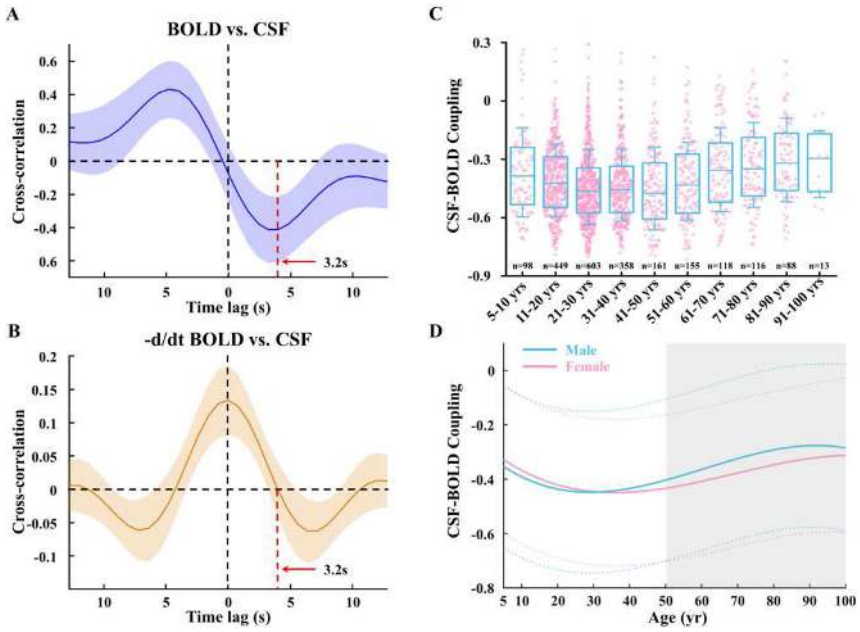

Figure2. The development Developmental trajectory of the CSF-BOLD coupling across human lifespan

Conclusions: In conclusion, the current study contributes to our understanding of the development of the glymphatic system across the lifespan, shedding light on its dynamic changes, gender-specific variations, and associations with sleep quality and cognitive function.

References

1. Xie, L. (2013), 'Sleep drives metabolite clearance from the adult brain', Science, vol. 342, no. 6156, pp. 373-377
2. Fultz, N. E. (2019), 'Coupled electrophysiological, hemodynamic, and cerebrospinal fluid oscillations in human sleep', Science, vol. 366, no. 6465, pp. 628-631
3. Han, F. (2021), 'Reduced coupling between cerebrospinal fluid flow and global brain activity is linked to Alzheimer disease–related pathology', PLoS biology, vol. 19, no. 6, pp. e3001233

Poster No 2606

Two Distinct Modes of Hemodynamic Responses in the Human Brain

Samira Epp[1], Gabriel Castrillón[1], Jessica Andrews-Hanna[2], Christine Preibisch[3], Valentin Riedl[3]

[1]Friedrich-Alexander University, Erlangen, Germany, [2]University of Arizona, Tucson, AZ, [3]Technical University of Munich, Munich, Germany

Introduction: The BOLD signal as measured by fMRI relies on the assumption that changes in the cerebral blood flow (CBF) in response to neural activity exceed changes in the cerebral metabolic rate of oxygen (CMRO2) – this is the canonical hemodynamic response model. The interpretation of positive BOLD responses as increases in neuronal activity and vice versa for negative responses is based on this assumption. Yet, several studies reported regional variability of hemodynamic responses, especially between cortical and subcortical regions. These observations raise doubts to what extent the canonical hemodynamic response can be generalized to the entire cortex. Our study aimed to investigate oxygen metabolism in relation to both positive and negative BOLD responses across the human cortex. To this end, we utilized a quantitative fMRI approach to examine the voxel-wise relationship between ΔCMRO2 and ΔBOLD signal during various task conditions.

Methods: Data during a calculation (CALC) and control (CTLR) task were acquired on a 3T MR scanner from 40 healthy subjects (22 w, 18 m; mean age 32.1 ± 9.2y), additional autobiographical memory (MEM) data from a subset of 30 subjects. The CALC task was designed to evoke negative BOLD responses in mostly the default mode network (DMN) and positive BOLD responses in other networks. The MEM task should evoke positive BOLD responses in the DMN. We employed CTRL as an active baseline, with matched visual input and button presses compared to CALC and MEM. Quantitative fMRI included 1) Spin-echo T2 mapping, GRASE, 8 echoes 2) Gradient-echo T2* mapping; 12 echoes 3) Dynamic susceptibility imaging (DSC); single-shot GRE-EPI; with contrast agent 4) Pseudo-continuous arterial spin labeling (pCASL); 2D EPI readout. BOLD fMRI was acquired using single-shot EPI, TR=1.2s, 400 dynamic scans, 30s block design. R2' maps were calculated via R2' = 1/(T2*) - 1/T2, OEF via OEF = (R2')/(c · CBV), CBF maps from pCASL; and CMRO2 via CMRO2 = OEF · CBF · CaO2. Group BOLD results, output from partial least squares analyses, were used as masks in standard space.

Results: The disparity between ΔBOLD and ΔCMRO2 at the voxel level for the CALC vs CTRL contrast is shown in Fig.1. 30% of voxels with significant positive ΔBOLD and canonical hemodynamics, whereas 66% with significant negative ΔBOLD exhibited inverse ΔCMRO2 and weak or missing ΔCBF. Pooling all voxels with significant ΔBOLD in MEM or CALC vs CTRL, separately for concordant and discordant voxels, revealed that concordant voxels regulate ΔCMRO2 via ΔCBF, whereas discordant voxels regulate ΔCMRO2 via ΔOEF (Fig. 2). To reveal if these different modes of hemodynamic responses were task-specific or location-specific, we identified voxels that showed both positive and negative ΔBOLD within the same voxels. Of these, 47% showed mixed modes of hemodynamics, dependent on the task. 34% of voxels consistently showed CBF-driven hemodynamics and 19% consistently showed OEF-driven hemodynamics. In this latter group of voxels, the sign of ΔBOLD was always opposing the sign of ΔCMRO2, independent of task. Additionally, they showed the lowest OEF levels in baseline, significantly lower than voxels with mixed or CBF-driven responses.

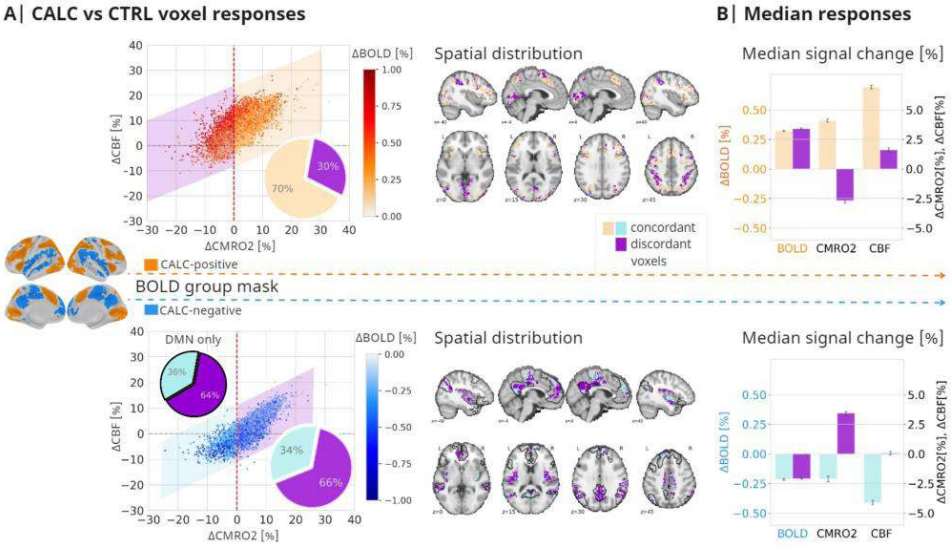

Figure 1. Dependence of BOLD responses on changes in CBF and CMRO2. A| Observed data from BOLD- and quantitative fMRI within BOLD group mask, separately for significant positive (orange, upper row) and negative (blue, lower row) BOLD responses, median across all subjects per voxel, colors indicate ΔBOLD [%]. Voxels with ΔBOLD concordant to ΔCMRO2 are depicted in pale, while voxels with discordant ΔBOLD are depicted in violet color and by violet shadings. The pie plots summarize the ratio of discordant to concordant voxels. In the lower panel, the pie plot with black contours additionally summarizes the ratio of discordant voxels within the DMN. Axial slices illustrate the spatial distribution of significant concordant and discordant BOLD voxels, with black contours depicting the DMN. **B|** The bar plots show median ΔCMRO2 [%] and ΔCBF [%] across voxels with either concordant or discordant ΔBOLD [%], within positive (upper row) and negative BOLD regions (lower row), error bars = 95% CI, 2000 bootstraps.

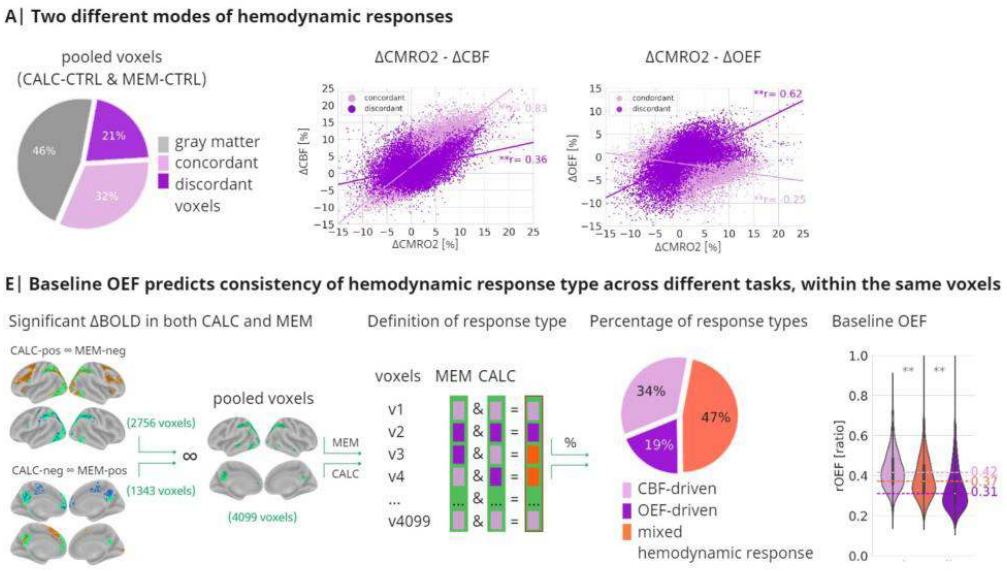

Figure 2. CMRO2 regulation via CBF versus OEF. A| Regulation of task CMRO2 responses. Of all gray matter voxels, 21% showed discordant and 32% showed concordant responses during either CALC vs. CTRL or MEM vs. CTRL contrasts. Correlation of ΔCMRO2 [%] with ΔCBF [%] and ΔOEF [%] across all task contrasts (CALC or MEM vs CTRL), separately for concordant (pale) and discordant (dark violet) voxels. ΔCMRO2 and ΔCBF showed a high correlation across concordant voxels ($r = 0.83$, $p < 0.01$), while discordant voxels showed only a weak correlation ($r = 0.36$, $p < 0.01$). ΔCMRO2 and ΔOEF showed a negative, weak correlation across concordant voxels correlation ($r = -0.25$, $p < 0.01$), but a positive, moderate correlation across discordant voxels ($r = 0.62$, $p < 0.01$). **B|** Conjunction voxels (green outlines) that showed either positive BOLD responses during CALC and negative BOLD responses during MEM (upper row) or vice versa (lower row). We pooled all conjunction voxels and defined the response type of each voxel. If the voxel behaved concordantly (same sign of ΔBOLD and ΔCMRO2) during both MEM and CALC conditions, as found in 34% of all pooled voxels, this voxel likely showed a CBF-driven hemodynamic response, see A). If it behaved discordantly in both conditions, as found in 16% of pooled voxels, it likely shows an OEF-driven hemodynamic response. If the voxel behaved concordantly in one conditions, but discordantly in the other, as found in 47% of voxels, its hemodynamic response type is defined to be mixed. These groups of voxels with different hemodynamic responses showed significantly different baseline OEF in CTRL, where CBF-driven voxels showed significantly higher OEF than mixed voxels, and OEF-driven voxels showed significantly lower OEF than mixed voxels. ** $p < 0.001$, independent sample permutation test on the median values, conducted for mixed versus other voxel types, 2000 permutations.

Conclusions: We identified a novel type of hemodynamic response in a substantial volume of the human cortex that, most critically, reverses the direction of the metabolic interpretation of BOLD signal changes. Using different task conditions, we induced significant ΔBOLD in approximately 50% of gray matter voxels, of which around 40% exhibited non-conforming hemodynamics during CALC, MEM or both tasks, regulating metabolic demand through OEF instead of changes in CBF. We identified lower OEF in the baseline state as a possible explanation for this phenomenon. Our findings strongly suggest that the common interpretation of positive ΔBOLD as increased neuronal activity and negative ΔBOLD as decreased neuronal activity may not withstand across the entire human cortex.

References

1. Drew et al. (2022), 'Neurovascular coupling: Motive unknown', Trends in Neurosciences
2. Hillman, E. M. C. (2014). 'Coupling Mechanism and Significance of the BOLD Signal: A Status Report.' Annual Review of Neuroscience, 37(1), 161–181.
3. Buxton, R. B. (2010). 'Interpreting oxygenation-based neuroimaging signals: The importance and the challenge of understanding brain oxygen metabolism.' Frontiers in Neuroenergetics.
4. Shaw, K., et al. (2021). 'Neurovascular coupling and oxygenation are decreased in hippocampus compared to neocortex because of 'microvascular differences.* Nature Communications, 12(1), 3190.
5. Shih et al. (2011).' Striatal and Cortical BOLD, Blood Flow, Blood Volume, Oxygen Consumption, and Glucose Consumption Changes in Noxious Forepaw Electrical Stimulation.' Journal of Cerebral Blood Flow & Metabolism, 31(3), 832–841.
6. Lin, P., et al. (2011). 'A Neuronal Basis for Task-Negative Responses in the Human Brain.' Cerebral Cortex, 21(4), 821–830.
7. Andrews-Hanna, J. R., Saxe, R., & Yarkoni, T. (2014). 'Contributions of episodic retrieval and mentalizing to autobiographical thought: Evidence from functional neuroimaging, resting-state connectivity, and fMRI meta-analyses.' NeuroImage, 91, 324–335.
8. Pike, G. B. (2012). 'Quantitative functional MRI: Concepts, issues and future challenges.' NeuroImage, 62(2), 1234–1240.
9. Christen, T., et al. (2012). 'Measuring brain oxygenation in humans using a multiparametric quantitative blood oxygenation level dependent MRI approach.' Magnetic Resonance in Medicine, 68(3), 905–911.
10. Kufer, J., et al. (2022). 'Imaging effective oxygen diffusivity in the human brain with multiparametric magnetic resonance imaging.' Journal of Cerebral Blood Flow & Metabolism, 42(2), 349–363.

Poster No 2607

Age-dependent changes in glymphatic system function in human brain using non-invasive MRI methods

Weiwei Zhao[1], Tianxin Mao[1], Hengyi Rao[1]

[1]*Center for Magnetic Resonance Imaging Research, Shanghai International Studies University, Shanghai, China*

Introduction: The glymphatic system (GS)[1] facilitates the exchange of cerebrospinal fluid (CSF) and brain interstitial fluid (ISF), resulting in the movement of fluid across the brain parenchyma to eliminate metabolic waste products[2]. The abnormal accumulation of this waste is a common feature in most neurodegenerative diseases[3]. Therefore, understanding the age-dependent trajectory of GS clearance function is crucial for comprehending brain aging and predicting neurodegenerative diseases. While interest in studying the GS in humans has markedly increased in the last decade, current approaches involving intrathecal gadolinium are challenging for research purposes and unsuitable for repeated measurements to assess changes in glymphatic transport across various physiological states. In this context, we discuss two potential non-invasive MRI methods for investigating the GS and its association with aging.

Methods: Forty-five healthy adults (23 females, mean age = 37.43 ± 10.29 years) participated in this study[4]. These participants were categorized into three groups with 10-year intervals (21-30, 31-40, 41-50), referred to as the 20s group, 30s group, and 40s group. Each participant underwent two MRI scans at the same time on two mornings. The imaging protocol included high-resolution T1-weighted anatomic imaging, resting-state functional MRI (rfMRI), and diffusion tensor imaging (DTI), all conducted using a 3T Siemens Trio system (Siemens Medical Systems, Erlangen, Germany) (for detailed MRI scan parameters, see[4]). The rfMRI data was pre-processed by SPM 12, where nuisance regressions of global signal, CSF signal, and motion parameters were omitted[5,6]. Consistent with prior studies[5,7], the cross-correlation between the gBOLD signal and CSF signal was calculated for each participant. The maximal anticorrelation was employed to quantify the strength of gBOLD-CSF coupling. The DTI images were pre-processed by FSL. The fractional anisotropy map of each subject was registered to the JHU-ICBM-FA template. The identification of the superior corona radiata (SCR) and the superior longitudinal fasciculus (SLF) as projection and association fibers at the lateral ventricle body level was based on the JHU-ICBM-DTI-81-white-matter Labeled Atlas. The diffusivity values of Dxx, Dyy, and Dzz of bilateral SLF and SCR were extracted, and the ALPS index was calculated using the following formula8: DTI-ALPS index = mean(Dxproj,Dxassoc)/mean(Dyproj,Dzassoc)

Results: In the 40s age group, the gBOLD-CSF coupling (-0.31±0.10) exhibited a significantly weaker connection compared to both the 20s (-0.35±0.11, p = 0.044) and 30s (-0.39±0.10, p = 0.002) groups (Figure 1). Although a linear correlation trend was observed between gBOLD-CSF coupling and age, the p-value did not reach statistical significance (p = 0.142). The ALPS index demonstrated a significant decrease in the 30s group (1.29±0.12) compared to both the 20s (1.39±0.12, p < 0.001) and 40s groups (1.38±0.11, p = 0.002). A quadratic relationship was observed between the ALPS index and age (R2 = 0.112, p = 0.001). The graphical representation of ALPS index versus age revealed a U-shaped pattern, reaching its nadir at 35 years of age, followed by an increase from approximately 40 years of age (Figure 2).

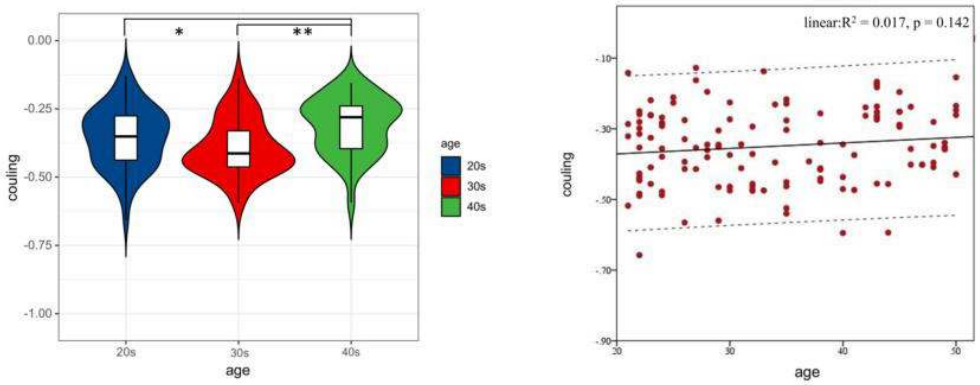

Fig 1. The results of age against gBOLD-CSF coupling.

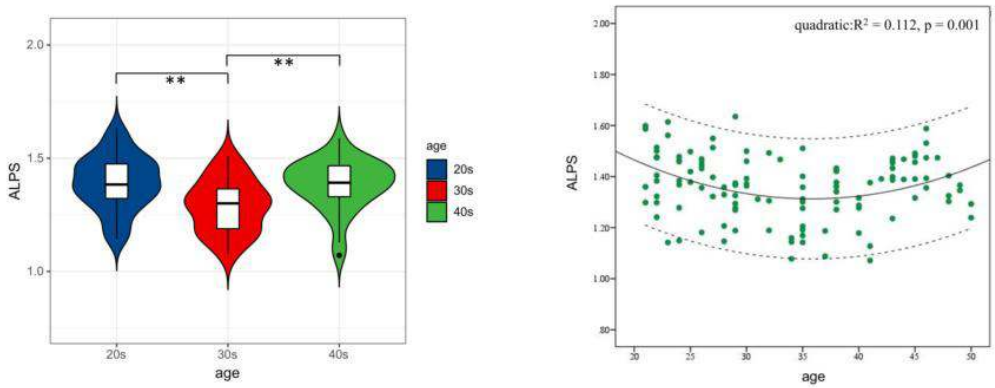

Fig 2. The results of age against ALPS index.

Conclusions: Two brain imaging modalities, rfMRI and DTI, were employed to assess their sensitivity to age-related changes in fluid transport. The gBOLD-CSF coupling and ALPS index were utilized to depict the clearance function of the GS from distinct perspectives, with the ALPS index revealing a U-shaped pattern in relation to age. Given the clinically relevant associations linking aging, glymphatic transport, and neurological disorders, both methodologies present an attractive avenue for gaining profound insights into the intricate interplay among vascular and CSF circulation, as well as ISF solute transport. These insights are crucial for future investigations pertaining to neurological diseases, cognitive function, or as reference values.

References

1. Iliff, J. J. et al. A paravascular pathway facilitates CSF flow through the brain parenchyma and the clearance of interstitial solutes, including amyloid β. Sci. Transl. Med. 4, 147 (2012).
2. Nedergaard, M. & Goldman, S. A. Glymphatic failure as a final common pathway to dementia. Science 370, 50–56 (2020).
3. Rasmussen, M. K., Mestre, H. & Nedergaard, M. The glymphatic pathway in neurological disorders. Lancet. Neurol. 17, 1016–1024 (2018).
4. Yang, F. N. et al. Sleep deprivation enhances inter-stimulus interval effect on vigilant attention performance. Sleep 41, (2018).
5. Fultz, N. E. et al. Coupled electrophysiological, hemodynamic, and cerebrospinal fluid oscillations in human sleep. Science (80-.). 366, 628–631 (2019).
6. Power, J. D. et al. Ridding fMRI data of motion-related influences: Removal of signals with distinct spatial and physical bases in multiecho data. Proc. Natl. Acad. Sci. U. S. A. 115, E2105–E2114 (2018).
7. Han, F. et al. Decoupling of Global Brain Activity and Cerebrospinal Fluid Flow in Parkinson's Disease Cognitive Decline. Mov. Disord. 36, 2066–2076 (2021).
8. Taoka, T. et al. Evaluation of glymphatic system activity with the diffusion MR technique: diffusion tensor image analysis along the perivascular space (DTI-ALPS) in Alzheimer's disease cases. Jpn. J. Radiol. 35, 172–178 (2017).

Poster No 2608

A Novel Imaging Biomarker in Cerebral Blood Flow in Patients with Sickle Cell Disease using fMRI

Brianna Kish[1], Jinxia Yao[1], Andrew John Frels[1], Jessica Budde[1], Vidhya Vijayakrishnan Nair[1], Andrew O'Brien[2], Ying Wang[2], Yunjie Tong[1]

[1]Purdue University, West Lafayette, IN, [2]Indiana University School of Medicine, Indianapolis, IN

Introduction: Sickle cell disease (SCD) is a genetic blood disorder characterized by production of abnormal hemoglobin (HgB) known as hemoglobin S (HgS), reducing blood oxygen-carrying capacity (Arkuszewski, 2013, DeBaun, 2006). To compensate the body increases cerebral blood flow but overcompensation can result in cerebral vascular shunting; blood velocity is increased until oxygen off-loading efficiency is reduced (Juttukonda, 2017). Studies have shown that shunting is more common in SCD patients than healthy individuals (Juttukonda, 2021). Systemic low-frequency oscillations (sLFOs) are a subset of low-frequency oscillations (0.01- 0.1 Hz) represented throughout the brain with high correlations and meaningful delay values in resting state BOLD-fMRI (Tong, 2017). In healthy subjects, sLFOs between the internal carotid arteries (ICA) and the superior sagittal sinus (SSS) have delays consistent with brain transit time (~5s) (Hoffmann, 2000). Using BOLD-fMRI, fluctuations in physiology can be measured via deoxy-hemoglobin concentration in blood; SCD is a blood disorder, so this allows changes to be captured (Heeger, 2002). In this study, we aim to investigate the hemodynamic mechanisms of sLFOs in SCD patients and their relationship with blood parameters.

Methods: Data from 23 participants with SCD were collected. 10 age and gender matched non-SCD controls were also enrolled. Each subject underwent a T1-weighted MRI, a resting state fMRI, and a blood draw. The blood tests included complete blood cell count, reticulocytes, and HgB electrophoresis. The fMRI data were preprocessed using FSL to correct

motion artifacts (Jenkinson, 2012). The SSS was identified and masked from the T1w image and then transformed into the fMRI space to extract the time series. The global mean signal (GMean) was generated by averaging the fMRI signal across the whole brain. Both signals were demeaned and filtered (0.01-0.1Hz) to acquire the sLFOs. Cross-correlation was performed between the SSS and GMean to calculate the maximum cross correlation coefficients (MCCC) and delay times. Pearson correlation was performed between the MCCC/delay times and 14 different blood measurements to determine any significant relationships.

Results: 90% of healthy subjects exhibit high positive MCCC values and negative delay times indicating that the GMean leads the SSS. However, only 11/23 SCD subjects displayed this standard behavior (MCCC 0.889, Delay -2.67 s). 12/23 SCD subjects show a negative MCCC value with the SSS leading the GMean (MCCC -0.748, Delay 3.708 s). In addition to a known relation with SCD, HgB, Hct, and HbS have significant correlations to MCCCs and delays. Negative MCCC subjects have significantly lower average HgB/Hct and higher HbS (Fig. 1A-C) compared with positive MCCC subjects. A significant positive correlation is observed between HgB/Hct and MCCC values in SCD patients with positive MCCCs while HbS exhibits a negative correlation to MCCC (Fig. 1D-F). Healthy subjects show a lower correlation. Similarly, the correlations between delays and blood measures in that cohort are weaker (Fig. 1G-I). Based on a particular model (Fig. 2A), fMRI signal flips sign when the oxygen saturation value from the corresponding voxel is greater than or equal to approximately 86% (Tong, 2019). This finding suggests that the SSS or GMean has a sign change. Since the SSS contains more venous blood, it is likely that oxygen saturation in the brain increases exceeding the threshold of 86%, thus flipping the GMean sign (Fig. 2B).

Conclusions: The present study employed fMRI to investigate the hemodynamics of SCD patients and identified a novel anti-correlation between the SSS-sLFO and the GMean-sLFO. The proposed model linked different degrees of shunting with anti-correlation and explained the high correlation between the MCCC values and blood measures. These findings represent significant advances in understanding the pathophysiology of SCD and offer potential biomarkers for measuring disease severity.

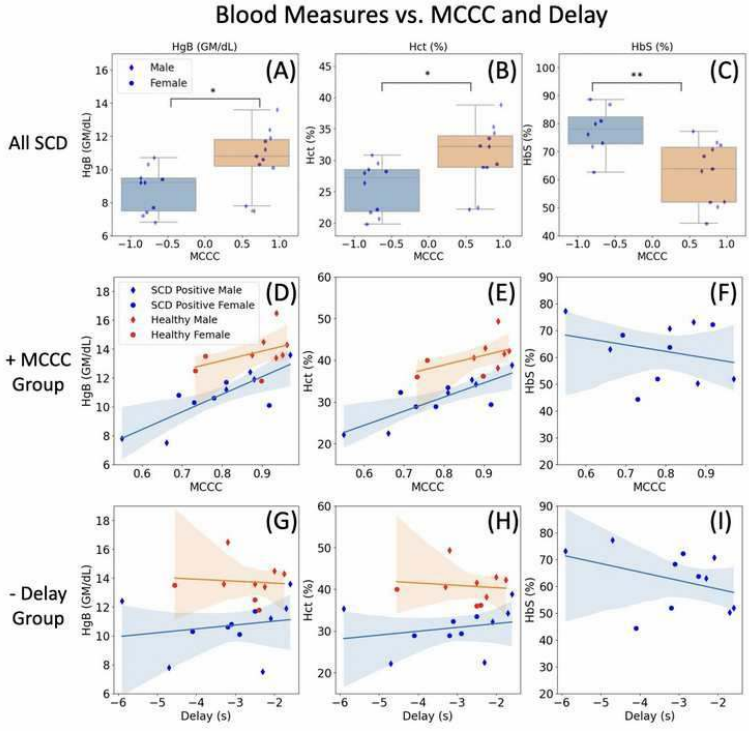

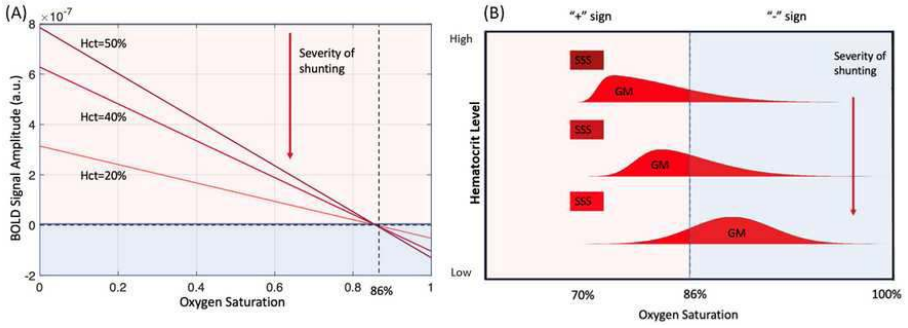

References
1. Arkuszewski, M. (2013), 'Sickle cell anemia: reference values of cerebral blood flow determined by continuous arterial spin labeling MRI', Neuroradiol J, vol. 26, no. 2, pp. 191–200
2. DeBaun, M.R. (2006), 'Etiology of strokes in children with sickle cell anemia', Ment Retard Dev Disabil Res Rev, vol. 12, no. 3, pp. 192–199
3. Heeger D. J. (2002), 'What does fMRI tell us about neuronal activity?', Nature Reviews Neuroscience, vol. 3, no. 2, pp. 142–151
4. Hoffmann O. (2000), 'Measurement of Cerebral Circulation Time by Contrast-Enhanced Doppler Sonography', Cerebrovascular Diseases, vol. 10, no. 2, pp. 142–146
5. Jenkinson M. (2011), 'FSL', Neuroimage, vol. 62, no. 2, pp. 782–790
6. Juttukonda M.R. (2017), 'Cerebral hemodynamics and pseudo-continuous arterial spin labeling considerations in adults with sickle cell anemia', NMR Biomed, vol. 30, no. 2, p. e3681
7. Juttukonda M.R. (2021), 'Reduced oxygen extraction efficiency in sickle cell anemia patients with evidence of cerebral capillary shunting', Journal of Cerebral Blood Flow & Metabolism, vol. 41, no. 3, p. 546
8. Tong Y. (2017), 'Perfusion information extracted from resting state functional magnetic resonance imaging', Journal of Cerebral Blood Flow and Metabolism, vol. 37, no. 2, pp. 564–576
9. Tong Y. (2019), 'The resting-state fMRI arterial signal predicts differential blood transit time through the brain', Journal of Cerebral Blood Flow and Metabolism, vol. 39, no. 6, pp. 1148–1160

Poster No 2609

White matter perfusion declines in aging are related to developmental trajectory, not fibre calibre

Tyler Robinson[1], Yutong Sun[1], Jordan Chad[1], Paul Chang[2], J. Jean Chen[3]

[1]Rotman Research Institute, Baycrest, Toronto, Ontario, [2]Rotman Reserach Institute, Baycrest, Toronto, Ontario, [3]Baycrest Health Sciences, Toronto, Ontario

Introduction: Our work recently uncovered tract-specific white-matter (WM) perfusion declines in aging, which may predate microstructural declines[7]. This study investigates the relationships between perfusion declines and WM development as well as physiology. Regions that develop first are often expected to deteriorate the last, i.e. "last-in-first-out"[5,8]. Alternatively, regions which develop most rapidly may also decline most rapidly in aging, or the "gains-predict-loss" model[8]. The validity of such theories remains uncertain, in part due to lack of clarity on the definition of developmental order[3,6,8]. Furthermore, it is informative to link perfusion to fibre metabolic need, which varies with fibre size(9). This study uses HCP-A data to elucidate the relationship amongst perfusion decline, fibre calibre and tract developmental order.

Methods: 535 data sets from healthy subjects (300 female, aged 36-100) were drawn from the HCP-A study (OMB Control# 0925-0667)[2], including diffusion-weighted MRI (93 directions at b=1500s/mm2 at 1.5mm isotropic resolution), and a multi-delay pseudo-continuous arterial spin labeling (pCASL) data set at 1.5mm3 voxel resolution. We corrected for eddy-current and susceptibility-related distortions via EDDY. FreeSurfer TRACULA (v 7.2.0)(10) was used to provide 10 bilateral tract segmentations in subject space. Cerebral blood flow (CBF) and arterial transit time (ATT) were assessed using FSL oxford_ ASL, and raw CBF and ATT values were normalized to the youngest 50 subjects to produce CBFperc, and ATTperc values. We defined 6 models to help explain perfusion age effects: Last-in-first-out models; (1) "Last-appearing-first-out" (LAFO): ordered by time of prenatal emergence[6] (2) "Last-myelinated-first-out" (LMFO): ordered by time of peak R1 ("myelination") at birth[3] Gain-predicts-loss models; (3) "Slowest-peak-first-out" (SPFO-MD): ordered by rate of MD change from adolescence to adult peak[8] (4) "Slowest-myelinated-first-out (SMFO): ordered by rate of R1 change from adolescence to adult peak[8] Physiological models: (5) "Axon-diameter-determined" (ADD): ordered by mean axon diameter at birth[4] (6) "Vascular-diameter-determined" (VDD): ordered by mean macrovascular density[1] The predictiveness of these models was assessed using multivariate regression in R (version 4.1.1), with sex as a covariate of no interest.

Results: Age-related declines in CBFperc and lengthening of ATT were identified in the majority of tracts. Both last-in-first-out models identified linear relationships between mean CBFperc/ATTperc and order of tract development (Fig. 1). In the LAFO model, tract order was negatively associated with both CBFperc and ATTperc. In the LMFO model, CBFperc associated positively with tract order while ATTperc associated negatively. The LAFO order was negatively associated with rates of age-related differences in both CBFperc and ATTperc. No interaction between tract-order and age-related CBFperc/ATTperc differences was observed in the LMFO model (Fig. 2). No contribution to CBF or ATT declines by tract order were detected in the gain-predicts-loss models (SPFO-MD, SMFO) or the physiological determinant models (ADD, VDD).

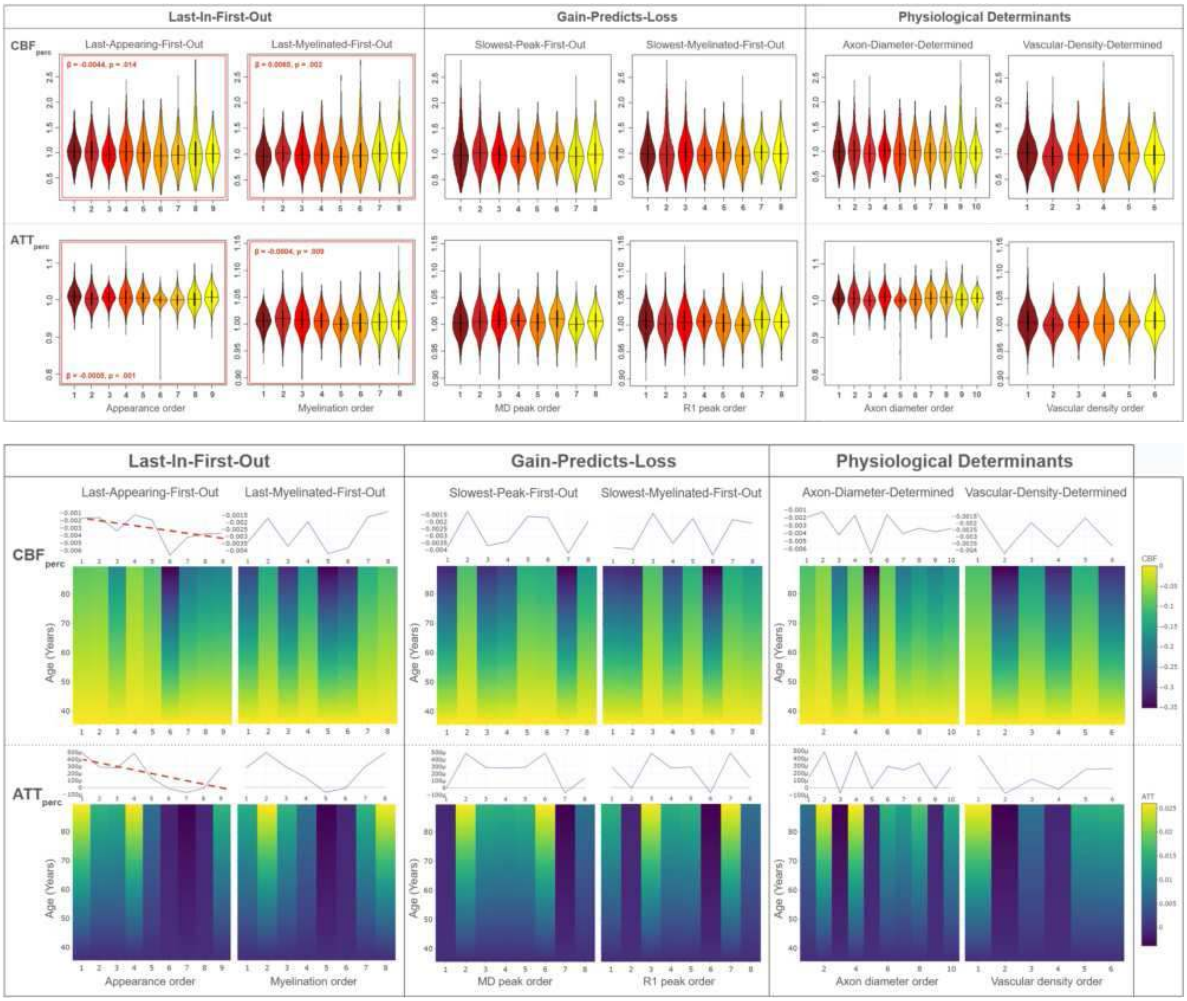

Conclusions: Our previous findings identified two main regimes of WM perfusion decline: namely reduced CBF with relatively preserved ATT, and prolonged ATT with relatively preserved CBF[7]. Our current findings suggest that later emerging tracts have both lower CBFperc and shorter ATTperc later in life. They also suggest that tracts last to fully myelinate have higher CBFperc and shorter ATTperc later in life. These include WM regions responsible for higher cognitive function, which may be preferentially perfused. However, in such regions, we also found evidence for faster decreases in CBFperc but preserved ATTperc in aging. These findings suggest that myelination order may determine the regime of perfusion decline aging, with distinctive functional consequences.

References

1. Bernier, M. (2023, June 03-08). Human cerebral white-matter vasculature imaged using the blood-pool contrast agent Ferumoxytol: bundle-specific vessels and vascular density [Conference presentation abstract]. Annual meeting of the International Society for Magnetic Resonance in Medicine, Toronto, ON, Canada. https://archive.ismrm.org/2020/0016.html
2. Bookheimer, S. Y. (2019). The Lifespan Human Connectome Project in Aging: An overview. NeuroImage, 185, 335–348.
3. Grotheer, M. (2022). White matter myelination during early infancy is linked to spatial gradients and myelin content at birth. Nature Communications, 13(1), 997.
4. Huang, S. Y. (2020). High-gradient diffusion MRI reveals distinct estimates of axon diameter index within different white matter tracts in the in vivo human brain. Brain Structure & Function, 225(4), 1277–1291.
5. Kiely, M. (2022). Insights into human cerebral white matter maturation and degeneration across the adult lifespan. NeuroImage, 247, 118727.
6. Ouyang, Y. (2021). Analysis of Age-Related White Matter Microstructures Based on Diffusion Tensor Imaging. Frontiers in Aging Neuroscience, 13, 664911.
7. Robinson, T. D. (2023). In search of a unifying theory of white matter aging: associations with age in perfusion detectable in advance of microstructure. In bioRxiv (p. 2023.06.30.547294). https://doi.org/10.1101/2023.06.30.547294
8. Slater, D. A. (2019). Evolution of white matter tract microstructure across the life span. Human Brain Mapping, 40(7), 2252–2268.
9. Stahon, K. E. (2016). Age-Related Changes in Axonal and Mitochondrial Ultrastructure and Function in White Matter. The Journal of Neuroscience: The Official Journal of the Society for Neuroscience, 36(39), 9990–10001.
10. Yendiki, A. (2011). Automated probabilistic reconstruction of white-matter pathways in health and disease using an atlas of the underlying anatomy. Frontiers in Neuroinformatics, 5, 23.

Poster No 2610

Predicting PETCO2 from RVT in Breath-Hold fMRI for Cerebrovascular Reactivity Mapping

Rebecca Clements[1], Kimberly Hemmerling[1], Elijah Huang[1], Max Wang[1], Molly Bright[1]

[1]*Northwestern University, Chicago, IL*

Introduction: Cerebrovascular reactivity (CVR), the response of blood vessels to a vasoactive stimulus, provides important information about cerebrovascular health[8,9]. Breath-hold tasks during fMRI provide a robust method for measuring CVR; typically, end-tidal CO2 (PETCO2) is measured and used to calculate CVR in standard units (%BOLD/mmHg). While PETCO2 allows for quantitative comparisons across subjects and sessions, it requires additional equipment and task compliance[10]. Respiration volume per time (RVT) is an alternative to PETCO2 that circumvents these requirements[2]; however, it is recorded in arbitrary units and only allows for relative CVR comparisons between brain regions of a single scan[10]. This work provides a more feasible method for quantitative CVR mapping by using machine learning to predict PETCO2 from RVT in breath-hold task data.

Methods: 185 physiological datasets were collected in 37 healthy adults; each consisted of expired CO2 pressure and chest position traces simultaneously recorded via nasal cannula, gas analyzer, and respiration belt at 100 Hz during a 5–7-minute repeated breath-hold task: 24-s paced breathing, 10-20-s breath-hold, 2-s exhale, and 6-s recovery. End-tidal CO2 peaks and belt trace minima/maxima were identified using a peak detection algorithm, manually verified, and used to calculate PETCO2 and RVT[2], which were downsampled to 10 Hz and convolved with the HRF and RRF, respectively[3,4]. Delay between PETCO2 and RVT was corrected by temporally shifting the PETCO2 trace by the delay with maximum cross-correlation with RVT. 31 datasets with RVT and PETCO2 cross-correlation<0.5 were excluded. Imitating the methods of Agrawal et al.[1], a 1D fully convolutional network was created to predict demeaned PETCO2 from RVT. For comparison, a model was also created to predict standardized PETCO2 from RVT (note, this model would only allow for CVR mapping in relative units). 4 different architectures with 1 (FCN-1L), 2 (FCN-2L), 4 (FCN-4L), and 6 (FCN-6L) convolutional layers were tested. For each model, training was executed using 5-fold cross validation with a weighted mean squared error (MSE) loss function, Adam optimizer, 15 epochs, and a learning rate of 0.01[1]. Model performance was assessed on the test set (20% of the dataset), and the model with the lowest test set mean absolute error was used for the below analysis. For 6 of the test set subjects, fMRI data was acquired with the physiological data (for detailed methods, see[5]). Using both the true and predicted demeaned PETCO2 regressors, CVR was mapped using phys2cvr[6,7]. Bland-Altman analysis was performed to assess agreement between average gray matter (GM) CVR values calculated with true and predicted demeaned PETCO2 regressors.

Results: The highest r value of the demeaned PETCO2 prediction models in breath-hold data was 0.680 (FCN-6L), which out-performs a previous study that predicted standardized PETCO2 from RVT in resting-state data with r=0.512[1]. Breath-holds evoke larger physiological fluctuations and thus may allow for more robust prediction of PETCO2. The demeaned and standardized PETCO2 prediction models had comparable performance (Fig.1); FCN-2L and FCN-6L produced the lowest MAE for the demeaned and standardized PETCO2 prediction models, respectively, and were used for all subsequent analysis. For one example subject, true and predicted PETCO2 regressors and the corresponding CVR maps are shown in Fig.2A/B. Across all 6 subjects, the CVR maps in standard units calculated using the demeaned predicted and true PETCO2 traces had an average GM CVR spatial correlation of 0.95±0.02. Bland-Altman analysis indicated no significant proportional bias in average GM CVR estimation(Fig.2C).

Conclusions: Quantitative PETCO2 can be predicted from RVT in breath-hold data and used to map CVR. Future work will assess whether a trial-by-trial version of our approach can mitigate the effects of poor task compliance and missing PETCO2 data on CVR estimation.

	Demeaned $PETCO_2$ Prediction Models				Standardized $PETCO_2$ Prediction Models			
	FCN-1L	FCN-2L	FCN-4L	FCN-6L	FCN-1L	FCN-2L	FCN-4L	FCN-6L
r	0.637 ± 0.297	0.677 ± 0.310	0.677 ± 0.306	0.680 ± 0.309	0.631 ± 0.312	0.664 ± 0.323	0.680 ± 0.315	0.689 ± 0.306
MAE (mmHg)	2.70 ± 0.664	2.13 ± 0.867	2.20 ± 0.896	2.14 ± 0.888	0.639 ± 0.253	0.568 ± 0.252	0.556 ± 0.261	0.548 ± 0.255
MAPE (%)	1.72 ± 0.521	3.41 ± 2.29	3.65 ± 2.72	3.56 ± 2.62	3.89 ± 1.44	3.44 ± 1.47	3.38 ± 1.45	3.09 ± 1.44
MSE ($mmHg^2$)	11.1 ± 5.29	8.32 ± 6.87	8.79 ± 7.38	8.45 ± 7.19	0.700 ± 0.584	0.609 ± 0.568	0.596 ± 0.579	0.581 ± 0.560

Figure 1. Performance of the quantitative and standardized $PETCO_2$ prediction models

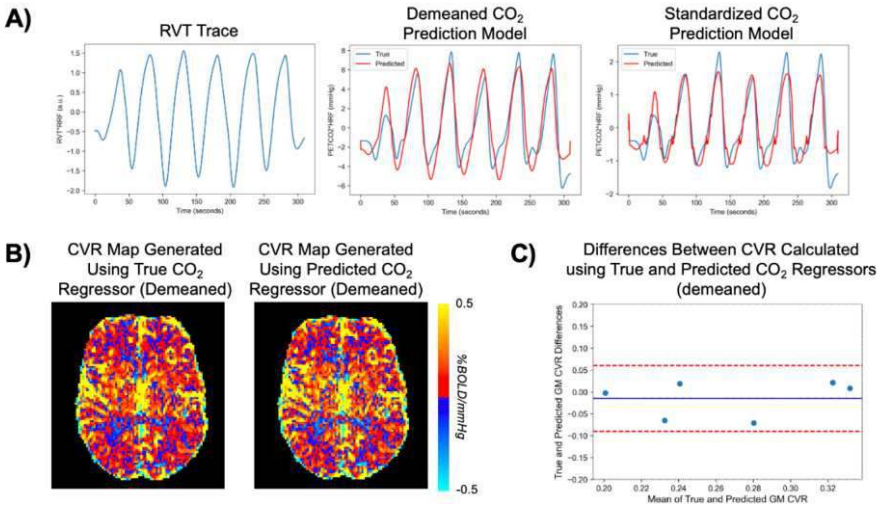

Figure 2. Sections A and B show results for one example subject. A shows the RVT trace and true and predicted $PETCO_2$ traces for the demeaned prediction model (FCN-2L) and standardized prediction model (FCN-6L). B shows CVR maps generated using the true and predicted (FCN-6L) demeaned $PETCO_2$ traces. C shows the results of the Bland-Altman analysis for 6 subjects, performed to assess differences between average GM CVR calculated using true and predicted (FCN-6L) demeaned $PETCO_2$ traces. The upper and lower limits of 95% agreement for GM CVR were 0.06 and -0.09 %BOLD/mmHg.

References

1. Agrawal, V. (2023), 'Generating dynamic carbon-dioxide traces from respiration-belt recordings: Feasibility using neural networks and applications in functional magnetic resonance imaging', Frontiers in Neuroimaging, vol. 2.
2. Birn, R. (2006), 'Separating respiratory-variation-related fluctuations from neuronal-activity-related fluctuations in fMRI', Neuroimage, vol. 31, no. 4, pp. 1536-1548.
3. Birn, R. (2008), 'The respiration response function: the temporal dynamics of fMRI signal fluctuations related to changes in respiration', vol. 40, no. 2, pp. 644-654.
4. Friston, K. (1998), 'Event-related fMRI: Characterizing differential responses', Neuroimage, vol. 7, no. 1, pp. 30-40.
5. Hoggarth, M. (2020), 'Impact of Acute Intermittent Hypoxia on BOLD fMRI measures of cerebrovascular reactivity', ISMRM Annual Meeting.
6. Moia, S. (2023), 'physiopy/phys2cvr: A tool to compute Cerebrovascular Reactivity maps and associated lag maps', Zenodo.
7. Moia, S. (2020), 'Voxelwise optimization of hemodynamic lags to improve regional CVR estimates in breath-hold fMRI', IEEE, pp. 1489-1492.
8. Papassin, J. (2021), 'Impaired cerebrovascular reactivity is associated with recurrent stroke in patients with severe intracranial arterial stenosis: A CO2 BOLD fMRI Study', Journal of Neuroradiology, vol. 48.5, no. 5, pp. 339-345.
9. Reinhard, M. (2014), 'Cerebrovascular reactivity predicts stroke in high-grade carotid artery disease', Neurology, vol. 83, no. 16, pp. 1424-1431.
10. Zvolanek, K. (2023), 'Comparing end-tidal CO2, respiration volume per time (RVT), and average gray matter signal for mapping cerebrovascular reactivity amplitude and delay with breath-hold task BOLD fMRI', Neuroimage, vol. 272, no. 120038.

Poster No 2611

The Effect of Stimulus Timing and Hemodynamic Delay on Measured BOLD fMRI Cerebrovascular Reactivity

Rebecca Clements[1], Molly Bright[1]

[1]Northwestern University, Chicago, IL

Introduction: Cerebrovascular reactivity (CVR), the response of blood vessels to a vasoactive stimulus, is an important indicator of cerebrovascular health. CVR is often measured using BOLD fMRI combined with breath-holds (BHs) or CO2 inhalation. During the scan, end-tidal CO2 (PETCO2) is measured and used as a regressor in a general linear model to calculate CVR in units of %BOLD/mmHg. However, due to measurement and physiological delays, there is a spatially varying offset in timing between the recorded PETCO2 and the BOLD response[6]. Despite several methods to account for this offset and improve CVR estimations[1,7,9], many existing CVR studies do not correct for delay[8,10]. The validity of these studies is not well understood, particularly in patient groups with prolonged delays. This work aims to use simulated and real fMRI data to understand how stimulus timing and hemodynamic delay affect CVR accuracy when delay is not corrected.

Methods: BOLD fMRI data were simulated for 10, 15, and 20s repeated BHs alternating with 30s rest periods using a time-scaled ramp design convolved with the canonical HRF (Fig1A). BOLD fMRI data were also simulated for 20, 40, 60, and

80s of hypercapnia induced using gas inhalation, alternating with similar length rest periods, by convolving a block design with the HRF (Fig1B). Simulated timeseries, which were approximately 8.5 minutes total (TR=1s), were shifted from 0-28s in 2s increments. Missing values were replaced by the mean of the simulated dataset. CVR was calculated in each simulated dataset using a general linear model, with unshifted data as the independent variable (representing the PETCO2 regressor) and shifted data as the dependent variable (representing the fMRI time series), both of which were downsampled to a 2s TR to better represent a typical fMRI TR. In these "ideal" simulations, CVR should be 1 (arbitrary units), as variance in the simulated data is fully attributed to simulated CO2 changes without scaling. Percent error of the CVR estimate was calculated for each simulated CO2 protocol and shift. Real 18s repeated BH fMRI data for 15 healthy adults (25±5y, 5M) were used to better understand how delay affects CVR accuracy in noisier data (see[4] for methods). Both uncorrected and delay corrected CVR maps were calculated for each scan using phys2cvr[6,7]. Using FSL's Harvard-Oxford cortical atlas in native space, average uncorrected CVR, delay-corrected CVR, delay, and percent error of uncorrected CVR were calculated within gray matter in each cortical parcel(Fig2A). 15s repeated BH fMRI data were also acquired in a 31yo male with unilateral Moyamoya disease (occluded right MCA; see[2]). Uncorrected and delay-corrected CVR maps, and the percent error of the CVR calculation for each cortical parcel (separated by L and R hemispheres), were calculated.

Results: For all simulations, as the shift (delay) increased, the CVR percent error also increased (Fig1C). As the length of the hypercapnia period decreased, CVR percent error increased at a faster rate. This suggests that longer periods of hypercapnia mitigate, but do not fully account for, the effects of delay on CVR accuracy when delay is not corrected. Features of real data, such as task-correlated motion, could further increase CVR error. In real fMRI data, as the absolute value of delay increased, the number of parcels with CVR percent error>20% increased substantially (Fig2B). Similarly, in the participant with Moyamoya disease, the parcels in the affected right hemisphere had greater delay values and CVR errors (Fig2C). This supports the simulation results, suggesting that as hemodynamic delay increases, the importance of CVR delay correction also increases.

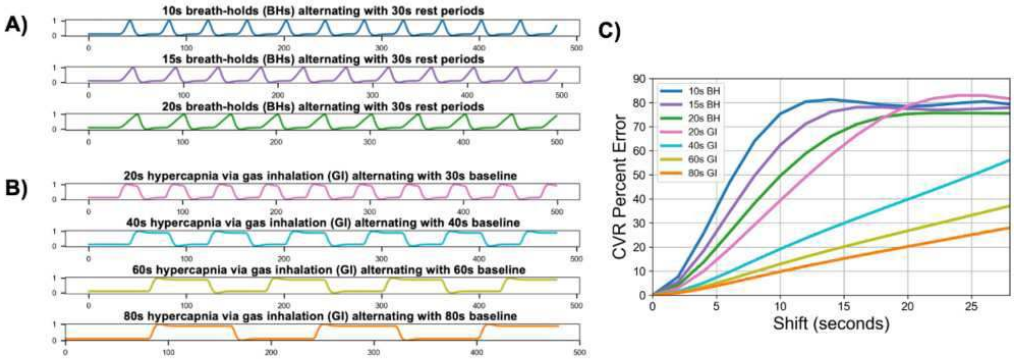

Figure 1. A shows the simulated fMRI data for 10, 15 and 20 second breath-holds without any shift applied, and B shows the simulated data for 20-, 40-, 60-, and 80-seconds gas hypercapnia via gas inhalation (GI) without any shift applied. C shows the effect of the applied shift on CVR percent error for each simulated dataset.

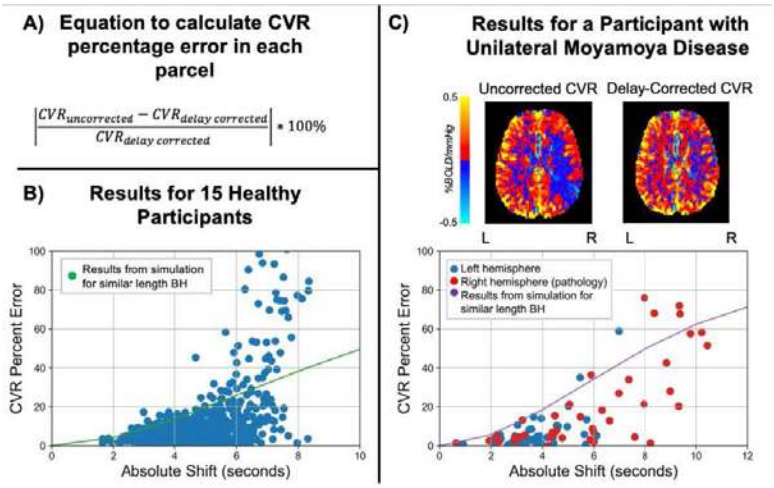

Figure 2. A shows the equation for calculating CVR percent error, which was used in each cortical parcel for each participant. B shows the CVR percent error and associated absolute delay for each cortical parcel in each healthy subject. For reference, the simulation results for a similar length breath-hold that was done for the healthy participants (20s) is also plotted in green. C shows the uncorrected and delay corrected CVR maps for a participant with unilateral Moyamoya disease (occluded right MCA), as well as the CVR percent error and associated absolute delay for each cortical parcel in each hemisphere. The simulation results for a similar length BH that was done by the Moyamoya participant (15s) is plotted in purple for comparison.

Conclusions: Delay correction is essential for accurate CVR results, even when long periods of hypercapnia are induced. Measuring hemodynamic delay not only leads to more accurate CVR measurements, but could also provide a complementary biomarker for cerebrovascular diseases[3,5].

References

1. Bhogal, A. (2021), 'abhogal-lab/seeVR: Current version', Zenodo.
2. Clements, R. (2023), 'Mapping the vascular default mode network using a breath-hold fMRI task', OHBM Annual Meeting.
3. Donahue, M. (2016), 'Time delay processing of hypercapnic fMRI allows quantitative parameterization of cerebrovascular reactivity and blood flow delays', Journal of Cerebral Blood Flow and Metabolism, vol 36, no. 10, pp. 1767-1779.
4. Hoggarth, M. (2020), 'Impact of Acute Intermittent Hypoxia on BOLD fMRI measures of cerebrovascular reactivity', ISMRM Annual Meeting.
5. Khalil, A. (2018), 'Non-invasive monitoring of longitudinal changes in cerebral hemodynamics in acute ischemic stroke using BOLD signal delay', Journal of Cerebral Blood Flow and Metabolism, vol 40, no, 1, pp. 23-34.
6. Moia, S. (2020), 'Voxelwise optimization of hemodynamic lags to improve regional CVR estimates in breath-hold fMRI', IEEE, pp. 1489-1492.
7. Moia, S. (2023), 'physiopy/phys2cvr: A tool to compute Cerebrovascular Reactivity maps and associated lag maps', Zenodo.
8. Papassin, J. (2021), 'Impaired cerebrovascular reactivity is associated with recurrent stroke in patients with severe intracranial arterial stenosis: A CO2 BOLD fMRI study', Journal of Neuroradiology, vol 48, no. 5, pp. 339-345.
9. 'Quantiphyse', http://www.quantiphyse.org/.
10. Sobcyzk, O. (2020), 'Cerebrovascular Reactivity Assays Collateral Function in Carotid Stenosis', Frontiers in Physiology, vol 11, p. 1031.

Poster No 2612

Bedside Neuromonitoring in Pediatric ECMO Patients Using High-Density Diffuse Optical Tomography

Sophia McMorrow[1], Tessa George[1], Chloe Sobolewski[1], Dalin Yang[1], Sung Min Park[1], Kelsey King[2], Ahmed Said[1], Adam Eggebrecht[1]

[1]Washington University School of Medicine in St. Louis, St. Louis, MO, [2]Roosevelt University, St. Louis, MO

Introduction: Extracorporeal membrane oxygenation (ECMO) is a form of life support for patients with severe, reversible respiratory or cardiac failure. ECMO patients are susceptible to neurological complications including seizures, hemorrhage, and infarction, resulting in an increased risk of neurodevelopmental, behavioral, and functional deficits[1,2]. Conventional neuroimaging techniques suffer limited sensitivity to detect early signs of brain injury or pose additional risks such as transportation to imaging facilities[3]. Thus, there is a clear and present need for continuous bedside neuromonitoring with high sensitivity and specificity. Herein, we establish the feasibility of high-density diffuse optical tomography (HD-DOT) for continuous neuromonitoring in pediatric ECMO patients with image quality comparable to functional magnetic resonance imaging[4]. Specifically, we assess the feasibility of HD-DOT for bedside assessment of high bandwidth cerebral oxygenation and functional connectivity.

Methods: We used an HD-DOT system optimized for pediatric patients with 80 dual-wavelength sources (685nm & 830nm) and 78 avalanche-photodiode detectors that together support over 1200 usable measurements per wavelength. Data were collected from four patients (age 2 weeks, 9 months, 28 months, and 16 years), with multi-day longitudinal data in three patients. Data collection periods were 1-3 hours. Raw data quality metrics, including mean light levels and temporal variance in HD-DOT measurements, were analyzed using NeuroDOT data processing pipelines5 to identify high-quality[4,6], low-motion[7] data for further analysis. Patient-specific facial landmarks and an age-appropriate anatomical atlas were used to model light propagation and depth sensitivity of the HD-DOT array (Fig. 1A-1D). Unfiltered 10 Hz HD-DOT measurements were converted to relative hemoglobin concentrations and aligned with 0.2 Hz physiology measurements for analysis of high bandwidth cerebral oxygenation (Fig. 1). The HD-DOT array field of view was intersected with the Gordon parcellation[8], and HD-DOT data was bandpass filtered at low bandwidths (0.009-0.08 Hz) for analysis of low frequency temporal correlation (functional connectivity; Fig. 2).

Results: We present example results from one neonatal patient on veno-arterial ECMO that included a clamp trial. Clamp trials are pre-planned periods of temporary separation from ECMO support to test the patient's ability to come off ECMO. HD-DOT measurements sampling superficial tissue reveal notable changes in concentrations of deoxygenated (HbR) and oxygenated hemoglobin (HbO) and their difference (HbD) in response to clamp trial events (Fig. 1E). Concurrently recorded physiology data changed similarly (Fig. 1F). After superficial signal regression, relative hemoglobin concentrations in cerebral tissue reveal temporal variation distinct from the response in superficial signals in response to clamp trial events. (Fig. 1G). Analysis of low frequency temporal correlation relative to parcels in the motor and visual cortex reveal consistent bilateral correlation during baseline periods and disrupted correlation during the clamp trial (Fig. 2E). These changes were quantified via test-

retest analyses relative to an initial baseline period, which reveal consistent spatial patterns during quiescence and strong disruptions during the clamp trial (Fig. 2F).

Conclusions: We establish feasibility of HD-DOT for bedside neuromonitoring for pediatric ECMO patients, a valuable step towards understanding brain health during ECMO support. Future analyses will investigate spatial-temporal variation in cortical hemoglobin changes and the relationship between cerebral hemodynamics and physiological parameters and outcomes. Overall, these investigations hold potential for illuminating associations between brain health in pediatric patients on ECMO and outcomes.

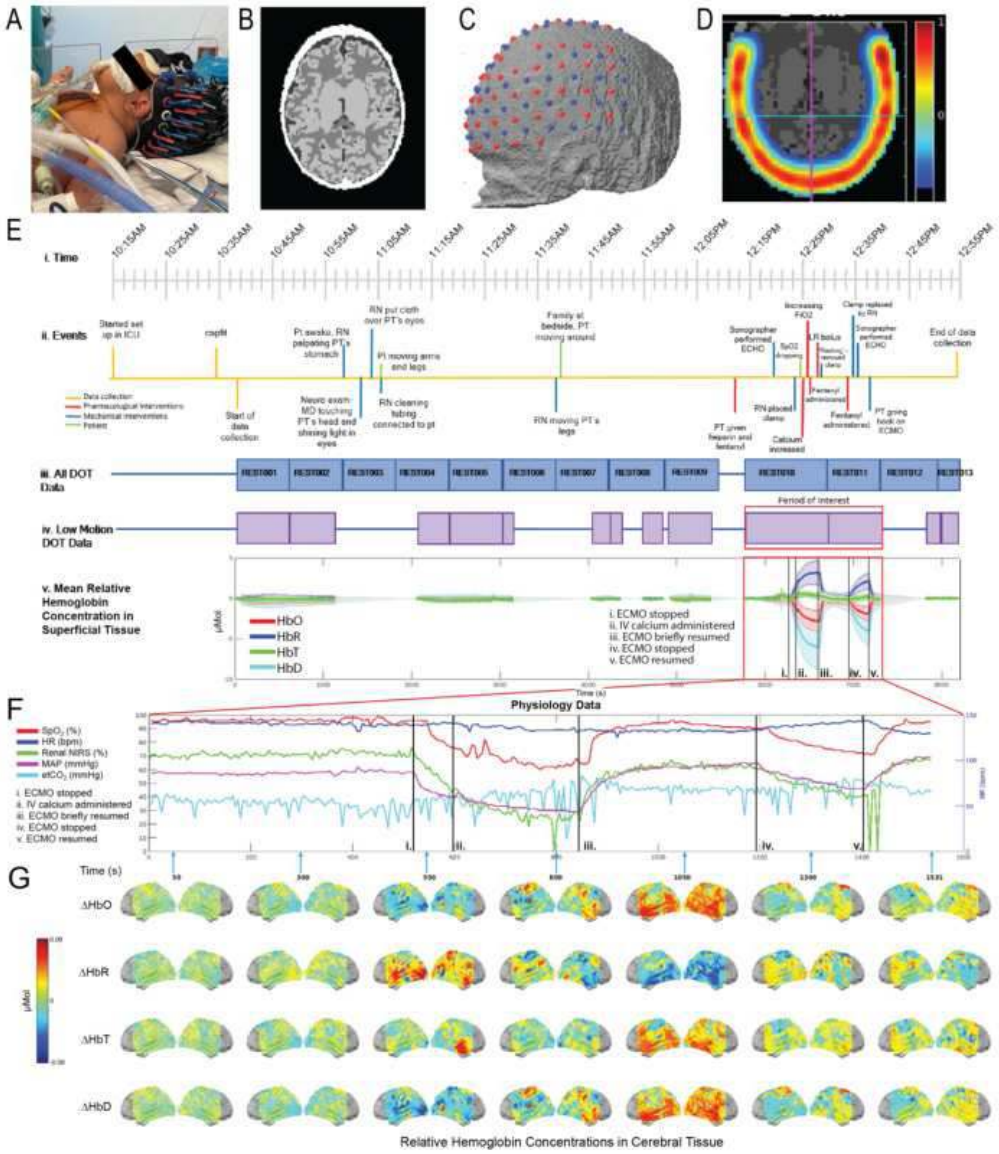

Figure 1 | Results for one sample patient. A Neonatal patient supported on ECMO wearing HD-DOT cap. **B** Age-appropriate atlas used to model light propagation. **C** Head model with the HD-DOT optode array. **D** Sensitivity matrix representing depth sensitivity of HD-DOT array. **E** Timelines of example data collection during ECMO course, including **i)** time of day; **ii)** relevant events in clinical care and data collection; **iii)** Boxes representing individual runs of HD-DOT data; **iv)** low motion HD-DOT data retained for further analysis. Red box: period of interest including a clamp trial; and **v)** mean HD-DOT measurements sampling superficial tissue converted to relative concentrations of deoxygenated hemoglobin (HbR), oxygenated hemoglobin (HbO), total hemoglobin (HbT), and hemoglobin difference (HbD) using the modified Beer-Lambert Law and a differential path length factor of 6. These measurements show notable and immediate changes in response to events during the clamp trial, represented by vertical black lines. When ECMO flow stops, HbR increases, while HbO and HbD decrease. Hemoglobin concentrations return to baseline levels when ECMO resumes. **F** Concurrently recorded 0.2 Hz phsyiology measurements during the period of interest reveal that oxygen saturation (SpO_2), mean arterial pressure (MAP), and renal near-infrared spectroscopy (NIRS) decrease when ECMO stops, and return to baseline when ECMO resumes, mirroring changes in superficial hemoglobin concentrations. **G** Relative concentrations of HbO, HbR, HbT, and HbD in cerebral tissue show temporal variation in response to clamp trial events. Blue arrows align timepoints with physiology data.

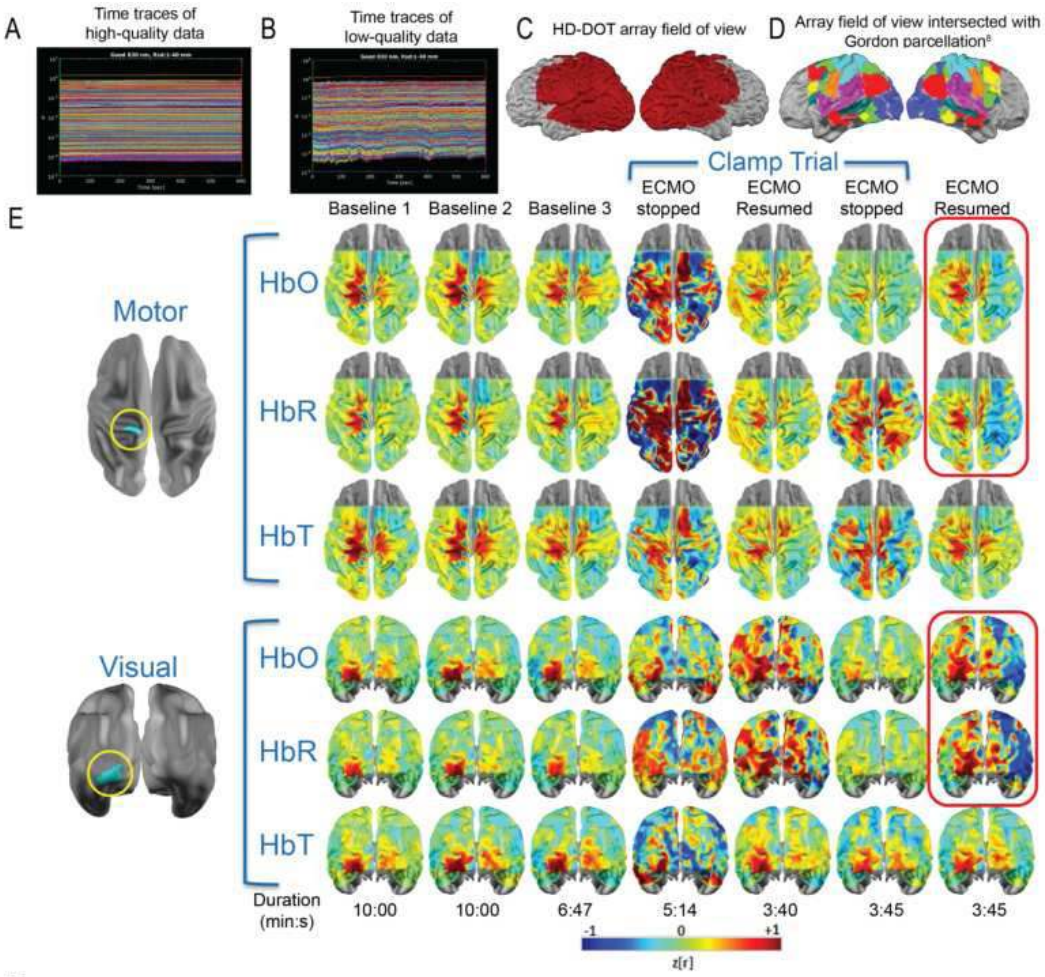

Figure 2 | Longitudinal mapping of functional connectivity. A Example time traces of high quality HD-DOT data indicating stable and robust optode coupling. **B** Example time traces of low-quality HD-DOT data indicative of movement and disruptions in optode coupling. **C** Lateral view of the HD-DOT array field of view. **D** HD-DOT array field of view overlapped with the Gordon parcellation[8]. **E** Fisher z transformed Pearson correlation maps relative to parcels in the motor and visual cortex for HbO, HbR, and HbT. Maps of low frequency temporal correlation reveal consistent spatial patterns of bilateral correlation during baseline periods and disrupted correlation in response to stopping ECMO flow during the clamp trial. Red boxes: Maps reveal hemispheric wide disruption for HbO and HbR when ECMO is resumed. **F** Changes in spatial patterns were quantified via test-retest analyses relative to an initial baseline period (baseline 1), which reveal consistent patterns of spatial correlation during quiescence with strong disruption during the clamp trial.

References

1. Eggebrecht, A. T. et al. (2014). "Mapping distributed brain function and networks with diffuse optical tomography." Nature Photonics, vol. 8, no. 6 pp. 448-454.
2. Ferradal, S. L. et al. (2016). "Functional Imaging of the Developing Brain at the Bedside Using Diffuse Optical Tomography." Cerebral Cortex vol. 26, no. 4, pp. 1558-1568.
3. Gordon, E. M. et al. (2016). "Generation and Evaluation of a Cortical Area Parcellation from Resting-State Correlations." Cerebral Cortex vol. 26, no. 1, pp. 288-303.
4. https://www.nitrc.org/projects/neurodot
5. Lin, N. et al. (2018). "Neuromonitoring in the neonatal ECMO patient." Seminars in Perinatology 42(2): 111-121.
6. Sadhwani, A. et al. (2019). "Early Neurodevelopmental Outcomes in Children Supported with ECMO for Cardiac Indications." Pediatric Cardiology vol. 40, no. 5, pp. 1072-1083.
7. Said, A. S. et al. (2020). "Neurological Monitoring and Complications of Pediatric Extracorporeal Membrane Oxygenation Support." Pediatric Neurology vol. 108, 31-39.
8. Sherafati, A. et al. (2020). "Global motion detection and censoring in high-density diffuse optical tomography." Hum Brain Mapping vol. 41, no, 14, pp. 4093-4112.

Poster No 2613

Respiration recording for fMRI: breathing belt versus spine coil sensor

Marilena Wilding[1], Anja Ischebeck[1], Natalia Zaretskaya[1]

[1]*Karl-Franzens-University, Graz, Styria*

Introduction: Physiological signals such as pulse and respiration contribute strongly to non-neuronal signal change of the blood oxygenation level-dependent (BOLD) contrast in fMRI. This has been observed not only during task-based but also during resting-state fMRI measurements. Both approaches are susceptible to effects of cardiac and respiratory signals, either through the introduction of spurious correlations or through possible systemic confounds due to time-locking of noise to the stimulus/task, respectively (Birn et al., 2009; Caballero-Gaudes & Reynolds, 2017; Murphy et al., 2013). Over the last decades, a variety of techniques evolved, aiming at detecting and removing physiological artifacts in fMRI time series. These follow either a data-driven or a reference-based approach, i.e., they rely on externally recorded physiological data. To record cardiac and respiratory signals, typically pulse oximetry or electrocardiography (ECG) and a respiration belt are used, respectively. New technologies allow to capture respiratory signal directly with a sensor placed within the spine coil in the patient table, eliminating the need of a respiration belt. However, little is known about the effectiveness of these new technologies and how they compare to the standard respiration belt recording.

Methods: In the current study, we evaluated these two different respiratory activity recording devices in their effectiveness for eliminating physiological noise in task-based and resting-state fMRI. We recorded respiration using a breathing belt that is placed around a person's diaphragm and detects changes in abdominal circumference due to inhalation and expiration (belt). Simultaneously, respiratory activity was captured by a body coil sensor below the spine, embedded in the scanner table (spine), which generates a local magnetic field that varies with moving body tissue during breathing (Runge et al., 2019). To investigate the performance of physiological noise correction based on either belt or spine in both data types, we recorded physiological signals with both devices during a perception task (n= 24; 12 female, mean age= 23.61) as well as during a resting-state session (n= 56; 35 female, mean age= 24.22). Physiological signals were processed using the RETROICOR (retrospective image correction) algorithm (Glover et al., 2000), where the periodic effects of pulsation- and respiration-related motion are modelled as a Fourier expansion of the cardiac and respiratory phase, using the PhysIO toolbox (Kasper et al., 2017). This ultimately resulted in 18 physiological regressors per device, which were then added to the different analyses. For the resting-state data, we compared ROI-to-ROI functional connectivity (FC) between denoised signals derived with the two devices. For the task data, we examined potential differences in stimulus-related activity between the denoised time series. In addition, the remaining noise after the application of the belt-derived or spine-derived physiological noise correction was compared in both datasets by analyzing the standard deviation (SD) of the general linear model (GLM) residuals.

Results: We observed no significant differences in ROI-to-ROI resting-state FC or stimulus-related activity between functional data denoised with either belt or spine regressors. However, we found that signal corrected with belt-derived regressors showed more residual noise than spine-corrected signal in task-induced activity (Fig. 1). Apart from this, belt recording contained artifacts like belt detachment and signal clipping, which were not present in the spine recording. Consequently, some subjects had to be removed due to technical issues during the belt recording.

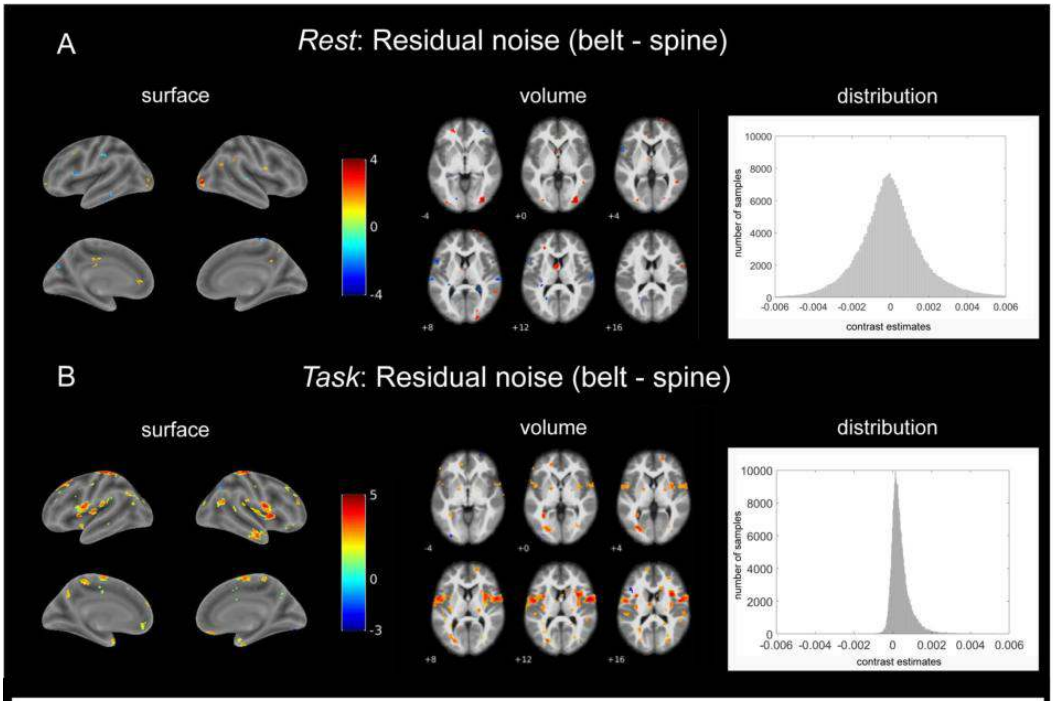

Figure 1. Comparison of residual noise in *belt*-denoised and *spine*-denoised data in the resting-state dataset (A) and in the task-based dataset (B). We observed higher noise values in the *belt*-denoised data, but only in the task-dataset. Insets on the right show the distribution of contrast estimates for the contrast "belt vs. spine" within the brain mask for each dataset, with residual SD as dependent variable.

Conclusions: Our results suggest that body coil sensors are at least as well suited for physiological noise removal as the established breathing belt. It additionally offers an advantage in terms of signal quality, artifact proneness and acquisition comfort.

References

1. Birn, R.M., 2012. The role of physiological noise in resting-state functional connectivity. NeuroImage 62, 864–870. https://doi.org/10.1016/j.neuroimage.2012.01.016
2. Birn, R.M., 2009. fMRI in the presence of task-correlated breathing variations. NeuroImage 47, 1092–1104. https://doi.org/10.1016/j.neuroimage.2009.05.030
3. Caballero-Gaudes, C., 2017. Methods for cleaning the BOLD fMRI signal. NeuroImage 154, 128–149. https://doi.org/10.1016/j.neuroimage.2016.12.018
4. Glover, G.H., 2000. Image-based method for retrospective correction of physiological motion effects in fMRI: RETROICOR. Magn. Reson. Med. 44, 162–167. https://doi.org/10.1002/1522-2594(200007)44:1<162::AID-MRM23>3.0.CO;2-E
5. Kasper, L., 2017. The PhysIO Toolbox for Modeling Physiological Noise in fMRI Data. J. Neurosci. Methods 276, 56–72. https://doi.org/10.1016/j.jneumeth.2016.10.019
6. Murphy, K., 2013. Resting-state FMRI confounds and cleanup. NeuroImage 349–359. https://doi.org/doi:10.1016/j.neuroimage.2013.04.001
7. Runge, V.M., 2019. Motion in Magnetic Resonance: New Paradigms for Improved Clinical Diagnosis. Invest. Radiol. 54, 383–395. https://doi.org/10.1097/RLI.0000000000000566

Poster No 2614

Mapping Between fMRI and Electrophysiological Networks Encoding Depressive Symptoms

John Alvarez[1], Niki Sabetfakhri[1], Joline Fan[1], Natalya Slepneva[1], Julian Motzkin[1], Melanie Morrison[1], Leo Sugrue[1], Kristin Sellers[1], Edward Chang[1], Andrew Krystal[1], A Moses Lee[1]

[1]University of California, San Francisco, San Francisco, CA

Introduction: Multiple prior imaging studies have implicated a role for network abnormalities in depression. Non-invasive methods like resting-state functional magnetic resonance imaging (rs-fMRI) are able to comprehensively characterize the spatial organization of functional connectivity (FC) networks while invasive intracranial electroencephalography (iEEG) can characterize the dynamics of networks with unparalleled temporal resolution across varying time scales. Here, we leverage the complementary spatiotemporal strengths of these modalities, which provide a unique opportunity to investigate the electrophysiological basis of canonical fMRI networks while characterizing their relationship to depressive symptoms.

Methods: Two participants with severe treatment-resistant depression underwent a brain mapping protocol, involving extensive fMRI followed by 10-day iEEG monitoring to identify personalized targets for therapeutic deep brain stimulation. iEEG leads recorded from bilateral contacts in the orbitofrontal cortex, subgenual cingulate, ventral striatum, hippocampus, and amygdala (Figure 1A). iEEG data was preprocessed and segmented into 5-minute recordings sessions corresponding with subjects' symptom self-reports (Figure 1B-C). We computed mean iEEG-FC for each recording session across canonical frequency bands by calculating mean phase-locking values (PLV) and band-limited power (BLP) correlations between electrode pairs (Figure 1B-C). rs-fMRI data was preprocessed using fMRIprep. We then used spherical regions of interest derived from electrode locations to calculate fMRI-FC (Figure 1D). Pearson correlation was calculated between fMRI-FC and iEEG-FC. We then trained a support vector machine (SVM) model on parcellated networks' cortical and subcortical FC patterns to predict network affiliations of iEEG electrodes (Figure 1E). We quantified correspondence between spatial organization of iEEG and fMRI networks using mutual information analysis and permutation testing. To characterize iEEG network dynamics, we calculated temporal correlations between z-scored intranetwork electrode pairs and determined if networks exhibited significantly correlated dynamics based upon permutation testing. Pearson correlations were calculated between self-reported depression scores and iEEG network FC. We then ran permutation tests to identify networks across frequency bands that significantly correlated with depressive symptoms.

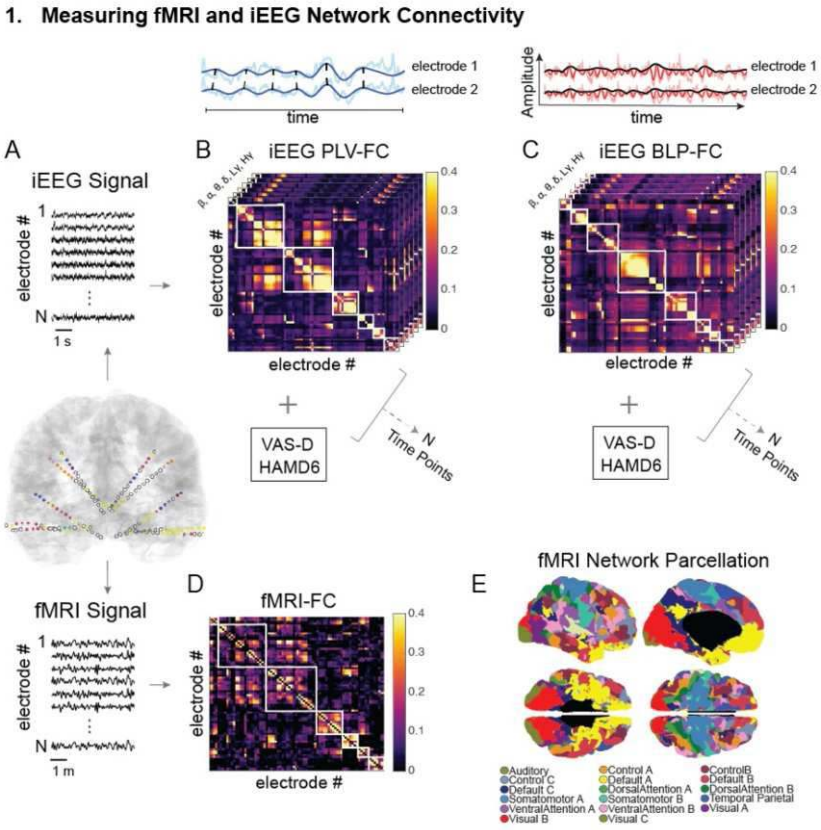

Figure 1: A) TRD subjects implanted with ten iEEG electrodes. Schematic representation of iEEG and fMRI signals. B) iEEG PLV-FC (blue) and C) iEEG BLP-FC (red) calculated for each 5-min iEEG recording segment, corresponding with subjects' symptom self-report times over a 10-day recording period. D) fMRI-FC matrix constructed using 6mm ROIs derived from electrode locations. E) Whole-brain fMRI-FC networks acquired using personalized network parcellations.

Results: We demonstrate that there is a significant spatial correspondence between iEEG functional connectivity (FC) and fMRI BOLD-FC corresponding regions-of-interest near the electrodes. These spatial correlations between BOLD-FC and iEEG phase-locking value (PLV) and band-limited power (BLP) were observed across frequency bands after correcting for distance ($p<.0001$, permutation test). We then demonstrate that electrophysiological networks share a similar topological organization with each individual's canonical fMRI networks based upon a mutual information metric ($p<.001$, permutation test). These electrophysiological networks have correlated intranetwork dynamics within specific frequency bands. In turn, fluctuations in the intranetwork FC within subcomponents of the default mode network (DMN) correlated with depression (VAS-D/HAMD6) over the course of days within the two subjects ($p<.05$, permutation test).

Conclusions: Together, these results support a model in which synchronous, correlated electrophysiological activity gives rise to the spontaneous spatial fluctuations in BOLD characterizing canonical fMRI networks. Further, these results suggest that the dynamics of DMN subnetworks encode variation in depressive symptoms over time.

References
1. Esteban, O. (2018) 'FMRIPrep: A robust preprocessing pipeline for functional MRI', Nature Methods, 16(1), pp. 111–116.
2. Kong, R. (2019). 'Spatial Topography of Individual-Specific Cortical Networks Predicts Human Cognition, Personality, and Emotion.' Cerebral Cortex, 29(6), 2533–2551.
3. Scangos, K.W. (2021) 'Closed-loop neuromodulation in an individual with treatment-resistant depression', Nature Medicine, 27(10), pp. 1696–1700.
4. Schaefer, A. (2017) 'Local-global parcellation of the human cerebral cortex from intrinsic functional connectivity MRI', Cerebral Cortex, 28(9), pp. 3095–3114.
5. Yeo, B.T. (2011) 'The organization of the human cerebral cortex estimated by intrinsic functional connectivity', Journal of Neurophysiology, 106(3), pp. 1125–1165.

Poster No 2615

Filler word-related high-gamma modulations in the left inferior frontal gyrus

Ayame Yamagishi[1], Yu Kitazawa[2,3], Riri Kimura[1], Risa Hikino[1], Hiroshi Uda[3,4], Naoto Kuroda[3,5], Shin-ichiro Osawa[5,6], Keiya Iijima[7], Kyoko Suzuki[8], Nobukazu Nakasato[5], Masaki Iwasaki[7], Eishi Asano[3,9]

[1]Department of Medicine, Yokohama City University, Yokohama, Japan, [2]Department of Neurology and Stroke Medicine, Yokohama City University, Yokohama, Japan, [3]Department of Pediatrics, Children's Hospital of Michigan, Detroit Medical Center, Wayne State University, Detroit, MI, [4]Department of Neurosurgery, Osaka Metropolitan University Graduate School of Medicine, Osaka, Japan, [5]Department of Epileptology, Tohoku University Graduate School of Medicine, Sendai, Japan, [6]Department of Neurosurgery, Tohoku University Graduate School of Medicine, Sendai, Japan, [7]Department of Neurosurgery, National Center Hospital, National Center of Neurology and Psychiatry, Tokyo, Japan, [8]Department of Behavioral Neurology and Cognitive Neuroscience, Tohoku University Graduate School of Medicine, Sendai, Japan, [9]Department of Neurology, Children's Hospital of Michigan, Detroit Medical Center, Wayne State University, Detroit, MI

Introduction: The left inferior frontal gyrus (IFG) is believed to play an essential role in extracting meaningful words relevant to verbal questions. Previous studies reported neural activation in the left IFG prior to speech production.[1,2] However, the temporal characteristics of left IFG activation related to utterance of filler words like "um" and "y'know" remains uncertain. We conducted research on filler-related high-gamma modulations to clarify when the left IFG is activated during use of filler words.

Methods: We studied 40 right-handed Japanese-speaking patients with drug-resistant focal epilepsy who underwent intracranial EEG (iEEG) recording followed by surgical resection. During the iEEG recording, participants performed an auditory descriptive naming task consisting of 96 questions. We excluded trials in which patients didn't respond to the question or stated "I have no idea" from the analysis. To characterize the dynamics of left IFG high-gamma modulations (70-110 Hz) associated with filler words and question answers, we conducted a time-frequency analysis of the iEEG signals on 15 patients who uttered filler words ten or more times during the naming task. The baseline period was set from 600 to 400 ms before the question onset, and we determined when IFG high-gamma activity was augmented as compared to the baseline.

Results: Approximately 300-750 ms prior to the vocalization of filler words and answers, there was a significant increase in high-gamma activity in the left IFG. Further, a more pronounced high-gamma augmentation in the left IFG was observed following the filler word uses as compared to the answer vocalization (Figures 1 and 2).

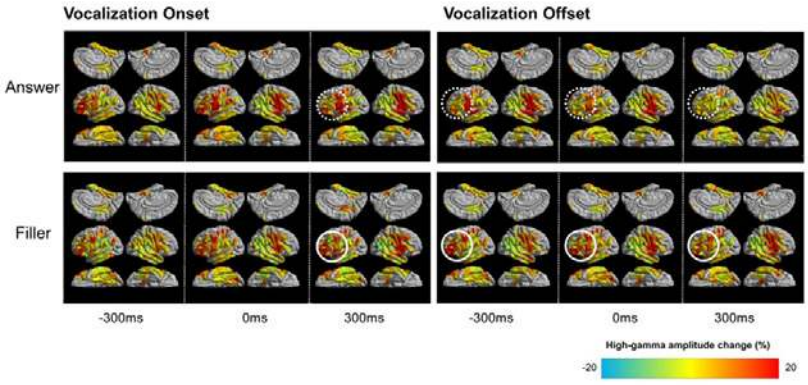

Fig. 1. Speech-related high-gamma modulations at the whole-brain level.
The left panel shows snapshots at -300, 0, and 300 ms time-locked to the vocalization onset and the right panel shows those to the vocalization offset. Upper rows represent question answer-related activity and lower represents filler words-related activity. 300 ms prior to the vocalization of filler words and answers, a significant increase in high-gamma activity was observed in the left inferior frontal gyrus. Following the filler word onset, a more pronounced high-gamma augmentation occurred in the left inferior frontal gyrus compared to following the question answer onset.

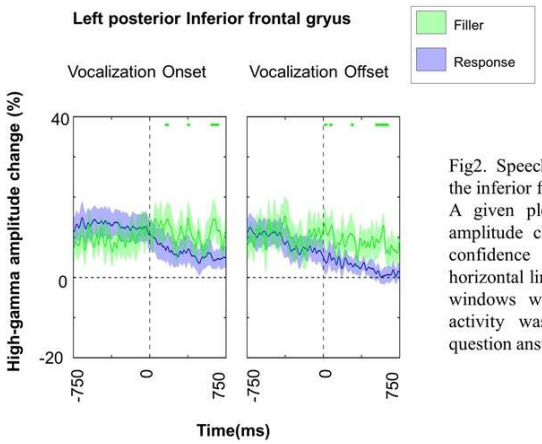

Fig2. Speech-related high-gamma enhancement in the inferior frontal gyrus.
A given plot displays the average high-gamma amplitude change as a solid line, with the 95% confidence interval shaded. The solid green horizontal lines at the top of the graph indicate time windows when filler words-related high-gamma activity was significantly greater than that of question answer-related activity.

Conclusions: Our investigation disclosed unique neural dynamics within the left IFG related to the utterance of filler words compared to question answers. The usage of filler words might signal increased neural requirements within the left IFG, implying that the utterance of such words necessitates the engagement of this region for lexical retrieval efforts.

References

1. Nakai Y, et al. Three- and four-dimensional mapping of speech and language in patients with epilepsy. Brain. 2017;140:1351-1370.
2. Kitazawa Y, et al. Intra– and inter–hemispheric network dynamics supporting object recognition and speech production. NeuroImage. 2023;270:119954.

Poster No 2616

Filler word-related high-gamma modulations in the sensorimotor cortex

Risa Hikino[1], Yu Kitazawa[1], Riri Kimura[2], Ayame Yamagishi[3], Hiroshi Uda[4], Naoto Kuroda[5], Shin-ichiro Osawa[6], Keiya Iijima[7], Kyoko Suzuki[8], Nobukazu Nakasato[6], Masaki Iwasaki[7], Eishi Asano[4]

[1]Yokohama City University, Yokohama, Kanagawa, [2]Yokohama City University, Saitama, Urawa, [3]Yokohama City University, Kawasaki, Kanagawa, [4]Wayne State University, Detroit, MI, [5]Department of Pediatrics, Children's Hospital of Michigan, Detroit Medical Center, Wayne State Unive, Detroit, MI, [6]Department of Epileptology, Tohoku University Graduate School of Medicine, Sendai, Miyagi, [7]Department of Neurosurgery, National Center Hospital, National Center of Neurology and Psychiatry, Tokyo, Tokyo, [8]Department of Behavioral Neurology and Cognitive Neuroscience, Tohoku University Graduate School of, Sendai, Miyagi

Introduction: The sensorimotor cortex plays a crucial role in speech production. Previous studies have reported excitation in the bilateral sensorimotor cortex around the onset of speech production[1,2]. However, the spatiotemporal dynamics of the sensorimotor cortex associated with filler word utterances, such as "um" and "well", commonly used to fill the silence during conversations, remains unclear. Therefore, we conducted intracranial EEG-based research to clarify when the sensorimotor cortex is activated.

Methods: A total of 40 patients with drug-resistant focal epilepsy who underwent resective epilepsy surgery were studied. They participated in an auditory descriptive naming task, comprising 96 questions while intracranial EEG recordings were performed. Trials in which patients didn't respond to the question or stated "I have no idea" were excluded from the analysis. To characterize the dynamics of high-gamma modulations (70-110 Hz) in the sensorimotor cortex related to filler word and ordinary answer utterances, we performed a time-frequency analysis on 15 participants who uttered ten or more filler words during the task.

Results: Both filler words and ordinary word answers induced a significant high-gamma augmentation in the bilateral sensorimotor cortices beginning just before the vocalization onset. After the offset of utterance, filler words induced more enhanced high-gamma augmentation in the bilateral sensorimotor cortices, compared to ordinary word answers.

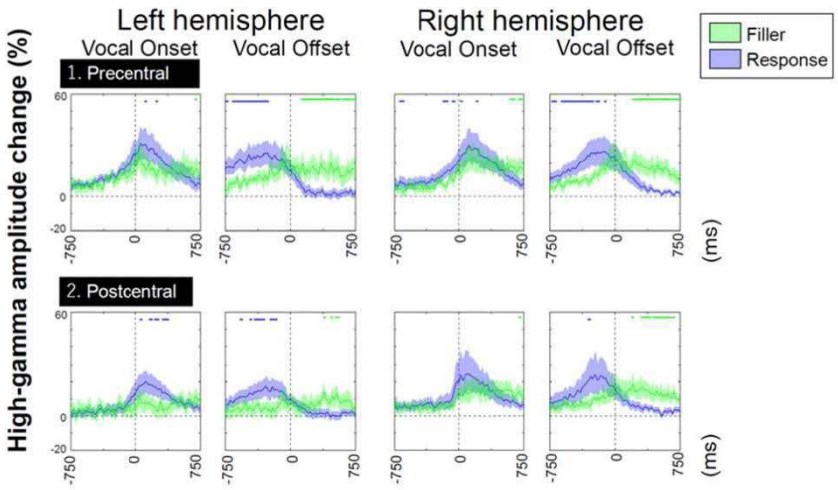

Fig. 1. Speech-related high-gamma modulations in sensorimotor cortices.
A given plot presents the percent change in high-gamma amplitudes at precentral and postcentral regions. Green: filler word utterance. Blue: ordinary word response. Shade: 95% bootstrap confidence intervals. Horizontal bars indicate the time period when a high gamma amplitude change significantly exceeded the other.

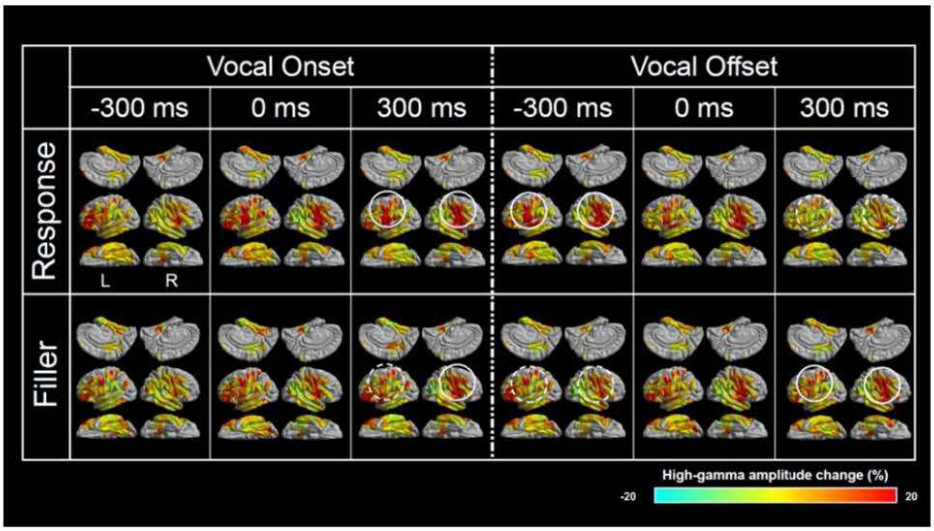

Fig. 2. Cortical high-gamma modulations around the vocalization onset and offset.
A given panel represents task-related high-gamma amplitude changes at -300, 0, and 300 ms from the vocalization onset and offset. The upper row represents ordinary word answer-related activity, whereas the lower represents filler word-related activity.

Conclusions: This study successfully identified the shared and differential neural dynamics associated with utterance of filler words and ordinary word answers in the sensorimotor cortex. Persistence of sensorimotor high-gamma augmentation following the offset of filler word utterances may indicate its involvement in response preparation after using filler words.

References

1. Nakai Y, et al. Three- and four-dimensional mapping of speech and language in patients with epilepsy. Brain. 2017;140:1351-1370.
2. Kitazawa Y, et al. Intra– and inter–hemispheric network dynamics supporting object recognition and speech production. NeuroImage. 2023;270:119954.

Poster No 2617

Coupling of Low Frequency Hemodynamic Oscillations between the Brain and Spinal Cord

Andrew John Frels[1], Vidhya Vijayakrishnan Nair[1], Yunjie Tong[1]

[1]*Purdue University, West Lafayette, IN*

Introduction: In functional Magnetic Resonance Imaging (fMRI), the primary contrast is Blood Oxygen Level Dependent (BOLD) signal. It is widely used as a signal of neuronal activity as it tracks increases and decreases in regional blood flow due to neurovascular coupling. Hemodynamic Low Frequency Oscillations (LFO) are BOLD fMRI signals between 0.01 Hz and 0.1 Hz that have been shown to strongly couple to neuronal activation and systemic physiological processes[1]. Delay times between LFOs are consistent with blood arrival and can be used to track cerebral circulation[2,3]. The Central Nervous System (CNS) is comprised of the brain and spinal cord (SC). The presence of LFO signals in the brain is well documented but LFOs as physiological oscillations in the SC have not been investigated; they have only been used to examine direct SC neuronal activity, not brain-SC interactivity[4,5]. There is no evidence on how physiological SC-LFOs couple to brain LFOs. Thus, the primary goal of this study is to investigate the coupling between brain and SC physiological LFO signals across time and frequency. This coupling information could inform a new marker for vascular connectivity between in the CNS. This is important from the perspective of CNS cerebrospinal fluid movement as hemodynamic LFOs have been shown to drive CSF motion in the brain[4]. Future studies could then understand the pathophysiology of traumatic brain or SC injury related degradation of glymphatic clearance.

Methods: All MRI data were acquired using a 3T SIEMENS MRI scanner with a 64-channel head coil, including structural T1-weighted MPRAGE and fMRI. Data from 11 participants were included in the analysis. The fMRI data were preprocessed using the FMRIB Software Library[6]. To obtain the global mean signal the high-res (T1w) brain mask was registered to the processed fMRI space and the time series was extracted[3]. All fMRI scans had arching in the cervical spine due to magnetic phenomena from distortions caused by bone/tissue interfaces[7] preventing conventional registration of SC masks from T1w space to fMRI space. Instead, the SC was masked in the fMRI space using an in-house algorithm. The SC was defined from the bottom of the scan to the voxel below the cerebellum to ensure inter-subject repeatability; time series were then directly extracted. To assess coupling between the SC and brain in the LFO range, maximum cross-correlation coefficients (MCCC) and delay times were calculated between SC and brain LFOs. For frequency analyses, the power spectra of the SC and brain time series were studied and cross spectral analyses were performed to examine the overlap in frequency content between the signals.

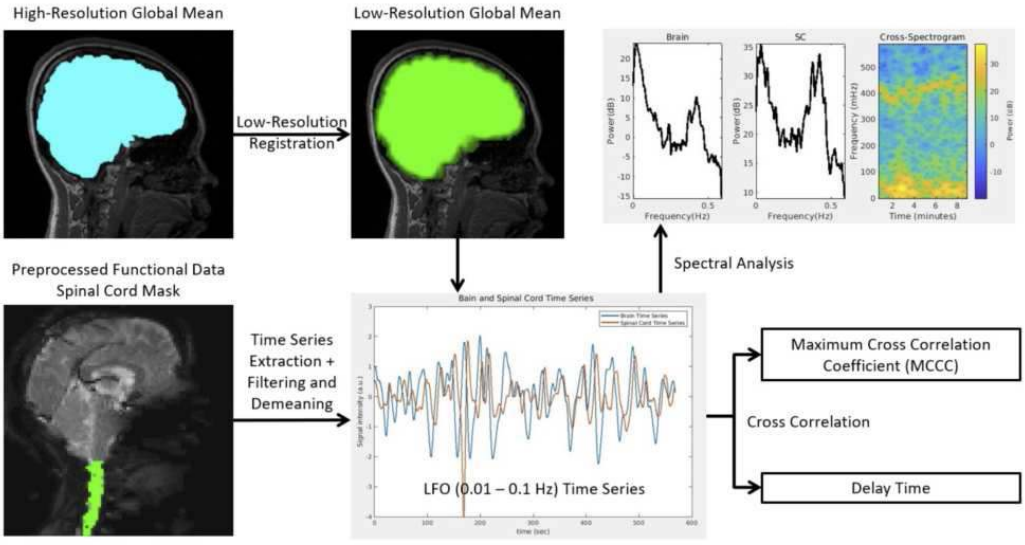

Figure 1. Methodology and Time Series Example

Results: Significant MCCCs are found between brain and SC time series in the LFO range indicating meaningful delays. These delays fall into two categories: a negative delay indicates the brain leads the SC while a positive delay shows the SC leads the brain (Fig. 2a-c). Seven subjects have a negative delay (mean=-3.86s) and a positive MCCC while four have a positive delay (mean=4.69s) and a negative MCCC. Variances are hypothesized to originate from the differing lengths of arterial pathways to the brain and SC between subjects. In the frequency analysis (Fig. 2d,e) it can be seen that LFO signals are dominant in the SC and brain. There exists a clear overlap in frequency between the brain and SC, with the highest power in the LFO range.

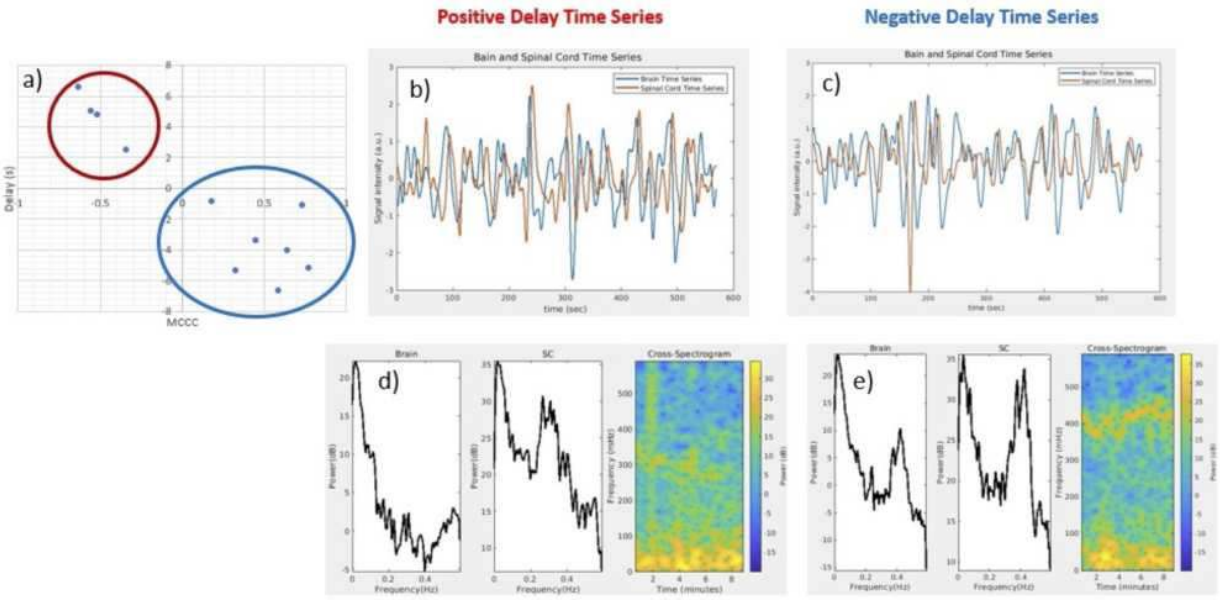

Figure 2. Results showing plot of MCCC vs Delay and example group Time Series and Power Spectra

Conclusions: Our research demonstrates a robust correlation between brain activity and SC-LFOs in both temporal and spectral domains. This investigation is the first study to confirm a significant physiological interconnection between brain and SC LFOs in healthy adult subjects. The findings of this study provide a critical basis for future explorations into spinal cord injuries. In subsequent studies, fMRI can be employed to assess and monitor hemodynamic coherence between the brain and SC, thereby facilitating the evaluation of recovery processes.

References

1. Tong, Y. & Frederick, B. de B. Time lag dependent multimodal processing of concurrent fMRI and near-infrared spectroscopy (NIRS) data suggests a global circulatory origin for low-frequency oscillation signals in human brain. Neuroimage 53, 553–564 (2010).
2. Tong, Y., Yao, J. (Fiona), Chen, J. J. & Frederick, B. de B. The resting-state fMRI arterial signal predicts differential blood transit time through the brain. Journal of Cerebral Blood Flow and Metabolism 39, 1148–1160 (2019).
3. Yao, J. et al. Cerebral circulation time derived from fMRI signals in large blood vessels. Journal of Magnetic Resonance Imaging 50, 1504–1513 (2019).
4. Barry, R. L., Vannesjo, S. J., By, S., Gore, J. C. & Smith, S. A. Spinal cord MRI at 7T. Neuroimage 168, 437–451 (2018).
5. Yang, H. C. et al. Coupling between cerebrovascular oscillations and CSF flow fluctuations during wakefulness: An fMRI study. Journal of Cerebral Blood Flow & Metabolism 42, 1091 (2022).
6. Jenkinson, M., Beckmann, C. F., Behrens, T. E. J., Woolrich, M. W. & Smith, S. M. FSL. Neuroimage 62, 782–790 (2012).
7. Stroman, P. W. et al. The current state-of-the-art of spinal cord imaging: Methods. Neuroimage 84, 1070–1081 (2014).

Poster No 2618

Investigation of functional MRI using phase-based EPT: Comparison with simulations

Kyu-Jin Jung[1], Chuanjiang Cui[1], SooHyoung Lee[1], Ji-Won Chun[2], Dong-Hyun Kim[1]

[1]Department of Electrical and Electronic Engineering, Yonsei University, Seoul, Korea, Republic of, [2]Department of Medical Informatics, Catholic University of Korea College of Medicine, Seoul, Korea, Republic of

Introduction: Functional magnetic resonance imaging (fMRI) provides insight into brain activity by the blood oxygenation level-dependent (BOLD) effect[1]. These changes are usually detectable through the gradient-recalled echo-planar imaging (EPI). Beyond the endeavors to enhance BOLD signals, significant efforts for another aspect have been made to decipher the physiological mechanisms underpinning the BOLD effect process[2-4]. On the other hand, only a handful of studies have attempted to clarify the relationship between brain activation and conductivity by applying electrical properties tomography (EPT) algorithms[4-6]. Despite these few attempts, a clear correlation remains yet elusive, with some studies even showing conflicting results[5,6]. Motivated by this ambiguity, we embarked on an investigation of the relationship between BOLD signals and conductivity changes, which can be reconstructed from the B1 phase with bSSFP sequence, employing the phase-based EPT algorithm[7,8]. Additionally, we analyzed trends in both phase and conductivity information using RF simulation, which provides ground-truth.

Methods: Six volunteers were scanned on a 3T MRI system (MAGNETOM Vida, Siemens Healthineers). For each volunteer, 2D EPI and bSFFP sequences were used (described in Figure 1 (A)). The phase information (φ) from bSSFP was used to reconstruct conductivity maps by employing the phase-based EPT algorithm[8]. In the right finger-tapping experiment, we used a block design for both sequences, consisting of 80 dynamics. These were divided into four alternating blocks of resting and tasking states. Initially, EPI scan was performed on the subject to map the BOLD signal, following which we selected a specific slice where activated BOLD signals were noticeable. This identical slice was subsequently scanned using the bSSFP sequence with signal averaging twelve-times to ensure sufficient SNR levels for the EPT reconstruction. Using GLM, we estimated beta maps for BOLD characteristics at $p<0.05$. To address uncertainties in B1 phase and conductivity activation function, we employed correlation analyses with a significance of $r<0.05$. Additionally, we used the finite-difference time-domain electromagnetic simulation program, Sim4Life, to investigate the relationship between the phase and conductivity due to brain activation in ideal conditions.

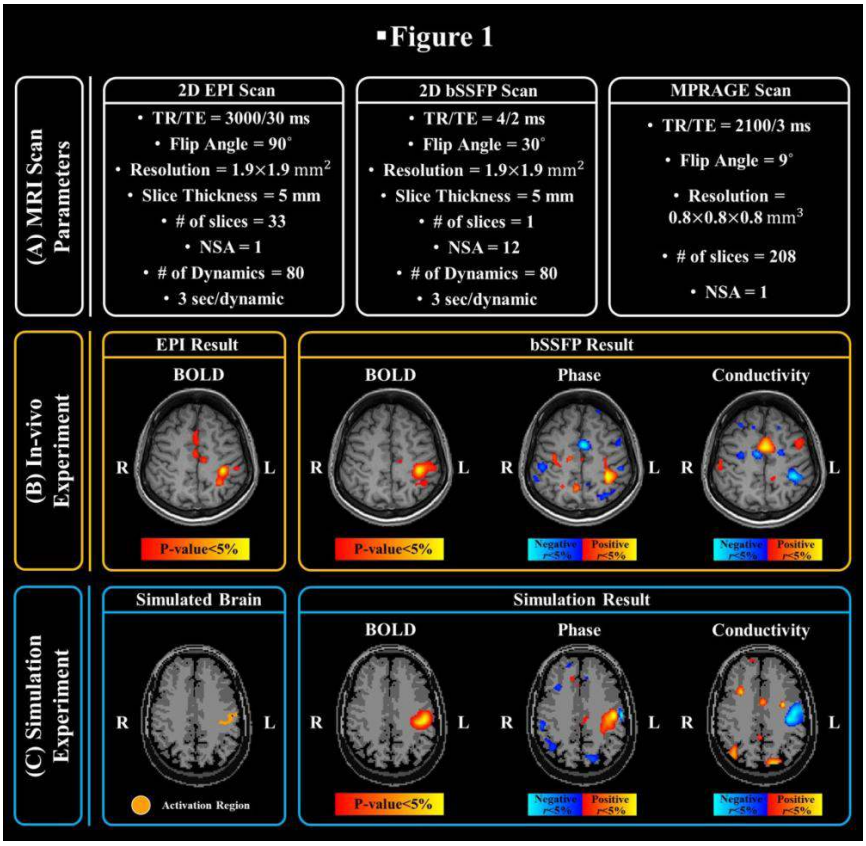

Results: In Figure 1 (B), using EPI BOLD as the reference, bSSFP BOLD, phase, and conductivity changes were observed for in-vivo. Phase change showed a positive correlation around the motor cortex, similar to the trends observed in BOLD, while reconstructed conductivity demonstrated a negative correlation. Similar to the correlation results observed in in-vivo studies, comparable trends were also noted in the simulation, as depicted in Figure 1 (C). Figure 2 presents the averaged results of the temporal-series signals in the non-activated (right motor cortex) and activated (left motor cortex) across six subjects. BOLDs and phase showed an increase in temporal series during the activation state, while conductivity exhibited a decrease. These trends of change are more pronounced when comparing activated and non-activated regions, with phase showing an increase of 0.017% in the signal during activation, while conductivity decreased by 0.37%.

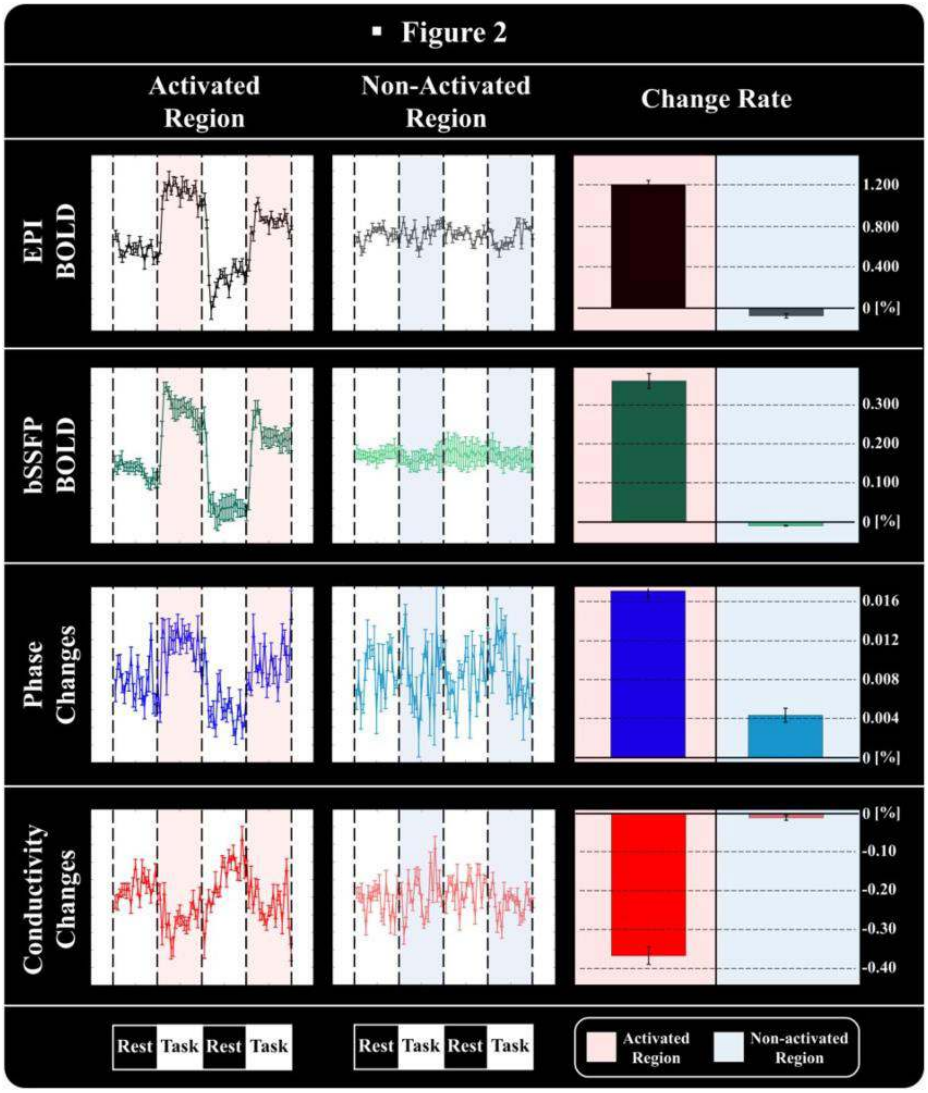

Conclusions: We explored the phase and conductivity changes during brain activation. Similar activation trends in in-vivo and simulation were observed in both phase and conductivity. This study considered how brain activation might affect conductivity, potentially influenced by ion concentration and blood oxygenation. It is known that ion concentration increases conductivity[7], but other factors (such as red cell[9]/hemoglobin concentrations[10]) may impact this effect. This conflict during brain activation highlights the need to understand which factor more significantly impacts conductivity changes.

References

1. Ogawa S., et al. (1992), 'Intrinsic signal changes accompanying sensory stimulation: functional brain mapping with magnetic resonance imaging', In proceedings of the National Academy of Science, Vol. 89, no. 13, pp. 951-5955.
2. Ip, I.B., et al. (2017), 'Combined fMRI-MRS acquires simultaneous glutamate and BOLD-fMRI signals in the human brain', Neuroimage, Vol. 155, no. 15, pp. 113-119.
3. Balla, D.Z., et al. (2014), 'Functional quantitative susceptibility mapping (fQSM)', Neuroimage, Vol 100, no. 15, pp. 112-124.
4. Helle M. & Katscher U (2019), 'Electrical Properties Tomography based Functional Magnetic Resonance Imaging (EPT-fMRI)', In proceedings of ISMRM 27th Annual Meeting & Exhibition, p. 3759.
5. Jung, K.J., et al. (2023), 'Investigation of electrical conductivity changes during functional activity of the brain via phase-based MR-EPT: Preliminary observation', In proceedings of 2023 ISMRM Annual Meeting & Exhibition, p. 0922.
6. Jahng, G.H., et al. (2023), 'High-frequency Conductivity Signal Changes Measured with Functional MREPT during Visual Stimulation', In proceedings of 2023 ISMRM Annual Meeting & Exhibition, p. 0923.
7. Katscher U. & van den Berg C.A.T. (2017), 'Electric properties tomography: Biochemical, physical and technical background, evaluation and clinical applications', NMR Biomed. Vol. 30, no. 8, p. 3729.
8. Lee, J., Shin, J., & Kim, D.H. (2016), 'MR-based conductivity imaging using multiple receiver coils', Magnetic resonance in medicine, Vol. 76, no. 2, pp. 530-539.
9. Hirsch F.G., et al. (1950), 'The electrical conductivity of blood: 1. Relationship to erythrocyte concentration', Blood, Vol. 5, no. 11, pp. 1017-1035.
10. Altaf I.M. & Ahmad A. (2017), 'Dielectric properties of human blood of patients Suffering from iron deficiency anemia', International Journal of Science, Environment and Technology, Vol. 6, no. 1, pp. 916-922.

Poster No 2619

Filler word-related cortical high-gamma modulations in the visual and auditory cortex

Riri Kimura[1], Yu Kitazawa[2], Ayame Yamagishi[3], Risa Hikino[2], Hiroshi Uda[4], Naoto Kuroda[5], Shin-ichiro Osawa[6], Keiya Iijima[7], Kyoko Suzuki[8], Nobukazu Nakasato[6], Masaki Iwasaki[9], Eishi Asano[4]

[1]Yokohama City University, Saitama, Urawa, [2]Yokohama City University, Yokohama, Kanagawa, [3]Yokohama City University, Kawasaki, Kanagawa, [4]Wayne State University, Detroit, MI, [5]Department of Pediatrics, Children's Hospital of Michigan, Detroit Medical Center, Wayne State Unive, Detroit, MI, [6]Department of Epileptology, Tohoku University Graduate School of Medicine, Sendai, Miyagi, [7]Department of Neurosurgery, National Center Hospital, National Center of Neurology and Psychiatry, Tokyo, Tokyo, [8]Department of Behavioral Neurology and Cognitive Neuroscience, Tohoku University Graduate School of, Sendai, Miyagi, [9]National Center Hospital, Tokyo, Tokyo

Introduction: A previous study of three participants reported high-gamma band EEG activation, an intracranial measure of neural excitation, in the visual association cortex when patients uttered filler words such as "um" or "like" during an visual task.[1] The present study of a large cohort of patients determined whether and when visual and auditory cortices are involved in uttering filler words.

Methods: We investigated 40 patients with drug-resistant focal epilepsy who underwent epilepsy surgery. During intracranial EEG (iEEG) recordings, patients engaged in an auditory descriptive naming task, which comprised 96 questions such as "When do you eat breakfast?" Using time-frequency iEEG analysis, we identified differential cortical high-gamma modulations between "filler words" and "ordinary word responses" in the superior temporal gyrus (STG) and lateral occipital gyrus (LOG). This analysis focused on patients who uttered ten or more filler words during the naming task.

Results: Fifteen patients uttered filler words ten or more times. In the STG, significant high-gamma augmentation was observed immediately after the onset of ordinary and filler words. Notably, there was a greater high-gamma augmentation during ordinary word compared to filler word utterance (Fig. 1). Conversely, in the left LOG, significant high-gamma augmentation was observed around the filler word offset alone (Fig. 1 and 2).

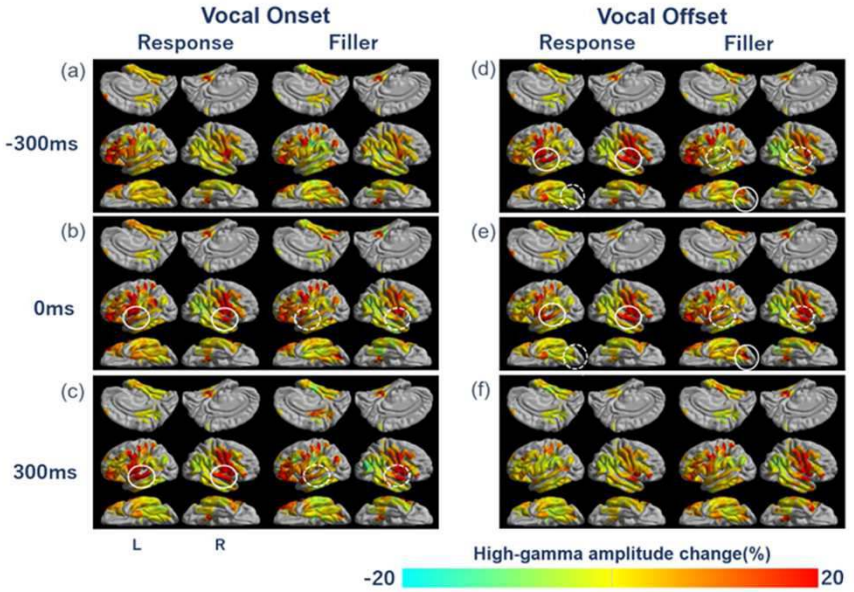

Figure 1: Cortical high-gamma modulations associated with the utterance of ordinary and filler words. High-gamma amplitude modulations at 300 ms pre-response, response onset, and 300-ms post-response are presented. In the bilateral superior temporal gyrus, significant high-gamma augmentation was found with the onset of ordinary and filler words, with greater high-gamma augmentation seen in ordinary word responses (b-e). In the left lateral occipital gyrus, significant high-gamma augmentation was noted around the vocalization offset, specifically in the case of filler words (d-e).

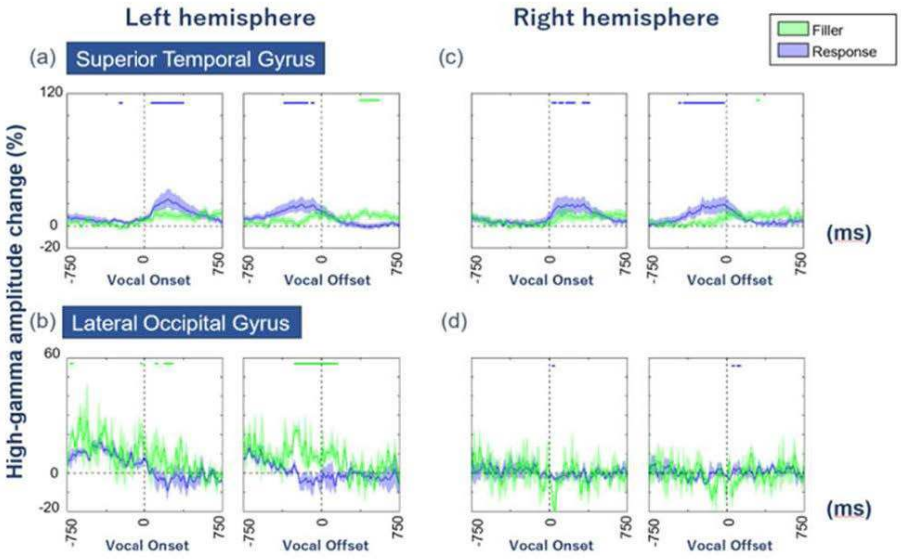

Figure 2: Cortical high-gamma modulations in the lateral occipital gyrus and superior temporal gyrus. Green: filler words. Blue: ordinary word responses. Solid line: mean high-gamma amplitude change. Shade: 95% confidence interval. Horizontal lines at the top of the graph indicate the time periods when high-gamma amplitude change for either filler words or ordinary word responses was significantly higher than the other.

Conclusions: This study demonstrated differential activation in auditory and visual cortices associated with filler and ordinary word utterances. The less enhanced activation in the STG during filler word utterance, compared to ordinary word responses, may imply a reduced need of monitoring of own filler words. Conversely, the more enhanced activation in the left LOG during filler word utterance, compared to ordinary word responses, could suggest the involvement of the visual association cortex in a form of visual scene scanning to facilitate word retrieval.

References

1. Sugiura A, et al. Neural dynamics during the vocalization of 'uh' or 'um'. Scientific Reports. 2020;10:1–8.

Poster No 2620

Axial deoxy-hemoglobin variation as a source of BOLD lag structure: evaluation on HCP-lifespan data

Toshihiko Aso[1], Takuya Hayashi[2]

[1]RIKEN Center for Biosystems Dynamics Research, Kobe, Hyogo, [2]RIKEN Center for Biocystems Dynamics Research, Kobe, Hyogo

Introduction: The longstanding controversy regarding the global signal regression (GSR) in resting-state fMRI stems from the lack of an integrated model. Despite the literature revealing cardiorespiratory components, they are not separable without special settings (Birn 2006; Chang 2009). In addition, the global component is not spatially uniform; GS can be decomposed into a set of spontaneous low-frequency oscillation (sLFO) with varying lag across voxels (Fig. 1A-B). sLFO was originally found as a systemic fluctuation common to NIRS and fMRI signals (Tong 2011), but the lag tracking allows estimation of sLFO from the fMRI data (Fig. 1C) with the "lag maps" reflecting vascular anatomy. Removal of this whole structure is a "tailored" GSR reducing more variance (-40%) than GS (Erdoğan 2016; Aso 2019). Since the mechanism of BOLD sLFO remains unsettled (Tong 2019), especially in the non-brain tissues, we proposed an axial deoxy-hemoglobin variation model (Aso 2019) which explains the absence of lag structure in CBV-based fMRI (Aso & Hayashi 2020). Indeed, physiological SaO2 or recently found hematocrit fluctuation can directly affect the tissue susceptibility: M = TE • B0 • CBV0 • [deoxy-Hb]β (Hoge 1999) This model states equivalence of the sLFO phase with moving blood, which is yet to be proven. Here we take advantage of the quality and sample size of HCP-lifespan data to elucidate several issues: 1) Are respiration volume per unit time (RVT) and heart rate variation (HR) the sources of correlation between GS amplitude and lag map robustness? (Aso & Hayashi 2023), 2) Is sLFO the source of correlation between GS and RVT/HR?, and 3) Is the age-related change of lag map (Aso 2020) reproducible in the high quality data?

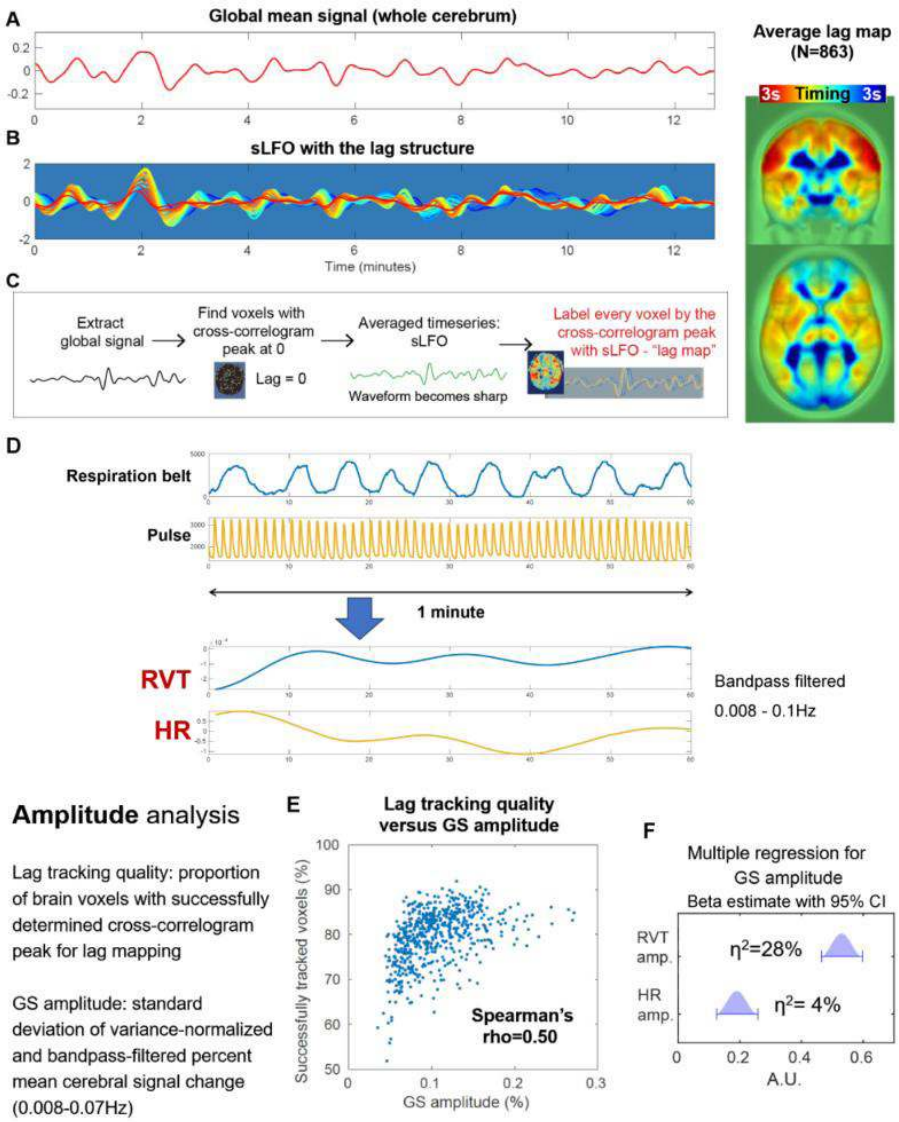

Methods: The 22.5 minutes of rsfMRI data from 863 subjects (HCP-A:714; D:149, >12 years) were processed. Only 582 had good physiological traces and were used for the main analysis, but the aging analysis involved all subjects. The perfusion lag mapping was done after minimally brain-masked preprocessing and smoothing at 4 mm FWHM, with 7.2-s tracking range both up- and downstream from the GS phase (https://github.com/RIKEN-BCIL/BOLDLagMapping). RVT was calculated using Power's toolbox (https://www.jonathanpower.net) after de-spiking the original sweeps. HR was obtained by finding the pulse rate for every peak and linearly interpolating the value (Fig. 1D).

Results: Lag mapping was successful (>70% of voxels) in most subjects, especially those with high GS amplitude (Fig. 1E). GS amplitude strongly followed RVT amplitude compared to HR, while both were significant (Fig. 1F). The known temporal relationships between RVT/HR and fMRI signals were replicated (Fig. 2A-B) but, interestingly, sLFO was more correlated than GS indicating the direct relationship. Furthermore, the best fitted sLFO waveform with HR/RVT was in the arterial side of the vasculature, in agreement with the model that sLFO exists in the inflow (Fig. 2C). Finally, the voxel-wise regression revealed both up- and downward shift of timing in the deep and superficial venous territory, roughly replicating previous works (Fig. 2D-E). This change was not accounted for by atrophy (Fig. 2F)

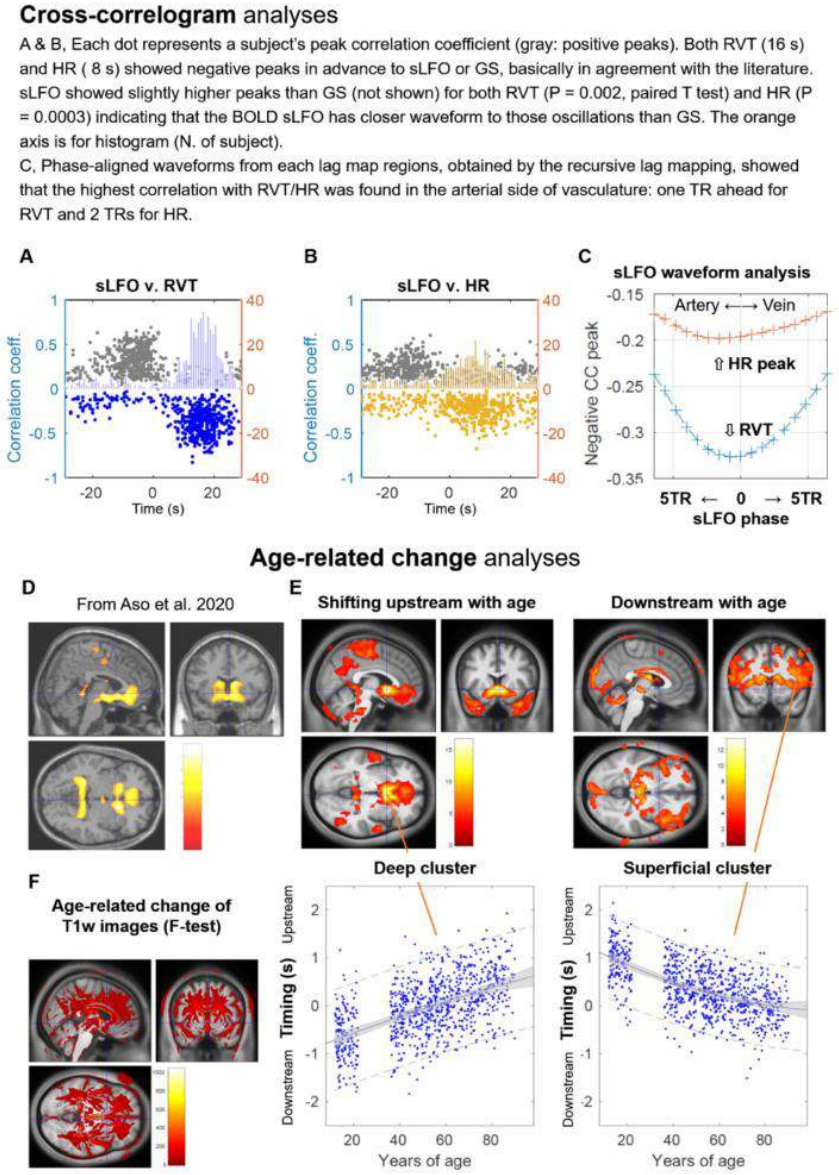

Conclusions: The known relationship of GS with RVT/HR were found to be due to sLFO; it runs through the cerebral vasculature to create a major part of the GS. The result also suggests the sLFO estimated from the fMRI data, without peripheral measurement, is valid. The higher correlation of RVT/HR with sLFO from the arterial side of the vasculature is also a new finding supporting an intrinsic signal source of fluctuating deoxy-Hb that is correlated with, but cannot be fully accounted for by RVT or HR. This model allows a simple interpretation of the age-related change confirmed here, a lifelong alteration of the venous drainage pattern starting in adolescence. Such a perfusion component would systematically affect the functional connectivity analysis and therefore needs to be treated.

References

1. Aso T, BOLD signal-based perfusion lag mapping in monkey brain. In: Annual Meeting of The Organization for Human Brain Mapping. 2020.
2. Aso T, Reliability of BOLD perfusion lag mapping depends on global signal amplitude. In: Annual Meeting of The Organization for Human Brain Mapping. 2023.
3. Aso T, Sugihara G, Murai T, Ubukata S, Urayama SI, Ueno T, et al. A venous mechanism of ventriculomegaly shared between traumatic brain injury and normal ageing. Brain. 2020 May 6;143(6):1843–56.
4. Aso T,. Axial variation of deoxyhemoglobin density as a source of the low-frequency time lag structure in blood oxygenation level-dependent signals. PLoS One. 2019 Sep 23;14(9):e0222787.
5. Birn RM, Diamond JB, Smith MA, Bandettini PA. Separating respiratory-variation-related fluctuations from neuronal-activity-related fluctuations in fMRI. Neuroimage. 7/2006;31(4):1536–48.
6. Chang C, Influence of heart rate on the BOLD signal: the cardiac response function. Neuroimage. 2009 Feb 1;44(3):857–69.
7. Erdoğan SB, Correcting for Blood Arrival Time in Global Mean Regression Enhances Functional Connectivity Analysis of Resting State fMRI-BOLD Signals. Front Hum Neurosci [Internet]. 2016 Jun 28 [cited 2018 Nov 25];10. Available from: http://journal.frontiersin.org/Article/10.3389/fnhum.2016.00311/abstract

8. Hoge RD, Investigation of BOLD signal dependence on cerebral blood flow and oxygen consumption: The deoxyhemoglobin dilution model. Magn Reson Med. 1999;42(5):849–63.
9. Tong Y, Low Frequency Systemic Hemodynamic "Noise" in Resting State BOLD fMRI: Characteristics, Causes, Implications, Mitigation Strategies, and Applications. Front Neurosci. 2019 Aug 14;13:787.
10. Tong Y, Partitioning of Physiological Noise Signals in the Brain with Concurrent Near-Infrared Spectroscopy and fMRI. J Cereb Blood Flow Metab. 12/2011;31(12):2352–62.

Poster No 2621

Edge-centric functional connectivity dynamics across the menstrual cycle

Brendan Williams[1], Anastasia Christakou[1]

[1]*University of Reading, Reading, Berkshire*

Introduction: The menstrual cycle is a recurring endocrine event characterized by fluctuations in hormones preparing the female reproductive system for pregnancy. These hormones include sex steroid hormones, which are also able to cross the blood-brain-barrier and have direct effects on brain physiology and neuronal activity. Previous work has begun to characterise functional connectivity changes across the menstrual cycle[1] e.g., default-mode network (DMN) connectivity dynamics are affected by menstrual cycle phase and oral contraceptive use[2], and DMN connectivity strength is positively correlated with estradiol levels[3]. However, menstrual cycle research has mostly focused on cross sectional or sparse repeated samples data (for exception, see[4]). Resting state analyses also often focus on distinct 'canonical' resting state networks, yet recent edge-centric functional connectivity work (which provides a temporal decomposition of static correlational-based resting state) has demonstrated that overlapping communities exist within 'canonical' resting state networks[5,6]. Here, we use an existing dense sampling dataset and an edge-centric approach to investigate community dynamics in 'canonical' networks across the menstrual cycle.

Methods: The Day2Day dataset is a dense sampling neuroimaging dataset collected from eight individuals between July 2013 and February 2014 (median 46.5 sessions, median interval between sessions 4.85 days)[7]. rsfMRI was acquired in each session [TR=2000ms, TE=30ms, FOV=216×216×129mm, FA=80°, voxels=3mm3, distance factor=20%, GRAPPA=2, 150 volumes], and concurrent measures of estradiol and menstrual cycle day were taken (menstrual cycle day converted to percentile for analysis). Resting state data were preprocessed using fMRIprep[8], and image postprocessing was performed using the XCP-D pipeline[9]. Functional data were parcellated using the Schaefer parcellation[10], and edge functional connectivity and community clustering (using k-means in Matlab) was calculated as in Faskowitz et al[6].

Results: We show – using a 10 cluster solution – that our edge communities, their similarity, and normalised network-level entropies replicate results presented by Faskowitz et al[6] (fig 1A,B & 2A). Next we generated subject-wise edge communities using group community structure as a seed. Similarity between subject-wise and group communities was assessed using variation of information, with community distance ranging from 0.91-1.10 within networks, to 1.61-2.10 across all node pairs. We then used subject-wise communities to generate session-wise communities for each participant. For each 'canonical' network, we correlated measures of session-wise community similarity (fig 1C), entropy (fig 2B), and entropy variability (fig 1E, and 2D, operationalised as the standard deviation nodal entropy in each network), with estradiol levels (fig 1D,F) and menstrual cycle day (fig 2C,E). Estradiol was positively correlated with session-level community similarity in DMN C, and negatively correlated with peripheral visual network similarity (fig 1D). Estradiol was also negatively correlated with DMN A entropy variability (fig 1F). Cycle day was positively correlated with network entropy in DMN and limbic networks and negatively correlated with entropy variability in DMN B (fig 2C,E) (correlations were FDR corrected).

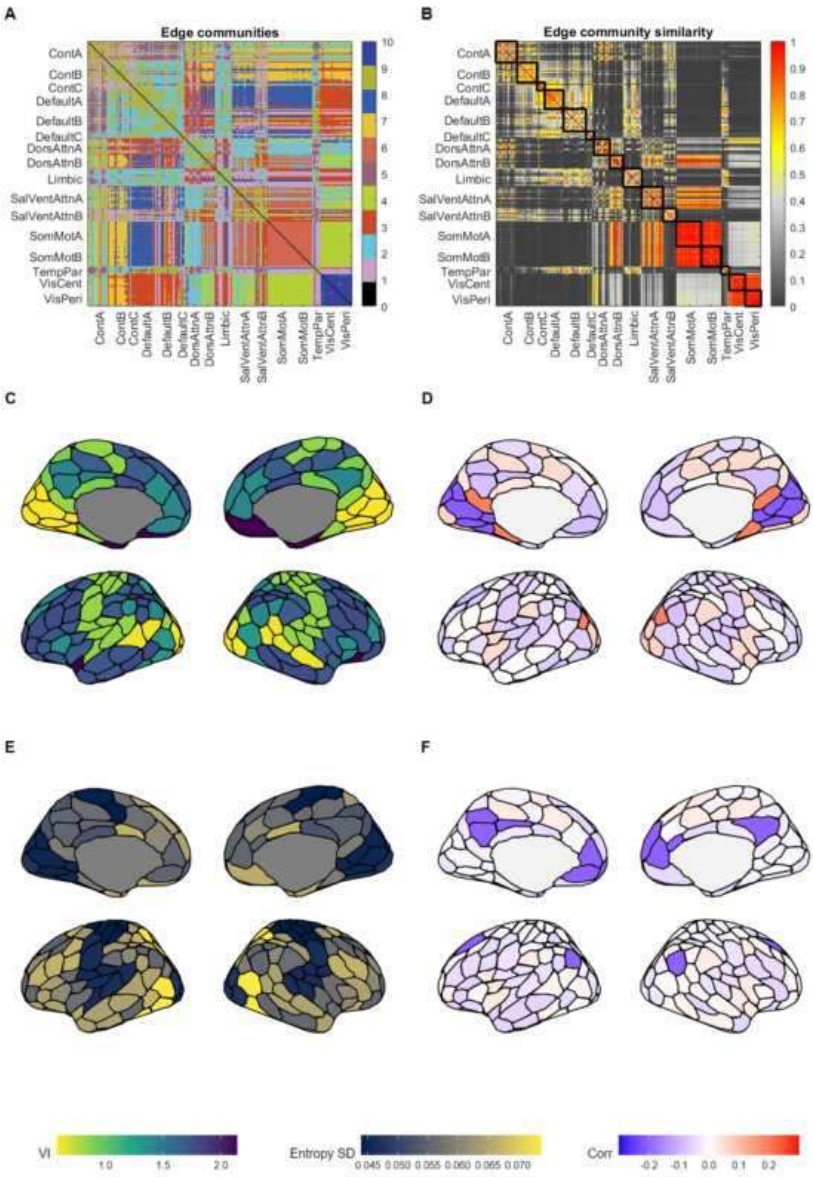

Figure 1: Edge community clustering (A) and similarity of edge community clustering for node pairs (B) mapped onto an [NxN] matrix for data pooled across all sessions. Network-level variation of information between session-wise and subject-wise community clustering (C) in Default C network was positively correlated with estradiol levels ($r(221)=0.190$, $p=0.034$), while estradiol was negatively correlated with peripheral visual network variation of information ($r(221)=-0.209$, $p=0.028$) (D). Session-wise variability in network-level entropy (E) of Default A network was negatively correlated with estradiol levels ($r(221)=-0.202$, $p=0.039$) (F). All results are FDR corrected, and all non-significant correlations are presented visually with 50% opacity.

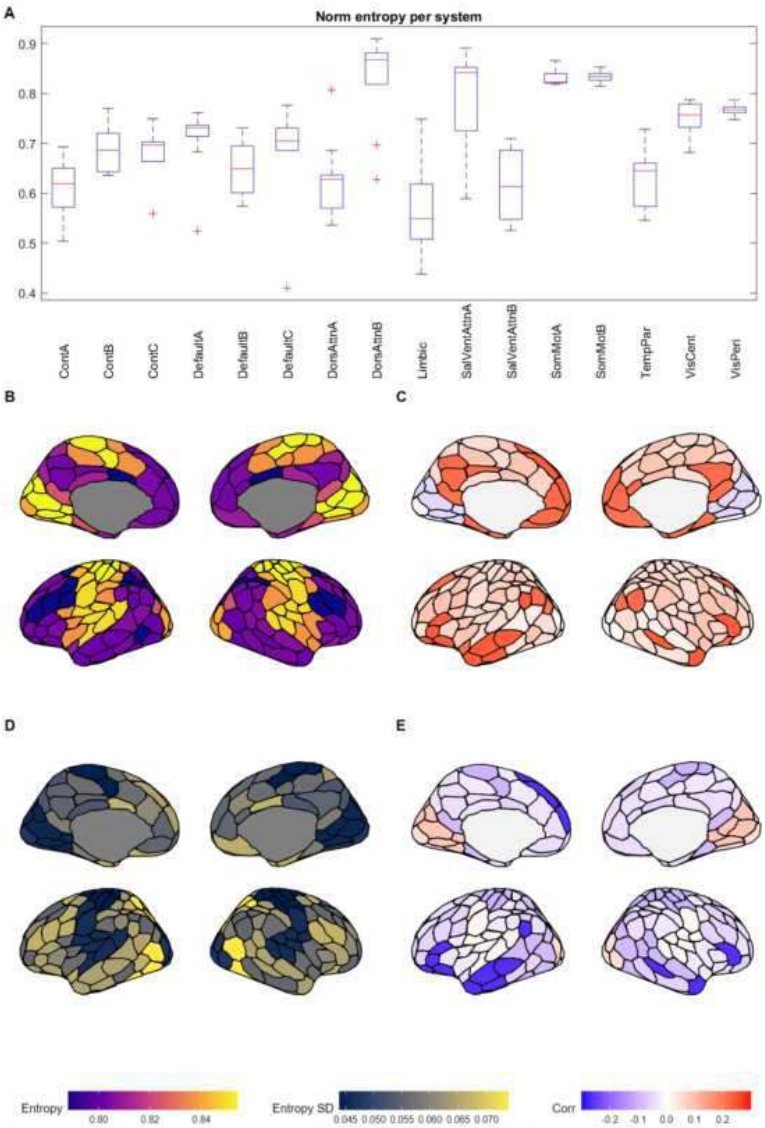

Figure 2: Normalised entropy values using data pooled across all sessions for each 'canonical' resting state network (A). Network-level entropy calculated using session-wise community clustering (B) in the default mode, and limbic networks was positively correlated with menstrual cycle day (Default A $r(143)=0.218$, $p=0.0492$, Default B $r(143)=0.238$, $p=0.0492$, Default C $r(143)=0.212$, $p=0.0492$, limbic $r(143)=0.207$, $p=0.0492$) (C). Session-wise variability in network-level entropy (D) of Default B network was negatively correlated with menstrual cycle day ($r(143)=-0.265$, $p=0.020$) (E). All results are FDR corrected, and all non-significant correlations are presented visually with 50% opacity.

Conclusions: We show that edge community structure within 'canonical' resting state networks varies as a function of the menstrual cycle. In particular, community structure within DMN appears to vary across the menstrual cycle. As estradiol levels increase DMN community structure of individuals more closely reflects the group average, and entropy variability across the network decreases. Additionally, diversity of community membership in DMN (entropy) increases as the menstrual cycle progresses. This work demonstrates changes in brain network configuration across the menstrual cycle, and the potential role of estradiol in shaping network dynamics.

References

1. Dubol M, Epperson CN, Sacher J, Pletzer B, Derntl B, Lanzenberger R, et al. Neuroimaging the menstrual cycle: A multimodal systematic review. Front Neuroendocrinol. 2021 Jan 1;60:100878.
2. Petersen N, Kilpatrick LA, Goharzad A, Cahill L. Oral contraceptive pill use and menstrual cycle phase are associated with altered resting state functional connectivity. NeuroImage. 2014 Apr 15;90:24–32.
3. Hidalgo-Lopez E, Mueller K, Harris T, Aichhorn M, Sacher J, Pletzer B. Human menstrual cycle variation in subcortical functional brain connectivity: a multimodal analysis approach. Brain Struct Funct. 2020 Mar 1;225(2):591–605.
4. Pritschet L, Santander T, Taylor CM, Layher E, Yu S, Miller MB, et al. Functional reorganization of brain networks across the human menstrual cycle. NeuroImage. 2020 Oct 15;220:117091.

5. Betzel RF, Faskowitz J, Sporns O. Living on the edge: network neuroscience beyond nodes. Trends Cogn Sci. 2023 Nov 1;27(11):1068–84.
6. Faskowitz J, Esfahlani FZ, Jo Y, Sporns O, Betzel RF. Edge-centric functional network representations of human cerebral cortex reveal overlapping system-level architecture. Nat Neurosci. 2020 Dec;23(12):1644–54.
7. Filevich E, Lisofsky N, Becker M, Butler O, Lochstet M, Martensson J, et al. Day2day: investigating daily variability of magnetic resonance imaging measures over half a year. BMC Neurosci. 2017 Aug 24;18(1):65.
8. Esteban O, Markiewicz CJ, Blair RW, Moodie CA, Isik AI, Erramuzpe A, et al. fMRIPrep: a robust preprocessing pipeline for functional MRI. Nat Methods. 2019 Jan;16(1):111–6.
9. Mehta K, Salo T, Madison T, Adebimpe A, Bassett DS, Bertolero M, et al. XCP-D: A Robust Pipeline for the post-processing of fMRI data [Internet]. bioRxiv; 2023 [cited 2023 Nov 30]. p. 2023.11.20.567926. Available from: https://www.biorxiv.org/content/10.1101/2023.11.20.567926v1
10. Schaefer A, Kong R, Gordon EM, Laumann TO, Zuo XN, Holmes AJ, et al. Local-Global Parcellation of the Human Cerebral Cortex from Intrinsic Functional Connectivity MRI. Cereb Cortex. 2018 Sep 1;28(9):3095–114.

Poster No 2623

Neurovascular coupling of D2/D3 dopamine receptors using simultaneous PET/MR in humans

Christian Schmitz[1], Xenia Hart[1], Moritz Spangemacher[1], Jana Roth[1], Karen Büsing[2], Robert Becker[1], Gabriele Ende[1], Gerhard Gründer[1]

[1]Central Institute of Mental Health, Mannheim, Baden-Wurttemberg, [2]University Hospital Mannheim, University of Heidelberg, Mannheim, Baden-Wurttemberg

Introduction: The dopamine (DA) system is a major therapeutic target in multiple psychiatric disorders such as schizophrenia or substance use disorder. Even though pharmaceutical substances that modulate DA transmission are frequently used, e.g. antipsychotic drugs, (NICE, 2014; SIGN, 2013), the scope of the functional effects as well as the long-term side effects induced by substances acting on the dopamine system is widely unknown. The neurovascular coupling of the dopamine system can be used to evaluate the functional domain of the DA system by investigating the functional effects of drugs that modify or intervene with the dopamine transmission. For example, translational studies have shown neurovascular coupling of the DA system using functional magnetic resonance imaging (fMRI) in combination with different DA agonistic interventions (Sander, 2013). Even though there is clear evidence for the neurovascular coupling of D2/3 receptors in animal models, major knowledge gaps remain regarding the dynamic relationship between DA neurochemistry and hemodynamic dopaminergic activity in humans. With this study, we want to evaluate the hemodynamic changes induced by the DA agonist apomorphine as a pharmacological challenge first time in humans and correlate the functional changes with the D2/3R non-displaceable binding potential (BP).

Methods: We are piloting the use of combined PET/fMRI imaging on a high resolution Siemens Biograph mMR (Siemens AG, Germany) with a pharmacological intervention in 9 healthy humans (four males and five females of mean age 35.1 years (SD 9.3; range 24–46 years). Using [18F]fallypride, a selective dopamine D2/3 receptor-tracer, we are determining the average dopamine non-displaceable binding potential (BPND)) based on a simplified reference tissue model (Vernaleken, 2011). In addition, we are using the dopamine receptor D2 agonist apomorphine as pharmacological challenge in order to evaluate the hemodynamic changes and correlate the activity changes with the D2/3R BP. Simultaneously, the cerebrovascular blood flow (CBF) in the striatum is measured with a multi-delay pseudo-continuous arterial spin labelling sequence (Wang, 2013).

Results: The preliminary data of 9 healthy subjects shows an average dopamine BPND of 19.3 in the striatal areas. We can show a median increase of CBF upon the injection of apomorphine of 1.75±2.6 ml/100g/min in this region. The BPND and the increase of CBF show a significant pearson correlation of r=.362 (p =.0019).

Conclusions: With our study approach, we are able to show that the simultaneous investigation of dopamine BPND and CBF is feasible. We demonstrate that the DA agonist apomorphine induces an increased blood flow in striatal areas that is correlated with the D2/3R BPND. Thus, with the use of simultaneous PET/fMR-imaging this study introduces a new methodology for investigating neurovascular coupling of the DA system first time in humans and delineates a possible mechanistic and diagnostic entry-point of pathologies of the dopamine system like dopamine supersensitivity or tardive dyskinesia.

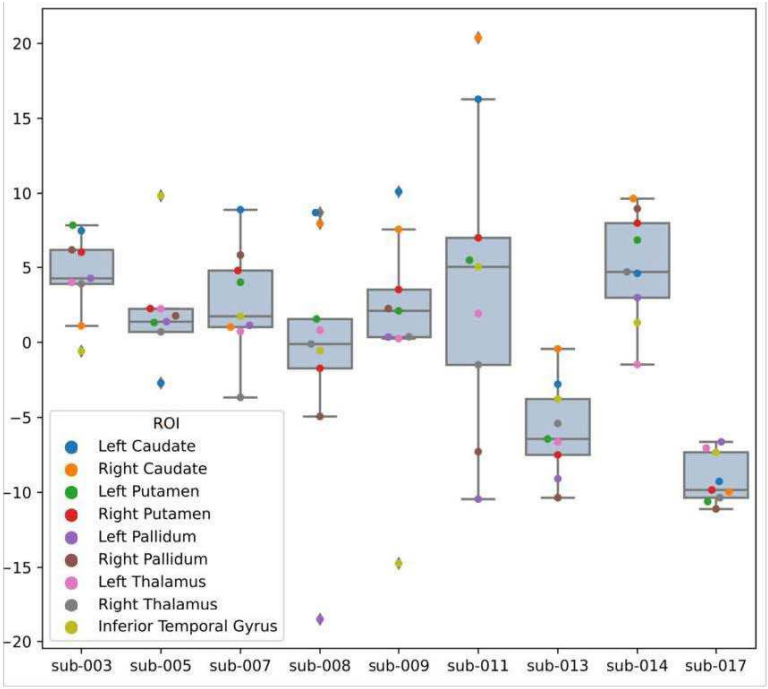

Figure 1 Median cerebrovascular blood flow (CBF) change in the striatum upon the administration of the dopamine agonist apomorphine. For each subject the different striatal areas are depicted: Left and right caudate nucleus, left and right putamen, left and right pallidum, left and right thalamus, combined inferior temporal gyrus.

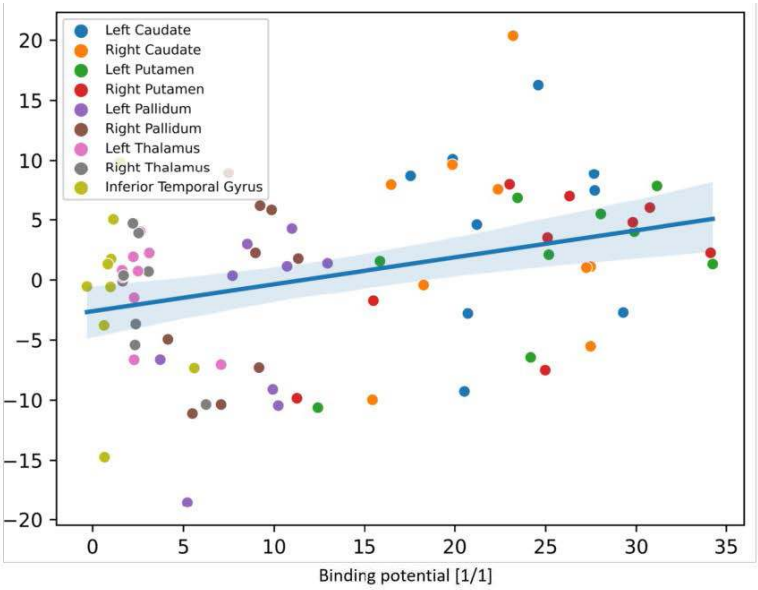

Figure 2 Scatter plot of the cerebrovascular blood flow (CBF) change in the striatum upon the administration of the dopamine agonist apomorphine and average dopamine BP_{ND} for each striatal region and each subject. The Pearson correlation coefficient of these values is r=.339 (p=.002).

References

1. NICE, National Institute of Health and Care Excellenece (2014), Psychosis and schizophrenia in adults: prevention and management. Clinical Guideline 178
2. SIGN, Scottish Intercollegiate Guidelines Network (2013), Management of schizophrenia. A national clinical guideline. Guideline 131
3. Sander CY, Hooker JM, Catana C, Normandin MD, Alpert NM, Knudsen GM, Vanduffel W, Rosen BR, Mandeville JB (2013). Neurovascular coupling to D2/D3 dopamine receptor occupancy using simultaneous PET/functional MRI. Proc Natl Acad Sci USA :11169-74
4. Vernaleken I, Peters L, Raptis M, Lin R, Buchholz HG, Zhou Y, Winz O, Rösch F, Bartenstein P, Wong DF, Schäfer WM, Gründer G (2011), The applicability of SRTM in [(18)F]fallypride PET investigations: impact of scan durations. J Cereb Blood Flow Metab. 2011 Sep;31(9):1958-66.
5. Wang DJ, Alger JR, Qiao JX, Gunther M, Pope WB, Saver JL, Salamon N, Liebeskind DS; UCLA Stroke Investigators (2013), Multi-delay multi-parametric arterial spin-labeled perfusion MRI in acute ischemic stroke - Comparison with dynamic susceptibility contrast enhanced perfusion imaging. Neuroimage Clin. 6;3:1-7

Poster No 2626

Ketamine treatment for MDD based on digital twin brain model

Ruonan Zheng[1], Junyang Zhang[1], Chen Wang[1], Zhichao Wang[1], Yang He[1], Yanling Zhou[2], Yuping Ning[2], Zhang Yu[3], Tianzi Jiang[4]

[1]Zhejiang Lab, Hangzhou, Zhejiang, [2]The Affiliated Brain Hospital of Guangzhou Medical University, Guangzhou, Guangdong, [3]Zhejiang Lab, Hang Zhou, Zhejiang, [4]Brainnetome Center, Institute of Automation, Chinese Academy of Sciences, Beijing, Beijing

Introduction: Ketamine has gained popularity as an antidepressant due to its rapid and effective action. However, the mechanisms by which ketamine improves emotional states remain unclear. By leveraging the unique biological characteristics of ketamine as an N-methyl-D-aspartate receptors (NMDAR) antagonist, we have utilized a digital twin brain model[1] to investigate ketamine's influence on brain circuitry. This approach has enabled us to explore the underlying neural mechanism of ketamine from the perspective of excitatory/inhibitory balance.

Methods: We recruited 40 patients with major depressive disorder (MDD) and 38 normal controls (NC). After quality control and excluding missing data, this study used 31 MDD patients who underwent ketamine treatment (6 sub-anaesthetic doses of ketamine by intravenous infusion over 12 days), including 19 effective (MDDa) and 12 ineffective (MDDb) patients according to Montgomery-Asberg Depression Rating Scale. All subjects underwent structural (voxel-size=1mm isotropic) and functional MRI (voxel-size=3.4mm, thickness=4mm, TR=2s) data using 3.0 T Philips Achieva scanner. More details regarding the study design and MRI data acquisition have been described in previous studies[2,3]. We simulated the spontaneous brain activity at the whole-brain level using a network model with each node representing a brain region and the links between nodes representing white matter connections. We used the dynamic mean field (DMF) model[4] to simulate the neural activity in each brain region. Additionally, ketamine binds directly to NMDAR, which prevents binding with upstream excitatory neurotransmitters and releasing excitatory/inhibitory neurotransmitters. Based on which, we modified the model (Fig. 1D).We hypothesized similar neural dynamics within each functional network and used the same set of parameters for each network. We simulated functional dynamics of each brain network using the digital twin brain model and hemodynamic model (Fig. 1) and evaluated the model by comparing the real and simulated functional connectivity matrix using Pearson correlation coefficient (PCC). We predicted the effectiveness of ketamine treatment by measuring the changes between the simulation models before and after and the real states using a grid search on the parameter space of Jexc/Jinh.

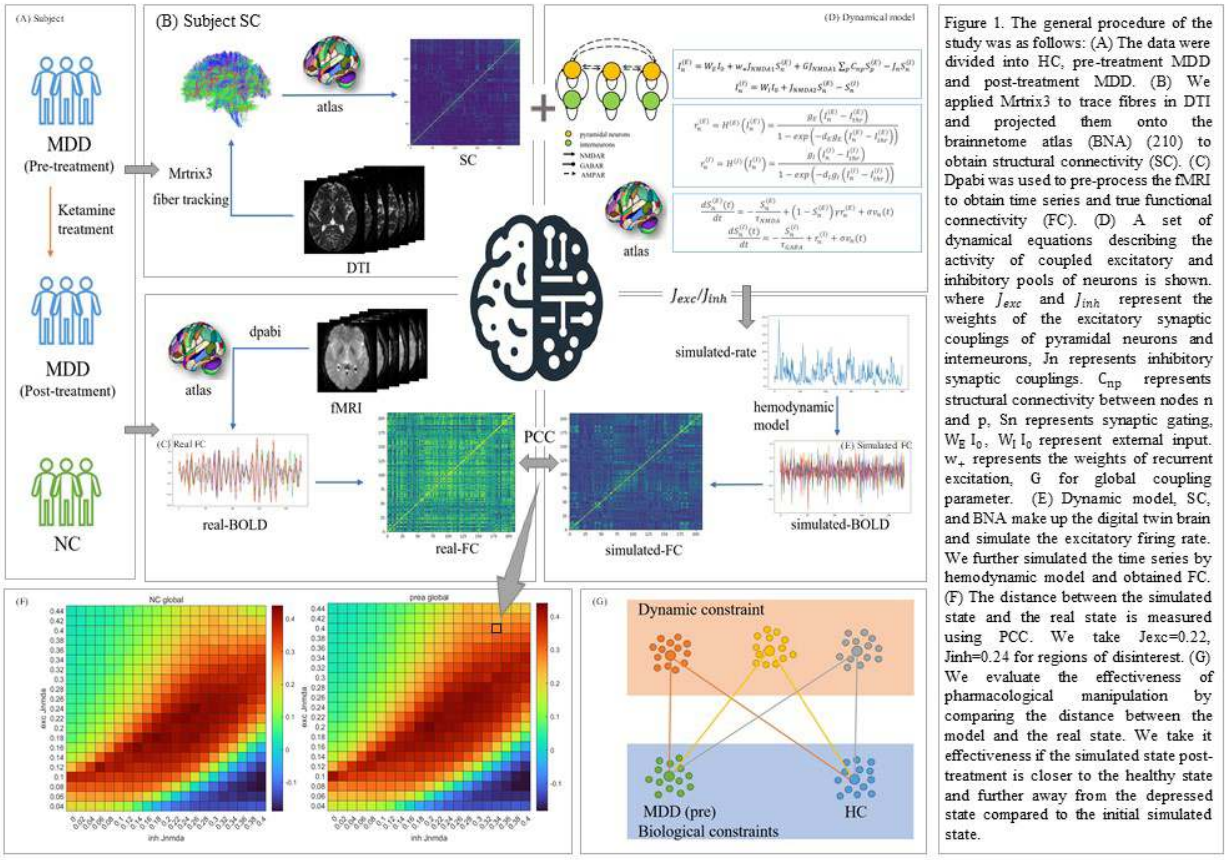

Figure 1. The general procedure of the study was as follows: (A) The data were divided into HC, pre-treatment MDD and post-treatment MDD. (B) We applied Mrtrix3 to trace fibres in DTI and projected them onto the brainnetome atlas (BNA) (210) to obtain structural connectivity (SC). (C) Dpabi was used to pre-process the fMRI to obtain time series and true functional connectivity (FC). (D) A set of dynamical equations describing the activity of coupled excitatory and inhibitory pools of neurons is shown. where J_{exc} and J_{inh} represent the weights of the excitatory synaptic couplings of pyramidal neurons and interneurons, Jn represents inhibitory synaptic couplings. C_{np} represents structural connectivity between nodes n and p, Sn represents synaptic gating, $W_E I_0$, $W_I I_0$ represent external input. w_+ represents the weights of recurrent excitation, G for global coupling parameter. (E) Dynamic model, SC, and BNA make up the digital twin brain and simulate the excitatory firing rate. We further simulated the time series by hemodynamic model and obtained FC. (F) The distance between the simulated state and the real state is measured using PCC. We take Jexc=0.22, Jinh=0.24 for regions of disinterest. (G) We evaluate the effectiveness of pharmacological manipulation by comparing the distance between the model and the real state. We take it effectiveness if the simulated state post-treatment is closer to the healthy state and further away from the depressed state compared to the initial simulated state.

Results: Using different functional network as regions of interest, we observed significant differences in the frontoparietal network (FPN) between MDDa and NC (Fig. 2A a, b). The FPN in NC models leaned towards excitation, whereas the FPN in MDDa models exhibited a bias towards inhibition, resembling the real state. Post-treatment modeling of MDDa's FPN revealed a shift closer to state I(Fig. 2d), indicating a reduction in NMDAR synaptic coupling among interneurons. Simulations of Jexc/Jinh pairs for the FPN in MDDa (Fig. 2B) suggested that inhibiting only the interneurons aligns closest to a healthy state. For MDDb, we found no significant pre-treatment inhibition bias or post-treatment inhibition of interneurons in the FPN model (Fig. 2C).

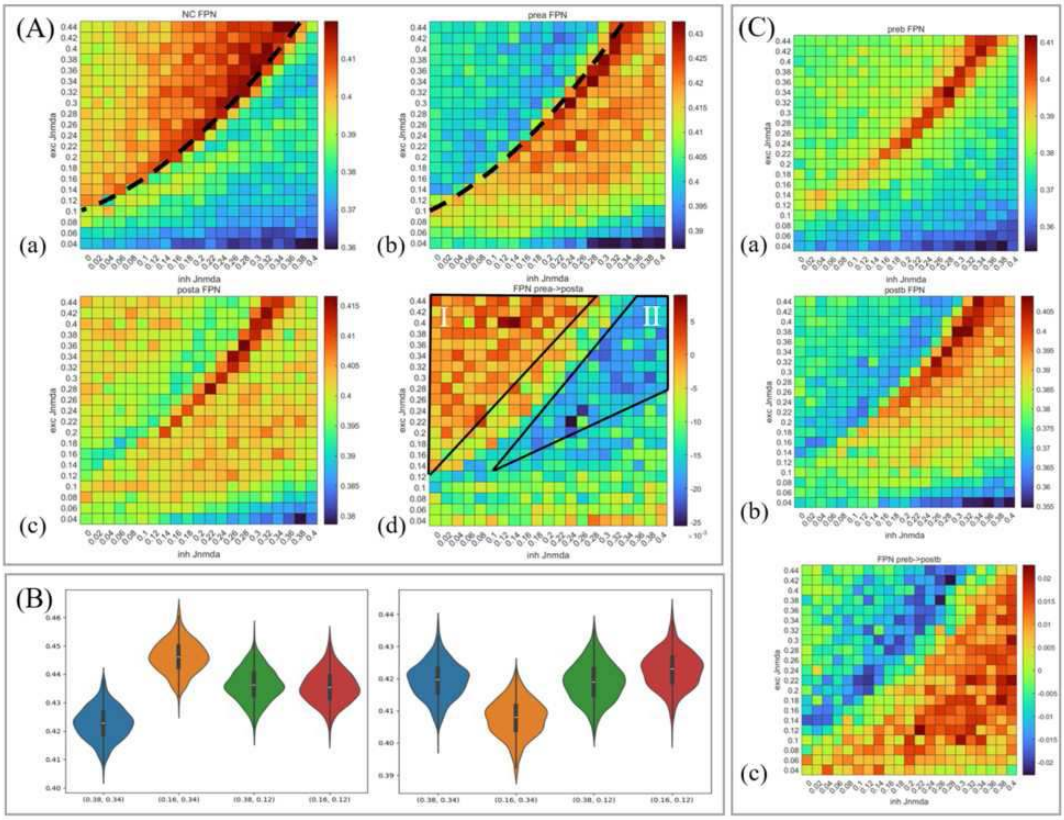

Figure2. (A) (a-c) represent the parameter space of the models for NC, MDDa (pre-treatment) and MDDa (post-treatment), respectively. (d) shows the changes of distance from each pair of parameter model before and after treatment to the real state. (B) We simulate four pairs of $J_{exc}/J_{inh}$of FPN model for MDDa, representing the pre-treatment state, that is, the point closest to the depressive state and farthest from the healthy state (mean(-NC)=0.4204, mean(-MDD)=0.4189), only reducing J_{inh} (mean(-NC)=0.4448, mean(-MDD)=0.4080), only reducing J_{exc} (mean(-NC)=0.4337, mean(-MDD)=0.4191), and reducing both (mean(-NC)=0.4347, mean(-MDD)=0.4221). (C) (a, b) denote the parameter space of the models before and after MDDb treatment, respectively. (c) denotes the change in distance to the healthy and depressed states for each pair of parameter models before and after treatment

Conclusions: In this study, we used the digital twin brain model to investigate the circuit-level mechanism of antidepressant action of ketamine. Our findings suggest that in NC, the FPN is typically excited, but in depression, it tends to be inhibited. Specifically, in MDDa, ketamine appears to inhibit FPN interneurons, eliciting antidepressant responses. Conversely, the results from MDDb provide a contrasting perspective for the ineffective response. Our study provides a computational perspective of depression symptoms and the neural mechanism of ketamine treatment.

References

1. Xiong, H. et al. (2023). The Digital Twin Brain: A Bridge between Biological and Artificial Intelligence. Intelligent Computing 2, 0055.
2. Zhou, Y.-L. et al. (2020). Volumetric changes in subcortical structures following repeated ketamine treatment in patients with major depressive disorder: a longitudinal analysis. Transl Psychiatry 10, 1–9.
3. Wang, C. et al. (2019). Association between depression subtypes and response to repeated-dose intravenous ketamine. Acta Psychiatrica Scandinavica 140, 446–457.
4. Deco, G. et al. (2014). How Local Excitation-Inhibition Ratio Impacts the Whole Brain Dynamics. Journal of Neuroscience 34, 7886–7898.

Poster No 2627

Specific effects of serotonergic psychedelics on whole-brain functional connectivity

Mihai Avram[1], Lydia Fortea[2], Felix Müller[3], Lea Wollner[1], Ricarda Coennen[1], Alexandra Korda[1], Helena Rogg[1], Friederike Holze[4], Patrick Vizeli[3], Anna Becker[3], Laura Ley[3], Joaquim Radua[2], Matthias Liechti[3], Stefan Borgwardt[1]

[1]University of Lübeck, Lübeck, Germany, [2]University of Barcelona, Barcelona, Spain, [3]University Hospital Basel, Basel, Switzerland, [4]Neurobiology Research Unit, Rigshospitalet, Copenhagen, Hovestaden

Introduction: Psychedelics have garnered considerable attention due to their potential to alleviate symptoms of various psychiatric disorders[1,2,3]. Despite therapeutic promise, their precise neurobiological mechanisms underlying such effects remain incompletely understood. Comparing psychedelics with substances having partly overlapping neurophysiological effects could provide valuable insights into their mechanisms of action. This comparison forms the basis of our investigation, which discusses the findings from two independent studies derived from clinical trials NCT03019822 and NCT04227756. The former study compared the effects of LSD to d-amphetamine and MDMA, while the latter compared LSD to other psychedelics, namely psilocybin and mescaline.

Methods: Both studies employed a randomized, double-blind, placebo-controlled, cross-over design to compare the acute effects in healthy volunteers (study 1: n=25, mean age 28±4 years, 14 women; Study 2: n=26, mean age 27.5±2.6 years, 13 women)[4,5]. Functional MRI data, assessed during peak effects, were acquired on the same MRI scanner with the same sequence and were preprocessed with the same pipeline using C-PAC[6]. We used a network parcellation approach[7] to investigate connectivity within-network (integrity), between-network (segregation), and globally (i.e., degree centrality; DC). Between-group differences were investigated with repeated-measures ANOVAs, followed by post-hoc pairwise t-tests. Statistical analyses conducted in R, underwent correction for multiple comparisons (FDR).

Results: In study 1, LSD reduced integrity in the visual (VIS), default mode (DMN), and frontoparietal networks (FPN), compared to placebo. The amphetamines reduced integrity in auditory-sensorimotor (ASM), salience (SAL), FPN, and VIS, but not in DMN. LSD findings were largely replicated in study 2, with integrity decreases in DMN and VIS, compared to placebo. Psilocybin reduced integrity in VIS and trend-wise DMN, while mescaline reduced integrity in VIS and DMN, albeit to a lesser extent than LSD. Regarding segregation, in study 1, LSD produced more pronounced effects (i.e., decreases) compared to placebo than the amphetamines but similar effects as the other psychedelics in study 2. Unlike the amphetamines, no increase in segregation was observed for any psychedelic. Direct comparisons revealed no differences between LSD and psilocybin, but LSD showed more extensive connectivity than mescaline and the latter more extensive connectivity than psilocybin. Regarding global connectivity, in study 1, LSD increased DC compared to placebo in basal ganglia, thalamus, and auditory cortices. Compared to placebo, d-amphetamine and MDMA increased DC in small clusters covering dorsolateral prefrontal cortex and fusiform gyrus, respectively. LSD increased DC in sensorimotor areas compared to both amphetamines. In study 2, the LSD vs. placebo findings were replicated among additional clusters found in sensorimotor cortices and cerebellum. Psilocybin also increased DC in sensorimotor areas, cerebellum, and middle cingulum. Mescaline did not increase DC compared to placebo. All substances decreased DC in visual areas compared to placebo, with additional decreases in sensorimotor areas for amphetamines and in posterior cingulate/precuneus for psychedelics, respectively.

Conclusions: We found profound changes in connectivity following the administration of distinct psychoactive compounds. A specific decrease in DMN integrity was observed following psychedelics. While psychedelics only decreased segregation, some increases were observed for amphetamines. LSD increased global connectivity in the basal ganglia and thalamus, aligning with prior reports[8]. These outcomes significantly contribute to our understanding of psychedelics' specific impacts on various brain networks, shedding light on their unique neurobiological effects and paving the way for further exploration into their therapeutic potential.

References

1. Carhart-Harris, R., Giribaldi, B., Watts, R., Baker-Jones, M., Murphy-Beiner, A., Murphy, R., ... & Nutt, D. J. (2021). Trial of psilocybin versus escitalopram for depression. New England Journal of Medicine, 384(15), 1402-1411.
2. Holze, F., Gasser, P., Müller, F., Dolder, P. C., & Liechti, M. E. (2023). Lysergic acid diethylamide–assisted therapy in patients with anxiety with and without a life-threatening illness: a randomized, double-blind, placebo-controlled phase II study. Biological Psychiatry, 93(3), 215-223.
3. Bogenschutz, M. P., Ross, S., Bhatt, S., Baron, T., Forcehimes, A. A., Laska, E., ... & Worth, L. (2022). Percentage of heavy drinking days following psilocybin-assisted psychotherapy vs placebo in the treatment of adult patients with alcohol use disorder: a randomized clinical trial. JAMA psychiatry, 79(10), 953-962
4. Holze, F., Vizeli, P., Müller, F., Ley, L., Duerig, R., Varghese, N., Eckert, A., Borgwardt, S., Liechti, M.E. (2020). Distinct acute effects of LSD, MDMA, and D-amphetamine in healthy subjects. Neuropsychopharmacol. 45, 462–47.

5. Ley, L., Holze, F., Arikci, D., Becker, A. M., Straumann, I., Klaiber, A., ... & Liechti, M. E. (2023). Comparative acute effects of mescaline, lysergic acid diethylamide, and psilocybin in a randomized, double-blind, placebo-controlled cross-over study in healthy participants. Neuropsychopharmacology, 1-9.
6. Avram, M., Müller, F., Rogg, H., Korda, A., Andreou, C., Holze, F., ... & Borgwardt, S. (2022). Characterizing thalamocortical (dys) connectivity following d-amphetamine, LSD, and MDMA administration. Biological Psychiatry: Cognitive Neuroscience and Neuroimaging, 7(9), 885-894.
7. Yeo, B. T., Krienen, F. M., Sepulcre, J., Sabuncu, M. R., Lashkari, D., Hollinshead, M., ... & Buckner, R. L. (2011). The organization of the human cerebral cortex estimated by intrinsic functional connectivity. Journal of neurophysiology.
8. Müller, F., Lenz, C., Dolder, P., Lang, U., Schmidt, A., Liechti, M., & Borgwardt, S. (2017). Increased thalamic resting-state connectivity as a core driver of LSD-induced hallucinations. Acta Psychiatrica Scandinavica, 136(6), 648-657.

Poster No 2628

Relationship between obesity, related comorbidities, and neuroinflammation in young and older adults

Filip Morys[1], Max Tweedale[1], Christina Tremblay[1], Alexandre Pastor-Bernier[1], Houman Azizi[1], Alain Dagher[1]

[1]Montreal Neurological Institute and Hospital, McGill University, Montreal, Quebec

Introduction: Obesity causes persistent, low-grade systemic metabolic inflammation[1]. Studies describe negative effects of such inflammation and other obesity-related factors on the brain[1]. Recently, studies also suggest that brain derangements might constitute a risk factor for excess weight gain[2–4]. For example, inflammation in the hypothalamus — initiated by a plethora of factors, e.g. genetics, overnutrition or high-fat diets — can often precede the onset of obesity and lead to altered homeostatic food-intake processes[5,6]. Such phenomena can lead to a vicious cycle of food intake, whereby overnutrition leads to changes in the brain, which can further lead to overnutrition, obesity, thus increasing brain damage. Inflammation caused by obesity and related metabolic derangements would not only be visible in the hypothalamus, but also in other vulnerable brain areas. At the same time, only hypothalamic inflammation would lead to altered food intake. Here, we looked at diffusion weighted imaging data from magnetic resonance (MR DWI) to assess inflammation in several subcortical brain structures in two large-scale cohorts of different ages. We investigated the relationship of the inflammation measures with obesity and related comorbidities to explore mechanisms linking excess weight with neuroinflammation.

Methods: We used data from the UK Biobank (UKB; n=26,242; mean age=63 years; body mass index, BMI=26.15 kg/m^2; 13,801 women) and Human Connectome Project (HCP, n=819; age=29 years; BMI=26.50 kg/m^2; 428 women) samples of healthy participants with no neurological disorders[7,8]. We processed DWI data using Tractoflow to derive diffusion tensor imaging (DTI) measures of fractional anisotropy (FA), mean diffusivity (MD), axial diffusivity (AD), and radial diffusivity (RD), which could reflect neuroinflammation in grey matter structures[3,9]. We investigated the hypothalamus, caudate nucleus, putamen, pallidum, nucleus accumbens, and hippocampus as regions of interest. Using linear regression we related the DTI measures to measures of adiposity (BMI) and other comorbidities (hypertension, c-reactive protein reflecting systemic inflammation (only UKB), blood glycated haemoglobin levels (HbA1c), blood glucose levels (only UKB), and blood lipid levels (only UKB)). Results were corrected for multiple comparisons using false discovery rate correction.

Results: In the HCP sample of young adults, we only found significant negative associations between DTI measures and BMI, predominantly for hippocampus and pallidum, but no associations between DTI measures and SBP, DBP, or HbA1c (Fig. 1). In the older UKB sample, we found consistently positive associations between FA and most investigated obesity-related measures in all brain structures except the caudate nucleus, where the association was opposite (Fig. 2). Other diffusivity measures had weaker and negative associations with investigated variables in most structures, except for the caudate nucleus.

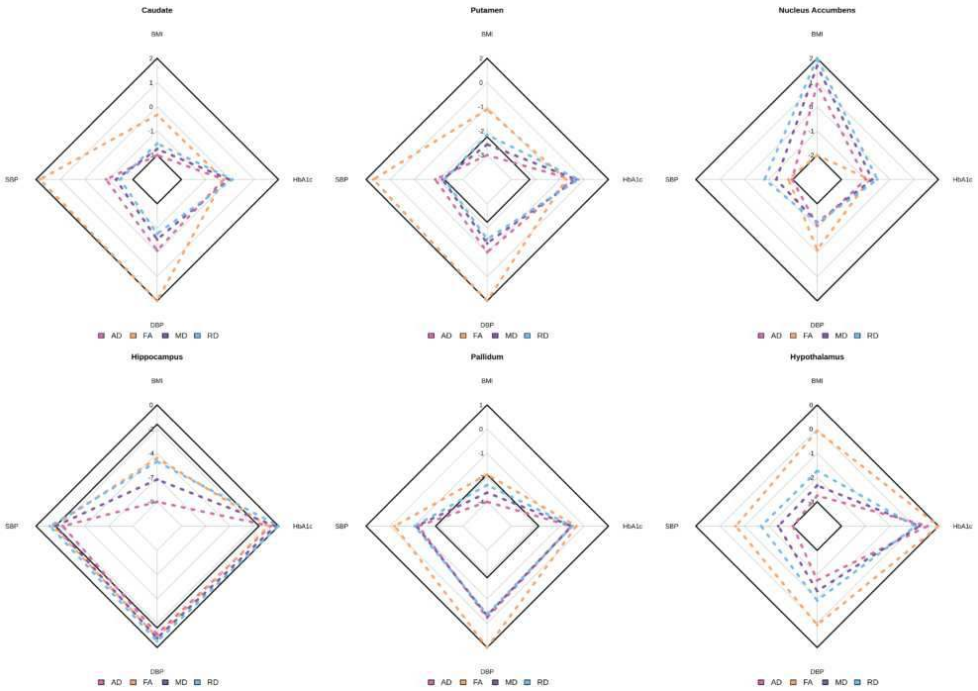

Figure 1 Associations between diffusion tensor imaging measures in subcortical brain structures and obesity-related variables in the HCP sample. Values above and below black lines on radar charts represent significant associations. BMI - body mass index. HbA1c - glycated haemoglobin, SBP - systolic blood pressure, DBP - diastolic blood pressure, AD - axial diffusivity, FA - fractional anisotropy, MD - mean diffusivity, RD - radial diffusivity.

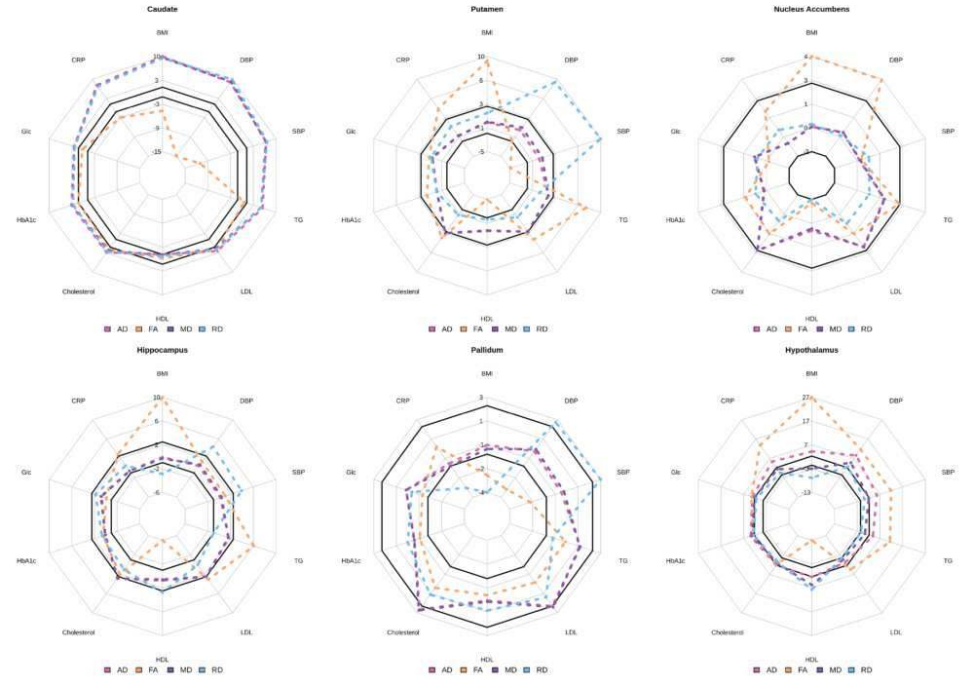

Figure 2 Associations between diffusion tensor imaging measures in subcortical brain structures and obesity-related variables in the UKB sample. Values above and below black lines on radar charts represent significant associations. BMI - body mass index. HbA1c - glycated haemoglobin, SBP - systolic blood pressure, DBP - diastolic blood pressure, CRP - C-reactive protein, TG - triglycerides, LDL - low density lipoprotein cholesterol, HDL - high density lipoprotein cholesterol, Glc - glucose, AD - axial diffusivity, FA - fractional anisotropy, MD - mean diffusivity, RD - radial diffusivity.

Conclusions: DTI measures were weakly associated with obesity-related measures in the investigated subcortical structures in the young, healthy sample. Some associations, for example positive relationship between DTI measures and BMI in the hippocampus or pallidum, might suggest an ongoing process of neuroinflammation, however, these effects seem to be small and not present in all the tested brain structures. Conversely, we observed significant associations between obesity-related measures and DTI measures in most of the subcortical structures in the older sample. Positive associations with FA might indicate a process of gliosis that restricts water diffusion in grey matter through increases in cellularity[3]. Because this process seems to be ongoing in multiple subcortical structures not directly related to food intake, it seems that it is an effect, rather than a cause, of obesity and related comorbidities. In sum, we are showing that obesity could be related to neuroinflammation and thus leads to neurodegeneration.

References
1. Morys F, Dadar M, Dagher A. Association Between Midlife Obesity and Its Metabolic Consequences, Cerebrovascular Disease, and Cognitive Decline. J Clin Endocrinol Metab. 2021;106:e4260–e4274.
2. Morys F, Yu E, Shishikura M, Paquola C, Vainik U, Nave G, et al. Neuroanatomical correlates of genetic risk for obesity in children. Transl Psychiatry. 2023;13:1.
3. Sewaybricker LE, Huang A, Chandrasekaran S, Melhorn SJ, Schur EA. The significance of hypothalamic inflammation and gliosis for the pathogenesis of obesity in humans. Endocr Rev. 2022. 17 October 2022. https://doi.org/10.1210/endrev/bnac023.
4. Jais A, Brüning JC. Hypothalamic inflammation in obesity and metabolic disease. J Clin Invest. 2017;127:24–32.
5. Szalanczy AM, Key C-CC, Solberg Woods LC. Genetic variation in satiety signaling and hypothalamic inflammation: merging fields for the study of obesity. J Nutr Biochem. 2022;101:108928.
6. Sonnefeld L, Rohmann N, Geisler C, Laudes M. Is human obesity an inflammatory disease of the hypothalamus? Eur J Endocrinol. 2023;188:R37–R45.
7. Miller KL, Alfaro-Almagro F, Bangerter NK, Thomas DL, Yacoub E, Xu J, et al. Multimodal population brain imaging in the UK Biobank prospective epidemiological study. Nat Neurosci. 2016;19:1523–1536.
8. Van Essen DC, Ugurbil K, Auerbach E, Barch D, Behrens TEJ, Bucholz R, et al. The Human Connectome Project: a data acquisition perspective. Neuroimage. 2012;62:2222–2231.
9. Theaud G, Houde J-C, Boré A, Rheault F, Morency F, Descoteaux M. TractoFlow: A robust, efficient and reproducible diffusion MRI pipeline leveraging Nextflow & Singularity. Neuroimage. 2020;218:116889.

Poster No 2629

Unraveling the Intricate Connections between Brain Aging, Body Composition, and Metabolic Indices

Huei-Yu Tsai[1], Han-Jui Lee[2,3], Chen-Yuan Kuo[1,4], Yu-Chung Tsao[5], Pei-Lin Lee[6], Kun-Hsien Chou[1,7], Chung-Jung Lin[2], Ching-Po Lin[1,6,8]

[1]Institute of Neuroscience, National Yang Ming Chiao Tung University, Taipei, Taiwan, [2]Department of Radiology, Taipei Veterans General Hospital, Taipei, Taiwan, [3]School of Medicine, National Yang Ming Chiao Tung University, Taipei, Taiwan, [4]Department of Neurology, Neurological Institute, Taipei Veterans General Hospital, Taipei, Taiwan, [5]Division of Occupational Medicine, Chang Gung Memorial Hospital, Taoyuan, Taiwan, [6]Center for Healthy Longevity and Aging Sciences, National Yang Ming Chiao Tung University, Taipei, Taiwan, [7]Brain Research Center, National Yang Ming Chiao Tung University, Taipei, Taiwan, [8]Department of Education and Research, Taipei City Hospital, Taipei, Taiwan

Introduction: The demographic shift toward an aging population poses a contemporary challenge, necessitating a comprehensive understanding of aging's multifaceted impact. Previous research has demonstrated the diverse effects of aging on brain structure, cognitive function, body composition, and metabolic processes[1,2]. These age-related changes significantly influence the risk of morbidity and disability in the elderly, exhibiting substantial individual variations[3]. While neuroimaging-derived indicators of brain biological age have emerged as a recognized measure of brain health[2], a gap persists in understanding the association among brain biological age, body composition, and metabolic profiles. This study addressed this gap by investigating the intricate relationship between brain biological age, metabolic indices, and specific body compositions defined by MR imaging. Through identifying these key factors, our research aimed to provide clinicians and the general population with valuable insights for navigating a healthier aging trajectory in the future.

Methods: A total of 458 subjects (age range: 20.5-82.5 years, 280 males and 178 females) were retrospectively recruited from Taipei Veterans General Hospital. Participants underwent abdominal and brain MRI scans using two 3T MRI scanners, with a comprehensive collection of biochemical markers, including total cholesterol, low-density lipoprotein, high-density lipoprotein, triglycerides, fasting glucose (Glu), high-sensitivity C-reactive protein (hs-CRP), aspartate aminotransferase (AST), and other relevant metabolic indices. Body composition metrics, such as total abdominal muscle area (TAMA), skeletal muscle index (SMI), and body surface area (BSA), were quantified using abdominal MRI. Additionally, brain T1-weighted MRI data were gathered from 2675 healthy participants (age range:18-92 years, 1247 males and 1428 females) as a training dataset to construct the structural covariance network (SCN)-based brain age prediction model. The brain age model was developed followed previously described procedures[4]. We extracted 800 SCN based features for both gray matter volume and density to construct a brain age estimator. The radial basis function (RBF) kernel-based support vector regression (SVR) brain age estimator was then applied to the study cohort to estimate individual brain predicted age and brain age gap (BAG). Subsequently, the partial correlation analyses were used to examine associations between BAG, body compositions, and metabolic indices adjusting for confounding variables including age, age2, gender, total intracranial volume, smoking, and drinking. The significance threshold was set at a false discovery rate-corrected p-value < 0.05. Additionally, general linear models were employed to explore the potential interaction effect between gender, significant metabolic and body composition indices on BAG.

Results: Our brain age prediction model accurately predicted chronological age in the training dataset (MAE = 4.26 years, r = 0.945) and satisfactory generalizability in the study dataset (MAE = 6.11 years, r = 0.900) (Fig 1). Our results showed significant negative correlations between BAG and TAMA, BMI-adjusted SMI, and BSA. Conversely, BAG exhibited positive correlations with hs-CRP, AST, and Glu (Table 1). Additionally, the change of BAG in male group was also associated with TAMA, BMI-adjusted SMI, BSA, hs-CRP and Glu, but not in female group. However, the interaction between gender and these biomarkers on BAG was not significant.

Figure 1. The performance of brain age prediction model in the training datasets and the generalizability in the clinical datasets

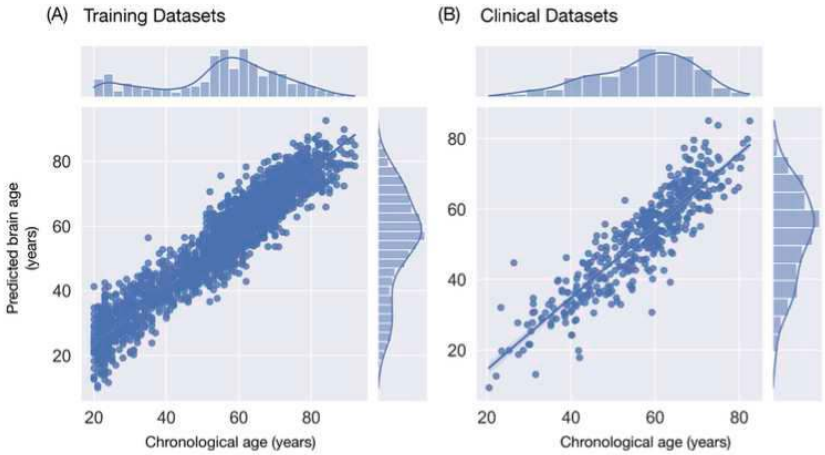

Table 1. Adjusted correlation map between brain age gap and biomarkers of body composition and metabolic indices

	Male†	Female†	All††
BMI	-0.075	-0.049	-0.062
BSA	-0.161*	-0.160	-0.157*
Total Abdominal Muscle Area	-0.158	-0.122	-0.146*
SMI	-0.092	-0.065	-0.084
BSA-adjusted SMI	-0.041	-0.033	-0.041
BMI-adjusted SMI	-0.138	-0.121	-0.134*
Total Abdominal Area	0.029	-0.045	0.003
Total Fat Area	-0.014	-0.034	-0.020
Subcutaneous Fat Area	-0.061	-0.050	-0.050
Visceral Fat Area	-0.029	-0.012	-0.025
Visceral Fat (%)	0.134	0.058	0.106
Muscle-to-Fat Ratio	-0.142	-0.032	-0.105
Liver Fat (%)	0.105	0.033	0.083
Liver Fat (%), right lobe	0.097	0.020	0.073
Liver Fat (%), left lobe	0.129	0.061	0.108
Fasting glucose	0.180*	0.084	0.149*
HbA1c	0.075	0.029	0.062
Triglyceride	0.067	-0.024	0.043
Cholesterol	-0.072	0.026	-0.029
LDL	-0.093	-0.003	-0.053
HDL	-0.026	0.166	0.061
hs-CRP	0.155*	0.086	0.121*
AST	0.108	0.193	0.123*
ALT	0.020	0.109	0.041
Creatinine	0.037	0.071	0.040
eGFR	0.004	-0.081	-0.027
Hematocrit	-0.071	0.003	-0.037
Hemoglobin	-0.035	-0.050	-0.037

* corrected $p < 0.05$
† Age, age square, total intracranial volume (TIV) total brain volume, smoking, and drinking are adjusted.
†† Sex is additionally adjusted in all subjects.
BMI, body mass index; BSA, body surface area; SMI, skeletal muscle index; Visceral Fat (%), visceral fat fraction; Liver fat (%), liver fat fraction; LDL, low-density lipoprotein; HDL, high-density lipoprotein; eGFR, estimated glomerular filtration rate; hs-CRP, high-sensitivity C-reactive protein; AST, aspartate aminotransferase; ALT, alanine aminotransferase.

Conclusions: In summary, our study provided insights into the associations between body composition, biochemical markers and BAG. The observed correlations suggested that lower skeletal muscle mass, increasing hs-CRP, and increasing blood glucose were associated with a larger BAG. These findings contributed to understanding the factors influencing brain aging and highlighted the importance of healthy aging interventions in future research.

References

1. Peters, R., Ageing and the brain. Postgrad Med J, 2006. 82(964): p. 84-8.
2. Ponti, F., et al., Aging and Imaging Assessment of Body Composition: From Fat to Facts. Front Endocrinol (Lausanne), 2019. 10: p. 861.
3. Wrigglesworth, J., et al., Factors associated with brain ageing - a systematic review. BMC Neurol, 2021. 21(1): p. 312.
4. Kuo, C.-Y., et al., Large-scale structural covariance networks predict age in middle-to-late adulthood: A novel brain aging biomarker. Cerebral Cortex, 2020. 30(11): p. 5844-5862.

Poster No 2630

Two distinctive brain correlates for top-down regulation of heart rate induced by acupuncture

Changjin Jung[1], Kyungmo Park[2]

[1]KIOM, Daejeon, Korea, Republic of, [2]Kyung Hee University, Yongin, Korea, Republic of

Introduction: Increasing studies with acupuncture have demonstrated both heart rate (HR) acceleration and deceleration, which may associate homeostatic mechanism of autonomic nervous system (LI, 2022). Even within repeated identical stimuli of an acupuncture protocols, phasic HR responses demonstrated discrepancy, suggesting a top-down interference to low-level regulation of HR. Existing findings consolidates the top-down regulatory mechanisms of heart rate, including orienting, arousal, affective, social, and cognitive responses (THAYER, 2009). However, underpinning linkages between these regulatory mechanisms and acupuncture remain unclear. Acupuncture is a compound interventional procedure including two components such as invasive needle stimulation and contextual manipulation for treatment. Here, we hypothesized that these two components would induce different brain mechanisms, contributing to HR changes. For instance, acupuncture stimuli to skin surface induce somatosensory afference accompanied by involuntary attention on body (i.e. orienting response). While, contextual manipulation for acupuncture treatment attracts voluntary attention on body (i.e. cognitive process). In present study, we aimed to investigate top-down regulatory mechanisms of HR differently induced by these two components of acupuncture.

Methods: Participants received electrical stimuli via inserted needle on the upper lateral side at the left leg (ST-36) for the somatosensory afferent (Sa) and/or visual cue informing the contextual manipulation (Cm) for treatment during fMRI scan. In REAL session (n = 23), both Sa and Cm were simultaneously conducted. In ZOMB session (n = 23), Sa were conducted; but we informed participants that an electrical diagnostic measurement would perform with the visual cue. In PHNT session (n = 18); there was no Sa; but participants received visual cue for contextual manipulation. In CONT session (n = 21), non-meaningful visual cue without Sa was performed for the control condition. Thus, we used two-by-two factorial design for two components of acupuncture. During the scan we acquired photoplethysmography to assess HR. We divided each fMRI data into 15 samples along the timeseries, corresponding to period of each stimulus interval. Then, whole samples (n = 1260) were merged to perform tensor-independent component analysis (tICA), which produces three matrices for spatial maps of ICs, timeseries and estimated scores of ICs for the samples. In accordance with the two-by-two factorial design, three-way ANOVA with interaction terms was performed for the estimated scores of each IC with Sa, Cm, and HR factors. We assessed interaction effects between Sa/Cm and HR factors representing Sa/Cm-specific association with HR (SaHR/CmHR). Since the spatial maps of ICs depended on the dimensionality of IC, we assessed statistic power of SaHR and CmHR for all possible dimensionality of IC. We identified the optimized dimensionality at 6 for our hypothesis (2nd IC for SaHR [IC-SaHR], $p < 0.01$; 1st IC for CmHR [IC-CmHR], $p < 0.01$).

Results: HR demonstrated both acceleration and deceleration in the experimental protocols (REAL: 62% decelerations; ZOMB: 59% decelerations; PHNT: 49% decelerations; CONT: 50% decelerations). The significant HR decelerations showed for REAL ($p < 0.00001$) and ZOMB ($p < 0.0001$). Spatial map of IC-SaHR showed functional couplings for facilitations in inferior frontal gyrus and visual cortex; and inhibitions in cingulate cortex, anterior insular, and somatosensory cortex. While, spatial map of IC-CmHR showed functional couplings for facilitations in anterior insular and dorsolateral prefrontal cortex; and inhibitions in default mode network (DMN) (Fig. 1).

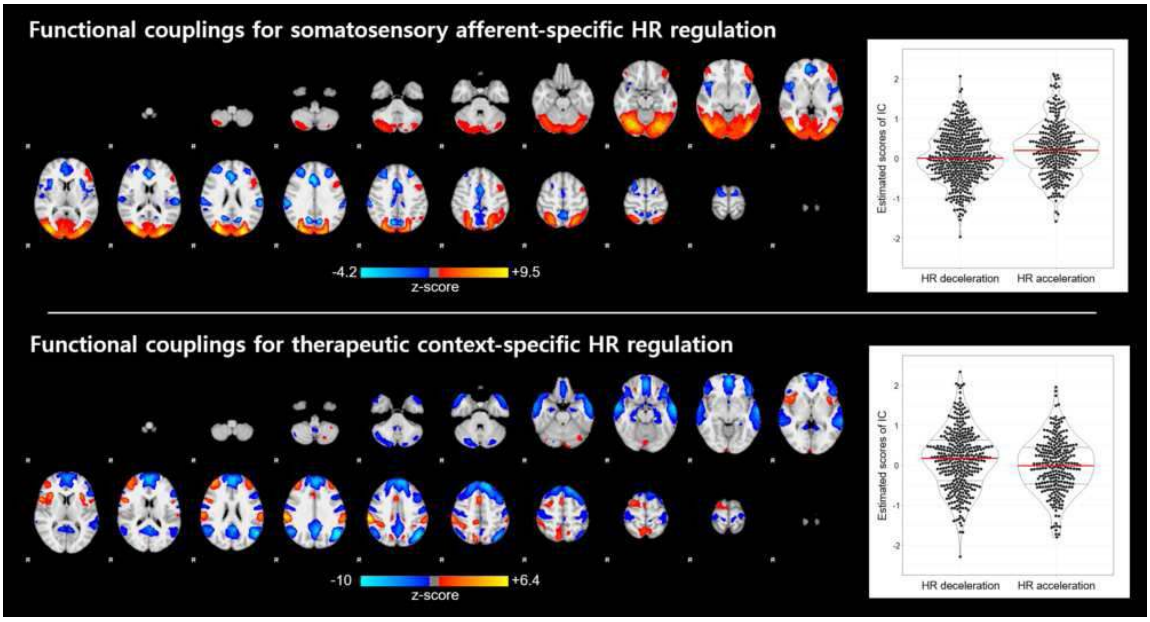

Figure 1. Top-down heart rate (HR) regulatory mechanisms, differently induced by two components of acupuncture.

Conclusions: The HR decelerations could be associated with suppression of coordinated inhibitions in cingulate cortex, anterior insular, and somatosensory cortex. Inhibition of DMN could decelerate HR.

References

1. Li, Y. W.; Li, W.; Wang, S. T.; Gong, Y. N. et al. The autonomic nervous system: A potential link to the efficacy of acupuncture. Front Neurosci, 16, p. 1038945, 2022.
2. Thayer, J. F.; Lane, R. D. Claude Bernard and the heart-brain connection: further elaboration of a model of neurovisceral integration. Neurosci Biobehav Rev, 33, n. 2, p. 81-88, Feb 2009.

Poster No 2631

QSM for identification of microstructural pathology in sports-related mild Traumatic Brain Injury

Christi Essex[1], Catherine Morgan[2], Samantha Holdsworth[2], Kieran O'Brien[3], Mayan Bedggood[1], Amabelle Voice-Powell[1], Richard Faull[2], Alice Theadom[1], Mangor Pedersen[1]

[1]Auckland University of Technology, Auckland, New Zealand, [2]The University of Auckland, Auckland, New Zealand, [3]Siemens Healthineers, Brisbane, Australia

Introduction: Brain iron accumulation is a putative biomarker of dementias and other neuropathological processes (Zecca et al., 2004). Despite evidence linking exposure to head trauma and risk factors for premature neuropathy (Daglas & Adlard, 2018), little is known about iron levels following sports-related mild Traumatic Brain Injury (sr-mTBI). Quantitative susceptibility mapping (QSM), an advanced MRI method, measures an intrinsic magnetic property of biomaterials (including iron, calcium, and myelin) (Wei et al., 2023) related to tissue composition. Recent advances in QSM image reconstruction have streamlined and simplified this process but require further validation. The aims of this study were to 1) investigate the presence of iron in subcortical grey matter as a marker of cellular pathology in acute sr-mTBI using QSM; and 2) assess the utility of developments in QSM processing for clinical research.

Methods: An observational, case-control study design was used to investigate differences in tissue magnetic susceptibility in basal ganglia sub-regions of 13 male contact sports players aged 16-35 years (M = 22.80, SD = 4.90) with acute sr-mTBI (< 14 days) and twelve age-matched male controls (M = 20.70, SD = 3.68). QSM was used to quantify iron deposition at high spatial resolution (1mm isotropic voxels) using data acquired on a Siemens MAGNETOM Vida Fit scanner (Siemens Healthcare, Erlangen, Germany) at 3 Tesla with a 3D Gradient Echo (GRE) sequence (TR = 30ms, TE = 20ms, FA= 15°, slice thickness = 1mm). Image processing with Morphology Enabled Dipole Inversion (MEDI) (Liu et al., 2012) was performed in-line on the scanner using a prototype sequence (Siemens Healthineers) which automates QSM image reconstruction. Images were skullstripped, coregistered and normalised to MNI152 standard space using FSL and fitted with the CIT168 mask (Pauli et al., 2018) to identify and partition the basal ganglia into 16 functionally and structurally distinct regions of interest (ROI). Maximum voxel-wise susceptibility values were extracted from each ROI with MATLAB version 9.13.0 (R2022b; MathWorks Inc., Natick,

MA) and compared between groups using Bonferroni-adjusted Mann-Whitney U tests. Spearman's rho correlation coefficients were used to investigate the expected relationship between brain iron and age (Li et al., 2014).

Results: No significant difference in magnetic susceptibility was observed in participants with sr-mTBI compared to controls for any ROI after post-hoc correction ($p > 0.003$). A trend for elevated susceptibility in the Globus Pallidus externus (GPe) of participants with sr-mTBI was noted ($U = 38$, $p = 0.03$) (see Figure 1). Susceptibility values were moderately, but not significantly, correlated with age for most basal nuclei ($p > 0.003$).

Figure 1

Tissue Magnetic Susceptibility of the Globus Pallidus externus

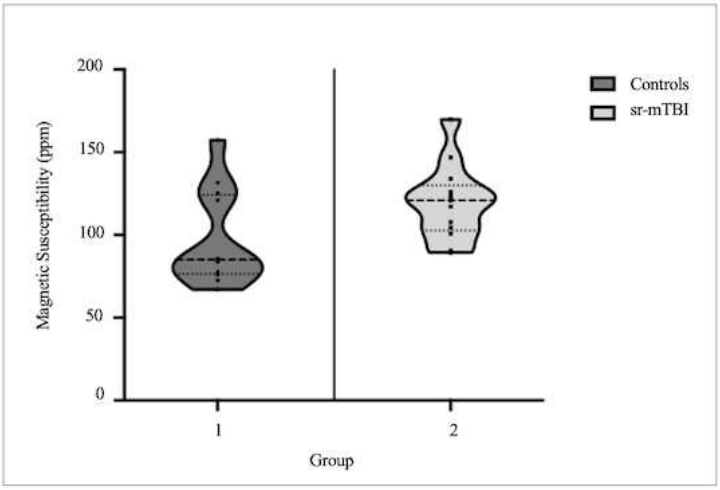

Note. Violin plot representing the trend for increased magnetic susceptibility in the Globus Pallidus externus of sr-mTBI participants compared to controls.

Conclusions: The lack of significant findings suggests this study was underpowered to detect changes in brain iron composition likely to be subtle at acute-stage mTBI. This is particularly salient given the association of iron deposition with age (Li et al., 2014) and exposure to repeated mTBI (Juan at al., 2023). However, the trend for increased GPe susceptibility in the sr-mTBI cohort hints at a possible role for iron accumulation shortly after injury. The Globus Pallidus is abnormally in iron and ferritin (Rouault, 2013), and appears particularly vulnerable to iron-mediated cellular pathology in neurodegenerative disease (Kruer et al., 2012). Prior research has evidenced increased iron in Pallidal nuclei at 6 (Lu et al., 2015) and 18 months (Raz et al., 2011) post-mTBI. Our observed MRI-based susceptibility values were consistent and comparable between groups and fell within expected range for the relative iron content of each ROI; suggesting our current imaging protocol may be used not only to research effects of sr-mTBI but other disorders of the central nervous system. Together, results indicate further research and increased study power is necessary to elucidate the underlying pathophysiological mechanisms of acute sr-mTBI.

References

1. Juan, S. M. (2023), 'Alterations in iron content, iron-regulatory proteins and behaviour without tau pathology at one year following repetitive mild traumatic brain injury', Acta Neuropathologica Communications, vol. 11, no. 1
2. Kruer, M. (2012), 'Neuroimaging features of Neurodegeneration with brain iron accumulation', American Journal of Neuroradiology, vol. 33, no. 3, pp. 407-414
3. Li, W. (2014), 'Differential developmental trajectories of magnetic susceptibility in human brain gray and white matter over the lifespan', Human Brain Mapping, vol. 35, no. 6, pp. 2698-2713
4. Liu, J. (2012), 'Morphology enabled dipole inversion for quantitative susceptibility mapping using structural consistency between the magnitude image and the susceptibility map', NeuroImage, vol. 59, no. 3, pp. 2560-2568
5. Lu, L. (2015), 'Iron deposition is positively related to cognitive impairment in patients with chronic mild traumatic brain injury: Assessment with susceptibility weighted imaging', BioMed Research International, vol. 2015, pp. 1-7
6. Pauli, W. M. (2018), 'A high-resolution probabilistic in vivo atlas of human subcortical brain nuclei', Scientific Data, vol. 5, no. 1
7. Raz, E. (2011), 'Brain iron quantification in mild traumatic brain injury: A magnetic Field correlation study', American Journal of Neuroradiology, vol. 32, no. 10, pp. 1851-1856
8. Rouault, T. A. (2013), 'Iron metabolism in the CNS: Implications for neurodegenerative diseases', Nature Reviews Neuroscience, vol. 14, no. 8, pp. 551-564
9. Wei, H. (2023), 'Editorial: Quantitative susceptibility mapping: technical advances and clinical applications', Frontiers in Neuroscience, vol. 17
10. Zecca, L. (2004). 'Iron, brain ageing and neurodegenerative disorders', Nature Reviews Neuroscience, vol. 5, no. 11, pp. 863-873

Poster No 2632

Brain Iron and Neurotransmitter Analysis for PFAS-Linked Psychosis Risk by 3D UTE MRI and 1H-MRS

Zhen Jiang[1], Xin Shen[2], Lisa Brown[3], Liz Lee[4], Humberto Monsivais[1], Zoe Kourtzi[4], Jason Cannon[1], Daniel Foti[3], Alexandra Lipka[1,5,6], Uzay Emir[1,7]

[1]School of Health Science, College of Health and Human Sciences, Purdue University, West Lafayette, IN, [2]Radiology and Biomedical Imaging, University of California San Francisco, San Francisco, CA, [3]Department of Psychological Sciences, Purdue University, West Lafayette, IN, [4]University of Cambridge, Cambridge, United Kingdom, [5]College of Engineering, Purdue University, West Lafayette, IN, [6]High Field MR Centre, Department of Biomedical Imaging and Image-guided Therapy, Medical University of Vienna, Vienna, Austria, [7]Weldon School of Biomedical Engineering, Purdue University, West Lafayette, IN

Introduction: Perturbations in excitatory and inhibitory neurotransmitters have been studied in disorders with psychotic features (Nakahara et al. 2022). The potential association between brain iron concentration and neurotransmitters (Unger et al. 2009) provides an opportunity to investigate the connection between PFAS exposure and risk for psychosis. This study postulates the developmental PFAS exposure as a potential environmental risk factor, that may trigger the presence of psychotic symptoms. To test this hypothesis, we analyzed potential correlations between brain iron concentration and Glutamate (Glu) levels, GABA levels, Glu/GABA ratio. 3D high-resolution UTE MRI was used for brain iron mapping. Metabolite levels of brain neurotransmitters in individuals were measured using 1H-MRS.

Methods: The study population included 15 individuals aged 19 to 30, classified into healthy and psychotic groups (undisclosed). All the subjects were scanned using a whole-body 3T MRI system (Siemens Healthineers, Erlangen, Germany) with a vendor-supplied 20-channel receiver head coil. A 3D high-resolution rosette UTE sequence was used for all scans, detailed in (Shen et al. 2023). Image reconstruction was performed in MATLAB (MathWorks, USA) with ESPIRiT calibration and non-uniform fast Fourier transform in BART (Berkeley Advanced Reconstruction Toolbox). All images were co-registered to a standard template (MNI-152), in addition to brain tissue extraction via BET (Smith 2002) and bias field correction via AFNI and SPM12. The brain iron map was calculated by the fitting model from (Shen et al. 2023): C_iron=-1/0.1078·log ((1157-S_iron)/404.4). Where C_iron represents the iron concentration in the unit of mM, S_iron is signal intensity in the processed brain image. The Brainnetome masks were then applied to compute the iron concentration in regions of interest (ROIs). The 1H-MRS data was measured by semi-adiabatic localization using an adiabatic selective refocusing (semi-LASER) sequence (TE = 32 ms; TR = 3.5 s; 32 averages; Deelchand et al. 2015) and variable power RF pulses with optimized relaxation delays (VAPOR), water suppression, and outer volume saturation. Unsuppressed water spectra acquired from the same volume of interest were used to remove residual eddy current effects and to reconstruct the phased array spectra with MRspa. Two voxels of interest were manually centered in the posterior cingulate (8 mL) and the hippocampus (3.36 mL) based on the individual's T1-weighted image. Absolute and relative concentrations of GABA and Glu were acquired. A total of 246 ROIs underwent equal variances t-test to evaluate the differences of iron concentration between the two groups. Correlation analyses were then conducted between ROI iron concentration (p-value ≤ 0.05) and Glu, GABA, Glu/GABA ratio in corresponding subregions of the brain.

Results: Significant differences in iron concentration without multiple comparisons were observed between the two groups (Table 1). Specifically, the iron concentration in PhG_L_6_6 showed a significant positive correlation with Glu levels (r = 0.54, p-value = 0.0377), as illustrated in Figure 1.

ROI ID	ROI Name	p value
OrG_L_6_3	Orbital Gyrus (OG)	0.0446
PrG_R_6_3	Precentral Gyrus (PrG)	0.0303
PCL_R_2_2	Paracentral Lobule (PCL)	0.0159
PhG_R_6_5	Parahippocampal Gyrus (PhG)	0.0434
PhG_L_6_6	Parahippocampal Gyrus	0.0327
PhG_R_6_6	Parahippocampal Gyrus	0.0453
SPL_L_5_1	Superior parietal lobe (SPL)	0.0319
CG_R_7_2	Cingulate Gryus (CG)	0.0057

Table 1: ROIs with p value less or equal to 0.05.

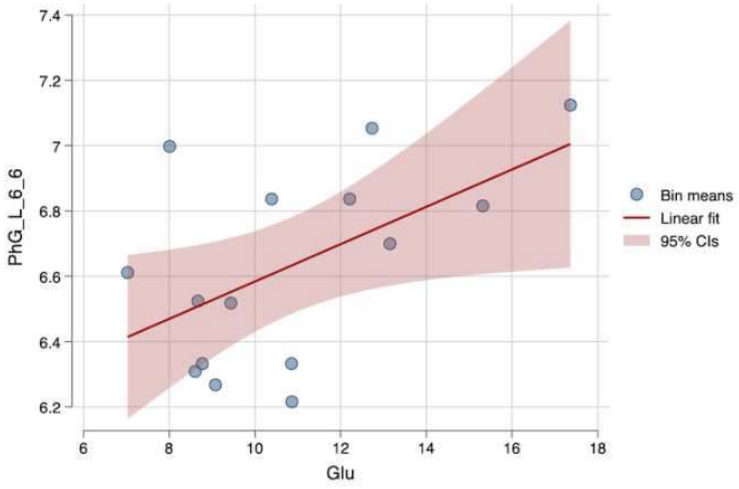

(a)

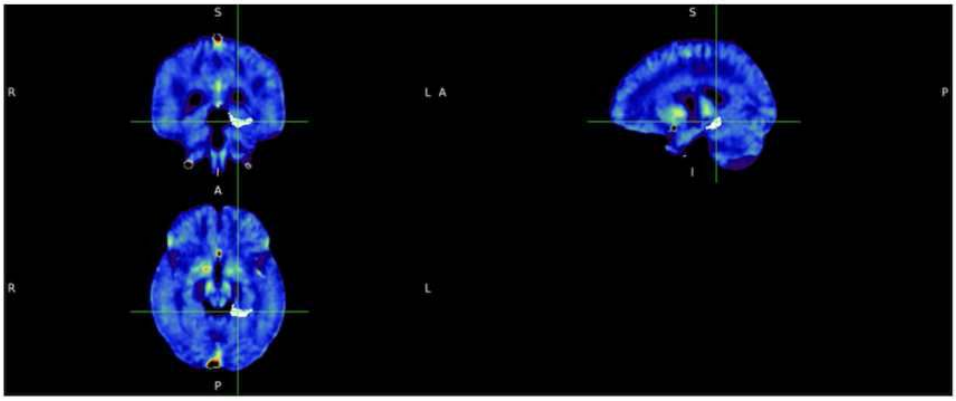

(b)

Figure 3: (a) correlation between iron concentration and Glu in PhG_L_6_6. (b) PhG_L_6_6 Brainnetome binary mask on the average iron map.

Conclusions: Our results highlight significant iron concentration differences between individuals at high risk for psychosis and individuals without psychotic risk, suggesting iron as a potential psychosis biomarker. The positive correlation between iron concentration and Glu levels suggests neurodegenerative processes (Ward et al. 2014) may occur with elevated glutamate in PhG. Furthermore, UTE MRI demonstrated clinical potential in psychotic disorders. Future studies will include additional individuals, multiple comparisons. Multivariate analysis will be performed to mitigate unrelated factors (e.g. age, gender). Further investigation into the relationship between PFAS and risk for psychosis will include gathering individuals' PFAS concentrations from blood samples and correlating them with brain iron concentration, GABA, Glu, Glu/GABA ratio.

References

1. Tomomi Nakahara et al., "Glutamatergic and GABAergic Metabolite Levels in Schizophrenia-Spectrum Disorders: A Meta-Analysis of 1H-Magnetic Resonance Spectroscopy Studies," Molecular Psychiatry 27, no. 1 (January 2022): 744–57, https://doi.org/10.1038/s41380-021-01297-6.
2. Erica Unger et al., "Dopamine D2 Receptor Expression Is Altered by Changes in Cellular Iron Levels in PC12 Cells and Rat Brain Tissue," The Journal of Nutrition 138 (January 1, 2009): 2487–94, https://doi.org/10.3945/jn.108.095224.
3. Josephine M. Brown-Leung and Jason R. Cannon, "Neurotransmission Targets of Per- and Polyfluoroalkyl Substance Neurotoxicity: Mechanisms and Potential Implications for Adverse Neurological Outcomes," Chemical Research in Toxicology 35, no. 8 (August 15, 2022): 1312–33, https://doi.org/10.1021/acs.chemrestox.2c00072.
4. Xin Shen et al., "High-Resolution 3D Ultra-Short Echo Time MRI with Rosette k-Space Pattern for Brain Iron Content Mapping," Journal of Trace Elements in Medicine and Biology 77 (May 1, 2023): 127146, https://doi.org/10.1016/j.jtemb.2023.127146.
5. Stephen M. Smith, "Fast Robust Automated Brain Extraction," Human Brain Mapping 17, no. 3 (November 2002): 143–55, https://doi.org/10.1002/hbm.10062..
6. Dinesh K. Deelchand et al., "Two-Site Reproducibility of Cerebellar and Brainstem Neurochemical Profiles with Short-Echo, Single-Voxel MRS at 3T," Magnetic Resonance in Medicine 73, no. 5 (2015): 1718–25, https://doi.org/10.1002/mrm.25295.
7. Roberta J. Ward et al., "The Role of Iron in Brain Ageing and Neurodegenerative Disorders," The Lancet Neurology 13, no. 10 (October 1, 2014): 1045–60, https://doi.org/10.1016/S1474-4422(14)70117-6.

Poster No 2633

Brief seizures induce severe postictal hypoxia in people with epilepsy

Antis George[1], Sarah Vinette[1], Jospeph Peedicail[1], Daniel Pittman[1], William Wilson[1], Paolo Federico[1]

[1]*University of Calgary, Calgary, Alberta*

Introduction: Recent animal work has demonstrated that seizures can result in vasoconstriction-induced hypoperfusion and hypoxia in brain regions involved in the seizure and is a putative mechanism of postictal impairments (Farrell et al., 2016). We have previously shown that arterial spin labeling MRI and CT- perfusion can be used to detect postictal hypoperfusion localizing to the seizure onset zone (SOZ) in people with medication resistant focal epilepsy (Gaxiola-Valdez et al., 2017; Li et al., 2019). However, postictal hypoxia has yet to be directly measured. Hypoperfusion and hypoxia are related pathophysiological concepts, however, they are not always correlated. In fact, only approximately 50% of postictal hypoxia is mediated by vasoconstriction and hypoperfusion while dysfunctional metabolism accounts for the remaining 50% (Villa et al., 2023). The extent of postictal symptoms is related to the resultant hypoxia. Therefore, measurement of oxygen levels in the area of brain generating seizures is superior to perfusion measurements. This is the first report of brain tissue hypoxia following seizures in patients with medication resistant focal epilepsy.

Methods: Eight adult patients with medication resistant focal epilepsy undergoing intracranial video-EEG monitoring were recruited. Patients underwent implantation of an oxygen sensing probe in their presumed SOZ at the same time as depth electrode implantation. Using a continuous oxygen detection system with high temporal resolution, the partial pressure of oxygen (pO2) was measured before, during and importantly, after a seizure. Oxygen dynamics associated with focal aware (FAS), focal impaired awareness (FIAS) and focal to bilateral tonic-clonic seizures (FBTCS) were analyzed. Severe hypoxia was defined as a pO2 of ≤10 mmHg.

Results: Our data show an enduring severe hypoxia (i.e., ≤10 mmHg) following a FAS, FIAS and FBTCS localized to the SOZ. Patients with FBTCS spent more time hypoxic relative to the other seizure types and had longer mean seizure duration. Although patients that had FBTCS had worse postictal hypoxia this is likely a function of seizure duration which was positively correlated with severity of hypoxia.

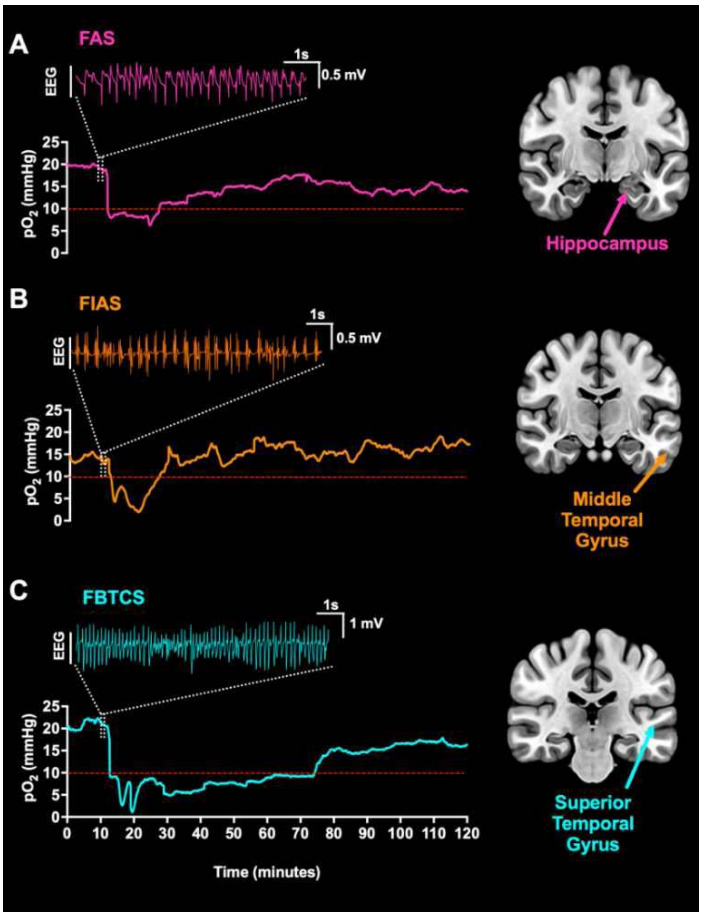

Figure. Brief seizures induce severe postictal hypoxia.

Conclusions: This work provides important proof-of-concept that postictal hypoxia can be measured in people with epilepsy. Following a FAS, FIAS or FBTCS, the area of the brain involved in the seizure becomes severely hypoxic. FBTCS are associated with worse postictal hypoxia compared to other seizure types. While epilepsy has long and correctly been considered an electrical disorder, the vascular system plays an important causal role, highlighting that seizures cause vascular insufficiency leading to brain tissue hypoxia.

References

1. Farrell J.S. (2016). 'Postictal behavioural impairments are due to a severe prolonged hypoperfusion/hypoxia event that is COX-2 dependent'. Elife. 22;5:e19352.
2. Gaxiola-Valdez I. (2017). 'Seizure onset zone localization using postictal hypoperfusion detected by arterial spin labelling MRI'. Brain. 140(11):2895-911
3. Li E. (2019). 'CT perfusion measurement of postictal hypoperfusion: localization of the seizure onset zone and patterns of spread'. Neuroradiology.1;61:991-1010.
4. Villa B.R. (2023). 'Postictal hypoxia involves reactive oxygen species and is ameliorated by chronic mitochondrial uncoupling'. Neuropharmacology.238:109653.

Organization for
Human Brain Mapping

Advancing Understanding of the Human Brain

ORGANIZATION FOR HUMAN BRAIN MAPPING

www.humanbrainmapping.org

1935 County Road B2 W, Ste 165
Roseville, MN 55113
info@humanbrainmapping.org
952-641-2294